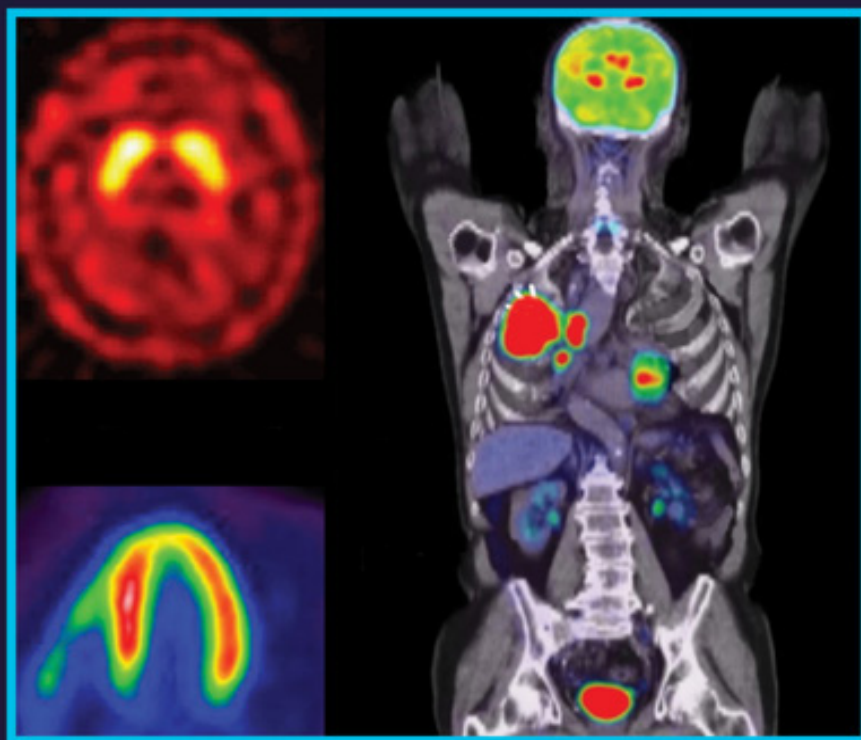


Second Edition

Handbook of **Radiopharmaceuticals**

Methodology and Applications



Edited by
Michael R. Kilbourn
Peter J. H. Scott

WILEY

**HANDBOOK OF
RADIOPHARMACEUTICALS:
METHODOLOGY
AND APPLICATIONS**

HANDBOOK OF RADIOPHARMACEUTICALS

METHODOLOGY AND APPLICATIONS

Second Edition

Edited by

MICHAEL R. KILBOURN

*University of Michigan
Ann Arbor, USA*

PETER J.H. SCOTT

*University of Michigan
Ann Arbor, USA*

WILEY

This second edition first published 2021
© 2021 John Wiley & Sons Ltd.

Edition History

John Wiley & Sons, Ltd. (1e, 2003)

All rights reserved. No part of this publication may be reproduced, stored in a retrieval system, or transmitted, in any form or by any means, electronic, mechanical, photocopying, recording or otherwise, except as permitted by law. Advice on how to obtain permission to reuse material from this title is available at <http://www.wiley.com/go/permissions>.

The right of Michael R. Kilbourn and Peter J.H. Scott to be identified as the authors of the editorial material in this work has been asserted in accordance with law.

Registered Offices

John Wiley & Sons, Inc., 111 River Street, Hoboken, NJ 07030, USA
John Wiley & Sons Ltd, The Atrium, Southern Gate, Chichester, West Sussex, PO19 8SQ, UK

Editorial Office

The Atrium, Southern Gate, Chichester, West Sussex, PO19 8SQ, UK

For details of our global editorial offices, customer services, and more information about Wiley products visit us at www.wiley.com.

Wiley also publishes its books in a variety of electronic formats and by print-on-demand. Some content that appears in standard print versions of this book may not be available in other formats.

Limit of Liability/Disclaimer of Warranty

In view of ongoing research, equipment modifications, changes in governmental regulations, and the constant flow of information relating to the use of experimental reagents, equipment, and devices, the reader is urged to review and evaluate the information provided in the package insert or instructions for each chemical, piece of equipment, reagent, or device for, among other things, any changes in the instructions or indication of usage and for added warnings and precautions. While the publisher and authors have used their best efforts in preparing this work, they make no representations or warranties with respect to the accuracy or completeness of the contents of this work and specifically disclaim all warranties, including without limitation any implied warranties of merchantability or fitness for a particular purpose. No warranty may be created or extended by sales representatives, written sales materials or promotional statements for this work. The fact that an organization, website, or product is referred to in this work as a citation and/or potential source of further information does not mean that the publisher and authors endorse the information or services the organization, website, or product may provide or recommendations it may make. This work is sold with the understanding that the publisher is not engaged in rendering professional services. The advice and strategies contained herein may not be suitable for your situation. You should consult with a specialist where appropriate. Further, readers should be aware that websites listed in this work may have changed or disappeared between when this work was written and when it is read. Neither the publisher nor authors shall be liable for any loss of profit or any other commercial damages, including but not limited to special, incidental, consequential, or other damages.

Library of Congress Cataloging-in-Publication Data

Names: Kilbourn, Michael R., editor. | Scott, Peter J. H., editor.
Title: Handbook of radiopharmaceuticals : methodology and applications /
edited by Michael R. Kilbourn, University of Michigan and Peter J.H.
Scott, University of Michigan.
Description: Second edition. | Hoboken, NJ : Wiley, 2021. | Revised edition
of: Handbook of radiopharmaceuticals : radiochemistry and applications /
editors, Michael J. Welch, Carol S. Redvanly. c2003. | Includes
bibliographical references and index.
Identifiers: LCCN 2020025975 (print) | LCCN 2020025976 (ebook) | ISBN
9781119500544 (cloth) | ISBN 9781119500551 (adobe pdf) | ISBN
9781119500568 (epub)
Subjects: LCSH: Radiopharmaceuticals—Handbooks, manuals, etc.
Classification: LCC RS431.R34 H36 2021 (print) | LCC RS431.R34 (ebook) |
DDC 615.8/42—dc23
LC record available at <https://lcn.loc.gov/2020025975>
LC ebook record available at <https://lcn.loc.gov/2020025976>

Cover Design: Wiley

Cover Image: Radio logical image of human body organs, Creative Commons

Set in 9/13pt Ubuntu by SPi Global, Chennai, India

10 9 8 7 6 5 4 3 2 1

Contents

About the Editors	vii		
List of Contributors	ix		
Foreword	xv		
Preface	xvii		
Abbreviations	xix		
PART I: Introduction to Radiopharmaceuticals	1		
Chapter 1: Targeted Diagnostic Radiopharmaceuticals: Design Options for Small-Molecule Radiotracers	3		
<i>Michael R. Kilbourn</i>			
Chapter 2: Concepts and Issues for Therapeutic Radiopharmaceuticals	23		
<i>Alexandra R. Sowa Dumond and Peter J.H. Scott</i>			
PART II: Production of Radionuclides	43		
Chapter 3: Production of Short Half-Life PET Radionuclides	45		
<i>Michael R. Kilbourn, Melissa E. Rodnick and Mara Clark</i>			
Chapter 4: Production of Radionuclides Used in SPECT	71		
<i>Salma Jivan and Thomas J. Ruth</i>			
Chapter 5: Production of Therapeutic Radionuclides	89		
<i>C. Shaun Loveless and Suzanne E. Lapi</i>			
PART III: Synthetic Methods for Radiopharmaceuticals	107		
Chapter 6: Synthesis of ¹³N- and ¹⁵O-Labeled Radiopharmaceuticals	109		
<i>Krishna R. Pulagam, Vanessa Gómez-Vallejo, Fernando López-Gallego, Luka Rejc and Jordi Llop</i>			
Chapter 7: Radiochemistry with Carbon-11	143		
<i>Stephen Thompson, Steven Kealey, Selena Milicevic Sephton and Franklin I. Aigbirhio</i>			
Chapter 8: Fluorine-18 Radiochemistry	251		
<i>Allen F. Brooks, Katarina J. Makaravage, Jay Wright, Melanie S. Sanford and Peter J. H. Scott</i>			
Chapter 9: Labeling with Gallium-68	291		
<i>Benjamin P. Burke and Stephen J. Archibald</i>			
Chapter 10: Cu-Mediated Radiohalogenation of Organoboranes	325		
<i>Sean W. Reilly and Robert H. Mach</i>			
Chapter 11: The Radiochemistry of Zirconium	343		
<i>Jason P. Holland</i>			

Chapter 12: ^{99m}Tc Radiopharmaceutical Chemistry	375	PART V: Major Applications of Radiopharmaceuticals	533
<i>Dionysia Papagiannopoulou</i>			
PART IV: Practical Aspects of Radiopharmaceutical Production and Use	435	Chapter 18: Radiopharmaceuticals in Oncology	535
		<i>Jeroen A.C.M. Goos, Outi Keinänen, Brian M. Zeglis, and Jason S. Lewis</i>	
Chapter 13: Automated Synthesis Modules for PET Radiochemistry	437	Chapter 19: Neurological Applications of Radiopharmaceuticals	571
<i>Laura Bruton and Peter J.H. Scott</i>		<i>Mehdi Djekidel and Nicolaas I. Bohnen</i>	
Chapter 14: Automation of PET Radiopharmaceutical Quality Control	457	Chapter 20: Cardiac Applications of Radiopharmaceuticals	607
<i>Arkadij Mikhailovich Elizarov</i>		<i>John P. Bois and Robert J. Gropler</i>	
Chapter 15: Moving PET Drugs from the Lab to the Patient in the USA	491	Chapter 21: Radiopharmaceuticals in Pediatric Nuclear Medicine	653
<i>David W. Dick</i>		<i>Scott E. Snyder, Elizabeth R. Butch and Barry L. Shulkin</i>	
Chapter 16: Moving from the Lab to the Patient in Asia	501	Chapter 22: PET Imaging in Drug Discovery and Development	703
<i>Dae Yoon Chi</i>		<i>David J. Donnelly, Ph.D</i>	
Chapter 17: Moving a Radiotracer from Bench to Bedside in Europe	515	Index	727
<i>Koen Vermeulen, Alfons Verbruggen, Guy Bormans and Frederik Cleeren</i>			

About the Editors

Michael R. Kilbourn is an emeritus professor of radiology at the University of Michigan Medical School. He retired from the university after 25 years of directing and expanding the PET Cyclotron and Radiochemistry program, where he pursued research efforts directed at the design, development, and application of novel PET radiotracers for Parkinson's and Alzheimer's diseases.

Peter J.H. Scott is an associate professor of radiology and a member of the Interdepartmental Program in Medicinal Chemistry at the University of Michigan. He is director of the University of Michigan Positron Emission Tomography (**PET**) Center and runs a research group developing new radiochemistry methodology and novel PET radiotracers. His laboratory is funded by the US Department of Energy, the National Institutes of Health, and the Alzheimer's Association and has multiple collaborations with academic institutions and biotech and pharmaceutical companies all over the world. Professor Scott has edited four other books for Wiley, including two volumes of *Radiochemical Syntheses*.

List of Contributors

Franklin I. Aigbirhio

Molecular Imaging Chemistry Laboratory,
Wolfson Brain Imaging Centre,
Department of Clinical Neurosciences
University of Cambridge,
Cambridge Biomedical Campus
Cambridge, UK

Stephen J. Archibald

Positron Emission Tomography
Research Centre,
Department of Biomedical Sciences,
Faculty of Health Sciences
University of Hull
Hull, UK

Nicolaas I. Bohnen

Department of Radiology
University of Michigan
Ann Arbor, MI, US

Department of Neurology
University of Michigan
Ann Arbor, MI, USA

Neurology Service and GRECC
VAAAHS
Ann Arbor, MI, USA

John P. Bois

Department of Cardiovascular Diseases
Mayo Clinic
Rochester, MN, USA

Guy Bormans

Laboratory for Radiopharmaceutical
Research,
Department of Pharmaceutical and
Pharmacological Sciences
University of Leuven
Leuven, Belgium

Allen F. Brooks

Department of Radiology
University of Michigan
Ann Arbor, MI, USA

Laura Bruton

Department of Radiology
University of Michigan
Ann Arbor, MI, USA

Benjamin P. Burke

Positron Emission Tomography
Research Centre,
Department of Biomedical Sciences,
Faculty of Health Sciences
University of Hull
Hull, UK

Elizabeth R. Butch

Department of Diagnostic Imaging
St. Jude Children's Research Hospital
Memphis, TN, USA

Dae Yoon Chi

Department of Chemistry
Sogang University
Seoul
Korea

Mara Clark

Department of Radiology
University of Michigan
Ann Arbor, MI, USA

Frederik Cleeren

Laboratory for Radiopharmaceutical
Research,
Department of Pharmaceutical and
Pharmacological Sciences
University of Leuven
Leuven, Belgium

David W. Dick

Department of Radiology
University of Iowa
Iowa City, IA, USA

Mehdi Djekidel

Nuclear Medicine and Molecular Imaging
Sidra Medicine
Qatar

David J. Donnelly

Bristol-Myers Squibb Pharmaceutical
Research and Development
Princeton, NJ, USA

Arkadij Elizarov

Trace-Ability
Los Angeles, California
USA

Vanessa Gómez-Vallejo

Radiochemistry and Nuclear
Imaging Group
CIC biomaGUNE
San Sebastián,
Spain

Jeroen A.C.M. Goos

Department of Radiology
Memorial Sloan-Kettering
Cancer Center
New York, NY, USA

Robert J. Gropler

Mallinckrodt Institute of Radiology
Washington University School
of Medicine,
St Louis, MO, USA

Jason P. Holland

Department of Chemistry
University of Zurich
Zurich, Switzerland

Salma Jivan,

Helen Wills Neuroscience Institute,
University of California
Berkeley, CA, USA

Steven Kealey

Molecular Imaging Chemistry Laboratory,
Wolfson Brain Imaging Centre,
Department of Clinical Neurosciences
University of Cambridge
Cambridge Biomedical Campus
Cambridge, UK

Outi Keinänen

Department of Chemistry,
Hunter College
The City University of New York
New York, NY, USA

Michael R. Kilbourn

Department of Radiology
University of Michigan
Ann Arbor, MI, USA

Suzanne E. Lapi

Department of Radiology
University of Alabama at Birmingham
Birmingham, AL, USA;

Department of Chemistry
University of Alabama at Birmingham
Birmingham, AL, USA

Jason S. Lewis,

Department of Radiology
Memorial Sloan-Kettering Cancer Center
Birmingham, AL, USA;

Molecular Pharmacology Program and the
Radiochemistry and Molecular Imaging
Probes Core
Memorial Sloan Kettering Cancer Center
Birmingham, AL, USA;

Departments of Radiology and
Pharmacology
Weill Cornell Medical College
New York, NY, USA

Jordi Llop

Radiochemistry and Nuclear
Imaging Group
CIC biomaGUNE
San Sebastián
Spain

Fernando López-Gallego

Heterogeneous Biocatalysis Laboratory
Instituto de Síntesis Química y Catálisis
Homogénea (ISQCH-CSIC),
University of Zaragoza
Zaragoza
Spain;

ARAID, Aragon I+D foundation
Zaragoza
Spain

C. Shaun Loveless

Department of Radiology
University of Alabama at Birmingham
Birmingham, AL, USA;

Department of Chemistry
Washington University in St. Louis
St Louis, MO, USA

Robert H. Mach

Department of Radiology,
Perelman School of Medicine
University of Pennsylvania
Philadelphia, PA, USA

Katarina J. Makaravage

Department of Chemistry
University of Michigan
Ann Arbor, MI, USA

Dionysia Papagiannopoulou

Department of Pharmaceutical Chemistry,
School of Pharmacy
Aristotle University of Thessaloniki
Thessaloniki
Greece

Krishna R. Pulagam

Radiochemistry and Nuclear
Imaging Group
CIC biomaGUNE
San Sebastián
Spain

Sean W. Reilly

Department of Radiology,
Perelman School of Medicine
University of Pennsylvania
Philadelphia, PA, USA

Luka Rejc

Radiochemistry and Nuclear
Imaging Group
CIC biomaGUNE
San Sebastián
Spain;

Faculty of Chemistry and Chemical
Technology,
University of Ljubljana
Ljubljana
Slovenia

Melissa E. Rodnick,

Department of Radiology
University of Michigan
Ann Arbor, MI, USA

Thomas J. Ruth

TRIUMF and BC Cancer Research Centre
Vancouver,
British Columbia,
Canada

Melanie S. Sanford

Department of Chemistry
University of Michigan
Ann Arbor, MI, USA

Peter J.H. Scott

Department of Radiology
University of Michigan
Ann Arbor, Michigan
USA

Selena M. Sephton

Molecular Imaging Chemistry Laboratory,
Wolfson Brain Imaging Centre,
Department of Clinical Neurosciences
University of Cambridge
Cambridge Biomedical Campus
Cambridge, UK

Barry L. Shulkin

Department of Diagnostic Imaging
St. Jude Children's Research Hospital
Memphis, TN, USA

Scott E. Snyder

Department of Diagnostic Imaging
St. Jude Children's Research Hospital
Memphis, TN, USA

Alexandra R. Sowa Dumond

Department of Radiology
University of Michigan
Ann Arbor, MI, USA

Stephen Thompson

Molecular Imaging Chemistry Laboratory,
Wolfson Brain Imaging Centre,
Department of Clinical Neurosciences
University of Cambridge
Cambridge Biomedical Campus
Cambridge, UK

Alfons Verbruggen

Laboratory for Radiopharmaceutical
Research,
Department of Pharmaceutical and Phar-
macological Sciences
University of Leuven
Leuven, Belgium

Koen Vermeulen

Laboratory for Radiopharmaceutical
Research,
Department of Pharmaceutical and Phar-
macological Sciences
University of Leuven
Leuven, Belgium

Jay Wright

Department of Radiology
University of Michigan
Ann Arbor, MI, USA

PhD program in chemistry
Graduate Center of the City University
of New York,
New York, NY, USA;

Brian M. Zeglis

Department of Radiology
Memorial Sloan-Kettering Cancer Center
New York, NY, USA;

Departments of Radiology and
Pharmacology
Weill Cornell Medical College
New York, NY, USA

Department of Chemistry, Hunter College
The City University of New York
New York, NY, USA;

Foreword

When Mike Welch and Carol Redvanly edited the first edition of the *Handbook of Radiopharmaceuticals* in 2003, the field of radiopharmaceutical sciences was undergoing a number of important changes. [¹⁸F]Fludeoxyglucose ([¹⁸F]FDG) had been recently approved by the US Food and Drug Administration (**FDA**), and reimbursement coverage was in place from the US Centers for Medicare and Medicaid Services. This was creating a burgeoning market for commercial production and distribution of [¹⁸F]FDG, which in turn drove innovation in both radiopharmaceutical manufacture and clinical scanner technology. At the same time, increasing numbers of radiochemistry facilities were stimulating the development of many different radiopharmaceuticals for research applications.

This innovation and research have continued over the intervening years, and as we complete this new edition at the start of the *Roaring Twenties*, we have been reflecting that it is another exciting and transformative time in the fields of nuclear medicine and radiopharmaceutical sciences! New radiopharmaceuticals continue to be approved by the FDA, including PET radiotracers for brain and cancer imaging and theranostics for cancer treatment. These radiopharmaceuticals are transforming the lives of the patients we diagnose and treat in our clinicals every day. Coupled with lobbying efforts by the Society of Nuclear Medicine and Molecular Imaging (**SNMMI**) and others to inform reimbursement policy, significant efforts by industrial partners to develop the radiochemistry and PET imaging suites of the future, initiatives by academic colleagues to standardize the nomenclature of our science,¹ and the expected impact of artificial intelligence on our discipline, nuclear medicine has been invigorated and is transforming from a research technique into a powerful standard of care.

This growth in nuclear medicine is apparent in day-to-day operations around the world. In an established market like the United States, over 1.5 million clinical PET scans currently occur, and yet we have been impressed to see the number of clinical PET scans taking place at the University of Michigan double between 2014 and 2019. There is also substantial growth occurring in developing markets, and at the 2019 International Symposium of Radiopharmaceutical Sciences (**ISRS**) that took place in Beijing, it was remarked that a new PET scanner is being installed in China every two weeks! The concomitant growth in the use of radiotherapeutics means that innovation in the radiopharmaceutical sciences to meet these new demands is as important today as when the first edition of the *Handbook* was published.

¹ See Coenen et al., *Nucl Med Biol.* 2017;55:v-xi, doi: 10.1016/j.nucmedbio.2017.09.004.

We were both attracted to the fields of nuclear medicine and radiopharmaceutical sciences early in our careers for a number of reasons. First, radiopharmaceutical sciences is an exciting application of basic science with immediate impact on patient care; second, the translational aspect of the research is appealing; and finally, we thoroughly enjoy the diverse and multidisciplinary nature of the work. Our field exists at the intersection of medicine, biology, chemistry, physics, and engineering, and, with the exception of Antarctica, research applications and clinical uses of nuclear medicine are occurring on every continent.

The articles in the new edition of the *Handbook* demonstrate that the field of radiopharmaceutical sciences remains as multidisciplinary as ever. We have tried to keep this new edition faithful to the format of the original and asked authors to provide knowledge updates in their various sub-disciplines (radionuclide production, radiochemistry, applications of radiopharmaceuticals) that have occurred since the first edition was published. However, the evolution of the radiopharmaceutical sciences since that time, particularly in regards to current Good Manufacturing Practice (**cGMP**), regulatory oversight, and novel approaches to quality control, have necessitated the addition of new chapters in these areas.

We look forward to how our field continues to develop in the next 20 years, as we witness new technology and applications in the radiopharmaceutical sciences that might find their way into a future edition of the *Handbook* and continue the legacy of Mike Welch and the other visionaries who started our field.

Michael R. Kilbourn
Peter J.H. Scott
June 2020
Ann Arbor MI, USA

Preface

The first edition of the *Handbook of Radiopharmaceuticals* was published near the start of the twenty-first century. Dedicated by Michael J. Welch and Carol Redvanly to the memory of Alfred P. Wolf, that volume provided students and researchers with a comprehensive review of the field of radiochemistry and its growing importance in medicine.

This second edition of the *Handbook* is dedicated to the memories of Michael Welch and the many other notable scientists and physicians that the field has lost in recent years, many of whom served as mentors or colleagues of the contributing authors to this edition. The radiochemical sciences and medical imaging have grown tremendously just in the past two decades, and as we enter the third decade of the twenty-first century, there is the expectation that the future holds untold important and impactful advances. In this edition of the *Handbook*, we have emphasized chapters that bring the reader up to date on the exciting developments of recent years. We thank the editorial team at John Wiley & Sons as well as all of the authors, the majority of whom are new contributors, for their valuable time and effort in bringing this new edition of the *Handbook* to reality.

Michael R. Kilbourn
Peter J.H. Scott
June 2020
Ann Arbor MI, USA

Abbreviations

5-HT1A	serotonin 1A receptor
ACh	acetylcholine
AChE	acetylcholinesterase
AcOH	acetic acid
ACPC	1-aminocyclopentanecarboxylic acid
AD	Alzheimer's disease
ADC	antibody drug conjugate
ADM	s-adenosyl-L-methionine
AI	artificial intelligence
ALARA	as low as reasonably achievable
AMDP	aminomethylenediphosphonate
AMT	α -Methyl-L-tryptophan
ATP	adenosine triphosphate
ATTR	amyloid transthyretin
BACE	beta-secretase
BAT	brown adipose tissue
BBB	blood-brain barrier
B _{max}	maximum concentration of target binding sites
BOx	benzoxazole
BP	binding potential
BP	British Pharmacopeia
Bq	becquerel
BTA	aryl-benzothiazole
BZD	benzodiazepine
CAD	coronary artery disease
cAMP	cyclic adenosine monophosphate
CBF	cerebral blood flow
CBS	compton backscattered
[¹⁴ C]ACHC	aminocyclohexanecarboxylic acid
[¹⁴ C]DASB	[¹⁴ C]3-amino-4-(2-dimethylaminomethylphenylsulfanyl)-benzonitrile
[¹⁴ C]DOPA	[¹⁴ C] dihydroxyphenylalanine
[¹⁴ C]DTBZ	[¹⁴ C]Dihydrotetraabenazine
[¹⁴ C]HED	[¹⁴ C]hydroxyephedrine
[¹⁴ C]PiB	[¹⁴ C]Pittsburgh compound B (PiB ([N-methyl- ¹⁴ C]6-Me-BTA-1))
CFR	Code of Federal Regulations
cGMP	current Good Manufacturing Practice
Ci	curie
ClogD	calculated distribution coefficient at pH 7.4
ClogP	calculated partition coefficient
CMC	chemistry, manufacturing, and controls

CMO	contract manufacturing organization
CNS	central nervous system
COMT	catecholamine O-methyl transferase
CSF	cerebrospinal fluid
CT	computed tomography
CTA	clinical trial application
CV	cardiovascular
CXCR4	CXC-chemokine receptor-4
Da	daltons
DAT	dopamine transporter
DBU	1,8-diazabicyclo[5.4.0]undec-7-ene
DDD	drug discovery and development
DIPE	di-isopropyl ether
DMA	<i>N,N</i> -dimethylacetamide
DMF	<i>N,N</i> -dimethylformamide
DMF	drug master file
DMSO	dimethyl sulfoxide
DNA	deoxyribose nucleic acid
DOTA	1,4,7,10-tetraazacyclododecane-1,4,7,10-tetraacetic acid
DPA	dipicolylamine
DPzA	dipyrazolylamine
Dx	dextran
EANM	European Association of Nuclear Medicine
EC	electron capture
ECD	[^{99m} Tc]ethylcysteine dimer
eCTD	electronic common technical document
EGFR	epidermal growth factor receptor
eLINACS	electron linear accelerators
EMA	European Medicines Agency
EOB	end-of-bombardment
EOS	end-of-synthesis
EP	European Pharmacopeia
EPI	epinephrine
EtOH	ethanol
EU	European Union
eV	electron volt
FA	fatty acid
FAAH	fatty acid amide hydrolase
[¹⁸ F]FACBC	1-amino-3-[¹⁸ F]fluorocyclobutanecarboxylic acid (Fluciclovine, Axumin)
FDA	Food and Drug Administration
[¹⁸ F]FDG	2-deoxy-2-[¹⁸ F]fluoro-D-glucose
FDH	formate dehydrogenase
[¹⁸ F]FDOPA	6-[¹⁸ F]fluorodihydroxyphenylalanine
[¹⁸ F]FES	[¹⁸ F]fluoroestradiol
[¹⁸ F]FET	2-[¹⁸ F]fluoroethyl)-L-tyrosine
[¹⁸ F]FMISO	[¹⁸ F]fluoromisonidazole

[¹⁸ F]FMT	[¹⁸ F]fluoromethyltyrosine
[¹⁸ F]FPEB	[¹⁸ F]3-fluoro-5-(pyridin-2-ylethynyl)benzotrile
[¹⁸ F]FSPG	(S-4-(3-[¹⁸ F]fluoropropyl)-L-glutamic acid
g	gram
GABA	gamma amino butyric acid
GC	gas chromatography
GIST	gastrointestinal stromal tumors
GLP	Good Laboratory Practice
GMP	Good Manufacturing Practice
HBED	<i>N,N'</i> -bis(2-hydroxybenzyl)ethylenediamine- <i>N,N'</i> -diacetic acid
HDA	hexadecanoic acid
HER	human epidermal growth factor receptor
HEU	highly enriched uranium
HITS	high-throughput screening
HIV/AIDS	human immunodeficiency virus/ acquired immunodeficiency syndrome
HMPAO	[^{99m} Tc]hexamethylpropyleneamine oxime
HMR	heart mediastinal ratio
HPLC	high-performance liquid chromatography
HSA	human serum albumin
HYNIC	hydrazinonicotinamide
IAEA	International Atomic Energy Agency
IB	investigators brochure
IBZM	iodobenzamide
ICH	International Council for Harmonization of Technical Requirements for Pharmaceuticals for Human Use
ID	injected dose
ID/g	injected dose per gram
IHC	immunohistochemistry
IMPd	investigational medicinal product dossier
IMZ	iomazenil
IND	investigational new drug
iNOS	inducible nitric oxide synthase
IVS	interventricular septum
K _d	equilibrium dissociation constant, affinity of ligand toward the target
LAF	laminar air flow
LET	linear energy transfer
LV	left ventricular
MAA	macroaggregated albumin
mAb	monoclonal antibody
MAO	monoamine oxidase
MCA	multi-channel analyzer
MCNPX	Monte Carlo N-Particle eXtended
MCP-1	monocyte chemoattractant protein-1
mCRPC	metastatic castration resistant prostate cancer
MDP	methylenediphosphonate
MeV	mega electron volt

MIBG	meta-iodobenzylguanidine
Min	minutes
mmol	millimoles
MMP	matrix metalloproteinases
μmol	micromoles
MPI	myocardial perfusion imaging
MPI	myocardial perfusion reserve
MPTP	1-methyl-4-phenyl-1,2,3,6-tetrahydropyridine
MRI	magnetic resonance imaging
MR2	muscarinic receptor 2
NA	natural abundance
NDA	new drug application
NE	norepinephrine
NET	neuroendocrine tumors
NK-1	neurokinin-1 receptor
nM	nanomolar
NOS	nitric oxide synthase
NOTA	1,4,7-triazacyclononane-triacetic acid
NPH	normal pressure hydrocephalus
NPs	nanoparticles
OCT	organic cation transporter
PBR	peripheral benzodiazepine receptor
PC	prostate cancer
PD	pharmacodynamics
PD-L1	program death ligand 1 receptor
PET	positron emission tomography
Pgp	p-glycoprotein
PHEN	phenylephrine
p.i.	post-injection
PiB	Pittsburgh Compound B
PIDA	phenyliodonium diacetate
PK	pharmacokinetics
pKa	acid dissociation constant
PRRT	peptide receptor radionuclide therapy
PSMA	prostate-specific membrane antigen
PTFE	polytetrafluoroethane
QA	quality assurance
QC	quality control
QMA	quaternary methyl ammonium
QNB	quinclidinyl benzilate
R&D	research and development
RBA	relative binding affinity
RCY	radiochemical yield
RDRC	Radioactive Drug Research Committee
RGD	arginine-glycine-aspartic acid
RIT	radioimmunotherapy

RLD	reference listed drug
RLT	radioligand therapy
RV	right ventricular
SERT	serotonin transporter
S _N Ar	nucleophilic aromatic substitution
SPE	solid phase extraction
SPECT	single photon emission computed tomography
SSRIs	selective serotonin reuptake inhibitors
SSTR-2	somatostatin receptor 2
SUV	standardized uptake value
TACN	triazamacrocyclic 1,4,7-triazacyclononane
TAT	targeted alpha therapy
TATE	(Tyr ³ -Thr ⁶)-octreotide
TBA	tetrabutylammonium
TBAF	tetra- <i>n</i> -butylammonium fluoride
TCEP	tris(2-carboxyethyl)phosphine
Tf	triflate
THF	tetrahydrofuran
TNBC	triple-negative breast cancer
TOC	(Tyr ³)-octreotide
TSPO	translocator protein, 18 kDa
TTR	transthyretin
USP	United States Pharmacopeia
UV	ultraviolet
VA	ventriculo-atrial
VACHT	vesicular transporter for acetylcholine
VMAT2	vesicular monoamine transporter type 2
VP	ventriculo-peritoneal
WHO	World Health Organization

PART I

Introduction to Radiopharmaceuticals

Chapter 1

Targeted Diagnostic Radiopharmaceuticals: Design Options for Small-Molecule Radiotracers

Michael R. Kilbourn

Department of Radiology, University of Michigan, Ann Arbor, MI 48109, USA

1.1 INTRODUCTION

The field of nuclear medicine has seen many important technical developments in the past seven decades, including improved radionuclide availability, new techniques for radiopharmaceutical synthesis, better imaging devices, and novel methods for image reconstruction and analysis. The importance of radiolabeled compounds used in nuclear medicine imaging is perhaps embodied in the proposal by Haberkorn et al. [1] that “Molecules are the future of nuclear medicine.” Many established radiopharmaceuticals currently in routine clinical care are used to image general physiological properties of organs (flow, volume, clearance, and metabolism), and research efforts have not stopped in that area, as represented by such radiopharmaceuticals as [¹⁸F]fluoromisonidazole [2] for hypoxia, [¹⁸F]flurpiridaz [3] for cardiac blood flow, and [¹⁸F]FROStrace for reactive oxygen species [4]. The emphasis in radiotracer design has more recently shifted to what

Handbook of Radiopharmaceuticals: Methodology and Applications, Second Edition.

Edited by Michael R. Kilbourn and Peter J.H. Scott.

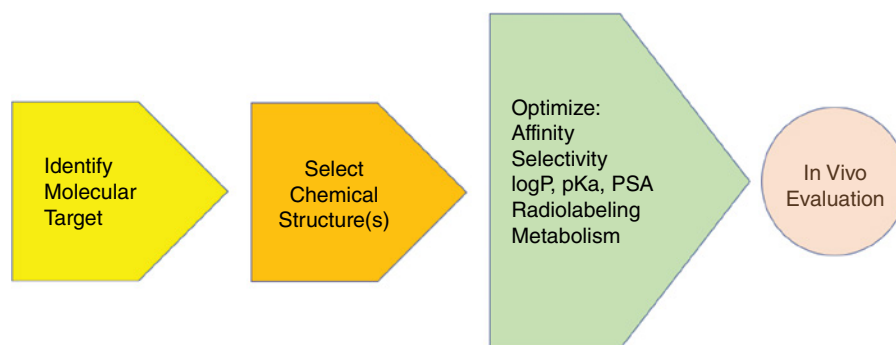
© 2021 John Wiley & Sons Ltd. Published 2021 by John Wiley & Sons Ltd.

are now termed “targeted” radiopharmaceuticals, in which radiolabeled compounds are designed specifically to indicate the presence or function of a single specific biochemical target, most often a particular macromolecule (e.g. protein, lipid, nucleic acid) whose numbers or functions have been identified as altered in pathological conditions.

The use of radiolabeled molecules for specific biochemical targets is, of course, not new and not limited to in vivo nuclear medicine imaging. In vitro studies of receptor binding or enzyme action have extensively used compounds labeled with longer-lived tritium, carbon-14, or iodine radionuclides. The steady improvements of imaging instrumentation (SPECT/computed tomography [CT], PET/CT, and PET/magnetic resonance imaging [MRI]) and their more widespread availability have spurred the continued development of small molecules as potential in vivo diagnostic radiopharmaceuticals. Adopting the concept of targeted radiotracer development for in vivo imaging is easy, but as noted in 1982 by Fowler and Wolf [5], “The site-specific delivery or targeting of radiotracers which probe particular aspects of the metabolism and function of a target organ or tissue is a particularly challenging aspect of radiotracer development.”

The processes for the development of new radiotracers are as varied as the investigators involved, but the early steps are usually very similar, as represented in Figure 1.1. All radiopharmaceutical development starts with the goal of imaging a specific biochemical process and then begins the search for appropriate chemical matter to radiolabel. There are several general requirements that apply to targeted radiotracers for any tissue. First and most obvious is that the molecules chosen must be amenable to radiolabeling, through isotopic substitution, addition of or substitution by small radionuclide-bearing groups, or attachment of a radionuclide-bearing pendant group in a manner that does not interfere with the desired properties of the molecule (e.g. affinity or specificity). The molecules chosen for radiolabeling should be specific or at least predominantly selective for the target to provide sufficient target-to-background distributions for in vivo imaging. The labeled compounds must be chemically stable and not easily metabolized to form radiolabeled species that would interfere with the interpretation of the radioactivity distribution after intravenous injection. Some consideration must be given to avoiding compounds that are clearly excluded from

Figure 1.1 Radiopharmaceutical development pathway.



target tissues due to the action of efflux transporters such as *p*-glycoprotein (**PGP**) and breast cancer resistance protein (**BCRP**). If the data is available, selection of compounds with more rapid *in vivo* pharmacokinetics may be favored: when using short-lived radionuclides, prolonged tissue retention is not useful; and for many applications of *in vivo* imaging, the ability to determine both the uptake and washout of a radiotracer in a dynamic fashion provides information useful for pharmacokinetic modeling. Finally, the development of radiotracers for imaging in the central nervous system (**CNS**) faces the additional requirement of passing the blood-brain barrier (**BBB**), a membrane system that efficiently excludes many compounds: CNS entry can be achieved using an active transport process or through passive diffusion, with the latter requiring consideration of the molecular size and lipophilicity.

In the following chapters of this *Handbook of Radiopharmaceuticals*, methods for producing radionuclides and radiopharmaceuticals, methods for evaluating new candidate radiotracers, and the many exciting applications of radiolabeled compounds for *in vivo* nuclear medicine imaging are discussed in detail. If radiopharmaceuticals are indeed the “future of nuclear medicine,” where do the ideas for new radiotracer structures come from? Although often the origins of a radiotracer are not clear, there are nevertheless a variety of sources of chemical structures that can be identified as useful for targeted radiotracer design (Table 1.1), and this chapter will focus on the early step of identifying appropriate chemical structures suitable for development into small-molecule radiotracers (for discussion purposes, small molecules are considered to have MW <600). Many of the examples arise from the field of positron emission tomography (**PET**) radiopharmaceutical chemistry, simply because it has often proven easier to radiolabel small molecules with carbon-11 or fluorine-18. There are, however, important examples of radioiodinated single-photon emission computed tomography (**SPECT**) agents – e.g. [¹²³I]ioflupane (DaTscan®), [¹²³I/¹³¹I]meta-iodobenzylguanidine ([¹²³I/¹³¹I]MIBG), and [¹²³I]iodobenzamide ([¹²³I]IBZM) – and efforts have been made to incorporate technetium-99m into relatively small molecules with some success ([^{99m}Tc]TRODAT-1). Although the sources for radiotracer development listed in Table 1.1 are discussed separately, it should be understood that combinations of the methods are often used to arrive at a molecule that can be successfully employed for *in vivo* imaging of biochemistry in living human subjects.

Endogenous compounds
 Established therapeutic drugs
 Pharmaceutical industry
In vitro assay reagents
 High-throughput screening
 Natural products (plant derived)

Table 1.1 Sources of leads for chemical matter for design and development of new *in vivo* imaging radiopharmaceuticals.

1.2 LABEL AN ENDOGENOUS COMPOUND OR DERIVATIVE

The radiolabeling of an endogenous chemical species is perhaps the simplest and oldest concept in radiotracer design: one of the earliest syntheses with carbon-11 was that of [^{11}C]acetic acid [6]. If the radiolabeling is done at a sufficiently high specific activity, then there should be no concerns regarding pharmacological effects or toxicology, as the mass of compound injected is likely far below normal physiological concentrations. It is also likely that the metabolism of an endogenous compound is very well known. A large number of endogenous compounds and derivatives have been radiolabeled and used for imaging studies: an incomplete listing of such radiopharmaceuticals is given in Table 1.2. The labeling of endogenous compounds has been primarily done using PET radionuclides (^{11}C , ^{13}N , ^{18}F), simply because of the simplicity in isotopic substitutions (e.g. ^{11}C for ^{12}C) or the observation that incorporation of the small fluorine atom is often well tolerated [7]. For example, many natural and non-natural amino acids have been synthesized with ^{11}C , ^{13}N , or ^{18}F radiolabels, using a variety of approaches to prepare radiotracers in a regiospecific or stereospecific fashion. Incorporating SPECT radionuclides into endogenous compounds is more challenging but has in some cases been successful with radioiodinated aromatic or non-natural amino acids [8].

Radiolabeled endogenous compounds may not seem to fit the simple concept of targeted radiotracers, as the biochemical processes they address are often ubiquitous, but they have proven useful when the target is enhanced or reduced in a pathophysiological condition. The best-known and most-used radiopharmaceutical based on an endogenous compound is 2-deoxy-2- ^{18}F fluoro-D-glucose (^{18}F FDG). As the PET radiopharmaceutical used daily in clinical medicine, ^{18}F FDG can be considered to target a specific biochemical process: the metabolism of glucose. The localization of radioactivity is, however, dependent on the action of one of the family of glucose transporters followed by enzyme-mediated phosphorylation to form 2-deoxy-2- ^{18}F fluoro-D-glucose-6-phosphate. That metabolite is effectively retained in cells, and ^{18}F FDG is a classic example of a metabolic trapping radiotracer. The powerful applications of ^{18}F FDG are the result of

Table 1.2 Examples of endogenous molecules and derivatives used as in vivo imaging radiopharmaceuticals.

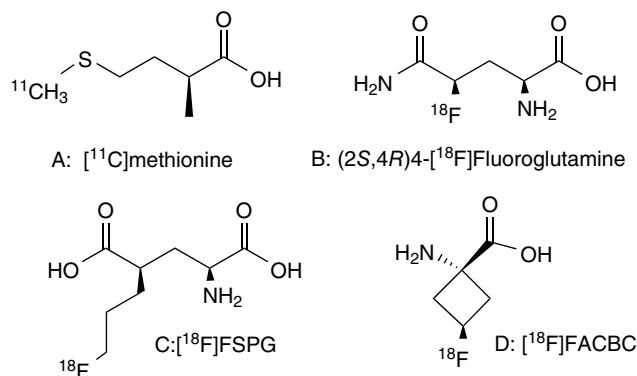
Type of molecule	Radiotracer example
Amino acids	^{11}C methionine
Fatty acids	^{11}C palmitate
Sugars	^{11}C glucose, 2- ^{18}F fluoro-2-deoxyglucose (FDG)
Nucleosides	^{11}C thymidine, ^{18}F fluorothymidine
Carboxylic acids	^{11}C pyruvic acid, ^{11}C ascorbic acid
Choline	^{11}C choline, ^{18}F fluorocholine
Steroids	^{18}F fluoroestradiol
Biogenic amines	^{11}C epinephrine, ^{18}F fluorodopamine
Arachidonic acid	^{11}C arachidonic acid

the localized changes in glucose metabolism, with both increases (in tumors) or decreases (in the brain in degenerative diseases) providing valuable information about physiology.

The tissue localization of radioactivity from [¹⁸F]FDG represents the action of a transporter and an enzyme, in that order. For endogenous compounds, the involvement of multiple biochemical steps in radiotracer uptake and localization is very common [9]. [¹⁸F]Fluorothymidine ([¹⁸F]FLT) has been successfully used for tumor imaging, with the mechanism of tumor retention proposed as trapping following phosphorylation by thymidine kinase, but the uptake of the radiotracer is also dependent on the equilibrative nucleoside transporter 1 (**ENT1**, *SLC29A1*). The successful accumulation and imaging of a radiotracer can also represent the actions of two transporters: for retention of the SPECT radiotracer [¹²³I]MIBG into neuroendocrine tumors or the uptake of the PET radiotracer [¹¹C]hydroxyephedrine ([¹¹C]HED) into presynaptic adrenergic neurons of the heart, it is a combination of transport by the neuronal membrane norepinephrine transporter (**NET**, *SLC6A2*) and the vesicular monoamine transporter type 2 (**VMAT2**, *SLC18A2*). The use of either radiotracer in the heart provides a measure of the integrity of the adrenergic innervation [10]. The brain radiotracers [¹¹C]dihydroxyphenylalanine ([¹¹C]DOPA) and 6-[¹⁸F]fluorodihydroxyphenylalanine ([¹⁸F]FDOPA) are examples where the specific localization of radioactivity in the synaptic vesicles of presynaptic dopaminergic neurons results from a combination of actions by, in order, the large amino acid transporter 1 (**LAT1**, *SLC7A5*) in the BBB, an intra-neuronal enzyme (dihydroxyphenylalanine [**DOPA**] decarboxylase) that converts the radiotracers to radiolabeled neurotransmitters ([¹¹C]dopamine and 6-[¹⁸F]fluorodopamine), and a second intra-neuronal transporter (the VMAT2) that moves those species inside neuronal storage vesicles. Thus, [¹¹C]DOPA and [¹⁸F]FDOPA target dopamine biosynthesis but represent a combination of three biochemical processes. Furthermore, the radioactivity distribution and retention from [¹¹C]DOPA and [¹⁸F]FDOPA are also dependent on the actions of two metabolic enzymes, **COMT** (catecholamine *O*-methyl transferase) and **MAO** (monoamine oxidase). Despite this complexity, [¹⁸F]FDOPA remains a useful radiotracer for human PET studies.

Many of the endogenous amino acids have been isotopically radiolabeled with nitrogen-13 or carbon-11, and numerous amino acid derivatives have been radiolabeled using fluorine-18 (incorporation of a single fluorine atom or a small fluorinated substituent) or radioisotopes of iodine [11–14]. The complex biochemical fates of the amino acids nicely demonstrate the potential – and difficulties – in the design and use of endogenous molecules as imaging agents. The movement of radiolabeled amino acids into and within cells is accomplished by no less than 51 transporters [15], and amino acids are involved in protein synthesis, neurotransmitter synthesis, redox balance (formation of glutathione and NADH/NADP⁺ coupling) [16], and energy-producing metabolism [17]. For the purposes of *in vivo* imaging, the natural amino acids may be not optimal, as their tissue localization reflects their multiple metabolic pathways; but that has not prevented their use in human studies, as exemplified by tumor imaging with [¹¹C]methionine (Figure 1.2) as a purported marker of protein synthesis. The design of a derivative of a natural amino acid such as (2-[¹⁸F]fluoroethyl)-*L*-tyrosine ([¹⁸F]FET) [18] or non-natural amino acids such as [¹¹C]ACHC (aminocyclohexanecarboxylic acid) [19] or [¹⁸F]FACBC

Figure 1.2 Targeted radiopharmaceuticals based on structures of amino acids.



(1-amino-3- ^{18}F)fluorocyclobutanecarboxylic acid: Fluciclovine, Axumin[®], Figure 1.2) [20] provides radiotracers that cannot be incorporated into proteins and are resistant to metabolism: such radiotracers target only the transporters primarily involved in their movement into tissues or tumors. The application of radiolabeled amino acids to probe tumor metabolism is exemplified by the synthesis of 4- ^{18}F fluoroglutamine (Figure 1.2), which is transported via the cysteine/glutamate antiporter (X_c^- , *SLC7A11*) into tumor cells where it can be subject to further metabolism or incorporation into macromolecules [21]. Finally, the potential use of an amino acid derivative to study cellular redox status is suggested for the radiotracer ^{18}F FSPG (S-4-(3- ^{18}F fluoropropyl)-L-glutamic acid, Figure 1.2) [22].

Most of the radiopharmaceutical examples in Table 1.2 are radiolabeled substrates for enzymes or transporters but are not radioligands that image specific binding to receptors. Why? The endogenous ligands for receptors usually have binding affinities too low for imaging specific binding in vivo: as an example, the affinity of dopamine for dopamine receptors is micromolar and does not match the <10 nM binding affinities of successful in vivo dopamine D2/D3 receptor imaging agents. One exception to this general limitation of receptor binding agents is the radiopharmaceutical ^{18}F fluoroestradiol (^{18}F FES). In vivo studies with radiolabeled estradiol started as early as 1967, with attempts to construct compartmental models for the specific binding of tritiated estradiol following intravenous administration and ex vivo tissue distribution studies [23]. The potential use of radiolabeled estrogens for breast cancer imaging stimulated years of effort to radiolabel estradiol, both with SPECT isotopes (16α - ^{123}I iodoestradiol [24] and 16α - ^{77}Br iodoestradiol [25]) and subsequently with fluorine-18 for PET imaging. Those efforts culminated in 16α - ^{18}F fluoroestradiol as a high-affinity radioligand for the estrogen receptor (reported K_d as low as 0.13 nM in cell studies [26]) that has subsequently been used by numerous institutions to image and characterize the receptor status of primary breast tumors [27]. The story of estrogen receptor imaging does not, however, end with ^{18}F FES. The recent identification of two types of estrogen receptors (ER- α and ER- β) may prompt research into radiotracers that show subtype specificity: whether these will be estradiol derivatives, derived from therapeutic agents, or newly designed xenobiotics cannot be predicted. Estradiol can be considered an endogenous compound that was

slightly modified to become an in vivo imaging agent targeting a specific receptor, but it could just as well have been used as an example of a clinically used drug successfully converted into an in vivo imaging agent, as discussed in the next section.

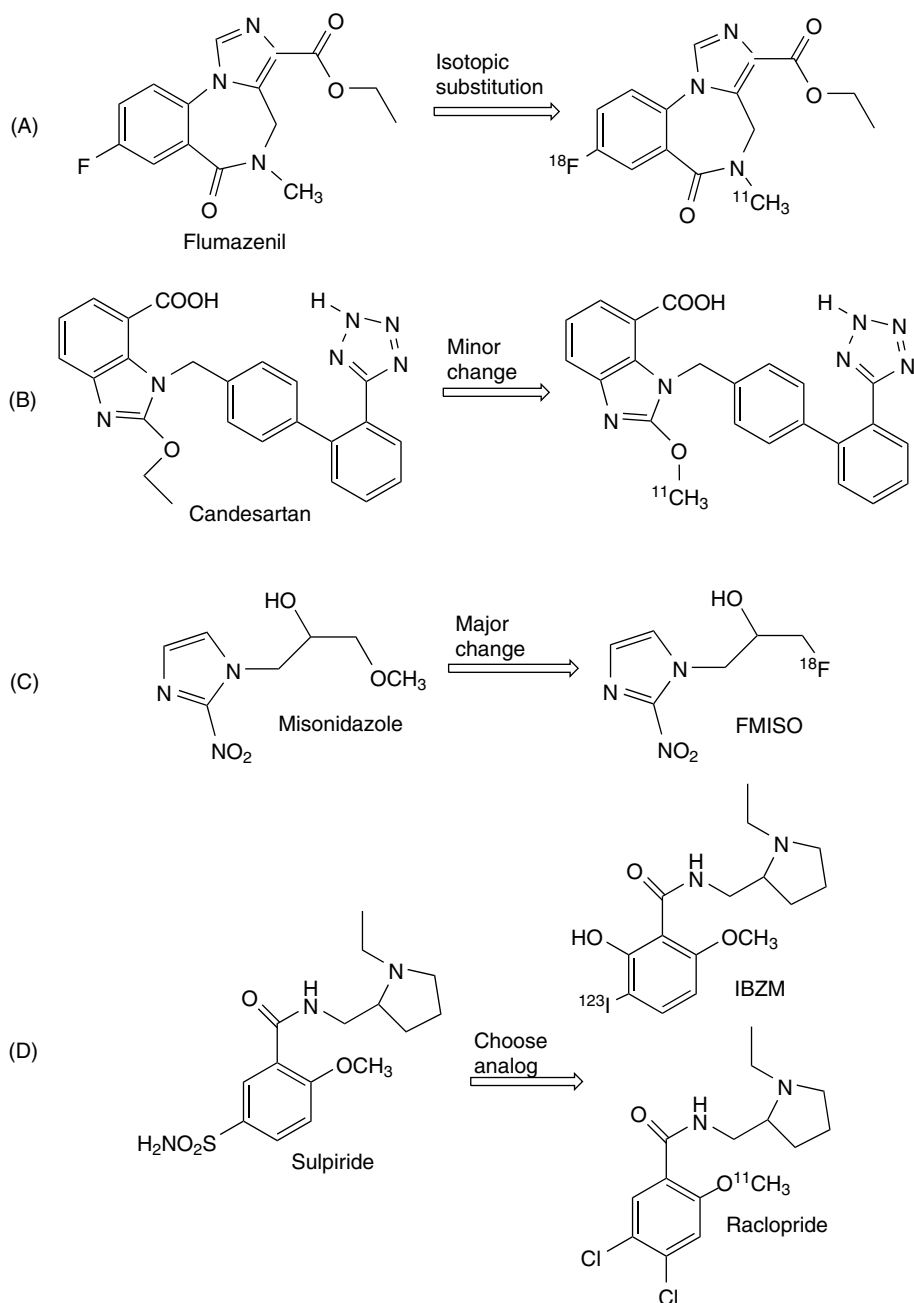
1.3 LABEL A PHARMACEUTICAL OR DERIVATIVE

The radiolabeling of a candidate drug molecule with a long-lived radionuclide (^3H or ^{14}C) to evaluate its disposition and metabolism has long been part of pharmaceutical development programs. The in vivo distribution of such new molecules can also be directly studied using isotopic substitutions with PET isotopes (e.g. ^{11}C for ^{12}C , ^{18}F for ^{19}F). In recent years, many of the large pharmaceutical companies have added capabilities for radiochemical syntheses with PET or SPECT radioisotopes, allowing them to develop radiotracers useful as in vivo biomarkers for preclinical evaluation of new drug candidates. Those efforts have yielded a number of radiotracers with impact on their drug development programs and led some investigators to form generalized concepts for successful biomarker development [28, 29]. The decades of effort by medicinal chemists in the pharmaceutical industry have resulted in the syntheses of many thousands of compounds, of which only a very small fraction have been eventually developed into marketable drugs. Whereas such libraries of compounds are used by in-house radiotracer development programs at pharmaceutical companies, they often remain inaccessible to academic researchers interested in radiopharmaceutical development: increased access to such chemical matter would be highly desired but will require more extensive industry-academia collaborations [30]. A number of clinically used drug molecules or compounds reported by pharmaceutical companies have, however, been the basis for successful radiopharmaceutical development in several different fashions, as exemplified in Figure 1.3 and discussed in this chapter.

In a few cases, it has been possible to radiolabel a therapeutic drug molecule using isotopic substitutions with carbon-11 or fluorine-18 (a large proportion of drugs have fluorine substituents [31]). Examples of drugs directly converted to in vivo imaging agents include [^{11}C or ^{18}F]flumazenil (Romazicon[®]: antagonist of the GABA_A receptor-benzodiazepine binding site), [^{11}C]methylphenidate (Ritalin[®]: dopamine transporter [**DAT**] antagonist), [^{18}F]altanserin (5HT_2A receptor antagonist), [^{11}C]elacridar (PGP inhibitor), [^{11}C]L-DOPA (levodopa, a dopamine precursor), [^{11}C]erlotinib (Tarceva[®]: epidermal growth factor receptor [**EGFR**] inhibitor), [^{11}C]metomidate (Hypnodil[®]: hypnotic), and [^{11}C]verapamil (Verelan[®]: calcium channel blocker). The monoamine oxidase inhibitor deprenyl (Selegiline[®]) was first radiolabeled by isotopic substitution with carbon-11 and then underwent a *second* isotopic substitution with deuterium to improve human brain imaging pharmacokinetics [32]. Radiotracers based on drugs that have been discontinued from therapeutic human use, such as [^{11}C]rolipram (phosphodiesterase-4 inhibitor), or which are only used as veterinary drugs, such as [^{11}C]carfentanil (Wildnil[®]: opiate agonist used as an animal tranquilizer), have also found applications in human studies.

In other cases, the molecular structure of a clinical drug molecule needed to be slightly modified to accommodate the radionuclide, to improve pharmacokinetics or

Figure 1.3 Targeted radiopharmaceuticals based on structures of known therapeutic drugs.



metabolism or to simplify its radiochemical synthesis. To design a radiotracer for SPECT imaging in epilepsy, the fluorine in flumazenil was replaced with radioiodine, yielding the compound [^{123}I]iomazenil. The heart drugs candesartan (Cilexetil[®]) and losartan (Cozaar[®]) are angiotensin II receptor antagonists where small changes in structure (substitution

of methyl groups for ethyl or propyl substituents) were necessary to accommodate easy radiochemical labeling with [^{11}C]methyl iodide; but the slight molecular modification (e.g. ethyl to methyl group) did not result in significant loss of in vitro affinities, and the resultant molecules proved useful as in vivo radioligands for cardiac imaging [33]. As discussed earlier, 16- α -[^{18}F]fluoroestradiol is a simple fluorinated derivative of the clinical drug estradiol.

A larger, more significant change in molecular structure might be needed, however, as exemplified for the hypoxic radiosensitizer misonidazole: to provide for incorporation of the radionuclide, the methoxy group of misonidazole was replaced by a fluorine atom in the synthesis of [^{18}F]FMISO (fluoromisonidazole) that is widely used in PET imaging [2]. Even more fortuitous was the discovery of a substituted diphenylsulfide (403U76) as an inhibitor of neuronal serotonin reuptake; that molecular structure provided the lead to a large number of carbon-11, fluorine-18, and radioiodine labeled diphenylsulfides that have been developed for in vivo imaging of the serotonin transporter (**SERT**, *SLC6A4*) [34].

Sometimes an analog of the clinical drug is chosen for radiolabeling and evaluation as an in vivo imaging agent: this may be due to the different pharmacokinetics required for an in vivo imaging agent intended for intravenous injection as compared to a chronic orally administered drug. Examples are the numerous substituted benzamides that were synthesized by medicinal chemists in the pharmaceutical industry [35]. These were investigated as potential antipsychotics based on pharmacological activity as dopamine receptor antagonists, and sulpiride (Dogmatil[®]) was developed into the clinical drug. It was, however, not chosen for development as a radioligand for in vivo brain imaging studies of dopamine receptors. Instead, an iodobenzamide ([^{123}I]IBZM) and [^{11}C]raclopride were synthesized as analogs of sulpiride, and both have been used for more than 30 years for SPECT and PET imaging of the D2/D3 receptor in the human brain [36, 37]. Numerous other benzamides have subsequently been radiolabeled, but only recently has sulpiride been carbon-11 labeled [38]: not as a dopaminergic radioligand, but rather as a substrate for organic cation transporters OCT1 (*SLC22A1*) and OCT2 (*SLC22A2*), and multidrug and toxin extrusion-type transporters MATE1 (*SLC47A1*) and MATE2 (*SLC47A2*).

There is also the possibility of “refining” an old drug into a new, useful in vivo radiopharmaceutical. The benzoisoquinoline tetrabenazine (Xenazine[®]) was invented in the late 1950s as an atypical antipsychotic, and in recent years it has been used in clinical care for treating selected movement disorders. In 1990, isotopic substitution was used to synthesize [^{11}C]TBZ; and in vivo PET imaging of its intended target, the VMAT2 in the brain, was successfully achieved in humans [39]. Significant improvements in the imaging of the VMAT2 were achieved when it was recognized that the brain pharmacokinetics actually represented a mixture of four stereoisomeric metabolites: application of modern methods for chiral chromatographic resolution allowed for the isolation, identification (absolute configuration), and carbon-11 labeling of a single high-affinity stereoisomer (+)- α -[^{11}C]dihydro-tetrabenazine ((+)- α -[^{11}C]DTBZ) [40]. This radiotracer optimization illustrates two useful concepts: understanding the metabolism of a drug (the metabolites may actually be higher affinity for the target site!) and using only single diastereomers of

drugs with multiple chiral centers. Furthermore, the efforts in radiotracer development may have impacted the design of a new VMAT2 inhibitor (valbenazine, Ingrezza), a pro-drug form of the single isomer (+)- α -DTBZ, which has been recently introduced into clinical use.

The radiolabeling of a class of clinical drugs does not always work, however. The selective serotonin reuptake inhibitors (**SSRIs**) such as fluoxetine (Prozac), citalopram (Celexa), and related compounds constitute an important and highly successful group of clinical drugs in psychiatry. The radiolabeling of such drugs with carbon-11 or fluorine-18 failed to produce useful in vivo imaging agents for human PET studies of the SERT largely due to the high non-specific binding of those lipophilic drugs [41, 42].

Established clinical drugs and the pharmaceutical industry are thus a rich source of chemical matter for potential development into an in vivo imaging agent. One advantage of a clinical drug is that the pharmacology, toxicology, and metabolism are already established in humans, and the doses in clinical use are likely orders of magnitude higher than the trace mass doses present in radiopharmaceuticals: this makes obtaining regulatory approvals much simpler. However, in many cases, a clinically used therapeutic drug does not work as a radiotracer, as the desired pharmacokinetics in blood and target tissues from an oral drug dose [43] usually do not match the relatively rapid pharmacokinetics desired for an in vivo imaging radiotracer labeled with short-lived radionuclides.

1.4 FROM IN VITRO REAGENTS TO IN VIVO IMAGING

The compounds synthesized as part of drug development represent only a portion of the vast numbers of chemical structures that have been synthesized. There are examples of the development of in vivo imaging radiotracers based on chemicals that were useful for in vitro purposes but were never developed as drugs (Figure 1.4).

Two examples of radiotracers used for in vivo brain β -amyloid imaging have origins in the chemical compounds used for in vitro tissue staining. The neutral fluorescent probe **DDNP** (1,1-dicyano-2-[6-(dimethylamino)naphthalen-2-yl]propene) was developed by Jacobsen et al. [44] as a reagent for microscopy studies but was then later radiolabeled with fluorine-18: the resultant radioligand [^{18}F]FDDNP was used for in vivo PET imaging of amyloid and tau in human brains [45]. Thioflavin-T, a dye used in histochemistry to selectively stain amyloid in post-mortem brain tissues, was selected by Mathis and Klunk as the starting point for the design of a brain-penetrant amyloid imaging agent [46]. The structure of thioflavin-T includes a positively charged quaternary heterocyclic nitrogen, which prevented its use directly as a brain imaging agent (it would not penetrate the BBB). The syntheses of a series of derivatives was thus undertaken, with the most important step being the removal of the methyl group on the quaternary nitrogen, eventually yielding several candidate compounds for radiolabeling; the best compound then chosen for labeling with carbon-11 was designated 6-Me-BTA-1, or more commonly known as **PIB** (Pittsburgh compound B) (Figure 1.3). [^{11}C]PIB (*N*-methyl- ^{11}C]6-Me-BTA-1) has now been used for many thousands of human PET studies.

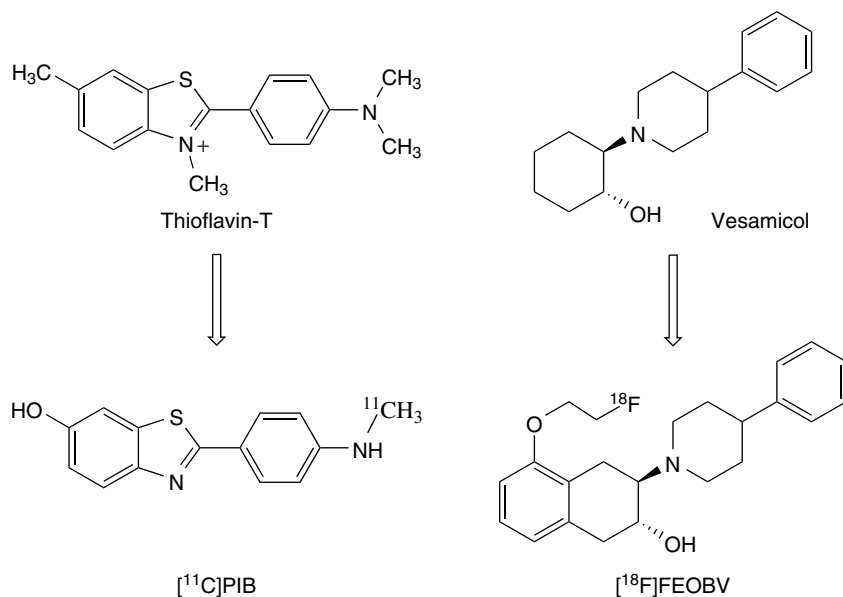


Figure 1.4 Targeted radiopharmaceuticals based on structures of in vitro chemical probes.

Two further examples of compounds that became radiotracers but not drugs come from studies of the cholinergic system in the brain. Quinclidinyl benzilate (**QNB**) was synthesized by chemists at Hoffman-La Roche in the 1950s and is useful as an in vitro tritiated radioligand for studies of the muscarinic cholinergic receptor, but QNB only drew human use interest as, unfortunately, a possible chemical war agent. However, when labeled with radioiodine, QNB was converted to radiotracers (¹²³I]QNB) successfully used for in vivo imaging, including one of the earliest examples of receptor-targeted human SPECT imaging [47]. Another example is vesamicol, a potent neuromuscular blocking agent [48] subsequently identified as a high-affinity inhibitor of the vesicular transporter for acetylcholine (**VAcHT**, *SLC18A3*). Multiple research groups pursued the radiolabeling of vesamicol and derivatives with radioiodine, carbon-11, and fluorine-18 with the goal of identifying in vivo imaging biomarkers for presynaptic cholinergic neurons [49], and the radiotracer [¹⁸F]FEOBV (Figure 1.3) is in current use in human PET studies [50, 51].

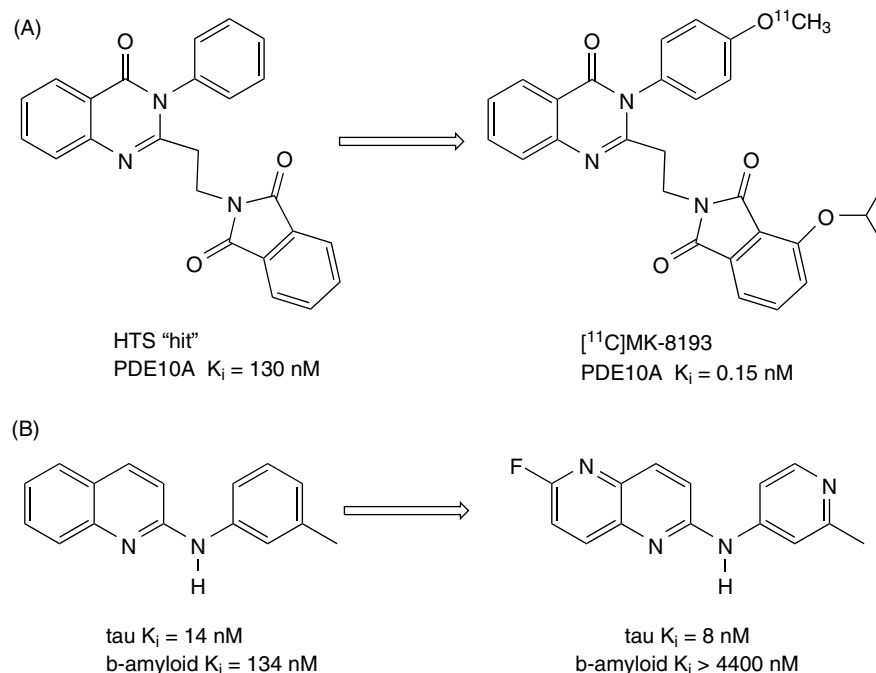
Finally, there are the recently reported radiolabeled substrates for MAOs that function as in vivo metabolic trapping agents [52]. These radiotracers can be considered as derived from the neurotoxin **MPTP** (1-methyl-4-phenyl-1,2,3,6-tetrahydropyridine), but with a structural modification (insertion of an ether oxygen between the phenyl and tetrahydropyridine rings) that retains the reactivity with MAO but removes the neurotoxicity concerns. The radiotracers derived from QNB, vesamicol, and MPTP are examples of successful use of highly toxic chemicals as starting materials for radiotracer development, which is only possible because the structural modifications or high specific activities of the radiopharmaceuticals allow their administration at very low and safe mass doses.

1.5 DO HIGH-THROUGHPUT SCREENING OF A CHEMICAL LIBRARY

High-throughput screening (**HTS**) is a technique that screens a chemical library (often many thousands of compounds) against an *in vitro* assay in the search for “hits”: that is, chemical structures that appear to interact with the target. In the pharmaceutical industry, the structures identified as hits provide leads for the development of new chemical matter, where structural refinements are then made to obtain optimal candidate drug molecules. HTS has been used by PET research groups in both industry and academia to identify scaffolds for successful *in vivo* imaging agent development.

The phosphodiesterase 10A (**PFD10A**) enzyme was discovered in 1999 and has become of significant interest for the development of drugs useful in a variety of psychiatric diseases. The research group at Merck undertook the development of a PDE10A radioligand useful for clinical studies of new candidate drug molecules [53] and employed HTS to identify a scaffold (Figure 1.3) with encouraging properties of moderate ligand binding ($K_i = 130$ nM), lipophilicity ($\text{clogP} = 3.9$), and polar surface area (**PSA** = 75). Syntheses of a series of derivatives of that scaffold identified four compounds with high affinity for the PDE10A binding site, each of which was then radiolabeled with carbon-11 and studied in rat and rhesus monkey brains. The result was the selection of [^{11}C]MK-8193 (Figure 1.5) as a high affinity ($K_i = 0.15$ nM), highly selective *in vivo* radioligand for the PDE10A binding site.

Figure 1.5 Targeted radiopharmaceuticals based on structures derived from high-throughput screening.



A significant application of HTS methods has been in the design of radiotracers for the proteinopathies, particularly those associated with neurological diseases: β -amyloid, tau, and synuclein. As there are no endogenous “ligands” for these proteins that accumulate in the brain, and protein structural information is very limited, the screening of chemical libraries with a diversity of molecular structures has been a useful mechanism in the search for possible radiotracer structures. The use of HTS is often more difficult for academic research groups, simply due to the lack of access to the chemical libraries and the equipment needed for performing the tedious *in vitro* assays, or the cost of performing the assays, or both. This has not, however, totally prevented its use, as exemplified by the efforts of the Tohoku University research group [54], who screened over 2000 chemicals in the search for a chemical scaffold suitable for the development of tau imaging agents. Their efforts resulted in the development and evaluation of [^{18}F]THK5351 as one of the several new radiochemicals that have now been investigated for PET imaging of tau in Alzheimer’s disease subjects.

The encouraging studies with [^{18}F]THK5351 and other proposed tau radioligands (e.g. [^{18}F]1451, [^{18}F]MK-6240, [^{11}C]PBB3, and others) provided insights into the some of the structural features needed for tau selectivity and binding, allowing chemists at Janssen Pharmaceutica [55] to employ a mini-HTS of only 4000 compounds to identify a compound (Figure 1.5) with high affinity ($K_i = 14 \text{ nM}$) and encouraging selectivity over β -amyloid binding ($K_i = 134 \text{ nM}$). Structural explorations involving syntheses of derivatives with varying ring nitrogen numbers and positions, and placement of a fluorine substituent in a position with potential for radiolabeling with ^{18}F , yielded their best candidate molecule (Figure 1.3) with an improved affinity ($K_i = 7.9 \text{ nM}$) and selectivity over β -amyloid binding ($K_i > 4400 \text{ nM}$).

These examples demonstrate the potential power of HTS for radiopharmaceutical design, but challenges remain. At the start, what is the correct (or needed) library size of chemical compounds [56]? Should searches be restricted to smaller focused libraries, or would searches of the vast virtual libraries (now containing billions of structures [57]) provide the lead structures needed for the development of new radiotracers for the plethora of biochemical targets (receptors, transporters, enzymes, ion channels) that are being identified by advances in genetics and biochemistry, but for which there are currently no known ligands? It must also be recognized that HTS screens most often identify lead structures with affinities for the target that may be far lower than needed for an *in vivo* radiotracer, and significant time and effort may be needed to achieve a new chemical entity with the needed affinities and **ADME** (absorption, distribution, metabolism, and excretion) properties for *in vivo* imaging applications.

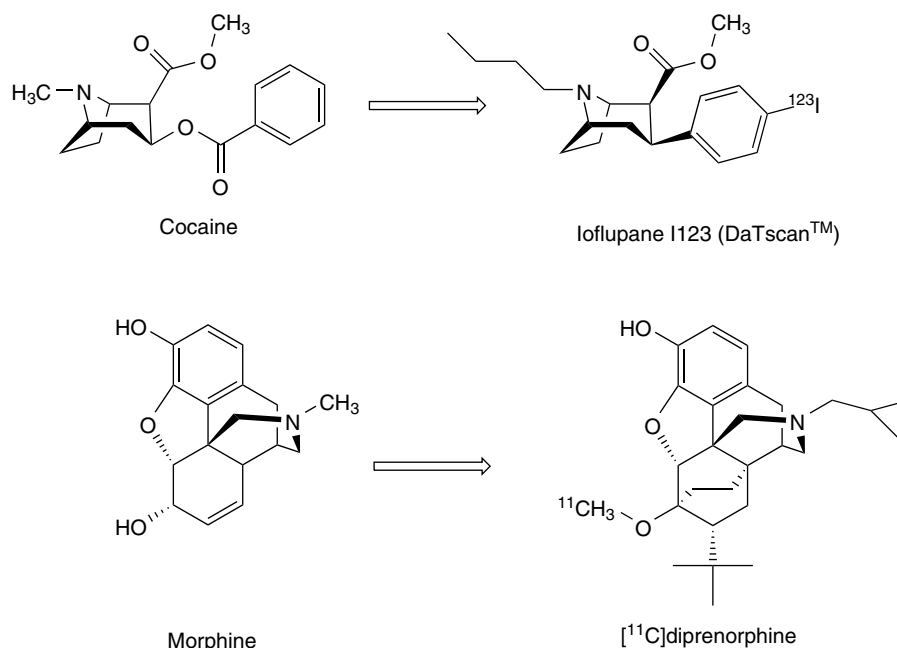
1.6 LABEL A NATURAL PRODUCT OR DERIVATIVE

Natural products have for many years been a source of chemical structures for drug development [58], and there are important examples of *in vivo* radiopharmaceuticals that are derived from natural products.

Cocaine is the neuroactive alkaloid isolated from leaves of the coca plant (Erythroxylaceae family). It is pharmacologically active at a number of transporters and receptors in the human brain, but the most significant effect of cocaine is at the neuronal membrane DAT. In 1989, Fowler et al. isotopically radiolabeled cocaine with carbon-11 [59], but applications of [^{11}C]cocaine for studies of the DAT in neurodegenerative diseases proved challenging due to its very rapid pharmacokinetics in the human brain. Fortunately, an earlier interest by medicinal chemists in developing cocaine antagonists had led to the syntheses of a very large number of compounds based on the 3-phenyltropane structure [60, 61], and that provided chemical leads useful for syntheses of a large number of analogs and derivatives labeled with radioiodine, carbon-11, and fluorine-18 [5]. These efforts led to radiotracers selective for the neuronal membrane dopamine (DAT), serotonin (SERT), and norepinephrine (NET) transporters [62]. Several of these radiolabeled 3-phenyltropanes have been used in human studies, and the radioiodinated compound DaTscan (loflupane 1123, Figure 1.6) has been approved for clinical studies of Parkinson's disease and related conditions.

A second example of natural products used as radiopharmaceuticals comes from the opiate receptors. Morphine is a high-affinity opiate receptor agonist first isolated from plant sources (e.g. opium poppy) in the first decade of the 1800s and marketed for human use since 1827. The extensive synthetic efforts of medicinal chemists produced numerous synthetic opioids that act as agonists or antagonists with varying selectivity for the three receptor subtypes (μ , δ , and κ receptors). Two such synthetic opioids, diprenorphine (μ receptor) (Figure 1.6) and naltrindole (δ receptor), were selected for carbon-11 or fluorine-18 labeling and have been used for opiate receptor PET studies in the human

Figure 1.6 Targeted radiopharmaceuticals based on structures of natural products.



brain [63, 64]. Morphine and cocaine are, of course, somewhat unique examples of plant-derived natural products. Both compounds have been or are in use as medicines, but both are also addictive and included on regulatory lists as controlled substances: development and use of radiolabeled forms of such compounds can at times be challenging from a regulatory standpoint.

There are times when natural products have been simply too complex for radiolabeling, had physical or metabolic properties inconsistent with use as an in vivo radiotracer, or had no obvious site for radiolabeling: examples are reserpine (a potent inhibitor of vesicular monoamine transporters), tetrahydrocannabinol (**THC**: one of the many alkaloids active at the cannabinoid receptor), and colchicine (binding to microtubules). Fortunately, for each of these targets, smaller and simpler chemical structures were pursued to yield useful in vivo imaging radiotracers [39, 65, 66].

1.7 SUMMARY

As described in the previous sections, there are multiple routes to new radiopharmaceutical design, and all have yielded radiotracers useful for human imaging studies. For all of these approaches, radiotracer development has drawn from known chemical structures, although often with small to very significant modifications required to achieve the desired attributes of specificity, biodistribution, pharmacokinetics, and metabolism needed for in vivo radiopharmaceuticals. The design and evaluation of new radiopharmaceuticals remains an exciting but challenging field, and one with a tremendous potential impact on our understanding of physiology and disease.

REFERENCES

1. Haberkorn, U., Mier, W., Kopka, K. et al. (2017). Identification of ligands and translation to clinical applications. *J. Nucl. Med.* 58 (Suppl 2): 27S–33S.
2. Xu, Z., Li, X.F., Zou, H. et al. (2017). ¹⁸F-Fluoromisonidazole in tumor hypoxia imaging. *Oncotarget* 8: 94969–94979.
3. Yu, M., Nekolla, S.G., Schwaiger, M., and Robinson, S.P. (2011). The next generation of cardiac positron emission tomography imaging agents: discovery of flurpiridaz F-18 for detection of coronary disease. *Semin. Nucl. Med.* 41: 305–313.
4. Hou, C., Hsieh, C.J., Lee, H. et al. (2018). Development of a positron emission tomography radiotracer for imaging elevated levels of superoxide in neuroinflammation. *ACS Chem. Neurosci.* 9: 578–586.
5. Fowler, J.S. and Wolf, A.P. (1982). *The Synthesis of Carbon-11, Fluorine-18, and Nitrogen-13 Radiotracers for Biomedical Applications*. NAS-NS-3201, 124. Oak Ridge, TN: US Department of Energy.
6. Kamen, M.D. (1951). *Radioactive Tracers in Biology*, 2e, 224–243. New York, NY: Academic Press.

7. Pekosak, A., Filp, U., Poot, A.J., and Windhorst, A.D. (2018). From carbon-11-labeled amino acids to peptides in positron emission tomography: the synthesis and clinical application. *Mol. Imag. Biol.* 20: 510–532.
8. McConathy, J., Yu, W., Jarkas, N. et al. (2012). Radiohalogenated nonnatural amino acids as PET and SPECT tumor imaging agents. *Med. Res. Rev.* 32: 868–905.
9. Kilbourn, M.R. (2017). Small molecule PET tracers for transporter imaging. *Semin. Nucl. Med.* 47: 536–552.
10. Raffel, D.M. and Wieland, D.M. (2010). Development of mIBG as a cardiac innervation imaging agent. *JACC Cardiovasc. Imaging* 3: 111–116.
11. Da Silva, E.S., Gomez-Vallejo, V., Baz, Z. et al. (2016). Efficient enzymatic preparation of [¹³N]-labelled amino acids: towards multipurpose synthetic systems. *Chemistry* 12: 13619–13626.
12. Ermert, J. and Coenen, H.H. (2013). Methods for ¹¹C- and ¹⁸F-labelling of amino acids and derivatives for positron emission tomography imaging. *J. Labelled Compd. Radiopharm.* 56: 225–236.
13. Sun, A., Liu, X., and Tang, G. (2017). Carbon-11 and fluorine-18 labeled amino acid tracers for positron emission tomography imaging of tumors. *Front. Chem.* 5: 124.
14. Goodman, M.M., Yu, W., and Jarkas, N. (2018). Synthesis and biological properties of radiohalogenated α,α -disubstituted amino acids for PET and SPECT imaging of amino acid transporters (AATs). *J. Labelled Compd. Radiopharm.* 61: 272–290.
15. Kandasamy, P., Gyimesi, G., Kanai, Y., and Hediger, M.A. (2018). Amino acid transporters revisited: new views in health and disease. *Trends Biochem. Sci* 43: 752–789.
16. Vucetic, M., Cormerais, Y., Parks, S.K., and Pousssegur, J. (2017). The central role of amino acids in cancer redox homeostasis: vulnerability points of the cancer redox code. *Front. Oncol.* 7: 319.
17. Yang, L., Venneti, S., and Nagrath, D. (2017). Glutaminolysis: a hallmark of cancer metabolism. *Annu. Rev. Biomed. Eng.* 19: 163–194.
18. Langen, K.-F., Soffels, G., Filss, C. et al. (2017). Imaging of amino acid transport in brain tumors: positron emission tomography with *O*-(2-[¹⁸F]fluoroethyl)-*L*-tyrosine. *Methods* 130: 124–134.
19. Koeppe, R.A., Mangner, T., Betz, A.L. et al. (1990). Use of [¹¹C]aminocyclohexanecarboxylate for the measurement of amino acid uptake and distribution volume in human brain. *J. Cereb. Blood Flow Metab.* 5: 727–739.
20. Shoup, T.M., Olson, J., Hoffman, J.M. et al. (1999). Synthesis and evaluation of [¹⁸F] 1-amino-3-fluorocyclobutane – 1-carboxylic acid to image brain tumors. *J. Nucl. Med.* 40: 331–338.
21. Ploessl, K., Wang, L., Lieberman, B.P. et al. (2012). Comparative evaluation of ¹⁸F-labeled glutamic acid and glutamine as tumor metabolic imaging agents. *J. Nucl. Med.* 53: 1616–1624.
22. McCormick, P.N., Greenwood, H.E., Glaser, M. et al. (2018). Assessment of tumor redox status through (*S*)-4-(3-[¹⁸F]fluoropropyl)-*L*-glutamic acid positron emission tomography imaging of system X_c⁻ activity. *Cancer Res.* in press DOI <https://doi.org/10.1158/0008-5472.CAN-18-2634>.

23. Eisenfeld, A.J. (1967). Computer analysis of the distribution of [³H]estradiol. *Biochim. Biophys. Acta* 136: 498–507.
24. Hochberg, R.B. and Rosner, W. (1980). Interaction of 16α-[¹²⁵I]iodoestradiol with estrogen receptor and other steroid-binding proteins. *Proc. Natl. Acad. Sci. U.S.A.* 77: 328–332.
25. Katzenellenbogen, J.A., Senderoff, S.G., McElvany, K.D. et al. (1981). 16α-[⁷⁷Br] bromoestradiol-17β: a high specific-activity, γ-emitting tracer with uptake in rat uterus and induced mammary tumors. *J. Nucl. Med.* 22: 42–47.
26. Salem, K., Kumar, M., Klopping, K.C. et al. (2018). Determination of binding affinity of molecular imaging agents for steroid hormone receptors in breast cancer. *Am. J. Nucl. Med. Mol. Imaging* 8: 119–126.
27. Mintun, M.A., Welch, M.J., Siegel, B.A. et al. (1988). Breast cancer: PET imaging of estrogen receptors. *Radiology* 169: 45–48.
28. Zhang, L. and Villalobos, A. (2016). Strategies to facilitate the discovery of novel CNS PET ligands. *EJNMMI Radiopharm. Chem.* 1: 13.
29. Van de Bittner, G.C., Ricq, E.L., and Hooker, J.M. (2014). A philosophy for CNS radio-tracer design. *Acc. Chem. Res.* 47: 3127–3134.
30. Bernard-Gauthier, V., Collier, T.L., Liang, S.H., and Vasdev, N. (2017). Discovery of PET radiopharmaceuticals at the academic-industry interface. *Drug Disc Today Technol.* 25: 19–26.
31. Swallow, S. (2015). Fluorine in medicinal chemistry. *Prog. Med. Chem.* 54: 65–133.
32. Fowler, J.S., Logan, J., Shumay, E. et al. (2015). Monoamine oxidase: radiotracer chemistry and human studies. *J. Labelled Compd. Radiopharm.* 58: 51–64.
33. Hadizad, T., Kirkpatrick, S.A., Mason, S. et al. (2009). Novel O-[¹¹C]methylated derivatives of candesartan as angiotensin II AT(1) receptor imaging ligands: radiosynthesis and ex vivo evaluation in rats. *Bioorg. Med. Chem.* 17: 7971–7977.
34. Stehouwer, J.S. and Goodman, M.M. (2013). ¹¹C and ¹⁸F PET radioligands for the serotonin transporter (SERT). *J. Labelled Compd. Radiopharm.* 56: 114–119.
35. Florvall, L. and Ogren, S.-O. (1982). Potential neuroleptic agents. 2,6-Dialkoxybenzamide derivatives with potent dopamine receptor blocking activities. *J. Med. Chem.* 25: 1280–1286.
36. Kung, H.F., Guo, Y.Z., Billings, J. et al. (1988). Preparation and biodistribution of [¹²⁵I] IBZM, a potential CNS D-2 receptor imaging agent. *Int. J. Radiat. Appl. Instrum. Part B* 15: 195–201.
37. Ehrin, E., Farde, L., de Paulis, T. et al. (1985). Preparation of ¹¹C-labelled raclopride, a new potent dopamine receptor antagonist: preliminary PET studies of cerebral dopamine receptors in the monkey. *Int. J. Appl. Radiat. Isot.* 36: 269–273.
38. Takano, H., Ito, S., Zhang, X. et al. (2017). Possible role of organic cation transporters in the distribution of [¹¹C]sulpiride, a dopamine D2 receptor antagonist. *J. Pharm. Sci.* 106: 2558–2565.
39. Kilbourn, M.R., DaSilva, J.N., Frey, K.A. et al. (1993). In vivo imaging of vesicular monoamine transporters in human brain using [¹¹C]tetrabenazine and positron emission tomography. *J. Neurochem.* 60: 2315–2318.

40. Kilbourn, M.R. and Koeppe, R.A. (2018). Classics in neuroimaging: radioligands for the vesicular monoamine transporter 2. *ACS Chem. Neurosci.* <https://doi.org/10.1021/acscchemneuro.8b00429>.
41. Hume, S.P., Pascali, C., Pike, V.W. et al. (1991). Citalopram: labelling with carbon-11 and evaluation in rat as a potential radioligand for PET studies of 5-HT reuptake sites. *Int. J. Radiat. Appl. Instrum. Part B* 18: 339–351.
42. Shiue, C.Y., Shiue, C.G., Cornish, K.G., and O'Rourke, M.F. (1995). PET study of the distribution of [¹¹C]fluoxetine in a monkey brain. *Nucl. Med. Biol.* 22: 613–616.
43. Smith, D.A., Beaumont, K., Naurer, T.S., and Di, L. (2018). Relevance of half-life in drug design. *J. Med. Chem.* 61: 4273–4282.
44. Jacobsen, A., Petric, A., Hogenkamp, D. et al. (1996). 1,1-Dicyano-2-[6-(dimethylamino)naphthalen-2-yl]propene (DDNP): a solvent polarity and viscosity sensitive fluorophore for fluorescence microscopy. *J. Am. Chem. Soc.* 118: 5572–5579.
45. Agdeppa, E.D., Kepe, V., Liu, J. et al. (2001). Binding characteristics of radiofluorinated 6-dialkylamino-2-naphthylethylidene derivatives as positron emission tomography probes for β -amyloid plaques in Alzheimer's disease. *J. Neurosci.* 21: RC189.
46. Mathis, C.A., Lopresti, B.J., Ikonovic, M.D., and Klunk, W.E. (2017). Small-molecule PET tracers for imaging proteinopathies. *Semin. Nucl. Med.* 47: 553–575.
47. Eckelman, W.C., Reba, R.C., Rzeszutarski, W.J. et al. (1984). External imaging of cerebral muscarinic acetylcholine receptors. *Science* 223: 291–293.
48. Brittain, R.T., Levy, G.P., and Tyers, M.B. (1969). The neuromuscular blocking action of 2-(4-phenylpiperidino)cyclohexanol (AH 5183). *Eur. J. Pharmacol.* 8: 93–99.
49. Kilbourn, M.R. (2013). PET radioligands for the vesicular transporters for monoamines and acetylcholine. *J. Labelled Compd. Radiopharm.* 56: 167–171.
50. Petrou, M., Frey, K.A., Kilbourn, M.R. et al. (2013). In vivo human imaging of cholinergic nerve terminals with the novel PET radiotracer [¹⁸F](–)5-fluoroethoxybenzovesamicol ([¹⁸F]FEOBV): biodistribution, dosimetry, and tracer kinetic analysis. *J. Nucl. Med.* 55: 396–404.
51. Aghourian, M., Legnault-Denis, C., Soucy, J.P. et al. (2017). Quantification of brain cholinergic denervation in Alzheimer's disease using PET imaging with [¹⁸F]-FEOBV. *Mol. Psychiatry* 22: 1531–1538.
52. Brooks, A.F., Shao, X., Quesada, C. et al. (2015). In vivo metabolic trapping radiotracers for imaging monoamine oxidase-A and -B enzymatic activity. *ACS Chem. Neurosci.* 16: 1965–1971.
53. Cox, C.D., Hostetler, E.D., Flores, B.A. et al. (2015). Discovery of [¹¹C]MK-8193 as a PET tracer to measure target engagement of phosphodiesterase 10A (PDE10A) inhibitors. *Bioorg. Med. Chem. Lett.* 25: 4893–4898.
54. Okamura, N., Harada, R., Ishiki, A. et al. (2018). The development and validation of tau PET tracers: current status and future directions. *Clin. Transl. Imaging* 6: 305–316.
55. Rejc, L., Smid, L., Kepe, V. et al. (2018). Design, syntheses, and in vitro evaluation of new fluorine-18 radiolabeled tau-labeling molecular probes. *J. Med. Chem.* 60: 8741–8757.

56. Lowe, D. (2018). How big should your screening collection be? *MedChemComm* 9: 1397–1398.
57. Walters, W.P. (2018). Virtual chemical libraries. *J. Med. Chem.* <https://doi.org/10.1021/acs.jmedchem.8b01048>.
58. Thomford, N.E., Senthebane, D.A., Rowe, A. et al. (2018). Natural products for drug discovery in the 21st century: innovations for novel drug discovery. *Int. J. Mol. Sci.* 19: 1578.
59. Fowler, J.S., Volkow, N.D., Wolf, A.P. et al. (1989). Mapping cocaine binding sites in the human and baboon brain in vivo. *Synapse* 4: 371–377.
60. Clarke, R.L., Daum, S.J., Gambino, A.J. et al. (1973). Compounds affecting the central nervous system. 4. 3 β -Phenyltropane-2-carboxylic acid esters and analogs. *J. Med. Chem.* 16: 1260–1267.
61. Singh, S. (2000). Chemistry, design, and structure-activity relationship of cocaine antagonists. *Chem. Rev.* 100: 925–1024.
62. Riss, P.J., Stockhofe, K., and Roesch, F. (2013). Tropane-derived ¹¹C-labelled and ¹⁸F-labelled DAT ligands. *J. Labelled Compd. Radiopharm.* 56: 149–153.
63. Frost, J.J., Mayberg, H.S., Sadzot, B. et al. (1990). Comparison of [¹¹C]diprenorphine and [¹¹C]carfentanil binding to opiate receptors in humans by positron emission tomography. *J. Cereb. Blood Flow Metab.* 10: 484–492.
64. Madar, I., Lever, J.R., Kinter, C.M. et al. (1996). Imaging of delta opioid receptors in human brain by N1-(¹¹C)methyl)naltrindole and PET. *Synapse* 24: 19–28.
65. Spinelli, F., Mu, L., and Amatemay, S.M. (2018). Radioligands for positron emission tomography imaging of cannabinoid type 2 receptor. *J. Labelled Compd. Radiopharm.* 61: 299–308.
66. Sai, K.K.S., Prabhakaran, J., Ramanathan, G. et al. (2018). Radiosynthesis and evaluation of [¹¹C]HD-800, a high affinity brain permeant PET tracer for imaging microtubules. *ACS Med. Chem. Lett.* 9: 452–456.

Chapter 2

Concepts and Issues for Therapeutic Radiopharmaceuticals

Alexandra R. Sowa Dumond and Peter J.H. Scott

*Department of Radiology, University of Michigan, Ann Arbor, MI,
48109, USA*

2.1 INTRODUCTION

The time since the publication of the first edition of the *Handbook of Radiopharmaceuticals* has seen enormous growth in radiotherapy applications within nuclear medicine and the radiopharmaceutical sciences. *Radiotherapy* is an overarching term that can refer to different applications of radiation toward the treatment of disease. Types of radiotherapy include: (i) external beam radiation, the use of single or multiple beams of radiation produced by a linear accelerator and aimed at a tumor; (ii) brachytherapy, which involves implanting a radiation source near a tumor; and (iii) targeted radiotherapy (also referred to as *radioimmunotherapy* or *radioligand therapy [RLT]*), which involves targeting radiation to a tumor through the use of pharmaceuticals labeled with radionuclides that decay via Auger, alpha (α), beta (β), or gamma (γ) emission. Clinically, the growth in radiotherapy has been in the use of targeted radiotherapeutics for the treatment of cancer, as shown in this chapter, but other emerging applications are also highlighted, including preclinical treatment of infections. Due to the selective nature of radiotherapeutics, targeted radiotherapy offers precise treatment of different subtypes of cancer such as prostate cancer (**PC**), neuroendocrine tumors (**NETs**), and lymphoma, while limiting off-target radiation toxicity effects that can be caused by other therapies such as external beam radiation [1]. In the United States, targeted radiotherapeutic protocols are typically

outpatient procedures, and depending on the mode of decay of different radionuclides, safety precautions must be taken after a patient receives therapy. These include a patient not using public transportation, using a single set of dishes and silverware that is washed separately, and limiting contact with other household members, including recommended use of a separate bathroom.

In its simplest form, a radiotherapeutic is a radionuclide coupled with a targeting moiety such as a monoclonal antibody (**mAb**), peptide, or smaller drug-like molecule. Depending on the radionuclide of choice, the radionuclide can either be bonded to the targeting moiety directly (e.g. ^{131}I ; Figure 2.1a,b) or complexed with an appropriate chelating group in the case of radioactive metal ions (e.g. ^{177}Lu , ^{225}Ac ; Figure 2.1c,d). The disease-targeting moiety can be directly coupled to the radionuclide, creating a one-step radiotherapeutic that is administered to the patient (Figure 2.1a–d). Alternatively, therapy can also involve a two-step biorthogonal process where an antibody for a particular target is administered first, followed by a radiolabeled small molecule that attaches to the antibody *in vivo* (Figure 2.1e). The latter biorthogonal approach is beneficial when the biological equilibration of the primary antibody, which can take days, is much longer than the half-life of the therapeutic radionuclide of choice. Letting the antibody reach the target first, and then treating with radiolabeled small molecules that have faster kinetics and quickly associate with a pre-targeted antibody, increases the effectiveness of the therapy and reduces off-target effects. The most common pre-targeted radiotherapy approach exploits the affinity of biotin for streptavidin or avidin, and recent reviews discuss the ability of pre-targeted radiotherapy to treat systemic malignancies [2, 3].

Nomenclature for targeted radiotherapy is fairly complex, with multiple terms frequently used interchangeably. Radioimmunotherapy (**RIT**), for example, targets diseased cells with mAbs complexed with a radionuclide. *RLT* is another commonly used term.

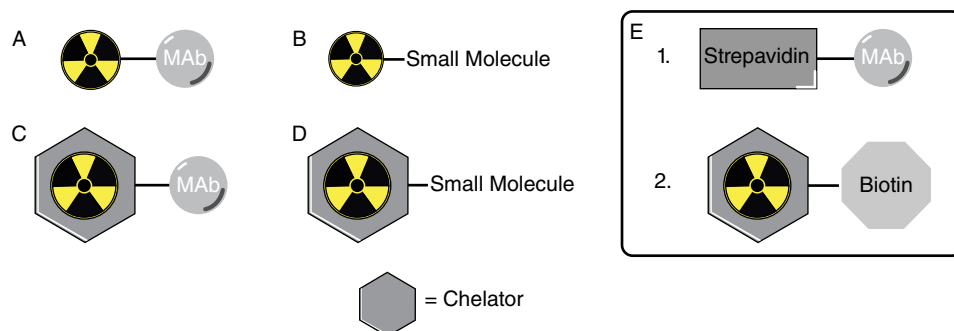


Figure 2.1 (a) Radioisotope bonded directly to a monoclonal antibody. (b) Radioisotope bonded directly to a small molecule. (c) Monoclonal antibody bonded to a chelator that complexes a radiometal. (d) Small molecule bonded to a chelator complexed with a radiometal. (e) Example of a two-step radiotherapeutic approach. Step 1: Tumor-targeting mAb linked to Streptavidin. Step 2: Biotin linked to a chelated radiometal.

One would infer that if *radioimmunotherapy* refers to the use of mAbs, then *radioligand* therapy would refer to non-mAb radiotherapeutics. Radiotherapeutics targeting peptide receptors specifically are sometimes referred to as peptide receptor radionuclide therapy (**PRRT**). As with positron emission tomography (**PET**) and single-photon emission computed tomography (**SPECT**), PRRT, RIT, and RLT benefit the most from exploiting a specific target that is expressed solely on (or inside) cancerous cells in high concentrations (high B_{\max}) and is found in comparatively very low levels in healthy, non-cancerous tissues. Such targeted radiotherapeutics are known as *endoradiotherapies* because they are administered intravenously, as opposed to external beam radiation therapy.

RIT is a powerful tool in cancer treatment that expands on the ability to target specific cells with antibodies. While immunotherapy uses epitope-specific antibodies to target specific cells, the cytotoxic effect of the antibody is limited to the cell on which the antibody binds. When a radionuclide is bound (or chelated) to an antibody, the therapeutic effect is greater [4]. RIT finds the most utility in cancers prone to radiosensitive tumors, such as leukemia and lymphoma. Achieving a significant response in solid tumors can require much higher radiation doses. However, with the development of more specific antibodies and the use of more powerful radionuclides, such as alpha emitters, the benefits of RIT are also having an impressive impact on the treatment of, for example, pancreatic and prostate cancers [5]. Solid tumors are more effectively treated using a pre-targeted RIT approach if injecting the treatment intravenously, or injecting the treatment into the tumor itself (intratumoral injection) or the region/body cavity in which the tumor resides (compartmental injection) [2].

The selection of a radionuclide determines the mode and energy of decay, and therefore the range of effect and potency of a radiotherapeutic. Considerations when selecting a radionuclide for use in radiotherapy include not only characteristics of the radionuclide, but also the feasibility of chemistry with the nuclide, as well as its availability. Matching the half-life of the radionuclide to the physiological half-life of the therapeutic is important to the success of the treatment. Linear energy transfer (**LET**) is an important consideration when choosing a radionuclide. LET ($L\Delta$) is a measure of how much energy a radionuclide deposits into an area. It is calculated by dividing the amount of energy that an ionizing particle emitted by the radionuclide transfers to the material ($dE\Delta$) by the range of the particle in tissue (dx) according to the following equation:

$$L = dE / dx$$

A higher LET indicates a more concentrated area of energy deposition and results in less toxicity to neighboring healthy cells. In larger and/or heterogeneous tumors, a lower LET may be more beneficial as the radiation will travel deeper into the tumor [6]. Radionuclides with lower energy/longer range, and therefore lower LET (e.g. beta emitters), are preferred for treating bulky/poorly vascularized tumors, while radionuclides with higher-energy/shorter-range radionuclides, and therefore higher LET (e.g. alpha emitters), are better for treating small tumors and decreasing toxicity. Beta emitters are more

likely to cause single-strand DNA breaks, while alpha emitters, with higher energy and LET, are more likely to cause double-strand DNA breaks, increasing their effectiveness. Of the therapeutic particle-emitting radionuclides, beta emitters, such as lutetium-177 (^{177}Lu) and yttrium-90 (^{90}Y), appear to be the most commonly used, likely due to their availability and straightforward labeling chemistry. A general comparison of the properties of therapeutic isotope classes can be seen in Table 2.1, while example radionuclides in each category are provided in Table 2.2.

Alpha particles are more desirable for RIT of smaller malignancies, but until recently, the availability of the isotopes and methods of incorporating them into radiopharmaceuticals have been somewhat lacking. This has shifted in recent years, as there has been an increase in efforts toward incorporating alpha-emitting radioisotopes such as bismuth-213 (^{213}Bi), radium-223 (^{223}Ra), and actinium-225 (^{225}Ac) into bioactive molecules because of the higher LET [7]. Use of alpha emitters can lead to a decrease in toxicity and off-target effects compared to beta emitters, but as mentioned previously, alpha-emitting radioisotopes lack the range to target large, heterogeneous, and/or poorly vascularized tumors. Often, alpha-emitting radionuclides decay through a chain of multiple emissions. For example, actinium-225 has a decay chain that includes four alpha decays (Figure 2.2), allowing smaller doses to be administered to patients. Radionuclides that decay through such a chain are sometimes referred to as nano or *in vivo* generators [8].

Radiotherapy used in the clinic typically employs powerful alpha- or beta-emitting radionuclides, but recent studies have found that Auger electron-emitting radionuclides also have therapeutic potential [9]. Auger electrons are negatively charged particles produced by radionuclides that decay via electron capture (EC). With comparably low energy (Table 2.1), and therefore short range within tissue, these particles were not initially

Table 2.1

Comparison of therapeutic atomic particles.

Particle	Energy	Range	LET (linear energy transfer)
Beta (β)	50–2300 keV	0.05–12 mm	0.2 keV mm ⁻¹
Auger electron	eV keV	2–500 nm	4–26 keV mm ⁻¹
Alpha (α)	5–9 MeV	40–100 μm	80 keV mm ⁻¹

Table 2.2 Properties of select therapeutic isotopes (properties of other radioisotopes can be found in Chapters 3–5 on the production of therapeutic radionuclides).

Primary decay mode	Isotope	Mean particle energy	
		(MeV)	Half-life
α	^{225}Ac	6	10 d
	^{223}Ra	5.7	11.4 d
	^{211}At	5.9	7.2 h
	^{213}Bi	6	45.6 min
β	^{89}Sr	1.492	8 d
	^{90}Y	2.28	64 h
	^{177}Lu	0.149	6.6 d
Electron capture (Auger emission)	^{111}In	0.86	2.8 d

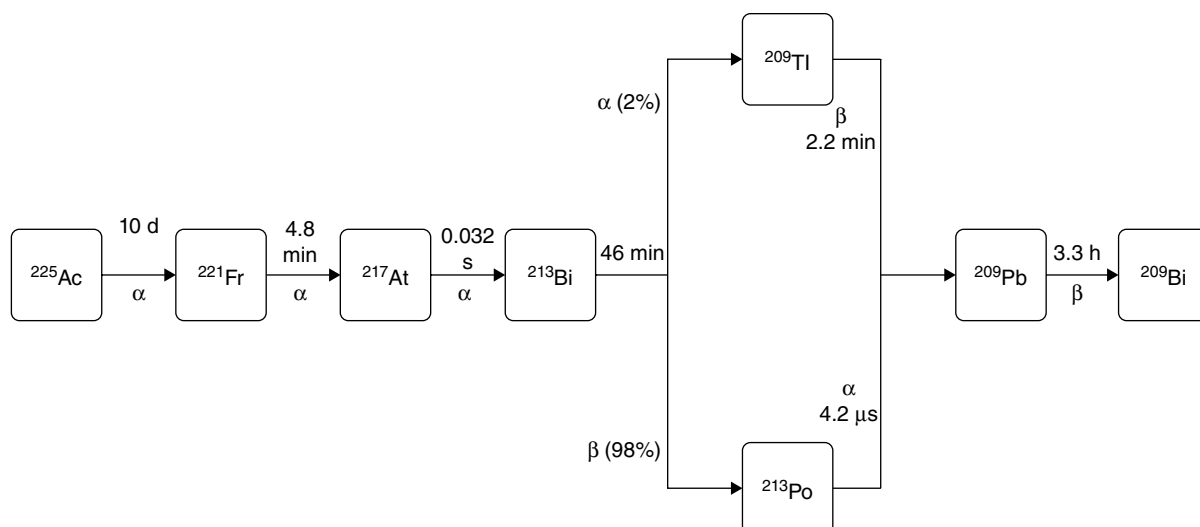


Figure 2.2 Decay chain of ^{225}Ac .

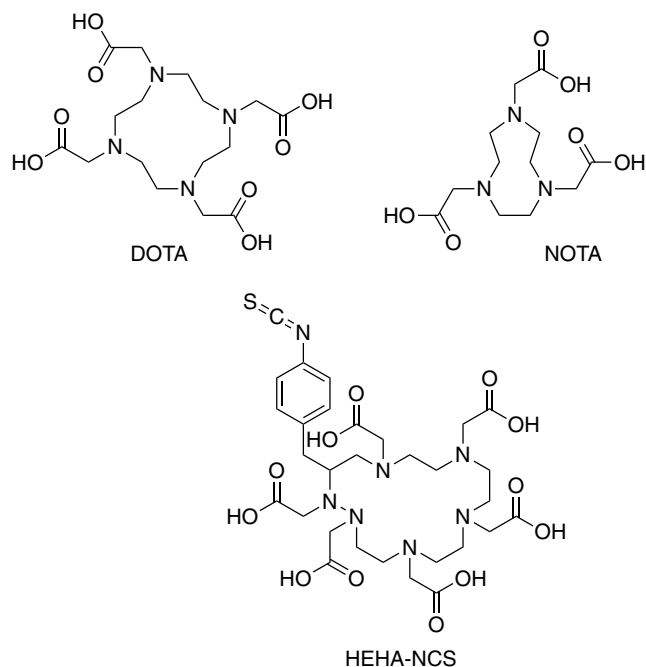
thought to be good candidates for RLT. However, when an Auger electron is emitted, the atom from which it is emitted is left positively charged. It is thought that the neutralization of this atom is compounded with the effect of the Auger electron, resulting in more significant biological effects than just an Auger emission by itself [9]. The challenge with all radiotherapeutics is the ability to position the radionuclide within range of the tumor DNA so that the emitted particles are able to inflict damage and induce cell death. This challenge is especially important for isotopes that emit either alpha particles or Auger electrons due to the short range of the particles.

The majority of commonly used therapeutic radionuclides (except iodine and astatine) are radioactive metal ions that require chelation to a mAb, peptide, or other targeting molecule. In such cases, a chelating moiety is bound to the antibody, peptide, or molecule, and the metal is chelated (examples of chelators are shown in Figure 2.3). The chelating group is determined by the molecule it will be bound to, and both the size and charge of the radionuclide to be chelated. Continual efforts have expanded the library of chelators available with the goal of improving the incorporation of different radionuclides into radiotherapeutics [10, 11].

2.2 THERANOSTICS

Theranostics (*therapeutic + diagnostic*) is a term used to describe pairs of radiolabeled molecules that can be used for both treatment and imaging of disease. There are two main ways that a radiopharmaceutical can be considered a theranostic. First, a radiopharmaceutical can be chelated to two different isotopes with different decay mechanisms and, therefore, different uses. To achieve both excellent images and effective treatment, the same drug/antibody can be bound to either an imaging isotope or a radiotherapy

Figure 2.3 Examples of chelators used in radiotherapeutics.



isotope. For example, new theranostic pairs targeting somatostatin receptors (**SSTRs**) on NETs and prostate-specific membrane antigen (**PSMA**) expressed in PC have been widely utilized in recent years. In each case, the diagnostic agents are (typically) labeled with ^{68}Ga for PET imaging. The same molecules can also be labeled with alpha (^{213}Bi or ^{225}Ac) or beta emitters (^{90}Y or ^{177}Lu) for radiotherapy (see the following discussion and Chapter 18 for specific examples). Radionuclides that have isotopes with use in both therapy and imaging are referred to as *true theranostic pairs*, and examples include scandium-44 and -47 ($^{44}\text{Sc}/^{47}\text{Sc}$) as well as copper-64 and -67 ($^{64}\text{Cu}/^{67}\text{Cu}$). The use of such pairings is especially beneficial in cases where even small changes to the radiotracer or therapeutic disturb its pharmacokinetics. The second theranostic approach involves the use of a single radionuclide, which decays via both a therapeutic particle (alpha or beta) and mechanism suitable for imaging (e.g. positron or gamma). ^{177}Lu is one example of such a radionuclide, as it is a beta-emitting therapeutic isotope but also emits low-energy gamma photons that can provide scintigraphic data. While isotopes such as ^{177}Lu are used for both therapy and imaging, it does remain beneficial to have two separate isotopes for these functions that behave similarly in all aspects besides decay. For example, pairing an isotope that is largely a beta emitter (e.g. ^{47}Sc , ^{177}Lu) with an isotope with a high percentage of positron emission (e.g. ^{44}Sc , ^{68}Ga) can give better images and/or therapeutic results than using an isotope with a split decay path.

2.3 EXAMPLES OF RADIOTHERAPEUTICS

2.3.1 ¹³¹I-MIBG

At the beginning of the new millennium, applications of targeted radiotherapy were fairly limited. Perhaps the best-known example was meta-iodobenzylguanidine (**MIBG**), a nor-epinephrine mimic developed at the University of Michigan in the 1970s [12] (Figure 2.4). The uptake of MIBG is either through norepinephrine transporters or through a non-saturable, passive mechanism [13]. MIBG was originally labeled with either iodine-123 or iodine-131, both for imaging purposes; however, the beta emission of iodine-131 was later noted as being useful for radiotherapy [14]. ¹³¹I-MIBG was approved in June 2018 by the Food and Drug Administration (**FDA**) for radiotherapy of certain cancers. Production of ¹³¹I-MIBG with no-carrier-added (**n.c.a**) iodine has shown better results than traditional ¹³¹I-MIBG as there is less non-radioactive product in the higher-specific-activity dose. Prior to treatment, patients' thyroid glands are protected against free radioiodine by pretreatment with, for example, potassium iodide. Hyperthyroidism can still develop in patients after treatment, however, and should be accounted for. ¹³¹I-MIBG has shown better uptake in low-grade/well-differentiated tumors than higher-grade/poorly differentiated tumors. The most common toxicity with ¹³¹I-MIBG treatment is hematotoxicity. This is more common in patients with metastasis in the bone marrow, and the risk increases as the whole-body dose increases [13]. Results of treatment with ¹²³I-MIBG over a 14-month period can be seen in Figure 2.5 [15].

Recently, the parent benzoguanidine molecule has been labeled with astatine-211 (Figure 2.6), which decays via alpha particle emission, resulting in a more powerful treatment for brain tumors, especially smaller tumors. The use of the alpha-emitting astatine-211 has also resulted in less toxicity among patients, although further studies are needed to fully characterize this treatment path [13].

2.3.2 Radiotherapy of Bone Metastases

Radionuclide therapy is a common treatment for painful bone metastases in many types of cancer. Radionuclides such as radium-223 and strontium-89 have a natural affinity for bone with increased metabolic activity, while other radionuclides require the formation of a complex with bone-seeking cations such as phosphates. In the latter case, beta-emitting radiophosphorus in the form of ³²P-sodium orthophosphate has been used in the treatment of bone pain. The ease of oral administration and comparable affordability make radiophosphorus a popular treatment option throughout the world [16].

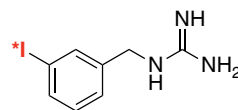


Figure 2.4
Meta-iodobenzylguanidine.

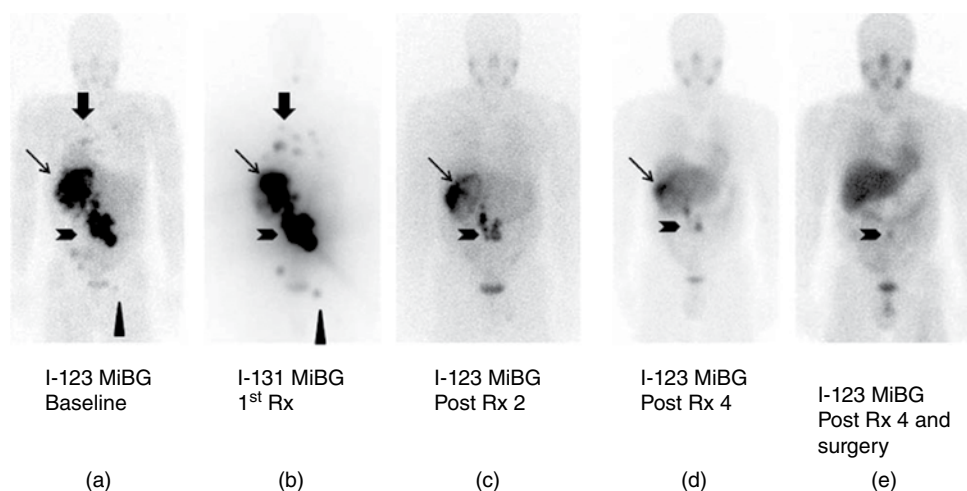
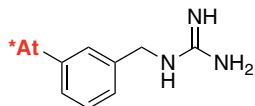


Figure 2.5 Serial I-123 MIBG anterior whole-body images. (a) The patient had unresectable primary PHEO of the right adrenal (upper thin arrow) and metastatic disease to retroperitoneal nodes (chevron), pelvis (arrowhead), and ribs and bilateral lung (thick upper arrow). He received four treatments consisting of 204–243 mCi and cumulative 873 mCi of I-131 MIBG over a 14-month period. (b) The initial I-131 MIBG is shown to illustrate tumor targeting post-first treatment; because of higher counts, lesions are seen better than on the diagnostic baseline scan. (c) MIBG imaging post-second treatment shows the disappearance of bone and lung lesions and shrinkage of other lesions. (d) Images post-fourth treatment show continued improvement that allowed for debulking surgery. (e) This panel shows images after the fourth I-131 MIBG treatment and 14 months post-surgery. Source (a–e): Reproduced from Carrasquillo et al. [15] with the permission of John Wiley and Sons. © 2012, Wiley Periodicals, Inc.

Figure 2.6 Meta-astatoben-zylguanidine.



Another beta emitter, ^{89}Sr , is paired with its true theranostic partner, the gamma-emitting ^{85}Sr , for biodistribution studies. While $^{89}\text{SrCl}_2$ localizes to metabolically active bone, a study comparing it to palliative radiotherapy suggested that the associated myelotoxicity, and decreased heme in the $^{89}\text{SrCl}_2$ -treated patients, lead to a lower survival rate versus local field radiotherapy [17]. ^{223}Ra RaCl₂ (Xofigo) was the first alpha emitter to be approved by the FDA in May 2013 and is indicated as the first-line treatment for castration-resistant PC with symptomatic bone metastases (Figure 2.7) [18, 19]. Clinical trials using Xofigo alone or in combination with other treatments are ongoing in patients with other cancers with skeletal metastases [19]. Like calcium, radium accumulates in areas of bone with increased levels of metabolism. Owing to the short range of alpha particles, ^{223}Ra RaCl₂ is able to target bone metastases without high toxicity to the surrounding

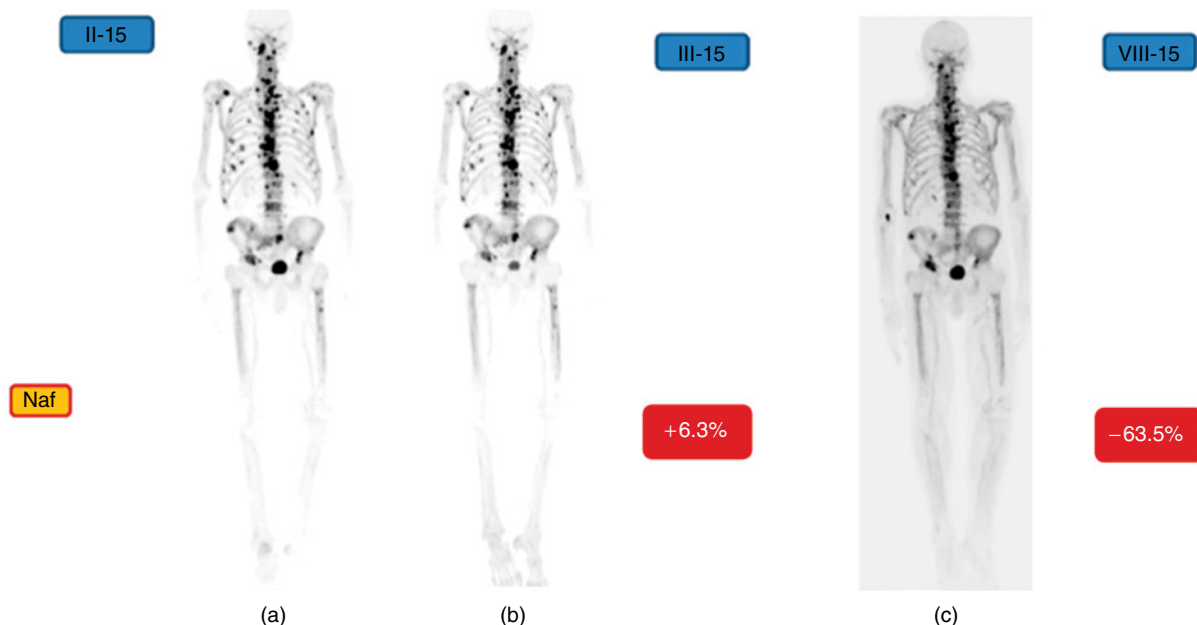


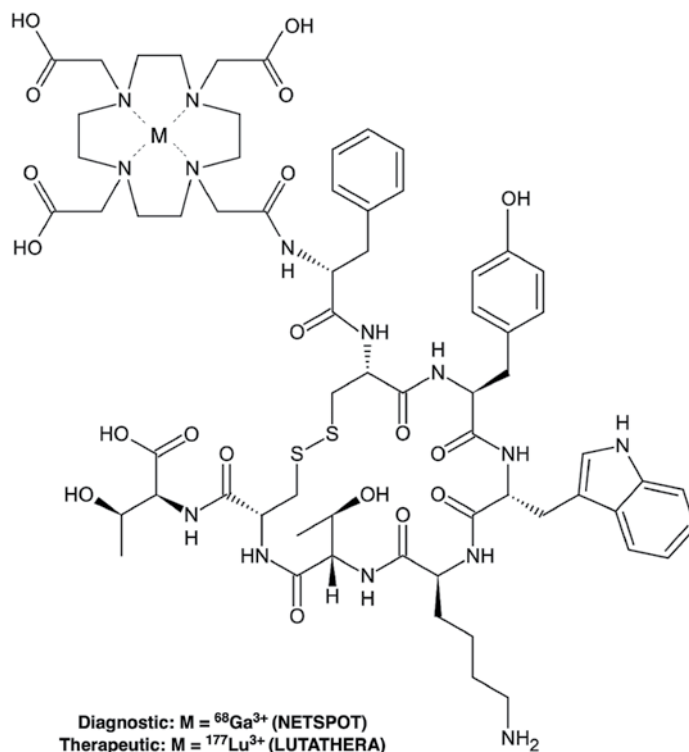
Figure 2.7 An old patient (83years) with Gleason score 6. (a) The NaF-PET before the Ra-223 treatment of six cycles is shown (II-15). Source: Imaged reproduced from Kairemo and Joensuu 2015 [18] under the terms and conditions of the Creative Commons Attribution license (<http://creativecommons.org/licenses/by/4.0>). (b) No essential response to the treatment was seen after the first cycle (+6.3% change, III-15). Source: Imaged reproduced from Kairemo and Joensuu 2015 [18] under the terms and conditions of the Creative Commons Attribution license (<http://creativecommons.org/licenses/by/4.0>). (c) After six cycles, a dramatic response was seen (-63.5% change, VIII-15). Many of the lesions have disappeared, especially in the thoracic girdle. Source: Imaged reproduced from Kairemo and Joensuu 2015 [18] under the terms and conditions of the Creative Commons Attribution license (<http://creativecommons.org/licenses/by/4.0>).

areas such as bone marrow [20]. Unfortunately, radium cannot be effectively chelated, so its use in other tumor-targeting radiotherapeutics is currently limited [21].

2.3.3 Somatostatin Receptor-Targeted Ligands

The discovery that SSTRs are expressed on NET cells has opened up new possibilities for diagnosing and treating patients with NETs. A number of radiopharmaceuticals targeting SSTRs have been developed, based on peptides such as (Tyr³)-octreotide (**TOC**) and (Tyr³-Thr⁶)-octreotide (**TATE**) with an affinity for SSTRs. These peptides can be functionalized with a chelating group such as DOTA (Figure 2.3) and labeled with diagnostic or therapeutic radionuclides. From an imaging perspective, [⁶⁸Ga]DOT-ATATE (Figure 2.8) is FDA approved and marketed in the United States under the name

Figure 2.8
NETSPOT and
Lutathera.



NETSPOT. In Europe, [^{68}Ga]DOTATOC is approved and marketed as SomaKit TOC. Substituting the radioisotope for the beta-emitting ^{177}Lu gives Lutathera (^{177}Lu -DOTATATE, Figure 2.8), a radiotherapeutic used for the treatment of SSTR-positive NETs, and the first approved PRRT [22]. Treatment of NETs with beta therapeutics such as Lutathera has proven effective for treating NETs. In addition to the treatment of NETs, Lutathera and related therapies such as ^{90}Y -DOTATOC are finding use in the treatment of other metastatic cancers that exhibit high expression of SSTRs, such as lung carcinoids (Figure 2.9) [23]. Prior to treatment with Lutathera, tumors are evaluated via imaging with NETSPOT or SomaKit TOC (and sometimes biopsy) to confirm SSTR expression and patient eligibility for therapy. Lutathera shows selectivity for SSTR2 over other SSTRs [21] and is approved by the FDA, European Medicines Agency (EMA), and Health Canada regulatory agencies.

In certain cases, tumors do not respond to beta therapy (with either Lutathera or alternate treatments such as ^{90}Y -DOTATOC), so alternate versions labeled with alpha emitters are also under development. For example, a clinical study of patients shown to be refractory to DOTATOC or beta-emitter-labeled DOTATOC therapy showed that the targeted alpha therapy (TAT) of ^{213}Bi -DOTATOC could halt the progression of the disease, as well as eliminate some tumor burden. In this study, the radiotherapeutic was administered intra-arterially to better directly target the tumors [24].

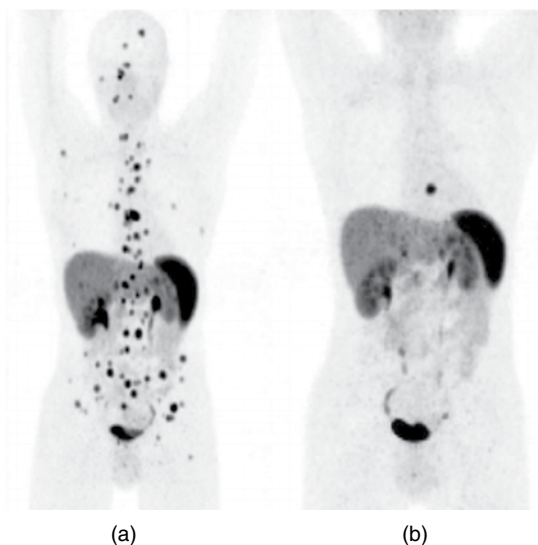


Figure 2.9 Atypical carcinoid patient referred for restaging with Ga-68 DOTATOC PET/CT and treated with three cycles of peptide receptor radionuclide therapy (PRRT; two cycles of Y-90 DOTATOC and one cycle of Lu-177 DOTATATE) showing excellent response. (a) Ga-68 DOTATOC maximum-intensity projection images before PRRT. Source: Reproduced From Prasad et al. 2015 [23], under a Creative Commons License (<https://creativecommons.org/licenses/by/2.0>). (b) Ga-68 DOTATOC maximum-intensity projection images 22 months after first PRRT. Source: Reproduced From Prasad et al. 2015 [23], under a Creative Commons License (<https://creativecommons.org/licenses/by/2.0>).

2.3.4 Prostate-Specific Membrane Antigen

Levels of prostate-specific antigen (**PSA**) are used in the evaluation and detection of PC. The development of peptide-based inhibitors of this antigen has resulted in both imaging and therapeutic agents with unparalleled results. Small molecule PSMA-targeting ligands are urea-based molecules that are internalized by PSMA (see [25] and Figure 2.10, for example). PSMA is significantly upregulated in PC, and this upregulation, in conjunction with the internalization of exogenous PSMA ligands, provides ideal conditions for RLT of PC and associated metastases. This treatment typically utilizes PSMA-617 [26, 27] but can also use PSMA-I&T (imaging and therapy) [28] and has shown promise in multiple human studies. For example, phase III clinical trials of ^{177}Lu -PSMA-617 are underway and, while ^{177}Lu -PSMA-617 is not yet approved, the studies have demonstrated that the agent is an effective treatment for PC (Figure 2.11). Side effects may include dry mouth syndrome as a result of off-target binding to PSMA expressed in salivary glands. Multiple techniques have been used to prevent/relieve these symptoms, including the use of Botox injections, or external cooling in the salivary/parotid glands, to block uptake of the radiotherapeutic and prevent the decrease in saliva production [29, 30].

Concomitant with the development of PSMA beta therapy, PSMA alpha therapy with ^{225}Ac or ^{211}At for the treatment of metastatic castration-resistant prostate cancer

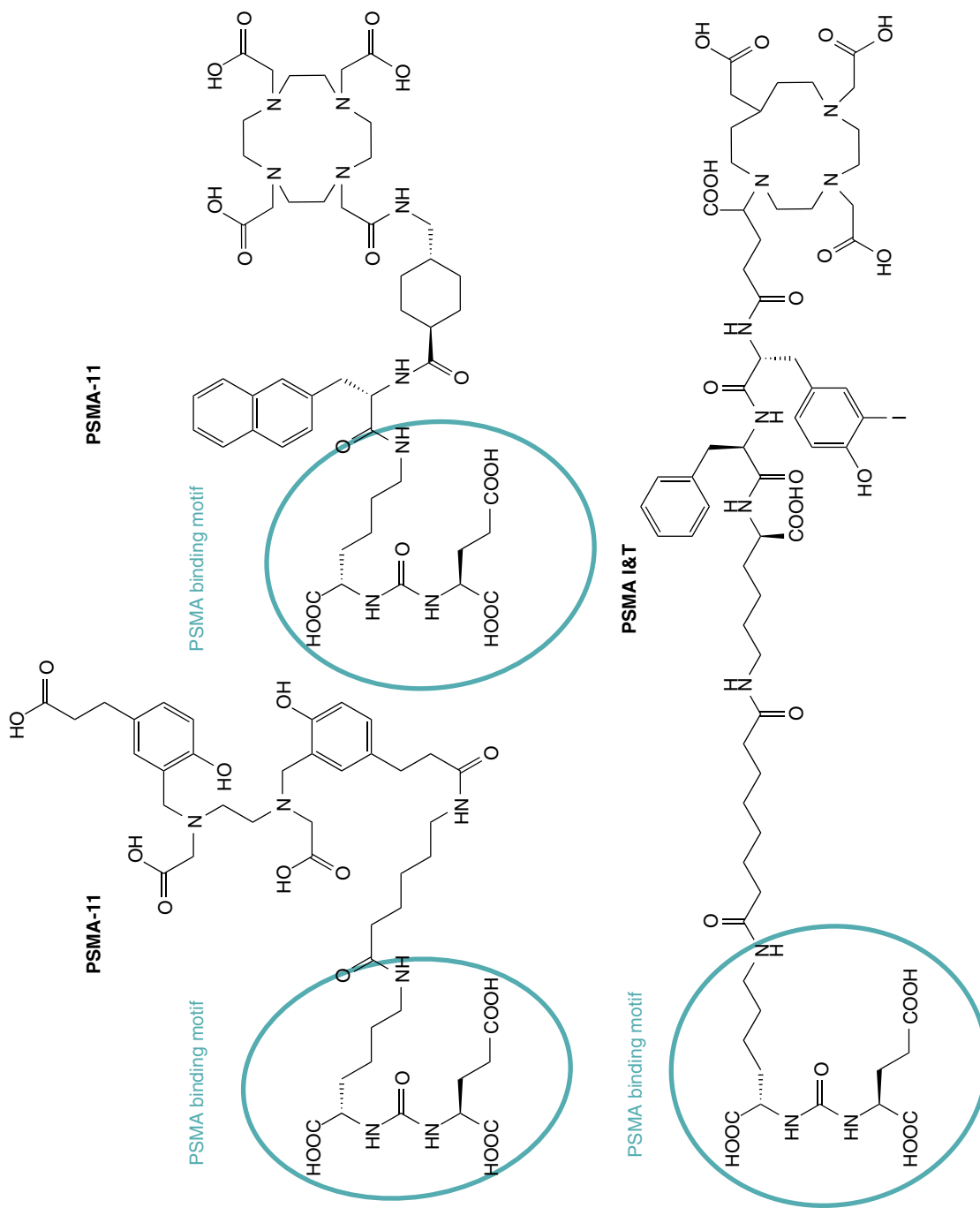


Figure 2.10 Chemical structures of small-molecule PSMA inhibitors PSMA-11, PSMA-617, and PSMA I&T. Source: Chatalic, K.L.S., Heskamp, S., Konijnenberg, M. et al. [25]. Licensed under CC BY 4.0.

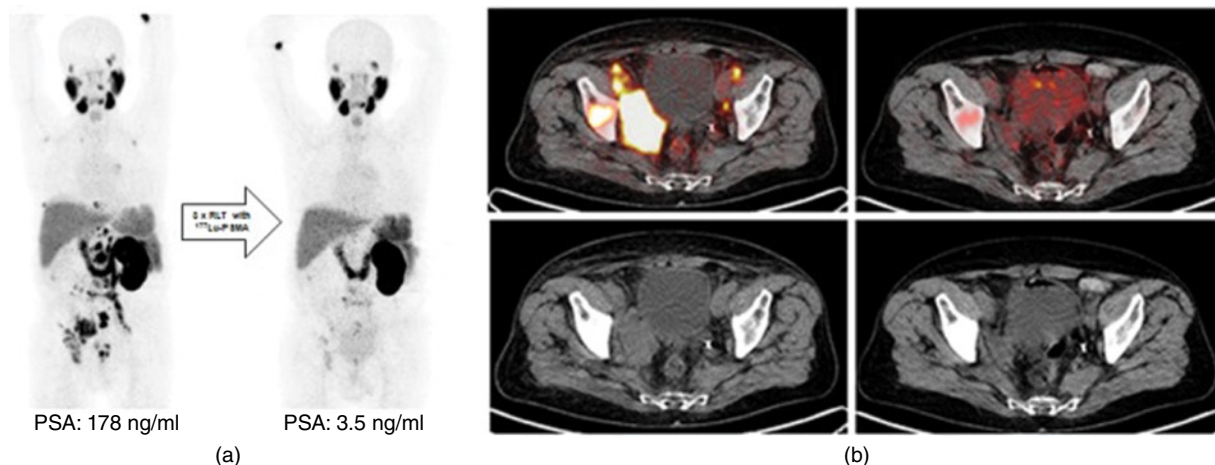


Figure 2.11 (a) ^{68}Ga -PSMA11-PET images of a 66-year-old patient with castration-resistant prostate cancer pretreated with docetaxel, abiraterone, and six cycles of ^{223}Ra radium. Maximum intensity projection (MIP) on the left side shows multiple bone and lymph node lesions. Patient was treated with three cycles of ^{177}Lu -PSMA-617 radioligand therapy with a cumulative activity of 13.5 GBq (reduced activity because of single kidney). The MIP images on the right side show significant reduction in prostate-specific membrane antigen (PSMA)-positive lesions in correlation with a PSA decline of 99%. Source: Reproduced from Rahbar et al. 2018 [27] under a Creative Commons License (<https://creativecommons.org/licenses/by-nc/4.0>). (b) Fused images of ^{68}Ga -PSMA11-positron emission tomography/computed tomography (PET/CT). Images in the upper row show a significant reduction in PSMA-positive lesions. Low-dose CT images (lower row) show a significant volume reduction in soft tissue lesions (especially in the right pelvis). Source: Reproduced from Rahbar et al. 2018 [27] under a Creative Commons License (<https://creativecommons.org/licenses/by-nc/4.0>).

(mCRPC) is also being investigated. With a higher LET and multiple alpha particles in their decay cascades, these isotopes have been successful in treating cancer with smaller doses as compared to beta-emitting isotopes. For example, ^{225}Ac -PSMA-617 has shown excellent results in patients with mCRPC. ^{225}Ac -PSMA treatment has also been successful in both chemotherapy-resistant and naïve patients, and where beta therapy with ^{177}Lu -PSMA failed [25, 31, 32].

TAT with ^{225}Ac -PSMA has also been employed in patients who have a contraindication for beta-emitting therapy (e.g. diffuse red marrow infiltration) and patients showing progression during or after treatment with ^{177}Lu -PSMA-617. Due to the transient nature of radionuclides, and because each of the nuclides in the decay chain has different properties, it is likely that they free themselves from the chelating group attached to the targeting moiety. When radiotherapeutics are bound to the cell surface, the dissociated radionuclide can be rapidly circulated away from the targeted area, potentially decreasing treatment efficacy and increasing toxicity. However, as PSMA-617 is internalized by the PSMA expressing cell, the parent radionuclide and its daughters remain internalized in the cancerous cell. Clinical studies have demonstrated positive results after two or three cycles of ^{225}Ac -PSMA-617 therapy in a range of PC patients (Figure 2.12) [31, 32].

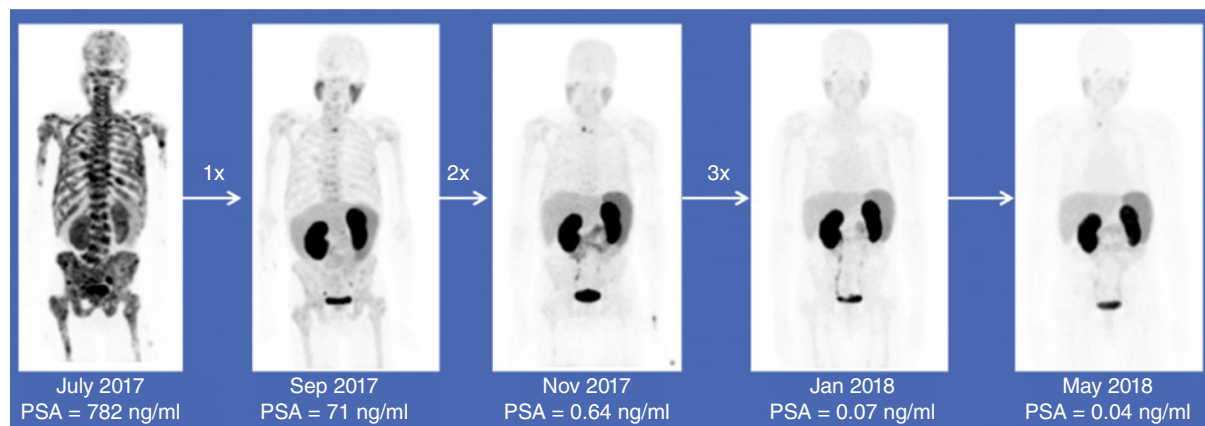


Figure 2.12 A treatment-naïve patient who presented with extensive bone metastasis at primary diagnosis achieved complete remission after three cycles of ^{225}Ac -PSMA-617 with de-escalating activities of 8/7/6 MBq. He also remained symptom-free on 11-month follow-up with his serum PSA remaining below the detectable level and the follow-up ^{68}Ga -PSMA-11 PET/CT scan remaining negative for disease recurrence. Source: Reproduced from Sathekge et al. 2019 [32] under the terms of the Creative Commons Attribution 4.0 International License (<http://creativecommons.org/licenses/by/4.0>).

2.3.5 Lymphoma and Leukemia

Immunotherapy and RIT strategies have been investigated for the treatment of leukemia and lymphomas. These mAb-based therapies are compatible with malignancies in the blood, bone marrow, and lymph nodes. As a large percentage of lymphomas are B-cell derived, the targeting of the B-cell specific epitope CD20 led to advances in lymphoma treatment. One such example is the use of ^{131}I -tositumomab, developed as Bexxar. Bexxar is a treatment using both the ^{131}I -labeled, CD20-specific antibody tositumomab as well as the non-radioactive version. The non-radioactive antibody is administered first with the goal of saturating the CD20 epitope on non-malignant B-cells. This is also thought to extend the time the radiolabeled antibody spends in circulation, allowing longer for perfusion of the therapeutic into the tumor [4]. Currently, Bexxar is no longer used in the clinic as GlaxoSmithKline stopped producing it in 2014.

Another CD20-targeting immunotherapy involving a two-part treatment regimen, Zevalin was first introduced as an alternative to Bexxar and boasted the use of yttrium-90 as an advantage. ^{90}Y has a half-life of 64 hours, or one-third that of ^{131}I ($t_{1/2} = 193$ hours). Also, as a pure beta emitter, the use of ^{90}Y means a decrease in the whole-body dose for the patient compared to the use of ^{131}I . The non-radioactive antibody rituximab is administered first, followed by ^{90}Y -ibritumomab tiuxetan. The FDA still requires imaging with the ^{111}In -labeled antibody to confirm normal distribution [4] prior to commencing treatment. During treatment, the initial administration of the non-radioactive rituximab is beneficial in the saturation of peripheral B-cells [6].

Comparing Bexxar and Zevalin, the most obvious difference is the radioisotope in use. ^{131}I has both beta and gamma emissions, with the advantage of simultaneously allowing

for imaging and therapy. Conversely, the gamma emissions detectable outside of the body give iodine a more complicated post-treatment protocol and a higher chance of those around the patient receiving a small dose of radiation. Zevalin, with its use of ^{90}Y , primarily has a beta emission, making post-treatment less complicated, but precautions are still taken with patients' interactions with family members or other people.

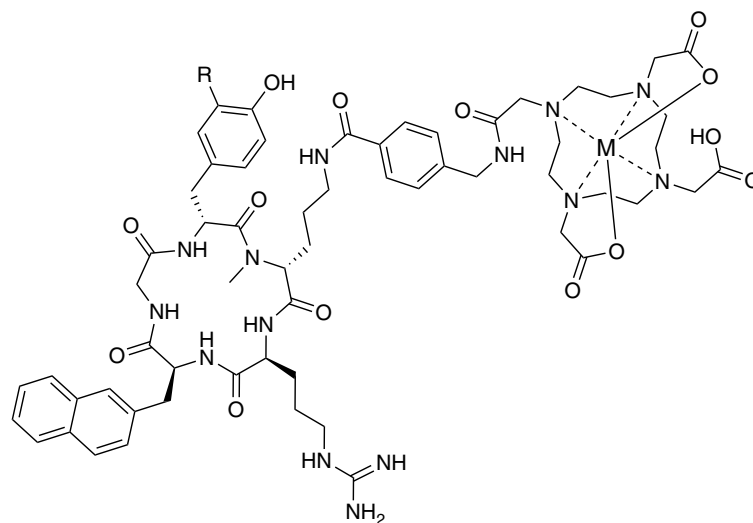
In the treatment of leukemia, CD33 has been identified as a myeloid leukemia cell-specific glycoprotein. Anti-CD33 antibodies such as M195 and lintuzumab carrying beta-emitting isotopes (e.g. ^{131}I , ^{90}Y) have previously shown promise in treating leukemia [33]. However, as beta particles have a lower LET (travel a further distance in tissue), such treatments came with side effects. In efforts to improve the therapeutic strategy, alpha therapeutics such as ^{213}Bi -lintuzumab have also been investigated. ^{213}Bi also emits a photon during decay, enabling *in vivo* imaging of the distribution of the therapeutic. A phase I/II clinical trial was completed with ^{213}Bi -lintuzumab, in conjunction with cytarabine chemotherapy. The pretreatment was implemented as it was believed that the chemotherapeutic would lessen the tumor burden to a level where the ^{213}Bi alpha therapy would have an increased effect on the tumors [7]. The proof of principle study demonstrated that this treatment is tolerable, and clinical responses were seen in 6 out of the 25 patients involved in the trial.

Hematological cancers such as lymphoma and leukemia are also characterized by an overexpression of CXC-chemokine receptor-4 (**CXCR4**). CXCR4 expression has been found to be upregulated in a number of human tumor cells. In addition, the high expression of these cells has been found to be an indicator in the presence and prevalence of distant metastases. This receptor and its only ligand, CXCL12, are key communicators in the proliferation of malignant cells. The targeting of the CXCR4/CXCL12 pair has resulted in the development of many treatment modalities, only one of which is FDA approved: AMD3100 (Plerixafor/Mozobil). [^{68}Ga]Pentixafor (Figure 2.13) was a product of efforts toward an imaging agent to better quantify patients' CXCR4 levels and therefore aid in confirming eligibility for a CXCR4/CXCL12 therapeutic strategy. While other PET drugs can be directly translated to therapy with the substitution of the radiometal (e.g. DOTATATE), small changes to ^{68}Ga -Pentixafor caused large changes in its affinity for CXCR4 [34]. To address this issue, the addition of iodine to the meta-position of the tyrosine in the peptide backbone allowed the use of the beta-emitting radionuclide lutetium-177 while maintaining CXCR4 affinity, resulting in ^{177}Lu -pentixather [34] (Figure 2.13). ^{177}Lu -Pentixather has been utilized in early clinical trials where preliminary results treating patients with extramedullary relapsed multiple myelomas were highly promising (Figure 2.14) [35].

2.3.6 Treatment of Viral, Fungal, and Infectious Diseases with Radiotherapy

While most radiotherapy is targeted at cancer, it is also being evaluated in the treatment of viral, fungal, and bacterial infectious diseases. In this context, radiotherapy is appealing for some of the same reasons it is an attractive strategy for cancer treatment: using

Figure 2.13 Pentixafor and Pentixather.



Diagnostic: R = H, M = $^{68}\text{Ga}^{3+}$ (Pentixafor)
Therapeutic: R = I, M = $^{177}\text{Lu}^{3+}$ (Pentixather)

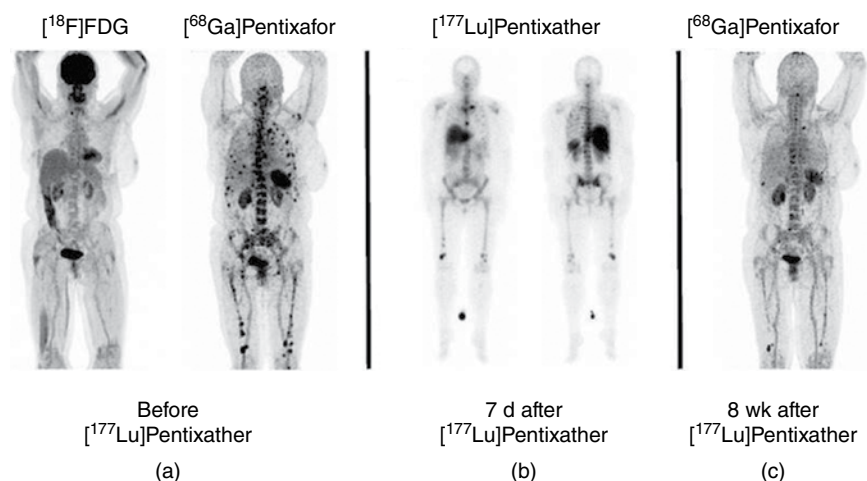


Figure 2.14 Example of partial response to CXCR4-directed treatment with ^{177}Lu Pentixather. (a) Maximum intensity projection (MIP) of ^{68}Ga Pentixafor- and ^{18}F FDG-PET/CT of patient #4 prior to Pentixather therapy, indicating high CXCR4-expression in multiple intramedullary ^{18}F FDG-negative myeloma lesions. Source: Reproduced from Lapa et al. 2017 [35] under a Creative Commons License (<https://creativecommons.org/licenses/by-nc/4.0>). (b) Scintigraphic images of patient #4 7 days after administration of 7.8 GBq ^{177}Lu Pentixather, confirming the long-lasting binding to the CXCR4-target after treatment. The patient is seen from ventral (left) and dorsal (right). Source: From Lapa et al. 2017 [35] under a Creative Commons License (<https://creativecommons.org/licenses/by-nc/4.0>). (c) MIP of ^{68}Ga Pentixafor-PET/CT eight weeks after ^{177}Lu Pentixather therapy, displaying partial response with the disappearance of most of the myeloma manifestations. In concordance, serological response was assessed as stable disease. Source: Reproduced from Lapa et al. 2017 [35] under a Creative Commons License (<https://creativecommons.org/licenses/by-nc/4.0>).

targeted molecules or antibodies leads to fewer off-target effects. In addition, radiotherapy is desirable for the treatment of infectious diseases because viral, fungal, and bacterial infections have become increasingly resistant to current standards of care. Many patients who experience these infections are already immunocompromised due to chemotherapy, HIV infections, or adjusting to organ transplants. Radiotherapy has already been shown to be tolerable in patients that fit these categories, most of all those with a history of chemotherapy treatments [36, 37]. *In vitro* and *in vivo* studies in mice of various antibodies labeled with alpha- and beta-emitting radioisotopes have shown the effectiveness of this therapy on infections such as *Streptococcus pneumoniae* or biofilms [38, 39]. However, applications of these treatments in a clinical setting have yet to be disclosed.

2.4 SUMMARY AND FUTURE OUTLOOK

Targeted radiotherapy is an exciting area of growth in the radiopharmaceutical sciences and nuclear medicine that is showing remarkable results primarily in the treatment of a variety of tumors and associated metastases, but also in other emerging areas such as treatment of infection. The therapeutics described in this chapter are in various states of investigation and regulatory approval, with a recent increase in the interest and use of alpha-emitting radionuclides such as ^{225}Ac and ^{211}At [40]. While targeted radiotherapy is advancing quickly thanks to many studies demonstrating an increase in response rates, there is still urgency around a reliable pipeline of both therapeutic radionuclides and formulated radiotherapeutics. For example, while ^{225}Ac -PSMA-617 has shown to be very effective in the attenuation of this disease, the current supply chain of ^{225}Ac is not sufficient to provide the necessary therapy to the current population living with mCRPC [41]. Reflecting this, there is significant research being done to establish reliable methods for the production of ^{225}Ac , which is essential to support the anticipated growth in alpha therapy use in the coming years.

REFERENCES

1. Govindan, S.V., Goldenberg, D.M., Hansen, H.J., and Griffiths, G.L. (2000). Advances in the use of monoclonal antibodies in cancer radiotherapy. *Pharm. Sci. Technol. Today* 3 (3): 90–98.
2. Larson, S.M., Carrasquillo, J.A., Cheung, N.K., and Press, O.W. (2015). Radioimmunotherapy of human tumours. *Nat. Rev. Cancer* 15 (6): 347–360.
3. Sharkey, R.M., Karacay, H., Cardillo, T.M. et al. (2005). Improving the delivery of radionuclides for imaging and therapy of cancer using pretargeting methods. *Clin. Cancer Res.* 11 (19): 7109s–7121s.
4. Goldsmith, S.J. (2010). Radioimmunotherapy of lymphoma: Bexxar and Zevalin. *Semin. Nucl. Med.* 40 (2): 122–135.
5. Poty, S., Francesconi, L.C., McDevitt, M.R. et al. (2018). α -Emitters for radiotherapy: from basic radiochemistry to clinical studies – part 2. *J. Nucl. Med.* 59 (7): 1020–1027.

6. Wiseman, G.A., White, C.A., Sparks, R.B. et al. (2001). Biodistribution and dosimetry results from a phase III prospectively randomized controlled trial of Zevalin™ radio-immunotherapy for low-grade, follicular, or transformed B-cell non-Hodgkin's lymphoma. *Crit. Rev. Oncol. Hematol.* 39: 181–194.
7. Rosenblat, T.L., McDevitt, M.R., Mulford, D.A. et al. (2010). Sequential cytarabine and α -particle immunotherapy with bismuth-213-lintuzumab (HuM195) for acute myeloid leukemia. *Clin. Cancer Res.* 16 (21): 5303–5311.
8. Poty, S., Francesconi, L.C., McDevitt, M.R. et al. (2018). α -emitters for radiotherapy: from basic radiochemistry to clinical studies – part 1. *J. Nucl. Med.* 59 (6): 878–884.
9. Kassis, A.I. (2003). Cancer therapy with Auger Electrons: are we almost there? *J. Nucl. Med.* 44 (9): 1479–1481.
10. Chappell, L.L., Deal, K.A., Dadachova, E., and Brechbiel, M.W. (2000). Synthesis, conjugation, and radiolabeling of a novel bifunctional chelating agent for ^{225}Ac radioimmunotherapy applications. *Bioconjugate Chem.* 11 (4): 510–519.
11. Kelly, J.M., Amor-Coarasa, A., Nikolopoulou, A. et al. (2017). Assessment of PSMA targeting ligands bearing novel chelates with application to theranostics: stability and complexation kinetics of $^{68}\text{Ga}^{3+}$, $^{111}\text{In}^{3+}$, $^{177}\text{Lu}^{3+}$ and $^{225}\text{Ac}^{3+}$. *Nucl. Med. Biol.* 55: 38–46.
12. Wieland, D.M., Brown, L.E., Rogers, W.L. et al. (1981). Myocardial imaging with a radioiodinated norepinephrine storage analog. *J. Nucl. Med.* 22 (1): 22–31.
13. Kayano, D. and Kinuya, S. (2018). Current consensus on I-131 MIBG therapy. *Nucl. Med. Mol. Imaging* 52 (4): 254–265.
14. Voo, S., Bucerius, J., and Mottaghy, F.M. (2011). I-131-MIBG therapies. *Methods* 55 (3): 238–245.
15. Carrasquillo, J.A., Pandit-Taskar, N., and Chen, C.C. (2012). Radionuclide therapy of adrenal tumors. *J. Surg. Oncol.* 106 (5): 632–642.
16. Lewington, V.J. (2005). Bone-seeking radionuclides for therapy. *J. Nucl. Med.* 46 (Suppl. 1): 38S–47S.
17. Oosterhof, G.O.N., Roberts, J.T., De Reijke, T.M. et al. (2003). Strontium (89) chloride versus palliative local field radiotherapy in patients with hormonal escaped prostate cancer: a phase iii study of the European Organisation for Research and Treatment of Cancer Genitourinary Group. *Eur. Urol.* 44 (5): 519–526.
18. Kairemo, K. and Joensuu, T. (2015). Radium-223-dichloride in castration resistant metastatic prostate cancer – preliminary results of the response evaluation using F-18-Fluoride PET/CT. *Diagnostics* 5: 413–427.
19. Makvandi, M., Dupis, E., Engle, J.W. et al. (2018). α -Emitters and targeted α therapy in oncology: from basic science to clinical investigations. *Target Oncol.* 13 (2): 189–203.
20. Hoskin, P., Sartor, O., O'Sullivan, J.M. et al. (2014). Efficacy and safety of radium-223 dichloride in patients with castration-resistant prostate cancer and symptomatic bone metastases, with or without previous docetaxel use: a prespecified subgroup analysis from the randomised, double-blind, phase 3 ALSYMPCA trial. *Lancet Oncol.* 15 (12): 1397–1406.
21. Hagemann, U.B., Wickstroem, K., Wang, E. et al. (2016). In vitro and in vivo efficacy of a novel CD33-targeted thorium-227 conjugate for the treatment of acute myeloid leukemia. *Mol. Cancer Ther.* 15 (10): 2422–2431.

22. Hennrich, U. and Kopka, K. (2019). Lutathera®: the first FDA- and EMA-approved radiopharmaceutical for peptide receptor radionuclide therapy. *Pharmaceuticals (Basel)* 12 (3): 114.
23. Prasad, V., Steffen, I.G., Pavel, M. et al. (2015). Somatostatin receptor PET/CT in restaging of typical and atypical lung carcinoids. *EJNMMI Res.* 5: 53.
24. Kratochwil, C., Giesel, F.L., Bruchertseifer, F. et al. (2014). ²¹³Bi-DOTATOC receptor-targeted α -radionuclide therapy induces remission in neuroendocrine tumours refractory to β radiation: a first-in-human experience. *Eur. J. Nucl. Med. Mol. Imaging* 41 (11): 2106–2119.
25. Chatalic, K.L.S., Heskamp, S., Konijnenberg, M. et al. (2016). Towards personalized treatment of prostate cancer: PSMA I&T, a promising prostate-specific membrane antigen-targeted theranostic agent. *Theranostics* 6 (6): 849–861.
26. Fendler, W.P., Rahbar, K., Herrmann, K. et al. (2017). ¹⁷⁷Lu-PSMA radioligand therapy for prostate cancer. *J. Nucl. Med.* 58 (8): 1196–1200.
27. Rahbar, K., Afshar-Oromieh, A., Jadvar, H., and Ahmadzadehfar, H. (2018). PSMA theranostics: current status and future directions. *Mol. Imaging* 17: 1–9.
28. Baum, R.P., Langbein, T., Singh, A. et al. (2018). Injection of botulinum toxin for preventing salivary gland toxicity after PSMA radioligand therapy: an empirical proof of a promising concept. *Nucl. Med. Mol. Imaging.* 52 (1): 80–81.
29. Yilmaz, B., Nisli, S., Ergul, N. et al. (2019). Effect of external cooling on ¹⁷⁷Lu-PSMA uptake by the parotid glands. *J. Nucl. Med.* 60 (10): 1388–1393.
30. Hofman, M., Violet, J., Sandhu, S. et al. (2018). High activity, pain reduction and low toxicity with Lutetium-177 PSMA617 theranostics in metastatic castrate-resistant prostate cancer (mCRPC): results of a phase II prospective trial. *J. Nucl. Med.* 59 (Suppl 1): 531.
31. Kratochwil, C., Bruchertseifer, F., Giesel, F.L. et al. (2016). ²²⁵Ac-PSMA-617 for PSMA-targeted α -radiation therapy of metastatic castration-resistant prostate cancer. *J. Nucl. Med.* 57 (12): 1941–1944.
32. Sathekge, M., Bruchertseifer, F., Knoesen, O. et al. (2019). ²²⁵Ac-PSMA-617 in chemotherapy-naïve patients with advanced prostate cancer: a pilot study. *Eur. J. Nucl. Med. Mol. Imaging* 46 (1): 129–138.
33. Jurcic, J.G. (2000). Antibody immunotherapy for leukemia. *Curr. Oncol. Rep.* 2 (2): 114–122.
34. Kircher, M., Herhaus, P., Schottelius, M. et al. (2018). CXCR4-directed theranostics in oncology and inflammation. *Ann. Nucl. Med.* 32 (8): 503–511.
35. Lapa, C., Herrmann, K., Schirbel, A. et al. (2017). CXCR4-directed endoradiotherapy induces high response rates in extramedullary relapsed Multiple Myeloma. *Theranostics* 7 (6): 1589–1597.
36. Dadachova, E. and Casadevall, A. (2009). Radioimmunotherapy of infectious diseases. *Semin. Nucl. Med.* 39 (2): 146–153.
37. Helal, M. and Dadachova, E. (2018). Radioimmunotherapy as a novel approach in HIV, bacterial, and fungal infectious diseases. *Cancer Biother. Radiopharm.* 33 (8): 330–335.
38. Dadachova, E. (2008). Radioimmunotherapy of infection with Bi-labeled antibodies. *Curr. Radiopharm.* 1 (3): 234–239.

39. Dadachova, E. and Casadevall, A. (2014). Radiolabeled antibodies for therapy of infectious diseases. *Microbiol. Spectr.* 2 (6): 0023.
40. Uccelli, L., Martini, P., Cittanti, C. et al. (2019). Therapeutic radiometals: worldwide scientific literature trend analysis (2008–2018). *Molecules* 24 (3): 640.
41. Robertson, A.K.H., Ramogida, C.F.R., Scaffer, P., and Radchenko, V. (2018). Development of ^{225}Ac radiopharmaceuticals: TRIUMF perspectives and experiences. *Curr. Radiopharm.* 11 (3): 156–172.

PART II

Production of Radionuclides

Chapter 3

Production of Short Half-Life PET Radionuclides

Michael R. Kilbourn, Melissa E. Rodnick and Mara Clark
Department of Radiology, University of Michigan, Ann Arbor, MI, 48109, USA

3.1 INTRODUCTION

The number of positron-emitting radionuclides is remarkably large, with a significant number available using cyclotron irradiations of natural or enriched target materials (Tables 3.1 and 3.2). However, routine applications of positron emission tomography (PET) imaging in humans has predominantly utilized the four short-lived positron emitters carbon-11, oxygen-15, nitrogen-13, and fluorine-18, with growing use of the isotopes rubidium-82 and gallium-68. All six have half-lives under two hours and high theoretical molar activities (radioactivity/mass) (Table 3.1). Significant efforts have been expended in trying to optimize the production of these isotopes via the small cyclotrons ($E < 30$ MeV) commonly used for radiopharmaceutical preparation. The cyclotron targets for production and the processing equipment for the isolation and purification of radionuclides are readily available from commercial vendors, as are the radionuclide generators for ^{82}Rb and ^{68}Ga . The development of many new methods for incorporating metal radionuclides into radiopharmaceuticals has resulted in an increasing demand for a slew of novel positron-emitting isotopes (Table 3.2) for use as diagnostic or theranostic radionuclides for nuclear medicine, with some of them available from low-energy (< 20 MeV) medical cyclotrons [1]. None of the radionuclides in Table 3.2 are pure positron emitters, and the impact of other emissions on their imaging potential has been reviewed [2]. Examples of the chemistry and applications of these newer PET

Handbook of Radiopharmaceuticals: Methodology and Applications, Second Edition.

Edited by Michael R. Kilbourn and Peter J.H. Scott.

© 2021 John Wiley & Sons Ltd. Published 2021 by John Wiley & Sons Ltd.

radionuclides are discussed in later chapters of this handbook. This chapter discusses the production methods for the most commonly used short-lived PET radionuclides, with an emphasis on the methods used with the typical low- to medium-energy (15–30 MeV) cyclotrons used for the production of radiopharmaceuticals for PET imaging studies. For a more thorough review of all positron-emitting radionuclides, a series of articles by Qaim is recommended [3–6].

3.2 PRODUCTION OF COMMONLY USED PET RADIONUCLIDES: ^{18}F , ^{11}C , ^{13}N , ^{15}O , ^{82}Rb , AND ^{68}Ga

The characteristics of the group of most-used radionuclides (^{18}F , ^{11}C , ^{13}N , ^{15}O , ^{82}Rb , and ^{68}Ga) for human PET imaging studies are shown in Table 3.1. The history of use of positron-emitting isotopes in human studies now spans more than 50 years, but the applications of these radionuclides in imaging studies have steadily increased, as has the acceptance and regulatory approval of PET radiopharmaceuticals for use in clinical nuclear medicine. As a result, the nuclear reactions and target materials used to generate them have in practice been reduced to a small number of well-understood, reliable production strategies. Of the radionuclides in Table 3.1, ^{11}C , ^{13}N , and ^{15}O have half-lives so short (<20 minutes) that their production very close to the site of use (the PET scanner) is required, most often by a cyclotron located very near the PET imaging suite. Fluorine-18, with a nearly two-hour half-life, can be shipped to imaging sites remote from the cyclotron production site. The radionuclides ^{82}Rb and ^{68}Ga are widely available due to their access from mother/daughter radionuclide generators [7–9], although recent developments in direct cyclotron production of ^{68}Ga will require proximity of imaging equipment to an available cyclotron facility. The very short half-life of ^{82}Rb requires the generator to also be placed in close proximity to the PET scanner.

A very thorough discussion of the theory, design, engineering, and operation of cyclotron targets is available in the free publication from the International Atomic Energy

Table 3.1 Commonly used radionuclides for human PET imaging studies.

Radionuclide	$T_{1/2}$ (min)	Method	Nuclear reaction	Max molar activity (TBq μmol^{-1})
Rubidium-82	1.25	Generator	$^{82}\text{Sr}/^{82}\text{Rb}$	5564
Oxygen-15	2.03	Cyclotron	$^{16}\text{O}(p,pn)^{15}\text{O}$ $^{14}\text{N}(d,n)^{15}\text{O}$	3394
Nitrogen-13	9.98	Cyclotron	$^{16}\text{O}(p,\alpha)^{13}\text{N}$	699.3
Carbon-11	20.4	Cyclotron	$^{14}\text{N}(p,\alpha)^{11}\text{C}$	341.1
Gallium-68	67.71	Generator	$^{68}\text{Ge}/^{68}\text{Ga}$	102.3
		Cyclotron	$^{68}\text{Zn}(p,n)^{68}\text{Ga}$	
Fluorine-18	109.8	Cyclotron	$^{18}\text{O}(p,n)^{18}\text{F}$ $^{20}\text{Ne}(d,\alpha)^{18}\text{F}$	63.3

Only the most often used nuclear reaction or radionuclide generator for each is shown.

Radionuclide	$T_{1/2}$	Production method
Astatine-77	26 h	$^{77}\text{Se}/^{77}\text{As}$ generator
Bromine-75	1.6 h	$^{76}\text{Se}(p,2n)^{76}\text{Br}$ $^{77}\text{Se}(p,3n)^{76}\text{Br}$
Bromine-76	16 h	$^{77}\text{Se}(p,2n)^{76}\text{Br}$
Cobalt-55	17.6 h	$^{56}\text{Fe}(p,2n)^{56}\text{Co}$
Copper-61	3.3 h	$^{61}\text{Ni}(p,n)^{61}\text{Cu}$ $^{64}\text{Zn}(p,\alpha)^{61}\text{Cu}$
Copper-64	12.7 h	$^{64}\text{Ni}(p,n)^{64}\text{Cu}$
Gallium-66	9.5 h	$^{66}\text{Zn}(p,n)^{66}\text{Ga}$
Iodine-122	3.6 min	$^{122}\text{Xe}/^{122}\text{I}$ generator
Iodine-124	4.18 d	$^{124}\text{Te}(p,n)^{124}\text{I}$ $^{124}\text{Te}(d,2n)^{124}\text{I}$
Potassium-38	7.6 min	$^{35}\text{Cl}(\alpha,n)^{35}\text{K}$ $^{40}\text{As}(p,3n)^{35}\text{K}$
Manganese-52	5.6 d	$^{52}\text{Cr}(^3\text{He},t)^{52}\text{Mn}$
Rubidium-81	4.6 h	$^{82}\text{Kr}(p,2n)^{82}\text{Rb}$
Scandium-44	3.9 h	$^{44}\text{Ti}/^{44}\text{Sc}$ generator $^{44}\text{Ca}(p,n)^{44}\text{Sc}$
Technetium-94m	52 min	$^{94}\text{Mo}(p,n)^{94\text{m}}\text{Tc}$
Titanium-45	3.08 h	$^{45}\text{Sc}(p,n)^{45}\text{Ti}$
Yttrium-86	14.7 h	$^{86}\text{Sr}(p,n)^{86}\text{Y}$
Zirconium-89	78.4 h	$^{89}\text{Y}(p,n)^{89}\text{Zr}$

Table 3.2 Less common cyclotron-produced PET radionuclides used for animal or human PET imaging studies.

Agency [10]. In the following sections are brief descriptions of the methods typically used to produce the common PET radionuclides for present-day radiopharmaceutical preparation.

3.2.1 Fluorine-18

Fluorine-18 ($T_{1/2} = 109.8$ minutes) is the single most-used PET radionuclide in the world, largely due to the widespread use of the radiopharmaceutical 2-deoxy-2- ^{18}F fluoro-D-glucose (^{18}F FDG) for both research and clinical care. Not surprisingly, the long history of interest in this PET radionuclide encouraged exploration of a variety of methods for its production using both nuclear reactors and particle accelerators (Table 3.3), but today it is almost exclusively done using the $^{18}\text{O}(p,n)^{18}\text{F}$ reaction. However, other methods of producing fluorine-18 were crucial to the introduction of ^{18}F -labeled compounds into human PET imaging and remain viable, if seldom used.

^{18}F Fluoride ion was first used for patient studies in the 1960s: the method of preparation at that time was using the neutron flux of a nuclear reactor to irradiate Li_2CO_3 powder, yielding ^{18}F fluoride ion from the nuclear reactions $^6\text{Li}(n,^4\text{He})^3\text{H}$ and $^{16}\text{O}(^3\text{H},n)^{18}\text{F}$ [11]. The ^{18}F fluoride ion from reactors was used for the original synthesis of 5- ^{18}F fluoroDOPA in 1973 [12]. ^{18}F Fluoride ion was also obtained at cyclotron

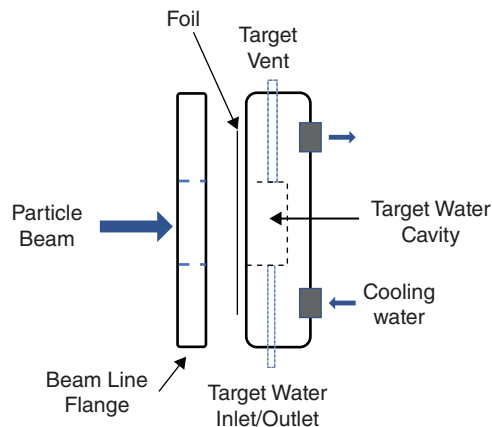
Table 3.3 Nuclear reactions used for cyclotron production of fluorine-18.

Nuclear reaction	Particle energy range (MeV)
$^{20}\text{Ne}(d,^4\text{He})^{18}\text{F}$	0–15
$^{16}\text{O}(^3\text{He},p)^{18}\text{F}$	1–15
$^{18}\text{O}(p,n)^{18}\text{F}$	4–14
$^{20}\text{Ne}(^3\text{He},^4\text{He})^{18}\text{F}$	10–40
$^{16}\text{O}(^4\text{He},np)^{18}\text{Ne}: ^{18}\text{F}$	10–52
$^{16}\text{O}(^3\text{He},n)^{18}\text{Ne}: ^{18}\text{F}$	15–40
$^{16}\text{O}(^4\text{He},np)^{18}\text{F}$	20–40
$^{20}\text{Ne}(p,2pn)^{18}\text{F}$	30–40
$^6\text{Li}(n,^4\text{He})^3\text{H}, ^{16}\text{O}(^3\text{H},n)^{18}\text{F}$	Reactor

installations by using large-volume (10–15 ml) water targets and the $^{16}\text{O}(\alpha,np)^{18}\text{F}$ reaction [13]. At present, [^{18}F]fluoride ion used for clinical PET studies (bone imaging) and radiopharmaceutical syntheses is most efficiently produced using the proton irradiation of [^{18}O]water targets. This choice is a combination of the much higher yields obtained with the $^{18}\text{O}(p,n)^{18}\text{F}$ reaction [14] and the ever-increasing diversity of methods for radiochemistry using [^{18}F]fluoride [15–17].

The proton irradiation of small-volume oxygen-18 enriched water targets yields aqueous solutions of [^{18}F]fluoride ion, the chemical form of the radionuclide most useful for subsequent syntheses to form useful ^{18}F radiopharmaceuticals. The design of such targets has not really changed from that reported years ago [18, 19]: either a small-volume cavity is created by machining a cavity into a solid metal target and covered with a thin metal foil (Figure 3.1) or, alternatively, a double-foil design with a central spacer is used to create the target volume [20, 21]. Ports into the cavity allow the introduction and removal of the target water, as well as the potential for pressurization (often used to minimize cavitation during beam irradiation). The target is then filled with enriched [^{18}O]water (usually less than 3 ml to conserve the enriched water) and irradiated with

Figure 3.1 Schematic diagram of a small-volume water target.



protons: the cross-section for the nuclear reaction is in the 2–15 MeV range, which is easily reached by low-energy cyclotrons. Water targets having many different cavity sizes and shapes have been utilized with various metal compositions, among them Ag, Ti, Nb, Ta, and Au [18–26]. Although the conceptual design of a small-volume [^{18}O]water target was quite simple, extensive efforts to improve these targets were expended to achieve three goals: (i) improve the chemical reactivity of the [^{18}F]fluoride from [^{18}O]water targets by decreasing ionic impurities; (ii) increase yields from such targets, important for the development of distribution systems for the fluorine-18 radiopharmaceuticals and in particular [^{18}F]FDG; and (iii) improve molar activities (radioactivity/mass) of [^{18}F]fluoride for use in syntheses of organic radiopharmaceuticals.

The particle irradiation of [^{18}O]water targets produces metal ions in the water, with both nonradioactive and radioactive ions present at the end of bombardment. The target body and foil are potential metallic ion sources, and much effort was spent in understanding the impact of the foil material. For example, many targets were initially equipped with Havar foils, an alloy with high tensile strength and a high melting point. It is an alloy of eight metals (Co, Cr, Ni, W, Mo, Mn, Be, and Fe), and numerous long-lived radioactive species (isotopes of Ni, Co, Mn, Cu, and Cd) have been observed in proton-irradiated water [18, 27]. Lower concentrations of metal ion impurities were found by replacing Havar with materials such as silver, titanium, or niobium [20]: using Nb, Pt, Ta, Ti, or Zr-sputtered Havar foils provided a better inert surface with the tensile strength of the Havar foil [28]. The potential for the target body being a source of metal ions in solution can be minimized by target designs that reduce or eliminate the proportion of the particle beam hitting the rear metal surface of the target cavity.

The formation of anionic contaminants of proton-irradiated [^{18}O]water has been less well studied, but the presence of nitrate, nitric, and chloride ions at concentrations 3–20 times that of the fluoride ion have been reported [29]. The impact of such anions on subsequent radiochemical syntheses has also not been fully examined, but with the development of better methods for fluorine-18 radiochemistry, the impact of both anion and metal ion contaminants on the reactivity of the [^{18}F]fluoride ion from water targets has been minimized. The processes used for radiochemical syntheses of, for example, [^{18}F]FDG also effectively remove the trace amounts of the metallic radioisotopes [30].

The increasing importance of [^{18}F]FDG in clinical medicine undoubtedly was the stimulus in the development of target systems capable of producing very large amounts of [^{18}F]fluoride ion, a necessary step for the widespread geographic distribution of [^{18}F]FDG. The high-level production has been addressed in target design by modifications of target materials, foil composition and thickness, target thickness, particle beam profile, and/or target cooling and over-pressurization. Those efforts achieved [^{18}O]water targets capable of withstanding high-beam currents (80–150 μA) [31] with a report of production of as much as 1 TBq of [^{18}F]fluoride ion using dual-target irradiations.

In contrast to the need to produce such high quantities of [^{18}F]fluoride ion, which is not necessary for non-commercial uses (most hospital-based research or clinical PET imaging programs), the molar activity of ^{18}F obtained from [^{18}O]water targets is very important to all users. The theoretical maximum molar activity for fluorine-18 is 63.3 TBq μmol^{-1} , but

that has not yet been reported for [^{18}F]fluoride from any cyclotron target. The metals of the targets and foils, and the [^{18}O]water used as target material, are likely not the source of significant carrier fluoride ions, but numerous studies have identified that using fluorinated tubing, valves, and fittings resulted in measurable dilutions of the molar activity [32, 33]. A particularly poor early choice of materials was Teflon (polytetrafluoroethane [**PTFE**]). The elimination of any target components constructed with fluorine-containing polymers, and the use of, for example, polypropylene or polyether ether ketone (**PEEK**) plastic lines for the filling and emptying of the target, significantly improves the molar activity for [^{18}F]fluoride with reported values as high as 43 TBq μmol^{-1} [34], although routine molar activities are probably in the 2–10 TBq μmol^{-1} range.

The production of ^{18}F can also be done using an [^{18}O]O₂ gas target. The interest in this target design was mostly as an option to the production of the radionuclide in neon gas targets (discussed shortly) for the formation of ^{18}F -labeled fluorine gas. As with water targets, a variety of metal surfaces were investigated (Ni, Al, Ag, Au, Cu), with the best result using aluminum targets. Upon irradiation of ^{18}O -enriched oxygen gas with protons, the ^{18}F is found attached to the inner target surface (chemical species undefined). Removal of the gas content allows recovery of the enriched ^{18}O -oxygen, and subsequent re-filling with a 1% F₂ in krypton gas mixture followed by a short proton irradiation produces [^{18}F]F₂, which can then be swept out of the target with an inert gas flow. This procedure produces [^{18}F]F₂ in a necessarily carrier-added fashion, with much lower molar activities (<1000 GBq mmol⁻¹) [35].

Before the advent of the small-volume [^{18}O]water targets, most of the production of fluorine-18 for radiopharmaceutical chemistry was done using the deuteron irradiation of neon-20 gas targets ($^{20}\text{Ne}(\text{d},\alpha)^{18}\text{F}$ nuclear reaction). The major interest in these targets was the production of fluorine-18 labeled fluorine gas for use in electrophilic fluorination reactions, an important need (at the time) for the syntheses of such important radiopharmaceuticals as [^{18}F]FDG and 6- ^{18}F fluoroDOPA: today, both of these radiopharmaceuticals can be made in much higher yields from [^{18}F]fluoride ion. The deuteron irradiation of a gas target filled with neon-20 containing a trace amount (0.1%) of fluorine gas produces carrier-added [^{18}F]F₂ suitable for radiochemical syntheses. A variety of metal target materials, target gas compositions, and irradiation conditions were explored in attempts to improve yields and increase the yields and molar activities of the [^{18}F]F₂ produced [36–38], but the best results were obtained with nickel, Inconel (Ni-Cr alloy), and aluminum target materials. The targets were routinely passivated with cold fluorine gas to improve recovery of the radionuclide, but that also resulted in the formation of low-molar-activity, carrier-added [^{18}F]fluorine gas.

The neon gas targets can also be used to provide ^{18}F in two other chemical forms: H[^{18}F]F and [^{18}F]fluoride ion. Irradiation of a hydrogen-neon gas mixture produces [^{18}F]HF, and the product can be swept out of the target using a recirculating gas system [39, 40] or after irradiation by heating the target (>370 °C) [40] and using a gas purge: the [^{18}F]HF is trapped at low temperature or by, for example, solid-supported cesium hydroxide. When done in targets that have not been passivated with cold fluorine gas (in contrast to targets intended for [^{18}F]F₂ production), such H[^{18}F] targets can yield very high molar activity ^{18}F for

radiochemical syntheses, as exemplified in the synthesis of [¹⁸F]fluoroethanol with a value of 4.6 TBq μmol⁻¹ [41]. The production of aqueous [¹⁸F]fluoride ion from a neon target is also possible: irradiation is done using a neon gas target that is constructed such that the fluorine-18 that is “stuck” on the inner target surface at the end of irradiation can be removed by washing with a small volume (e.g. 4.5 ml) of water. This method of aqueous [¹⁸F]fluoride ion production may produce fewer metal ion impurities compared to a [¹⁸O]water target, but it also requires much longer beam times to produce far less radionuclide.

3.2.2 Carbon-11

The 20.4 minute half-life radionuclide carbon-11 can be produced by nuclear reactions using cyclotron-produced proton, deuteron, or helium-3 beams (Table 3.4), but the common method for producing this isotope for radiopharmaceutical syntheses uses the ¹⁴N(p,α)¹¹C nuclear reaction and irradiation of a nitrogen gas target [42]. The design for ¹¹C gas targets is conceptually simple and has not changed much from early configurations [42, 43]: a metal cylinder is fitted with a thin metal foil at one end to allow entry of the irradiating protons, a cooling system to remove heat from the target body, a gas cooling flow for the entry window, and ports for pressurization of the cylinder with the desired target gas and post-irradiation removal of the irradiated gas (a simple diagram of a typical ¹¹C gas target is shown in Figure 3.2). A common target body material is aluminum, but targets take many different shapes and sizes depending on the energy of the proton beam, the beam current, and the desired length of irradiation. Targets

Nuclear reaction	Particle energy range (MeV)
¹⁰ B(d,n) ¹¹ C	3–12
¹¹ B(p,n) ¹¹ C	5–20
¹⁴ N(p,α) ¹¹ C	7–15
¹² (³ He, ⁴ He) ¹¹ C	7–15
¹⁴ (d,n ⁴ He) ¹¹ C	10–15
¹² C(p,pn) ¹¹ C	20–50

Table 3.4 Nuclear reactions used for cyclotron production of carbon-11.

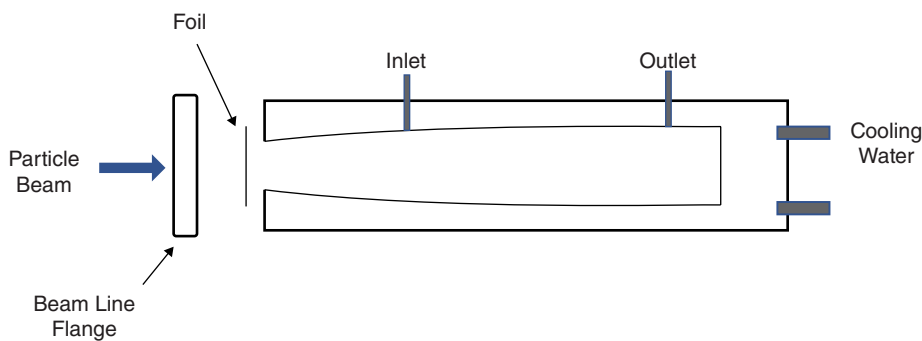


Figure 3.2 Schematic diagram of a carbon-11 gas target.

are operated at high pressure to provide sufficient gas density to allow the use of the entire cross-section for the $^{14}\text{N}(p,\alpha)^{11}\text{C}$ reaction (5–20 MeV) available to typical low-energy (<30 MeV) cyclotrons.

Two forms of carbon-11 are readily available from nitrogen gas targets. In the presence of a trace amount of oxygen, the product from irradiation is [^{11}C]carbon dioxide, which can be simply trapped upon release of the target gas and then used directly for radiochemical syntheses. Under reducing conditions, done via the proton irradiation of nitrogen-hydrogen gas mixtures, the product obtained is [^{11}C]methane [42, 44, 45] which can also be trapped after the release of the target gas. Both [^{11}C]CO₂ and [^{11}C]CH₄ can be converted using rapid online systems to a variety of useful single-carbon reagents including [^{11}C]CO, [^{11}C]methyl iodide, [^{11}C]methyl triflate, [^{11}C]methanol, [^{11}C]formaldehyde, [^{11}C]phosgene, [^{11}C]cyanide ion, or [^{11}C]fluoroform [17, 45, 46].

Both the [^{11}C]CO₂ and [^{11}C]CH₄ targets produce sufficient amounts of radioactivity (>74 GBq) for radiopharmaceutical syntheses, and thus most of the effort over the years has been devoted to improving the molar activity (radioactivity/mass) of the finished ^{11}C radiopharmaceuticals. The general design of targets has not changed. However, to obtain high molar activities, close attention must be paid to the quality of target gas materials (typically, using nitrogen gas of 99.9999% purity) and using materials and connection fittings that minimize the possibility of dilution of the molar activity by environmental carbon dioxide. To obtain ultra-high specific-activity ^{11}C -labeled radiopharmaceuticals from the subsequent radiochemical synthesis step, the target system needs to be coupled with a radiochemical synthesis system that has also been rigorously designed and maintained to prevent unintentional addition of carbon-12. A few institutions have devoted the time and resources to building such systems using either [^{11}C]CO₂ or [^{11}C]CH₄ targets, and molar activities of radiochemicals with specific activities in the 4–20 TBq μmol^{-1} have been reported [47, 48]. It is likely, however, that commercially available carbon-11 target systems and synthesis systems are not routinely operated to produce radionuclide with molar activities matching these select few examples: molar activities of ^{11}C radiopharmaceuticals typically used for human PET studies are more often in the range of 400–4000 GBq μmol^{-1} .

3.2.3 Nitrogen-13

The formation of nitrogen-13 ($T_{1/2} = 9.98$ minutes) dates back to 1934 when Joliot and Curie demonstrated the $^{10}\text{B}(\alpha,n)^{13}\text{N}$ nuclear reaction [48]. Nitrogen-13 can be produced by a variety of additional nuclear reactions (Table 3.5), but the predominant method used currently for nitrogen-13 production for radiopharmaceuticals is via the $^{16}\text{O}(p,\alpha)^{13}\text{N}$ reaction on ordinary [^{16}O]water. The water targets used for N-13 production are similar or, in many cases, identical to those used for F-18 production, except that larger volumes might be used as the target material is obviously of essentially no cost. A small-volume water target, such as that shown in Figure 3.1, for example, can be used for both ^{18}F and ^{13}N production.

The chemical form of nitrogen-13 from ^{16}O -water is mostly a mixture of nitrogen oxides ([^{13}N]NO_x) and [^{13}N]NH₃ [49], which is not particularly useful. However, they can

Nuclear reaction	Particle energy range (MeV)
$^{13}\text{C}(p,n)^{13}\text{N}$	1–6
$^{10}\text{B}(^4\text{H},n)^{13}\text{N}$	4–6
$^{13}\text{C}(p,n)^{13}\text{N}$	4–9
$^{11}\text{B}(^4\text{He},2n)^{13}\text{N}$	6–10
$^{16}\text{O}(p,^4\text{He})^{13}\text{N}$	8–15
$^{14}\text{N}(p,pn)^{13}\text{N}$	14–30

Table 3.5 Nuclear reactions used for cyclotron production nitrogen-13.

be rapidly reduced by chemical means (DeVarde's alloy) to form the useful species [^{13}N]ammonia, which in itself is used as a radiopharmaceutical (cardiac blood flow imaging) or as a synthetic precursor (e.g. amino acid syntheses). As an alternative, [^{13}N]NH₃ can be formed by in-target methods, using either over-pressurization of the water target with hydrogen or methane gas [50] or the irradiation of water containing a small amount of ethanol [49]. The nitrogen-13 from water targets can also be processed into such small chemical species as nitric oxide or molecular nitrogen, both used for *in vivo* ventilation studies. The production of nitrogen-13 in water targets is subject to the same concerns for contamination by metallic radionuclides as discussed for ^{18}O -water targets. In those instances where the radioactivity is volatilized, such as during DeVarde alloy reduction and distillation of [^{13}N]NH₃ or conversion to a volatile gas ([^{13}N]N₂, [^{13}N]NO), metal ions are of no further concern. However, when in-target production methods of [^{13}N]ammonia are employed, removal of the metal ions by select ion-exchange columns may be necessary.

The production of nitrogen-13 is also possible using several other nuclear reactions (Table 3.5) and used to prepare [^{13}N]NH₃, but none of them are routinely used in recent years. Interestingly, the formation of [^{13}N]N₂ occurs simultaneously during a typical proton irradiation of nitrogen ($^{14}\text{N}(p,n)^{13}\text{N}$) for production of carbon-11 but is discarded during the subsequent processing and synthesis steps; if desired, it can be isolated and purified for independent use [51].

Most reports of nitrogen-13 production and use did not address, and in many cases did not even report, the molar activity for the radionuclide. This was due to little interest in it when nitrogen-13 was used to prepare such radiolabeled compounds as [^{13}N]ammonia or [^{13}N]amino acids, where molar activity is not important for *in vivo* biological studies. However, if an attempt is made to carefully exclude sources of nitrogen-15, then molar activities as high as 6200 GBqmmol⁻¹ have been reported, making the ^{13}N potentially useful for the syntheses of radiopharmaceuticals (e.g. receptor ligands) that require such high values.

3.2.4 Oxygen-15

Oxygen-15 is a very short-lived radionuclide ($T_{1/2} = 2.04$ minutes) with a few potential nuclear reactions for production (Table 3.6). When made using a low-energy cyclotron

Table 3.6 Nuclear reactions used for cyclotron production of oxygen-15.

Nuclear reaction	Particle energy range (MeV)
$^{14}\text{N}(\text{d},\text{n})^{15}\text{O}$	2–10
$^{15}\text{N}(\text{p},\text{n})^{15}\text{O}$	4–10
$^{12}\text{C}(\text{He},\text{n})^{15}\text{O}$	12–18
$^{16}\text{O}(\text{p},\text{pn})^{15}\text{O}$	20–26.5

($E < 20$ MeV), this is done by deuteron irradiation of nitrogen gas containing a small amount (1%) of oxygen ($^{14}\text{N}(\text{d},\text{n})^{15}\text{O}$ nuclear reaction) [52, 54]. Rapid conversions of the ^{15}O obtained to other small molecules ($^{15}\text{O}\text{CO}_2$, $^{15}\text{O}\text{CO}$, $^{15}\text{O}\text{H}_2\text{O}$) is done using flow-through processing systems (e.g. furnaces, filters, traps) [53]. An example of the incorporation of oxygen-15 into an organic molecule is the reaction of ^{15}O with an organoborane [54] to form ^{15}O butanol, an alternative to ^{14}C butanol that had been previously introduced as a blood flow agent.

When a higher-energy cyclotron (>25 MeV) is available, oxygen-15 can also be produced by proton irradiation of oxygen-16 gas or water using the $^{16}\text{O}(\text{p},\text{pn})^{15}\text{O}$ nuclear reaction (the cross-section starts at 15 MeV and is very high at >20 MeV). Water targets are constructed in a similar fashion to that used for ^{13}N or ^{18}F production, except that the volume is not restricted as the target material is of no cost (^{16}O -water) and the molar activity of the ^{15}O water formed is of no consequence. The high yields of this nuclear reaction were particularly useful for the rapid sequential production of $^{15}\text{O}\text{H}_2\text{O}$ for brain activation PET studies [55]. The short half-life of oxygen-15 places severe restraints on its use, as the cyclotron production system must be located very close to the PET scanner [56] or a very fast and efficient transfer system must be employed.

3.2.5 Tandem Targets and Dual-Use targets

A wide variety of cyclotrons have been utilized for the production of the common PET radionuclides ^{11}C , ^{18}F , ^{15}O , and ^{13}N , and low-energy medical cyclotrons currently available often include the ability to perform dual-target irradiations. That makes feasible the simultaneous production of two different radionuclides for independent uses. In past years, simultaneous dual-isotope production was simply not possible as only single external beamlines were available: the best that was done was rapid sequential production of two isotopes through the use of target-switching systems or the utilization of a single target for production of more than one radionuclide. As examples of the latter approach, small-volume water targets can obviously be used for either ^{13}N or ^{18}F production depending on the target material loaded (^{16}O - or ^{18}O -water, respectively), and a gas target can be employed for the production of two radionuclides as done for oxygen-15 ($^{16}\text{O}(\text{p},\text{n})^{15}\text{O}$) and fluorine-18 ($^{20}\text{Ne}(\text{p},2\text{pn})^{18}\text{F}$) [57]. Target-switching or dual use also worked best when changing particles (e.g. protons to deuterons) was not necessary, as that often required a time delay.

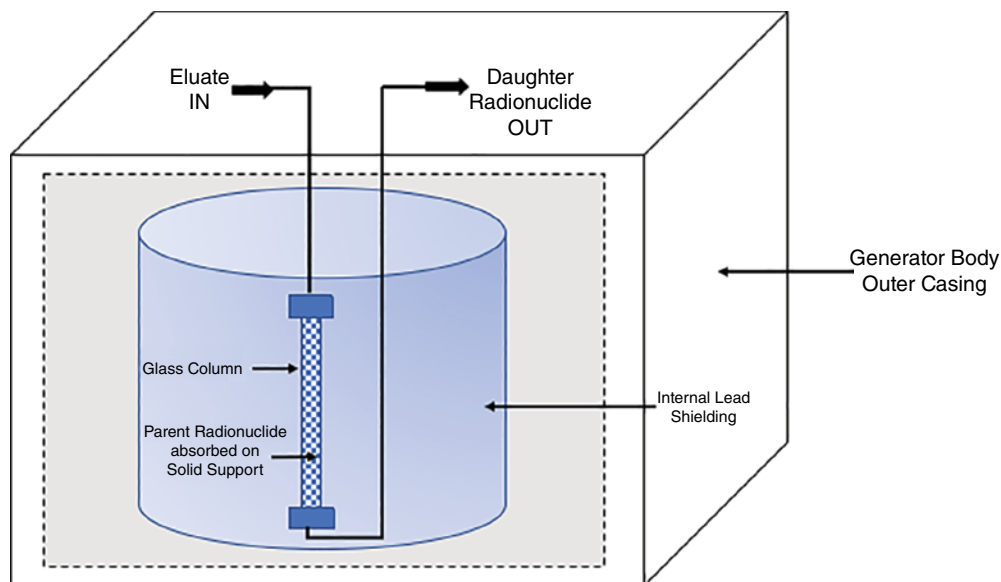


Figure 3.3 Schematic diagram of the design concept used for ^{82}Rb and ^{68}Ga generators.

To achieve the true simultaneous production of two different radionuclides from a single beamline, several investigators developed tandem systems using inline combinations of gas and water targets. The concept is actually simple: position a second target at the back of the first, separated by a suitable thin foil, but design it such that the incident particle energies on each target are appropriate for the cross-sections of the two desired radionuclides. Two different tandem targets were designed to take advantage of the availability of higher-energy protons from 30 to 50 MeV cyclotrons. Placement of an oxygen gas target in front and a [^{16}O]water target in the back allowed for simultaneous formation of oxygen-15 ($^{16}\text{O}(p,pn)^{15}\text{O}$) and nitrogen-13 ($^{16}\text{O}(p,\alpha)^{13}\text{N}$), with the front gas target used to attenuate the beam energy to match the lower-energy cross-section for nitrogen-13 production in the rear target [58]. Alternatively, a tandem water target design placing a [^{16}O]water target in front and a second small-volume water target in back allowed simultaneous production of oxygen-15 in front, and either ^{13}N or ^{18}F in the rear target (depending on using ^{16}O - or ^{18}O -water target material) [59]. Finally, a dual ^{11}C and ^{18}F target was reported using a nitrogen gas target in front that was “thin” to the particle beam, allowing protons of sufficient energy to pass through a rear foil assembly and into a typical small-volume [^{18}O]water target placed at the rear [60].

3.2.6 Rubidium-82 and Gallium-68

Two isotopes routinely used in human PET studies, ^{82}Rb and ^{68}Ga , have been available from generator systems that utilize parent isotopes with sufficiently long half-lives (^{68}Ge

$T_{1/2} = 275$ days; and ^{82}Sr $T_{1/2} = 25.55$ days) that such generators can be shipped to remote sites of use. The conceptual design of such generators is quite simple (Figure 3.3), with the long-lived parent radionuclide absorbed on a solid phase that is carefully selected to allow rapid elution of the daughter radionuclide in a solution useful either directly as a radiopharmaceutical (as for ^{82}Rb) or as a synthetic precursor (as for ^{68}Ga), without a significant breakthrough of the parent radionuclide into the eluate.

More recently, targetry needed for the production of ^{68}Ga directly using small medical cyclotrons has been introduced into the nuclear medicine community and offers an additional option for use of that PET radionuclide.

3.2.7 Rubidium-82

Rubidium-82 is a very short half-life nuclide available from a $^{82}\text{Sr}/^{82}\text{Rb}$ parent/daughter radionuclide generator [9]: the parent ^{82}Sr is produced by proton irradiation of a molybdenum target [61]. The strontium-82 is loaded onto a tin oxide column and the rubidium-82 selectively eluted using a 0.9% NaCl solution; the eluate is used immediately for PET imaging studies. The generators can be eluted every 10 minutes, making them particularly useful for repeated studies of cardiac blood flow. Quality control efforts for the eluted radioactivity center on determining the extent of the breakthrough of ^{82}Sr . The generators have a limited useful lifetime of approximately four to eight weeks before replacement is necessary to continue clinical studies.

The short half-life requires that the generator be located in close proximity to the PET scanner, but the parent ^{82}Sr nuclide has a sufficiently long half-life of 25.5 days to allow shipment to facilities that may not have local cyclotron access. Studies with ^{82}Rb have been done for decades, with the radiopharmaceutical gaining US Food and Drug Administration (FDA) approval in 1989, and it is used in many institutions around the world [62]. Rubidium generators (e.g. Ruby Fill and Cardiogen-82) are commercially available.

3.2.8 Gallium-68

Using gallium-68 for medical imaging was first described in the 1960s [63], but it had a small clinical footprint for much of the following four decades. Gallium-68 is an attractive alternative to fluorine-18 due to its availability from a generator system, thus supporting PET imaging capabilities at imaging facilities without a cyclotron. Additional attributes of ^{68}Ga make it a desirable PET trace. It is a positron-emitting (89% β^+) radionuclide with a relatively short half-life ($T_{1/2} = 67.71$ minutes), which decays to the stable isotope zinc-68. The $^{68}\text{Ga}^{3+}$ cation is small with an ionic radius of 0.62 Å, and it behaves as a relatively hard Lewis acid with an affinity for binding ligands containing oxygen and nitrogen donors: it is therefore suitable for conjugation not only to both large biomolecular vectors using bifunctional chelators, but also to small molecules with rapid pharmacokinetic profiles such as peptides and peptidomimetics [64, 65]. This synthetic diversity, together with the availability of ^{68}Ga from both generator systems and directly from

cyclotrons, has resulted in the rapid growth in interest in the development of gallium-68 radiopharmaceuticals [66, 67].

3.3 $^{68}\text{Ge}/^{68}\text{Ga}$ GENERATORS

The most common source of ^{68}Ga for radiopharmaceutical syntheses has been the $^{68}\text{Ge}/^{68}\text{Ga}$ parent/daughter radionuclide generator. The parent isotope ^{68}Ge (half-life of 270.95 days) is produced by proton irradiation of natural gallium ($^{69}\text{Ga}(p,2n)^{68}\text{Ge}$) [68], and ^{68}Ge spontaneously decays to ^{68}Ga via an electron capture reaction. The first $^{68}\text{Ge}/^{68}\text{Ga}$ generator was described in 1960 as a “Positron Cow,” where ^{68}Ga was separated from ^{68}Ge via liquid-liquid extraction [69]. Such systems using liquid-liquid extractions [69, 70] have disadvantages for designing a generator for routine clinical use, prompting the development of generators employing solid-phase ion-exchange systems. Building on the concept by researchers who had developed ion-exchange chromatographic columns for the $^{99}\text{Mo}/^{99\text{m}}\text{Tc}$ generator [71], Greene and Tucker developed an alumina column that could be loaded with ^{68}Ge ; elution with an EDTA solution directly yielded ^{68}Ga -EDTA [72]. Though ^{68}Ga -EDTA proved a successful and clinically used radiopharmaceutical, the generator was limited as it exclusively produced that single chemical species, and methods to free the ^{68}Ga from the thermodynamically stable EDTA complex were difficult and low-yielding [63]. More successful, and still used today, are ionic $^{68}\text{Ge}/^{68}\text{Ga}$ generators utilizing inorganic matrices containing TiO_2 , SnO_2 , ZrO_2 , or CeO_2 , which selectively adsorb ^{68}Ge and allow ^{68}Ga desorptions upon elution with dilute hydrochloric acid solutions. Such solid-phase generators have a shelf life of 6–12 months and provide the ^{68}Ga -EDTA that is useful for subsequent radiopharmaceutical syntheses. The eluted ^{68}Ga must be tested for levels of breakthrough of ^{68}Ge [73–75], defined as either the activity of ^{68}Ge relative to that of the generator column or, alternatively, the percentage of ^{68}Ge relative to the eluted ^{68}Ga . Provided the eluted ^{68}Ga radioactivity meets established breakthrough limits, it can then be used for radiopharmaceutical syntheses.

The generator system is simple in design with a small footprint, consisting of a self-shielded body containing a chromatographic column to which the parent is embedded, and an inlet and outlet for the solvent system that will selectively elute the daughter from the column (Figure 3.3). As of 2019, there were multiple commercially available $^{68}\text{Ge}/^{68}\text{Ga}$ generators, with two of them – allPharm, Eckert-Ziegler GmbH (Germany); and Galli Ad, IRE ELiT (Belgium) – having marketing authorization in Europe and the USA. Those two generators, along with generators from iThemba Labs (South Africa), itG (Isotope Technologies Garching, Germany), and Obninsk (Russia), all utilize dilute hydrochloric acid instead of an EDTA solution for elution, yielding cationic $^{68}\text{GaCl}_3$ and making them appropriate for subsequent ^{68}Ga labeling chemistry. The allPharm, Galli Ad, and Obninsk generators employ a TiO_2 column system, whereas the iThemba system is SnO_2 based, and the itG generator utilizes a unique organic matrix of dodecyl gallate attached to high-performance liquid chromatography (HPLC)-grade silica gel [73, 76, 77]. The use of the non-metallic solid phase by the itG generator allows for elution of ^{68}Ga at lower HCl concentrations (0.05 M HCl), with lower retention of metal ions (Zn, Fe, Ti)

by the matrix leading to less contamination of the ^{68}Ga eluate. All of the available ionic generators produce ^{68}Ga with low and acceptable ^{68}Ge breakthrough, and all have been routinely used for ^{68}Ga -radiopharmaceutical production for human PET imaging studies.

Despite $^{68}\text{Ge}/^{68}\text{Ga}$ generators having played a major role in the development of and access to ^{68}Ga -based radiopharmaceuticals, the commercial $^{68}\text{Ge}/^{68}\text{Ga}$ generator supply has been inconsistent and has not kept pace with the clinical demand for ^{68}Ga . Additionally, there remain technical challenges associated with generators [78]. The low quantities that can be eluted from available generators (approximately 1.85–3.7 GBq, 50–100 mCi) limit the numbers of patient studies that can be scheduled in a single day (often only two to four possible). The ^{68}Ga elution quantities decline steadily with use and time, making consistent patient scheduling difficult. Finally, as elution quantities of ^{68}Ga decrease, the percentages of the breakthrough radionuclide ^{68}Ge increase, eventually exceeding allowable limits and requiring the use of a new, fresh generator.

3.3.1 Cyclotron Production of ^{68}Ga

To meet the growing demand for gallium-68 labeled radiopharmaceuticals, the direct production of ^{68}Ga using a cyclotron has garnered much interest by the international nuclear medicine community, including publication of a technical document from the IAEA [79], publication in late 2018 of a European Pharmacopeia monograph for the direct accelerator-based production of $[^{68}\text{Ga}]\text{GaCl}_3$ [80], and the development and patenting of the equipment and processes involved [81, 82].

Of several possible nuclear reactions, the formation of ^{68}Ga by proton irradiation of ^{68}Zn ($^{68}\text{Zn}(p,n)^{68}\text{Ga}$) is the mostly widely utilized method on a cyclotron. Targetry options include both solid and liquid targets. The proton irradiation of highly enriched ^{68}Zn produces ^{68}Ga , but also small amounts of the longer-lived isotopes ^{66}Ga and ^{67}Ga ; the isotopic contamination is attributed to the trace amounts of ^{66}Zn and ^{67}Zn present in the isotopically enriched ^{68}Zn , as commonly the available targets are not 100% pure ^{68}Zn . More significant is the production of the isotopic contaminant ^{67}Ga that occurs with the use of proton energies above 12.2 MeV, due to the competing $^{68}\text{Z}(p,2n)^{67}\text{Ga}$ nuclear reaction. For that reason, incident proton energies are often degraded appropriately to produce ^{68}Ga of high radionuclidic purity while utilizing enough current to support the production of sufficient yields for clinical applications. Regardless, if opting for liquid or solid target approaches to the direct production of ^{68}Ga , an efficient means for purifying the ^{68}Ga from the irradiated ^{68}Zn is required.

3.3.2 Solid Target Production of ^{68}Ga

Four types of targets are used for solid target production of ^{68}Ga : foils, pressed, fused, and electroplated [79]. The ^{68}Zn foils are purchased commercially, but the availability of highly enriched foils has been limited. A pressed target is a metal disk with a central cavity into which a hydraulically pressed ^{68}Zn pellet is positioned [83], and a fused target is produced by melting zinc pellets into a recess on an aluminum disk [84]. The most

widely reported solid targets for ^{68}Ga production have, however, been the electroplated targets, using ^{68}Zn electrodeposited onto a copper, nickel, platinum, or silver support backing [85–88]. Such targets are capable of yielding curie amounts of ^{68}Ga suitable for radiopharmaceutical syntheses. The general production process for preparation, irradiation, and processing of such targets involves multiple steps: formation of the solid electroplated target, transfer of the target to the target holder, irradiation, transfer of the target to a hot cell, and dissolution of the target to provide impure ^{68}Ga in an acidic solution. This is then followed by chemical separation and purification of the desired ^{68}Ga from the target ^{68}Zn (discussed in a later section). The recovery of the target ^{68}Zn metal and finally reformation of the solid target is feasible but may not be practical on a routine basis. Of the multiple steps in the process, the one resulting in the most significant exposure to the personnel involved is the step of chemical separation and purification of the ^{68}Ga . The solid target has to be retrieved and moved to a hot cell after irradiation for processing: if accomplished by manual retrieval of the target, a very high personal radiation dose burden arises from the radioactive field of the target itself in addition to any surrounding metal contaminants and/or cyclotron components that were activated in the irradiation process. For that reason, high-yielding routine production of ^{68}Ga from solid targets necessitates an automated target transfer system and optimally an automated system rather than manual operations for the subsequent processing steps.

Foils, pressed, and electroplated targets have the additional option of being able to undergo ^{68}Ga extraction by thermal diffusion rather than target dissolution [89, 90]. This occurs by heating the irradiated zinc and etching the ^{68}Ga activity off of the zinc surface with a dilute acid. The isolation yields for the process are high (approximately 60–70%) and have a short processing time (under 10 minutes). If desired, zinc foils can be reused without going through the target reformation process, although the ^{68}Ga yields will decrease with continual use. The reported example [89] of gallium extraction by thermal diffusion was primarily performed manually in a model system by measuring ^{66}Ga and ^{68}Ga (produced from irradiated natural zinc) to minimize the effective dose to the radiochemist and projected possible yields scaled to the abundance of the starting zinc isotopes. While the proof-of-concept studies are encouraging, an automated approach to performing the thermal diffusion separation would be necessary for a commercial setting.

If multi-curie yields of ^{68}Ga are required, solid target production is needed [87, 91]: a solid target will always have a higher concentration of zinc and thus a larger cross-section for the nuclear reaction when compared to a liquid target. These higher production yields are, however, associated with the limitation that appropriate infrastructure will be needed for solid target production, handling, and processing. This is a high capital investment that may not be available for a developing site or a viable modification option for established cyclotron facilities.

3.3.3 Liquid Target Production of ^{68}Ga

Liquid targets, in which an aqueous solution of the enriched target material (usually [^{68}Zn] $\text{Zn}(\text{NO}_3)_2$) is irradiated with low-energy protons, offer increased simplicity as they present

a similar workflow to the production of [^{18}F]fluoride ion and are instantly compatible with laboratory setups in existing PET centers. When compared to the cyclotron production of the other short-lived PET radionuclides (^{15}O , ^{13}N , ^{11}C , ^{18}F), the targetry development is actually quite recent, but the targets are very similar to those utilized for fluorine-18 production and share many of the operating considerations and problems.

3.3.4 General Considerations for Liquid Targets for ^{68}Ga Production

The design and operation of aqueous targets for radionuclide production, including ^{68}Ga , share many of the challenges met with small-volume (approximately 2 ml) water targets for fluorine-18 production [92]. Surfaces in contact with the aqueous target volume (target body, innermost foil) are typically made of inert metals (e.g. niobium or titanium), with additional foils (e.g. aluminum or Havar backing foils) chosen to maintain good stability in the face of increased intra-target pressures resulting from proton-induced radiolysis of the water media: the combined foil system should be designed to keep the incident proton energy below the 12.2 MeV threshold to avoid ^{67}Ga formation. Targets may be over-pressurized with inert gas, which aids in maintaining the target solution within the beam strike region. Whereas with fluorine-18 production, the composition of valves and tubing is carefully selected to minimize dilution of the molar radioactivity with fluorine-19, for the ^{68}Ga targets the tubing and valves associated with target loading and unloading must be chosen to be inert to the acidic solutions utilized, and all target materials and chemicals utilized carefully chosen to minimize contamination by metal ions.

The proton irradiation of aqueous solutions, as for ^{68}Ga targets, produces several other radionuclide contaminants that must be appropriately accounted for and removed in the subsequent steps of processing. At the end-of-bombardment (**EOB**), a large portion of the radioactivity delivered to a hot cell consists of gaseous ^{13}N produced by the $^{16}\text{O}(p,\alpha)^{13}\text{N}$ reaction. Small amounts of ^{18}F are also produced via the $^{18}\text{O}(p,n)^{18}\text{F}$ reaction (typically, [^{16}O]water contains trace amounts of [^{18}O]water), and volatile ^{11}C species are generated from the nitrate anion through the $^{14}\text{N}(p,\alpha)^{11}\text{C}$ reaction. While these co-contaminants will not interfere with subsequent metal-coordinating ^{68}Ga reactions, the crude ^{68}Ga solution produced on the cyclotron needs to be delivered to a hot cell with appropriate ventilation to accommodate significant amounts of radioactive gas. Finally, as with any irradiation of an aqueous solution in a metal target, there is the possibility of contamination of the desired radionuclide (in this case, ^{68}Ga) with trace amounts of other radioactive and nonradioactive metallic species arising from the target body or the foil material [93, 94].

The maximum theoretical molar activity of ^{68}Ga is actually higher than for ^{18}F and ^{11}C (Table 3.1), but to date, there has been minimal discussion of the molar activities achieved from ^{68}Zn cyclotron targets: although it was reported the molar activity from cyclotron production ($368\text{ GBq}\mu\text{mol}^{-1}$) was significantly higher than from a $^{68}\text{Ge}/^{68}\text{Ga}$ generator [87], it was still a small percentage of the theoretical ($102.3\text{ TBq}\mu\text{mol}^{-1}$). In general, rather low effective specific activities are reported for final ^{68}Ga -radiopharmaceuticals. This seems to be due to the excess chemical precursors used to effectively chelate the ^{68}Ga

and the difficulties encountered in trying to separate the chemical precursor from the final ^{68}Ga -chelated radiotracer. The result is that, at present, typical reported “effective” molar activities (radioactivity per total mass of ligand, chelated plus unchelated) obtained for finished human ^{68}Ga radiopharmaceuticals are often in the range of 25–50 GBq nmol⁻¹ [95, 96], although a higher value (1200 MBq nmol⁻¹) was reported for use in animal studies [97]. These values do not come close to those obtained with ^{18}F or ^{11}C labeled radiotracers, which limits applications of such ^{68}Ga -radiotracers to receptor targets with high tissue concentrations. In the future, perhaps, preparation and application of true high-molar-activity ^{68}Ga -radiotracers might be achieved.

3.3.5 Aqueous ^{68}Ga Target Development

Initial work with liquid targets for the production of radiometals via irradiation of nitrate salts was performed by Vogg et al. with the irradiation of $\text{Sr}(\text{NO}_3)_2$ to produce ^{86}Y [98]. This laid the groundwork for subsequent investigations of metallic radionuclide production via cyclotron irradiation of salt solutions, and Jensen and Clark published the initial work on cyclotron production of ^{68}Ga using proton irradiation of a liquid target containing an aqueous solution of $^{68}\text{ZnCl}_2$ [99]. A significant improvement by Pandey et al. was to use 1.7 M $^{68}\text{Zn}[\text{Zn}(\text{NO}_3)_2]$ in 0.2 M nitric acid as a target solution [93], as compared to irradiation of chloride salts, which resulted in decreased rates of water radiolysis, decreased the target pressure during irradiation and increased the Havar foil life, and reduced long-lived radiometal contaminants. While that target system was useful for producing ^{68}Ga and purified $^{68}\text{Ga}[\text{GaCl}_3]$, the methods were plagued by low and inconsistent yields and a time-consuming $^{68}\text{Ga}/^{68}\text{Ga}[\text{GaCl}_3]$ separation/purification process. This was a great starting point for liquid target ^{68}Ga production, but the process needed to be optimized to provide a high-yielding and reproducible method appropriate for routine clinical use.

Subsequent studies at the Mayo Clinic evaluated irradiations of varying $^{68}\text{Zn}[\text{Zn}(\text{NO}_3)_2]$ (0.6–1.42 M) concentrations in nitric acid (0.8–1.2 N) for 60 minutes at 30–50 μA [100]. The highest yields reported were an impressive 9.85 ± 2.09 Gbq (266 ± 57 mCi) (EOB, decay corrected) using the target solution of 1.42 M $^{68}\text{Zn}[\text{Zn}(\text{NO}_3)_2]$ in 1.2 N HNO_3 , with irradiations for 60 minutes at 40 μA . The ^{68}Ga produced in this manner underwent purification and $^{68}\text{Ga}[\text{GaCl}_3]$ formation and was further used to synthesize ^{68}Ga -PSMA-HBED under Current Good Manufacturing Practice (**cGMP**) compliance. This method provided clinically useful cyclotron production of ^{68}Ga from a liquid target, with one possible complication being the potential degradative effects of irradiation of targets with high zinc and nitric acid concentrations.

The institutions in Europe and the United States that have pursued the optimization of liquid targets for ^{68}Ga production have focused on using low nitric acid concentrations in the target media. A collaborative effort between GE Healthcare and Mayo Clinic [91] reported high yields of $^{68}\text{Ga}[\text{GaCl}_3]$ at 30 minutes past EOB of 2.5 ± 0.1 GBq (68 ± 4 mCi) (EOB + 30 minutes) using a target of 1.0 M $^{68}\text{Zn}[\text{Zn}(\text{NO}_3)_2]$ in 0.2 N HNO_3 and irradiations of 26 μA for 60 minutes. A high radionuclidic purity of >99.8% was obtained, which is well above the >98% European Pharmacopoeia acceptance guideline. Investigators in

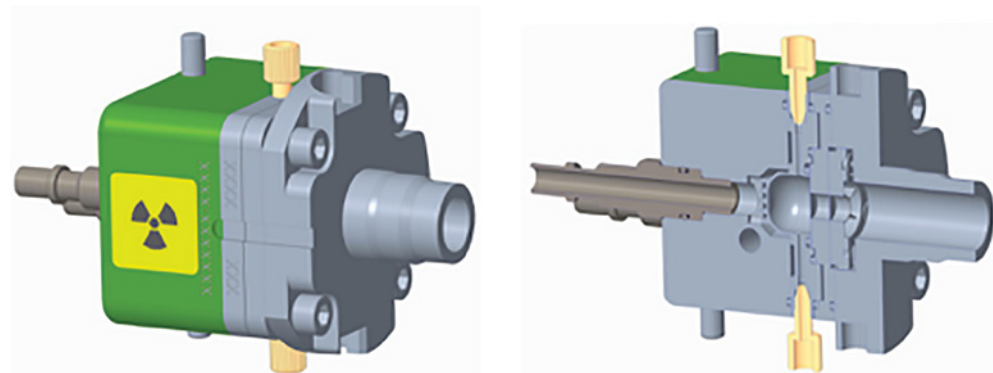
Italy reported ^{68}Ga yields of EOB of $4.3 \pm 0.3 \text{ GBq}$ ($116 \pm 8 \text{ mCi}$) (EOB) using $1.7 \text{ M } [^{68}\text{Zn}] \text{Zn}(\text{NO}_3)_2$ in 0.2 N HNO_3 and irradiations of 32 minutes at $46 \mu\text{A}$, with a high radionuclidic purity of $>99.9\%$ up to three hours EOB [101]. The University of Michigan utilized similar irradiation and synthetic conditions ($1.0 \text{ M } [^{68}\text{Zn}] \text{Zn}(\text{NO}_3)_2$ in 0.2 N HNO_3 , 60 minutes, $30 \mu\text{A}$) to produce $3.1 \pm 0.4 \text{ GBq}$ ($112 \pm 16 \text{ mCi}$) (EOB), which could be converted to $1.5 \pm 0.2 \text{ GBq}$ ($54 \pm 8 \text{ mCi}$) (EOB + 30 minutes) of $[^{68}\text{Ga}]\text{GaCl}_3$ and then to $1.2 \pm 0.2 \text{ GBq}$ ($45 \pm 6 \text{ mCi}$) of $[^{68}\text{Ga}]\text{Ga-PSMA-11}$ at 40 minutes EOB, all with high radionuclidic purity of $>99.8\%$.

At the end of 2019, there were commercially available liquid targets (IBA and GE Healthcare) for cyclotron production of ^{68}Ga . For both systems, the targetry is similar and functions to irradiate a $[^{68}\text{Zn}]\text{Zn}(\text{NO}_3)_2$ solution in dilute nitric acid. As a representative example, the design of the GE Healthcare ^{68}Ga liquid target is shown in Figure 3.4. The GE ^{68}Ga PETtrace Liquid Target is a small volume (including the target lines/dead volume, the total target fill volume is approximately 2.2 ml) constructed of a niobium target body and an entry foil pack consisting of an external 200 μm aluminum foil (for particle energy degradation), an intermediate 25 μm Havar foil for support, and an internal 25 μm niobium foil for chemical inertness with the target media. The thick aluminum foil serves as a degrader and provides additional protection against target foil failures and the acidic target solution being sucked into the cyclotron vacuum chamber.

3.3.6 Processing Cyclotron-Produced ^{68}Ga for Radiopharmaceutical Use

The process for ^{68}Ga purification is similar whether the radionuclide is obtained from solid or liquid targets and involves the steps needed to separate the desired ^{68}Ga from radionuclidic and chemical impurities and deliver a form (usually $^{68}\text{GaCl}_3$) useful for radiopharmaceutical syntheses. A variety of solid phases have been utilized for ^{68}Ga purification [79]: the two-column process [80, 91] used at the University of Michigan for liquid target processing is representative of the methods employed by many institutions. The irradiated target solution is transferred via lines from the cyclotron vault to a hot

Figure 3.4 The GE ^{68}Ga PETtrace liquid target used for cyclotron production of ^{68}Ga .



cell and diluted with a volume of water to reduce the nitric acid concentration to <0.1 M, and the ^{68}Ga is initially trapped on a hydroxamate resin. The resin is washed with dilute (0.1 N) nitric acid: this separates the ^{68}Ga from the ^{68}Zn , which is not retained on the resin. The column is then eluted with 1.5 N HCl, and the eluted $^{68}\text{GaCl}_3$ is trapped on a second column containing a triphenylphosphine oxide (**TOPO**) based resin. That resin can be washed with a NaCl/dilute HCl and finally eluted with water to provide a dilute acidic solution of the desired $^{68}\text{GaCl}_3$. Although $^{68}\text{GaCl}_3$ is not the final radiopharmaceutical of clinical value, quality control analyses are often performed on this intermediate to assure it is appropriate for use in radiopharmaceutical preparations. The important measures are radiochemical (percentage of ^{68}Ga as $^{68}\text{GaCl}_3$) and radionuclidic purities (^{66}Ga and ^{67}Ga impurities; ^{68}Ge breakthrough for generator eluate), and concentrations of the metal ions Fe and Zn (<10 $\mu\text{g GBq}^{-1}$ for each).

3.3.7 Future of Gallium-68

The University of Michigan and Mayo Clinic have performed full validation of their cyclotron-produced $^{68}\text{Ga}[\text{GaCl}_3]$ and $^{68}\text{Ga}[\text{Ga-PSMA-11}]$, and FDA-approved clinical studies with $^{68}\text{Ga}[\text{Ga-PSMA-11}]$ began in early 2019. The commercial availability of liquid targetry and/or automated chemical processing systems for the production of ^{68}Ga -radiopharmaceuticals will undoubtedly contribute to the continued development of new radiopharmaceuticals for PET imaging applications.

REFERENCES

1. Synowicki, M.A., Perk, L.R., and Nijssen, J.W.F. (2018). Production of novel diagnostic radionuclides in small medical cyclotrons. *EJNMMI Radiopharm. Chem.* 3: 3.
2. Conti, M. and Eriksson, L. (2016). Physics of pure and non-pure positron emitters for PET: a review and discussion. *EJNMMI Phys.* 3: 8.
3. Qaim, S.M. (2015). Nuclear data for medical radionuclides. *J. Radioanal. Nucl. Chem.* 305: 233–245.
4. Qaim, S.M. (2008). Decay data and production yields of some non-standard positron emitters used in PET. *Q. J. Nucl. Med. Mol. Imaging* 52: 111–120.
5. Qaim, S.M. (2011). Development of novel positron emitters for medical applications: nuclear and radiochemical aspects. *Radiochim. Acta* 99: 611–625.
6. Qaim, S.M. (2012). The present and future of medical radionuclide production. *Radiochim. Acta* 100: 635–651.
7. Hnatowich, D.J. (1977). A review of radiopharmaceutical development with short-lived generator-produced radionuclides other than $^{99\text{m}}\text{Tc}$. *Int. J. Appl. Radiat. Isot.* 28: 169–181.
8. Lebowitz, E. and Richards, P. (1974). Radionuclide generator systems. *Semin. Nucl. Med.* 4: 257–268.
9. Yano, Y., Chu, P., Budinger, T.F. et al. (1977). Rubidium-82 generators for imaging studies. *J. Nucl. Med.* 18: 46–50.

10. International Atomic Energy Agency. (2008). Technical report 465: Cyclotron produced radionuclide: principle and practice.
11. Thomas, C.C., Sondel, J.A., and Kerns, R.C. (1965). Production of carrier-free fluorine-18. *Int. J. Appl. Radiat. Isot.* 16: 71–74.
12. Firnaeu, G., Nahmias, C., and Garnett, S. (1973). The preparation of [¹⁸F]5-fluoro-DOPA with reactor-produced fluorine-18. *Int. J. Appl. Radiat. Isot.* 24: 182–184.
13. Clark, J.C. and Silvester, D.J. (1966). A cyclotron method for the production of fluorine-18. *Int. J. Appl. Radiat. Isot.* 17: 151–154.
14. Guillaume, M., Luxen, A., Nebeling, B. et al. (1991). Recommendations for fluorine-18 production. *Appl. Radiat. Isot.* 42: 749–762.
15. Brooks, A.F., Topczewski, I., Sanford, M.S., and Scott, P.J.H. (2014). Late-stage [¹⁸F] fluorination: new solutions to old problems. *Chem. Sci.* 5: 4545.
16. Preshlock, S., Tredwell, M., and Gouverneur, V. (2016). ¹⁸F-Labeling of arenes and heteroarenes for application in positron emission tomography. *Chem. Rev.* 116: 719–766.
17. Deng, X., Rong, J., Wang, L. et al. (2018). The chemistry for positron emission tomography: recent advances in ¹¹C-, ¹⁸F-, ¹³N- and ¹⁵O-labeling reactions. *Angew. Chem. Int. Ed.* (in press) DOI <https://doi.org/10.1002/anie.201805501>.
18. Kilbourn, M.R., Hood, J.T., and Welch, M.J. (1984). A simple oxygen-18 water target for fluorine-18 production. *Int. J. Appl. Radiat. Isot.* 35: 599–602.
19. Wieland, B.W., Hendry, G.O., Schmidt, D.G. et al. (1986). Efficient small-volume O-18 water targets for producing F-18 fluoride with low-energy protons. *J. Labelled Compd. Radiopharm.* 23: 1205–1207.
20. Kilbourn, M.R., Jerabek, P.A., and Welch, M.J. (1985). An improved [¹⁸O]water target for [¹⁸F]fluoride production. *Int. J. Appl. Radiat. Isot.* 36: 327–328.
21. Berridge, M.S. and Kjellstrom, R. (1999). Designs and use of silver [¹⁸O]water targets for [¹⁸F]fluoride production. *Appl. Radiat. Isot.* 50: 699–705.
22. Siikanen, J., Ohlsson, T., Medema, J. et al. (2013). A niobium water target for routine production of [¹⁸F]fluoride with a MC 17 cyclotron. *Appl. Radiat. Isot.* 72: 133–136.
23. Nye, J.A., Avila-Rodriguez, M.A., and Nickels, R.J. (2006). A grid-mounted niobium body target for production of reactive [¹⁸F]fluoride. *Appl. Radiat. Isot.* 64: 536–539.
24. Zeisler, S.K., Becker, D.W., Pavan, R.A. et al. (2000). A water-cooled spherical niobium target for the production of [¹⁸F]fluoride. *Appl. Radiat. Isot.* 53: 449–453.
25. Tewson, T.J., Berridge, M.S., Bolomey, L. et al. (1988). Routine production of reactive fluorine-18 fluoride salts from an oxygen-18 water target. *Nucl. Med. Biol.* 15: 499–504.
26. Mirzaii, M., Afarideh, H., Hadji-Saeid, S.M. et al. (2004). Production of [¹⁸F] fluoride with a high-current two-layer spherical gold target. *Nukleonika* 49: 23–27.
27. Metzger, R.L., Lasche, G.P., Eckerman, K.F., and Leggett, R.W. (2018). Long-lived contaminants in cyclotron-produced radiopharmaceuticals: measurement and dosimetry. *J. Radioanal. Nucl. Chem.* 318: 7–10.
28. Gagnon, K., Wilson, J.S., Sant, E. et al. (2011). Assessing the performance and longevity of Nb, Pt, Ta, Ti, Zr, and ZrO₂-sputtered Havar foils for the high-power production of reactive [¹⁸F]F⁻ by proton irradiation of [¹⁸O]H₂O. *Appl. Radiat. Isot.* 69: 1330–1336.

29. Solin, O., Bergman, J., Haaparanta, M., and Reissell, A. (1988). Production of ^{18}F from water targets. Specific radioactivity and anionic contaminants. *Int. J. Appl. Radiat. Isot.* 39: 1065–1071.
30. Bowden, L., Vintro, L.L., Mitchell, P.I. et al. (2009). Radionuclide impurities in proton-irradiated ^{18}O H_2O for production of $^{18}\text{F}^-$: activities and distribution in the ^{18}F FDG synthesis process. *Appl. Radiat. Isot.* 67: 248–255.
31. Eberl, S., Eriksson, T., Svedberg, O. et al. (2012). High beam current operation of a PETtrace™ cyclotron for ^{18}F -production. *Appl. Radiat. Isot.* 70: 922–930.
32. Savisto, N., Bergman, J., Aromaa, J. et al. (2018). Influence of transport line material on the molar activity of cyclotron produced ^{18}F fluoride. *Nucl. Med. Biol.* 64: 8–15.
33. Berridge, M.S., Apana, S.M., and Hersh, J.M. (2009). Teflon radiolysis as the major source of carrier in fluorine-18. *J. Labelled Compd. Radiopharm.* 52: 453–548.
34. Fuechtner, F., Preusche, S., Maeding, P. et al. (2008). Factors affecting the specific activity of ^{18}F fluoride from a ^{18}O water target. *Nuclearmedizin* 47: 116–119.
35. Hess, E., Blessing, G., Coenen, H.H., and Qaim, S.M. (2000). Improved target system for production of high purity ^{18}F fluoride via the $^{18}\text{O}(p,n)^{18}\text{F}$ reaction. *Appl. Radiat. Isot.* 52: 1431–1440.
36. Bida, G.T., Ehrenkaufer, R.L., Wolf, A.P. et al. (1980). The effect of target-gas purity on the chemical form of F-18 during $^{18}\text{F}\text{-F}_2$ production using the neon/fluorine target. *J. Nucl. Med.* 21: 758–762.
37. Bishop, A., Satyamurthy, N., Bida, G. et al. (1996). Metals suitable for fluorine gas target bodies. First use of aluminum for the production of $^{18}\text{F}\text{F}_2$. *Nucl. Med. Biol.* 23: 181–188.
38. Helus, F., Uhler, V., Wolber, G. et al. (1994). Contribution to cyclotron targetry II. Testing of the target construction materials for ^{18}F production via $^{20}\text{Ne}(d,\alpha)^{18}\text{F}$. Recovery of ^{18}F from various metal surfaces. *J. Radioanal. Nucl. Chem.* 182: 445–450.
39. Straatmann, M.G. and Welch, M.J. (1977). Fluorine-18-labeled diethylaminosulfur trifluoride (DAST): a F-for-OH fluorinating agent. *J. Nucl. Med.* 18: 151–157.
40. Ehrenfauser, R.E., MacGregor, R.R., Wolf, A.P. et al. (1983). Production of H^{18}F by deuteron irradiation of a neon-hydrogen gas target. *Radiochim. Acta* 33: 49–56.
41. Tewson, T.J. and Welch, M.J. (1999). Preparation and preliminary biodistribution of “no carrier added” fluorine-18 fluoroethanol. *J. Nucl. Med.* 21: 559–564.
42. Christman, D.R., Finn, R.D., Karlstrom, K.I., and Wolf, A.P. (1975). The production of ultra high activity ^{11}C -labeled hydrogen cyanide, carbon dioxide, carbon monoxide and methane via the $^{14}\text{N}(p,\alpha)^{11}\text{C}$ reaction (XV). *Int. J. Appl. Radiat. Isot.* 26: 435–442.
43. Clark, J.C. and Buckingham, P.D. (1971). The preparation and storage of carbon-11 labelled gases for clinical use. *Int. J. Appl. Radiat. Isot.* 22: 639–646.
44. Gillings, N., Jorgensen, J., Larsen, P. et al. (2012). Optimization of ^{11}C methane yields from a high pressure gas target. 14th International Workshop on Targets and Target Chemistry.
45. Dahl, K., Halldin, C., and Schou, M. (2017). New methodologies for the preparation of carbon-11 labeled radiopharmaceuticals. *Clin. Transl. Imaging* 5: 275–289.

46. Haskell, M.B. and Pike, V.W. (2017). [¹¹C]Fluoroform, a breakthrough for versatile labeling of PET radiotracer trifluoromethyl groups in high molar activity. *Chemistry* 23: 8156–8160.
47. Andersson, J., Truong, P., and Halldin, C. (2009). In-target produced [¹¹C]methane: increased specific activity. *Appl. Radiat. Isot.* 67: 106–110.
48. Joliot, F. and Curie, I. (1934). Artificial production of a new kind of radio-element. *Nature* 133: 201–202.
49. Tilbury, R.S. and Dahl, J.R. (1979). ¹³N species formed by proton irradiation of water. *Radiat. Res.* 79: 22–33.
50. Krasikova, R.N., Fedorova, O.S., Korsakov, M.V. et al. (1999). Improved [¹³N]ammonia yield from the proton irradiation of water using methane gas. *Appl. Radiat. Isot.* 51: 395–401.
51. Le Bars, D. (2001). A convenient production of [¹³N]nitrogen for ventilation studies using a nitrogen gas target for ¹¹C production. *J. Labelled Compd. Radiopharm.* 44: 1–5.
52. Clark, J.C., Matthews, C.M.E., Sylvester, D.J., and Vonberg, D.D. (1967). Using cyclotron-produced isotopes at Hammersmith Hospital. *Nucleonics* 25: 54–62.
53. Welch, M.J. and Kilbourn, M.R. (1985). A remote system for the routine production of oxygen-15 labeled radiopharmaceuticals. *J. Labelled Compd. Radiopharm.* 22: 1193–1200.
54. Berridge, M.S., Franceschini, M.P., Tewson, T.J., and Gould, K.L. (1986). Preparation of oxygen-15 butanol or positron tomography. *J. Nucl. Med.* 27: 834–837.
55. Herscovitch, P., Raichle, M.E., Kilbourn, M.R., and Welch, M.J. (1987). Positron emission tomographic measurement of cerebral blood flow and permeability-surface area product of water using ¹⁵O-water and ¹¹C-butanol. *J. Cereb. Blood Flow Metab.* 7: 527–542.
56. Sajjad, M., Liow, J.-S., and Moreno-Cantu, J. (2000). A system for continuous production and infusion of [¹⁵O]H₂O for PET activation studies. *Appl. Radiat. Isot.* 52: 205–210.
57. Ruth, T.J. (1985). The production of ¹⁸F-F₂ and ¹⁵O-O₂ sequentially from the same target chamber. *Int. J. Appl. Radiat. Isot.* 36: 107–110.
58. Koh, K., Finn, R., Wooten, T. et al. (1983). External tandem target system for efficient production of short-lived positron emitting radionuclides. *IEEE Trans. Nucl. Sci.* 30: 3062–3066.
59. Mulholland, G.K., Kilbourn, M.R., and Moskwa, J.J. (1990). Direct simultaneous production of [¹⁵O]water and [¹³N]ammonia or [¹⁸F]fluoride ion by 26 MeV proton irradiation of a double-chamber water target. *Appl. Radiat. Isot.* 41: 1193–1199.
60. Yang, S.D., Kim, S.W., Hur, M.G. et al. (2007). Design and evaluation of the tandem target for a simultaneous production of [¹¹C]CH₄ and [¹⁸F]fluoride. *Nucl. Med. Biol.* 34: 117–120.
61. Grant, P.M., O'Brien, H.A., and Kahn, M. (1975). The isolation of ⁸²Sr from 200 to 600 MeV proton-irradiated Mo targets for biomedical applications. *J. Inorg. Nucl. Chem.* 37: 413–417.

62. Yoshinaga, K., Klein, R., and Tamaki, N. (2010). Generator-produced rubidium-82 positron emission tomography myocardial perfusion imaging – from basic aspects to clinical applications. *J. Cardiol.* 55: 163–173.
63. Yano, Y. and Anger, H.O. (1964). A gallium-68 positron cow for medical use. *J. Nucl. Med.* 5: 485–488.
64. Green, M.A. and Welch, M.J. (1989). Gallium radiopharmaceutical chemistry. *Nucl. Med. Biol.* 16: 435–448.
65. Spang, P., Hermann, C., and Roesch, F. (2016). Bifunctional gallium-68 chelators: past, present and future. *Semin. Nucl. Med.* 46: 373–394.
66. Martiniova, L., De Palatis, L., Etchebehere, E. et al. (2016). Gallium-68 in medical imaging. *Curr. Radiopharm.* 9: 187–207.
67. Tanzey, S.S., Thompson, S., Scott, P.J.H. et al. (2018). Gallium-68: methodology and novel radiotracers for positron emission tomography (2010–2017). *Pharm. Pat. Anal.* 7: 193–227.
68. Aardenah, K. and van der Walt, T.N. (2006). Ga₂O for target, solvent extraction for radiochemical separation and SnO₂ for the preparation of a ⁶⁸Ge/⁶⁸Ga generator. *J. Radioanal. Nucl. Chem.* 268: 25–32.
69. Gleason, G.I. (1960). A positron cow. *Int. J. Appl. Radiat. Isot.* 8: 90–94.
70. Ehrhard, G.J. and Welch, M.J. (1978). A new germanium-68/gallium-68 generator. *J. Nucl. Med.* 19: 925–929.
71. Stang, L.G., Tucker, W.D., Doering, R.F., et al. (1958). In radioisotopes in scientific research, VII, pp. 50-70. Proc. 1st UNESCO Int. Conf. Paris, 1957, Pergamon Press, NY.
72. Greene, M.W. and Tucker, W.D. (1961). An improved gallium-68 cow. *Int. J. Appl. Radiat. Isot.* 12: 62–63.
73. Amor-Coarasa, A., Kelly, J.M., Gruca, M. et al. (2017). Continuation of comprehensive quality control of the itG ⁶⁸Ge/⁶⁸Ga generator and production of ⁶⁸Ga-DOTOTOC and ⁶⁸Ga-PSMA-HBED-CC for clinical research studies. *Nucl. Med. Biol.* 53: 37–39.
74. Eppard, E., Loktionova, N.S., and Rosch, F. (2013). Quantitative online isolation of ⁶⁸Ge from ⁶⁸Ge/⁶⁸Ga generator eluates for purification and immediate quality control of breakthrough. *Appl. Radiat. Isot.* 82: 45–48.
75. Eppard, E., Loktionova, N.S., and Rosch, F. (2014). ⁶⁸Ga content quality control of ⁶⁸Ge/⁶⁸Ga generator eluates and ⁶⁸Ga radiopharmaceuticals – a protocol for determining the ⁶⁸Ge content using thin layer chromatography. *Appl. Radiat. Isot.* 91: 92–96.
76. Nanabala, R., Anees, M.K., Sasikumar, A. et al. (2016). Preparation of [⁶⁸Ga]PSMA-11 for PET-CT imaging using a manual synthesis module and organic matrix based ⁶⁸Ge/⁶⁸Ga generator. *Nucl. Med. Biol.* 43: 463–469.
77. Tworowska, I., Raganathan, D., Thamake, S. et al. (2016). Radiosynthesis of clinical doses of ⁶⁸Ga-DOTOTATE (GalioMedix™) and validation of organic-matrix-based ⁶⁸Ge/⁶⁸Ga generators. *Nucl. Med. Biol.* 43: 19–26.
78. Rosch, F. (2013). Past, present and future of ⁶⁸Ge/⁶⁸Ga generators. *Appl. Radiat. Isot.* 76: 24–30.
79. International Atomic Energy Agency (2019). *Gallium-68 Cyclotron Production*, IAEA-TECDOC-1863. Vienna, Austria.

80. European Pharmacopoeia. (2018). Gallium (^{68}Ga) chloride (accelerator-produced) solution for radiolabelling. Monograph 2464, PA/PH/Exp. 14/T (18) 13 ANP.
81. Pandey, M.K. and DeGrado, T.R. (2019). Rapid isolation of cyclotron-produced gallium-68. US Patent 2019/0198187 A1.
82. Abbasi, A.A. and Easwaramoorthy, B. (2018). Method and system for producing gallium-68 radioisotope by solid targeting in a cyclotron. World Patent WO 2016/197084 A1.
83. Alnahwi, A., Tremblay, S., Ait-mohand, S. et al. (2019). Large-scale routine production of ^{68}Ga using ^{68}Zn -pressed target. *J. Nucl. Med.* 60 (Suppl 1): 634.
84. Zeisler, S., Limoges, A., Kumlin, J. et al. (2019). Fused zinc target for the production of gallium radioisotopes. *Instruments* 3: 10.
85. Szelecsényi, F., Kovács, Z., Nagatsu, K. et al. (2012). Investigation of direct production of ^{68}Ga with low energy multiparticle accelerator. *Radiochim. Acta* 100: 591.
86. Sadeghi, M., Kakavand, T., Rajabifar, S. et al. (2009). Cyclotron production of ^{68}Ga via proton-induced reaction on ^{68}Zn target. *Nukleonika* 54: 25–28.
87. Lin, M., Waligorski, G.J., and Lepera, C.G. (2018). Production of curie quantities of ^{68}Ga with a medical cyclotron via the $^{68}\text{Zn}(p,n)^{68}\text{Ga}$ reaction. *Appl. Radiat. Isot.* 133: 1–3.
88. Tieu, W., Hollis, C.A., Kuan, K.K.W. et al. (2019). Rapid and automated production of [^{68}Ga]gallium chloride and [^{68}Ga]Ga-DOTA-TATE on a medical cyclotron. *Nucl. Med. Biol.* 74–75: 12–18.
89. Tolmachev, V. and Lundqvist, H. (1996). Rapid separation of gallium from zinc targets by thermal diffusion. *Appl. Radiat. Isot.* 47: 297–299.
90. de Andrade Martins, P. and Osso, J.A. (2013). Thermal diffusion of ^{67}Ga from irradiated Zn targets. *Appl. Radiat. Isot.* 82: 279–282.
91. Nair, M., Happel, S., Eriksson, T. et al. (2017). Cyclotron production and automated new 2-column processing of [^{68}Ga]GaCl₃. *Eur. J. Nucl. Med. Mol. Imaging* 44 (Suppl 2): S119–S956.
92. Oehlke, E., Hoehr, C., Hou, X. et al. (2015). Production of Y-86 and other radiometals for research purposes using a solution target system. *Nucl. Med. Biol.* 42: 842–849.
93. Pandey, M.K., Byrne, J.F., Jiang, H. et al. (2014). Cyclotron production of ^{68}Ga via the $^{68}\text{Zn}(p,n)^{68}\text{Ga}$ reaction in aqueous solution. *Am. J. Nucl. Med. Mol. Imaging* 4: 303–310.
94. Alves, F., Alves, V.H.P., Do Carmo, S.J.C. et al. (2017). Production of copper-64 and gallium-68 with a medical cyclotron using liquid targets. *Mod. Phys. Lett. A* 32: 1740013.
95. Zha, Z., Song, J., Choi, S.R. et al. (2016). ^{68}Ga -Bivalent polypegylated styrylpyridine conjugates for imaging A β plaques in cerebral amyloid angiopathy. *Bioconjugate Chem.* 27: 1314–1323.
96. Velikyan, I., Sundin, A., Eriksson, B. et al. (2010). In vivo binding of [^{68}Ga]-DOTOTOC to somatostatin receptors in neuroendocrine tumours – impact of peptide mass. *Nucl. Med. Biol.* 37: 265–275.
97. Wurzer, A., Pollmann, J., Schmidt, A. et al. (2018). Molar activity of Ga-68 labeled PSMA inhibitor conjugates determines PET imaging results. *Mol. Pharmaceutics* 15: 4296–4302.

98. Vogg, A., Lang, R., Meier-Böke, P. et al. (2004). Cyclotron production of radionuclides in aqueous target matrices as alternative to solid state targetry: production of Y-86 as example. 6th International Conference on Nuclear and Radiochemistry, Aachen, Germany.
99. Jensen, M. and Clark, J.C. (2010). Direct production of Ga-68 from proton bombardment of concentrated aqueous solutions of [Zn-68] Zinc Chloride. 13th Workshop on Targetry and Target Chemistry. Roskilde, Denmark.
100. Pandey, M.K., Byrne, J.F., Schlasner, K.N. et al. (2019). Cyclotron production of ⁶⁸Ga in a liquid target: effects of solution composition and irradiation parameters. *Nucl. Med. Biol.* 74–75: 49–55.
101. Riga, S., Cicoria, G., Pancaldi, D. et al. (2018). Production of Ga-68 with a General Electric PETtrace cyclotron by liquid target. *Physica Med.*

Chapter 4

Production of Radionuclides Used in SPECT

Salma Jivan¹ and Thomas J. Ruth²

¹*Biomedical Isotope Facility, Berkeley Lab, Helen Wills Neuroscience Institute, University of California, Berkeley, Berkeley, CA 94720, USA*

²*Life Sciences Division, TRIUMF and BC Cancer Research Centre, Vancouver, BC V6T 2A3, Canada*

4.1 INTRODUCTION

This chapter describes the production and isolation methods for obtaining the radionuclides used in single photon emission computed tomography (**SPECT**). The radionuclides used in SPECT are produced in reactors or from proton bombardment of targets at cyclotron facilities. Table 4.1 lists the radionuclides used in the majority of procedures. The table also includes the half-life, major decay mode, as well as decay product for each of these radionuclides.

The following sections present the radionuclide with a description of how it is produced along with typical separation/purification approaches presently used. However, it should be noted that since these radionuclides are produced commercially, the exact procedures used by the various manufacturers are proprietary and thus may not reflect what is used by each producer.

Table 4.1 Table of SPECT radionuclides.

Isotope	Half-life	Primary decay (keV)	Decay product
^{99m} Tc	6 h	140	⁹⁹ Tc (2.1×10^5 yr)
¹³¹ I	8 d	364, 637	¹³¹ Xe (stable)
²⁰¹ Tl	72 h	70–80 (X-rays)	²⁰¹ Hg (stable)
⁶⁷ Ga	78 h	93, 185	⁶⁷ Zn (stable)
¹¹¹ In	67 h	245, 172	¹¹¹ Cd (stable)
¹²³ I	13 h	159	¹²³ Te (9.2×10^{16} yr)
¹³³ Xe	5 d	81	¹³³ Cs (stable)

Source: Based on NRC (National Research Council). 2007. *Advancing Nuclear Medicine Through Innovation*. Washington, DC: The National Academies Press. Available at <https://doi.org/10.17226/11985>.

4.2 TECHNETIUM-99m

SPECT imaging is dominated by ^{99m}Tc, which accounts for more than 80% of all procedures. Historically, ^{99m}Tc is derived from a ⁹⁹Mo generator, which is extracted from the fission products of ²³⁵U. The year 2018 marked the 60th anniversary of the development of the ⁹⁹Mo/^{99m}Tc generator at Brookhaven National Laboratory in New York (<https://www.bnl.gov/newsroom/news.php?a=213162>).

The development of this generator opened the field of nuclear medicine to a simple source of radioactivity that could be supplied internationally. The 66-hour half-life of ⁹⁹Mo allowed for remote producers to produce the isotope and prepare a generator to be shipped to hospitals or central pharmacies. Over the next several decades, chemists developed tracers that can be used in the diagnoses of various disease conditions. Table 4.2 provides some examples of the use of ^{99m}Tc.

The thermal neutron fission of ²³⁵U provides the most efficient source of ⁹⁹Mo. Figure 4.1 illustrates the fission yield curve for various isotopes as a function of atomic mass. Note that the yield in Figure 4.1 shows that the two maxima are for atomic masses at $A = 100$ and 130 .

As can be seen from the curve, the isotopes of interest to medicine (^{99m}Tc, ¹³¹I, ¹³³Xe) are produced in large abundance (3–5% of each fission). For several decades, highly enriched ²³⁵U (**HEU**; >93%) was the target of choice because the uranium targets could be made in the form of pellets or compact plates for ease of dissolution. Such targets occupied a relatively small space in a reactor's core due to the high density of uranium and high enrichment.

More recently, there has been a push from the nuclear safeguards community for removal of highly enriched fissile material from civilian use because a relatively small quantity of enriched ²³⁵U could be used to produce a nuclear bomb. As part of this effort, a study performed by the US National Academy of Sciences indicated that conversion from HEU to low enriched ²³⁵U (**LEU**; defined as <20% ²³⁵U) could be technically achieved within a reasonable cost structure [2]. At the time of this writing (2018), several of the international producers have converted from HEU to LEU targets, and new facilities have been designed from the start to use LEU [3]. The conversion has been challenging and costly, resulting in some disruption of supply.

^{99m} Tc radiopharmaceutical	Primary use
Sestamibi (Cardiolite)	Myocardial perfusion imaging
Tetrofosmin (Myoview)	Myocardial perfusion imaging
Medronate (methylene diphosphonate, MDP)	Bone imaging
Tc-99m oxidronate (TechnoScan; hydroxydiphosphonate, HDP)	Bone imaging
Pyrophosphate	Avid infarct imaging
Mebrofenin (Choletec)	Hepatobiliary imaging
Mertiatide (MAG-3)	Renal imaging
Glucaptate	Renal imaging
Tc-99m pentatate (diethylene triamine pentaacetic acid, DTPA)	Renal imaging and function studies
Pertechnetate	Imaging thyroid, salivary glands, ectopic gastric mucosa, parathyroid glands, dacrycystography, cystography
Macroaggregated albumin (MAA)	Pulmonary perfusion
Exametazime, HMPAO (Ceretec)	Cerebral perfusion imaging
Bicisate, ethyl cysteinate dimer (ECD) (Neurolite)	Cerebral perfusion imaging

Table 4.2 Examples of radiopharmaceuticals labelled with ^{99m}Tc along with their primary usage.

Source: Based on NRC (National Research Council). 2007. *Advancing Nuclear Medicine Through Innovation*. Washington, DC: The National Academies Press. Available at <https://doi.org/10.17226/11985>.

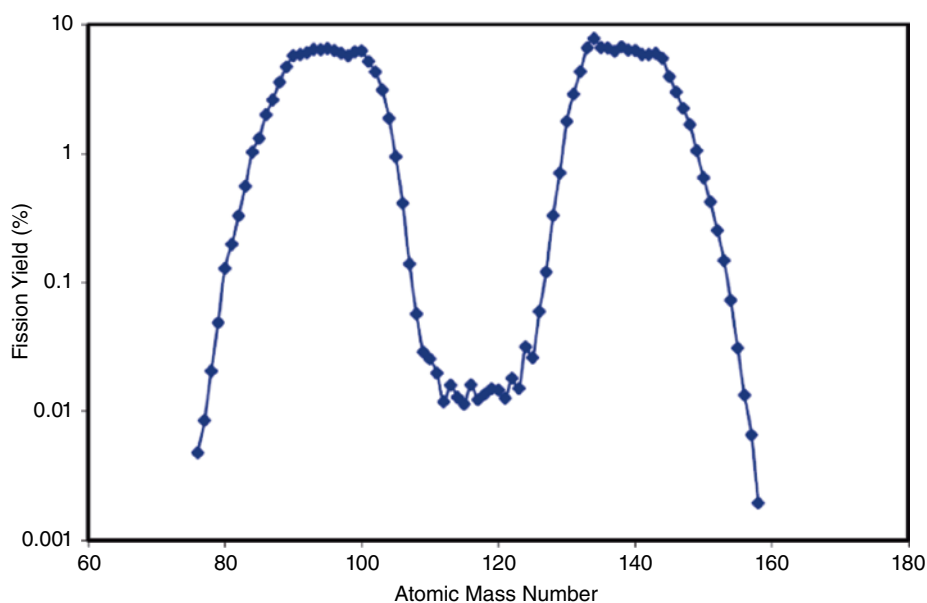


Figure 4.1 Fission yield for thermal neutron fission of ²³⁵U. Source: Data from Handbook of Nuclear Data for Safeguards: Database Extensions, August 2008. Prepared by A.L. Nichols, D.L. Aldama, and M. Verpelli. INDC International Nuclear Data Committee. International Atomic Energy Agency 2008. Retrieved from: <https://www-nds.iaea.org/sgnucdat/c1.htm>.

However, a larger disruption in the 2008–2009 period, with the two largest producers lasting more than one year, caused great concern for the nuclear medicine community [4]. Subsequently, several initiatives began to explore alternative routes to ^{99}Mo and/or $^{99\text{m}}\text{Tc}$ [5]. These included building new reactors or repurposing existing reactors as well as developing new technologies to produce these radionuclides. Again, as of this writing, only two new approaches have demonstrated the ability to produce useful quantities. NorthStar Medical Technologies, LLC has made use of an old technology, $^{98}\text{Mo}(n,\gamma)^{99}\text{Mo}$, to produce low-specific-activity ^{99}Mo . However, this product is not compatible with existing generator systems because of the large mass of Mo in the product (^{98}Mo and ^{99}Mo). Thus, a new generator approach had to be built. Such a new generator system (Radiogenix) was designed to supply $^{99\text{m}}\text{Tc}$ of sufficiently high concentration to be compatible with existing pharmaceutical *kits* to be used in the clinic (<https://www.northstarm.com/products/northstar-solutions-radiogenix-system>). It is too early to determine how successful this approach will be in supplementing the supply of $^{99}\text{Mo}/^{99\text{m}}\text{Tc}$.

The other approach developed by two Canadian consortia makes use of small medical cyclotrons (16–24 MeV protons) to produce $^{99\text{m}}\text{Tc}$ directly via the $^{100}\text{Mo}(p,2n)$ reaction [6, 7]. While this approach has been demonstrated to produce sufficient quantities for regional distribution, it has not been adopted for clinical use as of this writing.

It is beyond the scope of this chapter to provide a more in-depth discussion of this aspect of $^{99\text{m}}\text{Tc}$ availability.

4.3 IODINE-131

While ^{131}I is a fission product that can be extracted during the processing for ^{99}Mo , it is more efficient to produce via the $^{130}\text{Te}(n,\gamma) \rightarrow ^{131}\text{I}$ reaction. In either case, there is a need for a neutron source [5]. I-131 decays by beta emission and has two primary gamma rays at 364 and 637 keV.

For many years, ^{131}I – radiopharmaceuticals were used in diagnosing various diseases. However, with an eight-day half-life and relatively high photon energies, an alternative iodine isotope was sought. The best candidate was ^{123}I (discussed in a later section) [8]. With the introduction of ^{123}I radiopharmaceuticals, the use of ^{131}I has diminished. As can be seen from Figure 4.2, ^{131}I is used primarily for therapeutic purposes.

4.4 XENON-133

Xenon-133 (5d; photon at 81 keV) is also a ^{235}U fission product. As a noble gas, it is released upon the dissolution of the uranium target. Thus, the ^{133}Xe needs to be trapped in the gas stream during dissolution. The demand for ^{133}Xe is primarily in North America. Other jurisdictions use $^{99\text{m}}\text{Tc}$ tracers for ventilation studies [5].

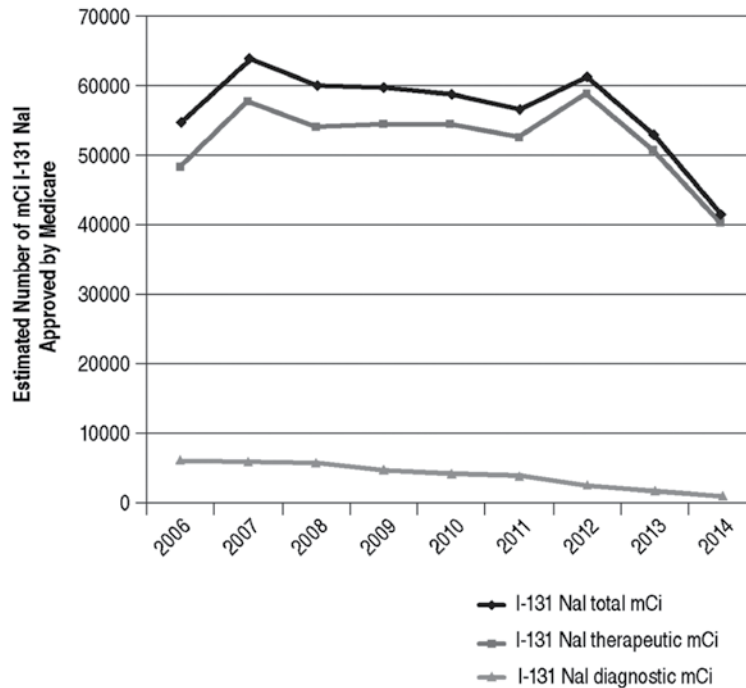


Figure 4.2 I-131 usage based on US Medicare beneficiaries (National Research Council [NRC]). Note that 1mCi is equivalent to 37GBq. Source: Based on NRC (National Research Council). 2016. Molybdenum-99 for Medical Imaging. Washington, DC: The National Academies Press. Available <https://doi.org/10.17226/23563>.

4.5 CYCLOTRON-PRODUCED RADIONUCLIDES

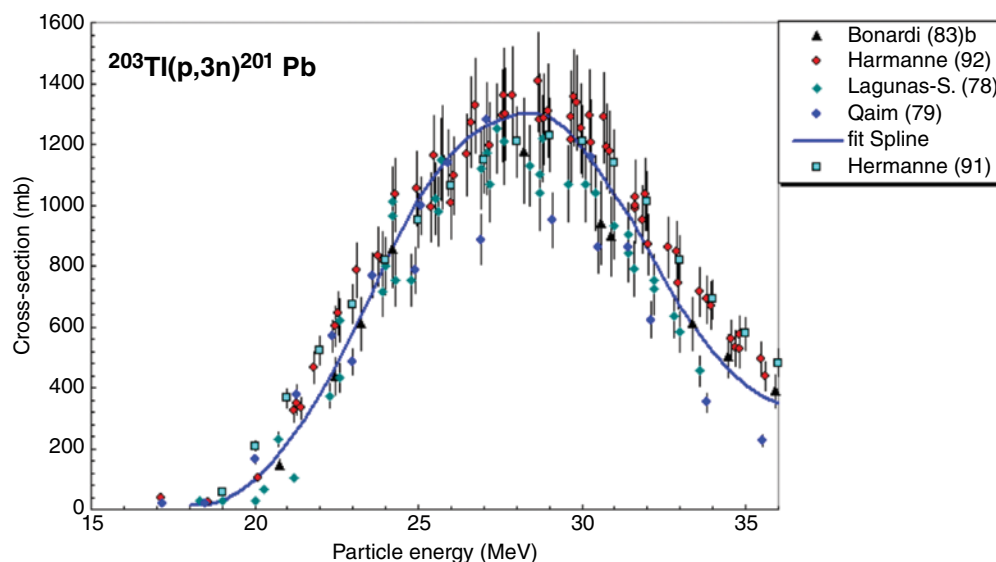
The radionuclides ^{201}Tl , ^{67}Ga , ^{123}I , and ^{111}In are made by proton bombardment of their respective target materials on high-beam-current cyclotrons owned and operated by commercial entities [9] (ref. Tec Doc 468). The typical cyclotron has a maximum proton energy of approximately 30 MeV and beam currents typically greater than 200 μA , with some as high as 1 mA. Such cyclotrons have remotely operated target changers to lower the radiation exposure to staff.

4.6 THALLIUM-201

Thallium has a +1 oxidation state, making it a useful analog of potassium. It is used extensively in cardiac imaging even though there are $^{99\text{m}}\text{Tc}$ -tracers (see Table 4.2) that deliver lower radiation exposure to the patient and can be prepared from generator-produced $^{99\text{m}}\text{Tc}$ [10].

With a half-life of 73.06 hours, ^{201}Tl can be produced in a central location and shipped to end users at great distances. Tl-201 decays by electron capture with the emission of gamma rays at 167 and 135 keV, which are ideal for use in a gamma camera [11–13].

Figure 4.3 Pb-201 production cross-section for the eventual extraction of ^{201}Tl . Source: Based on IAEA charged particle cross section database for medical radioisotope production, updated 2003–2004. www-nds.iaea.org/medical.



The production cross-section is shown in Figure 4.3, which is for the $^{203}\text{Tl}(p,3n)^{201}\text{Pb}$ reaction. The ^{201}Tl is obtained by waiting for the 9.3 hour ^{201}Pb to decay approximately 32 hours (more than three half-lives). There are two stable isotopes of thallium: ^{203}Tl (29.52%) and ^{205}Tl (70.48%). Thus, the target for producing ^{201}Tl must be enriched in $\text{Tl} = 203$.

Two methods that are generally used to achieve the separation and isolation of ^{201}Tl from the Tl/Pb target mixture may include ion-exchange resins and solvent/solvent extraction. The detailed procedure for the extraction can be found in International Atomic Energy Agency (IAEA) Technical Report Series 432 [15].

Because the target is composed of enriched ^{203}Tl (>97% to >98%),¹ it must be separated from the Pb isotopic product using chemical and electrodeposition methods.

For clinical use, the final product is checked for radionuclidic and chemical purity using multichannel pulse-height analysis with a gamma spectrometer. In addition to the ^{201}Tl gamma peaks, the impurities are also determined. The main gamma peaks are the X-rays (70.8 and 80.2 keV) and photons (135 and 167 keV) of ^{201}Tl ; photons (368 keV) of ^{200}Tl ; and photons (439 keV) of ^{202}Tl .

The radiochemical purity of the ^{201}Tl is checked by paper chromatography to differentiate Tl^+ and Tl^{3+} [16]. Chemical purity is assessed for the quantity of hydrazine in the ^{201}Tl solution by spectrophotometric adsorption analysis [16, 17]. Figure 4.4 illustrates the potential radionuclidic impurities found in the target mix, which are highly dependent upon the irradiation energy and length of irradiation [18].

Pb-200 (21.5 hours) decays to ^{200}Tl (26 hours), and $^{202\text{m}}\text{Pb}$ (3.54 hours) decays to ^{202}Tl (12.23 days).

¹ All enrichments are typical and provided by Isoflex, San Francisco, California.

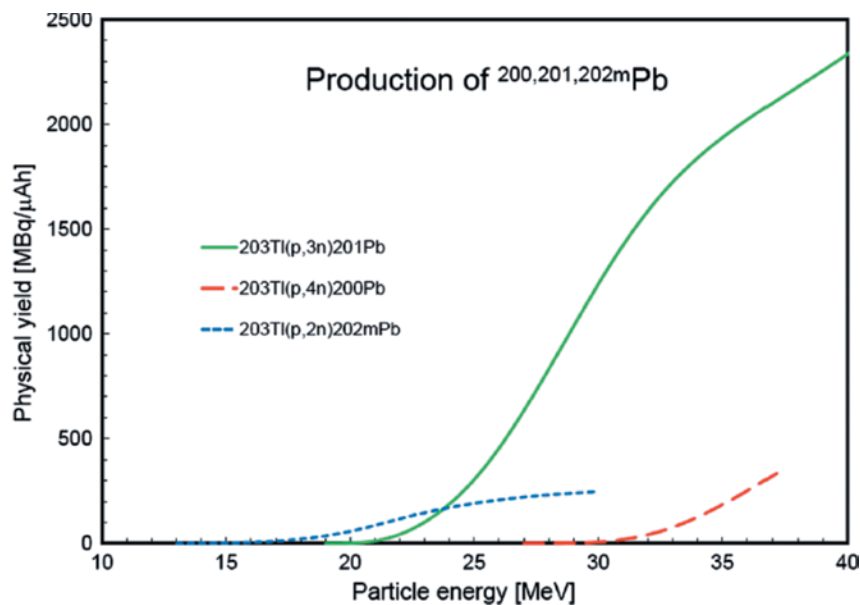


Figure 4.4 Yield curves for $^{200,201,202m}\text{Pb}$ based on excitation curves or the three proton reactions on Tl isotopes found in the enriched ^{203}Tl target. Source: Tárkányi, F.T., Ignatyuk, A.V., Hermanne, A. et al. Recommended nuclear data for medical radioisotope production: diagnostic gamma emitters. *J Radioanal Nucl Chem* 319, 487–531 (2019). Licensed under CCBY 4.0.

4.7 GALLIUM-67

Gallium-67 ($t_{1/2} = 3.26$ days) behaves in the body similarly to ferric iron and is often used as a trivalent citrate compound for imaging in the detection and localization of certain neoplasms and inflammatory lesions. It decays to stable ^{67}Zn by electron capture. The decay emissions include gamma-rays of 93.3 keV (37.0%), 184.6 keV (20.4%), and 300.2 keV (16.6%).

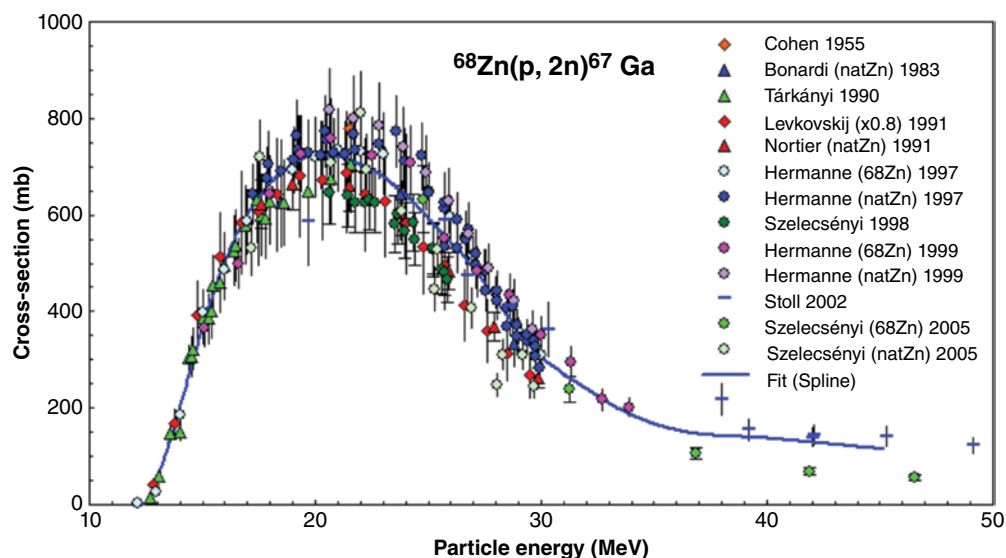
Figure 4.5 shows the excitation function for the production of ^{67}Ga via the $^{68}\text{Zn}(p,2n)$ reaction. An enriched ^{68}Zn target is required because of the large number of stable zinc isotopes. The target is often plated onto a copper backing plate for irradiation in the cyclotron.

There are several methods for the separation of ^{67}Ga from the zinc target. Two commonly used methods entail ion-exchange separation and solvent/solvent extraction [19, 20].

After irradiation, the ^{68}Zn target is dissolved in concentrated HCl, followed by separation of Ga-67 from ^{68}Zn by Dowex 50W-X8 resin. Ga-67 is recovered as Ga-citrate by dissolving the residue in a solution of 2–4% sodium citrate solution.

For the alternative approach, the irradiated ^{68}Zn target is dissolved in 7.5M HCl, followed by extraction of Ga-67 in di-isopropyl ether (**DIPE**). Zn-68 remains in the acidic

Figure 4.5 Excitation function for the production of ^{67}Ga . Source: Based on IAEA charged particle cross section database for medical radioisotope production, updated 2003–2004. www-nds.iaea.org/medical.



aqueous layer. Ga-67 is back-extracted from DIPE with a small volume of sterile water. To the solution containing Ga-67 is added 0.5 ml of 2.5% sodium citrate, and the solution is carefully evaporated to dryness. The residue is dissolved in saline containing a sufficient amount of sodium citrate for radiopharmaceuticals manufacturing [21].

For the recovery of the enriched ^{68}Zn , the acidic aqueous layer containing the target material is allowed to decay for approximately a month and pooled together from multiple targets. Zn-68 is precipitated as zinc sulfide with a Na_2S solution, followed by dissolution in concentrated HCl. Zn-68 is precipitated from the acid solution as zinc hydroxide by adding sufficient NaOH to attain basic pH [6–8]. Controlled drying provides ^{68}Zn as an oxide, which is used to prepare additional targets.

The radionuclidic impurity levels in the separated gallium citrate depend upon the radioisotopic enrichment of the target material and the efficiency of the separation method. Co-production of high-energy ^{66}Ga (9.3 hours; through p,2n reaction) should also be taken into account while processing the irradiated target. Sufficient time must be allowed post-irradiation for the short-lived Ga isotopes to decay to an acceptable level (pharmacopeia standard). Final ^{67}Ga products must have low levels of contaminants within acceptable human toxicity [22] and pharmacopoeial limits.

It is essential to ensure through chromatographic method a lower than acceptable level of free ^{67}Ga (<5%) and assurance of >95% as Ga-citrate.

4.8 INDIUM-111

Because indium forms stable chelates, it is used to label large molecules for imaging and therapy despite relatively poor decay emissions. In-111 decays by electron capture with a half-life of 2.83 days. There are two prominent gamma rays: 71.3 and 245.4 keV [15]. Table 4.3 provides a list of the primary ^{111}In radiopharmaceuticals [1].

Radiopharmaceutical	Trade name	Primary use
Indium-111 chloride	Indiclor In-111Cl	Labeling monoclonal antibodies and peptides (OncoScint and Octreoscan)
Indium-111 pentetate (DTPA)	Indium DTPA In-111	Imaging of cerebrospinal fluid kinetics
Indium-111 oxyquinoline (oxine)	Indium-111 oxine	Labeling leukocytes and platelets
Indium-111 capromab pendetide	ProstaScint	Monoclonal antibody for imaging prostate cancer
Indium-111 pentetreotide	Octreoscan	Imaging neuroendocrine tumors

Table 4.3 List of commercial Indium-111 radio-pharmaceuticals.

Source: Based on NRC (National Research Council). 2007. *Advancing Nuclear Medicine Through Innovation*. Washington, DC: The National Academies Press. Available at <https://doi.org/10.17226/11985>.

The target material is enriched Cd-112 (typically >98%). It can be either electroplated or pressed as a powder into a target holder (see target preparation) [15].

Enriched ^{112}Cd as a metal is used to produce ^{111}In from the $^{112}\text{Cd}(p, 2n)$ reaction. The excitation function is shown in Figure 4.6 [14].

In-111 is isolated from the cadmium target by dissolving in acid, separated by solvent extraction, and further purified by a second step extraction. An alternative approach uses ion-exchange chromatography. Both methods give similar recoveries of the ^{111}In [23].

To recover enriched target material, the pooled solution containing ^{112}Cd from several irradiated targets is boiled to remove residual organic solvent and made basic to precipitate ^{112}Cd (pH > 12). Cd-112 is precipitated as a sulfide with sodium sulfide solution followed by dissolution in concentrated HCl. Cd is then reprecipitated as $\text{Cd}(\text{OH})_2$ with a base. The hydroxide can be converted to oxide by heating at 90–130 °C.

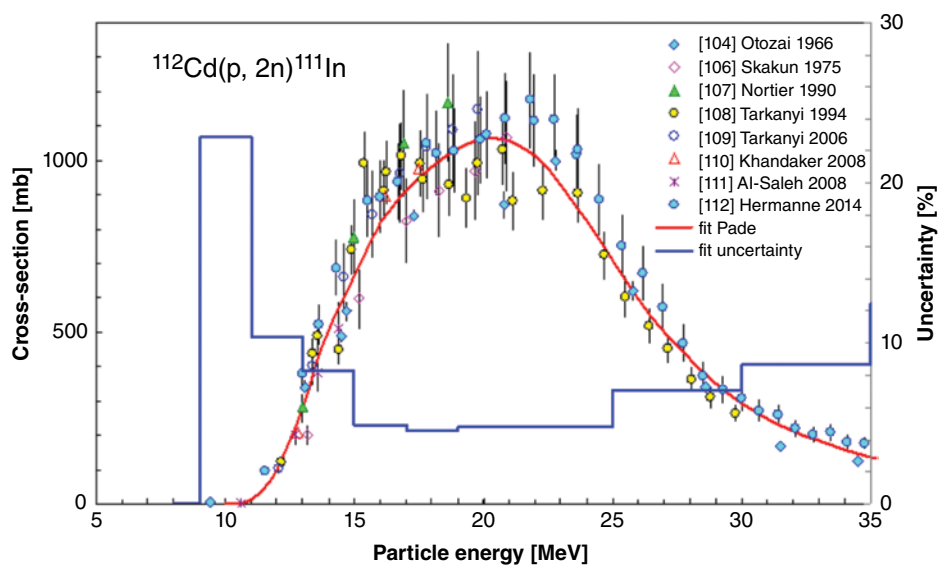


Figure 4.6 Excitation function for the production of ^{111}In . Source: Based on IAEA charged particle cross section database for medical radioisotope production, updated 2003–2004. www.nds.iaea.org/medical.

Physico-chemical tests for $^{111}\text{InCl}_3$ can be carried out to check the quality of the final product. The radionuclidic purity of the final product is checked by gamma-ray spectroscopy. Radiochemical purity is assessed by paper chromatography [24, 25]. The chemical purity of the final product is tested by checking for the presence of Cu, Fe, and Al [26].

4.9 IODINE-123

I-123, with a half-life of 13.2 hours, is probably the most widely used cyclotron-produced radiohalogen. It has gradually replaced ^{131}I as the isotope of choice for diagnostic radiopharmaceuticals containing radioiodine. It gives a much lower radiation dose to the patient due to the shorter half-life and lower gamma-ray energy of 159 keV. This photon energy is ideally suited for use in a SPECT camera [8]. Like the photons from $^{99\text{m}}\text{Tc}$, the gamma ray penetrates tissue very effectively without an excessive radiation dose. For this reason, it has, in many instances, replaced reactor-produced ^{131}I . A great number of radiopharmaceuticals have been labeled using ^{123}I , and the number is increasing (see Table 4.4).

The preferred method for preparing ^{123}I with high specific activity is via the irradiation of enriched ^{124}Xe . This approach produces three isobars – ^{123}Cs , ^{123}Xe , and ^{123}I – with half-lives of 5.9 minutes, 2.1 hours, and 13.2 hours, respectively.

The enriched ^{124}Xe (>99.8%) target material is a gas, and the target vessel typically contains 1–2 l of gas at elevated pressure. The real danger here is the possibility of rupturing a foil, which may result in the loss of the target gas into the cyclotron and then into the atmosphere. Several designs have been published to reduce or eliminate the possibility of such a loss [27–32]. In most cases, the xenon gas is trapped in a loop contained at liquid nitrogen temperatures. These loops, if properly constructed, can trap more than 99% of the xenon gas in the targets. This type of target has been tested extensively and has proven to be reliable in routine operation (Figure 4.7).

The separation of the radioiodine from the target matrix is accomplished by isolating the ^{123}Xe from the matrix; it is then allowed to decay to ^{123}I in a separate vessel. This separation is usually not difficult since the xenon is very unreactive and can generally be readily extracted from the target.

During much of the 1970s and 1980s, ^{123}I was produced by bombarding enriched ^{124}Te (99.90–99.93%) via the $^{124}\text{Te}(p,2n)$ reaction (see Figure 4.8). The targets were prepared by electrodeposition of metallic tellurium or by using tellurium oxide in a pressed target.

Table 4.4 Examples of some ^{123}I radiopharmaceuticals.

^{123}I – radiopharmaceutical	Application
<i>o</i> -Iodohippuran	Renal function imaging
<i>N</i> -Isopropyl- <i>p</i> -iodoamphetamine	Cerebral blood-flow imaging
Iododeoxyuridine	Cancer imaging
<i>p</i> -Iodophenylalanine	Glioma imaging and therapy
Octreotide	Targets somatostatin receptors

Source: Based on NRC (National Research Council). 2007. *Advancing Nuclear Medicine Through Innovation*. Washington, DC: The National Academies Press. Available at <https://doi.org/10.17226/11985>.

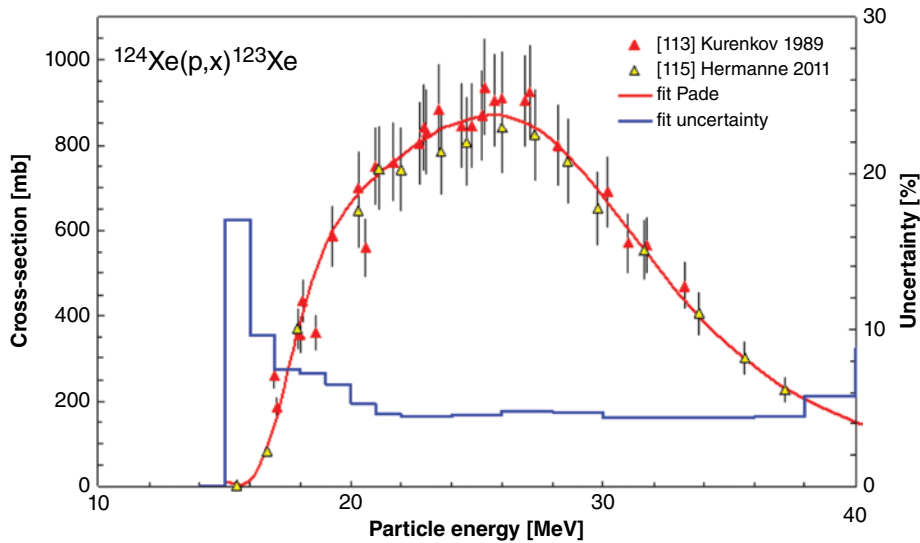


Figure 4.7 Cumulative excitation function for producing ^{123}Xe , including direct and decay processes. Source: Based on IAEA charged particle cross section database for medical radioisotope production, updated 2003–2004. www-nds.iaea.org/medical.

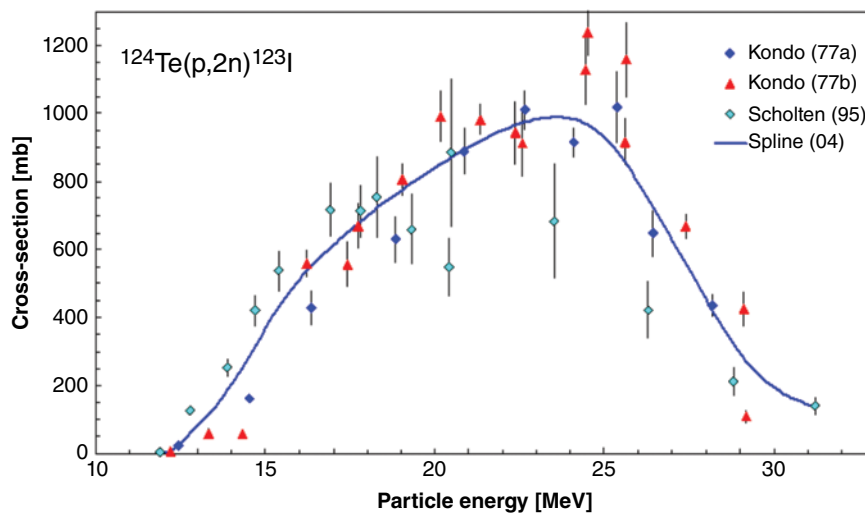


Figure 4.8 Excitation function for the production of ^{123}I from the bombardment of enriched ^{124}Te . Source: Based on IAEA charged particle cross section database for medical radioisotope production, updated 2003–2004. www-nds.iaea.org/medical.

Solid targets made from powdered tellurium have also been widely used for the production of ^{123}I [33–41]. The tellurium powder has often been mixed with aluminum powder to increase the heat-transfer characteristics of the target. A common problem with these targets is melting of the elemental tellurium and consequent loss of the radioiodine from the matrix.

Other types of alloy targets have been used for the production of ^{123}I , such as a tellurium–gold alloy [41]. This technique has been used extensively when the thermal conductivity of the primary material is low and/or the melting point is low. Tellurium oxide has also been used to produce ^{123}I . The oxide has the advantage of a high melting point and, therefore, a low loss of iodine from the matrix during irradiation.

With this method, ^{123}I was isolated through dry or wet distillation or through a chemical process. A common method of extraction is the use of dry distillation. In this approach, the tellurium powder or tellurium oxide powder is heated to near the melting point with a flow of gas over the plate. The ^{123}I is distilled out of the matrix and carried by the sweep gas to a collection vessel, where it is trapped. This vessel usually contains a base solution, and the iodine is in the chemical form of iodide. A wet chemical method can also be used by dissolving the Te and then oxidizing the iodide to iodine and distilling it from the solution [33].

Te-124 can be recovered through a straightforward chemical process. Te-124 from a number of targets after a lengthy cooling period is dissolved in a HCl/hydrogen peroxide mixture, followed by reduction of Te^{+6} to Te^{+4} with acid, and then free tellurium metal is precipitated by the addition of hydrazine hydrate and sodium sulfite [15].

I-123 produced through the (p,2n) reaction on enriched ^{124}Te is contaminated with co-produced ^{124}I , which limits the shelf-life of products prepared from the direct production method. Thus, the radionuclidic purity must be assessed before further use.

In addition, it is essential to monitor and control the presence of several different iodine species, such as iodate and periodate. These species may also be generated during the storage of high-specific-activity products [42]. Stabilization of radioiodine predominantly as iodide can be achieved by the addition of a small amount of a reductant such as sodium sulfite. It should be noted, however, that the presence of a reductant is known to interfere with the radiolabeling of proteins.

Iodine batches produced through irradiation of solid Te and TeO_2 targets are submitted to chemical purity tests on aluminum and tellurium. Use is made of emission spectrometry or colorimetry. The iodine batches produced through both targets meet all criteria of the Pharmacopoeia. The chemical impurities determined by colorimetric spot tests are typically $\text{Te} < 0.5 \mu\text{g mCi}^{-1}$; $\text{Al} < 0.25 \mu\text{g mCi}^{-1}$.

4.A. APPENDIX

References associated with the excitation functions, compiled by the IAEA [18]:

$^{203}\text{Tl}(p,3n)^{201}\text{Pb}$

M. Bonardi, C. Birattari, and A. Salomone. ^{201}Tl production for medical use by (p,xn) nuclear reactions on Tl and Hg natural and enriched targets. Proc. Int. Conf. Nuclear Data for Science and Technology, May 1983, Antwerp, Belgium (ed. K.H. Bockhoff), 1983, pp. 916–918.

Additional information in: F. Girardi, L. Goetz, E. Sabbioni, E. Marafante, M. Merlini, E. Acerbi, C. Birattari, M. Castiglioni, and F. Resmini. Preparation of ^{203}Pb compounds for studies on pathways and effects of lead pollution. Int. J. Appl. Rad. Isot 26 (1975) 267.

$^{68}\text{Zn}(p,2n)^{67}\text{Ga}$

Results of measurements for the $^{nat}\text{Zn}(p,xn)^{67}\text{Ga}$ process can be used for evaluation between 17 and 30 MeV. In this energy range, the contribution of the $^{67}\text{Zn}(p,n)^{67}\text{Ga}$

reaction can be neglected due to the low isotopic abundance of ^{67}Zn in a natural zinc matrix and the magnitude of the cross-section of the $^{67}\text{Zn}(p,n)^{67}\text{Ga}$ reaction. The influence of the $^{70}\text{Zn}(p,4n)^{67}\text{Ga}$ process to the production cross-sections is also negligible because of the very low isotopic abundance of ^{70}Zn in natural zinc (0.62%).

B.L. Cohen and E. Newman. (p,pn) and (p,2n) cross sections in medium weight elements. *Phys. Rev.* 99 (1955) 718. Exfor: B0050.

M. Bonardi and C. Birattari. Optimization of irradiation parameters for ^{67}Ga production from $^{\text{nat}}\text{Zn}(p,xn)$ nuclear reactions. *J. Radioanal. Chem.* 76 (1983) 311. Exfor: O1062.

F. Tarkanyi, F. Szelecsenyi, Z. Kovacs, and S. Sudar. Excitation functions of proton induced nuclear reactions on enriched ^{66}Zn , ^{67}Zn and ^{68}Zn . Production of ^{67}Ga and ^{66}Ga . *Radiochim. Acta* 50 (1990) 19. Exfor: D4004.

V.N. Levkovskij. Activation cross section nuclides of average masses ($A = 40\text{--}100$) by protons and α -particles with average energies ($E = 10\text{--}50\text{ MeV}$), book: Levkovskij, Activation cross section by protons and alphas, Moscow, 1991. Exfor: A0510 Cross-sections must be normalized by a factor of 0.8, as was pointed out in S. Takács, F. Tárkányi, M. Sonck, and A. Hermanne. Investigation of the $^{\text{nat}}\text{Mo}(p,x)^{96\text{mg}}\text{Tc}$ nuclear reaction to monitor proton beams: new measurements and consequences on the earlier reported data. *Nucl. Instrum. Methods B* 198 (2002) 183.

F.M. Nortier, S.J. Mills, and G.F. Steyn. Excitation functions and yields of relevance to the production of ^{67}Ga by proton bombardment of $^{\text{nat}}\text{Zn}$ and $^{\text{nat}}\text{Ge}$ up to 100 MeV. *Int. J. Radiat. Appl. Instrum. Part A* 42 (1991) 353. Exfor: A0498.

A. Hermanne. Evaluated cross section and thick target yield data of Zn+p processes for practical applications. Private communication (1997). Exfor: D4093 Target: natural Zn and enriched ^{68}Zn .

F. Szelecsényi, T.E. Boothe, S. Takács, F. Tárkányi, and E. Tavano. Evaluated cross section and thick target yield data bases of Zn+p processes for practical applications. *Appl. Radiat. Isot.* 49 (1998) 1005.

A. Hermanne, F. Szelecsenyi, M. Sonck, S. Takacs, F. Tarkanyi, and P. Van Den Winkel. New cross section data on $^{68}\text{Zn}(p,2n)^{67}\text{Ga}$ and $^{\text{nat}}\text{Zn}(p,xn)^{67}\text{Ga}$ nuclear reactions for the development of a reference data base. *J. Radioanal. Nucl. Chem.* 240 (1999) 623. Exfor: D4088.

T. Stoll, S. Kastleiner, Yu.N. Shubin, H.H. Coenen, and S.M. Qaim. Excitation functions of proton induced reactions on ^{68}Zn from threshold up to 71 MeV, with specific reference to the production of ^{67}Cu . *Radiochim. Acta* 90 (2002) 309.

F. Szelecsényi, G.F. Steyn, Z. Kovács, T.N. van der Walt, K. Suzuki, K. Okada, and K. Mukai. New cross-section data for the $^{66}\text{Zn}(p,n)^{66}\text{Ga}$, $^{68}\text{Zn}(p,3n)^{66}\text{Ga}$, $^{\text{nat}}\text{Zn}(p,x)^{66}\text{Ga}$, $^{68}\text{Zn}(p,2n)^{67}\text{Ga}$ and $^{\text{nat}}\text{Zn}(p,x)^{67}\text{Ga}$ nuclear reactions up to 100 MeV. *Nucl. Instrum. Methods B* 234 (2005) 375. Exfor: E1935.

$^{111}\text{Cd}(p,2n)^{111}\text{In}$

K. Otozai, S. Kume, A. Mito, H. Okamura, R. Tsujino, Y. Kanchiku, T. Katoh, and H. Gotoh. Excitation functions for the reactions induced by protons on Cd up to 37 MeV. Nucl. Phys. 80 (1966) 335. Exfor: P0019.

E.A. Skakun, A.P. Kljucharev, Yu.N. Rakivnenko, and I.A. Romanij. Excitation functions of (p,n)- and (p,2n)-reactions on cadmium isotopes. Izv. Rossiiskoi Akademii Nauk, Ser. Fiz. 39 (1975) 24.

F.M. Nortier, S.J. Mills, and G.F. Steyn. Excitation functions and production rates of relevance to the production of ^{111}In by proton bombardment of ^{nat}Cd and ^{nat}In up to 100 MeV. Int. J. Radiat. Appl. Instrum. Part A 41 (1990) 1201.

F. Tárkányi, F. Szelecsényi, P. Kopecký, T. Molnár, L. Andó, P. Mikecz, Gy. Tóth, and A. Rydl. Cross sections of proton induced nuclear reactions on enriched ^{111}Cd and ^{112}Cd for the production of ^{111}In for use in nuclear medicine. Appl. Radiat. Isot. 45 (1994) 239.

F. Tárkányi, B. Király, F. Ditrói, S. Takács, J. Csikai, A. Hermanne, M.S. Uddin, M. Hagiwara, M. Baba, T. Ido, Yu.N. Shubin, and S.F. Kovalev. Activation cross-sections on cadmium: proton induced nuclear reactions up to 80 MeV. Nucl. Instrum. Methods B 245 (2006) 379.

M.U. Khandaker, K. Kim, M.W. Lee, K.S. Kim, G.N. Kim, Y.S. Cho, and Y.O. Lee. Production cross-sections for the residual radionuclides from the $^{nat}\text{Cd}(p,x)$ nuclear processes. Nucl. Instrum. Methods Phys. Res. B266 (2008) 4877–4887.

F.S. Al-Saleh. Cross sections of proton induced nuclear reactions on natural cadmium leading to the formation of radionuclides of indium. Radiochim. Acta 96 (2008) 461–465.

A. Hermanne, R. Adam-Rebeles, P. Van den Winkel, F. Tárkányi, and S. Takács. Production of ^{111}In and $^{114\text{m}}\text{In}$ by proton induced reactions: an update on excitation functions, chemical separation-purification and recovery of target material. Radiochim. Acta 102 (2014) 1111–1126.

$^{124}\text{Xe}(p,2n)^{123}\text{Cs}/^{124}\text{Xe}(p,pn)^{123}\text{Xe}$

N.V. Kurenkov, A.B. Malinin, A.A. Sebyakin, and N.I. Venikov. Excitation functions of proton-induced nuclear reactions on ^{124}Xe : production of ^{123}I . J. Radioanal. Nucl. Chem. 135 (1989) 39–50.

F. Tárkányi, S.M. Qaim, G. Stocklin, M. Sajjad, R.M. Lambrecht, and H. Schweickert. Excitation functions of (p,2n) and (p,pn) reactions and differential and integral yields of ^{123}I in proton induced nuclear reactions on highly enriched ^{124}Xe . Appl. Radiat. Isot. 42 (1991) 221–228.

A. Hermanne, F. Tárkányi, S. Takács, R. Adam-Rebeles, A. Ignatyuk, S. Spellerberg, and R. Schweickert. Limitation of the long-lived ^{121}Te contaminant in production of ^{123}I through the $^{124}\text{Xe}(p,x)$ route. Appl. Radiat. Isot. 69 (2011) 358–368.

$^{124}\text{Te}(p,2n)^{123}\text{I}$

K. Kondo, R.M. Lambrecht, and A.P. Wolf. ^{123}I production for radiopharmaceuticals-XX. Excitation functions of the $^{124}\text{Te}(p,2n)^{123}\text{I}$ and $^{124}\text{Te}(p,n)^{124}\text{I}$ reactions and effect of target enrichment on radionuclidic purity. *Int. J. Appl. Radiat. Isot.* 28 (1977) 395.

K. Kondo, R.M. Lambrecht, E.F. Norton, and A.P. Wolf. Cyclotron isotopes and radiopharmaceuticals-XXII. Improved targetry and radiochemistry for production of ^{123}I and ^{124}I . *Int. J. Appl. Radiat. Isot.* 28 (1977) 765.

B. Scholten, Z. Kovács, F. Tárkányi, and S.M. Qaim. Excitation functions of $^{124}\text{Te}(p,xn)^{124,123}\text{I}$ reactions from 6 to 31 MeV with special reference to the production of ^{124}I at a small cyclotron. *Appl. Radiat. Isot.* 46 (1995) 255.

REFERENCES

1. National Research Council (NRC) (2007). *Advancing Nuclear Medicine Through Innovation*. Washington, DC: The National Academies Press. <https://doi.org/10.17226/11985>.
2. National Research Council (NRC) (2009). *Medical Isotope Production Without Highly Enriched Uranium*. The National Academies Press. www.nap.edu/catalog/12569.
3. Nuclear Energy Agency. (2017). The supply of medical radioisotopes: results from the third self-assessment of the global Mo-99/Tc-99m supply chain. <https://www.oecd-nea.org/globalsearch/download.php?doc=80142>.
4. Ruth, T.J. (2009). The medical isotope shortage. American Physical Society. <https://www.aps.org/units/fps/newsletters/200910/ruth.cfm>
5. National Research Council (NRC) (2016). *Molybdenum-99 for Medical Imaging*. Washington, DC: The National Academies Press. <https://doi.org/10.17226/23563>.
6. Bénard, F., Buckley, K.R., Ruth, T.J. et al. (2014). Implementation of multi-curie production of $^{99\text{m}}\text{Tc}$ by conventional medical cyclotrons. *J. Nucl. Med.* 55: 1017–1022. <https://doi.org/10.2967/jnumed.113.133413>.
7. Andersson, J.D., Thomas, B., Selivanova, S.V. et al. (2018). Robust high-yield ~1 TBq production of cyclotron based sodium [$^{99\text{m}}\text{Tc}$]pertechnetate. *Nucl. Med. Biol.* 60: 63–70. <https://doi.org/10.1016/j.nucmedbio.2018.02.003>.
8. Mandel, S.J., Shankar, L.K., Benard, F. et al. (2001). Superiority of iodine-123 compared with iodine-131 scanning for thyroid remnants in patients with differentiated thyroid cancer. *Clin. Nucl. Med.* 26: 6–9.
9. IAEA. (2009). Cyclotron produced radionuclides: physical characteristics and production methods. Technical report 468. https://www-pub.iaea.org/MTCD/Publications/PDF/trs468_web.pdf.
10. Weiner, R.E. and Thakur, M.L. (1995). Metallic radionuclides: applications in diagnostic and therapeutic nuclear medicine. *Radiochim. Acta* 70 (71): 273–287.
11. Belgrave, E. and Lebowitz, E. (1973). Development of ^{201}Tl for medical use. *J. Nucl. Med.* 13: 781.
12. Lebowitz, E., Greene, M.W., Fairchild, R. et al. (1975). Thallium-201 for medical use. I. *J. Nucl. Med.* 16: 151–155.

13. Lebowitz, E., Greene, M.W., Bradley-Moore, P. et al. (1974). ^{201}Tl for medical use. *J. Nucl. Med.* 14: 421–422.
14. IAEA. (2019). Charged particle cross section database for medical radioisotope production. www-nds.iaea.org/medical.
15. IAEA. (2004). Standardized high current solid targets for cyclotron production of diagnostic and therapeutic radionuclides. Technical report 432. https://www-pub.iaea.org/MTCD/publications/PDF/TRS432/TRS432_web.pdf.
16. Fernandes, L. and Gonçalves Da Silva, C.P. (1993). Quality control of $^{201}\text{TlCl}$ solution obtained at IPEN-CNEN/SP. *J. Radioanal. Nucl. Chem.* 172: 313–318.
17. Novak, M. and Hlatky, J. (1988). Determination of flow concentrations of hydraxzine in waters of both the primary and secondary circuits of NPPs with VVER. *J. Radioanal. Nucl. Chem.* 126: 337–344.
18. Tárkányi, F.T., Ignatyuk, A.V., Hermanne, A. et al. Recommended nuclear data for medical radioisotope production: diagnostic gamma emitters. *J. Radioanal. Nucl. Chem.* <https://doi.org/10.1007/s10967-018-6142-4>.
19. Helus, F. and Maier-Borst, W. (1973). A comparative investigation of methods used to produce ^{67}Ga with a cyclotron. *J. Labelled Compd. Radiopharm.* 1: 317, IAEA/SM/171/21. IAEA, Vienna.
20. El-Azony, K.M., Ferieg, K.H., and Saleh, Z.A. (2003). Direct separation of ^{67}Ga citrate from zinc and copper target materials by anion exchange. *Appl. Radiat. Isot.* 59: 329–331.
21. Das, M.K. and Ramamoorthy, N. (1995). ^{67}Ga galliumcitrate 1: production experience at Variable Energy Cyclotron Center, Calcutta. *Indian J. Nucl. Med.* 10: 63.
22. Casarett, L.J. and Doull, J. (1980). *Casarett and Doull's Toxicology: The Basic Science of Poisons*. New York, NY: Macmillan.
23. Szelecsényi, F., Tárkányi, F., Andó, L. et al. (1992). Excitation functions of proton induced nuclear reactions on ^{111}Cd and ^{112}Cd . Production of ^{111}In . In: *Nuclear Data for Science and Technology* (ed. S.M. Qaim), 603–605. Berlin: Springer-Verlag.
24. Chattopadhyay, S., Das, M.K., Sarkar, B.R., and Ramamoorthy, N. (1997). Radiochemical separation of high purity ^{111}In from cadmium, copper, aluminium and traces of iron: use of a cation exchange resin with hydrobromic acid and hydrochloric acid. *Appl. Radiat. Isot.* 48: 1063–1067.
25. Macdonald, N.S., Neely, H.H., Wood, R.A. et al. (1975). Methods for compact cyclotron production of indium-111 for medical use. *Int. J. Appl. Radiat. Isot.* 26: 631–633.
26. Vogel, A.I., Mendham, J., Denney, R.C. et al. (2000). *Vogel's Textbook of Quantitative Chemical Analysis*. Harlow, UK; New York, NY: Prentice Hall.
27. Firouzbakht, M.L., Teng, R.R., Schlyer, D.J., and Wolf, A.P. (1987). Production of high purity iodine-123 from xenon-124 at energies between 15 and 34 MeV. *Radiochim. Acta* 41: 1–4.
28. Godart, J., Barat, J.L., and Menthe, A. (1978). In beam collection of ^{123}Xe for carrier-free ^{123}I production. *Int. J. Appl. Radiat. Isot.* 28: 967–969.
29. Graham, D., Trevena, I.C., Webster, B., and Williams, D. (1985). Production of high purity iodine-123 using xenon-124. *J. Nucl. Med.* 26: 105.

30. Tárkányi, F., Qaim, S.M., Stöcklin, G. et al. (1991). Excitation functions of (p,2n) and (p,pn) reactions and differential and integral yields of ^{123}I in proton induced nuclear reactions on highly enriched ^{124}Xe . *Appl. Radiat. Isot.* 42: 221–228.
31. Firouzbakht, M.L., Schlyer, D.J., and Wolf, A.P. (1992). Production of iodine-123 from xenon-124: cross-sections and yields. *Radiochim. Acta* 56: 167–171.
32. Firouzbakht, M.L., Schlyer, D.J., and Wolf, A.P. (1995). "Failsafe" gas target for the production of I-123 from Xe-124. In: *Proceedings of the Sixth Workshop on Targetry and Target Chemistry, 17–19 August, Vancouver, BC, Canada*, 79–81. TRIUMF.
33. Acerbi, E., Birattari, C., Castiglioni, M., and Resmini, F. (1975). Production of ^{123}I for medical purposes at the Milan AVF cyclotron. *Int. J. Appl. Radiat. Isot.* 26: 741–747.
34. Barrall, R.C., Beaver, J.E., Hupf, H.B., and Rubio, F.F. (1981). Production of Curie quantities of high purity I-123 with 15 MeV protons. *Eur. J. Nucl. Med.* 6: 411–415.
35. Clem, R.G. and Lambrecht, R.M. (1991). Enriched ^{124}Te targets for production of ^{123}I and ^{124}I . *Nucl. Instrum. Methods A* 303: 115–118.
36. Guillaume, M., Lambrecht, R.M., and Wolf, A.P. (1975). Cyclotron production of ^{123}Xe and high purity ^{123}I : a comparison of tellurium targets. *Int. J. Appl. Radiat. Isot.* 26: 703–707.
37. Hupf, H.B., Eldridge, J.S., and Beaver, J.E. (1968). Production of iodine-123 for medical applications. *Int. J. Appl. Radiat. Isot.* 19: 345–351.
38. Kondo, K., Lambrecht, R.M., Norton, E.F., and Wolf, A.P. (1977). Improved target and chemistry for the production of ^{123}I and ^{124}I . *Int. J. Appl. Radiat. Isot.* 28: 765–771.
39. Mahunka, I., Ando, L., Mikecz, P. et al. (1996). Iodine-123 production at a small cyclotron for medical use. *J. Radioanal. Nucl. Chem. Lett.* 213: 135–142.
40. Michael, H., Rosezin, H., Apelt, H. et al. (1981). Some technical improvements in the production of ^{123}I via the $^{124}\text{Te}(p,2n)^{123}\text{I}$ reaction at a compact cyclotron. *Int. J. Appl. Radiat. Isot.* 32: 581–587.
41. Lambrecht, R.M., Mantescu, C., Redvanly, C., and Wolf, A.P. (1972). Preparation of high purity carrier-free ^{123}I -iodine monochloride as iodination reagent for synthesis of radiopharmaceuticals. IV. *J. Nucl. Med.* 13: 266–273.
42. Sajjad, M., Lambrecht, R.M., and Bakr, S. (1990). Autoradiolytic decomposition of reductant-free Sodium ^{124}I and ^{123}I iodide. *Radiochim. Acta* 50: 123.

Chapter 5

Production of Therapeutic Radionuclides

C. Shaun Loveless^{1,2} and Suzanne E. Lapi^{1,3}

¹*Department of Radiology, University of Alabama at Birmingham, Birmingham, AL, 35294, USA*

²*Department of Chemistry, Washington University in St. Louis, St. Louis, MI, 63130, USA*

³*Department of Chemistry, University of Alabama at Birmingham, Birmingham, AL, 35294, USA*

5.1 INTRODUCTION

Therapeutic radionuclides decay by the emission of alpha particles, emission of beta particles, or electron capture, which leads to the emission of Auger electrons. These decay particles have high linear energy transfer (**LET**) and thus deposit the majority of their energy over very short distances (μm - mm). The majority of radionuclides used for clinical radiotherapy are neutron-rich beta emitters and are produced in nuclear reactors by neutron capture reactions on stable targets or through fission. Other radionuclides that decay by alpha emission or electron capture routes may be produced via charged-particle reactions using cyclotrons or linear accelerators. While neutron capture and charged-particle reactions are used to produce the majority of therapeutic radionuclides, photonuclear reactions using electron linear accelerators (**eLINACs**) are actively being investigated as a potential new route to produce and supply previously inaccessible or hard-to-obtain radionuclides. This chapter covers these different production pathways and highlights commonly used isotopes produced through these routes.

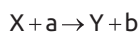
Handbook of Radiopharmaceuticals: Methodology and Applications, Second Edition.

Edited by Michael R. Kilbourn and Peter J.H. Scott.

© 2021 John Wiley & Sons Ltd. Published 2021 by John Wiley & Sons Ltd.

5.2 NUCLEAR REACTIONS AND ISOTOPE PRODUCTION BASICS

For nuclear reactions important to the production of radionuclides, we can consider a particle incident on a stationary target giving rise to a radioactive product and a light particle or gamma ray, as shown here



where X is the stationary target, a is the incident particle, Y is the radioactive product, and b is the light particle or gamma ray. This can be written in short form as X(a,b)Y. For instance, if one produces ^{153}Sm via neutron bombardment of ^{152}Sm , the reaction can be written as $^{152}\text{Sm}(n,\gamma)^{153}\text{Sm}$. The reaction rate depends on the flux of particles hitting the target, target thickness, target density, and cross-section, which is proportional to the probability of the nuclear reaction taking place. The cross-section (σ) is given in units of area (m^2); however, the smaller units of barn ($1 \text{ b} = 10^{-24} \text{ cm}^2$) or millibarn are typically used in practice. The reaction rate (R) in atoms/second of a neutron-induced reaction is

$$R = \varphi \sigma N_{\text{tgt}}$$

where φ is the neutron flux per area per second and N_{tgt} is the total number of target atoms. The corresponding reaction rate for a charged-particle reaction is

$$R = Inx\sigma$$

where I is the particle current incident on the target (particles/s), n is the number of nuclei/ cm^3 of target, and x is the target thickness (cm).

As these reactions often produce radioactive nuclei that are decaying, the overall change in the number of atoms present in the target is

$$dN / dt = R - \lambda N$$

where λ (which can be calculated by $\ln(2)/t_{1/2}$) is the decay constant (in s^{-1}) of the radionuclide of interest, and N is the number of atoms of the product. Eventually, at long irradiation times, the production rate will equal the rate of decay, and the number of radioactive nuclei in the target will be at a steady state. This is known as the *saturation* point. Typically, irradiations for radionuclide production are conducted for a maximum of two half-lives.

5.3 REACTOR PRODUCTION OF THERAPEUTIC RADIONUCLIDES

Nuclear reactors use fissile material (generally ^{235}U) to generate neutrons. Each fission event typically results in two to three additional neutrons that sustain a chain reaction in the reactor fuel by inducing additional fission events. These neutrons can also be used to produce radionuclides in targets via two general mechanisms: (i) by direct neutron reactions such as neutron capture, or (n,p) reactions; or (ii) by inducing additional fission events in targets composed of fissile material.

5.3.1 Production of Radionuclides via Direct Neutron-Induced Reactions

The cross-section (probability of reaction) of neutron capture, (n, γ), reactions generally increases as the incident neutron energy decreases. Thus, these reactions are carried out with low-energy or *slow neutrons*. Generally, target materials are solid metal or oxide powders, but they can also be liquid or gas. Neutron capture reactions typically result in a radioactive product of the same element as the initial target material. Hence, there is typically a large amount of non-radioactive or “cold” material that cannot be chemically separated from the product of interest. The ratio of radioactive atoms to the mass of material is relatively low, and the material is said to have low *molar activity* (Bq mol^{-1}). For example, the beta emitters ^{177}Lu ($t_{1/2} = 6.65$ days), ^{90}Y ($t_{1/2} = 2.67$ days), and ^{186}Re ($t_{1/2} = 3.72$ days) can be produced by neutron capture on the stable isotopes ^{176}Lu , ^{89}Y , and ^{185}Re , respectively [1]. Typically, isotopically enriched targets are used to produce radionuclidically pure products. As the radioactive product is the same element as the target material, no separation chemistry is required after irradiation, and the target is simply dissolved for downstream chemistry [2]. The cross-sections for neutron capture reactions are typically much higher than for other types of reactions, and thus very large quantities of radioisotopes can be produced via this route. For example, the cross-section at low neutron energies for the $^{176}\text{Lu}(n,\gamma)$ reaction is ~ 2100 b. Thus, a 10 mg sample of ^{176}Lu irradiated for three days at a typical neutron flux of $3 \times 10^{13} \text{ n cm}^{-2}$ would yield 3.58 GBq of ^{177}Lu . However, this represents a conversion rate of ^{176}Lu to ^{177}Lu of only 1.4% and thus results in low molar activity.

In some cases, particles containing the target isotope can be irradiated, giving rise to intrinsically radiolabeled particles. Radioactive gold and samarium nanoparticles (**NPs**) have been produced by exposing premade stable gold or samarium particles to a neutron flux [3, 4]. In the case of gold, solid gold particles were prepared for irradiation; however, Hashikin et al. reported on the preparation of stable ^{152}Sm incorporated into particles composed of a commercially available resin, which were irradiated after preparation.

When the radioactive product is created from a nuclear reaction, the resulting nucleus has a significant amount of kinetic energy. By careful selection of the target material and purification process, this recoil energy can be used to partially purify the radioactive

nuclides from the stable target material, even if the target material is of the same element. This process, discovered by L. Szilard and T.A. Chalmers in 1934 and published in *Nature*, was used to separate ^{128}I ($t_{1/2} = 24.9$ minutes) from neutron-irradiated ethyl iodide, $\text{C}_2\text{H}_5\text{I}$. This method of capturing a recoiling radioactive atom has been used to generate radionuclides with higher molar activity (Bq mol^{-1}) than would otherwise be possible from direct neutron capture reactions [5].

Radionuclide products may also be generated from the decay of a radionuclide resulting from a direct neutron capture event. Typically, the “parent” radionuclide is produced in the nuclear reaction, whereas the “daughter” radionuclide is the decay product used for downstream chemistry and applications. In this manner, one can obtain high-purity radionuclides with little or no non-radioactive contaminant (also referred to as *no-carrier-added*). For example, as discussed previously, ^{177}Lu can be produced via the $^{176}\text{Lu}(n,\gamma)^{177}\text{Lu}$ reaction. However, this radionuclide can also be produced via neutron irradiation of Yb: $^{176}\text{Yb}(n,\gamma)^{177}\text{Yb} \rightarrow \beta^- \rightarrow ^{177}\text{Lu}$ [6]. In the case of receptor-targeted therapy where a high-molar-activity product is desirable, this route may be preferable to the direct neutron capture reaction. The challenge with this method is the lower yields: the final product must be separated from the target material, and the enriched target material must be recycled [6].

Radionuclides with high molar activity can also be produced with higher energy or *fast* neutrons, which induce (n,p) reactions. Typically, the production yields for these reactions are much lower than the direct neutron capture reactions. As an example, several groups have reported the production of ^{64}Cu ($t_{1/2} = 12.7$ hours) via the $^{64}\text{Zn}(n,p)^{64}\text{Cu}$ reaction [7]. In a similar study, ^{47}Sc ($t_{1/2} = 3.35$ days) production rates via the $^{47}\text{Ti}(n,p)$ reaction have also been reported [8]. In these proof of principle studies, Kolsky et al. reported the purification of ^{47}Sc from neutron-irradiated natural Ti and enriched targets by cation-exchange chromatography using Dowex AG 50W resin. The optimized technique resulted in the near-quantitative recovery (>95%) of ^{47}Sc with yields of 3.2 GBq for irradiation times of up to 10 days at a neutron flux of $1.5 \times 10^{14} \text{ n cm}^{-2}$ [9].

In rare cases, radionuclides may be produced via double neutron capture. For example, the radionuclide generator $^{188}\text{W}/^{188}\text{Re}$ can be produced in this manner via the $^{186}\text{W}(n,\gamma)(n,\gamma)^{188}\text{W}$ reaction [10, 11]. This production route requires a very high neutron flux and is only feasible at a few sites in the world.

Examples of therapeutic radionuclides and characteristics that can be produced by neutron-induced reactions are shown in Table 5.1.

5.3.2 Production of Radionuclides via Fission

Neutrons can also be used to induce fission in target materials. Many radionuclides are produced via fission events where the ^{235}U nucleus splits asymmetrically into two fission products: one with mass number (A) = 80–110 and the other with $A = 130$ –150. One of the most commonly used therapeutic radionuclides, ^{131}I ($t_{1/2} = 8$ days), is mainly produced via fission of uranium. ^{90}Sr ($t_{1/2} = 28.8$ years), the parent of the therapeutic ^{90}Y ($t_{1/2} = 2.67$ days),

Radionuclide	Half-life	Primary decay mode	Mean particle energy (keV)	Production route
⁴⁷ Sc	3.35 d	β ⁻	143 204	⁴⁷ Ti(n,p) ⁴⁷ Sc
⁹⁰ Y	64.05 h	β ⁻	934	⁸⁹ Y(n,γ) ⁹⁰ Y
¹⁰⁵ Rh	35.37	β ⁻	70 74 179	¹⁰⁴ Ru(n,γ) ¹⁰⁵ Ru → ¹⁰⁵ Rh
¹⁰³ Pd	16.99 d	EC	Auger	¹⁰² Pd(n,γ) ¹⁰³ Pd
¹¹¹ Ag	7.45 d	β ⁻	224 279 360	¹¹⁰ Pd(n,γ) ¹¹¹ Pd → ¹¹¹ Ag
^{117m} Sn	13.8 d	IT (1)	Auger	¹¹⁶ Sn(n,γ) ^{117m} Sn
¹³¹ I	8.03 d	β ⁻	69 97 192	¹³⁰ Te(n,γ) ¹³¹ Te → ¹³¹ I
¹⁴⁹ Pm	53.1 h	β ⁻	256 369	¹⁴⁸ Nd(n,γ) ¹⁴⁹ Nd → ¹⁴⁹ Pm
¹⁵³ Sm	46.3 h	β ⁻	200 225 264	¹⁵² Sm(n,γ) ¹⁵³ Sm
¹⁶⁶ Ho	26.8 h	β ⁻	651 694	¹⁶⁵ Ho(n,γ) ¹⁶⁶ Ho
¹⁷⁷ Lu	6.65 d	β ⁻	47.6 112 149	¹⁷⁶ Lu(n,γ) ¹⁷⁷ Lu ¹⁷⁶ Yb(n,γ) ¹⁷⁷ Yb → ¹⁷⁷ Lu
¹⁸⁶ Re	3.72 d	β ⁻	306 359	¹⁸⁵ Re(n,γ) ¹⁸⁶ Re
^{195m} Pt	4.01 d	β ⁻	Auger	¹⁹⁴ Pt(n,γ) ^{195m} Pt ¹⁹⁵ Pt(n,n'γ) ^{195m} Pt ¹⁹⁴ Ir(n,γ) ^{195m} Ir → ^{195m} Pt

Table 5.1 Radionuclides produced by neutron-induced reactions.

can also be produced via fission. This reaction route results in the coproduction of a substantial number of radionuclides and requires significant chemistry in order to provide radiochemically pure products. Further, the number of available nuclear reactors that routinely produce radionuclides by fission is small. In many cases, these research or commercial reactors are nearing or have exceeded their operating lifetime and serve as the primary supply point for critically important medical radionuclides. The future decommissioning of these reactors and concern over the use of highly enriched uranium targets has generated interest in developing new methods of producing therapeutic radionuclides commonly derived via fission.

5.4 PRODUCTION OF THERAPEUTIC RADIONUCLIDES USING CHARGED-PARTICLE REACTIONS

Charged particles for the production of therapeutic radionuclides can be accelerated via cyclotrons or linear accelerators. As the stopping power (MeV mm^{-1}) of charged particles is much higher than neutrons or photons, smaller targets can typically be used. However, the substantial heat deposited by the beam in the target material should be considered when designing targets for the production of radionuclides via these reactions.

Charged-particle reactions typically lead to proton-rich radionuclides, which are mainly used for diagnostic purposes. However, high-energy proton-induced reactions on heavy target nuclei and alpha particle-induced reactions can be used to produce some alpha emitters. Additionally, recent studies with lower-energy medical cyclotrons have shown the feasibility of producing radionuclides that decay by electron capture, which results in the emission of Auger electrons. The emitted Auger electrons can be used for therapeutic applications due to their high LET.

5.4.1 Production of Beta Emitters via Charged-Particle Reactions

A handful of beta-emitting radionuclides are accessible via charged-particle reactions. Of these, ^{67}Cu ($t_{1/2} = 2.58$ days) is likely the most widely studied. This radionuclide can be produced via high-energy proton bombardment on enriched zinc metal or oxide targets via the $^{68}\text{Zn}(p,2p)^{67}\text{Cu}$ reaction [12, 13]. While the maximum cross-section for this reaction is relatively low (10 mb), high yields can be obtained with high-current irradiations. Separation of this isotope from the target material and coproduced cobalt radionuclides is typically accomplished via ion-exchange techniques.

While low-specific-activity ^{186}Re ($t_{1/2} = 3.72$ days) can be readily produced via neutron capture on stable rhenium targets in a reactor, this isotope can also be produced via proton or deuteron bombardment of enriched ^{186}W or Osmium targets [14, 15]. As the irradiation of natural isotopic composition targets results in the production of a variety of radioactive rhenium products, enriched targets are typically used for the production of this radionuclide. For the proton or deuteron production of ^{186}Re from tungsten targets, the cross-section reaches a maximum of 80 mb at 10 MeV and 600 mb at 15 MeV, respectively [16]. Targets prepared of tungsten metal, oxides, carbides, and sulfides have been reported [14, 15]. Purification of the radionuclide from the target material can be accomplished via dry distillation techniques or wet chemical separation using liquid-liquid extraction or ion-exchange methods [15, 17–19].

The production of ^{47}Sc ($t_{1/2} = 3.35$ days) has been reported via the proton or deuteron irradiation of Ti or Ca targets via a number of different reactions: $^{48}\text{Ca}(p,2n)^{47}\text{Sc}$, $^{46}\text{Ca}(d,n)^{47}\text{Sc}$, $^{44}\text{Ca}(\alpha,p)^{47}\text{Sc}$, $^{48}\text{Ti}(p,2p)^{47}\text{Sc}$, and $^{50}\text{Ti}(p,\alpha)^{47}\text{Sc}$ [9, 20–22]. While the Ca production route has a significantly higher cross-section, the enriched target material is more

expensive, and the beam current tolerated is limited due to the poor thermal conductivity of the calcium oxide or carbonate material. Purification of scandium radioisotopes is dependent on the target material used for production. Calcium metal targets rapidly dissolve in water, whereas the carbonate form will dissolve in a weak acid. Following this, the scandium radioisotopes can be separated from the target material using ion-exchange chromatography and/or extraction techniques [23–28]. Titanium targets are more difficult to dissolve and typically require the use of strong acid such as sulfuric (H_2SO_4) under reflux conditions and/or the use of hydrofluoric acid (**HF**). Following target dissolution, the scandium radioisotopes are typically purified using ion-exchange chromatography [68]. For enriched titanium and calcium targets, recycling of the target material may be required.

5.4.2 Production of Alpha Emitters via Charged-Particle Reactions

The production of alpha emitters can be achieved via high-energy proton routes or irradiation of targets with alpha beams. Both of these nuclear reaction routes have limited availability due to infrastructure requirements.

Several high-energy facilities have focused on the development of charged-particle reaction routes for the production of ^{225}Ac ($t_{1/2} = 10$ days), which is currently available in limited quantities from generators produced with legacy nuclear material [29]. ^{225}Ac can be used as a therapeutic radionuclide directly or can be used for the formation of a $^{225}\text{Ac}/^{213}\text{Bi}$ generator where the daughter nuclide (^{213}Bi) can be used as the therapeutic radionuclide [30, 31]. The production of ^{225}Ac via irradiation of thorium targets with high-energy protons has the potential to lead to wide-scale applications with this therapeutic radionuclide [32–34]. One drawback to this production method is the coproduction of ^{227}Ac ($t_{1/2} = 21.8$ years), a long-lived contaminant that limits the usable time window or *expiry* of the produced ^{225}Ac . The purification chemistry is challenging; however, recent publications have reported the development of ion-exchange methods leading to high recovery yields and purity [35, 36]. Other groups have explored the feasibility of the production of ^{225}Ac via the $^{226}\text{Rn}(p,2n)$ reaction [37]. However, the challenges of working with a long-lived radioactive target material (^{226}Rn , $t_{1/2} = 1600$ years) make this a difficult production path.

The short-lived ^{149}Tb is unique in that it decays by both alpha emission and positron decays. While promising for applications involving both diagnosis and therapy, production has thus far been limited to a single site via spallation reactions on tantalum targets [12].

The radiohalogen alpha emitter ^{211}At ($t_{1/2} = 7.2$ hours) can be produced via alpha irradiation of naturally monoisotopic bismuth targets via the $^{209}\text{Bi}(\alpha,2n)^{211}\text{At}$ reaction [38, 39]. Careful monitoring of the alpha beam energy is necessary to avoid the $^{209}\text{Bi}(\alpha,3n)^{210}\text{At}$ reaction as the decay of ^{210}At leads to the long-lived alpha emitter ^{210}Po ($t_{1/2} = 138$ days). While the short half-life of ^{211}At prevents widespread distribution, a network of regional sites could enable multiple clinical trials with this isotope. Purification of the radionuclide can be accomplished via dry distillation or wet chemistry techniques [39, 40].

5.4.3 Production of Auger Electron Emitters via Charged-Particle Reactions

Recently, interest has increased in the use of Auger electron emitters for targeted therapy. The short tissue range of Auger electrons limits their use to the development of therapeutics that can be transported into or are in close proximity to the cell nucleus. However, advances in the production of Auger electron-emitting radiometals and radiohalogens are enabling progress in the field.

While the radionuclide ^{111}In ($t_{1/2} = 2.80$ days) is typically used for imaging applications via planer or single photon emission computer tomography (**SPECT**), its utility as a therapeutic radionuclide has also been reported [41, 42]. Limouris et al. showed the therapeutic effect of Auger electrons of ^{111}In -octreotide in a small patient trial ($n = 13$) targeting liver neuroendocrine carcinoma metastases [43]. Moreover, the production methods for this radionuclide via proton irradiation of enriched ^{111}Cd targets are well established and used for commercial production.

Cobalt-58m ($t_{1/2} = 9.1$ hours) production has been studied by several groups as an Auger electron-emitting radionuclide and as a potential therapeutic analog to the positron-emitting isotope ^{55}Co [44]. Cobalt-58m can be readily produced via proton irradiation of enriched ^{58}Fe or deuteron irradiation of ^{57}Fe [44, 45]. After irradiation, the iron target is dissolved in acid, and the radiocobalt can be purified via ion-exchange techniques.

The radiolanthanide ^{165}Er ($t_{1/2} = 10.36$ hours) has also been suggested as an Auger electron-emitting radionuclide with therapeutic applications. This radionuclide can be produced via the proton or deuteron irradiation of holmium targets or indirectly via the higher-energy reaction routes: $^{\text{nat}}\text{Er}(p,xn)^{165}\text{Tm}$ ($t_{1/2} = 1.25$ days) \rightarrow EC/ β^+ \rightarrow ^{165}Er or $^{166}\text{Er}(p,2n)^{165}\text{Tm} \rightarrow$ EC/ β^+ \rightarrow ^{165}Er [46–49]. For the lower-energy holmium reaction routes, the target material is dissolved and separated using anion exchange. In the case of the higher-energy reaction, a two-step process is necessary to achieve a high-specific-activity product. In this scenario, the ^{165}Tm is first separated from the Er target material and allowed to decay, and then the ^{165}Er is purified from the ^{165}Tm [49].

The production of several other radiometals is ongoing at several sites. For example, the Auger electron emitter ^{135}La ($t_{1/2} = 19.5$ hours) can be produced via irradiation of natural barium targets [50]. Additionally, $^{119\text{g}}\text{Sb}$ ($t_{1/2} = 38.2$ hours) has been suggested as a therapeutic pair with the imaging isotope ^{117}Sb [51, 52]. Both of these antimony radionuclides can be produced via proton irradiation of electroplated enriched tin isotopes: ^{119}Sn for $^{119\text{g}}\text{Sb}$, and ^{117}Sn for ^{117}Sb . For production of both radiolanthanum and radioantimony, the irradiated target is dissolved in acid, and the radionuclides are purified using a weak anion exchange resin [51, 52]. In the case of the enriched tin targets, the enriched material is recycled.

Several Auger electron-emitting radiohalogens have also been studied as potential therapeutics. In contrast to radioactive metals, the radiohalogens may afford different strategies for incorporation into target molecules used in radiotherapy. For example, the long-lived iodine radionuclide ^{125}I ($t_{1/2} = 59.4$ days) has been investigated as a therapeutic radionuclide [53].

Production of the Auger electron-emitting radiohalogens ^{77}Br ($t_{1/2} = 2.38$ days) and $^{80\text{m}}\text{Br}$ ($t_{1/2} = 4.42$ hours) via proton or deuteron irradiation of isotopically enriched selenium targets has been investigated by several groups. These radionuclides can be used as therapeutic pairs with their diagnostic counterparts, ^{75}Br ($t_{1/2} = 97$ minutes) and ^{76}Br ($t_{1/2} = 16.2$ hours), respectively. As elemental selenium has poor thermal and chemical properties for a target material, refractory compounds of selenium such as Cu_2Se or NiSe typically are used [54]. Isolation of the produced radiobromine is typically achieved via dry distillation techniques or thermal diffusion; however, wet chemistry methods have also been reported [54–56]. The production of ^{77}Br and $^{80\text{m}}\text{Br}$ via the irradiation of krypton gas targets has also been explored [57]. While the yield of the krypton reactions is lower than that obtained by selenium irradiation, this route offers the potential advantages of decreased radionuclidic impurities and simple separation chemistry.

5.5 PRODUCTION OF THERAPEUTIC RADIONUCLIDES USING PHOTONUCLEAR REACTIONS

Photonuclear reactions occur via the absorption of photons by atomic nuclei followed by the ejection of protons (γ, p), neutrons (γ, n), or heavy particles (γ, x) and can be used to produce neutron-rich beta emitters, proton-rich positron emitters, and alpha emitters. Historically, photonuclear reactions have not been used to produce significant quantities of therapeutic radionuclides due to the low flux densities ($\gamma \text{ s}^{-1}$) attainable at γ ray sources, limiting the yield of produced radioactivities. However, research in this area is increasing due to developments in accelerator technology leading to a new generation of eLINACs capable of electron beam currents up to or exceeding 100 mA. Two methods, bremsstrahlung radiation and Compton backscattering, can be used to obtain photons with energy sufficient to induce these reactions.

Bremsstrahlung radiation is generated by the deceleration of high-energy electrons produced by an eLINAC in the electric field of nuclei contained in a *converter* material, as shown in Figure 5.1.

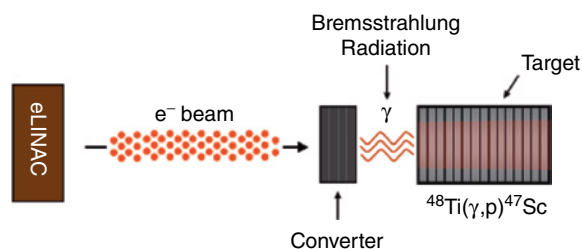


Figure 5.1 An example of a photonuclear reaction to produce ^{47}Sc . An electron beam and converter are needed to generate a bremsstrahlung photon beam, which can then be used to induce a photonuclear reaction.

The kinetic energies lost by the decelerating electrons are emitted as photons with a continuous spectrum of energies. Importantly, the use of dense, high Z material (e.g. tungsten or tantalum) as a converter increases the energy loss of the accelerated electrons, shifting the peak photon intensity to higher energies. Alternatively, the direct collision of laser beams with high-energy (>100 MeV) electrons can result in Compton backscattered (**CBS**) photons with a well-defined energy range [58].

The most recent generation of eLINACs can produce bremsstrahlung or CBS photons with flux densities up to 10^{14} – 10^{15} γ s^{-1} . At a flux density of this magnitude, similar in magnitude to thermal neutron flux densities (10^{13} – 10^{16} n cm^{-2} s^{-1}), therapeutic radionuclides could be produced in high specific activity and supplied via different photonuclear reactions. Early studies of photonuclear production have focused on modeling the yield and specific activity of radionuclides that are inaccessible or can only be produced in limited quantities with nuclear reactors or charged-particle accelerators [58]. To date, the photonuclear production of a limited number of therapeutic radionuclides has been experimentally investigated. Moreover, unlike the extensive nuclear data available to inform therapeutic radionuclide production via neutron capture and charged-particle reactions, cross-section data on photonuclear reactions is limited. Therefore, the successful development of photonuclear production will require future work to expand the existing nuclear data sets on these reactions. Early research on four therapeutic radionuclides that could be produced by photonuclear reactions is illustrated next.

The therapeutic radionuclide ^{47}Sc (discussed earlier) has been produced using both charged particles and neutrons. Alternatively, ^{47}Sc can be produced directly or indirectly via the $^{48}\text{Ti}(\gamma, p)^{47}\text{Sc}$ reaction and $^{48}\text{Ca}(\gamma, n)^{47}\text{Ca} \rightarrow \beta^- \rightarrow ^{47}\text{Sc}$. Rotsch et al. investigated the direct route using natural titanium, a 35 or 40 MeV electron beam, and a tantalum or tungsten converter. A typical four-hour irradiation yielded approximately 180 MBq. Following chemical purification, >90% of the ^{47}Sc was recovered with chemical purities suitable for direct radiolabeling [59]. The indirect route produces ^{47}Ca ($t_{1/2} = 4.54$ days), which decays by emission of a 1.3 MeV γ ray and a beta particle to ^{47}Sc . The ^{47}Ca can be produced using either natural calcium or enriched ^{48}Ca , with the latter resulting in a higher molar activity. Rane et al. investigated the indirect route using Monte Carlo N-Particle eXtended (**MCNPX**) radiation transport code to predict the production rate on an enriched ^{48}Ca target using bremsstrahlung photons generated by a 40 MeV electron beam, 1 mA beam current, and tungsten converter. The predicted values were then validated using a 39 MeV electron beam, 12.5 μA beam current, and tungsten converter. Based on these parameters, an enriched target will result in tens of MBq/g of ^{47}Ca . Calcium-47 incorporated into a $^{47}\text{Ca}/^{47}\text{Sc}$ generator system, at equilibrium with its radioactive daughter ^{47}Sc , would provide a similar amount of this promising therapeutic radionuclide [60]. Further, with the long half-life of ^{47}Ca , this generator could be distributed regionally. For both production routes, enriched targets should be used to optimize yield, molar activities, and radionuclidic purity.

The therapeutic radionuclide ^{225}Ac (discussed earlier) can be obtained via the chemical separation of a radioactive ^{229}Th ($t_{1/2} = 7932$ years) sample undergoing decay to its ^{225}Ac

daughter ($^{229}\text{Th} \rightarrow ^{225}\text{Ra} \rightarrow ^{225}\text{Ac}$). However, the current supply of ^{229}Th is limited and generates approximately 37 GBq of ^{225}Ac per year. Alternatively, ^{225}Ac can be produced indirectly by the $^{226}\text{Ra}(\gamma, n)^{225}\text{Ra}$ photonuclear reaction. Radium-225 ($t_{1/2} = 14.9$ days) produced by this route could be incorporated into a $^{225}\text{Ra}/^{225}\text{Ac}$ generator. The use of ^{225}Ac as a therapeutic radionuclide would require hundreds of MBqs and tens of GBqs for clinical trials and commercial supply, respectively [61]. Melville and Allen investigated the use of charged-particle and photonuclear reactions to produce ^{225}Ac . In this study, an 18 MeV electron beam, 26 μA beam current, and tungsten converter were used to generate bremsstrahlung photons. The measured rate on a low-power medical eLINAC was 14.2 $\text{kBq} \mu\text{A}^{-1} \text{h}^{-1}$ [61]. Further, this group showed that increasing the eLINAC power and maximum electron beam energy to 40 MeV will double the number of photons, with energy near the peak cross-section from 25% to 56% [61]. Thus, the extrapolated rate on a high-power eLINAC with a 40 MeV electron beam, 1 mA beam current, and similar tungsten converter would be approximately 30 $\text{kBq} \mu\text{A}^{-1} \text{h}^{-1}$. At this rate, a two-week irradiation could produce up to 10 GBq; however, much work must be done in the future to realize this method of production for ^{225}Ac .

The nuclear isomers $^{195\text{m}}\text{Pt}$ ($t_{1/2} = 4.02$ days) and $^{117\text{m}}\text{Sn}$ ($t_{1/2} = 13.8$ days) decay by emission of an imageable 99 and 159 keV γ ray, respectively, and low-energy conversion and Auger electrons. Both isomers have been suggested as potential therapeutic radionuclides. Platinum-195m could allow combined chemo- and radiotherapy with cisplatin-based drugs. Platinum-195m can be produced via the $^{194}\text{Pt}(n, \gamma)^{195\text{m}}\text{Pt}$ reaction in a nuclear reactor; however, $^{195\text{m}}\text{Pt}$ produced by this reaction is destroyed by the $^{195\text{m}}\text{Pt}(n, \gamma)^{196}\text{Pt}$ reaction, resulting in a low specific activity [58]. Platinum-195m can be produced by the photonuclear reactions, $^{195}\text{Pt}(\gamma, \gamma')^{195\text{m}}\text{Pt}$ and $^{197}\text{Au}(\gamma, np)^{195\text{m}}\text{Pt}$. Dykiy et al. irradiated cisplatin, $^{\text{nat}}\text{PtCl}_2(\text{NH}_3)_2$, with bremsstrahlung photons generated from a 26 and 34 MeV electron beam; however, the recoil energies (several keV) associated with the many platinum radionuclides produced (^{191}Pt , $^{193\text{m}}\text{Pt}$, $^{195\text{m}}\text{Pt}$, and ^{197}Pt) led to disassociation and formation of $(\text{PtCl}_4)^{2-}$ and $(\text{PtCl}_6)^{2-}$. In the same work, using a 34 MeV electron beam, $^{195\text{m}}\text{Pt}$ was produced using gold NPs irradiated with bremsstrahlung photons. The $^{195\text{m}}\text{Pt}$ was chemically separated and used to synthesize $^{195\text{m}}\text{PtCl}_2(\text{NH}_3)_2$. Following radiosynthesis, the $^{195\text{m}}\text{Pt}$ -cisplatin was used in cell viability studies to show improved cell-killing efficacy relative to normal cisplatin compounds [62]. Tin-117m has been used in clinical studies for palliative care in patients with bone metastases [63, 64]. Tin-117m can be produced via the $^{117}\text{Sn}(n, n\gamma)^{117\text{m}}\text{Sn}$ reaction; however, the thermal neutron cross-section is small, resulting in a low molar activity [58]. Tin-117m can be produced by the photonuclear reactions $^{117}\text{Sn}(\gamma, \gamma')^{117\text{m}}\text{Sn}$ and $^{118}\text{Sn}(\gamma, n)^{117\text{m}}\text{Sn}$. Danagulyan et al. measured the cumulative cross-section of the $^{118}\text{Sn}(\gamma, n)^{117\text{m}}\text{Sn}$ reaction using a 40 MeV electron beam, 10 μA beam current, tantalum converter, and 98.5% enriched ^{118}Sn target. The measured cross-section was 17.5 ± 1.7 mb. Although the magnitude of this cross-section is small, the advantage of photonuclear production of $^{117\text{m}}\text{Sn}$ is the absence of other coproduced radionuclides. The only radiocontaminants are the short-lived $^{117\text{m}}\text{In}$ ($t_{1/2} = 116.2$ minutes) and $^{117\text{g}}\text{In}$ ($t_{1/2} = 43.2$ minutes) [65]. In both cases, the utility of these radionuclides have been shown; however, the existing production methods using neutron capture results in low specific

activities. Photonuclear production of these promising nuclear isomers could result in much higher specific activities. Compared to previous work using neutron capture reactions, this could increase the specific activities by a factor of 1700 and 12, respectively [58].

5.6 ADDITIONAL OPPORTUNITIES FOR THERAPEUTIC RADIONUCLIDE PRODUCTION

Therapeutic radionuclides may also be produced by in-flight projectile fragmentation. This technique uses the high-energy collision of heavy nuclei with a light target. The heavy ion fragments into a number of product radionuclides that are used for downstream experiments. Typically, this method will generate many radionuclides but select only one for study via an electromagnetic separation. The unwanted radionuclides are diverted and stopped in a solid or liquid media, often referred to as a *beam dump*. Facilities capable of producing the beams necessary to induce these reactions are exceedingly rare. Moreover, these facilities are often dedicated to studying questions in basic nuclear science.

Recent studies have focused on developing new methods to characterize the contents of these beam dumps and strategies to chemically extract a single target radionuclide from a mixture of tens to hundreds of different radionuclides. Mastren et al. showed that ^{67}Cu (also discussed earlier) coproduced in a large ensemble of radionuclides ranging in atomic number from ~ 19 to 34 and captured in an aqueous beam dump could be separated with high yield ($74\% \pm 4\%$) and $>99\%$ radiochemical purity [66]. Abel et al. modeled the production rate of therapeutic radionuclides expected at the Facility for Rare Isotope Beams located at Michigan State University. In this work, it was shown that ^{47}Ca for a $^{47}\text{Ca}/^{47}\text{Sc}$ generator, ^{211}Rn ($t_{1/2} = 14.6$ hours) for a $^{211}\text{Rn}/^{211}\text{At}$ generator, and ^{225}Ac for direct targeted alpha therapy or a $^{225}\text{Ac}/^{213}\text{Bi}$ generator could have production rates up to 37 GBq d^{-1} , 15.9 GBq d^{-1} , and 1.7 GBq wk^{-1} , respectively [67].

5.7 SUMMARY

A variety of nuclear reaction routes are available that lead to the high-yield production of therapeutic radionuclides that decay by alpha, beta, or Auger electron emission. In several cases, there may be multiple routes leading to the radionuclide of interest. Important considerations for the production of therapeutic radionuclides include target material chemistry and cost, specific activity requirements, and infrastructure needs. Interestingly, as novel accelerators become more common or accelerator technologies advance, rarely used routes like photonuclear reactions and in-flight fragmentation may become feasible future means of producing and supplying therapeutic radionuclides.

REFERENCES

1. Pourhabib, Z., Ranjbar, H., Bahrami Samani, A., and Shokri, A.A. (2019). Experimental and theoretical study of rhenium radioisotopes production for manufacturing of new compositional radiopharmaceuticals. *Appl. Radiat. Isot.* 145: 176–179.
2. Chakravarty, R., Chakraborty, S., Chirayil, V., and Dash, A. (2014). Reactor production and electrochemical purification of ^{169}Er : a potential step forward for its utilization in in vivo therapeutic applications. *Nucl. Med. Biol.* 41 (2): 163–170.
3. Khorshidi, A. (2016). Gold nanoparticles production using reactor and cyclotron based methods in assessment of $^{196,198}\text{Au}$ production yields by ^{197}Au neutron absorption for therapeutic purposes. *Mater. Sci. Eng. C* 68: 449–454.
4. Hashikin, N.A.A., Yeong, C.-H., Abdullah, B.J.J. et al. (2015). Neutron activated samarium-153 microparticles for transarterial radioembolization of liver tumour with post-procedure imaging capabilities. *PLoS One* 10 (9): e0138106.
5. Vimalnath, K.V., Rajeswari, A., Chakraborty, S., and Dash, A. (2014). Large scale production of ^{51}Cr for medical application in a medium flux research reactor: a comparative investigation of Szilard–Chalmers process and direct (n, γ) route. *Appl. Radiat. Isot.* 91: 104–108.
6. Valery, A.T., Oleg, I.A., Evgeny, G.R. et al. (2015). Production of no-carrier added lutetium-177 by irradiation of enriched ytterbium-176. *Curr. Radiopharm.* 8 (2): 95–106.
7. Karimi, Z., Sadeghi, M., and Mataji-Kojouri, N. (2018). ^{64}Cu , a powerful positron emitter for immunoimaging and theranostic: production via (nat)ZnO and (nat)ZnO-NPs. *Appl. Radiat. Isot.* 137: 56–61.
8. Deilami-Nezhad, L., Moghaddam-Banaem, L., Sadeghi, M., and Asgari, M. (2016). Production and purification of scandium-47: a potential radioisotope for cancer theranostics. *Appl. Radiat. Isot.* 118: 124–130.
9. Kolsky, K.L., Joshi, V., Mausner, L.F., and Srivastava, S.C. (1998). Radiochemical purification of no-carrier-added scandium-47 for radioimmunotherapy. *Appl. Radiat. Isot.* 49 (12): 1541–1549.
10. Aydia, M.I., El-Said, H., El-Sadek, A.A., and El-Azony, K.M. (2018). Preparation and characterization of zirconium silico ^{188}W -tungstate as a base material for $^{188}\text{W}/^{188}\text{Re}$ generator. *Appl. Radiat. Isot.* 142: 203–210.
11. Gohlke, S., Beets, A.L., Oetjen, K. et al. (2000). Simple new method for effective concentration of ^{188}Re solutions from alumina-based ^{188}W – ^{188}Re generator. *J. Nucl. Med.* 41 (7): 1271–1278.
12. Müller, C., van der Meulen, N.P., Benešová, M., and Schibli, R. (2017). Therapeutic radiometals beyond ^{177}Lu and ^{90}Y : production and application of promising α -particle, β^- -particle, and Auger electron emitters. *J. Nucl. Med.* 58 (Supplement 2): 91S–96S.
13. Mausner, L.F., Kolsky, K.L., Joshi, V., and Srivastava, S.C. (1998). Radionuclide development at BNL for nuclear medicine therapy. *Appl. Radiat. Isot.* 49 (4): 285–294.
14. Gott, M.D., Hayes, C.R., Wycoff, D.E. et al. (2016). Accelerator-based production of the $^{99\text{m}}\text{Tc}$ – ^{186}Re diagnostic-therapeutic pair using metal disulfide targets (MoS_2 , WS_2 , OsS_2). *Appl. Radiat. Isot.* 114: 159–166.

15. Richards, V.N., Rath, N., and Lapi, S.E. (2015). Production and separation of ^{186}Re from proton bombardment of ^{186}W . *Nucl. Med. Biol.* 42 (6): 530–535.
16. Ali, S.K.I., Khandaker, M.U., and Kassim, H.A. (2018). Evaluation of production cross-sections for ^{186}Re theranostic radionuclide via charged-particle induced reactions on tungsten. *Appl. Radiat. Isot.* 135: 239–250.
17. Fassbender, M.E., Ballard, B., Birnbaum, E.R. et al. (2013). Proton irradiation parameters and chemical separation procedure for the bulk production of high-specific-activity ^{186}Re using WO_3 targets. *Radiochim. Acta* 101, 339 (5).
18. Moustapha, M.E., Ehrhardt, G.J., Smith, C.J. et al. (2006). Preparation of cyclotron-produced ^{186}Re and comparison with reactor-produced ^{186}Re and generator-produced ^{188}Re for the labeling of bombesin. *Nucl. Med. Biol.* 33 (1): 81–89.
19. Novgorodov, A.F., Bruchertseifer, F., Brockmann, J. et al. (2000). Thermochromatographic separation of no-carrier-added ^{186}Re or ^{188}Re from tungsten targets relevant to nuclear medical applications. *Radiochim. Acta* 88 (3–4): 163.
20. Chaple, I.F. and Lapi, S.E. (2018). Production and use of the first-row transition metal PET radionuclides $^{43,44}\text{Sc}$, ^{52}Mn , and ^{45}Ti . *J. Nucl. Med.* 59 (11): 1655–1659.
21. Müller, C., Domnanich, K.A., Umbricht, C.A., and Meulen, N.P. (2018). Scandium and terbium radionuclides for radiotheranostics: current state of development towards clinical application. *Br. J. Radiol.* 91 (1091): 20180074.
22. Minegishi, K., Nagatsu, K., Fukada, M. et al. (2016). Production of scandium-43 and -47 from a powdery calcium oxide target via the $^{nat/44}\text{Ca}(\alpha, x)$ -channel. *Appl. Radiat. Isot.* 116: 8–12.
23. Valdovinos, H.F., Hernandez, R., Barnhart, T.E. et al. (2015). Separation of cyclotron-produced ^{44}Sc from a natural calcium target using a dipentyl pentylphosphonate functionalized extraction resin. *Appl. Radiat. Isot.* 95: 23–29.
24. Severin, G.W., Engle, J.W., Valdovinos, H.F. et al. (2012). Cyclotron produced ^{44}gSc from natural calcium. *Appl. Radiat. Isot.*: including data, instrumentation and methods for use in agriculture, industry and medicine 70 (8): 1526–1530.
25. Domnanich, K.A., Eichler, R., Müller, C. et al. (2017). Production and separation of ^{43}Sc for radiopharmaceutical purposes. *EJNMMI Radiopharm. Chem.* 2 (1): 14.
26. van der Meulen, N.P., Bunka, M., Domnanich, K.A. et al. (2015). Cyclotron production of ^{44}Sc : from bench to bedside. *Nucl. Med. Biol.* 42 (9): 745–751.
27. Walczak, R., Krajewski, S., Szkliniarz, K. et al. (2015). Cyclotron production of ^{43}Sc for PET imaging. *EJNMMI Phys.* 2 (1): 33.
28. Hoehr, C., Oehlke, E., Benard, F. et al. (2014). ^{44}gSc production using a water target on a 13 MeV cyclotron. *Nucl. Med. Biol.* 41 (5): 401–406.
29. AKH, R., Ramogida, C.F., Schaffer, P., and Radchenko, V. (2018). Development of ^{225}Ac radiopharmaceuticals: TRIUMF perspectives and experiences. *Curr. Radiopharm.* 11 (3): 156–172.
30. Ma, D., McDevitt, M.R., Finn, R.D., and Scheinberg, D.A. (2001). Breakthrough of ^{225}Ac and its radionuclide daughters from an $^{225}\text{Ac}/^{213}\text{Bi}$ generator: development of new methods, quantitative characterization, and implications for clinical use. *Appl. Radiat. Isot.* 55 (5): 667–678.

31. Morgenstern, A., Apostolidis, C., and Kratochwil, C. (2018). An overview of targeted alpha therapy with ^{225}Ac and ^{213}Bi . *Curr. Radiopharm.* 11 (3): 200–208.
32. Jonathan, W.E. (2018). The production of Ac-225. *Curr. Radiopharm.* 11 (3): 173–179.
33. Griswold, J.R., Medvedev, D.G., Engle, J.W. et al. (2016). Large scale accelerator production of ^{225}Ac : effective cross sections for 78–192 MeV protons incident on ^{232}Th targets. *Appl. Radiat. Isot.* 118: 366–374.
34. Weidner, J.W., Mashnik, S.G., John, K.D. et al. (2012). ^{225}Ac and ^{223}Ra production via 800 MeV proton irradiation of natural thorium targets. *Appl. Radiat. Isot.* 70 (11): 2590–2595.
35. Radchenko, V., Engle, J.W., Wilson, J.J. et al. (2015). Application of ion exchange and extraction chromatography to the separation of actinium from proton-irradiated thorium metal for analytical purposes. *J. Chromatogr. A* 1380: 55–63.
36. McAlister, D.R. and Horwitz, E.P. (2018). Selective separation of radium and actinium from bulk thorium target material on strong acid cation exchange resin from sulfate media. *Appl. Radiat. Isot.* 140: 18–23.
37. Apostolidis, C., Molinet, R., McGinley, J. et al. (2005). Cyclotron production of Ac-225 for targeted alpha therapy 11 dedicated to Prof. Dr. Franz Baumgärtner on the occasion of his 75th birthday. *Appl. Radiat. Isot.* 62 (3): 383–387.
38. Martin, T.M., Bhakta, V., Al-Harbi, A. et al. (2014). Preliminary production of ^{211}At at the Texas A&M University Cyclotron Institute. *Health Phys.* 107 (1): 1–9.
39. Michael, R.Z. and Marek, P. (2011). Astatine-211: production and availability. *Curr. Radiopharm.* 4 (3): 177–185.
40. Lindegren, S., Bäck, T., and Jensen, H.J. (2001). Dry-distillation of astatine-211 from irradiated bismuth targets: a time-saving procedure with high recovery yields. *Appl. Radiat. Isot.* 55 (2): 157–160.
41. Rosenkranz, A.A., Slastnikova, T.A., Karmakova, T.A. et al. (2018). Antitumor activity of Auger electron emitter ^{111}In delivered by modular nanotransporter for treatment of bladder cancer with EGFR overexpression. *Front. Pharmacol.* 9: 1331.
42. Cai, Z., Chattopadhyay, N., Yang, K. et al. (2016). ^{111}In -labeled trastuzumab-modified gold nanoparticles are cytotoxic in vitro to HER2-positive breast cancer cells and arrest tumor growth in vivo in athymic mice after intratumoral injection. *Nucl. Med. Biol.* 43 (12): 818–826.
43. Limouris, G., Dimitropoulos, N., Kontogeorgakos, D. et al. (2005). Evaluation of the therapeutic response to In-111-DTPA octreotide-based targeted therapy in liver metastatic neuroendocrine tumors according to CT/MRI/US findings. *Cancer Biother. Radiopharm.* 20 (2): 215–217.
44. Valdovinos, H.F., Hernandez, R., Graves, S. et al. (2017). Cyclotron production and radiochemical separation of ^{55}Co and ^{58m}Co from ^{54}Fe , ^{58}Ni and ^{57}Fe targets. *Appl. Radiat. Isot.* 130: 90–101.
45. Thisgaard, H., Elema, D.R., and Jensen, M. (2011). Production and dosimetric aspects of the potent Auger emitter ^{58m}Co for targeted radionuclide therapy of small tumors. *Med. Phys.* 38 (8): 4535–4541.

46. Vaudon, J., Frealle, L., Audiger, G. et al. (2018). First steps at the cyclotron of orléans in the radiochemistry of radiometals: ^{52}Mn and ^{165}Er . *Instruments* 2 (3).
47. Sadeghi, M., Enferadi, M., and Tenreiro, C. (2010). Nuclear model calculations on the production of Auger emitter ^{165}Er for targeted radionuclide therapy. *J. Mod. Phys.* 01 (04): 9.
48. Beyer, G.J., Zeisler, S.K., and Becker, D.W. (2004). The Auger-electron emitter ^{165}Er : excitation function of the $^{165}\text{Ho}(p,n)^{165}\text{Er}$ process. *Radiochim. Acta* 92 (4–6): 219.
49. Zandi, N., Sadeghi, M., and Afarideh, H. (2013). Evaluation of the cyclotron production of ^{165}Er by different reactions. *J. Radioanal. Nucl. Chem.* 295 (2): 923–928.
50. Fonslet, J., Lee, B.Q., Tran, T.A. et al. (2017). ^{135}La as an Auger-electron emitter for targeted internal radiotherapy. *Phys. Med. Biol.* 63 (1): 015026.
51. Thisgaard, H. and Jensen, M. (2009). Production of the Auger emitter ^{119}Sb for targeted radionuclide therapy using a small PET-cyclotron. *Appl. Radiat. Isot.* 67 (1): 34–38.
52. Thisgaard, H. and Jensen, M. (2008). ^{119}Sb – a potent Auger emitter for targeted radionuclide therapy. *Z. Med. Phys.* 35 (9): 3839–3846.
53. Kiess, A.P., Minn, I., Chen, Y. et al. (2015). Auger Radiopharmaceutical Therapy Targeting Prostate-Specific Membrane Antigen. *J. Nucl. Med.* 56 (9): 1401–1407.
54. Ogawa, K., Kanbara, H., Kiyono, Y. et al. (2013). Development and evaluation of a radiobromine-labeled sigma ligand for tumor imaging. *Nucl. Med. Biol.* 40 (4): 445–450.
55. Tolmachev, V., Löfvqvist, A., Einarsson, L. et al. (1998). Production of ^{76}Br by a low-energy cyclotron. *Appl. Radiat. Isot.* 49 (12): 1537–1540.
56. Breunig, K., Spahn, I., Spellerberg, S., and Coenen Heinz, H. (2015). Production of no-carrier-added radiobromine: new nickel selenide target and optimized separation by dry distillation. *Radiochim. Acta* 103 (5): 397.
57. Mease, R.C., DeJesus, O.T., Gatley, S.J. et al. (1991). Production of no carrier added ^{80}mBr for investigation of Auger electron toxicity. *Int. J. Radiat. Appl. Instrum. Part A. Appl. Radiat. Isot.* 42 (1): 57–61.
58. Habs, D. and Köster, U. (2011). Production of medical radioisotopes with high specific activity in photonuclear reactions with γ -beams of high intensity and large brilliance. *Appl. Phys. B* 103 (2): 501–519.
59. Rotsch, D.A., Brown, M.A., Nolen, J.A. et al. (2018). Electron linear accelerator production and purification of scandium-47 from titanium dioxide targets. *Appl. Radiat. Isot.* 131: 77–82.
60. Rane, S., Harris, J.T., and Starovoitova, V.N. (2015). ^{47}Ca production for $^{47}\text{Ca}/^{47}\text{Sc}$ generator system using electron linacs. *Appl. Radiat. Isot.* 97: 188–192.
61. Melville, G. and Allen, B. (2009). Cyclotron and linac production of Ac-225. *Appl. Radiat. Isot.* 67 (4): 549–555.
62. Dykiy, M.P., Dovbnya, A.N., Lyashko, Y.V. et al. (2007). Photonuclear production of $^{193\text{m},195\text{m}}\text{Pt}$ and synthesis of radioactive cisplatin. *J. Labelled Compd. Radiopharm.* 50 (5–6): 480–482.
63. Atkins, H.L., Mausner, L.F., Srivastava, S.C. et al. (1995). Tin-117m(4+)-DTPA for palliation of pain from osseous metastases: a pilot study. *J. Nucl. Med.* 36 (5): 725–729.

64. Srivastava, S.C., Atkins, H.L., Krishnamurthy, G.T. et al. (1998). Treatment of metastatic bone pain with tin-117m Stannic diethylenetriaminepentaacetic acid: a phase I/II clinical study. *Clin. Cancer Res.* 4 (1): 61.
65. Danagulyan, A., Hovhannisyan, G., Bakhshyan, T.M. et al. (2015). Formation of medical radioisotopes ^{111}In , $^{117\text{m}}\text{Sn}$, ^{124}Sb , and ^{177}Lu in photonuclear reactions. *Phys. At. Nucl.* 78: 447–452.
66. Mastren, T., Pen, A., Loveless, S. et al. (2015). Harvesting ^{67}Cu from the collection of a secondary beam cocktail at the national superconducting cyclotron laboratory. *Anal. Chem.* 87 (20): 10323–10329.
67. Abel, E.P., Avilov, M., Ayres, V. et al. (2018). Isotope harvesting at FRIB: additional opportunities for scientific discovery. arXiv preprint arXiv:1812.03984.
68. Loveless, C.S., Blanco, J.R., Diehl, G.L. SE Cyclotron Production and Separation of Scandium Radionuclides from Natural Titanium Metal and Titanium Dioxide Targets *J Nucl Med.* 2020.

PART III

Synthetic Methods for Radiopharmaceuticals

Chapter 6

Synthesis of ^{13}N - and ^{15}O -Labeled Radiopharmaceuticals

Krishna R. Pulagam¹, Vanessa Gómez-Vallejo¹,
Fernando López-Gallego^{2,3}, Luka Rejc^{1,4}, and Jordi Llop¹

¹*Radiochemistry and Nuclear Imaging Group, CIC biomaGUNE, Basque Research and Technology Alliance (BRTA), 20014, Donostia San Sebastián, Spain*

²*Heterogeneous Biocatalysis Laboratory, CIC biomaGUNE, Basque Research and Technology Alliance (BRTA), 20014, Donostia San Sebastián, Spain*

³*IKERBASQUE, Basque Foundation for Science, 48013 Bilbao, Spain*

⁴*Faculty of Chemistry and Chemical Technology, University of Ljubljana, SI-1000, Ljubljana, Slovenia*

6.1 NITROGEN-13

Nitrogen-13 was discovered more than 80 years ago when Irene Curie and Frederic Joliot irradiated boron nitride with α -particles to produce nitrogen-13 via the $^{10}\text{B}(\alpha, n)^{13}\text{N}$ nuclear reaction [1]. After treatment of the irradiated sample with sodium hydroxide, the authors detected the distillation of a radioactive compound that produced a radioactive

white precipitate when contacted with a paper soaked in hydrochloric acid. This precipitate was identified as ammonium chloride, and Joliot and Curie concluded that the radionuclide formed was nitrogen-13 and estimated its physical half-life to be close to 14 minutes. Within the same year, the first production of nitrogen-13 using a cyclotron was reported by Cockcroft et al. [2]. The authors irradiated either ^{13}C -enriched graphite with accelerated protons or natural graphite with accelerated deuterons to produce, in both cases, nitrogen-13. The half-life was determined to be 10.5 ± 0.5 minutes, a value that better resembles the currently accepted physical half-life of nitrogen-13 (9.97 minutes). Joliot and Curie got the Nobel Prize in 1935 for “their synthesis of new radioactive elements,” while Cockcroft and Walton received the Nobel Prize in 1951 for “their pioneer work on the transmutation of atomic nuclei by artificially accelerated atomic particles.”

After these pioneering studies, nitrogen-13 has progressively been incorporated in the toolbox of positron emission tomography (PET) chemists, who have developed strategies for the in-cyclotron production of different ^{13}N -labeled species, which have been used directly in different applications or further employed to prepare more complex labeled molecules. This chapter will cover the main alternatives for the production of nitrogen-13 and the application of this radionuclide to the preparation of labeled molecules.

6.1.1 Nuclear Reactions for the Production of Nitrogen-13

Nitrogen-13 can be produced in biomedical cyclotrons using different nuclear reactions (see Table 6.1), the most commonly used reactions being those first described by Cockcroft et al. [2], i.e. $^{12}\text{C}(d,n)^{13}\text{N}$ and $^{13}\text{C}(p,n)^{13}\text{N}$ together with $^{16}\text{O}(p,\alpha)^{13}\text{N}$. In addition to accelerated ion-induced nuclear reactions, nitrogen-13 can also be produced by neutron irradiation of natural nitrogen via the $^{14}\text{N}(n,2n)^{13}\text{N}$ nuclear reaction. This nuclear reaction requires the use of a neutron source, which is not widely available; additionally, because the irradiated material and the radionuclide are isotopes of the same element, low molar activity values are achieved. Because of this, neutron irradiation has barely been applied to produce ^{13}N .

Table 6.1 Methods for the production of ^{13}N using nuclear reactions.

Target material	Nuclear reaction	In-target product
CO_2 (trace N_2)	$^{12}\text{C}(d,n)^{13}\text{N}$	$[^{13}\text{N}]\text{N}_2$
Graphite	$^{12}\text{C}(d,n)^{13}\text{N}$	$[^{13}\text{N}]\text{CN}$
Charcoal	$^{12}\text{C}(d,n)^{13}\text{N}$	$[^{13}\text{N}]\text{N}_2$ + trapped $[^{13}\text{N}]\text{CN}$
^{13}C -enriched charcoal	$^{13}\text{C}(p,n)^{13}\text{N}$	Trapped $[^{13}\text{N}]\text{CN}$
H_2O /ethanol	$^{16}\text{O}(p,\alpha)^{13}\text{N}$	$[^{13}\text{N}]\text{NH}_3$
H_2O	$^{16}\text{O}(p,\alpha)^{13}\text{N}$	$[^{13}\text{N}]\text{NH}_3$ + $[^{13}\text{N}]\text{NO}_3^-$ + $[^{13}\text{N}]\text{NO}_2^-$
NaNO_3 (aq)	$^{14}\text{N}(n,2n)^{13}\text{N}$	$[^{13}\text{N}]\text{NH}_3$
Al_4C_3	$^{12}\text{C}(d,n)^{13}\text{N}$	Matrix-trapped ^{13}N
CH_4 (flowing)	$^{12}\text{C}(d,n)^{13}\text{N}$	$[^{13}\text{N}]\text{NH}_3$ + $[^{13}\text{N}]\text{HCN}$ + $[^{13}\text{N}]\text{CH}_3\text{NH}_2$

6.1.2 Production of $[^{13}\text{N}]\text{N}_2$

Dinitrogen is an inert gas, and its chemical modification for conducting radiolabeling reactions is challenging. Because of this, the main applications of $[^{13}\text{N}]\text{N}_2$ have been limited to nitrogen fixation experiments [3, 4] as well as ventilation studies both in animal species [5, 6] and in human subjects [7].

$[^{13}\text{N}]\text{N}_2$ is unintentionally produced in biomedical cyclotrons worldwide on a daily basis when N_2/O_2 mixtures are irradiated to produce $[^{11}\text{C}]\text{CO}_2$ via the $^{14}\text{N}(p,\alpha)^{11}\text{C}$ nuclear reaction. In addition to the formation of $[^{11}\text{C}]\text{CO}_2$, this process leads to the formation of $[^{14}\text{O}]\text{O}_2$, $[^{15}\text{O}]\text{O}_2$, $[^{11}\text{C}]\text{CO}$, and $[^{13}\text{N}]\text{N}_2$; the last is as a result of the $^{14}\text{N}(p,pn)^{13}\text{N}$ nuclear reaction, which produces recoil ^{13}N atoms that can undergo isotopic exchange reactions with N_2 , ultimately resulting in the in situ formation of $[^{13}\text{N}]\text{N}_2$. After elimination of short-lived oxygen isotopes by simple radioactive decay and of $[^{11}\text{C}]\text{CO}$ and $[^{11}\text{C}]\text{CO}_2$ by oxidation of the first and subsequent trappings of $[^{11}\text{C}]\text{CO}_2$, pure $[^{13}\text{N}]\text{N}_2$ can be produced in sufficient amounts to conduct ventilation studies (c. 10 GBq in 30-minutes irradiation of the target at 20 μA ; Figure 6.1) [8].

Before the development of this convenient and straightforward approach, more sophisticated methods had been developed. The first paper that specifically mentioned

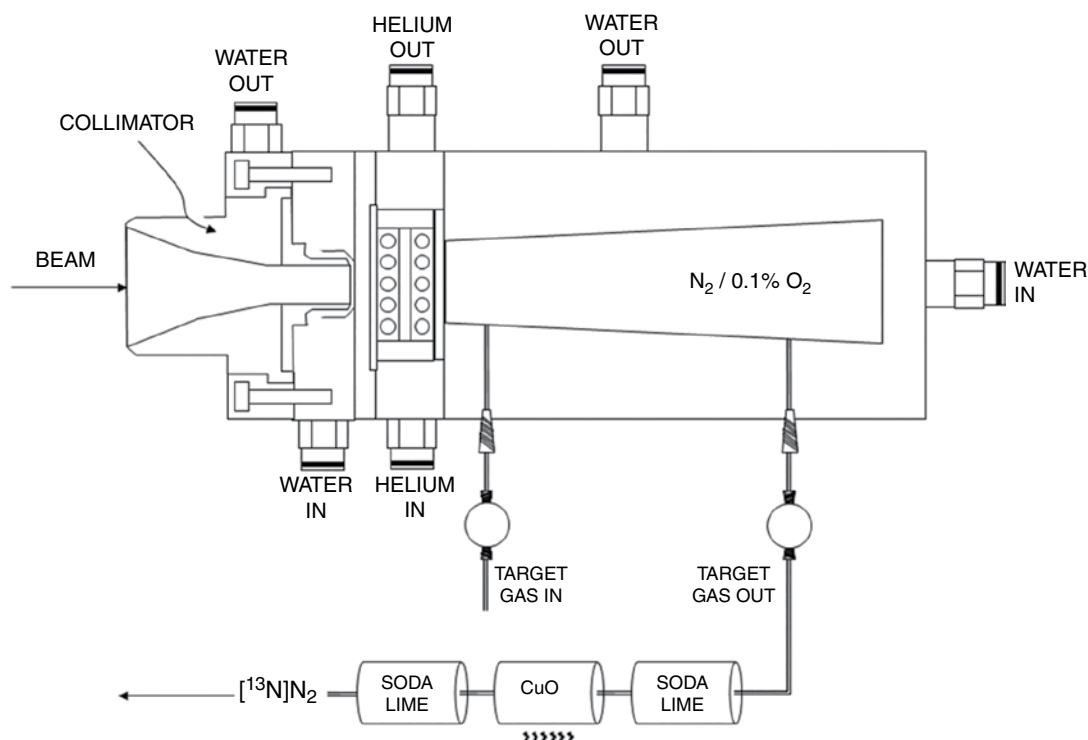


Figure 6.1 Schematic representation of the system used for the production of $[^{13}\text{N}]\text{N}_2$ by irradiation of an N_2/O_2 mixture, as used for the production of $[^{11}\text{C}]\text{CO}_2$. Source: Based on the target Nirta® -C11 provided by IBA.

the production of $[^{13}\text{N}]\text{N}_2$ and its use in plant fixation experiments was published in 1940 [9]. In this study, ^{13}N was produced via the $^{12}\text{C}(d,n)^{13}\text{N}$ nuclear reaction by irradiation of charcoal using 8-MeV deuterons. Combustion of the irradiated material under a stream of O_2 and in the presence of CuO resulted in a mixture of radioactive gases containing $[^{13}\text{N}]\text{CN}$, $[^{13}\text{N}]\text{NH}_3$, $[^{13}\text{N}]\text{NO}$, and $[^{13}\text{N}]\text{N}_2$, which could be isolated by purification over different chemical and cryogenic traps. With the same nuclear reaction, a continuous flow production of $[^{13}\text{N}]\text{N}_2$ could be achieved by flushing the irradiated granulated charcoal with argon gas and passing the gas mixture through combustion tubes packed with copper at high temperature (750°C) and then through diluted H_2SO_4 and alkaline sulfite solutions [10]. With this procedure, a continuous flow containing ^{13}N activity in the range $1\text{--}2\text{ GBq min}^{-1}$ using a deuteron current of $40\ \mu\text{A}$ in the target could be produced.

Liquid targets have also been applied to the production of $[^{13}\text{N}]\text{N}_2$. By proton (18 MeV) irradiation of 0.1 M aqueous ammonia solutions at $10\ \mu\text{A}$, Parks and Krohn demonstrated that 75% of the radioactivity was due to the presence of $[^{13}\text{N}]\text{N}_2$, which could be recovered with a spirometer and stored in a specially designed reservoir outside the cyclotron vault [11] (see Figure 6.2 for the scheme of the production system). $[^{13}\text{N}]\text{NO}_3^-$ (16%), $[^{13}\text{N}]\text{NO}_2^-$ (6%), and $[^{13}\text{N}]\text{NH}_4^+$ (3%) were also formed. Of note, this method leads to low molar activities, because the radiolytic oxidation of ammonia results in the formation of nonradioactive N_2 (up to 3 mmol under the experimental conditions assayed by the authors).

The direct production of $[^{13}\text{N}]\text{N}_2$ in the target has also been achieved by irradiation of ^{13}C -enriched charcoal with protons (energy = 19 MeV). In this case, the ^{13}C -enriched charcoal (ca. 0.8 g, 97% enriched) was packed into a carbon (natural abundance) cylinder that was spring-loaded into a quartz tube, preheated at 800°C , and irradiated at $10\ \mu\text{A}$ [12].

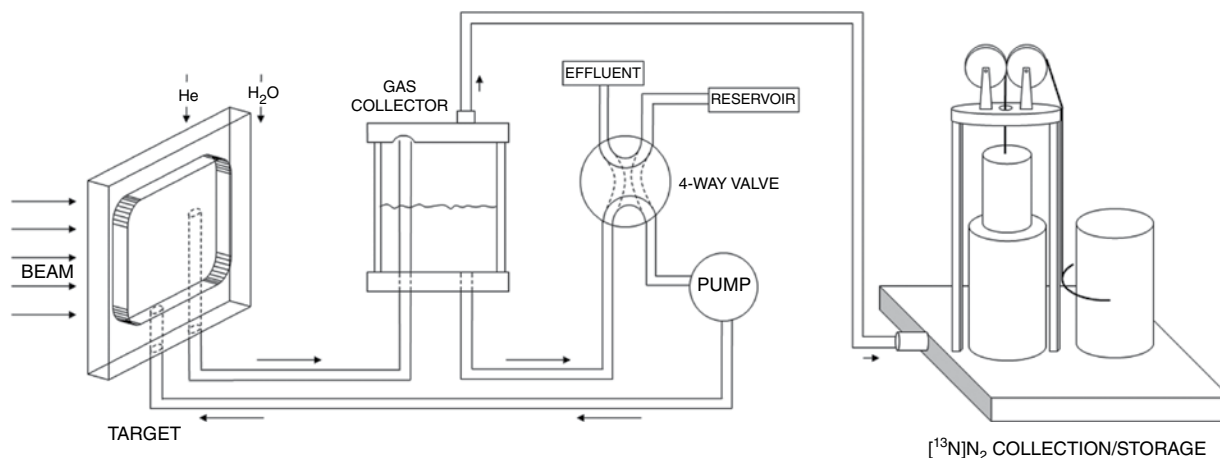


Figure 6.2 Schematic representation of the liquid recirculation system for the production and accumulation of $[^{13}\text{N}]\text{N}_2$. All components except the target were outside the cyclotron vault. The whole target solution (volume $\sim 60\text{ ml}$) was typically circulated at 1 cm s^{-1} by using a variable-speed pump. Radioactive $[^{13}\text{N}]\text{N}_2$ was collected in the spirometer (right). The four-way valve was used to replace the target solution without interrupting irradiation.

The target was flushed with helium gas to transfer the radioactive species into a liquid-cooled charcoal trap. As much as 99.7% of the generated radioactivity under these conditions was $[^{13}\text{N}]\text{N}_2$. When lower target-intensity values were used, other species, i.e. $[^{13}\text{N}]\text{NO}$ and $[^{13}\text{N}]\text{N}_2\text{O}$, were majorly formed (22.6% and 44.9%, respectively).

Strategies to generate $[^{13}\text{N}]\text{N}_2$ from other radioactive precursors produced in the cyclotron have been reported. The clearest example is the oxidation of cyclotron-produced $[^{13}\text{N}]\text{NH}_3$ (see the next section) with NaOBr in the presence of NH_4Cl to give $[^{13}\text{N}]\text{N}_2$ [13, 14]. The addition of NH_4Cl resulted in low molar activity values. The molar activity values could be slightly improved by increasing the amount of both NH_4Cl and NaOBr, which also resulted in an increase in radiochemical yield [4].

6.1.3 Production of $[^{13}\text{N}]\text{NH}_3$

Ammonia is the most widely used ^{13}N -labeled radiotracer, and it has been widely applied as an accurate noninvasive diagnostic tool for the quantification of myocardial perfusion in clinical settings [15, 16] and to explore different phenomena in preclinical studies [17–19]. Additionally, it is used as the precursor for a wide range of more sophisticated tracers (discussed later).

^{13}N -labeled ammonia was the first ^{13}N -labeled compound ever reported, and it was first produced by Joliot and Curie in an attempt to prove the identity of the radionuclide that they had produced by irradiation of boron nitride with α -particles [1]. They treated the irradiated sample with sodium hydroxide and distilled a radioactive compound that produced ammonium chloride when contacted with hydrochloric acid. After this pioneering work, other attempts to successfully produce $[^{13}\text{N}]\text{NH}_3$ using solid targets were reported, all based on the same principle but using particle accelerators for the production of the radionuclide. For example, Hunter and Monahan produced ^{13}N by irradiation of Al_4C_3 with 8–12-MeV deuterons. The authors treated the target with a solution of KOH and distilled $[^{13}\text{N}]\text{NH}_3$ that was trapped in an acidic solution [20]. Although no details about irradiation time and the amount of target material were reported, 740 GBq of carrier-free $[^{13}\text{N}]\text{NH}_3$ could be produced using a target intensity of 30 μA . Almost simultaneously, Welch and Lifton reported the formation of ^{13}N -labeled compounds produced during irradiation of different carbides with deuterons, with the relative amounts depending on the integrated current on the target material [21]. They found that by varying the carbide and irradiation conditions, different chemical species could be obtained, including $[^{13}\text{N}]\text{NH}_3$, $[^{13}\text{N}]\text{CH}_3\text{CN}$, and $[^{13}\text{N}]\text{CN}^-$. The maximum percentage of $[^{13}\text{N}]\text{NH}_3$ was obtained after irradiation of Al_4C_3 , with relative values in the range 75–90% depending on the integrated current in the target. It is noteworthy that this irradiation results in the formation of the short-lived β^- -emitter ^{28}Al (half-life = 2.24 minutes) via the $^{27}\text{Al}(d,p)^{28}\text{Al}$ nuclear reaction (maximum cross-section at around 5 MeV) [22].

An alternative method using a gas-phase target was developed one year later, and it was based on the deuteron irradiation (8 MeV) of methane continuously flowing in a Pyrex glass-lined target chamber [23]. Ten minutes of irradiation at 5 μA resulted in 740 MBq of $[^{13}\text{N}]\text{NH}_3$, which could be trapped in an isotonic saline solution. Minor

impurities were $[^{13}\text{N}]\text{CH}_3\text{NH}_2$ (2%), $[^{13}\text{N}]\text{C}_2\text{H}_5\text{NH}_2$ (<0.2%), and $[^{13}\text{N}]\text{HCN}$ (<3%), as determined by gas chromatography.

The use of liquid targets for the production of $[^{13}\text{N}]\text{NH}_3$ was described one year later [24], to overcome the limitations of the low molar activity obtained using the methane target (0.2–0.4 GBq μmol^{-1} or, as reported in the original publication, 30 μg of carrier ammonia in 10–20 mCi). Following suggestions by Tilbury that the $^{16}\text{O}(p,\alpha)^{13}\text{N}$ reaction proceeded with a high yield, Krizek et al. investigated this nuclear reaction in liquid targets by irradiating water with protons. With 15-minutes irradiation at 10 μA , they could produce 7.9 GBq of ^{13}N (end-of-bombardment [EOB]) mainly as $[^{13}\text{N}]\text{NO}_3^-$, which was reduced with titanium hydroxide to yield 3.5 GBq of $[^{13}\text{N}]\text{NH}_3$ with a molar activity close to 8 GBq μmol^{-1} , clearly superior to the activity obtained using the methane target. Other reducing agents [25], such as Devarda's alloy in the presence of NaOH and TiCl_3 in the presence of NaOH, were successfully assayed, and a fully automated process was first described in 1973 [26].

A few years later, Tilbury and Dahl showed that the integrated dose in the target played a pivotal role in the formation of $[^{13}\text{N}]\text{NH}_3$ relative to the other two major species generated during beam delivery, i.e. $[^{13}\text{N}]\text{NO}_3^-$ and $[^{13}\text{N}]\text{NO}_2^-$, with $[^{13}\text{N}]\text{NO}_3^-$ being the major species at high doses (>80% for doses >3 μAh) [27], but with $[^{13}\text{N}]\text{NH}_3$ ammonia accounting for ca. 40% of the radioactivity at low integrated doses (0.01 μAh). This is due to the fact that the nitrogen-13 nuclei produced by the $^{16}\text{O}(p,\alpha)^{13}\text{N}$ nuclear reaction first pick up hydrogen atoms, either by hydrogen abstraction from water or by reaction with other hydrogenous species. These reactions produce OH radicals, which can induce the radiolytic oxidation of $[^{13}\text{N}]\text{NH}_3$ to its oxoanions. If we assume that this mechanism is correct, it is clear that the formation of the oxoanions could be prevented by "inactivating" or "removing" the radicals formed during hydrogen abstraction. This was achieved by using a cryogenic target containing frozen water [28]. The authors irradiated water in the solid state using protons with an effective energy of 15.7 MeV and found that nearly all nitrogen activity was in the form of $[^{13}\text{N}]\text{NH}_3$, irrespective of the beam current in the range 1–20 μA , with only traces of $[^{13}\text{N}]\text{NO}_3^-$ and $[^{13}\text{N}]\text{NO}_2^-$ present, because the low temperature decreased radiolysis.

The use of frozen targets has major inconveniences. Hence, the addition of radical scavengers to liquid water to prevent the formation of the oxoanions was investigated. The major breakthrough was reported by Wieland et al. [29], who demonstrated that the addition of a small amount of ethanol (5–10 mM concentration) to the irradiated water resulted in more than 96% of the radioactivity being produced as $[^{13}\text{N}]\text{NH}_3$, irrespective of the beam intensity (15–30 μA) and irradiation time (8–20 minutes). Similar results could be achieved with the addition of acetic acid, which at concentrations >5 mM also yielded more than 95% of the radioactivity as $[^{13}\text{N}]\text{NH}_3$, with equivalent saturation yields to those achieved after the addition of ethanol. Currently, the production of ^{13}N by proton irradiation of ethanol/water solutions is widely established worldwide, using a target configuration similar to that shown in Figure 6.3.

Other, less convenient strategies to prevent the formation of $[^{13}\text{N}]\text{NO}_3^-$ and $[^{13}\text{N}]\text{NO}_2^-$ include the pressurization of the water target with (i) hydrogen with [30] and without [30–32] addition of ethanol in the irradiated solution, and (ii) methane [33].

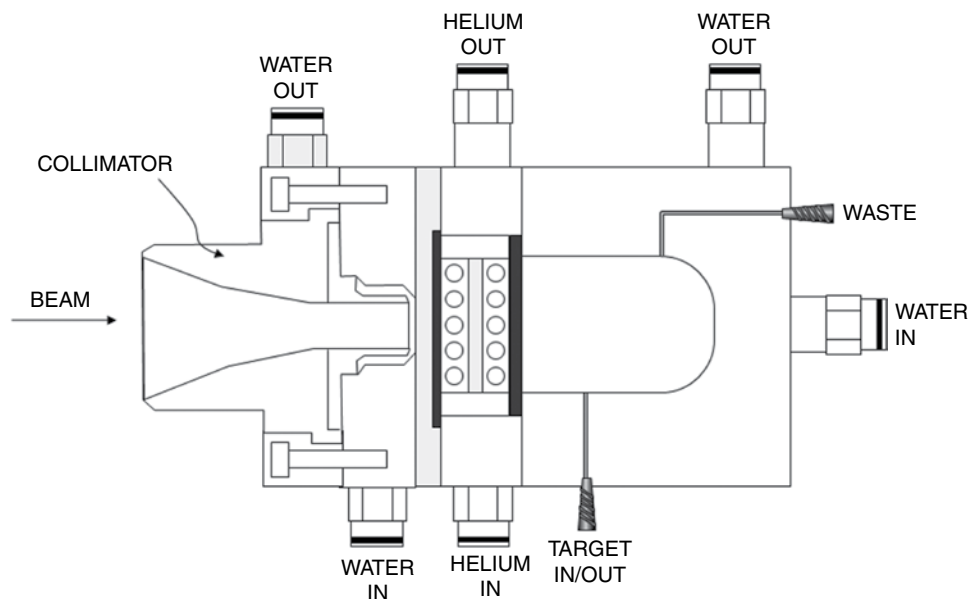


Figure 6.3 Typical target design for the production of $[^{13}\text{N}]\text{NH}_3$ by irradiation of 5 mM ethanol aqueous solution with protons. Source: Based on the target Nirta® -N13 provided by IBA.

6.1.4 Production of $[^{13}\text{N}]\text{NO}_3^-$, $[^{13}\text{N}]\text{NO}_2^-$, and $[^{13}\text{N}]\text{N}_2\text{O}$

As mentioned earlier, $[^{13}\text{N}]\text{NO}_3^-$ is formed as the predominant species by proton irradiation of water in the absence of a scavenger, after a sufficient dose has been imposed on the target [24]. Usually, $[^{13}\text{N}]\text{NO}_2^-$ and $[^{13}\text{N}]\text{NH}_3$ are also found in the irradiated solution, eventually together with the radionuclides produced in the target chamber or target window, e.g. ^{48}V if the target window is made of titanium. All cationic species can be efficiently removed by passing them through a small column containing cation-exchange resin, while $[^{13}\text{N}]\text{NO}_2^-$ can be eliminated by acidifying it with 10% H_2SO_4 and boiling it to decompose nitrous acid and expel it as NO_x [34].

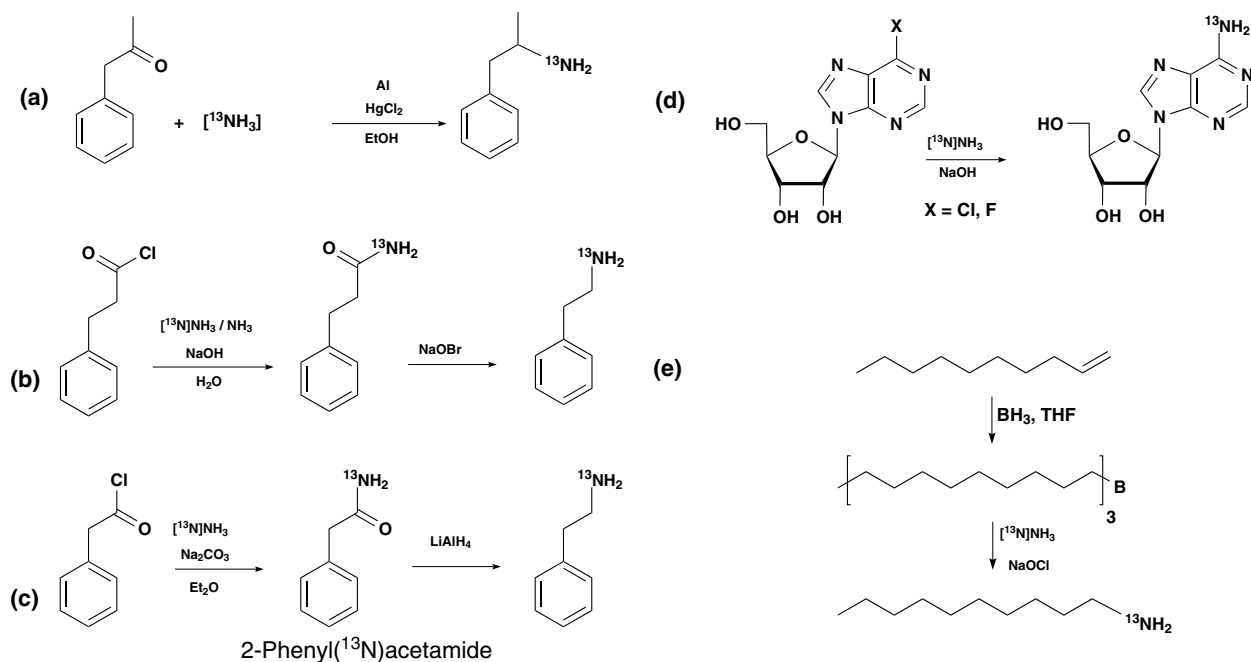
For the production of $[^{13}\text{N}]\text{NO}_2^-$, the most efficient route is the reduction of $[^{13}\text{N}]\text{NO}_3^-$ produced by proton irradiation of water. The first methods reported in the literature [11] exploited the reducing capacity of a freshly prepared cadmium-copper amalgam [35], providing a maximal ratio of $[^{13}\text{N}]\text{NO}_2^-$ to $[^{13}\text{N}]\text{NO}_3^-$ of 6 with 95% of the activity recovered from the column. Later, the reduction efficiency could be improved by using a copper-plated cadmium column, prepared by sequential treatment of cadmium with 2N HCl, 0.3N HNO_3 , and 2N HCl, each lasting for 20 minutes, and with intercalating washing steps with distilled water until the pH is neutral, followed by treatment with 0.08 M CuSO_4 solution and replacement of the solvent with 0.15 M NH_4Cl before packing the column [36]. Under these conditions, radiochemical purity greater than 97% could be obtained in the eluent of the cadmium column. This value could be increased to 99.2% by adding a subsequent step consisting of rotatory evaporation at pH = 11.0 to remove $[^{13}\text{N}]\text{NH}_3$. The reduction

with the use of copper-plated columns or variants of these has been successfully applied by different research groups [37–45]. Recently, an enzymatic method for the efficient, metal-free reduction of $[^{13}\text{N}]\text{NO}_3^-$ to $[^{13}\text{N}]\text{NO}_2^-$ has been reported [46] (see Section 6.1.11).

The production of $[^{13}\text{N}]\text{N}_2\text{O}$ has been achieved by pyrolysis of $[^{13}\text{N}]\text{NH}_4\text{NO}_3$ or $\text{NH}_4[^{13}\text{N}]\text{NO}_3$ in sulfuric acid and in the presence of an excess of NH_4NO_3 [47]. In both cases, the formation of $[^{13}\text{N}]\text{N}_2\text{O}$ was achieved, although 30–40% of the radioactivity was due to the presence of $[^{13}\text{N}]\text{N}_2$. This value could be decreased to c. 2% by addition of an excess of $(\text{NH}_4)_2\text{SO}_4$.

6.1.5 ^{13}N -Labeled Amines and Amides

Reactions typically used in classical organic chemistry have been applied to the preparation of ^{13}N -labeled amines and amides, the latter usually not isolated and used just as intermediates for the preparation of amines. One of the approaches for the preparation of ^{13}N -labeled amines was based on the reaction of $[^{13}\text{N}]\text{NH}_3$ with ketones or aldehydes to form the corresponding imine, which can then be reduced to the corresponding primary amine. This method was applied, for example, in the preparation of ^{13}N -labeled amphetamine (Scheme 6.1a) by reaction of $[^{13}\text{N}]\text{NH}_3$ with phenylacetone in the presence



Scheme 6.1 (a) Synthesis of $[^{13}\text{N}]$ amphetamine via formation of the imine. (b, c) Synthesis of $[^{13}\text{N}]$ PEA (phenethylamine) via Hofmann rearrangement (b) and reduction of the amide (c). (d) Synthesis of $[^{13}\text{N}]$ adenosine by ammonolysis of 6-chloro- and 6-fluoro-9- β -D-ribo-furanosyl purine. (e) Synthesis of ^{13}N -labeled alkylamines by amination of organoboranes (example shown for 1- $[^{13}\text{N}]$ aminodecane).

of carrier ammonia and aluminum/mercuric chloride as the reducing agent [48]. Overall radiochemical yields around 3.5% could be obtained; however, the molar activity of the final tracer was low (c. 300 MBqmmol⁻¹) due to the presence of the carrier, which was required to prevent the formation of the secondary amine, because under no-carrier-added conditions the primary ¹³N-labeled amine competes with [¹³N]NH₃ to react with the carbonyl compound.

Alternatively, amines can also be produced by Hofmann rearrangement. For example, ¹³N-labeled β-phenethylamine was prepared by the reaction of phenylpropionyl chloride with an aqueous solution containing [¹³N]NH₃, carrier ammonia, and sodium hydroxide [49] to yield, initially, [¹³N]phenylpropionamide, which in the presence of sodium hypobromide underwent rearrangement to produce the corresponding amine (Scheme 6.1b). When the reaction was carried out in the absence of the carrier ammonia, yields dramatically decreased from 50% to 5%, since the appropriate molar ratio of sodium hypobromite/amide, which is essential for obtaining good yields, is difficult to achieve under no-carrier-added conditions. High specific activity values under no-carrier-added conditions can be obtained by using an alternative strategy based on the reduction of the corresponding ¹³N-labeled amide (Scheme 6.1c). In the first step, phenylacetyl chloride was reacted with [¹³N]NH₃ to yield the corresponding amide, which was reduced in the presence of lithium aluminum hydride to yield the corresponding amine with a good radiochemical yield (60–70%) even without the addition of a carrier [50]. The main disadvantage of this method is that the reaction needs to be conducted in LiAlH₄-compatible solvents and under an inert atmosphere.

The third reaction that has been applied to the preparation of ¹³N-labeled amines is aminolysis, by replacement of a halogen atom by ammonia. This method was applied to the synthesis of ¹³N-labeled adenosine starting from two different substrates: 6-chloro-9-β-D-ribofuranosylpurine and 6-fluoro-9-β-D-ribofuranosylpurine (Scheme 6.1d). The reaction resulted in good yields in the presence of carrier ammonia (close to 25% for the fluoro derivative under optimal conditions), while the yields were slightly lower (around 10%) in no-carrier-added conditions. In the latter, the addition of NaOH was required to maintain a basic pH, while the addition of a base was not necessary under carrier-added conditions, where the concentration of ammonia was sufficient to keep appropriate pH values.

Finally, the preparation of ¹³N-labeled alkylamines has also been achieved by amination of organoboranes [51]. Experimentally, [¹³N]NH₃, produced by proton irradiation followed by reduction with Devarda's alloy, was distilled into a solution of tetrahydrofuran (THF) containing the corresponding tri-n-alkylborane, which was prepared by reaction of the corresponding terminal alkene with borane/THF solution (Scheme 6.1e). This was followed by the addition of carrier ammonia and sodium hypochlorite. The formation of the amine, which presumably proceeds via the in situ formation of chloramine, offered good yields (40–60%) in an overall time of 25–30 minutes, and the mild reaction conditions allowed the extrapolation of the method to functionalized amines such as γ-aminobutyric acid [52]. This method was later optimized by using polymeric borane reagents, which facilitated the purification of the amines [53, 54].

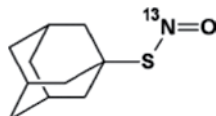
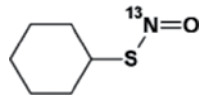
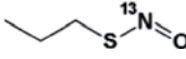
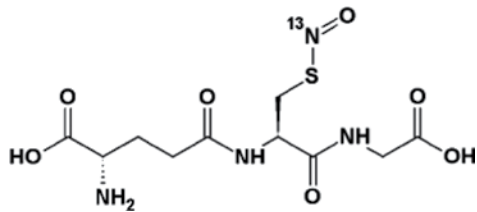
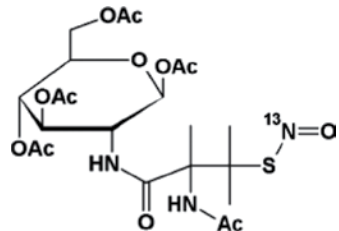
6.1.6 ^{13}N -Labeled Nitrosothiols

The synthesis of ^{13}N nitrosothiols was first reported in 1995 [44]. In this pioneering study, $^{13}\text{N}\text{NO}_3^-$ was reduced to $^{13}\text{N}\text{NO}_2^-$ using an activated cadmium column. The resulting ^{13}N -labeled nitrite was trapped in an anion exchange column, which was eluted with a solution of different thiols in acidic media (citric acid) to yield the corresponding ^{13}N -labeled thiols in close to quantitative amounts and ready for injection after filtration (in an overall production time of five minutes). The methodology was further extended, following a similar approach, to the preparation of *S*-nitrosoglutathione [55], although in this case the nitrosation reaction was conducted in a vial, and later to the preparation of a small library of both hydrophilic and hydrophobic ^{13}N -labeled nitrosothiols in a fully automated process that included reactions in solid phase and purification using high-performance liquid chromatography (HPLC) [41]. Decay-corrected radiochemical yields in the range 33.8–60.6% were reported, with molar activity values above $5\text{ GBq }\mu\text{mol}^{-1}$ and overall preparation times <13 minutes. The preparation of ^{13}N nitrosothiols was later assayed under microfluidic conditions [37]. Radiochemical purities (so-called *radiochemical conversion* in the original publication, as they were determined from chromatographic profiles) clearly exceeding those obtained in solid-phase reactions could be achieved in three out of five cases (compounds 2–4; see Table 6.2), while equivalent results were obtained for compounds 1 and 5.

6.1.7 ^{13}N -Labeled Nitrosamines

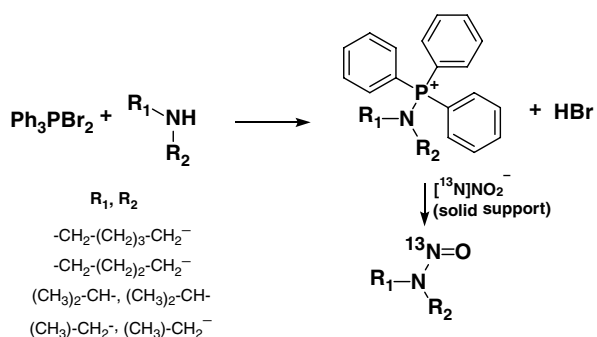
The synthesis of ^{13}N -labeled nitrosamines was also first reported in 1995 [44], following a parallel strategy to that applied to the synthesis of ^{13}N -labeled nitrosothiols. However, in this case, a solution of a secondary amine was used to elute the resin-trapped $^{13}\text{N}\text{NO}_2^-$ at pH 2–4.5. The authors reported decay-corrected radiochemical yields $>30\%$ and observed variations in the reaction rate depending on the secondary amine, although individual values for specific compounds were not provided. In an attempt to extend the methodology to the preparation of other ^{13}N -labeled nitrosamines, Gómez-Vallejo et al. reproduced the experimental conditions to perform the ^{13}N -nitrosation reaction with different secondary amines, but the formation of the labeled nitrosamines could not be observed [40]. The authors postulated that the lack of reactivity was due to the low nucleophilicity of the secondary amines, especially under acidic conditions. Good radiochemical yields could be achieved by the previous activation using $\text{Ph}_3\text{P}/\text{Br}_2$ to form in situ bromotriphenylphosphonium bromide, which slowly reacts with the secondary amine to yield triphenyl(amin-1-yl)phosphonium bromide, which can then undergo the nitrosation reaction (see Scheme 6.2). With this methodology, four different ^{13}N -labeled nitrosamines were prepared with decay-corrected radiochemical yields in the range 34–40.7% and overall production times <10 minutes, including purification by HPLC [40].

Table 6.2 Radiochemical purity for the preparation of different ^{13}N -labeled nitrosothiols by solid-phase-supported synthesis and microfluidics.

Entry	^{13}N -labeled nitrosothiol	Radiochemical purity (solid support) ^a	Radiochemical purity (microfluidics) ^b
1		72.5 ± 3.9	53.6 ± 8.8
2		60.3 ± 5.5	99.5 ± 0.2
3		74.5 ± 2.1	98.4 ± 1.1
4		48.7 ± 6.3	99.6 ± 0.3
5		66.2 ± 5.8	57.3 ± 6.5

a Source: Obtained from Gómez-Vallejo, V., Kato, K., Oliden, I. et al. [41].

b Source: Obtained from Gaja, V., Gómez-Vallejo, V., Cuadrado-Tejedor, M. et al. [37].

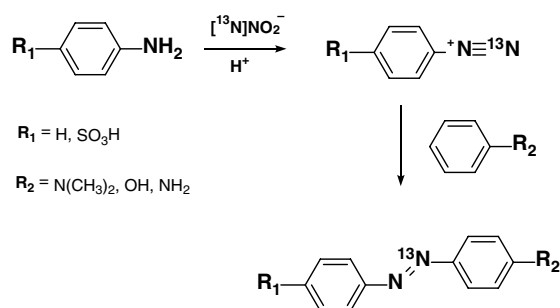


Scheme 6.2 Synthesis of *N*-[^{13}N] nitrosamines by following the combined approach (resin-supported [^{13}N] $\text{NO}_2 + \text{Ph}_3\text{P}/\text{Br}_2/\text{amine}$).

6.1.8 ^{13}N -Labeled Azo Compounds

Aromatic azo compounds can be readily synthesized by azo coupling involving an electrophilic substitution reaction of an aryl ring, which is usually substituted with electron-donating groups on an aryl diazonium cation. The latter can be easily prepared by the reaction of an aromatic amine with sodium nitrite in acidic conditions. This efficient reaction has been employed in the preparation of ^{13}N -labeled azo compounds [39]. First, $[^{13}\text{N}]\text{NO}_3^-$ produced by proton irradiation of purified water was reduced into $[^{13}\text{N}]\text{NO}_2^-$ using activated cadmium. The resulting $[^{13}\text{N}]\text{NO}_2^-$ was reacted with aromatic amines to generate the corresponding ^{13}N -labeled diazonium salts, which were finally coupled with aromatic amines and phenols to yield ^{13}N -labeled diazonium salts (Scheme 6.3).

Scheme 6.3 Synthesis of ^{13}N -labeled azo compounds.



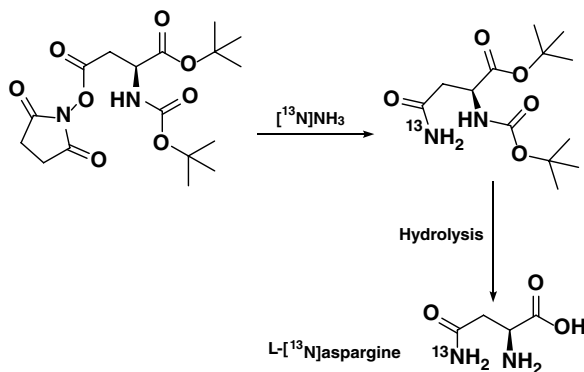
In the first study that reported this synthesis method [39], the formation of the ^{13}N -labeled diazonium salt was carried out in an anionic exchange resin-filled cartridge, while the subsequent reaction for the formation of the labeled azo compound was carried out in a vial. Chromatographic purities (so-called radiochemical conversion, or RCC, in the original publication) in the range 40.0–58.3%, overall non-decay-corrected radiochemical yields in the range 7.7–19.1%, and molar activity values close to $5 \text{ GBq } \mu\text{mol}^{-1}$ were obtained in an overall synthesis time of 13–16 minutes, including purification. The reaction was later assayed under microfluidic conditions [37], resulting in slightly improved chromatographic purities (49.3–93.9%), although in this case, radiochemical yields after purification and specific activity values were not reported.

Selected ^{13}N -labeled azo compounds were evaluated as β -amyloid markers in a mouse model of Alzheimer's disease [38]. One of the compounds assayed showed increased binding potential values in the cortex of Tg2576 animals when compared with age-matched littermates.

6.1.9 Synthesis of ^{13}N -Labeled Amino Acids: Chemical Methods

Amino acids can be readily synthesized using biocatalysis (see the next section). However, attempts to radiolabel amino acids at the *R* group have been carried out. These

methods are time-consuming and offer poor radiochemical yields, so they have barely been explored. In one of the few examples found in the literature, the synthesis of L-[¹³N]asparagine was performed by reaction of L- α -N-Boc-aspartate with [¹³N]NH₃, followed by hydrolysis (Scheme 6.4) [56]. First, the β -carboxylic group of the protected L-aspartic acid was activated with *N*-hydroxysuccinimide to yield α -N-t-Boc- α -t-Bu- β -N-hydroxysuccinimidyl aspartic ester, which was refluxed for 10 minutes with [¹³N]NH₃. After one-minute hydrolysis with 1 M HCl solution, the labeled asparagine was purified by cation exchange. Unfortunately, no yields were reported in this study. Another example is the preparation of a γ -amino acid, reported by Kabalka et al., although a completely different approach was used in this case (see Section 6.1.5) [52].



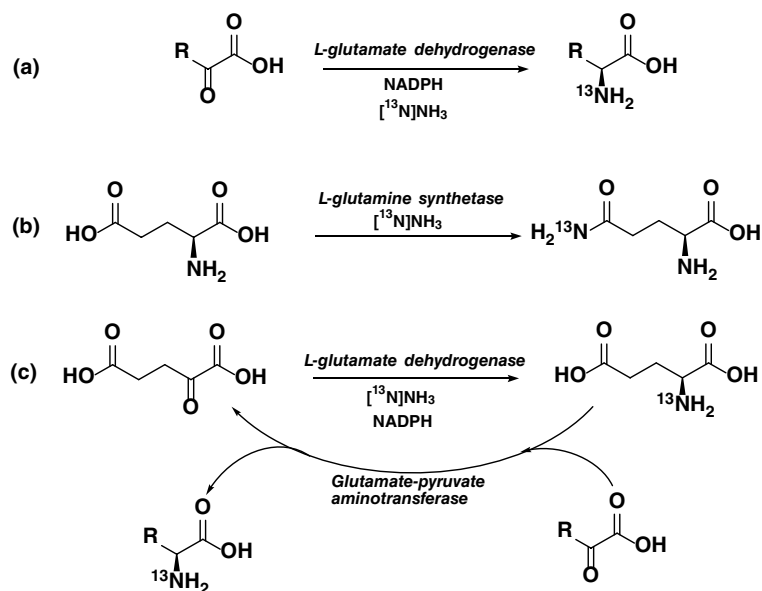
Scheme 6.4
Synthesis of L-[¹³N]asparagine by a synthetic chemistry method.

6.1.10 Biocatalysis (I): Synthesis of ¹³N-Labeled Amino Acids

Biocatalysis, although surprisingly underutilized in radiochemistry, constitutes a powerful tool for organic chemistry. The excellence of enzymes to catalyze chemical reactions lies in their exquisite chemical selectivity and high turnover numbers. Due to the tightly regulated cell metabolism, enzymes have evolved to work under rather low substrate concentrations with high efficiency. This substrate-limiting situation resembles the conditions in radiochemical reactions, where the concentration of the radioactive precursors is extremely low.

The enzymatic synthesis of amino acids labeled with nitrogen-13 is a paradigmatic example of the success of biocatalysis in radiochemistry. A battery of ¹³N-labeled amino acids have been enzymatically produced using ammonia ([¹³N]NH₃) as a radioactive precursor. Up to now, [¹³N]NH₃ has been enzymatically incorporated into amino acids through three main biosynthetic schemes (Scheme 6.5): (i) using amino acid dehydrogenases that catalyze the reductive amination of α -ketoacids using nicotinamide adenine dinucleotide (**NADH**) as redox cofactor and [¹³N]NH₃ as the amine source [57–63]; (ii) using amino acid synthetases that catalyze the insertion of [¹³N]NH₃ into the ω -carboxylic group of acidophosphate (**ATP**) [56, 58, 64]; and (iii) using a bi-enzymatic system integrated with an amino

Scheme 6.5 Main enzymatic routes to incorporate [^{13}N] NH_3 into amino acids, using (a) amino acid dehydrogenases, (b) amino acid synthetases, and (c) a bi-enzymatic system formed by an amino acid dehydrogenase and a transaminase.



acid dehydrogenase (usually glutamate dehydrogenase) that catalyzes the reductive amination of α -ketoglutarate to produce L- ^{13}N glutamate, which is concurrently used by a transaminase that transfers the radiolabeled amine group to the target α -ketoacid to form the desired L- ^{13}N -amino acid [58, 64].

These biosynthetic strategies have often been performed with soluble enzymes, which may turn into a potential source of pyrogenic proteins; the presence of such contaminants consequently requires a time-consuming purification process [65]. This problem is smartly solved by immobilizing the enzymes on solid carriers through covalent and irreversible bonds that avoid protein leaching. Several immobilized enzymes, including multi-enzyme systems, have been successfully applied to the heterogeneous synthesis of ^{13}N -labeled glutamine, glutamate, asparagine, citrulline, aspartate, alanine, serine, and glycine [57–59, 62–64, 66]. These amino acids have been obtained with different radiochemical yields, ranging from 10% for L- ^{13}N asparagine using an asparagine synthetase [67] to 70% for L- ^{13}N glutamate using a glutamate dehydrogenase [59]. The glutamate dehydrogenase is very versatile since it is able to synthesize a plethora of L- ^{13}N amino acids beyond glutamate [57, 66]. Some of these enzymatically synthesized amino acids were tested for *in vivo* studies (both in animals and in humans) to assess their bio-distribution and metabolism [59, 66]. In 1983, Lambrecht et al. [68] synthesized L- ^{13}N glutamate through a semi-automatic approach. To this end, the authors used a glutamate dehydrogenase immobilized on porous glass beads for a short time (10 minutes). As a result, this system yielded the labeled amino acid with high purity and high molar activity ($1.11 \text{ GBq } \mu\text{mol}^{-1}$). Later on, the same group expanded this methodology to manufacture β - ^{13}N aminobutyric acid (^{13}N GABA) [69]. Finally, the system was fully automatized to yield pure L- ^{13}N glutamate [61].

In the past five years, a fruitful collaboration between biotechnologists and radiochemists has materialized for the construction of more efficient biocatalytic systems to synthesize L-[¹³N]-amino acids in one pot through only one enzymatic step. Herein, L-alanine dehydrogenase from *Bacillus subtilis* catalyzed the non-carrier-added synthesis of L-[¹³N]alanine, [¹³N]glycine, and L-[¹³N]serine, starting from their corresponding α -ketoacids and using NADH as the redox cofactor and [¹³N]NH₃ as the amine source [60]. This one-pot methodology shows superior performance compared with other enzymatic methods previously published [64], since it enables the preparation of up to three different enantiomerically pure L-[¹³N]amino acids with chromatographic yields >98% in only 15 minutes. This setup enabled the manufacturing of sufficient amounts of different radiolabeled amino acids to perform *in vivo* studies in small rodents. Following this study, L-amino acid dehydrogenase was immobilized on different carriers and through different chemistries to search for the optimal immobilization protocol that maximizes both activity and stability of the final heterogeneous biocatalysts. These immobilized biocatalysts efficiently operated five separate batches with chromatographic yields of L-[¹³N]alanine >95%.

One of the limitations of this system is the necessity of an exogenous cofactor, which is usually added in large excess in the reaction mixture. In situ recycling of the cofactor is therefore mandatory to enhance the purity of the radiotracers and the efficiency of the radiochemical reaction. With a formate dehydrogenase (**FDH**) from *Candida boidinii* added to the reaction tube, NADH was in situ recycled, allowing a 50-fold decrease in the cofactor concentration without compromising radiochemical yields.

6.1.11 Biocatalysis (II): Other Applications

Besides amino acids, [¹³N]NH₃ has been incorporated into other biological molecules by means of carbamyl phosphate synthase and carbamoyl transferases. Following this scheme, Gelbard et al. co-immobilized carbamyl phosphate synthetase with either aspartate transcarbamylase or ornithine transcarbamylase to synthesize [¹³N]carbamyl phosphate, L-[ω -¹³N]citrulline, and [carbamyl-¹³N]-L-aspartate [58]. In this multi-enzymatic sequence, the carbamyl phosphate synthetase uses [¹³N]NH₃ as the ammonia source, carbamic acid as substrate, and ATP as the cofactor to synthesize radiolabeled carbamyl phosphate, whose carbamyl group is concurrently transferred to either ornithine or the aspartate using the corresponding transcarbamylase to achieve the corresponding carbamylated amino acid. These amino acid derivatives were obtained with moderate radiochemical yields of around 15%.

Biocatalysis has also been applied to the preparation of [¹³N]NO₂⁻, which, as mentioned in other sections, has been employed in the preparation of nitrosothiols [41, 44, 55], nitrosamines [40, 44], azo derivatives [38, 39], triazoles [70], and tetrazoles [43] (for the last two, see the later discussion). Typically, [¹³N]NO₂⁻ is produced from the reduction of cyclotron-generated [¹³N]NO₃⁻. This reduction can easily be performed by chemical methods using cadmium-copper activated columns, albeit with potential toxicity issues. To increase the safety of the process, da Silva et al. have recently reported an innovative

methodology to quantitatively reduce $[^{13}\text{N}]\text{NO}_3^-$ to $[^{13}\text{N}]\text{NO}_2^-$ under innocuous conditions by using a nitrate reductase immobilized on agarose activated with diethyl-aminoethyl groups [46]. With this heterogeneous biocatalyst, quantitative reduction of $[^{13}\text{N}]\text{NO}_3^-$ is achieved in four minutes, and the immobilized enzyme can be reused up to seven reaction cycles without activity loss. The potential of this heterogeneous biocatalyst was confirmed by applying enzymatically prepared $[^{13}\text{N}]\text{NO}_2^-$ to the synthesis of *S*- $[^{13}\text{N}]$ nitrosoglu-tathione in a two-step/one-pot process.

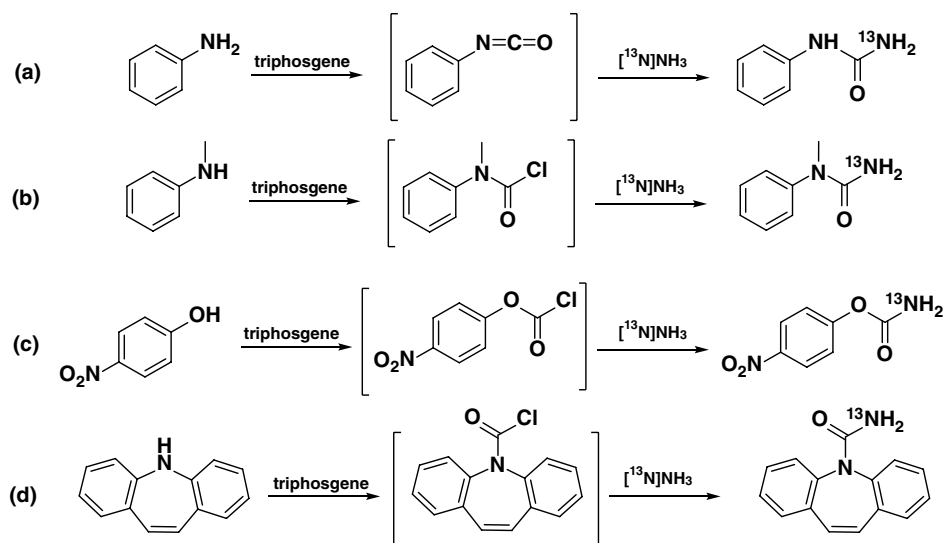
6.1.12 ^{13}N -Labeled Nanoparticles

Nanoparticles (NPs) have recently emerged as key tools in a wide range of applications. This has raised serious concerns about their potential toxicological effects after administration to or incorporation into living organisms. Incorporation of a positron emitter into the NP structure followed by *in vivo* imaging has been postulated as a suitable imaging tool for the evaluation of the biodistribution pattern and biological fate of different types of NPs. In a pioneering study, Pérez-Campaña et al. reported the radiolabeling of Al_2O_3 nanoparticles by proton irradiation to induce *in situ* the $^{16}\text{O}(p,\alpha)^{13}\text{N}$ nuclear reaction. Despite the short half-life of the radionuclide, this approach provided valuable information about the biodistribution of NPs with different sizes after intravenous administration in rodents [71].

6.1.13 Other ^{13}N -Labeled Compounds

Nitrogen-13 has sporadically been used for the preparation of radiotracers that do not fall into any of the categories mentioned previously. One of the most interesting examples is the preparation of $[^{13}\text{N}]$ cisplatin [72], which was synthesized in three steps. First, K_2PtI_4 was produced by reaction of K_2PtCl_4 with potassium iodide. This compound was reacted with aqueous $[^{13}\text{N}]\text{NH}_3$ under carrier-added conditions to form $\text{cis-Pt}([^{13}\text{N}]\text{NH}_3)_2\text{I}_2$, which, after the addition of AgNO_3 , filtration, and collection in NaCl , yielded $\text{cis-Pt}([^{13}\text{N}]\text{NH}_3)_2\text{Cl}_2$. After purification by HPLC, the radiochemical yield and molar activity were 27.1% and $11 \text{ GBq}\mu\text{mol}^{-1}$ (EOB), respectively. The radiochemical yield could be improved modestly to 31.8% by directly sparging $[^{13}\text{N}]\text{NH}_3$ into K_2PtI_4 [73]; a more substantial increase (80%) was obtained by using a solid-support synthesis method [74].

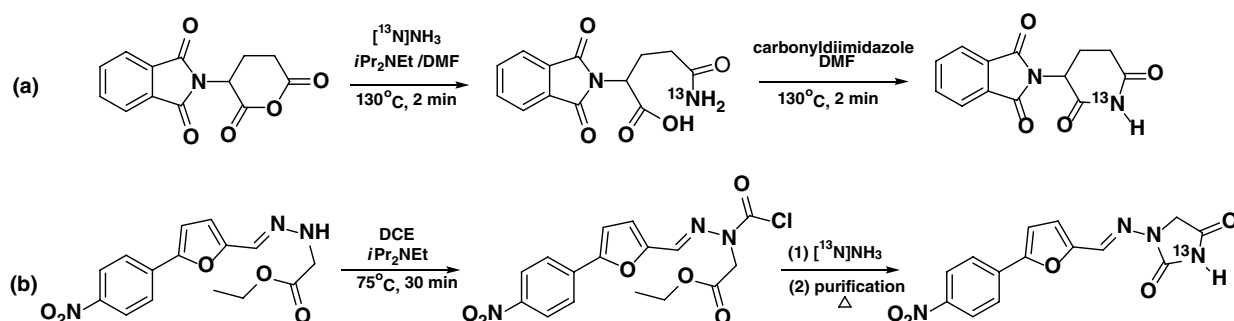
^{13}N -labeled carbamates and ureas have also been prepared using $[^{13}\text{N}]\text{NH}_3$ as the labeling reagent. $[^{13}\text{N}]$ urea could be synthesized by reaction of ammonium cyanate with $[^{13}\text{N}]\text{NH}_3$ [75]. After purification in a solid-phase extraction cartridge, decay-corrected radiochemical yields of 56% could be achieved in an overall time of 10 minutes. In this process, carrier urea was added before the purification, resulting in a very low molar activity of the final tracer (c. $2.6 \times 10^{-5} \text{ GBq}\mu\text{mol}^{-1}$). The preparation of non-carrier-added $[^{13}\text{N}]$ urea and different $[^{13}\text{N}]$ carbamate analogs using one-pot synthesis was reported many years later, using as the labeling reagent anhydrous $[^{13}\text{N}]\text{NH}_3$ [76], which was reacted with a primary amine, a secondary amine, or an alcohol previously treated with triphosgene; this reaction step yields the intermediate isocyanate (Scheme 6.6a), carbamoyl



Scheme 6.6 One-pot synthesis of [^{13}N]urea (a, b) and [^{13}N]carbamate (c) analogs using non-carrier added [^{13}N] NH_3 ; (d) synthesis of [^{13}N]carbamazepine following a parallel strategy.

chloride (Scheme 6.6b), or chloroformate (Scheme 6.6c), respectively. This strategy was also applied to the preparation of [^{13}N]carbamazepine (Scheme 6.6d) with high radiochemical yield (56–74%, decay corrected and based on [^{13}N] NH_3) and high molar activity (22–33 $\text{GBq}\mu\text{mol}^{-1}$).

The same group reported the use of anhydrous [^{13}N] NH_3 for the radiosynthesis of [^{13}N] thalidomide [77] and [^{13}N]dantrolene [78] (Scheme 6.7). For thalidomide (Scheme 6.7a), [^{13}N] NH_3 was reacted with *N*-phthaloylglutamic anhydride to produce [^{13}N] ammonolysis. Under no-carrier-added conditions, low yields were achieved in this step (20%), although a significant improvement was achieved by the addition of *i*- Pr_2NEt (76%). This step was followed by cyclization with carbonyldiimidazole to yield the desired tracer. After purification by HPLC, 570–780 MBq of pure (98%) tracer could be obtained, resulting in a decay-corrected radiochemical yield of $56\% \pm 12\%$ and molar activity values of $49 \pm 24 \text{GBq}\mu\text{mol}^{-1}$. For the preparation of [^{13}N]dantrolene (Scheme 6.7b), the authors reacted ethyl 2-[2-[5-(4-nitrophenyl)furfurylidene]hydrazino] acetate with triphosgene in



Scheme 6.7 Synthesis of [^{13}N]thalidomide (a) and [^{13}N]dantrolene (b).

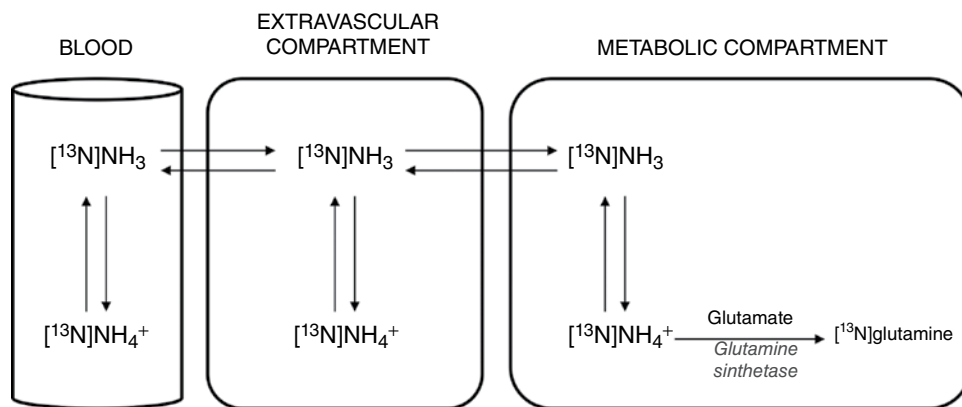
the presence of *i*-Pr₂NEt to produce the corresponding carbonyl chloride. After removal of excess COCl₂ and without further purification, the mixture was reacted with [¹³N]NH₃ to induce [¹³N]ammonolysis. In this process, controlling the initial amount of triphosgene was essential to achieve good yields under no-carrier-added conditions, as the excess of COCl₂ reacted with [¹³N]NH₃, thus preventing the desired [¹³N]ammonolysis. Final cyclization to yield [¹³N]dantrolene was achieved by purification using HPLC followed by heating of the collected fraction. The process was fully automated, resulting in non-corrected radiochemical yields close to 5% and molar activities around 30 GBq μmol⁻¹.

The preparation of ¹³N-labeled peptides is the final example in which [¹³N]NH₃ is used as the labeling agent. The only study in the literature in which the preparation of the opioid tetrapeptide H-Tyr-D-Met(O)-Phe-Gly-[¹³N]NH₂ is described is the study by Saji et al. [79]. This preparation was achieved by amidation of the activated *p*-nitrophenol ester with [¹³N]NH₃, with a decay-corrected radiochemical yield of 48% in an overall production time of 25 minutes.

[¹³N]NO₂⁻ has also been reported in other applications than those presented so far. Very recently, the preparation of ¹³N-labeled polysubstituted triazoles has been achieved via Huisgen cycloaddition following a four-step process [70]. First, cyclotron-produced [¹³N]NO₃⁻ was reduced to [¹³N]NO₂⁻ using a cadmium column. In the second step, ¹³N-labeled diazonium salts were formed by reaction of [¹³N]NO₂⁻ with aromatic amines under acidic conditions. These were reacted with NaNO₂ and hydrazine hydrate in acidic media to yield the corresponding ¹³N-labeled azides, which were finally reacted with alkynes or aldehydes in the presence of a catalyst to yield the labeled triazoles (Scheme 6.8). Full automation of the process was reported for only one triazole (compound 6 in Scheme 6.8), which could be obtained in decay-corrected radiochemical yields of 11% ± 2% and molar activity of 4.6 ± 0.2 GBq μmol⁻¹ in an overall production time of 25 minutes. In a different study, and by incorporation of the label into two different positions, either in the diazonium salt or in the hydrazine, the same authors demonstrated that the formation of the aryl azides proceeds under a stepwise mechanism via acyclic zwitterionic intermediates [42]. More recently, the formation of ¹³N-labeled tetrazoles was achieved by reaction of ¹³N-labeled azide (by reaction of [¹³N]NO₂⁻ with hydrazine hydrate in acid media) with a nitrile in the presence of a Cu-Cr-Al catalyst. Despite the confirmation of the presence of the desired labeled compound by chromatographic co-elution with the reference standard, the isolation of the compounds was not carried out in this work [43].

[¹³N]NO₂⁻ has also been used for the preparation of ¹³N-labeled nitrosocarbamates [45] and nitrosoureas [80] (Scheme 6.9). ¹³N-labeled 1,3-bis(2-chloroethyl)-1-nitrosourea ([¹³N]BCNU, Scheme 6.9) was prepared by treating a solution containing cyclotron-produced [¹³N]NO₃⁻ and carrier HNO₃ with bis(2-chloroethyl)urea in the presence of acetic acid and copper dust. The desired labeled compound was obtained by extraction with chloroform and subsequent evaporation, in decay-corrected radiochemical yields of 20–40% and overall times of 15–20 minutes. By means of a parallel procedure, its carbamate analog *N*-nitroso-*N*-chloroethyl-1-chloroethyl carbamate ([¹³N]BCNC) was also successfully prepared a few years later with radiochemical yields in the range 4–11% [81].

Figure 6.4 Schematic display of the physiological behavior of $[^{13}\text{N}]\text{NH}_3$ in the myocardium following intravenous injection. $[^{13}\text{N}]\text{NH}_3$ freely diffuses across cellular membranes and is metabolically trapped in the form of $[^{13}\text{N}]\text{glutamine}$.



^{13}N activity from the vascular space [85] and can be interpreted in terms of tissue perfusion. In this scenario, PET with ammonia has become an accurate and well-validated tool for the assessment of myocardial perfusion and blood flow in coronary artery disease (CAD) or suspected CAD and their effects on ventricular function. A description of the acquisition protocols, image interpretation, and a detailed overview of all the medical applications fall beyond the scope of this chapter. For recent reviews on these topics, the reader is referred to [16, 86, 87].

Because $[^{13}\text{N}]\text{NH}_3$ is widely used as a radiopharmaceutical tool in the clinical arena, there are precise guidelines for its quality control in both the European and US Pharmacopeia. Tests to be performed during the quality control on the injectable solution include (data from European Pharmacopeia): (i) determination of the pH, which should be between 5.5 and 8.5; (ii) presence of aluminum $<2\text{ mg l}^{-1}$, as determined by a colorimetric test; (iii) radionuclide purity, with a determined half-life in the range 9–11 minutes and $<1\%$ of gamma-emitting impurities; and (iv) radiochemical purity $>99\%$, as determined by liquid chromatography. Additionally, the solution should comply with sterility criteria and bacterial endotoxin limits like any other PET radiopharmaceutical. Major radiochemical impurities are usually $[^{13}\text{N}]\text{NO}_2^-$ and $[^{13}\text{N}]\text{NO}_3^-$ produced during the irradiation, $[^{18}\text{F}]\text{F}^-$ produced during irradiation via the $^{18}\text{O}(p,n)^{18}\text{F}$ nuclear reaction (note that the natural abundance of ^{18}O is close to 0.2%), and $[^{15}\text{O}]\text{H}_2\text{O}$ formed due to the $^{16}\text{O}(p,pn)^{15}\text{O}$ nuclear reaction. The anionic species can easily be eliminated by trapping $[^{13}\text{N}]\text{NH}_4^+$ in a cation exchange resin, while the ^{15}O -labeled water is eliminated by simple radioactive decay (half-life = 122.2 seconds).

6.2 OXYGEN-15

Oxygen-15 is an unstable isotope of oxygen. It decays through the emission of a positron and has a half-life of 2.07 minutes (Table 6.3). It was discovered in 1934 when Livingston and McMillan irradiated nitrogen gas with deuterons [88]. The resulting gas mixture was found to be radioactive, with an estimated efficiency of activation of one nitrogen atom

Isotope	Half-life	E_{\max} (MeV) ^a	E_{mean} (MeV) ^b	R_{\max} (mm) ^c
¹⁵ O	2.07 min	1.732	0.735	8.4

Table 6.3 Main properties of ¹⁵O.

- a Maximum energy of the emitted positrons.
 b Mean energy of the emitted positrons.
 c Maximum range in water.

per million incident deuterons. The identity of the radioactive nuclide was confirmed by mixing the irradiated gas with O₂ and H₂, passing the mixture over heated platinized asbestos, and finally leading it through a CaCl₂ drying tube. The activity was trapped entirely in the drying tube, thereby indirectly confirming the formation of radioactive isotope oxygen-15.

The high abundance of oxygen in molecular species involved in biological processes presents an opportunity for radioactive oxygen-15 to be used as a radiomarker of biologically active molecules without changing their original structure. A possible role of ¹⁵O as a radiotracer was first recognized in the middle of the twentieth century; however, its short half-life and low availability at the time led early investigators to divert their research interests to other radiotracers [89, 90]. It was not until Ter-Pogossian and Powers, of Washington University, St. Louis, used [¹⁵O]O₂ to assess the distribution of oxygen in murine experimental neoplasms that the idea of ¹⁵O as a radiotracer was revived [91]. This encouraged the development of new strategies for the faster and more efficient incorporation of ¹⁵O into new ¹⁵O-labeled radiotracers and gave a breath of fresh air to the field, opening new avenues for the exploitation of ¹⁵O in biomedical research.

6.2.1 Production of Oxygen-15

Storage or transportation of oxygen-15 is unfeasible due to its short half-life ($t_{1/2} = 2.07$ minutes); hence, the production of ¹⁵O-labeled species is limited to fast nuclear and radiochemical reactions and the performance of the reactions on site.

Oxygen-15 is produced in low-energy proton and deuteron accelerators. By carefully selecting the target material and the type of irradiation, one can produce the radionuclide in different chemical forms (Table 6.4).

Target material	Nuclear reaction	In-target product
N ₂	¹⁴ N(<i>d,n</i>) ¹⁵ O	[¹⁵ O]O ₂ + [¹⁵ O]N ₂ O + [¹⁵ O]NO ₂ + [¹⁵ O]O ₃
N ₂ /O ₂	¹⁴ N(<i>d,n</i>) ¹⁵ O	[¹⁵ O]O ₂
N ₂ /CO ₂	¹⁴ N(<i>d,n</i>) ¹⁵ O	[¹⁵ O]CO ₂
N ₂ /H ₂	¹⁴ N(<i>d,n</i>) ¹⁵ O	[¹⁵ O]H ₂ O
N ₂ /CH ₄	¹⁴ N(<i>d,n</i>) ¹⁵ O	[¹⁵ O]CH ₃ OH + [¹⁵ O]C ₂ H ₅ OH + [¹⁵ O]H ₂ O
O ₂	¹⁶ O(<i>p,pn</i>) ¹⁵ O	[¹⁵ O]O ₂
H ₂ O	¹⁶ O(<i>p,pn</i>) ¹⁵ O	[¹⁵ O]H ₂ O
[¹⁵ N]N ₂ /H ₂	¹⁵ N(<i>p,n</i>) ¹⁵ O	[¹⁵ O]H ₂ O

Table 6.4 Nuclear reactions used for the production of ¹⁵O.

Three main strategies are used: irradiation of ^{15}N or ^{16}O -bearing targets with protons and irradiation of ^{14}N -bearing targets with deuterons. This, in turn, leads to the production of $[^{15}\text{O}]\text{N}_2\text{O}$, $[^{15}\text{O}]\text{O}_2$, $[^{15}\text{O}]\text{CO}_2$, $[^{15}\text{O}]\text{H}_2\text{O}$, $[^{15}\text{O}]\text{alcohols}$, or $[^{15}\text{O}]\text{O}_3$, depending on the strategy used. On the downside, undesired chemical and radiochemical impurities form in the target during the irradiation. The full spectrum of the crude ^{15}O -labeled mixture has rarely been fully characterized, but evidence suggests that careful control of the irradiation energy and the specific chemical composition of the initial target improve the purity of the ^{15}O -labeled product. Nevertheless, impurities need to be removed post-irradiation to produce ^{15}O -labeled species that can be injected into patients or used as reagents in further radiochemical reactions.

6.2.2 Oxygen-15-Labeled Species

6.2.2.1 Early Beginnings: $[^{15}\text{O}]\text{N}_2\text{O}$

Early reports on the production of ^{15}O -bearing molecules date from 1958 [92]. Irradiation of an air target with deuterons initiated the $^{14}\text{N}(d,n)^{15}\text{O}$ reaction to produce $[^{15}\text{O}]\text{N}_2\text{O}$. A wide energy range of the deuterons used for bombardment caused the production of radiology-based chemical and radiochemical impurities, such as $[^{15}\text{O}]\text{O}_2$, $[^{15}\text{O}]\text{NO}_2$, and $[^{15}\text{O}]\text{O}_3$. The development of low-energy deuteron accelerators (3–4 MeV) enabled the production of 99.95% pure $[^{15}\text{O}]\text{N}_2\text{O}$ gas upon irradiation of N_2 target gas at a low (0.5 μA) beam, and purification through a zeolite column [93]. Regardless of these improvements, $[^{15}\text{O}]\text{N}_2\text{O}$ has no reported applicability in biomedical research and is mostly considered an unwanted side product of in-target radiolysis in the production of $[^{15}\text{O}]\text{O}_2$ [94, 95].

6.2.2.2 $[^{15}\text{O}]\text{O}_2$

One of the most widely used nuclear reactions for the production of ^{15}O radioisotopes has been the irradiation of O_2/N_2 (0.1–4% of O_2) mixtures with deuterons via the $^{14}\text{N}(d,n)^{15}\text{O}$ reaction to produce $[^{15}\text{O}]\text{O}_2$ [96]. The lower content of oxygen in the target, compared with the air-filled target used by Dyson et al. [92], resulted in the formation of fewer impurities. Primarily $[^{15}\text{O}]\text{O}_2$ was formed in the presence of trace amounts of $[^{15}\text{O}]\text{N}_2\text{O}$. Beam intensity clearly determined the selectivity of irradiation, producing 96.7% or 99.3% pure $[^{15}\text{O}]\text{O}_2$, the rest being $[^{15}\text{O}]\text{N}_2\text{O}$, at 5 or 50 μA beam, respectively.

With the development and widespread distribution of proton-only cyclotron accelerators, alternative methods for the production of $[^{15}\text{O}]\text{O}_2$ using proton irradiation have been explored by exploiting the $^{16}\text{O}(p,pn)^{15}\text{O}$ and $^{15}\text{N}(p,n)^{15}\text{O}$ reactions [97].

The use of $[^{15}\text{O}]\text{O}_2$ is not limited to oxygen biodistribution studies; $[^{15}\text{O}]\text{O}_2$ has also been used as a radioactive precursor for the synthesis of $[^{15}\text{O}]\text{CO}_2$ [98], $[^{15}\text{O}]\text{H}_2\text{O}$ [99], $[^{15}\text{O}]\text{CO}$ [100, 101], and $[^{15}\text{O}]\text{butanol}$ [102–105].

6.2.2.3 Production of $[^{15}\text{O}]\text{CO}_2$ and $[^{15}\text{O}]\text{CO}$

There are two main strategies to produce $[^{15}\text{O}]\text{CO}_2$: (i) in-target production of $[^{15}\text{O}]\text{CO}_2$, which entails the irradiation of N_2 gas mixtures containing 0.25–5% of CO_2 with

deuterons [95]; and (ii) post-irradiation treatment of [^{15}O]O₂ with activated charcoal at 600 °C [98]. The choice of the methodology will depend mainly on the type of cyclotron available. However, one might consider different limitations of the two strategies. The post-irradiation treatment involves an additional step, diminishing the yield of production due to the fast radioactive decay of ^{15}O . On the other hand, in-target production instigates the $^{12}\text{C}(d,n)^{13}\text{N}$ nuclear reaction, producing [^{13}N]N₂, which is sometimes impossible to remove. Fine-tuning of the reaction conditions by adding low amounts of CO₂ (0.25%) in the N₂ gas target and increasing the strength of irradiation from 5 to 40 μA resulted in 98% and 99.5% purity, respectively, but the problem of [^{13}N]N₂ removal remained [95]. As an alternative for the two previously mentioned approaches, a method based on the metal-oxide-catalyzed isotopic exchange between [^{15}O]O₂ and CO₂ has been described [106].

Unlike that of [^{15}O]CO₂, the production of [^{15}O]CO requires careful control of the amount of oxygen. The first report on the production of [^{15}O]CO described the irradiation of oxygen-free nitrogen in a recirculating target system with an active carbon tube heated to 900 °C [96]. While the major product observed was indeed [^{15}O]CO, the product was most likely predominantly a result of radiolysis-driven exchange reactions between [^{15}O]O₂ and CO in the target. Attempts to optimize in-target conversion involved an introduction of a source of hot carbon within the target volume [107] and post-irradiation modification of [^{15}O]O₂ with carbon at 900–950 °C [100, 101]. In both cases, the control of the O₂ carrier in the target is crucial for reducing the final content of non-radiolabeled CO. This is especially important when [^{15}O]CO is considered for biological applications because of its potential toxicity.

6.2.2.4 Production of [^{15}O]H₂O

[^{15}O]Water is by far the most used ^{15}O -labeled radiotracer in biological applications. The nontoxic nature of water and its large abundance in biological systems are exploited in preclinical and clinical studies to measure blood flow throughout the living organism. Similarly to ^{15}O -labeled species described earlier, [^{15}O]H₂O can also be produced by irradiation with deuterons ($^{14}\text{N}(d,n)^{15}\text{O}$) or protons ($^{16}\text{O}(p,pn)^{15}\text{O}$).

The first attempts to produce [^{15}O]H₂O were based on palladium- or platinum-catalyzed reactions of [^{15}O]O₂ with H₂ at elevated temperatures [95, 101, 108]. The latest modification uses an in-flow system, in which [^{15}O]O₂ is first produced and transferred to the hot cell, where it is mixed with H₂ and circulated through a palladium catalyst-filled oven to produce [^{15}O]H₂O. The product is trapped in a saline solution and is then ready for use in biological studies [99]. Other early reports describe the isotopic exchange of [^{15}O]CO₂ with water [109] and the irradiation of 5% H₂ in an N₂ mixture with deuterons, which in turn predominantly produce [^{15}O]H₂O [110–112].

More recently, the $^{15}\text{N}(p,n)^{15}\text{O}$ nuclear reaction for the in-target production of [^{15}O]H₂O from 5% H₂ in [^{15}N]N₂ has been exploited [97]. In this procedure, the irradiated mixture is passed through a cold trap at –40 °C to capture [^{15}O]H₂O, followed by the recovery of the unreacted [^{15}N]N₂ gas. For the extraction of [^{15}O]H₂O, the cold trap is heated and flushed with an inert gas, after which the activity is transferred to the radiochemistry lab.

6.2.2.5 Production of [¹⁵O]O₃

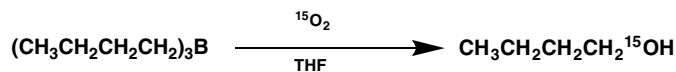
Like [¹⁵O]N₂O, [¹⁵O]O₃ has mainly been described as an impurity produced during the production of ¹⁵O-labeled species in several ¹⁵O-production systems [113]. The potential benefit of [¹⁵O]O₃ in the investigation of environmental exposure to ozone has encouraged the development of a heterogeneous target-based method that produces high-specific-activity [¹⁵O]ozone [114]. In this study, the authors describe the production of [¹⁵O]O₃ in the reaction between a matrix of silica micro-fibers irradiated with high energy (22–27 MeV) protons, and a low concentration of oxygen (0.5% O₂) in Ne. The product is finally purified by cryopurification.

6.2.3 Radiochemistry of Oxygen-15

Most of the oxygen-15 radiochemistry involves in-target production of ¹⁵O-labeled species or post-irradiation treatment of primary in-target produced products. As mentioned earlier, its short half-life limits ¹⁵O to extremely fast modifications. This makes the involvement of the radionuclide in radiochemical conversions and its incorporation into organic molecules, to produce highly specific and high-yielding products, extremely difficult. Nevertheless, a few attempts of such reactions have been described in the literature.

6.2.3.1 Synthesis of [¹⁵O]Butanol

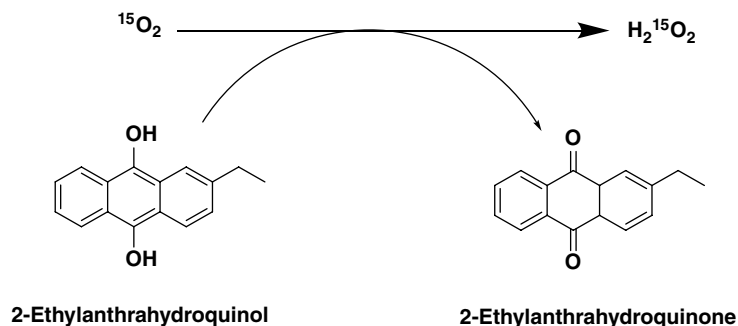
The reaction of [¹⁵O]O₂ with tri-*n*-butylborane in THF to synthesize [¹⁵O]butanol was first described by Kabalka et al. [105] (Scheme 6.10). Further improvements involved the use of solid-support-immobilized tri-*n*-butylborane on alumina Sep-Pak cartridges, which enabled the automation of multi-dose preparation systems [103, 104, 115].



Scheme 6.10 Synthesis of ¹⁵O-labeled butanol.

6.2.3.2 Synthesis of [¹⁵O]H₂O₂

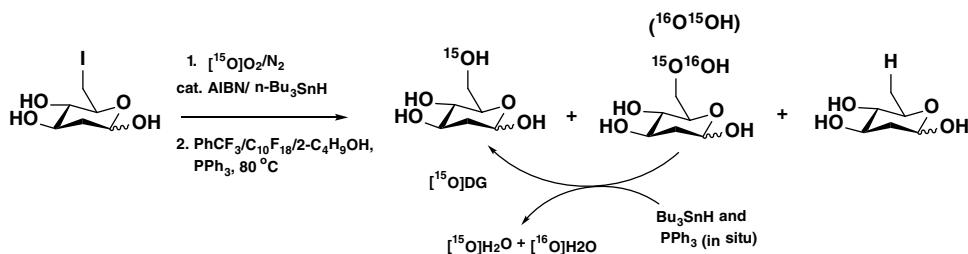
Another successful example of the use of solid-support synthesis in radiochemical reactions is the conversion of [¹⁵O]O₂ into [¹⁵O]H₂O₂ [116]. The method is based on a previously reported redox-reaction-based preparation of [¹⁸O]H₂O₂ and involves autoxidation of 2-ethylantrahydroquinol with [¹⁵O]O₂, resulting in the formation of 2-ethylantrahydroquinone and consequently [¹⁵O]H₂O₂ (Scheme 6.11). When a C-18 Sep-Pak cartridge is conditioned with a solution of 2-ethylantrahydroquinol, the reaction can be performed by simply passing [¹⁵O]O₂ through the cartridge and finally eluting the [¹⁵O]H₂O₂ product with a saline solution.



Scheme 6.11 Synthesis of ^{15}O -labeled hydrogen peroxide.

6.2.3.3 Synthesis of [^{15}O]DG

A few years ago, the single-step synthesis of 6- ^{15}O -2-deoxy-D-glucose (^{15}O]DG) from 2,6-dideoxy-6-iodo-D-glucose was reported (Scheme 6.12) [117]. To overcome the challenges related to the short half-life of oxygen-15, a specially adapted hot-air-jacketed reaction vessel, equipped with a sintered glass bottom through which ^{15}O -oxygen gas was introduced as fine bubbles, was implemented. Additionally, a non-protected iodinated sugar precursor was used to reduce the reaction time from several hours to a few minutes and make the reaction possible even under mild conditions. The iodo-activated precursor was first reacted with cold O_2 in the presence of perfluorodecaline, azobisisobutyronitrile (**AIBN**), and tributyltin hydride, which initialized the formation of DG, hydroperoxide, and 2,6-dideoxy-D-glucose, before introducing radioactive ^{15}O gas (Scheme 6.12). The addition of triphenylphosphine in trifluorotoulene instantaneously converted any remaining hydroperoxide to obtain ^{15}O]DG. The crude was purified through a series of Sep-Pak cartridges to obtain the final solution containing ^{15}O]DG in around 70% radiochemical purity, while ^{15}O]water accounted for the rest of the radioactivity. An efficient and short production (only eight minutes from the start of the bombardment to the injection) allowed the authors to demonstrate the applicability of ^{15}O]DG in PET imaging. The new strategy expanded the toolbox of ^{15}O -radiochemistry and created a possibility for metabolite studies with ^{15}O]DG and eventually the expansion of this method to the production of a variety of ^{15}O -labeled alcohols.



Scheme 6.12 Synthesis of 6- ^{15}O -2-deoxy-D-glucose.

6.2.4 Clinical Applications of ^{15}O -Labeled Tracers

The only ^{15}O -labeled tracer currently included in the European Pharmacopeia is $[^{15}\text{O}]\text{H}_2\text{O}$. Tests to be performed during the quality control of the injectable solution include the determination of (i) the pH, which should be between 5.5 and 8.5; (ii) the radionuclidic purity, with a determined half-life in the range 1.9–2.2 minutes and <1% of gamma-emitting impurities; (iii) the chemical purity, with a limit for main impurities, ammonia, and nitrate of 10 mg l^{-1} each; and (iv) the radiochemical purity, which should be >99%, as determined by liquid chromatography. For this assay, the injected radioactivity is circulated through the radioactivity detector before and after being eluted through a 250-mm aminopropylsilylated silica column with a phosphate buffer (pH = 3) at 1 ml min^{-1} . The area under the second radioactive peak (i.e. the amount of radioactivity exiting from the column) should be at least 99% of the amount of radioactivity before it entered the column. Additionally, the solution should comply with sterility criteria and bacterial endotoxin limits like any other PET radiopharmaceutical.

6.2.5 Administration of Oxygen-15-Labeled Tracers

In biomedical research, the success of administration is as important as the quality of the radiotracer; hence, research focuses on the development of reliable and safe administration methods. The choice of administration method will depend on the aggregate state of the radiotracer.

For gaseous ^{15}O -labeled tracers, inhalation of a regulated mixture of radiotracer in air is performed continuously [118–121] or as a bolus [119] via a medically accepted breathing system. When the activity is administered continuously, a steady-state delivery system capable of regulating the target beam current, target gas flow, and air dilution flow to maintain a constant delivery of radiotracer is used. The radioactivity can be administered through a facemask, nasal tubes, or a ventilator.

In bolus administration of gaseous products, a flexible vessel is filled with a dose of radiotracer and administered via a mouthpiece and a one-way non-rebreathing valve or a ventilator. In this case, the activity is prepared before inhalation and has a much higher concentration than the one used in the steady-state method.

In contrast, $[^{15}\text{O}]\text{water}$ is injected intravenously as a bolus solution in saline or as a steady-state infusion. The first biological studies with $[^{15}\text{O}]\text{H}_2\text{O}$ required the manual preparation of doses [95, 122, 123], posing a higher exposure risk for the personnel involved in the experiments. Together with the rise in functional brain PET studies that demanded multiple-dose deliveries per subject, this encouraged the development of automated systems for $[^{15}\text{O}]\text{H}_2\text{O}$ delivery [124–126], which made the experiments safer and more reliable.

6.3 FUTURE PERSPECTIVES

Only a few groups in the world are working on the development of new strategies for the preparation of ^{13}N -labeled compounds, and probably nobody dedicates efforts to the

development of ^{15}O -labeling strategies. Both radionuclides have short half-lives, resulting in three main inconveniences: (i) their use is restricted to organizations with access to a cyclotron; (ii) rapid and efficient methods must be applied to the preparation of radiotracers to minimize radioactivity loss; and (iii) only fast processes can be investigated, because the time window for image acquisition is short.

That said, the stable isotopes of nitrogen and oxygen are present in the majority of biologically active molecules. Hence, a wide range of molecules can potentially be labeled with ^{13}N or ^{15}O . Additionally, the short half-life enables repeated experiments within the same individual. These facts, combined with the development of smaller/cheaper cyclotrons, may facilitate the incorporation of these radionuclides into the toolbox of PET chemists. New strategies would help tackle the preparation of multi-radioisotope-labeled tracers as the driving force for the investigation of biological processes, providing crucial information on metabolism, mechanisms of diseases, and more.

ACKNOWLEDGMENTS

The authors thank the Spanish Ministry of Science and Competitiveness for financial support (Project CTQ2017-87637-R).

REFERENCES

1. Joliot, F. and Curie, I. (1934). Artificial production of a new kind of radio-element. *Nature* 133: 201–202.
2. Cockcroft, J.D., Gilbert, C.W., and Walton, E.T.S. (1934). Production of induced radioactivity by high velocity protons. *Nature* 133: 328.
3. Wolk, C.P., Austin, S.M., Bortins, J., and Galonsky, A. (1974). Autoradiographic localization of ^{13}N after fixation of ^{13}N -labeled nitrogen gas by a heterocyst-forming blue-green alga. *J. Cell Biol.* 61: 440–453.
4. Kasel, M.C.K., Schueller, M.J., and Ferrieri, R.A. (2010). Optimizing $[^{13}\text{N}]\text{N}_2$ radiochemistry for nitrogen-fixation in root nodules of legumes. *J. Labelled Compd. Radiopharm.* 53: 592–597.
5. Wellman, T.J., Winkler, T., Costa, E.L.V. et al. (2010). Measurement of regional specific lung volume change using respiratory-gated PET of inhaled ^{13}N -nitrogen. *J. Nucl. Med.* 51: 646–653.
6. Richard, J.C., Janier, M., Lavenne, F. et al. (2005). Quantitative assessment of regional alveolar ventilation and gas volume using ^{13}N - N_2 washout and PET. *J. Nucl. Med.* 46: 1375–1383.
7. Suzuki, T. and Iio, M. (1991). Quantitative regional alveolar volume and specific ventilation (V/VA) in healthy subjects measured with positron emission tomography. *Respir. Circu.* 39: 445–448.
8. Le Bars, D. (2001). A convenient production of $[^{13}\text{N}]$ nitrogen for ventilation studies using a nitrogen gas target for ^{11}C production. *J. Labelled Compd. Radiopharm.* 44: 1–5.

9. Ruben, S., Hassid, W.Z., and Kamen, M.D. (1940). Radioactive nitrogen in the study of N_2 fixation by non-leguminous plants. *Science* 91: 578–579.
10. Nicholas, D.J.D., Silvester, D.J., and Fowler, J.F. (1961). Use of radioactive nitrogen in studying nitrogen fixation in bacterial cells and their extracts. *Nature* 189: 634–636.
11. Parks, N.J. and Krohn, K.A. (1978). The synthesis of ^{13}N labeled ammonia, dinitrogen, nitrite, and nitrate using a single cyclotron target system. *Int. J. Appl. Radiat. Isot.* 29: 754–757.
12. Ferrieri, R.A., Schlyer, D.J., Wieland, B.W., and Wolf, A.P. (1983). On-line production of ^{13}N -nitrogen gas from a solid enriched ^{13}C -target and its application to ^{13}N -ammonia synthesis using microwave radiation. *Int. J. Appl. Radiat. Isot.* 34: 897–900.
13. Vaalburg, W., Steenhoek, A., Paans, A.M.J. et al. (1981). Production of ^{13}N -labelled molecular nitrogen for pulmonary function studies. *J. Labelled Compd. Radiopharm.* 18: 303–308.
14. Lindner, L., Helmer, J., and Brinkman, G.A. (1979). Water “loop”-target for the in-cyclotron production of ^{13}N by the reaction $^{16}O(p,\alpha)^{13}N$. *Int. J. Appl. Radiat. Isot.* 30: 506–507.
15. Plein, S. and Sivananthan, M. (2001). The role of positron emission tomography in cardiology. *Radiography* 7: 11–20.
16. Slomka, P., Berman, D.S., Alexanderson, E., and Germano, G. (2014). The role of PET quantification in cardiovascular imaging. *Clin. Transl. Imaging* 2: 343–358.
17. Martín, A., San Sebastián, E., Gómez-Vallejo, V., and Llop, J. (2012). Positron emission tomography with [^{13}N]ammonia evidences long-term cerebral hyperperfusion after 2h-transient focal ischemia. *Neuroscience* 213: 47–53.
18. Vaquero, J.J., Gao, D.W., García-Villaba, C. et al. (2012). Approach to assessing myocardial perfusion in rats using static [^{13}N]ammonia images and a small-animal PET. *Mol. Imaging Biol.* 14: 541–545.
19. Cruz, N.F., Dienel, G.A., Patrick, P.A., and Cooper, A.J.L. (2017). Organ distribution of ^{13}N following intravenous injection of [^{13}N]ammonia into portacaval-shunted rats. *Neurochem. Res.* 42: 1683–1696.
20. Hunter, W.W. and Monahan, W.G. (1971). ^{13}N -ammonia: a new physiologic radiotracer for molecular medicine. *J. Nucl. Med.* 12: 368–368.
21. Welch, M.J. and Litton, J.F. (1971). The fate of nitrogen-13 formed by the $^{12}C(d,n)^{13}N$ reaction in inorganic carbides. *J. Am. Chem. Soc.* 93: 3385–3388.
22. Bem, P., Bittmann, L., Burjan, V. et al. (2007). The activation of Cu and Al by deuterons at energies up to 20 MeV. In: *International Conference on Nuclear Data for Science and Technology*, 1003–1006.
23. Monahan, W.G., Tilbury, R.S., and Laughlin, J.S. (1972). Uptake of ^{13}N -labeled ammonia. *J. Nucl. Med.* 13: 274–277.
24. Krizek, H., Lembares, N., Dinwoodie, R. et al. (1973). Production of Radiochemically pure $^{13}NH_3$ for biomedical studies using the $^{16}O(p,\alpha)^{13}N$ reaction. *J. Nucl. Med.* 14: 629–630.
25. Vaalburg, W., Kamphuis, J.A.A., Beerling-van der Molen, H.D. et al. (1975). An improved method for the cyclotron production of ^{13}N -labelled ammonia. *Int. J. Appl. Radiat. Isot.* 26: 316–318.

26. Ido, T. and Iwata, R. (1973). Fully automated synthesis of $^{13}\text{NH}_3$. *J. Labelled Compd. Radiopharm.* 18: 244–246.
27. Tilbury, R.S. and Dahl, J.R. (1979). ^{13}N species formed by proton irradiation of water. *Radiat. Res.* 79: 22–33.
28. Firouzbakht, M.L., Schlyer, D.J., Wolf, A.P., and Fowler, J.S. (1999). Mechanism of nitrogen-13-labeled ammonia formation in a cryogenic water target. *Nucl. Med. Biol.* 26: 437–441.
29. Wieland, B., Bida, G., Padgett, H. et al. (1991). In-target production of [^{13}N]ammonia via proton irradiation of dilute aqueous ethanol and acetic acid mixtures. *Appl. Radiat. Isot.* 42: 1095–1098.
30. Berridge, M.S. and Landmeier, B.J. (1993). In-target production of [^{13}N]ammonia: target design, products, and operating parameters. *Appl. Radiat. Isot.* 44: 1433–1441.
31. Mulholland, G.K., Kilbourn, M.R., and Moskwa, J.J. (1990). Direct simultaneous production of [^{15}O]water and [^{13}N]ammonia or [^{18}F]fluoride ion by 26 MeV proton irradiation of a double chamber water target. *Int. J. Radiat. Appl. Instrum. Part A* 41: 1193–1199.
32. Korsakov, M.V., Krasikova, R.N., and Fedorova, O.S. (1996). Production of high yield [^{13}N]ammonia by proton irradiation from pressurized aqueous solutions. *J. Radioanal. Nucl. Chem.* 204: 231–239.
33. Krasikova, R.N., Fedorova, O.S., Korsakov, M.V. et al. (1999). Improved [^{13}N]ammonia yield from the proton irradiation of water using methane gas. *Appl. Radiat. Isot.* 51: 395–401.
34. Wieneke, J. and Nebeling, B. (1990). Improved method for ^{13}N -application in short-term studies on NO_3^- fluxes in barley and squash plants. *Z. Pflanzenernähr. Bodenkd.* 153: 117–123.
35. Wood, E.D., Armstrong, F.A.J., and Richards, F.A. (1967). Determination of nitrate in sea water by cadmium-copper reduction to nitrite. *J. Mar. Biol. Assoc. U. K.* 47: 23–31.
36. McElfresh, M.W., Meeks, J.C., and Parks, N.J. (1979). The synthesis of ^{13}N -labelled nitrite of high specific activity and purity. *J. Radioanal. Chem.* 53: 337–344.
37. Gaja, V., Gómez-Vallejo, V., Cuadrado-Tejedor, M. et al. (2012). Synthesis of ^{13}N -labelled radiotracers by using microfluidic technology. *J. Labelled Compd. Radiopharm.* 55: 332–338.
38. Gaja, V., Gomez-Vallejo, V., Puigivila, M. et al. (2014). Synthesis and evaluation of ^{13}N -labelled Azo compounds for beta-amyloid imaging in mice. *Mol. Imaging Biol.* 16: 538–549.
39. Gomez-Vallejo, V., Borrell, J.I., and Llop, J. (2010). A convenient synthesis of ^{13}N -labelled azo compounds: a new route for the preparation of amyloid imaging PET probes. *Eur. J. Med. Chem.* 45: 5318–5323.
40. Gomez-Vallejo, V., Kato, K., Hanyu, M. et al. (2009). Efficient system for the preparation of [^{13}N]labeled nitrosamines. *Bioorg. Med. Chem. Lett.* 19: 1913–1915.
41. Gómez-Vallejo, V., Kato, K., Oliden, I. et al. (2010). Fully automated synthesis of ^{13}N -labeled nitrosothiols. *Tetrahedron Lett.* 51: 2990–2993.

42. Joshi, S.M., de Cozar, A., Gomez-Vallejo, V. et al. (2015). Synthesis of radiolabelled aryl azides from diazonium salts: experimental and computational results permit the identification of the preferred mechanism. *Chem. Commun.* 51: 8954–8957.
43. Joshi, S.M., Mane, R.B., Pulagam, K.R. et al. (2017). The microwave-assisted synthesis of 5-substituted 1:H-tetrazoles via [3+2] cycloaddition over a heterogeneous Cu-based catalyst: application to the preparation of ¹³N-labelled tetrazoles. *New J. Chem.* 41: 8084–8091.
44. Vavrek, M.T. and Mulholland, G.K. (1995). Simple general synthesis of NCA [¹³N]nitrosothiols and [¹³N]nitrosamines. *J. Labelled Compd. Radiopharm.* 37: 118.
45. Pettit, W.A., Tilbury, R.S., Digenis, G.A., and Mortara, R.H. (1977). A convenient synthesis of ¹³N-BCNU. *J. Labelled Compd. Radiopharm.* 13: 119–122.
46. da Silva, E.S., Gómez-Vallejo, V., Llop, J., and López-Gallego, F. (2015). Efficient nitrogen-13 radiochemistry catalyzed by a highly stable immobilized biocatalyst. *Catal. Sci. Technol.* 5: 2705–2713.
47. Nickles, R.J., Gatley, S.J., Hichwa, R.D. et al. (1978). The synthesis of ¹³N-labelled nitrous oxide. *Int. J. Appl. Radiat. Isot.* 29: 225–227.
48. Finn, R.D., Christman, D.R., and Wolf, A.P. (1981). A rapid synthesis of nitrogen-13 labelled amphetamine. *J. Labelled Compd. Radiopharm.* 18: 909–913.
49. Tominaga, T., Inoue, O., Irie, T. et al. (1985). Preparation of ¹³N-β-phenethylamine. *Int. J. Appl. Radiat. Isot.* 36: 555–560.
50. Tominaga, T., Inoue, O., Suzuki, K. et al. (1986). Synthesis of ¹³N-labelled amines by reduction of ¹³N-labelled amides. *Appl. Radiat. Isot.* 37: 1209–1212.
51. Kothari, P.J., Finn, R.D., Kabalka, G.W. et al. (1986). Synthesis of nitrogen-13 labeled alkylamines via amination of organoboranes. *Int. J. Radiat. Appl. Instrum.* 37: 469–470.
52. Kabalka, G.W., Wang, Z., Green, J.F., and Goodman, M.M. (1992). Synthesis of isomerically pure nitrogen-13 labeled gamma-aminobutyric acid and putrescine. *Int. J. Radiat. Appl. Instrum.* 43: 389–391.
53. Kabalka, G.W., Goodman, M.M., Green, J.F. et al. (1993). Synthesis of nitrogen-13 labeled amines using organoborane polymers. *J. Labelled Compd. Radiopharm.* 32: 165.
54. Kabalka, G.W., Green, J.F., Goodman, M.M. et al. (1991). Synthesis of organoborane polymers for use in the preparation of nitrogen-13 labeled amines. *J. Labelled Compd. Radiopharm.* 30: 409–410.
55. Llop, J., Gomez-Vallejo, V., Bosque, M. et al. (2009). Synthesis of S-[¹³N]nitrosoglutathione (¹³N-GSNO) as a new potential PET imaging agent. *Appl. Radiat. Isot.* 67: 95–99.
56. Elmaleh, D., Hnatowitch, D., and Kulprathipanja, S. (1979). A novel synthesis of ¹³N-l-asparagine. *J. Labelled Compd. Radiopharm.* 16: 92–93.
57. Cooper, A.J.L. and Gelbard, A.S. (1981). The use of immobilized glutamate dehydrogenase to synthesize ¹³N-labeled l-amino acids. *Anal. Biochem.* 111: 42–48.
58. Gelbard, A.S., Kaseman, D.S., Rosenspire, K.C., and Meister, A. (1985). Enzymatic syntheses of phosphate, l-citrulline, and N-carbamyl l-aspartate labeled with either ¹³N or ¹¹C. *Int. J. Nucl. Med. Biol.* 12: 235–242.

59. Gelbard, A.S., Benua, R.S., Reiman, R.E. et al. (1980). Imaging of the human heart after administration of l-(N-13)glutamate. *J. Nucl. Med.* 21: 988–991.
60. da Silva, E.S., Gomez-Vallejo, V., Baz, Z. et al. (2016). Efficient enzymatic preparation of ¹³N-Labelled amino acids: towards multipurpose synthetic systems. *Chemistry* 22: 13619–13626.
61. Helus, F., Weber, K., Zeisler, S., and Maier-Borst, W. (1991). An automatic system for the enzymatic synthesis of ¹³N-glutamate. *J. Radioanal. Nucl. Chem. Lett.* 155: 9–13.
62. da Silva, E.S., Gómez-Vallejo, V., Llop, J., and López-Gallego, F. (2017). Structural, kinetic and operational characterization of an immobilized l-aminoacid dehydrogenase. *Process Biochem.* 57: 80–86.
63. Gelbard, A.S., Cooper, A.J.L., Asano, Y. et al. (1990). Methods for the enzymatic synthesis of tyrosine and phenylalanine labeled with nitrogen-13. *Int. J. Radiat. Appl. Instrum.* 41: 229–233.
64. Baumgartner, F.J., Barrio, J.R., Henze, E. et al. (1981). ¹³N-labeled L-amino acids for in vivo assessment of local myocardial metabolism. *J. Med. Chem.* 24: 764–766.
65. Gelbard, A.S. (1981). Biosynthetic methods for incorporating positron-emitting radionuclides into compounds of biomedical interest. *J. Labelled Compd. Radiopharm.* 18: 933–945.
66. Barrio, J.R., Baumgartner, F.J., Henze, E. et al. (1983). Synthesis and myocardial kinetics of N-13 and C-11 labeled branched-chain l-amino acids. *J. Nucl. Med.* 24: 937–944.
67. Elmaleh, D.R., Hnatowich, D.J., and Kulprathipanja, S. (1979). A novel synthesis of ¹³N-l-asparagine. *J. Labelled Compd. Radiopharm.* 16: 92–93.
68. Lambrecht, R.H.D., Slegers, G., Claeys, A. et al. (1983). Enzymatic synthesis of radiopharmaceutically pure ¹³N-labelled l-glutamate. *Radiochem. Radioanal. Lett.* 58: 39–48.
69. Lambrecht, R.H.D., Slegers, G., Mannens, G., and Claeys, A. (1986). Enzymatic synthesis of ¹³N-labeled γ-amino-butyric acid. *J. Labelled Compd. Radiopharm.* 23: 1114–1115.
70. Joshi, S.M., Gómez-Vallejo, V., Salinas, V., and Llop, J. (2016). Synthesis of ¹³N-labelled polysubstituted triazoles: via Huisgen cycloaddition. *RSC Adv.* 6: 109633–109638.
71. Perez-Campana, C., Gomez-Vallejo, V., Puigivila, M. et al. (2013). Biodistribution of different sized nanoparticles assessed by positron emission tomography: a general strategy for direct activation of metal oxide particles. *ACS Nano* 7: 3498–3505.
72. de Spiegeleer, B., Slegers, G., Vandecasteele, C. et al. (1986). Microscale synthesis of nitrogen-13-labeled cisplatin. *J. Nucl. Med.* 27: 399–403.
73. Ginos, J.Z., Cooper, A.J.L., Dhawan, V. et al. (1987). [¹³N]cisplatin PET to assess pharmacokinetics of intra-arterial versus intravenous chemotherapy for malignant brain tumors. *J. Nucl. Med.* 28: 1844–1852.
74. Holschbach, M., Hamkens, W., Steinbach, A. et al. (1997). [¹³N]cisplatin: a fast and efficient on-line synthesis using a solid state support. *Appl. Radiat. Isot.* 48: 739–744.
75. Krizek, H., Harper, P.V., and Mock, B. (1977). Adapting the old to new needs: ¹³N labeled urea. *J. Labelled Compd. Radiopharm.* 13: 207.

76. Kumata, K., Takei, M., Ogawa, M. et al. (2009). One-pot radiosynthesis of [¹³N]urea and [¹³N]carbamate using no-carrier-added [¹³N]NH₃. *J. Labelled Compd. Radiopharm.* 52: 166–172.
77. Kumata, K., Takei, M., Ogawa, M. et al. (2010). Radiosynthesis of ¹³N-labeled thalidomide using no-carrier-added [¹³N]NH₃. *J. Labelled Compd. Radiopharm.* 53: 53–57.
78. Kumata, K., Ogawa, M., Takei, M. et al. (2012). Radiosynthesis of [¹³N]dantrolene, a positron emission tomography probe for breast cancer resistant protein, using no-carrier-added [¹³N]ammonia. *Bioorg. Med. Chem.* 20: 305–310.
79. Saji, H., Tsutsumi, D., Kiso, Y. et al. (1992). Synthesis and biological evaluation of a ¹³N-labeled opioid peptide. *Int. J. Radiat. Appl. Instrum.* 19: 455–460.
80. Pettit, W.A., Mortara, R.H., Digenis, G.A., and Reed, M.F. (1975). Preparation of nitroso-¹³N-labeled nitrosoureas. *J. Med. Chem.* 18: 1029–1031.
81. Digenis, G.A., Cheng, Y.C., McQuinn, R.L. et al. (1981). ¹³N-labeling of a substituted nitrosourea, its carbamate, and nitrosocarbaryl: in vivo and in vitro studies. In: *Short-Lived Radionuclides in Chemistry and Biology* (eds. J.W. Root and K.A. Krohn), 351–367. American Chemical Society.
82. Schelbert, H.R., Phelps, M.E., Hoffman, E.J. et al. (1979). Regional myocardial perfusion assessed with N-¹³ labeled ammonia and positron emission computerized axial tomography. *Am. J. Cardiol.* 43: 209–218.
83. Schelbert, H.R., Phelps, M.E., Huang, S.C. et al. (1981). N-¹³ ammonia as an indicator of myocardial blood flow. *Circulation* 63: 1259–1272.
84. Krivokapich, J., Smith, G.T., Huang, S.C. et al. (1989). ¹³N ammonia myocardial imaging at rest and with exercise in normal volunteers. Quantification of absolute myocardial perfusion with dynamic positron emission tomography. *Circulation* 80: 1328–1337.
85. Rosenspire, K.C., Schwaiger, M., Mangner, T.J. et al. (1990). Metabolic fate of [¹³N] ammonia in human and canine blood. *J. Nucl. Med.* 31: 163–167.
86. Bratis, K., Mahmoud, I., Chiribiri, A., and Nagel, E. (2013). Quantitative myocardial perfusion imaging by cardiovascular magnetic resonance and positron emission tomography. *J. Nucl. Cardiol.* 20: 860–870.
87. Brunken, R.C. (2012). Cardiovascular positron emission tomography (PET). In: *Nuclear Cardiology Review: A Self-Assessment Tool* (eds. W.A. Jaber and M.D. Cerqueira), 83–103. Lippincott Williams & Wilkins.
88. Livingston, M.S. and McMillan, E. (1934). The production of radioactive oxygen. *Phys. Rev.* 46: 437–438.
89. Siri, W.E. (1949). *Isotopic Tracers and Nuclear Radiations with Applications to Biology and Medicine*. New York/Toronto/London: McGraw-Hill Book Co. Inc.
90. Kamen, M.D. (1957). The isotopes of oxygen, nitrogen, phosphorus and sulphur. In: *Isotopic Tracers in Biology* Chapter XI, 3e (ed. M.D. Kamen), 339–360. Academic Press.
91. Ter-Pogossian, M.M. and Herscovitch, P. (1985). Radioactive oxygen-¹⁵ in the study of cerebral blood flow, blood volume, and oxygen metabolism. *Semin. Nucl. Med.* 15: 377–394.

92. Dyson, N.A., Hugh-Jones, P., Newbery, G.R., and West, J.B. (1959). The preparation and use of oxygen-18 with particular reference to its value in the study of pulmonary malfunction. Second United Nations Conference of the Peaceful Uses of Atomic Energy (UN Geneva 1958).
93. Van Der Linde, S.C., Jansen, W.P.A., De Goeij, J.J.M. et al. (2000). In-target production of high specific radioactivity [¹⁵O]nitrous oxide by deuteron irradiation of nitrogen gas. *Appl. Radiat. Isot.* 52: 77–85.
94. Diksic, M., Yamamoto, Y.L., and Feindel, W. (1983). An on-line synthesis of [¹⁵O]N₂O: new blood-flow tracer for PET imaging. *J. Nucl. Med.* 24 (7): 603–607.
95. Clark, J.C. (1975). *Short-Lived Radioactive Gases for Clinical Use* (eds. J.C. Clark and P.D. Buckingham). London/Boston: Butterworth.
96. Welch, M.J. and Ter-Pogossian, M.M. (1968). Preparation of short half-lived radioactive gases for medical studies. *Radiat. Res.* 36: 580–587.
97. Powell, J. and O’Neil, J.P. (2006). Production of [¹⁵O]water at low-energy proton cyclotrons. *Appl. Radiat. Isot.* 64: 755–759.
98. Nichols, A.B., Cochavi, S., Hales, C.A. et al. (1978). Scintigraphic detection of pulmonary emboli by serial positron imaging of inhaled ¹⁵O-labeled carbon dioxide. *N. Engl. J. Med.* 299: 279–284.
99. Sajjad, M., Liow, J.S., and Moreno-Cantu, J. (2000). A system for continuous production and infusion of [¹⁵O]H₂O for PET activation studies. *Appl. Radiat. Isot.* 52: 205–210.
100. Strijckmans, K., Vandecasteele, C., and Sambre, J. (1985). Production and quality control of ¹⁵O₂ and C¹⁵O₂ for medical use. *Int. J. Appl. Radiat. Isot.* 36: 279–283.
101. Berridge, M.S., Terris, A.H., and Cassidy, E.H. (1990). Low-carrier production of [¹⁵O] oxygen, water and carbon monoxide. *Int. J. Radiat. Appl. Instrum.* 41: 1173–1175.
102. Berridge, M.S., Cassidy, E.H., and Terris, A.H. (1990). A routine, automated synthesis of oxygen-15-labeled butanol for positron tomography. *J. Nucl. Med.* 31: 1727–1731.
103. Goodman, M.M., DeVinney, J.L., Kabalka, G.W. et al. (1991). Computer-controlled synthesis of oxygen-15 butanol and water: automated production and dispensing systems. *J. Labelled Compd. Radiopharm.* 30: 166–168.
104. Kabalka, G.W., Green, J.F., Goodman, M.M. et al. (1994). The synthesis of oxygen-15 butanol via the oxidation of tributylborane adsorbed on solid surfaces. *J. Labelled Compd. Radiopharm.* 35: 186–188.
105. Kabalka, G.W., Lambrecht, R.M., Sajjad, M. et al. (1985). Synthesis of ¹⁵O-labeled butanol via organoborane chemistry. *Int. J. Appl. Radiat. Isot.* 36: 853–855.
106. Iwata, R., Ido, T., Fujisawa, Y., and Yamazaki, S. (1988). On-line interconversion of [¹⁵O] O₂ and [¹⁵O]CO₂ via metal oxide by isotopic exchange. *Int. J. Radiat. Appl. Instrum. Part A* 39: 1207–1211.
107. Votaw, J.R., Satter, M.R., and Sunderland, J.J. (1986). The Edison lamp: O-15 carbon monoxide production in the target. *J. Labelled Compd. Radiopharm.* 23: 1211–1213.
108. West, J.B. and Dollery, C.T. (1961). Absorption of inhaled radioactive water vapour. *Nature* 189: 588.
109. Welch, M.J., Lifton, J.F., and Seck, J.A. (1969). Tracer studies with radioactive oxygen-15. Exchange between carbon dioxide and water. *J. Phys. Chem.* 73: 3351–3356.

110. Ruiz, H.V. and Wolf, A.P. (1978). Direct synthesis of oxygen-15 labelled water at high specific activities. *J. Labelled Compd. Radiopharm.* 15: 185–189.
111. Harper, P.V. and Wickland, T. (1981). Oxygen-15 labeled water for continuous intravenous administration. *J. Labelled Compd. Radiopharm.* 18: 186.
112. Hagami, E., Murakami, M., Takahashi, K. et al. (1986). Studies on the direct synthesis of [O-15]-H₂O. *Kakuigaku* 23: 351–358.
113. Buckingham, P.D. and Forse, G.R. (1963). The preparation and processing of radioactive gases for clinical use. *Int. J. Appl. Radiat. Isot.* 14: 439–444.
114. Wieland, B.W., McKinney, C.J., and Coleman, R.E. (1996). Duke cyclotron radionuclides for clinical and preclinical use. In: *3rd Topical Meeting on Industrial Radiation and Radioisotope Measurements and Applications*, 107. American Nuclear Society.
115. Bauer, B. and Wagner, R. (1991). Improved synthesis of (¹⁵O) butanol for clinical use. *J. Labelled Compd. Radiopharm.* 30: 69–71.
116. Takahashi, K., Murakami, M., Hagami, E. et al. (1989). Radiosynthesis of ¹⁵O-labeled hydrogen peroxide. *J. Labelled Compd. Radiopharm.* 27: 1167–1175.
117. Yorimitsu, H., Murakami, Y., Takamatsu, H. et al. (2005). Ultra-rapid synthesis of ¹⁵O-labeled 2-deoxy-d-glucose for positron emission tomography (PET). *Angew. Chem. Int. Ed.* 44: 2708–2711.
118. Le Bars, D., Lavenne, F., Sasse, K. et al. (1991). Development of an inexpensive programmable logic controller for clinical gases regulation. *J. Labelled Compd. Radiopharm.* 30: 113–114.
119. Wagner, R., Arenz, W., Richerzhagen, N., and Wienhard, K. (1993). Single-breath inhalation or rebreathing of gases labelled with positron emitters: some technical aspects of dispensing and waste gas management. *Appl. Radiat. Isot.* 44: 1065–1068.
120. Jackson, J.R., Dembowski, B.S., Ehrenkauffer, R.L. et al. (1993). [¹⁵O]H₂O, [¹⁵O]O₂ and [¹⁵O]CO gas production, monitoring and quality control system. *Appl. Radiat. Isot.* 44: 631–634.
121. Löttgen, J., Wagner, R., Richerzhagen, N., and Wienhard, K. (1994). Automatic control device for the continuous administration of ¹⁵O labelled gaseous tracers for PET measurements. *Appl. Radiat. Isot.* 45: 923–928.
122. Welch, M.J., Lifton, J.F., and Ter-Pogossian, M.M. (1969). Preparation of millicurie quantities of oxygen-15 labeled water. *J. Labelled Compd.* 5: 168–172.
123. Welch, M.J. and Kilbourn, M.R. (1985). A remote system for the routine production of oxygen-15 radiopharmaceuticals. *J. Labelled Compd. Radiopharm.* 22: 1193–1200.
124. Meyer, G.J., Schober, O., Bossaller, C. et al. (1984). Quantification of regional extravascular lung water in dogs with positron emission tomography, using constant infusion of ¹⁵O-labeled water. *Eur. J. Nucl. Med.* 9: 220–228.
125. Ferrieri, R.A., Alexoff, D.L., Schlyer, D.J., and Wolf, A.P. (1994). Remote processing, delivery and injection of H₂[¹⁵O] produced from a N₂/H₂ gas target using a simple and compact apparatus. *Appl. Radiat. Isot.* 45: 1149–1154.
126. Palmer, B.M., Sajjad, M., and Rottenberg, D.A. (1995). An automated [¹⁵O]H₂O production and injection system for PET imaging. *Nucl. Med. Biol.* 22: 241–249.

Chapter 7

Radiochemistry with Carbon-11

Stephen Thompson, Steven Kealey, Selena Milicevic
Sephton and Franklin I. Aigbirhio

*Molecular Imaging Chemistry Laboratory, Wolfson Brain Imaging
Centre, Department of Clinical Neurosciences, University of Cam-
bridge, Cambridge, CB2 0SZ, UK*

7.1 INTRODUCTION

7.1.1 History

In 1934, Lauritsen et al. found that when boron oxide was irradiated with deuterons, a radionuclide with a half-life of 20 minutes was formed [1]. This was subsequently identified as carbon-11, formed by the $^{10}\text{B}(\text{d},\text{n})^{11}\text{C}$ nuclear reaction and isolated in the form of $[^{11}\text{C}]\text{CO}_2$ and $[^{11}\text{C}]\text{CO}$ [2]. In 1939, the $^{14}\text{N}(\text{p},\alpha)^{11}\text{C}$ reaction was first described by Barkas [3], whereby high-energy cyclotron-produced protons were bombarded on a nitrogen-14 target to produce carbon-11. Eighty years on, this remains the most common method of producing ^{11}C and is used at positron emission tomography (**PET**) centres across the world.

Carbon-11 decays into stable boron-11 and has a physical half-life of 20.4 minutes. Decay occurs primarily (99.8%) by positron emission, with the emitted positron having a mean energy of 0.386 MeV and a mean range of 1.2 mm in water [4]. The remaining decay (0.2%) occurs by electron capture. The utility of ^{11}C as a radiolabel for biological application is immediately obvious – the ubiquitous nature of carbon in biologically relevant molecules allows for a radioactive analogue (isotopologue) to be produced by substitution of a stable $^{12/13}\text{C}$ for ^{11}C . The first chemical manipulation with ^{11}C was reported by Long in

1939, in which [^{11}C] CO_2 was converted to potassium [^{11}C]oxalate [5]. Later that year, Ruben et al. reported the first biological application of ^{11}C in their study on [^{11}C] CO_2 uptake during photosynthesis [6]. The first human experiments with ^{11}C were performed in 1945 by Tobias et al. with a study on [^{11}C]CO uptake and bodily distribution following inhalation of the gas [7].

The availability of carbon-14 (half-life 5730 years) after World War II precipitated a downturn in research activities with ^{11}C until the early 1960s. The emergence of medical cyclotrons in the 1960s and PET in the late 1970s has driven ^{11}C radiochemistry research to meet the demands for new or improved tracers at an expanding array of biological targets [8]. This review chapter highlights core aspects of ^{11}C radiochemistry and notable advances since the publication of the previous edition of *Handbook of Radiopharmaceuticals* in 2003 [9].

7.1.2 Synthetic Considerations

In addition to the usual synthetic considerations, incorporation of cyclotron-derived ^{11}C into the molecule of interest is complicated by the inherent challenges of working with radioactivity: i.e. need for shielding and automation, time restrictions, and small scale of radiolabelling reactions with short-lived radionuclides. For a typical production of a ^{11}C -labelled PET tracer for clinical use, the radiosynthesis, purification, and quality control must be complete within approximately three half-lives (~1 hour) to have sufficient radioactivity in the final dose for a successful PET scan. In practice, this restricts the use of ^{11}C to centres with a cyclotron on-site, or to those centres in close proximity. The requirement for rapid chemistry means a convergent synthetic approach is often pursued in which the radiolabel is introduced late in the sequence, ideally in the final step, to minimize loss of activity by radioactive decay.

The theoretical molar activity of ^{11}C in the absence of isotopic dilution from naturally occurring carbon ($^{12/13}\text{C}$) is 341 000 GBq· μmol^{-1} . In practice, molar activities in the 100–1000 GBq· μmol^{-1} range are observed for ^{11}C -labelled tracers, meaning ^{11}C is outnumbered by $^{12/13}\text{C}$ in a ratio of ~1 : 1000. Even when accounting for isotopic dilution, the total amount of ^{11}C + $^{12/13}\text{C}$ in the final dose of a PET radiotracer is typically in the nanomole range. Fortunately, the nanomole amount of radiolabelling reagents lends itself to rapid chemical reactions due to the large stoichiometric excess (10–1000 fold) of non-radioactive reagents present in the reaction mixture (based on typical conditions involving 0.1–10 mg of precursor with a molecular mass of 300 g· mol^{-1} reacting with 10 GBq of ^{11}C -labelling reagent with a molar activity of 300 GBq· μmol^{-1}). Under these conditions, the amount of precursor effectively remains constant throughout the reaction, and the resultant pseudo first-order reaction kinetics allows reactions to occur within minutes.

7.1.3 Biological Considerations

The physical properties of carbon-11 are ideally suited to imaging biological processes as its half-life is of a similar order of magnitude to many biological processes involving small

molecules, including incorporation into biomolecules, transport across membranes, and binding to receptors. From a patient-scanning perspective, the short half-life allows multiple PET studies to be performed in the same subject in one day, and also reduces the radiation dose to the subject.

Substituting $^{12/13}\text{C}$ for ^{11}C gives a structurally and biologically indistinguishable radio-labelled isotopologue (albeit for a negligible kinetic isotope effect), well suited for studying *in vivo* properties of endogenous molecules. Carbon-11 is available in high molar activity, enabling low masses of unlabelled compound to be administered, often below pharmacologically active levels, resulting in minimal perturbation of the biological system under investigation and minimizing the likelihood of any toxic effects.

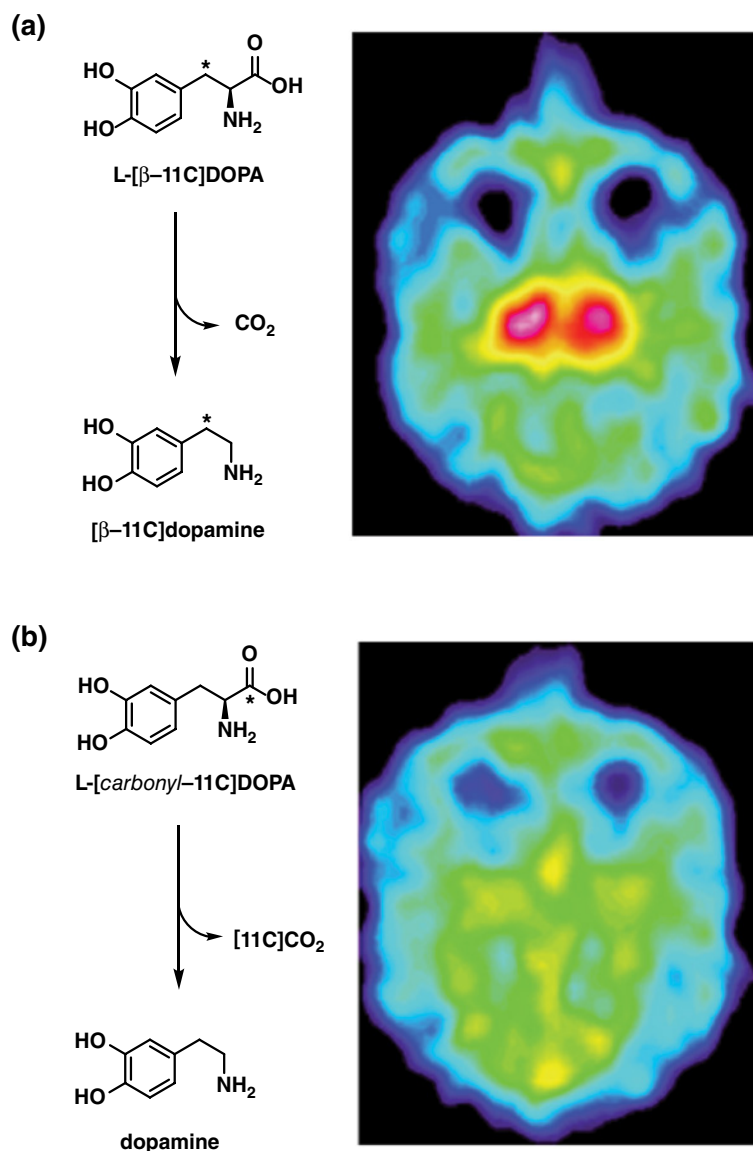
The presence of multiple carbon atoms in most bioactive molecules offers a choice of sites for radiolabelling with carbon-11. This is advantageous in the context of both the radiochemistry used to incorporate the label and facilitates studies of *in vivo* metabolism and biochemistry. For example, WAY100365, a 5-HT₁ antagonist, has been radiolabelled with carbon-11 at the methoxy position and the carbonyl position. [*Methyl*- ^{11}C]WAY100635 is metabolized to a compound that crosses the blood-brain barrier and has an affinity for the 5-HT₁ receptor, confounding analysis of the resultant images. In contrast, the radiolabelled metabolites of [*carbonyl*- ^{11}C]WAY100635 do not cross the blood-brain barrier, and this compound has been widely used to investigate the serotonergic system [10]. Similarly, the rate of decarboxylation of L-DOPA to dopamine could be measured using L-DOPA labelled with carbon-11 at different positions (Figure 7.1) [11, 12]. With the carbon-11 label in the methylene (β) position, decarboxylation gives [^{11}C]dopamine, and radioactivity accumulates in the striatum (Figure 7.1a). However, decarboxylation of L-[*carbonyl*- ^{11}C]DOPA gives unlabelled dopamine and no accumulation of radioactivity in the striatum (Figure 7.1b). Calculated influx rate constants were used as a measure of the rate of decarboxylation of L-DOPA. Similar studies using differential labelling to interrogate *in vivo* metabolism have also been reported using [^{11}C]pyruvate [12] and [^{11}C]glutamate [13, 14].

7.2 SYNTHESIS OF COMMON CARBON-11 PRECURSORS

7.2.1 Primary Precursors

The chemical composition of cyclotron-generated ^{11}C is dictated by the choice of additive gas within the [^{14}N]N₂ target; trace amounts of O₂ (0.05–1.0%) give rise to [^{11}C]carbon dioxide ([^{11}C]CO₂), while H₂ (5–10%) gives rise to [^{11}C]methane ([^{11}C]CH₄) [15]. Although [^{11}C]CO₂ is the feedstock for the majority of ^{11}C -labelling reactions, its susceptibility to isotopic dilution from atmospheric CO₂ is reflected in the molar activity of products (c. 50–500 GBq· μmol^{-1}), which are usually lower than those obtained from [^{11}C]CH₄ (c. 500–2000 GBq· μmol^{-1}). A number of techniques may be adopted to minimize this, such

Figure 7.1 Labeling of L-DOPA at differential positions allowed for the determination of the rate of decarboxylation to dopamine by the accumulation of [^{11}C]dopamine in the striatum. Source: From Gunnar Antoni, (2015). Reproduced with permission of John Wiley & Sons.



as: (i) pre-conditioning the cyclotron target, (ii) flushing delivery lines with an inert gas and preconditioning synthesis modules, (iii) maintaining leak-tightness throughout systems, and (iv) avoiding solution-phase reactions for further derivatisations or using high-purity, fresh reagents for these reactions. Radiochemical conversions of [^{11}C]CO $_2$ /[^{11}C]CH $_4$ are also complicated by their delivery from the cyclotron at high dilution in an inert gas stream, which may also contain trace amounts of hydrogen/nitrogen and nitrous oxide impurities derived from the target gas mixture. Purification and preconcentration may be achieved using a cryogenic [16, 17] or solid-phase [18, 19] trap-and-release process to

capture $[^{11}\text{C}]\text{CO}_2/[^{11}\text{C}]\text{CH}_4$ from the gas stream and carry volatile impurities to exhaust. $[^{11}\text{C}]\text{CO}_2/[^{11}\text{C}]\text{CH}_4$ can then be released as a more concentrated bolus by heating the trap under a controlled flow of sweep gas.

7.2.2 Secondary Precursors

Primary ^{11}C -labelling reagents may be converted into more reactive or synthetically useful species to provide access to a broader range of functional groups. For example, $[^{11}\text{C}]\text{CH}_4$ has limited scope for direct incorporation into biologically relevant molecules but can be readily converted into the useful radiolabelling reagent $[^{11}\text{C}]\text{methyl iodide}$ ($[^{11}\text{C}]\text{CH}_3\text{I}$). A summary of well-known ^{11}C reagents that can be derived from $[^{11}\text{C}]\text{CO}_2$ and $[^{11}\text{C}]\text{CH}_4$ is shown in Figure 7.2, and their synthesis is described in the following sections.

7.2.2.1 $[^{11}\text{C}]\text{Carbon Monoxide}$

Although $[^{11}\text{C}]\text{CO}$ can be produced directly from the cyclotron as a by-product of $[^{11}\text{C}]\text{CO}_2$ formation, it is more commonly formed via gas-phase reduction of $[^{11}\text{C}]\text{CO}_2$ over zinc or molybdenum at elevated temperature (Figure 7.3a). Recently, solution-phase (Figure 7.3b) and electrochemical (Figure 7.3c) methods to produce $[^{11}\text{C}]\text{CO}$ have also been reported.

Reduction of $[^{11}\text{C}]\text{CO}_2$ over zinc at 400°C produces $[^{11}\text{C}]\text{CO}$ in near-quantitative radiochemical yield (**RCY**) [20, 21]. This method has been reported to suffer from declining RCY over successive runs, necessitating regular replacement of the zinc [22], which in itself may be problematic due to inconsistent conversion yields following replacement [23]. The limited reproducibility is due to (i) zinc deactivation arising from reaction with oxygen and/or nitrogen oxides derived from the target [24–26], (ii) adsorption of $[^{11}\text{C}]\text{CO}/\text{CO}_2$ at

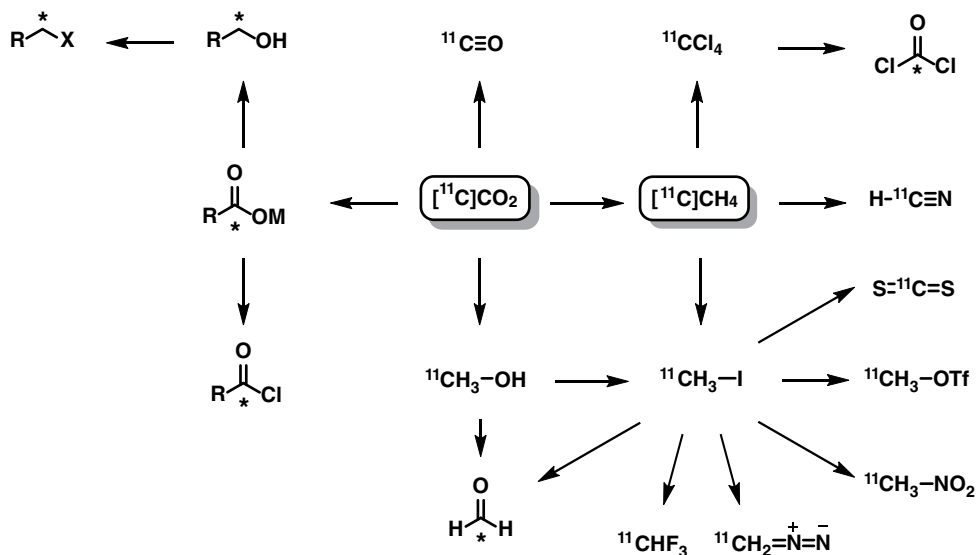
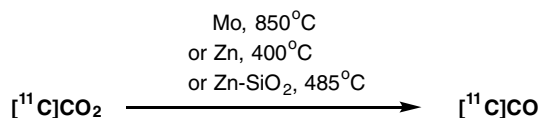


Figure 7.2
Common secondary ^{11}C -labelling reagents derived from $[^{11}\text{C}]\text{CO}_2$ and $[^{11}\text{C}]\text{CH}_4$.

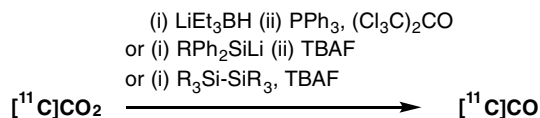
Figure 7.3

Methods for reduction of $[^{11}\text{C}]\text{CO}_2$ to $[^{11}\text{C}]\text{CO}$.

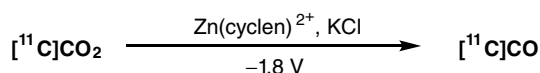
(a) Gas phase:



(b) Solution phase:



(c) Electrochemical:



the metal surface [25], and (iii) technical issues arising from the reduction temperature being close to the melting point of zinc (420°C) [27]. In 2017, Dahl et al. reported a modified method in which the zinc reductant is supported on fused silica particles, allowing for a higher reduction temperature of 485°C , achieving RCYs of $93\% \pm 3\%$ over 20 runs [28].

Gas-phase reduction using molybdenum at 850°C provides a reliable route to $[^{11}\text{C}]\text{CO}$, albeit with lower RCYs (~ 70 to 80% using molybdenum powder [23] or mesh [27]). Yields are consistent throughout ~ 100 production cycles, which may in part be attributable to the conversion temperature being significantly below the melting point of molybdenum (2623°C). Furthermore, the molybdenum(IV) oxide formed by reaction of $[^{11}\text{C}]\text{CO}_2$ with molybdenum is itself able to reduce $[^{11}\text{C}]\text{CO}_2$, which may improve the performance of the converter [27].

Solution-phase techniques are an alternative means of generating $[^{11}\text{C}]\text{CO}$ without the need for high-temperature ovens and associated apparatus. Roeda et al. report a two-step process using lithium triethylborohydride and triphenylphosphine-hexachloroacetone to convert $[^{11}\text{C}]\text{CO}_2$ to $[^{11}\text{C}]\text{formyl chloride}$, which decomposes to give $[^{11}\text{C}]\text{CO}$ in near-quantitative yield [29]. In 2015, two groups published separate reports of $[^{11}\text{C}]\text{CO}$ production through the use of lithiated silyl reagents [30, 31]. These reagents, which must be prepared in advance, capture $[^{11}\text{C}]\text{CO}_2$ through the formation of the corresponding ^{11}C -silacarboxylic acid, which can then release $[^{11}\text{C}]\text{CO}$ upon addition of a fluoride source such as tetra-*n*-butylammonium fluoride (**TBAF**). Near-quantitative $[^{11}\text{C}]\text{CO}$ conversions within 10 minutes were reported when using $^t\text{BuPh}_2\text{SiLi}$ [30]. A simplified method using commercially available disilane reagents allows the fluoride source to be added before $[^{11}\text{C}]\text{CO}_2$ delivery and is capable of producing $[^{11}\text{C}]\text{CO}$ in 74% RCY within 10 minutes [32]. A proof of principle electrochemical methodology has also been reported, which uses a screen-printed electrode immersed in a solution of Zn(cyclen)^{2+}

electrocatalyst and is able to reduce cyclotron-produced $[^{11}\text{C}]\text{CO}_2$ to $[^{11}\text{C}]\text{CO}$ in up to 10% RCY [33].

7.2.2.2 $[^{11}\text{C}]\text{Methyl Iodide}$

In 1973, Comar and co-workers first reported the synthesis of $[^{11}\text{C}]\text{CH}_3\text{I}$ by LiAlH_4 reduction of $[^{11}\text{C}]\text{CO}_2$ to $[^{11}\text{C}]\text{CH}_3\text{OH}$ followed by iodination with concentrated hydroiodic acid, as shown in Figure 7.4a [36]. $[^{11}\text{C}]\text{CH}_3\text{I}$ is a potent electrophile that readily undergoes reaction with amines, phenols, and other suitable nucleophiles. $[^{11}\text{C}]\text{CH}_3\text{I}$ is also a precursor to other useful reagents for radiolabelling with ^{11}C , including $[^{11}\text{C}]\text{CH}_3\text{OTf}$, $[^{11}\text{C}]\text{HCHO}$, and $[^{11}\text{C}]\text{CS}_2$. The versatility of $[^{11}\text{C}]\text{CH}_3\text{I}$ has led to the extensive development of reliable and repeatable automated methods, the radiosynthesis of the most widely used intermediate in carbon-11 radiochemistry.

7.2.2.2.1 $[^{11}\text{C}]\text{CH}_3\text{I}$ by the “Wet Method”

The first reported method for producing $[^{11}\text{C}]\text{CH}_3\text{I}$ [37] was further optimized by Långström and colleagues [38] and has since evolved from a multi-reactor, manual process to a simple, semi-automated, single-reactor process (Figure 7.4b) [34]. The “wet method” involves the cryogenic trapping and concentration of $[^{11}\text{C}]\text{CO}_2$, followed by its release into a solution of LiAlH_4 in tetrahydrofuran (**THF**) or Et_2O (hence the “wet method”), where $[^{11}\text{C}]\text{CO}_2$ is reduced to $[^{11}\text{C}]\text{CH}_3\text{O}^-$. The organic solvent is evaporated before the addition of concentrated aqueous HI, hydrolysing any salts and releasing $[^{11}\text{C}]\text{CH}_3\text{OH}$, which rapidly undergoes substitution with HI to give $[^{11}\text{C}]\text{CH}_3\text{I}$. The $[^{11}\text{C}]\text{CH}_3\text{I}$ is distilled from the solution through a $\text{P}_2\text{O}_5/\text{NaOH}$ trap (for drying and scrubbing of excess HI) into a second reactor and used for further reaction. Alternatively, P_2I_4 [39] or PPh_3I_2 [40] can be used for iodination of $[^{11}\text{C}]\text{CH}_3\text{OH}$. These reagents are less corrosive than HI, improving the lifetime of the synthesis apparatus and reducing failure rates.

The wet method reliably produces $[^{11}\text{C}]\text{CH}_3\text{I}$ in >80% RCY from $[^{11}\text{C}]\text{CO}_2$ [41]. The molar activity of $[^{11}\text{C}]\text{CH}_3\text{I}$ varies between 0.55–222 GBq· μmol^{-1} , often lower than that produced using alternative methods [42], likely due to (i) $[^{12/13}\text{C}]\text{CO}_2$ present in the target and delivery gases; (ii) ingress of $[^{12/13}\text{C}]\text{CO}_2$ into the target system during target filling, bombardment, or emptying [42–44]; (iii) absorption of $[^{12/13}\text{C}]\text{CO}_2$ by the LiAlH_4 [45]; (iv) $[^{12/13}\text{C}]\text{CO}_2$ dissolved in the solvents used for synthesis; or (v) iodination of residual volatile organic materials to give contaminating $[^{12/13}\text{C}]\text{CH}_3\text{I}$ [46, 47].

7.2.2.2.2 $[^{11}\text{C}]\text{CH}_3\text{I}$ by the “Gas-Phase” Method

The “gas-phase” synthesis of $[^{11}\text{C}]\text{CH}_3\text{I}$ was developed independently by Link et al. [48] and Larson et al. [49] in an effort to improve the molar activity of $[^{11}\text{C}]\text{CH}_3\text{I}$ by avoiding the use of LiAlH_4 solutions and highly corrosive HI. The reported gas-phase radiosynthesis involves a reduction of $[^{11}\text{C}]\text{CO}_2$ to $[^{11}\text{C}]\text{CH}_4$ by H_2 over a nickel catalyst at c. 400 °C, followed by a radical iodination [21]. The radical iodination is performed in a quartz tube in a furnace between 700 °C and 720 °C, where $[^{11}\text{C}]\text{CH}_4$ reacts with I_2 vapour to give gaseous $[^{11}\text{C}]\text{CH}_3\text{I}$ (Figure 7.5a). Link et al. described a single-pass process where the

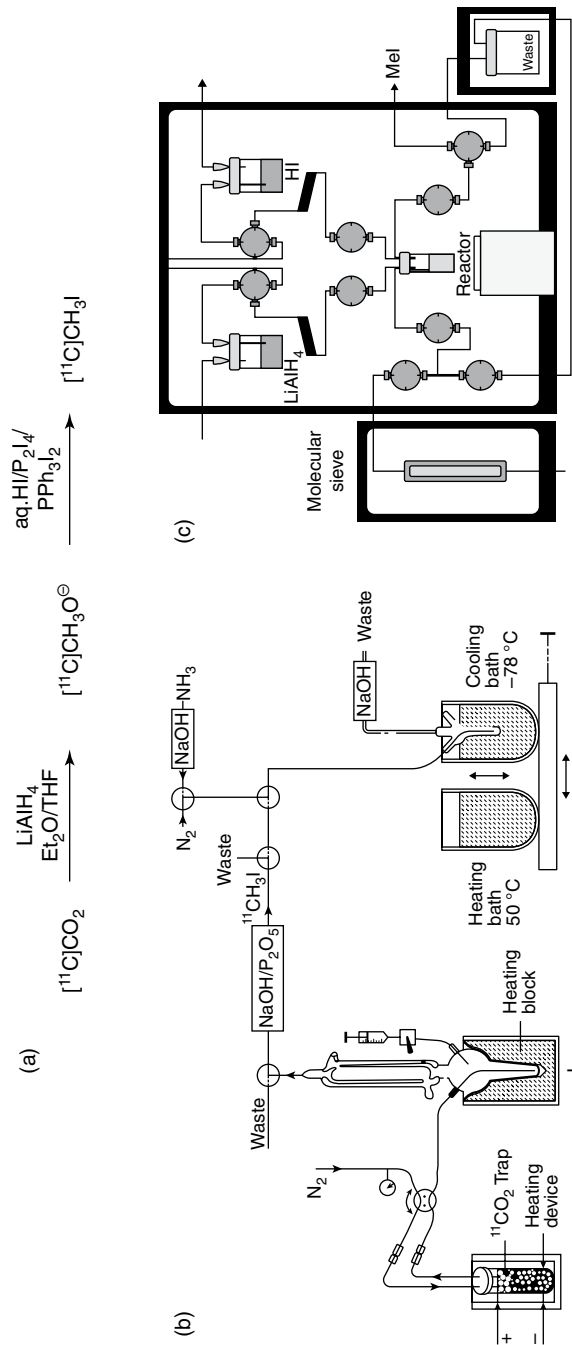


Figure 7.4 (a) Production of $[^{11}\text{C}]\text{CH}_3\text{I}$ by the “wet method.” (b) Diagrammatic representation of an early single-reactor system for producing $[^{11}\text{C}]\text{CH}_3\text{I}$ by the wet method. LiAlH_4 would be loaded in an ethereal solvent into reactor I, while hydroiodic acid would be added into the reactor from the syringe. The resultant $[^{11}\text{C}]\text{CH}_3\text{I}$ can then be trapped in reactor II. Source: From Långström, B., Antoni, G., Gullberg, P. et al. [34]. © SNMMI. (c) Diagrammatic representation of a modern, single reactor system for production of $[^{11}\text{C}]\text{CH}_3\text{I}$ using the “wet” method. Source: From Gómez-Vallejo, V. and Llop, J. [35]. © 2009 Elsevier.

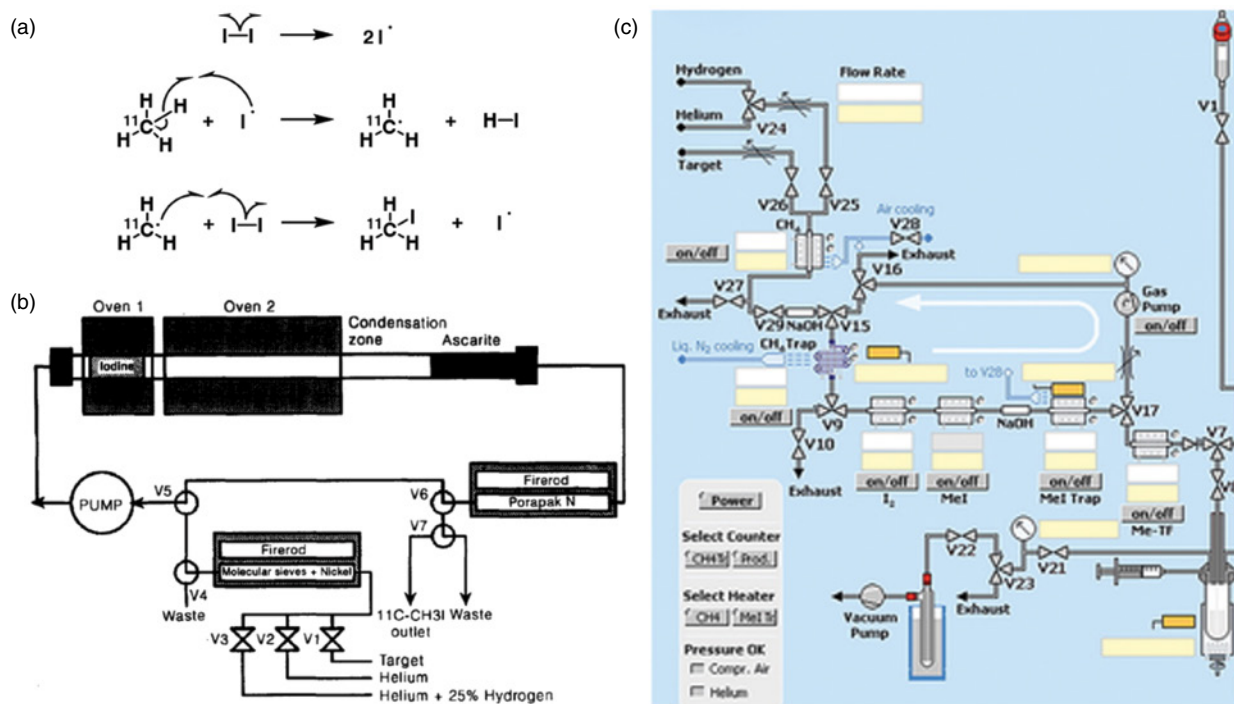


Figure 7.5 (a) Production of $[^{11}\text{C}]\text{CH}_3\text{I}$ from $[^{11}\text{C}]\text{CH}_4$ and molecular iodine by radical iodination in the gas phase. Sources: Link, J.M., Krohn, K.A., and Clark, J.C. [48]; and Larsen, P., Ulin, J., Dahlstrøm, K., and Jensen, M.[49] (b) Schematic diagram of the recirculating pump, ovens, and trapping cartridges for synthesizing $[^{11}\text{C}]\text{CH}_3\text{I}$ from $[^{11}\text{C}]\text{CO}_2$ described by Larsen et al. Source: Larsen, P., Ulin, J., Dahlstrøm, K., and Jensen, M.[49]. © 1997. Reproduced with the permission of Elsevier. (c) Schematic diagram of the $[^{11}\text{C}]\text{CH}_3\text{I}$ production components of a modern GE Tracerlab FX_{c-Pro} module, with the white arrow indicating the recirculation pathway. Source: Shao, X., Hoareau, R., Runkle, A.C. et al. [50]. © 2011. Reproduced with the permission of John Wiley & Sons.

$[^{11}\text{C}]\text{CH}_4$ passes once through the heated iodination furnace and $[^{11}\text{C}]\text{CH}_3\text{I}$ is condensed in a cooled glass trap upon exit. $[^{11}\text{C}]\text{CH}_3\text{I}$ was obtained in <55% RCY from $[^{11}\text{C}]\text{CH}_4$ and gave ^{11}C -methylated products with a molar activity of $451 \text{ GBq}\cdot\mu\text{mol}^{-1}$ at the end of bombardment (EOB) [48], representing a significant improvement in molar activity over the wet method. Some of the highest molar activities for carbon-11 labelled compounds, averaging $4700 \text{ GBq}\cdot\mu\text{mol}^{-1}$ and as high as $9700 \text{ GBq}\cdot\mu\text{mol}^{-1}$, have been prepared using single-pass gas-phase methods [46, 51, 52]. These ultra-high molar activity productions start from cyclotron-produced $[^{11}\text{C}]\text{CH}_4$ rather than $[^{11}\text{C}]\text{CO}_2$. Introduction of organic contaminants that can react to form $[^{12/13}\text{C}]\text{CH}_3\text{I}$ is also limited, as the gas bolus passes through the apparatus only once.

Larsen et al. described a similar process but including a pump that recirculates $[^{11}\text{C}]\text{CH}_4$ through the iodine furnace, improving the yield of $[^{11}\text{C}]\text{CH}_3\text{I}$ (Figure 7.5b). A Porapak-N cartridge (a porous divinylbenzene polymer bead-bed) was incorporated into the

recirculation loop, which traps $[^{11}\text{C}]\text{CH}_3\text{I}$ from the gas stream and allows any unreacted $[^{11}\text{C}]\text{CH}_4$ to circulate back into the iodine furnace. Once radioactivity is trapped on the cartridge plateaus, conversion of $[^{11}\text{C}]\text{CH}_4$ to $[^{11}\text{C}]\text{CH}_3\text{I}$ is complete and recirculation is stopped. Heating of the Porapak-N cartridge in an inert gas flow releases the trapped $[^{11}\text{C}]\text{CH}_3\text{I}$, which can then be transferred to the reaction vessel. The average non-decay corrected RCY of $[^{11}\text{C}]\text{CH}_3\text{I}$ from $[^{11}\text{C}]\text{CH}_4$ was 66%, and the $[^{11}\text{C}]\text{CH}_3\text{I}$ produced by this method had a molar activity of $>550\text{ GBq}\cdot\mu\text{mol}^{-1}$ [49]. The efficiency, reproducibility, ease of automation, and high molar activities that can be achieved have made this recirculation-based method the most widely used in radiochemistry facilities for the production of $[^{11}\text{C}]\text{CH}_3\text{I}$. Several manufacturers offer commercially available systems that automate the entire $[^{11}\text{C}]\text{CH}_3\text{I}$ process (Figure 7.5c).

7.2.2.3 Other Methods

Alternative methods for the generation of $[^{11}\text{C}]\text{CH}_3\text{I}$ are based upon the recoil synthesis of $[^{11}\text{C}]\text{CH}_3\text{I}$ by the $^{14}\text{N}(\text{p},\alpha)^{11}\text{C}$ reaction in an N_2/HI flow target system [53], giving $[^{11}\text{C}]\text{CH}_3\text{I}$ in 25% RCY over 40 minutes. Single-pass iodination of $[^{11}\text{C}]\text{CH}_4$ by iodine radicals in a glow-discharge helium plasma, rather than a high-temperature furnace, was reported to give $[^{11}\text{C}]\text{CH}_3\text{I}$ in 13% RCY [54]. These alternate methods are rarely used as their yields are lower than those obtained using the gas-phase method, and the equipment used is not commercially available.

7.2.2.3 $[^{11}\text{C}]\text{Methyl Triflate}$

$[^{11}\text{C}]\text{Methyl trifluoromethylsulfonate}$ ($[^{11}\text{C}]\text{methyl triflate}$, $[^{11}\text{C}]\text{CH}_3\text{OTf}$) is inherently more reactive, less volatile, and more efficiently trapped in the reaction solvent than $[^{11}\text{C}]\text{CH}_3\text{I}$. Reactions can therefore be conducted at lower temperatures and with less precursor [55, 56]. The synthesis of $[^{11}\text{C}]\text{CH}_3\text{OTf}$ by a single pass of gaseous $[^{11}\text{C}]\text{CH}_3\text{I}$ through a column of silver triflate-impregnated graphitized carbon at 200°C was reported by Jewett in 1992 [57]. This gas-phase synthesis system is easily appended to the outlet of a gas-phase system for $[^{11}\text{C}]\text{CH}_3\text{I}$ production (Figure 7.5c) and provides $[^{11}\text{C}]\text{CH}_3\text{OTf}$ in near-quantitative conversions. The synthesis of $[^{11}\text{C}]\text{CH}_3\text{OTf}$ from $[^{11}\text{C}]\text{CH}_3\text{Br}$ has also been reported [58, 59].

7.2.2.4 Other ^{11}C -Alkylating Agents

$[^{11}\text{C}]\text{CH}_3\text{Br}$ has also been used as a ^{11}C -methylating reagent, requiring the use of lower furnace temperatures (550°C vs. 720°C) for radical bromination compared to iodination [58]. The synthesis of $[^{11}\text{C}]\text{CD}_3\text{I}$ from $[^{11}\text{C}]\text{CD}_4$ (produced by bombardment of a 95%/5% N_2/D_2 mixture) for investigation of *in vivo* kinetic isotope effects has also been reported [60].

The longer-chain $1\text{-}^{11}\text{C}$ -alkyl halides [61–64], $\alpha\text{-}^{11}\text{C}$ -benzyl iodides [63, 65–68], $[2\text{-}^{11}\text{C}]\text{isopropyl iodide}$ [63, 69], and $[2\text{-}^{11}\text{C}](2\text{-iodoethyl})\text{benzene}$ [70] have also been

reported as ^{11}C -alkylating agents. These are most often prepared using processes analogous to the wet method for $[^{11}\text{C}]\text{CH}_3\text{I}$ radiosynthesis. $[^{11}\text{C}]\text{CO}_2$ is first reacted with freshly prepared alkyl- or phenyl-Grignard reagents to generate a ^{11}C -carboxylate species, and then reduced with LiAlH_4 and iodinated with concentrated aq. HI to produce the corresponding ^{11}C -alkyl halides (Figure 7.6a).

Långström and co-workers have also reported the radiosyntheses of $[2\text{-}^{11}\text{C}]\text{ethyl iodide}$ [71], $[1\text{-}^{11}\text{C}]\text{propyl iodide}$, and $[1\text{-}^{11}\text{C}]\text{butyl iodide}$ [72] from $[^{11}\text{C}]\text{CO}$ rather than $[^{11}\text{C}]\text{CO}_2$ in an effort to obtain ^{11}C -alkylated products with higher molar activities. $[^{11}\text{C}]\text{Ethyl iodide}$ was formed in 55% RCY via Pd(0)-catalysed ^{11}C -carbonylation reaction with CH_3I , followed by hydride reduction of the intermediate mixture of $[2\text{-}^{11}\text{C}]\text{acetic acid}$ and methyl $[2\text{-}^{11}\text{C}]\text{acetate}$ (Figure 7.6b). $[1\text{-}^{11}\text{C}]\text{Propyl}$ and $[1\text{-}^{11}\text{C}]\text{butyl iodide}$ were obtained in 58% and 34% RCY, respectively, via Pd(0)-catalysed formylation of ethene or propene with $[^{11}\text{C}]\text{CO}$ and H_2 , followed by hydride reduction and iodination of the intermediate alkyl aldehyde/carboxylic acid mixture (Figure 7.6c). Sterically more hindered 1-iodo-2- $[^{11}\text{C}]\text{methylpropane}$ was prepared in 59% RCY over three steps from $[^{11}\text{C}]\text{CO}_2$ using a Grignard reaction as a key transformation.

7.2.2.5 $[^{11}\text{C}]\text{Hydrogen Cyanide}$

$[^{11}\text{C}]\text{Hydrogen cyanide}$ ($[^{11}\text{C}]\text{HCN}$) production was first reported by Cramer and Kistiaowsky in 1940 via high-temperature reaction of $[^{11}\text{C}]\text{CO}_2$ with potassium metal and ammonia within a sealed tube reactor [73, 74]. Today, it is usually synthesized via the platinum catalysed reaction of $[^{11}\text{C}]\text{CH}_4$ with ammonia at $\sim 1000^\circ\text{C}$ (Figure 7.7) [74–76].

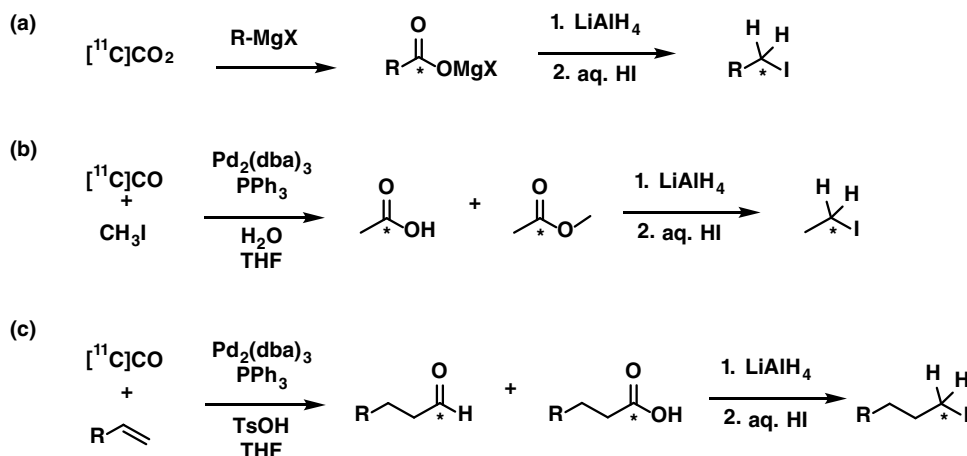


Figure 7.6 Synthesis of longer chain $[^{11}\text{C}]\text{alkyl iodides}$ from $[^{11}\text{C}]\text{CO}_2$ or $[^{11}\text{C}]\text{CO}$.

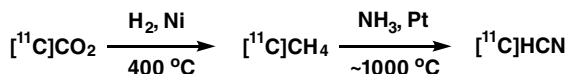


Figure 7.7 Radio-synthesis of $[^{11}\text{C}]\text{HCN}$.

Residual NH_3 , which interferes with subsequent reactions, is removed through an in-line P_2O_5 trap. The synthesis is reproducible and gives yields of over 95% [74, 76]. Direct production of $[^{11}\text{C}]\text{HCN}$ in a cyclotron target filled with nitrogen and hydrogen (1%) has also been reported [77].

7.2.2.6 $[^{11}\text{C}]\text{Phosgene}$

$[^{11}\text{C}]\text{Phosgene}$ ($[^{11}\text{C}]\text{COCl}_2$) is a versatile labelling reagent; however, its synthesis requires specialized apparatus that has restricted its widespread use. Initial methods to access $[^{11}\text{C}]\text{COCl}_2$ utilised $[^{11}\text{C}]\text{CO}$ as a starting material, via reaction with PtCl_4 at 280°C [78, 79], or direct reaction with chlorine gas under UV irradiation [80–82]; however, low molar activities were observed due to $[^{12/13}\text{C}]\text{CO}$ contamination arising from PtCl_4 or Cl_2 (Figure 7.8a).

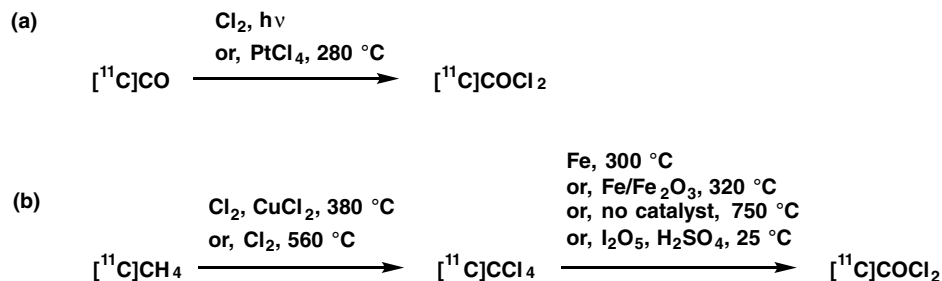
In 1987, Landais et al. reported an alternative synthesis starting from $[^{11}\text{C}]\text{CH}_4$. In this method, $[^{11}\text{C}]\text{CH}_4$ is reacted with Cl_2 in the presence of a CuCl_2 catalyst to give $[^{11}\text{C}]\text{CCl}_4$, which is then oxidised by an iron catalyst to $[^{11}\text{C}]\text{COCl}_2$ [83]. Moderate molar activities ($<40\text{ GBq}\cdot\mu\text{mol}^{-1}$) were reported [83, 84], which could be significantly improved by removing the CuCl_2 and increasing the temperature of the chlorination oven [85]. An improvement in yield for the second step was subsequently reported through the use of an $\text{Fe}/\text{Fe}_2\text{O}_3$ catalyst for the oxidation of $[^{11}\text{C}]\text{CCl}_4$ [86] and, in a further iteration, in the absence of catalyst at 750°C [87]. In 2010, Ogawa et al. reported the room-temperature conversion of $[^{11}\text{C}]\text{CCl}_4$ to $[^{11}\text{C}]\text{COCl}_2$ using a Kitagawa gas detector tube filled with I_2O_5 and fuming H_2SO_4 (Figure 7.8b) [88].

7.2.2.7 $[^{11}\text{C}]\text{Formaldehyde}$

$[^{11}\text{C}]\text{Formaldehyde}$ ($[^{11}\text{C}]\text{HCHO}$) is usually produced through the reduction of $[^{11}\text{C}]\text{CO}_2$ to $[^{11}\text{C}]\text{CH}_3\text{OH}$ followed by partial re-oxidation in the presence of a catalyst such as ferric molybdenum oxide [89], silver [90, 91], or XeF_2 [92] (Figure 7.9a). Enzymatic oxidation has been used to convert $[^{11}\text{C}]\text{CH}_3\text{OH}$ to $[^{11}\text{C}]\text{HCHO}$ [93, 94]; however, the product is obtained as an aqueous solution, which may limit its subsequent reactivity.

The solution-phase reduction of $[^{11}\text{C}]\text{CO}_2$ using LiAlH_4 is likely to contribute to low molar activities, leading the Fowler group to develop an alternative method utilizing high molar activity $[^{11}\text{C}]\text{CH}_3\text{I}$ as the starting reagent [95]. In this approach, trimethylamine *N*-oxide was used to convert $[^{11}\text{C}]\text{CH}_3\text{I}$ to $[^{11}\text{C}]\text{HCHO}$ in 89% RCY in a reproducible and robust process, with no erosion of molar activity (Figure 7.9b).

Figure 7.8 Radio-synthesis of $[^{11}\text{C}]\text{phosgene}$.



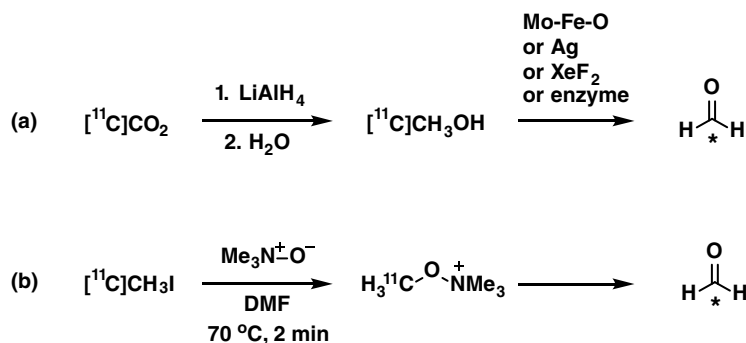


Figure 7.9 Radio-synthesis of $[^{11}\text{C}]$ formaldehyde.

7.2.2.8 $[^{11}\text{C}]$ Carbon Disulfide

The production of $[^{11}\text{C}]\text{CS}_2$ was first reported in 1984 by Niisawa and co-workers via microwave discharge of $[^{11}\text{C}]\text{CO}_2$ in hydrogen sulfide gas [96]; however, $[^{11}\text{C}]\text{CS}_2$ did not receive further attention until Miller et al. reported new methods (Figure 7.10) for its production from $[^{11}\text{C}]\text{CH}_3\text{I}$ in 2012 [97]. In their first report, $[^{11}\text{C}]\text{CS}_2$ was generated by gas-phase reaction of $[^{11}\text{C}]\text{CH}_3\text{I}$ with P_2S_5 at $400\text{ }^\circ\text{C}$. An improved method in which the toxic and malodorous P_2S_5 was replaced with elemental sulfur was subsequently reported, allowing for the rapid, quantitative formation of $[^{11}\text{C}]\text{CS}_2$ at $500\text{ }^\circ\text{C}$ [98].

7.2.2.9 Other Secondary Precursors

7.2.2.9.1 $[^{11}\text{C}]$ Fluoroform

The CF_3 group is present in many pharmaceuticals; however, existing radiolabelling approaches using fluorine-18 suffer from poor molar activities, leading Haskali and Pike to develop a novel carbon-11 radiolabelling approach using high molar activity $[^{11}\text{C}]$ fluoroform ($[^{11}\text{C}]\text{CF}_3\text{H}$) [99]. In this process, $[^{11}\text{C}]\text{CF}_3\text{H}$ can be produced in 53% RCY by passing $[^{11}\text{C}]\text{CH}_4$ through a column containing CoF_3 at $270\text{ }^\circ\text{C}$ (Figure 7.11a). The hydrofluoric acid side product is removed from the gas stream using an in-line MeCN/dry ice trap, allowing $[^{11}\text{C}]\text{CF}_3\text{H}$ to be collected in chilled ethanol or *N,N*-dimethylformamide (DMF) (Figure 7.11b).

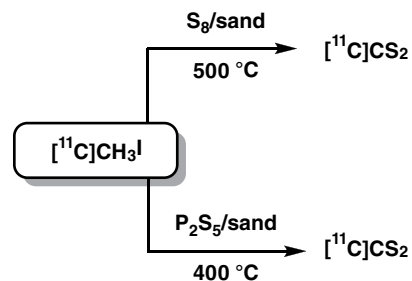


Figure 7.10 Radio-synthesis of $[^{11}\text{C}]$ carbon disulfide.

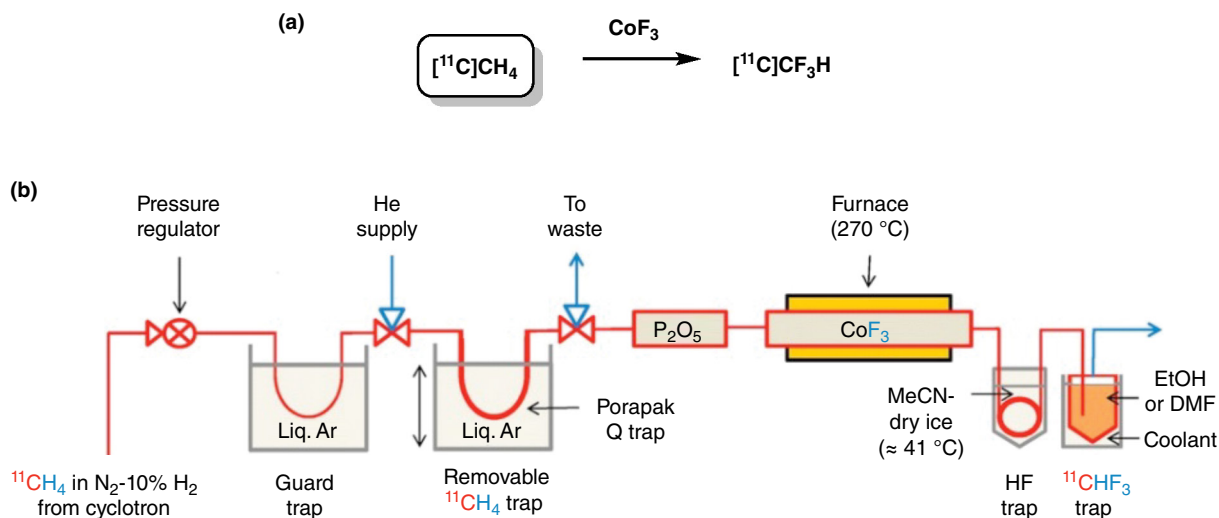


Figure 7.11 Apparatus for producing $[^{11}\text{C}]\text{CHF}_3$ from $[^{11}\text{C}]\text{CH}_4$ and CoF_3 . Source: From Mohammad B. Haskali, et. al. (2017). Reproduced with permission of John Wiley & Sons.

7.2.2.9.2 $[^{11}\text{C}]\text{Nitromethane}$

The solution-phase synthesis of $[^{11}\text{C}]\text{nitromethane}$ ($[^{11}\text{C}]\text{CH}_3\text{NO}_2$) was first reported by Schoeps et al. [100] in 1988 via reaction of $[^{11}\text{C}]\text{CH}_3\text{I}$ with AgNO_2 , and a year later as a gas-phase process using a AgNO_2 column at 80°C , as shown in Figure 7.12a [101]. The reaction is fast and typically uses an additional NaHCO_3 column, which is attached to the AgNO_2 outlet to help remove nitrogen oxide by-products of pyrolysis. Longer-chain ^{11}C -alkyl iodides could also be converted to the respective nitro species in 50–70% RCY (based on ^{11}C -alkyl iodide).

7.2.2.9.3 $[^{11}\text{C}]\text{Diazomethane}$

In 1986, Crouzel et al. reported the radiosynthesis of $[^{11}\text{C}]\text{diazomethane}$ ($[^{11}\text{C}]\text{CH}_2\text{N}_2$) in a two-step process from $[^{11}\text{C}]\text{CH}_4$ (Figure 7.12b) [102]. In the first step, $[^{11}\text{C}]\text{CH}_4$ undergoes partial chlorination at 310°C , giving rise to $[^{11}\text{C}]\text{CHCl}_3$, which is then delivered to a solution of hydrazine and KOH in ethanol. $[^{11}\text{C}]\text{CH}_2\text{N}_2$ was obtained in 30% RCY and molar activities of up to $130\text{GBq}\cdot\mu\text{mol}^{-1}$.

7.2.2.9.4 $[^{11}\text{C}]\text{Methyl Azide}$

$[^{11}\text{C}]\text{Methyl azide}$ ($[^{11}\text{C}]\text{CH}_3\text{N}_3$) can be formed in one step from $[^{11}\text{C}]\text{CH}_3\text{I}$, as shown in Figure 7.12c, providing the opportunity to perform Huisgen cycloaddition reactions with alkynes to form ^{11}C -labelled 1,2,3-triazoles. $[^{11}\text{C}]\text{CH}_3\text{N}_3$ synthesis was first reported by Schirmacher et al. in 2008 through reaction of $[^{11}\text{C}]\text{CH}_3\text{I}$ with NaN_3 in a solution containing the 18-crown-6 cryptand [103] and was later performed on a cartridge containing $\text{Na}^+/\text{15-crown-5}/\text{N}_3^-$ in acetonitrile [104].

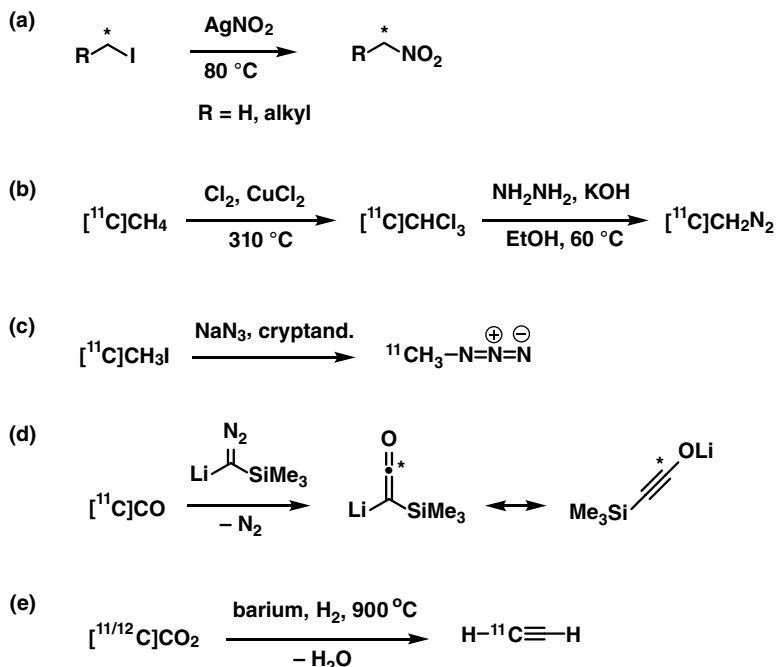


Figure 7.12 Radio-syntheses of secondary precursors. (a) [^{11}C]nitromethane; (b) [^{11}C]diazomethane; (c) [^{11}C]methyl azide; (d) lithium [^{11}C]trimethylsilylynolate; (e) [^{11}C]acetylene.

7.2.2.9.5 [^{11}C]Ynolates

Ynolates are triple-bond analogues of enolates, which may be promising reagents for ketylation reactions in radiotracer synthesis. The synthesis of lithium [^{11}C]trimethylsilylynolate (Figure 7.12d) has been reported by reaction of [^{11}C]CO with in situ-prepared lithiated silyldiazomethane [105].

7.2.2.9.6 [^{11}C]Acetylene

Acetylene is a useful reagent in organic synthesis; however, its complex synthesis with ^{11}C has limited its use as a radiolabelling reagent. In 2005, Nazih et al. [106] reported a simplified synthetic procedure based on the method described by Madsen et al. [107]. In this process, [$^{11/12}\text{C}$]CO₂ is trapped at room temperature on barium within a quartz reaction tube and then heated to 900°C under hydrogen flow to produce [^{11}C]acetylene in 50–75% RCY and with molar activities of up to 6 GBq·μmol⁻¹ (Figure 7.12e).

7.3 TECHNOLOGICAL INNOVATIONS IN LABELLING METHODS

7.3.1 The “On-Cartridge” Method

Early ^{11}C -methylation reactions involved trapping the labelling agent in a solution containing the precursor within a small reaction vial. This technique remains widely used and

is regularly incorporated into automated processes. Since this method involves multiple time-consuming transfers of reagents to and from the reactor, intermediate vials, and the purification system, it is susceptible to incomplete transfer of materials and hence diminished RCYs.

Efforts to streamline these processes led to the development of reactions that take place on an inert solid support, known as “on-cartridge” reactions. Three variations of such on-cartridge reactions have been described. First, the precursors for radiolabelling may be loaded onto an inert solid support, such as polymer resins [108, 109], silica [110], C₁₈-modified silica [111], or stainless steel powder [112]. After loading with precursor, a small volume of solvent, gaseous [¹¹C]CH₃I or [¹¹C]CH₃OTf in N₂ carrier gas, is gently flowed over the solid support, where the reaction then takes place. Second, [¹¹C]CH₃I or [¹¹C]CH₃OTf can be trapped on the solid support and a solution of the precursor flowed over the trapped ¹¹C-methylating agent. Third, the precursor may be covalently attached to a solid support, which is then released after reaction with the labelling agent [113]. This strategy is attractive as unreacted precursor remains resin bound, and purification of the ¹¹C-labelled product is greatly simplified. For all methods, once the reaction is complete, the entire reaction mixture can be eluted into the purification system to isolate the ¹¹C-labelled product.

The principal advantage of using the on-cartridge method lies in the speed with which ¹¹C radiopharmaceuticals can be produced. Transfers of the reaction mixture are minimized, as are losses of the volatile ¹¹C-methylating agents into the headspace of the reactor, all contributing to improving both RCY and molar activities, whilst being amenable for transfer into a simple “kit” form [114]. The on-cartridge method has been used for the synthesis of a number of radiopharmaceuticals, including [¹¹C]methyl jasmonate [115], [*methyl*-¹¹C]-L-methionine [116, 117], [*N-methyl*-¹¹C]choline [116, 118, 119], and [¹¹C]Pittsburgh compound B ([¹¹C]PIB) [114].

7.3.2 The “Loop” Method

Wilson et al. [17, 120, 121] described the “loop” method for radiosynthesis, where the precursor in a suitable solvent was coated as a thin film onto the inner surface of a high-performance liquid chromatography (HPLC) loop connected directly to an HPLC purification system. [¹¹C]CH₃I was then passed through the loop in a stream of inert gas and trapped in the thin solvent film, where it underwent rapid reaction with the precursor. The reaction mixture could then be directly eluted onto the HPLC system for purification. At the same time, Iwata et al. [122, 123] described a similar procedure using a dedicated polytetrafluoroethane (PTFE) loop. The large surface area presented by the thin film of precursor/solvent on the inner surface of the loop ensures efficient trapping of the labelling agent, while the resultant high concentration of precursor in the film ensures a rapid reaction even in the absence of heating.

The loop method is particularly attractive due to its operational simplicity, and it can be easily incorporated into existing commercial synthesis systems (Figure 7.13) [50, 124, 125] or used with cheaper dedicated automated systems [126, 127]. The use of EtOH as

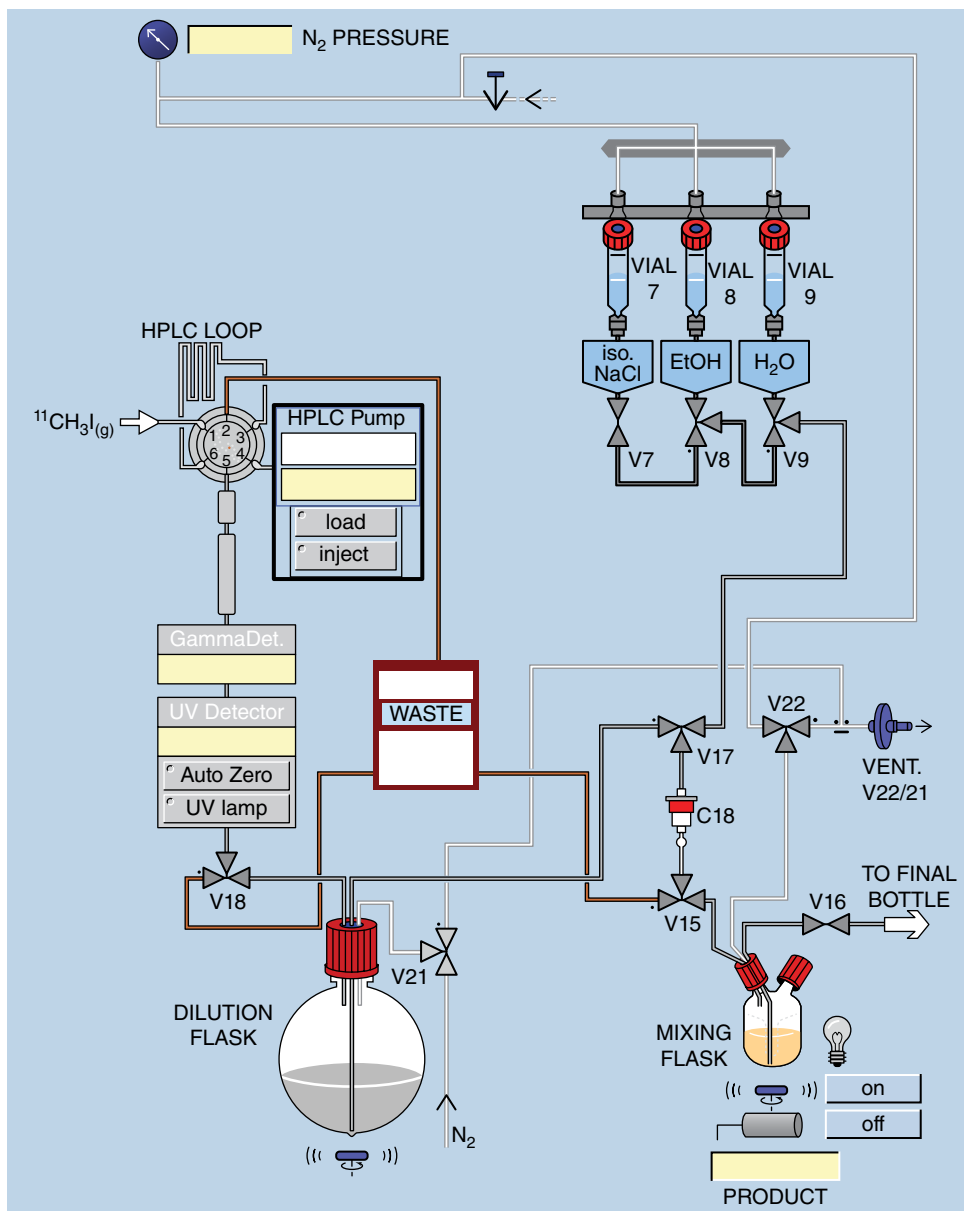


Figure 7.13 Modification of a commercial GE FxFN module for “loop” synthesis. Source: Wilson, A.A., Garcia, A., Houle, S., and Vasdev, N. [124] © 2009 John Wiley & Sons.

a solvent for both trapping and purification has made the process practically simpler by eliminating the reformulation step [128]. A number of radiotracers, including [¹¹C] raclopride, [¹¹C] rolopram, [¹¹C] 3-amino-4-(2-dimethylaminomethylphenylsulfanyl)-benzotrile ([¹¹C]DASB), [¹¹C] PIB [129], [*methyl*-¹¹C]-L-methionine [130], [¹¹C] carfentanil [131], [¹¹C] methylphenidate [132], and [¹¹C] metomidate [133], have all been prepared using the loop method, in generally greater RCY compared with vial-based methods.

7.3.3 Microfluidic Chemistry

There have been numerous efforts to adapt more PET radiosyntheses for operation using microfluidic devices. The advantages include inherent compatibility with small masses and volumes of reagents, improved heat transfer, and facile automation [134–137]. The first application in ^{11}C synthesis of ^{11}C -methyl esters from carboxylic acids was accomplished in 65% RCY using a $0.2\ \mu\text{l}$ T-shaped microreactor. The precursor and a base in DMF (5 mM) were infused by syringe pump through one arm of the T, and $[^{11}\text{C}]\text{CH}_3\text{I}$ was infused through the other arm [138]. Similarly, $[^{11}\text{C}]\text{DASB}$ [139] and $[^{11}\text{C}]\text{raclopride}$ [140, 141] were prepared using microfluidic methods.

7.3.4 Purification and Quality Control of Carbon-11-Radiolabelled Products

The time taken to purify and perform quality control of the resultant ^{11}C radiopharmaceutical contributes to the total synthesis time, and time savings at these steps can lead to significant improvements in RCY and molar activity of the final product [142].

Solid-phase extraction (**SPE**) has proven useful for radiotracers such as [*N*-methyl- ^{11}C]choline and 2 β -carbomethoxy-3 β -(4-fluorophenyl) [*N*-methyl- ^{11}C]tropane ($[^{11}\text{C}]\beta\text{-CFT}$), where large differences in polarity between the precursor and the ^{11}C -labelled product exist [143]. Owing to the large difference in the amount of precursor and radiolabelled product (mg vs. μg), the precursor peak often tails into the product peak using conventional reverse-phase HPLC. To circumvent this problem, modified reverse-phase HPLC stationary phases [144] or hydrophilic interaction chromatography (**HILIC**) [145] has been used to develop methods where the ^{11}C -labelled product elutes *before* the precursor. Such an approach has been used for the purification of $[^{11}\text{C}]\text{raclopride}$, $[^{11}\text{C}]\text{FLB457}$, $[^{11}\text{C}]\text{carfentanil}$, $[^{11}\text{C}]\text{DASB}$, $[^{11}\text{C}]\text{WAY1000635}$, and $[^{11}\text{C}]\text{SCH23390}$.

Additional improvements toward reducing the time taken for quality-control testing include: (i) use of shorter columns packed with smaller particles, where analysis times can be reduced to as little as one minute [145]; (ii) use of ultra-high performance liquid chromatography-based methods where analysis times are 2–3 minutes [146]; and (iii) use of liquid chromatography with tandem mass spectrometry methods, as reported by Shetty et al. [147], which allows for the simultaneous determination of radiopharmaceutical identity, molar activity, and half-life.

7.4 METHODOLOGY FOR THE INCORPORATION OF CARBON-11 INTO BIOACTIVE MOLECULES

7.4.1 Reactions with $[^{11}\text{C}]\text{CO}_2$

CO_2 is a centrosymmetric molecule with no overall dipole, rendering it a weak electrophile with poor solubility in organic solvents. To compensate for its low reactivity, large stoichiometric excesses and/or high pressures are often employed during reactions with

CO₂; however, this is not feasible for radiolabelling experiments due to the small quantities of [¹³C]CO₂ available. Consequently, the direct use of [¹³C]CO₂ was initially limited to Grignard-type chemistry involving highly reactive nucleophiles. In the last decade, however, new synthetic methodologies have been developed using non-nucleophilic bases as fixation agents, which serve to dramatically enhance [¹³C]CO₂ solubility and reactivity.

7.4.1.1 Carboxylation Using Reactive Nucleophiles

7.4.1.1.1 ¹³C–C Bond Formation

Grignard reagents react rapidly with [¹³C]CO₂ and are trapped in solution through the rapid formation of the corresponding magnesium ¹³C-carboxylate species. These may be quenched or further derivatised as required using a variety of methods (Figure 7.14a–d), including: (a) aqueous workup to produce the corresponding *carboxyl*-¹³C-carboxylic acid [148], e.g. [¹³C]acetate [149, 150] and [¹³C]palmitate [108, 150]; (b) heating the carboxylate with primary or secondary amines to produce *carboxyl*-¹³C-amides [151], which can be subsequently reduced using NaBH₄ to yield ¹³C-labelled tertiary amines [152]; (c) reaction with activating agents such as thionyl chloride or phthaloyl dichloride to produce *carboxyl*-¹³C-acid chlorides, e.g. [¹³C]acetyl chloride [153], [¹³C]propionyl chloride [154, 155], ¹³C-cycloalkanecarbonyl chlorides [156–158], and [¹³C]acryloyl chloride [159], which are used as ¹³C-acylating reagents to generate ¹³C-amides or ¹³C-esters via reaction with amines or alcohols; and (d) reduction of the carboxylate intermediate using LiAlH₄, followed by halogenation, to give access to 1-¹³C-alkyl halides, which can then be used as ¹³C-alkylating reagents in subsequent reactions [64, 160].

Organolithium reagents are more reactive than Grignard reagents and can undergo double addition with [¹³C]CO₂ to form *carboxyl*-¹³C-ketones; however, careful control of reaction conditions is required to avoid side reactions. For example, [¹³C]acetone may be obtained via reaction of methyl lithium with [¹³C]CO₂, followed by hydrolysis (Figure 7.14e) [161–163]. [¹³C]Acetone is a useful building block for the introduction of *N*-isopropyl groups via reductive alkylation [163] and has been used to radiolabel tracers such as [¹³C]practolol [164] and [¹³C]pindolol [165]. ¹³C-Carboxylation of ^tBuLi produces lithium [¹³C]pivalate, which has been used to radiolabel a ^tBu-substituted benzimidazole [166].

7.4.1.1.2 ¹³C–H Bond Formation

¹³C–H bond formation can be achieved by reaction of metal hydrides with [¹³C]CO₂: LiAlH₄ gives rise to [¹³C]methanol (Figure 7.15a), which forms the basis of the wet method for [¹³C]methyl iodide production [16] (see Section 7.2.2.2.1). LiEt₃BH partially reduces [¹³C]CO₂ to give lithium [¹³C]formate, which can then be alkylated, providing ¹³C-formate esters (Figure 7.15b) [29]. These can be used as ¹³C-formylating reagents, as exemplified by the synthesis of [¹³C]benzimidazole [167].

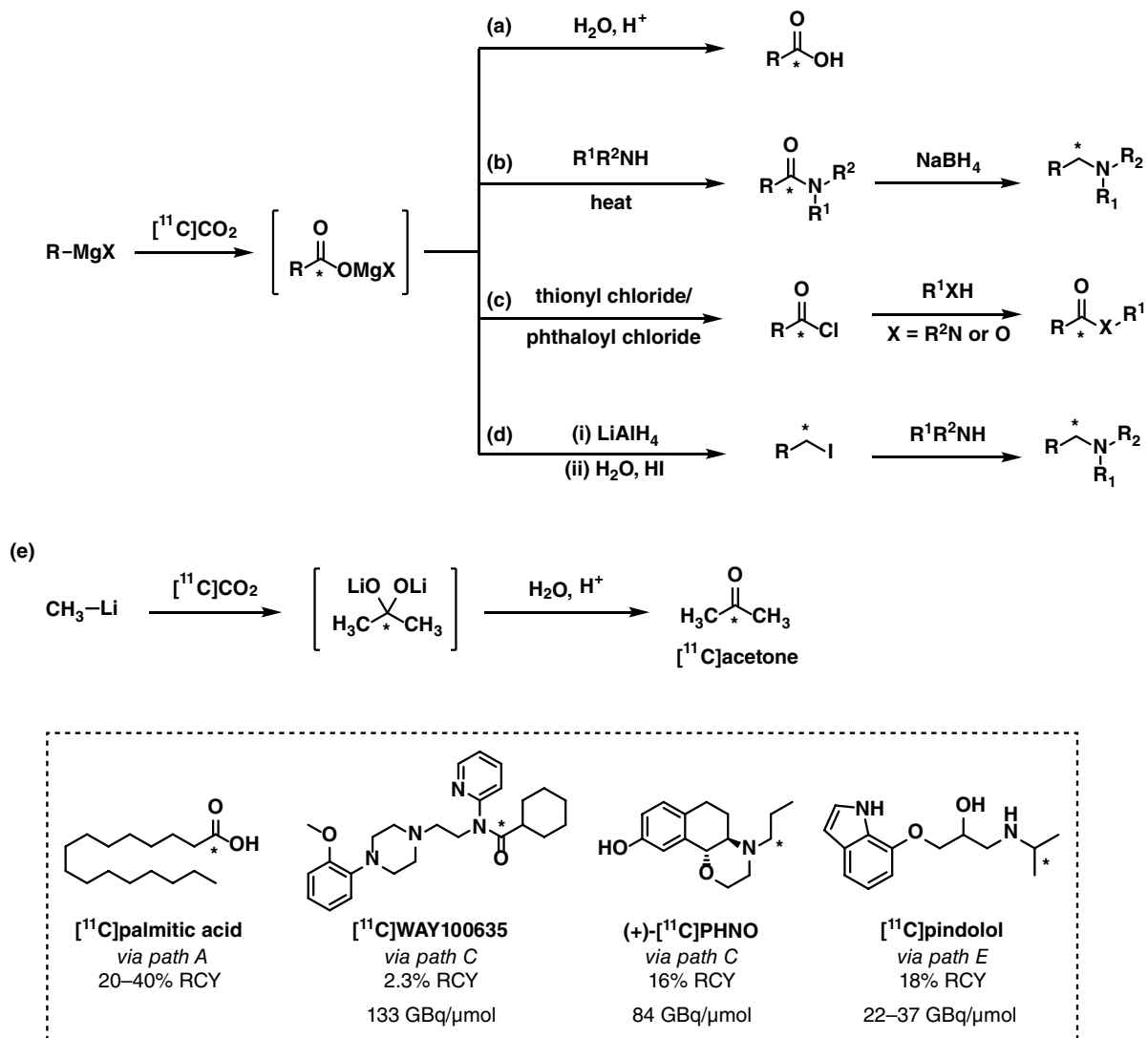
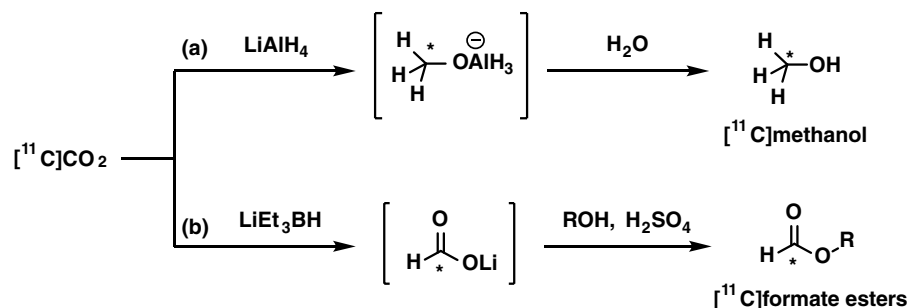


Figure 7.14 Reactions of [¹¹C]CO₂ with organometallic reagents.

Figure 7.15

Reaction of [¹¹C]CO₂ with metal hydride reagents.



7.4.1.1.3 ^{11}C –N Bond Formation

Deprotonated amine bases can react directly with $[^{11}\text{C}]\text{CO}_2$ at room temperature, as demonstrated by Chakraborty et al. in their synthesis of *carbonyl*- ^{11}C urea using lithium bis(trimethylsilyl)amide (LiHMDS) (Figure 7.16a) [168]. This reaction proceeds via a ^{11}C -carbodiimide intermediate, which is subsequently hydrolysed to produce $[^{11}\text{C}]\text{urea}$; however, the scope of this methodology cannot be extended to the formation of substituted ^{11}C -ureas.

Van Tilberg et al. showed the viability of the aza-Wittig reaction for ^{11}C -carboxylations using commercially available phenyl triphenylphosphinimine [169]. Quantitative $[^{11}\text{C}]\text{CO}_2$ trapping was observed at -60°C , and the resultant phenyl $[^{11}\text{C}]\text{isocyanate}$ underwent reaction with various amines to produce unsymmetrical *carbonyl*- ^{11}C -ureas in non-isolated RCYs of 8–49% (Figure 7.16b). In 2018, Del Vecchio et al. used this methodology to form cyclic *carbonyl*- ^{11}C -ureas in 25–85% non-isolated RCY from in situ generated phosphinimines, synthesised by reaction of *o*-azidoanilines with dimethylphenylphosphine (Figure 7.16c) [170]. A variety of aliphatic unsymmetrical ^{11}C -ureas as well as five pharmaceutically active ^{11}C -ureas were labelled using this procedure, with isolated RCYs of 34–48% and molar activities of 32–75 GBq μmol^{-1} .

The ability of silylated amines to react with $[^{11}\text{C}]\text{CO}_2$ to give *carbonyl*- ^{11}C -carbamic acids has been exploited for ^{11}C -methylation as an alternative to $[^{11}\text{C}]\text{CH}_3\text{I}/\text{CH}_3\text{OTf}$ labelling. In the method developed by Ram et al., $[^{11}\text{C}]\text{CO}_2$ is delivered at -80°C to a solution of trimethylsilyl amine, heated to form an *O*-silylcarbamate, and then reduced using LiAlH_4 to produce the corresponding ^{11}C -methylated tertiary amine (Figure 7.16d) [171–174]. This approach has been used to synthesise radiotracers $[^{11}\text{C}]\text{imipramine}$ [171], $[^{11}\text{C}]\text{chlorpromazine}$ [172], and $[^{11}\text{C}]\text{tamoxifen}$ [174].

Direct one-pot ^{11}C -methylation of aliphatic and aromatic amines using $[^{11}\text{C}]\text{CO}_2$ has also been achieved using phenylsilane as a reductant in the presence of a zinc-*N*-heterocyclic carbene complex (Figure 7.16e) [175]. In this process, $[^{11}\text{C}]\text{CO}_2$ is delivered at 0°C to a diglyme solution containing the reducing reagents and heated at 150°C for 20 minutes to yield ^{11}C -methylated amines in 24–75% RCY. The amyloid- β imaging agent $[^{11}\text{C}]\text{PIB}$ was radiolabelled under these conditions, but with lower molar activity than that obtained via $[^{11}\text{C}]\text{CH}_3\text{OTf}$ labelling (15 GBq μmol^{-1} vs. 50 GBq μmol^{-1} , respectively).

7.4.1.2 Fixation-Agent Promoted ^{11}C -Carboxylation

In 1999, Coenen et al. reported that in the presence of a tertiary amine base, non-activated amines such as aniline could react with $[^{11}\text{C}]\text{CO}_2$ to form the corresponding *carbonyl*- ^{11}C -carbamate salts, albeit using low-temperature trapping (Figure 7.17a) [176]. Subsequent treatment of the ^{11}C -carbamate with POCl_3 and reaction with excess amine gave symmetrical ^{11}C -ureas via an intermediate ^{11}C -isocyanate. The use of amines to improve $[^{11}\text{C}]\text{CO}_2$ capture was also observed by van Tilburg et al. in their study on phosphinimine ^{11}C -carboxylation (vide supra) [169].

These findings, as well as advances in “green” CO_2 capture chemistry, laid the groundwork for what is arguably the most significant breakthrough in ^{11}C chemistry since the

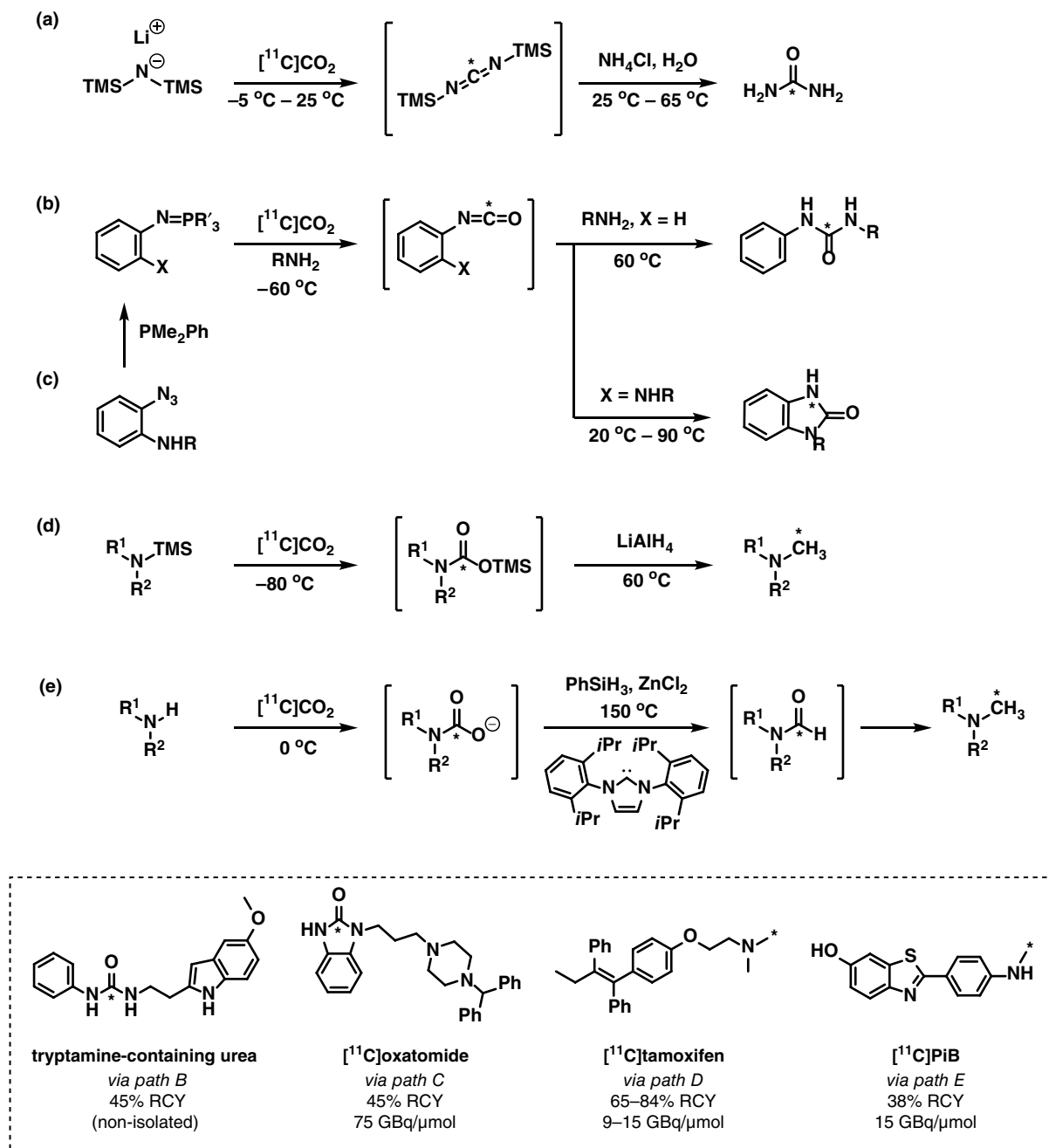


Figure 7.16 Reactions of activated amines with [¹¹C]CO₂.

advent of [¹¹C]CH₃I in the 1970s – the use of strong non-nucleophilic bases as [¹¹C]CO₂ fixation agents to promote ¹¹C-carboxylation reactions with less reactive substrates. This was first described by Hooker et al. using the amidine base 1,8-diazabicyclo[5.4.0]undec-7-ene

(DBU) [177] and then Wilson et al. using the phosphazine base 2-*tert*-butylimino-2-diethylamino-1,3-dimethylperhydro-1,3,2-diazaphosphorine (BEMP) [178], enabling $[^{11}\text{C}]\text{CO}_2$ to react rapidly under mild reactions conditions without the need for specialised laboratory apparatus (Figure 7.17b). This chemistry was applied to *carbonyl*- ^{11}C -carbamate synthesis via reaction of aliphatic primary [177] and secondary [178] amines with $[^{11}\text{C}]\text{CO}_2$ in the presence of an alkylating agent in good RCY. Anilines, however, proved to be more challenging substrates. Biologically active molecules, including the serotonin-receptor antagonist $[^{11}\text{C}]\text{metergoline}$ [177], the κ -opioid agonist $[^{11}\text{C}]\text{GR103545}$ [178], and the histone deacetylase inhibitor $[^{11}\text{C}]\text{MS-275}$ [179], have been radiolabelled using this technique.

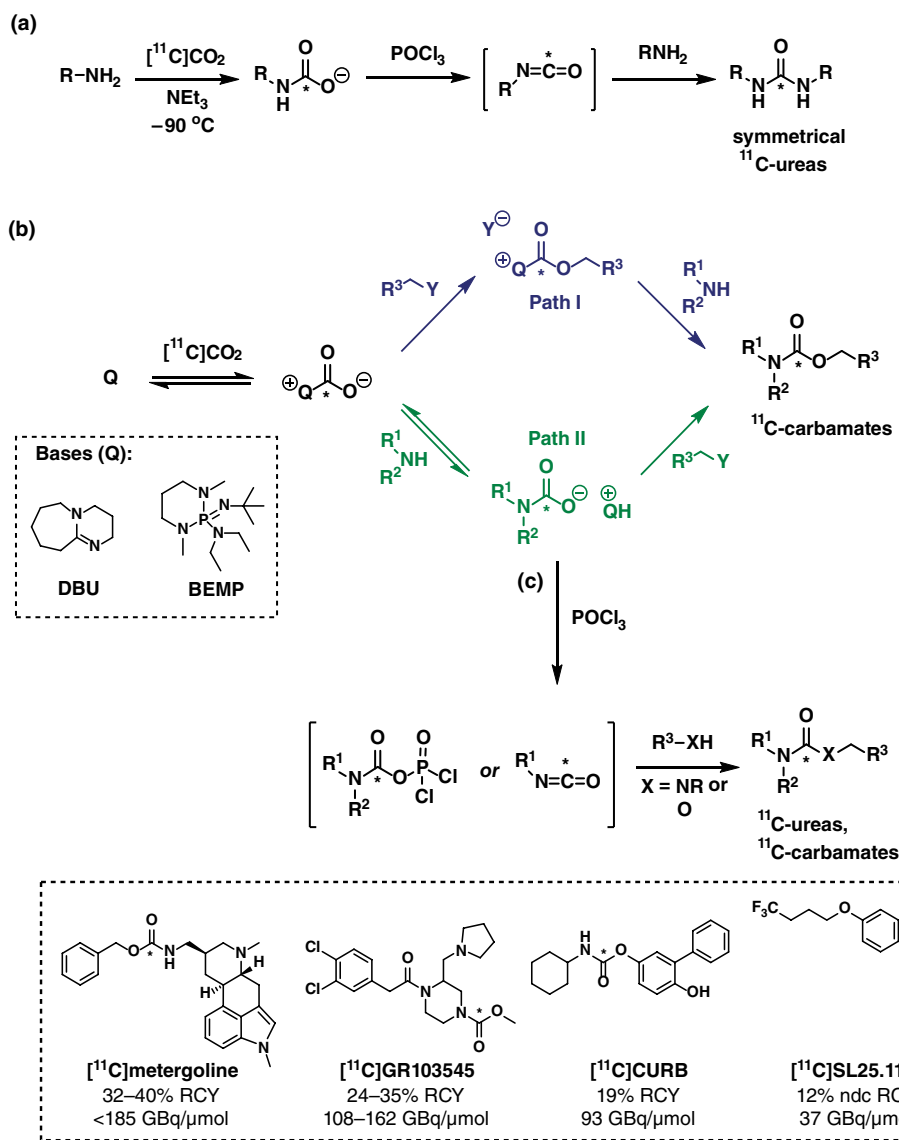


Figure 7.17
Reaction of amines with $[^{11}\text{C}]\text{CO}_2$ in the presence of fixation agents.

When evaluating DBU and BEMP as fixation agents, Wilson et al. found that the latter offered superior ^{11}C CO₂ trapping and product yields, allowing ^{11}C -carbamate formation to proceed at room temperature in approximately one minute [178]. Mechanistically, there are two possible reaction pathways following the formation of the base- ^{11}C carbamate intermediate, depending on the order of the subsequent reactions with the amine and alkylating agent (Figure 7.17b, Paths I and II). Investigating this, Wilson et al. obtained optimal product yields when the order of reagent addition was tailored to Path II (^{11}C CO₂ fixation in the presence of the amine, followed by addition of alkylating agent), and that when this order was reversed, yields were very low [178].

In 2011, Wilson et al. extended this methodology to the synthesis of unsymmetrical *carboxyl*- ^{11}C -ureas and *carboxyl*- ^{11}C -carbamates (Figure 7.17c) [180] using the dehydrating agent POCl₃ to convert the ^{11}C -carbamate intermediate into an ^{11}C -isocyanate, which can undergo reaction with a second amine or alcohol. Numerous PET tracers containing ^{11}C carbamate [180–184] and ^{11}C -urea [184–187] functional groups have been synthesized using this approach, including the clinically validated fatty acid amide hydrolase (**FAAH**) inhibitor ^{11}C CURB [188] and the monoamine oxidase B (MAO-B) inhibitor ^{11}C SL25.1188, previously only accessible in low yields from ^{11}C phosgene [189].

This methodology was later transferred to an automated “in-loop” system consisting of three HPLC loops connected to an eight-port, two-way valve (Figure 7.18) [190]. The loops are first pre-loaded with reagent solutions: reactor loop A with amine and fixation base; the reagent loop with the dehydrating agent, POCl₃; and reactor loop B with the second nucleophile (alcohol or amine). The reaction then proceeds in stages: first, ^{11}C CO₂ is passed into and fixed in reactor loop A to form the intermediate ^{11}C -carbamate ion, followed by the addition of POCl₃ into reactor loop A from the reagent loop to form the ^{11}C -isocyanate. The ^{11}C -isocyanate can then be eluted into reactor loop B, where it reacts with the nucleophile. The ^{11}C -labelled product can then

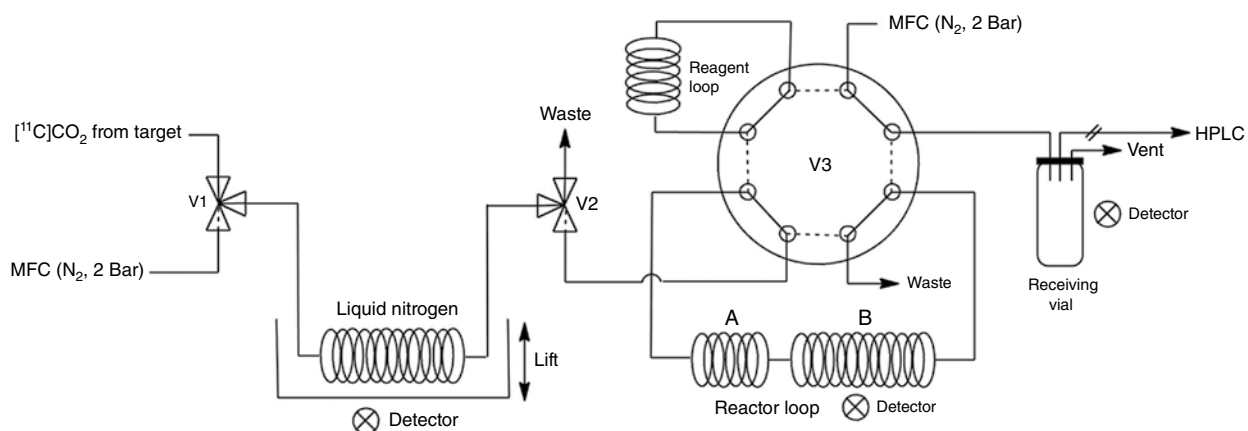


Figure 7.18 In-loop ^{11}C CO₂-fixation setup. Source: From Dahl, K., Collier, T.L., Cheng, R. et al. [190] © 2018 John Wiley & Sons.

be eluted into the receiving vial. [^{13}C]SL25.1188 and two novel FAAH inhibitors were synthesized using this method, and in all cases, non-isolated RCYs were higher than for the corresponding vial reactions.

Dheere et al. reported an alternative pathway to access symmetrical [191] and unsymmetrical [192] *carbonyl*- ^{13}C -ureas, utilising the Mitsunobu reaction to facilitate reaction of poorly nucleophilic amines such as anilines (Figure 7.19a). This reaction proceeds in three stages: (i) DBU-mediated [^{13}C]CO₂ fixation to form a ^{13}C -carbamate intermediate, (ii) addition of Mitsunobu reagents (tributylphosphine and di-*t*-butyl azodicarboxylate) to form an oxyphosphonium species, and (iii) reaction with a second amine upon gentle heating. This provides ^{13}C -ureas in high RCYs of 69–94%. The scope of this methodology was later extended to the production of ^{13}C -amides via reaction of the oxyphosphonium intermediate with Grignard reagents (Figure 7.19b) and applied to the synthesis the hormone [^{13}C]melatonin [193]. In 2018, Downey et al. performed a proof-of-concept loop-based Mitsunobu radiolabelling reaction to synthesise the model compound *N,N'*-[*carbonyl*- ^{13}C]dibenzylurea with a RCY of 72%, in a process lasting only three minutes [194].

7.4.1.3 C–C Bond Formation via Boronic Esters

Base-mediated [^{13}C]CO₂ fixation chemistry has also been exploited for ^{13}C –C bond formation, providing a milder alternative to Grignard chemistry. This was first reported in 2012 by Riss et al. using boronic esters to form *carbonyl*- ^{13}C -carboxylic acids through a copper(I)-mediated process (Figure 7.20) [195]. Boronic esters can be incorporated onto highly functionalised molecules and are less sensitive to moisture and oxygen than Grignard reagents, allowing for easier handling and storage. Tetramethylethylenediamine (**TMEDA**), acting as both fixation agent and chelating ligand for copper, was identified as the optimal base, providing near-quantitative [^{13}C]CO₂ trapping and high yields for a broad range of functionalised ^{13}C -carboxylic acids, with electron-deficient and amino-substituted aromatics being the most challenging substrates. ^{13}C -Carboxylic acids could be further derivatised in a one-pot process using alkylating, chlorinating, or coupling agents (Figure 7.20a–c), as exemplified by the synthesis an oxytocin receptor ligand [195], the retinoic acid X receptor agonist [^{13}C]bexarotene [196], the μ -opioid agonist [^{13}C]AH-7921 [197], and a ligand for γ -hydroxybutyric acid (GABA) binding sites 3-hydroxycyclopent-1-ene-[^{13}C]carboxylic acid [198].

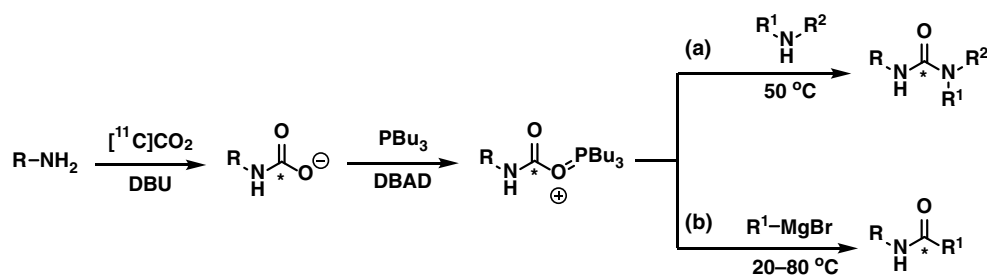
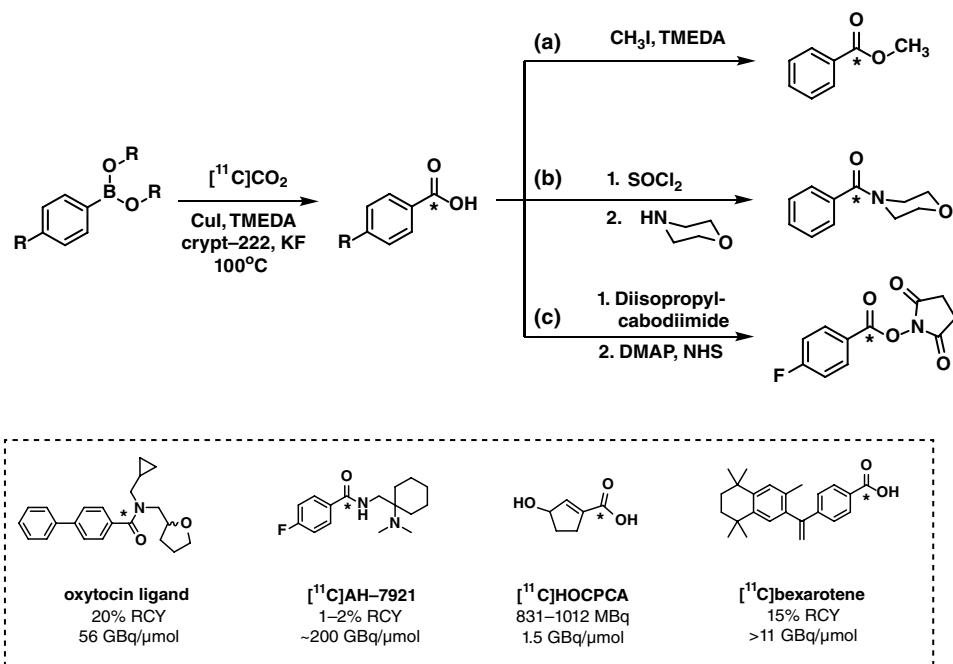


Figure 7.19 [^{13}C]CO₂ fixation and subsequent Mitsunobu reaction to form [^{13}C]ureas and [^{13}C]amides.

Figure 7.20 Cu(I)-mediated ^{11}C -carboxylation of boronic esters and subsequent derivatisation reactions.



7.4.2 Reactions with [^{11}C]CO

[^{11}C]CO was one of the very first ^{11}C radiotracers to be investigated in humans [7]; yet despite its ease of production and the prevalence of the carbonyl group in biologically relevant molecules, it was not exploited as a radiolabelling reagent until relatively recently due to the challenges associated with its handling and reactivity. The poor solubility of CO in common organic solvents means conventional carbonylations are typically performed using a large stoichiometric excess of CO and often require high temperatures, elevated pressures, and extended reaction times; conditions that are difficult to achieve with low-mass, low-concentration [^{11}C]CO. These conditions, however, allow for the use of stoichiometric catalyst loadings, favouring increased reaction rates and fast conversions.

The palladium(0)-catalysed Heck carbonylation [199, 200], which couples an electrophile and a nucleophile with CO, has been extensively investigated for ^{11}C -radiolabelling due to its compatibility with a wide range of nucleophilic substrates (Figure 7.21). Early attempts involved Stille-type coupling of organotin reagents and aryl halides to generate *carbonyl*- ^{11}C -ketones, following delivery of [^{11}C]CO at atmospheric pressure (Figure 7.21a) [201–203]. While ^{11}C -ketones were generally produced in high radiochemical purity, RCYs were low (~10%), with the majority of [^{11}C]CO passing unreacted through the solution. The principal challenge in ^{11}C -carbonylation chemistry, therefore, is to transfer sufficient quantities of [^{11}C]CO into solution in order to react. Over the years, a number of technological and chemical approaches have been developed to overcome this problem.

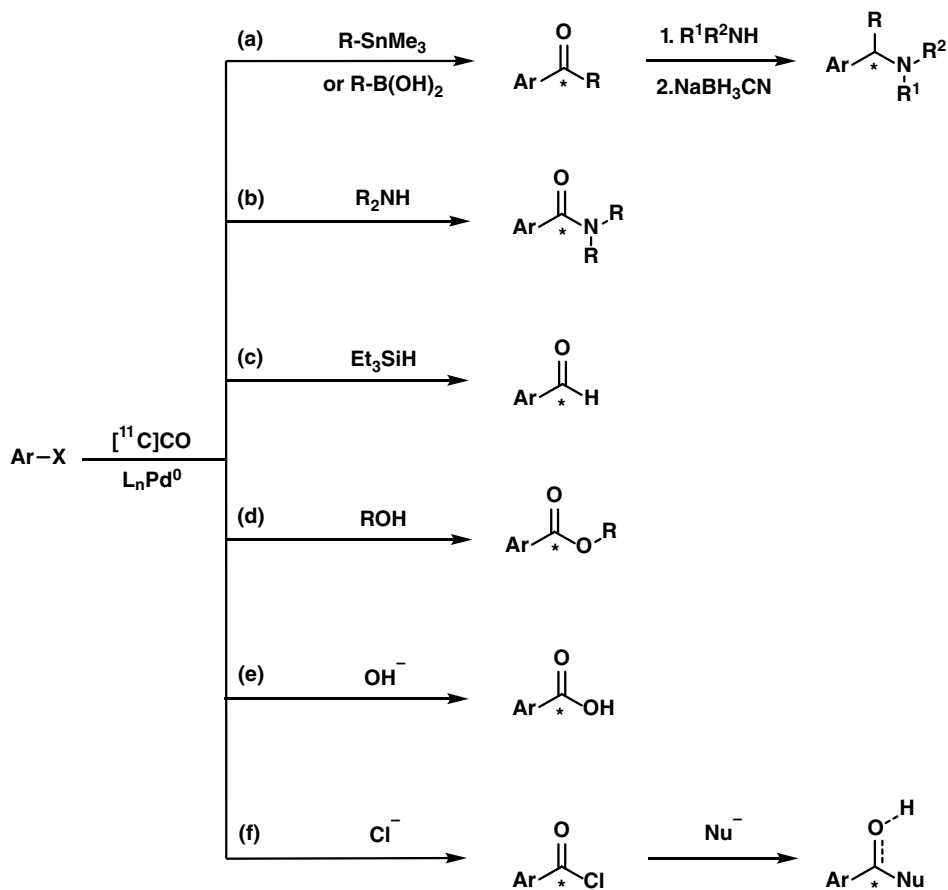


Figure 7.21 Scope of palladium(0)-catalysed ^{11}C -carbonylation reactions.

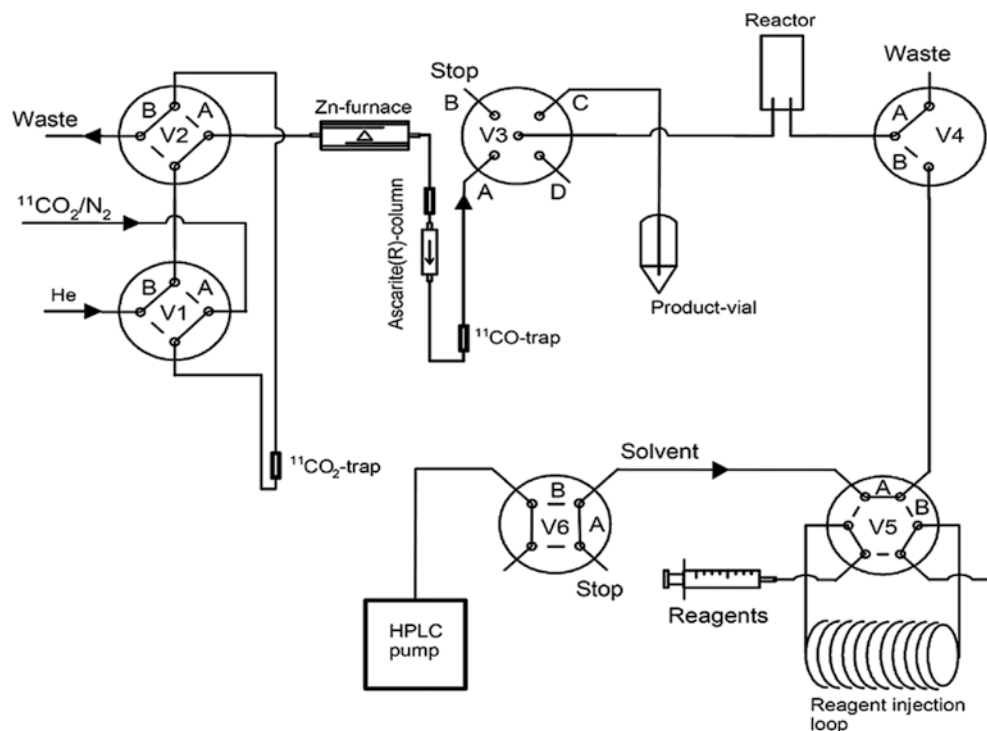
7.4.2.1 Preconcentration and Recirculation Systems

Preconcentrating $[\text{}^{11}\text{C}]\text{CO}$ on a liquid-nitrogen-cooled silica trap prior to delivery to the reaction media has been reported to increase $[\text{}^{11}\text{C}]\text{CO}$ incorporation to around 30–40% [204, 205]. A gas-handling system in which $[\text{}^{11}\text{C}]\text{CO}$ is recirculated through the reagent solution leads to a further improvement, enabling ^{11}C -ketones to be obtained in 36–62% RCY [204].

7.4.2.2 High-Pressure Carbonylation Methods

An alternative means of increasing $[\text{}^{11}\text{C}]\text{CO}$ solubility is to increase the gas pressure within a sealed vessel. To achieve this, Långström et al. developed a micro-autoclave reactor capable of performing ^{11}C -carbonylations at high pressures (~35 MPa, 350 atm) and temperatures (~200 °C) (Figure 7.22) [207]. In this process, preconcentrated $[\text{}^{11}\text{C}]\text{CO}$ is transferred into the micro-autoclave chamber; the coupling reagent solution is then added using an HPLC pump that compresses the gas to <2% of the liquid volume, thus producing a pseud one-phase system [208, 209]. An alternative high-pressure reactor was reported

Figure 7.22 A high-pressure micro-autoclave reaction system. Source: From Rahman, O. [206]. © 2015 John Wiley & Sons.



in 2002, in which the reactant solution is pushed through the [^{11}C]CO trapping loop and into the microreactor [210].

The micro-autoclave was initially used for the synthesis of *carbonyl*- ^{11}C -amides in good RCY and with excellent molar activity via Pd(0)-catalysed reaction of aryl halides and amines with [^{11}C]CO [211], and has since been used to prepare ^{11}C -radiolabelled ketones, amides, aldehydes, esters, carboxylic acids, and derivatives such as amines, alkyl iodides, and acyl chlorides (Figure 7.21a–e) [23, 209].

In 2017, Dahl and Nordeman reported the direct synthesis of *carbonyl*- ^{11}C -benzoyl chlorides via Pd(0)-catalysed ^{11}C -carbonylation of aryl halides (Figure 7.21f) [212]. The ^{11}C -benzoyl chloride could undergo further reactions with various nucleophiles to form the corresponding ^{11}C -labelled carboxylic acids, amides, esters, or aldehydes as well as alcohols and ketones [213]. In 2017, Altomonte et al. reported that the use of reactive diaryliodonium salts in place of aryl halides in the Heck ^{11}C -carbonylation enabled ^{11}C -carboxylic acids and ^{11}C -amides to be formed at room temperature [214].

High-pressure ^{11}C -carbonylations have been used to radiolabel numerous drug-like molecules, as shown in Figure 7.23 [215], including the α -amino-3-hydroxy-5-methyl-4-isoxazolepropionic acid (AMPA) receptor modulator [^{11}C]CX546 [210], the mGluR1 ligand [^{11}C]FIMX [216], the translocator protein 18 kDa (**TSPO**) receptor ligands ^{11}C -PK11195 [217] and [^{11}C]DAA1106 [218], the AT1 receptor ligand [^{11}C]eprosartan [219], the β -secretase 1 (BACE-1) inhibitor [^{11}C]BSI-IV [220], histamine H_3R ligands [221], the histone deacetylase

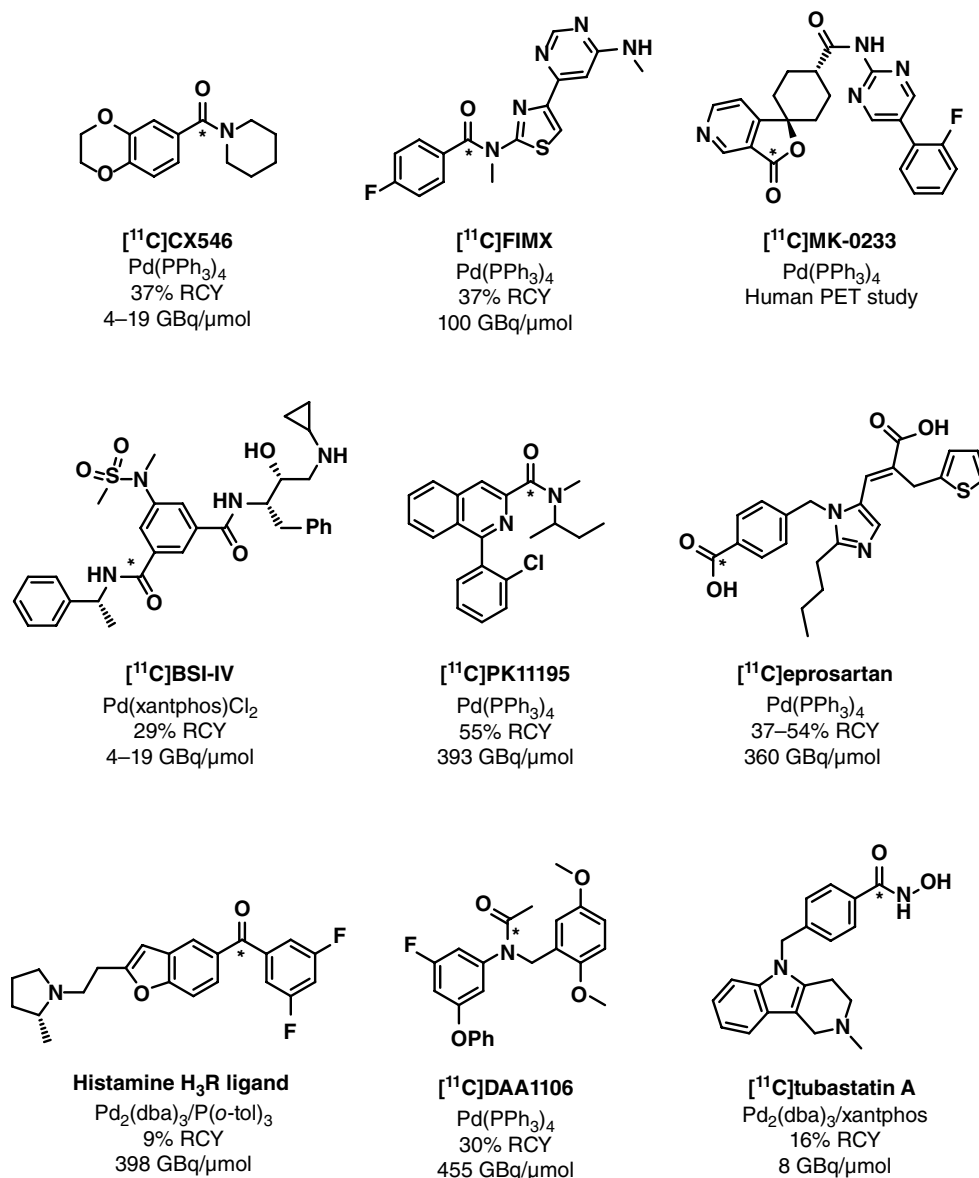


Figure 7.23 PET radioligands synthesised via high-pressure Pd(0)-catalysed ¹¹C-carbonylation reactions.

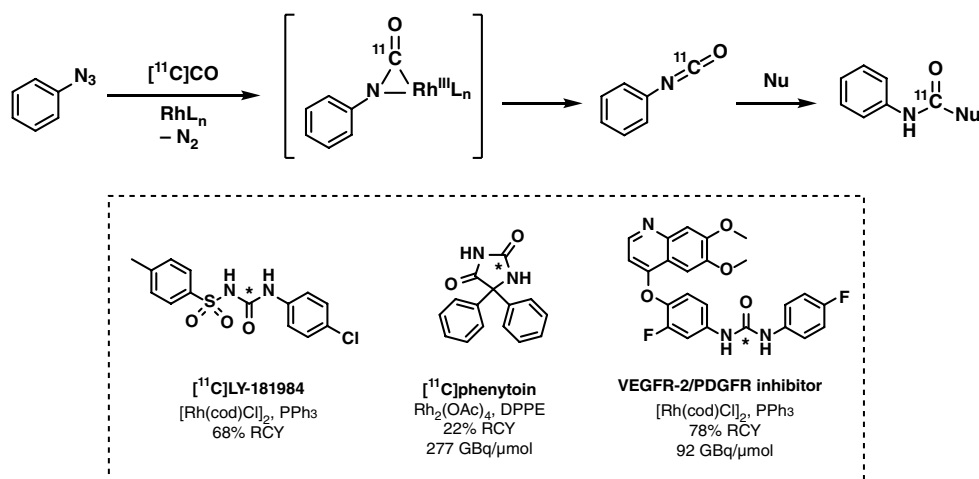
6 inhibitor [¹¹C]tubastatin-A [222], and the neuropeptide Y5 receptor antagonist [¹¹C]MK-0233 [223, 224], which has been studied in humans [225]. Aberg and Långström used this approach to synthesise a library of 12 potential irreversible epidermal growth factor receptor (EGFR) inhibitors from 4 substituted vinyl iodides and 3 different amino-quinazolines through Pd(0)-catalysed ¹¹C-carbonylation reactions using a single set of reaction conditions [226]. A semi-automated dispensing system for performing multiple carbonylation reactions with a single batch of [¹¹C]CO has been developed by Van der Wildt et al. and may facilitate combinatorial ¹¹C-radiolabelling strategies [227].

The scope of the micro-autoclave system has been explored beyond Pd(0)-catalysis. ^{11}C -Labelled ureas [228–231] and carbamates [228] have been produced by Rh(I)-catalysed ^{11}C -carbonylation of azides, providing an alternative to $[^{11}\text{C}]\text{CO}_2$ or $[^{11}\text{C}]\text{COCl}_2$ radiolabelling (Figure 7.24). This reaction is thought to proceed via an ^{11}C -isocyanate intermediate, which can then react with a nucleophile to generate the corresponding ^{11}C -carbonyl compound. A *carbonyl*- ^{11}C -malonate has been produced using a diazo starting material instead of an azide. This could be further functionalised at the α -carbonyl position by deprotonation and reaction with an alkylating agent [232]. Rh(I)-catalysed ^{11}C -carbonylations have been used to synthesise bioactive molecules such as the cytotoxic sulfonyleurea $[^{11}\text{C}]\text{LY-181984}$ [231], the Pgp substrate $[^{11}\text{C}]\text{phenytoin}$ [24], and a dual vascular endothelial growth factor receptor-2/platelet-derived growth factor receptor β (VEGFR-2/PDGFR β) inhibitor [230].

The transition metal-catalysed reactions described so far are limited to methyl, benzyl, aryl, and vinyl halides as the electrophilic coupling partner to avoid competing β -hydrogen elimination at the metal centre following oxidative addition. To extend the labelling of aliphatic substrates, Långström et al. explored metal-free photoinitiated radical ^{11}C -carbonylations of alkyl iodides using a modified micro-autoclave equipped with a sapphire window to allow irradiation of UV light to prepare ^{11}C -labelled aliphatic amides [233, 234], esters [234–236], and carboxylic acids [208, 236–238] (Figure 7.25a). Reactions generally proceeded in good RCY, although in some cases photosensitisers such as acetone, benzophenone, or di-*t*-butyl peroxide were added to improve yields [234, 236].

Selenium-catalysed high-pressure ^{11}C -carbonylations have also been investigated for the conversion of amines, amino alcohols, and alcohols into cyclic and acyclic *carbonyl*- ^{11}C -ureas, *carbonyl*- ^{11}C -carbamates, and *carbonyl*- ^{11}C -carbonates, respectively (Figure 7.25b) [239]. These reactions are thought to proceed via initial formation of $[^{11}\text{C}]\text{carbonyl}$ selenide, which can then undergo reaction with an amine to produce an intermediate ^{11}C -isocyanate. Subsequent nucleophilic attack of the isocyanate yields the

Figure 7.24
High-pressure rhodium(I)-catalysed ^{11}C -carbonylation to form carbamyl derivatives.



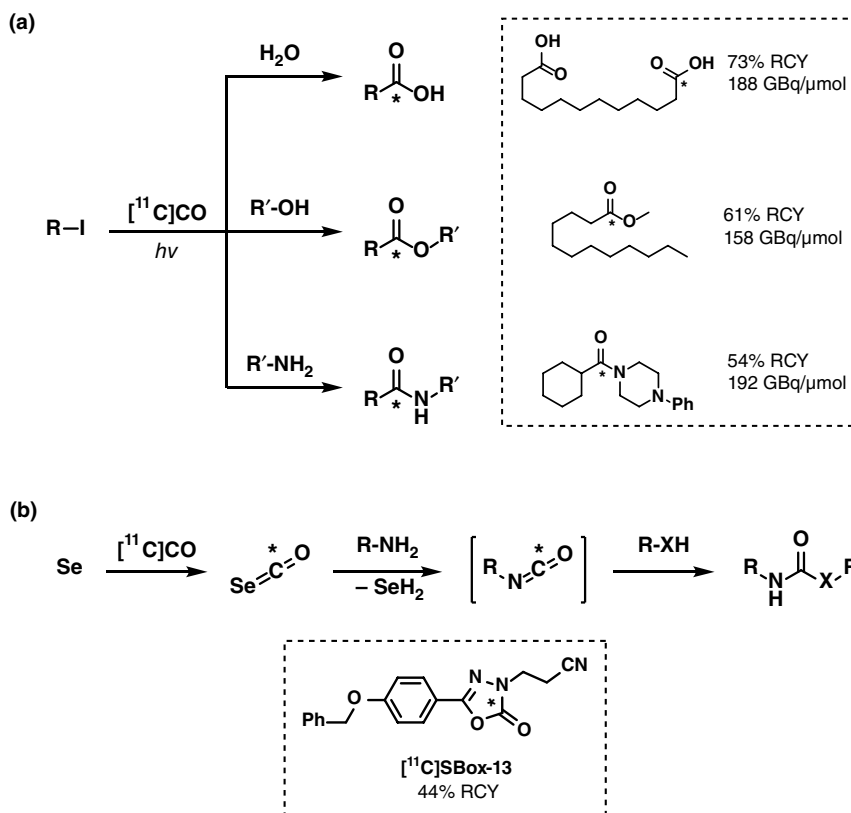


Figure 7.25 UV and selenium-mediated ^{11}C -carbonylation reactions to form $[^{11}\text{C}]$ carbonyl compounds.

corresponding ^{11}C -carbamoyl product. This method was used to synthesise the oxazolidinone MAO-B radioligand $[^{11}\text{C}]\text{SBox-13}$, previously accessed via $[^{11}\text{C}]\text{COCl}_2$.

7.4.2.3 Low-Pressure Carbonylation Methods

Despite the success of high-pressure ^{11}C -carbonylation, its technical complexity and lack of commercial availability have prompted researchers to explore alternative approaches. In 2004, Audrain et al. reported on the use of $\text{BH}_3 \cdot \text{THF}$ as a complexation agent to enhance $[^{11}\text{C}]\text{CO}$ solubility at atmospheric pressure via coordination of BH_3 to the lone electron pair of CO [240]. This process was used to synthesise a model *carbonyl*- ^{11}C -amide and model *carbonyl*- ^{11}C -lactone in moderate RCY via Pd(0)-catalysed ^{11}C -carbonylation. In 2009, Kealey et al. used a copper(I) tris(pyrazolyl)borate (CuTp^*) complex to coordinate $[^{11}\text{C}]\text{CO}$, observing near-quantitative $[^{11}\text{C}]\text{CO}$ trapping at room temperature without the need for a preconcentration step [241]. $[^{11}\text{C}]\text{CO}$ was released by addition of a competing phosphine ligand and used directly in a one-pot Pd(0)-catalysed ^{11}C -carbonylation to form model *carbonyl*- ^{11}C -amides and *carbonyl*- ^{11}C -carboxylic acids [241–243], including the NPY-Y5 radioligand $[^{11}\text{C}]\text{MK-0233}$ (Figure 7.26) [244].

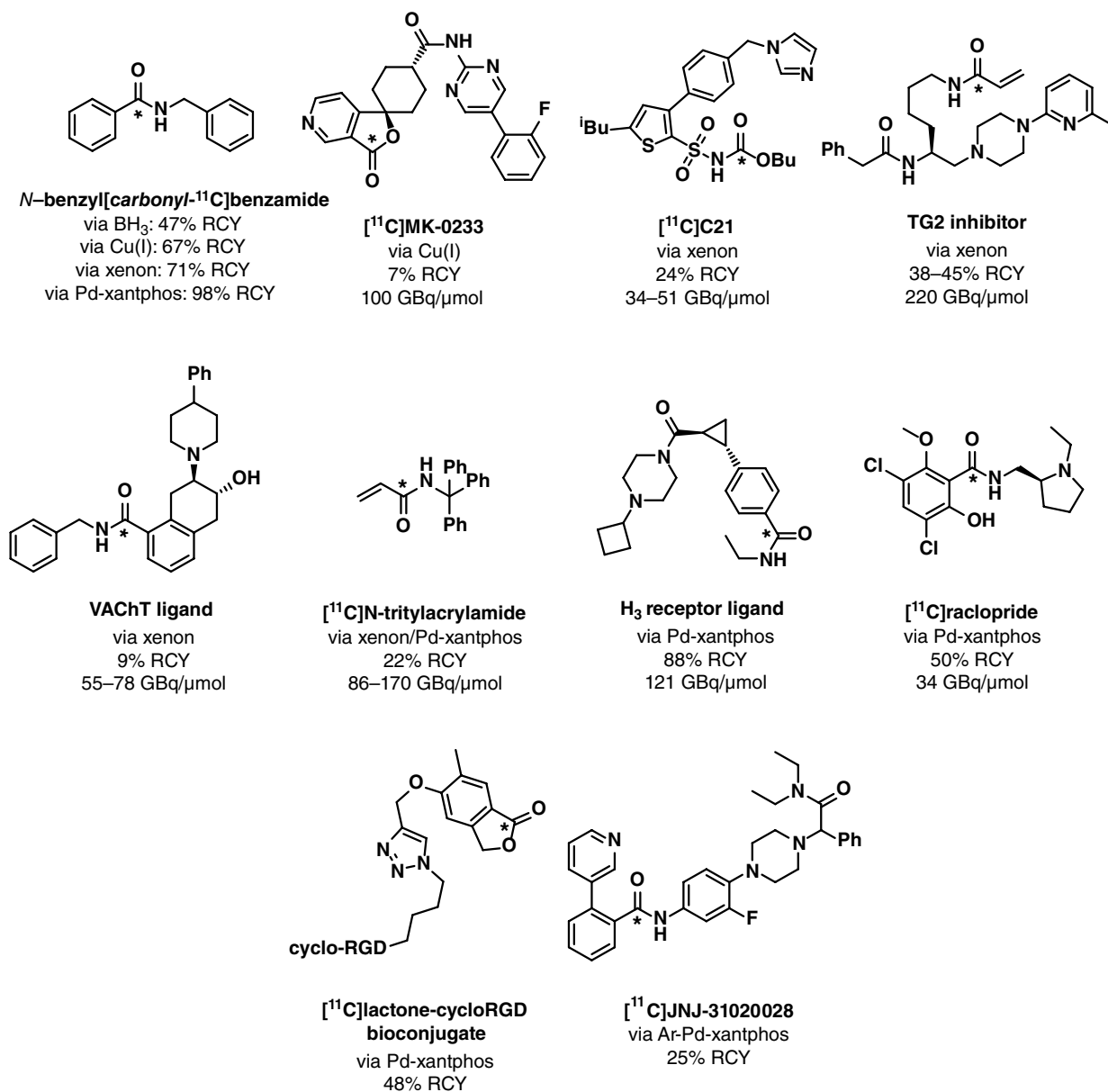


Figure 7.26 Example compounds synthesised via low-pressure Pd(0)-catalysed ¹¹C-carbonylation methods.

During these experiments, it was observed that replacing the Pd(0) with a Pd(II) species led to the formation of homocoupled *N,N'*-[carbonyl-¹¹C]dibenzylurea as a major side product. This reaction was further developed for the synthesis of ¹¹C-labelled symmetrical and unsymmetrical ureas (Figure 7.27a). Urea formation is thought to proceed via a Pd(II)-mediated oxidative carbonylation process, as previously reported using

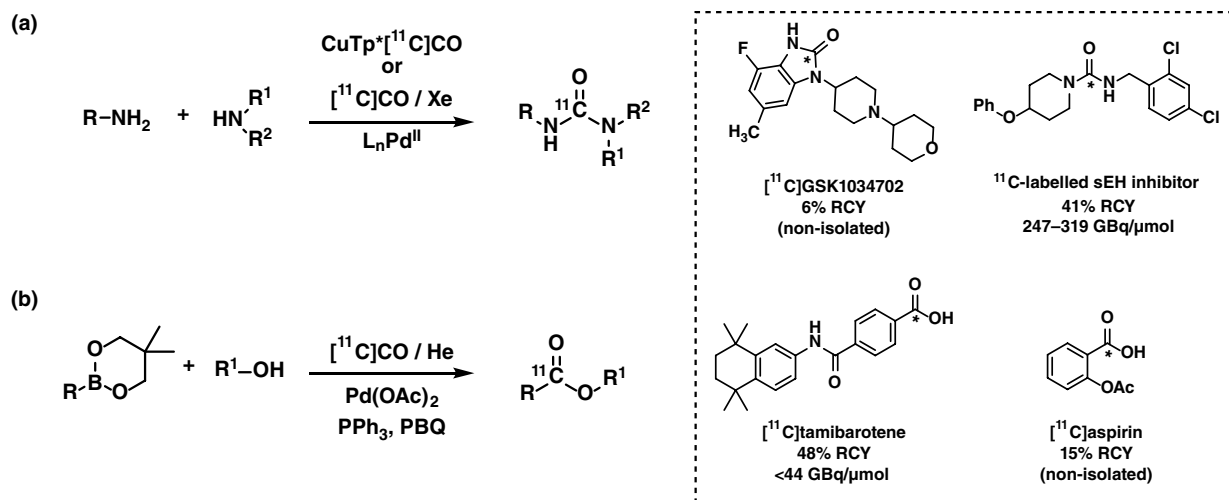


Figure 7.27 Pd(II)-mediated oxidative ^{11}C -carbonylation reactions.

^{12}CO [245]. Using $\text{Pd}(\text{PPh}_3)_2\text{Cl}_2$, homocoupling reactions of primary aliphatic amines produced the corresponding N,N' -disubstituted ^{11}C -ureas in good RCY. Secondary amines were unreactive under these conditions. This difference in reactivity allowed for the formation of unsymmetrical N,N,N' -trisubstituted ^{11}C -ureas using a mixture of a primary and reactive secondary amines, as was used to prepare the M1 muscarinic acetylcholine receptor radiotracer [*carboxyl*- ^{11}C]GSK1034702 and later by Roslin et al. to isolate a ^{11}C -urea inhibitor of soluble epoxide hydrolase [246].

Pd(II)-mediated oxidative carbonylation chemistry has also been used to couple aryl/heteroaryl boronic esters and alcohols with $[^{11}\text{C}]\text{CO}$ to produce *carboxyl*- ^{11}C -esters in 6–80% RCY (based on trapped $[^{11}\text{C}]\text{CO}$) (Figure 7.27b) [247, 248]. These reactions were performed at ambient pressure without additional complexation agents, with the co-oxidant *p*-benzoquinone. ^{11}C -Esters could be further converted to the ^{11}C -carboxylic acids or ^{11}C -amides by reaction with NaOH or aqueous ammonia, respectively, as demonstrated by the syntheses of [^{11}C]aspirin and the synthetic retinoid [^{11}C]tamibarotene.

A breakthrough in the handling of $[^{11}\text{C}]\text{CO}$ was made by Eriksson et al. in 2012 through the use of xenon as a soluble carrier gas, obviating the need for chemical complexation agents [22]. Since xenon is 160 times more soluble than helium in THF, it could be used to sweep $[^{11}\text{C}]\text{CO}$ from a silica trap and into an unvented reaction vial filled with solvent. While this does not increase the solubility of CO itself, it does enable it to be transferred quickly and quantitatively into a small volume reactor without a significant pressure increase. This technically and chemically simple setup has been used for radiolabelling a wide range of substrates via Pd(0) [22], Pd(II) [246], and Rh(I) [249] catalysed processes with RCYs comparable to those obtained using high-pressure conditions or complexation agents. Radiotracers prepared using the xenon- $[^{11}\text{C}]\text{CO}$ trapping method include a sulfonyl *carboxyl*- ^{11}C -carbamate as a non-peptide AT_2 receptor agonist [249], benzovesamicol analogues as potential tracers for the vesicular acetylcholine transporter [250], and

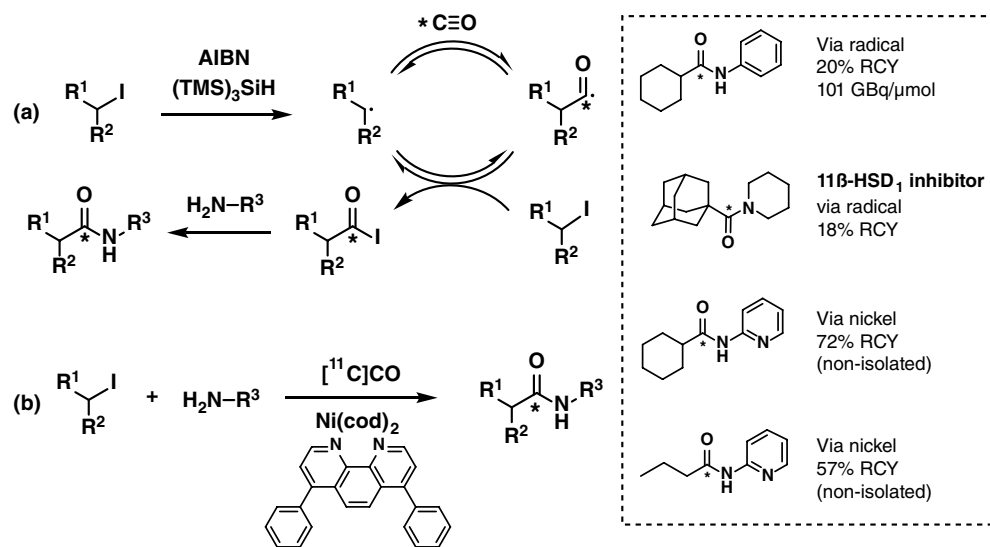
carbonyl- ^{11}C -acrylamides as transglutaminase inhibitor radiotracers (Figure 7.26) [251]. In 2017, Filp et al. reported the synthesis of [^{11}C]acrylamides from [^{11}C]CO and their use as Michael addition substrates with Schiff base glycine derivatives to form amino acids [^{11}C]glutamate and [^{11}C]glutamine [252].

The xenon- ^{11}C CO method has also been used to develop a thermally initiated radical ^{11}C -carbonylation to produce alkyl *carbonyl*- ^{11}C -amides. In a parallel to the high-pressure UV-initiated radical reactions performed by the Långström group, Chow et al. used the radical initiator azobisisobutyronitrile (**AIBN**) to promote the ^{11}C -carbonylation of alkyl iodides and amines at ambient pressure to form a range of alkyl ^{11}C -amides including the 11β -HSD1 inhibitor [*carbonyl*- ^{11}C]adamantan-1-yl(piperidin-1-yl)methanone (Figure 7.28a) [253]. Using isopropanol instead of an amine allowed the formation of ^{11}C -esters via an initial radical dehalogenation of the alkyl halide to form an alkyl and then acyl radical after the addition to [^{11}C]CO. This species could be either quenched by the starting alkyl iodide to form an acyl iodide, or oxidized to an acylium ion, which then reacts with an amine to produce the ^{11}C -labelled alkyl amide.

Alternatively, Rahman et al. used $\text{Ni}(\text{cod})_2$ in the presence of the supporting ligand bathophenanthroline to couple non-activated alkyl iodides with amines and [^{11}C]CO at ambient pressure at 100°C (Figure 7.28b) [254]. Model ^{11}C -amides were obtained in 33–72% RCY highest being for weaker nucleophiles and sterically hindered electrophiles, in contrast to the usual reactivity observed in Pd(0) catalysis.

In 2006, Buchwald et al. showed that aminocarbonylation reactions could be performed at low CO pressures in the presence of a Pd(0) catalyst supported by the wide bite-angle bidentate phosphine ligand xantphos [255]. This led Dahl et al. to explore the synthesis of [*carbonyl*- ^{11}C]N-benzylbenzamide and optimize this method for use with [^{11}C]CO. A series of Pd reagents were screened, showing that xantphos and $(\text{Pd}(\pi\text{-cinnamyl})\text{Cl})_2$ was a particularly efficient catalyst system, allowing exceptional

Figure 7.28 ^{11}C -carbonylation reactions of alkyl iodides to form [^{11}C]amides.



[¹¹C]CO incorporation and high RCY (13–98%) for substituted ¹¹C-*N*-benzylbenzamides, ¹¹C-carboxylic acids, ¹¹C-aldehydes, ¹¹C-ketones, and ¹¹C-lactones [256]. A subsequent report described a further improvement in RCY through microwave irradiation [257]. The efficiency of the Pd-xantphos system has seen it become increasingly adopted as a first-choice reagent for ¹¹C-carbonylation reactions, as exemplified by its use in the synthesis of a histamine type-3 receptor radioligand [256] and the D₂ radioligand [*carbonyl*-¹¹C]raclopride (Figure 7.26) [258].

In 2015, Anderson et al. reported an efficient ¹¹C-aminocarbonylation strategy designed to optimise RCYs for structurally demanding motifs [259]. Since oxidative addition can be a slow step, it was reasoned that pre-formed aryl-palladium-xantphos complexes might undergo more efficient reaction with [¹¹C]CO as stoichiometric reagents. PET radiotracers [*carbonyl*-¹¹C]raclopride, [¹¹C]olaparib, and [¹¹C]JNJ-31020028 were successfully radiolabelled at low pressures using this approach (Figure 7.29a). This methodology was applied to the ¹¹C-*N*-acetylation of peptides, allowing native peptides [*carbonyl*-¹¹C]acetyl-LULUPhol, [*carbonyl*-¹¹C]acetyl-cRGDFK, and [¹¹C]lacosamide to be synthesised in good RCY and with high molar activity under mild conditions (Figure 7.29b) [260].

Cornilleau et al. used an alternative strategy for ¹¹C-labelling complex biomolecules, whereby a 2-iodobenzylalcohol moiety was appended via click chemistry, making it amenable to radiolabelling via Pd(0)-catalysed intramolecular cyclisation with [¹¹C]CO [261]. Following the high-yielding radiosynthesis of the unconjugated test substrate, a bioconjugated glucose derivative and a cyclo-**RGD** peptide bioconjugate were radiolabelled (Figure 7.29c) in good RCY.

7.4.2.4 Flow-Based Carbonylation Methods

A number of flow-based approaches to performing ¹¹C-carbonylations have been investigated, making use of micro-reactors that are well suited to the small scale of radiolabelling reactions. The microtube system developed by Miller et al. uses a heterogeneous silica-bound Pd catalyst packed into a PTFE tube [262]. The 45 cm tube (internal diameter [i.d.] = 1 mm) is first loaded with a solution of aryl halide and amine, and then [¹¹C]CO is delivered into the tube and heated at 75 °C for 12 minutes, after which the crude product mixture is eluted into a vial under a flow of THF. Model [*carbonyl*-¹¹C]-*N*-benzylbenzamides were obtained in 33–79% RCY with excellent reproducibility. The same group later reported the use of a glass-microfluidic device to perform gas-liquid amino-¹¹C-carbonylation reactions inside a 5 m channel (i.d. ≈ 200 μm) using an annular flow of [¹¹C]CO gas co-infused with a solution of cross-coupling reagents [263]. In a 7–8 minute reaction performed at 150 °C, the same model *carbonyl*-¹¹C-amides were this time obtained in 56–88% RCY. In an alternative approach, Kealey et al. performed liquid-liquid amino-¹¹C-carbonylation reactions using a preformed CuTp*-¹¹C]CO solution rather than [¹¹C]CO gas, within a 2 m silica glass capillary (i.d. = 100 μm) in a commercially available microfluidic device, as exemplified in the synthesis of [¹¹C]MK-0233 [244]. In 2015, Dahl et al. used microfluidics to perform amino-¹¹C-carbonylation reactions in a gas-liquid segmented microfluidic process [264]. Using a 5 m fused silica capillary (i.d. = 200 μm) at 100 °C, 12 different

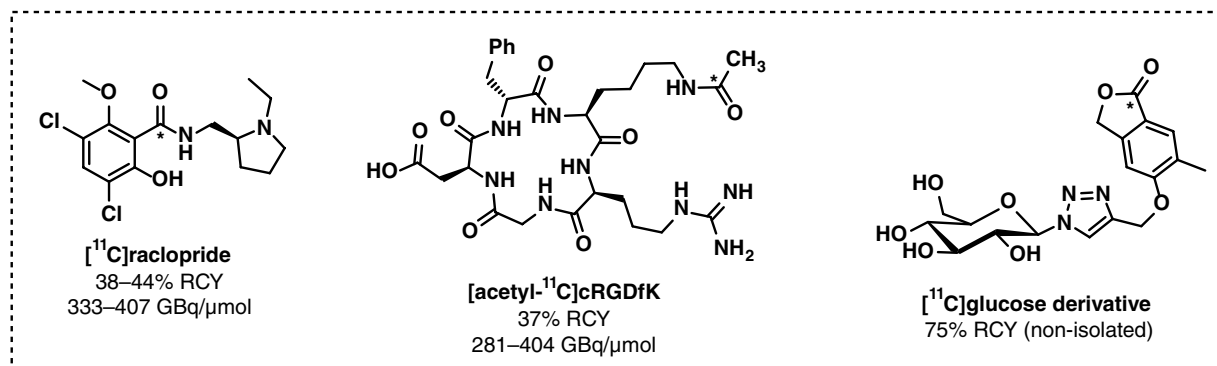
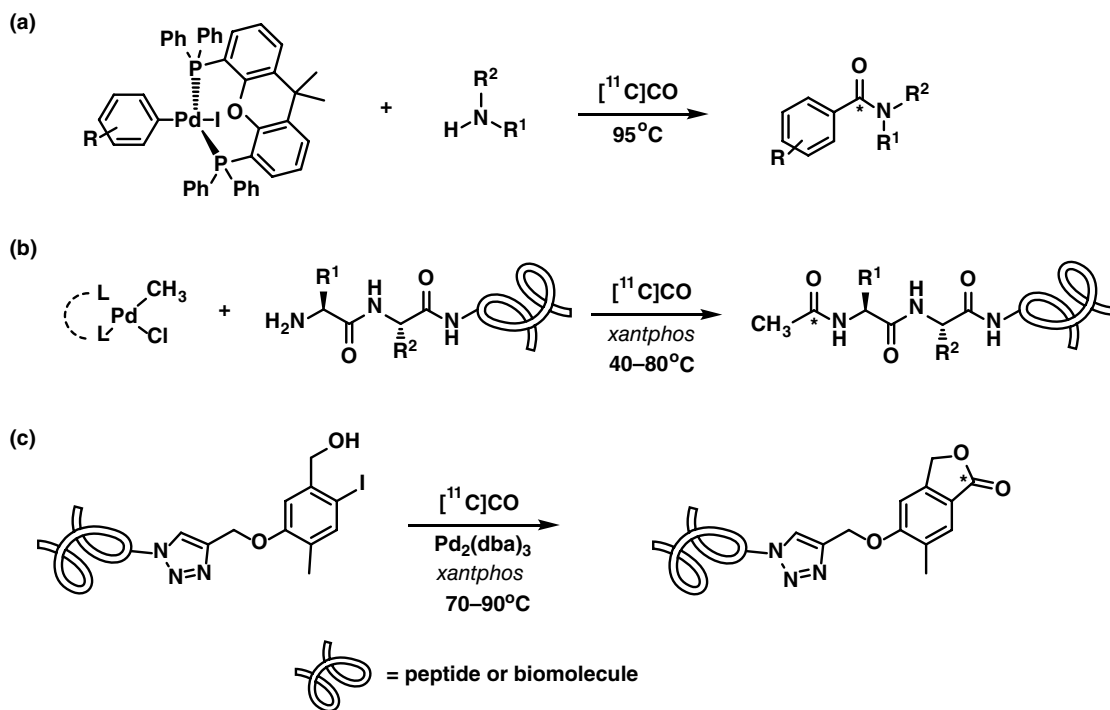


Figure 7.29 Complex molecules access via Pd-xantphos mediated ¹¹C-carbonylation reactions.

¹¹C-labelled compounds were produced in 38–99% RCY, including the D₂ receptor ligands [*carbonyl*-¹¹C]raclopride and [*carbonyl*-¹¹C]FLB 457.

7.4.3 Alkylations with [¹¹C]Alkyl Halides

Methyl groups are common motifs in both natural and synthetic products providing potential sites for labelling with carbon-11. The rapid adoption of [¹¹C]CH₃I (and later [¹¹C]CH₃OTf) as “go-to” reagents for labelling with carbon-11 led to significant market forces to develop commercially available automated systems for the production of [¹¹C]CH₃I and [¹¹C]CH₃OTf

as well as the radiolabelling, purification, and reformulation of radiopharmaceuticals labelled with these agents [50, 265]. “Kit” setups [266] have further spurred the growth of PET imaging in the clinic by simplifying radiopharmaceutical manufacture.

$[^{11}\text{C}]\text{CH}_3\text{I}$ is the simplest alkyl iodide, and the lack of steric hindrance at the electrophilic site makes it the ideal electrophile for use in nucleophilic substitution reactions with amines, amides, alcohols, thiols, or enols. Polar aprotic solvents like acetonitrile, DMF, acetone, 2-butanone, and dimethyl sulfoxide (**DMSO**) are most commonly used, although protic solvents such as ethanol have also been reported [267]. Forcing conditions may be used to accelerate radiolabelling reactions; however, precursor decomposition or undesired side reactions with the solvent may occur [268, 269]. Bases (e.g. hydrides, hydroxides, and carbonates) can be used to either deprotonate the substrate to increase nucleophilicity or quench acidic by-products. The choice of base is dictated by the pK_a of the substrate and the stability of the precursor. To overcome the challenges in controlling the stoichiometry of the base in the reaction due to the limited solubility of inorganic bases in organic solvents, TBAF has been shown to be a suitable base for both *N*- and *O*-alkylation with $[^{11}\text{C}]\text{CH}_3\text{I}$ in DMSO [270, 271].

7.4.3.1 $[^{11}\text{C}]\text{Methyl Iodide vs. } [^{11}\text{C}]\text{Methyl Triflate as Labelling Agents}$

$[^{11}\text{C}]\text{CH}_3\text{OTf}$ is a more reactive methylating agent with a higher boiling point than that of $[^{11}\text{C}]\text{CH}_3\text{I}$ (94–99 °C vs. 41–43 °C) being frequently employed for labelling less nucleophilic substrates. While the synthesis of $[^{11}\text{C}]\text{CH}_3\text{OTf}$ requires an additional step compared to $[^{11}\text{C}]\text{CH}_3\text{I}$, its production via in-line gas-phase synthesis from either $[^{11}\text{C}]\text{CH}_3\text{I}$ or $[^{11}\text{C}]\text{CH}_3\text{Br}$ adds minimal time to the process but dramatically improves RCY as well as molar activities (Figure 7.30a–e). Further advantages include improved trapping in the reaction solvent; shorter reaction times, allowing for lower reaction temperatures; and a reduction in the mass of precursor required as well as by-products formed. Head-to-head comparisons of the application of $[^{11}\text{C}]\text{CH}_3\text{OTf}$ or $[^{11}\text{C}]\text{CH}_3\text{I}$ for labelling of amines, anilines [55], thiols, amides [282], phenols, and carboxylic acids [56, 283] have been reported.

7.4.3.2 *N*-Alkylation

N-alkylation with $[^{11}\text{C}]\text{CH}_3\text{I}$ or $[^{11}\text{C}]\text{CH}_3\text{OTf}$ is the most widely used strategy for radiolabelling with carbon-11 due to the abundance of methylated aliphatic amine motifs amongst bioactive molecules. The excess of desmethylamine precursor and minimal amounts of ^{11}C -methylating agent ensure that poly- ^{11}C -methylation is negligible despite the intermediate $[^{11}\text{C}]\text{methylamine}$ being more nucleophilic. A base is not needed in the reaction, as the parent amines are often sufficiently nucleophilic, and the excess precursor can function as the base. For example, $[^{11}\text{C}]\text{DASB}$ (Figure 7.31a), a serotonin transporter ligand, is synthesised by selective ^{11}C -methylation (aliphatic over aromatic) of the desmethyl precursor using $[^{11}\text{C}]\text{CH}_3\text{I}$ in DMSO at 100 °C for five minutes in 66% ± 6.9% ($n = 60$) RCY [284]. ^{11}C -Methylation of an aromatic amine is often achieved using $[^{11}\text{C}]\text{CH}_3\text{OTf}$, exemplified by the synthesis of an amyloid- β PET radiotracer $[^{11}\text{C}]\text{PIB}$ (Figure 7.31b) [272]. When the aromatic amine is particularly electron-deficient and

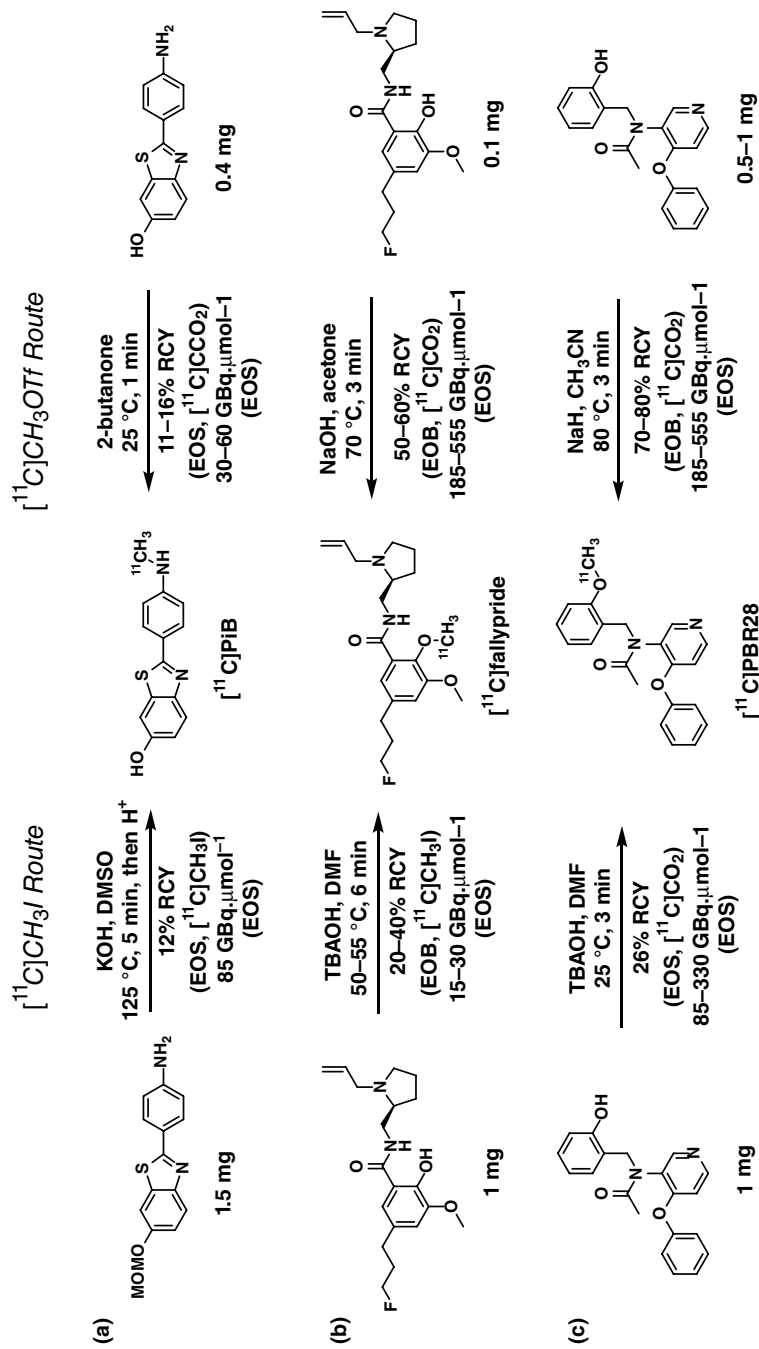
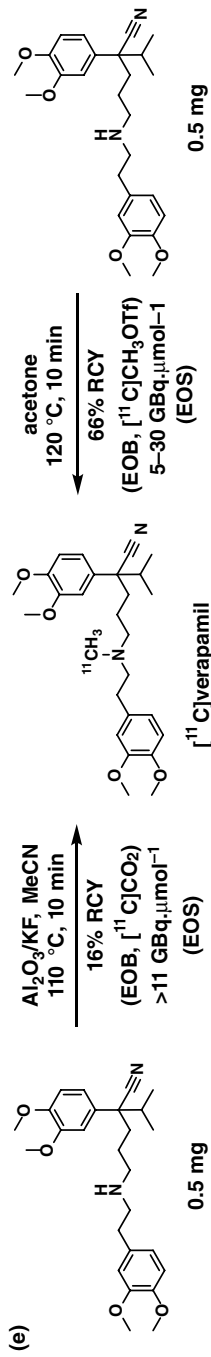
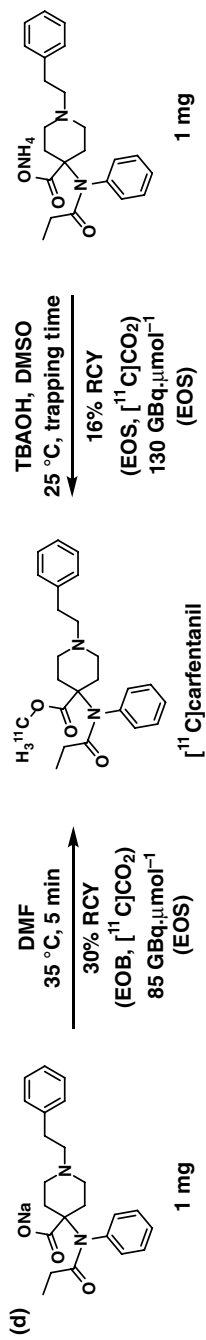


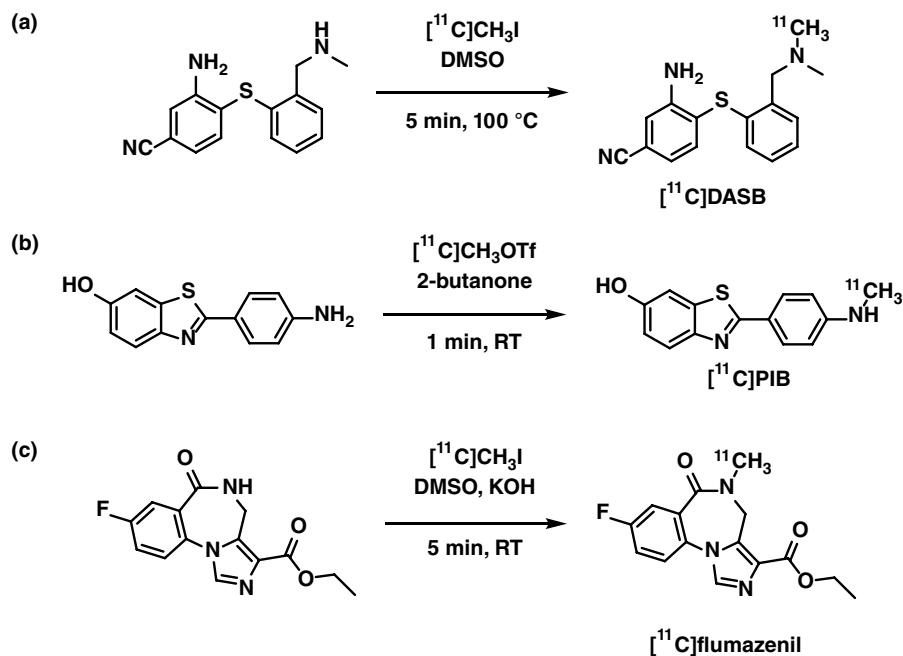
Figure 7.30 Comparison of reaction conditions and yields for the synthesis of (a) [¹¹C]PIB. Sources: Mathis, C.A., Wang, Y., Holt, D.P. et al. [272] and Wilson, A.A., Garcia, A., Chestakova, A. et al. [129]. (b) [¹¹C]fallypride. Sources: Mukherjee, J., Shi, B., Christian, B.T. et al. [273]; and Gao, M., Wang, M., Mock, B.H. et al. [274]. (c) [¹¹C]PBR28. Sources: Briard, E., Zoghbi, S.S., Imaizumi, M. et al. [275] and Wang, M., Yoder, K.K., Gao, M. et al. [276].



(d) [^{11}C]carfentanil. Sources: Dannals, R.F., et al., [277] and Jewett, D.M., et al., [279]. (e) [^{11}C]verapamil [279, 280] using either [^{11}C]CH $_3$ I (left) or [^{11}C]CH $_3$ OTf (right). Sources: Elsinga, P.H., et al., [279] and Wegman, T.D., et al., [280].

Figure 7.31

N-¹¹C-Methylation is used to synthesise [¹¹C]DASB, [¹¹C]PIB, and [¹¹C]flumazenil.



poorly nucleophilic, [¹¹C]CH₃OTf may not be sufficiently reactive. To address such cases, Pike et al. showed that solid, inorganic bases like Li₃N and Li₂O in combination with [¹¹C]CH₃I in DMF effectively ¹¹C-methylated a range of nitroanilines and pyrroles at room temperature with ultrasonication in moderate RCYs [269]. Carbon-11-methylated secondary and tertiary amides are also common targets, in which case the presence of a base is required. [¹¹C]Flumazenil (Figure 7.31c), a GABA_A receptor antagonist, was radiolabelled on a solid-supported thin film of KOH in DMSO, in 5–10% RCY, with a molar activity of 520–600 GBq·μmol⁻¹ (End-of-synthesis [EOS]) [112].

[¹¹C](CH₃)₂NH has been reported as a precursor for introducing ¹¹C-methyl groups using electrophilic precursors. [¹¹C](CH₃)₂NH is prepared by ¹¹C-methylation of CH₃NH₂ and has been used in nucleophilic substitutions with primary benzyl bromides in *N,N*-dimethylacetamide (**DMA**) in the presence of Hunig's base (Figure 7.32a) [284]. Unlike benzyl bromides, allyl and simple alkyl bromides react sluggishly under these conditions.

Palladium-mediated *N*-methyl-¹¹C-acetylation of alkyl and benzylamines and anilines using [¹¹C]CH₃I in the presence of Cp₂Fe₂(CO)₄ as a CO source has been reported by Norde-man et al. [285]. *N*-methyl-¹¹C-acetylated products were obtained in good RCYs at 160 °C for 10 minutes in THF; however, sterically hindered substrates performed poorly (Figure 7.32b).

7.4.3.3 O-Alkylation

¹¹C-Methylated phenols and esters are also common radiolabelled motifs. Their precursors are poor nucleophiles when protonated. However, their conjugate bases, phenolates, and carboxylates, respectively, are potent nucleophiles and react rapidly with [¹¹C]CH₃I

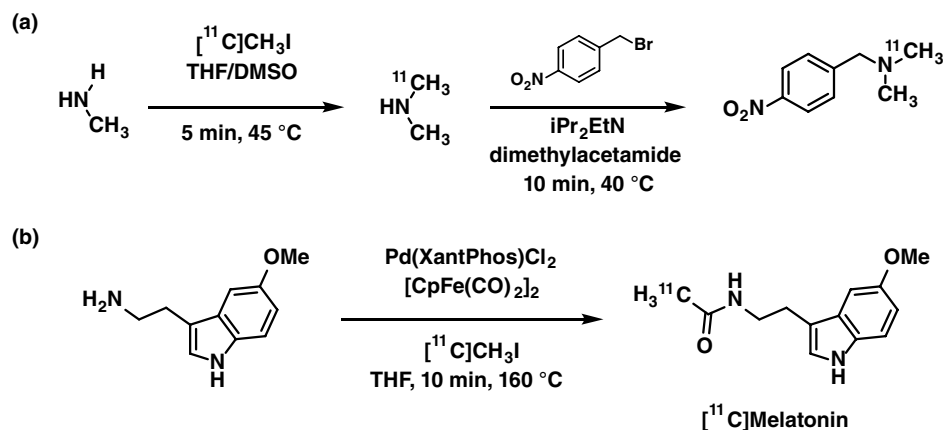


Figure 7.32 (a) Radiolabeling of amines using [^{11}C]dimethylamine and (b) *N*-acetylation of amines with a CO -source and [^{11}C]CH $_3$ I.

and [^{11}C]CH $_3$ OTf. Thus, tetra-*n*-butylammonium hydroxide or an alkali hydroxide is usually required in the reaction mixture unless preformed salt is being used. ^{11}C -Methylation of phenols and carboxylic acids [286] can also be accomplished using [^{11}C]CH $_2$ N $_2$ [102].

[*Methyl*- ^{11}C]Raclopride, a D2-selective dopamine receptor antagonist, was labelled using the loop method at the phenolic position of preformed desmethylraclopride tetra-*n*-butylammonium (**TBA**) salt with [^{11}C]CH $_3$ OTf in 2-butanone (Figure 7.33a) [125]. A nucleophilic tertiary amine and a secondary amide within the molecule remain unreacted. Similarly, an oestrogen receptor ligand (Figure 7.33b) can be methylated at the carboxylic acid in the presence of an unprotected phenol [288]. This is a result of the difference in pK_a between acids and phenols (c. 2–4 vs. 7–11, respectively). [^{11}C]Metomidate, an agent for imaging of adenoma, was esterified in DMF with [^{11}C]CH $_3$ I from the carboxylic acid TBA salt (Figure 7.33c). Instead of using [^{11}C]CH $_3$ I, Ackermann et al. employed either $\text{BF}_3 \cdot \text{Et}_2\text{O}$ [289] and 1,3-dichlorodibutylstannoxane [290] as mediators to accomplish esterification with [^{11}C]CH $_3$ OH in moderate RCY through addition-elimination or transesterification, respectively.

O-alkylations of other functional groups are less common. ^{11}C -Methyl carbamates are usually prepared using [^{11}C]methyl chloroformate [291] or via ^{11}C -methylation of a carbamic acid, made either by bubbling CO_2 through a solution of the amine precursor or by transcarboxylation from the DBU- CO_2 adduct. Labelling of [^{11}C]GR103545, a κ -opioid receptor agonist, was achieved in 8.2% RCY using [^{11}C]CH $_3$ OTf at room temperature in five minutes (Figure 7.33d) [292]. The use of [^{11}C]CH $_3$ OTf proved critical, as the reaction with [^{11}C]CH $_3$ I required heating, resulting in partial decarboxylation of the carbamic acid and production of the *N*- ^{11}C -methylated compound as a byproduct [293]. The ^{11}C -methylation of the hydroxyl group of an oxime has also been reported, illustrated by the synthesis of [^{11}C]ABP688 and similar compounds as mGlu $_5$ antagonists in the presence of NaH and [^{11}C]CH $_3$ I at 90 °C for five minutes (Figure 7.33e) [294, 295].

7.4.3.4 *S*-Alkylation

The most widely used radiopharmaceutical labelled at sulfur is [*methyl*- ^{11}C]-L-methionine, which is used for imaging of the rate of amino acid transport and protein biosynthesis.

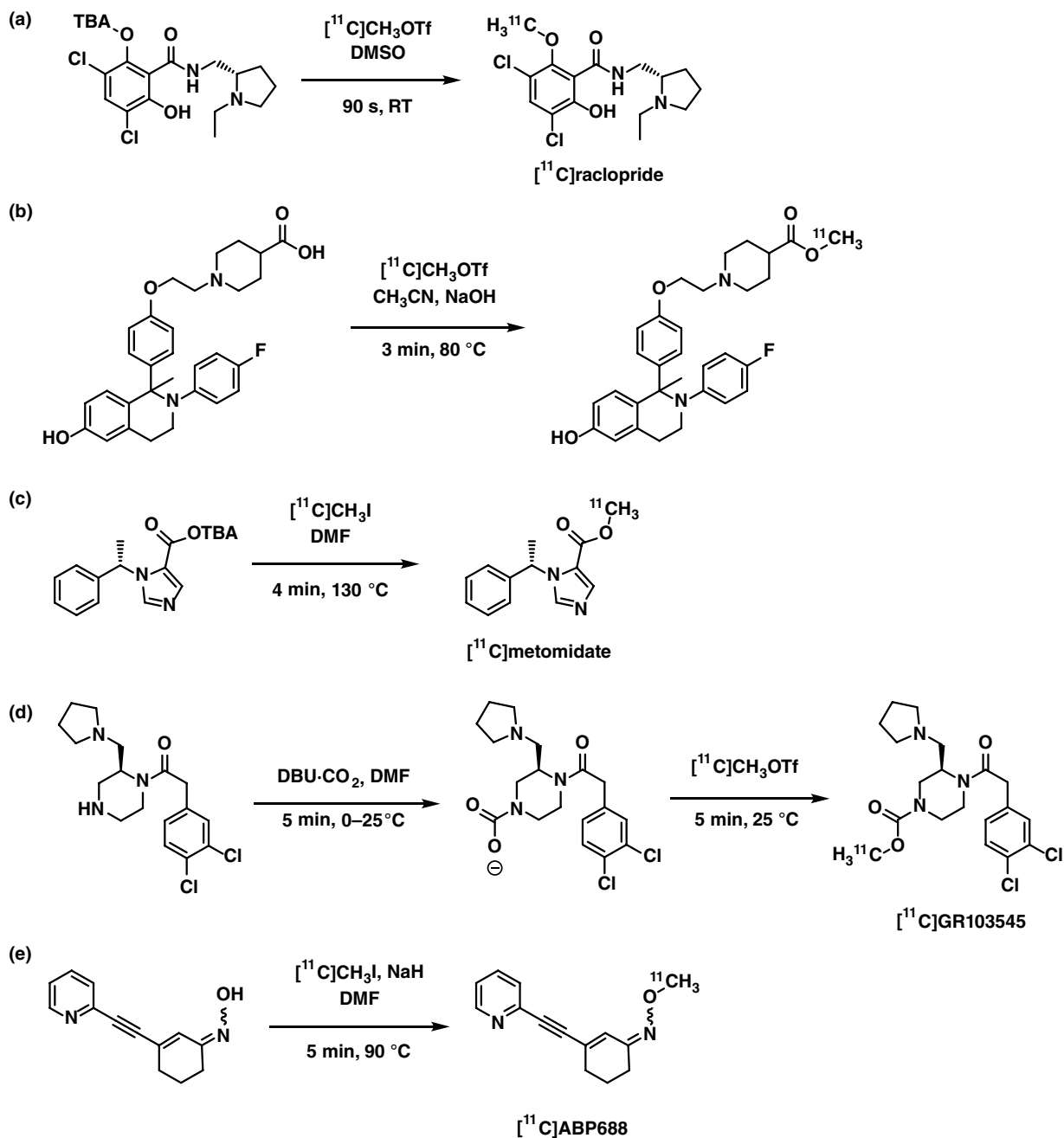


Figure 7.33 O-¹¹C-methylation is used to synthesize [¹¹C]raclopride, [¹¹C]metomidate, and a ¹¹C-labelled oestrogen receptor ligand.

Reaction of the free thiol with $[^{11}\text{C}]\text{CH}_3\text{I}$ occurs in the presence of base through the highly nucleophilic thiolate anion (Figure 7.34a) in RCYs of 38% [38, 130]. A challenge in labeling free thiols is their propensity to oxidize to the disulfide, which is no longer easily ^{11}C -methylated. Alternatively, L-homoserine thiolactone or other masked thiols [296] have been used as precursors to [*methyl*- ^{11}C]-L-methionine. Both loop [130] and solid-supported methods [297] have been reported. Other ^{11}C -methyl thioether-based PET radiotracers, including the amyloid plaque agent [^{11}C]MeS-IMPY, have been radiolabelled using $[^{11}\text{C}]\text{CH}_3\text{I}$, a masked thiol precursor, and a phosphazine base (Figure 7.34b) [298]. As part of cysteine residues in peptides and proteins, thiols can be radiolabelled with $[^{11}\text{C}]\text{CH}_3\text{OTf}$ to provide access to e.g. [^{11}C]methylalbumin in a single step [299].

Radiolabelled sulfoxides and sulfones have been explored as motifs for introducing carbon-11 into biomolecules. ^{11}C -Methyl sulfones are usually accessed from reaction of

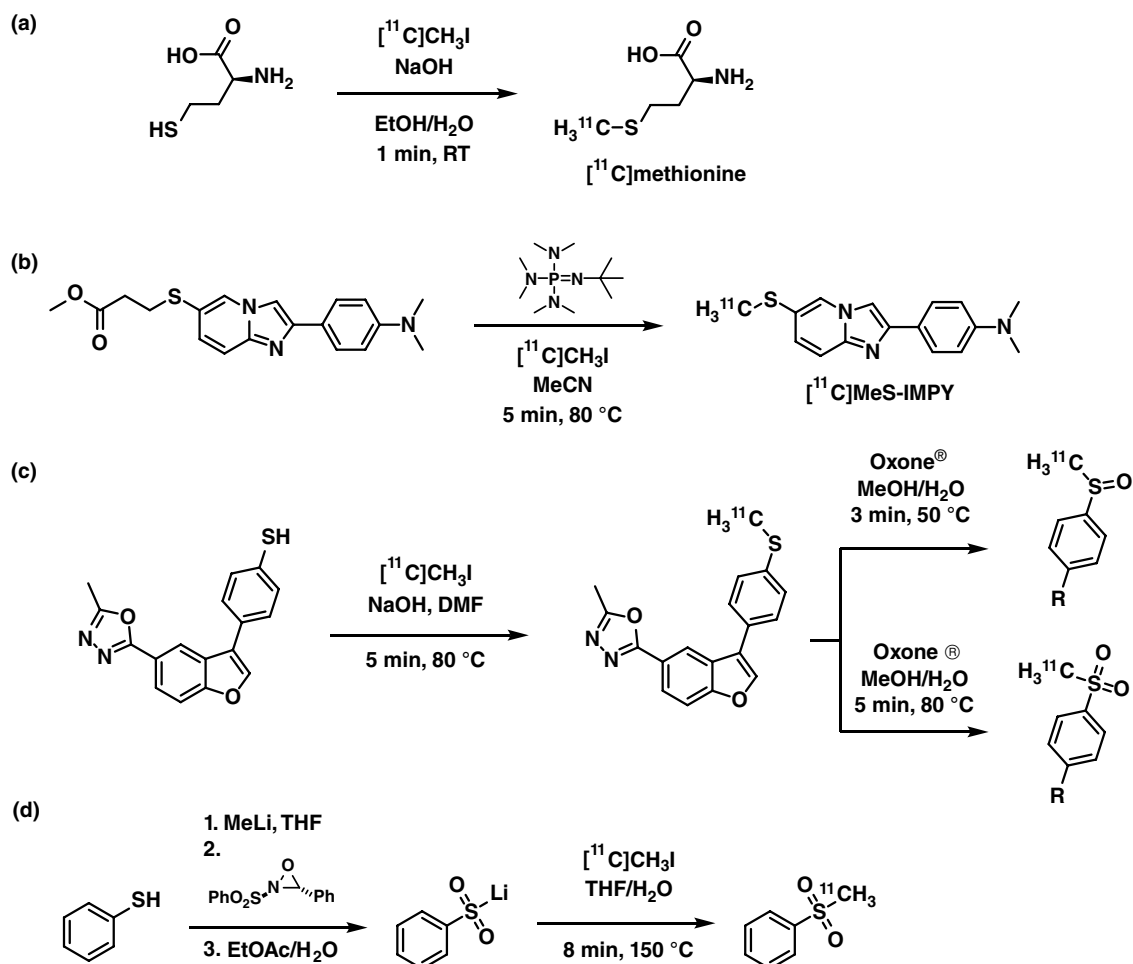


Figure 7.34 S-alkylation with $[^{11}\text{C}]\text{CH}_3\text{I}$ is used for the synthesis of [^{11}C]-L-methionine. [^{11}C]Methyl sulfones and [^{11}C]methyl sulfoxides can also be produced by ^{11}C -methylation followed by oxidation.

a thiol with $[^{11}\text{C}]\text{CH}_3\text{I}$ or $[^{11}\text{C}]\text{CH}_3\text{OTf}$, followed by complete oxidation to the ^{11}C -methyl sulfone [300]. With careful control of the conditions (lower temperature and shorter time), the ^{11}C -methyl sulfoxide can be accessed, though ^{11}C -methyl sulfone is often also produced as a by-product (Figure 7.34c) [301]. Lasne et al. have described an alternative approach via selective oxidation of a lithium thiolate by *N*-sulfonyloxaziridine to give a lithium sulfinate that can react with $[^{11}\text{C}]\text{CH}_3\text{I}$ (Figure 7.34d) to give a ^{11}C -methyl sulfone [302]. The advantage of this approach is that it introduces carbon-11 at the last synthetic step. Mesylating agent $[^{11}\text{C}]\text{methanesulfonyl chloride}$ ($[^{11}\text{C}]\text{MsCl}$) has also been prepared by ^{11}C -methylation of NaSH with $[^{11}\text{C}]\text{CH}_3\text{I}$, followed by oxidation and chlorination [303], and was shown to rapidly ^{11}C -mesylate alcohols and amines.

7.4.3.5 C-Alkylation

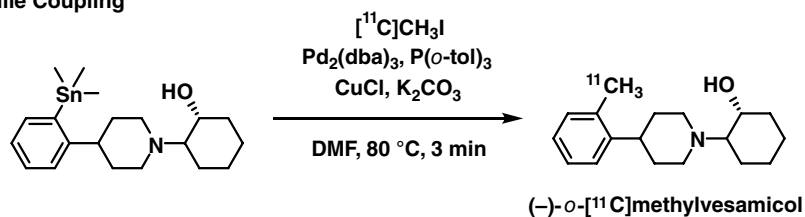
The development of ^{11}C -alkylation reactions at carbon centres has largely been driven by transition metal-mediated ^{11}C -methylation reactions. Additionally, the synthesis of (chiral) amino acids by alkylation at the alpha-carbon of glycine derivative is also a commonly used strategy for the formation of C– ^{11}C bonds.

7.4.3.5.1 Transition Metal-Mediated ^{11}C -Methylation

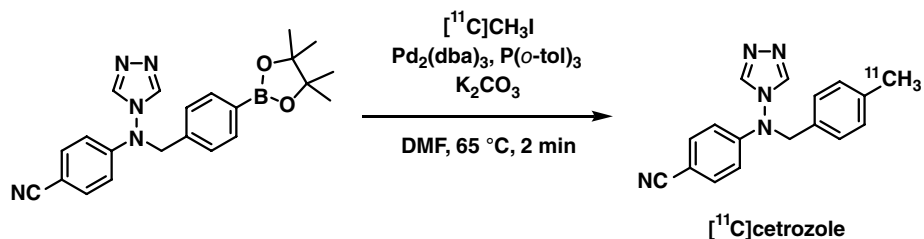
Metal-mediated couplings between $[^{11}\text{C}]\text{CH}_3\text{I}$ and appropriate organometallic reagents have been used extensively for ^{11}C –C bond formation [304, 305]. Specifically, Stille and Suzuki couplings have been applied for the synthesis of PET radiotracers, including (-)-*o*- $[^{11}\text{C}]\text{methylvesamicol}$ (Figure 7.35a) and $[^{11}\text{C}]\text{cetrozole}$ (Figure 7.35b). Other cross-couplings, including the Negishi coupling, have also been reported but are used less frequently. The general mechanism for these cross-couplings (Figure 7.35c) occurs as follows: the Pd(0) (usually in the presence of triarylphosphine ligands) undergoes oxidative addition into a C–X bond to generate Pd(II) species; then transmetalates with an appropriate coupling partner e.g. an organostannane or organoboron; and finally, reductive elimination regenerates the Pd(0), which is free to enter into another catalytic cycle. In the case of radiochemical cross-coupling, the alkyl halide ($[^{11}\text{C}]\text{CH}_3\text{I}$ in most cases) is the limiting reagent, and the Pd-reagent is used stoichiometrically; the catalytic cycle does not begin again, as all the $[^{11}\text{C}]\text{CH}_3\text{I}$ is consumed in a single cycle.

The combination of trace amounts of $[^{11}\text{C}]\text{CH}_3\text{I}$ and stoichiometric Pd-reagents and coupling partners increases the rate of individual steps in the reaction cycle so that the reactions are complete in minutes rather than hours. The rate of the oxidative addition of Pd(0) into $[^{11}\text{C}]\text{CH}_3\text{I}$ is the rate-determining step in the Suzuki reaction. Due to the large excess of Pd(0), the rate of this step is increased, providing the $^{11}\text{C}\text{-CH}_3\text{-Pd(II)-I}$ intermediate rapidly. Maximum conversions are achieved when the $^{11}\text{C}\text{-CH}_3\text{-Pd(II)-I}$ intermediate is prepared *before* the addition of the organometallic coupling partner. In contrast, the transmetalation step is rate-determining for the Stille coupling. Here, the rate-determining step is accelerated by the large excess of the organostannane reagent. The reductive elimination step in Pd-mediated couplings is usually rapid.

(a) Stille Coupling



(b) Suzuki Coupling



(c) General Mechanism

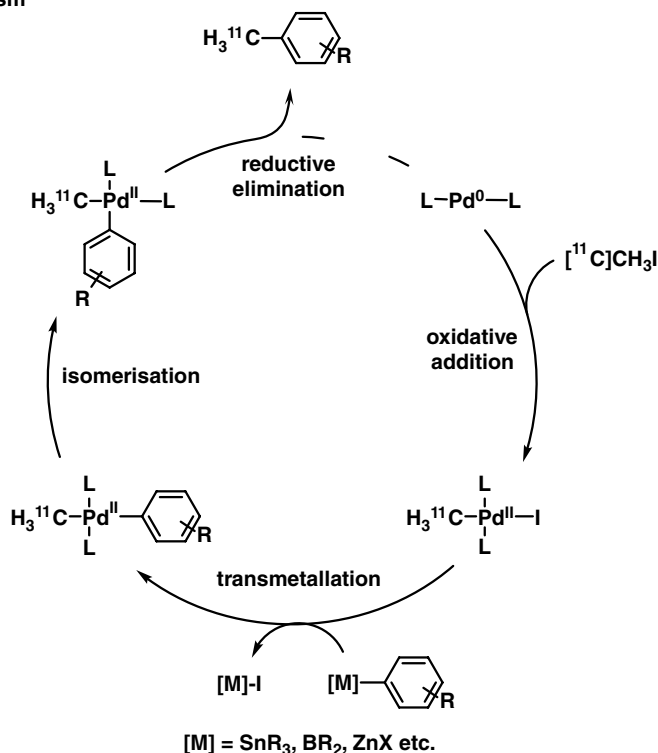


Figure 7.35 Suzuki and Stille coupling reactions with $[^{11}\text{C}]\text{CH}_3\text{I}$, and the proposed mechanism of Pd-mediated couplings with $[^{11}\text{C}]\text{CH}_3\text{I}$.

7.4.3.5.2 Stille Coupling Reactions

The first application of the Stille coupling with $[^{11}\text{C}]\text{CH}_3\text{I}$ was reported by the Långström group in 1995 [306]. Coupling of aryl- and vinyl-trialkylstannanes in polar aprotic solvents

at 90 °C over four minutes gave the corresponding *methyl*-¹¹C-toluenes and ¹¹C-methyl alkenes, respectively, in 30–54% RCY. Extensive optimization of the Stille reaction toward use for PET radiochemistry with [¹¹C]CH₃I was reported by Suzuki, Noyori, and Långström using substoichiometric amounts of [^{12/13}C]CH₃I [307]. Aryltrimethylstannanes were found to be more reactive than their tributyl congeners; however, they promote the formation of [¹¹C]ethane and can also transfer a ¹²C-methyl group and thus reduce the molar activity of the final product. Trimethylstannanes are also more toxic, requiring rigorous quality control, especially in the case of clinical/Good Manufacturing Practice (**GMP**) productions. The use of the sterically demanding P(*o*-tolyl)₃ ligand facilitates the transmetalation and reductive elimination steps. The addition of CuCl is thought to generate an aryl-Cu intermediate that transfers the aryl group more rapidly than the aryl-Sn species, further accelerating the rate-limiting step. The optimized reaction therefore involved methylation of aryltributylstannanes using Pd₂(dba)₃, P(*o*-tolyl)₃, CuCl, and K₂CO₃ in DMF at 60 °C for five minutes, providing ^{12/13}C-methylated products in excellent yields. This optimized method was used with [¹¹C]CH₃I to synthesise the methyl ester of (15*R*)-[¹¹C]TIC (Figure 7.36a), the prodrug form of a prostaglandin receptor ligand, in 85% RCY and with a molar activity of 100 GBq·μmol⁻¹; it was used for imaging prostaglandin receptors in the human brain [308].

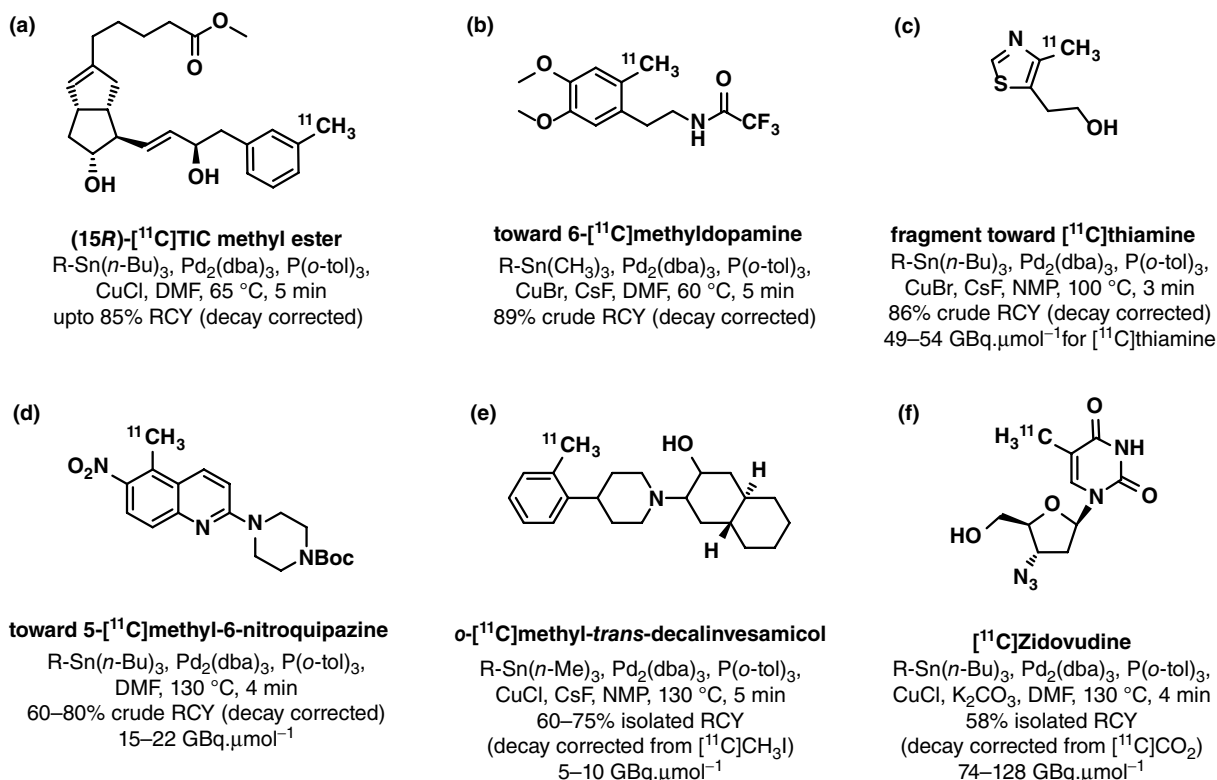


Figure 7.36 Bioactive molecules labelled with carbon-11 using a Stille coupling.

The Stille coupling of electron-rich arenes and heteroarenes such as a protected dopamine analogue [309] (Figure 7.36b) and the fragment toward [^{11}C]thiamine [310] (Figure 7.36c) was achieved using a CuBr/CsF system [311, 312]. Electron-poor arenes such as the protected precursor to 5- ^{11}C -methyl-6-methylquinazepine [313] (Figure 7.36d) have also been successfully synthesised using the Stille coupling. Vinyltrialkylstannanes [311] and alkynyltrialkylstannanes [308, 314] have also been shown to be active in the Stille coupling, giving ^{11}C -methylated products in RCY >85% or 75%, respectively. Despite concerns over the toxicity of organostannanes, the wide functional group tolerance of the reaction, illustrated by successful synthesis of the unprotected ^{11}C -labelled vesamicol derivative [315] (Figure 7.36e) and [^{11}C]zidovudine [316] (Figure 7.36f), has contributed to the application of the Stille coupling to the synthesis of a wide range of ^{11}C -labelled bioactive molecules.

The preparation of stannylated precursors for the Stille reaction remains a challenge. To address this, ^{11}C -methylstannanes, which are able to react with more readily available aryl or vinyl halides, were developed. Långström and colleagues reported the synthesis of 5- ^{11}C -methyl-1-aza-5-stanna-bicyclo[3.3.3]undecane in 20–90% RCY by reaction of the chlorostannane with [^{11}C]CH₃Li (Figure 7.37a) [317]. 5- ^{11}C -Methyl-1-aza-5-stanna-bicyclo[3.3.3]undecane was shown to undergo efficient Stille coupling with a range of aryl halides, providing ^{11}C -methylated products in 9–90% RCY. Huiban et al. used a ^{11}C -methylstannate derived from Lappert's stannane and more readily available [^{11}C]CH₃I (Figure 7.37b). TBAF-activated ^{11}C -methylstannate underwent an efficient Stille coupling with a series of bromoquinolines and halonaphthalenes at 120 °C in 63–78% RCY using Pd₂(dba)₃ in the absence of any ligand [312]. The tin by-product is less toxic than the organotin by-products of the conventional Stille coupling. In a follow-up investigation, the authors compared the conventional Stille coupling with [^{11}C]CH₃I with the modified Stille coupling with the [^{11}C]methylstannate toward the ^{11}C -methylation of bioactive quinolines and quinolinamides. Radiochemical yields were found to be higher when using the ^{11}C -methylstannate in the case of [^{11}C]SB222200, a NK-3 receptor antagonist. (Figure 7.37b) [318]. Automation of the process resulted in even higher radiochemical purity (>99% vs. >95%) of the ^{11}C -methylated product.

7.4.3.5.3 Suzuki Coupling Reactions

The same report by Andersson et al. that described the first Stille cross-coupling with [^{11}C]CH₃I also described the first Suzuki cross-coupling with [^{11}C]CH₃I [306]. [$1\text{-}^{11}\text{C}$]Heptane was prepared from 9-hexyl-9-borabicyclo[3.3.1]nonane (9-hexyl-9-BBN) with Pd(PPh₃)₄ in the presence of NaOH or K₃PO₄ at 90 °C for 4 minutes. Similarly, Hostetler et al. reported the synthesis of $\omega\text{-}^{11}\text{C}$ -palmitic acid derivatives [319]. ^{11}C -Methylation of arenes via microwave-mediated Suzuki coupling was achieved by the same group using aryl boronic acids or esters to give *methyl*- ^{11}C -toluenes [320]. Similar RCY was observed with either Pd(PPh₃)₄ or Pd(dppf)₂Cl₂ in DMF; the former, however, gave an insoluble Pd(0) precipitate. During their optimization of the Suzuki cross-coupling, they showed that it was necessary to form the reactive [^{11}C]CH₃-Pd(II)-I complex prior to the addition of the boronic acid or ester to achieve consistently high RCYs. The authors demonstrated the

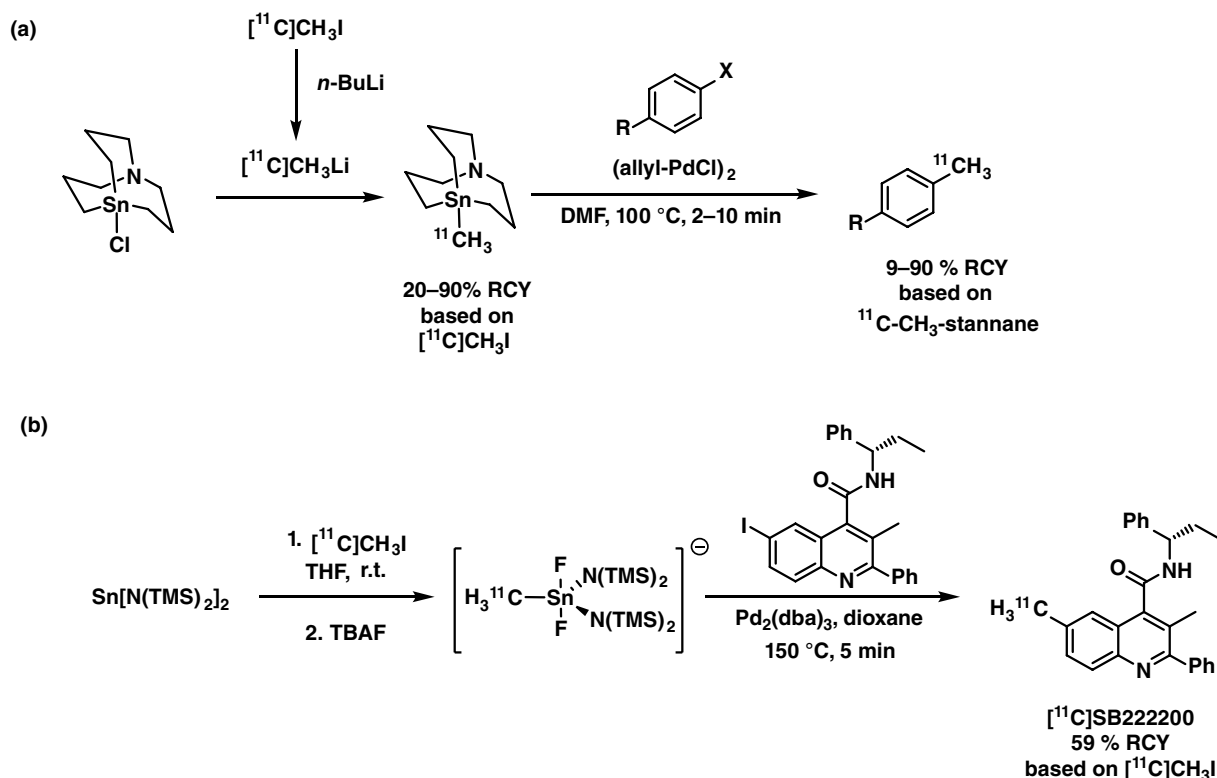


Figure 7.37 Synthesis and utilization of ^{11}C -methylstannanes and ^{11}C -methylstannates for coupling with aryl halides.

synthesis of a range of substituted ^{11}C -toluenes, highlighting the reaction's tolerance to both *ortho*-substituted and protic functional groups. Doi et al. performed a systematic study of the Pd-mediated reaction between sub-stoichiometric quantities of $^{12/13}\text{C}$ CH_3I and excess of a boronic acid/ester as a proxy for the development of the reaction with ^{11}C CH_3I [321]. The highest RCYs (87–94%) were achieved with $\text{Pd}_2(\text{dba})_3$ and $P(o\text{-tolyl})_3$ at 60°C in five minutes. Using these conditions, *p*- ^{11}C xylene was radiolabelled in 96% RCY from the BPin precursor; and ^{11}C celecoxib, a cyclooxygenase-2 (COX-2) inhibitor, was isolated in 63% RCY with a molar activity of $83\text{ GBq}\cdot\mu\text{mol}^{-1}$ (Figure 7.38a) [321]. ^{11}C -Methylation of aniline-bearing boronic acids and esters was accomplished in 49–82% crude RCY using the $\text{Pd}_2(\text{dba})_3/P(o\text{-tolyl})_3/\text{K}_2\text{CO}_3$ system, as illustrated for the synthesis of ^{11}C CIMBI-712 (Figure 7.38b) [322]. Electron-deficient arenes have also been shown to undergo efficient Suzuki coupling with ^{11}C CH_3I , using the corresponding boronic acid precursor, $\text{Pd}_2(\text{dppf})_2\text{Cl}_2$ as catalyst, under microwave heating, and has been used for the synthesis of ^{11}C MTEB, an mGluR5 antagonist (Figure 7.38c) [323].

Vinyl boronic esters have also been shown to be competent coupling partners in the Suzuki reaction with ^{11}C CH_3I and have been used to prepare all-*trans*- ^{11}C retinoic acid

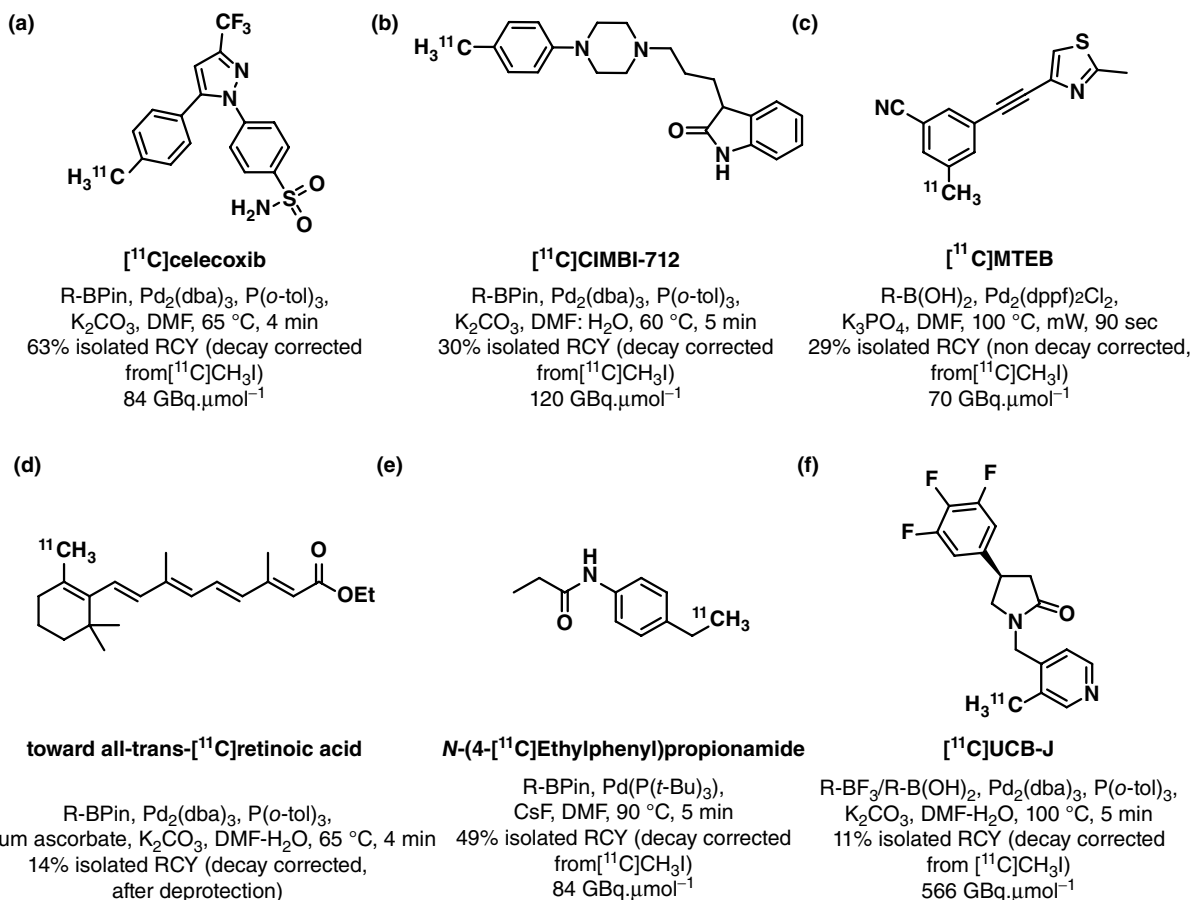


Figure 7.38 Various PET radiotracers prepared by the application of the Suzuki reaction.

in good RCY (Figure 7.38d) [324]. Benzyl and cinnamyl boronic acids and esters have also been employed for the sp^3 - sp^3 Suzuki coupling reaction with [¹¹C]CH₃I [325]. Optimized reaction conditions employed the electron-rich and bulky P(*t*-Bu)₃ ligand in combination with CsF as base. *N*-(4-[¹¹C]Ethylphenyl)propionamide was synthesized in 90% crude and 49% isolated RCY at 90 °C for 5 minutes (Figure 7.38e). Aryl-trifluoroborates as the radiolabelling precursors have been used in the synthesis of [¹¹C]UCB-J, a PET radiotracer for imaging of the synaptic vesicle protein SV2A (Figure 7.38f) [326]. The boronic acid precursor can also be used; however, it results in the production of protodeborated by-products. Protodeborylation is a common side reaction in Suzuki couplings, giving rise to analogues that are difficult to separate and can compete for the same binding site as the desired PET ligand. Using the trifluoroborate precursor was found to significantly reduce the amount of by-product formed. There is some debate as to whether the trifluoroborate truly undergoes the cross-coupling, or whether trace amounts of boronic acid are the reactive cross-coupling partner [327].

7.4.3.5.4 Negishi Coupling Reactions

Kealey et al. described the rapid, microwave-assisted synthesis of organozinc reagents for use in Negishi-type Pd-mediated ^{11}C -methylations by reaction of aryl halides with Rieke zinc at 180°C [328]. The organozinc reagent in THF was then cannulated into a second vial containing $\text{Pd}(\text{PPh}_3)_2\text{Cl}_2$ in DMA and $[^{11}\text{C}]\text{CH}_3\text{I}$, which had been trapped in the solution at room temperature. After five minutes ^{11}C -labeled toluene derivatives were obtained. Electron-poor substrates were slowest to react, requiring additional heating to $100\text{--}120^\circ\text{C}$. The process was successfully automated, and an mGluR₅ agonist $[^{11}\text{C}]\text{MPEP}$ was prepared in 26% RCY and with a molar activity of $46\text{ GBq}\cdot\mu\text{mol}^{-1}$, as shown in Figure 7.39a. In contrast to Stille and Suzuki cross-couplings, $[^{11}\text{C}]\text{CH}_3\text{I}$ could be added to a solution that already contained the organometallic reagent, simplifying further automation. The application of the traditional Negishi coupling is restricted by the harsh conditions needed (180°C and a strong reductant) to prepare the reactive organozinc precursor of a complex radiopharmaceutical.

As stated by Kealey et al. [328], preparation of $[^{11}\text{C}]\text{CH}_3\text{ZnI}$ would facilitate the use of the Negishi coupling toward a wider range of radiopharmaceuticals. Recently, Llop et al. have reported the synthesis of $[^{11}\text{C}]\text{CH}_3\text{ZnI}$ by the trapping of $[^{11}\text{C}]\text{CH}_3\text{I}$ gas on a cartridge containing iodine-activated zinc, $\text{Pd}(\text{PPh}_3)_4$, and the aryl halide in anhydrous DMF. After heating of the cartridge at 65°C for five minutes and elution of the reaction mixture, *methyl*- ^{11}C -toluenes were obtained in good RCY for electron-poor arenes and moderate-to-low RCY for electron-rich arenes. Automated radiosynthesis of $[^{11}\text{C}]\text{thymidine}$ was achieved in 53% crude and 6.1% isolated RCY and with a molar activity of $>50\text{ GBq}\cdot\mu\text{mol}^{-1}$ using $[^{11}\text{C}]\text{CH}_3\text{ZnI}$ (Figure 7.39b).

7.4.3.5.5 Miscellaneous Mediated Coupling Reactions

Wüst et al. reported a Sonogashira-like coupling reaction for the synthesis of substituted ^{11}C -methylpropynes [329] in 49–64% crude RCY using $[^{11}\text{C}]\text{CH}_3\text{I}$, $\text{Pd}_2(\text{dba})_3$, or AsPh_3 as a ligand and TBAF as a non-nucleophilic base in THF at 60°C for three minutes. A steroid derivative, $17\alpha\text{-(3'-}[^{11}\text{C}]\text{prop-1-yn-1-yl)-3-methoxy-3-17}\beta\text{-estradiol}$, was prepared in 27–47% isolated RCY, as shown in Figure 7.40a.

^{11}C -Methylalkenes have been prepared via a Pd-mediated cross-coupling of $[^{11}\text{C}]\text{CH}_3\text{I}$ and alkenyl-zirconocene derivatives, which are accessed through regioselective intermolecular insertion of alkynes into the Zr-H bond of the Schwartz reagent (Cp_2ZrHCl) [330]. Addition of $\text{Pd}(\text{PPh}_3)_4$ to the alkenyl-zirconocene and distillation of $[^{11}\text{C}]\text{CH}_3\text{I}$ into the solution yield ^{11}C -methylalkenes in 62–75% crude RCY (Figure 7.40b). Ester- or nitro-containing substrates were not compatible with the Schwartz reagent.

Alkenes prepared by a Wittig reaction between benz- or butyraldehydes and the phosphonium ylide generated from $[^{11}\text{C}]\text{CH}_3\text{I}$ and $\text{P}(o\text{-tolyl})_3$ were shown to undergo efficient Pd-mediated Heck reactions with a series of substituted aryl iodides (Figure 7.40c) [331]. A one-pot procedure, using $\text{Pd}_2(\text{dba})_3/\text{P}(o\text{-tolyl})_3$, afforded ^{11}C -labelled alkene and stilbene products in 43–55% crude and 34–40% isolated RCY.

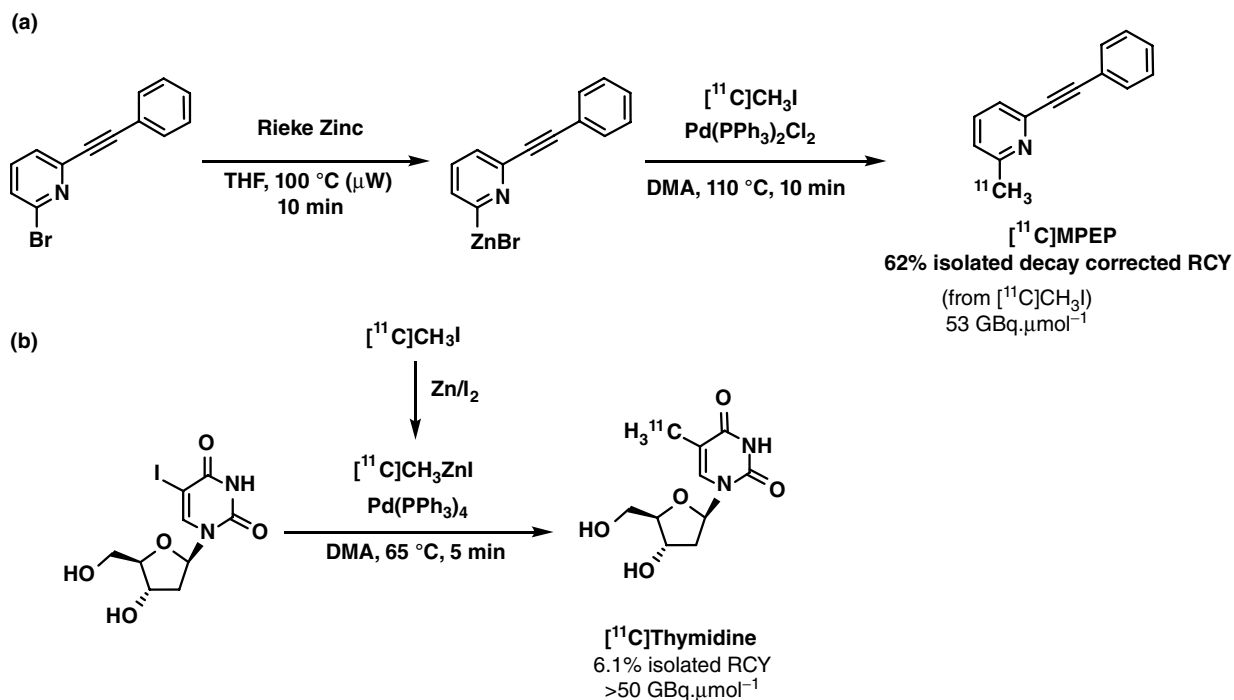


Figure 7.39 Negishi coupling reactions with [¹¹C]CH₃I and [¹¹C]CH₃ZnI.

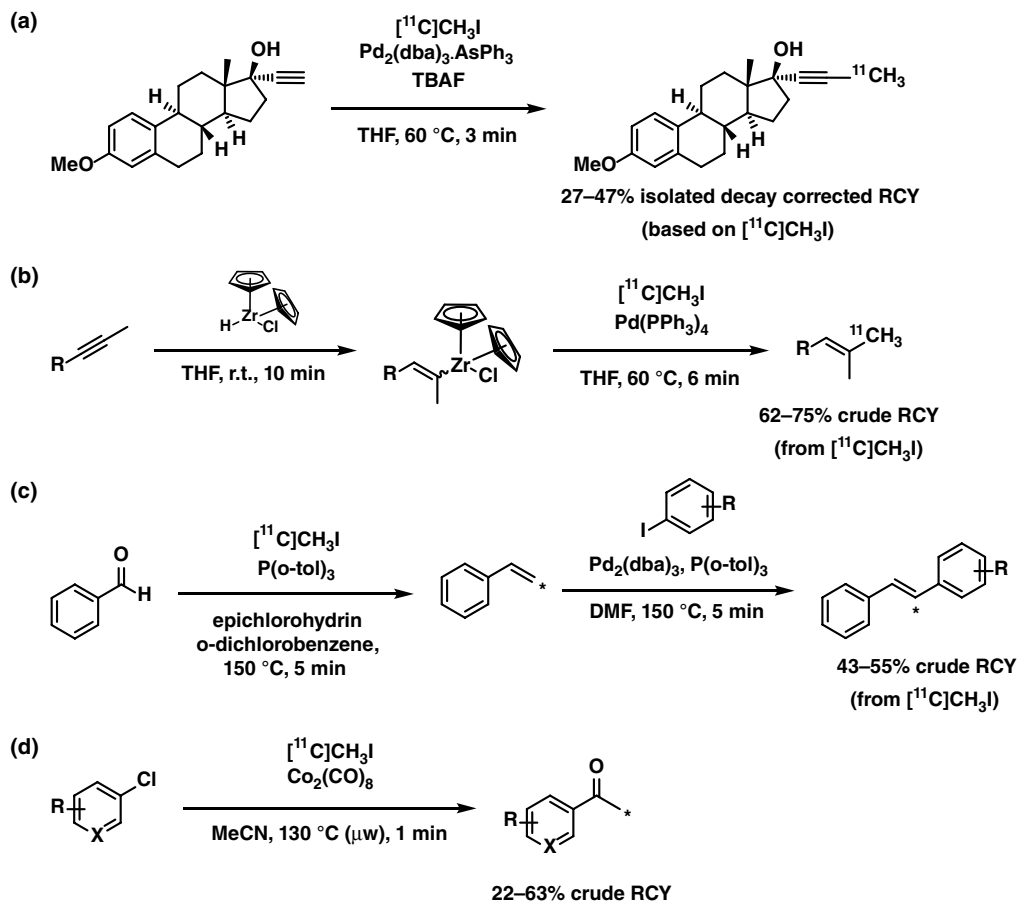
The synthesis of aryl [¹¹C]methyl ketones (Figure 7.40d) by the coupling of aryl chlorides with [¹¹C]CH₃I in the presence of Co₂(CO)₈ as a CO source and mediator was recently reported by Dahl et al. [332]. [¹¹C]CH₃I was trapped in a solution of the aryl chloride in MeCN, transferred to a vial containing Co₂(CO)₈, and then heated in a microwave. Radiochemical yields of 22–63% were observed, and electron-poor arenes gave higher RCYs. [*methyl*-¹¹C]Acetophenone was synthesized in 43% RCY on a preparative scale with a molar activity of 230 GBq.μmol⁻¹.

7.4.3.5.6 Metal-Free Coupling Reactions

Wittig reactions using ¹¹C-methyltriphenylphosphonium ylides and aldehydes afford ¹¹C-alkenes labelled in the terminal-alkene position [333, 334]. The Horner-Wadsworth-Emmons reaction between an α-¹¹C-methyl phosphonate and aldehydes was shown to furnish disubstituted ¹¹C-methylalkenes in 60–89% crude RCY [335, 336]. Carbanions generated by lithium-halogen exchange of bromoarenes have also successfully been alkylated with [¹¹C]CH₃I [337].

Enolates have proved useful substrates for ¹¹C-alkylation with a ¹¹C-labelled electrophile, and this strategy has been extensively applied toward the synthesis of ¹¹C-labelled amino acid derivatives [14, 338]. Welch et al. [339] reported the ¹¹C-alkylation of the enolate derived from a glycinate Schiff base derivative with various electrophiles. Using this approach, *D,L*-[¹¹C]phenylalanine (Figure 7.41a) was prepared in 23–31% RCY after

Figure 7.40 Miscellaneous metal-mediated ^{11}C -C coupling reactions.



deprotection, by alkylation of the glycinate Schiff base with $[\alpha\text{-}^{11}\text{C}]\text{BnCl}$. Enolates derived from *N*-(diphenylmethylene)imines have been extensively used to access racemic and enantiomerically enriched amino acids, including aminolevulinic acid analogues [340] and α -aminoisobutyric acid [341].

Chiral aldehydes and chiral alcohols have been used as chiral auxiliaries to access enantiomerically enriched amino acids from the respective chiral imine and ester derivatives of glycine [342]. Enantioenriched L - $[3\text{-}^{11}\text{C}]$ alanine (>90% ee) has been prepared from $[^{11}\text{C}]\text{CH}_3\text{I}$ using this approach, but larger electrophiles like $[\alpha\text{-}^{11}\text{C}]\text{BnI}$ showed lower yields [67, 343–345]. Chiral imidazolidinones have also been used as chiral auxiliaries and have been stereoselectively ^{11}C -alkylated, yielding L - $[3\text{-}^{11}\text{C}]$ alanine, L - $[3\text{-}^{11}\text{C}]$ phenylalanine, and L - $[3\text{-}^{11}\text{C}]$ lysine, all in >90% enantiomeric excess (ee) (Figure 7.41b) [346]. Alternatively, ^{11}C -alkylation of L -proline-based chiral nickel complexes of a glycine equivalent (Figure 7.41c) gave L - $[3\text{-}^{11}\text{C}]$ alanine, L - $[3\text{-}^{11}\text{C}]$ phenylalanine, and L - $[3\text{-}^{11}\text{C}]$ -tyrosine in 80–90% ee and 12–60% RCY [347]. ^{11}C -Methylation of chiral nickel complexes derived from aromatic amino acid derivatives showed poor RCYs [348].

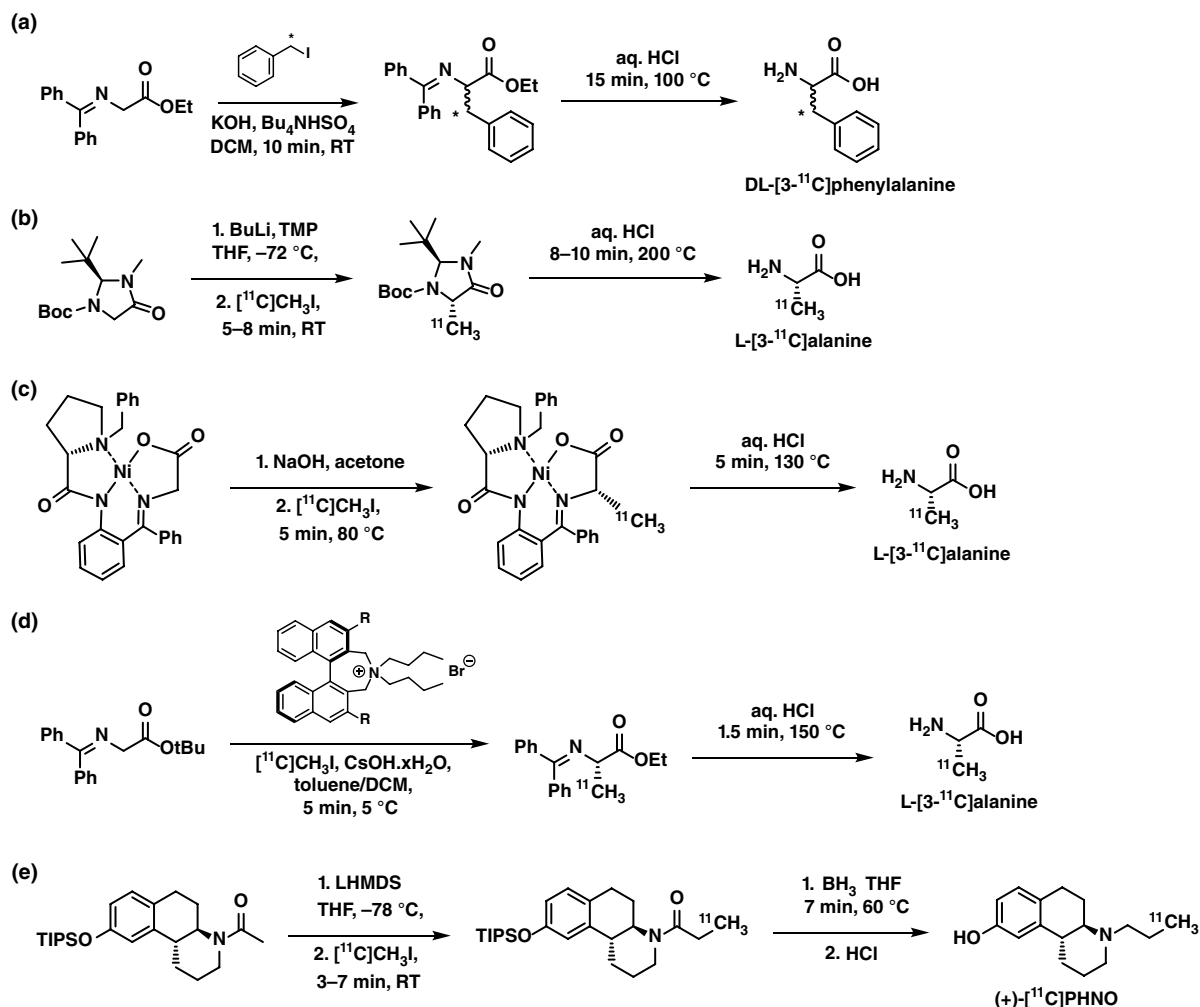


Figure 7.41 ^{11}C -Alkylations at carbon are often used to access enantioenriched amino acids. The synthesis of a propyl group from a *N*-acetyl precursor has also been described.

Filp, Pekořak, and Windhorst described the stereoselective ^{11}C -alkylation of achiral *N*-diphenylmethylenimine glycinate precursors employing chiral phase-transfer catalysis (PTC). The combination of chiral cinchonium alkaloid or chiral ammonium bis-naphthyl derivatives with an excess of solid CsOH was found to induce stereoselectivity during the ^{11}C -alkylation reaction of glycinate Schiff base derivatives with $[^{11}\text{C}]\text{CH}_3\text{I}$ or $[\alpha\text{-}^{11}\text{C}]\text{BnI}$ in toluene or toluene/dichloromethane mixtures. L-[3- ^{11}C]Alanine was synthesised using an automated method in 20% RCY and >90% ee (Figure 7.41d) [348]. Similar RCY and stereoselectivity were observed for the radiosynthesis of L-[3- ^{11}C]phenylalanine [349]. Using the pseudoenantiomer of the catalyst, the D-enantiomers of the ^{11}C -labelled amino acids could be accessed, albeit in lower RCY and enantiomeric excesses. Di- and tetrapeptides

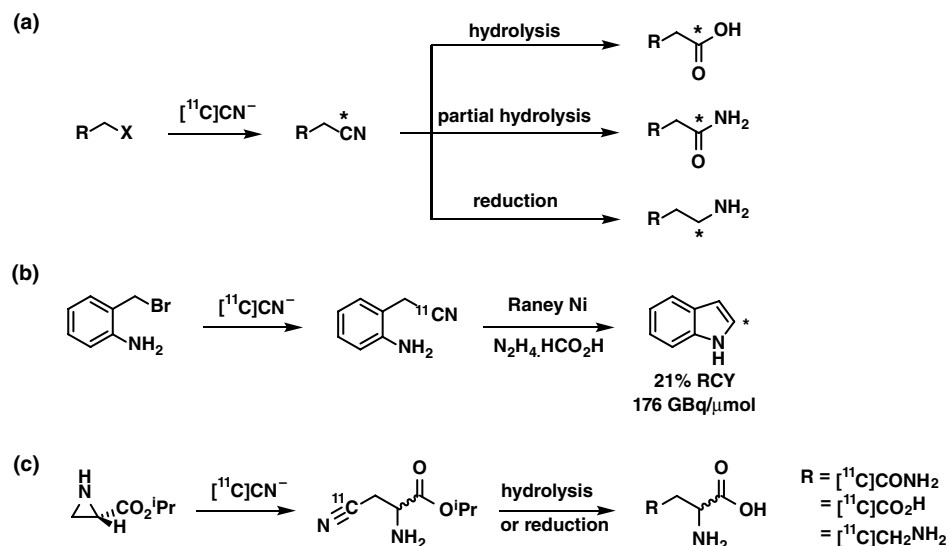
were radiolabelled using this method, including the pharmacophore of somatostatin receptor-targeting peptides, which were obtained in >90% ee [350, 351].

Takashima-Hirano et al. [352] and Kato et al. [353] reported the ^{11}C -methylation of enolates generated from arylacetates to give 3- ^{11}C -arylpropionates in 26–76% RCY. A similar reaction using the amide enolate generated in a reaction of *N*-acetyl amide with *n*-BuLi gave the *N*-3- ^{11}C -propionyl derivative, albeit in low RCY due to side reactions [354]. Garcia-Arguello et al. used similar ^{11}C -methylation for the synthesis of dopamine D2/3 receptor agonist (+)-[3- ^{11}C]PHNO [489]. The authors showed that a protected *N*-acetyl amide derivative could be deprotonated by LiHMDS at -78°C and reacted with [^{11}C]CH $_3$ I at room temperature to give the *N*-3- ^{11}C -propionyl derivative. Reduction by BH $_3$ •THF and acidic deprotection gave (+)-[3- ^{11}C]PHNO in 9% RCY in 60 minutes using an automated synthesiser (Figure 7.41e).

7.4.4 Reactions with [^{11}C]Cyanide

[^{11}C]Cyanide ([^{11}C]CN $^-$) is a reactive nucleophile that undergoes substitution reactions with alkyl halides to produce organic nitriles, which may be further derivatized to obtain ^{11}C -labelled carboxylic acids [355–359], amides [360, 361], or amines [362] (Figure 7.42a). The wide reactivity of the nitrile group allows for more complex transformations: for example, ^{11}C -cyanation of 2-nitrobenzyl bromide followed by nickel-catalyzed intramolecular cyclisation has been used to radiolabel [2- ^{11}C]indole (Figure 7.42b) [363]. Additionally, [^{11}C]CN $^-$ participates in ring-opening reactions, as exemplified by the reaction of aziridine derivatives to produce ^{11}C -labelled amino acids. In this process, the intermediate ^{11}C -cyanoalanine could be converted in one step to the formamide (asparagine), the acid (aspartic acid), or the amine (2,4-diamino-butyric acid) (Figure 7.42c) [364].

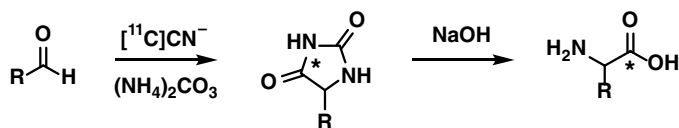
Figure 7.42 Applications of [^{11}C]cyanide as a nucleophile to give [^{11}C]nitriles, which may be further hydrolysed or reduced to give other functional groups.



^{11}C -Amino acids may be synthesised by the Bucherer-Bergs reaction (often referred to as the Bucherer-Strecker method). This multicomponent reaction combines an aldehyde or ketone with ammonium carbonate and carrier-added $[^{11}\text{C}]$ cyanide and is typically performed at high temperature and pressure. The resultant ^{11}C -hydantoin intermediate is subsequently hydrolysed to yield the corresponding *carbonyl*- ^{11}C -amino acid (Figure 7.43a). This approach has been used to access a range of radiolabelled aromatic (e.g. tyrosine [365], tryptophan [366], phenylglycine [367], and L-DOPA [368]) and aliphatic amino acids (e.g. leucine [369], glycine [370], α -aminoisobutyric acid [371, 372], and 1-aminocyclopentanecarboxylic acid [**ACPC**] [373–375]). An automated apparatus for the production of a range of amino acids has been described [376].

The Strecker reaction allows *carbonyl*- ^{11}C -amino acids to be synthesised without carrier addition, via reaction of $[^{11}\text{C}]\text{CN}^-$ with an aldehyde or ketone in the presence of ammonia, followed by hydrolysis of the intermediate α -amino- ^{11}C -nitrile (Figure 7.43b). This was originally performed using aldehyde-bisulfite adducts in place of the parent aldehydes to generate ^{11}C -labelled amino acids such as ACPC [76], alanine [377, 378], phenylalanine, and tyrosine [379]. The analogous reaction of aldehyde-bisulfite adducts in the absence of ammonia generates ^{11}C -cyanohydrins, which may be further derivatized, as exemplified by the synthesis of ^{11}C -labelled lactic acid [380, 381], dopamine [382], and octopamines [383].

(a) Bucherer-Bergs



(b) Strecker

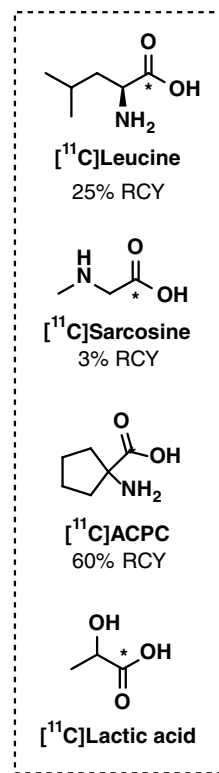
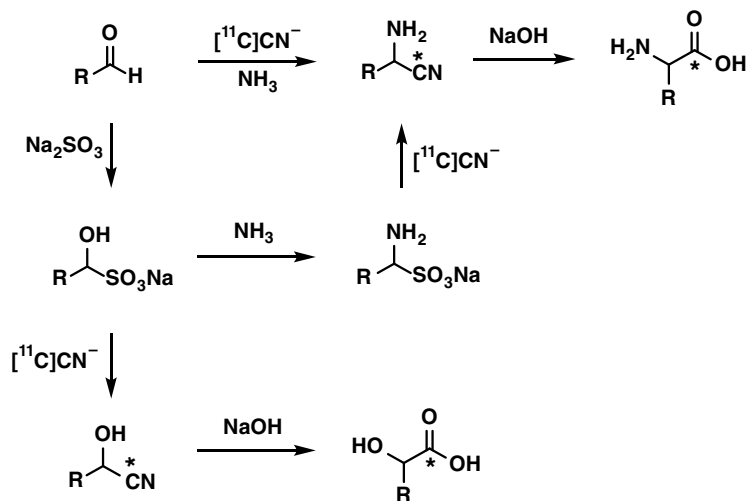
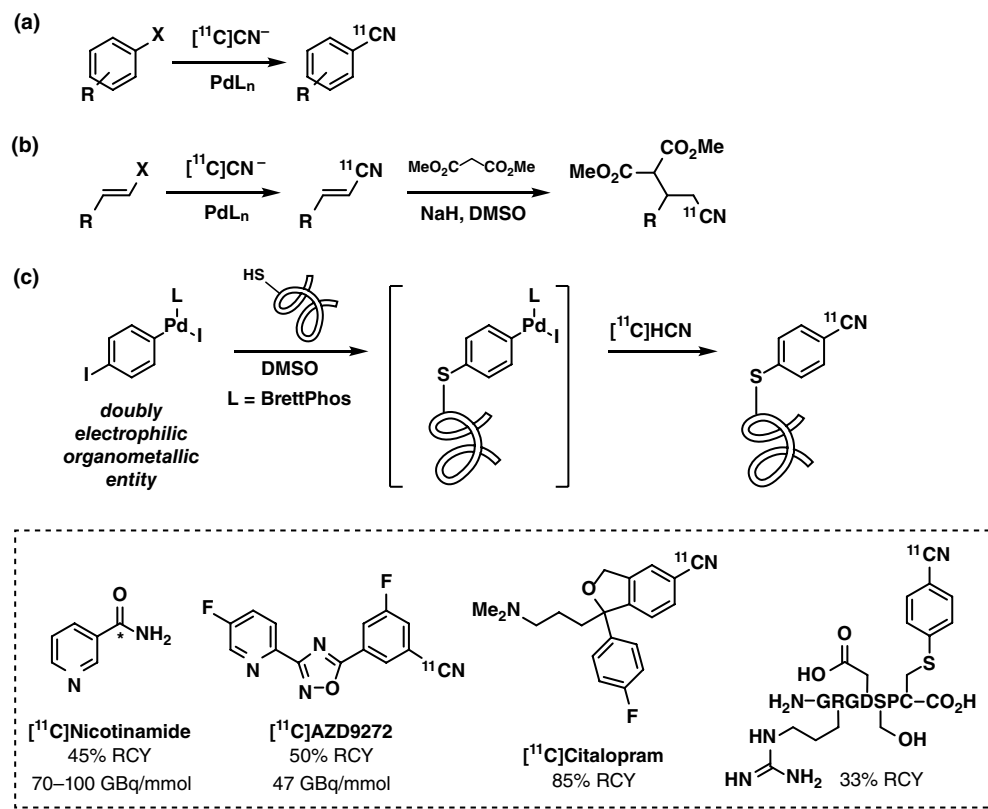


Figure 7.43 Reaction of $[^{11}\text{C}]$ cyanide with carbonyl-containing compounds.

A direct Strecker approach, starting from the parent aldehyde, has been used to generate an α -amino- ^{11}C nitrile as an intermediate in the synthesis of ^{11}C levetiracetam [384]. In this process, $^{11}\text{C}\text{CN}^-$ reacts with an imine generated in situ from reaction of an aldehyde with ammonia. This approach has been used by Xing et al. to synthesise a series of *carbonyl*- ^{11}C -amino acids, including ^{11}C sarcosine, ^{11}C methionine, *N*-phenyl- ^{11}C glycine, and ^{11}C glycine in moderate to good RCY via ^{11}C -cyanation of mixtures of aldehydes and simple amines [385].

Novel methodologies for metal-catalyzed $^{12}/^{13}\text{C}$ -cyanations may be translated to the radiochemistry laboratory to provide new radiolabeling strategies with ^{11}C cyanide [386]. Aryl ^{11}C -nitriles may be accessed via metal-catalysed coupling of $^{11}\text{C}\text{CN}^-$ and aryl halides, an early example being the reaction of fluoroaryl chromium complexes with $^{11}\text{C}\text{KCN}$ [387]. In 1994, Andersson and Långström explored Pd-mediated ^{11}C -cyanation reactions with a range of aromatic electrophiles (Figure 7.44a), achieving excellent RCYs of aryl ^{11}C -nitriles (e.g. ^{11}C nicotinamide) within five minutes [388]. A diverse array of radioligands have been synthesised using this approach, including mGluR₅ antagonists ^{11}C AZD9272 (Figure 7.44) [389] and ^{11}C SP203 [390], ^{11}C -oligothiophenes for amyloid imaging [391], and the aromatase inhibitor ^{11}C letrozole [392]. ^{11}C -Nitriles prepared by Pd-mediated reactions can also be further derivatized, illustrated by the synthesis

Figure 7.44 Palladium-mediated ^{11}C -cyanation reactions.



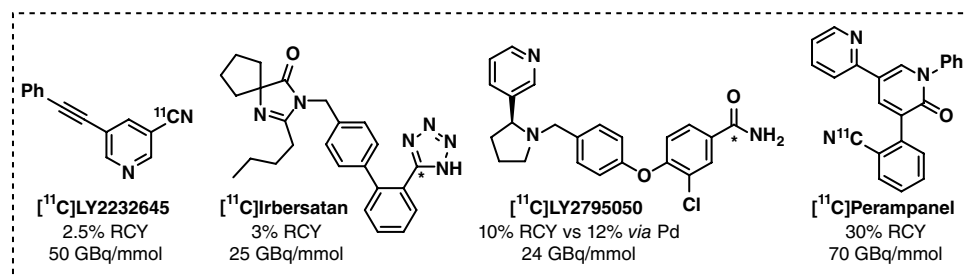
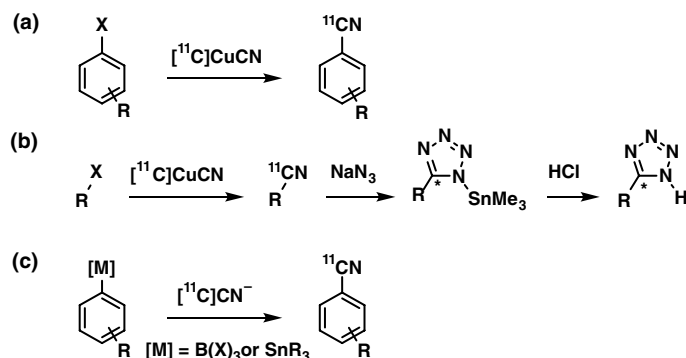
of *carbonyl*- ^{11}C -enzamides targeting poly(ADP-ribose) (PARP) synthetase [393], and tuberculosis chemotherapeutics [^{11}C]isonicotinohydrazide and [^{11}C]pyrazine-2-carboxamide [394].

In an effort to improve yields, Buchwald, Hooker, and coworkers explored the ^{11}C -cyanation of aryl halides using biaryl phosphine Pd(0) catalysts (Figure 7.44a) [395]. They postulated that performing oxidative addition before [^{11}C]CN⁻ delivery could reduce reaction times and that biaryl phosphine ligands would obviate the need for harsh reaction conditions. By mixing the Pd-ligand complex and aryl halide 30 minutes prior to [^{11}C]CN⁻ delivery, ^{11}C -cyanation reactions were found to proceed rapidly at ambient temperature with excellent functional group tolerance. This process was used for radiolabelling a range of pharmacologically active compounds, e.g. [^{11}C]citalopram (Figure 7.44). Vinyl bromides are similarly converted to vinyl ^{11}C -nitriles, which may participate in subsequent Michael addition reactions with suitable nucleophiles (Figure 7.44b) [396]. Buchwald and Hooker further extended Pd-mediated ^{11}C -cyanation chemistry to radiolabel the cysteine residue of unprotected peptides with aryl ^{11}C -nitriles (Figure 7.44c) using a doubly reactive electrophile precursor [397]. This reaction demonstrated good chemoselectivity over other functional groups present on the peptide, providing ^{11}C -labelled peptides such as the integrin-targeting RGD peptide shown in Figure 7.44 in good RCY.

Unlike most Pd(0)-mediated reactions, Cu-mediated reactions do not require stringent air- and moisture-free conditions. Ponchant et al. explored the Rosenmund-von Braun ^{11}C -cyanation reaction between [^{11}C]CuCN and aryl halides (Figure 7.45a) [398], which was found to proceed in good RCYs with aryl iodide substrates. In some cases, yields were lower than those obtained under Pd-mediation [399]; however, the Cu-mediated reaction requires no special handling of reagents. ^{11}C -Cyanations with [^{11}C]CuCN have been used to prepare a library of potential PET imaging agents for the AMPA receptor [400, 401] and the orexin-2 receptor [401, 402] and employed in the multistep synthesis of the ^{11}C -tetrazoles, LY202157 [403], and irbesartan [404], where the resultant nitrile participates in a subsequent [1 + 3] cycloaddition reaction with NaN₃ (Figure 7.45b). Recently, this methodology has been extended to enable copper-mediated ^{11}C -cyanation of aryl boronic acids [405, 406] and aryl stannanes [406] (Figure 7.45c). These reactions are compatible with a variety of substituted aryl and heteroaryl substrates and have been applied to the synthesis of the κ -opioid receptor ligand [^{11}C]LY2795050 [407] and the epilepsy drug [^{11}C]perampanel [406].

[^{11}C]CN⁻ is readily converted into other reactive labelling precursors, including cyanate ([^{11}C]NCO⁻), thiocyanate ([^{11}C]NCS⁻), and cyanogen bromide ([^{11}C]CNBr) (Figure 7.46). [^{11}C]CNBr is prepared by solution-phase reaction of [^{11}C]HCN with bromine [408] or by gas-phase reaction with pyridinium tribromide [409]. [^{11}C]CNBr is notable for its umpolung reactivity, providing an electrophilic source of [^{11}C]cyanide and allowing an opportunity for reaction with nucleophiles such as amines (including proteins) [410] to give ^{11}C -cyanamides or ^{11}C -guanidine derivatives [411–414], alcohols (including polysaccharides) [415] to give ^{11}C -cyanates, or thiols to give ^{11}C -thiocyanates. [^{11}C]NCO⁻ is prepared by oxidation of [^{11}C]CN⁻ with KMnO₄ [380, 416, 417]. Aminolysis of [^{11}C]NCO⁻ with

Figure 7.45 Cu-mediated ^{11}C -cyanation reactions.



ammonium sulfate at $185\text{ }^{\circ}\text{C}$ gives $[^{11}\text{C}]$ urea [416, 417], which can be used for the synthesis of ^{11}C -labelled heterocycles such as $2\text{-}^{11}\text{C}$ -pyrimidines, including $[2\text{-}^{11}\text{C}]$ thymine and $[2\text{-}^{11}\text{C}]$ thymidine [418]. ^{11}C -Ureas can also be used to prepare ^{11}C -hydantoins, as shown by Emran et al. in the radiosynthesis of 5,5-diphenyl- $[2\text{-}^{11}\text{C}]$ hydantoin [419]. $[^{11}\text{C}]$ SCN $^{-}$ can be prepared from $[^{11}\text{C}]$ NaCN or $[^{11}\text{C}]$ CNBr by reaction with S_8 or Na_2S , respectively [420, 421]. $[^{11}\text{C}]$ SCN $^{-}$ is particularly useful as an intermediate and can be converted to a range of other functional groups, including thiozones, thiocyanates, isothiocyanates, and sulfonyl-tetrazoles [422], and incorporated into heterocycles such as the myeloperoxidase (MPO) inhibitor $[^{11}\text{C}]$ AZD3241 [423].

7.4.5 Reactions with $[^{11}\text{C}]$ Formaldehyde

$[^{11}\text{C}]$ HCHO is not widely used as a precursor for radiolabelling with carbon-11, but the intermediate oxidation state of this reagent has allowed for its use in a wide range of reactions for incorporating a one-carbon unit into complex scaffolds. $[^{11}\text{C}]$ HCHO has found application in the synthesis of saturated and unsaturated heterocycles labelled with carbon-11. Saeed et al. prepared $[^{11}\text{C}]$ methylenetetrahydrofolate, a candidate PET radiotracer for imaging proliferating cells, by cyclization of enzymatically produced tetrahydrofolate with $[^{11}\text{C}]$ HCHO, as shown in Figure 7.47a [424]. $[^{11}\text{C}]$ Methylenetetrahydrofolate has also previously been prepared from $[^{11}\text{C}]$ HCHO in situ in a multistep bioreactor system for the synthesis of ^{11}C -labelled nucleosides [425]. $[^{11}\text{C}]$ HCHO has been used in the radiosynthesis of two selective $5\text{HT}_{2\text{C}}$ agonists: $[^{11}\text{C}]$ WAY163909 and $[^{11}\text{C}]$ vabicaserin

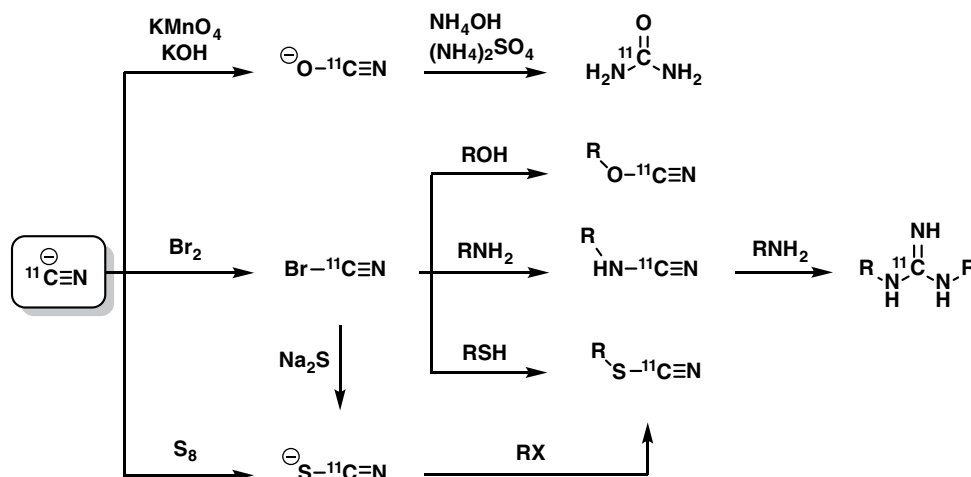
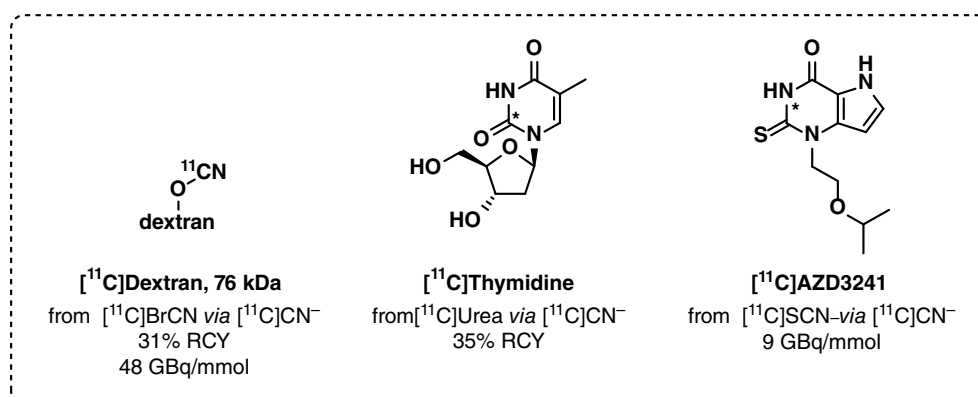


Figure 7.46

Further derivatization of $[^{11}\text{C}]$ cyanide to other useful radiolabelling precursors, and radiotracers prepared from $[^{11}\text{C}]$ cyanide-derived precursors, including $[^{11}\text{C}]$ cyanogen bromide, $[^{11}\text{C}]$ urea, and $[^{11}\text{C}]$ thiocyanate.



(Figure 7.47b) [426]. These compounds were prepared via a Pictet-Spengler cyclization with $[^{11}\text{C}]\text{HCHO}$ in modest RCYs of 1.5% and 1.3%, and products had 43 or 31 $\text{GBq}\cdot\mu\text{mol}^{-1}$ molar activity, respectively. Under the acidic reaction conditions required for the cyclization, $[^{12/13}\text{C}]\text{HCHO}$ is released from the reaction solvent DMF, necessitating substitution of the solvent for *N,N*-diethylformamide (**DEF**) to achieve acceptable molar activities of the desired products. The Pictet-Spengler reaction with $[^{11}\text{C}]\text{HCHO}$ has also been used for radiolabelling cyclic RGD peptides (Figure 7.47c) with carbon-11 at a tryptophan residue in only 35 minutes [427]. Mathews and co-workers prepared $[^{11}\text{C}]$ adenosine 5'-monophosphate ($[^{11}\text{C}]$ AMP) by cyclisation of the carboxamide phosphate precursor (Figure 7.47d) with $[^{11}\text{C}]\text{HCHO}$ in the presence of palladium on carbon in 2% RCY and with molar activity of $90\text{GBq}\cdot\mu\text{mol}^{-1}$ in 35 minutes [428]. $[^{11}\text{C}]\text{HCHO}$ has also been used to cyclize a 2-oxoacetaldehyde derivative to afford $[^{11}\text{C}]$ atipamezole in 24% RCY in the presence of ZnO and NH_4OH [429].

D-Serine is an important co-transmitter of *N*-methyl-D-aspartate (NMDA) receptors and had been prepared by ^{11}C -hydroxymethylation of chiral nickel(II) complex using

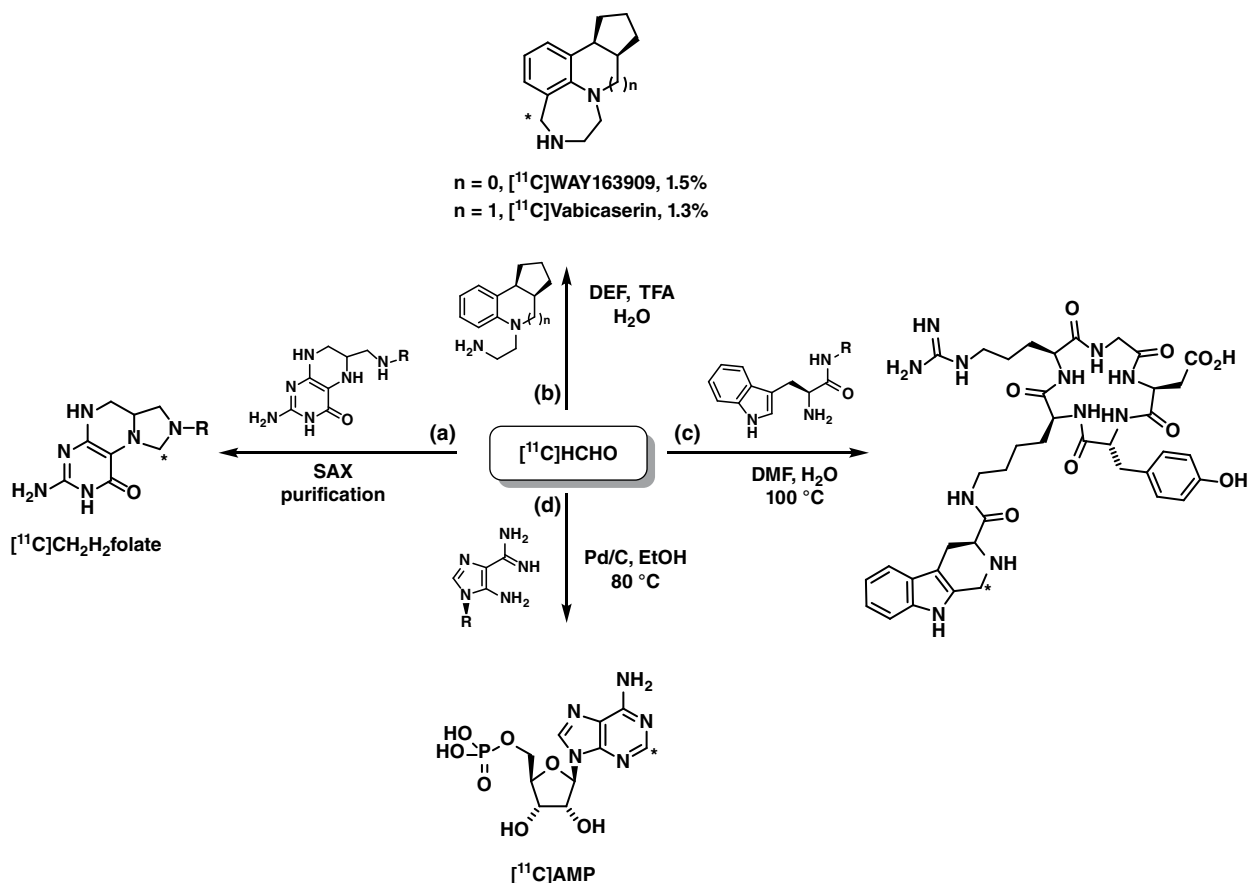


Figure 7.47 Applications of [^{11}C]HCHO in cyclizations with amines.

[^{11}C]HCHO, as illustrated in Figure 7.48a, in 80% diastereomeric excess and RCY 50% (based on starting [^{11}C]CH₃I) [430]. [^{11}C]HCHO has also been used to prepare 1,1'-[^{11}C]methylene-di-(2-naphthol), a candidate PET tracer for Alzheimer's disease, and was prepared in an automated synthesizer from [^{11}C]HCHO and 2-naphthol under acidic conditions in 48% RCY and with molar activity of 32 GBq μmol^{-1} (Figure 7.48b) [430].

The reactivity of [^{11}C]HCHO has facilitated its use for radiolabelling proteins by reductive amination [431]. Non-selectively *N*- ^{11}C -methylated human serum albumin, fibrinogen, and luteinizing hormone were produced in good RCYs of up to 40%, as illustrated in Figure 7.48c. More recently, small-molecule amines have been radiolabelled by reductive amination in phosphate-buffered saline with [^{11}C]HCHO and NaBH₃CN (Figure 7.48d), as an alternative to radiolabelling amines with [^{11}C]CH₃I or [^{11}C]CH₃OTf [432].

7.4.6 Reactions with [^{11}C]Phosgene

Despite its challenging synthesis, gaseous [^{11}C]COCl₂ is a simple reagent to use under the automated paradigm used for the preparation of carbon-11 radiotracers. [^{11}C]COCl₂

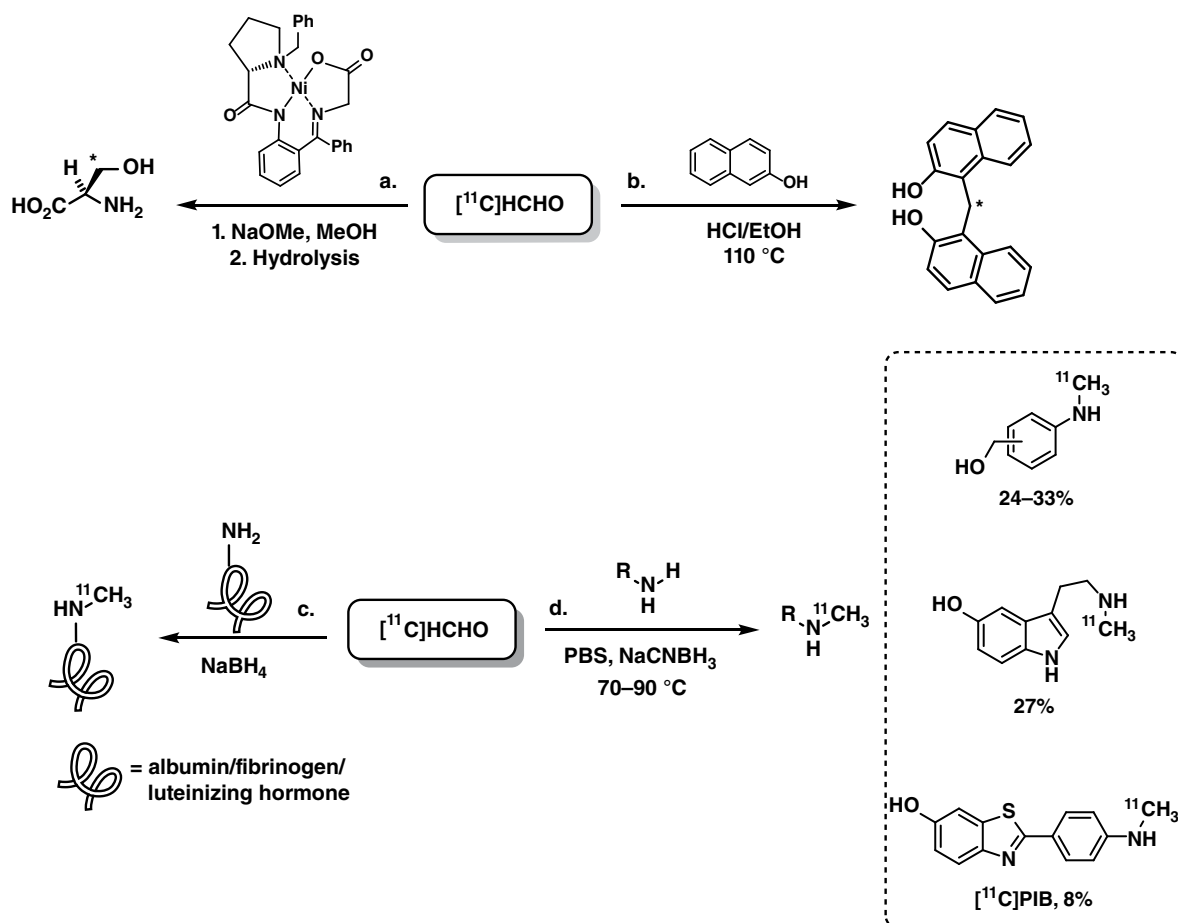


Figure 7.48 Applications of $[^{11}\text{C}]\text{HCHO}$ for alkylation reactions.

is soluble in various organic solvents, including acetonitrile and toluene, and it is typically trapped from a gas stream at ambient or below ambient temperatures in a solution already containing precursor [433]. With the rise of applications of $[^{11}\text{C}]\text{CO}_2$ and $[^{11}\text{C}]\text{CO}$ chemistries for the radiosynthesis of ^{11}C -carbonyl compounds, the use of $[^{11}\text{C}]\text{COCl}_2$ is likely to see decline in usage due to its difficult radiosynthesis and difficulties in obtaining asymmetrically substituted products.

Radiolabelling of candidate PET tracers with $[^{11}\text{C}]\text{COCl}_2$ is challenging as it is reactive toward two equivalents of a nucleophile. Preparation of symmetrically substituted ^{11}C -carbonyl-labelled-agents is, therefore, fairly straightforward and involves heating a solution containing both $[^{11}\text{C}]\text{COCl}_2$ and the amine (or alcohol) of interest. Such symmetrical molecules are, however, rarely of interest, and often the challenge in using $[^{11}\text{C}]\text{COCl}_2$ lies in the preparation of asymmetrically substituted ^{11}C -ureas and ^{11}C -carbonates, or in the preparation of ^{11}C -carbamates. Without selective means for their preparation, the synthesis of asymmetrically substituted carbonyl compounds relies on the use

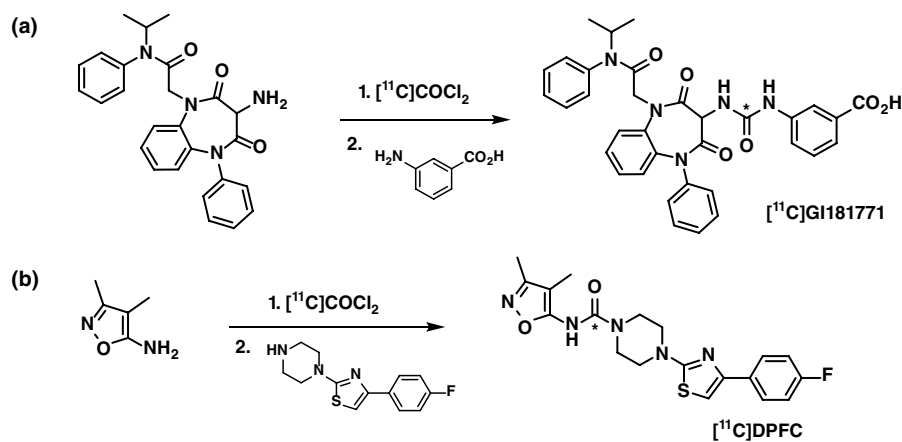
of precursors with significant differences in reactivity and their stepwise reaction with $[^{11}\text{C}]\text{COCl}_2$.

^{11}C -Isocyanates prepared by reaction of $[^{11}\text{C}]\text{COCl}_2$ with a primary amine in the presence of a tertiary amine is one strategy used to prepare asymmetrically substituted ^{11}C -carbonyl-radiolabelled products; however, extensive optimization of the reaction conditions is often required. ^{11}C -Isocyanates can also be prepared from *N,N*-bis(trimethylsilyl) alkylamines [434], from *N*-alkyl-sulfinylamines, or directly from *N,N*-organoureas [435]. Dolle et al. performed a detailed optimization of reaction conditions leading to a two-step one-pot radiosynthesis of $[^{11}\text{C}]\text{GI181771}$ (Figure 7.49a), a cholecystokinin-A (CCK-A) agonist [436]. The intermediate ^{11}C -isocyanate derivative was formed at room temperature, followed by reaction with an aniline derivative at 70°C to afford the desired asymmetric *carbonyl*- ^{11}C -urea in up to 10% RCY and with molar activity of $55\text{ GBq}\cdot\mu\text{mol}^{-1}$. Similarly, Shimoda et al. described that the coupling of $[^{11}\text{C}]\text{COCl}_2$ and an aminoisoxazole at -15°C in an effort to minimize symmetrical ^{11}C -urea formation during the synthesis of $[^{11}\text{C}]\text{DPFC}$ for PET imaging of fatty acid amide hydrolase, as shown in Figure 7.49b [437].

Asakawa et al. developed the radiosynthesis of a glycyrrhetic acid derivative with the aim of establishing a PET radiotracer for double imaging of kinases and proteasomes in tumors [438]. To avoid symmetrical ^{11}C -urea formation, $[^{11}\text{C}]\text{COCl}_2$ was reacted with the hydrochloride salts of the corresponding amines, as shown in Figure 7.50. The amine hydrochlorides retained sufficient nucleophilicity to react with $[^{11}\text{C}]\text{COCl}_2$ but were not sufficiently reactive to add to the intermediate ^{11}C -isocyanate. The second, free amine coupling partner was then added and underwent rapid reaction with the ^{11}C -isocyanate to give the desired asymmetric $[^{11}\text{C}]\text{urea}$ in 33% (Figure 7.50a) or 69% (Figure 7.50b) RCY depending on the sequence of reactions. The automation of the process afforded the ^{11}C -glycyrrhetic acid derivative in 5% RCY and with a molar activity of $48\text{ GBq}\cdot\mu\text{mol}^{-1}$ molar activity. The use of amine hydrochlorides for the synthesis of asymmetric ^{11}C -ureas via intermediary ^{11}C -isocyanates was also demonstrated in the radiosynthesis of $[^{11}\text{C}]\text{Sorafenib}$ [439] and for the preparation of three potential ^{11}C -labelled PET radiotracer candidates for imaging carbonic anhydrase IX in tumors [440].

Figure 7.49

Formation of asymmetric ^{11}C -ureas using $[^{11}\text{C}]\text{COCl}_2$.



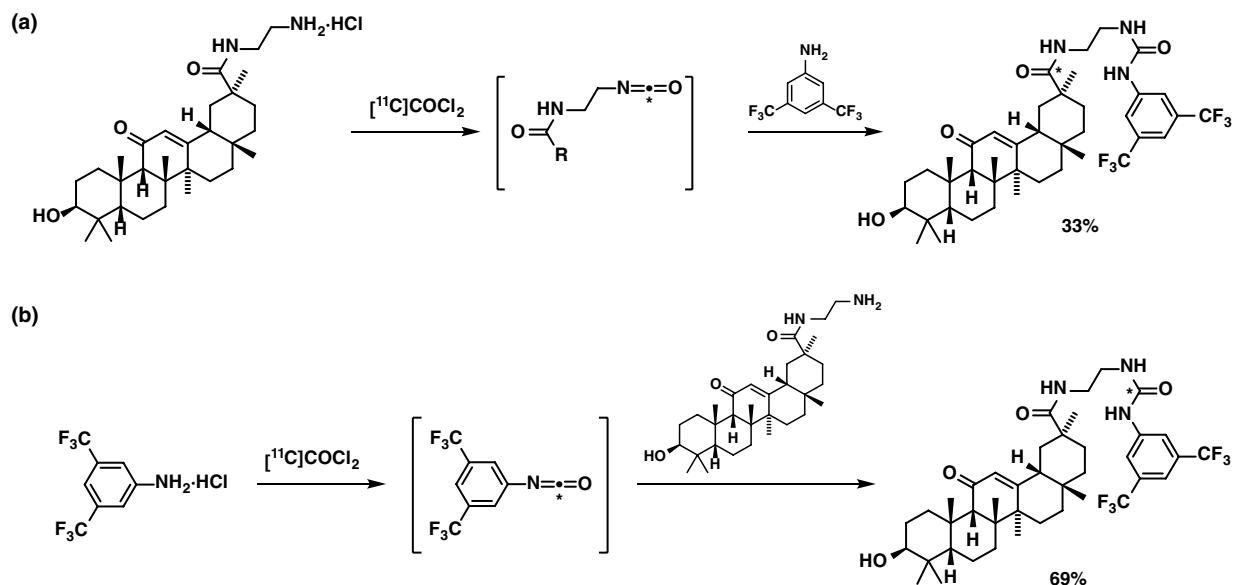


Figure 7.50 Synthesis of asymmetric ^{11}C -ureas via ^{11}C -isocyanate intermediates.

Lemoucheux et al. demonstrated an alternative approach to the synthesis of unsymmetrical ^{11}C -ureas from $[^{11}\text{C}]\text{COCl}_2$ using the debenzoylation of tertiary amines (Figure 7.51). The intermediate ^{11}C -carbamoyl chlorides could undergo further reaction with primary or secondary amines to afford unsymmetrical ^{11}C -ureas in up to 76% RCY [441]. In addition to the formation of unsymmetrical ureas, the authors showed the further derivatization of the intermediate ^{11}C -carbamoyl chlorides to ^{11}C -carbamates and ^{11}C -amides upon reaction with NaOEt or Grignard reagents, respectively.

Carbonyl- ^{11}C -Carbamates can be prepared from $[^{11}\text{C}]\text{COCl}_2$ by reaction of an intermediate ^{11}C -carbamoyl chloride or ^{11}C -isocyanate with an excess of an alcohol in a process analogous to the preparation of *carbonyl*- ^{11}C -ureas. Carbon-11-labelled ligands for the central nicotinic acetylcholine receptor (nAChR) were prepared via treatment of an intermediate $[^{11}\text{C}]\text{isocyanate}$ with an excess of alkoxide to give the ^{11}C -carbamate in 7% RCY and with 30% molar activity (Figure 7.52a) [442]. Symmetrical $[^{11}\text{C}$ -ureas, themselves prepared from ^{11}C - COCl_2 , have been subjected to alcoholysis to give the ^{11}C -carbamates. Using this approach, Lidstrom et al. prepared ^{11}C -estramustine and $[^{11}\text{C}]\text{estramustine}$ phosphate for the imaging of prostate cancer. To accomplish this, $[^{11}\text{C}]\text{COCl}_2$ was reacted with bis(2-chloroethyl)amine in THF to generate the symmetrical ^{11}C -urea, before selectively deprotonated estradiol was added to give the ^{11}C -carbamate products, as shown in (Figure 7.52b) [443].

Carbonyl- ^{11}C -Carbamates can also be prepared by first reacting $[^{11}\text{C}]\text{COCl}_2$ with an excess of an alcohol to give symmetrical ^{11}C -carbonates. Aminolysis of these symmetrical ^{11}C -carbonates gives the corresponding ^{11}C -carbamates such as $[^{11}\text{C}]\text{MTFC}$ (Figure 7.53a), $[^{11}\text{C}]\text{TPZU}$ (Figure 7.53b), and $[^{11}\text{C}]\text{SAR127303}$ (Figure 7.53c), which have found application in the imaging of serine proteases such as fatty acid amide hydrolase

Figure 7.51 The use of ^{11}C -carbonyl chlorides generated from $[^{11}\text{C}]\text{COCl}_2$, and their elaboration to ^{11}C -ureas, ^{11}C -carbamates, and $[^{11}\text{C}]$ amides.

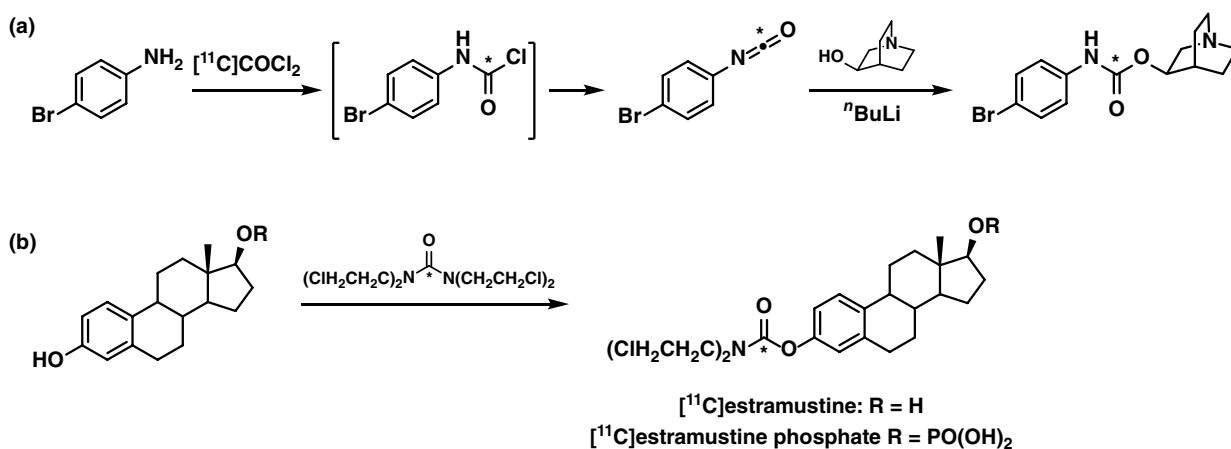
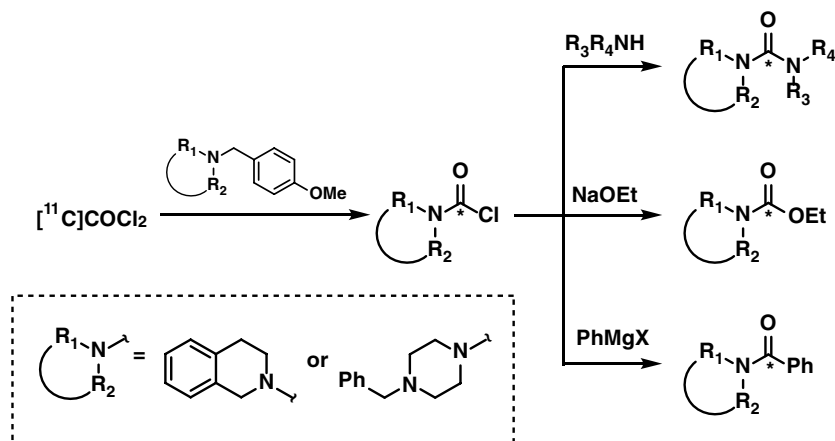


Figure 7.52 Preparation of ^{11}C -carbamates from $[^{11}\text{C}]$ phosgene.

and monoacylglycerol hydrolase [444–446]. Two structurally isomeric ^{11}C -carbamates for imaging of TSPO, $[^{11}\text{C}]\text{PK13162}$ and $[^{11}\text{C}]\text{PK13168}$ (Figure 7.53d), were radiolabelled via an intermediate ^{11}C -chloroformate in 33% and 66% RCYs, respectively, and with molar activity ranging from 50 to 140 $\text{GBq}\cdot\mu\text{mol}^{-1}$ [447]. It was postulated that the phenolic groups are sufficiently reactive toward $[^{11}\text{C}]\text{COCl}_2$ at -10°C to afford corresponding ^{11}C -chloroformates, which were further treated with diethylamine and heated to 110°C for three minutes to give the desired ^{11}C -carbamate products.

$[^{11}\text{C}]\text{COCl}_2$ is often used in cyclization reactions, incorporating carbon-11 into the rings of various heterocycles, as shown in Figure 7.54 [448, 449]. $[^{11}\text{C}]\text{COCl}_2$ reacts efficiently with 1,3- and 1,2-diamines, and 1-amino-2-hydroxyphenyls upon heating, to afford cyclized products in high RCY. Perimidinone analogue $[^{11}\text{C}]\text{RPR72840A}$, a potential PET radiotracer for imaging the serotonin reuptake system [450], and $[^{11}\text{C}]$ uric acid have been prepared using this method [451]. $[^{11}\text{C}]\text{COCl}_2$ has also been applied to the synthesis of

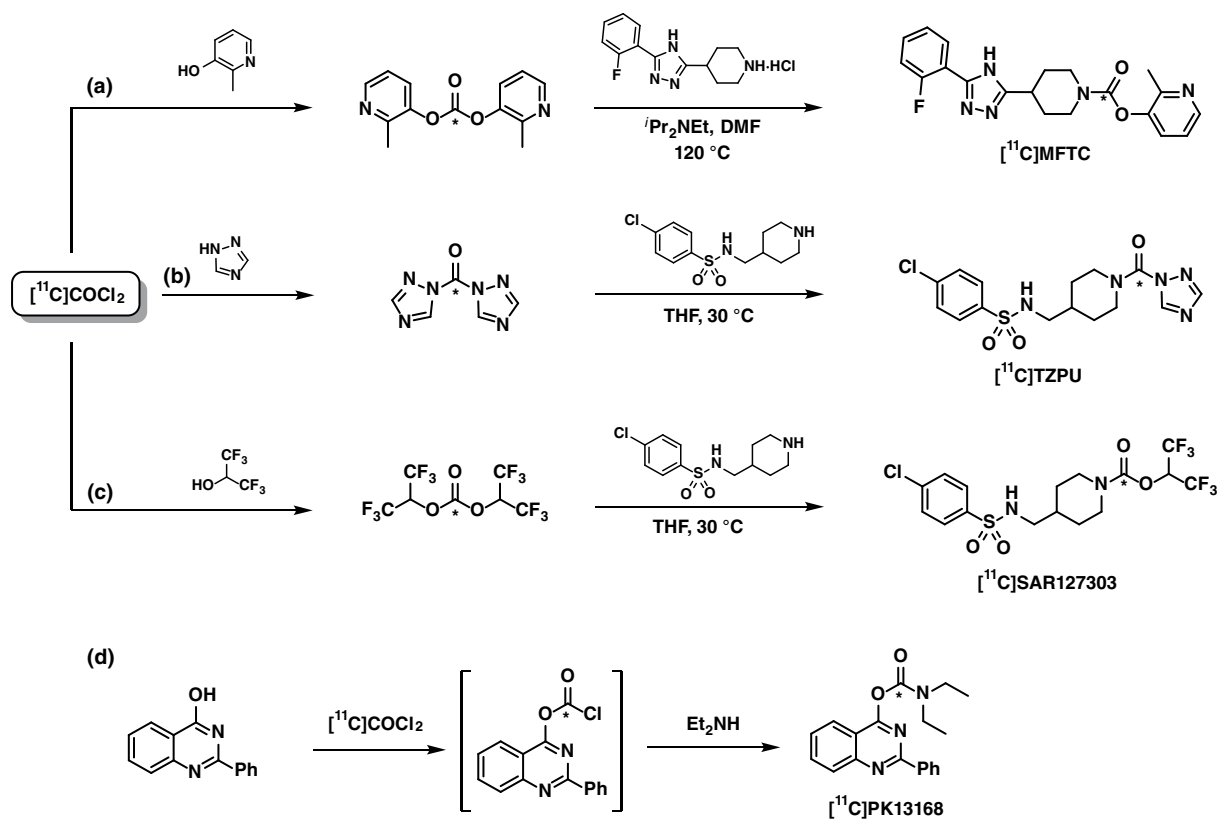


Figure 7.53 Synthesis of ^{11}C -carbamates via symmetrical ^{11}C -carbonates or ^{11}C -chloroformates.

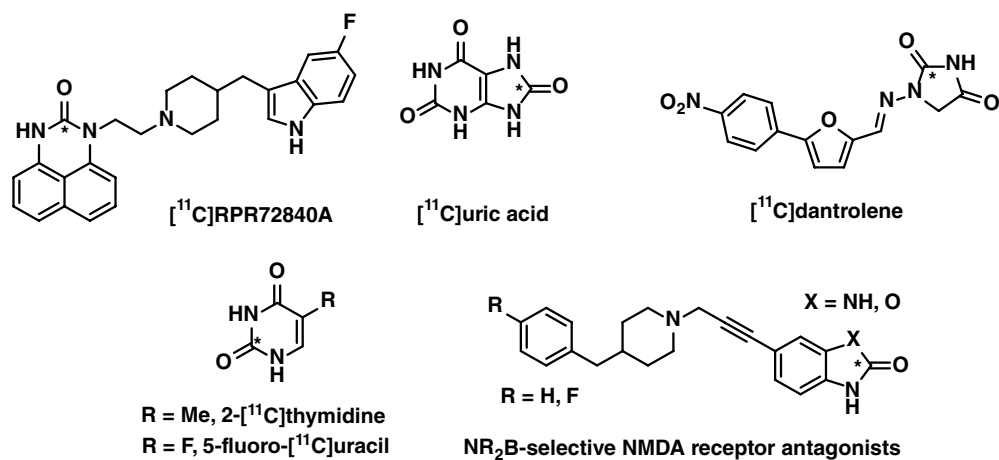


Figure 7.54 Compounds prepared by cyclization reaction with ^{11}C COCl₂.

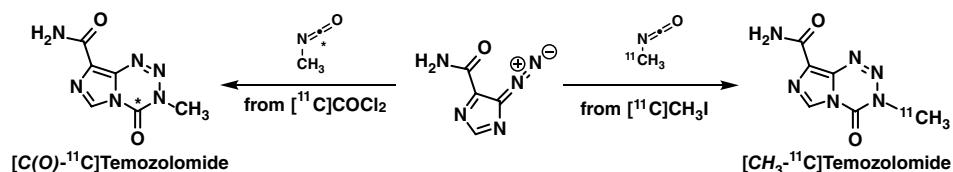
^{11}C -hydantoins. ^{11}C Dantrolene, a ligand for breast cancer resistance protein, was radio-labeled with ^{11}C COCl_2 in a multi-step one-pot sequence by Takada et al. in 34% RCY and with 47 GBq· μmol^{-1} molar activity [452]. ^{11}C -Pyrimidines, including ^{11}C thymidine and 5-fluoro- ^{11}C uracil, have also been prepared from ^{11}C COCl_2 , from the appropriate β -aminoacrylamide salts [453]. ^{11}C -Benzoxazolones [454] and ^{11}C -benzimidazolones [455, 456], also prepared from ^{11}C COCl_2 , have been explored as potential PET radiotracers for imaging the NR2B subunit of the NMDA receptor.

Methyl isocyanate labelled at two different positions has been used to prepare Temozolomide labelled at two different positions (e.g. 3- N - ^{11}C methyl or 4- ^{11}C carbonyl) depending on the method used to prepare carbon-11-labelled methyl isocyanate, as shown in Figure 7.55 [457]. For example, reaction of ^{11}C CH_3I with silver cyanate provides [*methyl*- ^{11}C]methyl isocyanate, whereas using ^{11}C COCl_2 yields [*carbonyl*- ^{11}C]methyl isocyanate, in 20% and 15% RCYs, respectively. Cyclization of each agent with the appropriate diazoimidazole provided differentially labelled ^{11}C temozolamide for the elucidation of the mechanism of action of this anticancer drug.

7.4.7 Reactions with ^{11}C Carbon Disulfide

It was not until 2012, when the Miller group disclosed their facile production of ^{11}C CS_2 , that the reagent received much attention in the radiochemistry literature [97]. ^{11}C CS_2 and ^{11}C CO_2 are similar in that they are both electrophilic at the central carbon atom and undergo reaction with nucleophiles at this position. ^{11}C CS_2 is, however, more reactive than ^{11}C CO_2 , due to the weaker C=S double bonds. In their seminal report, the Miller group showed the reaction of ^{11}C CS_2 with a range of amines in acetonitrile, giving rise to the corresponding ^{11}C -dithiocarbamate salts in only five minutes (Figure 7.56a) [97]. The only observed side product was carbon-11 labelled quaternary ammonium salt in under 5%. The resultant ^{11}C -dithiocarbamates undergo alkylation with alkyl halides or react with POCl_3 to give potentially electrophilic substituted ^{11}C -isothiocyanates. ^{11}C CS_2 has been used for the synthesis of ^{11}C -thioureas upon reaction with an excess of amine in either acetonitrile or DMSO, as shown in Figure 7.56b [98]. The resultant ^{11}C -thioureas could also be alkylated to give ^{11}C -isothioureas. ^{11}C Carbon disulfide has also been used for the synthesis of ^{11}C -thiocarbamates, exemplified by the synthesis of ^{11}C Tanaproget, a potential PET radiotracer for quantification of levels of the progesterone receptor in breast cancer. The acyclic precursor, shown in Figure 7.56c, was labelled using ^{11}C CS_2 at 150 °C in DMSO [98].

Figure 7.55 Preparation of ^{11}C temozolamide labelled at different positions.



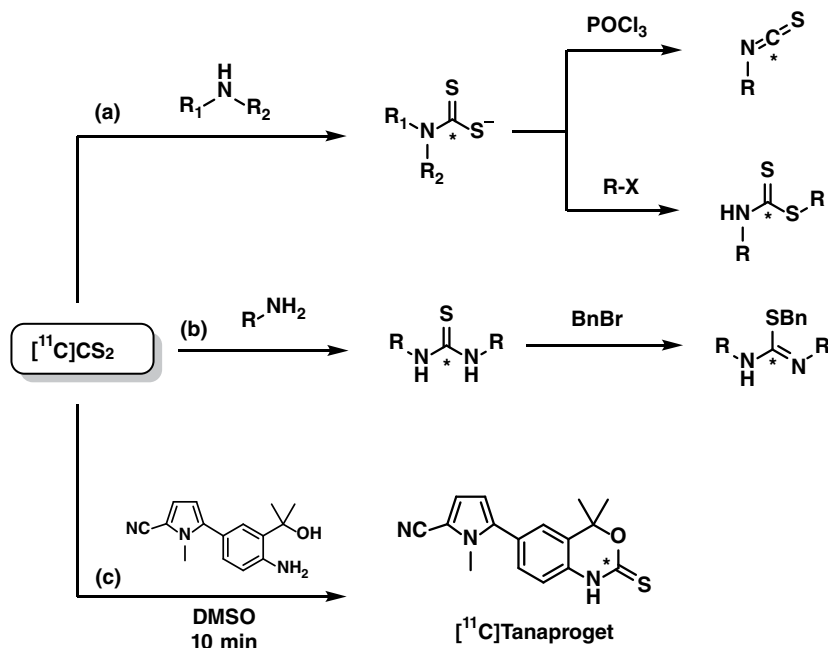


Figure 7.56 Application of the $[^{11}C]CS_2$ to the synthesis of ^{11}C -isothiocyanates, ^{11}C -dithiocarbamates, ^{11}C -thioureas, ^{11}C -isothioureas, and ^{11}C -hiocarbamates.

As an alternative to the preparation of $[^{11}C]$ thiocyanate from $[^{11}C]$ cyanide, $[^{11}C]$ thiocyanate can be prepared from $[^{11}C]CS_2$ by trapping in acetonitrile before the addition of an ammonia solution and heating to $90^\circ C$, as shown in Figure 7.57a [422]. The reaction of

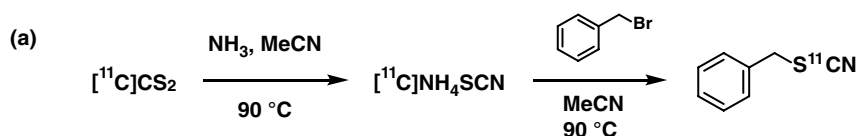
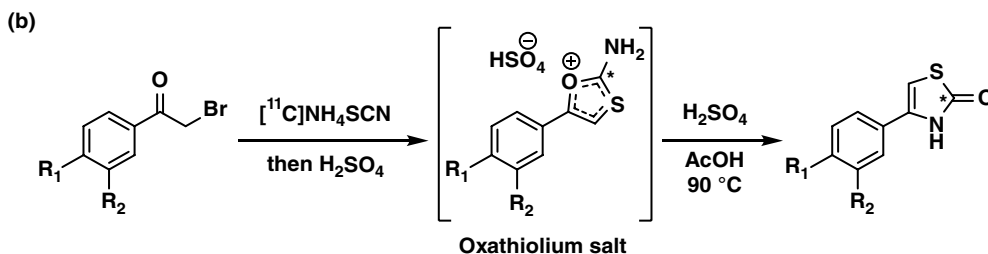
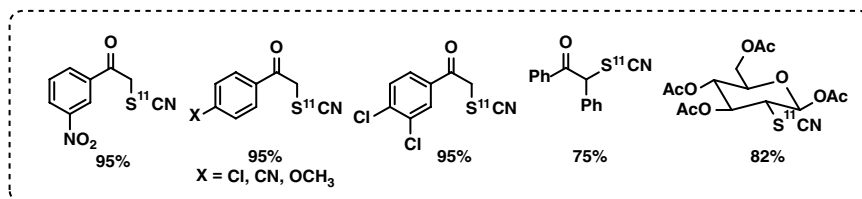


Figure 7.57 Reaction of $[^{11}C]CS_2$ for the preparation of ^{11}C -isothiocyanates.



$[^{11}\text{C}]\text{NH}_4\text{SCN}$ with benzyl bromide afforded quantitative conversion to benzyl $[^{11}\text{C}]$ thiocyanate. Several different α -ketobromides and alkyl bromides were subjected to the same reaction conditions to give alkyl ^{11}C -thiocyanates. The ^{11}C -thiocyanatophenones could be further converted to ^{11}C -thiazolones by treatment with sulfuric acid (Figure 7.57b).

7.4.8 Other Chemical Reactions with Carbon-11

7.4.8.1 $[^{11}\text{C}]$ Fluoroform

The prevalence of the CF_3 group in pharmaceuticals has led to significant efforts to develop a method for incorporating a radionuclide with high molar activity into this motif. Much of this effort has focused on the use of fluorine-18; however, existing methods all give radiolabelled products with low molar activity ($30 \text{ GBq}\cdot\mu\text{mol}^{-1}$ for the best case, commonly below $10 \text{ GBq}\cdot\mu\text{mol}^{-1}$). Haskali and Pike developed the synthesis of $[^{11}\text{C}]\text{CF}_3\text{H}$, which proved a versatile synthon for incorporating a radiolabelled CF_3 group into candidate PET probes using methods developed for $[^{18}\text{F}]\text{CF}_3\text{H}$ and $[^{18}\text{F}]\text{CuCF}_3$ [99]. For example, the addition of a solution of $[^{11}\text{C}]\text{CF}_3\text{H}$ in DMF to a solution of benzophenone in the presence of $t\text{BuOK}$ afforded $[^{11}\text{C}]$ trifluoromethylbenzhydrol quantitatively (Figure 7.58a). Similarly, $[^{11}\text{C}]\text{CF}_3\text{H}$ undergoes reaction with disulfides to give ^{11}C -trifluoromethyl sulfides, as shown in Figure 7.58b. $[^{11}\text{C}]\text{CF}_3\text{H}$ could also be converted to $[^{11}\text{C}]\text{CuCF}_3$ (Figure 7.58c), which reacts with aryl iodides (Figure 7.58d) and aryl boronic acids (Figure 7.58e) via a Cu-mediated process. Reaction of with 4-nitrophenylboronic acid gave 99% RCY of the coupled product, with a molar activity of $>500 \text{ GBq}\cdot\mu\text{mol}^{-1}$. Diazonium salts also undergo reaction with $[^{11}\text{C}]\text{CuCF}_3$ in good RCY, as shown in (Figure 7.58e). Three known PET radiotracers were prepared in excellent RCYs of up to 93%, with molar activity of up to $400 \text{ GBq}\cdot\mu\text{mol}^{-1}$, using this newly developed precursor [99].

7.4.8.2 $[^{11}\text{C}]$ Nitromethane

Deprotonation of $[^{11}\text{C}]\text{CH}_3\text{NO}_2$ provides a nucleophilic $[^{11}\text{C}]$ nitronate anion, which undergoes facile addition to carbonyl compounds (the nitroaldol reaction), as well as to other electrophiles. The ^{11}C -nitroalcohols obtained from the nitroaldol reaction can be dehydrated in situ to give α,β -unsaturated- γ - ^{11}C -alkylnitrates. For example, the radiosynthesis of β - $[^{11}\text{C}]$ nitrostyrene is achieved from $[^{11}\text{C}]\text{CH}_3\text{NO}_2$ in up to 85% RCY, as shown in Figure 7.59a [100]. A moderately selective asymmetric variant of the nitroaldol reaction with $[^{11}\text{C}]\text{CH}_3\text{NO}_2$ has also been developed using a La-Li-2,2'-bis(diphenylphosphino)-1,1'-binaphthyl (BINAP) bimetallic catalyst, providing enantioenriched ^{11}C -nitroalcohols, as shown in Figure 7.59b [458]. The ^{11}C -alkylnitrates may themselves be useful, but the versatility of the nitroaldol reaction with $[^{11}\text{C}]\text{CH}_3\text{NO}_2$ lies in the ability to convert the nitro group in the product into other functional groups, including amines (via reduction) and aldehydes (via the Nef reaction). A number of bioactive molecules including $[^{11}\text{C}]$ indole (Figure 7.59c) [459], $[1\text{-}^{11}\text{C}]$ glucose and $[1\text{-}^{11}\text{C}]$ mannose [460], and 2-(hydroxymethyl)-2-nitro- $[^{11}\text{C}]$ propane-1,3-diol ($[^{11}\text{C}]$ TRIS) [461] have been prepared in this way.

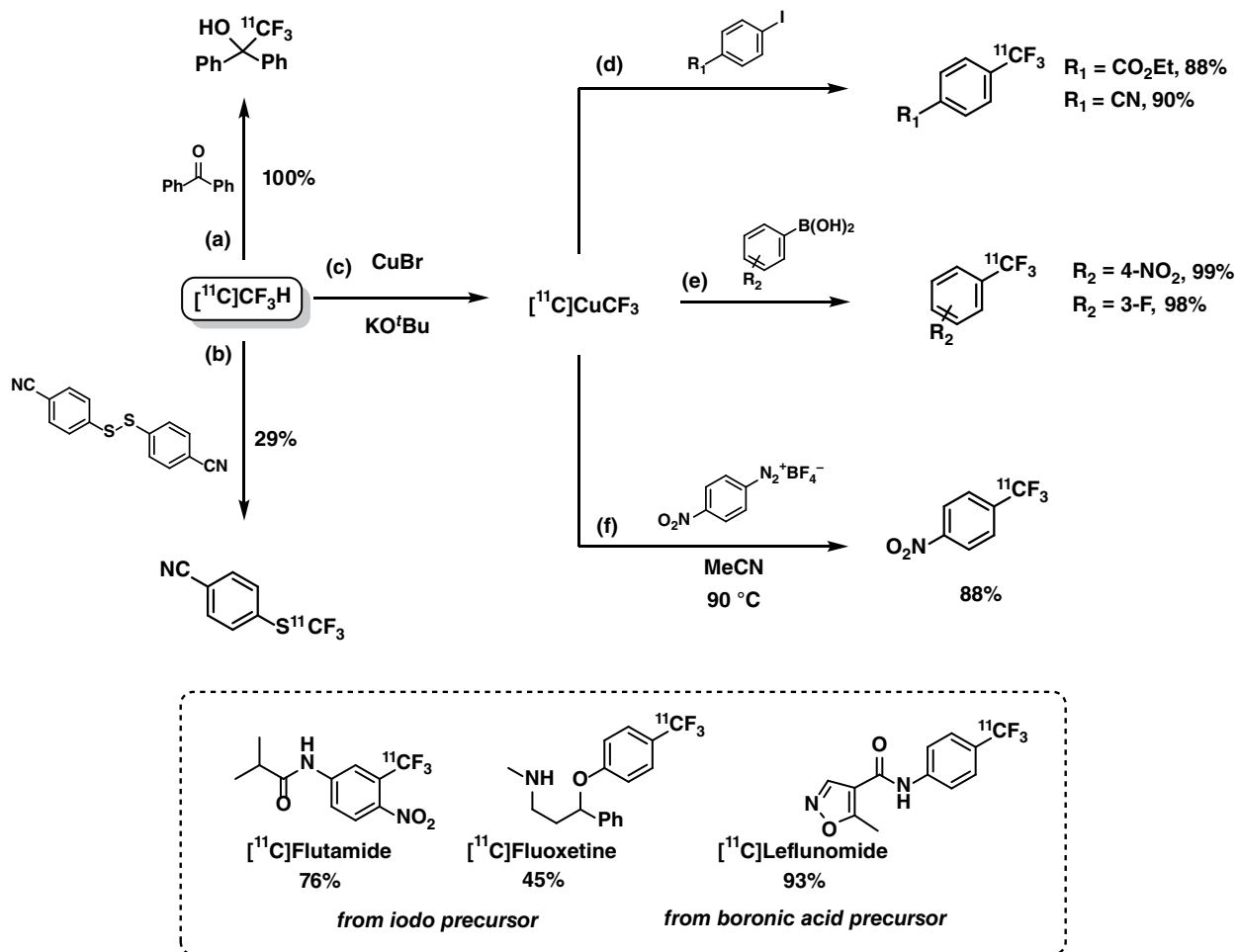


Figure 7.58 Applications of $[\text{}^{11}\text{C}]\text{CF}_3\text{H}$ for the introduction of a carbon-11 labelled CF_3 group.

$[\text{}^{11}\text{C}]\text{CH}_3\text{NO}_2$ has also been used in additional reactions. Maeding et al. employed $[\text{}^{11}\text{C}]\text{CH}_3\text{NO}_2$ in a reaction with various pyrylium salts to obtain ^{11}C -nitrobenzenes, as shown in Figure 7.59d [462]. Addition of $[\text{}^{11}\text{C}]\text{CH}_3\text{NO}_2$ to activated carbonyl compounds was employed for the synthesis of ethyl $[\text{}^{11}\text{C}]\text{nitroacetate}$, which was converted to $[\text{}^{11}\text{C}]\text{ethyl glycinate}$ (Figure 7.59e) [463]. $[\text{}^{11}\text{C}]\text{CH}_3\text{NO}_2$ has also been exploited for Michael additions with α,β -unsaturated compounds, including methyl *p*-chlorocinnamate for the synthesis of $[4\text{-}^{11}\text{C}]\text{baclofen}$ [464].

7.4.8.3 $[\text{}^{11}\text{C}]\text{Diazomethane}$

$[\text{}^{11}\text{C}]\text{Diazomethane}$ is an alternative agent for the transfer of a ^{11}C -radiolabelled methyl group to suitable nucleophiles. The ubiquitous use of $[\text{}^{11}\text{C}]\text{CH}_3\text{I}$ and $[\text{}^{11}\text{C}]\text{CH}_3\text{OTf}$, and the challenging multistep synthesis of $[\text{}^{11}\text{C}]\text{diazomethane}$, means this reagent is rarely used.

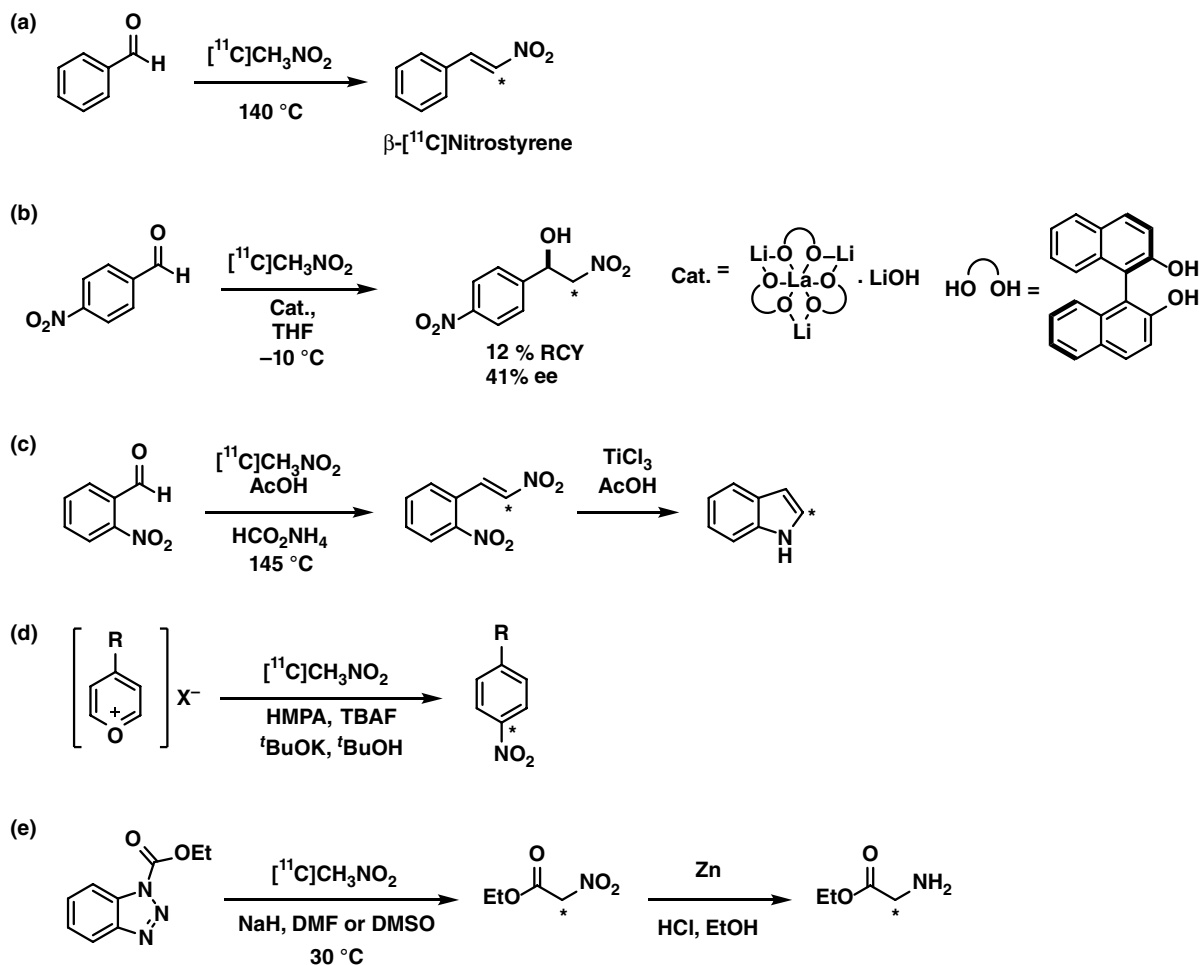


Figure 7.59 Applications of $[^{11}\text{C}]\text{CH}_3\text{NO}_2$ for nitroaldol reactions and addition reactions.

Some examples of compounds prepared by reaction with $[^{11}\text{C}]\text{diazomethane}$ include the ^{11}C -methyl ester of *N*-nitro-*L*-arginine, a nitric oxide synthase inhibitor [465], and the calcium-channel antagonist $[^{11}\text{C}]\text{S12968}$ (Figure 7.60a) and its enantiomer $[^{11}\text{C}]\text{S12967}$ [466].

7.4.8.4 $[^{11}\text{C}]\text{Methyl Azide}$

$[^{11}\text{C}]\text{CH}_3\text{N}_3$ has been employed as a reagent for the Cu-catalyzed alkyne-azide cycloaddition (**CuAAC**) as a rapid, biorthogonal approach to labelling both peptides and nucleotides with carbon-11. Schirmacher and coworkers [103] reported the radiolabelling of an alkyne-modified peptide with $[^{11}\text{C}]\text{CH}_3\text{N}_3$ in up to 55% RCY and with molar activity of $25 \text{ GBq}\cdot\mu\text{mol}^{-1}$ (Figure 7.60b). The authors also explored the in situ generation of $[^{11}\text{C}]\text{CH}_3\text{N}_3$ from $[^{11}\text{C}]\text{CH}_3\text{I}$ and NaN_3 ; however, this method was unreliable due to the variable trapping of $[^{11}\text{C}]\text{CH}_3\text{I}$, and more reliable production of the product was observed

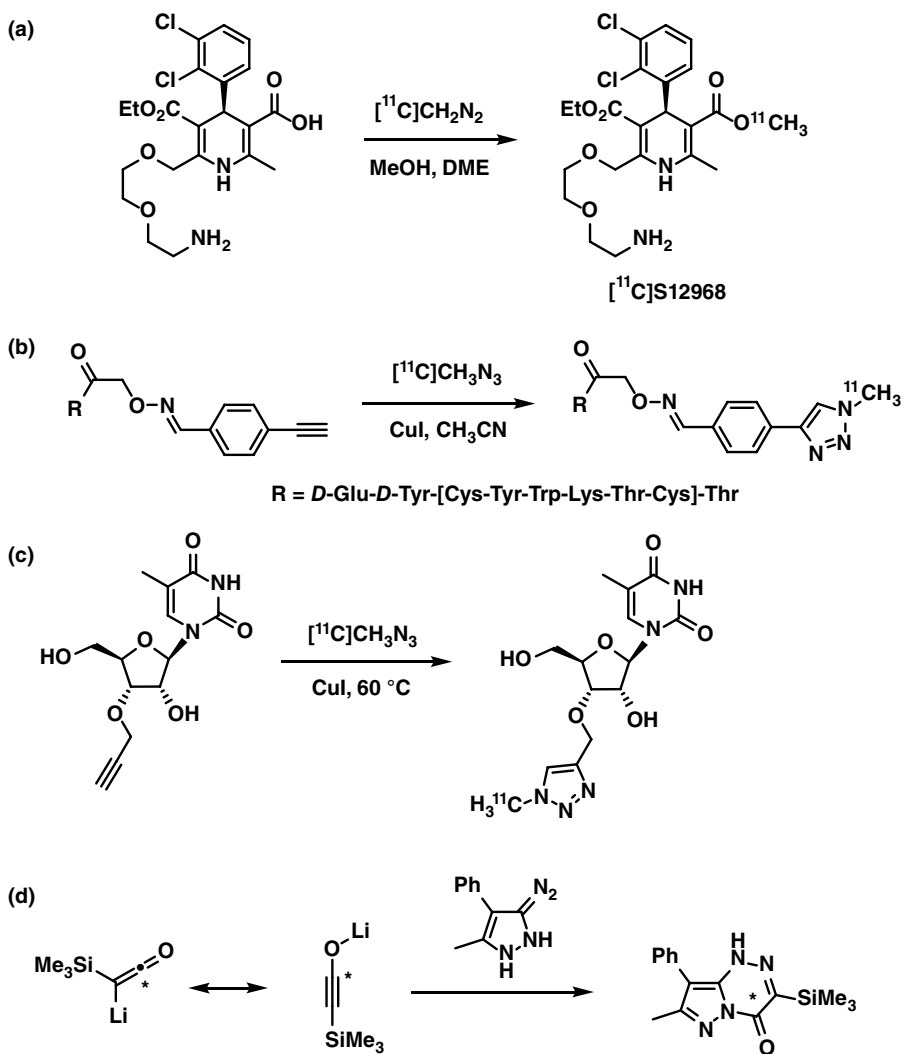


Figure 7.60

Carbon-11 radio-labelling using [^{11}C]diazomethane, [^{11}C]methyl azide, and [^{11}C]trimethylsilylyl ynolates.

when [^{11}C]CH $_3$ N $_3$ was prepared in a separate step. Similarly, Bordenave et al. explored the CuAAC reaction between [^{11}C]CH $_3$ N $_3$ and alkyne-bearing nucleosides and oligonucleosides as PET radiotracers to image cell proliferation, as shown in Figure 7.60c. A ^{11}C -radiolabeled thymidine analogue was prepared in this way in 48% RCY.

7.4.8.5 [^{11}C]Lithium Trimethylsilylylolate

[^{11}C]Lithium trimethylsilylylolate (Figure 7.60d) has been prepared as a novel reagent for the incorporation of carbon-11 into heteroaromatic rings. The reaction of [^{11}C]lithium trimethylsilylylolate with the diazopyrazole derivative gave the bicyclic ^{11}C -pyrazolotriazine product in 40% RCY, but with poor molar activity (0.006 GBq· μmol^{-1}) [105].

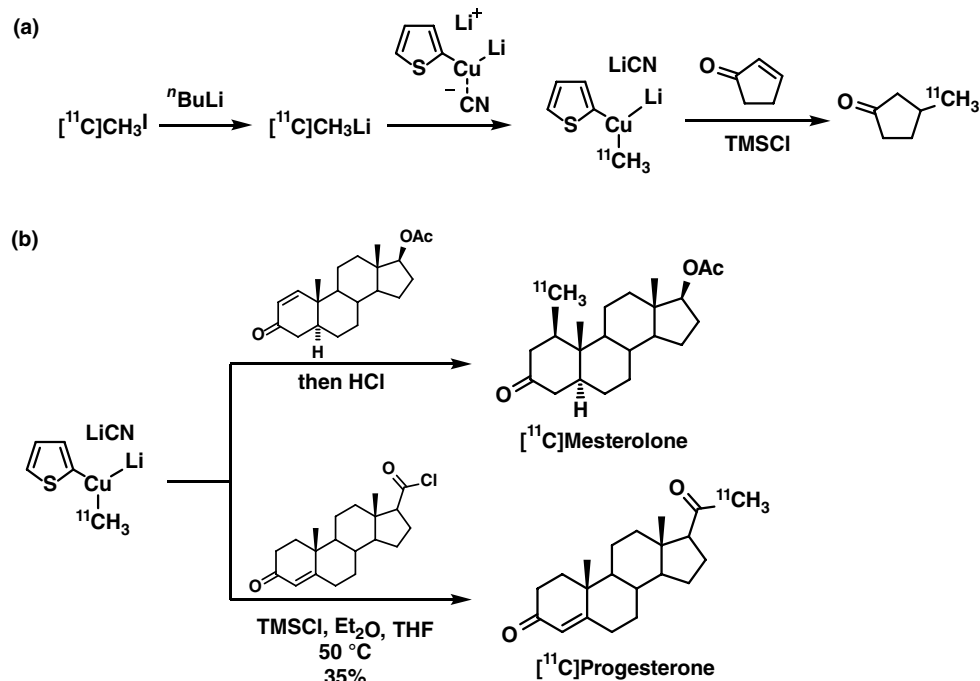
7.4.8.6 Lithium [^{11}C]methyl(2-thienyl)cuprate

The 1,4-addition of organocuprates to α,β -unsaturated carbonyls is a well-established synthetic method, but it has seen limited application to radiochemistry. The Långström group first explored 1,4-conjugate addition of lithium [^{11}C]methyl(2-thienyl)cuprate to α,β -unsaturated ketones, affording the addition products in 35–50% RCY (Figure 7.61a) [467]. Lithium [^{11}C]methyl(2-thienyl)cuprate was prepared by addition of [^{11}C]CH₃Li to lithium (2-thienyl)cyanocuprate or lithium (2-thienyl)iodocuprate. [^{11}C]CH₃Li was produced by lithium-halogen exchange between [^{11}C]CH₃I and ⁿBuLi. Lithium [^{11}C]methyl(2-thienyl)cuprate was used for the radiosynthesis of [^{11}C]mesterolone (Figure 7.61b), a PET radiotracer for imaging the androgen receptor in prostate cancer, in 31% RCY and with molar activity of 40 GBq· μmol^{-1} after deprotection. The Långström group also reported the radiosynthesis of [^{11}C]progesterone labeled in the C21-position (Figure 7.61a) by reaction of lithium [^{11}C]methyl(2-thienyl)cuprate with the corresponding acid chloride, in 35% RCY and with molar activity of 14 GBq μmol^{-1} [468].

7.4.9 Enzymatic Reactions with Carbon-11

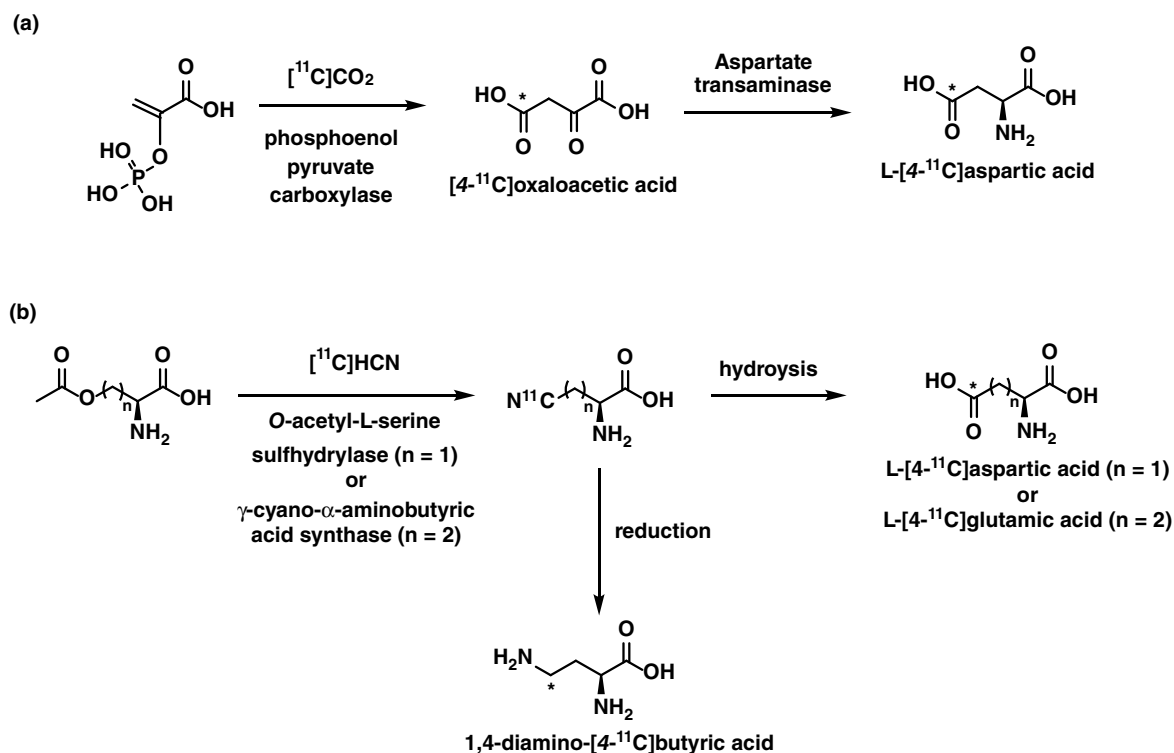
Enzymes are attractive catalysts for the incorporation of carbon-11 into biomolecules as they can perform complex reactions under mild conditions to give highly functionalized radiolabelled products, which may be hard to access through chemical routes [469]. Additionally, enzymes usually operate under conditions where substrate concentrations

Figure 7.61 Uses of lithium [^{11}C]methyl(2-thienyl)cuprate for addition reactions.



are similar to the concentration of reagents encountered in PET radiochemistry (nM to μM). Enzymatic reactions offer several advantages over traditional synthetic transformations, including their exceptional substrate selectivity, ability to facilitate reactions under physiological conditions, and ability to provide enantiomerically pure products. These same advantages do simultaneously limit the widespread application of enzymes in PET radiochemistry. The use of enzymes in radiochemical syntheses is hampered by the limited substrate tolerance, sensitivity to radiolabelling conditions (solvent, heating, pH, and ionic strength), and particularly, in this case, sensitivity to radiolysis. The use of immobilized enzymes has somewhat facilitated their use as it simplifies separation of the enzyme from the radiolabelled product, but concerns may arise from any residual potentially immunogenic protein. Despite these concerns, many enzymes have been explored for the synthesis of ^{11}C -radiolabelled PET agents. Enzymes have been used to incorporate primary and secondary precursors (such as $[^{11}\text{C}]\text{CO}_2$ / $[^{11}\text{C}]\text{HCO}_3^-$ and $[^{11}\text{C}]\text{CN}^-$) into biological molecules, as well as for further chemical transformations of molecules that have been radiolabelled with carbon-11 either chemically or enzymatically.

The preparation of enantiopure ^{11}C -radiolabelled amino acids has been the primary focus of applications of enzymes for PET as their chemical preparation is challenging (*vide supra*). In an effort to prepare L-[4- ^{11}C]aspartic acid, Barrio et al. employed immobilized phosphoenol pyruvate carboxylase for the fixation of $[^{11}\text{C}]\text{CO}_2$ with phosphoenol pyruvate to give [4- ^{11}C]oxaloacetic acid (Figure 7.62a). Further reaction with immobilized



aspartate transaminase provided L-[4-¹¹C]aspartic acid in 10% RCY [470]. [¹¹C]HCN has also been used as a substrate for enzymatic incorporation to provide amino acids. Enzymatic reaction of [¹¹C]HCN with *O*-acetylserine or *O*-acetylhomoserine gives β-[¹¹C]cyano-L-alanine and γ-[¹¹C]cyano-α-amino-L-butyric acid, respectively (Figure 7.62b). These products can be further hydrolysed to provide L-[4-¹¹C]aspartic acid and L-[5-¹¹C]glutamic acid [471]. Reduction of β-[¹¹C]cyano-L-alanine has been used to prepare 1,4-diamino-[4-¹¹C]butyric acid [472]. Other amino acids that have been radiolabelled by enzymatic means from simple precursors include [3-¹¹C]serine, prepared in a three-step enzymatic sequence from [¹¹C]methanol [473]; and L-[methyl-¹¹C]methionine, prepared from [¹¹C]methanethiol catalysed by immobilized γ-cyano-α-aminobutyric acid synthase [474].

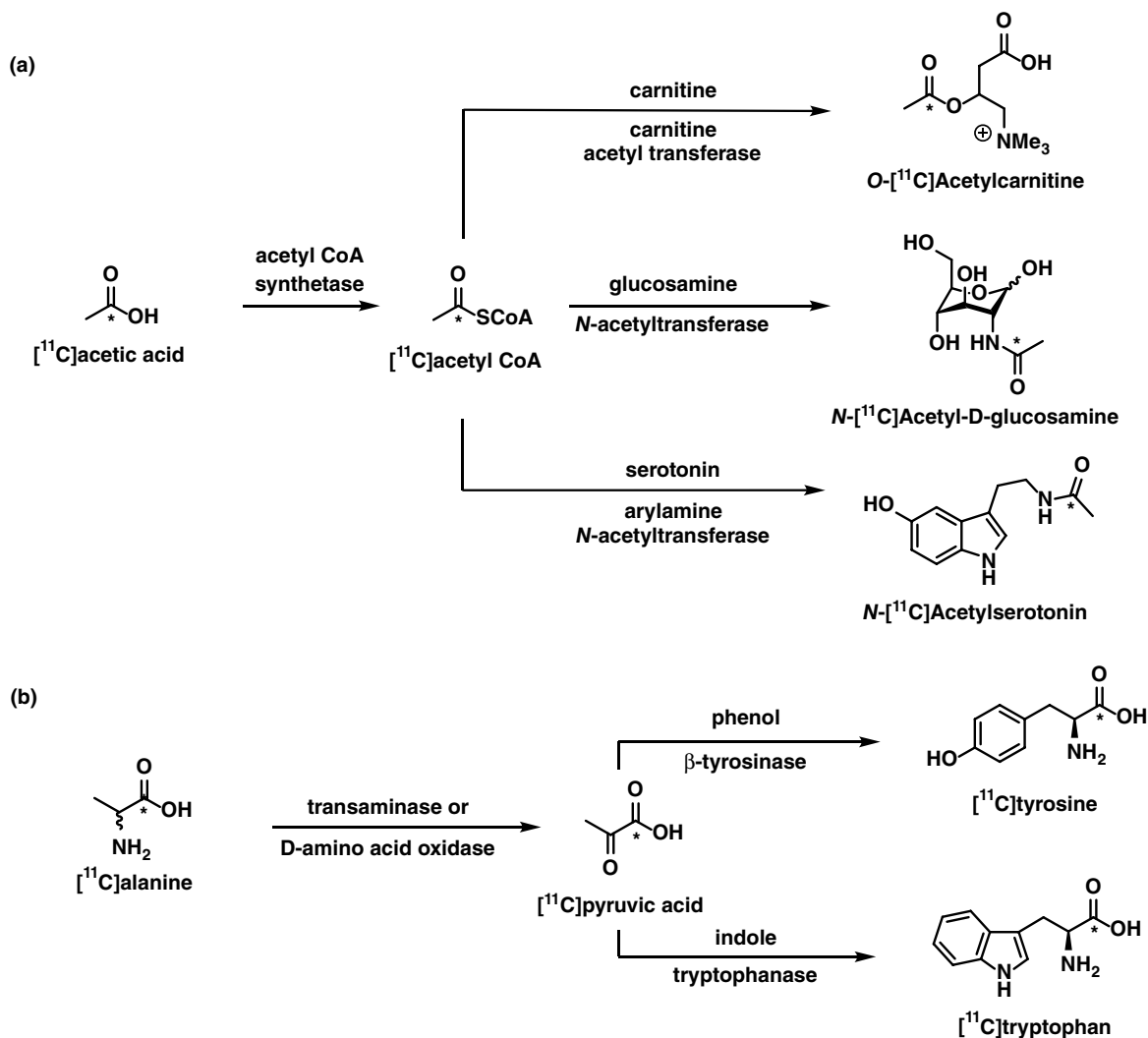


Figure 7.63 Enzymatic incorporation of chemically prepared ¹¹C-labelled intermediates.

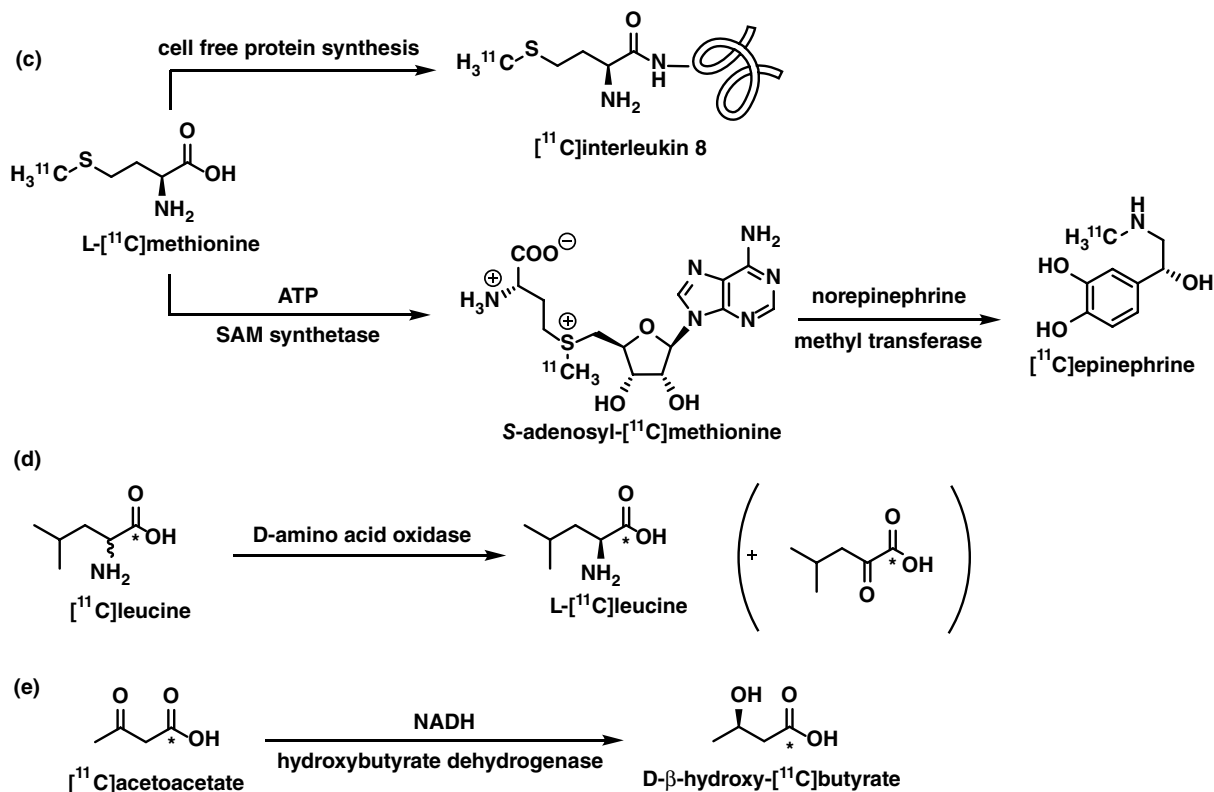


Figure 7.63 (Continued)

The second approach is to use a chemically prepared ^{11}C -labelled substrate for the enzyme (e.g. ^{11}C -acetate, $\text{L-}^{11}\text{C}$ -alanine, or $\text{L-}^{11}\text{C}$ -methionine) in an enzymatic reaction to generate a more complex ^{11}C -labelled biomolecules. This strategy has been applied to the incorporation of ^{11}C -acetyl groups via ^{11}C -acetyl co-enzyme A (CoA), prepared from ^{11}C -acetate by acetyl CoA-synthetase (Figure 7.63a) [475]. Further enzymatic reactions catalysed by acetyl transferases have been used and provide $O\text{-}^{11}\text{C}$ -acetylcarnitine [476, 477], $N\text{-}^{11}\text{C}$ -acetyl-D-glucosamine [478], and $N\text{-}^{11}\text{C}$ -acetylserotonin [479]. Similarly, chemically produced ^{11}C -alanine can be used for the enzymatic synthesis of ^{11}C -pyruvate catalysed by either a transaminase or a D-amino acid oxidase, as shown in Figure 7.63b [480]. ^{11}C -Pyruvate has been used as a substrate for the enzymatic synthesis of ^{11}C -tyrosine and ^{11}C -tryptophan [481–483]. In both cases, using either ^{11}C -acetate or ^{11}C -alanine labelled at either the carboxyl- or methyl-position provides PET radiotracers labelled at different sites, which have been used as a means to investigate *in vivo* metabolism of these tracers [476]. $\text{L-}^{11}\text{C}$ -[methyl- ^{11}C]Methionine prepared chemically from ^{11}C - CH_3I has also been used for the direct incorporation of radiolabelled amino acids into peptides, such as the single-chain variable fragment of an antibody and interleukin-8 (Figure 7.63c) [484–486]. $\text{L-}^{11}\text{C}$ -[methyl- ^{11}C]Methionine has also been combined with *S*-adenosylmethionine synthetase

and methyl transferases to selectively transfer a ^{11}C -methyl group to an appropriate nor-methyl precursor such as for the preparation of (–)- ^{11}C adrenaline [487]. Enzymes have also been used for the chiral resolution of chemically produced racemic ^{11}C -labelled compounds [480]. Barrio et al. described the application of immobilized D-amino acid oxidase and catalase as an efficient means to access enantioenriched L- ^{11}C leucine (Figure 7.63d) [369]. Alternatively, the ability of enzymes to stereoselectively generate chiral products from achiral precursors can be exploited, as described by Tremblay et al., where enzymatic reduction of a ketone stereoselectively provided D-β-hydroxy- ^{11}C butyrate, as shown in Figure 7.63e [488].

REFERENCES

1. Lauritsen, C.C., Crane, H.R., and Harper, W.W. (1934). Artificial production of radioactive substances. *Science* 79 (2045): 234–235.
2. Crane, H.R. and Lauritsen, C.C. (1934). Radioactivity from carbon and boron oxide bombarded with deuterons and the conversion of positrons into radiation. *Physiol. Rev.* 45 (6): 430–432.
3. Barkas, W.H. (1939). Some new reactions in light nuclei with high energy protons. *Physiol. Rev.* 56 (3): 287–287.
4. Conti, M. and Eriksson, L. (2016). Physics of pure and non-pure positron emitters for PET: a review and a discussion. *EJNMMI Phys.* 3 (1): 8.
5. Long, F.A. (1939). A study of the interchange between chromioxalate ion and oxalate ion, using radio-carbon. *J. Am. Chem. Soc.* 61 (3): 570–572.
6. Ruben, S., Hassid, W.Z., and Kamen, M.D. (1939). Radioactive carbon in the study of photosynthesis. *J. Am. Chem. Soc.* 61 (3): 661–663.
7. Tobias, C.A., Lawrence, J.H., Roughton, F.J.W. et al. (1945). The elimination of carbon monoxide from the human body with reference to the possible conversion of CO to CO_2 . *Am. J. Physiol. Content* 145 (2): 253–263.
8. Dahl, K., Halldin, C., and Schou, M. (2017). New methodologies for the preparation of carbon-11 labeled radiopharmaceuticals. *Clin. Transl. Imaging* 5 (3): 275–289.
9. Welch, M.J. and Redvanly, C.S. (2002). *Handbook of Radiopharmaceuticals* (eds. M.J. Welch and C.S. Redvanly). Chichester, UK: Wiley.
10. Pike, V.W., McCarron, J.A., Lammertsma, A.A. et al. (1996). Exquisite delineation of 5-HT_{1A} receptors in human brain with PET and [Carbonyl- ^{11}C]WAY-100635. *Eur. J. Pharmacol.* 301 (1–3): R5–R7.
11. Torstenson, R., Tedroff, J., Hartvig, P. et al. (1999). A comparison of ^{11}C -labeled L-DOPA and L-fluorodopa as positron emission tomography tracers for the presynaptic dopaminergic system. *J. Cereb. Blood Flow Metab.* 19 (10): 1142–1149.
12. Antoni, G. (2015). Development of carbon-11 labelled PET tracers - radiochemical and technological challenges in a historic perspective. *J. Labelled Compd. Radiopharm.* 58 (3): 65–72.
13. Cohen, M.B., Spolter, L., Chia, C.C. et al. (1982). The varying tissue distribution of L-glutamic acid labelled at three different sites. *Int. J. Appl. Radiat. Isot.* 33 (8): 613–617.

14. Pekošak, A., Filp, U., Poot, A.J., and Windhorst, A.D. (2018). From carbon-11-labeled amino acids to peptides in positron emission tomography: the synthesis and clinical application. *Mol. Imaging Biol.* 20 (4): 510–532.
15. McQuade, P., Rowland, D., Lewis, J., and Welch, M. (2005). Positron-emitting isotopes produced on biomedical cyclotrons. *Curr. Med. Chem.* 12 (7): 807–818.
16. Crouzel, C., Långström, B., Pike, V.W., and Coenen, H.H. (1987). Recommendations for a practical production of [¹¹C]methyl iodide. *Int. J. Radiat. Appl. Instrum. A Appl. Radiat. Isot.* 38 (8): 601–603.
17. Wilson, A.A., Garcia, A., Jin, L., and Houle, S. (2000). Radiotracer synthesis from [¹¹C]-iodomethane: a remarkably simple captive solvent method. *Nucl. Med. Biol.* 27 (6): 529–532.
18. Kim, D., Alexoff, D.L., Schueller, M. et al. (2014). The design and performance of a portable handheld ¹¹CO₂ delivery system. *Appl. Radiat. Isot.* 94: 338–343.
19. Mock, B.H., Vavrek, M.T., and Mulholland, G.K. (1995). Solid-phase reversible trap for [¹¹C]carbon dioxide using carbon molecular sieves. *Nucl. Med. Biol.* 22 (5): 667–670.
20. Clark, J.C. and Buckingham, P.D. (1971). The preparation and storage of carbon-11 labelled gases for clinical use. *Int. J. Appl. Radiat. Isot.* 22 (11): 639–646.
21. Christman, D.R., Finn, R.D., Karlstrom, K.I., and Wolf, A.P. (1975). The production of ultra high activity ¹¹C-labeled hydrogen cyanide, carbon dioxide, carbon monoxide and methane via the reaction (XV). *Int. J. Appl. Radiat. Isot.* 26 (8): 435–442.
22. Eriksson, J., Hoek, J., and Windhorst, A.D. (2012). Transition metal mediated synthesis using [¹¹C]CO at low pressure - a simplified method for ¹¹C-carbonylation. *J. Labelled Compd. Radiopharm.* 55 (6): 223–228.
23. Dahl, K., Itsenko, O., Rahman, O. et al. (2015). An evaluation of a high-pressure ¹¹CO carbonylation apparatus. *J. Labelled Compd. Radiopharm.* 58 (5): 220–225.
24. Verbeek, J., Eriksson, J., Syvänen, S. et al. (2012). [¹¹C]phenytoin revisited: synthesis by [¹¹C]CO carbonylation and first evaluation as a P-Gp tracer in rats. *EJNMMI Res.* 2 (1): 36.
25. Clark, J.C. and Buckingham, P.D. (1975). *Short-Lived Radioactive Gases for Clinical Use*. Oxford: Butterworth-Heinemann.
26. Kasyutich, V.L., McMahon, A., Barnhart, T., and Martin, P.A. (2008). On-line monitoring of cyclotron target-gas output by means of tunable lead salt diode laser absorption spectroscopy. *Appl. Phys. B* 93 (2–3): 701–711.
27. Zeisler, S.K., Nader, M., Theobald, A., and Oberdorfer, F. (1997). Conversion of no-carrier-added [¹¹C]carbon dioxide to [¹¹C]carbon monoxide on molybdenum for the synthesis of ¹¹C-labelled aromatic ketones. *Appl. Radiat. Isot.* 48 (8): 1091–1095.
28. Dahl, K., Ulin, J., Schou, M., and Halldin, C. (2017). Reduction of [¹¹C]CO₂ to [¹¹C]CO using solid supported zinc. *J. Labelled Compd. Radiopharm.* 60 (13): 624–628.
29. Roeda, D., Crouzel, C., and Dollé, F. (2004). A rapid, almost quantitative conversion of [¹¹C]carbon dioxide into [¹¹C]carbon monoxide via [¹¹C]formate and [¹¹C]formyl chloride. *Radiochim. Acta* 92 (4–6): 329–332.
30. Nordeman, P., Friis, S.D., Andersen, T.L. et al. (2015). Rapid and efficient conversion of ¹¹CO₂ to ¹¹CO through silacarboxylic acids: applications in Pd-mediated carbonylations. *Chem. Eur. J.* 21 (49): 17601–17604.

31. Taddei, C., Bongarzone, S., Haji Dheere, A.K., and Gee, A.D. (2015). [^{11}C]CO₂ to [^{11}C]CO conversion mediated by [^{11}C]silanes: a novel route for [^{11}C]carbonylation reactions. *Chem. Commun.* 51 (59): 11795–11797.
32. Taddei, C., Bongarzone, S., and Gee, A.D. (2017). Instantaneous conversion of [^{11}C]CO₂ to [^{11}C]CO via fluoride-activated disilane species. *Chem. Eur. J.* 23 (32): 7682–7685.
33. Anders, D.A., Bongarzone, S., Fortt, R. et al. (2017). Electrochemical [^{11}C]CO₂ to [^{11}C]CO conversion for PET imaging. *Chem. Commun.* 53 (20): 2982–2985.
34. Långström, B., Antoni, G., Gullberg, P. et al. (1987). Synthesis of L- and D-[Methyl- ^{11}C]methionine. *J. Nucl. Med.* 28 (6): 1037–1040.
35. Gómez-Vallejo, V. and Llop, J. (2009). Specific activity of [^{11}C]CH₃I synthesized by the “Wet” method: main sources of non-radioactive carbon. *Appl. Radiat. Isot.* 67 (1): 111–114.
36. Comar, D., Maziere, M., and Crouzel, C. (1973). Synthese et Metabolisme de l'iodomethylate de Chlorpromazine- ^{11}C . In: *Radiopharmaceuticals and Labelled Compounds*, vol. 1, 461–469. Vienna: International Atomic Energy Agency.
37. Comar, D., Cartron, J.-C., Maziere, M., and Marazano, C. (1976). Labelling and metabolism of methionine-methyl- ^{11}C . *Eur. J. Nucl. Med.* 1 (1): 11–14.
38. Långström, B. and Lundqvist, H. (1976). The preparation of ^{11}C -methyl iodide and its use in the synthesis of ^{11}C -methyl-L-methionine. *Int. J. Appl. Radiat. Isot.* 27 (7): 357–363.
39. Oberdorfer, F., Hanisch, M., Helus, F., and Maier-Borst, W. (1985). A new procedure for the preparation of ^{11}C -labelled methyl iodide. *Int. J. Appl. Radiat. Isot.* 36 (6): 435–438.
40. Holschbach, M. and Schüller, M. (1993). A new and simple on-line method for the preparation of n.c.a. [^{11}C]methyl iodide. *Appl. Radiat. Isot.* 44 (4): 779–780.
41. Ferrieri, R.A. (2003). Synthetic precursors labeled with carbon-11 and fluorine-18. In: *Handbook of Radiopharmaceuticals: Radiochemistry and Applications* (eds. M.J. Welch and C.S. Redvanly), 230–282.
42. Itsenko, O., Gómez-Vallejo, V., Llop, J., and Kozirowski, J. (2013). On ^{11}C chemistry reviews - surveying and filling the gaps. *Curr. Org. Chem.* 17 (19): 2067–2096.
43. Gomez-Vallejo, V., Gaja, V., Kozirowski, J., and Llop, J. (2012). Specific activity of ^{11}C -labelled radiotracers: a big challenge for PET chemists. In: *Positron Emission Tomography - Current Clinical and Research Aspects*, vol. 2 (ed. C.-H. Hsieh), 183–210. InTech.
44. Ermert, J., Stüsgen, S., Lang, M. et al. (2008). High molar activity of [^{11}C]TCH346 via [^{11}C]methyl triflate using the “Wet” [^{11}C]CO₂ reduction method. *Appl. Radiat. Isot.* 66 (5): 619–624.
45. Matarrese, M., Soloviev, D., Todde, S. et al. (2003). Preparation of [^{11}C] radioligands with high specific radioactivity on a commercial PET tracer synthesizer. *Nucl. Med. Biol.* 30 (1): 79–83.
46. Zhang, M.-R. and Suzuki, K. (2005). Sources of carbon which decrease the specific activity of [^{11}C]CH₃I synthesized by the single pass I₂ method. *Appl. Radiat. Isot.* 62 (3): 447–450.

47. Iwata, R., Ido, T., Ujiie, A. et al. (1988). Comparative study of specific activity of [¹¹C] methyl iodide: a search for the source of carrier carbon. *Int. J. Radiat. Appl. Instrum. A Appl. Radiat. Isot.* 39 (1): 1–7.
48. Link, J.M., Krohn, K.A., and Clark, J.C. (1997). Production of [¹¹C]CH₃I by single pass reaction of [¹¹C]CH₄ with I₂. *Nucl. Med. Biol.* 24 (1): 93–97.
49. Larsen, P., Ulin, J., Dahlstrøm, K., and Jensen, M. (1997). Synthesis of [¹¹C]iodomethane by iodination of [¹¹C]methane. *Appl. Radiat. Isot.* 48 (2): 153–157.
50. Shao, X., Hoareau, R., Runkle, A.C. et al. (2011). Highlighting the versatility of the tracerlab synthesis modules. Part 2: fully automated production of [¹¹C]-labeled radiopharmaceuticals using a tracerlab FXC-pro. *J. Labelled Compd. Radiopharm.* 54 (14): 819–838.
51. Noguchi, J. and Suzuki, K. (2003). Automated synthesis of the ultra high specific activity of [¹¹C]Ro15-4513 and its application in an extremely low concentration region to an ARG study. *Nucl. Med. Biol.* 30 (3): 335–343.
52. Andersson, J., Truong, P., and Halldin, C. (2009). In-target produced [¹¹C]methane: increased specific radioactivity. *Appl. Radiat. Isot.* 67 (1): 106–110.
53. Wagner, R., Stöcklin, G., and Schaack, W. (1981). Production of carbon-11 labelled methyl iodide by direct recoil synthesis. *J. Labelled Compd. Radiopharm.* 18 (11): 1557–1566.
54. Eriksson, J., Ulin, J., and Långström, B. (2006). [¹¹C]Methyl iodide from [¹¹C]methane and iodine using a non-thermal plasma method. *J. Labelled Compd. Radiopharm.* 49 (13): 1177–1186.
55. Någren, K., Müller, L., Halldin, C. et al. (1995). Improved synthesis of some commonly used PET radioligands by the use of [¹¹C]methyl triflate. *Nucl. Med. Biol.* 22 (2): 235–239.
56. Lundkvist, C., Sandell, J., Någren, K. et al. (1998). Improved syntheses of the PET radioligands, [¹¹C]FLB 457, [¹¹C]MDL 100907 and [¹¹C]β-CIT-FE, by the use of [¹¹C] methyl triflate. *J. Labelled Compd. Radiopharm.* 41 (6): 545–556.
57. Jewett, D.M. (1992). A simple synthesis of [¹¹C]methyl triflate. *Int. J. Radiat. Appl. Instrum.* 43 (11): 1383–1385.
58. Mock, B.H., Mulholland, G.K., and Vavrek, M.T. (1999). Convenient gas phase bromination of [¹¹C]methane and production of [¹¹C]methyl triflate. *Nucl. Med. Biol.* 26 (4): 467–471.
59. Fei, X., Mock, B.H., DeGrado, T.R. et al. (2004). An improved synthesis of PET dopamine D₂ receptors radioligand [¹¹C]raclopride. *Synth. Commun.* 34 (10): 1897–1907.
60. Madsen, J., Elfving, B., Andersen, K. et al. (2004). Gas phase production of [¹¹C] methyl iodide-D₃. Synthesis and biological evaluation Of S-[N-methyl-¹¹C]citalopram and deuterated analogues. *J. Labelled Compd. Radiopharm.* 47 (6): 335–348.
61. Slegers, G., Sambre, J., Goethals, P. et al. (1986). Synthesis of [1-¹¹C]iodoethane for the preparation of [¹¹C]ethyl labelled radiopharmaceuticals. *Int. J. Radiat. Appl. Instrum. A Appl. Radiat. Isot.* 37 (4): 279–282.
62. Långström, B., Antoni, G., Gullberg, P. et al. (1986). The synthesis of 1-¹¹C-labelled ethyl, propyl, butyl and isobutyl iodides and examples of alkylation reactions. *Int. J. Radiat. Appl. Instrum. A Appl. Radiat. Isot.* 37 (11): 1141–1145.

63. Antoni, G. and Langstrom, B. (1987). Asymmetric synthesis of L-2-amino[3-¹¹C]butyric acid, L-[3-¹¹C]norvaline and L-[3-¹¹C]valine. *Acta Chem. Scand.*: 511–517.
64. Rotteveel, L., Poot, A.J., Funke, U. et al. (2017). Radiosynthesis of 1-Iodo-2-[¹¹C]methylpropane and 2-methyl-1-[¹¹C]propanol and its application for alkylation reactions and C—C bond formation. *J. Labelled Compd. Radiopharm.* 60 (12): 566–576.
65. Antoni, G. and Långström, B. (1987). Synthesis of racemic [3-¹¹C]-labelled alanine, 2-aminobutyric acid, norvaline, norleucine, leucine and phenylalanine and preparation of L-[3-¹¹C]alanine and L-[3-¹¹C]phenylalanine. *J. Labelled Compd. Radiopharm.* 24 (2): 125–143.
66. Dannals, R.F., Långström, B., Ravert, H.T. et al. (1988). Synthesis of radiotracers for studying muscarinic cholinergic receptors in the living human brain using positron emission tomography: [¹¹C]dexetimide and [¹¹C]levetimid. *Int. J. Radiat. Appl. Instrum. A Appl. Radiat. Isot.* 39 (4): 291–295.
67. Fasth, K.-J., Antoni, G., and Långström, B. (1988). Asymmetric synthesis of L-[3-¹¹C]alanine and L-[3-¹¹C]phenylalanine by a phase-transfer alkylation reaction. *J. Chem. Soc. Perkin Trans. 1* 0 (12): 3081–3084.
68. Fasth, K.J., Antoni, G., and Långström, B. (1990). Synthesis of some α-¹¹C-labelled substituted benzyl iodides. *Int. J. Radiat. Appl. Instrum. A Appl. Radiat. Isot.* 41 (6): 611–613.
69. Zhang, M.-R., Ogawa, M., Maeda, J. et al. (2006). [2-¹¹C]isopropyl-, [1-¹¹C]ethyl-, and [¹¹C]methyl-labeled phenoxyphenyl acetamide derivatives as positron emission tomography ligands for the peripheral benzodiazepine receptor: radiosynthesis, uptake, and in vivo binding in brain. *J. Med. Chem.* 49 (9): 2735–2742.
70. Halldin, C., Bjurling, P., Stålnacke, C.-G. et al. (1989). ¹¹C-labelling of dimethylphenethylamine in two different positions and biodistribution studies. *Int. J. Radiat. Appl. Instrum. A Appl. Radiat. Isot.* 40 (7): 557–560.
71. Eriksson, J., Antoni, G., and Långström, B. (2004). Synthesis of [1-¹¹C]ethyl iodide from [¹¹C]carbon monoxide and its application in alkylation reactions. *J. Labelled Compd. Radiopharm.* 47 (11): 723–731.
72. Eriksson, J., Antoni, G., and Långström, B. (2006). Synthesis of [1-¹¹C]propyl and [1-¹¹C]butyl iodide from [¹¹C]carbon monoxide and their use in alkylation reactions. *J. Labelled Compd. Radiopharm.* 49 (12): 1105–1116.
73. Cramer, R.D. and Kistiakowsky, G.B. (1941). Synthesis of radioactive lactic acid. *J. Biol. Chem.* 137 (3): 549–555.
74. Labaree, D.C., Ropchan, J.R., Nabulsi, N., and Huang, Y. (2017). A modification to improve the reliability of [¹¹C]CN⁻ production in the GE radiochemistry system. *J. Labelled Compd. Radiopharm.* 60 (12): 592–595.
75. Christman, D.R., Finn, R.D., Karlstrom, K.I., and Wolf, A.P. (1973). Production of carrier-free H¹¹CN for medical use and radiopharmaceutical syntheses. IX. *J. Nucl. Med.* 14 (11): 864–866.
76. Iwata, R., Ido, T., Takahashi, T. et al. (1987). Optimization of [¹¹C]HCN production and no-carrier-added [1-¹¹C]amino acid synthesis. *Int. J. Radiat. Appl. Instrum. A Appl. Radiat. Isot.* 38 (2): 97–102.
77. Lamb, J.F., James, R.W., and Winchell, H.S. (1971). Recoil synthesis of high specific activity ¹¹C-cyanide. *Int. J. Appl. Radiat. Isot.* 22 (8): 475–479.

78. Roeda, D., Van Zanten, B., and Crouzel, C. (1978). The production of ^{11}C -phosgene without added carrier. *Radiochem. Radioanal. Lett.* 33: 175–178.
79. Crouzel, C., Roeda, D., Berridge, M. et al. (1983). ^{11}C -labelled phosgene: an improved procedure and synthesis device. *Int. J. Appl. Radiat. Isot.* 34 (11): 1558–1559.
80. Brinkman, G.A., Haas-Lisewska, I., Veenboer, J.T., and Lindner, L. (1978). Preparation of $^{11}\text{COCl}_2$. *Int. J. Appl. Radiat. Isot.* 29 (11): 701–702.
81. Roeda, D. and Westera, G. (1981). A U.V.-induced on-line synthesis of ^{11}C -phosgene and the preparation of some of its derivatives. *Int. J. Appl. Radiat. Isot.* 32 (12): 931–932.
82. Diksic, M., Jolly, D., and Farrokhzad, S. (1982). On-line synthesis of “No-Carrier-Added” ^{11}C]phosgene. *Int. J. Nucl. Med. Biol.* Y: 283–285.
83. Landais, P. and Crouzel, C. (1987). A new synthesis of carbon-11 labelled phosgene. *Int. J. Radiat. Appl. Instrum. A Appl. Radiat. Isot.* 38 (4): 297–300.
84. Brady, F., Luthra, S.K., Tochon-Danguy, H.J. et al. (1991). Asymmetric synthesis of a precursor for the automated radiosynthesis of S-(3'-t-Butylamino-2'-Hydroxypropoxy)-benzimidazol-2- ^{11}C]one (S- ^{11}C]CGP 12177) as a preferred radioligand for β -adrenergic receptors. *Int. J. Radiat. Appl. Instrum.* 42 (7): 621–628.
85. Link, J.M. and Krohn, K.A. (1997). A simplified production of high specific activity ^{11}C]labelled phosgene, $^{11}\text{COCl}_2$. *J. Labelled Compd. Radiopharm.* 40 (4): 306–308.
86. Nishijima, K.I., Kuge, Y., Seki, K.I. et al. (2002). A simplified and improved synthesis of ^{11}C]phosgene with iron and iron (III) oxide. *Nucl. Med. Biol.* 29 (3): 345–350.
87. Bramoullé, Y., Roeda, D., and Dollé, F. (2010). A simplified ^{11}C]phosgene synthesis. *Tetrahedron Lett.* 51 (2): 313–316.
88. Ogawa, M., Takada, Y., Suzuki, H. et al. (2010). Simple and effective method for producing ^{11}C]phosgene using an environmental CCl_4 gas detection tube. *Nucl. Med. Biol.* 37 (1): 73–76.
89. Christman, D., Crawford, E.J., Friedkin, M., and Wolf, A.P. (1972). Detection of DNA synthesis in intact organisms with positron-emitting [methyl- ^{11}C]thymidine. *Proc. Natl. Acad. Sci. USA* 69 (4): 988–992.
90. Berger, G., Mazière, M., Marazano, C., and Comar, D. (1978). Carbon 11 labeling of the psychoactive drug O-methyl-bufotenine and its distribution in the animal organism. *Eur. J. Nucl. Med.* 3 (2): 101–104.
91. Roeda, D. and Dollé, F. (2003). Preparation of ^{11}C]formaldehyde using a silver-containing ceramic catalyst. *J. Labelled Compd. Radiopharm.* 46 (5): 449–458.
92. Nader, M., Thobald, A., and Oberdorfer, F. (1997). Novel synthesis of ^{11}C]formaldehyde and its application in the labelling of α -(n- ^{11}C -Methylamino)isobutyric acid. *J. Labelled Compd. Radiopharm.* 40 (11): 730–731.
93. Slegers, G., Lambrecht, R.H., Vandewalle, T. et al. (1984). Enzymatic synthesis of C-11 formaldehyde: concise communication. *J. Nucl. Med.* 25 (3): 338–342.
94. Hughes, J.A. and Jay, M. (1995). Preparation of ^{11}C] formaldehyde using a hollow fiber membrane bioreactor. *Nucl. Med. Biol.* 22 (1): 105–109.
95. Hooker, J.M., Schönberger, M., Schieferstein, H., and Fowler, J.S. (2008). A simple, rapid method for the preparation of ^{11}C]formaldehyde. *Angew. Chemie Int. Ed.* 47 (32): 5989–5992.

96. Niisawa, K., Ogawa, K., Saito, J. et al. (1984). Production of no-carrier-added ^{11}C -carbon disulfide and ^{11}C -hydrogen cyanide by microwave discharge. *Int. J. Appl. Radiat. Isot.* 35 (1): 29–33.
97. Miller, P.W. and Bender, D. (2012). [^{11}C]Carbon disulfide: a versatile reagent for PET radiolabelling. *Chem. Eur. J.* 18 (2): 433–436.
98. Haywood, T., Kealey, S., Sánchez-Cabezas, S. et al. (2015). Carbon-11 radiolabelling of organosulfur compounds: ^{11}C synthesis of the progesterone receptor agonist tanaproget. *Chem. Eur. J.* 21 (25): 9034–9038.
99. Haskali, M.B. and Pike, V.W. (2017). [^{11}C]Fluoroform, a breakthrough for versatile labeling of PET radiotracer trifluoromethyl groups in high molar activity. *Chem. Eur. J.* 23 (34): 8156–8160.
100. Schoeps, K.-O., Halidin, C., Stone-Elander, S. et al. (1988). Preparation of ^{11}C -nitromethane and an example of its use as a radiolabeling precursor. *J. Labelled Compd. Radiopharm.* 25 (7): 749–758.
101. Schoeps, K.-O., Stone-Elander, S., and Halidin, C. (1989). On-line synthesis of [^{11}C]nitroalkanes. *Int. J. Radiat. Appl. Instrum. A Appl. Radiat. Isot.* 40 (3): 261–262.
102. Crouzel, C., Amano, R., and Fournier, D. (1987). Synthesis of carbon-11 labelled diazomethane. *Int. J. Radiat. Appl. Instrum. A Appl. Radiat. Isot.* 38 (8): 669–670.
103. Schirmacher, R., Lakhri, Y., Jolly, D. et al. (2008). Rapid in situ synthesis of [^{11}C]methyl azide and its application in ^{11}C click-chemistry. *Tetrahedron Lett.* 49 (33): 4824–4827.
104. Bordenave, T., Hazari, P.P., James, D. et al. (2013). ^{11}C click chemistry using [^{11}C]methyl azide: simplified, versatile, and practical alternative access to [^{11}C]nucleosides and [^{11}C]oligonucleotides for PET imaging. *Eur. J. Org. Chem.* 2013 (7): 1214–1217.
105. Nader, M.W. and Oberdorfer, F. (2011). [^{11}C]Lithium trimethylsilyl ynoate: a new [^{11}C] precursor and its application in heterocyclic synthesis. *Tetrahedron Lett.* 52 (18): 2309–2311.
106. Nazih, R., Blauser, J.P., Mock, B.H., and DeGrado, T.R. (2005). A facile synthesis of [^{11}C]acetylene. *Appl. Radiat. Isot.* 63 (3): 305–309.
107. Madsen, M.T., Hichwa, R.D., and Nickles, R.J. (1981). An investigation of ^{11}C -methane, ^{13}N -nitrous oxide and ^{11}C -acetylene as regional cerebral blood flow agents. *Phys. Med. Biol.* 26 (5): 875–882.
108. Jewett, D.M., Ehrenkauf, R.L., and Ram, S. (1985). A captive solvent method for rapid radiosynthesis: application to the synthesis of [^{11}C]palmitic acid. *Int. J. Appl. Radiat. Isot.* 36 (8): 672–674.
109. Leonard Watkins, G., Jewett, D.M., Keith Mulholland, G. et al. (1988). A captive solvent method for rapid N-[^{11}C]methylation of secondary amides: application to the benzodiazepine, 4'-chlorodiazepam (RO5-4864). *Int. J. Radiat. Appl. Instrum. A Appl. Radiat. Isot.* 39 (5): 441–444.
110. Iwata, R., Pascali, C., Yuasa, M. et al. (1992). On-line [^{11}C]methylation using [^{11}C]methyl iodide for the automated preparation of ^{11}C -radiopharmaceuticals. *Int. J. Radiat. Appl. Instrum. A Appl. Radiat. Isot.* 43 (9): 1083–1088.

111. Wilson, A.A., DaSilva, J.N., and Houle, S. (1996). Solid-phase radiosynthesis of [¹¹C]WAY 100635. *J. Labelled Compd. Radiopharm.* 38 (2): 149–154.
112. Cleij, M.C., Clark, J.C., Baron, J.-C., and Aigbirhio, F.I. (2007). Rapid preparation of [¹¹C]flumazenil: captive solvent synthesis combined with purification by analytical sized columns. *J. Labelled Compd. Radiopharm.* 50 (1): 19–24.
113. Maclean, D., Zhu, J., Chen, M. et al. (2003). Safety-catch linker strategies for the production of radiopharmaceuticals labeled with positron-emitting isotopes. *J. Am. Chem. Soc.* 125 (34): 10168–10169.
114. Boudjemeline, M., Hopewell, R., Rochon, P.-L. et al. (2017). Highly efficient solid phase supported radiosynthesis of [¹¹C]PiB using TC18 cartridge as a “3-in-1” production entity. *J. Labelled Compd. Radiopharm.* 60 (14): 632–638.
115. Herth, M.M., Thorpe, M.R., and Ferrieri, R.A. (2005). Synthesis of the phytohormone [¹¹C]methyl jasmonate via methylation on a C18 Sep Pak cartridge. *J. Labelled Compd. Radiopharm.* 48 (5): 379–386.
116. Lodi, F., Trespidi, S., Di Pierro, D. et al. (2007). A simple tracerlab module modification for automated on-column [¹¹C]methylation and [¹¹C]carboxylation. *Appl. Radiat. Isot.* 65 (6): 691–695.
117. Pascali, C., Bogni, A., Iwata, R. et al. (1999). High efficiency preparation of L-[S-methyl-¹¹C]methionine by on-column [¹¹C]methylation on C18 Sep-Pak. *J. Labelled Compd. Radiopharm.* 42 (8): 715–724.
118. Pascali, C., Bogni, A., Itawa, R. et al. (2000). [¹¹C]Methylation on a C18 Sep-Pak cartridge: a convenient way to produce [N-methyl-¹¹C]choline. *J. Labelled Compd. Radiopharm.* 43 (2): 195–203.
119. Hockley, B.G., Henderson, B., and Shao, X. (2012). Synthesis of [¹¹C]choline chloride ([¹¹C]CHL). In: *Radiochemical Syntheses* (eds. P.J.H. Scott and B.G. Hockley), 167–175. Hoboken, NJ, USA: Wiley.
120. Wilson, A.A., Garcia, A., Bell, T. et al. (2001). Further progress on a remarkably simple captive solvent method for [¹¹C]-methylations. *J. Labelled Compd. Radiopharm.* 44 (S1): S999–S1001.
121. Studenov, A.R., Jivan, S., Adam, M.J. et al. (2004). Studies of the mechanism of the in-loop synthesis of radiopharmaceuticals. *Appl. Radiat. Isot.* 61 (6): 1195–1201.
122. Iwata, R., Pascali, C., Bogni, A. et al. (2001). A simple loop method for the automated preparation of [¹¹C]raclopride from [¹¹C]methyl triflate. *Appl. Radiat. Isot.* 55 (1): 17–22.
123. Iwata, R., Pascali, C., Bogni, A. et al. (2002). A combined loop-SPE method for the automated preparation of [¹¹C]doxepin. *J. Labelled Compd. Radiopharm.* 45 (4): 271–280.
124. Wilson, A.A., Garcia, A., Houle, S., and Vasdev, N. (2009). Utility of commercial radio-synthetic modules in captive solvent [¹¹C]-methylation reactions. *J. Labelled Compd. Radiopharm.* 52 (11): 490–492.
125. Shao, X. and Kilbourn, M.R. (2009). A simple modification of GE tracerlab FX C pro for rapid sequential preparation of [¹¹C]carfentanil and [¹¹C]raclopride. *Appl. Radiat. Isot.* 67 (4): 602–605.

126. Holt, D.P., Ravert, H.T., Dannals, R.F., and Pomper, M.G. (2006). Synthesis of [¹¹C] gefitinib for imaging epidermal growth factor receptor tyrosine kinase with positron emission tomography. *J. Labelled Compd. Radiopharm.* 49 (10): 883–888.
127. Verdurand, M., Bort, G., Tadino, V. et al. (2008). Automated radiosynthesis of the Pittsburg compound-B using a commercial synthesizer. *Nucl. Med. Commun.* 29 (10): 920–926.
128. Shao, X., Schnau, P.L., Fawaz, M.V., and Scott, P.J.H. (2013). Enhanced radiosyntheses of [¹¹C]raclopride and [¹¹C]DASB using ethanolic loop chemistry. *Nucl. Med. Biol.* 40 (1): 109–116.
129. Wilson, A.A., Garcia, A., Chestakova, A. et al. (2004). A rapid one-step radiosynthesis of the β-amyloid imaging radiotracer N-methyl-[¹¹C]2-(4'-methylaminophenyl)-6-hydroxybenzothiazole ([¹¹C]-6-OH-BTA-1). *J. Labelled Compd. Radiopharm.* 47 (10): 679–682.
130. Gómez, V., Gispert, J.D., Amador, V., and Llop, J. (2008). New method for routine production of L-[methyl-¹¹C]methionine in loop synthesis. *J. Labelled Compd. Radiopharm.* 51 (1): 83–86.
131. Studenov, A.R., Jivan, S., Buckley, K.R., and Adam, M.J. (2003). Efficient in-loop synthesis of high specific radioactivity [¹¹C]carfentanil. *J. Labelled Compd. Radiopharm.* 46 (9): 837–842.
132. Moran, M.D., Wilson, A.A., Stableford, W.T. et al. (2011). A rapid one-step radiosynthesis of [¹¹C]-D-threo-methylphenidate. *J. Labelled Compd. Radiopharm.* 54 (3): 168–170.
133. Burton, T.J., Mackenzie, I.S., Balan, K. et al. (2012). Evaluation of the sensitivity and specificity of (11)C-metomidate positron emission tomography (PET)-CT for lateralizing aldosterone secretion by Conn's adenomas. *J. Clin. Endocrinol. Metab.* 97 (1): 100–109.
134. Rensch, C., Jackson, A., Lindner, S. et al. (2013). Microfluidics: a groundbreaking technology for PET tracer production? *Molecules* 18 (7): 7930–7956.
135. Wang, M.-W., Lin, W.-Y., Liu, K. et al. (2010). Microfluidics for positron emission tomography probe development. *Mol. Imaging* 9 (4): 7290.2010.00027.
136. Miller, P.W. (2009). Radiolabelling with short-lived PET (positron emission tomography) isotopes using microfluidic reactors. *J. Chem. Technol. Biotechnol.* 84 (3): 309–315.
137. Audrain, H. (2007). Positron emission tomography (PET) and microfluidic devices: a breakthrough on the microscale? *Angew. Chemie Int. Ed.* 46 (11): 1772–1775.
138. Lu, S.-Y., Watts, P., Chin, F.T. et al. (2004). Syntheses of ¹¹C- and ¹⁸F-labeled carboxylic esters within a hydrodynamically-driven micro-reactor. *Lab Chip* 4 (6): 523.
139. Ungersboeck, J., Philippe, C., Haeusler, D. et al. (2012). Optimization of [¹¹C]DASB-synthesis: vessel-based and flow-through microreactor methods. *Appl. Radiat. Isot.* 70 (11): 2615–2620.
140. Kawashima, H., Kimura, H., Nakaya, Y. et al. (2015). Application of microreactor to the preparation of C-11-labeled compounds via O-[¹¹C]methylation with [¹¹C]CH₃I: rapid synthesis of [¹¹C]raclopride. *Chem. Pharm. Bull.* 63 (9): 737–740.

141. Haroun, S., Sanei, Z., Jivan, S. et al. (2013). Continuous-flow synthesis of [¹¹C]raclopride, a positron emission tomography radiotracer, on a microfluidic chip. *Can. J. Chem.* 91 (5): 326–332.
142. Passchier, J. (2009). Fast high performance liquid chromatography in PET quality control and metabolite analysis. *Q. J. Nucl. Med. Mol. imaging* 53 (4): 411–416.
143. Zheng, Q.-H. and Mock, B.H. (2005). Purification of carbon-11 PET radiotracers from unlabeled precursors by preparative HPLC and SPE. *Biomed. Chromatogr.* 19 (9): 671–676.
144. Lehel, S., Madsen, J., and Gillings, N. (2009). HPLC methods for the purification of [¹¹C]-labelled radiopharmaceuticals: reversal of the retention order of products and precursors. *J. Labelled Compd. Radiopharm.* 52 (5): 177–181.
145. Nakao, R., Ito, T., Hayashi, K. et al. (2009). Rapid and efficient purification of positron emission tomography probes by hydrophilic interaction chromatography. *J. Chromatogr. A* 1216 (18): 3933–3940.
146. Nics, L., Steiner, B., Klebermass, E.-M. et al. (2018). Speed matters to raise molar radioactivity: fast HPLC shortens the quality control of C-11 PET-tracers. *Nucl. Med. Biol.* 57: 28–33.
147. Shetty, H.U., Morse, C.L., Zhang, Y., and Pike, V.W. (2013). Characterization of fast-decaying PET radiotracers solely through LC-MS/MS of constituent radioactive and carrier isotopologues. *EJNMMI Res.* 3 (1): 3.
148. Ram, S. and Lee Ehrenkaufer, R. (1988). Synthesis of ¹¹C-radiopharmaceuticals using direct fixation of [¹¹C]carbon dioxide and [¹¹C]carbon monoxide. *Int. J. Radiat. Appl. Instrum. B Nucl. Med. Biol.* 15 (4): 345–355.
149. Tang, X., Tang, G., and Nie, D. (2013). Fully automated synthesis of ¹¹C-acetate as tumor PET tracer by simple modified solid-phase extraction purification. *Appl. Radiat. Isot.* 82: 81–86.
150. Pike, V.W., Eakins, M.N., Allan, R.M., and Selwyn, A.P. (1981). Preparation of carbon-11 labelled acetate and palmitic acid for the study of myocardial metabolism by emission-computerised axial tomography. *J. Radioanal. Chem.* 64 (1–2): 291–297.
151. Aubert, C., Huard-Perrio, C., and Lasne, M.-C. (1997). Rapid synthesis of aliphatic amides by reaction of carboxylic acids, grignard reagent and amines: application to the preparation of [¹¹C]amides. *J. Chem. Soc. Perkin Trans.* 10 (19): 2837–2842.
152. Perrio-Huard, C., Aubert, C., and Lasne, M.-C. (2000). Reductive amination of carboxylic acids and [¹¹C]magnesium halide carboxylates. *J. Chem. Soc. Perkin Trans.* 10 (3): 311–316.
153. Mäding, P., Zessin, J., Pleiß, U. et al. (2006). Synthesis of a ¹¹C-labelled taxane derivative by [¹¹C]acetylation. *J. Labelled Compd. Radiopharm.* 49 (4): 357–365.
154. Zhu, Y.C., Prenant, C., Crouzel, C. et al. (1992). Synthesis of [¹¹C]-ohmefentanyl, a novel, highly potent and selective agonist for opiate μ -receptors. *J. Labelled Compd. Radiopharm.* 31 (11): 853–860.
155. Plisson, C., Huiban, M., Pampols-Maso, S. et al. (2012). Automated preparation of the dopamine D2/3 receptor agonist ligand [¹¹C]-(+)-PHNO for human PET imaging studies. *Appl. Radiat. Isot.* 70 (2): 380–387.

156. Matarrese, M., Sudati, F., Soloviev, D. et al. (2002). Automation of [¹¹C]Acyl chloride syntheses using commercially available ¹¹C-modules. *Applied Radiation and Isotopes* 57: 675–679.
157. Hwang, D.-R., Simpson, N.R., Montoya, J. et al. (1999). An improved one-pot procedure for the preparation of [¹¹C-carbonyl]-WAY100635. *Nucl. Med. Biol.* 26 (7): 815–819.
158. Luthra, S.K., Pike, V.W., and Brady, F. (1985). The preparation of carbon-11 labelled diprenorphine: a new radioligand for the study of the opiate receptor system in vivo. *J. Chem. Soc., Chem. Commun.* 0 (20): 1423.
159. Ben-David, I., Rozen, Y., Ortu, G., and Mishani, E. (2003). Radiosynthesis of ML03, a novel positron emission tomography biomarker for targeting epidermal growth factor receptor via the labeling synthon: [¹¹C]acryloyl chloride. *Appl. Radiat. Isot.* 58 (2): 209–217.
160. Pekošak, A., Filp, U., Rotteveel, L. et al. (2015). Improved synthesis and application of [¹¹C]benzyl iodide in positron emission tomography radiotracer production. *J. Labelled Compd. Radiopharm.* 58 (8): 342–348.
161. Berger, G., Maziere, M., Prenant, C., and Comar, D. (1980). Synthesis of carbon-11-labelled acetone. *Int. J. Appl. Radiat. Isot.* 31 (9): 577–578.
162. Studenov, A.R., Berridge, M.S., Soloviev, D.V. et al. (1999). High yield synthesis of [¹¹C]-acetone through selective quenching of methyl lithium. *Nucl. Med. Biol.* 26 (4): 431–435.
163. van der Meij, M., Carruthers, N.I., Herscheid, J.D.M. et al. (2003). Reductive N-alkylation of secondary amines with [2-¹¹C]acetone. *J. Labelled Compd. Radiopharm.* 46 (11): 1075–1085.
164. Berger, G., Prenant, C., Sastre, J. et al. (1983). Synthesis of a β-blocker for heart visualization: [¹¹C]practolol. *Int. J. Appl. Radiat. Isot.* 34 (11): 1556–1557.
165. Prenant, C., Sastre, J., Crouzel, C., and Syrota, A. (1987). Synthesis of ¹¹C-pindolol. *J. Labelled Compd. Radiopharm.* 24 (2): 227–232.
166. Schou, M., Varnäs, K., Jucaite, A. et al. (2013). Radiolabeling of the cannabinoid receptor agonist AZD1940 with carbon-11 and PET microdosing in non-human primate. *Nucl. Med. Biol.* 40 (3): 410–414.
167. Schou, M. and Halldin, C. (2012). Radiolabeling of two ¹¹C-labeled formylating agents and their application in the preparation of [¹¹C]benzimidazole. *J. Labelled Compd. Radiopharm.* 55 (13): 460–462.
168. Chakraborty, P.K., Mangner, T.J., and Chugani, H.T. (1997). The synthesis of no-carrier-added [¹¹C]urea from [¹¹C]carbon dioxide and application to [¹¹C]uracil synthesis. *Appl. Radiat. Isot.* 48 (5): 619–621.
169. van Tilburg, E.W., Windhorst, A.D., van der Mey, M., and Herscheid, J.D.M. (2006). One-pot synthesis of [¹¹C]ureas via triphenylphosphinimines. *J. Labelled Compd. Radiopharm.* 49 (4): 321–330.
170. Del Vecchio, A., Caillé, F., Chevalier, A. et al. (2018). Late-stage isotopic carbon labeling of pharmaceutically relevant cyclic ureas directly from CO₂. *Angew. Chemie Int. Ed.* 57 (31): 9744–9748.

171. Ram, S., Ehrenkauffer, R.E., and Jewett, D.M. (1986). Rapid reductive-carboxylation of secondary amines, one pot synthesis of N'-(4-¹¹C-methyl)imipramine. *Int. J. Radiat. Appl. Instrum. A Appl. Radiat. Isot.* 37 (5): 391–395.
172. Ram, S. and Spicer, L.D. (1989). Synthesis of ¹¹C-labeled chlorpromazine directly from [¹¹C]carbon dioxide. *Int. J. Radiat. Appl. Instrum. A Appl. Radiat. Isot.* 40 (5): 413–416.
173. Ram, S., Ehrenkauffer, R.E., and Spicer, L.D. (1989). Synthesis of the labeled D1 receptor antagonist SCH 23390 using [¹¹C]carbon dioxide. *Int. J. Radiat. Appl. Instrum. A Appl. Radiat. Isot.* 40 (5): 425–427.
174. Ram, S. and Spicer, L.D. (1989). Direct incorporation of [¹¹C]carbon dioxide for labeling bioactive molecules. An application to [¹¹C] labeled tamoxifen. *J. Labelled Compd. Radiopharm.* 27 (6): 661–668.
175. Liger, F., Eijsbouts, T., Cadarossanesaib, F. et al. (2015). Direct [¹¹C]methylation of amines from [¹¹C]CO₂ for the synthesis of PET radiotracers. *Eur. J. Org. Chem.* 2015 (29): 6434–6438.
176. Schirbel, A., Holschbach, M.H., and Coenen, H.H. (1999). N.C.A.[¹¹C]CO₂ as a safe substitute for phosgene in the carbonylation of primary amines. *J. Labelled Compd. Radiopharm.* 42 (6): 537–551.
177. Hooker, J.M., Reibel, A.T., Hill, S.M. et al. (2009). One-pot, direct incorporation of [¹¹C]CO₂ into carbamates. *Angew. Chemie Int. Ed.* 48 (19): 3482–3485.
178. Wilson, A.A., Garcia, A., Houle, S., and Vasdev, N. (2010). Direct fixation of [¹¹C]-CO₂ by amines: formation of [¹¹C-carbonyl]-methylcarbamates. *Org. Biomol. Chem.* 8 (2): 428–432.
179. Hooker, J.M., Kim, S.W., Alexoff, D. et al. (2010). Histone deacetylase inhibitor MS-275 exhibits poor brain penetration: pharmacokinetic studies of [¹¹C]MS-275 using positron emission tomography. *ACS Chem. Neurosci.* 1 (1): 65–73.
180. Wilson, A.A., Garcia, A., Houle, S. et al. (2011). Synthesis and application of isocyanates radiolabeled with carbon-11. *Chem. Eur. J.* 17 (1): 259–264.
181. Vasdev, N., Sadovski, O., Garcia, A. et al. (2011). Radiosynthesis of [¹¹C]SL25.1188 via [¹¹C]CO₂ fixation for imaging monoamine oxidase B. *J. Labelled Compd. Radiopharm.* 54 (10): 678–680.
182. Kawamura, K., Hashimoto, H., Ogawa, M. et al. (2013). Synthesis, metabolite analysis, and in vivo evaluation of [¹¹C]Irinotecan as a novel positron emission tomography (PET) probe. *Nucl. Med. Biol.* 40 (5): 651–657.
183. Wilson, A.A., Hicks, J.W., Sadovski, O. et al. (2013). Radiosynthesis and evaluation of [¹¹C-carbonyl]-labeled carbamates as fatty acid amide hydrolase radiotracers for positron emission tomography. *J. Med. Chem.* 56 (1): 201–209.
184. Hicks, J.W., Parkes, J., Tong, J. et al. (2014). Radiosynthesis and ex vivo evaluation of [¹¹C-carbonyl]carbamate- and urea-based monoacylglycerol lipase inhibitors. *Nucl. Med. Biol.* 41 (8): 688–694.
185. Hicks, J.W., Wilson, A.A., Rubie, E.A. et al. (2012). Towards the preparation of radiolabeled 1-Aryl-3-benzyl ureas: radiosynthesis of [¹¹C-carbonyl] AR-A014418 by [¹¹C]CO₂ fixation. *Bioorg. Med. Chem. Lett.* 22 (5): 2099–2101.

186. Hicks, J.W., Parkes, J., Sadovski, O. et al. (2013). Synthesis and preclinical evaluation of [^{11}C -carbonyl]PF-04457845 for neuroimaging of fatty acid amide hydrolase. *Nucl. Med. Biol.* 40 (6): 740–746.
187. Mossine, A.V., Brooks, A.F., Jackson, I.M. et al. (2016). Synthesis of diverse ^{11}C -labeled PET radiotracers via direct incorporation of [^{11}C]CO₂. *Bioconjugate Chem.* 27 (5): 1382–1389.
188. Boileau, I., Bloomfield, P.M., Rusjan, P. et al. (2014). Whole-body radiation dosimetry of ^{11}C -carbonyl-URB694: a PET tracer for fatty acid amide hydrolase. *J. Nucl. Med.* 55 (12): 1993–1997.
189. Rusjan, P.M., Wilson, A.A., Miler, L. et al. (2014). Kinetic modeling of the monoamine oxidase B radioligand [^{11}C]SL25.1188 in human brain with high-resolution positron emission tomography. *J. Cereb. Blood Flow Metab.* 34 (5): 883–889.
190. Dahl, K., Collier, T.L., Cheng, R. et al. (2018). “In-Loop” [^{11}C]CO₂ fixation: prototype and proof of concept. *J. Labelled Compd. Radiopharm.* 61 (3): 252–262.
191. Dheere, A., Bongarzone, S., Taddei, C. et al. (2015). Synthesis of ^{11}C -labelled symmetrical ureas via the rapid incorporation of [^{11}C]CO₂ into aliphatic and aromatic amines. *Synlett* 26 (16): 2257–2260.
192. Haji Dheere, A.K., Yusuf, N., and Gee, A. (2013). Rapid and efficient synthesis of [^{11}C] ureas via the incorporation of [^{11}C]CO₂ into aliphatic and aromatic amines. *Chem. Commun.* 49 (74): 8193.
193. Bongarzone, S., Runser, A., Taddei, C. et al. (2017). From [^{11}C]CO₂ to [^{11}C]amides: a rapid one-pot synthesis via the Mitsunobu reaction. *Chem. Commun.* 53 (38): 5334–5337.
194. Downey, J., Bongarzone, S., Hader, S., and Gee, A.D. (2018). In-loop flow [^{11}C]CO₂ fixation and radiosynthesis of *N,N'*-[^{11}C]dibenzylurea. *J. Labelled Compd. Radiopharm.* 61 (3): 263–271.
195. Riss, P.J., Lu, S., Telu, S. et al. (2012). CuI-catalyzed ^{11}C carboxylation of boronic acid esters: a rapid and convenient entry to ^{11}C -labeled carboxylic acids, esters, and amides. *Angew. Chemie Int. Ed.* 51 (11): 2698–2702.
196. Rotstein, B.H., Hooker, J.M., Woo, J. et al. (2014). Synthesis of [^{11}C]bexarotene by Cu-mediated [^{11}C]carbon dioxide fixation and preliminary PET imaging. *ACS Med. Chem. Lett.* 5 (6): 668–672.
197. Rafique, W., Khanapur, S., Spilhaug, M.M., and Riss, P.J. (2017). Reaching out for sensitive evaluation of the Mu opioid receptor in vivo: positron emission tomography imaging of the agonist [^{11}C]AH7921. *ACS Chem. Neurosci.* 8 (9): 1847–1852.
198. Jensen, C.H., Hansen, H.D., Bay, T. et al. (2017). Radiosynthesis and evaluation of [^{11}C]3-hydroxycyclopent-1-enecarboxylic acid as potential PET ligand for the high-affinity γ -hydroxybutyric acid binding sites. *ACS Chem. Neurosci.* 8 (1): 22–27.
199. Schoenberg, A., Bartoletti, I., and Heck, R.F. (1974). Palladium-catalyzed carboalkoxylation of aryl, benzyl, and vinylic halides. *J. Org. Chem.* 39 (23): 3318–3326.
200. Schoenberg, A. and Heck, R.F. (1974). Palladium-catalyzed amidation of aryl, heterocyclic, and vinylic halides. *J. Org. Chem.* 39 (23): 3327–3331.
201. Andersson, Y. and Långström, B. (1995). Synthesis of ^{11}C -labelled ketones via carbonylative coupling reactions using [^{11}C]carbon monoxide. *J. Chem. Soc. Perkin Trans.* 10 (4): 287–289.

202. Al-Qahtani, M.H. and Pike, V.W. (2000). Rapid mild syntheses of [¹¹C]benzophenones by Pd(0)-catalysed ¹¹C-carbonylative coupling of Iodoarenes with phenyltributylstannane in DME-water. *J. Labelled Compd. Radiopharm.* 43 (8): 825–835.
203. Al-Qahtani, M.H. and Pike, V.W. (2000). Palladium(II)-mediated ¹¹C-carbonylative coupling of diaryliodonium salts with organostannanes—a new, mild and rapid synthesis of aryl [¹¹C]ketones. *J. Chem. Soc. Perkin Trans. 1* 0 (6): 1033–1036.
204. Lidström, P., Kihlberg, T., and Långström, B. (1997). [¹¹C]carbon monoxide in the palladium-mediated synthesis of ¹¹C-labelled ketones. *J. Chem. Soc. Perkin Trans. 1* 0 (18): 2701–2706.
205. Nader, M. and Oberdorfer, F. (2002). Syntheses of [Carbonyl-¹¹C]2-(2-Benzoylphenoxy)-N-phenylacetamide from [¹¹C]carbon monoxide by the Suzuki and the Stille reactions. *Appl. Radiat. Isot.* 57 (5): 681–685.
206. Rahman, O. (2015). [¹¹C]carbon monoxide in labeling chemistry and positron emission tomography tracer development: scope and limitations. *J. Labelled Compd. Radiopharm.* 58 (3): 86–98.
207. Kihlberg, T., Langstrom, B., Ferm, T., and Eriksson, J. (2008). Methods and apparatus for production and use of ¹¹C-carbon monoxide in labeling synthesis. US patent application 20080095693.
208. Itsenko, O., Kihlberg, T., and Långström, B. (2006). Labeling of aliphatic carboxylic acids using [¹¹C]carbon monoxide. *Nat. Protoc.* 1 (2): 798–802.
209. Långström, B., Itsenko, O., and Rahman, O. (2007). [¹¹C]carbon monoxide, a versatile and useful precursor in labelling chemistry for PET-ligand development. *J. Labelled Compd. Radiopharm.* 50 (9–10): 794–810.
210. Hostetler, E.D. and Burns, H.D. (2002). A remote-controlled high pressure reactor for radiotracer synthesis with [¹¹C]carbon monoxide. *Nucl. Med. Biol.* 29 (8): 845–848.
211. Kihlberg, T. and Långström, B. (1999). Biologically active ¹¹C-labeled amides using palladium-mediated reactions with aryl halides and [¹¹C]carbon monoxide. *J. Org. Chem.* 64 (25): 9201–9205.
212. Dahl, K. and Nordeman, P. (2017). ¹¹C-carbonylation through in situ generated ¹¹C-benzoyl chlorides with tetrabutylammonium chloride as chloride source. *Eur. J. Org. Chem.* 2017 (18): 2648–2651.
213. Roslin, S., Dahl, K., and Nordeman, P. (2018). Reaction of ¹¹C-benzoyl chlorides with metalloids reagents: ¹¹C-labeling of benzyl alcohols, benzaldehydes, and phenyl ketones from [¹¹C]CO. *J. Labelled Compd. Radiopharm.* 61 (5): 447–454.
214. Altomonte, S., Telu, S., Lu, S., and Pike, V.W. (2017). Pd(0)-mediated ¹¹C-carbonylation of aryl(Mesityl)iodonium salts as a route to [¹¹C]arylcarboxylic acids and derivatives. *J. Org. Chem.* 82 (22): 11925–11932.
215. Kealey, S., Gee, A., and Miller, P.W. (2014). Transition metal mediated [¹¹C]carbonylation reactions: recent advances and applications. *J. Labelled Compd. Radiopharm.* 57 (4): 195–201.
216. Hong, J., Lu, S., Xu, R. et al. (2015). [Carbonyl-¹¹C]4-Fluoro-N-methyl-N-(4-(6-[methylamino]pyrimidin-4-yl)thiazol-2-yl)benzamide ([¹¹C]FIMX) is an effective radioligand for PET imaging of metabotropic glutamate receptor 1 (mGluR1) in monkey brain. *Nucl. Med. Biol.* 42 (12): 967–974.

217. Rahman, O., Kihlberg, T., and Långström, B. (2002). Synthesis of N-methyl-N-(1-methylpropyl)-1-(2-chlorophenyl)isoquinoline-3-[¹¹C]carboxamide ([¹¹C-carbonyl] PK11195) and some analogues using [¹¹C]carbon monoxide and 1-(2-chlorophenyl)isoquinolin-3-yl triflate. *J. Chem. Soc. Perkin Trans. 1* 0 (23): 2699–2703.
218. Rahman, O. and Långström, B. (2007). Synthesis of N-(2,5-dimethoxybenzyl)-N-(5-fluoro-2-phenoxyphenyl)[carbonyl-¹¹C]acetamide ([carbonyl-¹¹C]DAA1106) and analogues using [¹¹C]carbon monoxide and palladium(0) complex. *J. Labelled Compd. Radiopharm.* 50 (13): 1192–1199.
219. Åberg, O., Lindhe, Ö., Hall, H. et al. (2009). Synthesis and biological evaluation of [carboxyl-¹¹C]eprosartan. *J. Labelled Compd. Radiopharm.* 52 (8): 295–303.
220. Nordeman, P., Estrada, S., Odell, L.R. et al. (2014). ¹¹C-labeling of a potent hydroxyethylamine BACE-1 inhibitor and evaluation in vitro and in vivo. *Nucl. Med. Biol.* 41 (6): 536–543.
221. Siméon, F., Culligan, W., Lu, S., and Pike, V. (2017). ¹¹C-labeling of aryl ketones as candidate histamine subtype-3 receptor PET radioligands through Pd(0)-mediated ¹¹C-carbonylative coupling. *Molecules* 22 (5): 792.
222. Lu, S., Zhang, Y., Kalin, J.H. et al. (2016). Exploration of the labeling of [¹¹C]tubastatin A at the hydroxamic acid site with [¹¹C]carbon monoxide. *J. Labelled Compd. Radiopharm.* 59 (1): 9–13.
223. Hostetler, E., Sanabria, S., Krause, S. et al. (2006). Neuropeptide-Y Y5 (NPY5) receptor: occupancy studies in rhesus monkey using a novel NPY5 PET tracer. *Neuroimage* 31: T16.
224. Burns, H.D., Gibson, R.E., Hamill, T.G., and Fukami, T. (2003). Radiolabeled neuropeptide Y Y5 receptor antagonists. International patent WO2003010175A2.
225. Erondu, N., Gantz, I., Musser, B. et al. (2006). Neuropeptide Y5 receptor antagonism does not induce clinically meaningful weight loss in overweight and obese adults. *Cell Metab.* 4 (4): 275–282.
226. Åberg, O. and Långström, B. (2012). Combinatorial synthesis of labelled drugs and PET tracers: synthesis of a focused library of ¹¹C-carbonyl-labelled acrylamides as potential biomarkers of EGFR expression. *J. Labelled Compd. Radiopharm.* 55 (14): 477–483.
227. Van der Wildt, B., Shen, B., and Chin, F.T. (2018). A [¹¹C]CO dispensing system for rapid screening of carbonylation reactions. *J. Labelled Compd. Radiopharm.* 61 (14): 1110–1114.
228. Doi, H., Barletta, J., Suzuki, M. et al. (2004). Synthesis of ¹¹C-labelled N,N'-diphenylurea and ethyl phenylcarbamate by a rhodium-promoted carbonylation via [¹¹C]isocyanatobenzene using phenyl azide and [¹¹C]carbon monoxide. *Org. Biomol. Chem.* 2 (21): 3063–3066.
229. Barletta, J., Karimi, F., and Långström, B. (2006). Synthesis of [¹¹C-carbonyl]hydroxyureas by a rhodium-mediated carbonylation reaction using [¹¹C]carbon monoxide. *J. Labelled Compd. Radiopharm.* 49 (5): 429–436.
230. Ilovich, O., Åberg, O., Långström, B., and Mishani, E. (2009). Rhodium-mediated [¹¹C]carbonylation: a library of N-phenyl-N'-{4-(4-quinolyloxy)-phenyl}-[¹¹C]-urea derivatives as potential PET angiogenic probes. *J. Labelled Compd. Radiopharm.* 52 (5): 151–157.

231. Åberg, O. and Långström, B. (2011). Synthesis of substituted [^{13}C]Ureas and [^{13}C]sulphonylureas by Rh(I)-mediated carbonylation. *J. Labelled Compd. Radiopharm.* 54 (1): 38–42.
232. Barletta, J., Karimi, F., Doi, H., and Långström, B. (2006). Synthesis of diethyl [carbonyl- ^{13}C]malonate from [^{13}C]carbon monoxide by rhodium-promoted carbonylation and its application as a reaction intermediate. *J. Labelled Compd. Radiopharm.* 49 (9): 801–809.
233. Itsenko, O., Kihlberg, T., and Långström, B. (2004). Photoinitiated carbonylation with [^{13}C]carbon monoxide using amines and alkyl iodides. *J. Org. Chem.* 69 (13): 4356–4360.
234. Itsenko, O., Norberg, D., Rasmussen, T. et al. (2007). Radical carbonylation with [^{13}C]carbon monoxide promoted by oxygen-centered radicals: experimental and DFT studies of the mechanism. *J. Am. Chem. Soc.* 129 (29): 9020–9031.
235. Itsenko, O., Kihlberg, T., and Långström, B. (2005). Synthesis of aliphatic [carbonyl- ^{13}C]esters using [^{13}C]carbon monoxide. *Eur. J. Org. Chem.* 2005 (17): 3830–3834.
236. Itsenko, O. and Långström, B. (2005). Photoinitiated free radical carbonylation enhanced by photosensitizers. *Org. Lett.* 7 (21): 4661–4664.
237. Itsenko, O. and Långström, B. (2005). Radical-mediated carboxylation of alkyl iodides with [^{13}C]carbon monoxide in solvent mixtures. *J. Org. Chem.* 70 (6): 2244–2249.
238. Itsenko, O., Kihlberg, T., and Långström, B. (2005). Carboxylation of alkyl iodides with [^{13}C] and (^{13}C)carbon monoxide: using sulfoxides as oxygen nucleophiles. *Synlett* 2005 (20): 3154–3156.
239. Kihlberg, T., Karimi, F., and Långström, B. (2002). [^{13}C]Carbon monoxide in selenium-mediated synthesis of ^{13}C -carbamoyl compounds. *J. Org. Chem.* 67 (11): 3687–3692.
240. Audrain, H., Martarello, L., Gee, A., and Bender, D. (2004). Utilisation of [^{13}C]labelled boron carbonyl complexes in palladium carbonylation reaction. *Chem. Commun.* 0 (5): 558.
241. Kealey, S., Miller, P.W., Long, N.J. et al. (2009). Copper(I) scorpionate complexes and their application in palladium-mediated [^{13}C]carbonylation reactions. *Chem. Commun.* 0 (25): 3696.
242. Jennings, L.E., Kealey, S., Miller, P.W. et al. (2011). N-heterocyclic carbenes as ligands in palladium-mediated [^{13}C]radiolabelling of [^{13}C]amides for positron emission tomography. *J. Labelled Compd. Radiopharm.* 54 (3): 135–139.
243. Buscemi, G., Miller, P.W., Kealey, S. et al. (2011). Rapid carbonylative coupling reactions using palladium(i) dimers: applications to ^{13}C -radiolabelling for the synthesis of PET tracers. *Org. Biomol. Chem.* 9 (9): 3499.
244. Kealey, S., Plisson, C., Collier, T.L. et al. (2011). Microfluidic reactions using [^{13}C]carbon monoxide solutions for the synthesis of a positron emission tomography radiotracer. *Org. Biomol. Chem.* 9 (9): 3313.
245. Díaz, D.J., Darko, A.K., and McElwee-White, L. (2007). Transition metal-catalyzed oxidative carbonylation of amines to ureas. *Eur. J. Org. Chem.* 2007 (27): 4453–4465.
246. Roslin, S., Brandt, P., Nordeman, P. et al. (2017). Synthesis of ^{13}C -labelled ureas by palladium(II)-mediated oxidative carbonylation. *Molecules* 22 (10): 1688.

247. Takashima-Hirano, M., Ishii, H., and Suzuki, M. (2012). Synthesis of [^{11}C]Am80 via novel Pd(0)-mediated rapid [^{11}C]carbonylation using arylboronate and [^{11}C]carbon monoxide. *ACS Med. Chem. Lett.* 3 (10): 804–807.
248. Ishii, H., Minegishi, K., Nagatsu, K., and Zhang, M.-R. (2015). Pd(0)-mediated [^{11}C] carbonylation of aryl and heteroaryl boronic acid pinacol esters with [^{11}C]carbon monoxide under ambient conditions and a facile process for the conversion of [carbonyl- ^{11}C]esters to [carbonyl- ^{11}C]amides. *Tetrahedron* 71 (10): 1588–1596.
249. Stevens, M.Y., Chow, S.Y., Estrada, S. et al. (2016). Synthesis of ^{11}C -labeled sulfonyl carbamates through a multicomponent reaction employing sulfonyl azides, alcohols, and [^{11}C]CO. *ChemistryOpen* 5 (6): 566–573.
250. Roslin, S., De Rosa, M., Deuther-Conrad, W. et al. (2017). Synthesis and in vitro evaluation of 5-substituted benzovesamicol analogs containing N-substituted amides as potential positron emission tomography tracers for the vesicular acetylcholine transporter. *Bioorg. Med. Chem.* 25 (19): 5095–5106.
251. van der Wildt, B., Wilhelmus, M.M.M., Bijkerk, J. et al. (2016). Development of carbon-11 labeled acryl amides for selective PET imaging of active tissue transglutaminase. *Nucl. Med. Biol.* 43 (4): 232–242.
252. Filp, U., Pees, A.L., Taddei, C. et al. (2017). Efficient synthesis of ^{11}C -acrylesters, ^{11}C -acrylamides and their application in Michael addition reactions for PET tracer development. *Eur. J. Org. Chem.* 2017 (34): 5154–5162.
253. Chow, S.Y., Odell, L.R., and Eriksson, J. (2016). Low-pressure radical ^{11}C -aminocarbonylation of alkyl iodides through thermal initiation. *Eur. J. Org. Chem.* 2016 (36): 5980–5989.
254. Rahman, O., Långström, B., and Halldin, C. (2016). Alkyl iodides and [^{11}C]CO in nickel-mediated cross-coupling reactions: successful use of alkyl electrophiles containing a β hydrogen atom in metal-mediated [^{11}C]carbonylation. *ChemistrySelect* 1 (10): 2498–2501.
255. Martinelli, J.R., Freckmann, D.M.M., and Buchwald, S.L. (2006). Convenient method for the preparation of Weinreb amides via Pd-catalyzed aminocarbonylation of aryl bromides at atmospheric pressure. *Org. Lett.* 8 (21): 4843–4846.
256. Dahl, K., Schou, M., Amini, N., and Halldin, C. (2013). Palladium-mediated [^{11}C]carbonylation at atmospheric pressure: a general method using xantphos as supporting ligand. *Eur. J. Org. Chem.* 2013 (7): 1228–1231.
257. Dahl, K., Schou, M., Rahman, O., and Halldin, C. (2014). Improved yields for the palladium-mediated ^{11}C -carbonylation reaction using microwave technology. *Eur. J. Org. Chem.* 2014 (2): 307–310.
258. Rahman, O., Takano, A., Amini, N. et al. (2015). Synthesis of ([^{11}C]carbonyl)raclopride and a comparison with ([^{11}C]methyl)raclopride in a monkey PET study. *Nucl. Med. Biol.* 42 (11): 893–898.
259. Andersen, T.L., Friis, S.D., Audrain, H. et al. (2015). Efficient ^{11}C -carbonylation of isolated aryl palladium complexes for PET: application to challenging radiopharmaceutical synthesis. *J. Am. Chem. Soc.* 137 (4): 1548–1555.

260. Andersen, T.L., Nordeman, P., Christoffersen, H.F. et al. (2017). Application of methyl bisphosphine-ligated palladium complexes for low pressure N - ^{11}C -acetylation of peptides. *Angew. Chemie Int. Ed.* 56 (16): 4549–4553.
261. Cornilleau, T., Audrain, H., Guillemet, A. et al. (2015). General last-step labeling of biomolecule-based substrates by [^{12}C], [^{13}C], and [^{11}C] carbon monoxide. *Org. Lett.* 17 (2): 354–357.
262. Miller, P.W., Long, N.J., de Mello, A.J. et al. (2007). Rapid multiphase carbonylation reactions by using a microtube reactor: applications in positron emission tomography ^{11}C -radiolabeling. *Angew. Chemie Int. Ed.* 46 (16): 2875–2878.
263. Miller, P.W., Audrain, H., Bender, D. et al. (2011). Rapid carbon-11 radiolabelling for PET using microfluidics. *Chem. Eur. J.* 17 (2): 460–463.
264. Dahl, K., Schou, M., Ulin, J. et al. (2015). ^{11}C -carbonylation reactions using gas–liquid segmented microfluidics. *RSC Adv.* 5 (108): 88886–88889.
265. Mock, B. (2013). Automated C-11 methyl iodide/triflate production: current state of the art. *Curr. Org. Chem.* 17 (19): 2119–2126.
266. Jolly, D., Hopewell, R., Kovacevic, M. et al. (2017). Development of “[^{11}C]kits” for a fast, efficient and reliable production of carbon-11 labeled radiopharmaceuticals for positron emission tomography. *Appl. Radiat. Isot.* 121: 76–81.
267. Shao, X., Fawaz, M.V., Jang, K., and Scott, P.J.H. (2014). Ethanolic carbon-11 chemistry: the introduction of green radiochemistry. *Appl. Radiat. Isot.* 89: 125–129.
268. Klein, A.T. and Holschbach, M. (2001). Labelling of the solvent DMSO as side reaction of methylations with n.c.a. [^{11}C]CH₃I. *Appl. Radiat. Isot.* 55 (3): 309–313.
269. Cai, L., Xu, R., Guo, X., and Pike, V.W. (2012). Rapid room-temperature ^{11}C -methylation of arylamines with [^{11}C]methyl iodide promoted by solid inorganic-bases in DMF. *Eur. J. Org. Chem.* 2012 (7): 1303–1310.
270. Adam, M.J., Jivan, S., Huser, J.M., and Lu, J. (2000). ^{11}C -methylations using ^{11}C -methyl iodide and tetrabutylammonium fluoride. *Radiochim. Acta* 88 (3–4): 207–210.
271. Kikuchi, T., Minegishi, K., Hashimoto, H. et al. (2013). The use of tetrabutylammonium fluoride to promote N - and O - ^{11}C -methylation reactions with iodo[^{11}C]methane in dimethyl sulfoxide. *J. Labelled Compd. Radiopharm.* 56 (13): 672–678.
272. Mathis, C.A., Wang, Y., Holt, D.P. et al. (2003). Synthesis and evaluation of ^{11}C -labeled 6-substituted 2-arylbenzothiazoles as amyloid imaging agents. *J. Med. Chem.* 46 (13): 2740–2754.
273. Mukherjee, J., Shi, B., Christian, B.T. et al. (2004). ^{11}C -Fallypride: radiosynthesis and preliminary evaluation of a novel dopamine D2/D3 receptor PET radiotracer in non-human primate brain. *Bioorg. Med. Chem.* 12 (1): 95–102.
274. Gao, M., Wang, M., Mock, B.H. et al. (2010). An improved synthesis of dopamine D2/D3 receptor radioligands [^{11}C]fallypride and [^{18}F]fallypride. *Appl. Radiat. Isot.* 68 (6): 1079–1086.
275. Briard, E., Zoghbi, S.S., Imaizumi, M. et al. (2008). Synthesis and evaluation in monkey of two sensitive ^{11}C -labeled aryloxyanilide ligands for imaging brain peripheral benzodiazepine receptors in vivo. *J. Med. Chem.* 51 (1): 17–30.

276. Wang, M., Yoder, K.K., Gao, M. et al. (2009). Fully automated synthesis and initial PET evaluation of [^{11}C]PBR28. *Bioorg. Med. Chem. Lett.* 19 (19): 5636–5639.
277. Dannals, R.F., Ravert, H.T., James Frost, J. et al. (1985). Radiosynthesis of an opiate receptor binding radiotracer: [^{11}C]carfentanil. *Int. J. Appl. Radiat. Isot.* 36 (4): 303–306.
278. Jewett, D.M. (2001). A simple synthesis of [^{11}C]carfentanil using an extraction disk instead of HPLC. *Nucl. Med. Biol.* 28 (6): 733–734.
279. Elsinga, P.H., Franssen, E.J., Hendrikse, N.H. et al. (1996). Carbon-11-labeled daunorubicin and verapamil for probing P-glycoprotein in tumors with PET. *J. Nucl. Med.* 37 (9): 1571–1575.
280. Wegman, T.D., Maas, B., Elsinga, P.H., and Vaalburg, W. (2002). An improved method for the preparation of [^{11}C]verapamil. *Appl. Radiat. Isot.* 57 (4): 505–507.
281. Någren, K. and Halldin, C. (1998). Methylation of amide and thiol functions with [^{11}C]methyl triflate, as exemplified by [^{11}C]NMSP [^{11}C]flumazenil and [^{11}C]methionine. *J. Labelled Compd. Radiopharm.* 41 (9): 831–841.
282. Kawamura, K. and Ishiwata, K. (2004). Improved synthesis of [^{11}C]SA4503, [^{11}C]MPDX and [^{11}C]TMSX by use of [^{11}C]methyl triflate. *Ann. Nucl. Med.* 18 (2): 165–168.
283. Haeusler, D., Mien, L.-K., Nics, L. et al. (2009). Simple and rapid preparation of [^{11}C]DASB with high quality and reliability for routine applications. *Appl. Radiat. Isot.* 67 (9): 1654–1660.
284. Jacobson, O. and Mishani, E. (2008). [^{11}C]-Dimethylamine as a labeling agent for PET biomarkers. *Appl. Radiat. Isot.* 66 (2): 188–193.
285. Dahl, K. and Nordeman, P. (2017). ^{11}C -acetylation of amines with [^{11}C]methyl iodide with bis(cyclopentadienyldicarbonyliron) as the CO source. *Eur. J. Org. Chem.* 2017 (38): 5785–5788.
286. Patt, M., Solbach, C., and Wüllner, U. (2007). Synthetic approaches and bio-distribution studies of [^{11}C]methyl-phenidate. *J. Pharm. Pharmaceut. Sci.* 10 (2): 312–320.
287. Gao, M., Wang, M., Miller, K.D. et al. (2008). Synthesis and preliminary biological evaluation of new carbon-11 labeled tetrahydroisoquinoline derivatives as SERM radioligands for PET imaging of ER expression in breast cancer. *Eur. J. Med. Chem.* 43 (10): 2211–2219.
288. Ackermann, U., Tochon-Danguy, H.J., and Scott, A.M. (2004). BF_3 etherate catalysed formation of [^{11}C]methyl esters: a novel radiolabelling technique. *J. Labelled Compd. Radiopharm.* 47 (8): 523–530.
289. Ackermann, U., Blanc, P., Falzon, C.L. et al. (2006). Synthesis of ^{11}C labelled methyl esters: transesterification of enol esters versus BF_3 catalysed esterification—a comparative study. *Radiat. Phys. Chem.* 75 (1): 48–52.
290. Ravert, H.T., Mathews, W.B., Musachio, J.L., and Dannals, R.F. (1995). Synthesis of carbon-11 labeled methylcarbamates from [^{11}C]-methylchloroformate. *J. Labelled Compd. Radiopharm.* 36 (4): 365–371.
291. Nabulsi, N.B., Zheng, M.-Q., Ropchan, J. et al. (2011). [^{11}C]GR103545: Novel one-pot radiosynthesis with high specific activity. *Nucl. Med. Biol.* 38 (2): 215–221.
292. Schoultz, B., Årstad, E., Marton, J. et al. (2008). A new method for radiosynthesis of ^{11}C -labeled carbamate groups and its application for a highly efficient synthesis of the kappa-opioid receptor tracer [^{11}C]GR103545. *Open Med. Chem. J.* 2: 72–74.

293. Ametamey, S.M., Kessler, L.J., Honer, M. et al. (2006). Radiosynthesis and preclinical evaluation of ^{11}C -ABP688 as a probe for imaging the metabotropic glutamate receptor subtype 5. *J. Nucl. Med.* 47 (4): 698–705.
294. Sephton, S.M., Mu, L., Müller, A. et al. (2013). Synthesis and in vitro/in vivo pharmacological evaluation of [^{11}C]-ThioABP, a novel radiotracer for imaging MGLuR5 with PET. *Medchemcomm* 4 (3): 520.
295. Ishiwata, K., Ido, T., and Vaalburg, W. (1988). Increased amounts of D-enantiomer dependent on alkaline concentration in the synthesis of l-[methyl- ^{11}C]methionine. *Int. J. Radiat. Appl. Instrum. A Appl. Radiat. Isot.* 39 (4): 311–314.
296. Mitterhauser, M., Wadsak, W., Krcaj, A. et al. (2005). New aspects on the preparation of [^{11}C]methionine—a simple and fast online approach without preparative HPLC. *Appl. Radiat. Isot.* 62 (3): 441–445.
297. Cai, L., Liow, J.-S., Zoghbi, S.S. et al. (2008). Synthesis and evaluation of N-methyl and S-methyl ^{11}C -labeled 6-methylthio-2-(4'-N,N-dimethylamino)phenylimidazo[1,2-a]pyridines as radioligands for imaging β -amyloid plaques in Alzheimer's disease. *J. Med. Chem.* 51 (1): 148–158.
298. Chin, J., Vesnaver, M., Bernard-Gauthier, V. et al. (2013). Direct one-step labeling of cysteine residues on peptides with [^{11}C]methyl triflate for the synthesis of PET radiopharmaceuticals. *Amino Acids* 45 (5): 1097–1108.
299. Majo, V.J., Prabhakaran, J., Simpson, N.R. et al. (2005). A general method for the synthesis of aryl [^{11}C]methylsulfones: potential PET probes for imaging cyclooxygenase-2 expression. *Bioorg. Med. Chem. Lett.* 15 (19): 4268–4271.
300. Kumata, K., Yui, J., Xie, L. et al. (2015). Radiosynthesis and preliminary PET evaluation of glycogen synthase kinase 3β (GSK- 3β) inhibitors containing [^{11}C]methylsulfanyl, [^{11}C]methylsulfinyl or [^{11}C]methylsulfonyl groups. *Bioorg. Med. Chem. Lett.* 25 (16): 3230–3233.
301. Martin, C., Sandrinelli, F., Perrio, C. et al. (2006). Oxidation of aromatic lithium thioates into sulfinate salts: an attractive entry to aryl sulfones labeled with carbon-11. *J. Org. Chem.* 71 (1): 210–214.
302. McCarron, J.A. and Pike, V.W. (2003). Synthesis of no-carrier-added [^{11}C]methanesulfonyl chloride as a new labeling agent for PET radiopharmaceutical development. *J. Labelled Compd. Radiopharm.* 46 (12): 1127–1140.
303. Pretze, M., Große-Gehling, P., and Mamat, C. (2011). Cross-coupling reactions as valuable tool for the preparation of PET radiotracers. *Molecules* 16 (2): 1129–1165.
304. Doi, H. (2015). Pd-mediated rapid cross-couplings using [^{11}C]methyl iodide: groundbreaking labeling methods in ^{11}C radiochemistry. *J. Labelled Compd. Radiopharm.* 58 (3): 73–85.
305. Andersson, Y., Cheng, A., Långström, B. et al. (1995). Palladium-promoted coupling reactions of [^{11}C]methyl iodide with organotin and organoboron compounds. *Acta Chem. Scand.* 49: 683–688.
306. Suzuki, M., Doi, H., Björkman, M. et al. (1997). Rapid coupling of methyl iodide with aryltributylstannanes mediated by palladium(0) complexes: a general protocol for the synthesis of $^{11}\text{CH}_3$ -labeled PET tracers. *Chem. Eur. J.* 3 (12): 2039–2042.

307. Suzuki, M., Doi, H., Hosoya, T. et al. (2004). Rapid methylation on carbon frameworks leading to the synthesis of a PET tracer capable of imaging a novel CNS-type prostacyclin receptor in living human brain. *Trends Anal. Chem.* 23 (8): 595–607.
308. Al-Momani, E., Zlatopolskiy, B.D., Machulla, H.-J. et al. (2012). Radiosynthesis of carbon-11 labeled 6-methyldopamine ($[^{11}\text{C}]\text{MeDA}$). *Appl. Radiat. Isot.* 70 (8): 1475–1479.
309. Doi, H., Mawatari, A., Kanazawa, M. et al. (2015). Synthesis of ^{11}C -labeled thiamine and fursultiamine for in vivo molecular imaging of vitamin B_1 and its prodrug using positron emission tomography. *J. Org. Chem.* 80 (12): 6250–6258.
310. Suzuki, M., Sumi, K., Koyama, H. et al. (2009). Pd^0 -mediated rapid coupling between methyl iodide and heteroarylstannanes: an efficient and general method for the incorporation of a positron-emitting ^{11}C radionuclide into heteroaromatic frameworks. *Chem. Eur. J.* 15 (45): 12489–12495.
311. Huiban, M., Huet, A., Barré, L. et al. (2006). Methyl transfer reaction from monomethyltin reagent under palladium(0) catalysis: a versatile method for labelling with carbon-11. *Chem. Commun.* 0 (1): 97–99.
312. Sandell, J., Halldin, C., Sovago, J. et al. (2002). PET examination of $[^{11}\text{C}]5$ -methyl-6-nitroquipazine, a radioligand for visualization of the serotonin transporter. *Nucl. Med. Biol.* 29 (6): 651–656.
313. Hosoya, T., Wakao, M., Kondo, Y. et al. (2004). Rapid methylation of terminal acetylenes by the Stille coupling of methyl iodide with alkynyltributylstannanes: a general protocol potentially useful for the synthesis of short-lived $^{11}\text{CH}_3$ -labeled PET tracers with a 1-propynyl group electronic supplementary. *Org. Biomol. Chem.* 2 (1): 24.
314. Kitamura, Y., Kozaka, T., Miwa, D. et al. (2016). Synthesis and evaluation of a new vesamicol analog O- $[^{11}\text{C}]$ methyl-trans-decalinvesamicol as a PET ligand for the vesicular acetylcholine transporter. *Ann. Nucl. Med.* 30 (2): 122–129.
315. Zhang, Z., Doi, H., Koyama, H. et al. (2014). Efficient syntheses of $[^{11}\text{C}]$ zidovudine and its analogs by convenient one-pot palladium(0)-copper(I) co-mediated rapid C- $[^{11}\text{C}]$ methylation. *J. Labelled Compd. Radiopharm.* 57 (8): 540–549.
316. Forngren, T., Samuelsson, L., and Långström, B. (2004). A ^{11}C -methyl stannane(5- $[^{11}\text{C}]$ methyl-1-aza-5-stanna-bicyclo[3.3.3]undecane) for use in palladium-mediated $[^{11}\text{C}]$ C–C bond forming reactions with organohalides. *J. Labelled Compd. Radiopharm.* 47 (1): 71–78.
317. Bourdier, T., Huiban, M., Huet, A. et al. (2008). Tetra- and monoorganotin reagents in palladium-mediated cross-coupling reactions for the labeling with carbon-11 of PET tracers. *Synthesis* 2008 (6): 978–984.
318. Hostetler, E.D., Fallis, S., McCarthy, T.J. et al. (1998). Improved methods for the synthesis of $[\omega\text{-}^{11}\text{C}]$ palmitic acid. *J. Org. Chem.* 63 (4): 1348–1351.
319. Hostetler, E.D., Terry, G.E., and Donald Burns, H. (2005). An improved synthesis of substituted $[^{11}\text{C}]$ toluenes via Suzuki coupling with $[^{11}\text{C}]$ methyl iodide. *J. Labelled Compd. Radiopharm.* 48 (9): 629–634.
320. Takashima-Hirano, M., Takashima, T., Katayama, Y. et al. (2011). Efficient sequential synthesis of PET probes of the COX-2 inhibitor $[^{11}\text{C}]$ celecoxib and its major metabolite $[^{11}\text{C}]$ SC-62807 and in vivo PET evaluation. *Bioorg. Med. Chem.* 19 (9): 2997–3004.

321. Andersen, V.L., Herth, M.M., Lehel, S. et al. (2013). Palladium-mediated conversion of para-aminoarylboronic esters into para-aminoaryl- ^{11}C -methanes. *Tetrahedron Lett.* 54 (3): 213–216.
322. Hamill, T.G., Krause, S., Ryan, C. et al. (2005). Synthesis, characterization, and first successful monkey imaging studies of metabotropic glutamate receptor subtype 5 (MGlur5) PET radiotracers. *Synapse* 56 (4): 205–216.
323. Suzuki, M., Takashima-Hirano, M., Ishii, H. et al. (2014). Synthesis of ^{11}C -labeled retinoic acid, [^{11}C]ATRA, via an alkenylboron precursor by Pd(0)-mediated rapid C-[^{11}C] methylation. *Bioorg. Med. Chem. Lett.* 24 (15): 3622–3625.
324. Koyama, H., Zhang, Z., Ijuin, R. et al. (2013). Pd0-mediated rapid coupling of methyl iodide with excess amounts of benzyl- and cinnamylboronic acid esters: efficient method for incorporation of positron-emitting ^{11}C radionuclide into organic frameworks by coupling between two sp^3 -hybridized carbons. *RSC Adv.* 3 (24): 9391.
325. Nabulsi, N.B., Mercier, J., Holden, D. et al. (2016). Synthesis and preclinical evaluation of ^{11}C -UCB-J as a PET tracer for imaging the synaptic vesicle glycoprotein 2A in the brain. *J. Nucl. Med.* 57 (5): 777–784.
326. Boscutti, G., Huiban, M., and Passchier, J. (2017). Use of carbon-11 labelled tool compounds in support of drug development. *Drug Discov. Today Technol.* 25: 3–10.
327. Kealey, S., Passchier, J., and Huiban, M. (2013). Negishi coupling reactions as a valuable tool for [^{11}C]methyl-arene formation; first proof of principle. *Chem. Commun.* 49 (96): 11326.
328. Wüst, F., Zessin, J., and Johannsen, B. (2003). A new approach for ^{11}C -C bond formation: synthesis of 17 α -(3'-[^{11}C]prop-1-yn-1-yl)-3-methoxy-3,17 β -estradiol. *J. Labelled Compd. Radiopharm.* 46 (4): 333–342.
329. Wuest, F.R. and Berndt, M. (2006). ^{11}C -C bond formation by palladium-mediated cross-coupling of alkenylzirconocenes with [^{11}C]methyl iodide. *J. Labelled Compd. Radiopharm.* 49 (2): 91–100.
330. Björkman, M. and Långström, B. (2000). Functionalisation of ^{11}C -labelled olefins via a Heck coupling reaction. *J. Chem. Soc. Perkin Trans.* 10 (18): 3031–3034.
331. Dahl, K., Schou, M., and Halldin, C. (2016). Direct and efficient (carbonyl)cobalt-mediated aryl acetylation using [^{11}C]methyl iodide. *Eur. J. Org. Chem.* 2016 (16): 2775–2777.
332. Murakami, Y., Kuroda, A., Osoda, K., and Nishimura, S. (2003). Rapid synthesis of ^{11}C -labeled FK506 for positron emission tomography. *Tetrahedron Lett.* 44 (4): 641–644.
333. Kihlberg, T., Gullberg, P., and Långström, B. (1990). [^{11}C]Methylenetriphenylphosphorane, a new ^{11}C -precursor, used in a one-pot Wittig synthesis of [β - ^{11}C]styrene. *J. Labelled Compd. Radiopharm.* 28 (10): 1115–1120.
334. Tateishi, H., Tsuji, A.B., Kato, K. et al. (2017). Synthesis and evaluation of ^{11}C -labeled Coumarin analog as an imaging probe for detecting monocarboxylate transporters expression. *Bioorg. Med. Chem. Lett.* 27 (21): 4893–4897.
335. Takashima, M., Kato, K., Ogawa, M., and Magata, Y. (2013). One-pot sequential reactions for the synthesis of versatile ^{11}C -labeled olefin frameworks. *RSC Adv.* 3 (44): 21275.

336. Karramkam, M., Demphel, S., Hinnen, F. et al. (2003). Methylation of the thiophene ring using carbon-11-labelled methyl iodide: formation of 3-[¹¹C]methylthiophene. *J. Labelled Compd. Radiopharm.* 46 (3): 255–261.
337. Popkov, A. and Elsinga, P. (2013). Asymmetric synthesis of carbon-11 labelled α -amino acids for PET. *Curr. Org. Chem.* 17 (19): 2127–2137.
338. Kilbourn, M.R., Dischino, D.D., and Welch, M.J. (1984). Synthesis of DL-[3-¹¹C]phenylalanine. *Int. J. Appl. Radiat. Isot.* 35 (7): 603–605.
339. Suzuki, C., Kato, K., Tsuji, A.B. et al. (2013). Synthesis and in vitro cellular uptake of ¹¹C-labeled 5-aminolevulinic acid derivative to estimate the induced cellular accumulation of protoporphyrin IX. *Bioorg. Med. Chem. Lett.* 23 (16): 4567–4570.
340. Kato, K., Tsuji, A.B., Saga, T., and Zhang, M.-R. (2011). An efficient and expedient method for the synthesis of ¹¹C-labeled α -aminoisobutyric acid: a tumor imaging agent potentially useful for cancer diagnosis. *Bioorg. Med. Chem. Lett.* 21 (8): 2437–2440.
341. Långström, B. and Stridsberg, B. (1979). Syntheses of racemic [1-¹¹C]-alanine and partially resolved [3-¹¹C]-alanine. *Int. J. Appl. Radiat. Isot.* 30 (3): 151–153.
342. Antoni, G., Långström, B., Datema, R. et al. (1986). Asymmetric synthesis of L-[3-¹¹C]alanine. *Acta Chem. Scand.* 40b: 152–156.
343. Fasth, K.J., Antoni, G., Långström, B. et al. (1990). Asymmetric synthesis of L-[beta-¹¹C]alanine using a glycine derivative with two chiral handles, (1R,2S,3R)-8-phenylmenthan-3-yl N-[(1R,2R,5R)-2-hydroxypinan-3-ylidene]glycinate. *Acta Chem. Scand.* 44: 527–530.
344. Någren, K. (1979). Asymmetric synthesis of L-[3-¹¹C]alanine utilizing a sultam-derived glycine equivalent. *J. Labelled Compd. Radiopharm.* 40: 758–759.
345. Fasth, K.-J., Hörnfeldt, K., Långström, B. et al. (1995). Asymmetric synthesis of ¹¹C-labelled L- and D-amino acids by alkylation of imidazolidinone derivatives. *Acta Chem. Scand.* 49: 301–304.
346. Fasth, K.J., Långström, B., Sauerwein, B. et al. (1990). Asymmetric synthesis of L-[beta-¹¹C]amino acids using a chiral nickel complex of the Schiff base of (S)-O-[(N-benzylpropyl)amino]benzophenone and glycine. *Acta Chem. Scand.* 44: 720–725.
347. Popkov, A., Nádvořník, M., Kružberská, P. et al. (2007). Towards stereoselective radiosynthesis of α -[¹¹C]methyl-substituted aromatic α -amino acids – a challenge of creation of quaternary asymmetric centre in a very short time. *J. Labelled Compd. Radiopharm.* 50 (5–6): 370–374.
348. Pekošak, A., Filp, U., Škrinjar, J. et al. (2017). A rapid and highly enantioselective C–11 C bond formation of l-[¹¹C]phenylalanine via chiral phase-transfer catalysis. *Org. Biomol. Chem.* 15 (3): 570–575.
349. Filp, U., Pekošak, A., Poot, A.J., and Windhorst, A.D. (2017). Stereocontrolled [¹¹C] alkylation of N-terminal glycine Schiff bases to obtain dipeptides. *Eur. J. Org. Chem.* 2017 (37): 5592–5596.
350. Pekošak, A., Rotstein, B.H., Collier, T.L. et al. (2017). Stereoselective ¹¹C labeling of a “native” tetrapeptide by using asymmetric phase-transfer catalyzed alkylation reactions. *Eur. J. Org. Chem.* 2017 (5): 1019–1024.

351. Takashima-Hirano, M., Shukuri, M., Takashima, T. et al. (2010). General method for the ^{11}C -labeling of 2-arylpropionic acids and their esters: construction of a PET tracer library for a study of biological events involved in COXs expression. *Chem. Eur. J.* 16 (14): 4250–4258.
352. Kato, K., Kikuchi, T., Nengaki, N. et al. (2010). Tetrabutylammonium fluoride-promoted α - ^{11}C methylation of α -arylesters: a simple and robust method for the preparation of ^{11}C -labeled ibuprofen. *Tetrahedron Lett.* 51 (45): 5908–5911.
353. Takashima-Hirano, M., Tazawa, S., Takahashi, K. et al. (2011). Efficient synthesis of ^{11}C ramelteon as a positron emission tomography probe for imaging melatonin receptors involved in circadian rhythms. *Chem. Pharm. Bull.* 59 (8): 1062–1064.
354. Takahashi, T., Ido, T., Hatano, K. et al. (1990). Synthesis of 1- ^{11}C -labeled fatty acid from ^{11}C HCN. *Int. J. Radiat. Appl. Instrum.* 41 (7): 649–654.
355. Best, M., Gifford, A.N., Kim, S.W. et al. (2012). Rapid radiosynthesis of ^{11}C and ^{14}C azelaic, suberic, and sebacic acids for in vivo mechanistic studies of systemic acquired resistance in plants. *J. Labelled Compd. Radiopharm.* 55 (1): 39–43.
356. Zhang, Z., Ding, Y.S., Studenov, A.R. et al. (2002). Novel synthesis of ^{11}C γ -vinyl- γ -aminobutyric acid (^{11}C GVG) for pharmacokinetic studies of addiction treatment. *J. Labelled Compd. Radiopharm.* 45 (3): 199–211.
357. Lee, S., Alexoff, D.L., Shea, C. et al. (2015). Tetraethylene glycol promoted two-step, one-pot rapid synthesis of indole-3- ^{11}C acetic acid. *Tetrahedron Lett.* 56 (3): 517–520.
358. Reid, A.E., Kim, S.W., Seiner, B. et al. (2011). Radiosynthesis of C-11 labeled auxin (3-indolyl ^{11}C acetic acid) and its derivatives from gramine. *J. Labelled Compd. Radiopharm.* 54 (8): 433–437.
359. Qu, W., Oya, S., Lieberman, B.P. et al. (2012). Preparation and characterization of L- ^{11}C -glutamine for metabolic imaging of tumors. *J. Nucl. Med.* 53 (1): 98–105.
360. Gleede, T., Riehl, B., Shea, C. et al. (2015). Investigation of SN2 ^{11}C cyanation for base-sensitive substrates: an improved radiosynthesis of L- ^{11}C -glutamine. *Amino Acids* 47 (3): 525–533.
361. Somawardhana, C.W., Sajjad, M., and Lambrecht, R.M. (1991). Solid state support for the synthesis of ^{11}C -putrescine. *Int. J. Radiat. Appl. Instrum.* 42 (6): 555–558.
362. Lee, S.J., Fowler, J.S., Alexoff, D. et al. (2015). An efficient and practical synthesis of ^{11}C indole via superfast nucleophilic ^{11}C cyanation and RANEY® nickel catalyzed reductive cyclization. *Org. Biomol. Chem.* 13 (46): 11235–11243.
363. Gillings, N.M. and Gee, A.D. (2001). Synthesis of ^{11}C amino acids via ring-opening of aziridine-2-carboxylates. *J. Labelled Compd. Radiopharm.* 44 (13): 909–920.
364. Halldin, C., Schoeps, K.-O., Stone-Elander, S., and Wiesel, F.-A. (1987). The Bucherer-Strecker synthesis of D- and L-(^{11}C)tyrosine and the in vivo study of L-(^{11}C)tyrosine in human brain using positron emission tomography. *Eur. J. Nucl. Med.* 13 (6): 288–291.
365. Zalutsky, M.R., Wu, J., Harper, P.V., and Wickland, T. (1981). Synthesis of ^{11}C -DL-tryptophan and its purification using high-pressure liquid chromatography. *Int. J. Appl. Radiat. Isot.* 32 (3): 182–184.

366. Halldin, C. and Långström, B. (1985). Synthesis of racemic [2-¹¹C]phenylglycine. *J. Labelled Compd. Radiopharm.* 22 (6): 631–640.
367. Adam, M.J., Grierson, J.R., Ruth, T.J. et al. (1987). Routine synthesis of carbon-11-carboxyl-labeled L-DOPA. *J. Nucl. Med.* 28 (10): 1599–1603.
368. Barrio, J.R., Keen, R.E., Ropchan, J.R. et al. (1983). L-[1-¹¹C]leucine: routine synthesis by enzymatic resolution. *J. Nucl. Med.* 24 (6): 515–521.
369. Johnström, P., Stone-Elander, S., Ericson, K. et al. (1987). ¹¹C-labelled glycine: synthesis and preliminary report on its use in the investigation of intracranial tumours using positron emission tomography. *Int. J. Radiat. Appl. Instrum. A Appl. Radiat. Isot.* 38 (9): 729–734.
370. Schmall, B., Conti, P.S., Bigler, R.E. et al. (1984). Synthesis and quality assurance of [¹¹C]alpha-aminoisobutyric acid (AIB), a potential radiotracer for imaging and amino acid transport studies in normal and malignant tissues. *Int. J. Nucl. Med. Biol.* 11 (3–4): 209–214.
371. Dunzendorfer, U., Schmall, B., Bigler, R.E. et al. (1981). Synthesis and body distribution of alpha-aminoisobutyric acid-L-¹¹C in normal and prostate cancer-bearing rat after chemotherapy. *Eur. J. Nucl. Med.* 6 (11): 535–538.
372. Sambre, J., Vandecasteele, C., Goethals, P. et al. (1985). Routine production of H¹¹CN and [¹¹C]-1-aminocyclopentanecarboxylic acid. *Int. J. Appl. Radiat. Isot.* 36 (4): 275–278.
373. Hayes, R.L., Washburn, L.C., Wieland, B.W. et al. (1976). Carboxyl-labeled ¹¹C-1-aminocyclopentanecarboxylic acid, a potential agent for cancer detection. *J. Nucl. Med.* 17 (8): 748–751.
374. Hayes, R.L., Washburn, L.C., Wieland, B.W. et al. (1978). Synthesis and purification of ¹¹C-carboxyl-labeled amino acids. *Int. J. Appl. Radiat. Isot.* 29 (3): 186–187.
375. Fissekis, J.D., Nielsen, C.M., Tirelli, S. et al. (1991). A remote control process for the routine synthesis of branched chain [1-¹¹C]α amino acids. *Int. J. Radiat. Appl. Instrum.* 42 (12): 1169–1176.
376. Takahashi, T., Någren, K., and Aho, K. (1990). An alternative synthesis of DL-[1-¹¹C]alanine from [¹¹C]HCN. *Int. J. Radiat. Appl. Instrum.* 41 (12): 1187–1191.
377. Bjurling, P. and Långström, B. (1990). Synthesis of 1- and 3-¹¹C-labelled L-lactic acid using multi-enzyme catalysis. *J. Labelled Compd. Radiopharm.* 28 (4): 427–432.
378. Studenov, A.R., Szalda, D.E., and Ding, Y.-S. (2003). Synthesis of no-carrier-added C-11 labeled D- and L-enantiomers of phenylalanine and tyrosine for comparative PET studies. *Nucl. Med. Biol.* 30 (1): 39–44.
379. Winstead, M.B., Chern, C., Lin, T.-H. et al. (1978). Synthesis and preliminary scintigraphic evaluation of in vivo distribution of ¹¹C-hydroxyurea/isohydroxyurea and ¹¹C-cyanate. *Int. J. Appl. Radiat. Isot.* 29 (7): 443–447.
380. Drandarov, K., Schubiger, P.A., and Westera, G. (2006). Automated no-carrier-added synthesis of [1-¹¹C]-labeled D- and L-enantiomers of lactic acid. *Appl. Radiat. Isot.* 64 (12): 1613–1622.
381. Christman, D.R., Hoyte, R.M., and Wolf, A.P. (1970). Organic radiopharmaceuticals labeled with isotopes of short half-life. I. ¹¹C-1-dopamine hydrochloride. *J. Nucl. Med.* 11 (8): 474–478.

382. Maeda, M., Koga, Y., Fukumura, T., and Kojima, M. (1990). [¹¹C]octopamine synthesis using [¹¹C]cyanide: chemical and enzymatic approaches for the [¹¹C]cyanohydrin synthesis. *Int. J. Radiat. Appl. Instrum.* 41 (5): 463–469.
383. Cai, H., Mangner, T.J., Muzik, O. et al. (2014). Radiosynthesis of ¹¹C-levetiracetam: a potential marker for PET imaging of SV2A expression. *ACS Med. Chem. Lett.* 5 (10): 1152–1155.
384. Xing, J., Brooks, A.F., Fink, D. et al. (2017). High-yielding automated convergent synthesis of no-carrier-added [¹¹C-carbonyl]-labeled amino acids using the Strecker reaction. *Synlett* 28 (3): 371–375.
385. Sundermeier, M., Zapf, A., and Beller, M. (2003). Palladium-catalyzed cyanation of aryl halides: recent developments and perspectives. *Eur. J. Inorg. Chem.* 2003 (19): 3513–3526.
386. Balatoni, J.A., Adam, M.J., and Hall, L.D. (1989). Synthesis of ¹¹C-labeled aromatics using aryl chromium tricarbonyl intermediates. *J. Labelled Compd. Radiopharm.* 27 (12): 1429–1435.
387. Andersson, Y. and Långström, B. (1994). Transition metal-mediated reactions using [¹¹C]cyanide in synthesis of ¹¹C-labelled aromatic compounds. *J. Chem. Soc. Perkin Trans. 1* 0 (11): 1395–1400.
388. Andersson, J.D., Seneca, N., Truong, P. et al. (2013). Palladium mediated ¹¹C-cyanation and characterization in the non-human primate brain of the novel MGLUR5 radioligand [¹¹C]AZD9272. *Nucl. Med. Biol.* 40 (4): 547–553.
389. Siméon, F.G., Liow, J.S., Zhang, Y. et al. (2012). Synthesis and characterization in monkey of [¹¹C]SP203 as a radioligand for imaging brain metabotropic glutamate 5 receptors. *Eur. J. Nucl. Med. Mol. Imaging* 39 (12): 1949–1958.
390. Nordeman, P., Johansson, L.B.G., Bäck, M. et al. (2016). ¹¹C and ¹⁸F radiolabeling of tetra- and pentathiophenes as PET-ligands for amyloid protein aggregates. *ACS Med. Chem. Lett.* 7 (4): 368–373.
391. Kil, K.E., Biegón, A., Ding, Y.S. et al. (2009). Synthesis and PET studies of [¹¹C-cyano] letrozole (Femara®), an aromatase inhibitor drug. *Nucl. Med. Biol.* 36 (2): 215–223.
392. Andersson, Y., Bergström, M., and Långström, B. (1994). Synthesis of ¹¹C-labelled benzamide compounds as potential tracers for poly(ADP-ribose) synthetase. *Appl. Radiat. Isot.* 45 (6): 707–714.
393. Liu, L., Xu, Y., Shea, C. et al. (2010). Radiosynthesis and bioimaging of the tuberculosis chemotherapeutics isoniazid, rifampicin and pyrazinamide in baboons. *J. Med. Chem.* 53 (7): 2882–2891.
394. Lee, H.G., Milner, P.J., Placzek, M.S. et al. (2015). Virtually instantaneous, room-temperature [¹¹C]-cyanation using biaryl phosphine Pd(0) complexes. *J. Am. Chem. Soc.* 137 (2): 648–651.
395. Antoni, G. and Långström, B. (1992). Synthesis of ¹¹C-labelled α,β -unsaturated nitriles. *Int. J. Radiat. Appl. Instrum.* 43 (7): 903–905.
396. Zhao, W., Lee, H.G., Buchwald, S.L., and Hooker, J.M. (2017). Direct ¹¹CN-labeling of unprotected peptides via palladium-mediated sequential cross-coupling reactions. *J. Am. Chem. Soc.* 139 (21): 7152–7155.

397. Ponchant, M., Hinnen, F., Demphel, S., and Crouzel, C. (1997). [^{11}C]Copper(II) cyanide: a new radioactive precursor for ^{11}C -cyanation and functionalization of haloarenes. *Appl. Radiat. Isot.* 48 (6): 755–762.
398. Siméon, F., Sobrio, F., Gourand, F., and Barré, L. (2001). Total synthesis and radiolabeling of an efficient Rt-PA inhibitor: [^{11}C] (Z,Z)-BABCH. A first route to [^{11}C] labelled amidines. *J. Chem. Soc. Perkin Trans. 1* 0 (7): 690–694.
399. Oi, N., Tokunaga, M., Suzuki, M. et al. (2015). Development of novel PET probes for central 2-amino-3-(3-hydroxy-5-methyl-4-isoxazolyl)propionic acid receptors. *J. Med. Chem.* 58 (21): 8444–8462.
400. Taddei, C. and Gee, A.D. (2018). Recent progress in [^{11}C]carbon dioxide ([^{11}C]CO₂) and [^{11}C]carbon monoxide ([^{11}C]CO) chemistry. *J. Labelled Compd. Radiopharm.* 61 (3): 237–251.
401. Oi, N., Suzuki, M., Terauchi, T. et al. (2013). Synthesis and evaluation of novel radioligands for positron emission tomography imaging of the orexin-2 receptor. *J. Med. Chem.* 56 (16): 6371–6385.
402. Ponchant, M., Galéa, H., Bottlaender, M. et al. (2000). [Tetrazoyl- ^{11}C]LY202157 synthesis for in vivo studies of the NMDA receptor channel complex. *J. Labelled Compd. Radiopharm.* 43 (13): 1311–1320.
403. Ponchant, M., Demphel, S., Hinnen, F., and Crouzel, C. (1997). Radiosynthesis of [tetrazoyl- ^{11}C]irbesartan, a non-peptidic angiotensin II antagonist. *Eur. J. Med. Chem.* 32 (9): 747–752.
404. Ma, L., Placzek, M.S., Hooker, J.M. et al. (2017). Cyanation of arylboronic acids in aqueous solutions. *Chem. Commun.* 53 (49): 6597–6600.
405. Makaravage, K.J., Shao, X., Brooks, A.F. et al. (2018). Copper(II)-mediated [^{11}C]cyanation of arylboronic acids and arylstannanes. *Org. Lett.* 20 (6): 1530–1533.
406. Brooks, A., Makaravage, K., Shao, X. et al. (2017). Cu-mediated radiocyanation with [^{11}C]KCN for the preparation of [^{11}C]LY2795050, a selective kappa opioid antagonist. *J. Nucl. Med.* 58 (suppl 1): 402.
407. Westerberg, G., Långström, B., Ragnarsson, U. et al. (1993). Synthesis of [^{11}C]- and [^{13}C]-cyanogen bromide, useful electrophilic labelling precursors. *Acta Chem. Scand.* 47: 974–978.
408. Westerberg, G. and Långström, B. (1997). On-line production of [^{11}C]cyanogen bromide. *Appl. Radiat. Isot.* 48 (4): 459–461.
409. Westerberg, G. and Långström, B. (1994). Labelling of proteins with ^{11}C in high specific radioactivity: [^{11}C]albumin and [^{11}C]transferrin. *Appl. Radiat. Isot.* 45 (7): 773–782.
410. Raffel, D.M., Jung, Y.W., Gildersleeve, D.L. et al. (2007). Radiolabeled phenethylguanidines: novel imaging agents for cardiac sympathetic neurons and adrenergic tumors. *J. Med. Chem.* 50 (9): 2078–2088.
411. Derdau, V. (2018). New trends and applications in cyanation isotope chemistry. *J. Labelled Compd. Radiopharm.* 61 (14): 1012–1023.
412. Jacobson, G.B., Westerberg, G., Markides, K.E., and Långström, B. (1996). Synthesis of ^{11}C -labeled guanidines in supercritical ammonia. *J. Am. Chem. Soc.* 118 (29): 6868–6872.

413. Westerberg, G., Kärger, W., Onoe, H., and Långström, B. (1994). [¹¹C]Cyanogen bromide in the synthesis of 1,3-di(2-tolyl)-[¹¹C]guanidine. *J. Labelled Compd. Radiopharm.* 34 (8): 691–696.
414. Westerberg, G., Bergström, M., Gustafson, S. et al. (1995). Labelling of polysaccharides using [¹¹C]cyanogen bromide. In vivo and in vitro evaluation of ¹¹C-hyaluronan uptake kinetics. *Nucl. Med. Biol.* 22 (2): 251–256.
415. Emran, A.M., Boothe, T.E., Finn, R.D. et al. (1983). Preparation of ¹¹C-urea from no-carrier-added ¹¹C-cyanide. *Int. J. Appl. Radiat. Isot.* 34 (7): 1013–1014.
416. Emran, A.M., Boothe, T.E., Finn, R.D. et al. (1985). Optimized production of high specific activity [¹¹C]urea. *Int. J. Appl. Radiat. Isot.* 36 (9): 739–740.
417. Vander Borght, T., Labar, D., Pauwels, S., and Lambotte, L. (1991). Production of [2-¹¹C]thymidine for quantification of cellular proliferation with PET. *Int. J. Radiat. Appl. Instrum.* 42 (1): 103–104.
418. Emran, A.M., Boothe, T.E., Finn, R.D. et al. (1986). Use of ¹¹C as a tracer for studying the synthesis of radiolabelled compounds—II: 2-[¹¹C]-5,5-diphenylhydantoin from [¹¹C]cyanide. *Int. J. Radiat. Appl. Instrum. A Appl. Radiat. Isot.* 37 (10): 1033–1038.
419. Westerberg, G. and Långström, B. (1994). Synthesis of sodium [¹¹C]thiocyanate using [¹¹C]cyanogen bromide. *J. Labelled Compd. Radiopharm.* 34 (6): 545–548.
420. Stone-Elander, S., Roland, P., Halldin, C. et al. (1989). Synthesis of [¹¹C]sodium thiocyanate for in vivo studies of anion kinetics using positron emission tomography (PET). *Int. J. Rad. Appl. Instrum. B* 16 (7): 741–746.
421. Haywood, T., Cesarec, S., Kealey, S. et al. (2018). Ammonium [¹¹C]thiocyanate: revised preparation and reactivity studies of a versatile nucleophile for carbon-11 radiolabelling. *Medchemcomm* 9 (8): 1311–1314.
422. Johnström, P., Bergman, L., Varnäs, K. et al. (2015). Development of rapid multistep carbon-11 radiosynthesis of the myeloperoxidase inhibitor AZD3241 to assess brain exposure by PET microdosing. *Nucl. Med. Biol.* 42 (6): 555–560.
423. Saeed, M., Tewson, T.J., Erdahl, C.E., and Kohen, A. (2012). A fast chemoenzymatic synthesis of [¹¹C]-N5,N10-methylenetetrahydrofolate as a potential PET tracer for proliferating cells. *Nucl. Med. Biol.* 39 (5): 697–701.
424. Hughes, J.A., Hartman, N.G., and Jay, M. (1995). Preparation of [¹¹C]-thymidine and [¹¹C]-2'-arabino-2'-fluoro-β-5-methyl-uridine (FMAU) using a hollow fiber membrane bioreactor system. *J. Labelled Compd. Radiopharm.* 36 (12): 1133–1145.
425. Neelamegam, R., Hellenbrand, T., Schroeder, F.A. et al. (2014). Imaging evaluation of 5HT2 cagonists, [¹¹C]WAY-163909 and [¹¹C]vabicaserin, formed by Pictet-Spengler cyclization. *J. Med. Chem.* 57 (4): 1488–1494.
426. Hanyu, M., Takada, Y., Hashimoto, H. et al. (2013). Carbon-11 radiolabeling of an oligopeptide containing tryptophan hydrochloride via a Pictet-Spengler reaction using carbon-11 formaldehyde. *J. Pept. Sci.* 19 (10): 663–668.
427. Mathews, W.B., Nakamoto, Y., Abraham, E.H. et al. (2005). Synthesis and biodistribution of [¹¹C]adenosine 5'-monophosphate ([¹¹C]AMP). *Mol. Imaging Biol.* 7 (3): 203–208.

428. Roeda, D., Sipil, H.T., Bramoull, Y. et al. (2002). Synthesis of [^{11}C]atipamezole, a potential PET ligand for the A2-adrenergic receptor in the brain. *J. Labelled Compd. Radiopharm.* 45 (1): 37–47.
429. Popkov, A. and Itsenko, O. (2015). An asymmetric approach to the synthesis of a carbon-11 labelled gliotransmitter D-serine. *J. Radioanal. Nucl. Chem.* 304 (1): 455–458.
430. Straatmann, M.G. and Welch, M.J. (1975). A general method for labeling proteins with ^{11}C . *J. Nucl. Med.* 16 (5): 425–428.
431. Wu, C., Li, R., Dearborn, D., and Wang, Y. (2012). Reductive amination with [^{11}C]formaldehyde: a versatile approach to radiomethylation of amines. *Int. J. Org. Chem.* 02 (03): 202–223.
432. Roeda, D. and Dolle, F. (2010). [^{11}C]Phosgene: a versatile reagent for radioactive carbonyl insertion into medicinal radiotracers for positron emission tomography. *Curr. Top. Med. Chem.* 10 (16): 1680–1700.
433. Crouzel, C., Hinnen, F., and Maitre, E. (1995). Radiosynthesis of methyl and heptyl [^{11}C]isocyanates from [^{11}C]phosgene, application to the synthesis of carbamates: [^{11}C]physostygmine and [^{11}C]heptylphysostigmine. *Appl. Radiat. Isot.* 46 (3): 167–170.
434. Brown, G.D., Henderson, D., Steel, C. et al. (2001). Two routes to [^{11}C -carbonyl]organo-isocyanates utilizing [^{11}C]phosgene ([^{11}C]organo-Isocyanates from [^{11}C]phosgene). *Nucl. Med. Biol.*: 991–998.
435. Dollé, F., Martarello, L., Bramoullé, Y. et al. (2005). Radiosynthesis of carbon-11-labelled G1181771, a new selective CCK-A agonist. *J. Labelled Compd. Radiopharm.* 48 (7): 501–513.
436. Shimoda, Y., Yui, J., Zhang, Y. et al. (2015). Radiosynthesis and evaluation of N-(3,4-dimethylisoxazol-5-yl)piperazine-4-[4-(4-fluorophenyl)thiazol-2-yl]-1- ^{11}C carboxamide for in vivo positron emission tomography imaging of fatty acid amide hydrolase in brain. *RSC Adv.* 5 (128): 106122–106127.
437. Asakawa, C., Ogawa, M., Fujinaga, M. et al. (2012). Utilization of [^{11}C]phosgene for radiosynthesis of N-(2-{3-[3,5-bis(trifluoromethyl)]phenyl} ^{11}C ureido}ethyl) glycyrrhetinamide, an inhibitory agent for proteasome and kinase in tumors. *Bioorg. Med. Chem. Lett.* 22 (11): 3594–3597.
438. Asakawa, C., Ogawa, M., Kumata, K. et al. (2011). Sorafenib: radiosynthesis and preliminary PET study of brain uptake in P-Gp/Bcrp knockout mice. *Bioorg. Med. Chem. Lett.* 21 (8): 2220–2223.
439. Asakawa, C., Ogawa, M., Kumata, K. et al. (2011). Radiosynthesis of three [^{11}C]Ureido-substituted benzenesulfonamides as PET probes for carbonic anhydrase IX in tumors. *Bioorg. Med. Chem. Lett.* 21 (23): 7017–7020.
440. Lemoucheux, L., Rouden, J., Ibazizene, M. et al. (2003). Debenzylation of tertiary amines using phosgene or triphosgene: an efficient and rapid procedure for the preparation of carbamoyl chlorides and unsymmetrical ureas. Application in carbon-11 chemistry. *J. Org. Chem.* 68 (19): 7289–7297.
441. Dolle, F., Valette, H., Hinnen, F. et al. (2001). Synthesis and preliminary evaluation of a carbon-11-labelled agonist of the A7 nicotinic acetylcholine receptor. *J. Labelled Compd. Radiopharm.* 44 (11): 785–795.

442. Lidström, P., Bonasera, T.A., Marquez-M, M. et al. (1998). Synthesis and in vitro evaluation of [carbonyl-¹¹C]estramustine and [carbonyl-¹¹C]estramustine phosphate. *Steroids* 63 (4): 228–234.
443. Kumata, K., Yui, J., Hatori, A. et al. (2015). Development of [¹¹C]MFTC for PET imaging of fatty acid amide hydrolase in rat and monkey brains. *ACS Chem. Neurosci.* 6 (2): 339–346.
444. Wang, L., Mori, W., Cheng, R. et al. (2016). Synthesis and preclinical evaluation of sulfonamidobased [¹¹C-carbonyl]-carbamates and ureas for imaging monoacylglycerol lipase. *Theranostics* 6 (8): 1145–1159.
445. Cheng, R., Mori, W., Ma, L. et al. (2018). In vitro and in vivo evaluation of ¹¹C-labeled azetidincarboxylates for imaging monoacylglycerol lipase by PET imaging studies. *J. Med. Chem.* 61 (6): 2278–2291.
446. Damont, A., Roeda, D., and Dollé, F. (2013). The potential of carbon-11 and fluorine-18 chemistry: illustration through the development of positron emission tomography radioligands targeting the translocator protein 18 KDa. *J. Labelled Compd. Radiopharm.* 56 (3–4): 96–104.
447. Miller, P.W., Kato, K., and Långström, B. (2014). Carbon-11, nitrogen-13, and oxygen-15 chemistry: an introduction to chemistry with short-lived radioisotopes. In: *The Chemistry of Molecular Imaging*, vol. 9781118093 (eds. N. Long and W.-T. Wong), 79–103. Hoboken, NJ: Wiley.
448. Del Vecchio, A., Destro, G., Taran, F., and Audisio, D. (2018). Recent developments in heterocycle labeling with carbon isotopes. *J. Labelled Compd. Radiopharm.* 61 (13): 988–1007.
449. Roeda, D., Tavitian, B., Coulon, C. et al. (1997). Synthesis of [¹¹C]RPR-72840A and its evaluation as a radioligand for the serotonin reuptake site in positron emission tomography. *Bioorg. Med. Chem.* 5 (2): 397–403.
450. Yashio, K., Katayama, Y., Takashima, T. et al. (2012). Synthesis of [¹¹C]uric acid, using [¹¹C]phosgene, as a possible biomarker in PET imaging for diagnosis of gout. *Bioorg. Med. Chem. Lett.* 22 (1): 115–119.
451. Takada, Y., Ogawa, M., Suzuki, H., and Fukumura, T. (2010). Radiosynthesis of [2-¹¹C-carbonyl]dantrolene using [¹¹C]phosgene for PET. *Appl. Radiat. Isot.* 68 (9): 1715–1720.
452. Seki, K.I., Nishijima, K.I., Sanoki, K. et al. (2009). New [¹¹C]phosgene based synthesis of [¹¹C]pyrimidines for positron emission tomography. *Heterocycles* 77 (2): 1307–1321.
453. Roger, G., Dollé, F., De Bruin, B. et al. (2004). Radiosynthesis and pharmacological evaluation of [¹¹C]EMD-95885: a high affinity ligand for NR2B-containing NMDA receptors. *Bioorg. Med. Chem.* 12 (12): 3229–3237.
454. Roger, G., Lagnel, B., Besret, L. et al. (2003). Synthesis, radiosynthesis and in vivo evaluation of 5-[3-(4-benzylpiperidin-1-yl)prop-1-ynyl]-1,3-dihydrobenzimidazol-2-[¹¹C]one, as a potent NR1A/2B subtype selective NMDA PET radiotracer. *Bioorg. Med. Chem.* 11 (24): 5401–5408.
455. Labas, R., Sobrio, F., Bramoullé, Y. et al. (2010). Radiosynthesis of N-[4-(4-fluorobenzyl)piperidin-1-yl]-N'-(2-[¹¹C]oxo-1,3-dihydrobenzimidazol-5-yl)oxamide, a NR2B-selective NMDA receptor antagonist. *J. Labelled Compd. Radiopharm.* 53 (2): 63–67.

456. Brown, G.D., Luthra, S.K., Brock, C.S. et al. (2002). Antitumor imidazotetrazines. 40. 1 radiosyntheses of [4-¹¹C-Carbonyl]- and [3-N-¹¹C-methyl]-8-carbamoyl-3-methylimidazo[5,1-d]-1,2,3,5-tetrazin-4(3H)-one (temozolomide) for positron emission tomography (PET) studies. *J. Med. Chem.* 45 (25): 5448–5457.
457. Kato, K., Gustavsson, S.Å., and Långström, B. (2008). Asymmetric nitroaldol reaction using nitromethane labeled with ¹¹C. *Tetrahedron Lett.* 49 (41): 5837–5839.
458. Zessin, J. and Steinbach, J. (1998). ¹¹C-labelling of heterocyclic aromatic compounds in ring positions: synthesis of [2-¹¹C]indole. *J. Labelled Compd. Radiopharm.* 41 (7): 669–676.
459. Schoeps, K.O., Långström, B., Stone-Elander, S., and Halldin, C. (1991). Synthesis of [1-¹¹C]D-glucose and [1-¹¹C]D-mannose from on-line produced [¹¹C]nitromethane. *Int. J. Rad. Appl. Instrum. A* 42 (9): 877–883.
460. Kato, K., Zhang, M.R., Minegishi, K. et al. (2011). Nitroaldol reaction of nitro[¹¹C] methane to form 2-(hydroxymethyl)-2-nitro[2-¹¹C]propane-1,3-diol and [¹¹C]TRIS. *J. Labelled Compd. Radiopharm.* 54 (3): 140–144.
461. Mäding, P., Steinbach, J., and Johannsen, B. (2000). No-carrier-added ¹¹C-labelling of benzenoid compounds in ring positions by condensation of nitro-[¹¹C]methane with pyrylium salts. *J. Labelled Compd. Radiopharm.* 43 (6): 565–583.
462. Kato, K., Zhang, M.R., and Suzuki, K. (2007). Rapid C-carboxylation of nitro[¹¹C] methane for the synthesis of ethyl nitro[2-¹¹C]acetate. *Mol. Biosyst.* 4 (1): 53–55.
463. Kato, K., Zhang, M.-R., and Suzuki, K. (2009). Synthesis of (R,S)-[4-¹¹C]baclofen via Michael addition of nitromethane labeled with short-lived ¹¹C. *Bioorg. Med. Chem. Lett.* 19 (21): 6222–6224.
464. Roeda, D., Crouzel, C., Brouillet, E., and Valette, H. (1996). Synthesis and in vivo distribution of no-carrier-added N(ω)-nitro-L-arginine [¹¹C]methyl ester, a nitric oxide synthase inhibitor. *Nucl. Med. Biol.* 23 (4): 509–512.
465. Dollé, F., Hinnen, F., Valette, H. et al. (1997). Synthesis of two optically active calcium channel antagonists labelled with carbon-11 for in vivo cardiac PET imaging. *Bioorg. Med. Chem.* 5 (4): 749–764.
466. Neu, H., Bonasera, T.A., and Langström, B. (1998). Lithium[¹¹C]methyl(2-thienyl) cuprate·LiCN in 1,4-addition to α,β-unsaturated ketones, ¹¹C and ¹³C labelling of the androgen mesterolone. *J. Labelled Compd. Radiopharm.* 41 (3): 227–234.
467. Lidström, P., Neu, H., and Långström, B. (1997). Syntheses of [21-¹¹C] and [21-¹³C]progesterone. *J. Labelled Compd. Radiopharm.* 39 (8): 695–704.
468. da Silva, E.S., Gómez-Vallejo, V., López-Gallego, F., and Llop, J. (2018). Biocatalysis in radiochemistry: enzymatic incorporation of PET radionuclides into molecules of biomedical interest. *J. Labelled Compd. Radiopharm.* 61 (4): 332–354.
469. Barrio, J.R., Egbert, J.E., Henze, E. et al. (1982). L-[4-¹¹C]aspartic acid: enzymatic synthesis, myocardial uptake, and metabolism. *J. Med. Chem.* American Chemical Society: 93–96.
470. Antoni, G., Omura, H., Ikemoto, M. et al. (2001). Enzyme catalysed synthesis of L-[4-¹¹C] aspartate and L-[5-¹¹C] glutamate. *J. Labelled Compd. Radiopharm.* 44 (4): 287–294.
471. Antoni, G., Omura, H., Bergström, M. et al. (1997). Synthesis of L-2,4-diamino[4-¹¹C] butyric acid and its use in some in vitro and in vivo tumour models. *Nucl. Med. Biol.* 24 (6): 595–601.

472. Svärd, H., Jigerius, S.B., and Långström, B. (1990). The enzymatic synthesis of L-[3-¹¹C]serine. *Int. J. Radiat. Appl. Instrum.* 41 (6): 587–591.
473. Kaneko, S., Ishiwata, K., Ishii, S.I. et al. (1999). Enzymatic synthesis of carbon-11 labeled methionine and its derivatives with immobilized γ -cyano- γ -aminobutyric acid synthase. *Appl. Radiat. Isot.* 51 (3): 285–291.
474. Mannens, G., Slegers, G., Lambrecht, R., and Goethals, P. (1988). Enzymatic synthesis of carbon-11 acetyl coenzyme A. *J. Labelled Compd. Radiopharm.* 25 (7): 695–705.
475. Jacobson, G.B., Watanabe, Y., Valind, S. et al. (1997). Synthesis of O-[¹¹C]acetyl CoA, O-[¹¹C]acetyl-L-carnitine, and L-[¹¹C]carnitine labelled in specific positions, applied in PET studies on rhesus monkey. *Nucl. Med. Biol.* 24 (5): 471–478.
476. Davenport, R.J., Pike, V.W., Dowsett, K. et al. (1997). Automated chemoenzymatic synthesis of no-carrier-added [carbonyl-¹¹C]propionyl L-carnitine for pharmacokinetic studies. *Appl. Radiat. Isot.* 48 (7): 917–924.
477. Mannens, G., Slegers, G., Goethals, P., and Claeys, A. (1990). Enzymatic synthesis of carbon-11 N-acetyl-D-glucosamine. *J. Labelled Compd. Radiopharm.* 28 (1): 53–64.
478. Mannens, G., Slegers, G., and Goethals, P. (1990). Enzymatic synthesis of [¹¹C]N-acetylserotonin. *J. Labelled Compd. Radiopharm.* 28 (3): 311–320.
479. Ikemoto, M., Sasaki, M., Haradahira, T. et al. (1999). Synthesis of L-[β -¹¹C]amino acids using immobilized enzymes. *Appl. Radiat. Isot.* 50 (4): 715–721.
480. Bjurling, P., Antoni, G., Malmborg, P. et al. (1991). Multi-enzymatic syntheses of L-tyrosine and L-DOPA. ¹¹C labeling in two positions. *Acta Radiol. Suppl.* 376: 107–108.
481. Bjurling, P., Antoni, G., Watanabe, Y., and Langstrom, B. (1990). Enzymatic synthesis of carboxy-¹¹C-labelled L-tyrosine, L-DOPA, L-tryptophan and 5-hydroxy-L-tryptophan. *Acta Chamaica Scand.* 44: 178–182.
482. Harada, N., Nishiyama, S., Sato, K., and Tsukada, H. (2000). Development of an automated synthesis apparatus for L-[3-¹¹C] labeled aromatic amino acids. *Appl. Radiat. Isot.* 52 (4): 845–850.
483. Carlson, E.D., Gan, R., Hodgman, C.E., and Jewett, M.C. (2012). Cell-free protein synthesis: applications come of age. *Biotechnol. Adv.* Elsevier: 1185–1194.
484. Matsuda, T., Furumoto, S., Higuchi, K. et al. (2012). Rapid biochemical synthesis of ¹¹C-labeled single chain variable fragment antibody for immuno-PET by cell-free protein synthesis. *Bioorg. Med. Chem.* 20 (22): 6579–6582.
485. Harada, R., Furumoto, S., Yoshikawa, T. et al. (2012). Synthesis of [¹¹C]interleukin 8 using a cell-free translation system and L-[¹¹C]methionine. *Nucl. Med. Biol.* 39 (1): 155–160.
486. Gueguen, P., Morgat, J.-L., Maziere, M. et al. (1982). Enzymatic synthesis of ¹¹C-labelled S-adenosylmethionine. *J. Labelled Compd. Radiopharm.* 19 (2): 157–170.
487. Tremblay, S., Ouellet, R., Bénard, F., and Cunnane, S.C. (2008). Automated synthesis of ¹¹C- β -hydroxybutyrate by enzymatic conversion of ¹¹C-acetoacetate using β -hydroxybutyrate dehydrogenase. *J. Labelled Compd. Radiopharm.* 51 (5): 242–245.
488. Garcia-Arguello, S.F., Fortt, R., Steel, C.J. et al. (2013). Radiosynthesis of the D2/3 agonist [3-¹¹C]-(+)-PHNO using [¹¹C]iodomethane *Appl. Radiat. Isot* **73**: 79–83.-

Chapter 8

Fluorine-18 Radiochemistry

Allen F. Brooks

*Department of Radiology, University of Michigan, Ann Arbor,
MI, 48109, USA*

Katarina J. Makaravage

*Department of Chemistry, University of Michigan, Ann Arbor,
MI, 48109, USA*

Jay Wright

*Department of Radiology, University of Michigan, Ann Arbor,
MI, 48109, USA*

Melanie S. Sanford

*Department of Chemistry, University of Michigan, Ann Arbor,
MI, 48109, USA*

Peter J. H. Scott

*Department of Radiology, University of Michigan, Ann Arbor,
MI, 48109, USA*

8.1 INTRODUCTION

Between the publication of the first edition of the *Handbook of Radiopharmaceuticals* and this new edition, interest in fluorine-18, its applications, and utilization have continued to grow. This is reflected in the increasing number of publications and patents containing fluorine-18 as a key feature of the work (Figure 8.1). Cyclotron produced fluorine-18

Handbook of Radiopharmaceuticals: Methodology and Applications, Second Edition.

Edited by Michael R. Kilbourn and Peter J.H. Scott.

© 2021 John Wiley & Sons Ltd. Published 2021 by John Wiley & Sons Ltd.

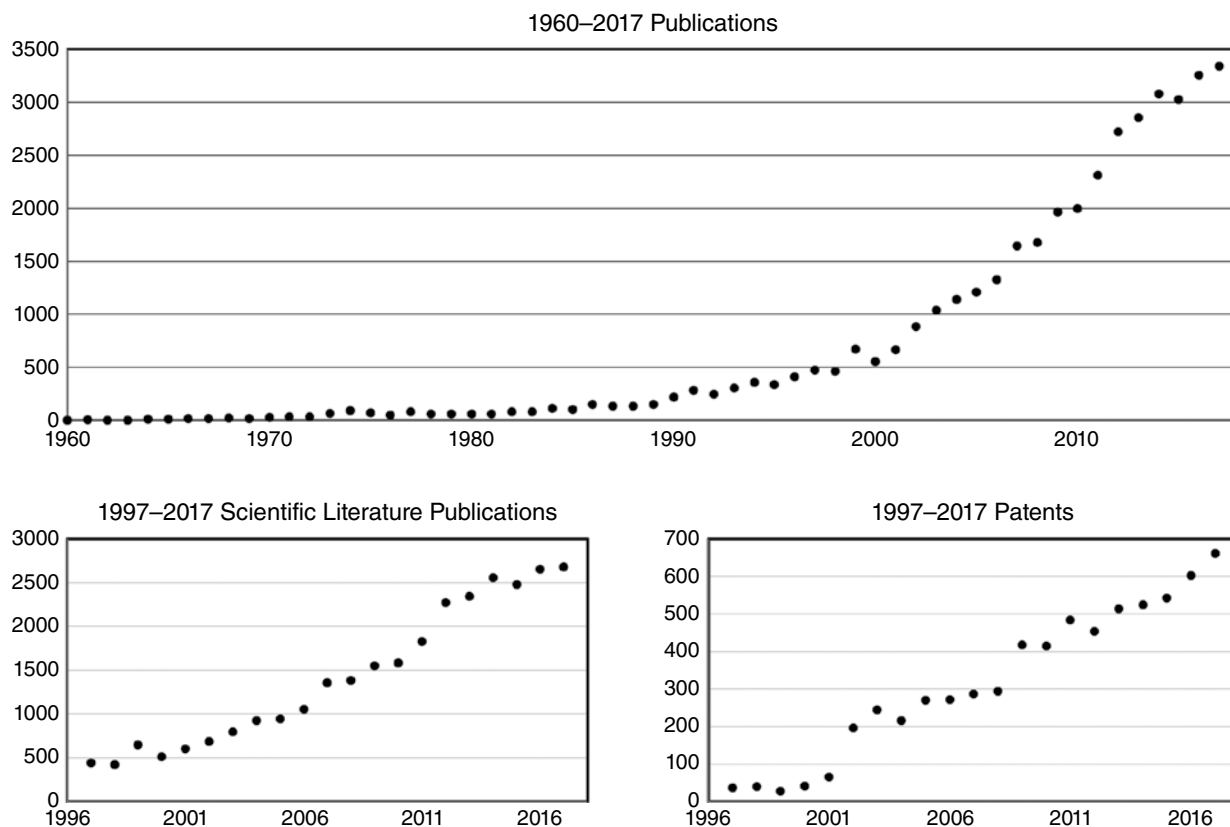


Figure 8.1 Fluorine-18 scientific and patent literature. Source: Data from Scopus.

is readily available primarily from commercial nuclear pharmacies (which require it for [^{18}F]fluorodeoxyglucose ([^{18}F]FDG) production) and academic medical research centers, which has been a factor in this growth as more sites and researchers can start programs with smaller investments in infrastructure. Alongside this increased interest, the trend toward the utilization of nucleophilic [^{18}F]F $^{-}$ sources such as [^{18}F]KF, over [^{18}F]F $^{+}$ sources like [^{18}F]F $_2$, has continued. This is due to the amount of high-molar-activity [^{18}F]fluoride that can be conveniently produced in easy-to-handle aqueous solutions. For example, the bulk of new methodology research and positron emission tomography (PET) tracer development with fluorine-18 has utilized small medical cyclotrons to produce [^{18}F]fluoride ([^{18}F]F $^{-}$) via proton irradiation of [^{18}O]H $_2$ O according to the $^{18}\text{O}(\text{p},\text{n})^{18}\text{F}$ nuclear reaction. New fluorine-18 radiochemistry has been extensively reviewed in recent years [1–20], and this chapter will focus on highlighting key new methods utilizing [^{18}F]F $^{-}$ as a reagent for the production of fluorine-18 PET imaging agents.

At the time of the previous edition of the *Handbook*, the two main approaches to radiolabeling with [^{18}F]fluoride were nucleophilic substitution reactions ($\text{S}_{\text{N}}2$) of aliphatic compounds and nucleophilic aromatic substitution ($\text{S}_{\text{N}}\text{Ar}$) of aromatic compounds. For challenging substrates (e.g. electron-rich arenes) or molecules previously labeled with a

carbon-11 methyl group, an alternative approach involving the use of prosthetic groups such as the [^{18}F]fluoroethyl tosylate group [21] or *N*-succinimidyl 4- ^{18}F fluorobenzoate [22, 23] were employed. These approaches are still used extensively in fluorine-18 radiochemistry, but they only allow for the labeling of a limited set of potential molecules of interest for study by PET imaging.

In the past 15 years, extensive work has been done to improve the chemical space that can be labeled with fluorine-18. A significant challenge is improving the reactivity of [^{18}F]KF to a level comparable to reagents such as anhydrous HF and F^+ sources. To facilitate this, many productive collaborations between radiochemists and organometallic chemists have developed, and the results have disrupted many of the established notions, dogma, and limitations of fluorine-18 chemistry previously accepted.

8.1.1 Elutions and Solvents

A standard procedure is often undertaken to process [^{18}F]fluoride obtained as a solution in [^{18}O]H₂O from a cyclotron. Typically, [^{18}F]fluoride is trapped on a quaternary methylammonium (**QMA**) ion-exchange resin that has been preconditioned with carbonate or bicarbonate, allowing recovery of [^{18}O]H₂O. The [^{18}F]fluoride is then eluted with a basic solution such as aqueous K₂CO₃ to generate [^{18}F]KF. The [^{18}F]KF is then combined with acetonitrile containing Kryptofix 222 (K_{2.2.2}), a phase-transfer reagent, and the resulting [^{18}F]KF·K_{2.2.2} reagent is azeotropically dried in order to allow for solubility and reactivity in the radiofluorination step to follow. While this approach is general, a pitfall is that S_N2 reactions with fluoride are prone to undesirable competing elimination reactions.

Furthermore, the use of additional base in the preconditioning of the QMA and elution of fluoride can exacerbate this problem (e.g. accelerate deleterious deprotection processes). Moreover, carbonate and bicarbonate are not compatible with many catalysts or reagents, as they form unproductive mixtures. For example, copper species can form unreactive copper carbonates, inhibiting the desired radiofluorination process and decreasing overall radiochemical yield (**RCY**). In addition, K_{2.2.2} as a nitrogen base can also degrade potential precursors and poison reaction mixtures. As the field has developed new methodologies over the past 15 years, PET radiochemists have given careful thought to how [^{18}F]fluoride is prepared as a reagent for radiolabeling in order to overcome these challenges.

The preparation of new [^{18}F]fluoride sources to improve reactivity is not a new avenue of research. Reports dating back to the 1990s overcame limitations associated with the use of carbonate and its ability to degrade precursors, reagents, and/or products through the use of other anions (e.g. triflate, oxalate) to condition and elute QMA cartridges. Recent work on elution scope has demonstrated that basic elution can be achieved provided that a sufficient amount of solvent anion is generated. This can simply be achieved using bases with conjugate pKa constants high enough to form ions of the solvent (e.g. hydroxide in the case of H₂O). When utilized in conjunction with preconditioning using less basic salts like KOTf, this results in [^{18}F]fluoride reagents that can be tolerated in a broader set of reaction conditions, such as copper-mediated radiofluorination (**CMRF**) [24]. For example, the Scott group was recently interested in preparing [^{18}F]AgF

to enable access to new CH activation methods for radiofluorination [25]. Several reports of [^{18}F]AgF were present in the literature prior to this [26–30] but required specialized equipment and conditions. Instead, by preconditioning the QMA with an anion that forms a soluble silver salt, such as triflate, acetate, or nitrate (using the corresponding potassium or sodium salt), [^{18}F]AgF can be conveniently produced [31]. In this example, changing the preconditioning agent enabled the production of a reactive silver salt that would otherwise have formed an unproductive carbonate/bicarbonate under standard elution conditions. In analogy, solvent protonation can also enable the production of different ions and ^{18}F fluoride sources. This was demonstrated in a recent report describing the production of [^{18}F]HF, in which elution with methanesulfonic acid or trifluoroacetic acid led to the protonation of H_2O , ethanol, or *N,N*-Dimethylformamide (**DMF**) to produce [^{18}F]HF [32]. The ability to prepare different forms of [^{18}F]fluoride offers scope to develop further radiofluorination methods in the future.

Choice of solvent is also essential in the design of efficient radiofluorination processes. Until recently, it has been accepted that the use of protic solvents would inhibit any nucleophilic radiofluorination since fluoride forms hydrogen bonds with them. This likely originates from nucleophilic ^{19}F fluorination chemistry, which in many cases has been demonstrated to occur with increased efficiency in the absence of hydrogen-bond donors (such as adventitious moisture) [33–37].

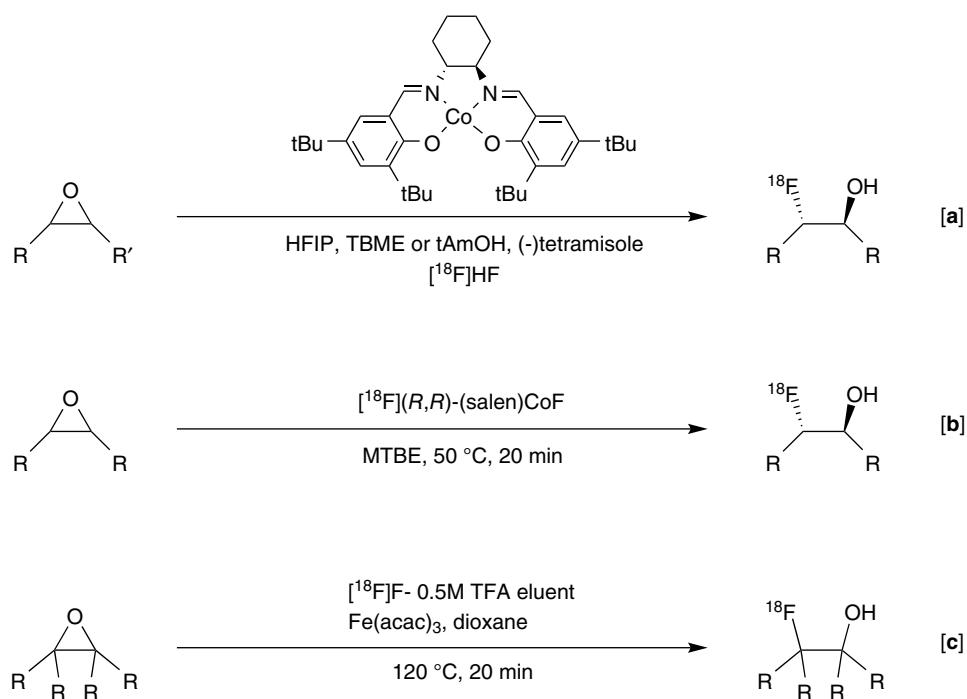
However, Stewart and co-workers described how the azeotropic drying of [^{18}F]fluoride can be conducted with ethanol instead of acetonitrile without reduction in subsequent reaction yield, offering a greener and cheaper alternative for fluorine-18 processing [38]. In this report, the authors demonstrated that several precursors, including the mannose triflate precursor of [^{18}F]FDG, could be labeled in a solvent composed of ethanol and H_2O (85 : 15). The use of ethanol over acetonitrile in the azeotropic drying step is of particular interest as it replaces a class II solvent, simplifying quality control analysis provided none are utilized in the production method (e.g. during the reaction, high-performance liquid chromatography (**HPLC**) purification, and/or solid-phase extraction), as was later disclosed by the Scott laboratory [39]. Furthermore, Sergeev and co-workers demonstrated that highly aqueous solvent mixtures could be utilized for the radiofluorination of sulfonates in the presence of titanium catalysts. The sulfonate was postulated to coordinate to the surface of TiO_2 particles, which could also desolvate the [^{18}F]fluoride and thus facilitate both $\text{S}_{\text{N}}2$ and $\text{S}_{\text{N}}\text{Ar}$ reactions [40]. The use of sulfonate precursor molecules for $\text{S}_{\text{N}}2$ was further explored in protic solvents by the Chi laboratory, where reaction was achieved through the formation of ionic liquids from protic solvents [41]. In their early work, 1-butyl-3-methylimidazolium triflate was utilized, and [^{18}F]fluoride was prepared with cesium carbonate elution. Notably, the $\text{S}_{\text{N}}2$ radiofluorination of mesylates in this medium did not require the removal of water prior to the reaction. Later, the same group also reported that if tert-butyl alcohol was utilized as a solvent and cesium carbonate was used for elution, no additive was required to convert the starting sulfonates to the corresponding [^{18}F]fluorinated products [42]. In spite of the preference for aprotic media in a majority of radiofluorination methods, protic solvents can also be utilized in fluorine-18 chemistry, providing the precursor and reaction conditions are judiciously selected [43].

8.2 ALIPHATIC FLUORINATION WITH FLUORINE-18

8.2.1 Metal-Catalyzed Fluorination Reactions

8.2.1.1 Fluorohydrins

The production of fluorohydrins is typically accomplished through a substitution reaction with a sulfonate or related leaving group. The alcohol precursor can be protected to mitigate the effect of the proton donor on fluoride reactivity. In several instances, a cyclic sulfonate is utilized for the installation of fluoride, and the resulting acyclic sulfonate is cleaved, resulting in a mixture of isomeric fluorohydrin products. Alternatively, a one-step radiofluorination may be achieved using an epoxide precursor, and this has been performed in reactions using HF as the fluorinating reagent [44–50]. In an improvement of this approach, methods using $[^{18}\text{F}]\text{Co}(\text{salen})$ fluorides have been developed separately by both the Zhuravlev (Scheme 8.1a) and Doyle (Scheme 8.1b) labs [51, 52]. In more recent work, the Scott and Sanford laboratories developed a method to prepare a putative $[^{18}\text{F}]\text{FeF}$ species from $[^{18}\text{F}]\text{HF}$ to open sterically hindered epoxides (Scheme 8.1c) [32].



Scheme 8.1 Radiofluorination of epoxides for the synthesis of $[^{18}\text{F}]$ fluorohydrins.

This method employed iron(III) acetylacetonate as a promoter and typically displayed regioselectivity for the more substituted epoxide carbon center (Scheme 8.1c). Notably, this selectivity is complementary to that offered by the Co(salen) catalyst systems.

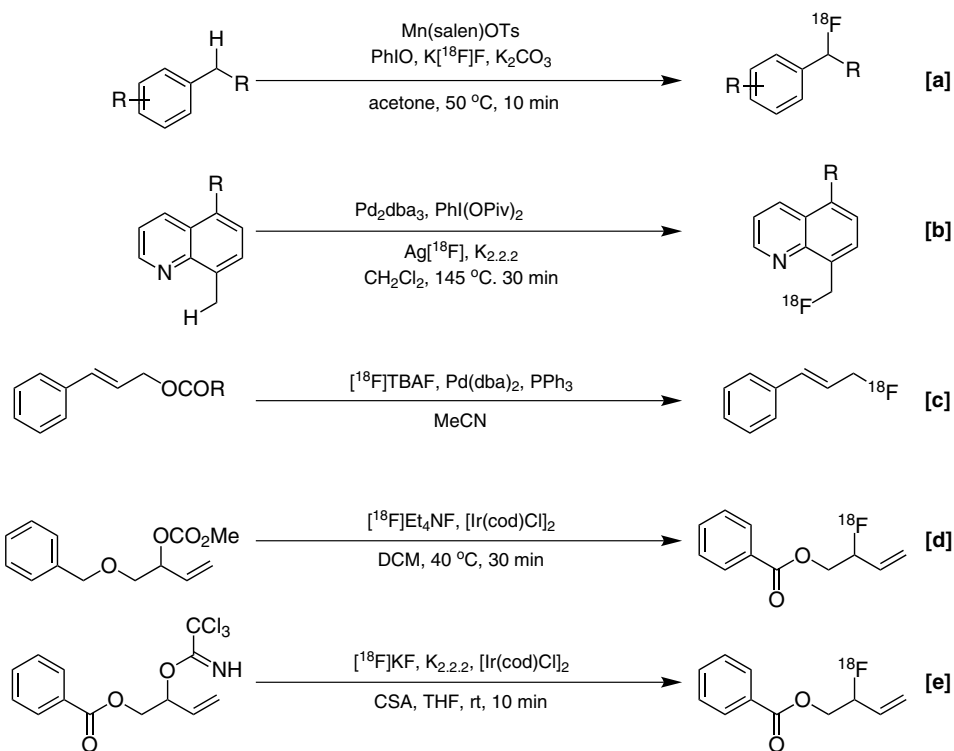
8.2.1.2 Benzylic and Allylic Fluorination

Novel methods for benzylic and allylic fluorinations have been developed and offer new opportunities to quickly screen scaffolds for suitability as drug molecules or imaging agents by PET, and manganese complexes have been successful in promoting this transformation [53, 54]. For example, in a collaboration between the Hooker and Groves labs, it was shown that benzylic C–H bonds can undergo radiofluorination in the presence of Mn(salen)OTs, [¹⁸F]KF, and an oxidant (Scheme 8.2a) [53]. The conditions performed well on a range of molecules, including those based on known small-molecule drugs. While the benzylic position offers greater activity for C–H activation and fluorination, the resulting benzyl fluorides can exhibit poor metabolic stability in some instances. Despite this drawback, this approach permits facile scaffold screening for further development and can facilitate the expedient production of fluorine-18 PET imaging agents. Furthermore, the recent development of Ag[¹⁸F]F production has led to the development of a C–H activation of methyl quinolines to produce benzylic [¹⁸F]fluorides (Scheme 8.2b) [31]. While this method is limited to quinolines, it demonstrates that benzylic methyl and methylene C–H bonds can be radiolabeled directly with Pd. Furthermore, this method illustrates the potential for further C–H radiofluorination processes to be developed.

Metal-catalyzed methods have also been developed to produce allylic fluorides by two separate laboratories [55–58]. In seminal work from the Gouverneur lab, a palladium-catalyzed method was developed that employed an allylic methyl carbonate group, which facilitated driving the radiofluorination to completion. An example was provided in the manuscript for radiofluorination (Scheme 8.2c), and the authors later described an improved method using an iridium catalyst. Utilizing allylic methyl carbonates alongside tetraethylammonium [¹⁸F]fluoride as the fluoride source with an Ir precatalyst, the desired radiofluorination was observed on three substrates (Scheme 8.2d). The use of iridium for allylic radiofluorination has also been investigated by the Nguyen group. In their method, an iridium catalyst and an allylic trichloroacetimidate precursor were utilized (Scheme 8.2e). The fluorine-19 method performed better with 3HF-TEA, which is not currently available as the corresponding fluorine-18 isotopolog. Later, the Nguyen laboratory further developed this method and described a general radiofluorination of allylic trichloroacetimidates using [¹⁸F]KF [59].

These methods provide access to benzylic and allylic [¹⁸F]fluorides for research use, initial development, and evaluation, but have several drawbacks. For example, some incorporate toxic class II solvents and rare-earth heavy metal catalysts. Transition metals like palladium and iridium are only allowed in a parenteral administration at a quantity not exceeding 10 μg day⁻¹, introducing difficulty for routine production and purification of PET imaging agents. Therefore, the development of methods with a metal that carries

a higher release amount, such as copper ($340 \mu\text{g day}^{-1}$), and greener solvents would be preferred.



Scheme 8.2 Metal-catalyzed methods for the production of benzylic $^{[18\text{F}]}$ fluorides and allylic $^{[18\text{F}]}$ fluorides.

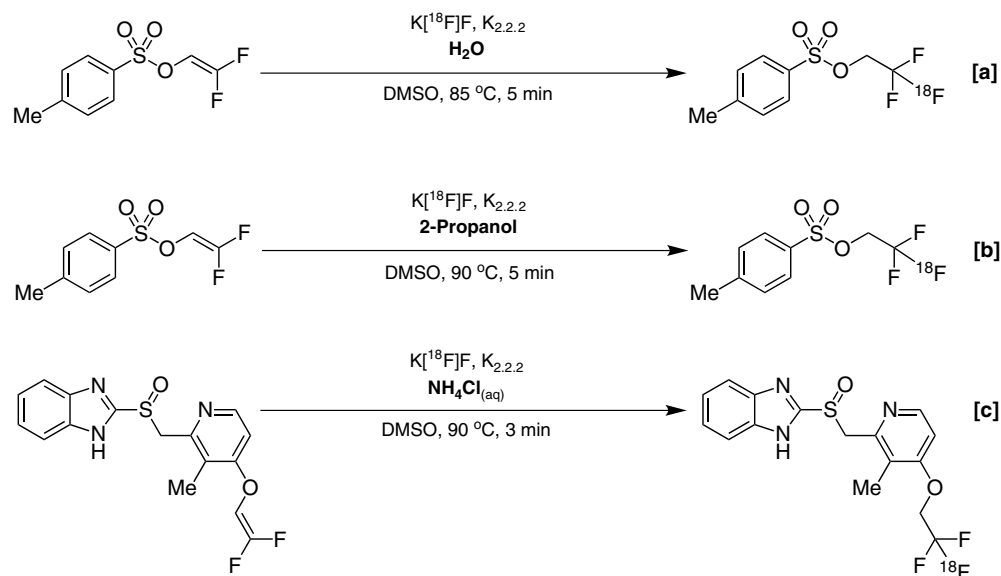
8.3 CF₃ CHEMISTRY

The trifluoromethyl group is an attractive moiety in drug design owing to its capability to improve drug pharmacokinetic properties, such as metabolic stability. Reflecting this, the development of methods to install the trifluoromethyl group has been the focus of many laboratories. Notably, the trifluoromethyl group represents a way to radiolabel many drug and drug-like scaffolds with the added benefit of improved stability when compared to terminal alkyl fluorides, which are prone to elimination. In previous decades, a small number of trifluoromethyl groups have been generated by preparing a difluoro-bromo/iodo methyl group and displacing the higher halide with either $\text{K}^{[18\text{F}]\text{F}}$ or $\text{H}^{[18\text{F}]\text{F}}$ [60–63]. These methods are difficult to implement on a variety of scaffolds owing to the challenge of forming the precursor and have seen limited use as a result. In the last 15 years, efforts have been undertaken to generate aliphatic trifluoromethyl groups, [64–66] including trifluoromethyl groups attached to a heteroatom (oxygen, sulfur or selenium) [63, 67–70], as well as aryl trifluoromethyl groups [54, 71–75].

8.3.1 Aliphatic [¹⁸F]Trifluoromethyl Methodology

An improved strategy for the generation of aliphatic trifluoromethyl groups was reported in 2011 in work from Riss and Aigbirhio [64]. In this method, a difluoroalkene was generated, typically by treatment of a trifluoromethylated substrate bearing an α -C-H bond with *n*-butyllithium to eliminate HF. The resulting difluoroalkene can be converted to the desired [¹⁸F]trifluoromethyl group by treatment with [¹⁸F]KF·K_{2.2.2} in dimethyl sulfoxide (**DMSO**) with a small amount of H₂O in the reaction mixture to provide the proton required to complete the mechanism (Scheme 8.3a). The reaction, unfortunately, also has a competing addition-elimination process that results in the formation of the [¹⁸F]difluoroalkene (i.e. the radiolabeled precursor). The scope of the reaction was limited to activated difluoroalkenes, but one of the best substrates, 2,2-difluorovinyl-4-tosylate, is also a potential prosthetic group since it can undergo a substitution reaction with a nucleophile following radiofluorination. The competing side reaction was a problem that the authors addressed in a follow-up report [30]. In the improved labeling method for this reaction (Scheme 8.3b), alternative quenching reagents to water were investigated to improve the ratio of [¹⁸F]trifluoro vs. [¹⁸F]difluoroalkene. The use of organic proton donors like 2-propanol was superior to H₂O, and improved yields and product ratios were observed (up to 10 : 1 trifluoromethyl : difluoroalkene). Later, this approach was adapted to the synthesis of [¹⁸F]N-methyl-lansoprazole and [¹⁸F]lansoprazole by the Scott laboratory [76]. In this work, lansoprazole, a Food and Drug Administration (**FDA**) approved pharmaceutical, was treated with *n*-butyllithium to prepare a difluoroalkene precursor.

Scheme 8.3 Aliphatic [¹⁸F]trifluoromethyl formation methods.

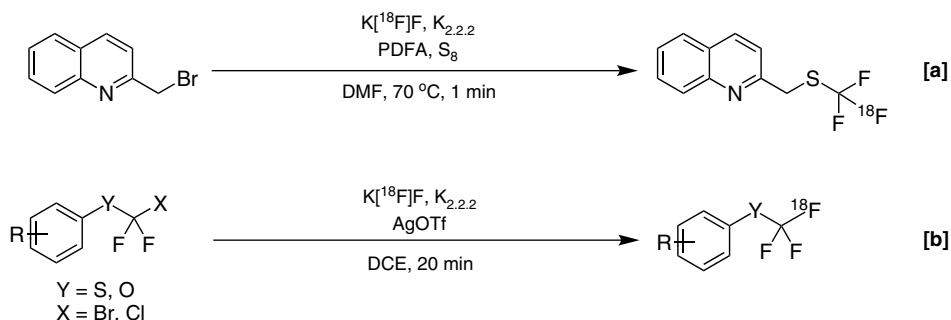


Their investigations showed that a saturated solution of ammonium chloride as a proton source offered the highest yields of labeled [¹⁸F]lansoprazole or

[¹⁸F]N-methyl-lansoprazole over the corresponding difluoroalkenes (Scheme 8.3c). Of the trifluoromethyl radiofluorinations developed over the last 15 years, this method offers the highest molar activity. [¹⁸F]N-methyl-lansoprazole has been advanced to clinical study with this synthesis, showcasing the suitability of this approach for clinical translation to PET imaging agents [77].

8.3.2 [¹⁸F]Trifluoromethyl Groups Attached to a Heteroatom (Sulfur and Oxygen)

Several labs have also investigated novel techniques to generate [¹⁸F]trifluoromethyl groups attached to heteroatoms. In a method reported by Liang and co-workers, a benzylic or aliphatic halide is treated with a combination of S₈, 2,2-Difluoro-2-(triphenylphosphonio)difluoroacetate (PDFA), and [¹⁸F]KF·K_{2.2.2} to generate the radiolabeled product through a difluorocarbene intermediate (Scheme 8.4a) [68]. In studies from the Gouverneur lab, it was shown that silver can also be used to mediate halide abstraction for the synthesis of [¹⁸F]-OCF₃ and [¹⁸F]-SCF₃ containing arenes (Scheme 8.4b) [78]. To date, these methods carry limited utility in PET imaging as they offer low molar activity. However, these types of products do have relevance in drug discovery, as there are biologically active compounds that contain a -SCF₃ or -OCF₃ moiety, such as the approved drug Cefazaflur.



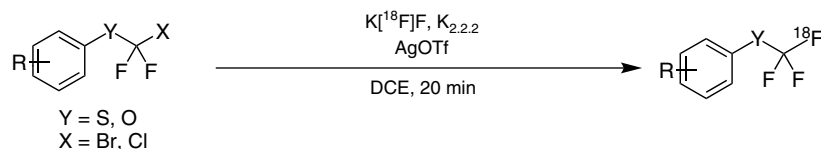
Scheme 8.4 [¹⁸F] trifluoromethyl groups attached to a heteroatom.

8.3.3 Aromatic [¹⁸F]Trifluoromethyl Methodology

Several laboratories have successfully developed improved methods for the production of aromatic [¹⁸F]trifluoromethyl compounds. Unfortunately, these methods to date have suffered from low molar activity, which limits their utility in PET imaging as they are not suitable methods to produce radioligands. However, these approaches may be utilized in the generation of radiotracers, substrates, and trapped metabolite PET imaging agents within applications where molar activity does not limit the ability to generate imaging data [79]. These newly developed approaches to form aromatic trifluoromethyl groups in general start by forming [¹⁸F]CuCF₃ from trifluoromethane, which can subsequently be

treated with aryl iodides or aryl boronic acids. Based on previous studies on the trifluoromethylation of aldehydes and ketones, Vugts and co-workers developed a method for forming $[^{18}\text{F}]\text{CHF}_3$, which subsequently enabled the $[^{18}\text{F}]$ trifluoromethylation of arenes (Scheme 8.5) [73, 74]. While this method currently offers the highest molar activity for this transformation, it is still 3–5 times lower than typically achieved by other methods.

Scheme 8.5 Aromatic $[^{18}\text{F}]$ trifluoromethylation methodology.

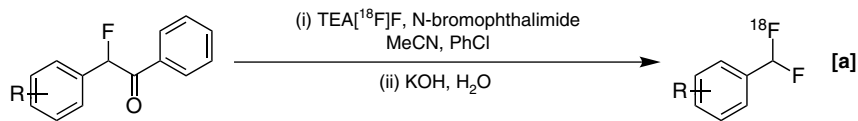


8.4 OTHER ALIPHATIC C–F BOND FORMATION METHODS

Several other methodologies to generate aliphatic $[^{18}\text{F}]$ fluorides of interest have been developed since the last edition of the *Handbook*. Efforts have been undertaken in a collaboration between the Ritter and Vasdev-Liang groups to generate $[^{18}\text{F}]$ difluoromethyl groups using aryl-pseudo halides [80]. In this method, a 2-fluoro-1,2-diphenylethan-1-one is treated with tetraethylammonium $[^{18}\text{F}]$ fluoride generated using tetraethylammonium bicarbonate for QMA cartridge elution, facilitating a halogen exchange.

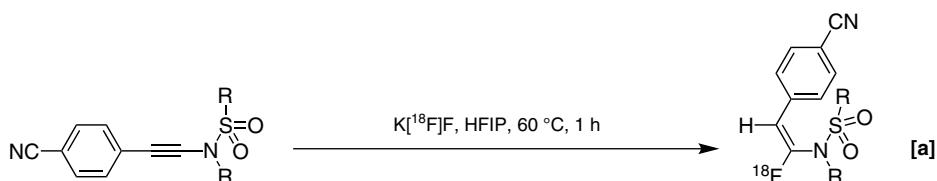
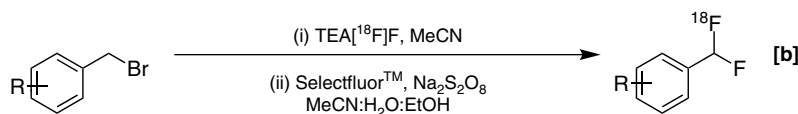
The reaction mixture is subsequently treated with N-bromophthalimide followed by aqueous potassium hydroxide to produce the desired difluoromethyl arene (Scheme 8.6a). This reaction suffers from poor molar activity as each molecule of precursor necessarily contains a fluorine-19 atom that becomes a part of the reaction mechanism to give the difluoro product. Liang followed this work with an alternate method to produce difluoromethylated arenes from benzylic bromides [81]. In this method, benzylic bromides are treated with tetraethylammonium $[^{18}\text{F}]$ fluoride, followed by the electrophilic fluoride source Selectfluor™ in the presence of $\text{Na}_2\text{S}_2\text{O}_8$ to afford the desired difluoromethylated arene (Scheme 8.6b). This approach afforded a higher molar activity than the earlier method but still three to fivefold lower than standard techniques. Two other late-stage labeling methodologies have also been developed. Zeng and co-workers developed a (radio)fluoroclick reaction to produce α -fluoroenamides from ynamides with $[^{18}\text{F}]\text{KF}$ with hexafluoroisopropanol (**HFIP**) as a solvent [82]. The reaction is promoted through a hydrogen-bonding cluster between the solvent and $[^{18}\text{F}]$ fluoride in the reaction mixture. Five substrates with a range of functional groups were amenable to the reaction conditions. This included an ynamide, which was radiofluorinated chemoselectively, leaving the azide group intact (Scheme 8.7a). Therefore, this chemistry may facilitate the late-stage installation of labeled prosthetic groups, which can be conveniently installed with an azide click reaction. The five products were obtained in good RCY (76–97%, decay corrected), although a long reaction time of one hour was utilized. In addition, Zeng and co-workers showed that three of the radiolabeled products were stable in serum for two

hours. Further work is required to demonstrate the use of this moiety for PET imaging *in vivo*. In particular, the safety and toxicity of fluoroenamides is not well established since they are not commonly featured in pharmaceuticals.



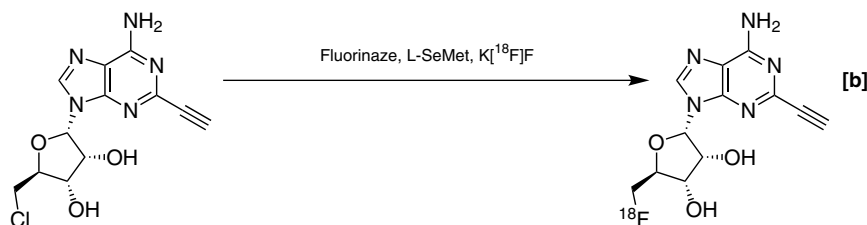
Scheme 8.6

Methods for the preparation of [¹⁸F]difluoro-methylarenes.



Scheme 8.7

Further new radiofluorination methods.



The other method utilizes fluorinase, which is the only known and well-characterized enzyme to use fluoride for substrate fluorination. This enzyme selectively converts S-adenosyl-L-methionine (**ADM**) to 5'-fluoro-5'-deoxyadenosine. Thompson and co-workers investigated the radiofluorination of other substrates with the aim of synthesizing prosthetic groups for peptides [83]. The authors replaced the methionine group of ADM with a chloride for an enzymatic transhalogenation in buffered water (Scheme 8.7b).

The incorporation of an acetylene at the C-2 position was also tolerated, enabling a subsequent click reaction to incorporate arginine-glycine-aspartic acid peptide for the production of a PET radioligand. The incorporation of fluorine-18 in buffered water is a noteworthy development as the labeling of peptides is frequently hampered by incompatible organic solvents. Therefore, this method carries the potential to conveniently radiolabel peptides and biomolecules, which would otherwise be challenging using other strategies.

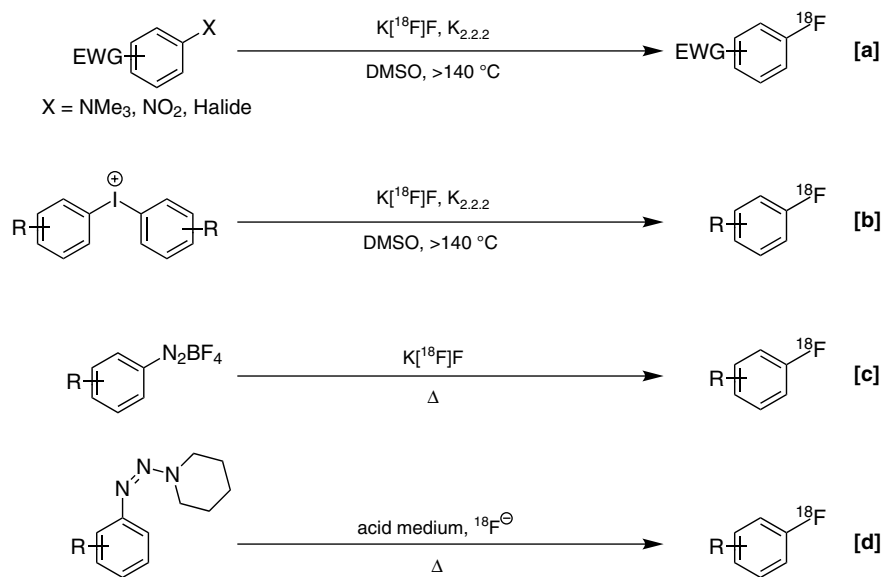
8.5 AROMATIC FLUORINATION WITH FLUORINE-18

8.5.1 Introduction

Aryl fluorides are prevalent in pharmaceuticals [84–88], and their ^{18}F isotopologs are important for PET imaging applications. As such, methods for synthesizing ^{18}F arenes are of great interest in the PET community [8, 16, 89, 90]. At the time of the previous edition of the *Handbook of Radiopharmaceuticals*, there were limited methodologies to incorporate fluorine-18 into an aromatic ring [91]. The most commonly used methods were electrophilic aromatic substitution (**SEAr**) and nucleophilic aromatic substitution (**SNAr**). An extensive discussion of these methods is beyond the scope of this chapter, although comprehensive reviews are available [1–7, 9, 13–20]. In general, the last decade has seen a shift away from traditional $\text{S}_{\text{E}}\text{Ar}$, because the carrier-added method of $^{18}\text{F}\text{F}_2$ production generally has limited site- and chemoselectivity, and the final products inherently have low molar activity due to the required carrier $^{19}\text{F}\text{F}_2$ gas. Furthermore, the requirement for carrier $^{19}\text{F}\text{F}_2$ gas requires specialized equipment that is not widely available. The preference is to use nucleophilic ^{18}F fluoride, which is readily available from small medical cyclotrons and possesses greater molar activity.

In the case of $\text{S}_{\text{N}}\text{Ar}$, radiofluorination of appropriately activated aromatic rings bearing standard leaving groups such as nitro, halo, and trialkylammonium groups remains a commonly used strategy for preparing ^{18}F arenes (Scheme 8.8a). For example, a microfluidic approach for radiofluorination of nitroarene precursors was recently described [92]. Radiofluorination of diaryliodonium salts is a newer alternative to $\text{S}_{\text{N}}\text{Ar}$ that was introduced in the 1990s and continues to be utilized (Scheme 8.8b) [93, 94].

Scheme 8.8
Nucleophilic
syntheses of
 ^{18}F arenes.



Diaryliodonium salts are often symmetrical, but there can be selectivity limitations in unsymmetrical substrates (*vide infra*) [95]. Other radiofluorination methodologies that are less commonly used due to their harsh conditions and limited scope are the Balz-Schiemann decomposition and the Wallach reaction (Scheme 8.8c and d). However, all of the existing methodologies have certain limitations, including forcing conditions and restricted substrate scopes, often stemming from challenging precursor syntheses and an electronic mismatch between nucleophilic [^{18}F]fluoride and the aromatic ring. To overcome these challenges, the last 10 years have seen a renaissance in fluorine-18 radiochemistry research and an introduction of many new methods that are compatible with a wide range of aromatic substrates. This section will highlight the new methodologies developed since c. 2000, as well as some of their applications.

8.5.2 Updated Methodologies

8.5.2.1 Electrophilic Radiofluorination

Electrophilic radiofluorination with [^{18}F]F₂ is not commonly used for the reasons outlined previously and suffers from low molar activity products and harsh reaction conditions. However, there are groups who currently research electrophilic radiofluorination and continue to explore improvements. Efforts to develop higher-molar-activity electrophilic methods, such as the use of a fluoromethane MeF electrical discharge chamber, have occurred in recent years with some success [96, 97]. However, these approaches are generally not technically routine or trivial and have consequently not seen widespread usage. To overcome harsh fluorinating conditions, a number of reports have investigated converting reactive [^{18}F]F₂ into new F⁺ reagents, such as [^{18}F]Selectfluor bis(triflate) and [^{18}F]-*N*-fluorobenzenesulfonimide (**NFSI**) (Figure 8.2) [98–100]. These reagents are milder and easier to handle in production laboratories but, again, suffer from the requirement of an [^{18}F]F₂ source in their production.

8.5.2.2 New Approaches to S_NAr

Since 2000, methods have been developed that have broadened the scope of nucleophilic aromatic substitution radiofluorination methods. For example, the mechanism of aromatic substitution of aromatic trimethylammonium salts has been studied, and it has been shown that the formation of [^{18}F]fluoromethane competes with the production of the radiofluorinated arene [101]. Furthermore, halogen exchange of arylfluorides

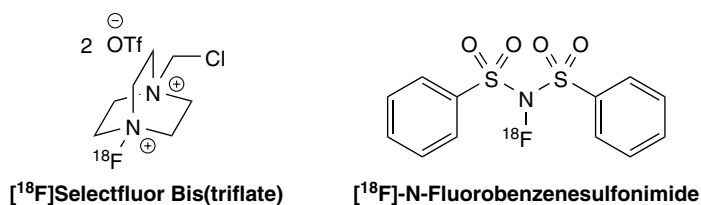
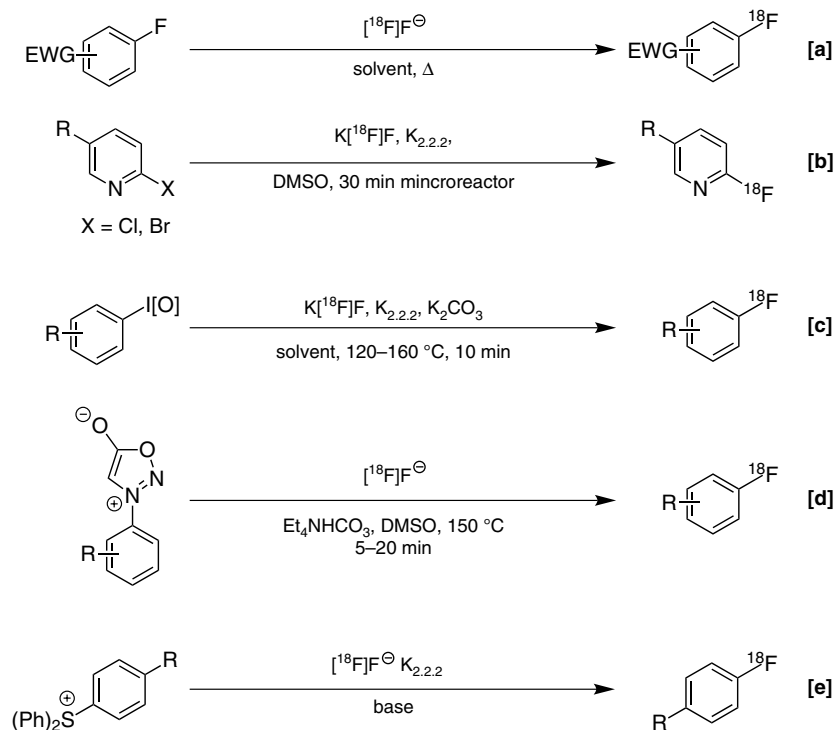


Figure 8.2 Electrophilic radiofluorination reagents.

with $[^{18}\text{F}]$ fluoride continues to be utilized [102, 103], although this is rarer due to molar activity limitations stemming from the inability to separate $[^{19}\text{F}]$ precursor from $[^{18}\text{F}]$ product (Scheme 8.9a). Improving the $\text{S}_{\text{N}}\text{Ar}$ of precursors with halide leaving groups has also been investigated using pyridine derivatives (Scheme 8.9b) [104] and oxidative strategies (Scheme 8.9c) [105]. Radiofluorination of anilines via conversion to *N*-arylsydnone was also recently reported, and density functional theory (**DFT**) calculations predict that this operates via a typical addition-elimination $\text{S}_{\text{N}}\text{Ar}$ mechanism (Scheme 8.9d) [106]. Triaryl-sulfonium salts can also be used to achieve radiofluorination via aromatic substitution (Scheme 8.9e) [107]. *p*-Electron-withdrawing groups provide the highest yields, while *m*-substituted and electron-rich substrates give trace products. Notably, this methodology has successfully been used to synthesize PET radiotracers [108, 109].

Scheme 8.9

Further nucleophilic syntheses of $[^{18}\text{F}]$ arenes.



Another approach to overcome the scope limitations of traditional $\text{S}_{\text{N}}\text{Ar}$ is to design prosthetic groups that can be radiolabeled by $\text{S}_{\text{N}}\text{Ar}$ and then attached to a larger molecule (Figure 8.3) [110–113]. While this allows biologically active molecules (e.g. peptides) to be radiolabeled, it requires multiple steps post- $[^{18}\text{F}]$ fluoride introduction, which can lead to low yields and reproducibility issues [22]. However, this method has been applied to the synthesis of many PET radiotracers and is routinely employed to introduce a $[^{18}\text{F}]$ fluorine into a molecule of interest [114, 115]. Methods for the synthesis of prosthetic groups are discussed later.

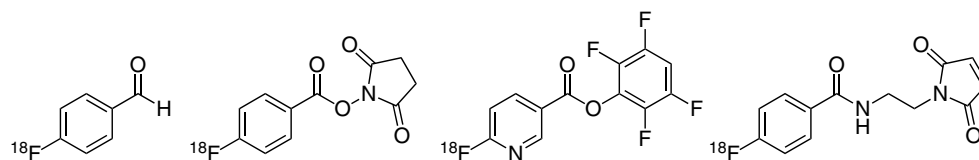
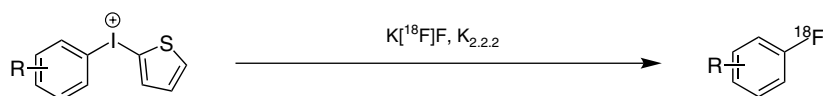


Figure 8.3 Examples of prosthetic groups prepared through S_NAr .

8.5.2.3 Aryliodonium Salts

Extending functional group tolerance to include precursors not amenable to S_NAr has been a focus of different research groups [116, 117]. To this end, diaryliodonium salts have been investigated heavily in the past 20 years, as these species can be employed for direct aromatic radiofluorination. Diaryliodonium salts are typically designed with an unreactive aryl auxiliary, and selectivity is generally observed for the most electron-deficient aryl substituent. However, regioselectivity issues can be encountered, and the auxiliary ring of electron-rich *meta*-substituted substrates can inadvertently fluorinate, decreasing the reaction efficiency [116, 118]. To overcome this, a method using (2-thienyl)aryliodonium salts has been reported (Scheme 8.10) [116]. In this study, electron-rich aryl moieties were radiofluorinated selectively when the corresponding diaryliodonium precursor contained an electron-rich 2-thienyl group, and this selectivity had previously been unattainable. However, the true reaction selectivity can be difficult to determine accurately due to the volatility of 2-fluorothiophene. In general, *o*- and *p*-substituted substrates can display good reactivity toward radiofluorination, while the functionalization of *meta*-substituted substrates is generally low yielding [119]. Electron-deficient substrates can be slow to radiofluorinate, although increased yields can be observed if a microreactor is used [118]. Issues of selectivity in unsymmetrical diaryliodonium salts are influenced by steric congestion around the iodine center, which has been termed the “*ortho*-effect” [119–123].



Scheme 8.10 [^{18}F] Fluorination of 2-thienyl iodonium salts.

Recently, a CMRF method was developed to overcome the electronic bias of diaryliodonium salts to favor the less-sterically congested product [124]. Unlike the metal-free iodonium methods, this procedure gave high conversions with electron-rich substrates. Diaryliodonium salts have had success in clinical applications to synthesize a number of PET radiotracers (Figure 8.4) including [^{18}F]fluorodopamine [125, 126], [^{18}F]F-DOPA [127], [^{18}F]4F-MHPG [128, 129], [^{18}F]UCB-H [130], [^{18}F]FIMX [131], an $\alpha\beta$ plaque imaging probe [132], and a novel potent MMP2/MMP9 inhibitor [133]. Furthermore, the radio-labeling of various synthons from diaryliodonium salts has been explored as a way to enhance the scope of structurally complex available PET radiotracers [134]. Despite these advantages, synthetic limitations such as precursor and reaction sensitivity to air/moisture and functional group tolerance can limit the application of diaryliodonium salts in

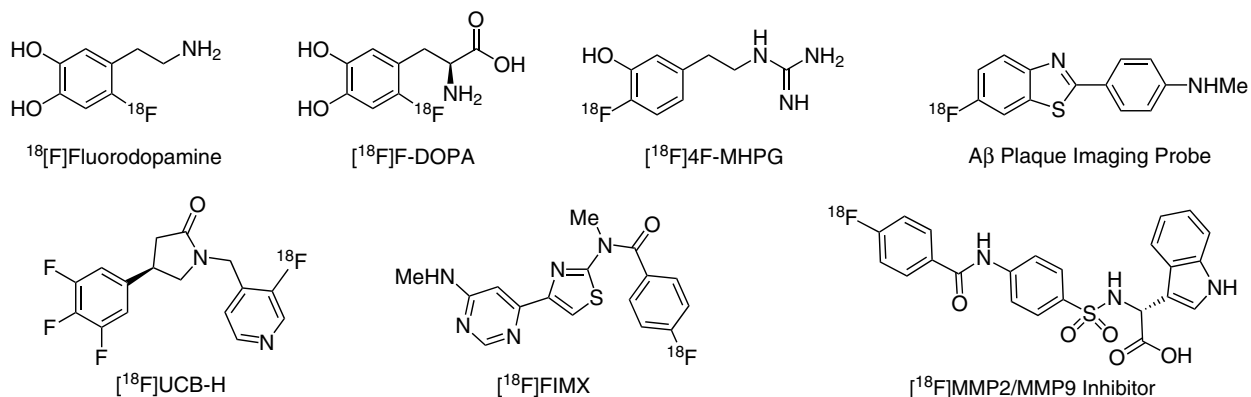


Figure 8.4 Radiotracers synthesized from diaryliodonium salts.

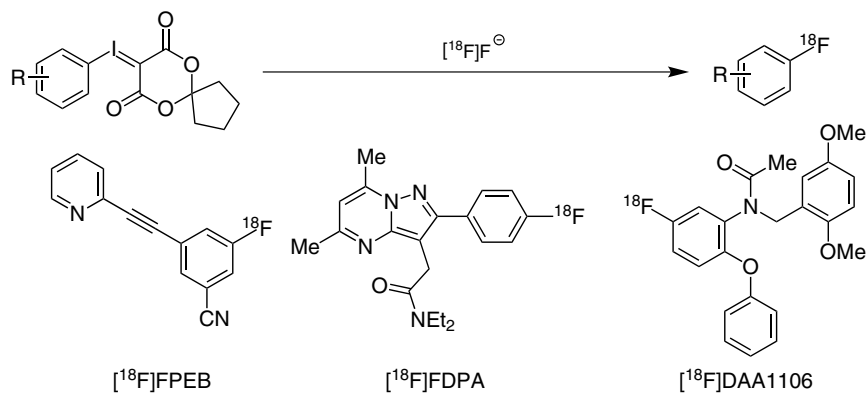
radiofluorination. In particular, diaryliodonium salts are known to be photosensitive [135] and can undergo side reactions that involve the formation of iodine radicals.

Most diaryliodonium salts are made from (diacetoxyiodo)arenes [136], and the direct radiolabeling of these intermediates with ^{18}F fluoride has been investigated to address precursor instability and broaden the scope of methodology available to the ^{18}F radiochemist [137].

Alternatively, iodonium salts can be prepared *in situ* prior to a radiofluorination to avoid handling issues [138]. Furthermore, some limitations of diaryliodonium salts were addressed by using iodonium salts with auxiliaries other than sacrificial arenes (Scheme 8.11) [81, 139]. For example, optimization studies by the Liang laboratory revealed that a five-membered spirocyclic iodonium ylide auxiliary can afford radiofluorinated arenes in excellent yields [140]. Additives such as organocatalysts to drive the radiofluorination have also been investigated [141], and spirocyclic iodonium ylides have been used to synthesize several PET radiotracers [139, 142] such as ^{18}F -3-fluoro-5-[(pyridin-3-yl)ethynyl]benzonitrile (^{18}F FPEB) [143–145], ^{18}F -N,N-diethyl-2-[4-(2-fluoroethoxy)phenyl]-5,7-dimethylpyrazolo[1,5-a]pyrimidine-3-acetamide (^{18}F FDPA) [146], and N-(2,5-dimethoxybenzyl)-N-(5- ^{18}F -fluoro-2-phenoxyphenyl)acetamide (^{18}F DAA1106) [147] (Scheme 8.11).

Scheme 8.11

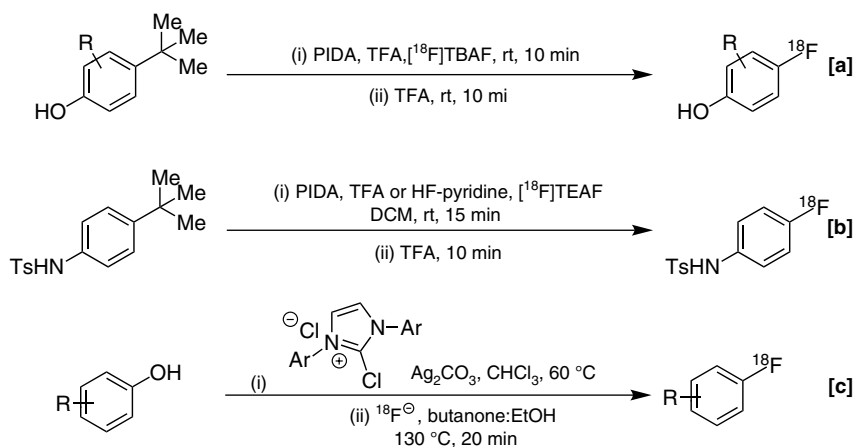
Radiotracers synthesized from spirocyclic iodonium ylides.



For some electron-rich precursors, reaction products consistent with an aryne mechanism compete with the desired product [148].

8.5.2.4 Phenols and Anilines

The radiofluorination of phenols and anilines using tert-butyl as a leaving group has also been investigated [149, 150]. This method allows for *p*-[¹⁸F]fluorophenols (Scheme 8.12a) and *p*-[¹⁸F]fluoroanilines (Scheme 8.12b) with some structural diversity. The substrate scope is limited to arenes bearing two mutually *para*-substituents, and the harshly oxidizing conditions conferred by phenyliodonium diacetate (**PIDA**) limits the functional group tolerance of this approach. While milder conditions have been developed for the synthesis of *p*-[¹⁸F]fluorophenol, they require two additional steps following the initial S_NAr radiofluorination [151, 152]. Furthermore, Ritter and co-workers have developed a direct radiofluorination of electron-deficient phenols using PhenoFluor and related reagents, which was proposed to proceed through a concerted nucleophilic aromatic substitution (C_SNAr) mechanism (Scheme 8.12c) [125].



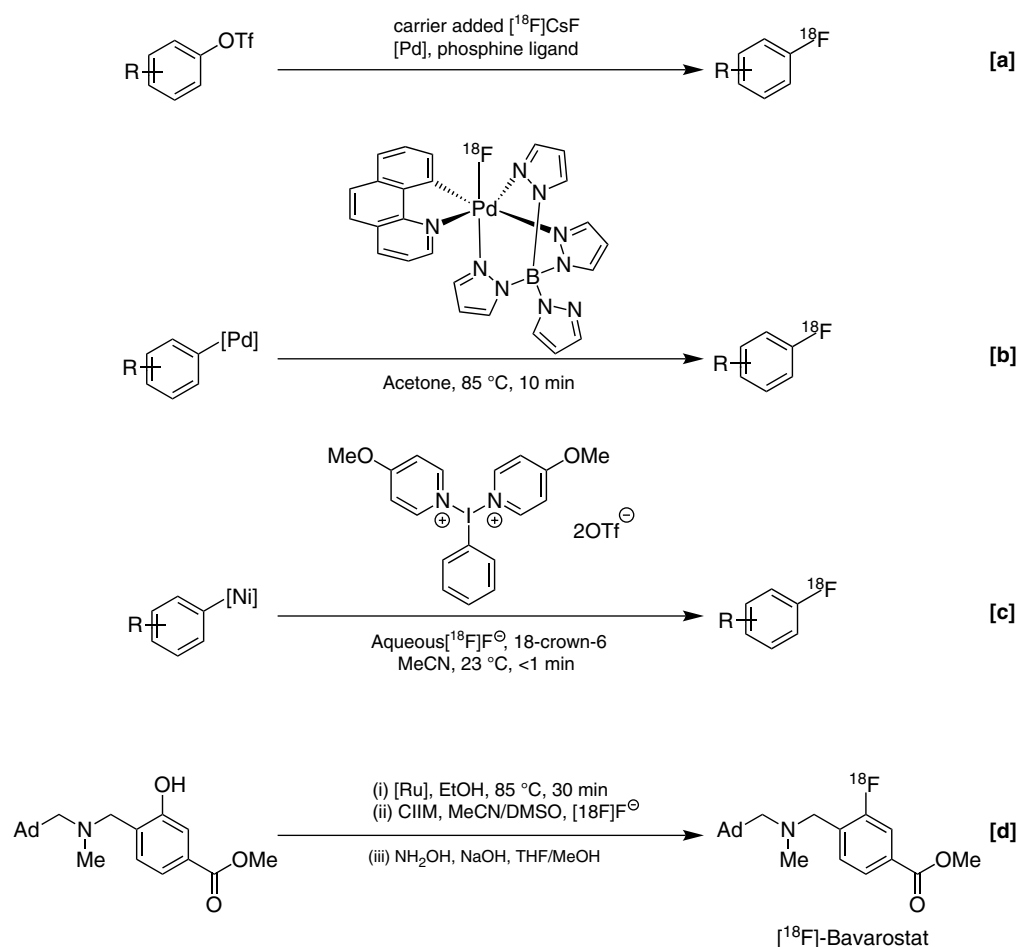
Scheme 8.12
Radiofluorination of phenols and anilines.

8.5.3 Transition-Metal-Mediated Late-Stage Aromatic Fluorination Using [¹⁸F]Fluoride

Since 2000, several new methodologies have been developed to install C(sp²)-¹⁸F bonds. A common class of methodology development includes the use of a transition-metal. Initially, attempts were made to adapt the Pd-mediated fluorination of aryl triflates reported by Buchwald [153, 154]. [¹⁸F]Radiofluorination of aryl triflates was realized but required carrier-added fluoride to obtain meaningful RCYs (Scheme 8.13a) [155]. A study by Ritter in 2011 described a Pd^{II}/Pd^{IV} catalytic cycle (Scheme 8.13b) that could promote a metal-mediated radiofluorination reaction [132]. In this report, a Pd complex was treated with [¹⁸F]fluoride to generate a Pd-¹⁸F complex, which could in turn react with another Pd complex to give the desired labeled product.

Scheme 8.13

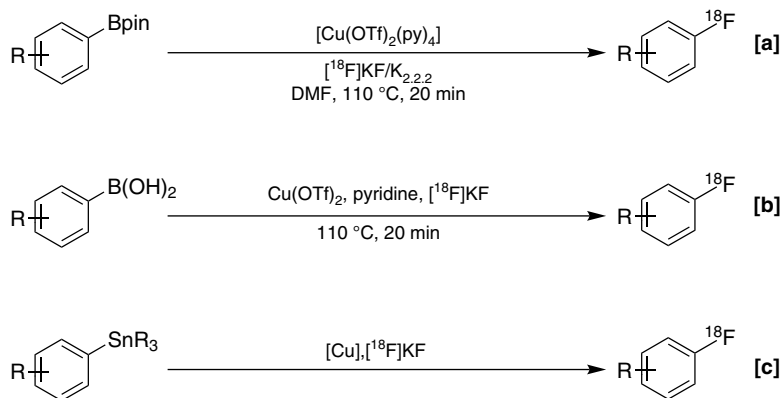
Transition metal-mediated radiofluorination of arenes.



The active Pd- ^{18}F complex was generated from nucleophilic [^{18}F]fluoride but conferred umpolung reactivity since it behaved as an electrophilic source of fluorine [156]. Later, the Pd- ^{18}F fluorination methodology was applied to synthesize known PET radiotracers on a clinical scale [157]. Further improvements were subsequently implemented, including the use of an aryl-Ni complex with aqueous [^{18}F]fluoride [158]. This update avoided the need to synthesize a M- ^{18}F complex alongside a M-aryl complex during the course of the reaction, simplifying the overall procedure (Scheme 8.13c) [159, 160]. Building on this work, the Ritter laboratory has also reported a Ru-mediated deoxyfluorination, which was later used to synthesize [^{18}F]bavarostat for non-human primate animal studies (Scheme 8.13d) [161, 162]. Owing to their specialized nature, the adoption of these methods for the clinical production of PET radiotracers has been somewhat slow to date.

Of the new transition-metal-promoted fluorination methods, CMRF has emerged as an operationally simple and powerful labeling technique that has been widely used by the PET radiochemistry community. Originally introduced by Sanford in 2013 for fluorination

of aryl iodonium salts, stannanes, and organoborons [163, 164], Sanford and Scott soon thereafter described an adapted CMRF of (mesityl)(aryl)iodonium salts (*vide supra*) [124]. Concurrently, a method for the CMRF of pinacol boronates (Bpin) was reported by Gouverneur (Scheme 8.14a) [165, 166], while Sanford and Scott have also disclosed the ^{18}F -fluorination of arylboronic acids (Scheme 8.14b) [167] and stannanes (Scheme 8.14c) [168]. Since these reports, there have been several updates, including a robustness screen to determine functional group tolerance [169], investigation into pyridine effects [170], order of addition studies, the use of pyridinium sulfates [171], the use of promoter alcohols [172], improved drying methods [173], and a comparison of CMRF with the spirocyclic iodonium ylide method (*vide supra*) [174, 175]. CMRF has proven to be a versatile approach for the late-stage fluorination of bioactive molecules to date, and the original reports have inspired the synthesis of numerous PET radiotracers (Figure 8.5) [115], such as 6- ^{18}F Fluorodihydroxyphenylalanine (^{18}F FDOPA) [176], ^{18}F DAA1106, (*vide supra*), amino acids [177, 178], 4- ^{18}F fluorobenzyltriphenylphosphonium cation (^{18}F FBnTP) [179], ^{18}F cabozantinib [180], and ^{18}F TRACK [181].



Scheme 8.14 Copper-mediated radiofluorination of arenes.

Other radiofluorination methodologies have been developed, but not widely implemented for various reasons. Of these, radiofluorination of $\text{C}(\text{sp}^2)\text{-H}$ bonds is an under-explored area with few methodologies available. In 2002, a $\text{C}(\text{sp}^2)\text{-H}$ radiofluorination using an electrochemical method was achieved using benzene as the model substrate

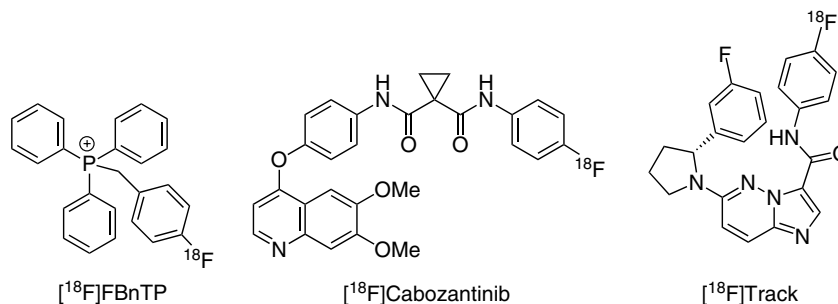
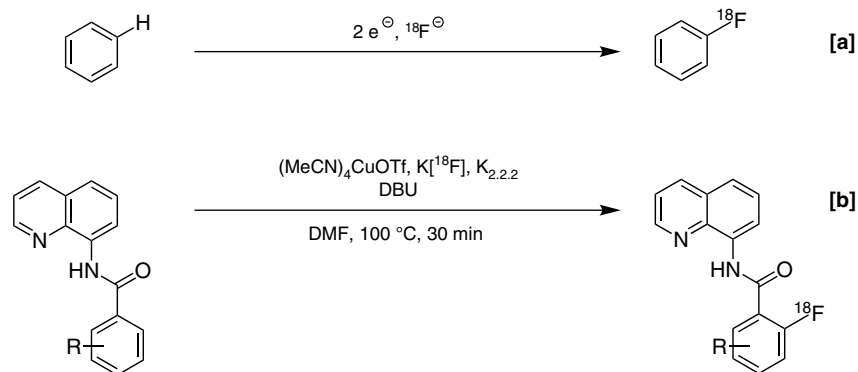


Figure 8.5 Select radiotracers synthesized with Cu-mediated radiofluorination.

(Scheme 8.15a) [182]. Limitations of this and subsequent electrochemical methods are that substituted precursors require carrier-added [^{18}F]fluoride and afford low yields, and possess selectivity issues [183, 184]. Furthermore, a recent radiofluorination using a cleavable 8-aminoquinoline directing group has been developed by employing a copper catalyst in conjunction with 1,8-Diazabicyclo[5.4.0]undec-7-ene (**DBU**) [25]. Carboxylic acid products can be obtained by simply cleaving the directing group (Scheme 8.15b). Notably, [^{18}F]KF outperformed [^{18}F]AgF, which was shown to be the optimal fluorine-19 source in the original report from Dauglulis [185].

Scheme 8.15
Radiofluorination of
aryl C–H bonds.



8.6 OTHER STRATEGIES FOR RADIOLABELING WITH FLUORINE-18

A challenge that PET radiochemists face is functional group compatibility with [^{18}F]fluoride. Overcoming this challenge to synthesize radiopharmaceuticals usually entails a two-step procedure consisting of initial radiofluorination and subsequent removal of protecting groups. However, given the growing popularity of technologies like immuno-PET [186], there are situations where this approach is infeasible. For example, scenarios requiring labeling of complicated molecules that are not compatible with fluorination/deprotection conditions, or sensitive biologics/macromolecules, require different labeling strategies. In such cases, it is often preferred to directly label a prosthetic group that can then be added to the molecule/macromolecule/biologic that is ill-suited for direct fluorination. To this end, a number of strategies have been developed, which are highlighted in this section.

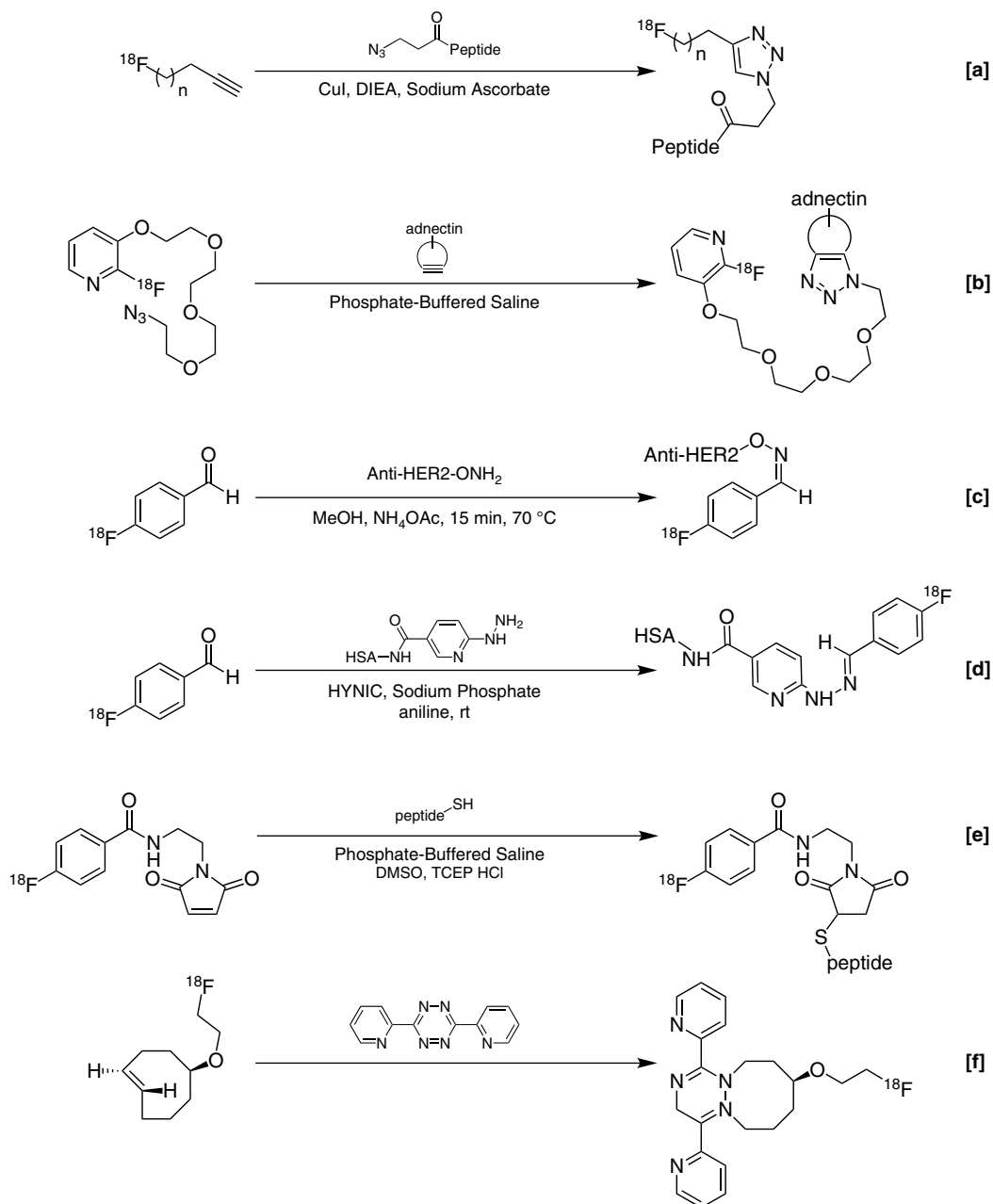
8.6.1 Prosthetic Group Methods

There is utility in the use of prosthetic groups, as they allow molecules to be investigated by PET imaging that would otherwise be difficult to radiolabel directly. This provides the potential to rapidly screen a number of peptides or small molecules of interest. Since the last edition of the *Handbook*, the use of classical prosthetic groups such as

[¹⁸F]fluoroethyltosylate and N-succinimidyl 4-[¹⁸F]fluorobenzoate (**[¹⁸F]SFB**) has continued. For example, a study design and workflow for screening radiotracers using [¹⁸F]SFB was described by the Sutcliffe lab [187]. In addition, new prosthetic groups continue to be developed, such as [¹⁸F]fluoroalkynes, which can be synthesized and used in a Cu(I)-catalyzed 1,3-dipolar cycloaddition (a class of click reaction) with molecules of interest containing a terminal azide (Scheme 8.16a) [188]. This concept of using click chemistry has been widely adopted by the radiochemistry community [189–192]. For example, clinical studies supporting drug development was fully realized in work from Donnelly and co-workers, where a 2-nitropyridine with an ether linkage to a polyethylene glycol chain that terminates with an azide is first radiolabeled by reaction with [¹⁸F]fluoride (Scheme 8.16b) [193]. This moiety was then combined with an anti-PD-L1 adnectin (a therapeutic protein) containing a strained alkyne to promote a cycloaddition for the attachment of the radiolabeled prosthetic group. The group at Bristol-Meyers Squibb took this through preclinical development and translated the use of this imaging agent and method to clinical trials, demonstrating the utility of this approach for the radiolabeling of biomolecules.

Click reactions are not limited to the 1,3-dipolar cycloadditions of azides and alkynes but can be any reaction that can occur in an orthogonal manner to “click” two molecules of interest together. Several other click methods have been developed, including the formation of oximes, hydrazones, thiol-Michael additions, and inverse-electron demand Diels-Alder reactions [194, 195]. In the oxime methods [¹⁸F]fluorobenzaldehyde is treated with a molecule of interest containing a hydroxylamine with an aniline catalyst (Scheme 8.16c) [196]. Glaser and co-workers found the oxime bond formation superior to both Si–F bond formation and Al-F-1,4,7-triazacyclononane-1,4,7-triacetic acid (NOTA) methods (vide infra) [197]. In analogy, Dirksen has utilized hydrazone-based prosthetic group strategies. In this study, both oxime and a hydrazone conjugates were investigated, and the use of aniline as a catalyst was critical for the appreciable radiolabeling of peptides and proteins (Scheme 8.16d) [198]. In the thiol-Michael approach, a maleimide bound to a labile moiety can be radiolabeled in the presence of tris(2-carboxyethyl)phosphine (**TCEP**) and subsequently attached to a biomolecule of interest that contains a thiol (such as a cysteine) to form a bond rapidly and orthogonally to other functional groups present (Scheme 8.16e) [199].

Finally, the inverse-electron demand Diels-Alder reaction provides another version of a click reaction recently developed for use with PET labeled prosthetic groups. The Conti lab demonstrated that tetrazine-trans-cyclooctenes may be synthesized from a [¹⁸F]cyclooctene derived prosthetic group and tetrazines via Diels-Alder cycloaddition. This approach is rapid and can be conducted at low concentrations, which is an important attribute given that high molar activity demands the use of small amounts of radio-labeled material for the prosthetic group (Scheme 8.16f) [195, 200]. This ability of this process to occur at low concentration was further explored and exploited by the Lewis lab to develop a method for pretargeting a protein of interest with an antibody that contains a cyclooctene. Once the antibody had been given sufficient time to bind its target, the tetrazine connected to a fluorine-18 containing moiety was injected [201]. *In vivo* experiments indicated targeted uptake of the tetrazine-labeled moiety, demonstrating that the Diels-Alder reaction could even occur at physiological dilution. This is an interesting development as it allows large biomolecules like antibodies that have biological



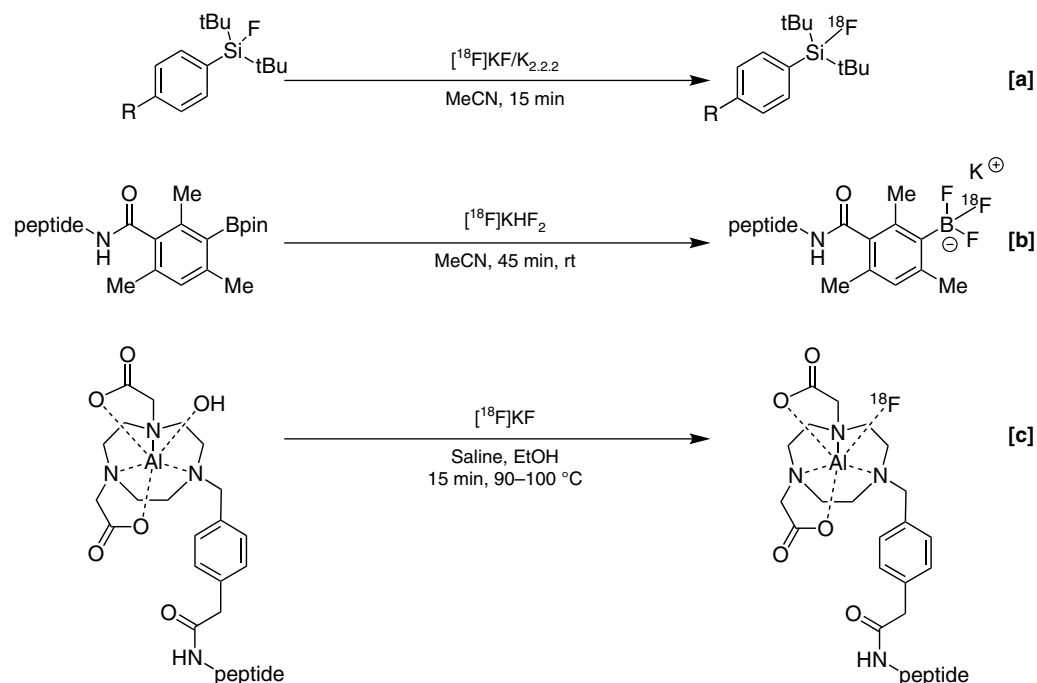
Scheme 8.16 Use of click reactions for prosthetic group radiolabeling.

half-lives (days) incompatible with the physical half-life of fluorine-18 to be imaged with fluorine-18 through pretargeting. Further investigations have been reported, although the method has not been advanced to clinical use, suggesting that further developments are required.

8.7 RADIOFLUORINATION BEYOND THE C-F BOND

8.7.1 Fluorine-Acceptor Chemistry

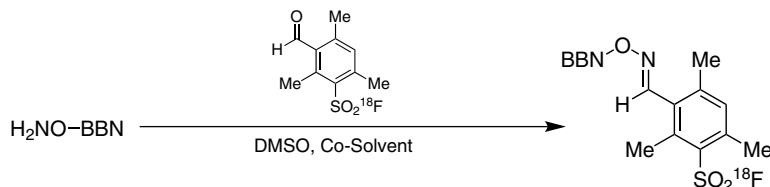
In recent years, radiochemists have begun to look beyond the C-¹⁸F bond in favor of other heteroatomic bonds to fluorine-18, and a number of attractive examples that exploit the mild conditions associated with fluorine-acceptor chemistry have been reported. Fluorine-acceptor chemistry takes advantage of stable fluorine bonds to aluminum, boron, and silicon. These atoms have strong Lewis acid character, and fluorine can be introduced under mild ion-exchange or chelation conditions. For example, the [¹⁸F]fluoroorganosilanes – [¹⁸F]fluorotriphenylsilane, [¹⁸F]fluoro-*t*-butyldiphenylsilane, and [¹⁸F]fluorodi-*t*-butylphenylsilane – were evaluated by Schirmmacher and co-workers [202]. They determined that di-*tert*-butyl substituted peptides gave the greatest *in vivo* stability in addition to ease of labeling with fluorine-18 to yield [¹⁸F]silyl fluorides (Scheme 8.17a). Development of one-step kit-like labeling of boronic acid ester peptides with fluorine-18 to give [¹⁸F]tetrafluoroborates has been reported by Perrin and co-workers. Unlike most methods, this chemistry does not require drying of fluoride and can be carried out under aqueous conditions (Scheme 8.17b) [203].



Scheme 8.17 Alternative approaches for ¹⁸F-labeling with silicon, boron, and aluminum.

Another kit-like preparation for radiolabeling involves the use of NOTA peptides with Al^{3+} hydroxide complexes [204]. In this example, fluorine-18 can displace hydroxide and form a strong Al–F bond (Scheme 8.17c). Finally, Inkster and colleagues disclosed syntheses of sulfonyl fluoride-based prosthetic groups such as $[\text{}^{18}\text{F}]$ 3-formyl-2,4,6-trimethylbenzenesulfonyl fluoride, which can be prepared from the corresponding sulfonyl chloride [205]. The prosthetic group was used for radiolabeling bombesin analogs (BBN-OH_2) through imine formation (Scheme 8.18).

Scheme 8.18 $[\text{}^{18}\text{F}]$
Sulfonyl fluoride-
based pros-
thetic group.



8.8 CONCLUSIONS AND FUTURE DIRECTIONS

To answer the increasing demand for novel radiopharmaceuticals labeled with fluorine-18, a number of research groups have initiated method-development programs for late-stage radiofluorination. Consequently, an impressive battery of novel methods for direct aliphatic and aromatic radiofluorination have been described in recent years, and continue to be reported [206]. Concurrently, the introduction of new prosthetic groups and strategies for generating ^{18}FB , ^{18}FSi , ^{18}FS , and ^{18}FAl bonds have improved the synthesis of established radiotracers, while also enabling ^{18}F -labeling of bioactive molecules in an increasingly complex chemical space that has been previously inaccessible to imaging scientists.

REFERENCES

1. Ametamey, S.M., Honer, M., and Schubiger, P.A. (2008). Molecular imaging with PET. *Chem. Rev.* 108 (5): 1501–1516. <https://doi.org/10.1021/cr0782426>.
2. Cai, L., Lu, S., and Pike, V.W. (2008). Chemistry with $[\text{}^{18}\text{F}]$ fluoride ion. *Eur. J. Org. Chem.* 2008 (17): 2853–2873. <https://doi.org/10.1002/ejoc.200800114>.
3. Miller, P.W., Long, N.J., Vilar, R. et al. (2008). Synthesis of ^{11}C , ^{18}F , ^{15}O , and ^{13}N radio-labels for positron emission tomography. *Angew. Chem. Int. Ed.* 47 (47): 8998–9033. <https://doi.org/10.1002/anie.200800222>.
4. Tredwell, M. and Gouverneur, V. (2012). ^{18}F labeling of arenes. *Angew. Chem. Int. Ed.* 51 (46): 11426–11437. <https://doi.org/10.1002/anie.201204687>.
5. Mason, N.S., Mathis, C.A., and Klunk, W.E. (2013). Positron emission tomography radioligands for *in vivo* imaging of $\text{A}\beta$ plaques. *J. Labelled Compd. Radiopharm.* 56 (3–4): 89–95. <https://doi.org/10.1002/jlcr.2989>.

6. Zimmer, L. and Le Bars, D. (2013). Current status of positron emission tomography radiotracers for serotonin receptors in humans. *J. Labelled Compd. Radiopharm.* 56 (3–4): 105–113. <https://doi.org/10.1002/jlcr.3001>.
7. Kovac, M., Mavel, S., and Anderluh, M. (2013). ¹⁸F-Labeled aryl-tracers through direct introduction of [¹⁸F]fluoride into electron-rich arenes. *Curr. Org. Chem.* 17 (15): 2921–2935.
8. Cole, E.L., Stewart, M.N., Littich, R. et al. (2014). Radiosyntheses using fluorine-18: the art and science of late stage fluorination. *Curr. Top. Med. Chem.* 14 (7): 875–900. <https://doi.org/10.2174/1568026614666140202205035>.
9. Brooks, A.F., Topczewski, J.J., Ichiishi, N. et al. (2014). Late-stage [¹⁸F]fluorination: new solutions to old problems. *Chem. Sci.* 5 (12): 4545–4553. <https://doi.org/10.1039/C4SC02099E>.
10. Brooks, A.F., Drake, L.R., Stewart, M.N. et al. (2016). Fluorine-18 patents (2009–2015). Part 1: novel radiotracers. *Pharm. Pat. Anal.* 5 (1): 17–47. <https://doi.org/10.4155/ppa.15.36>.
11. Mossine, A.V., Thompson, S., Brooks, A.F. et al. (2016). Fluorine-18 patents (2009–2015). Part 2: new radiochemistry. *Pharm. Pat. Anal.* 5 (5): 319–349. <https://doi.org/10.4155/ppa-2016-0028>.
12. Littich, R. and Scott, P.J.H. (2012). Novel strategies for fluorine-18 radiochemistry. *Angew. Chem. Int. Ed.* 51 (5): 1106–1109. <https://doi.org/10.1002/anie.201106785>.
13. Campbell, M.G. and Ritter, T. (2015). Modern carbon–fluorine bond forming reactions for aryl fluoride synthesis. *Chem. Rev.* 115 (2): 612–633. <https://doi.org/10.1021/cr500366b>.
14. Liang, S.H. and Vasdev, N. (2015). Total radiosynthesis: thinking outside “the box.”. *Aust. J. Chem.* 68 (9): 1319. <https://doi.org/10.1071/CH15406>.
15. Edwards, R. and Wirth, T. (2015). [¹⁸F]6-fluoro-3,4-dihydroxy-l-phenylalanine - recent modern syntheses for an elusive radiotracer. *J. Labelled Compd. Radiopharm.* 58 (5): 183–187. <https://doi.org/10.1002/jlcr.3285>.
16. Jacobson, O., Kiesewetter, D.O., and Chen, X. (2015). Fluorine-18 radiochemistry, labeling strategies and synthetic routes. *Bioconjugate Chem.* 26 (1): 1–18. <https://doi.org/10.1021/acs.chemrev.5b00493>.
17. Preshlock, S., Tredwell, M., and Gouverneur, V. (2016). ¹⁸F-labeling of arenes and heteroarenes for applications in positron emission tomography. *Chem. Rev.* 116 (2): 719–766. <https://doi.org/10.1021/acs.chemrev.5b00493>.
18. Deng, X., Rong, J., Wang, L. et al. (2019). Chemistry for positron emission tomography: recent advances in ¹¹C-, ¹⁸F-, ¹³N-, and ¹⁵O-labeling reactions. *Angew. Chem. Int. Ed.* 58 (9): 2580–2605. <https://doi.org/10.1002/anie.201805501>.
19. Coenen, H.H. and Ermert, J. (2018). ¹⁸F-labelling innovations and their potential for clinical application. *Clin. Transl. Imaging* 6 (3): 169–193. <https://doi.org/10.1007/s40336-018-0280-0>.
20. Gillis, E.P., Eastman, K.J., Hill, M.D. et al. (2015). Applications of fluorine in medicinal chemistry. *J. Med. Chem.* 58 (21): 8315–8359. <https://doi.org/10.1021/acs.jmedchem.5b00258>.
21. Kniess, T., Laube, M., Brust, P. et al. (2015). 2-[¹⁸F]fluoroethyl tosylate – a versatile tool for building ¹⁸F-based radiotracers for positron emission tomography. *Medchemcomm* 6 (10): 1714–1754. <https://doi.org/10.1039/C5MD00303B>.

22. Vaidyanathan, G. and Zalutsky, M.R. (2006). Synthesis of N-succinimidyl 4- ^{18}F fluorobenzoate, an agent for labeling proteins and peptides with ^{18}F . *Nat. Protoc.* 1 (4): 1655–1661. <https://doi.org/10.1038/nprot.2006.264>.
23. Scott, P.J.H., Shao, X., and Automated, F. (2010). High yielding production of N-succinimidyl 4- ^{18}F fluorobenzoate (^{18}F SFB), and its use in microwave-enhanced radiochemical coupling reactions. *J. Labelled Compd. Radiopharm.* 53 (9): 586–591. <https://doi.org/10.1002/jlcr.1785>.
24. Mossine, A.V., Brooks, A.F., Ichiishi, N. et al. (2017). Development of customized ^{18}F fluoride elution techniques for the enhancement of copper-mediated late-stage radiofluorination. *Sci. Rep.* 7 (1): 233. <https://doi.org/10.1038/s41598-017-00110-1>.
25. Lee, S.J., Makaravage, K.J., Brooks, A.F. et al. (2019). Copper-mediated aminoquinoline-directed radiofluorination of aromatic C–H bonds with K^{18}F . *Angew. Chem. Int. Ed.* 131 (10): 3151–3154. <https://doi.org/10.1002/anie.201812701>.
26. Gatley, S.J., Hichwa, R.D., Shaughnessy, W.J. et al. (1981). ^{18}F -labeled lower fluoroalkanes; reactor-produced gaseous physiological tracers. *Int. J. Appl. Radiat. Isot.* 32 (4): 211–214. [https://doi.org/10.1016/0020-708X\(81\)90051-X](https://doi.org/10.1016/0020-708X(81)90051-X).
27. Silver, G.S.J. (1982). Oxide assisted synthesis of fluoroalkanes; measurements with a fluoride electrode and with fluorine-18. *Int. J. Appl. Radiat. Isot.* 33 (4): 255–258. [https://doi.org/10.1016/0020-708X\(82\)90023-0](https://doi.org/10.1016/0020-708X(82)90023-0).
28. Clark, J.C., Goulding, R.W., and Palmer, A.J. (1973). *Radiopharmaceuticals and Labelled Compounds*. London: IAEA. 411 p. https://inis.iaea.org/collection/NCLCollectionStore/_Public/05/100/5100770.pdf.
29. Shalom, E., Takroui, K., Metsuyanin, N. et al. (2007). Semiautomated synthesis of a novel ^{18}F amine fluorocyanoborane for PET imaging studies. Radiosynthesis and *in vivo* characterization in rats. *Appl. Radiat. Isot.* 65 (2): 204–208. <https://doi.org/10.1016/j.apradiso.2006.08.014>.
30. Caires, C.C. and Guccione, S. (2010). Methods for silver-promoted fluorination of organic molecules. US patent 8,212,090, filed 10 December 2009 and issued 3 July 2012.
31. Lee, S.J., Brooks, A.F., Ichiishi, N. et al. (2019). C–H ^{18}F -fluorination of 8-methylquinolines with Ag^{18}F . *Chem. Commun.* 55 (20): 2976–2979. <http://xlink.rsc.org/?DOI=C9CC00641A>.
32. Verhoog, S., Brooks, A.F., Winton, W.P. et al. (2019). Ring opening of epoxides with ^{18}F FeF species to produce ^{18}F fluorohydrin PET imaging agents. *Chem. Commun.*: 2–6. <http://xlink.rsc.org/?DOI=C9CC02779C>.
33. Schimler, S.D., Cismesia, M.A., Hanley, P.S. et al. (2017). Nucleophilic deoxyfluorination of phenols via aryl fluorosulfonate intermediates. *J. Am. Chem. Soc.* 139 (4): 1452–1455. <https://doi.org/10.1021/jacs.6b12911>.
34. Sun, H. and DiMagno, S.G. (2005). Anhydrous tetrabutylammonium fluoride. *J. Am. Chem. Soc.* 127: 2050–2051. <https://doi.org/10.1021/JA0440497>.
35. Cox, D.P., Terpinski, J., and Lawrynowicz, W. (1984). “Anhydrous” tetrabutylammonium fluoride: a mild but highly efficient source of nucleophilic fluoride ion. *J. Org. Chem.* 49 (17): 3216–3219. <https://doi.org/10.1021/jo00191a035>.

36. Cismesia, M.A., Ryan, S.J., Bland, D.C. et al. (2017). Multiple approaches to the in situ generation of anhydrous tetraalkylammonium fluoride salts for S_NAr fluorination reactions. *J. Org. Chem.* 82 (10): 5020–5026. <https://doi.org/10.1021/acs.joc.7b00481>.
37. Schwesinger, R., Link, R., Wenzl, P. et al. (2006). Anhydrous phosphazanium fluorides as sources for extremely reactive fluoride ions in solution. *Chem. Eur. J.* 12 (2): 438–445. <https://doi.org/10.1002/chem.200500838>.
38. Stewart, M.N., Hockley, B.G., and Scott, P.J.H. (2015). Green approaches to late-stage fluorination: radiosyntheses of ^{18}F -labelled radiopharmaceuticals in ethanol and water. *Chem. Commun.* 51: 14805. <https://doi.org/10.1039/c5cc05919d>.
39. Mossine, A.V., Brooks, A.F., Henderson, B.D. et al. (2017). An updated radiosynthesis of [^{18}F]AV1451 for tau PET imaging. *EJNMMI Radiopharm. Chem.* 2 (1): 7. <https://doi.org/10.1186/s41181-017-0027-7>.
40. Sergeev, M.E., Morgia, F., Lazari, M. et al. (2015). Titania-catalyzed radiofluorination of tosylated precursors in highly aqueous medium. *J. Am. Chem. Soc.* 137 (17): 5686–5694. <https://doi.org/10.1021/jacs.5b02659>.
41. Wook, K.D., Ahn, D.-S., Oh, Y.-H. et al. (2006). A new class of S_N2 reactions catalyzed by protic solvents: facile fluorination for isotopic labeling of diagnostic molecules. *J. Am. Chem. Soc.* 128: 16394–16397. <https://doi.org/10.1021/ja0646895>.
42. Wook, K.D., Jeong, H.-J., Tae, L.S. et al. (2008). Facile nucleophilic fluorination reactions using tert-alcohols as a reaction medium: significantly enhanced reactivity of alkali metal fluorides and improved selectivity. *J. Org. Chem.* 73: 957–962. <https://doi.org/10.1021/jo7021229>.
43. Lee, J.-W., Oliveira, M.T., Bin, J.H. et al. (2016). Hydrogen-bond promoted nucleophilic fluorination: concept, mechanism and applications in positron emission tomography. *Chem. Soc. Rev.* 45 (17): 4638–4650. <http://xlink.rsc.org/?DOI=C6CS00286B>.
44. Turkman, N., Gelovani, J.G., and Alauddin, M.M. (2010). A novel method for stereospecific fluorination at the 2--arabino-position of pyrimidine nucleoside: synthesis of [^{18}F]-FMAU. *J. Labelled Compd. Radiopharm.* 53 (13): 782–786. <https://doi.org/10.1002/jlcr.1797>.
45. Kil, H.S., Cho, H.Y., Lee, S.J. et al. (2013). Alternative synthesis for the preparation of 16α -[^{18}F]fluoroestradiol. *J. Labelled Compd. Radiopharm.* 56 (12): 619–626. <https://doi.org/10.1002/jlcr.3076>.
46. Kiesewetter, D.O., Kilbourn, M.R., Landvatter, S.W. et al. (1984). Preparation of four fluorine-18-labeled estrogens and their selective uptakes in target tissues of immature rats. *J. Nucl. Med.* 25 (11): 1212–1221. <http://jnm.snmjournals.org/content/25/11/1212.full.pdf>.
47. Knott, K.E., Grätz, D., Hübner, S. et al. (2011). Simplified and automatic one-pot synthesis of 16α -[^{18}F]fluoroestradiol without high-performance liquid chromatography purification. *J. Labelled Compd. Radiopharm.* 54 (12): 749–753. <https://doi.org/10.1002/jlcr.1916>.
48. Amaraesekera, B., Marchis, P.D., Bobinski, K.P. et al. (2013). High-pressure, compact, modular radiosynthesizer for production of positron emitting biomarkers. *Appl. Radiat. Isot.* 78: 88–101. <https://doi.org/10.1016/J.APRADISO.2013.04.024>.

49. Ackermann, U., Lewis, J.S., Young, K. et al. (2016). Fully automated synthesis of [¹⁸F] fluoro-dihydrotestosterone ([¹⁸F]FDHT) using the FlexLab module. *J. Labelled Compd. Radiopharm.* 59 (10): 424–428. <https://doi.org/10.1002/jlcr.3417>.
50. Zhou, D., Lin, M., Yasui, N. et al. (2014). Optimization of the preparation of fluorine-18-labeled steroid receptor ligands 16alpha-[¹⁸F]fluoroestradiol (FES), [¹⁸F]fluoro furanyl norprogesterone (FFNP), and 16beta-[¹⁸F]fluoro-5alpha-dihydrotestosterone (FDHT) as Ra. *J. Labelled Compd. Radiopharm.* 57 (5): 371–377. <https://doi.org/10.1002/jlcr.3191>.
51. Revunov, E. and Zhuravlev, F. (2013). Co(salen)-mediated enantioselective radio-fluorination of epoxides. Radiosynthesis of enantiomerically enriched [¹⁸F]F-MISO via kinetic resolution. *J. Fluorine Chem.* 156: 130–135. <https://doi.org/10.1016/j.jfluchem.2013.09.006>.
52. Graham, T.J.A., Lambert, R.F., Ploessl, K. et al. (2014). Enantioselective radiosynthesis of positron emission tomography (PET) tracers containing [¹⁸F]fluoroalcohols. *J. Am. Chem. Soc.* 136 (14): 5291–5294. <https://doi.org/10.1021/ja5025645>.
53. Huang, X., Liu, W., Ren, H. et al. (2014). Late stage benzylic C-H fluorination with [¹⁸F]fluoride for PET imaging. *J. Am. Chem. Soc.* 136 (19): 6842–6845. <https://doi.org/10.1021/ja5039819>.
54. Carroll, L., Evans, H.L., Spivey, A.C. et al. (2015). Mn–Salen catalysed benzylic C–H activation for the synthesis of aryl[¹⁸F]CF₃-containing PET probes. *Chem. Commun.* 51 (40): 8439–8441. <https://doi.org/10.1039/C4CC05762G>.
55. Topczewski, J.J., Tewson, T.J., and Nguyen, H.M. (2011). Iridium-catalyzed allylic fluorination of trichloroacetimidates. *J. Am. Chem. Soc.* 133 (48): 19318–19321.
56. Braun, M.-G. and Doyle, A.G. (2013). Palladium-catalyzed allylic C–H fluorination. *J. Am. Chem. Soc.* 135 (35): 12990–12993. <https://doi.org/10.1021/ja407223g>.
57. Hollingworth, C., Hazari, A., Hopkinson, M.N. et al. (2011). Palladium-catalyzed allylic fluorination. *Angew. Chem. Int. Ed.* 50 (11): 2613–2617. <https://doi.org/10.1002/anie.201007307>.
58. Benedetto, E., Tredwell, M., Hollingworth, C. et al. (2013). Regio- and stereoretentive synthesis of branched, linear (E)- and (Z)-allyl fluorides from allyl carbonates under Ir-catalysis. *Chem. Sci.* 4: 89–96. <https://doi.org/10.1039/C2SC21789A>.
59. Mixdorf, J.C., Sorlin, A.M., Dick, D.W. et al. (2019). Iridium-catalyzed radiosynthesis of branched allylic [¹⁸F]fluorides. *Org. Lett.* 21 (1): 60–64.
60. Angelini, G., Speranza, M., Wolf, A.P. et al. (1990). ¹⁸F-to-halogen exchange reaction on a,a,a-trihalotoluenes. A useful route to no-carrier-added (NCA) ¹⁸F-labeled substituted a,a,a-trifluorotoluenes. *Radiochim. Acta* 50: 63–69. <https://doi.org/10.1524/ract.1990.50.12.63>.
61. Angelini, G., Speranza, M., Shiue, C.-Y. et al. (1986). H¹⁸F + Sb₂O₃: a new selective radio-fluorinating agent. *J. Chem. Soc., Chem. Commun.* 12: 924. <https://doi.org/10.1039/c39860000924>.
62. Kilbourn, M.R., Pavia, M.R., and Gregor, V.E. (1990). Synthesis of fluorine-18 Labeled GABA uptake inhibitors. *Int. J. Radiat. Appl. Instrumentation. Part A. Appl. Radiat. Isot.* 41 (9): 823–828. [https://doi.org/10.1016/0883-2889\(90\)90059-P](https://doi.org/10.1016/0883-2889(90)90059-P).

63. Verhoog, S., Pfeifer, L., Khotavivattana, T. et al. (2016). Silver-mediated ^{18}F -labeling of aryl- CF_3 and aryl- CHF_2 with ^{18}F -fluoride. *Synlett* 27 (01): 25–28. <https://doi.org/10.1055/s-0035-1560592>.
64. Riss, P.J., Aigbirhio, F.I., and Simple, A. (2011). Rapid procedure for nucleophilic radiosynthesis of aliphatic ^{18}F trifluoromethyl groups. *Chem. Commun.* 47 (43): 11873. <https://doi.org/10.1039/c1cc15342k>.
65. Riss, P.J., Ferrari, V., Brichard, L. et al. (2012). Direct, nucleophilic radiosynthesis of ^{18}F trifluoroalkyl tosylates: improved labelling procedures. *Org. Biomol. Chem.* 10 (34): 6980. <https://doi.org/10.1039/c2ob25802a>.
66. Shao, X., Schnau, P.L., Fawaz, M.V. et al. (2013). Enhanced radiosyntheses of ^{11}C raclopride and ^{11}C DASB using ethanolic loop chemistry. *Nucl. Med. Biol.* 40 (1): 109–116. <https://linkinghub.elsevier.com/retrieve/pii/S0969805112002533>.
67. Khotavivattana, T., Verhoog, S., Tredwell, M. et al. (2015). ^{18}F -labeling of aryl- SCF_3 , $-\text{OCF}_3$ and $-\text{OCHF}_2$ with ^{18}F fluoride. *Angew. Chem. Int. Ed.* 127 (34): 10129–10133. <https://doi.org/10.1002/ange.201504665>.
68. Zheng, J., Wang, L., Lin, J.-H. et al. (2015). Difluorocarbene-derived trifluoromethylthiolation and ^{18}F trifluoromethylthiolation of aliphatic electrophiles. *Angew. Chem. Int. Ed.* 54 (45): 13236–13240. <https://doi.org/10.1002/anie.201505446>.
69. Zheng, J., Cheng, R., Lin, J.-H. et al. (2017). An unconventional mechanistic insight into SCF_3 formation from difluorocarbene: preparation of ^{18}F -labeled $\alpha\text{-SCF}_3$ carbonyl compounds. *Angew. Chem. Int. Ed.* 56 (12): 3196–3200. <https://doi.org/10.1002/anie.201611761>.
70. Verhoog, S., Kee, C.W., Wang, Y. et al. (2018). ^{18}F -trifluoromethylation of unmodified peptides with 5- ^{18}F -(Trifluoromethyl)dibenzothiophenium trifluoromethanesulfonate. *J. Am. Chem. Soc.* 140 (5): 1572–1575. <https://doi.org/10.1021/jacs.7b10227>.
71. Huiban, M., Tredwell, M., Mizuta, S. et al. (2013). A broadly applicable ^{18}F trifluoromethylation of aryl and heteroaryl iodides for PET imaging. *Nat. Chem.* 5 (11): 941–944. <https://doi.org/10.1038/nchem.1756>.
72. Rühl, T., Rafique, W., Lien, V.T. et al. (2014). Cu(I)-mediated ^{18}F -trifluoromethylation of arenes: rapid synthesis of ^{18}F -labeled trifluoromethyl arenes. *Chem. Commun.* 50 (45): 6056–6059. <https://doi.org/10.1039/C4CC01641F>.
73. Van Der Born, D., Herscheid, J.D.M., Orru, R.V.A. et al. (2013). Efficient synthesis of ^{18}F trifluoromethane and its application in the synthesis of PET tracers. *Chem. Commun.* 49 (38): 4018–4020. <https://doi.org/10.1039/c3cc37833k>.
74. van der Born, D., Sewing, C., Herscheid, J.K.D.M. et al. (2014). A universal procedure for the ^{18}F trifluoromethylation of aryl iodides and aryl Boronic acids with highly improved specific activity. *Angew. Chem. Int. Ed.* 53 (41): 11046–11050. <https://doi.org/10.1002/anie.201406221>.
75. Ivashkin, P., Lemonnier, G., Cousin, J. et al. (2014). ^{18}F CuCF_3 : a ^{18}F trifluoromethylating agent for arylboronic acids and aryl iodides. *Chem. Eur. J.* 20 (31): 9514–9518. <https://doi.org/10.1002/chem.201403630>.
76. Fawaz, M.V., Brooks, A.F., Rodnick, M.E. et al. (2014). High affinity radiopharmaceuticals based upon lansoprazole for PET imaging of aggregated tau in Alzheimer's

- disease and progressive supranuclear palsy: synthesis, preclinical evaluation, and lead selection. *ACS Chem. Neurosci.* 5 (8): 718–730. <https://doi.org/10.1021/cn500103u>.
77. Kramer, V., Brooks, A.F., Haeger, A. et al. (2020). Evaluation of [¹⁸F]-*N*-methyl lansoprazole as a tau PET imaging agent in first-in-human studies. *ACS Chem. Neurosci.* 11 (3): 427–435.
 78. Khotavivattana, T., Verhoog, S., Tredwell, M. et al. (2015). ¹⁸F-Labeling of aryl-SCF₃, -OCF₃ and -OCHF₂ with [¹⁸F]fluoride. *Angew. Chem. Int. Ed.* 54 (34): 9991–9995. <https://doi.org/10.1002/anie.201504665>.
 79. Brooks, A.F., Drake, L.R., Shao, X. et al. (2018). Evaluation of enzyme substrate radiotracers as PET/MRS hybrid imaging agents. *ACS Med. Chem. Lett.* 9 (11): 1140–1143. <https://doi.org/10.1021/acsmchemlett.8b00402>.
 80. Shi, H., Braun, A., Wang, L. et al. (2016). Synthesis of ¹⁸F-difluoromethylarenes from aryl (pseudo) halides. *Angew. Chem. Int. Ed.* 55 (36): 10786–10790. <https://doi.org/10.1002/anie.201604106>.
 81. Yuan, G., Wang, F., Stephenson, N.A. et al. (2017). Metal-free ¹⁸F-labeling of aryl-CF₃H via nucleophilic radiofluorination and oxidative C–H activation. *Chem. Commun.* 53 (1): 126–129. <http://xlink.rsc.org/?DOI=C6CC07913J>.
 82. Zeng, X., Li, J., Ng, C.K. et al. (2018). (Radio)Fluoroclick reaction enabled by a hydrogen-bonding cluster. *Angew. Chem. Int. Ed.* 57 (11): 2924–2928. <https://doi.org/10.1002/anie.201711341>.
 83. Thompson, S., Onega, M., Ashworth, S. et al. (2015). A two-step fluorinase enzyme mediated ¹⁸F labelling of an RGD peptide for positron emission tomography. *Chem. Commun.* 51 (70): 13542–13545. <https://doi.org/10.1039/C5CC05013H>.
 84. Zhou, Y., Wang, J., Gu, Z. et al. (2016). Next generation of fluorine-containing pharmaceuticals, compounds currently in phase II–III clinical trials of major pharmaceutical companies: new structural trends and therapeutic areas. *Chem. Rev.* 116 (2): 422–518. <https://doi.org/10.1021/acs.chemrev.5b00392>.
 85. Wang, J., Sánchez-Roselló, M., Aceña, J.L. et al. (2014). Fluorine in pharmaceutical industry: fluorine-containing drugs introduced to the market in the last decade (2001–2011). *Chem. Rev.* 114 (4): 2432–2506. <https://doi.org/10.1021/cr4002879>.
 86. Shah, P. and Westwell, A.D. (2007). The role of fluorine in medicinal chemistry. *J. Enzyme Inhib. Med. Chem.* 22 (5): 527–540. <http://www.tandfonline.com/doi/full/10.1080/14756360701425014>.
 87. Müller, K. and Böhm, H.-J. (2009). Facilitating the design of fluorinated drugs. *Chem. Biol.* 16 (11): 1130–1131. <https://doi.org/10.1016/J.CHEMBIOL.2009.11.004>.
 88. Mei, H., Han, J., Fustero, S. et al. (2019). Fluorine-containing drugs approved by the FDA in 2018. *Chem. A Eur. J.* 25 (51): 11797–11819. <https://onlinelibrary.wiley.com/doi/abs/10.1002/chem.201901840>.
 89. Sander, K., Galante, E., Gendron, T. et al. (2015). Development of fluorine-18 labeled metabolically activated tracers for imaging of drug efflux transporters with positron emission tomography. *J. Med. Chem.* 58 (15): 6058–6080. <https://doi.org/10.1021/acs.jmedchem.5b00652>.

90. Zlatopolskiy, B.D., Zischler, J., Krapf, P. et al. (2015). Copper-mediated aromatic radiofluorination revisited: efficient production of PET tracers on a preparative scale. *Chem. Eur. J.* 21 (15): 5972–5979. <https://doi.org/10.1002/chem.201405586>.
91. Snyder, S.E. and Kilbourn, M.R. (2005). Chemistry of fluorine-18 radiopharmaceuticals. In: *Handbook of Radiopharmaceuticals*, 195–227. Chichester, UK: Wiley. Available from: <https://doi.org/10.1002/0470846380.ch6>.
92. Moore, T.M., Akula, M.R., Collier, L. et al. (2013). A rapid microfluidic synthesis of [¹⁸F]fluoroarenes from nitroarenes. *Appl. Radiat. Isot.* 71 (1): 47–50. <https://doi.org/10.1016/J.APRADISO.2012.09.013>.
93. Pike, V.W. and Aigbirhio, F.I. (1995). Reactions of cyclotron-produced [¹⁸F]fluoride with diaryliodonium salts—a novel single-step route to no-carrier-added [¹⁸F]fluoroarenes. *J. Chem. Soc., Chem. Commun.* 21: 2215–2216. <https://doi.org/10.1039/C39950002215>.
94. Pike, V.W. (2018). Hypervalent aryl iodine compounds as precursors for radiofluorination. *J. Labelled Compd. Radiopharm.* 61 (3): 196–227. <https://doi.org/10.1002/jlcr.3570>.
95. Shah, A., Pike, V.W., and Widdowson, D.A. (1998). The synthesis of [¹⁸F]fluoroarenes from the reaction of cyclotron-produced [¹⁸F]fluoride ion with diaryliodonium salts. *J. Chem. Soc. Perkin Trans. 1* 13: 2043–2046. <https://doi.org/10.1039/a802349b>.
96. Krzyczmonik, A., Keller, T., López-Picón, F.R. et al. (2019). Radiosynthesis and pre-clinical evaluation of an α2A-adrenoceptor tracer candidate, 6-[¹⁸F]fluoro-marsandine. *Mol. Imaging Biol.* 21 (5): 879–887. <https://doi.org/10.1007/s11307-019-01317-6>.
97. Bergman, J. and Solin, O. (1997). Fluorine-18-labeled fluorine gas for synthesis of tracer molecules. *Nucl. Med. Biol.* 24 (7): 677–683. [https://doi.org/10.1016/S0969-8051\(97\)00078-4](https://doi.org/10.1016/S0969-8051(97)00078-4).
98. Stenhagen, I.S.R., Kirjavainen, A.K., Forsback, S.J. et al. (2013). [¹⁸F]fluorination of an arylboronic ester using [¹⁸F]selectfluor bis(triflate): application to 6-[¹⁸F]fluoro-l-DOPA. *Chem. Commun.* 49 (14): 1386. <https://doi.org/10.1039/c2cc38646a>.
99. Teare, H., Robins, E.G., Kirjavainen, A. et al. (2010). Radiosynthesis and evaluation of [¹⁸F]selectfluor bis(triflate). *Angew. Chem. Int. Ed.* 49 (38): 6821–6824. <https://doi.org/10.1002/anie.201002310>.
100. Teare, H., Robins, E.G., Årstad, E. et al. (2007). Synthesis and reactivity of [¹⁸F]-N-fluorobenzenesulfonimide. *Chem. Commun.* 23: 2330–2332. <https://doi.org/10.1039/B701177F>.
101. Sun, H. and DiMugno, S.G. (2007). Competitive demethylation and substitution in N,N,N-trimethylanilinium fluorides. *J. Fluorine Chem.* 128 (7): 806–812. <https://doi.org/10.1016/J.JFLUCHEM.2007.03.009>.
102. Lazarova, N., Siméon, F.G., Musachio, J.L. et al. (2007). Integration of a microwave reactor with synthia to provide a fully automated radiofluorination module. *J. Labelled Compd. Radiopharm.* 50 (5–6): 463–465. <https://doi.org/10.1002/jlcr.1196>.
103. Iovkova, L., Wängler, B., Schirrmacher, E. et al. (2009). *para*-functionalized aryl-di-tert-butylfluorosilanes as potential labeling synthons for ¹⁸F radiopharmaceuticals. *Chem. Eur. J.* 15 (9): 2140–2147. <https://doi.org/10.1002/chem.200802266>.

104. Naumiec, G.R., Cai, L., Lu, S. et al. (2017). Quinuclidine and DABCO enhance the radiofluorination of 5-substituted 2-halopyridines. *Eur. J. Org. Chem.* 2017 (45): 6593–6603. <https://doi.org/10.1002/ejoc.201700970>.
105. Kwon, Y.-D., Son, J., and Chun, J.-H. (2018). Catalyst-free aromatic radiofluorination via oxidized Iodoarene precursors. *Org. Lett.* 20 (24): 7902–7906. <https://doi.org/10.1021/acs.orglett.8b03450>.
106. Narayanam, M., Ma, G., Champagne, P. et al. (2018). Nucleophilic ^{18}F -fluorination of anilines via N-arylsydnone intermediates. *Synlett* 29 (09): 1131–1135. <http://www.thieme-connect.de/DOI/DOI?10.1055/s-0036-1591948>.
107. Mu, L., Fischer, C.R., Holland, J.P. et al. (2012). ^{18}F -radiolabeling of aromatic compounds using triarylsulfonium salts. *Eur. J. Org. Chem.* 2012 (5): 889–892. <https://doi.org/10.1002/ejoc.201101730>.
108. Sander, K., Gendron, T., Yiannaki, E. et al. (2015). Sulfonium salts as leaving groups for aromatic labelling of drug-like small molecules with fluorine-18. *Sci. Rep.* 5 (1): 9941. <https://doi.org/10.1038/srep09941>.
109. Gendron, T., Sander, K., Cybulska, K. et al. (2018). Ring-closing synthesis of dibenzothiophene sulfonium salts and their use as leaving groups for aromatic ^{18}F -fluorination. *J. Am. Chem. Soc.* 140 (35): 11125–11132. <https://doi.org/10.1021/jacs.8b06730>.
110. Recent, O.S. (2001). Progress in fluorine-18 labelled peptide radiopharmaceuticals. *Eur. J. Nucl. Med.* 28 (7): 929–938. <https://doi.org/10.1007/s002590100508>.
111. Becaud, J., Mu, L., Karramkam, M. et al. (2009). Direct one-step ^{18}F -labeling of peptides via nucleophilic aromatic substitution. *Bioconjugate Chem.* 20 (12): 2254–2261. <https://doi.org/10.1021/bc900240z>.
112. Ermert, J., Hocke, C., Ludwig, T. et al. (2004). Comparison of pathways to the versatile synthon of no-carrier-added 1-bromo-4- ^{18}F fluorobenzene. *J. Labelled Compd. Radiopharm.* 47 (7): 429–441. <https://doi.org/10.1002/jlcr.830>.
113. Basuli, F., Zhang, X., Woodroffe, C.C. et al. (2017). Fast indirect fluorine-18 labeling of protein/peptide using the useful 6-fluoronicotinic acid-2,3,5,6-tetrafluorophenyl prosthetic group: a method comparable to direct fluorination. *J. Labelled Compd. Radiopharm.* 60 (3): 168–175. <https://doi.org/10.1002/jlcr.3487>.
114. Prante, O., Maschauer, S., and Banerjee, A. (2013). Radioligands for the dopamine receptor subtypes. *J. Labelled Compd. Radiopharm.* 56 (3–4): 130–148. <https://doi.org/10.1002/jlcr.3000>.
115. Preshlock, S., Calderwood, S., Verhoog, S. et al. (2016). Enhanced copper-mediated ^{18}F -fluorination of aryl boronic esters provides eight radiotracers for PET applications. *Chem. Commun.* 52 (54): 8361–8364. <https://doi.org/10.1039/C6CC03295H>.
116. Carroll, M.A., Nairne, J., and Woodcraft, J.L. (2007). Diaryliodonium salts: a solution to 3- ^{18}F fluoropyridine. *J. Labelled Compd. Radiopharm.* 50 (5–6): 452–454. <https://doi.org/10.1002/jlcr.1190>.
117. Yuan, Z., Cheng, R., Chen, P. et al. (2016). Efficient pathway for the preparation of aryl(isoquinoline)iodonium(III) salts and synthesis of radiofluorinated isoquinolines. *Angew. Chem. Int. Ed.* 55 (39): 11882–11886. <https://doi.org/10.1002/anie.201606381>.

118. Chun, J.-H., Lu, S., and Pike, V.W. (2011). Rapid and efficient radiosyntheses of *meta*-substituted [¹⁸F]fluoroarenes from [¹⁸F]fluoride ion and diaryliodonium-tosylates within a microreactor. *Eur. J. Org. Chem.* 2011 (23): 4439–4447. <https://doi.org/10.1002/ejoc.201100382>.
119. Ross, T.L., Ermert, J., Hocke, C. et al. (2007). Nucleophilic ¹⁸F-fluorination of hetero-aromatic iodonium salts with no-carrier-added [¹⁸F]fluoride. *J. Am. Chem. Soc.* 129: 8018–8025. <https://doi.org/10.1021/JA066850H>.
120. Yamada, Y. and Okawara, M. (1972). Steric effect in the nucleophilic attack of bromide anion on diaryl- and aryl-2-thienyliodonium ions. *Bull. Chem. Soc. Jpn.* 45 (6): 1860–1863. <https://doi.org/10.1246/bcsj.45.1860>.
121. Yamada, Y., Kashima, K., and Okawara, M. (1974). Substituent effect in the nucleophilic attack by the bromide ion on the *p*-tolyl-substituted phenyliodonium ions. *Bull. Chem. Soc. Jpn.* 47 (12): 3179–3180. <https://doi.org/10.1246/bcsj.47.3179>.
122. Lancer, K.M. and Wiegand, G.H. (1976). The *ortho* effect in the pyrolysis of iodonium halides. A case for a sterically controlled nucleophilic aromatic (SN) substitution reaction. *J. Org. Chem.* 41 (21): 3360–3364. <https://doi.org/10.1021/jo00883a004>.
123. Chun, J.-H., Lu, S., Lee, Y.-S. et al. (2010). Fast and high-yield microreactor syntheses of *ortho*-substituted [¹⁸F]fluoroarenes from reactions of [¹⁸F]fluoride ion with diaryliodonium salts. *J. Org. Chem.* 75 (10): 3332–3338. <https://doi.org/10.1021/jo100361d>.
124. Ichiishi, N., Brooks, A.F., Topczewski, J.J. et al. (2014). Copper-catalyzed [¹⁸F]fluorination of (Mesityl)(aryl)iodonium salts. *Org. Lett.* 16 (12): 3224–3227. <https://doi.org/10.1021/ol501243g>.
125. Neumann, C.N., Hooker, J.M., and Ritter, T. (2016). Concerted nucleophilic aromatic substitution with ¹⁹F⁻ and ¹⁸F⁻. *Nature* 534 (7607): 369–373. <https://doi.org/10.1038/nature17667>.
126. Vāvere, A.L., Neumann, K.D., Butch, E.R. et al. (2018). Improved, one-pot synthesis of 6-[¹⁸F]fluorodopamine and quality control testing for use in patients with neuroblastoma. *J. Labelled Compd. Radiopharm.* 61 (14): 1069–1080. <https://doi.org/10.1002/jlcr.3685>.
127. Edwards, R., Westwell, A.D., Daniels, S. et al. (2015). Convenient synthesis of diaryliodonium salts for the production of [¹⁸F]F-DOPA. *Eur. J. Org. Chem.* 2015 (3): 625–630. <https://doi.org/10.1002/ejoc.201403378>.
128. Jang, K.S., Jung, Y.-W., Sherman, P.S. et al. (2013). Synthesis and bioevaluation of [¹⁸F]4-fluoro-*m*-hydroxyphenethylguanidine ([¹⁸F]4F-MHPG): a novel radiotracer for quantitative PET studies of cardiac sympathetic innervation. *Bioorg. Med. Chem. Lett.* 23 (6): 1612–1616. <https://doi.org/10.1016/J.BMCL.2013.01.106>.
129. Raffel, D.M., Jung, Y.-W., Koeppe, R.A. et al. (2018). First-in-human studies of [¹⁸F] fluorohydroxyphenethylguanidines. *Circ. Cardiovasc. Imaging* 11 (12) <https://doi.org/10.1161/CIRCIMAGING.118.007965>.
130. Warnier, C., Lemaire, C., Becker, G. et al. (2016). Enabling efficient positron emission tomography (PET) imaging of synaptic vesicle glycoprotein 2A (SV2A) with a robust and one-step radiosynthesis of a highly potent ¹⁸F-labeled ligand

- (¹⁸F)UCB-H). *J. Med. Chem.* 59 (19): 8955–8966. <https://doi.org/10.1021/acs.jmedchem.6b00905>.
131. Xu, R., Zanotti-Fregonara, P., Zoghbi, S.S. et al. (2013). Synthesis and evaluation in monkey of [¹⁸F]4-fluoro-*N*-methyl-*N*-(4-(6-[methylamino]pyrimidin-4-yl)thiazol-2-yl)benzamide ([¹⁸F]FIMX): a promising radioligand for PET imaging of brain metabotropic glutamate recept. *J. Med. Chem.* 56 (22): 9146–9155. <https://doi.org/10.1021/jm4012017>.
 132. Lee, E., Kamlet, A.S., Powers, D.C. et al. (2011). A fluoride-derived electrophilic late-stage fluorination reagent for PET imaging. *Science* 334 (6056): 639–642. <https://doi.org/10.1126/science.1212625>.
 133. Selivanova, S.V., Stellfeld, T., Heinrich, T.K. et al. (2013). Design, synthesis, and initial evaluation of a high affinity positron emission tomography probe for imaging matrix metalloproteinases 2 and 9. *J. Med. Chem.* 56 (12): 4912–4920. <https://doi.org/10.1021/jm400156p>.
 134. Chun, J.-H. and Pike, V.W. (2013). Single-step syntheses of no-carrier-added functionalized [¹⁸F]fluoroarenes as labeling synthons from diaryliodonium salts. *Org. Biomol. Chem.* 11 (37): 6300. <https://doi.org/10.1039/c3ob41353e>.
 135. Irving, H. and Reid, R.W. (1960). 421. The photochemical decomposition of diphenyliodonium iodide. *J. Chem. Soc. (0)*: 2078. <https://doi.org/10.1039/jr9600002078>.
 136. Zhang, M.-R., Kumata, K., and Suzuki, K. (2007). A practical route for synthesizing a PET ligand containing [¹⁸F]fluorobenzene using reaction of diphenyliodonium salt with [¹⁸F]F⁻. *Tetrahedron Lett.* 48 (49): 8632–8635. <https://doi.org/10.1016/J.TETLET.2007.10.025>.
 137. Haskali, M.B., Telu, S., Lee, Y.-S. et al. (2016). An investigation of (Diacetoxyiodo) arenes as precursors for preparing no-carrier-added [¹⁸F]fluoroarenes from cyclotron-produced [¹⁸F]fluoride ion. *J. Org. Chem.* 81 (1): 297–302. <https://doi.org/10.1021/acs.joc.5b02332>.
 138. McCammant, M.S., Thompson, S., Brooks, A.F. et al. (2017). Cu-mediated C–H ¹⁸F-fluorination of electron-rich (hetero)arenes. *Org. Lett.* 19 (14): 3939–3942. <https://doi.org/10.1021/acs.orglett.7b01902>.
 139. Satyamurthy, N. and Barrio, J.R. (2010). No-carrier-added nucleophilic [F-18] fluorination of aromatic compounds. International patent WO/2010/117435.
 140. Rotstein, B.H., Stephenson, N.A., Vasdev, N. et al. (2014). Spirocyclic hypervalent iodine(III)-mediated radiofluorination of non-activated and hindered aromatics. *Nat. Commun.* 5 (1): 4365. <https://doi.org/10.1038/ncomms5365>.
 141. Jakobsson, J.E., Grønnevik, G., and Riss, P.J. (2017). Organocatalyst-assisted Ar–¹⁸F bond formation: a universal procedure for direct aromatic radiofluorination. *Chem. Commun.* 53 (96): 12906–12909. <https://doi.org/10.1039/C7CC07211B>.
 142. Rotstein, B.H., Wang, L., Liu, R.Y. et al. (2016). Mechanistic studies and radiofluorination of structurally diverse pharmaceuticals with spirocyclic Iodonium(III) ylides. *Chem. Sci.* 7 (7): 4407–4417. <https://doi.org/10.1039/C6SC00197A>.
 143. Calderwood, S., Collier, T.L., Gouverneur, V. et al. (2015). Synthesis of ¹⁸F-arenes from spirocyclic iodonium(III) ylides via continuous-flow microfluidics. *J. Fluorine Chem.* 178: 249–253. <https://doi.org/10.1016/J.JFLUCHEM.2015.08.006>.

144. Liang, S.H., Yokell, D.L., Jackson, R.N. et al. (2014). Microfluidic continuous-flow radiosynthesis of [¹⁸F]FPEB suitable for human PET imaging. *Med. Chem. Commun.* 5 (4): 432–435. <https://doi.org/10.1039/C3MD00335C>.
145. Stephenson, N.A., Holland, J.P., Kassenbrock, A. et al. (2015). Iodonium ylide-mediated radiofluorination of ¹⁸F-FPEB and validation for human use. *J. Nucl. Med.* 56 (3): 489–492. <https://doi.org/10.2967/jnumed.114.151332>.
146. Wang, L., Cheng, R., Fujinaga, M. et al. (2017). A facile radiolabeling of [¹⁸F]FDPA via spirocyclic iodonium ylides: preliminary PET imaging studies in preclinical models of neuroinflammation. *J. Med. Chem.* 60 (12): 5222–5227. <https://doi.org/10.1021/acs.jmedchem.7b00432>.
147. Kumata, K., Zhang, Y., Fujinaga, M. et al. (2018). [¹⁸F]DAA1106: automated radiosynthesis using spirocyclic iodonium ylide and preclinical evaluation for positron emission tomography imaging of translocator protein (18 kDa). *Bioorg. Med. Chem.* 26 (17): 4817–4822. <https://doi.org/10.1016/J.BMC.2018.08.017>.
148. Graskemper, J.W., Wang, B., Qin, L. et al. (2011). Unprecedented directing group ability of cyclophanes in arene fluorinations with diaryliodonium salts. *Org. Lett.* 13 (12): 3158–3161. <https://doi.org/10.1021/ol201080c>.
149. Gao, Z., Lim, Y.H., Tredwell, M. et al. (2012). Metal-free oxidative fluorination of phenols with [¹⁸F]fluoride. *Angew. Chem. Int. Ed.* 51 (27): 6733–6737. <https://doi.org/10.1002/anie.201201502>.
150. Buckingham, F., Calderwood, S., Checa, B. et al. (2015). Oxidative fluorination of N-arylsulfonamides. *J. Fluorine Chem.* 180: 33–39. <https://doi.org/10.1016/J.JFLUCHEM.2015.07.030>.
151. Ludwig, T., Ermert, J., and Coenen, H.H. (2002). 4-[¹⁸F]Fluoroarylkylethers via an improved synthesis of n.c.a. 4-[¹⁸F]fluorophenol. *Nucl. Med. Biol.* 29 (2): 255–262. [https://doi.org/10.1016/S0969-8051\(01\)00302-X](https://doi.org/10.1016/S0969-8051(01)00302-X).
152. Stoll, T., Ermert, J., Oya, S. et al. (2004). Application of n.c.a. 4-[¹⁸F]fluorophenol in diaryl ether syntheses of 2-(4-[¹⁸F]fluorophenoxy)-benzylamines. *J. Labelled Compd. Radiopharm.* 47 (7): 443–455. <https://doi.org/10.1002/jlcr.828>.
153. Watson, D.A., Su, M., Teverovskiy, G. et al. (2009). Formation of ArF from LPdAr(F): catalytic conversion of aryl triflates to aryl fluorides. *Science* 325 (5948): 1661–1664. <https://doi.org/10.1126/science.1178239>.
154. Lee, H.G., Milner, P.J., and Buchwald, S.L. (2013). An improved catalyst system for the Pd-catalyzed fluorination of (hetero)aryl Triflates. *Org. Lett.* 15 (21): 5602–5605. <https://doi.org/10.1021/ol402859k>.
155. Cardinale, J., Ermert, J., Kügler, F. et al. (2012). Carrier-effect on palladium-catalyzed, nucleophilic ¹⁸F-fluorination of aryl triflates. *J. Labelled Compd. Radiopharm.* 55 (12): 450–453. <https://doi.org/10.1002/jlcr.2973>.
156. Gouverneur, V. (2012). Flipping fluoride's reactivity. *Nat. Chem.* 4 (3): 152–154. <https://doi.org/10.1038/nchem.1280>.
157. Kamlet, A.S., Neumann, C.N., Lee, E. et al. (2013). Application of palladium-mediated ¹⁸F-fluorination to PET radiotracer development: overcoming hurdles to translation. Woloschak GE, editor. *PLoS One* 8 (3): e59187. <https://doi.org/10.1371/journal.pone.0059187>.

158. Lee, E., Hooker, J.M., and Ritter, T. (2012). Nickel-mediated oxidative fluorination for PET with aqueous [¹⁸F] fluoride. *J. Am. Chem. Soc.* 134 (42): 17456–17458. <https://doi.org/10.1021/ja3084797>.
159. Lee, E., Hooker, J.M., and Ritter, T. (2012). Nickel-mediated oxidative fluorination for PET with aqueous [¹⁸F] fluoride. *J. Am. Chem. Soc.* 134 (42): 17456–17458. <https://doi.org/10.1021/ja3084797>.
160. Campbell, M.G. and Ritter, T. (2014). Late-stage fluorination: from fundamentals to application. *Org. Process Res. Dev.* 18 (4): 474–480. <https://doi.org/10.1021/op400349g>.
161. Strebl, M.G., Campbell, A.J., Zhao, W.-N. et al. (2017). HDAC6 brain mapping with [¹⁸F]bavarostat enabled by a Ru-mediated deoxyfluorination. *ACS Cent. Sci.* 3 (9): 1006–1014. <https://doi.org/10.1021/acscentsci.7b00274>.
162. Beyzavi, M.H., Mandal, D., Strebl, M.G. et al. (2017). ¹⁸F-Deoxyfluorination of phenols via Ru π-complexes. *ACS Cent. Sci.* 3 (9): 944–948. <https://doi.org/10.1021/acscentsci.7b00195>.
163. Ichiishi, N., Canty, A.J., Yates, B.F. et al. (2013). Cu-catalyzed fluorination of diaryliodonium salts with KF. *Org. Lett.* 15 (19): 5134–5137. <https://doi.org/10.1021/ol4025716>.
164. Ye, Y. and Sanford, M.S. (2013). Mild copper-mediated fluorination of aryl stannanes and aryl trifluoroborates. *J. Am. Chem. Soc.* 135: 9. <https://doi.org/10.1021/ja400300g>.
165. Tredwell, M., Preshlock, S.M., Taylor, N.J. et al. (2014). A general copper-mediated nucleophilic ¹⁸F fluorination of arenes. *Angew. Chem. Int. Ed.* 53 (30): 7751–7755. <https://doi.org/10.1002/anie.201404436>.
166. Wilson, T.C., Cailly, T., and Gouverneur, V. (2018). Boron reagents for divergent radiochemistry. *Chem. Soc. Rev.* 47 (18): 6990–7005. <https://doi.org/10.1039/C8CS00499D>.
167. Mossine, A.V., Brooks, A.F., Makaravage, K.J. et al. (2015). Synthesis of [¹⁸F]arenes via the copper-mediated [¹⁸F]fluorination of boronic acids. *Org. Lett.* 17 (23): 5780–5783. <https://doi.org/10.1021/acs.orglett.5b02875>.
168. Makaravage, K.J., Brooks, A.F., Mossine, A.V. et al. (2016). Copper-mediated radiofluorination of arylstannanes with [¹⁸F]KF. *Org. Lett.* 18 (20): 5440–5443. <https://doi.org/10.1021/acs.orglett.6b02911>.
169. Taylor, N.J., Emer, E., Preshlock, S. et al. (2017). Derisking the Cu-mediated ¹⁸F-fluorination of heterocyclic positron emission tomography radioligands. *J. Am. Chem. Soc.* 139 (24): 8267–8276. <https://doi.org/10.1021/jacs.7b03131>.
170. Antuganov, D., Zykov, M., Timofeeva, K. et al. (2017). Effect of pyridine addition on the efficiency of copper-mediated radiofluorination of aryl pinacol boronates. *ChemistrySelect* 2 (26): 7909–7912. <https://doi.org/10.1002/slct.201701628>.
171. Antuganov, D., Zykov, M., Timofeev, V. et al. (2019). Copper-mediated radiofluorination of aryl pinacolboronate esters: a straightforward protocol by using pyridinium sulfonates. *Eur. J. Org. Chem.* 2019 (5): 918–922. <https://doi.org/10.1002/ejoc.201801514>.

172. Zischler, J., Kolks, N., Modemann, D. et al. (2017). Alcohol-enhanced Cu-mediated radiofluorination. *Chem. Eur. J.* 23 (14): 3251–3256. <https://doi.org/10.1002/chem.201604633>.
173. Zhang, X., Basuli, F., and Swenson, R.E. (2019). An azeotropic drying-free approach for copper-mediated radiofluorination without addition of base. *J. Labelled Compd. Radiopharm.* 62 (3): 139–145. <https://doi.org/10.1002/jlcr.3705>.
174. Petersen, I.N., Villadsen, J., Hansen, H.D. et al. (2017). ¹⁸F-labelling of electron rich iodonium ylides: application to the radiosynthesis of potential 5-HT_{2A} receptor PET ligands. *Org. Biomol. Chem.* 15 (20): 4351–4358. <https://doi.org/10.1039/C7OB00628D>.
175. Li, S., Cai, Z., Wu, X. et al. (2019). Synthesis and *in vivo* evaluation of a novel PET radiotracer for imaging of synaptic vesicle glycoprotein 2A (SV2A) in non-human primates. *ACS Chem. Neurosci.* 10 (3): 1544–1554. <https://doi.org/10.1021/acscemneuro.8b00526>.
176. Mossine, A.V., Tanzey, S.S., Brooks, A.F. et al. (2019). One-pot synthesis of high molar activity 6-[¹⁸F]fluoro-L-DOPA by Cu-mediated fluorination of a BPin precursor. *Org. Biomol. Chem.* 17 (38): 8701–8705. <https://doi.org/10.1039/C9OB01758E>.
177. Zarrad, F., Zlatopolskiy, B., Krapf, P. et al. (2017). A practical method for the preparation of ¹⁸F-labeled aromatic amino acids from nucleophilic [¹⁸F]fluoride and stannyl precursors for electrophilic radiohalogenation. *Molecules* 22 (12): 2231. <https://doi.org/10.3390/molecules22122231>.
178. Zlatopolskiy, B.D., Zischler, J., Schäfer, D. et al. (2018). Discovery of 7-[¹⁸F]fluorotryptophan as a novel positron emission tomography (PET) probe for the visualization of tryptophan metabolism *in vivo*. *J. Med. Chem.* 61 (1): 189–206. <https://doi.org/10.1021/acs.jmedchem.7b01245>.
179. Zhang, Z., Zhang, C., Lau, J. et al. (2016). One-step synthesis of 4-[¹⁸F]fluorobenzyltriphenylphosphonium cation for imaging with positron emission tomography. *J. Labelled Compd. Radiopharm.* 59 (11): 467–471. <https://doi.org/10.1002/jlcr.3436>.
180. Lien, V.T., Klaveness, J., and Olberg, D.E. (2018). One-step synthesis of [¹⁸F]cabozantinib for use in positron emission tomography imaging of c-met. *J. Labelled Compd. Radiopharm.* 61 (1): 11–17. <https://doi.org/10.1002/jlcr.3564>.
181. Bernard-Gauthier, V., Mossine, A.V., Mahringer, A. et al. (2018). Identification of [¹⁸F]TRACK, a fluorine-18-labeled tropomyosin receptor kinase (Trk) inhibitor for PET imaging. *J. Med. Chem.* 61 (4): 1737–1743. <https://doi.org/10.1021/acs.jmedchem.7b01607>.
182. Reischl, G., Kienzle, G.J., and Machulla, H.-J. (2002). Electrochemical radiofluorination: labeling of benzene with [¹⁸F]fluoride by nucleophilic substitution. *J. Radioanal. Nucl. Chem.* 254 (2): 409–411. <https://doi.org/10.1023/A:1021669126378>.
183. Reischl, G., Kienzle, G.J., and Machulla, H.-J. (2003). Electrochemical radiofluorination. Part 2. Anodic monofluorination of substituted benzenes using [¹⁸F]fluoride. *Appl. Radiat. Isot.* 58 (6): 679–683. [https://doi.org/10.1016/S0969-8043\(03\)00093-9](https://doi.org/10.1016/S0969-8043(03)00093-9).
184. Kienzle, G.J., Reischl, G., and Machulla, H.-J. (2005). Electrochemical radiofluorination. 3. Direct labeling of phenylalanine derivatives with [¹⁸F]fluoride after

- anodic oxidation. *J. Labelled Compd. Radiopharm.* 48 (4): 259–273. <https://doi.org/10.1002/jlcr.918>.
185. Truong, T., Klimovica, K., and Daugulis, O. (2013). Copper-catalyzed, directing group-assisted fluorination of arene and heteroarene C–H bonds. *J. Am. Chem. Soc.* 135 (25): 9342–9345. <https://doi.org/10.1021/ja4047125>.
 186. Knowles, S.M. and Wu, A.M. (2012). Advances in immuno-positron emission tomography: antibodies for molecular imaging in oncology. *J. Clin. Oncol.* 30 (31): 3884–3892. <https://doi.org/10.1200/JCO.2012.42.4887>.
 187. Gagnon, M.K.J., Hausner, S.H., Marik, J. et al. (2009). High-throughput *in vivo* screening of targeted molecular imaging agents. *Proc. Natl. Acad. Sci. U. S. A.* 106 (42): 17904–17909. <https://doi.org/10.1073/pnas.0906925106>.
 188. Marik, J. and Sutcliffe, J.L. (2006). Click for PET: rapid preparation of [¹⁸F]fluoropeptides using CuI catalyzed 1,3-dipolar cycloaddition. *Tetrahedron Lett.* 47 (37): 6681–6684. <https://doi.org/10.1016/J.TETLET.2006.06.176>.
 189. Wang, M., Yuan, Y., and Liang, G. (2012). “Click Chemistry” for molecular imaging. *Curr. Mol. Imaging* 1 (1): 87–95. <https://doi.org/10.2174/2211555211201010087>.
 190. Kettenbach, K., Schieferstein, H., and Ross, T.L. (2014). ¹⁸F-labeling using click cycloadditions. *Biomed Res. Int.* 2014: 361329. <https://doi.org/10.1155/2014/361329>.
 191. Choi, J.Y. and Lee, B.C. (2010). Click reaction: an applicable radiolabeling method for molecular imaging. *Nucl. Med. Mol. Imaging* 49 (4): 258–267. <https://doi.org/10.1007/s13139-015-0377-6>.
 192. Meyer, J.-P., Adumeau, P., Lewis, J.S. et al. (2016). Click chemistry and radiochemistry: the first 10 years. *Bioconjugate Chem.* 27 (12): 2791–2807. <https://doi.org/10.1021/acs.bioconjchem.6b00561>.
 193. Donnelly, D.J., Smith, R.A., Morin, P. et al. (2018). Synthesis and biologic evaluation of a novel ¹⁸F-labeled adnectin as a PET radioligand for imaging PD-L1 expression. *J. Nucl. Med.* 59 (3): 529–535. <https://doi.org/10.2967/jnumed.117.199596>.
 194. Keliher, E.J., Reiner, T., Thurber, G.M. et al. (2012). Efficient ¹⁸F-labeling of synthetic exendin-4 analogues for imaging Beta cells. *ChemistryOpen* 1 (4): 177–183. <https://doi.org/10.1002/open.201200014>.
 195. Selvaraj, R., Liu, S., Hassink, M. et al. (2011). Tetrazine-trans-cyclooctene ligation for the rapid construction of integrin $\alpha\beta 3$ targeted PET tracer based on a cyclic RGD peptide. *Bioorg. Med. Chem. Lett.* 21 (17): 5011–5014. <https://doi.org/10.1016/J.BMCL.2011.04.116>.
 196. Namavari, M., Padilla De Jesus, O., Cheng, Z. et al. (2008). Direct site-specific radiolabeling of an affibody protein with 4-[¹⁸F]fluorobenzaldehyde via oxime chemistry. *Mol. Imaging Biol.* 10 (4): 177–181. <https://doi.org/10.1007/s11307-008-0142-7>.
 197. Glaser, M., Iveson, P., Hoppmann, S. et al. (2013). Three methods for ¹⁸F labeling of the HER2-binding affibody molecule Z(HER2:2891) including pre-clinical assessment. *J. Nucl. Med.* 54 (11): 1981–1988. <https://doi.org/10.2967/jnumed.113.122465>.

198. Dirksen, A. and Dawson, P.E. (2008). Rapid oxime and hydrazone ligations with aromatic aldehydes for biomolecular labeling. *Bioconjugate Chem.* 19 (12): 2543–2548. <https://doi.org/10.1021/bc800310p>.
199. Cai, W., Zhang, X., Wu, Y. et al. (2006). A thiol-reactive ^{18}F -labeling agent, N-[2-(4- ^{18}F -fluorobenzamido)ethyl]maleimide, and synthesis of RGD peptide-based tracer for PET imaging of alpha v beta 3 integrin expression. *J. Nucl. Med.* 47 (7): 1172–1180. <https://jnm.snmjournals.org/content/47/7/1172.long>.
200. Li, Z., Cai, H., Hassink, M. et al. (2010). Tetrazine–trans-cyclooctene ligation for the rapid construction of ^{18}F labeled probes. *Chem. Commun.* 46 (42): 8043. <https://doi.org/10.1039/c0cc03078c>.
201. Meyer, J.-P., Houghton, J.L., Kozłowski, P. et al. (2016). ^{18}F -based pretargeted PET imaging based on bioorthogonal diels–alder click chemistry. *Bioconjugate Chem.* 27: 298–301. <https://doi.org/10.1021/acs.bioconjchem.5b00504>.
202. Schirmmayer, R., Bradtmöller, G., Schirmmayer, E. et al. (2006). ^{18}F -labeling of peptides by means of an organosilicon-based fluoride acceptor. *Angew. Chem. Int. Ed.* 45 (36): 6047–6050. <https://doi.org/10.1002/anie.200600795>.
203. Li, Y., Ting, R., Harwig, C.W. et al. (2011). Towards kit-like ^{18}F -labeling of Marimastat, a noncovalent inhibitor drug for *in vivo* PET imaging cancer associated matrix metalloproteases. *Medchemcomm* 2 (10): 942. <https://doi.org/10.1039/c1md00117e>.
204. McBride, W.J., Sharkey, R.M., Karacay, H. et al. (2009). A novel method of ^{18}F radiolabeling for PET. *J. Nucl. Med.* 50 (6): 991–998. <https://doi.org/10.2967/jnumed.108.060418>.
205. Inkster, J.A.H., Liu, K., Ait-Mohand, S. et al. (2012). Sulfonyl fluoride-based prosthetic compounds as potential ^{18}F labelling agents. *Chem. Eur. J.* 18 (35): 11079–11087. <https://doi.org/10.1002/chem.201103450>.
206. Wright, J. S., Kaur, T., Preshlock, S. et al. (2020). Copper-mediated late-stage radiofluorination: five years of impact on preclinical and clinical PET imaging. *Clin. Transl Imaging* 8 (3): 167–206. <https://doi.org/10.1007/s40336-020-00368-y>.

Chapter 9

Labeling with Gallium-68

Benjamin P. Burke and Stephen J. Archibald

*Positron Emission Tomography Research Centre, Department of
Biomedical Sciences, Faculty of Health Sciences, University of
Hull, Hull, HU6 7RX, UK*

9.1 INTRODUCTION

Gallium-68 has seen the largest growth in nuclear medicine usage of any isotope over the past 10 years. This is due to a combination of factors: the rise of PET/CT, the availability of the isotope (driven by the $^{68}\text{Ge}/^{68}\text{Ga}$ generator), the development of clinically desirable peptidic targeted agents, facile labeling processes, and the recognition of the potential in the theranostics market. Obtaining accurate ^{68}Ga positron emission tomography (**PET**) scan numbers is challenging, but based on generator sales, it can be estimated that over 200 000 scans are carried out annually worldwide (using the conservative figure of 100 scans per generator sold). Licensed ^{68}Ga -radiopharmaceuticals for targeting the somatostatin receptors (**SSTRs**) are now considered the clinical standard for imaging neuroendocrine tumors (**NETs**), and the prostate-specific membrane antigen (**PSMA**) ligands in development may shortly follow suit for prostate tumors. The likely future success of ^{68}Ga is built on the theranostic combination with ^{177}Lu , with more agents expected to transition into routine clinical practice over the coming years. The Society for Nuclear Medicine and Molecular Imaging (SNMMI) annual meeting has selected images with gallium-68 radiotracers as the "Image of the Year" for four out of the five years from 2015 to 2019, giving an accurate indication of the impact and level of interest in this isotope.

The short half-life ($t_{1/2} = 68$ minutes) and high percentage of radioactive decay by positron emission (88%) of ^{68}Ga are well suited to PET imaging, and whilst the positron energy is higher (max 1.9 MeV, mean 0.89 MeV) than for fluorine-18 (max 0.63 MeV, mean 0.25 MeV), the difference in image quality is marginal when using modern clinical PET

Handbook of Radiopharmaceuticals: Methodology and Applications, Second Edition.

Edited by Michael R. Kilbourn and Peter J.H. Scott.

© 2021 John Wiley & Sons Ltd. Published 2021 by John Wiley & Sons Ltd.

scanners [1–3]. The long-lived parent isotope, ^{68}Ge ($t_{1/2} = 271$ days), is generally produced on an accelerator with a natural gallium or gallium-containing target, prior to separation and incorporation onto a stationary phase for production of the $^{68}\text{Ge}/^{68}\text{Ga}$ generator. The use of $^{68}\text{Ge}/^{68}\text{Ga}$ generators (which can produce radioisotope for up to 12 months) allows for worldwide distribution and widespread use without the need for a cyclotron. When compared with routine clinically used cyclotron produced isotopes ($^{11}\text{C}/^{18}\text{F}$), the use of a ^{68}Ga generator offers some advantages. PET centers that do not have a cyclotron and rely on delivery of fluorine-18 tracers can introduce gallium-68 tracer production by a relatively simple modification of an existing technetium radiopharmacy suite [4]. If required to meet capacity demands, larger amounts of gallium-68 can be produced in a standard biomedical cyclotron using a solid target. Recently, production methods have been extended to solution targets, to allow cyclotron production of the isotope at sites that are not equipped to handle solid targetry. Overall, there are a number of models for the production of gallium-68 radiopharmaceuticals, adding to its potential utility.

The first major successes in this field were the ^{68}Ga -octreotide derivatives, which offer significantly increased diagnostic capability compared to the established ^{111}In derivatives used in clinical single-photon emission computed tomography (**SPECT**) imaging. This stimulated an increase in research activity due to the general applicability of peptide conjugates to many biological targets and diseases. Coupling this with the development of protocols improving the chemistry for radiolabeling to simplify tracer synthesis further adds to the future potential in this area. Cheaper and simpler protocols to access the tracers will drive down the at-patient costs and increase widespread availability, ensuring a bright future for gallium-68 PET imaging.

9.2 ISOTOPE PRODUCTION AND ITS EFFECT ON RADIOLABELING

There are two options used for ^{68}Ga production: by decay of ^{68}Ge ($t_{1/2} = 271$ days) in a generator, or from ^{68}Zn using a cyclotron. Over the past 20 years, there has been significant focus on the development of easy-to-use cGMP $^{68}\text{Ge}/^{68}\text{Ga}$ generators (*vide infra*); the majority of clinical ^{68}Ga imaging uses isotope produced by this method. Cyclotron-produced ^{68}Ga is a more recent development, driven by increasing demand for the isotope placing a strain on generator production capacity and the limit on the total amount of ^{68}Ga produced from each generator (some high-demand sites now have racks of generators in use at any one time).

The simplest way to produce ^{68}Ga on a cyclotron is by using a liquid target, as this does not require a change in infrastructure and is compatible with most cyclotron sites [5–8]. An amount of ^{68}Ga equivalent to the yield from one or two generators can be produced in around an hour (bombardment and separation). Standard synthesis units can be used for both processing of the feed from the cyclotron and synthesis of the radiotracer. There is potential corrosion from the use of concentrated acid, and care needs to be taken because the hot cell environment can contain radioactive gaseous waste, as ^{13}N compounds are a byproduct.

^{68}Ga can also be produced on a cyclotron using a solid target [9–11], with up to a 10-fold increase in the amount of ^{68}Ga produced in comparison with a generator. Irradiation times and separation chemistry are similar to using a liquid target, but with the increased practical complexities of handling the solid target. However, if a high-demand center is equipped to handle these challenges, the reward in terms of cost per dose will make this method viable. As with any cyclotron production, especially with metals, production of unwanted radiometal byproducts must be considered; with ^{68}Ga , the amount of the main contaminants, ^{66}Ga and ^{67}Ga , is inversely proportional to the isotopic purity of enriched ^{68}Zn target material [5, 9]. In addition, there are complexity considerations related to post-production isotope purification, which are not present with generator-produced ^{68}Ga .






$^{68}\text{Ge}/^{68}\text{Ga}$ generators provide isotope without the need for a cyclotron and can be incorporated into existing radiopharmacies with only minor facility modification. All modern generators can provide ionic ^{68}Ga in hydrochloric acid every few hours for up to a year. Whilst there may be some specific centers in which cyclotron-produced ^{68}Ga offers the best solution for routine clinical imaging (dependent on facility capability and clinical demand), the majority of centers will likely continue to use generator-produced isotope in the short term.

For radiolabeling, the characteristics of an ideal ^{68}Ga generator are:

- Low elution volume (high activity per volume)
- Low $[\text{H}]^+$ concentration (compatibility with direct kit synthesis or pre-purification)
- Low level of germanium-68 breakthrough
- Consistency of elution characteristics over the generator lifetime
- Low amount of metal ion contamination
- High isotope yield
- Simplicity of use
- Compatibility with licensed radiopharmaceuticals

Currently, five main $^{68}\text{Ge}/^{68}\text{Ga}$ generator products are being used globally (see Table 9.1). The most widely used generator – GalliaPharm, produced by Eckert & Ziegler (**EZAG**) – received marketing authorization in 2014. This was followed by the Galli Ad – produced by IRE ELiT – which received marketing authorization in 2018. The maximum generator size available is currently 50 mCi (1.85 GBq), although larger generators are currently in development. The level of breakthrough of ^{68}Ge has been one of the major limiting factors in gaining marketing authorization, so generators using TiO_2 -based columns are the only ones currently licensed. Ideally, ^{68}Ga will ultimately emulate $^{99\text{m}}\text{Tc}$, with the capability to use the generator eluate directly (for the lifetime of the generator) with a single-vial lyophilized kit to rapidly produce a radiotracer with high molar activity (i.e. both pre-purification and radiosynthesis using a synthesis module would become obsolete). To achieve this, the generator used must elute ^{68}Ga in a low volume of weak acid solution to be easily buffered; this eluate must maintain acceptable amounts

Table 9.1 Basic characteristics of the most common $^{68}\text{Ge}/^{68}\text{Ga}$ generators used globally.

	GalliaPharm – Eckert & Ziegler (EZAG)	iThemba Labs	Isotope Technologies Garching (ITG)	Galli Ad – IRE ELit	Obninsk
					
Column matrix	TiO ₂	SnO ₂	SiO ₂ /organic	TiO ₂	TiO ₂
Eluent	0.1 M HCl	0.6 M HCl	0.05 M HCl	0.1 M HCl	0.1 M HCl
Eluate volume	5 ml	6 ml	4 ml	1.1 ml	5 ml
Marketing	Europe, USA	—	—	Europe, USA	—
Authorization					
Key feature	Clinically established	Low cost	Metal-free	Low volume vacuum-based elution	Low cost

of ^{68}Ge breakthrough and low metal ion impurities across the generator life span. If any of these criteria are not met, a pre-purification step (*vide infra*) must be included, which increases the complexity of the radiosynthesis. Biodistribution dosimetry studies of ^{68}Ge in rats (with extrapolation to human) demonstrated that at least 16 mCi (600 MBq) can be administered before giving the patient an effective dose of 10 mSv [12]. A view on this issue posited by Irina Velikyan, and echoed here, is: "This amount exceeds the limit recommended by European Pharmacopoeia monographs (0.001%) by 35 000–50 000 times. These results imply that the $^{68}\text{Ge}(\text{IV})$ limit currently recommended by European Pharmacopoeia monograph could be increased at least 100 times without compromising patient safety" [13]. Increasing the limit for ^{68}Ge breakthrough would not cause a chemical problem for radiotracer synthesis because of the significant difference in coordination requirements for germanium(IV) compared to gallium(III). However, non-radioactive metal ion contamination, whilst not a realistic concern from a regulatory perspective (the limit of $10\ \mu\text{g GBq}^{-1}$ for iron and zinc in the European Pharmacopoeia monograph is high compared to what is observed in routine practice), even minor levels of contaminants can affect radiolabeling efficiency.

In a direct comparison, the eluate from both the SnO_2 (iThemba) and TiO_2 (EZAG) generators contains Fe, Cu, Mn, and Al ion levels in the 1–20 ppm range, making direct radiolabeling (without purification) more challenging; whereas the SiO_2 -based generator produced by Isotope Technologies Garching (ITG) has metal ion levels below 0.1 ppm [14]. DOTA-RGD₂ could be quantitatively radiolabeled at 20 μg levels after 15 minutes at 90 °C when using the eluate from a SiO_2 -based generator (ITG), whereas pre-purification was required to achieve quantitative radiolabeling when using the SnO_2 (iThemba) and TiO_2 (EZAG) generators. It should also be noted that titanium breakthrough from TiO_2 -based columns can often be significant and can interfere with radiolabeling, dependent on the chelator used [15, 16]. Green et al. used both the SiO_2 -based (ITG) and TiO_2 (EZAG) generators to make clinical doses of [^{68}Ga]Ga-DOTA-NOC over an extended period [17]. Radiolabeling can be carried out using the generator eluate from both generators; however, with the TiO_2 (EZAG) generator, more peptide (60 vs. 30 μg) was required for quantitative radiolabeling, and the elution had to be fractionated before use; the extent to which this should be a consideration depends on the required molar activity for imaging (*vide infra*). In a further study, the TiO_2 (EZAG) and SiO_2 -based (ITG) generators were compared with the eluate used for radiolabeling common chelators DOTA and NOTA [18]. At 5 μg at 95 °C, no difference was noted between the generators, whereas when the amount of chelator and/or temperature is decreased, the yield when using the TiO_2 (EZAG) generator decreases. Pre-purification of the eluate from the TiO_2 (EZAG) generator is required to mirror the yields achieved from the SiO_2 -based (ITG) generator without purification. Since the TiO_2 generator produced by IRE ELiT is a relatively new product, there have been no similar published studies to provide a relevant comparison. It could be assumed, given the column matrix is the same, that it should be similar to the TiO_2 (EZAG) generator. However, given the low elution volume and elution mechanism, fractionation would be more challenging, which may mean that any metal impurities (including ^{68}Ge) are concentrated in the 1.1 ml eluate. From a chemistry perspective, metal-free SiO_2 -based generators offer

the best compatibility with kit radiosynthesis, allowing for high-molar-activity tracers to be produced. However, at present, the only generators licensed for clinical use are TiO_2 based.

9.3 GALLIUM(III) CHEMISTRY AND GALLIUM-68 RADIOCHEMISTRY

Gallium is a group 13 p-block element with the electronic configuration $[\text{Ar}]3d^{10}4s^24p^1$. A full d-orbital makes the oxidation chemistry relatively simple, and whilst gallium(I) and gallium(II) exist, only gallium(III) is generally stable in aqueous solution. Gallium(III) has a small ionic radius with a high charge density and is classified as a hard Lewis acid, preferring to bind to non-polarizable hard Lewis bases, most commonly oxygen and nitrogen. The coordinating groups most often used for ^{68}Ga are amines, carboxylates, and phosphonates [19–22]. The bonding of gallium(III) is highly ionic and labile - requiring polydentate chelators, which relies on the chelate effect (i.e. five- and six-membered chelate rings) to ensure adequate stability. Gallium(III) forms complexes that are almost exclusively six-coordinate and have an octahedral geometry. Hence, linear, tripodal, and macrocyclic hexadentate (and higher) chelators are generally utilized.

Compared to other radioisotopes in nuclear medicine, ^{68}Ga poses an additional challenge for radiochemists in the form of hydroxide formation [23]. At low pH values (<3), gallium(III) is present in its ionic, or hexahydrate, form $[\text{Ga}(\text{H}_2\text{O})_6]^{3+}$. However, most chelators used in ^{68}Ga radiochemistry will protonate and be unusable at such a low pH. Above pH 7, soluble but unreactive $[\text{Ga}(\text{OH})_4]^-$ is exclusively present. To match chelator and isotope requirements, radiolabeling must be carried out in the pH range 3–7; however, in this range, other hydroxide species ($[\text{Ga}(\text{OH})]^{2+}$, $[\text{Ga}(\text{OH})_2]^+$, and $\text{Ga}(\text{OH})_3$) are present; see Figure 9.1 [24–26]. Whilst $\text{Ga}(\text{OH})_3$ is never the major species, it is practically the most important because of its low solubility; as $\text{Ga}(\text{OH})_3$ precipitates and is removed from solution, the equilibrium shifts, causing further $\text{Ga}(\text{OH})_3$ formation that also precipitates, to form colloidal species. $\text{Ga}(\text{OH})_3$ precipitation occurs under conditions that are the most amenable to common chelator radiolabeling conditions at pH 4–5 and increasing with temperature.

To make ^{68}Ga more available for subsequent reactions, an intermediate complex is often formed, which should be significantly more preferred than the formation of $\text{Ga}(\text{OH})_3$ but of low enough stability to allow the gallium(III) to be available for further reactions. The most common and effective of these “transfer reagents” are acetate, citrate, and 4-(2-hydroxyethyl)-1-piperazineethanesulfonic acid (HEPES), and most ^{68}Ga radiosynthesis is carried out using one of them *in situ* as part of the buffer medium [20, 23] – although there are strong reasons to avoid HEPES, where possible, from a regulatory perspective [27].

Citrate solutions are often used for instant thin-layer chromatography (ITLC) analysis of ^{68}Ga radiochemical reactions and give a clear indication of the amount of free gallium present; however, this technique is rarely able to distinguish between radiolabeled tracer

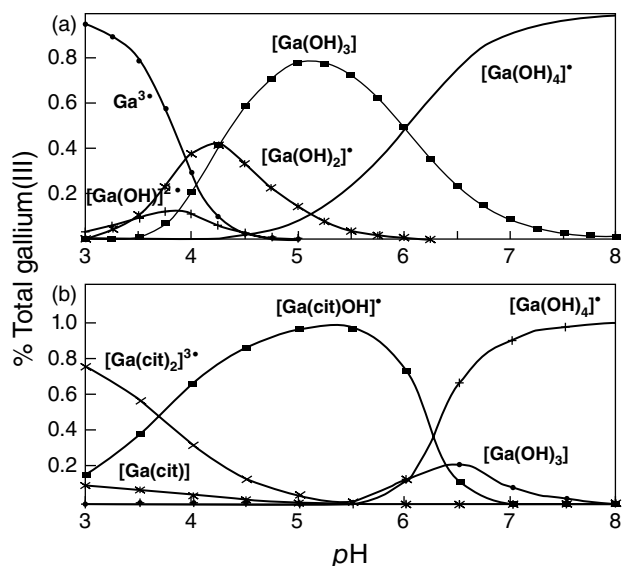


Figure 9.1 (a) Speciation of a 10^{-9} M Ga(III) aqueous solution. Source: Jackson, G.E. and Byrne, M.J. [24]. © 1996. SNMMI. (b) Speciation of a 10^{-9} M Ga(III) aqueous solution in the presence of 4×10^{-5} M citrate. Source: Jackson, G.E. and Byrne, M.J. © 1996. SNMMI.

and colloidal gallium. Therefore, an additional parallel iTLC method should be used to distinguish colloidal gallium, such as using a mobile phase of 1 M ammonium acetate in 50 : 50 methanol:water [15, 28]. A dual-TLC method, similar to that used routinely in technetium-99m radiopharmacies, should be exclusively adopted.

9.4 TRACER DESIGN AND CHELATOR CHOICE

To design an ideal chelator for ^{68}Ga , a range of criteria need to be met:

Fast radiolabeling

- Given the very short half-life of ^{68}Ga , radiolabeling within <10 minutes is essential. Longer radiosynthesis will limit the lifetime of the generator and the total number of patient doses that can be produced from one unit.

Quantitative (>95%) incorporation

- Purification can be time-consuming, adds complexity to any radiosynthetic procedure, and wastes valuable isotope, thus limiting practical utility.

Mild radiolabeling conditions

- The more efficient the radiolabeling of a chelator is at room temperature at an injectable pH (5–7), the better. Extremes of pH and/or temperature are often incompatible with conjugated biomolecules and lead to decomposition.

Low precursor concentration (high molar activity)

- Purification of radiolabeled tracer from excess starting material is time-consuming, often practically challenging, and may be incompatible with routine clinical production. Therefore, in practice, any unlabeled precursor will still be present on administration and will compete with the radiolabeled derivative, potentially blocking binding to the targeted proteins. Molar activity is expressed as the amount of radioactivity (Bq or Ci) bound per mole of biologically active molecule (mol) [29].

Metal ion selectivity

- If the chelator does not effectively discriminate from other metal cations (especially zinc(II), aluminum(III), and titanium(IV)), more precursor, time, or temperature will be required for radiolabeling, which can have a negative impact on one or more of synthesis time, process complexity, and molar activity.

Versatile and robust conjugation chemistry

- Conjugation of a bifunctional derivative of the chelator needs to be sufficiently robust to prevent cleavage of the ^{68}Ga complex from the biomolecule *in vivo*. A range of conjugation chemistries have been successfully carried out for both ^{68}Ga and other radiometals [30, 31].

High in vivo stability

- Upon administration, radiopharmaceuticals are in a challenging environment, at a very low concentration compared with potential competitors, such as other endogenous metal ions and biomolecules. Because of their chemical similarities, ^{68}Ga mimics iron(III) *in vivo*. Transferrin, the iron transport protein, has a high binding constant ($\log K = 20.3$) for gallium(III) [23], resulting in uptake in the liver and lungs. Therefore, chelators for ^{68}Ga are often designed to compete effectively with apo-transferrin for gallium binding. Complex stability measurements are usually carried out by competing apo-transferrin either directly, or in serum with the gallium-68 complex. Chelator stability is also often tested directly against excess competitor metal anions to ensure selectivity. However – given that *in vitro* experiments are carried out under idealized conditions using small volumes – high *in vitro* stability does not necessarily translate to *in vivo*, which must also be investigated [22]. It is important to consider that kinetic stability can be of high importance under these conditions and so should be taken in to account along with thermodynamic stability. This encourages the exploitation of hexadentate chelators and macrocycles.

The most common ^{68}Ga -radiopharmaceutical design is the conjugation of a bifunctional chelator (**BFC**) to a targeting vector – most often a small peptide [30]. In recent years, there have been a number of reviews of ^{68}Ga chelators, including recent developments, and a number of derivatives of each chelator have been designed to tune various properties (charge, lipophilicity, and functional group for conjugation) [19, 21, 22, 30]. Here, we focus on the most widely used chelators, principally those that have been taken through to clinical studies (see Figure 9.2). Each chelator is described, followed by a comparison of their relative properties.

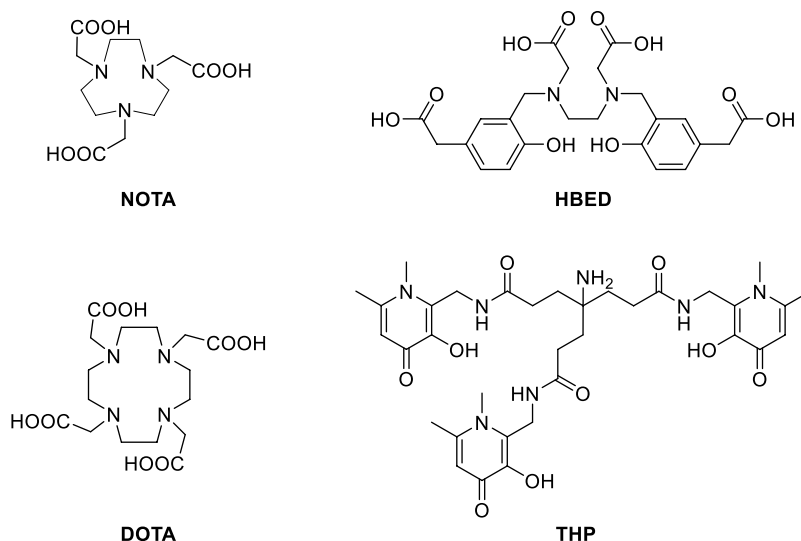


Figure 9.2
Chemical structures of common chelators used for ^{68}Ga radiolabeling.

9.4.1 NOTA: Chelator Characteristics

1,4,7-Triazacyclononane- N,N',N'' -triacetic acid (**NOTA**) is a macrocyclic chelator made from the triazamacrocycle 1,4,7-triazacyclononane (**TACN**) with acetate donors attached to the secondary amines. NOTA binds to gallium(III) with a N_3O_3 coordination sphere where the metal ion sits above the N_3 plane of the macrocycle with the acetate pendant arms wrapping around to form unstrained five-membered chelate rings. This gives a relatively high formation constant ($\log K_{\text{ML}}$) of 30.98 and high selectivity over other metal ions [32, 33]. Radiolabeling of NOTA with ^{68}Ga can be carried out at room temperature to form complexes that have high stability *in vivo* [34–36]. The only minor limitation for ^{68}Ga NOTA radiolabeling is the necessity for the reaction to be at slightly acidic pH (4–5), which may result in degradation of highly sensitive biomolecules; however, this is not usually a concern with peptide conjugates over the short radiolabeling time required (ca. 10 minutes) [15]. NOTA has three carboxylic acid groups that can be used for conjugation to the targeting moiety. However, sacrificing a carboxylate donor may reduce complex stability whilst modifying the overall charge, and so is not preferred. Using glutaric acid as a pendant arm on the TACN, rather than acetic acid, forms the 1,4,7-triazacyclononane-1-glutaric acid-4,7-acetic acid (NODAGA) chelator, which can be conjugated to a biomolecule without sacrificing the preferred donor atom set (due to the additional functional group on the pendant arm) and can increase the flexibility of the linker [37, 38]. Replacement of the carboxylic acid pendant arms with phosphonic and phosphinic acid groups has been carried out to form the chelators 1,4,7-triazacyclononane-1,4,7-tri(methylene phosphonic acid) (NOTP) and 3,3',3''-(((1,4,7-triazonane-1,4,7-triyl)tris(methylene)) tris(hydroxyphosphoryl))tripropanoic acid (TRAP), respectively, which can increase gallium(III) binding selectivity relative to other metal cations [39–44].

9.4.2 DOTA: Chelator Characteristics

1,4,7,10-Tetraazacyclododecane-1,4,7,10-tetraacetic acid (**DOTA**) is the most widely utilized general-purpose chelator, and a wide range of metals can adequately be chelated for nuclear imaging and radioisotope therapy applications (^{68}Ga , $^{64/67}\text{Cu}$, $^{44/47}\text{Sc}$, ^{111}In , ^{177}Lu , $^{86/90}\text{Y}$, ^{89}Zr , and ^{225}Ac , amongst others) [21, 30, 45, 46]. Whilst not optimal for all of these metal ions, the ability to accommodate a metal into the central macrocyclic cavity (smaller metal ions/6 coordinate geometry) or sitting above the N_4 plane of the macrocycle with the acetic acid pendant arms wrapping around (larger metal ions/octadentate) offers a useful compromise for multipurpose applications. This has resulted in it being the most widely used chelator for ^{68}Ga [28]. Crystal structures of Ga-DOTA complex show it has a N_4O_2 binding mode with steric strain in the macrocyclic backbone, as the central macrocyclic cavity size is slightly too large for the small ionic radius of gallium(III) [47]. The result of this is the relatively low formation constant of 21.33; with radiochemical reactions requiring elevated temperatures to quantitatively radiolabel at usable concentrations [48]. The labeling kinetics are slow as the metal ion needs to be located in the central cavity to form the stable complex. ^{68}Ga -DOTA complexes are generally accepted to have sufficient *in vivo* stability for most molecular imaging applications [30, 49, 50]. The DOTA binding mode leaves a free carboxylic acid group for conjugation to the targeting moiety, which also conveniently allows the formation of a neutral complex (three carboxylate groups balancing the charge of the gallium(III) ion). Hence, a BFC DOTA derivative is not required for gallium(III), simplifying the production of the conjugate. However, many derivatives of DOTA have been investigated, to either rigidify the backbone or provide alternate functional groups for specific conjugation reactions with biomolecules [45]. 1,4,7,10-Tetraazacyclododecane-1-(glutaric acid)-4,7,10-triacetic acid (DOTAGA) derivatives (analogous to the NODAGA derivatives) have become more popular to produce bioconjugate structures that retain the 8-coordinate binding mode for larger radiometals [51, 52]. Whilst this is not required for the 6-coordinate ^{68}Ga (although the additional negative charge can be used to influence biodistribution), it has started to replace DOTA when developing agents that can be radiolabeled with either ^{68}Ga and ^{177}Lu for matched-pair theranostics (*vide infra*) [46, 53].

9.4.3 HBED: Chelator Characteristics

N,N'-Bis(2-hydroxybenzyl)ethylenediamine-*N,N'*-diacetic acid (**HBED**) is an acyclic chelator developed from an ethylenediaminetetraacetic acid (**EDTA**) backbone with substituted phenol binding groups to give a high formation constant for gallium(III) of 38.51 [54]. Its most common derivative, *N,N'*-bis-[2-hydroxy-5-(carboxyethyl)benzyl]ethylenediamine-*N,N'*-diacetic acid (HBED-CC), has carboxylic acid groups that can be used for bioconjugation, and its acyclic nature lends itself to rapid kinetics of complex formation, even at room temperature [55]. HBED derivatives were not the main focus of initial research work to develop chelators for gallium-68 applications. However, its use in the design of the successful PSMA targeted tracer PSMA-11 indicated that it is fit for purpose as a

component of a radiotracer [56]. HBED is an average chelator for ^{68}Ga ; it does not have outstanding properties but has limited weaknesses. It can be radiolabeled rapidly at moderate concentrations at room temperature and is suitably stable for *in vivo* use. ^{68}Ga radiopharmaceuticals that use HBED as the BFC are present as a diastereomeric mixture that does not reach equilibrium when radiolabeling at room temperature [15, 56]. It must therefore be confirmed – for each tracer designed with this chelator – that this does not affect target binding, complex stability, and, ultimately, diagnostic ability. Historically, HBED was radiolabeled at elevated temperatures ($>90^\circ\text{C}$); however, there has been a shift recently to more routine synthesis at room temperature, especially in kit-radiosynthesis of [^{68}Ga]Ga-PSMA-11. These considerations should be taken into account when utilizing this chelator as a component in a radiopharmaceutical.

9.4.4 THP: Chelator Characteristics

Tris(hydroxypyridinone) (**THP**) is an acyclic chelator based on iron(III) chelating agents inspired by siderophores and contains three hydroxypyridinone units to provide an O_6 donor set. In contrast to the multipurpose DOTA, THP offers ideal characteristics for gallium(III) coordination. THP can be used to radiolabel biomolecules at room temperature at pH 6.5 almost instantaneously at low chelator concentrations, making its use ideal for kit radiolabeling of biomolecules, especially those that are sensitive to pH or temperature [15, 57–62].

9.4.5 Chelator Comparison

DOTA and HBED are the most commonly used chelators for ^{68}Ga : DOTA because of its success with SSTR-targeted agents, and ^{68}Ga -HBED because of its success with PSMA-11 (*vide infra*). Neither provides optimal coordination properties for ^{68}Ga , but both have been shown to be effective in the specific clinical situations to which they have been applied. They both have significant limitations, however, which may limit their utility in future applications. DOTA is not particularly selective for ^{68}Ga compared to other metal ions, so the resultant molar activity can be low, especially if generator eluate pre-purification is not carried out. DOTA requires heat for efficient radiolabeling, which limits its application to biomolecule conjugates that are not temperature sensitive. While HBED does not require heat for efficient kit radiolabeling without pre-purification, the formation of isomers – particularly an isomeric mixture that has not reached equilibrium – may cause problems in applications beyond PSMA-11, either through complex instability or variation in binding profile/pharmacokinetics between the two stereoisomers.

As neither DOTA nor HBED is ideal for ^{68}Ga , there has been significant ongoing research to develop optimized chelators that can be selectively radiolabeled at room temperature without pre-purification at low chelator concentration (to increase tracer molar activity), forming a complex that is stable *in vivo* and can be readily conjugated to biomolecules without dominating their characteristics. Both NOTA and THP can be radiolabeled with ^{68}Ga at room temperature at low chelator concentrations ($<5\ \mu\text{M}$), with

THP having the advantage of effective radiolabeling at pH 6.5 [15]. In direct competition studies, in which equimolar amounts of two chelators are combined and reacted with ^{68}Ga , THP showed >95% radiochemical yield when in competition with DOTA, NOTA, and HBED at room temperature at both pH 3.5 and 6.5.

The selection of a chelator when designing a novel bioconjugate depends on some key considerations:

- Is the targeting vector temperature or pH-sensitive?
- What is the commercial availability (and associated intellectual property) of the desired chelator?
- Should the synthesis ultimately be carried out in kit form? (At room temperature? In one step?)
- Is the design of an analogous sister therapeutic agent a key goal?
- How easily modifiable is the chelator or linking unit to modify the pharmacokinetic profile?

There is no one-size-fits-all chelator for all situations and applications.

Many other chelators have been developed or repurposed for ^{68}Ga radiolabeling; recent examples include the “DATA” compounds (that are carboxylate-substituted 6-amino-perhydro-1,4-diazepine (AAZTA) derivatives) [63–69], modified siderophores [70–73], and others [74–77]. The majority of these can be radiolabeled in mild conditions suitable for kit radiosynthesis and may be viable alternatives in radiopharmaceutical design. Of particular note is the recent translation of the hybrid chelator DATA into a clinical study as part of the room temperature single-vial kit in the form of DATA-TOC [78].

Attaching a chelator with ideal ^{68}Ga radiolabeling characteristics to a biomolecule known to bind to a target protein does not guarantee that a successful bioconjugate will be generated. Often, a range of related derivatives must be synthesized to optimize receptor binding *in vitro*. Linkers are usually introduced (with varying structures) to physically separate the binding unit from the chelator in an attempt to limit disruption to binding caused by the chelator. Relatively speaking, the introduction of a linker, chelator, and radiometal is a significant modification to the binding molecule/vector (in terms of molecular weight), which can cause a profound effect on binding. Therefore, once a targeting molecule has been identified for ^{68}Ga radiolabeling, the whole tracer should be designed iteratively rather than simply tagging a biomolecule, which can be effective for ^{18}F and ^{11}C radiolabeling strategies.

Additionally, if a bioconjugate is optimized *in vitro* for binding affinity, there is no guarantee that it will behave optimally *in vivo*. The selection of a lead compound based on binding affinity alone does not necessarily make the best tracer. Attaching a BFC (and often a linker) can have a profound impact on the *in vivo* pharmacokinetics, including biodistribution, target binding, and clearance. Hober and coworkers recently carried out a comprehensive preclinical chelator comparison study for imaging HER2 using a small protein [79], highlighting the key feature of variable clearance route and time when varying chelator/isotope combinations. Jain et al. compared

the biodistribution of three ^{68}Ga -labeled fatty acid derivatives with various chelators (diethylenetriaminepentaacetic acid (DTPA), NOTA, and NODAGA), observing that structurally similar tracers with similar molar activities and lipophilicities can behave very differently *in vivo*, likely because of variation of overall charge [80]. Significant differences were seen in uptake in target tissue (heart), blood clearance, and the level of hepatic clearance. The importance of chelator choice and linker design was demonstrated by the formation of two deferoxamine (DFO) conjugated PSMA derivatives and comparing them to PSMA-11 (PSMA-HBED-CC) [77]. Chelator replacement and linker modification caused dramatic changes in tumor uptake and clearance profile in preclinical studies. Importantly, the clearance profile was shown to correlate with both plasma protein binding and cellular dissociation constants, rather than lipophilicity. Baranski et al. modified the structure of PSMA-11 (PSMA-HBED-CC) by introducing varying numbers of amino acids in the linker [81]. This linker extension results in a significant modification of the biodistribution pattern when tested in preclinical studies, specifically by reducing uptake in dose-limiting organs whilst retaining tumor uptake levels. The lead tracer had similar tumor uptake whilst reducing spleen uptake from 17.88 ± 2.87 to $2.70 \pm 1.07 \text{ ID g}^{-1}$ and liver uptake from 139.44 ± 21.40 to $68.44 \pm 15.24 \text{ ID g}^{-1}$. Other structural modifications have also been carried out in an attempt to increase tumor-to-kidney ratios of PSMA analogs [82, 83].

In general, the most important properties that influence the *in vivo* profile of a radiotracer are charge and lipophilicity. The smaller the relative difference in size of the chelator to the binding unit, the larger the effect, with small molecules and peptides the most significantly perturbed. However, there are also examples in which large-molecular-weight biomolecules such as antibodies can be influenced by chelator attachment [20, 84], although in some applications, chelator modification or minor structural linker modifications have a more limited influence on the pharmacokinetic profile [70, 85–87]. It is important to note that varying only the metal center can also have an effect on the pharmacokinetics of the radiotracer, which can be very important in theranostic applications (*vide infra*) particularly if PET data is being used to calculate personalized dosimetry for therapeutic isotope administration.

9.5 PRACTICAL ASPECTS OF GALLIUM-68 RADIOLABELING

When ^{68}Ga first emerged into clinical use, cGMP radiosynthesis of novel unlicensed radiopharmaceuticals used flexible and programmable synthesis units that were designed for other radioisotopes [88]; they were not developed to handle the high reaction volumes from elution of $^{68}\text{Ge}/^{68}\text{Ga}$ generators (c. 5 ml). In addition, ^{68}Ge breakthrough levels in the generator elute were too high for administration, and other metal ions present in the eluate, including titanium(IV), aluminum(III), and zinc(II), can compete with ^{68}Ga for chelator binding and reduce radiolabeling efficiency. The simplest way to reduce the amount of ^{68}Ge and total volume is through fractionation, with 80% of the activity eluting in

the 1 ml fraction between 1.5 and 2.5 ml [89]. This method offers a workaround and has allowed radiopharmaceuticals to be synthesized for clinical studies (with the amount of ^{68}Ge breakthrough in the fraction used reduced by around 75%), but it does not solve the problem.

Meyer et al. proposed an ionic exchange method via the formation of $^{68}\text{Ga}[\text{GaCl}_4]^-$, allowing aqueous elution in a small volume [90]. However, the method is limited by the requirement for pre-dilution of the eluate, and the purification from other metal contaminants is not optimal. Zhernosekov et al. provided an elegant solution using a weak cation exchange cartridge to trap ^{68}Ga , followed by elution in a weak acid/acetone solution [91]. This can be used directly for radiolabeling or evaporated and reconstituted in aqueous buffer [92]. Introduction of cationic pre-purification allowed the full generator eluate to be used, the radioactivity to be concentrated, the acid concentration to be reduced, and most competing metal ions to be removed. All of these factors contribute to an increase in radiolabeling efficiency and dealing effectively with the issue of ^{68}Ge contamination.

Alternate eluent solutions were subsequently used to increase reactivity and/or biocompatibility. Eppard et al. replaced acetone with ethanol to elute purified ^{68}Ga from the cation exchange resin, to provide a more acceptable reaction mixture for the preparation and formulation of directly injectable ^{68}Ga -radiopharmaceuticals [93, 94]. Monolith technologies have more recently been developed for ethanol-based cationic ^{68}Ga purification, with lower elution volumes and acid concentrations required to achieve quantitative release [16]. These highly efficient, low-volume, small-size monolith columns allow integration of purification as part of a miniaturized lab-on-a-chip/microfluidic synthesis system, as they decrease backpressure in comparison to particle-packed columns.

Additionally, the presence of ethanol in ^{68}Ga radiosynthesis seems to improve reaction efficiency, even when compared with aqueous solutions, potentially via radiolysis stabilization by scavenging of free radicals [27, 95, 96]. Avoiding organic solvents entirely is also possible, with elution of the ion-exchange cartridge using a high-ionic-strength saline solution becoming a more widely used approach [97]. Alternatively, cation-exchange cartridge purification can also be combined with a subsequent anion cartridge step to release ^{68}Ga in a pure aqueous media [98], but this increases complexity.

Given the similarity to gallium(III), removal of iron(III) is challenging using pre-purification techniques, with amounts generally only reduced by an order of magnitude. Their chemical similarity also means chelators are often not particularly selective between these cations. Therefore, the easiest way to avoid iron(III) interfering with metal ion chelation is to ensure that its presence is limited in the first place. This can be achieved through generator design, quality of reagents used, and equipment used (spatulas, needles, etc. should be metal-free). The elution yield slowly decreases across the generator lifetime as the remaining ^{68}Ge decreases. A generator can be eluted multiple times daily, with the time allowed between elutions dictating subsequent yields. After one half-life (68 minutes), 50% of the activity can be eluted; 4 hours is required for >90% recovery. If the generator has been left without elution for a significant period (usually >48 hours), it is common practice to discard the first elution [27, 28]. A pre-elution is

sometimes carried out two to three hours before the first production elution to increase the reactivity of the subsequently eluted ^{68}Ga and increase molar activity of the product.

9.5.1 The Future of Pre-Purification in the Production of ^{68}Ga -Radiopharmaceuticals

Pre-purification of the ^{68}Ga eluate before radiosynthesis reduces volume, removes metal ion impurities, removes ^{68}Ge contamination, and decreases acid concentration (which can cause a problem in radiolabeling). However, ^{68}Ge breakthrough levels of current generators with marketing authorization are low enough for direct administration; synthesis units and kits have been developed to cope with the volume; and pre-purification is not required for the routine radiosynthesis of somatostatin and PSMA targeted imaging agents with adequate diagnostic performance (*vide infra*).

This leaves a question open regarding the future role of generator eluate processing. There are potential situations where pre-purification becomes more important, or even essential, for radiosynthesis:

- *Removal of metal ions: lowering of acid concentration and/or volume is required to produce a tracer with clinically useful diagnostic potential.* Purification of generator eluate increases the reactivity of ^{68}Ga with a chelator or bioconjugate, lowering the amount of precursor required for quantitative radiolabeling [16, 18]. Not carrying out pre-purification therefore limits the maximum molar activity of the produced tracers and restricts applications to those with high tissue receptor density [27, 99–102]. As recently discussed by Blower et al., molar activities of ^{111}In -based radiopharmaceuticals can be 50-fold higher than ^{68}Ga derivatives [28]. This needs to be addressed as a potential limitation to the expanding tracer portfolio and applicability to a wide range of clinical situations.
- *Reproducibility and robustness.* Radiolabeling using pre-purification (and using synthesis units) offers consistency, which is practically impossible without including this step. There is variability between generators in terms of acid concentration of eluate, ^{68}Ge breakthrough levels, volume, and metal ion contamination. There is also variability with the same generator over its lifetime (up to 12 months) and/or the amount of time that has passed since the previous elution. Pre-purification can take ^{68}Ga of variable quality and ensure that it is in a form that behaves consistently. Manufacturers of kit radiopharmaceuticals also have the challenge of developing kits that are compatible with the full range of clinically used generators (or cyclotron produced isotope), with variable volumes, acid concentrations, and contaminants. As options continue to diversify, there will be little point in developing a kit system that only works in an idealized situation or for a single generator.
- *Combining eluates from multiple generators.* Using pre-purification allows for multiple generators to feed a single production (by reducing volume and issues with contaminants). This is a situation that is becoming more important in routine clinical production as an increase in demand has resulted in the need to have multiple generators in use.

9.5.2 Synthesis Units vs. Kits

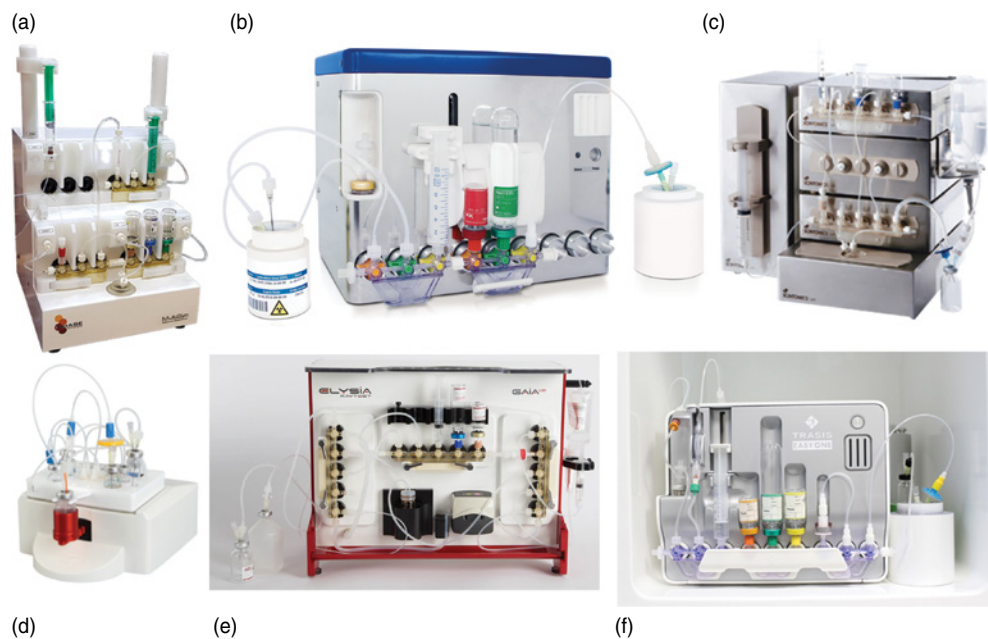
As ^{68}Ga -radiopharmaceuticals have become more popular, there have been significant changes in how they are produced clinically, moving on from manual radiosynthesis to flexible and programmable synthesis units for developmental and early clinical trials work [88]. As the synthesis of an increased range of standard radiopharmaceuticals was established for widespread use, there was a move to dedicated, user-friendly, cGMP-compliant synthesis units with single-use disposable cassettes for specific tracers. [1, 103]. A range of synthesis units are now marketed with disposable cassettes for individual tracers designed for ^{68}Ga (including those produced by iPHASE, ITM, Elysia-Raytest, Eckert and Ziegler, Scintomics, and Trasis), with varying features and flexibility (see Figure 9.3). More recently, there has been significant investment in the development of kit-based ^{68}Ga -radiopharmaceuticals in an attempt to emulate the simplicity and widespread success of $^{99\text{m}}\text{Tc}$ imaging agents, including examples that have received marketing authorization [78, 104–106].

The choice between using a synthesis unit, kits, or a combination of both depends on the specific goals of each center and the balance of routine clinical production vs. research. Overall, kits and synthesis units each have individual advantages and disadvantages, which are summarized in Table 9.2.

Production of kit-based ^{68}Ga -radiopharmaceuticals that have received marketing authorization is by far the easiest route to access these radiotracers. A traditional radiopharmacy can be retrofitted to produce ^{68}Ga products. The quality-control requirements

Figure 9.3

Common disposable cassette-based synthesis units used for ^{68}Ga radiolabeling. (a) Multisyn (iPHASE); Source: iPHASE Technologies. (b) iQS-Theranostics (ITM); Source: ITM Medical Isotopes GmbH (c) GRP2 (Scintomics); Source: Scintomics (d) Modular-Lab easy (Eckert & Ziegler); Source: Eckert & Ziegler (e) Gaia (Elysia-Raytest); Source: Elysia-Raytest (f) EASY ONE (Trasis). Source: Trasis.



Kits		Synthesis units	
Advantages	Disadvantages	Advantages	Disadvantages
<ul style="list-style-type: none"> • Simple • Less risk of contamination • Cheaper infrastructure • User dependent • Lower QC burden^a • Radiopharmacy compatible • Lower failure rate 	<ul style="list-style-type: none"> • Low flexibility • Radiation protection issues • Running costs^a • Limited molar activity • No pre-purification 	<ul style="list-style-type: none"> • Robust Flexibility • Pre-purification possible 	<ul style="list-style-type: none"> • Larger footprint • Initial cost • Longer time taken • Higher QC burden^a

^a Based on current kits with marketing authorization vs. unlicensed synthesis unit produced products.

for these products are also relatively simple and quick, with no major additional infrastructure required. This route, however, is very limiting and relies on future products all being kit-produced and gaining marketing approval before being introduced. The current products with marketing authorization are heated and two-step (addition of buffer to reaction vial); see Figure 9.4. There is significant interest in the development of single-vial room-temperature kit products, given their simplicity (*vide infra*). Production of unlicensed products (either kits moving toward authorization or products made on a synthesis unit) increases the quality-control requirements, both pre- and post-release. A center could transition from producing approved kit-based products to supporting the

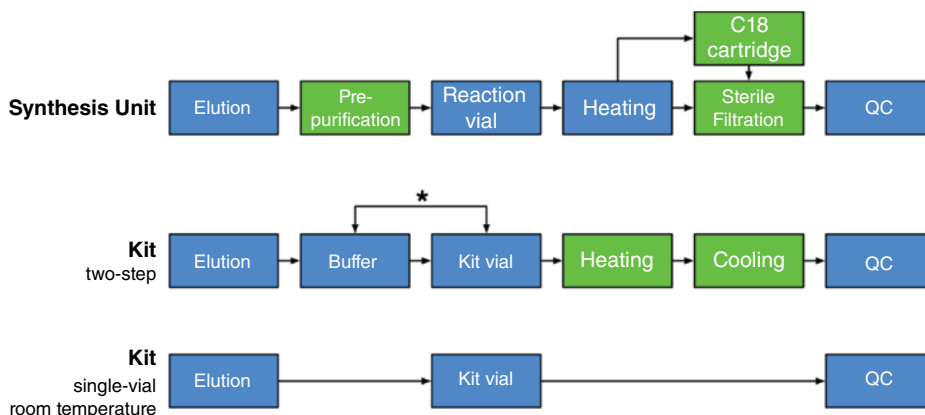


Figure 9.4 Steps for the production of ⁶⁸Ga-radio-pharmaceuticals (synthesis unit and kits).

Notes

- Inclusion is situation dependent
- ★ Order of addition is variable

development of unlicensed kits by ensuring that they have the required quality control (QC) equipment and adequate staffing levels to support this.

If there is a need to produce either first-in-human tracers or agents that have not yet been produced in kit form to support phase II/III clinical studies, the use of a synthesis unit is essential. Using a disposable cassette-based synthesis unit to produce ^{68}Ga -radiopharmaceuticals offers the best compromise between cGMP compliance and flexibility in the production of current and future tracers. In broad terms, ^{68}Ga synthesis procedures between different tracers are very similar, with only a limited number of variables to change: ligand amount, buffer type/amount, optional pre-purification, reaction temperature/time, and optional post-synthesis purification (see Figure 9.4). Hence, minor modification of automated step parameters is relatively simple, and facile modification of cassettes produced for other established tracers can be exploited. Using this approach, it is relatively easy to take a synthesis unit that is producing one tracer and modify it to produce a novel tracer for a first-in-human study, whilst remaining cGMP compliant.

One of the potential weaknesses of kit radiosynthesis compared to the use of synthesis units is the manual involvement of a human operator during synthesis: this has the potential to cause inconsistencies between users and can lead to radiation protection concerns for personnel in high-volume centers. Radiation protection may be a key consideration for routine ^{68}Ga -radiopharmaceutical production going forward and may have a significant influence on decisions for production methodologies selected. Facilities often underestimate the significance of high-energy positrons from ^{68}Ga (based on previous experiences with $^{99\text{m}}\text{Tc}$ or ^{18}F). For example, a 37 mCi (1 GBq) source of ^{68}Ga unshielded at 30 cm in a glass with 2 mm thickness (for example, in a kit) has a dose rate of 50 mSv h^{-1} – nearly 30-fold higher than ^{18}F and 250-fold higher than $^{99\text{m}}\text{Tc}$.

Recently, there has been some interest in automating kit radiosynthesis: for example, using the KitLab (Eckert and Ziegler, Germany) or MorGaNA (Tema Sinergie, Italy); see Figure 9.5. Such systems can integrate generator elution and be used to carry out kit radiosynthesis without manual manipulation; whilst both systems have their individual limitations, they may be appealing for high-throughput services. This blurring of the lines between kit radiosynthesis and automated synthesis units may lead to systems that allow

Figure 9.5

Integrated synthesis units. (a) KitLab (Eckert & Ziegler); Source: Eckert & Ziegler (b) MorGaNA (Tema Sinergie). Source: Tema Sinergie



for the re-inclusion of simple, disposable, pre-purification cartridges (if the quality of the clinical data can be improved by doing so). Alternatively, developers of a future ^{68}Ga -radiopharmaceutical may choose to market the product as a bespoke, integrated, simple automated kit/synthesis unit, which could include a pre-purification step and even quality control, giving hospitals a complete package for individual radiotracer production and analysis [16, 107–109].

9.6 CLINICAL TRACERS: DEVELOPMENT, RADIOSYNTHESIS, AND APPLICATIONS

The development of ^{68}Ga -radiopharmaceuticals is arguably the fastest-moving area in nuclear medicine, emerging from research studies 10 years ago to become the gold standard for some clinical situations. A detailed review of how ^{68}Ga -radiopharmaceuticals have been developed and their use in clinical practice (both current and potential future opportunities) is beyond the scope of this chapter. Herein, an overview of the key clinical ^{68}Ga -radiopharmaceuticals and their principal applications is given, followed by details of their respective radiosyntheses.

The recent increasing interest in ^{68}Ga is inextricably linked to the use of the beta emitter ^{177}Lu ($t_{1/2} = 6.7$ days) for radioligand therapy (**RLT**); which requires a targeting peptide that is coupled to a radioisotope emitting beta or alpha radiation that binds to specific receptors expressed on the surface of tumor cells. Matched-pair theranostics (in which ^{68}Ga PET is used for localization, characterization, staging, target identification, dosimetry, and treatment monitoring, and ^{177}Lu RLT is used for therapy) have prompted significant clinical interest in the past few years. $^{68}\text{Ga}/^{177}\text{Lu}$ theranostic combinations are central to the majority of ^{68}Ga -radiopharmaceuticals under development. The market interest in this area was demonstrated recently by Novartis' acquisition in 2018 of both Advanced Accelerator Applications (AAA) for \$3.9 billion (SomaKit TOC, NETSPOT, LUTATHERA) and Endocyte for \$2.1 billion ($[^{177}\text{Lu}]\text{LuPSMA-617}$).

9.6.1 Somatostatin Receptor (SSTRs) Targeting Radiotracers

Well-differentiated NETs often overexpress SSTRs on their cell surface [110, 111]. Targeting SSTRs for imaging has a long history, with ^{111}In -SPECT SSTR imaging one of the first examples of receptor-targeted peptide molecular imaging [112]. Octreoscan ($[^{111}\text{In}]\text{-DTPA-D-Phe1-octreotide}$, Curium Pharma) has been used clinically since the mid-1990s and was the first registered and commercially available radiometal-based peptide for imaging [1]. Imaging SSTRs can be used for disease staging and to influence treatment decisions, especially in selecting patients for SSTR peptide therapy [113, 114], or more recently for RLT. In 2001, $[^{68}\text{Ga}]\text{Ga-DOTA-TOC}$ was shown to have superior diagnostic capability compared to Octreoscan [49]; this led to a surge of research, which has resulted in the transition from ^{111}In SPECT to ^{68}Ga PET as the gold standard for imaging of NETs. This is

largely because of increased sensitivity, improved target-to-background contrast, and lower radiation dose [115, 116]. In addition, practical considerations also favor ^{68}Ga PET, with ^{111}In SPECT often requiring two scans on different days. Other peptides with slight modifications to the peptide sequence have subsequently been developed, notably DOTA-TATE and DOTA-NOC (see Figure 9.6) [117–119]. Peptide sequence modification causes a slight variation in the affinities for the various receptor subtypes; all three bind to SSTR2, whereas ^{68}Ga -DOTA-NOC also has a good affinity for SSTR3 and SSTR5; and ^{68}Ga -DOTA-TOC also binds SSTR5 (with a lower affinity than ^{68}Ga -DOTA-NOC), whereas ^{68}Ga -DOTA-TATE has a higher selectivity for SSTR2 [110, 120]. However, in practice, there is limited clinical evidence of differences in their diagnostic capability as SSTR2 expression is generally the most abundant on NETs relative to the other SSTRs. Individual affinity and specificity data for these and other SSTR-targeting radiopharmaceuticals have been summarized by Pauwels et al. [121].

In practice, all three tracers (TOC/TATE/NOC) are used routinely, and selection is more often governed by other factors, including local marketing authorization, commercial availability, tradition, individual clinician preference, and RLT considerations. This is borne out by the fact that in 2016, the Food and Drug Administration (FDA) approved NETSPOT (^{68}Ga -DOTA-TATE) and the European Commission approved SomaKit TOC (^{68}Ga -DOTA-TOC); both were commercialized by AAA (Saint-Genis-Pouilly, France), with the European market favoring the more established imaging product, whereas the US market approved the product with the same peptide as the subsequently approved ^{177}Lu -DOTA-TATE therapy [122–124]. LUTATHERA (^{177}Lu -DOTA-TATE) received European approval in 2017 and FDA approval in 2018 after the NETTER-1 trial demonstrated a significant effect, with progression-free survival at 65.2% at 20 months, compared to 10.8% for patients treated with high-dose peptide (see Figure 9.7) [125, 126].

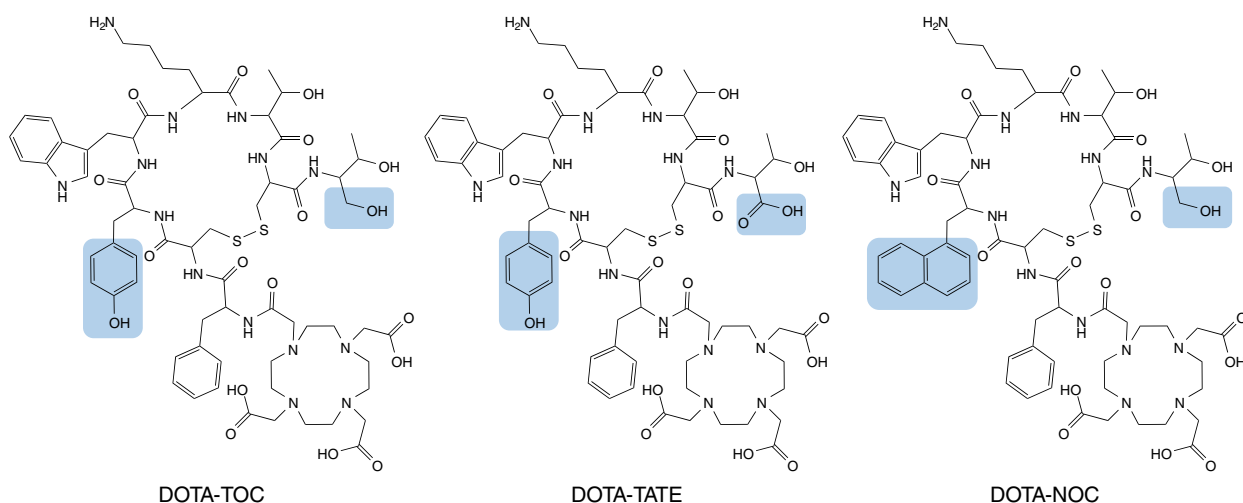


Figure 9.6 Chemical structures of common SSTR targeting ligands with structural differences highlighted.

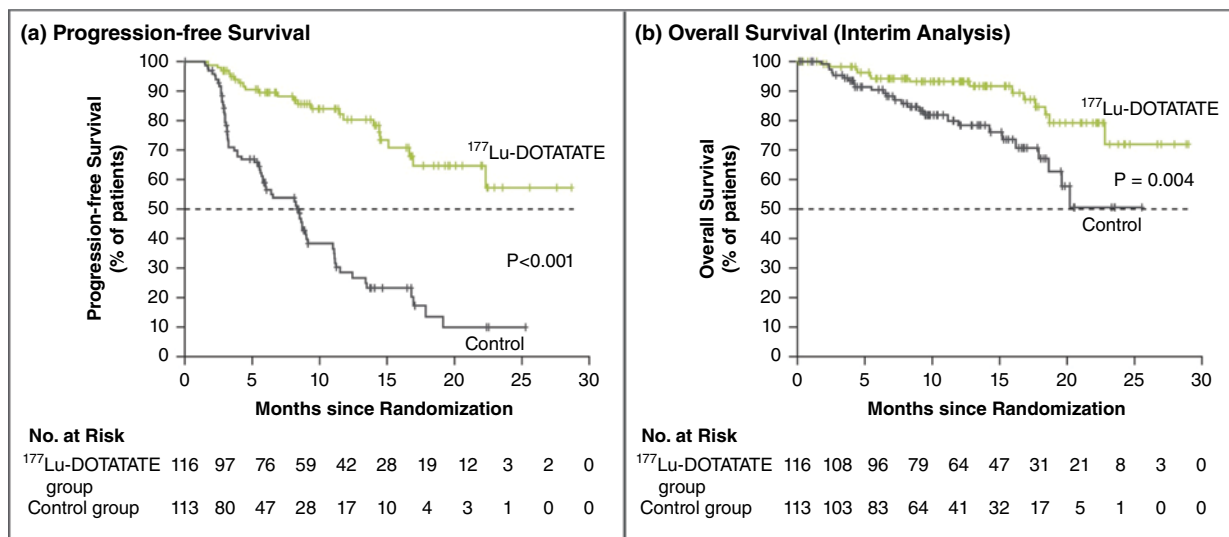


Figure 9.7 Interim analysis of NETTER-1 trial. (a) Kaplan–Meier analysis of progression-free survival. Source: Strosberg, J., El-Haddad, G., Wolin, E. et al. [125]. © 2017 Massachusetts Medical Society. (b) Overall survival. Source: Strosberg, J., El-Haddad, G., Wolin, E. et al. [125]. © 2017 Massachusetts Medical Society.

^{68}Ga]Ga-DOTA-TOC and ^{68}Ga]Ga-DOTA-TATE were commonly produced on synthesis units for a number of years and had become established tracers. Focus then switched to making production easier by moving away from synthesis units with the development of kit-based products – resulting in SomaKit TOC and NETSPOT reaching the market. Production in kit form allows for more widespread use, even in centers that had no experience of producing PET radiopharmaceuticals, as they could access the generator-produced isotope. Both products use DOTA as the chelator and therefore require heating (7 minutes at 95°C) to quantitatively radiolabel at a peptide amount ($40\ \mu\text{g}$) that is acceptable for administration.

When using kit ^{68}Ga radiopharmaceuticals, practical aspects for interfacing with the generator must be considered. For example, the radiolabeling of SomaKit TOC (^{68}Ga]Ga-DOTA-TOC) has been shown to be compatible with both the GalliaPharm (Eckert & Ziegler Radiopharma GmbH) and Galli Ad (IRE ELiT) generators. However, the differences in the generator elution mechanism mean a different setup is needed for radiolabeling. When using the Galli Ad generator, less buffer is used (because of the lower elution volume), water needs to be added (to keep the total reaction volume the same as with the GalliaPharm), and the reaction vial needs to be linked (in serial) to a secondary vacuum vial or pump (or transferred post-elution). In this case, use of the GalliaPharm generator is more straightforward, adding only buffer and eluting in to the reaction vial; however, it should be noted that this is a result of the design of SomaKit TOC for use with the GalliaPharm generator (before the Galli Ad received marketing authorization). Future kits will need to be compatible with all approved generators, or minor product variations marketed to map on to each generator.

^{68}Ga labeling of octreotide derivatives for PET imaging of SSTRs in NETs is the most established area in clinical ^{68}Ga radiopharmaceuticals, but it is still a highly active area of research [121]. There is significant interest in developing modified peptides that have a broader receptor affinity profile, to both increase tumor uptake and expand the range of tumors amenable to SSTR imaging. In addition, selective SSTR antagonists are being developed that do not internalize after receptor binding, with the theory that they would occupy more receptor sites than the agonists. This can result in higher overall tumor uptake. Given the success of SomaKit TOC and NETSPOT, and the desire for agents to be compatible with ^{177}Lu radiolabeling, any next-generation agents are likely to be DOTA-based and developed for production with a heated kit.

9.6.2 PSMA-Targeting Radiotracers

Prostate cancer is one of the most common cancers in men worldwide, with a reported 1.3 million new cases and 300 000 deaths in 2018 alone [127, 128]. Staging of disease has previously relied on morphologic visualization of tumor lesions using computed tomography (**CT**), magnetic resonance imaging (**MRI**), or bone scintigraphy. [^{18}F]2-Deoxy-2-fluoro-D-glucose ([^{18}F]FDG) has low uptake in most prostate cancer tumors; and choline derivatives ([^{11}C]choline, [^{18}F]fluoromethylcholine, and [^{18}F]fluoroethylcholine), although widely used, have limited accuracy in initial staging. Specific tumor localization in early biochemical recurrence is also very challenging using established methods [129, 130], especially in patients with “low” prostate-specific antigen (PSA) levels [131]; and whilst [^{18}F]fluciclovine (Axumin) has received approval, issues with specificity can result in false disease upstaging [132–134].

PSMA is a type II integral membrane glycoprotein that is significantly overexpressed in the majority of prostate cancers but has low expression in both benign tumors and non-target tissues, making it an ideal target for molecular imaging [128, 132]. PSMA-targeted radiopharmaceuticals can be used for initial staging, can identify patients for RLT, and give a more accurate indication of biochemical recurrence. Overall, this approach is key to the future of patient management in prostate cancer. PSMA-targeted radiopharmaceuticals are now preferred to [^{18}F]fluciclovine or choline derivatives for imaging patients with biochemical recurrence by the European Association of Urology [135].

A range of PSMA-targeted radiopharmaceuticals are being used in clinical practice (see Figure 9.8); and whilst at the time of writing, there are no PSMA-targeted radiopharmaceuticals with marketing authorization, the trial results published so far are exciting high levels of interest. There is no stand-out leader from the various agents available with regard to diagnostic and clinical utility, with the European Association of Nuclear Medicine (EANM) and SNMMI treating the three most common ^{68}Ga -PSMA agents ([^{68}Ga]Ga-PSMA-11, [^{68}Ga]Ga-PSMA-617, and [^{68}Ga]Ga-PSMA-I&T) as interchangeable [136]. Ultimately, the widespread use of one or more PSMA-targeted radiopharmaceuticals

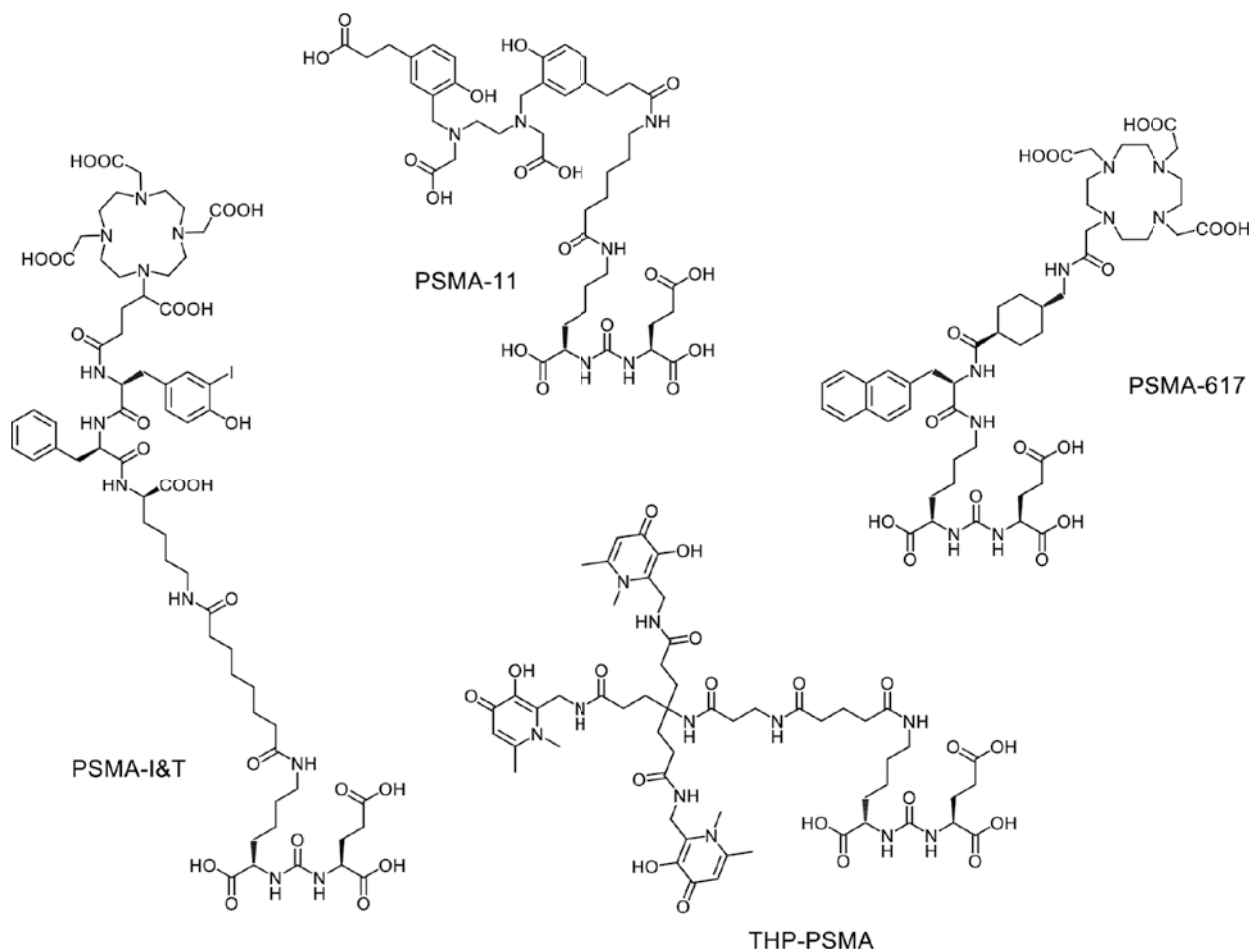


Figure 9.8 Chemical structures of common PSMA derivatives used for ^{68}Ga imaging.

or products is likely to be governed by factors other than diagnostic accuracy, including regulatory status, availability, price, simplicity of production, how well established the tracer is in clinical use, and availability of a therapeutic congener.

^{68}Ga]-PSMA-HBED-CC (^{68}Ga]-PSMA-11) is by far the most widely applied tracer in clinical practice, especially in Europe, with over 90% of ^{68}Ga -PSMA clinical trials using this tracer; it was first developed in 2012 by the Heidelberg group and rapidly translated to clinical studies [137, 138]. The peptide structure is also not covered by any patents, reducing barriers to widespread use. ^{68}Ga]-PSMA-11 incorporates HBED as a chelator, and most clinical studies are performed with tracer produced at elevated temperatures using a synthesis module. However, buoyed by the success of SSTR-targeted kit products, there has been significant interest in developing a PSMA kit. Advanced Nuclear

Medicine Ingredients (ANMI, now a Telix company) developed a kit for room temperature [^{68}Ga]Ga-PSMA-11 production (Illumet in the USA), in which the peptide and buffer are stored individually and mixed before adding to the gallium-68 and incubating at room temperature [139]. As mentioned previously, ^{68}Ga radiolabeling of HBED (as in [^{68}Ga]Ga-PSMA-11) forms multiple species (stereoisomers), which may have different complex stability, receptor affinity, and/or biodistribution [15, 140]. Radiolabeling at room temperature results in a more complex situation with the formation of the most thermodynamically stable isomer taking multiple hours or days [56]. Whilst this situation is chemically inelegant, concerns about individual aspects (stability, affinity, and/or biodistribution) can be rapidly alleviated if the diagnostic results are demonstrated to be adequate, especially if they are comparable with the well-established [^{68}Ga]Ga-PSMA-11 that is produced at elevated temperature. The presence of reversible stereoisomerisation is acknowledged in the draft European Monograph "Gallium (^{68}Ga) PSMA-11 Injection." Whilst a heated ^{68}Ga kit is practically much easier to use than a synthesis unit, room temperature kits are even more straightforward, with a decrease in synthesis time (especially for cooling) and elimination of additional practical cGMP considerations due to heating.

From the perspective of simplicity, there are clear advantages to having a single-vial, room temperature kit radiopharmaceutical. In addition to the reduction in production time and complexity, there is a lower risk of contamination, and fewer consumable items are required per production. Direct elution of licensed generators into a lyophilized reaction vial containing the required peptide, buffers, and stabilizers followed by rapid room temperature quantitative radiolabeling ready for administration is an optimally simplistic procedure. Isotopia (Israel) is developing a room temperature single-vial kit for [^{68}Ga]Ga-PSMA-11 production (IsoPROtrace-11), which uses less peptide (10 vs. 40 μg) than Illumet, therefore increasing molar activity. Theragnostics (UK) is also translating a room temperature single-vial kit (THP-PSMA) for ^{68}Ga PSMA imaging into clinical use and announced a global commercial partnership with GE Healthcare in late 2019. In this case, THP is used as the chelator [141–144], circumventing the issue of the formation of multiple species, and potentially avoiding the non-specific uptake seen with [^{68}Ga]Ga-PSMA-11 [145, 146]. However, given the disparity in the volume of clinical data compared to [^{68}Ga]Ga-PSMA-11, more work is required to confirm comparable diagnostic potential with similar flexibility for routine clinical use and variation in dose amounts.

DOTA-PSMA derivatives PSMA-617 and PSMA-I&T have also been developed for radiolabeling with ^{68}Ga for imaging and ^{177}Lu for therapy [53, 147–151]. Radiosynthesis using ^{68}Ga is routinely carried out using a synthesis unit; the inclusion of DOTA means any transition to kit form will likely require heated kits, similar to the licensed SSTR-targeted products. Both PSMA-617 and PSMA-I&T have shown significant promise in clinical therapeutic studies when radiolabeled with ^{177}Lu (see Figure 9.9) [153, 154]. The effectiveness of [^{177}Lu]Lu-PSMA-617 therapy is being evaluated in the VISION Study: an 80-institution, 750-participant, global phase 3 clinical trial in men with progressive metastatic castration-resistant prostate cancer.

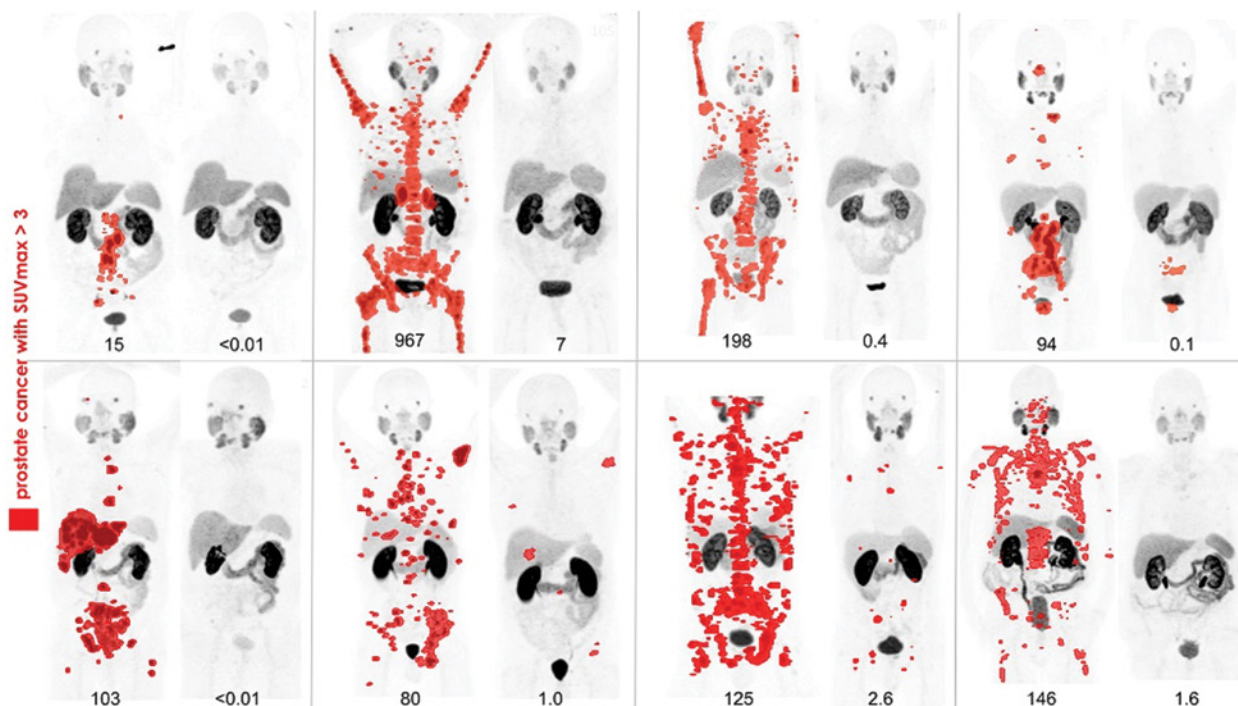


Figure 9.9 [^{68}Ga]Ga-PSMA-11 PET images at baseline (left) and three months after [^{177}Lu]Lu-PSMA-617 treatment of eight patients. Any disease with SUVmax >3 is shown in red. PSA values are given below each scan. SNMMI Image of the Year 2018. Source: SNMMI.

The clinical demand for PSMA-targeted tracers is high, and ^{68}Ga derivatives are desirable because of the accessibility of the generator-produced isotope and the potential for production in existing radiopharmacies, especially with the development of a single-vial room temperature kit. However, development in technology is moving rapidly, with other ^{68}Ga and ^{18}F derivatives (and even radiohybrids) being developed simultaneously which are likely to be viable alternatives to those presented here [128–130, 155–157]. $^{99\text{m}}\text{Tc}$ derivatives, although inferior, are still likely to be used in lower/middle income countries that have limited isotope and PET scanner access [158–160].

9.7 FUTURE PERSPECTIVES

9.7.1 General Development Areas

^{68}Ga radiopharmaceuticals have driven PET imaging forward and paved the way to exploit the huge potential of RLT. The longstanding promise of more personalized treatments and treatment stratification based on molecular imaging is now being realized. The pioneering path has been trodden by imaging NETs with targeting of SSTRs, demonstrating that accessible and routine imaging is possible, with the appetite for the new generation

of PSMA-targeted agents even greater. The development of further applications of ^{68}Ga radiopharmaceuticals is a highly active and fast-paced area, with many in clinical trials and most accompanied by a ^{177}Lu therapeutic sister product. The future of clinical ^{68}Ga will likely see a significant increase in global use, utilizing a wider range of radiopharmaceuticals that are produced by simplified methods, mirroring technetium-99m.

9.7.2 Advances in Kits and Tracer Production

The half-life of ^{68}Ga generally means radiopharmaceuticals must be produced on-site (and often for a single patient). However, the advent of simple kit radiolabeling, cyclotron-produced isotope, and a tracer with sufficient clinical demand makes it viable for distribution. A central location in a large metropolitan area could easily be used to serve multiple local hospitals. However, the dosimetry concerns for high-energy positron emitters are significantly exacerbated by increased activities resulting from cyclotron-produced activity, and this has to be taken into account to reduce operator doses when carrying out kit-based radiosyntheses. Once some of the key issues around kits have been resolved and optimal usage patterns established with regulators (combined with competition driving cost-effectiveness), the various models will be established for different types of centers. This will likely encompass centers that use solid targets for distribution, those that use solution targets for on-site supply of a range of gallium (and other) PET tracers, and dedicated gallium-68 radiopharmacies using generators. In all of these models, there is still a drive for better understanding of chelator use both for tracer design and to optimize labeling chemistry.

9.7.3 Chelator Library Impact on Labeling Chemistry

A fixed library of chelators are likely to be used in the future (particularly if the chelator is not subject to intellectual property). The relationship between linkers, chelator properties, and peptide will be used to predict and select combinations for optimal bio-distribution [161, 162]. The baseline understanding of the key chemical parameters and limitations on reactivity has been rapidly developed in recent years to give specific radiochemical knowledge for gallium-68 complex formation. Once this picture is complete, the development of the next-generation tracers will be streamlined.

9.7.4 Automation, Integration (Microfluidics), and Novel Chemical Processes (Pretargeted Click Reactions and Radiohybrids)

There are still significant opportunities for new technologies in both the simplification of new tracer development and the optimization of chemical labeling protocols. Microfluidic / lab-on-a-chip technology is ideal for radiochemical applications as chemical efficiency of the reaction is increased (mainly due to the high surface area of the channels), which can allow reactions to be driven to completion with lower amounts of

precursor, reduce labeling times, and/or reduce the temperature required [16, 163]. There has been a growing body of research applying this to radiometal reactions [16, 164, 165]. Multi-step processes can be incorporated into microfluidic chips; and, perhaps most importantly for ^{68}Ga tracers, there is the potential to miniaturize quality-control processes to also automate and reduce infrastructure requirements for this step. Disposable single-use devices can be developed from plastics and provide a good fit with more stringent regulatory requirements. Microfluidic chips have been developed to optimize key chemical processes such as click chemistry reactions with chelators [166]. Other innovative ways to increase chemical efficiency include emulsion-based labeling, which relies on the concentration of the reagents and orientation of substrates at the micellar surface to improve yields and reaction rates [167]. Specific chemical reactions and novel tracers are also being developed that improve currently used protocols and extend the use of gallium-68 to new applications.

There has been an increase in interest in imaging with antibody-based radioimmunotherapeutic agents, which are usually radiolabeled using isotopes with a longer half-life, particularly ^{89}Zr . The rise of ^{68}Ga use clinically may provide a more readily available source of isotope for PET antibody imaging by exploiting pre-targeted biorthogonal *in vivo* click to circumvent the disparity between their respective physical and biological half-lives [168]. The concept of a radiohybrid, introduced by Wester and coworkers, is an innovative way of maintaining identical properties with different isotope use. They have produced a molecular structure to target PSMA that incorporates both fluorine and gallium atoms, where the tracer can be labeled with either fluorine-18 or gallium-68 (with the other element present in its stable form) [156, 169]. This concept is likely to be extended and could improve consistency in the interpretation of PET scans with different isotopes. It also links well to opportunities in the use of therapeutic isotopes.

9.7.5 Therapeutic Isotope Congeners and Dosimetry

There is a desire for radioisotope therapies utilizing the same peptide precursor as ^{68}Ga for imaging (including dosimetry planning), switching, for example, to ^{177}Lu for therapy (e.g. NETSPOT and LUTATHERA); however, this approach is not currently compatible with the move toward single-vial room temperature ^{68}Ga kits. This point needs careful consideration, and there are opposing viewpoints. If ^{68}Ga imaging is used for staging, target identification, and therapy monitoring, then an alternate agent can be used for therapy. There is interest in using ^{68}Ga agents to calculate personalized ^{177}Lu lesion dosimetry, although the disparity in half-lives makes it inherently challenging, and as yet, the clinical benefit of this process is not well established (and the cost may be prohibitive for routine use). A key issue is the assumption that ^{68}Ga and ^{177}Lu radiolabeled versions of the same precursor have the same biodistribution and uptake in tumors, which is unverified [170, 171], and these parameters may not be sufficiently similar for accurate personalized dosimetry. If personalized dosimetry is important for successful (and even curative) RLT, as has been suggested recently [172, 173], and the related ^{68}Ga agent is not available or suitable, the ^{68}Ga radiopharmaceutical used for imaging could be selected

on cost, production simplicity, and imaging characteristics. This could potentially be followed by (or used simultaneously with) low-dose ^{177}Lu SPECT imaging for accurate dosimetry calculations prior to RLT. It is also worth noting that, whilst the main current interest is in the theranostic pairing of ^{68}Ga with ^{177}Lu , the use of alpha-emitting isotopes may be advantageous, with ^{225}Ac being the current leading candidate [174–176].

ACKNOWLEDGMENTS

The authors would like to thank representatives of the following companies for their engagement during the writing of this chapter: Eckert and Ziegler (Germany), IRE ELiT (Belgium), iThemba Labs (South Africa), Imaging Equipment Ltd. (UK), Telix Pharmaceuticals (Australia), Isotopia (Israel), Theragnostics (UK), and Curium Pharma (France). Other companies were approached for comment. The authors would also like to thank Stefano Boschi (University of Bologna, Italy) for his valuable and interesting conversations.

REFERENCES

1. Martiniova, L., Palatis, L.D., Etchebehere, E., and Ravizzini, G. (2016). *Curr. Radiopharm.* 9: 187–207.
2. Velikyan, I. (2011). *Med. Chem.* 7: 345–379.
3. Brandt, M., Cardinale, J., Aulsebrook, M.L. et al. (2018). *J. Nucl. Med.* 59: 1500–1506.
4. Maecke, H.R. and Andre, J.P. (2007). Ga-68-PET radiopharmacy: A generator-based alternative to F-18-radiopharmacy. In: *PET Chemistry: The Driving Force in Molecular Imaging*, vol. 62 (eds. P.A. Schubiger, L. Lehmann and M. Friebe), 215–242. Springer-Verlag.
5. Riga, S., Cicoria, G., Pancaldi, D. et al. (2018). *Phys. Med.* 55: 116–126.
6. Pandey, M.K. and Degrado, T.R. (2018). Rapid isolation of cyclotron-produced gallium-68. International patent WO2018039662A1.
7. Alves, F., Alves, V.H.P., Do Carmo, S.J.C. et al. (2017). *Mod. Phys. Lett. A* 32: 1740013.
8. Degrado, T.R., Pandey, M.K., and Byrne, J. 2015. Solution target for cyclotron production of radiometals. International patent WO2015175972A2.
9. Lin, M., Waligorski, G.J., and Lepera, C.G. (2018). *Appl. Radiat. Isot.* 133: 1–3.
10. Abbasi, A.A. and Easwaramoorthy, B.. 2016. Method and system for producing gallium-68 radioisotope by solid targeting in a cyclotron. International patent WO2016197084A1.
11. Zeisler, S. and Olsson, J.O.O. 2019. System, apparatus and method for producing gallium radioisotopes on particle accelerators using solid targets International patent WO2019023787A1.
12. Velikyan, I., Antoni, G., Sørensen, J., and Estrada, S. (2013). *Am. J. Nucl. Med. Mol. Imaging* 3: 154–165.
13. Velikyan, I. (2015). *J. Labelled Compd. Radiopharm.* 58: 99–121.
14. Chakravarty, R., Chakraborty, S., Ram, R. et al. (2016). *J. Labelled Compd. Radiopharm.* 59: 87–94.

15. Tsionou, M.I., Knapp, C.E., Foley, C.A. et al. (2017). *RSC Adv.* 7: 49586–49599.
16. He, P., Burke, B.P., Clemente, G.S. et al. (2016). *React. Chem. Eng.* 1: 361–365.
17. Green, M.A., Mathias, C.J., and Fletcher, J.W. (2016). *Appl. Radiat. Isot.* 116: 63–68.
18. Amor-Coarasa, A., Gruca, M., Hurez, S. et al. (2018). *J. Radioanal. Nucl. Chem. Art.* 317: 1485–1490.
19. Burke, B.P., Clemente, G.S., and Archibald, S.J. (2014). *J. Labelled Compd. Radiopharm.* 57: 239–243.
20. Bartholoma, M.D. (2012). *Inorg. Chim. Acta* 389: 36–51.
21. Price, T.W., Greenman, J., and Stasiuk, G.J. (2016). *Dalton Trans.* 45: 15702–15724.
22. Spang, P., Herrmann, C., and Roesch, F. (2016). *Semin. Nucl. Med.* 46: 373–394.
23. McInnes, L.E., Rudd, S.E., and Donnelly, P.S. (2017). *Coord. Chem. Rev.* 352: 499–516.
24. Jackson, G.E. and Byrne, M.J. (1996). *J. Nucl. Med.* 37: 379–386.
25. Green, M.A. and Welch, M.J. (1989). *Nucl. Med. Biol.* 16: 435.
26. Moerlein, S.M. and Welch, M.J. (1981). *Int. J. Nucl. Med. Biol.* 8: 277–287.
27. Velikyan, I. (2015). *Molecules* 20: 12913–12943.
28. Blower, J.E., Cooper, M.S., Imberti, C. et al. (2019). The radiopharmaceutical chemistry of the radionuclides of gallium and indium. In: *Radiopharmaceutical Chemistry* (eds. J.S. Lewis, A.D. Windhorst and B.M. Zeglis), 255–271. Cham: Springer International Publishing.
29. Coenen, H.H., Gee, A.D., Adam, M. et al. (2017). *Nucl. Med. Biol.* 55: V–XI.
30. Price, E.W. and Orvig, C. (2014). *Chem. Soc. Rev.* 43: 260–290.
31. Ramogida, C.F. and Orvig, C. (2013). *Chem. Commun.* 49: 4720–4739.
32. Wadas, T.J., Wong, E.H., Weisman, G.R., and Anderson, C.J. (2010). *Chem. Rev.* 110: 2858–2902.
33. Chakravarty, R., Chakraborty, S., Dash, A., and Pillai, M.R.A. (2013). *Nucl. Med. Biol.* 40: 197–205.
34. Knetsch, P.A., Petrik, M., Griessinger, C.M. et al. (2011). *Eur. J. Nucl. Med. Mol. Imaging* 38: 1303–1312.
35. Lang, L.X., Li, W.H., Guo, N. et al. (2011). *Bioconjugate Chem.* 22: 2415–2422.
36. Liu, Z.F., Niu, G., Wang, F., and Chen, X.Y. (2009). *Eur. J. Nucl. Med. Mol. Imaging* 36: 1483–1494.
37. Eisenwiener, K.P., Prata, M.I.M., Buschmann, I. et al. (2002). *Bioconjugate Chem.* 13: 530–541.
38. Cox, J.P.L., Craig, A.S., Helps, I.M. et al. (1990). *J. Chem. Soc., Perkin Trans. 1:* 2567–2576.
39. Notni, J., Hermann, P., Havlickova, J. et al. (2010). *Chem. Eur. J.* 16: 7174–7185.
40. Notni, J., Pohle, K., and Wester, H.J. (2012). *EJNMMI Res.* 2: 28.
41. Notni, J., Pohle, K., and Wester, H.J. (2013). *Nucl. Med. Biol.* 40: 33–41.
42. Notni, J., Simecek, J., Hermann, P., and Wester, H.J. (2011). *Chem. Eur. J.* 17: 14718–14722.
43. Mate, G., Simecek, J., Pniok, M. et al. (2015). *Molecules* 20: 13112–13126.
44. Gai, Y., Sun, L., Lan, X. et al. (2018). *Bioconjugate Chem.* 29: 3483–3494.
45. Stasiuk, G.J. and Long, N.J. (2013). *Chem. Commun.* 49: 2732–2746.

46. Kelly, J.M., Amor-Coarasa, A., Williams, C. Jr. et al. (2017). *Nucl. Med. Biol.* 55: 38–46.
47. Viola, N.A., Rarig, R.S., Ouellette, W., and Doyle, R.P. (2006). *Polyhedron* 25: 3457–3462.
48. Sun, Y.Z., Anderson, C.J., Pajeau, T.S. et al. (1996). *J. Med. Chem.* 39: 458–470.
49. Hofmann, M., Maecke, H., Borner, A.R. et al. (2001). *Eur. J. Nucl. Med.* 28: 1751–1757.
50. Gabriel, M., Decristoforo, C., Kendler, D. et al. (2007). *J. Nucl. Med.* 48: 508–518.
51. Weineisen, M., Simecek, J., Schottelius, M. et al. (2014). *EJNMMI Res.* 4: 63.
52. Bernhard, C., Moreau, M., Lhenry, D. et al. (2012). *Chem. Eur. J.* 18: 7834–7841.
53. Weineisen, M., Schottelius, M., Simecek, J. et al. (2015). *J. Nucl. Med.* 56: 1169–1176.
54. Ma, R., Motekaitis, R.J., and Martell, A.E. (1994). *Inorg. Chim. Acta* 224: 151–155.
55. Eder, M., Wangler, B., Knackmuss, S. et al. (2008). *Eur. J. Nucl. Med. Mol. Imaging* 35: 1878–1886.
56. Eder, M., Neels, O., Muller, M. et al. (2014). *Pharmaceuticals* 7: 779–796.
57. Berry, D.J., Ma, Y.M., Ballinger, J.R. et al. (2011). *Chem. Commun.* 47: 7068–7070.
58. Ma, M.T., Cullinane, C., Waldeck, K. et al. (2015). *EJNMMI Res.* 5: 52.
59. Ma, M.T., Cullinane, C., Imberti, C. et al. (2016). *Bioconjugate Chem.* 27: 309–318.
60. Cusnir, R., Imberti, C., Hider, R.C. et al. (2017). *Int. J. Mol. Sci.* 18: 116.
61. Nawaz, S., Mullen, G.E.D., Sunassee, K. et al. (2017). *EJNMMI Res.* 7: 86.
62. Imberti, C., Chen, Y.-L., Foley, C.A. et al. (2019). *Dalton Trans.* 48: 4299–4313.
63. Farkas, E., Nagel, J., Waldron, B.P. et al. (2017). *Chem. Eur. J.* 23: 10358–10371.
64. Nock, B.A., Kaloudi, A., Nagel, J. et al. (2017). *Dalton Trans.* 46: 14584–14590.
65. Pfister, J., Summer, D., Rangger, C. et al. (2015). *EJNMMI Res.* 5: 74.
66. Vagner, A., D’Alessandria, C., Gambino, G. et al. (2016). *ChemistrySelect* 1: 163–171.
67. Seemann, J., Waldron, B.P., Roesch, F., and Parker, D. (2015). *ChemMedChem* 10: 1019–1026.
68. Seemann, J., Eppard, E., Waldron, B.P. et al. (2015). *Appl. Radiat. Isot.* 98: 54–59.
69. Waldron, B.P., Parker, D., Burchardt, C. et al. (2013). *Chem. Commun.* 49: 579–581.
70. Petrik, M., Novy, Z., Zhai, C. et al. (2016). *Mol. Imaging Biol.* 18: 344–352.
71. Summer, D., Grossrubatscher, L., Rangger, C. et al. (2017). *Bioconjugate Chem.* 28: 1722–1733.
72. Zhai, C., Summer, D., Rangger, C. et al. (2015). *J. Labelled Compd. Radiopharm.* 58: 209–214.
73. Knetsch, P.A., Zhai, C.Y., Rangger, C. et al. (2015). *Nucl. Med. Biol.* 42: 115–122.
74. Lappchen, T., Holland, J.P., Kiefer, Y. et al. (2018). *EJNMMI Radiopharm. Chem.* 3: 6.
75. Lappchen, T., Kiefer, Y., Holland, J.P., and Bartholoma, M.D. (2018). *Nucl. Med. Biol.* 60: 45–54.
76. Price, T.W., Gallo, J., Kubicek, V. et al. (2017). *Dalton Trans.* 46: 16973–16982.
77. Gourni, E., Del Pozzo, L., Bartholoma, M. et al. (2017). *Mol. Imaging* 16 <https://doi.org/10.1177/1536012117737010>.
78. Sinnes, J.P., Nagel, J., Waldron, B.P. et al. (2019). *EJNMMI Res.* 9: 48.
79. von Witting, E., Garousi, J., Lindbo, S. et al. (2019). *Eur. J. Pharm. Biopharm.* 140: 109–120.

80. Jain, A., Mathur, A., Pandey, U. et al. (2016). *Bioorg. Med. Chem. Lett.* 26: 5785–5791.
81. Baranski, A.-C., Schaefer, M., Bauder-Wuest, U. et al. (2017). *Bioconjugate Chem.* 28: 2485–2492.
82. Kuo, H.-T., Pan, J., Zhang, Z. et al. (2018). *Mol. Pharmaceutics* 15: 3502–3511.
83. Moon, S.-H., Hong, M.K., Kim, Y.J. et al. (2018). *Bioorg. Med. Chem.* 26: 2501–2507.
84. Dearling, J.L.J., Voss, S.D., Dunning, P. et al. (2011). *Nucl. Med. Biol.* 38: 29–38.
85. Jain, A., Pandey, U., Gamre, N. et al. (2017). *J. Radioanal. Nucl. Chem. Art.* 313: 661–668.
86. Guleria, M., Das, T., Amirdhanayagam, J. et al. (2018). *Cancer Biother. Radiopharm.* 33: 8–16.
87. Satpati, D., Sharma, R., Sarma, H.D., and Dash, A. (2018). *Chem. Biol. Drug Des.* 91: 781–788.
88. Boschi, S., Lodi, F., Malizia, C. et al. (2013). *Appl. Radiat. Isot.* 76: 38–45.
89. Breeman, W.A.P., de Jong, M., de Blois, E. et al. (2005). *Eur. J. Nucl. Med. Mol. Imaging* 32: 478–485.
90. Meyer, G.J., Macke, H., Schuhmacher, J. et al. (2004). *Eur. J. Nucl. Med. Mol. Imaging* 31: 1097–1104.
91. Zhernosekov, K.P., Filosofov, D.V., Baum, R.P. et al. (2007). *J. Nucl. Med.* 48: 1741–1748.
92. Asti, M., De Pietri, G., Fraternali, A. et al. (2008). *Nucl. Med. Biol.* 35: 721–724.
93. Eppard, E., Homann, T., de la Fuente, A. et al. (2017). *J. Nucl. Med.* 58: 432–438.
94. Eppard, E., Wuttke, M., Nicodemus, P.L., and Rosch, F. (2014). *J. Nucl. Med.* 55: 1023–1028.
95. Perez-Malo, M., Szabo, G., Eppard, E. et al. (2018). *Inorg. Chem.* 57: 6107–6117.
96. Hasegawa, K., Kawachi, E., Uehara, Y. et al. (2017). *J. Labelled Compd. Radiopharm.* 60: 55–61.
97. Mueller, D., Breeman, W.A.P., Klette, I. et al. (2016). *Nat. Protoc.* 11: 1057–1066.
98. Loktionova, N.S., Belozub, A.N., Filosofov, D.V. et al. (2011). *Appl. Radiat. Isot.* 69: 942–946.
99. Wurzer, A., Pollmann, J., Schmidt, A. et al. (2018). *Mol. Pharm.* 15: 4296–4302.
100. Velikyan, I., Beyer, G.J., Bergstrom-Pettermann, E. et al. (2008). *Nucl. Med. Biol.* 35: 529–536.
101. Velikyan, I., Sundin, A., Eriksson, B. et al. (2010). *Nucl. Med. Biol.* 37: 265–275.
102. von Hacht, J.L., Erdmann, S., Niederstadt, L. et al. (2019). *PLoS One*: 14.
103. Velikyan, I. (2018). *Contrast Media Mol. Imaging* 2018 <https://doi.org/10.1155/2018/9713691>.
104. Chakraborty, S., Chakravarty, R., Vatsa, R. et al. (2016). *Nucl. Med. Biol.* 43: 116–123.
105. Chakravarty, R., Chakraborty, S., Radhakrishnan, E.R. et al. (2017). *Nucl. Med. Biol.* 46: 1–11.
106. Ebenhan, T., Schoeman, I., Rossouw, D.D. et al. (2017). *Mol. Imaging Biol.* 19: 469–482.
107. Taggart, M.P., Deakin, T., Thompson, L.F. et al. (2016). *Lab Chip* 16: 1605–1616.
108. Tarn, M.D., Maneuski, D., Alexander, R. et al. (2016). *Chem. Commun.* 52: 7221–7224.
109. Pfaff, S., Philippe, C., Pichler, V. et al. (2018). *Dalton Trans.* 47: 5997–6004.

110. Virgolini, I., Ambrosini, V., Bomanji, J.B. et al. (2010). *Eur. J. Nucl. Med. Mol. Imaging* 37: 2004–2010.
111. Velikyan, I. (2014). *Theranostics* 4: 47–80.
112. Krenning, E.P., Bakker, W.H., Kooij, P.P.M. et al. (1992). *J. Nucl. Med.* 33: 652–658.
113. Jamar, F., Fiasse, R., Leners, N., and Pauwels, S. (1995). *J. Nucl. Med.* 36: 542–549.
114. Lebtahi, R., Cadiot, G., Sarda, L. et al. (1997). *J. Nucl. Med.* 38: 853–858.
115. Kowalski, J., Henze, M., Schuhmacher, J. et al. (2003). *Mol. Imaging Biol.* 5: 42–48.
116. Buchmann, I., Henze, M., Engelbrecht, S. et al. (2007). *Eur. J. Nucl. Med. Mol. Imaging* 34: 1617–1626.
117. Wild, D., Bomanji, J.B., Benkert, P. et al. (2013). *J. Nucl. Med.* 54: 364–372.
118. Kayani, I., Bomanji, J.B., Groves, A. et al. (2008). *Cancer* 112: 2447–2455.
119. Wild, D., Schmitt, J.S., Ginj, M. et al. (2003). *Eur. J. Nucl. Med. Mol. Imaging* 30: 1338–1347.
120. Antunes, P., Ginj, M., Zhang, H. et al. (2007). *Eur. J. Nucl. Med. Mol. Imaging* 34: 982–993.
121. Pauwels, E., Deroose, C.M., Pauwels, E. et al. (2018). *Am. J. Nucl. Med. Mol. Imaging* 8: 311–331.
122. Werner, R.A., Bluemel, C., Allen-Auerbach, M.S. et al. (2015). *Ann. Nucl. Med.* 29: 1–7.
123. Bodei, L., Cremonesi, M., Grana, C.M. et al. (2011). *Eur. J. Nucl. Med. Mol. Imaging* 38: 2125–2135.
124. Zaknun, J.J., Bodei, L., Mueller-Brand, J. et al. (2013). *Eur. J. Nucl. Med. Mol. Imaging* 40: 800–816.
125. Strosberg, J., El-Haddad, G., Wolin, E. et al. (2017). *New Engl. J. Med.* 376: 125–135.
126. Strosberg, J., Wolin, E., Chasen, B. et al. (on behalf of the NETTER Study Group) (2018). *J. Clin. Oncol.* 36: 2578–2584.
127. Bray, F., Ferlay, J., Soerjomataram, I. et al. (2018). *CA Cancer J. Clin.* 68: 394–424.
128. Wester, H.J. and Schottelius, M. (2019). *Semin. Nucl. Med.* 49: 302–312.
129. Lutje, S., Herrmann, K., Slavik, R. et al. (2017). *Methods* 130: 42–50.
130. Jackson, I.M., Scott, P.J.H., and Thompson, S. (2017). *Semin. Nucl. Med.* 47: 493–523.
131. Treglia, G., Mestre, R.P., Ferrari, M. et al. (2019). *Am. J. Nucl. Med. Mol. Imaging* 9: 127–139.
132. Mena, E., Lindenberg, L.M., and Choyke, P.L. (2019). *Semin. Nucl. Med.* 49: 326–336.
133. Calais, J., Ceci, F., Eiber, M. et al. (2019). *Lancet Oncol.* 20: 1286–1294.
134. Calais, J., Ceci, F., Nguyen, K. et al. (2019). *J. Clin. Oncol.*: 37.
135. Mottet, N., van den Bergh, R.C.N., Briers, E. et al. 2018. *European Association of Urology guidelines*.
136. Fendler, W.P., Eiber, M., Beheshti, M. et al. (2017). *Eur. J. Nucl. Med. Mol. Imaging* 44: 1014–1024.
137. Eder, M., Schafer, M., Bauder-Wust, U. et al. (2012). *Bioconjugate Chem.* 23: 688–697.
138. Afshar-Oromieh, A., Malcher, A., Eder, M. et al. (2013). *Eur. J. Nucl. Med. Mol. Imaging* 40: 486–495.
139. Beheshti, M., Paymani, Z., Brillhante, J. et al. (2018). *Eur. J. Nucl. Med. Mol. Imaging* 45: 1188–1196.
140. Schuhmacher, J., Klivenyi, G., Hull, W.E. et al. (1992). *Nucl. Med. Biol.* 19: 809–824.

141. Hofman, M.S., Eu, P., Jackson, P. et al. (2018). *J. Nucl. Med.* 59: 625–631.
142. Young, J.D., Abbate, V., Imberti, C. et al. (2017). *J. Nucl. Med.* 58: 1270–1277.
143. Derlin, T., Schmuck, S., Juhl, C. et al. (2018). *Mol. Imag. Biol.* 20: 650–658.
144. Derlin, T., Schmuck, S., Juhl, C. et al. (2018). *Eur. J. Nucl. Med. Mol. Imaging* 45: 913–922.
145. Bialek, E.J. and Malkowski, B. (2019). *Nucl. Med. Commun.* 40: 175–184.
146. Rupp, N.J., Umbricht, C.A., Pizzuto, D.A. et al. (2019). *J. Nucl. Med.* 60: 1270–1276.
147. Afshar-Oromieh, A., Hetzheim, H., Kratochwil, C. et al. (2015). *J. Nucl. Med.* 56: 1697–1705.
148. Herrmann, K., Bluemel, C., Weineisen, M. et al. (2015). *J. Nucl. Med.* 56: 855–861.
149. Liu, C., Liu, T.L., Zhang, N. et al. (2018). *Eur. J. Nucl. Med. Mol. Imaging* 45: 1852–1861.
150. McCarthy, M., Langton, T., Kumar, D., and Campbell, A. (2017). *Eur. J. Nucl. Med. Mol. Imaging* 44: 1455–1462.
151. Benesova, M., Schafer, M., Bauder-Wust, U. et al. (2015). *J. Nucl. Med.* 56: 914–920.
152. Hofman, M., Violet, J., Sandhu, S. et al. (2018). *J. Nucl. Med.* 59: 531.
153. Rahbar, K., Ahmadzadehfar, H., Kratochwil, C. et al. (2017). *J. Nucl. Med.* 58: 85–90.
154. Baum, R.P., Kulkarni, H.R., Schuchardt, C. et al. (2016). *J. Nucl. Med.* 57: 1006–1013.
155. Kesch, C., Kratochwil, C., Mier, W. et al. (2017). *J. Nucl. Med.* 58: 687–688.
156. Wurzer, A., Di Carlo, D., Schmidt, A. et al. (2019). *J. Nucl. Med.*: 60.
157. Kelly, J.M., Amor-Coarasa, A., Ponnala, S. et al. (2019). *J. Nucl. Med.* 60: 656–663.
158. Banerjee, S.R., Foss, C.A., Castanares, M. et al. (2008). *J. Med. Chem.* 51: 4504–4517.
159. Banerjee, S.R., Pullambhatla, M., Foss, C.A. et al. (2013). *J. Med. Chem.* 56: 6108–6121.
160. Robu, S., Schottelius, M., Eiber, M. et al. (2017). *J. Nucl. Med.* 58: 235–242.
161. Mewis, R.E. and Archibald, S.J. (2010). *Coord. Chem. Rev.* 254: 1686–1712.
162. Burke, B.P., Seemann, J., and Archibald, S.J. (2016). *Advances in Inorganic Chemistry, Insights from Imaging in Bioinorganic Chemistry*, vol. 68 (eds. R. VanEldik and C.D. Hubbard), 301–339. Academic Press.
163. Rensch, C., Jackson, A., Lindner, S. et al. (2013). *Molecules* 18: 7930–7956.
164. Zeng, D.X., Desai, A.V., Ranganathan, D. et al. (2013). *Nucl. Med. Biol.* 40: 42–51.
165. Bignell, H.A., Tarn, M.D., Burke, B.P. et al. (2016). *Abs. Pap. Am. Chem. Soc.* 250: 1577–1578.
166. Whittenberg, J.J., Li, H.R., Zhou, H.Y. et al. (2017). *Bioconjugate Chem.* 28: 986–994.
167. Simms, R.W., Kim, D.H., Weaver, D.M. et al. (2012). *Chem. Eur. J.* 18: 6746–6749.
168. Fu, R.S., Carroll, L., Yahioglu, G. et al. (2018). *ChemMedChem* 13: 2466–2478.
169. Wurzer, A., Di Carlo, D., Schmidt, A. et al. (2019). *J. Nucl. Med.*: 60.
170. Fani, M., Del Pozzo, L., Abiraj, K. et al. (2011). *J. Nucl. Med.* 52: 1110–1118.
171. Kotzerke, J., Runge, R., Braune, A., and Wunderlich, G. (2019). *J. Nucl. Med.* 60: 436.
172. Violet, J., Jackson, P., Ferdinandus, J. et al. (2019). *J. Nucl. Med.* 60: 517–523.
173. Ilan, E., Sandström, M., Wassberg, C. et al. (2015). *J. Nucl. Med.* 56: 177–182.
174. Haberkorn, U., Giesel, F., Morgenstern, A., and Kratochwil, C. (2017). *J. Nucl. Med.* 58: 1017–1018.
175. Kratochwil, C., Bruchertseifer, F., Giesel, F.L. et al. (2016). *J. Nucl. Med.* 57: 1941–1944.
176. Sathekge, M., Bruchertseifer, F., Knoesen, O. et al. (2019). *Eur. J. Nucl. Med. Mol. Imaging* 46: 129–138.

Chapter 10

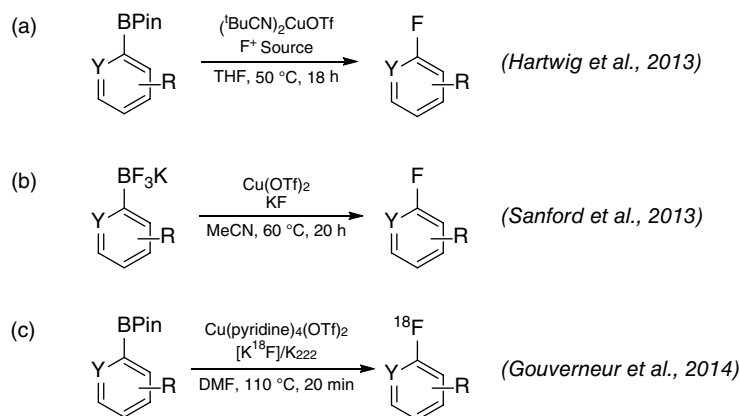
Cu-Mediated Radiohalogenation of Organoboranes

Sean W. Reilly and Robert H. Mach

*Department of Radiology, Perelman School of Medicine,
University of Pennsylvania, Philadelphia, PA 19104, USA*

10.1 INTRODUCTION AND BACKGROUND

The utilization of organoborane synthons for radiohalogenation dates back to the early 1980s when Kabalka et al. reported the radiosynthesis of ^{125}I -labeled radiopharmaceuticals using organoborane precursors in the presence of a mild oxidant [1]. This radioiodination method was described as a safer alternative to oxidative iododestannylation, which requires handling of toxic alkyltin reagents for stannane precursor development. However, this strategy did not tolerate electron-rich aryl substrates, thus limiting the scope of this radiosynthesis. Then, in 2013, Hartwig described an elegant Cu-mediated fluorination procedure that tolerated electron-rich and -poor arylboronate ester precursors under mild conditions (Scheme 10.1a) [2]. This report was immediately followed up by Sanford and co-workers, who disclosed a $\text{Cu}(\text{OTf})_2$ -mediated fluorination study using aryltrifluoroborates with KF (Scheme 10.1b) [3]. Building off these advances, Gouverneur was able to disclose the first Cu-mediated organoborane radiofluorination report (Scheme 10.1c) [4]. Since then, many Cu-mediated organoborane radiohalogenation methods have been developed, allowing these versatile boron intermediates to be utilized for F-, I-, Br, and At-radiolabeling reactions. To date, chlorine is the only halide to which this methodology has not been extended, as radiochloride labeling reports are mostly

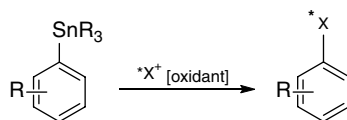


Scheme 10.1 Initial Cu-mediated fluorination strategies. (a) Cu-mediated fluorination of arylboronate esters. Source: Fier, P.S., Luo, J., and Hartwig, J.F. [2]. (b) $\text{Cu}(\text{OTf})_2$ -mediated fluorination of aryltrifluoroborates. Source: Ichiishi, N., Canty, A.J., Yates, B.F., and Sanford, M.S. [3]. (c) Cu-mediated radiofluorination of organoboranes. Source: Based on Gouverneur et al. 2014.

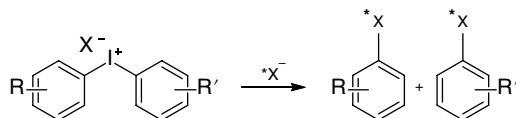
limited to traditional aryltin [5] or iodonium salt [6] precursors in order to access $^{34\text{m}}\text{Cl}$ -labeled molecules [7].

Cu complexes have been among the most reported additives in organoborane radiohalogenation, as these systems are more air-stable than other disclosed transition-metal species, such as $\text{Ni}(\text{COD})_2$ [8]. Furthermore, many Cu (II) systems in heavy halide radiohalogenation studies have displayed exceptional water tolerance, allowing the radiolabeling of organoborane precursors to be conducted in aqueous media. Although this tolerance is not quite as applicable to radiofluorination, as the presence of water can directly impair the nucleophilicity of the fluoride ion, it has helped to facilitate more rapid radiolabeling strategies of larger radiohalides by eliminating the need for a drying process. More importantly, the broad commercial availability of functionalized organoborane starting materials, combined with the non-toxic nature of boron, have made boryl precursors a more practical and safer alternative to organotin precursors. Furthermore, recent developments in C–B bond formation reactions have enabled many facile installment strategies of boron functional groups into complex molecular scaffolds [9]. Thus, preparation of organoborane precursors has generally become more straightforward than the synthesis of aryliodonium salts, where developing a complex precursor for radiolabeling can become problematic. Consequently, Cu-mediated radiohalogenation has become a robust and more attractive alternative to the traditional electrophilic and nucleophile radiolabeling pathways (Figure 10.1). This chapter will highlight the recent advances in Cu-mediated radiohalogenation of organoboranes and discuss how this

Electrophilic Radiohalogenation



Nucleophilic Radiohalogenation



Cu-Mediated Nucleophilic Radiohalogenation

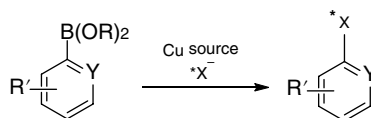


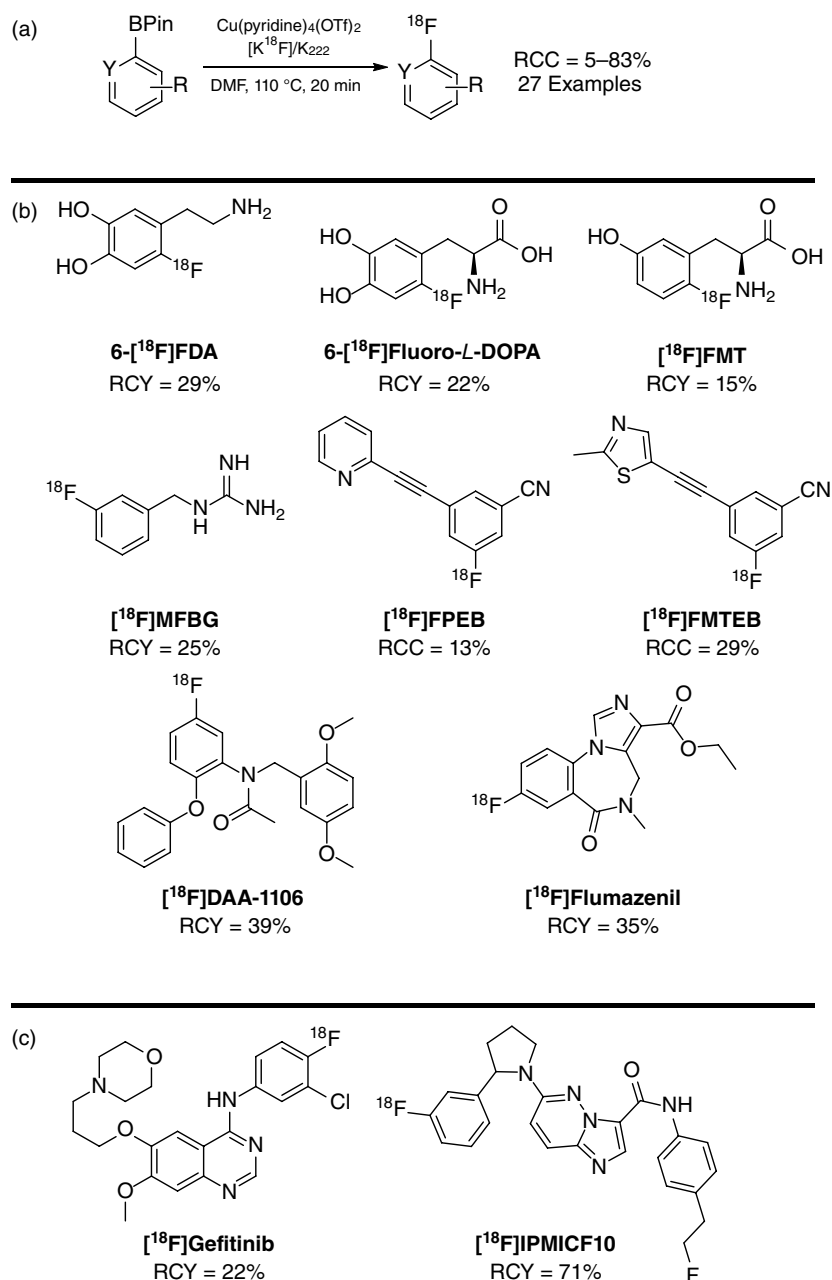
Figure 10.1
Common
methods
for radioha-
logenation.

method has enabled the development of highly efficient radiolabeling strategies for the less studied Br and At heavy halides.

10.2 Cu-MEDIATED RADIOFLUORINATION

Fluorine-18 (^{18}F) is the more commonly used radioisotope for positron emission tomography (PET) imaging applications due to the excellent imaging properties and relatively long half-life ($t_{1/2} = 110$ minutes) of the radiohalide [10]. Traditionally, $\text{S}_{\text{N}}\text{Ar}$ reactions have been among the more common methods used to introduce ^{18}F onto aryl rings of molecular scaffolds in order to prepare the desired PET tracer [11]. However, these strategies often employ harsh reaction conditions, with temperatures frequently above 150°C , and are generally limited to electron-deficient aromatics [12]. To address this limitation, novel synthetic advances in nucleophilic radiofluorination using diaryliodonium [13–15], triarylsulfonium [16], diaryl sulfoxides [17], iodonium ylide [18–20], and *N*-arylsydnone [21] precursors, and even electron-rich (hetero)arenes for C–H radiofluorination [22], among others [23], have been developed. In comparison to these elegant methods, Cu-mediated nucleophilic radiofluorination of organoborane precursors allows the use of electron-rich and -deficient aryl boron substrates that are stable and commercially available, making this a more practical and convenient strategy for late-stage radiofluorination of drug-like molecules.

In Gouverneur's initial 2014 Cu-mediated radiofluorination report, a broad class of aryl boronic esters was radiolabeled with ^{18}F in the presence of $\text{Cu}(\text{OTf})_2(\text{pyr})_4$

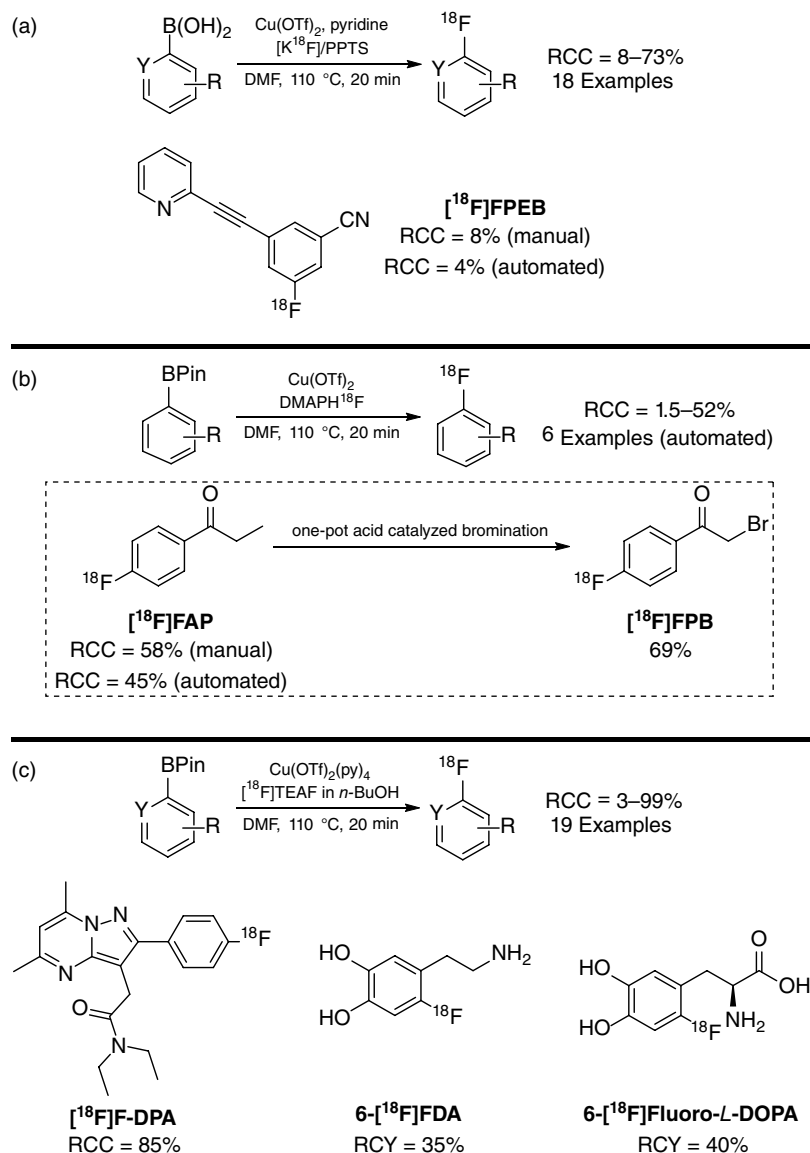


Scheme 10.2 Cu-mediated radiofluorination of organoboranes. (a) Radiofluorination of aryl boronic esters. Source: Based on Gouverneur et al. 2014. (b) Preparation of clinically relevant ¹⁸F-based PET radiotracers. Source: Preshlock, S., Tredwell, M., and Gouverneur, V. [11]. (c) Cu-mediated derisking study aimed toward establishing low-risk retrosynthetic routes for development of complex molecular radioligands. Source: Based on Gouverneur et al., 2017.

(Scheme 10.2a). Late-stage radiofluorination using this method also allowed access to clinically relevant PET tracers [^{18}F]DAA-1106 and 6- ^{18}F fluoro-L-DOPA, following a post-labeling Boc-deprotection step. This strategy was further optimized in Gouverneur's 2016 report, and was utilized to synthesize eight clinically relevant PET radiotracers under manual and automatic radiolabeling conditions (Scheme 10.2b) [24]. In this report, the authors found the use of *N,N*-dimethylacetamide (**DMA**) and $\text{K}_2\text{C}_2\text{O}_4$ quaternary methyl ammonium (**QMA**) cartridge eluent to be among the key changes made from their original investigation. To better understand the scope and limitations of the Cu-mediated organoborane radiofluorination approach, Gouverneur and co-workers performed an exhaustive screening technique [25] that was inspired by the work of Glorius [26]. The Gouverneur group examined how the presence of nearly 100 heterocycles, commonly used in drug development, can impact the ^{18}F -labeling efficiency of over 50 (hetero)aryl boronic esters. The data accumulated from this study resulted in the successful radiosynthesis of seven structurally complex bioactive compounds, including two that were accessed via last-step radiofluorination (Scheme 10.2c).

In 2015, Scott and Sanford disclosed the first Cu-mediated [^{18}F]fluorination study using boronic acid precursors (Scheme 10.3a) [27]. One of the aims of this investigation was to develop a reproducible process that could be automated on a commercial radiochemistry synthesis module. During their optimization studies, the authors noted the comparable radiochemical conversions (**RCCs**) obtained between $\text{Cu}(\text{OTf})_2(\text{py})_4$ and the more economical combination of $\text{Cu}(\text{OTf})_2$ and pyridine. They also found the combination of KOTf and K_2CO_3 to be an effective QMA ion-exchange eluent for both ^{18}F recovery and suppression of radioactivity loss throughout the azeotropic drying process. Under optimized conditions, the PET tracer [^{18}F]FPEB was conveniently synthesized in an automated module, illustrating the clinical promise of this method. Reaction conditions were further optimized by Scott and Sanford in 2017, reporting enhanced automated RCCs with dimethylaminopyridine (**DMAP**) (Scheme 10.3b) [28] or KOTf QMA eluents [29]. Using the DMAP elution strategy, the successful synthesis of [^{18}F]FAP was enabled, followed by a one-pot acid-catalyzed bromination to achieve the synthetically challenging PET tracer [^{18}F]FPB. Neumaier and co-workers found primary alcohols to enhance product RCCs when used as a QMA elution with Et_4NHCO_3 and as a subsequent co-solvent (Scheme 10.3c) [30]. This approach eliminated the need for azeotropic drying, a critical and cumbersome step for most ^{18}F radiolabeling strategies.

The scope of Cu-mediated late-stage radiofluorination using organoboranes has rapidly progressed to include a number of clinically relevant ^{18}F -labeled PET radiotracers with diverse ligand architectures (Figure 10.2). Vugts and co-workers reported a one-minute [^{18}F]trifluoromethylation method to prepare [^{18}F]4-trifluoromethylestrone at room temperature [31]. In 2015, Niwa, Hosoya disclosed a tandem Ni/Cu-catalyzed defluoroborylation strategy of fluoroarenes [32]. The authors applied this process to the radiosynthesis of a ^{18}F -labeled statin analogue by converting the cold F-19 parent compound into the desired boryl ester precursor, followed by subsequent Cu-mediated radiofluorination. Throughout 2017, Lin and co-workers utilized the Cu-mediated strategy to prepare three clinically relevant PET tracers [^{18}F]FBnTP [33], a negative membrane



Scheme 10.3 Cu-mediated radiofluorination of organoboranes optimization. (a) Cu-mediated radiofluorination of boronic acids. Source: Based on McCammant, M.S., Thompson, S., Brooks, A.F. et al. [22]. (b) Automation of Cu-mediated radiofluorination of boronic ester precursors. Source: Based on McCammant, M.S., Thompson, S., Brooks, A.F. et al. [22]. (c) Alcohol-enhanced Cu-mediated radiofluorination of boronic ester precursors. Source: Based on Zischler, J., Kolks, N., Modemann, D. et al. [30].

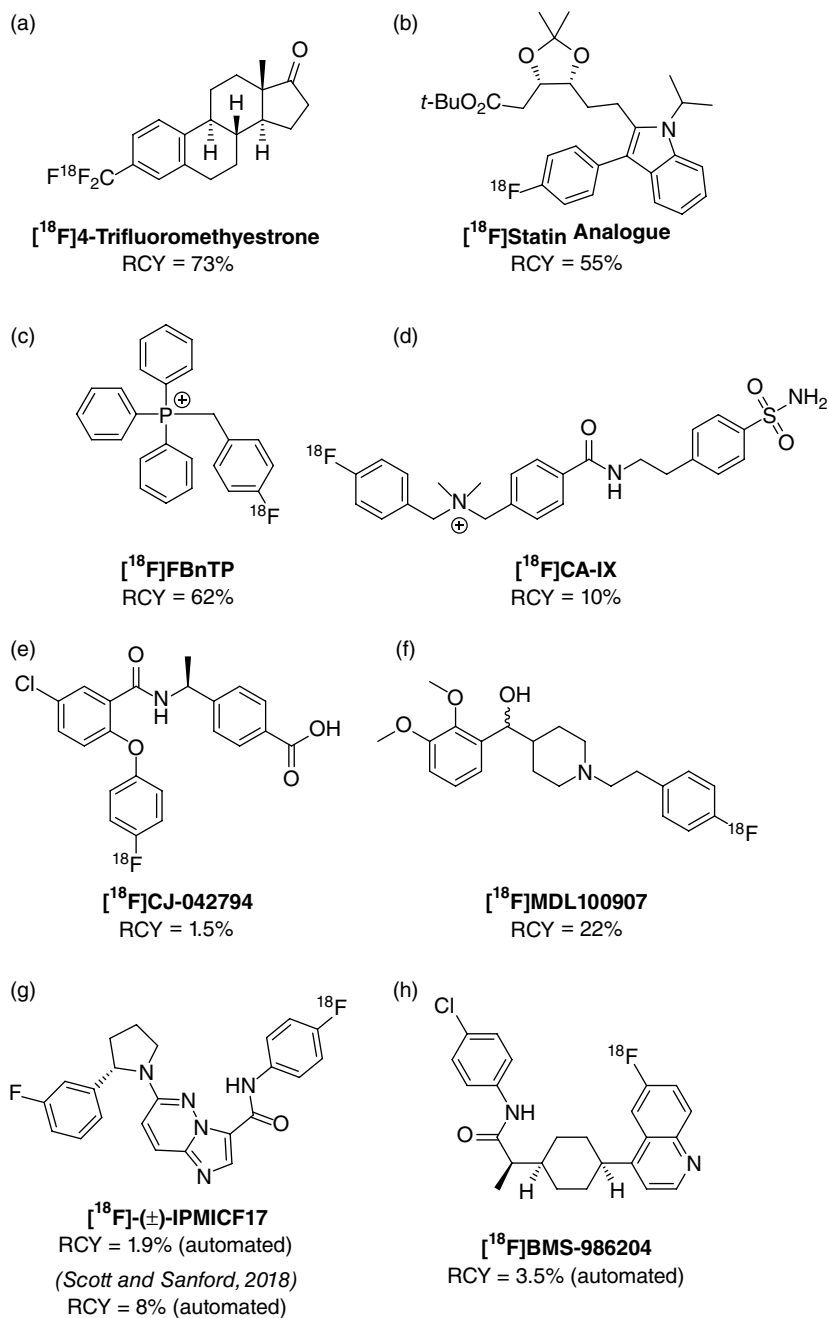


(Figure 10.2 Continued)

Figure 10.2 Radiosynthesis of clinically relevant ^{18}F -labeled PET radiotracers using late-stage Cu-mediated radiofluorination. Sources: (a) van der Born, D., Sewing, C., Herscheid, J.D.M. et al. [31]. (b) Niwa, T., Ochiai, H., Watanabe, Y., and Hosoya, T. [32]. (c, d, e) Zhang, Z., Zhang, C., Lau, J. et al. [33]. (f) Zhang, X., Dunlow, R., Blackman, B.N., and Swenson, R.E. [36]. (g) Mossine, A.V., Brooks, A.F., Ichiishi, N. et al. [28]. and Bernard-Gauthier, V., Mossine, A.V., Mahringer, A. et al. [29]. (h) Based on Cole, E., Donnelly, D., Wallace, M. et al. [38].

potential targeting tracer, ^{18}F CA-IX [34], a tumor hypoxia tracer, and ^{18}F CJ-042794 [35], a prostanoid EP4 receptor tracer, using the Cu-mediated strategy. Swenson et al. found this method to drastically improve the radiosynthesis of 5-HT_{2a} probe ^{18}F MDL100907, which traditionally suffered from low radiochemical yields (RCYs) due to the electron-rich aryl ring of the ligand [36]. Recently, Schirmacher and Bernard-Gauthier applied the optimization conditions from Neumaier's [30] and Scott's [37] Cu-mediate radiofluorination studies toward the production of structurally diverse ^{18}F -(±)-IPMICF17, a tropomyosin receptor kinase (Trk) inhibitor, to image Trk proteins in non-human primates [29]. The preparation of an indoleamine-2,3-dioxygenase (IDO) imaging probe ^{18}F BMS-986205 by Bonacorsi and co-workers [38] further illustrates the broad functional tolerance of this late-stage radiofluorination approach.

10.3 Cu-MEDIATED HEAVY HALIDE RADIOHALOGENATION

In contrast to F-18, heavy radiohalides have been evaluated for biomedical applications beyond imaging. Radiopharmaceuticals labeled with radioactive isotopes of iodine play a major role in non-invasive imaging modalities such as single-photon emission computed tomography (SPECT) (^{123}I , ^{125}I , and ^{131}I) and PET (^{124}I) imaging, as well as radiotherapeutics (^{131}I). Bromine has two radionuclides that fit the criteria for PET imaging (^{76}Br , $t_{1/2} = 16.2$ hours) and radiotherapeutic (^{77}Br , $t_{1/2} = 57$ hours) applications. Although astatine has no stable isotope and is one of the rarest known elements, the α -emitting radionuclide ^{211}At ($t_{1/2} = 7.2$ hours) is an attractive radioisotope for the production of targeted radiotherapy agents.

Traditional electrophilic heavy halide radiohalogenation methods require an oxidizing agent to generate the positive radionuclide species for the displacement of the leaving group. However, this strategy can result in degradation of the precursor and even production of volatile molecular iodine due to the oxidant, resulting in overall low RCCs and RCYs [39]. The high reactivity of the bromine intermediate generated in no-carrier-added oxidative electrophilic radiobromination commonly leads to unwanted side-product formation [40]. Electrophilic astatination of stannane precursors can result in astatine

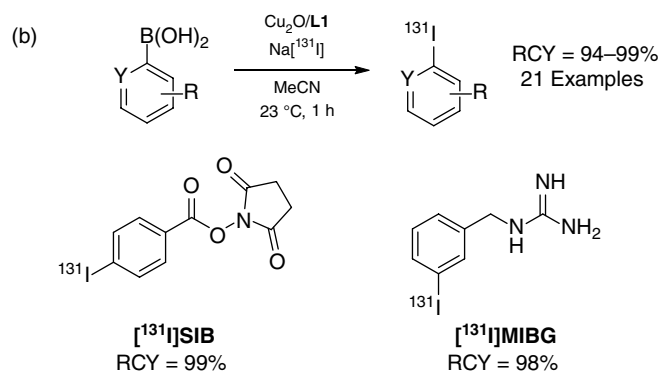
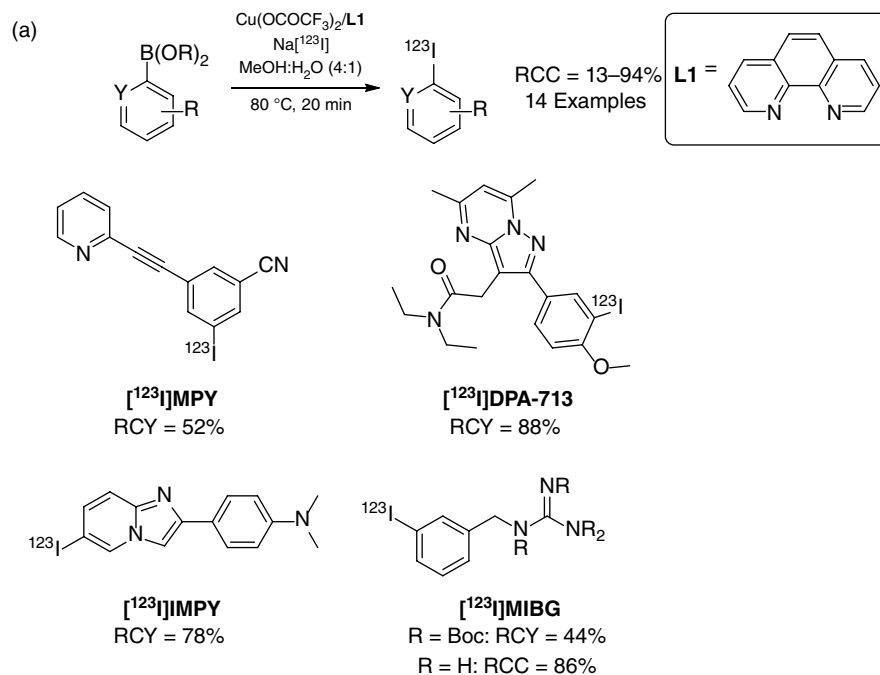
adopting multiple oxidation states, thus making it difficult to obtain the desired, and non-stable, At^{I} species for electrophilic substitution [41, 42]. Many of the reported nucleophilic displacement strategies for heavy halide radiohalogenation are energy-demanding processes and require elevated temperatures, making these techniques non-suitable for thermally labile compounds [43–45]. Thus, the limitations of these radiosynthetic methods to efficiently incorporate heavy radiohalides have made the development of new radiopharmaceuticals containing these radionuclides challenging.

In light of the advances in Cu-mediated organoborane radiofluorination, groups began to extend the scope of this strategy to include heavy radiohalides. In 2016, Gouverneur and Zhang simultaneously reported the first Cu-mediated radioiodination strategies using aryl boron precursors and $\text{Na}^{[123\text{I}]}$ (Scheme 10.4) [46, 47]. In Gouverneur's report, a broad scope of ^{123}I -labeled compounds using electron-rich and electron-poor (hetero) aromatic boronic esters and acids were achieved using copper catalyst $\text{Cu}(\text{OCOCF}_3)_2$ with 1,10-phenanthroline (L1) as the ligand (Scheme 10.4a). Additive L1 has also been utilized in previous Cu-catalyzed iodination studies [48, 49], presumably to generate the active Cu species.

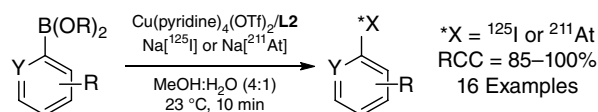
Gouverneur and co-workers found their optimized conditions to be suitable for the preparation of clinically relevant SPECT tracers ^{123}I]MPY, ^{123}I]DPA-713, ^{123}I]MPY, and ^{123}I]MIBG from the corresponding boronic ester precursors. In contrast to Gouverneur's report, Zhang and co-workers illustrated a room temperature ^{131}I -labeling method of aryl boronic acids at one hour using Cu_2O and L1 (Scheme 10.4b). The mild reaction conditions in this report afforded near-quantitative RCCs of aryl boronic acids containing formyl, nitro, cyano, hydroxyl, and ester function groups. The authors also successfully extended their scope to include the boronic acid precursor of ^{131}I]SIB, a versatile intermediate for the radioiodination of monoclonal antibodies.

In 2018, Mach and co-workers developed a divergent Cu-mediated radioiodination and astatination protocol that led to excellent RCCs and RCYs in just 10 minutes at room temperature [50]. In contrast to the reports by Gouverneur and Zhang, Mach's reaction conditions did not require the use of a ligand additive for radiolabeling simple aryl boronic esters and acids. Instead, Cu (II) source $\text{Cu}(\text{pyridine})_4(\text{OTf})_2$, alone, enabled RCCs between 85% and 100% of sterically crowded, and electron-rich and -poor aryl boronic esters (Scheme 10.5). The authors' use of methanolic reaction media coincides with Hartwig's Cu-catalyzed iodination report, in which protic media was found to enhance the transmetalation of the boronic ester, the hypothesized rate-limiting step in the catalytic cycle [48]. The RCCs and RCYs obtained for the desired ^{211}At -labeled small molecules were greater than those observed with ^{125}I . This trend is also consistent with Brechbiel's study, where the authors reported a much higher reactivity of astatide over iodide in nucleophilic substitution of arylodonium salts [43].

The Mach group then extended their investigation beyond simple molecules to several boronic ester precursors of olaparib derivatives, a Food and Drug Administration (FDA) approved poly(ADP-ribose) polymerase-1 (PARP-1) inhibiting cancer therapeutic

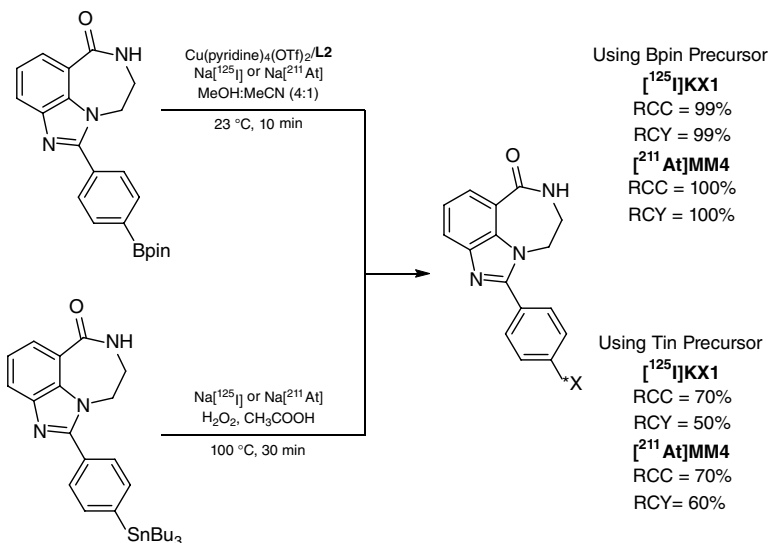
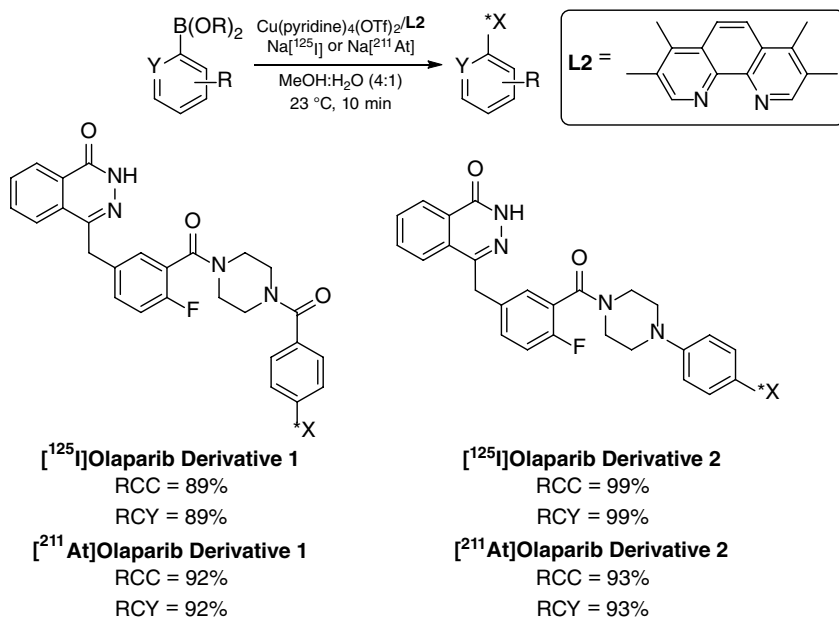


Scheme 10.4 Cu-mediated radioiodination of organoboranes. (a) Radioiodination of aryl boronic esters. Source: Based on Preshlock, S., Tredwell, M., and Gouverneur, V. [11]. (b) Room temperature radioiodination of aryl boronic acids. Source: Based on Zhang, Z., Zhang, C., Lau, J. et al. [33].



Scheme 10.5 Cu-mediated radioiodination and astatination of organoboranes. Source: Based on Reilly, S.W., Makvandi, M., Xu, K., and Mach, R.H. [50].

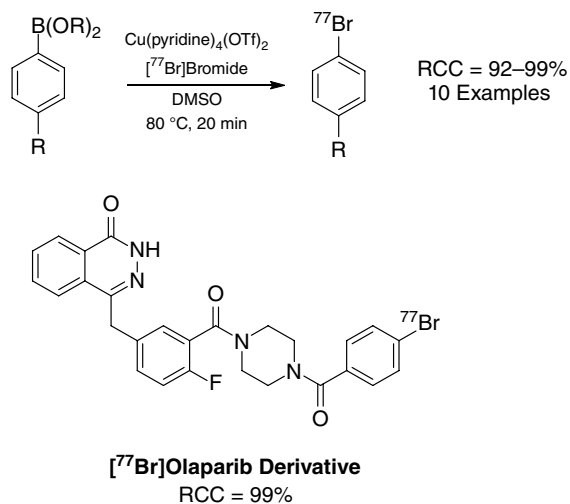
(Scheme 10.6) [51]. Initially, sluggish RCYs of the desired ^{125}I -labeled PARP-1 inhibitors were observed using optimized conditions. However, when utilizing a 1 : 1 ratio of $\text{Cu}(\text{pyridine})_4(\text{OTf})_2$ and electron-rich ligand 3,4,7,8-tetramethyl-1,10-phenanthroline (L2), excellent RCCs and RCYs were restored. Mach and co-workers also conducted a comparative radiolabeling study by preparing ^{125}I]KX1 and ^{211}At]MM4, PARP-1



Scheme 10.6 Radiosynthesis of ^{125}I - and ^{211}At -labeled PARP-1 inhibitors. Source: Based on Reilly, S.W., Makvandi, M., Xu, K., and Mach, R.H. [50].

inhibitors with applications in cancer imaging and radiotherapeutics, respectively, from both the boronic ester and stannane precursors (Scheme 10.6). Compared to the classical electrophilic organostannane radiohalogenation approach, Mach's late-stage radiolabeling method delivered higher RCCs and RCYs for both [¹²⁵I]KX1 and [²¹¹At]MM4 under optimized reaction conditions.

Zhou and co-workers then disclosed the first Cu-mediated organoborane radiobromination report in 2018 [52]. In their study, they found Cu(pyridine)₄(OTf)₂ to be the most efficient Cu source for labeling aryl boronic acids and esters with ⁷⁷Br at temperatures of 80–110 °C (Scheme 10.7). The authors noted near-quantitative RCCs in 40 minutes during the optimization studies; however, large amounts of reagents were required. Similar to the Cu-mediated heavy halide radiohalogenation studies by Gouverneur [46] and Mach [50], Zhou's method was also found to tolerate aqueous reaction media. Although the authors did not discuss why the scope was limited to *para*-substituted aryl boron precursors, this robust radiolabeling strategy afforded RCCs of 90% or greater throughout the investigation in just 10–20 minutes. This technique was also evaluated with a boronic ester precursor of an olaparib derivative, affording a RCC of 99%. Overall, the Zhou group found this method to be higher-yielding, as well as more reliable and facile, than their previously reported nucleophilic [44] and electrophilic [53] radiobromination strategies.



Scheme 10.7 Cu-mediated radiobromination of organoboranes. Source: Zhou, D., Chu, W., Voller, T., and Katzenellenbogen, J.A. [52]. Reproduced with the permission of Elsevier.

10.4 CONCLUSIONS

The overall advances made in Cu-mediated organoborane radiohalogenation have undoubtedly helped bridge the synthetic gaps in ^{18}F -based PET tracer development and heavy halide radiohalogenation. Development of radioligands with promising clinical applications previously found to be synthetically challenging, and subsequently underutilized, may now be more synthetically accessible using this robust radiolabeling approach. However, while this versatile method enables organic transformations that are quite challenging using traditional radiosynthetic techniques, replicating RCYs found in Cu-mediated radiohalogenation reports has been problematic since many of the protocols have been carried out in a “manual” format [37]. Thus, in order to extend this radiolabeling concept to clinical applications, a dependable and reproducible Cu-mediated protocol will be needed in order to tailor this method to automated radiosynthesis modules, due to the high level of radioactivity in patient-scale PET studies. Moreover, these automated synthetic and purification steps must also be in compliance with current Good Manufacturing Practice (cGMP) before translating this innovative radiosynthesis to the production of PET tracers for clinical research in humans [54, 55]. Although much progress has been achieved in Cu-mediated radiohalogenation of organoboranes, additional work in the aforementioned areas must be achieved before this method can be used on a widespread basis in radiosynthesis.

REFERENCES

1. Kabalka, G.W., Gooch, E.E., and Sastry, K.A.R. (1981). Rapid and mild syntheses of radioiodine-labeled radiopharmaceuticals. *J. Nucl. Med.* 22 (10): 908–912.
2. Fier, P.S., Luo, J., and Hartwig, J.F. (2013). Copper-mediated fluorination of arylboronate esters. Identification of a copper(III) fluoride complex. *J. Am. Chem. Soc.* 135 (7): 2552–2559.
3. Ichiishi, N., Canty, A.J., Yates, B.F., and Sanford, M.S. (2013). Cu-catalyzed fluorination of diaryliodonium salts with KF. *Org. Lett.* 15 (19): 5134–5137.
4. Tredwell, M., Preshlock, S.M., Taylor, N.J. et al. (2014). A general copper-mediated nucleophilic ^{18}F fluorination of arenes. *Angew. Chem. Int. Ed.* 53 (30): 7751–7755.
5. Takada, Y., Hanyu, M., Nagatsu, K., and Fukumura, T. (2012). Radiolabeling of aromatic compounds using $\text{K}[^{14}\text{C}]\text{Cl}$ and OXONE[®]. *J. Labelled Compd. Radiopharm.* 55 (10): 383–386.
6. Zhang, M.-R., Kumata, K., Takei, M. et al. (2008). How to introduce radioactive chlorine into a benzene ring using $^{36}\text{Cl}]\text{Cl}$. *Radiat. Isot.* 66 (10): 1341–1345.

7. Engle, J.W., Barnhart, T.E., Severin, G.W., and Nickles, R.J. (2011). The unrealized potential of ^{34}mCl for radiopharmaceutical research with PET. *Curr. Radiopharm.* 4 (2): 102–108.
8. Cant, A.A., Champion, S., Bhalla, R. et al. (2013). Nickel-mediated radioiodination of aryl and heteroaryl bromides: rapid synthesis of tracers for SPECT imaging. *Angew. Chem. Int. Ed.* 52 (30): 7829–7832.
9. Fyfe, J.W.B. and Watson, A.J.B. (2017). Recent developments in organoboron chemistry: old dogs, New Tricks. *Chem* 3 (1): 31–55.
10. Miller, P.W., Long, N.J., Vilar, R., and Gee, A.D. (2008). Synthesis of ^{11}C , ^{18}F , ^{15}O , and ^{13}N radiolabels for positron emission tomography. *Angew. Chem. Int. Ed.* 47 (47): 8998–9033.
11. Preshlock, S., Tredwell, M., and Gouverneur, V. (2016). ^{18}F -labeling of arenes and heteroarenes for applications in positron emission tomography. *Chem. Rev.* 116 (2): 719–766.
12. Adams, D.J. and Clark, J.H. (1999). Nucleophilic routes to selectively fluorinated aromatics. *Chem. Soc. Rev.* 28 (4): 225–231.
13. Pike, V.W. and Aigbirhio, F.I. (1995). Reactions of cyclotron-produced [^{18}F]fluoride with diaryliodonium salts – a novel single-step route to no-carrier-added [^{18}F]fluoroarenes. *J. Chem. Soc., Chem. Commun.* (21): 2215–2216.
14. Chun, J.-H., Lu, S., and Pike, V.W. (2011). Rapid and efficient radiosyntheses of meta-substituted [^{18}F]fluoroarenes from [^{18}F]fluoride ion and diaryliodonium – tosylates within a microreactor. *Eur. J. Org. Chem.* 2011 (23): 4439–4447.
15. Chun, J.-H. and Pike, V.W. (2013). Single-step syntheses of no-carrier-added functionalized [^{18}F]fluoroarenes as labeling synthons from diaryliodonium salts. *Org. Biomol. Chem.* 11 (37): 6300–6306.
16. Mu, L., Fischer, C.R., Holland, J.P. et al. (2012). ^{18}F -radiolabeling of aromatic compounds using triarylsulfonium salts. *Eur. J. Org. Chem.* 2012 (5): 889–892.
17. Chun, J.-H., Morse, C.L., Chin, F.T., and Pike, V.W. (2013). No-carrier-added [^{18}F]fluoroarenes from the radiofluorination of diaryl sulfoxides. *Chem. Commun.* 49 (21): 2151–2153.
18. Cardinale, J., Ermert, J., Humpert, S., and Coenen, H.H. (2014). Iodonium ylides for one-step, no-carrier-added radiofluorination of electron rich arenes, exemplified with 4-([^{18}F]fluorophenoxy)-phenylmethyl)piperidine NET and SERT ligands. *RSC Adv.* 4 (33): 17293–17299.
19. Rotstein, B.H., Stephenson, N.A., Vasdev, N., and Liang, S.H. (2014). Spirocyclic hypervalent iodine(III)-mediated radiofluorination of non-activated and hindered aromatics. *Nat. Commun.* 5: 4365.
20. Stephenson, N.A., Holland, J.P., Kassenbrock, A. et al. (2015). Iodonium ylide-mediated radiofluorination of ^{18}F -FPEB and validation for human use. *J. Nucl. Med.* 56 (3): 489–492.
21. Narayanam, M.K., Ma, G., Champagne, P.A. et al. (2017). Synthesis of [^{18}F]fluoroarenes by nucleophilic radiofluorination of *N*-arylsydones. *Angew. Chem. Int. Ed.* 56 (42): 13006–13010.

22. McCammant, M.S., Thompson, S., Brooks, A.F. et al. (2017). Cu-mediated C–H ¹⁸F-fluorination of electron-rich (hetero)arenes. *Org. Lett.* 19 (14): 3939–3942.
23. Brooks, A.F., Topczewski, J.J., Ichiishi, N. et al. (2014). Late-stage [(18)F]fluorination: new solutions to old problems. *Chem. Sci.* 5 (12): 4545–4553.
24. Preshlock, S., Calderwood, S., Verhoog, S. et al. (2016). Enhanced copper-mediated ¹⁸F-fluorination of aryl boronic esters provides eight radiotracers for PET applications. *Chem. Commun.* 52 (54): 8361–8364.
25. Taylor, N.J., Emer, E., Preshlock, S. et al. (2017). Derisking the Cu-mediated ¹⁸F-fluorination of heterocyclic positron emission tomography radioligands. *J. Am. Chem. Soc.* 139 (24): 8267–8276.
26. Collins, K.D. and Glorius, F. (2013). A robustness screen for the rapid assessment of chemical reactions. *Nat. Chem.* 5: 597.
27. Mossine, A.V., Brooks, A.F., Makaravage, K.J. et al. (2015). Synthesis of [¹⁸F]arenes via the copper-mediated [¹⁸F]fluorination of boronic acids. *Org. Lett.* 17 (23): 5780–5783.
28. Mossine, A.V., Brooks, A.F., Ichiishi, N. et al. (2017). Development of customized [¹⁸F] fluoride elution techniques for the enhancement of copper-mediated late-stage radiofluorination. *Sci. Rep.* 7 (1): 233.
29. Bernard-Gauthier, V., Mossine, A.V., Mahringer, A. et al. (2018). Identification of [¹⁸F] TRACK, a fluorine-18-labeled tropomyosin receptor kinase (Trk) inhibitor for PET imaging. *J. Med. Chem.* 61 (4): 1737–1743.
30. Zischler, J., Kolks, N., Modemann, D. et al. (2017). Alcohol-enhanced Cu-mediated radiofluorination. *Chem. Eur. J.* 23 (14): 3251–3256.
31. van der Born, D., Sewing, C., Herscheid, J.D.M. et al. (2014). A universal procedure for the [¹⁸F]trifluoromethylation of aryl iodides and aryl boronic acids with highly improved specific activity. *Angew. Chem. Int. Ed.* 53 (41): 11046–11050.
32. Niwa, T., Ochiai, H., Watanabe, Y., and Hosoya, T. (2015). Ni/Cu-catalyzed defluoroborylation of fluoroarenes for diverse C–H bond functionalizations. *J. Am. Chem. Soc.* 137 (45): 14313–14318.
33. Zhang, Z., Zhang, C., Lau, J. et al. (2016). One-step synthesis of 4-¹⁸F]fluorobenzyltriphenylphosphonium cation for imaging with positron emission tomography. *J. Labelled Compd. Radiopharm.* 59 (11): 467–471.
34. Zhang, Z., Lau, J., Zhang, C. et al. (2017). Design, synthesis and evaluation of ¹⁸F-labeled cationic carbonic anhydrase IX inhibitors for PET imaging. *J. Enzyme Inhib. Med. Chem.* 32 (1): 722–730.
35. Zhang, Z., Lau, J., Kuo, H.-T. et al. (2017). Synthesis and evaluation of ¹⁸F-labeled CJ-042794 for imaging prostanoid EP4 receptor expression in cancer with positron emission tomography. *Bioorg. Med. Chem. Lett.* 27 (10): 2094–2098.
36. Zhang, X., Dunlow, R., Blackman, B.N., and Swenson, R.E. (2018). Optimization of ¹⁸F-syntheses using ¹⁹F-reagents at tracer-level concentrations and liquid chromatography/tandem mass spectrometry analysis: improved synthesis of [¹⁸F]MDL100907. *J. Labelled Compd. Radiopharm.* 61 (5): 427–437.

37. Mossine, A.V., Brooks, A.F., Bernard-Gauthier, V. et al. (2018). Automated synthesis of PET radiotracers by copper-mediated ^{18}F -fluorination of organoborons: importance of the order of addition and competing protodeborylation. *J. Labelled Compd. Radiopharm.* 61 (3): 228–236.
38. Cole, E., Donnelly, D., Wallace, M. et al. (2018). Radiochemistry challenges and progression for incorporation of ^{18}F into a complex substituted 6- ^{18}F -fluoroquinoline BMS-986205 for IDO imaging. *J. Nucl. Med.* 59 (Supplement 1): 605.
39. Seevers, R.H. and Counsell, R.E. (1982). Radioiodination techniques for small organic molecules. *Chem. Rev.* 82 (6): 575–590.
40. Maziere, B. and Loc'h, C. (1986). Radiopharmaceuticals labelled with bromine isotopes. *Int. J. Radiat. Appl. Instrum. Part A* 37 (8): 703–713.
41. Visser Gerard, W.M. (1989). Inorganic astatine chemistry. *Radiochim. Acta* 47: 97.
42. Pozzi, O.R. and Zalutsky, M.R. (2007). Radiopharmaceutical chemistry of targeted radiotherapeutics, part 3: α -particle-induced radiolytic effects on the chemical behavior of ^{211}At . *J. Nucl. Med.* 48 (7): 1190–1196.
43. Guérard, F., Lee, Y.-S., Baidoo, K. et al. (2016). Unexpected behavior of the heaviest halogen astatine in the nucleophilic substitution of arylodonium salts. *Chem. Eur. J.* 22 (35): 12332–12339.
44. Zhou, D., Kim, S.H., Chu, W. et al. (2017). Evaluation of aromatic radiobromination by nucleophilic substitution using diaryliodonium salt precursors. *J. Labelled Compd. Radiopharm.* 60 (9): 450–456.
45. Moerlein, S.M., Hwang, D.R., and Welch, M.J. (1988). No-carrier-added radiobromination via cuprous chloride-assisted nucleophilic aromatic bromodeiodination. *Int. J. Radiat. Appl. Instrum. Part A* 39 (5): 369–372.
46. Wilson, T.C., McSweeney, G., Preshlock, S. et al. (2016). Radiosynthesis of SPECT tracers via a copper mediated ^{123}I iodination of (hetero)aryl boron reagents. *Chem. Commun.* 52 (90): 13277–13280.
47. Zhang, P., Zhuang, R., Guo, Z. et al. (2016). A highly efficient copper-mediated radioiodination approach using aryl boronic acids. *Chem. Eur. J.* 22 (47): 16783–16786.
48. Partridge, B.M. and Hartwig, J.F. (2013). Sterically controlled iodination of arenes via iridium-catalyzed C–H borylation. *Org. Lett.* 15 (1): 140–143.
49. Zhang, G., Lv, G., Li, L. et al. (2011). Copper-catalyzed halogenation of arylboronic acids. *Tetrahedron Lett.* 52 (16): 1993–1995.
50. Reilly, S.W., Makvandi, M., Xu, K., and Mach, R.H. (2018). Rapid Cu-catalyzed $[(^{211}\text{At})]$ astatination and $[(^{125}\text{I})]$ iodination of boronic esters at room temperature. *Org. Lett.* 20 (7): 1752–1755.
51. Wang, Y.-Q., Wang, P.-Y., Wang, Y.-T. et al. (2016). An update on poly(ADP-ribose)polymerase-1 (PARP-1) inhibitors: opportunities and challenges in cancer therapy. *J. Med. Chem.* 59 (21): 9575–9598.
52. Zhou, D., Chu, W., Voller, T., and Katzenellenbogen, J.A. (2018). Copper-mediated nucleophilic radiobromination of aryl boron precursors: convenient preparation of a radiobrominated PARP-1 inhibitor. *Tetrahedron Lett.* 59 (20): 1963–1967.

53. Zhou, D., Zhou, H., Jenks, C.C. et al. (2009). Bromination from the macroscopic level to the tracer radiochemical level: ^{76}Br radiolabeling of aromatic compounds via electrophilic substitution. *Bioconjugate Chem.* 20 (4): 808–816.
54. Sanford, M.S. and Scott, P.J.H. (2016). Moving metal-mediated ^{18}F -fluorination from concept to clinic. *ACS Cent. Sci.* 2 (3): 128–130.
55. Hoover, A.J., Lazari, M., Ren, H. et al. (2016). A transmetalation reaction enables the synthesis of $[^{18}\text{F}]5$ -fluorouracil from $[^{18}\text{F}]$ fluoride for human PET imaging. *Organometallics* 35 (7): 1008–1014.

Chapter 11

The Radiochemistry of Zirconium

Jason P. Holland

Department of Chemistry, University of Zurich, CH-8057, Zurich, Switzerland

11.1 INTRODUCTION

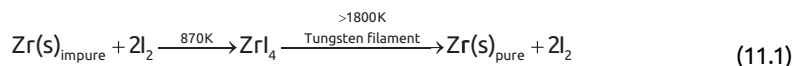
In the last two decades, the positron-emitting radionuclide zirconium-89 (^{89}Zr , $t_{1/2} = 78.41$ hours) has been the subject of increasing fundamental and clinical research activity centred around the development of radiolabelled antibodies, immunoglobulin fragments and other proteins for use in immuno-positron emission tomography (immuno-PET). Interest in ^{89}Zr stems from the excellent image quality reported in both preclinical and clinical studies, but also from the ease, efficiency, and reproducibility of the bioconjugation chemistry and radiochemistry required to make ^{89}Zr -labelled radiotracers. Other advantages include the low cost of production, automated isolation from the cyclotron target material (usually solid ^{89}Y foils), and the possibility to ship stock radionuclide solutions across continents. This chapter explores some of the fundamental properties of zirconium in aqueous environments, as well as the production, chemistry, and radiochemistry associated with the synthesis of ^{89}Zr -based radiotracers.

11.2 HISTORICAL BACKGROUND OF ZIRCONIUM

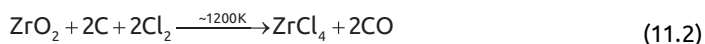
When asked to name one of the most abundant elements on Earth, most people would be unlikely to suggest zirconium. Nevertheless, zirconium is the 18th most abundant element in the Earth's crust, with estimated concentrations in the range $130\text{--}250\text{ mg kg}^{-1}$ [1, 2]. The most prevalent minerals that contain Zr ions include zircon (zirconium silicate, ZrSiO_4) and zirconium dioxide (ZrO_2). An interesting fact related to

nuclear chemistry is that in the geological sciences, zircon crystals play an important role in uranium-thorium-lead radiometric dating methods. Zircon crystals are exceedingly hard (hardness of 7.5 on the Mohs scale) and are highly resistant to both mechanical and chemical weathering. The relative concentrations of uranium, thorium and radiogenic lead, and the analysis of fission (or ion) tracks present in the zircon crystals allows geologists to estimate mineral ages from about 1 million years ago to over 4.4 billion years old (the current estimated age of the Earth) with a precision of 0.1–1.0%.

Element 40 is a second-row *d*-block transition metal and resides in group 4 of the Periodic Table. The first discovery is credited to Martin Heinrich Klaproth in 1789, who prepared ZrO_2 from zircon (Figure 11.1a). The elemental form of Zr was allegedly isolated by the prolific Swedish chemist Jöns Jacob Berzelius in 1824 (Figure 11.1b). However, due to the chemical similarities between zirconium and hafnium, pure forms of Zr were not obtained until much later. The crystal bar process (also known as the thermal iodide process or the Arkel-de Boer process) was invented by Anton Eduard van Arkel and Jan Hendrik de Boer in 1925 (Eq. (11.1)) [3].



Subsequently, William J. Kroll invented the chloride process (also known as the Kroll process) in 1940. This allowed pure forms of Zr(s) to be produced on large scales by adapting the methods used for isolating titanium (Eqs. (11.2) and (11.3)).

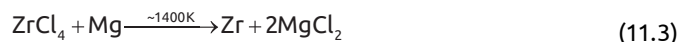


(a)
Klaproth
(1743–1817)



(b)
Berzelius
(1779–1848)

Figure 11.1 (a) Engraving of the German chemist Martin Heinrich Klaproth Source: Smithsonian Libraries. (b) Lithograph of the Swedish chemist Jöns Jacob Berzelius Electronic images were obtained from the Smithsonian Libraries Digital Collections (<https://library.si.edu>, accessed 16 January 2019). Source: Smithsonian Libraries.



Links between zirconium and the nuclear industry go deeper than just radionuclides. Zirconium has a very low absorption cross-section for thermal neutrons, which in combination with the high hardness, high resistance to corrosion, and high ductility, makes Zr a versatile metal. When zirconium is alloyed with other metals, including tin, niobium, chromium, and nickel (amongst others), the so-called zircalloys (containing ~95% Zr by weight) are common materials used as cladding for nuclear fuel rods.

11.3 RADIONUCLIDES OF ZIRCONIUM

Zirconium has three stable nuclides (Figure 11.2; ^{90}Zr [natural abundance (NA) = 51.45%], ^{91}Zr [NA = 11.22%], and ^{92}Zr [NA = 17.15%]) and two nuclides that are observationally stable (^{94}Zr , $t_{1/2} = 5.2 \times 10^{19}$ years [NA = 17.38%]; and ^{96}Zr , $t_{1/2} = 2.35 \times 10^{19}$ years [NA = 2.80%]). Interestingly, ^{94}Zr and ^{96}Zr have been predicted to undergo rare double- β ($\beta\beta$) decay yielding daughter nuclides ^{94}Mo and ^{96}Mo , respectively [4, 5]. The distinctive isotopic pattern is very useful in characterising zirconium ion coordination complexes by high-resolution mass spectrometry [6].

In total, there are 34 known isotopes of zirconium with mass numbers ranging from 78 to 112. At least six additional metastable states have also been reported (all nuclear data in this chapter are from the National Nuclear Decay Center [NNDC]; Brookhaven National Laboratory, Upton, NY; www.nndc.bnl.gov, accessed 17 January 2019). A subsection of the chart of nuclides showing some of the isotopes of zirconium encountered in the context of radiochemistry and nuclear medicine research is presented in Figure 11.3. In addition, a list of zirconium nuclides and their respective radioactive properties (isotopic mass,

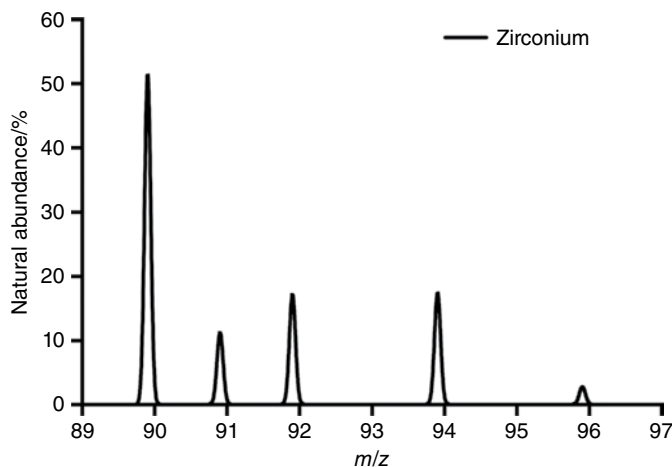
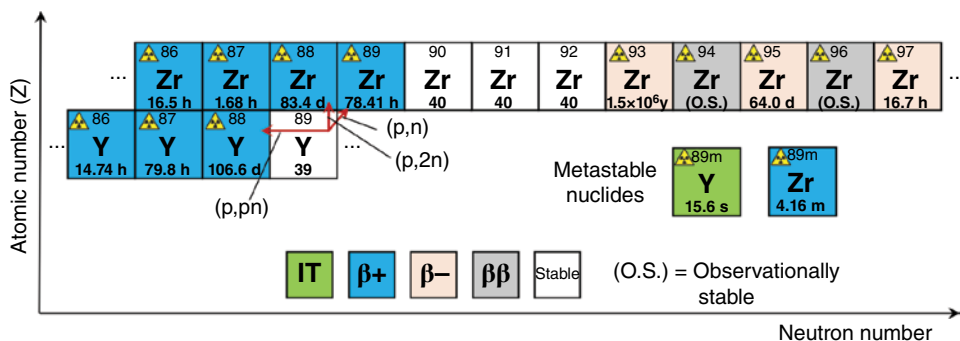


Figure 11.2 Natural isotopic abundance pattern of stable zirconium isotopes as observed by mass spectrometry.

Figure 11.3

Portion of the chart of nuclides showing relevant isotopes of zirconium and their respective decay modes.



half-life, decay mode, and primary daughters) is given in Table 11.1. In the broader context of radiochemistry, naturally occurring isotopes of zirconium, in particular ^{90}Zr , are target materials for cyclotron-induced (p,x)-type transmutation reactions to form various radionuclides of niobium. Of the radionuclides of element 41 that can be produced from solid metal zirconium targets, niobium-90 ($t_{1/2} = 14.60$ hours, $I(\beta^+) = 53\%$, $E_{\text{mean}}(\beta^+) = 0.35$ MeV) has been proposed as a potential alternative to copper-64 and zirconium-89 for immuno-PET. However, the concomitant release of high-energy and high-intensity γ -rays at 2186 keV (18.0%) and 2319 keV (82.0%) will likely prevent the clinical translation of ^{90}Nb compounds based on dosimetry concerns. The use of zirconium as a target is not considered further; but for more detailed information, the reader is referred to the publications by Rösch and co-workers [7–9]. The remainder of this chapter explores the production, chemistry, and radiochemistry of zirconium-89 for PET, but it is also worth mentioning that zirconium-97 ($t_{1/2} = 16.75$ hours, $I(\beta^-) = 100\%$, $E_{\text{mean}}(\beta^-) = 704$ keV, $E_{\text{max}}(\beta^-) = 1915.7$ keV) is a potent β^- emitter. At present, there are no known sources of zirconium-97, but if access to this radionuclide could be established, it would represent an ideal scenario in which the radioisotopes $^{89}\text{Zr}/^{97}\text{Zr}$ would form a matched pair for the synthesis of chemically identical diagnostic and radiotherapeutic agents.

11.4 ZIRCONIUM-89 PRODUCTION AND NUCLEAR CHEMISTRY

Zirconium-89 ($t_{1/2} = 78.41$ hours, $I(\beta^+) = 22.74\%$, $E_{\text{mean}}(\beta^+) = 395.5$ keV, $E_{\text{max}}(\beta^+) = 2399$ keV) is the most important radionuclide of element 40 and has been utilised in an increasing number of preclinical and clinical studies. The fact that zirconium-89 has been translated to human trials is testament to the sterling work performed over the last three to four decades by research groups in Europe and the United States, and throughout the world [10]. Many excellent review articles on zirconium-89 have appeared, but rapid advances in the field mean that the reader is urged to exercise caution when referring to the various reported methods therein [11–20].

Table 11.1 List of the observed nuclides of zirconium.

Nuclide	Isotopic mass (a.u.)	Half-life	Decay mode	Daughter nuclides
⁷⁸ Zr	77.95523	>170 ns	EC	⁷⁸ Y
⁷⁹ Zr	78.94916	56 ms	(β+, p) or β+	⁷⁸ Sr or ⁷⁹ Y
⁸⁰ Zr	79.9404	4.6 s	β+	⁸⁰ Y
⁸¹ Zr	80.93721	5.5 s	β+	⁸¹ Y
⁸² Zr	81.93109	32 s	β+	⁸² Y
⁸³ Zr	82.92865	41.6 s	β+	⁸³ Y
⁸⁴ Zr	83.92325	25.9 min	β+	⁸⁴ Y
⁸⁵ Zr	84.92147	7.86 min	β+	⁸⁵ Y
⁸⁶ Zr	85.91647	16.5 h	β+	⁸⁶ Y
⁸⁷ Zr	86.914816	1.68 h	β+	⁸⁷ Y
⁸⁸ Zr	87.910227	83.4 d	EC	⁸⁸ Y
⁸⁹ Zr	88.908890	78.41 h	EC, β+	⁸⁹ Y
^{89m} Zr (metastate)	587.8 keV	4.16 min	IT (93.8%), and β+ (6.2%)	⁸⁹ Zr and ⁸⁹ Y
⁹⁰ Zr	89.9047044	Stable		51.45% abundance
⁹¹ Zr	90.9056458	Stable		11.22% abundance
⁹² Zr	91.9050408	Stable		17.15% abundance
⁹³ Zr	92.9064760	1.61 × 10 ⁶ yr	β-	⁹³ Nb
⁹⁴ Zr	93.9063152	O.S.	ββ predicted	17.38% abundance
⁹⁵ Zr	94.9080426	64.0 d	β-	⁹⁵ Nb
⁹⁶ Zr	95.9082734	O.S. (2.35 × 10 ¹⁹ yr)	ββ	2.80% abundance
⁹⁷ Zr	96.9109531	16.75 h	β-	⁹⁷ Nb
⁹⁸ Zr	97.912735	30.7 s	β-	⁹⁸ Nb
⁹⁹ Zr	98.916512	2.1 s	β-	⁹⁹ Nb
¹⁰⁰ Zr	99.91776	7.4 s	β-	¹⁰⁰ Nb
¹⁰¹ Zr	100.92114	2.3 s	β-	¹⁰¹ Nb
¹⁰² Zr	101.92298	2.9 s	β-	¹⁰² Nb
¹⁰³ Zr	102.92660	1.32 s	β-, (β-n)	¹⁰³ Nb, ¹⁰² Nb
¹⁰⁴ Zr	103.92878	0.87 s	β-, (β-n)	¹⁰⁴ Nb, ¹⁰³ Nb
¹⁰⁵ Zr	104.93305	167 ms	β-, (β-n)	¹⁰⁵ Nb, ¹⁰⁴ Nb
¹⁰⁶ Zr	105.93591	180 ms	β-	¹⁰⁶ Nb
¹⁰⁷ Zr	106.94075	146 ms	β-	¹⁰⁷ Nb
¹⁰⁸ Zr	107.94396	77.4 ms	β-	¹⁰⁸ Nb
¹⁰⁹ Zr	108.94924	56 ms	β-	¹⁰⁹ Nb
¹¹⁰ Zr	109.95287	37.5 ms	β-	¹¹⁰ Nb
¹¹¹ Zr		24 ms	β-	¹¹¹ Nb
¹¹² Zr		30 ms	β-, (β-2n), (β-n)	¹¹² Nb, ¹¹¹ Nb, ¹¹⁰ Nb

O.S. = observationally stable.

Source: Data from the National Nuclear Decay Center (NNDC; Brookhaven National Laboratory, Upton, NY; www.nndc.bnl.gov, accessed 17 January 2019). O.S. = observationally stable.

Notwithstanding the recent advances in zirconium-89 radiochemistry, the first production and use of this radionuclide in both animal models and humans were reported in the 1940s and 1950s [21–23]. Whilst working at the Massachusetts Institute of Technology cyclotron facility, Shure and Deutsch were among the first to report the decay properties of ^{89}Zr after production via the $^{89}\text{Y}(\text{d},2\text{n})$ transmutation reaction [24]. Later in 1957, Dr John Mealey reported the first pharmacokinetic studies of zirconium-89 distribution in humans, which were performed at Massachusetts General Hospital and Harvard Medical School (Boston, USA) [23]. Experiments used a citrate formulation of ^{89}Zr ions produced after irradiation of ^{89}Y solid targets and purification/isolation by using classic ion-exchange methods (Dowex-1 resin, washing with HCl, and elution with HNO_3). Citrate was introduced to minimise colloid formation. Importantly, Mealey reported that “In preliminary chemical toxicity studies in mice, 100–200 times the contemplated dose per kilogram in man was well-tolerated. No ill-effects were observed in any of the animals.” After intravenous injection of “ ^{89}Zr -citrate” formulations in two patients undergoing neurosurgery, biopsy samples were taken at approximately 90 minutes and 3 hours post-administration. Concentrations of ^{89}Zr in bone, muscle, normal brain tissue, and brain tumour tissue were measured at 0.9, 7.6, 0.8, and 4.6 %ID/kg, respectively. Temporal excretion studies found that most of the ^{89}Zr activity was retained in the body with only 2.5 %ID/kg eliminated in the urine by 24 hours, and a total of only 7.6 %ID/kg eliminated after seven days. Conclusions were that “after intravenous injection of zirconium-89 in carrier-free dilute citrate solution, the radiozirconium is only very slowly cleared from the plasma due to formation of metal complexes with plasma proteins.” Although current knowledge of the pharmacokinetics of zirconium complexes in mammals is more detailed, these pioneering results paved the way for future use of both ^{89}Zr and other metal-based positron-emitting nuclides in humans.

From the 1970s onwards, many groups explored zirconium-89 radiochemistry [25–33], but modern methods for the production of zirconium-89 in high quantities, purity, and specific activity stem from the 1990s and the publications of Herscheid et al. [34–36]. Separation and radiolabelling chemistry was advanced further by Verel et al. [37, 38], and standardised methods were reported in 2010 [39].

Zirconium-89 for clinical use is now almost exclusively produced with small biomedical cyclotrons (with c. 9–19 MeV incident proton beam energy) via the $^{89}\text{Y}(\text{p},\text{n})^{89}\text{Zr}$ transmutation reaction. Cyclotron solid target designs are not standardised. Most centres that produce ^{89}Zr opt for custom-made solutions. Schematic diagrams and a photograph of a custom-made solid target designed by Dr Bruce Wieland and co-workers (BTI Targetry, Cary, North Carolina, USA) for irradiating metal foils using a GE PETtrace is shown in Figure 11.4. The irradiation target typically uses 100% naturally abundant ^{89}Y solid metal foils, although solution targets [40, 41], thick targets [42], and powdered/pressed targets [43] have been considered. When irradiating a solid ^{89}Y foil with protons, three principal reaction channels must be considered. Excitation functions for the $^{89}\text{Y}(\text{p},\text{n})^{89}\text{Zr}$, $^{89}\text{Y}(\text{p},\text{pn})^{88}\text{Y}$, and $^{89}\text{Y}(\text{p},2\text{n})^{88}\text{Zr}$ transmutation reactions are shown in Figure 11.5 and Eq. (11.4).

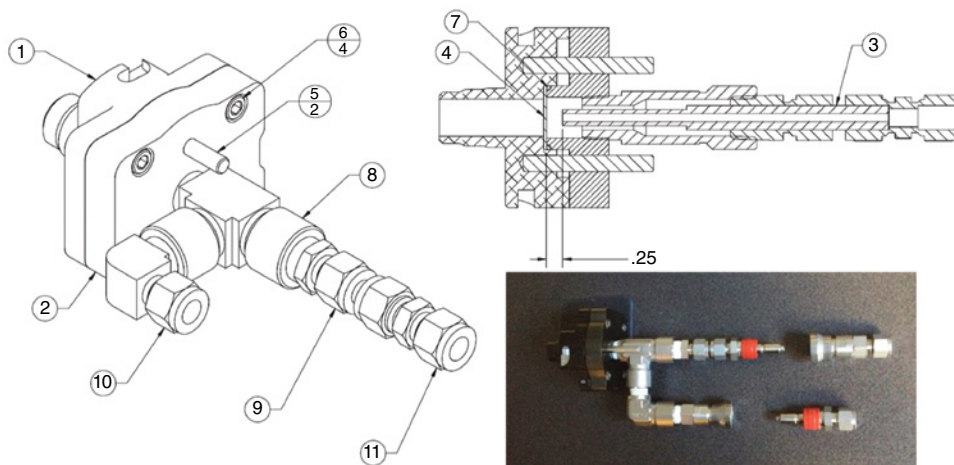


Figure 11.4 Figure showing design schematics and a photograph of a water-cooled solid-metal target assembly for use on a GE PETtrace cyclotron. Source: Design and schematics courtesy of Dr. Matthew Stockley, BTI Targetry.

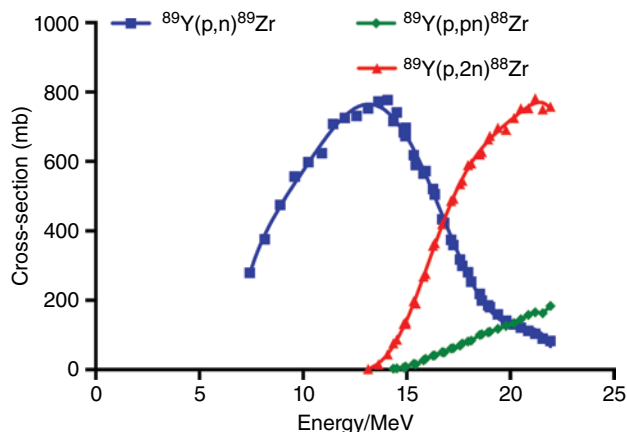
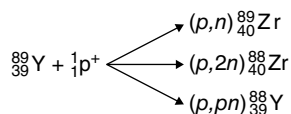


Figure 11.5 Experimentally measured excitation functions showing the cross-sections for the formation of ^{89}Zr (blue), ^{88}Y (green), and ^{88}Zr (red) during irradiation of a thin ^{89}Y foil with protons in the energy range ~7 to ~22 MeV.



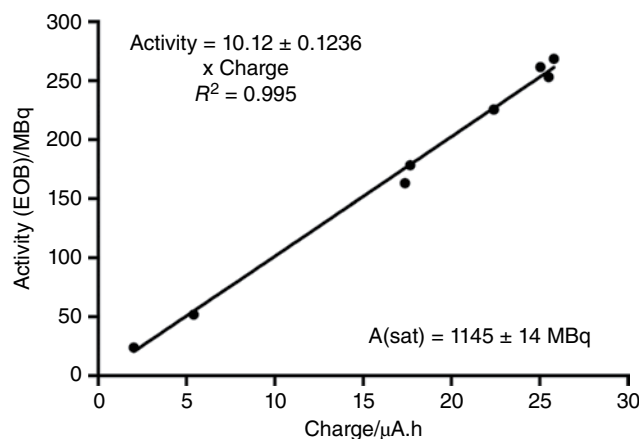
11.4

Calculated threshold energies for the transmutation of ^{89}Y to ^{89}Zr , ^{88}Y , and ^{88}Zr are 3.65, 11.60, and 13.08 MeV, respectively. In practice, proton beam energies in the range of approximately 13–15 MeV are used to ensure a balance between efficient production of clinically useful quantities and minimising the formation of long-lived ^{88}Y ($t_{1/2} = 106.626$ d h) and ^{88}Zr ($t_{1/2} = 83.4$ days) radionuclide impurities. Representative experimental data on the irradiation yields of ^{89}Zr with different irradiation energies and time are presented in Table 11.2 and Figure 11.6.

Table 11.2 Experimental data on the irradiation yields of ^{89}Zr using an ^{89}Y foil target.

Irradiation number	Approximate current (mA)	Duration (min)	Charge (mAh)	End of bombardment activity (MBq)
1	5	25	2.03	23.98
2	5.5	60	5.42	51.80
3	7	153	17.38	163.17
4	8	172	22.40	225.70
5	9	175	25.50	253.08
6	9	120	17.67	178.34
7	9	176	25.81	268.62
8	10	153	25.04	261.59

Figure 11.6 Plot of the activity yield (MBq) versus the incident charge (mAh) giving an activity at saturation of 1145 ± 14 MBq.



11.4.1 Decay Properties of Zirconium-89

Although not perfect, ^{89}Zr possesses favourable nuclear decay characteristics for use in the preparation of radiotracers that exhibit prolonged circulation and uptake times *in vivo*. Experimental data showing the γ -ray emission spectrum of ^{89}Zr are presented in Figure 11.7, and nuclear decay schemes for radioactive decay of ^{89}Zr and the metastable excited state $^{89\text{m}}\text{Zr}$ are shown in Figure 11.8a,b, respectively. In spite of the moderate complexity of the ^{89}Zr decay scheme, only two γ -ray lines at 511 and 909.2 keV have significant emission intensities. Nevertheless, when compared with the emission spectra of other common radionuclides like ^{11}C , ^{13}N , ^{18}F , and ^{64}Cu for PET imaging, the additional radiation burden imposed by the $\sim 99\%$ intensity emission of photons at 909.2 keV has important implications regarding radiation protection for nuclear medicine clinicians, patient dosimetry, and patient management. It also places stringent limitations on the maximum administered doses of ^{89}Zr -based radiopharmaceuticals (which is typically in the range 37–185 MBq in human trials). In spite of the excellent clinical performance reported for many different ^{89}Zr -radiolabelled antibodies, some members of the nuclear medicine community remain concerned about dosimetry. Improved patient management strategies

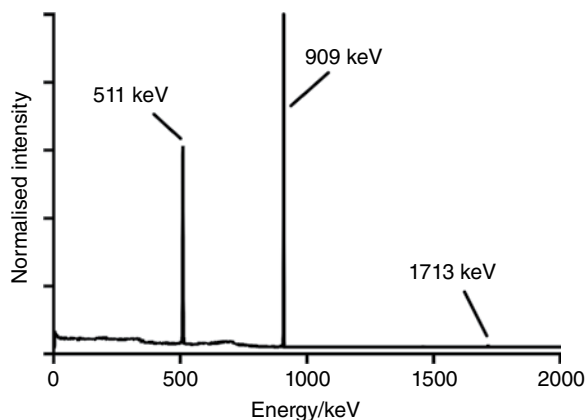


Figure 11.7
Experimental γ -ray emission spectrum of ^{89}Zr .

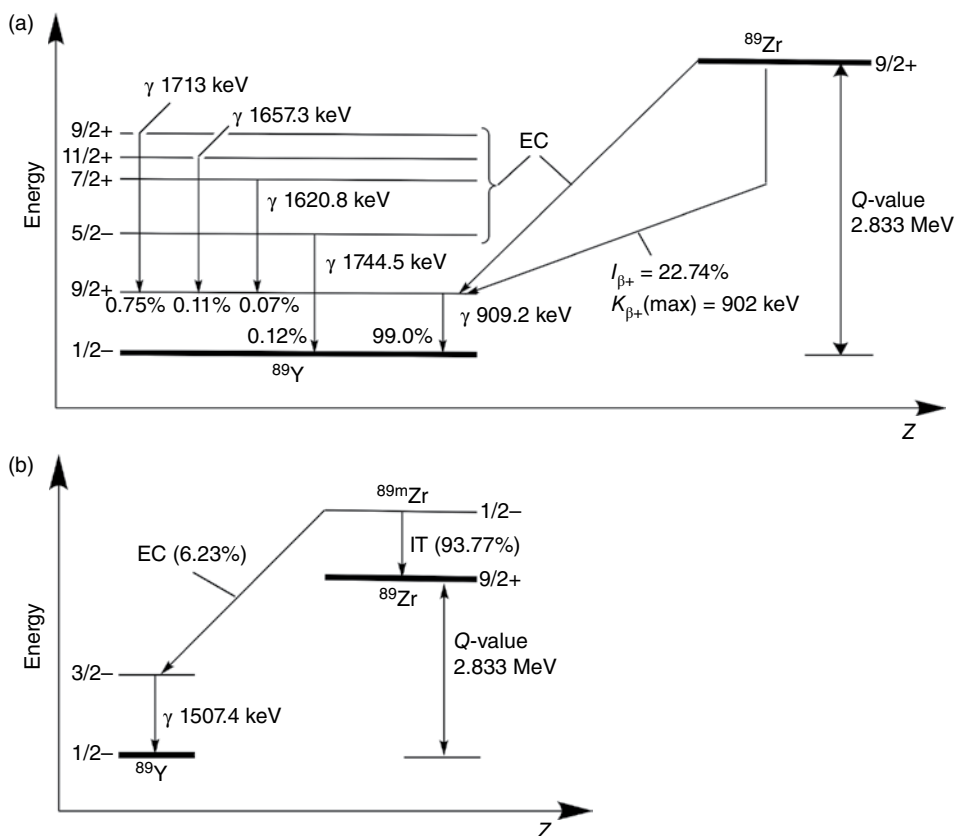


Figure 11.8 Nuclear energy level decay schemes for (a) ^{89}Zr (ground state) and (b) $^{89\text{m}}\text{Zr}$ meta-stable excited state ($t_{1/2} = 4.16$ minutes) formed during $^{89}\text{Y}(p,n)^{89}\text{Zr}$ production using a cyclotron.

and increased clinical experience are still required before ^{89}Zr -immuno-PET can receive more widespread acceptance in nuclear medicine.

Most radiochemists working on ^{89}Zr -radiotracers only encounter the ^{89}Zr ground state radionuclide. However, cyclotron production of ^{89}Zr typically produces high quantities

of the ^{89m}Zr excited state. For this reason, targets are usually left to “cool” for at least an hour prior to removing the ^{89}Y -foil and commencing the purification chemistry.

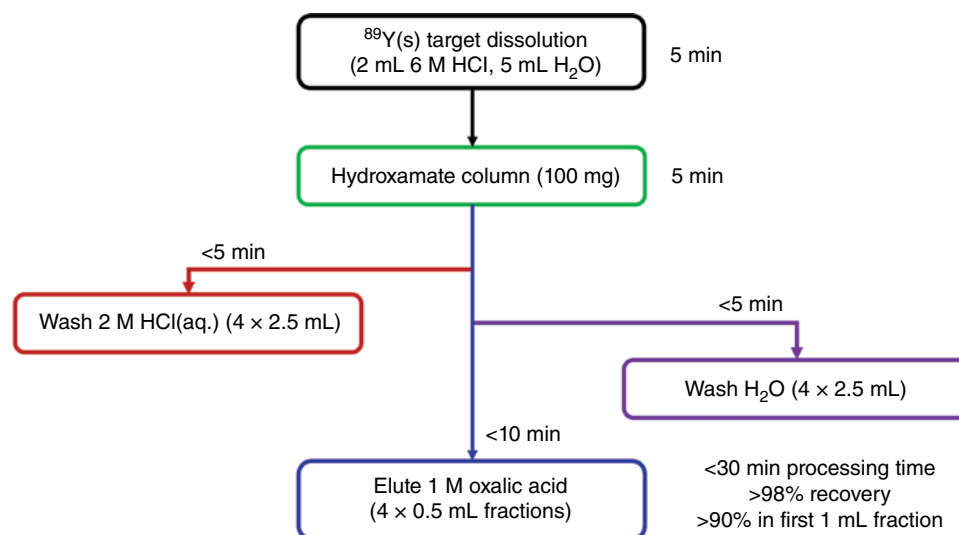
The comparatively low mean kinetic energy of the positrons emitted during the decay of ^{89}Zr (395.5 keV) means PET image resolution is essentially limited only by the physical resolution of the preclinical and clinical cameras used to record data sets and not by the nuclide itself. This means the spatial resolution of most reported ^{89}Zr -PET images is comparable to data reported using radiotracers labelled with ^{18}F or ^{64}Cu [10, 39, 44].

11.4.2 Separation Chemistry

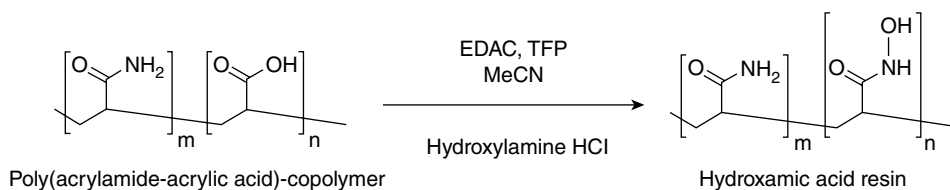
An overview of the manual steps involved in the purification of ^{89}Zr from the ^{89}Y target material is shown in Figure 11.9. The procedure has several important features. First, the ^{89}Y target (which is cheap and does not need recycling) is dissolved carefully by using a solution of 6 M HCl. This step generates copious amounts of heat and hydrogen gas, and the mixture is liable to boil. Hence, care should be taken to ensure that the solution is vented to prevent pressure buildup and that the mixture is sealed from ignition sources. While some research groups have opted for cooled reaction vessels to manage the heat produced from dissolution, this adaptation is not essential, and the temperature of the solution can be reduced effectively by controlled (stepwise or portion-wise) addition of the acid and later by diluting the mixture with cold water. It is essential to ensure that the final concentration of HCl is <2 M; otherwise, the separation chemistry will be compromised. It should be noted that all solutions should be prepared from the highest purity reagents. In addition, 18.2 M Ω -cm water is purified further by pretreatment using Chelex resin to ensure that other metal ions that may compete with Zr^{4+} ions during the separation and radiolabelling chemistries (in particular, Fe^{3+} ions) are removed.

Figure 11.9

Schematic flow-chart showing the steps and approximate timing involved in the manual separation of ^{89}Zr from the bulk ^{89}Y target material.



After dissolution, the mixture has a clear appearance, but some black precipitate/particulates remain. Although the black material has not been characterised, it is presumably a form of Y_2O_3 that precipitates during the addition of acid. The presence of the black precipitate does not impact the efficiency of the separation chemistry, and during the solid-phase extraction (SPE) step, it is completely removed by filtration. Once dissolved, the crude solution is passed onto a prepacked SPE cartridge containing ~100 mg of 'hydroxamate resin.' Commercial sources are now available, but during the early-to-late 2000s, research groups prepared these SPE cartridges manually. The 'hydroxamate' resin actually consists of a poly(acrylamide-acrylic acid) block co-polymer backbone in which the carboxylic acid groups have been transformed into hydroxamic acid groups via standard activated ester formation and amide bond formation using hydroxylamine in acetonitrile (Scheme 11.1) [39]. Loading the 'hydroxamate' resin takes <5 minutes with essentially >99% of the radioactivity retained on the SPE cartridge. Then, the resin is washed with dilute HCl to ensure the effective removal of the soluble fraction of Y^{3+} ions (and other metal ion impurities), followed by further washing with high-purity water. It should be noted that the resin remains white in colour with the exception of the top few millimetres, which trap the black particulate material. If the colour of the resin changes to orange/brown, this is a positive indication that the solutions are contaminated with Fe^{3+} ions. Ferric ions form strong dative covalent bonds with hydroxamate donors and give rise to intense metal-based electronic absorption at ~430 nm (molar absorption coefficient, $\epsilon \sim 2200 \text{ M}^{-1} \text{ cm}^{-1}$). At present, no methods have been reported for the effective separation of $^{89}\text{Zr}^{4+}$ ions from Fe^{3+} ions, and hence, if contamination is evident, it is best to abandon radiolabelling experiments, perform a full clean of the lab space to remove dust particles (which often contain rust), and prepare all solutions fresh.



Scheme 11.1
Chemical synthesis of the 'hydroxamate resin.'

After the washing steps, purified $^{89}\text{Zr}^{4+}$ ions are eluted from the SPE cartridge by washing with 1 M oxalic acid solution. The final product is obtained in <30 minutes processing time with high recovery of the activity and in high chemical and radiochemical purity. Measurements of the specific-activity using the aforementioned separation procedure gave a value in the range 195–496 MBq mg^{-1} of Zr (equivalent to a molar activity of 17.39–44.22 GBq μmol^{-1}) [39]. Given that the theoretical maximum molar activity of ^{89}Zr is 1478.74 GBq μmol^{-1} (449 056 Ci g^{-1} ; or 39.97 Ci μmol^{-1}), the estimated isotopic dilution factors (IDFs) for clinical-grade ^{89}Zr are in the range 33–87. This means the ^{89}Zr produced via this route is of comparable or even higher purity than standard productions of most ^{18}F - and ^{64}Cu -radiolabelled compounds [39, 45]. With such high molar activities (low IDF values), it is essential that the radiochemical kinetics of ^{89}Zr labelling reactions occurs

extremely fast to ensure efficient complexation and high radiochemical yields [45]. Radio-labelling efficiency depends strongly on the nature of the radiochemical species present in solution and on the thermodynamics and kinetics of the complexation reaction.

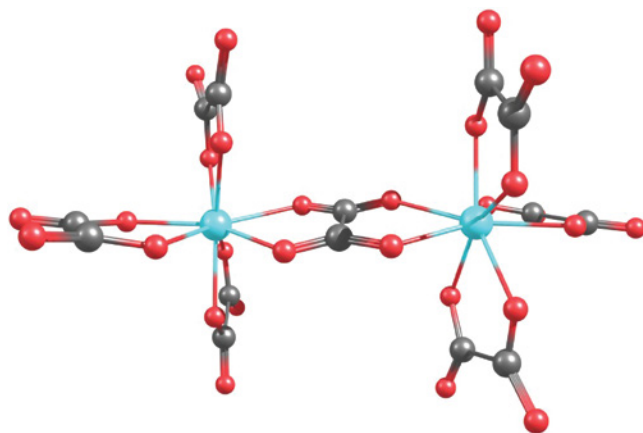
11.4.3 Zirconium Speciation in Aqueous Solution

In the elution step, the oxalate anions effectively displace the didentate hydroxamate donors under conditions of low pH (~1–2). Hydroxamate groups have pK_a values in the range 5.5–7.0, and thus are protonated under the elution conditions, making them weak donors. An underappreciated feature of this separation chemistry is that the ^{89}Zr -radioactivity is eluted as ' ^{89}Zr -oxalate' whose speciation is likely of the chemical formula $[\text{Zr}(\text{C}_2\text{O}_4)_4]^{4-}$ [46]. One of the major challenges of performing Zr chemistry in aqueous conditions is preventing the highly polar Zr^{4+} ions from hydrolysing [47, 48] or forming multinuclear hydroxylate complexes [49]. Oxalate anions have the effect of both solubilising Zr^{4+} ions and stabilising the complex against hydrolysis up to pH values over 7 [46].

Interestingly, Baggio et al. [50] have reported that Zr^{4+} in the presence of oxalate anions gives crystals showing a bridged dimeric structure in which both Zr^{4+} ions are 8-coordinate and one of the oxalate anions acts as a $\eta^4-\mu_2-\text{C}_2\text{O}_4$ bridging ligand. (Figure 11.10). Although the precise nature of the ^{89}Zr species in the oxalate solution remains uncertain, a wealth of empirical data has shown that the ' ^{89}Zr -oxalate' formulation is a suitable starting material for radiosynthesis.

In 2009, a method for the preparation of ' ^{89}Zr -chloride' was reported by myself and co-workers [39]. The rationale behind accessing a different formulation of $^{89}\text{Zr}^{4+}$ ions that do not contain oxalate ligands/oxalic acid was that powerful didentate ligands in high concentration can be thermodynamically and kinetically difficult to displace with some multidentate ligands (typically macrocyclic chelates) that have less accessible cavities. Our original method involved an initial (two-step) trap and release using a quaternary methyl ammonium ion (**QMA**) SPE cartridge followed by a practically cumbersome thermal hydrolysis step in which the ' ^{89}Zr -oxalate' mixture was boiled to dryness under

Figure 11.10 Single crystal X-ray structure of the bridged dimer $\text{K}_6[\{\text{Zr}(\text{C}_2\text{O}_4)_3\}_2(\mu-\text{C}_2\text{O}_4)]$ [50]. Note: potassium ions and water molecules incorporated inside the crystal are omitted for clarity.



a stream of nitrogen gas and in the presence of concentrated HNO₃. Hot nitric acid decomposes oxalic acid/oxalate, and subsequent reconstitution with 0.1 M HCl gave a ⁸⁹Zr-chloride' formulation. The exact chemical nature of the ⁸⁹Zr-chloride' species in solution remains unknown, but it is possible that the tetrameric zirconyl chloride structure, [Zr₄(OH)₈(H₂O)₁₆]Cl₈(H₂O)₁₂, is present. Although successful, this method has not been widely adopted. In addition, if the mixture is not heated to complete dryness, any residual oxalic acid will likely mean that the formulation is better described as ⁸⁹Zr-oxalate' in a HCl mixture. The two different speciations can be observed by the different distribution of ⁸⁹Zr-oxalate' and ⁸⁹Zr-chloride' in mice [39, 51].

In 2018, Graves et al. reported a streamlined approach toward chloride-based ⁸⁹Zr radiochemistry using a tributyl phosphate (TBP)-functionalized extraction resin [52]. This method eliminated the need for a QMA extraction and thermolysis, and an average Y/Zr separation factor of 1.5 × 10⁵ (n = 3) was obtained. One downside was that trace metal impurities, including radiochemically poisonous Fe³⁺ ions, were higher than in the original two-step QMA/thermolysis approach. Nevertheless, as work continues on new methods for accessing different initial formulations of ⁸⁹Zr⁴⁺ ions, it is likely that these studies will facilitate the investigation of a wider range of radiolabelling chemistry using different chelates.

11.5 ZIRCONIUM CHEMISTRY AND RADIOCHEMISTRY

11.5.1 Fundamentals

Although zirconium complexes are known in which the metal ion exists in oxidation states of 1+, 2+, 3+, and 4+, for the vast majority of zirconium complexes, the metal ion is found in the group oxidation state (Zr⁴⁺). The chemistry of Zr⁴⁺ ions is dominated by the fact that the ion has a very high charge-to-size ratio. In compounds containing Zr⁴⁺ ions, the metal centre exhibits a small covalent radius of 0.145 nm and ionic radius of 0.072 nm, and it has a value of 1.45 on the Pauling scale of electronegativity, making it an extremely electropositive element. Such high electropositivity is illustrated in the reduction potentials of various Zr⁴⁺ species (Eqs. (11.5)–(11.8)) and has important implications in the aqueous phase chemistry of zirconium.



The strongly negative reduction potentials of Zr^{4+} species mean that in aqueous environments, Zr ions with 1+, 2+, or 3+ charge reduce water and/or spontaneously disproportionate to give Zr^{4+} ions and $Zr(s)$ [1, 2]. Hence, existing aqueous phase radiochemistry of ^{89}Zr resides exclusively with the 4+ ion.

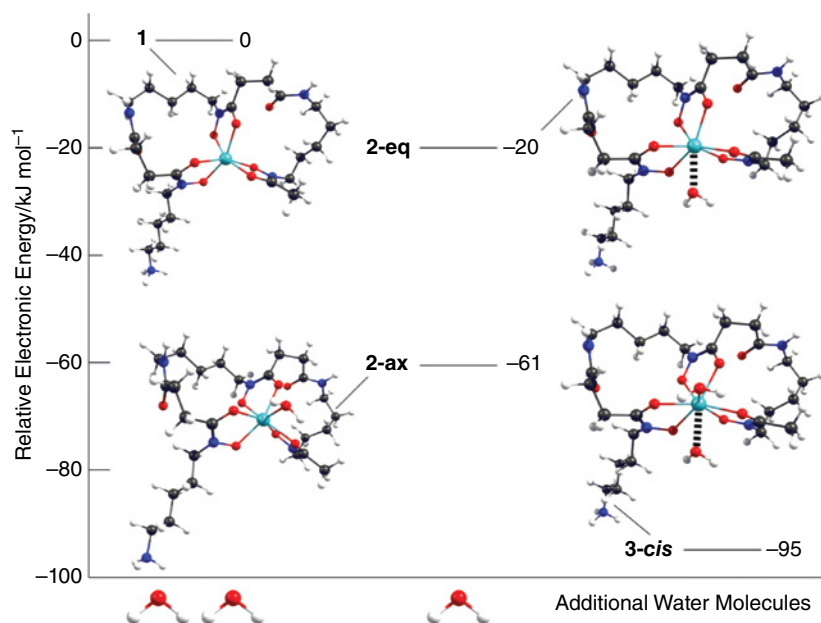
11.5.2 Coordination Compounds of Zirconium

Beyond radiochemistry, very few examples exist of Zr complexes that are stable in aqueous conditions. However, in non-aqueous environments, coordination complexes of Zr are more extensive, though still dominated by the 4+ ion. The organometallic compound zirconocene hydrochloride (Schwartz's reagent, $(C_5H_5)_4Zr_2H_2(CH_3)_2$) is a classic example of a covalent coordination complex containing Zr^{4+} ions. This compound is a common reagent used in organic reactions for chemical transformations of alkenes/alkynes and is also capable of selective reduction of amide bonds in the presence of other groups such as reducible esters. However, as with many organometallic compounds, Schwartz's complex is unstable in water and illustrates the major problem of zirconium chemistry: namely, how can the Zr^{4+} ion be stabilised against hydrolysis?

An additional complexity in zirconium coordination chemistry is that, in spite of the relatively small size, Zr^{4+} ions can form complexes with between six and eight donor atoms in the first coordination sphere. In 2010, co-workers and I reported the first computational study on the structure of the zirconium desferrioxamine B complex ($[Zr(HDFO)(H_2O)_n]^+$

Figure 11.11

Calculated relative energies of the $[Zr(HDFO)(H_2O)_n]^{2+}$ ($n = 0, 1, \text{ or } 2$) complexes.



where $n = 0, 1, \text{ or } 2$) in which the possibility of introducing coordinated water molecules was explored using density functional theory (DFT) [53]. Optimised structures and relative free energies (in kJ mol^{-1}) for four possible $[\text{Zr}(\text{HDFO})(\text{H}_2\text{O})_n]^{2+}$ species are shown in Figure 11.11. Note that in all structures, the DFO ligand is in the Λ -*N-cis-cis* geometric isomer. In total, eight geometric isomers can be made when DFO coordinates around a central metal cation, and each is optically active. Upon taking the thermodynamically most stable geometric isomer of the hexacoordinate $[\text{Zr}(\text{HDFO})]^{2+}$ complex (**1**), the addition of the first water molecule can occur in either a pseudo-axial or pseudo-equatorial site. Interestingly, the pseudo-axial site in which the water binds in the centre of a trigonal face produced by the carbonyl ($\text{C}=\text{O}$) oxygen atoms leads to a stable structure, but the opposite trigonal face (formed by the three $\text{N}-\text{O}$ donors) is inaccessible due to increased electron density that repels the water ligand. Addition of the water molecule was predicted to be thermodynamically feasible and spontaneous. The $[\text{Zr}(\text{HDFO})(\text{H}_2\text{O})]^{2+}$ structure with a pseudo-axial water (**2-ax**) molecule was found to be more stable than the addition of the water molecule in a pseudo-equatorial site (**2-eq**) and was calculated to be $\sim 61 \text{ kJ mol}^{-1}$ more stable than the hexadentate complex. The combination of both a pseudo-axial molecule and a pseudo-equatorial water molecule in $[\text{Zr}(\text{DFO})(\text{H}_2\text{O})_2]^{2+}$ stabilised the complex even further. However, it should be noted that the $\text{Zr}-\text{O}$ bond length of the water ligand in the pseudo-equatorial position of the 8-coordinate complex was very long (0.248 nm compared to 0.234 nm for the pseudo-axial $\text{Zr}-\text{O}$ bond length), indicating a 'loose' coordination and likely facile exchange with bulk solvent. The conclusions from this work were that (i) unlike most Zr complexes and many other radiometal complexes, coordination of a water molecule actually *stabilises* the

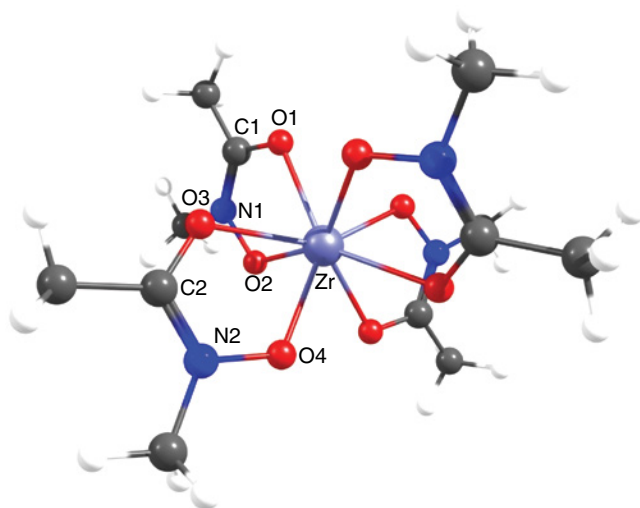


Figure 11.12 Structure of the 8-coordinate $\text{Zr}(\text{MeAHA})_4$ complex. Sources: Guérard, F., Lee, Y.S., Tripier, R. et al. [54]; and Holland, J.P. and Vasdev, N. [55].

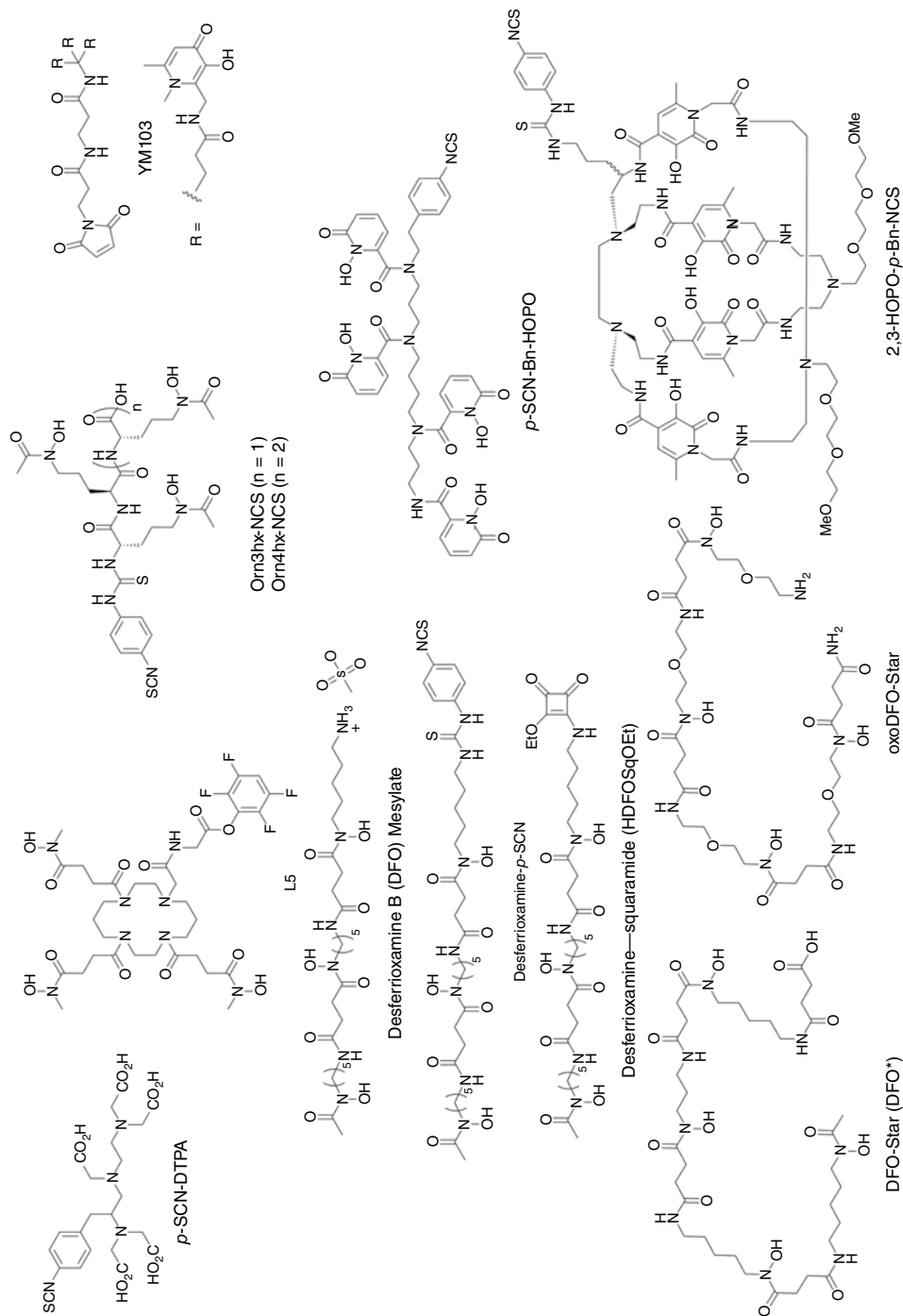


Figure 11.13 Chemical structure of selected bifunctional chelates that are potentially useful in the design of ^{89}Zr -based radiotracers.

Zr(DFO) complex; (ii) one water molecule fits comfortably in a pseudo-axial site, forming a potentially thermodynamically robust but still kinetically labile 7-coordinate complex; and (iii) Zr(DFO) can potentially expand the coordination sphere to accommodate up to eight donor atoms in the first shell.

Subsequent to these calculations, it was suggested that the comparatively high bone uptake observed in mice when using many different [^{89}Zr][Zr(DFO)]⁺ labelled antibodies is potentially the result of incomplete saturation of the first coordination sphere of the $^{89}\text{Zr}^{4+}$ ion, which facilitates hydrolysis. It should be noted that high accumulation of ^{89}Zr radioactivity in bone is a phenomenon that has been observed in mice but is not evident in human trials. Nevertheless, there is a definite need and scope for advancing ^{89}Zr radiochemistry by synthesising new ligands with different donor atom sets and with higher denticity (from six to eight donors).

In 2013, Guérard et al. reported the synthesis and single-crystal X-ray structure of the eight-coordinate Zr(MeAHA)₄ complex (Figure 11.12) [54]. This work confirmed that when steric constraints are not an issue (MeAHA ligands are very small), hydroxamate ligands can transchelate oxalate ligands from Zr⁴⁺ ions in eight-coordinate complexes. Further computational work by myself mapped out the thermodynamics of the MeAHA/oxalate exchange reaction using simulated ‘acidic’ and ‘basic’ conditions [55]. Indeed, the DFT studies found that the substitution reaction was thermodynamically feasible above pH values of approximately 4.19 (corresponding to the second pK_a value of oxalic acid). The calculations also yielded a set of design criteria for the design and synthesis of new ligands for $^{89}\text{Zr}^{4+}$ complexation.

In the last few years, many groups around the world have been working actively on the design and synthesis of new bifunctional ligands for $^{89}\text{Zr}^{4+}$ radiochemistry [11–20]. Structures of a number of promising bifunctional chelates are shown in Figure 11.13 [56–68]. The reader should note that the list is by no means comprehensive but is rather a selection of different bifunctional chelates that illustrate the current chemical scope of ligands for Zr coordination. Almost without exception [64], the reports claim that the new ligands, and in particular those that represent octadentate scaffolds, exhibit “superior” stability, imaging quality, and distribution in mice, which confirms that there is still room for improvement in Zr coordination chemistry. In spite of the very interesting chemistry that is emerging from exploring the expanded coordination space of Zr, the success of DFO in the clinical setting, and the fact that desferrioxamine is readily available as an approved GMP source, mean the jury is still out on whether any of these new chelates will supersede the existing technology.

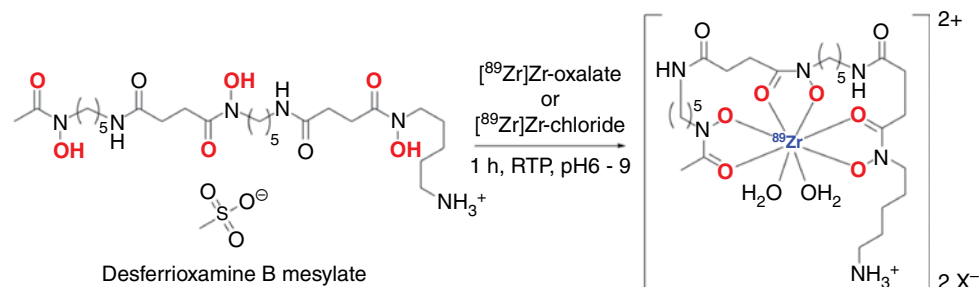
11.5.3 Radiolabelling with Zirconium-89

Methods for bioconjugation of proteins with chelates like DFO have been reported elsewhere and are not discussed further here [69]. In addition, ^{89}Zr has been employed as a radionuclide for developing alternative protein conjugation strategies [70–73]. The advantages of using [^{89}Zr][Zr(C₂O₄)₄]⁴⁻ (aq.) solutions in radiosynthesis include (i) stabilisation

of the $^{89}\text{Zr}^{4+}$ ion against hydrolysis and/or colloidal formation over a wide pH range; (ii) facile exchange of the oxalate ligands by multidentate chelates bearing powerful carboxylate, hydroxamate, or hydroxypyridinone (**HOPO**) donors; and (iii) rapid radiolabelling kinetics (Scheme 11.2). In most common radiolabelling methods, stock solutions of $[\text{}^{89}\text{Zr}][\text{Zr}(\text{C}_2\text{O}_4)_4]^{4-}$ containing 1 M oxalic acid are first neutralised carefully by using a base (for example, ~1 M solutions of Na_2CO_3 , NaHCO_3 , or NaOH , etc.). Neutralised solutions can be buffered by using carbonate solutions for pH values in the range ~7–9, or alternatively by using 4-(2-hydroxyethyl)-1-piperazineethanesulfonic acid (HEPES) for tighter control of pH values ~6.8–8.2. Other buffer systems may also work, but it is advisable to avoid those that contain phosphate groups, which may act as competitive ligands for Zr^{4+} ions.

Scheme 11.2

Radiosynthesis of $[\text{}^{89}\text{Zr}][\text{Zr}(\text{HDFO})(\text{H}_2\text{O})_n]^{2+}$.



In the manual synthesis of ^{89}Zr -radiolabelled antibodies conjugated with the DFO chelate, reactions are typically incubated at room temperature or heated up to 37°C for between 30 and 60 minutes. Mixtures may be agitated gently by hand or mixed by using a rocker but are not normally stirred or vortexed to avoid protein flocculation. Efficient mixing does increase radiolabelling rates, as illustrated by the work of Wright et al., who used microfluidic apparatus to prepare single patient doses of ^{89}Zr -radiolabelled trastuzumab [74]. After radiolabelling reactions are complete, mixtures are typically quenched with excess DTPA or EDTA solutions to strip any non-specifically bound ^{89}Zr from the protein fraction. Then, the ^{89}Zr -radiolabelled antibody component is purified and formulated for injection using manual or automated size-exclusion chromatography methods. For manual purification, columns containing PD-10 (Sephadex gel) are often used, or centrifugation spin-filtration is possible. Alternatively, preparative size-exclusion HPLC can be used. The advantage of HPLC methods is that chromatographic resolution can facilitate quantification (and separation) of any dimeric or multimeric protein aggregates that may form during the bioconjugation or radiolabelling steps. However, HPLC methods are more expensive and time-consuming, require specialist equipment, and are more challenging to maintain in a GMP environment.

If stock solutions of ' ^{89}Zr -chloride' are employed for radiolabelling, care must be taken to ensure that the pH of the mixture remains acidic. In the absence of oxalate anions (or other supporting ligands like citrate), hydrated Zr^{4+} ions are likely to aggregate and form metal clusters that may impact the success of radiolabelling reactions [39, 52].

11.6 PRECLINICAL AND CLINICAL REPORTS USING ZIRCONIUM-89-RADIOLABELLED PROTEINS

If one excludes the early human studies reported by Mealey [23], the first pilot experiments using ^{89}Zr -radiolabelled antibodies in patients were reported in 2006 [75, 76]. Since then, many preclinical studies and clinical trials using different ^{89}Zr -radiolabelled antibodies have been performed across the world. A non-comprehensive list of relevant reports is given in Table 11.3. Two recent articles by Jauw et al. [129] and Bensch et al. [130] have provided comparative (meta) studies on the experience gained from clinical trials with multiple different ^{89}Zr -radiolabelled antibodies. These comparative assessments provide a retrospective view of the *in vivo* biodistribution and tumour targeting of ^{89}Zr -immuno-PET radiotracers. As ^{89}Zr -immuno-PET radiopharmaceuticals advance beyond early-stage clinical trials, one important aspect of multicentre trials is harmonising the methods used to administer the radiotracers and acquire/interpret the images. Makris et al. pointed out that harmonisation of image quality is achievable, but more studies will be required before a standard ^{89}Zr -immuno-PET protocol can be adapted in a wider setting [131].

11.7 FUTURE DIRECTIONS AND EMERGING TECHNOLOGIES

With the evident success of ^{89}Zr -immuno-PET in the clinic, it is safe to say that ^{89}Zr -based radiopharmaceuticals are not only breaking new ground in nuclear medicine but also spurring the development of new chemistry and radiochemistry. The introduction of advanced technologies such as alternative chelates with improved thermodynamic, kinetic, and metabolic stability for Zr^{4+} ion coordination (*vide supra*); facile conjugation methods [132, 133]; automated production [134]; and an increasing number of highly specific radiotracers against emerging biomarkers means that zirconium-based radiopharmaceutical research (both fundamental and clinical) is accelerating. Two recent advances that have the potential to impact future production of ^{89}Zr -radiolabelled antibodies are given next.

11.7.1 Automated Production

In 2018, the team in Amsterdam reported a major advance in the automated radiosynthesis and purification of ^{89}Zr -radiolabelled antibodies. In this work, [^{89}Zr]Zr-DFO-*N*-sucetuximab and [^{89}Zr]Zr-DFO-*N*-suc-rituximab were produced with isolated radiochemical yields of $74.6\% \pm 2.0\%$ and $62.6\% \pm 3.0\%$, respectively. In both cases, radiochemical purity was $>95\%$, and the protein remained biochemically active with immunoreactive fractions $>87\%$. The importance of having an automated production method cannot be overstated.

Table 11.3 Overview of some influential studies using ⁸⁹Zr-radiolabelled antibodies/proteins in animals and in human trials that have been completed since 2006.

Radiotracer	Target/ biomarker	Animal model/patient cohort	Year/reference
Animal models			
[⁸⁹ Zr]mcAb-U36 chimeric monoclonal antibody (cmAb)	CD44v6	Head and neck squamous cell carcinoma (HNSCC): HNX-OE	2003, Verel et al. [38]
[⁸⁹ Zr]DN30	c-MET (CD)	Head and neck cancer: GLT-16 (high)/FaDu (low)	2008, Perk et al. [77]
[⁸⁹ Zr]trastuzumab	HER2/ <i>neu</i>	SK-OV-3 BT-474/negative MDA-MB-468 NCI-N87/negative MKN74 MDA-435	2009, Dijkers et al. [78] 2010, Holland et al. [79] 2012, Chang et al. [80] 2013, Janjigian et al. [81]
[⁸⁹ Zr]trastuzumab-F(ab') ₂	HER2/ <i>neu</i>	SKBR3/FaDu	2010, Oude Minnick et al. [82] 2012, Oude Minnick et al. [83]
[⁸⁹ Zr]cetuximab	EGFR	U-373 MG/HT29/T-47D	2008, Aerts et al. [84] 2005, Perk et al. [85]
[⁸⁹ Zr]transferrin	CD71 (TRFC)	Prostate cancer: HiMYC transgenic mice and MycCaP tumours Hormone-sensitive prostate cancer cell lines CWR22Pc and MDA PCa 2b Gliomas: TS543, U87-MG, LN-18, SF268 Diffuse large B-cell lymphoma: TDM8 Burkitt's lymphoma: Raji Breast cancers: MDA-MB-157/MDA-MB-231/Hs578T	2012, Holland et al. [86] 2013, Evans et al. [87] 2016, Doran et al. [88] 2017, Aggarwal et al. [89] 2018, Henry et al. [90]
[⁸⁹ Zr]7E11	PSMA internal epitope	Prostate cancer: LNCaP	2011, Ruggiero et al. [91]
[⁸⁹ Zr]AC-10	CD30	Lymphoma: Karpas 299/negative A-431	2016, Rylova et al. [92]
[⁸⁹ Zr]J591	PSMA	LNCaP/negative PC-3	2011, Holland et al. [53]
[⁸⁹ Zr]Mb (dimeric scFv-C _H 3)	PSMA	LNCaP/negative PC-3	2014, Viola-Villegas et al. [93]
[⁸⁹ Zr]Cys-Db (dimeric scFv)			
[⁸⁹ Zr]RO5323441	PlGF	Hepatocellular cancer: Huh7 Human renal cell carcinoma: ACHN	2013, Oude Minnick et al. [94]
[⁸⁹ Zr]bevacizumab	VEGF	Ovarian cancers: SK-OV-3, A2780/resistant CP70 Colorectal cancer: Colo205	2007, Nagengast et al. [95] 2010, Nagengast et al. [96] 2011, Nagengast et al. [97]
[⁸⁹ Zr]rituximab	CD20	Human B-cell lymphoma: huCD20TM	2012, Natarajan et al. [98]
[⁸⁹ Zr]cG250-F(ab) ₉ 2	CAIX (hypoxia)	Head and neck: SCCNij3	2010, Hoeben et al. [99]
[⁸⁹ Zr]cG250	CAIX (hypoxia)	Clear cell renal cell carcinoma: SK-RC-52 or NU-12	2013, Stillebroer et al. [100]

Table 11.3 (Continued)

Radiotracer	Target/ biomarker	Animal model/patient cohort	Year/reference
[⁸⁹ Zr]TRC105	CD105	Breast cancer lung metastasis: 4T1	2012, Hong et al. [101]
[⁸⁹ Zr]R1507	IGF-1R	Triple negative breast cancer	2010, Heskamp et al. [102]
[⁸⁹ Zr]onartuzumab	c-MET	MKN-45 (high), SNU-16 (moderate), U87-MG (low)	2012, Jagoda et al. [103]
[⁸⁹ Zr]059–053	CD147	Pancreatic cancer: MIA Paca-2, PANC- 1, BxPC-3, AsPC-1 (negative mouse A4)	2013, Sugyo et al. [104]
[⁸⁹ Zr]panitumumab	EGFR	Breast cancer: MDA-MB-468	2013, Bhattacharyya et al. [105] 2014, Wei et al. [106]
[⁸⁹ Zr]RG7356	CD44	MDA-MB-231/negative HepG2	2014, Vugts et al. [107]
[⁸⁹ Zr]αGPC3	Glypican-3 (GPC3)	Hepatocellular carcinoma: HepG2/ negative HLF and RH7777	2014, Sham et al. [108]
[⁸⁹ Zr]-AMA <i>Human trials</i>	Anti-mesothelin	Pancreatic cancer: HPAC and CAPAN-2	2015, ter Weele et al. [109]
[⁸⁹ Zr] Zevalin(ibrutinomab tiuxetan)	CD20	CD20+ B-cell non-Hodgkin's lym- phoma (NHL)	2006, Perk et al. [75] 2012, Rizvi et al. [110]
[⁸⁹ Zr]mcAb-U36 chi- meric monoclonal antibody (cmAb)	CD44v6	Head and neck squamous cell carcinoma (HNSCC)	2006, Börjesson et al. [76] 2009, Börjesson et al. [111]
[⁸⁹ Zr]trastuzumab	HER2/ <i>neu</i>	Metastatic breast cancer Esophagogastric cancer	2007, Dijkers et al. [112] 2010, Dijkers et al. [113] 2016, Laforest et al. [114] 2017, O'Donoghue et al. [115]
[⁸⁹ Zr]J591	PSMA	Prostate cancer	2013, Morris et al. [116] 2014, Pandit-Tasker et al. [117] 2015, Pandit-Tasker et al. [118] 2016, Pandit-Tasker et al. [119]
[⁸⁹ Zr]DF-IAB2M mini- body	PSMA	Prostate cancer	2016, Pandit-Tasker et al. [120]
[⁸⁹ Zr]panitumumab	EGFR	Metastatic colon cancer	2017, Lindenberg et al. [121]
[⁸⁹ Zr]bevacizumab	VEGF	Breast cancer	2012, van der Bilt et al. [122] 2013, Gaykema et al. [123] 2014, van Asselt et al. [124] 2015, Oosting et al. [125]
[⁸⁹ Zr]fresolimumab	Transforming growth factor β (TGF-β)	Glioma	2015, den Hollander et al. [126]
[⁸⁹ Zr]rituximab	CD20	B-cell lymphoma	2015, Muylle et al. [127]
[⁸⁹ Zr]cetuximab	EGFR	Colorectal cancer	2015, van Oordt et al. [128]

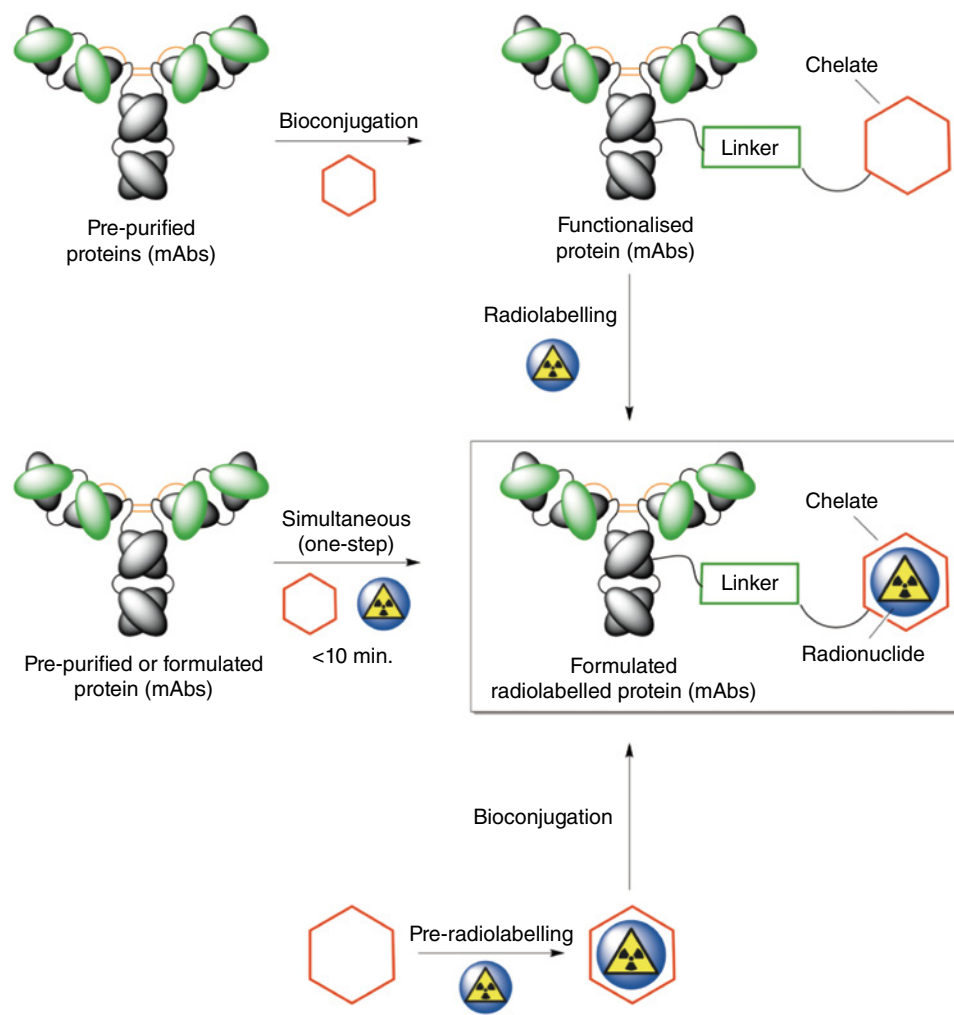
Note: the list is not intended to be comprehensive but rather demonstrates a range of compounds/targets that have been investigated.

Although radiometal labelling reactions are generally simple to perform, it remains true that manual synthesis of radiopharmaceuticals is not possible in most nuclear medicine facilities. Automation is highly desirable. If a disposable, cartridge-based system can be made available, it is conceivable that many more hospitals will be able to access ^{89}Zr -radiolabelled antibodies using in-house facilities.

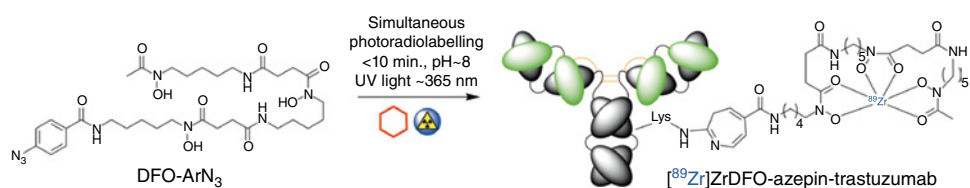
11.7.2 Simultaneous Bioconjugation and Radiolabelling

Conceptually, radiolabelled antibodies can be produced via three different routes (Scheme 11.3). The vast majority of radiolabelled antibodies are made via a two-step pre-conjugation approach. In the first step (bioconjugation), the protein is normally purified from source and conjugated to a suitable chelate, and then the intermediate

Scheme 11.3 Three conceptual approaches toward radiolabelled antibodies.



product is isolated, reformulated, characterised, and stored for subsequent use. In the second step, radiolabelling is performed to give access to the final radiolabelled product. An alternative two-step approach involves pre-radiolabelling the chelate and then performing the bioconjugation step using the radioactive intermediate. Although highly successful, these two-step approaches have a number of disadvantages, including the need to produce, isolate, characterise, and potentially store an intermediate product. As an alternative, our group is exploring the possibility of combining the bioconjugation and radiolabelling steps into a simultaneous, one-pot process using an emerging concept that combines photochemistry with radiochemistry (*photoradiochemistry*) [132, 133]. The approach involves a multicomponent reaction in which a photoactivatable chelate is mixed with the radionuclide and the protein at the same time, and then irradiated with ultraviolet light (Scheme 11.4). Radiolabelling of 'free' chelates that are not bound to protein can typically be accomplished in just a few seconds or minutes due to the enhanced rate of diffusion of small molecules. At the same time, photochemical activation of a substrate containing an aryl azide group generates extremely reactive aryl nitrene intermediates that rapidly isomerise and then undergo facile and chemoselective reactions with primary amines (lysine residues). In contrast to traditional coupling methods that usually functionalise lysine or cysteine residues using thermochemically initiated reactions, photochemical reactions occur at room temperature with greatly enhanced kinetics (estimates indicate upwards of three-orders of magnitude faster than standard approaches). The speed of photochemical reactions means the photoradiochemical approach can produce fully formulated radiolabelled antibodies from the native protein source in <10 minutes. In addition, we found that, unlike traditional conjugation chemistries, this photoradiochemical method is compatible with standard clinical formulations of many antibodies. This discovery circumvents the need to pre-purify the protein from a GMP-grade source. Further development is required before photoradiochemical methods can be translated to a clinical setting, but if the two examples highlighted in this section can be combined, ^{89}Zr -based radiopharmaceuticals will have a bright future.



Scheme 11.4 Illustration of the concept of the simultaneous, one-pot photoradiochemical conjugation and labelling of antibodies.

ACKNOWLEDGMENTS

J.P.H. the Swiss National Science Foundation (SNSF Professorship PP00P2_163683 and PP00P2_190093), the Swiss Cancer League (Krebsliga Schweiz; KLS-4257-08-2017), and the University of Zurich (UZH) for financial support. This project has received funding from the

REFERENCES

1. Cotton, F.A. and Wilkinson, G. (1972). *Advanced Inorganic Chemistry: A Comprehensive Text*. Wiley.
2. Earnshaw, A. and Greenwood, N. (1997). *Chemistry of the Elements*, 2e. Elsevier.
3. van Arkel, A.E. and de Boer, J.H. (1925). Darstellung von reinem Titanium-, Zirkonium-, Hafnium- und Thoriummetall. *Z. Anorg. Allg. Chem.*: 345–350.
4. Arnold, R., Augier, C., Baker, J. et al. (1999). Double beta decay of ^{96}Zr . *Nucl. Phys. A*.
5. Dokania, N., Degering, D., Lehnert, B. et al. (2018). An improved half-life limit of the double beta decay of ^{94}Zr into the excited state of ^{94}Mo . *J. Phys. G: Nucl. Part. Phys.* 45 (7): 75104.
6. Collier, T.L., Dahl, K., Stephenson, N.A. et al. (2018). Recent applications of a single quadrupole mass spectrometer in ^{11}C , ^{18}F and radiometal chemistry. *J. Fluorine Chem.* 210: 46–55.
7. Busse, S., Brockmann, J., and Rösch, F. (2002). Radiochemical separation of no-carrier-added radioniobium from zirconium targets for application of ^{90}Nb -labelled compounds. *Radiochim. Acta* 90 (37438): 411–415.
8. Radchenko, V., Filosofov, D.V., Bochko, O.K. et al. (2014). Separation of ^{90}Nb from zirconium target for application in immuno-pet. *Radiochim. Acta* 102 (5): 433–442.
9. Radchenko, V., Hauser, H., Eisenhut, M. et al. (2012). ^{90}Nb – a potential PET nuclide: production and labeling of monoclonal antibodies. *Radiochim. Acta* 100 (11): 857–863.
10. Holland, J.P., Williamson, M.J., and Lewis, J.S. (2010). Unconventional nuclides for radiopharmaceuticals. *Mol. Imaging* 9 (1): 1–10.
11. van Dongen, G.A.M.S., Visser, G.W.M., Lub-de Hooge, M.N. et al. (2007). Immuno-PET: a navigator in monoclonal antibody development and applications. *Oncologist* 12 (12): 1379–1389.
12. Deri, M.A., Zeglis, B.M., Francesconi, L.C., and Lewis, J.S. (2013). PET imaging with ^{89}Zr : from radiochemistry to the clinic. *Nucl. Med. Biol.* 40 (1): 3–14.
13. Zeglis, B.M., Houghton, J.L., Evans, M.J. et al. (2014). Underscoring the influence of inorganic chemistry on nuclear imaging with radiometals. *Inorg. Chem.* 53: 1880–1899.
14. Zhang, Y., Hong, H., and Cai, W. (2011). PET tracers based on zirconium-89. *Curr. Radiopharm.* 4: 131–139.
15. Van De Watering, F.C.J., Rijpkema, M., Perk, L. et al. (2014). Zirconium-89 labeled antibodies: a new tool for molecular imaging in cancer patients. *Biomed. Res. Int.*
16. Vugts, D.J., Visser, G.W., and van Dongen, G.A. (2013). ^{89}Zr -PET radiochemistry in the development and application of therapeutic monoclonal antibodies and other biologicals. *Curr. Top. Med. Chem.* 13: 446–457.
17. Heskamp, S., Raavé, R., Boerman, O. et al. (2017). ^{89}Zr -immuno-positron emission tomography in oncology: state-of-the-art ^{89}Zr radiochemistry. *Bioconjugate Chem.* 28 (9): 2211–2223.

18. Fischer, G., Seibold, U., Schirmacher, R. et al. (2013). ^{89}Zr , a radiometal nuclide with high potential for molecular imaging with pet: chemistry, applications and remaining challenges. *Molecules* 18 (6): 6469–6490.
19. Bhatt, N.B., Pandya, D.N., and Wadas, T.J. (2018). Recent advances in zirconium-89 chelator development. *Molecules* 23 (3): 638.
20. Dilworth, J.R. and Pascu, S.I. (2018). The chemistry of PET imaging with zirconium-89. *Chem. Soc. Rev.* 47 (8): 2554–2571.
21. Schubert, J. (1947). Treatment of plutonium poisoning by metal displacement. *Science* 105 (2728): 389–390.
22. Dobson, E.L. and Gofman, J.W. (1949). Studies with colloids containing radioisotopes of yttrium, zirconium, columbium, and lanthanum; the controlled selective localization of radioisotopes of yttrium, zirconium, and columbium in the bone marrow, liver, and spleen. *J. Lab. Clin. Med.* 34 (3): 305–312.
23. Mealey, J.J. (1957). Turn-over of carrier-free zirconium-89 in man. *Nature* 179: 673–674.
24. Shure, K. and Deutsch, M. (1951). Radiations from Zr^{89} . *Physiol. Rev.* 82 (122): 948.
25. Inarida, M. and Shimamura, A. (1970). Separation of carrier-free zirconium from yttrium target. *Rikagaku Kenkyusho Hokoku* 46: 63–65.
26. Link, J., Krohn, K., Eary, J. et al. (1986). ^{89}Zr for antibody labeling and positron emission tomography. *J. Labelled Compd. Radiopharm.* 23: 1296–1297.
27. Dejesus, O.T. and Nickles, R.J. (1990). Production and purification of ^{89}Zr , a potential PET antibody label. *Int. J. Radiat. Appl. Instrum. Part A* 41 (8): 789–790.
28. Lahiri, S., Mukhopadhyay, B., and Das, N.R. (1997). Simultaneous production of ^{89}Zr and $^{90,91\text{m},92\text{m}}\text{Nb}$ in α -particle activated yttrium and their subsequent separation by HDEHP. *Appl. Radiat. Isot.* 48 (7): 883–886.
29. Kandil, S.A., Spahn, I., Scholten, B. et al. (2007). Excitation functions of (α, xn) reactions on ^{nat}Rb and ^{nat}Sr from threshold up to 26 MeV: possibility of production of ^{87}Y , ^{88}Y and ^{89}Zr . *Appl. Radiat. Isot.* 65 (5): 561–568.
30. Zweit, J., Downey, S., and Sharma, H.L. (1991). Production of no-carrier-added zirconium-89 for positron emission tomography. *Int. J. Radiat. Appl. Instrum. Part A* 42 (2): 199–201.
31. Omara, H.M., Hassan, K.F., Kandil, S.A. et al. (2009). Proton induced reactions on ^{89}Y with particular reference to the production of the medically interesting radionuclide ^{89}Zr . *Radiochim. Acta* 97 (9): 467–471.
32. Taghilo, M. (2012). Cyclotron production of ^{89}Zr : a potent radionuclide for positron emission tomography. *Int. J. Phys. Sci.* 7 (14): 1321–1325.
33. Kandil, S.A., Scholten, B., Saleh, Z.A. et al. (2007). A comparative study on the separation of radiozirconium via ion-exchange and solvent extraction techniques, with particular reference to the production of ^{88}Zr and ^{89}Zr in proton induced reactions on yttrium. *J. Radioanal. Nucl. Chem.* 274 (1): 45–52.
34. Meijs, W.E., Herscheid, J.D.M., Haisma, H.J., and Pinedo, H.M. (1992). Evaluation of desferal as a bifunctional chelating agent for labeling antibodies with Zr-89. *Int. J. Radiat. Appl. Instrum. Part A*.

35. Meijs, W.E., Herscheid, J.D.M., Haisma, H.J. et al. (1994). Production of highly pure no-carrier added ^{89}Zr for the labelling of antibodies with a positron emitter. *Appl. Radiat. Isot.*
36. Meijs, W.E., Haisma, H.J., Klok, R.P. et al. (1997). Zirconium-labeled monoclonal antibodies and their distribution in tumor-bearing nude mice. *J. Nucl. Med.*
37. Verel, I., Visser, G.W.M., Boellaard, R. et al. (2003). ^{89}Zr immuno-PET: comprehensive procedures for the production of ^{89}Zr -labeled monoclonal antibodies. *J. Nucl. Med.* 44 (8): 1271–1281.
38. Verel, I., Visser, G.W.M., Boerman, O.C. et al. (2003). Long-lived positron emitters zirconium-89 and iodine-124 for scouting of therapeutic radioimmunoconjugates with PET. *Cancer Biother. Radiopharm.* 18 (4): 655–661.
39. Holland, J.P., Sheh, Y., and Lewis, J.S. (2009). Standardized methods for the production of high specific-activity zirconium-89. *Nucl. Med. Biol.* 36 (7): 729–739.
40. Pandey, M.K., Engelbrecht, H.P., Byrne, J.P. et al. (2014). Production of ^{89}Zr via the $^{89}\text{Y}(p,n)^{89}\text{Zr}$ reaction in aqueous solution: effect of solution composition on in-target chemistry. *Nucl. Med. Biol.* 41 (4): 309–316.
41. Pandey, M.K., Bansal, A., Engelbrecht, H.P. et al. (2016). Improved production and processing of ^{89}Zr using a solution target. *Nucl. Med. Biol.* 43 (1): 97–100.
42. Link, J.M., Krohn, K.A., and O'Hara, M.J. (2017). A simple thick target for production of ^{89}Zr using an 11 MeV cyclotron. *Appl. Radiat. Isot.* 122: 211–214.
43. Alnahwi, A., Tremblay, S., and Guérin, B. (2018). Comparative study with ^{89}Y -foil and ^{89}Y -pressed targets for the production of ^{89}Zr . *Appl. Sci.* 8 (9): 1579.
44. Carter, L.M., Poty, S., Sharma, S.K., and Lewis, J.S. (2018). Preclinical optimization of antibody-based radiopharmaceuticals for cancer imaging and radionuclide therapy – model, vector, and radionuclide selection. *J. Labelled Compd. Radiopharm.* 61 (9): 611–635.
45. Holland, J.P. (2018). Chemical kinetics of radiolabelling reactions. *Chem. Eur. J.* In press.
46. Kobayashi, T., Sasaki, T., Takagi, I., and Moriyama, H. (2009). Zirconium solubility in ternary aqueous system of Zr(IV)-OH-carboxylates. *J. Nucl. Sci. Technol.* 46 (2): 142–148.
47. Kobayashi, T., Sasaki, T., Takagi, I., and Moriyama, H. (2007). Solubility of zirconium (IV) hydrous oxides. *J. Nucl. Sci. Technol.* 44: 90–94.
48. Sasaki, T., Kobayashi, T., Takagi, I., and Moriyama, H. (2008). Hydrolysis constant and coordination geometry of zirconium(IV). *J. Nucl. Sci. Technol.* 45 (8): 735–739.
49. Davydov, Y.P., Davydov, D.Y., and Zemskova, L.M. (2006). Speciation of Zr(IV) radionuclides in solutions. *Radiochemistry* 48 (4): 358–364.
50. Baggio, R., Garland, M.T., and Percec, M. (1997). A binuclear zirconium(IV) oxalate complex with a μ -oxalate coordination mode. Crystal structure of $\text{K}_6[\{\text{Zr}(\text{C}_2\text{O}_4)_3\}_2(\mu\text{-C}_2\text{O}_4)]4\text{H}_2\text{O}$. *Inorg. Chem.* 36 (14): 3198–3200.
51. Abou, D.S., Ku, T., and Smith-Jones, P.M. (2011). In vivo biodistribution and accumulation of ^{89}Zr in mice. *Nucl. Med. Biol.* 38 (5): 675–681.
52. Graves, S.A., Kuttyreff, C., Barrett, K.E. et al. (2018). Evaluation of a chloride-based ^{89}Zr isolation strategy using a tributyl phosphate (TBP)-functionalized extraction resin. *Nucl. Med. Biol.* 64–65: 1–7.

53. Holland, J.P., Divilov, V., Bander, N.H. et al. (2010). ^{89}Zr -DFO-J591 for immunoPET of prostate-specific membrane antigen expression in vivo. *J. Nucl. Med.* 51 (8): 1293–1300.
54. Guérard, F., Lee, Y.S., Tripier, R. et al. (2013). Investigation of Zr(IV) and ^{89}Zr (IV) complexation with hydroxamates: progress towards designing a better chelator than desferrioxamine B for immuno-PET imaging. *Chem. Commun.* 49 (10): 1002–1004.
55. Holland, J.P. and Vasdev, N. (2014). Charting the mechanism and reactivity of zirconium oxalate with hydroxamate ligands using density functional theory: implications in new chelate design. *Dalton Trans.* 43 (26): 9872–9884.
56. Patra, M., Bauman, A., Mari, C. et al. (2014). An octadentate bifunctional chelating agent for the development of stable zirconium-89 based molecular imaging probes. *Chem. Commun.* 50 (78): 11523–11525.
57. Vugts, D.J., Klaver, C., Sewing, C. et al. (2017). Comparison of the octadentate bifunctional chelator DFO*-pPhe-NCS and the clinically used hexadentate bifunctional chelator DFO-pPhe-NCS for ^{89}Zr -immuno-PET. *Eur. J. Nucl. Med. Mol. Imaging* 44 (2): 286–295.
58. Pandya, D.N., Bhatt, N., Yuan, H. et al. (2017). Zirconium tetraazamacrocyclic complexes display extraordinary stability and provide a new strategy for zirconium-89-based radiopharmaceutical development. *Chem. Sci.* 8 (3): 2309–2314.
59. Tieu, W., Lifa, T., Katsifis, A., and Codd, R. (2017). Octadentate zirconium(IV)-loaded macrocycles with varied stoichiometry assembled from hydroxamic acid monomers using metal-templated synthesis. *Inorg. Chem.* 56 (6): 3719–3728.
60. Tinianow, J.N., Pandya, D.N., Pailloux, S.L. et al. (2016). Evaluation of a 3-hydroxypyridin-2-one (2,3-HOPO) based macrocyclic chelator for $^{89}\text{Zr}^{4+}$ and its use for immunoPET imaging of HER2 positive model of ovarian carcinoma in mice. *Theranostics* 6 (4): 511–521.
61. Deri, M.A., Ponnala, S., Zeglis, B.M. et al. (2014). Alternative chelator for ^{89}Zr radiopharmaceuticals: radiolabeling and evaluation of 3,4,3-(LI-1,2-HOPO). *J. Med. Chem.* 57 (11): 4849–4860.
62. Deri, M.A., Ponnala, S., Kozłowski, P. et al. (2015). P-SCN-Bn-HOPO: a superior bifunctional chelator for ^{89}Zr immunoPET. *Bioconjugate Chem.* 26 (12): 2579–2591.
63. Rudd, S.E., Roselt, P., Cullinane, C. et al. (2016). A desferrioxamine B squaramide ester for the incorporation of zirconium-89 into antibodies. *Chem. Commun.* 52 (80): 11889–11892.
64. Boros, E., Holland, J.P., Kenton, N. et al. (2016). Macrocyclic-based hydroxamate ligands for complexation and immunoconjugation of ^{89}Zr for positron emission tomography (PET) imaging. *ChemPlusChem* 81 (3): 274–281.
65. Briand, M., Aulsebrook, M.L., Mindt, T.L., and Gasser, G. (2017). A solid phase-assisted approach for the facile synthesis of a highly water-soluble zirconium-89 chelator for radiopharmaceutical development. *Dalton Trans.* 46 (47): 16387–16389.
66. Adams, C.J., Wilson, J.J., and Boros, E. (2017). Multifunctional desferriochrome analogues as versatile ^{89}Zr (IV) chelators for immunoPET probe development. *Mol. Pharmaceutics* 14 (8): 2831–2842.

67. Bhatt, N.B., Pandya, D.N., Xu, J. et al. (2017). Evaluation of macrocyclic hydroxyisophthalamide ligands as chelators for zirconium-89. *PLoS One* 12 (6): 1–13.
68. Pandya, D.N., Pailloux, S., Tatum, D. et al. (2015). Di-macrocyclic terephthalamide ligands as chelators for the PET radionuclide zirconium-89. *Chem. Commun.* 51 (12): 2301–2303.
69. Vosjan, M.J.W.D., Perk, L.R., Visser, G.W.M. et al. (2010). Conjugation and radiolabeling of monoclonal antibodies with zirconium-89 for PET imaging using the bifunctional chelate p-isothiocyanatobenzyl-desferrioxamine. *Nat. Protoc.* 5 (4): 739–743.
70. Vugts, D.J., Vervoort, A., Stigter-Van Walsum, M. et al. (2011). Synthesis of phosphine and antibody-azide probes for in vivo staudinger ligation in a pretargeted imaging and therapy approach. *Bioconjugate Chem.* 22 (10): 2072–2081.
71. Zeglis, B.M., Davis, C.B., Aggeler, R. et al. (2013). Enzyme-mediated methodology for the site-specific radiolabeling of antibodies based on catalyst-free click chemistry. *Bioconjugate Chem.* 24 (6): 1057–1067.
72. Zeglis, B.M., Mohindra, P., Weissmann, G.I. et al. (2011). Modular strategy for the construction of radiometalated antibodies for positron emission tomography based on inverse electron demand diels-alder click chemistry. *Bioconjugate Chem.* 22 (10): 2048–2059.
73. Houghton, J.L., Zeglis, B.M., Abdel-Atti, D. et al. (2016). Pretargeted immuno-PET of pancreatic cancer: overcoming circulating antigen and internalized antibody to reduce radiation doses. *J. Nucl. Med.* 57 (3): 453–459.
74. Wright, B.D., Whittenberg, J., Desai, A. et al. (2016). Microfluidic preparation of a ⁸⁹Zr-labeled trastuzumab single-patient dose. *J. Nucl. Med.* 57 (5): 747–752.
75. Perk, L.R., Visser, O.J., Stigter-Van Walsum, M. et al. (2006). Preparation and evaluation of ⁸⁹Zr-Zevalin for monitoring of ⁹⁰Y-Zevalin biodistribution with positron emission tomography. *Eur. J. Nucl. Med. Mol. Imaging* 33 (11): 1337–1345.
76. Börjesson, P.K.E., Jauw, Y.W.S., Boellaard, R. et al. (2006). Performance of immuno-positron emission tomography with zirconium-89-labeled chimeric monoclonal antibody U36 in the detection of lymph node metastases in head and neck cancer patients. *Clin. Cancer Res.* 12 (7): 2133–2140.
77. Perk, L.R., Stigter-Van Walsum, M., Visser, G.W.M. et al. (2008). Quantitative PET imaging of Met-expressing human cancer xenografts with ⁸⁹Zr-labelled monoclonal antibody DN30. *Eur. J. Nucl. Med. Mol. Imaging* 35 (10): 1857–1867.
78. Dijkers, E.C.F., Kosterink, J.G.W., Rademaker, A.P. et al. (2009). Development and characterization of clinical-grade ⁸⁹Zr-trastuzumab for HER2/neu immunoPET imaging. *J. Nucl. Med.* 50 (6): 974–981.
79. Holland, J.P., Caldas-Lopes, E., Divilov, V. et al. (2010). Measuring the pharmacodynamic effects of a novel Hsp90 inhibitor on HER2/neu expression in mice using ⁸⁹Zr-DFO-trastuzumab. *PLoS One*: 5, e8859–1.
80. Chang, A.J., DeSilva, R., Jain, S. et al. (2012). ⁸⁹Zr-radiolabeled trastuzumab imaging in orthotopic and metastatic breast tumors. *Pharmaceuticals* 5 (1): 79–93.
81. Janjigian, Y.Y., Viola-Villegas, N., Holland, J.P. et al. (2013). Monitoring afatinib treatment in HER2-positive gastric cancer with ¹⁸F-FDG and ⁸⁹Zr-trastuzumab PET. *J. Nucl. Med.* 54 (6): 936–943.

82. Oude Munnink, T.H., de Korte, M.A., Nagengast, W.B. et al. (2010). ⁸⁹Zr-trastuzumab PET visualises HER2 downregulation by the HSP90 inhibitor NVP-AUY922 in a human tumour xenograft. *Eur. J. Cancer* 46 (3): 678–684.
83. Oude Munnink, T.H., De Vries, E.G.E., Vedelaar, S.R. et al. (2012). Lapatinib and 17AAG reduce ⁸⁹Zr-trastuzumab-F(ab')₂ uptake in SKBR3 tumor xenografts. *Mol. Pharmaceutics* 9 (11): 2995–3002.
84. Aerts, H.J.W.L., Dubois, L., Perk, L. et al. (2008). Disparity between in vivo EGFR expression and ⁸⁹Zr-labeled cetuximab uptake assessed with PET. *J. Nucl. Med.* 50 (1): 123–131.
85. Perk, L.R., Visser, G.W.M., Vosjan, M.J.W.D. et al. (2005). ⁸⁹Zr as a PET surrogate radioisotope for scouting biodistribution of the therapeutic radiometals ⁹⁰Y and ¹⁷⁷Lu in tumor-bearing nude mice after coupling to the internalizing antibody cetuximab. *J. Nucl. Med.* 46 (11): 1898–1906.
86. Holland, J.P., Evans, M.J., Rice, S.L. et al. (2012). Annotating MYC status with ⁸⁹Zr-transferrin imaging. *Nat. Med.* 18 (10): 1586–1591.
87. Evans, M.J., Holland, J.P., Rice, S.L. et al. (2013). Imaging tumor burden in the brain with ⁸⁹Zr-transferrin. *J. Nucl. Med.* 54 (1): 90–95.
88. Doran, M.G., Carnazza, K.E., Steckler, J.M. et al. (2016). Applying ⁸⁹Zr-transferrin to study the pharmacology of inhibitors to BET bromodomain containing proteins. *Mol. Pharmaceutics* 13 (2): 683–688.
89. Aggarwal, R., Behr, S.C., Paris, P.L. et al. (2017). Real-time transferrin-based PET detects MYC-positive prostate cancer. *Mol. Cancer Res.* 15 (9): 1221–1229.
90. Henry, K.E., Dilling, T.R., Abdel-Atti, D. et al. (2017). Non-invasive ⁸⁹Zr-transferrin PET shows improved tumor targeting compared to ¹⁸F-FDG PET in MYC-overexpressing human triple negative breast cancer. *J. Nucl. Med.* jnumed.117.192286.
91. Ruggiero, A., Holland, J.P., Hudolin, T. et al. (2011). Targeting the internal epitope of prostate-specific membrane antigen with ⁸⁹Zr-7E11 immuno-PET. *J. Nucl. Med.* 52 (10): 1608–1615.
92. Rylova, S.N., Del Pozzo, L., Klingeberg, C. et al. (2016). Immuno-PET imaging of CD30-positive lymphoma using ⁸⁹Zr-desferrioxamine-labeled CD30-specific AC-10 antibody. *J. Nucl. Med.* 57 (1): 96–102.
93. Viola-Villegas, N.T., Sevak, K.K., Carlin, S.D. et al. (2014). Noninvasive imaging of PSMA in prostate tumors with ⁸⁹Zr-labeled huJ591 engineered antibody fragments: the faster alternatives. *Mol. Pharmaceutics* 11 (11): 3965–3973.
94. Oude Munnink, T.H., Tamas, K.R., Lub-de Hooge, M.N. et al. (2013). Placental growth factor (PLGF)-specific uptake in tumor microenvironment of ⁸⁹Zr-labeled PLGF antibody RO5323441. *J. Nucl. Med.* 54 (6): 929–935.
95. Nagengast, W.B., de Vries, E.G., Hospers, G.A. et al. (2007). In vivo VEGF imaging with radiolabeled bevacizumab in a human ovarian tumor xenograft. *J. Nucl. Med.* 48 (8): 1313–1319.
96. Nagengast, W.B., de Korte, M.A., Oude Munnink, T.H. et al. (2010). ⁸⁹Zr-bevacizumab PET of early antiangiogenic tumor response to treatment with HSP90 inhibitor NVP-AUY922. *J. Nucl. Med.* 51 (5): 761–767.

97. Nagengast, W.B., Lub-de Hooge, M.N., Oosting, S.F. et al. (2011). VEGF-PET imaging is a noninvasive biomarker showing differential changes in the tumor during sunitinib treatment. *Cancer Res.* 71 (1): 143–153.
98. Natarajan, A., Habte, F., and Gambhir, S.S. (2012). Development of a novel long-lived immunoPET tracer for monitoring lymphoma therapy in a humanized transgenic mouse model. *Bioconjugate Chem.* 23 (6): 1221–1229.
99. Hoeben, B.A.W., Kaanders, J.H.A.M., Franssen, G.M. et al. (2010). PET of hypoxia with ⁸⁹Zr-labeled cG250-F(ab')₂ in head and neck tumors. *J. Nucl. Med.* 51 (7): 1076–1083.
100. Stillebroer, A.B., Franssen, G.M., Mulders, P.F.A. et al. (2013). ImmunoPET imaging of renal cell carcinoma with ¹²⁴I- and ⁸⁹Zr-labeled anti-CAIX monoclonal antibody cG250 in mice. *Cancer Biother. Radiopharm.* 28 (7): 510–515.
101. Hong, H., Zhang, Y., Severin, G.W. et al. (2012). Multimodality imaging of breast cancer experimental lung metastasis with bioluminescence and a monoclonal antibody dual-labeled with ⁸⁹Zr and IRDye 800CW. *Mol. Pharmaceutics* 9 (8): 2339–2349.
102. Heskamp, S., van Laarhoven, H.W.M., Molkenboer-Kuening, J.D.M. et al. (2010). ImmunoSPECT and immunoPET of IGF-1R expression with the radiolabeled antibody R1507 in a triple-negative breast cancer model. *J. Nucl. Med.* 51 (10): 1565–1572.
103. Jagoda, E.M., Lang, L., Bhadrasetty, V. et al. (2012). Immuno-PET of the hepatocyte growth factor receptor met using the 1-armed antibody onartuzumab. *J. Nucl. Med.* 53 (10): 1592–1600.
104. Sugyo, A., Tsuji, A.B., Sudo, H. et al. (2013). Evaluation of ⁸⁹Zr-labeled human anti-CD147 monoclonal antibody as a positron emission tomography probe in a mouse model of pancreatic cancer. *PLoS One* 8 (4).
105. Bhattacharyya, S., Kurdziel, K., Wei, L. et al. (2013). Zirconium-89 labeled panitumumab: a potential immuno-PET probe for HER1-expressing carcinomas. *Nucl. Med. Biol.* 40 (4): 451–457.
106. Wei, L., Shi, J., Afari, G., and Bhattacharyya, S. (2014). Preparation of clinical-grade ⁸⁹Zr-panitumumab as a positron emission tomography biomarker for evaluating epidermal growth factor receptor-targeted therapy. *J. Labelled Compd. Radiopharm.* 57 (1): 25–35.
107. Vugts, D.J., Heuveling, D.A., Stigter-van Walsum, M. et al. (2014). Preclinical evaluation of ⁸⁹Zr-labeled anti-CD44 monoclonal antibody RG7356 in mice and cynomolgus monkeys: prelude to phase 1 clinical studies. *MAbs* 6 (2): 567–575.
108. Sham, J.G., Kievit, F.M., Grierson, J.R. et al. (2014). Glypican-3-targeted ⁸⁹Zr PET imaging of hepatocellular carcinoma. *J. Nucl. Med.* 55 (5): 799–804.
109. ter Weele, E.J., van Scheltinga, A.G.T.T., Kosterink, J.G.W. et al. (2015). Imaging the distribution of an antibody-drug conjugate constituent targeting mesothelin with ⁸⁹Zr and IRDye 800CW in mice bearing human pancreatic tumor xenografts. *Oncotarget* 6 (39).
110. Rizvi, S.N.F., Visser, O.J., Vosjan, M.J.W.D. et al. (2012). Biodistribution, radiation dosimetry and scouting of ⁹⁰Y-ibritumomab tiuxetan therapy in patients with

- relapsed B-cell non-Hodgkin's lymphoma using ^{89}Zr -ibritumomab tiuxetan and PET. *Eur. J. Nucl. Med. Mol. Imaging* 39 (3): 512–520.
111. Borjesson, P.K.E., Jauw, Y.W.S., de Bree, R. et al. (2009). Radiation dosimetry of ^{89}Zr -labeled chimeric monoclonal antibody U36 as used for immuno-PET in head and neck cancer patients. *J. Nucl. Med.* 50 (11): 1828–1836.
 112. Dijkers, E., Lub-de Hooge, M.N., Kosterink, J.G. et al. (2007). Characterization of ^{89}Zr -trastuzumab for clinical HER2 immunoPET imaging. *J. Clin. Oncol.* 25 (18_suppl): 3508.
 113. Dijkers, E.C., Oude Munnink, T.H., Kosterink, J.G. et al. (2010). Biodistribution of ^{89}Zr -trastuzumab and PET imaging of HER2-positive lesions in patients with metastatic breast cancer. *Clin. Pharmacol. Ther.* 87 (5): 586–592.
 114. Laforest, R., Lapi, S.E., Oyama, R. et al. (2016). [^{89}Zr]Trastuzumab: evaluation of radiation dosimetry, safety, and optimal imaging parameters in women with HER2-positive breast cancer. *Mol. Imaging Biol.* 18 (6): 952–959.
 115. O'Donoghue, J.A., Lewis, J.S., Pandit-Taskar, N. et al. (2017). Pharmacokinetics, bio-distribution, and radiation dosimetry for ^{89}Zr -trastuzumab in patients with esophago-gastric cancer. *J. Nucl. Med.* jnumed.117.194555.
 116. Morris, M.J., Pandit-Taskar, N., Carrasquillo, J.A. et al. (2013). Phase I trial of zirconium 89 (Zr^{89}) radiolabeled J591 in metastatic castration-resistant prostate cancer (mCRPC). *J. Clin. Oncol.* 31 (6).
 117. Pandit-Taskar, N., O'Donoghue, J.A., Beylergil, V. et al. (2014). ^{89}Zr -huJ591 immuno-PET imaging in patients with advanced metastatic prostate cancer. *Eur. J. Nucl. Med. Mol. Imaging* 41: 2093–2105.
 118. Pandit-Taskar, N., O'Donoghue, J.A., Durack, J.C. et al. (2015). A phase I/II study for analytic validation of ^{89}Zr -J591 immunoPET as a molecular imaging agent for metastatic prostate cancer. *Clin. Cancer Res.* 21 (23): 5277–5285.
 119. Pandit-Taskar, N., Veach, D.R., Fox, J.J. et al. (2016). Evaluation of castration-resistant prostate cancer with androgen receptor-axis imaging. *J. Nucl. Med.* 57 (Supplement_3): 73S–78S.
 120. Pandit-Taskar, N., O'Donoghue, J.A., Ruan, S. et al. (2016). First-in-human imaging with ^{89}Zr -DF-IAB2M anti-PSMA minibody in patients with metastatic prostate cancer: pharmacokinetics, biodistribution, dosimetry, and lesion uptake. *J. Nucl. Med.* 57 (12): 1858–1864.
 121. Lindenberg, L., Adler, S., Turkbey, I.B. et al. (2017). Dosimetry and first human experience with (^{89}Zr)-panitumumab. *Am. J. Nucl. Med. Mol. Imaging* 7 (4): 195–203.
 122. Van Der Bilt, A.R.M., AGT, T.V.S., Timmer-Bosscha, H. et al. (2012). Measurement of tumor VEGF-A levels with ^{89}Zr -bevacizumab PET as an early biomarker for the anti-angiogenic effect of everolimus treatment in an ovarian cancer xenograft model. *Clin. Cancer Res.* 18 (22): 6306–6314.
 123. Gaykema, S.B.M., Brouwers, A.H., Lub-de Hooge, M.N. et al. (2013). ^{89}Zr -bevacizumab PET imaging in primary breast cancer. *J. Nucl. Med.* 54 (7): 1014–1018.
 124. van Asselt, S.J., Oosting, S.F., Brouwers, A.H. et al. (2014). Everolimus reduces ^{89}Zr -bevacizumab tumor uptake in patients with neuroendocrine tumors. *J. Nucl. Med.* 55 (7): 1087–1092.

125. Oosting, S.F., Brouwers, A.H., van Es, S.C. et al. (2015). ^{89}Zr -bevacizumab PET visualizes heterogeneous tracer accumulation in tumor lesions of renal cell carcinoma patients and differential effects of antiangiogenic treatment. *J. Nucl. Med.* 56 (1): 63–69.
126. den Hollander, M.W., Bensch, F., Glaudemans, A.W.J.M. et al. (2015). TGF-antibody uptake in recurrent high-grade glioma imaged with ^{89}Zr -fresolimumab PET. *J. Nucl. Med.* 56 (9): 1310–1314.
127. Muylle, K., Flamen, P., Vugts, D.J. et al. (2015). Tumour targeting and radiation dose of radioimmunotherapy with ^{90}Y -rituximab in CD20+ B-cell lymphoma as predicted by ^{89}Zr -rituximab immuno-PET: impact of preloading with unlabelled rituximab. *Eur. J. Nucl. Med. Mol. Imaging* 42 (8): 1304–1314.
128. van Der Houven, W.M., Van Oordt, C., Gootjes, E.C. et al. (2015). Zr-cetuximab PET imaging in patients with advanced colorectal cancer. *Oncotarget* 6 (30).
129. Jauw, Y.W., Menke-van der Houven van Oordt, C.W., Hoekstra, O.S. et al. (2016). Immuno-positron emission tomography with zirconium-89-labeled monoclonal antibodies in oncology: what can we learn from initial clinical trials? *Front. Pharmacol.* 7: 131.
130. Bensch, F., Smeenk, M.M., van Es, S.C. et al. (2018). Comparative biodistribution analysis across four different ^{89}Zr -monoclonal antibody tracers-the first step towards an imaging warehouse. *Theranostics* 8 (16): 4295–4304.
131. Makris, N.E., Boellaard, R., Visser, E.P. et al. (2014). Multicenter harmonization of ^{89}Zr PET/CT performance. *J. Nucl. Med.* 55 (2): 264–267.
132. Patra, M., Eichenberger, L.S., Fischer, G., and Holland, J.P. (2019). Radiochemistry in a flash: photochemical conjugation and one-pot radiolabelling of antibodies for immuno-PET. *Angew. Chem. Int. Ed.* 58: 1928–1933. DOI: 10.1002/anie.20181328.
133. Eichenberger, L.S., Patra, M., and Holland, J.P. (2019). Photoactive chelates for radiolabelling proteins. *Chem. Commun.* 55, 2257–2260. DOI: 10.1039/C8CC09660K.
134. Poot, A.J., Adamzek, K.W.A., Windhorst, A.D. et al. (2018). Fully automated zirconium-89 labeling and purification of antibodies. *J. Nucl. Med.* 60(5):691–695.

Chapter 12

^{99m}Tc

Radiopharmaceutical Chemistry

Dionysia Papagiannopoulou

*Department of Pharmaceutical Chemistry, School of Pharmacy,
Aristotle University of Thessaloniki, 54124, Thessaloniki, Greece*

12.1 INTRODUCTION

Technetium-99m is a γ -emitting radionuclide ($E_{\gamma} = 141$ keV, 89% abundance, $t_{1/2} = 6$ hours) with diagnostic applications in nuclear medicine for planar scintigraphy and single photon emission computed tomography (**SPECT**). Its nuclear properties are ideal for imaging with γ cameras, it is produced from $^{99}\text{Mo}/^{99m}\text{Tc}$ generators with low cost and worldwide availability, and its radiopharmaceuticals can be easily prepared in the radiopharmacy via commercial kits. Today there exist numerous ^{99m}Tc radiopharmaceuticals for various diagnostic procedures (Table 12.1), of which the ^{99m}Tc perfusion imaging agents are the most common (Figure 12.1).

The development of new ^{99m}Tc radiopharmaceuticals is driven by the need to obtain disease-specific imaging agents. In this chapter, the bibliography has been surveyed from 2000 to the present, and the ^{99m}Tc -labelled imaging agents developed are summarized in the relevant sections. In these years, new ^{99m}Tc -labelling strategies have been developed, new ^{99m}Tc -complexes have been proposed as probes with superior properties over older ones, and many research efforts have focused on the design of new targeted ^{99m}Tc radiopharmaceuticals based on the advances of chemical biology in the identification of suitable targeting vectors.

Table 12.1 Technetium-99m radiopharmaceuticals.

^{99m} Tc-Radiopharmaceutical	Medical application
^{99m} Tc-Sestamibi	Myocardial perfusion, breast cancer imaging, parathyroid imaging
^{99m} Tc-Tetrofosmin	Myocardial perfusion
^{99m} Tc-Medronate (MDP)	Bone scintigraphy
^{99m} Tc-Oxidronate (HDP)	
d,l-[^{99m} Tc]Tc-HMPAO	Brain perfusion
l,l-[^{99m} Tc]Tc-ECD	Brain perfusion
[^{99m} Tc]Tc-MAG ₃	Renal perfusion
[^{99m} Tc]Tc-DMSA	Tc(III)DMSA: kidney scan Tc(V)DMSA: medullary thyroid carcinoma imaging
[^{99m} Tc]Tc-glucoheptate(GH)	Renal imaging
[^{99m} Tc]Tc-DTPA	Renal imaging/(aerosol) Lung ventilation
^{99m} Tc-Etifenin/Mebrofenin/ Disofenin	Hepatobiliary scintigraphy
^{99m} Tc-colloids	Liver/spleen scintigraphy, bone marrow imaging
^{99m} Tc-albumin macroaggregate	Lung perfusion+
[^{99m} Tc][TcO ₄] ⁻	Thyroid imaging, salivary glands, Meckel's diverticulum imaging
^{99m} Tc-Tilmanocept	Lymphoscintigraphy
^{99m} Tc-Tektrotyd	Imaging of tumors overexpressing somatostatin receptors (e.g. gastro-entero-pancreatic neuroendocrine tumors)
^{99m} Tc-Apcitide	Deep venous thrombosis imaging
^{99m} Tc-Nofetumomab Merpentan	Monoclonal antibody fragment Fab for small-cell lung cancer imaging
^{99m} Tc-Arcitumomab	Monoclonal antibody Fab' for colorectal cancer imaging
^{99m} Tc-Sulesomab	Monoclonal antibody Fab' for infection imaging
^{99m} Tc-Besilesomab	Monoclonal antibody for infection imaging
^{99m} Tc-red blood cells	Radionuclide angiography, blood pool, GI bleeding, spleen imaging (denaturated)
^{99m} Tc-white blood cells	Infection imaging

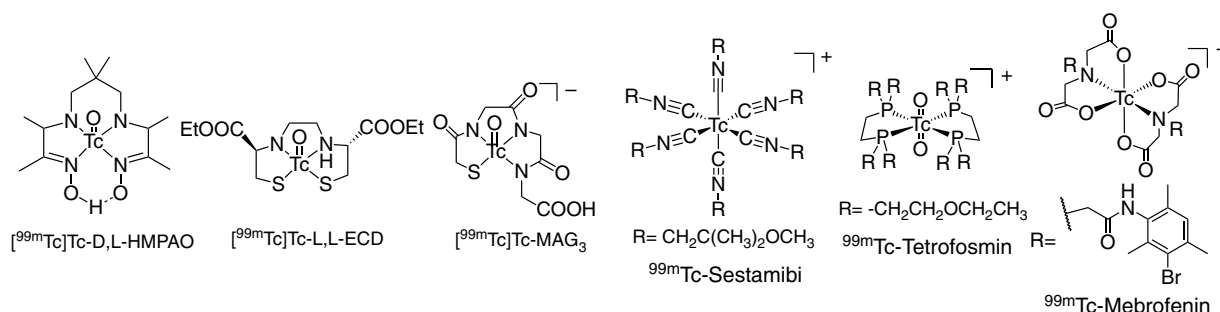


Figure 12.1 Structures of common ^{99m}Tc-radiopharmaceuticals.

12.2 TECHNETIUM-99m CHELATORS AND COMPLEXES

Various ^{99m}Tc -labelling strategies have been developed that, depending upon the type of chelator, lead to complexes with different physicochemical characteristics (Figure 12.2). ^{99m}Tc Oxotechnetium(V) complexes are widely used because they are formed in high yield and are stable, especially with suitable tetradentate ligands. The N_2S_2 chelators that have been used the most for the preparation of ^{99m}Tc oxotechnetium(V) complexes are the bisaminethiols (**BAT**) (also known as diaminedithiols, **DADT**), diamidedithiols (**DADS**), and monoamino monoamido dithiols (**MAMA**). The respective complexes ^{99m}Tc TcO-BAT and ^{99m}Tc TcO-MAMA are neutral and lipophilic and have been used as brain perfusion agents or for brain receptor imaging. The N_3S chelators used for the preparation of ^{99m}Tc oxotechnetium(V) complexes are mercaptoacetyltriglycine (**MAG3**) and similar cysteine-containing tripeptide or tetrapeptide chelators. These chelators may be incorporated at the end of a peptide sequence for the development of ^{99m}Tc -labelled peptides [1]. The respective complexes ^{99m}Tc TcO-MAG₃ and ^{99m}Tc TcO-DADT are anionic and exhibit high renal excretion. ^{99m}Tc Tc-MAG₃ is one of the most used renal imaging agents. The “3+1” mixed-ligand ^{99m}Tc oxotechnetium(V) complexes are formed by the coordination of a tridentate dithiolate (S,X,S) ligand (X = O, S or NR) and a monodentate

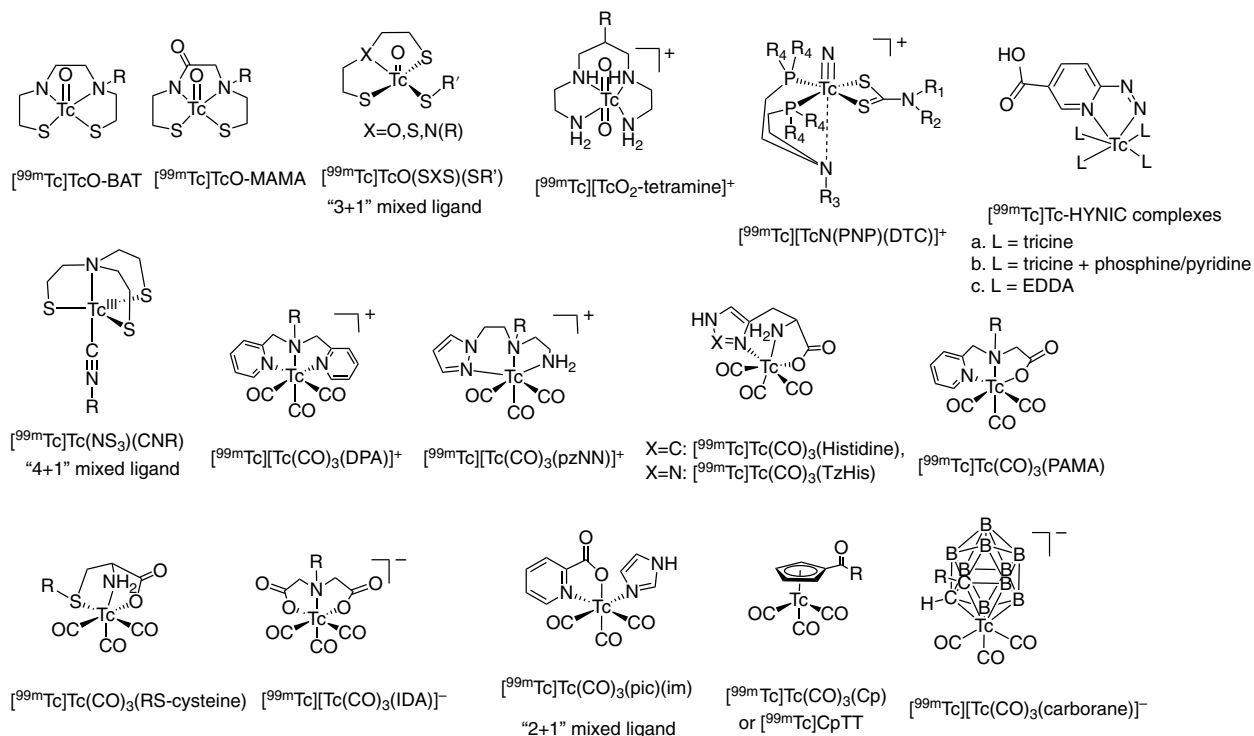


Figure 12.2 Structures of ^{99m}Tc -complexes.

thiolate. The complexes $[^{99m}\text{Tc}][\text{TcO}(\text{S},\text{X},\text{S})(\text{S})]$ are neutral and lipophilic and have been used for the development of brain perfusion as well as for brain receptor-targeted imaging agents. The *propyleneaminoxime chelator* forms neutral $[^{99m}\text{Tc}]$ oxotechnetium(V) complexes. *D,L*- $[^{99m}\text{Tc}]$ oxotechnetium-hexamethylpropyleneamineoxime is one of the most useful brain perfusion imaging agents. Cationic *trans*- $[^{99m}\text{Tc}]$ dioxotechnetium(V) complexes have also been applied in radiopharmaceuticals. Tetradentate ligands used for their preparation are the *tetramine chelators*, either acyclic (e.g. 1,4,7,11-tetraaza-undecane) or cyclic (e.g. cyclam), as well as the X_2P_2 -type (X = N or S) chelators. The latter ligand with two terminal hydroxymethylphosphine moieties as the P-donor forms hydrophilic ^{99m}Tc -complexes [2].

The $[^{99m}\text{Tc}]$ nitridotechnetium(V) complexes have been synthesized in the past in combination with *bidentate (S,S) chelators* such as the dithiocarbamate, which forms neutral symmetrical complexes, $[^{99m}\text{Tc}][\text{TcN}(\text{S},\text{S})_2]$. A complex of this type, $[^{99m}\text{Tc}]\text{TcN-NOET}$, was developed as a myocardial imaging agent. Of interest are the more recently developed asymmetrical complexes with an *aminodiphosphane (P,N,P) ligand* that forms the metal fragment $[^{99m}\text{Tc}][\text{TcN}(\text{P},\text{N},\text{P})]^{2+}$. This fragment can be combined with various bidentate chelators L and leads to asymmetrical mixed-ligand $[^{99m}\text{Tc}][\text{TcN}(\text{P},\text{N},\text{P})\text{L}]^{0/+}$ complexes, cationic or neutral depending on the nature of L. For the formation of these complexes, cysteine acting as a (S,N)⁻ or (S,O)²⁻ bidentate chelator, as well as dithiocarbamates or dithiols (S,S)⁻, can be used [3,4].

The $[^{99m}\text{Tc}]\text{Tc}$ -hydrazino complexes are formed by the coordination of the *6-hydrazinonicotinic acid (HYNIC) ligand*, which acts as a bifunctional chelating agent, complexed with technetium via the hydrazide-N, aromatic-N atoms and conjugated to biomolecules via the carboxylate moiety. For the formation of the hydrazine complexes, additional co-ligands are required to complete the coordination sphere, such as tricine alone, or in combination with N,N'-ethylenediamine-diacetic acid (**EDDA**), ternary phosphines (e.g. triphenylphosphine-3,3',3''-trisulfonate, **TPPTS**), or aromatic amines (e.g. nicotinic or isonicotinic acid). In the case of $[^{99m}\text{Tc}]\text{Tc-HYNIC-EDDA}$ complexes, tricine is required in the labeling mixture for ligand exchange and probably is not present in the final complex formed. In the case of the ternary ligands, tricine remains coordinated in the final complex. The technetium-99m HYNIC complexes have not been fully characterized at the macroscopic level. Their composition $[^{99m/99g}\text{Tc}][\text{Tc}(\text{HYNIC})(\text{co-ligand})]$ has been identified by ^{99g}Tc -carrier-added mass spectrometry studies of the labeling mixture. In these mixtures, more than one product can be formed, of which the formulas $[^{99m/99g}\text{Tc}][\text{Tc}(\text{HYNIC})(\text{tricine})_{1\text{or}2}]$ with co-ligand tricine, $[^{99m/99g}\text{Tc}][\text{Tc}(\text{HYNIC})(\text{EDDA})_{1\text{or}2}]$ with co-ligands tricine and EDDA, $[^{99m/99g}\text{Tc}][\text{Tc}(\text{HYNIC})(\text{tricine})(\text{TPTTS})]$ with co-ligands tricine and TPTTS, and $[^{99m/99g}\text{Tc}][\text{Tc}(\text{HYNIC})(\text{tricine})(\text{nicotinate})]$ with co-ligands tricine and nicotinate were identified [5–7]. Each of these complexes exhibits different pharmacokinetic properties and biological stability. The $[^{99m}\text{Tc}]\text{Tc-HYNIC-tricine}$ complexes are formed in high yield, but isomers are observed, and the biological stability is relatively low. The $[^{99m}\text{Tc}]\text{Tc-HYNIC-EDDA}$ complexes are more stable and exhibit better homogeneity; however, heating is required to obtain high labelling yield. The use of ternary ligands along with tricine improves both stability and homogeneity [5, 6]. Furthermore, if the peptide sequence conjugated to HYNIC has an additional donor (such as histidine or glutamate),

it has been proposed that it may also participate in the coordination sphere of the $^{99m}\text{Tc}[\text{Tc}-\text{HYNIC}]$ complex formed [8].

Organometallic $^{99m}\text{Tc}(\text{III})$ -complexes of the “4+1” *mixed-ligand system* are formed with the combination of the tripodal/tetradentate *tris(2-mercaptoethyl)amine (NS₃) chelator* and an *isocyanide* to form the neutral $^{99m}\text{Tc}[\text{Tc}(\text{NS}_3)(\text{CNR})]$ complex [9, 10]. Organometallic $^{99m}\text{Tc}(\text{I})$ -complexes with isocyanide or carbon monoxide ligands have been extensively applied in radiopharmaceutical design. These complexes are six-coordinate with high stability and inertness due to the metal–carbon bond and full-shell coordination, respectively. The $^{99m}\text{Tc}[\text{Tc}^{\text{I}}(\text{MIBI})_6]^+$ complex (^{99m}Tc -Sestamibi), where MIBI is 2-methoxy-isobutyl-isocyanide, is used as a myocardial and tumor imaging agent. The $^{99m}\text{Tc}[\text{Tc}^{\text{I}}\text{-tricarboxyl}]$ labeling approach is one of the most widely explored in the past two decades. By this approach, the “semi-aqua” precursor *fac*- $^{99m}\text{Tc}[\text{Tc}(\text{CO})_3(\text{H}_2\text{O})_3]^+$ is complexed with a variety of chelators. The tridentate ligands that are used for the preparation of ^{99m}Tc -tricarboxyl complexes may combine N, O, S, and P donor atoms. The (*N,N,N*) *chelators* usually contain at least one aromatic amine and form cationic $^{99m}\text{Tc}[\text{Tc}(\text{CO})_3(\text{N,N,N})]^+$ complexes in high yields [11, 12]. Chelators of this type include dipicolylamine (**DPA**) as well as its lysine-based analogues prepared by the single amino acid chelate (**SAAC**) strategy [13, 14], where the tridentate chelator is built via reductive amination on the ϵ -NH₂ group of a lysine residue. The (*N,N,O*) *chelators* that have been used are histidine and picolylamine acetic acid (**PAMA**), which form neutral $^{99m}\text{Tc}[\text{Tc}(\text{CO})_3(\text{N,N,O})]$ complexes [15, 16]. A histidine analogue that is equally potent is the *triazole-histidine* (TzHis) ligand, where 1,2,3-triazole takes the place of imidazole in His. The $^{99m}\text{Tc}[\text{Tc}(\text{CO})_3(\text{TzHis})]$ complexes are prepared by a two-step procedure that does not require intermediate purification: (i) the ligand is formed by “3+2” cycloaddition “click” of an azide with L-propargyl-glycine, and (ii) the product (TzHis) is reacted with $^{99m}\text{Tc}[\text{Tc}(\text{CO})_3(\text{H}_2\text{O})_3]^+$ precursor [17, 18]. Another type of tridentate ligand is (*N,O,O*) *chelator iminodiacetic acid*, which forms an anionic $^{99m}\text{Tc}(\text{CO})_3(\text{N,O,O})^-$ complex with lower lipophilicity [15]. In an analogous way, cationic $^{99m}\text{Tc}[\text{Tc}(\text{CO})_3(\text{N,S,N})]^+$ and neutral $^{99m}\text{Tc}[\text{Tc}(\text{CO})_3(\text{N,S,O})]$ with thioether-containing chelators, as well as phosphine-containing (*P,N,P*), (*P,S,S*), (*P,O,O*) chelators, form stable ^{99m}Tc -tricarboxyl complexes [19–22]. The “2+1” *mixed-ligand* $^{99m}\text{Tc}[\text{Tc}(\text{CO})_3]^+$ complexes are used as well and contain bidentate chelators such as 3-hydroxypyridone (*O,O*), dithiocarbamate (*S,S*), bipyridine (*N,N*), bisphosphine (*P,P*), and 2-picolinic acid (*N,O*). As monodentate ligands, phosphines (*P*), isocyanides (*CNR*), and aromatic amines have been used [23–29]. For labelling antibodies or immunoreactive constructs such as single-chain scFv fragments or affibodies with $^{99m}\text{Tc}[\text{Tc}(\text{CO})_3]^+$, a histidine tag added in the amino acid sequence has proven to be efficient for coordination with the metal through the imidazole moieties [30–32]. $^{99m}\text{Tc}[\text{Tc}(\text{CO})_3]^+$ complexes of ligands with η^5 hapticity, such as *cyclopentadienyls* and *carboranes*, have also been developed. The “piano stool” $^{99m}\text{Tc}[\text{Tc}(\text{CO})_3(\eta^5\text{-Cp})]$ complexes (^{99m}Tc CpTT) are compact in size and considered bioisosters to the phenyl ring. Their importance in radiopharmaceutical design is that they offer the possibility to obtain bioactive technetium-99m complexes via the “integrated” approach. The ^{99m}Tc CpTT complexes are prepared by various methodologies: (i) from $^{99m}\text{Tc}[\text{TcO}_4]^-$ by reaction with a carbonyl source (e.g. $\text{Cr}(\text{CO})_6$ or $\text{Mn}(\text{CO})_5\text{Br}$) and a ferrocene

as the cyclopentadienyl source (double ligand transfer) [33]; (ii) by reaction of $[^{99m}\text{Tc}] [\text{Tc}(\text{CO})_3(\text{H}_2\text{O})_3]^+$ with a ferrocene (single ligand transfer) [34, 35]; and (iii) by reaction of $[^{99m}\text{Tc}][\text{Tc}(\text{CO})_3(\text{H}_2\text{O})_3]^+$ with a cyclopentadiene-carbonyl derivative (e.g. ketone) or its dimer (e.g. Thiele's acid) [36, 37]. These complexes are neutral and lipophilic and have been used for the development of targeted radiopharmaceuticals. The isolobal to Cp^- ligand *nido-carborane* is prepared from dicarba-*closododecaboranes* followed by deprotonation, and the anionic $[^{99m}\text{Tc}][\text{Tc}(\text{CO})_3\text{C}_2\text{B}_9\text{H}_{10}]^-$ complex is formed. Carboranes have a similar size to the phenyl ring and demonstrate low toxicity [38].

12.3 MYOCARDIAL IMAGING AGENTS

Myocardial perfusion scintigraphy is one of the most frequently performed nuclear medicine procedures useful for the evaluation of the myocardial function. The lipophilic, cationic ^{99m}Tc radiopharmaceuticals that are mostly used for this procedure are ^{99m}Tc -Sestamibi and ^{99m}Tc -Tetrofosmin. These agents do not exhibit ideal myocardial extraction and furthermore display prolonged hepatic clearance that, due to the proximity of the liver to the heart, makes it difficult to assess the myocardial perfusion, especially in the lower areas of the left ventricle. Therefore, it is highly desirable to develop new myocardial agents with better organ distribution and faster hepatic clearance. More than two decades ago, a novel myocardial imaging agent was developed – the neutral nitridotechnetium complex $[^{99m}\text{Tc}][\text{TcN}(\text{NOET})_2]$ (NOET is N-ethoxy, N-ethyl-dithiocarbamate) – that exhibits better extraction properties compared to ^{99m}Tc -Sestamibi and ^{99m}Tc -Tetrofosmin as well as redistribution similar to ^{201}Tl . In 2000, a new class of nitrido technetium(V) complexes was developed based on the $[^{99m}\text{Tc}][\text{TcN}(\text{aminodiphosphane}, \text{PNP})]^{2+}$ metal fragment that, in combination with dithiocarbamate (DTC) as co-ligand, forms asymmetrical and monocationic complexes of the type $[^{99m}\text{Tc}][\text{TcN}(\text{PNP})(\text{DTC})]^+$. From this series of compounds, the complexes $[^{99m}\text{Tc}][\text{TcN}(\text{PNP3})(\text{DBODC})]^+$ and $[^{99m}\text{Tc}][\text{TcN}(\text{PNP5})(\text{DBODC})]^+$, where DBODC is bis-N-ethoxyethyl-dithiocarbamate, PNP3 is bis(dimethoxypropylphosphinoethyl)-methoxyethylamine, and PNP5 is bis(dimethoxypropylphosphinoethyl)-ethoxyethylamine, respectively (Figure 12.3), exhibited superior properties as myocardial imaging agents. In particular, high myocardial uptake of 3.65 ± 0.56 and $3.69 \pm 0.29\%$ ID/g was displayed by $[^{99m}\text{Tc}][\text{TcN}(\text{PNP3})(\text{DBODC})]^+$ and $[^{99m}\text{Tc}][\text{TcN}(\text{PNP5})(\text{DBODC})]^+$ at 10 minutes *p.i.*, respectively,

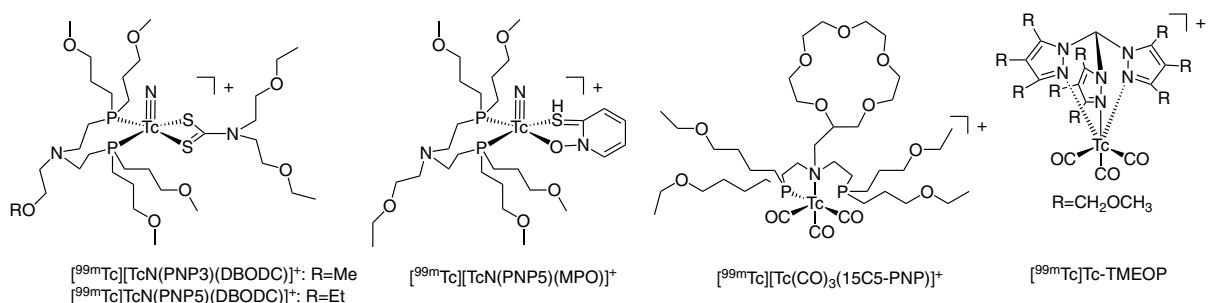


Figure 12.3 Structures of ^{99m}Tc -labelled myocardial imaging agents.

which was retained for a prolonged time, comparable to that of ^{99m}Tc -Sestamibi and ^{99m}Tc -Tetrofosmin [39, 40]. Furthermore, fast lung and liver washout was observed, with heart-to-lung and heart-to-liver ratios higher than those of ^{99m}Tc -Sestamibi and ^{99m}Tc -Tetrofosmin at 60 minutes and 120 minutes *p.i.* In preclinical evaluation, the heart-to-liver ratio of ^{99m}Tc [^{99m}Tc][TcN(PNP5)(DBODC)]⁺ was found to be 18.4 ± 2.0 , which was superior to ^{99m}Tc -Sestamibi and ^{99m}Tc -Tetrofosmin with ratios of 2.6 ± 0.2 and 5.8 ± 0.7 , respectively, at 60 minutes *p.i.* [41]. In subcellular experiments, ^{99m}Tc [^{99m}Tc][TcN(PNP5)(DBODC)]⁺ behaved as a substrate of the multi-drug resistance-associated protein P-glycoprotein and also displayed selective mitochondrial accumulation [42]. Another tracer of the same type that contains a crown-ether moiety, ^{99m}Tc [^{99m}Tc][TcN(N-(dithiocarbamate)-2-aminimethyl-15-crown-5)(N,N-bis[2-(bis(3-ethoxypropyl)phosphino)ethyl]methoxyethylamine)]⁺ (^{99m}Tc][TcN-15C5), was developed and exhibited similar biodistribution properties to ^{99m}Tc [^{99m}Tc][TcN(PNP5)(DBODC)]⁺ [43, 44]. In addition, the nitridotechnetium tracer ^{99m}Tc [^{99m}Tc][TcN(PNP5)(MPO)]⁺, where MPO is 2-mercaptopyridine N-oxide (Figure 12.3), was developed and displayed heart uptake of $2.62 \pm 0.34\%$ ID/g. Its heart-to-liver ratio of 12.75 ± 3.34 at 30 minutes *p.i.* was higher than that of ^{99m}Tc [^{99m}Tc][TcN(PNP5)(DBODC)]⁺ (6.01 ± 1.45) and ^{99m}Tc -Sestamibi (2.90 ± 0.22) [45]. In addition, ^{99m}Tc [^{99m}Tc][TcN(PNP5)(MPO)]⁺ and ^{99m}Tc -Sestamibi displayed almost identical subcellular distribution and localization mechanisms [46].

By a different approach, the cationic ^{99m}Tc technetium-tricarbonyl complexes were developed as well for myocardial perfusion imaging. First, complexes of the type ^{99m}Tc [^{99m}Tc][Tc(CO)₃(CNR)₃]⁺ with three isocyanide ligands were developed, which, although they exhibited myocardial uptake, did not display superior biodistribution properties [47, 48]. A series of ^{99m}Tc [^{99m}Tc][Tc(CO)₃(PNP)]⁺-type complexes were developed that exhibited high myocardial uptake, and among them, the crown-ether containing ligand ^{99m}Tc [^{99m}Tc][Tc(CO)₃(15C5-PNP)]⁺ (15C5-PNP: N-[15-crown-5]-2-yl]-N,N-bis[2-(bis(3-ethoxypropyl)phosphino)ethyl]amine) (Figure 12.3) exhibited approximately 2.5 times better heart-to-liver ratio than that of ^{99m}Tc -Sestamibi at 30 minutes *p.i.* and properties similar to ^{99m}Tc [^{99m}Tc][TcN(PNP5)(DBODC)]⁺ [22]. In preclinical evaluation, ^{99m}Tc [^{99m}Tc][Tc(CO)₃(15C5-PNP)]⁺ displayed favorable *in vivo* kinetics [49]. Furthermore, cationic ^{99m}Tc tris(pyrazolyl)methane-technetium-tricarbonyl complexes were developed with a tripodal chelator that offers multiple possibilities of functionalization. In particular, one of these complexes, ^{99m}Tc [^{99m}Tc][Tc(CO)₃{κ³-HC[3,4,5-(CH₃OCH₂)₃pz]₃}]⁺ (^{99m}Tc][Tc-TMEOP, Figure 12.3), exhibited high heart uptake and superior heart-to-liver ratio of 6.98 ± 1.66 compared to that of ^{99m}Tc -Sestamibi and ^{99m}Tc -Tetrofosmin (2.48 ± 0.30 and 2.66 ± 0.40 , respectively) at 40 minutes *p.i.* [50, 51]. The heart-to-liver ratio of ^{99m}Tc][Tc-TMEOP is comparable to that of ^{99m}Tc [^{99m}Tc][TcN(PNP5)(DBODC)]⁺ (6.01 ± 1.45 at 30 minutes *p.i.*) and ^{99m}Tc [^{99m}Tc][Tc(CO)₃(15C5-PNP)]⁺ (~5) but inferior to that of ^{99m}Tc [^{99m}Tc][TcN(PNP5)(MPO)]⁺ (12.75 ± 3.34). In preclinical evaluation, ^{99m}Tc][Tc-TMEOP displayed a heart-uptake mechanism similar to that of the other reported monocationic ^{99m}Tc cardiac agents and is associated with its accumulation in the mitochondria. Furthermore, cyclosporin A studies indicated that the fast liver and kidney clearance kinetics was mediated by **Pgp** [52, 53]. Additional studies on the metabolism of these ether tracers indicated that the position of the ether moieties on the pyrazole ring is crucial for its ability to exhibit significant myocardial uptake [54].

12.4 ^{99m}Tc -FATTY ACIDS DERIVATIVES

Heart disease can result in regional alterations of the myocardial fatty acid metabolism. Radiolabelled fatty acids (FA) such as 15-(*p*- ^{123}I iodophenyl)-3(*R,S*)-methyl pentadecanoic acid, are useful in the diagnosis of heart disease. The development of ^{99m}Tc -FA for this purpose is highly desirable due to the lower cost and wider availability of technetium-99m.

One effort was based on the [^{99m}Tc]oxotechnetium "3+1" mixed-ligand complexes of the type [SNS/S] and [SSS/S] bearing FA either on the monodentate thiol or on the tridentate chelator. These tracers exhibited low *in vivo* myocardial uptake [55, 56]. Also, a series of [^{99m}Tc]TcO-MAMA-FA complexes with hexanoic, dodecanoic, and hexadecanoic acids were developed. The highest initial myocardial uptake in mice was observed for [^{99m}Tc]TcO-MAMA-hexadecanoic acid (Figure 12.4) ($11.22 \pm 0.25\%$ ID/g at 0.5 minutes and $2.40 \pm 0.22\%$ ID/g at 5 minutes *p.i.*, respectively), which exhibited the highest heart-to-blood ratio of 3.6 at 2 minutes *p.i.* Furthermore, this tracer was able to undergo *in vivo* metabolism, since its metabolite [^{99m}Tc]TcO-MAMA-butanoic acid was detected in the urine [57]. In another approach, asymmetrical cationic, or neutral [^{99m}Tc][TcN(PNP) (L-FA)], complexes were developed, where L was 2,3-dimercaptopropanoic acid or dithiocarbamate linked to undecanoic and dodecanoic acids [58]. The ^{99m}Tc -tracers exhibited fast liver and lung washout, and the highest heart uptake was observed for the cationic dithiocarbamate tracer conjugated to dodecanoic acid, [^{99m}Tc][TcN(PNP3) (DTC11)] $^{+}$ (Figure 12.4), with values of 1.07 ± 0.02 and $0.59 \pm 0.03\%$ ID/g at 5 and 60 minutes *p.i.*, respectively. However, more detailed heart-extraction experiments showed

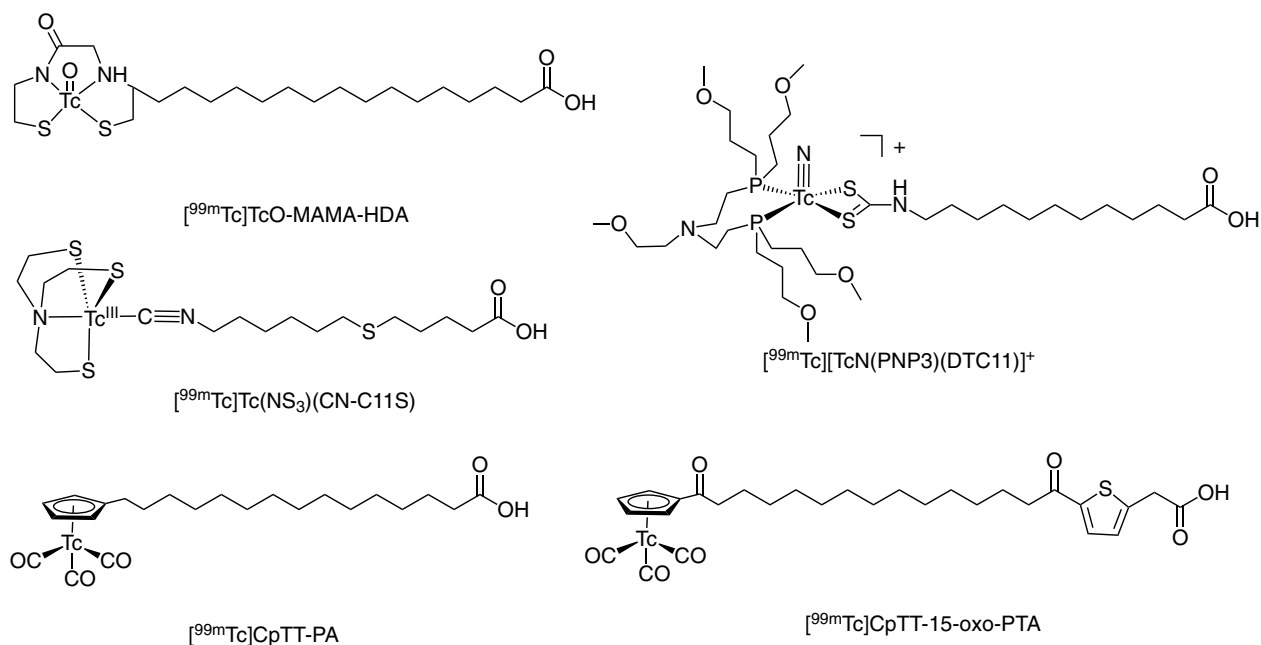


Figure 12.4 Structures of ^{99m}Tc -labelled fatty acids.

that the biodistribution profile was similar to that of the heart agents ^{99m}Tc -Sestamibi and $^{99m}\text{Tc}[\text{TcN}(\text{PNP})(\text{DBODC})]^+$, while its hepatic metabolism pattern was complex. In addition, similar $^{99m}\text{Tc}[\text{TcN}(\text{PNP})(\text{cysteinyI-FA})]$ complexes were developed where cysteine was coordinated either as $[\text{S},\text{N}]^{-1}$ or as $[\text{S},\text{O}]^{2-}$ bidentate ligand leading to either cationic or neutral complexes, respectively [59, 60]. The cationic tracer exhibited myocardial uptake of $9.88 \pm 2.99\%$ ID/g and $1.39 \pm 0.36\%$ ID/g at 2 and 30 minutes *p.i.*, respectively.

A series of "4+1" mixed-ligand ^{99m}Tc -complexes were developed with tris(2-mercaptoethyl)amine as the tetradentate ligand and isocyanide monodentate ligands of varying length FAs. Inserted in some of these FA monodentate ligands was either a sulfur heteroatom or a phenylene group to block/slow the β -oxidation. High myocardial extraction rates up to 26% injected dose (ID) were observed for these tracers in an isolated Langendorff rat heart model. *In vivo*, the tracers exhibited fast metabolism at 60 minutes *p.i.*, although no myocardial metabolism was observed. The highest heart uptake was 2% ID/g, and the heart-to-blood ratio was 8.6 ± 0.1 at 5 minutes *p.i.* for the derivative with the isonitrile ligand 5-[6-(isocyanoethyl)thio]pentanoic acid, $^{99m}\text{Tc}[\text{Tc}(\text{NS}_3)(\text{CN-C11S})]$ (Figure 12.4) [61, 62]. Furthermore, "4+1" mixed-ligand technetium-99m complexes were developed where the ^{99m}Tc -chelate was placed in a central position of the compound for improved myocardial profile following the sequence: carboxylic group, alkyl chain, ^{99m}Tc -chelate, and lipophilic tail. The myocardial first-pass extraction of the compounds was up to 20% of the injected dose (% ID) in the perfused heart, and the tracers exhibited fast liver clearance [63]. Some of these tracers were evaluated in isolated perfused rat heart models, where it was found that the myocardial extraction was between 15.2% and 33.0%. Further studies in knockout H-FABP $^{-/-}$ and H-FABP $^{+/+}$ mice, where H-FABP is an intracellular protein that binds and transports FA, showed that H-FABP plays an important role in the myocardial uptake and retention of these "4+1" ^{99m}Tc -FA tracers [64]. Metabolism studies showed that the tracers did not undergo mitochondrial metabolism [65].

The ^{99m}Tc technetium-tricarbonyl approach was also used for the development of ^{99m}Tc -labelled FAs [66–69]. From these tracers, the ^{99m}Tc technetium-tricarbonyl-cyclopentadienyl (CpTT) pentadecanoic acid, $^{99m}\text{Tc}[\text{CpTT-PA}]$ (Figure 12.4), exhibited high myocardial uptake and retention with values of 3.85 ± 0.58 and $1.27 \pm 0.28\%$ ID/g at 1 and 30 minutes *p.i.*, respectively, and maximum heart-to-blood ratio of 4.60 at 10 minutes *p.i.*. In comparison, 15-(p-[^{123}I]-iodophenyl)pentadecanoic acid exhibited heart uptake of 7.59 ± 1.00 and $4.19 \pm 1.66\%$ ID/g at 1 and 30 minutes *p.i.*, respectively, and maximum heart-to-blood ratio of 12.46 at 2 minutes *p.i.*. The tracer $^{99m}\text{Tc}[\text{CpTT-PA}]$ exhibited myocardial β -oxidation metabolism down to the $^{99m}\text{Tc}[\text{CpTT-propionic acid}]$ metabolite, as Langendorff perfusion study exhibited, where approximately 34% of the perfused $^{99m}\text{Tc}[\text{CpTT-PA}]$ was retained in the heart, and approximately 33% of the perfusate was present as the metabolite [67]. In another study, the tracer $^{99m}\text{Tc}[\text{CpTT-16-oxo-HDA}]$, where HDA is hexadecanoic acid, was developed and exhibited myocardial uptake and retention with values of 9.03 ± 0.17 and $2.16 \pm 0.19\%$ ID/g at 1 and 30 minutes *p.i.*, respectively, and maximum heart-to-blood ratio of 3.76 at 30 minutes *p.i.*. This tracer also

exhibited myocardial metabolism down to the [^{99m}Tc]CpTT-4-oxo-butyric acid metabolite [68]. To create steric hindrance in FA metabolism and enhance the myocardial retention of the radioactivity, the thiophene moiety was introduced in the β -position of the fatty acid chain in 15-[cyclopentadienyl-technetium-tricarbonyl]-15-oxo-pentadecanoyl thiopheneacetic acid ([^{99m}Tc]CpTT-15-oxo-PTA, Figure 12.4). This tracer showed myocardial uptake of 9.39 ± 1.10 and $1.48 \pm 0.14\%$ ID/g at 1 and 30 minutes *p.i.*, respectively, with a maximum heart-to-blood ratio of 5.7 at 15 minutes *p.i.*, while no heart metabolism was detected [69]. More recent modifications in [^{99m}Tc]CpTT-FA complexes did not result in a significant improvement [70, 71].

12.5 BRAIN IMAGING AGENTS

12.5.1 5-HT_{1A} Imaging Agents

The imaging of 5-HT_{1A} receptors may be useful in the assessment of neuropsychiatric and neurodegenerative disorders. For this purpose, the pharmacophore moiety *ortho*-methoxyphenyl-piperazine (**oMPP**) of the true 5-HT_{1A} antagonist WAY-100635 was conjugated to various neutral and lipophilic technetium complexes with the ability to cross the blood-brain barrier. In one effort, the [$^{99g/99m}\text{Tc}$]TcO-DADT complexes were developed where the N₂S₂ chelator was conjugated to 2-(1-piperazino)phenol via a 6-carbon alkyl chain (Figure 12.5). The ^{99}Tc -complex displayed a high affinity for the 5-HT_{1A} receptor with IC₅₀ value of 1.29 nM against the selective 5-HT_{1A} agonist [^3H]8-OH-DPAT, as well as good selectivity versus 5-HT_{2A} (IC₅₀ of 922 nM against [^3H]ketanserin). The ^{99m}Tc -tracer exhibited initial brain uptake of $0.56 \pm 0.07\%$ ID at 2.5 minutes *p.i.*, while *in vitro* autoradiography indicated its accumulation in 5-HT_{1A} receptor-rich brain regions [72]. The “4+1” concept was used as well for the development of M(NS₂)(CN-C4/5/6-*oMPP*) (M = Re or ^{99m}Tc) complexes where *oMPP* was conjugated to the isonitrile co-ligand via butyl (C4), pentyl (C5), and hexyl (C6) linkers (Figure 12.5). The Re-complexes exhibited a high affinity for 5-HT_{1A} with IC₅₀ values of 0.29 ± 0.01 , 0.62 ± 0.17 and 4.5 ± 0.1 nM, respectively. Biodistribution studies in rats of the ^{99m}Tc -complexes showed brain-uptake values between 0.3 and 0.5% ID/organ (5 minutes *p.i.*), while in autoradiography, specific accumulation in 5-HT_{1A} receptor-rich brain regions was displayed [73]. Furthermore, a series of technetium and rhenium “3+1” complexes were developed, where *oMPP* was conjugated either to the tridentate chelator or to the monothiol [74–77]. The complexes [ReO(S₂N(C3-*oMPP*)(TP or MeOTP))] with thiophenol (TP) or 4-methoxythiophenol (MeOTP) as co-ligands, where *oMPP* was conjugated to the tridentate SNS ligand via a propyl (C3) linker, exhibited the highest affinity for 5-HT_{1A} with IC₅₀ values of approximately 6 nM against [^3H]8-OH-DPAT [75, 76]. In the complexes where *oMPP* was conjugated to the monothiol, the analogous complexes MO(S₂NMe)(S-C6-*oMPP*) (M = Re or ^{99}Tc) (Figure 12.5) exhibited subnanomolar affinities for 5-HT_{1A} with IC₅₀ values of 0.24 ± 0.08 and 0.13 ± 0.01 nM for Re and ^{99}Tc complexes, respectively, as well as good selectivity versus 5-HT_{2A} [74]. Furthermore,

a different “3+1” complex of the type $\text{ReO}(\text{PNS})(\text{S-X-}o\text{MPP})$ was developed, where (P,N,S) is a phosphine-amide-thiol tridentate chelator and $o\text{MPP}$ was conjugated to the monothiol (S) with spacers of various lengths, X. The complex with the propyl spacer X exhibited a high affinity for 5-HT_{1A} with IC_{50} of 2.35 ± 0.02 nM as well as high selectivity versus 5-HT_{2A} . Biodistribution of the analogous ^{99m}Tc -tracer exhibited poor brain uptake [78]. Furthermore, neutral complexes of the type $\text{MN}(\text{PS})(\text{DTC})$ ($\text{M} = ^{99}\text{Tc}$, ^{99m}Tc) were developed, of which the $[\text{Re}^{99}\text{Tc}]\text{TcN}(\text{PSiso})(\text{DTC-}o\text{MPP})$ complex, where PSiso was diisopropyl-phosphinoethanethiol and DTC- $o\text{MPP}$ was a dithiocarbamate ligand conjugated to $o\text{MPP}$ via a butyl spacer (Figure 12.5), exhibited the highest affinity for 5-HT_{1A} receptors with IC_{50} of 1.5 ± 0.1 nM and good selectivity versus 5-HT_{2A} ($\text{IC}_{50} = 570 \pm 30$ nM against $[\text{H}^3]\text{ketanserin}$). The ^{99m}Tc -tracers exhibited negligible brain uptake, though [79]. The $\text{M}(\text{CO})_3^+$ ($\text{M} = \text{Re}$, ^{99m}Tc) approach was also used [80, 81], and from these tracers, the ones synthesized from the poly(mercaptoimidazolyl)borate scorpionate (DMIB) chelator are of interest. The ligand was conjugated to either one or two $o\text{MPP}$ moieties, and the respective rhenium-tricarbonyl complexes exhibited subnanomolar affinities for 5-HT_{1A} with IC_{50} values of 0.172 ± 0.003 for the Re-complex conjugated to two $o\text{MPP}$ moieties (Figure 12.5) and 0.71 ± 0.02 nM for the Re-complex conjugated to one $o\text{MPP}$ moiety with moderate to good selectivity versus 5-HT_{2A} . The ^{99m}Tc -tracer analogues exhibited an initial brain uptake of $1.38 \pm 0.46\%$ ID/g for the ^{99m}Tc -complex conjugated to two $o\text{MPP}$ moieties and $0.43 \pm 0.12\%$ ID/g for the ^{99m}Tc -complex conjugated to one $o\text{MPP}$ moiety at 5 minutes *p.i.*, with fast washout [82]. High brain uptake and specific retention in 5-HT_{1A} receptor-rich brain regions was also observed for a $[\text{Re}^{99m}\text{Tc}]\text{technetium-tricarbonyl-cyclopentadienyl}$ complex conjugated to $o\text{MPP}$ (Figure 12.5), where the brain uptake was $2.47 \pm 0.04\%$ ID/g at 5 minutes *p.i.*; furthermore, the hippocampus-to-cerebellum ratio in the brain was found to be 4.83, and the cortex-to-cerebellum ratio was 2.77 [83].

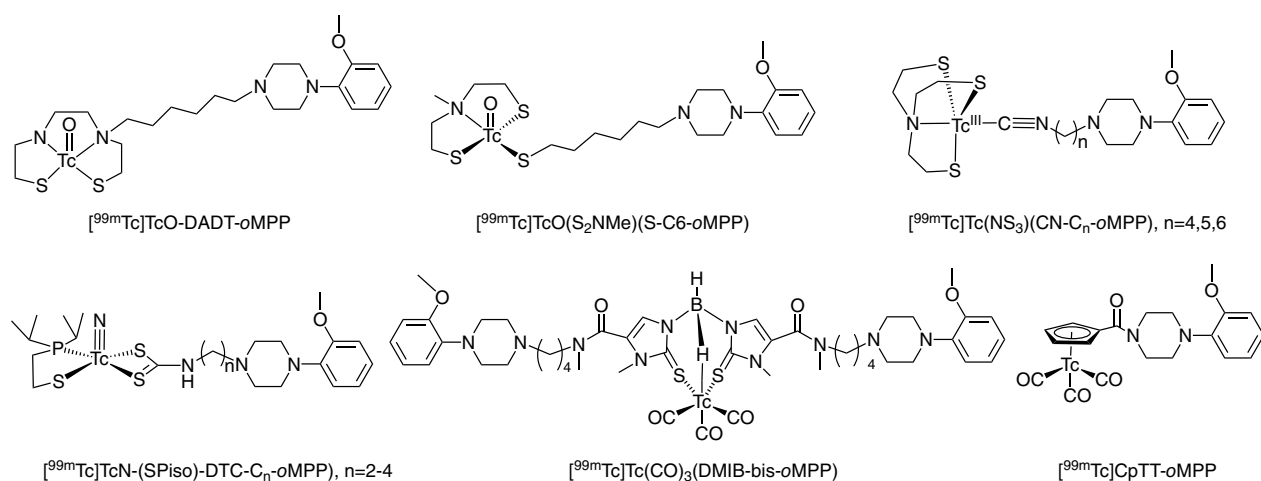


Figure 12.5 Structures of ^{99m}Tc -labelled 5-HT_{1A} receptor imaging agents.

12.5.2 Beta-Amyloid Imaging Agents

Imaging agents for β -amyloid plaques have proven to be useful in the diagnosis of patients with cognitive impairment suspected for Alzheimer's disease (AD). An ideal amyloid imaging agent should be able to cross the blood-brain barrier and bind with a high affinity to the β -amyloid, while the unbound radioactivity washes out quickly. The β -amyloid binding moieties that have mostly been explored are based on Thioflavin T and Chrysamine G dyes. Most of the efforts have used phenyl-benzothiazole as the pharmacophore unit, but modifications with benzofuran, benzoxazole, aurone, and flavone moieties were also made. A number of aryl-benzothiazole (BTA) derivatives were conjugated to the BAT or MAMA chelators, and their respective rhenium and technetium complexes were developed [84]. In a few studies, the suitable position of the BTA system for conjugation to the metal chelator was investigated [85, 86]. Promising results were obtained when the derivative 6-hydroxy-2-(4'-aminophenyl)-1,3-benzothiazole (6-BTA) was conjugated to the MAMA chelator via the 6-hydroxyl position and a 5-carbon spacer. The respective fluorescent Re-MAMA-6-BTA complex selectively bound to the β -amyloid aggregates in the brain sections of both transgenic mouse and AD patients. The analogous [^{99m}Tc]Tc-MAMA-6-BTA complex could cross the healthy mouse brain with high initial uptake ($1.34 \pm 0.16\%$ ID/g at 2 minutes *p.i.*) but with low blood clearance (4.43% ID/g at 60 minutes *p.i.*) [87]. More recently, the BAT chelator was conjugated to 2-aryl-6-hydroxy-benzothiazole pharmacophore moieties via the hydroxyl position-6 of benzothiazole with various spacers ranging from propyl (C3) up to hexyl (C6) as well as with the ethyleneoxy spacer [88, 89]. From these complexes, it was shown that the M-BAT-6-PhBTA complex (M = Re, ^{99m}Tc) where the 2-(*N*-4'-methylaminophenyl)-6-hydroxy-benzothiazole pharmacophore was used with a butyl spacer (Figure 12.6) exhibited the most promising *in vitro* and *in vivo* behavior, with binding affinity against [^{125}I]IMPY of K_i (Re-complex) = 8.8 ± 1.8 nM, and the highest *in vivo* brain uptake of the ^{99m}Tc -tracer of $2.11 \pm 0.11\%$ ID/g at 2 minutes *p.i.*. The significant brain uptake of this tracer was confirmed with *in vivo* SPECT/CT imaging of rhesus monkeys [89].

Furthermore, various [^{99m}Tc][$\text{Tc}(\text{CO})_3$] $^+$ -labelled benzothiazole derivatives were also developed [90, 91]. In one attempt, the cyclopentadienyl ligand was conjugated via an amide bond with the 6-hydroxyl-derivatized 2-(4'-aminophenyl)-6-hydroxy-benzothiazole with propyl and pentyl spacers. The $\text{Re}(\text{CO})_3(\text{cp-BTA})$ complexes exhibited moderate binding affinities to β -amyloid and, in addition, they were able to bind *in vitro* to β -amyloid in postmortem brain slices of transgenic mice and AD patients, although [^{99m}Tc][$\text{Tc}(\text{CO})_3(\text{cp-BTA})$] (Figure 12.6) exhibited poor brain uptake $<0.5\%$ ID/g [92]. Similar derivatives were prepared by amide linkage of cyclopentadienyl to the 2-aryl-6-hydroxy-benzothiazole moiety. The rhenium complexes displayed a high affinity for β -amyloid *in vitro* (the highest affinity was $K_i = 12.39 \pm 5.14$), and they could intensely stain β -amyloid deposits on brain sections of transgenic mice and AD patients. The ^{99m}Tc -radiotracers were prepared by double-ligand transfer reaction from the respective ferrocene precursor and were found to bind to β -amyloid deposits in blood vessels of the brain section of AD patients, while the highest initial brain uptake in normal mice was 1.06% ID/g at

2 minutes *p.i.*. Comparatively, the brain uptake between the amide and the ester derivatives was not significantly different [93].

In the direction of ^{99m}Tc -labelled benzofuran (**BF**) derivatives, 5-hydroxyl-2-(4'-dimethylaminophenyl)-benzofuran was conjugated to the BAT and MAMA chelators via a propyl chain at position-5. The Re-BAT-5-BF and Re-MAMA-5-BF complexes prepared displayed binding affinity to β -amyloid with K_i values of 11.5 ± 0.56 and 24.4 ± 0.77 nM, respectively. The analogous [^{99m}Tc]Tc-BAT-5-BF (Figure 12.6) and [^{99m}Tc]Tc-MAMA-5-BF were able to bind to β -amyloid plaques of transgenic mice in autoradiography brain tissue sections and exhibited initial brain uptake of 1.34 ± 0.12 and $0.74 \pm 0.15\%$ ID/g, respectively, at 2 minutes *p.i.*. In addition, [^{99m}Tc]Tc-BAT-5-BF exhibited maximum brain uptake of $1.37 \pm 0.18\%$ ID/g and fast washout, with blood percentage activity of $1.96 \pm 0.06\%$ ID/g, at 10 minutes *p.i.* [94].

In the development of ^{99m}Tc -benzoxazole (**BOx**) derivatives, 2-(*N,N*-dimethyl-4'-aminophenyl)-5-hydroxyl-benzoxazole was conjugated to the BAT and MAMA chelators via a pentyl spacer at position-5 of benzoxazole (5-BOx). The Re-BAT-C5-5-BOx and Re-MAMA-C5-5-BOx complexes exhibited *in vitro* binding affinity to β -amyloid with K_i values of 11.1 and 14.3 nM, respectively, against [^{125}I]IMPY. In addition, the Re complexes stained the β -amyloid plaques on the sections of transgenic mice. Biodistribution experiments in normal mice revealed that [^{99m}Tc]Tc-BAT-C5-5-BOx displayed moderate initial brain uptake (0.81% ID/g at 2 minutes), which quickly washed out from the brain (0.25% ID/g at 60 minutes) [95]. From a series of BOx derivatives, Re-BAT-C3-5-BOx where 2-(*N,N*-dimethyl-4'-aminophenyl)-5-hydroxy-benzoxazole was conjugated to the BAT chelator at position-5 via a propyl linker exhibited β -amyloid binding affinity of $K_i = 15.86 \pm 4.64$ nM against [^{125}I]IMPY. Its analogous ^{99m}Tc -tracer ([^{99m}Tc]Tc-BAT-C3-5-BOx, Figure 12.6) exhibited the highest brain uptake of $1.55 \pm 0.51\%$ ID/g at 2 minutes *p.i.* [96]. Derivatives of the quinoxaline type were also developed from the 2-(4'-aminophenyl)-6-hydroxy-quinoxaline scaffold that was conjugated via a propyl chain to the BAT chelator and where the 4'-aminophenyl moiety was either *N,N*-dimethylated (BAT-C3-PQ-1), *N*-methylated (BAT-C3-PQ-2), or unmethylated (BAT-C3-PQ-3). The binding affinity of [^{99m}Tc]Tc-BAT-C3-PQ-1 in β -amyloid aggregates was higher compared to the other two derivatives, and its biodistribution study revealed moderate initial brain uptake of $0.88 \pm 0.08\%$ ID/g with reasonable clearance from the brain [97].

In another approach, ^{99m}Tc -labelled chalcone (**Ch**) derivatives were developed based on the scaffold 4-*N,N*-dimethylamino-4'-hydroxy-chalcone, which was conjugated to the chelators BAT and MAMA via propyl (C3) and pentyl (C5) spacers at the 4'-hydroxyl position. All the ^{99m}Tc complexes exhibited binding to β -amyloid aggregates *in vitro*, and higher binding was obtained for the two C5 analogues [^{99m}Tc]Tc-BAT/MAMA-C5-4'-Ch. Biodistribution in normal mice showed that the [^{99m}Tc]Tc-BAT-C3-4'-Ch tracer (Figure 12.6) displayed the highest initial brain uptake (1.48% ID/g) at 2 minutes *p.i.* and fast brain washout (0.17% ID/g at 60 minutes) [98]. Furthermore, similar flavone and aurone complexes were developed, where the 6-hydroxy-4'-*N,N*-dimethylamino-flavone (**FL**) and the analogous aurone (**AR**) were conjugated to BAT via a propyl spacer at the 6-hydroxyl position. Both ^{99m}Tc -labelled derivatives showed specific binding in β -amyloid aggregates,

with the aurone exhibiting a higher binding affinity compared to the flavone (but lower compared to the previously mentioned chalcone one) as well as similar *in vivo* characteristics in biodistribution studies. [^{99m}Tc]Tc-BAT-FL and [^{99m}Tc]Tc-BAT-AR (Figure 12.6) exhibited low initial brain uptake of 0.64 and 0.79 %ID/g at 2 minutes *p.i.*, respectively, and fast elimination [99]. A [^{99m}Tc]Tc(CO)₃-flavonol derivate was also described with a binding affinity (of the respective Re complex) of $K_D = 11.16$ nM in β -amyloid aggregates, with low *in vivo* brain uptake (0.48 ± 0.05 % ID/g at 5 minutes *p.i.*) [100].

In an integrated approach, chalcone-mimics were developed by replacing the chalcone aromatic ring by the [^{99m}Tc]cyclopentadienyl-technetium-tricarbonyl moiety and by inserting extended conjugated π systems (ethenyl, dienyl, and trienyl) (Figure 12.6). Low binding affinities for β -amyloid were displayed with the highest that of the trienyl derivative with $K_i = 108 \pm 16$ nM, against [¹²⁵I]IMPY. Apparently, as shown from the crystal structure of these complexes, the metal-carbonyl core distorts the planarity of the system, which decreases their affinity. In terms of their brain uptake in normal mice, the ethenyl-, dienyl-, and trienyl-chalcone mimics exhibited high brain uptake of 4.10 ± 0.38 , 2.30 ± 0.27 , and 1.11 ± 0.34 % ID/g at 2 minutes *p.i.* [101].

A different pharmacophore, curcumin, was coordinated with [^{99m}Tc][Tc(CO)₃]⁺ in a bidentate (O,O) fashion with co-ligands imidazole and cyclohexylisocyanide (Figure 12.6). The analogous rhenium complexes were able to stain postmortem brain section of AD patients [102]. Furthermore, ^{99m}Tc-labelled dibenzylideneacetone (**DBAc**) derivatives were developed, where the dibenzylideneacetone scaffold was conjugated to BAT and MAMA chelators via propyl (C3) and pentyl (C5) chains. All the Re derivatives exhibited specific β -amyloid binding, and the highest measured binding affinity was $K_i = 13.6$ nM displayed by the Re-BAT-C5-DBAc complex. All the ^{99m}Tc tracers exhibited low brain uptake <0.5% ID/g [103].

The stilbene moiety has also been used for the design of ^{99m}Tc-probes. 3-Styrylpyridine derivatized with an oligoethyleneoxy linker was conjugated to the BAT chelator. The Re complex with the bisethyleneoxy linker exhibited a higher binding affinity with $K_i = 13.4 \pm 3.3$ nM against [¹²⁵I]IMPY. The analogous ^{99m}Tc tracer (Figure 12.6) exhibited brain uptake of 2.10 ± 0.22 % ID/g at 2 minutes *p.i.*. *In vivo* SPECT/CT imaging in six rhesus monkeys displayed an improvement in the brain uptake (1.94–2.63% ID within 20 minutes) [88].

12.6 RENAL IMAGING AGENTS

The most used renal imaging agent in nuclear medicine is [^{99m}Tc]Tc-MAG₃, which exhibits approximately 50–60% of the renal excretion of the gold standard *ortho*-[¹³¹I]iodohipurate ([¹³¹I]OIH), not currently used due to its suboptimal γ properties and β -radiation burden. In an effort to develop new renal tracers with improved properties, a series of [^{99m}Tc]technetium-tricarbonyl complexes were prepared with at least one dangling carboxylate group that favors renal tubular transport, and the tracers were compared to [¹³¹I]OIH (Figure 12.7). The first effort described the labeling of lanthionine (**LAN**) (a mixture of *meso*-LAN, *DD*- and *LL*-LAN isomers) to form [^{99m}Tc][Tc(CO)₃(LAN)]⁻ where

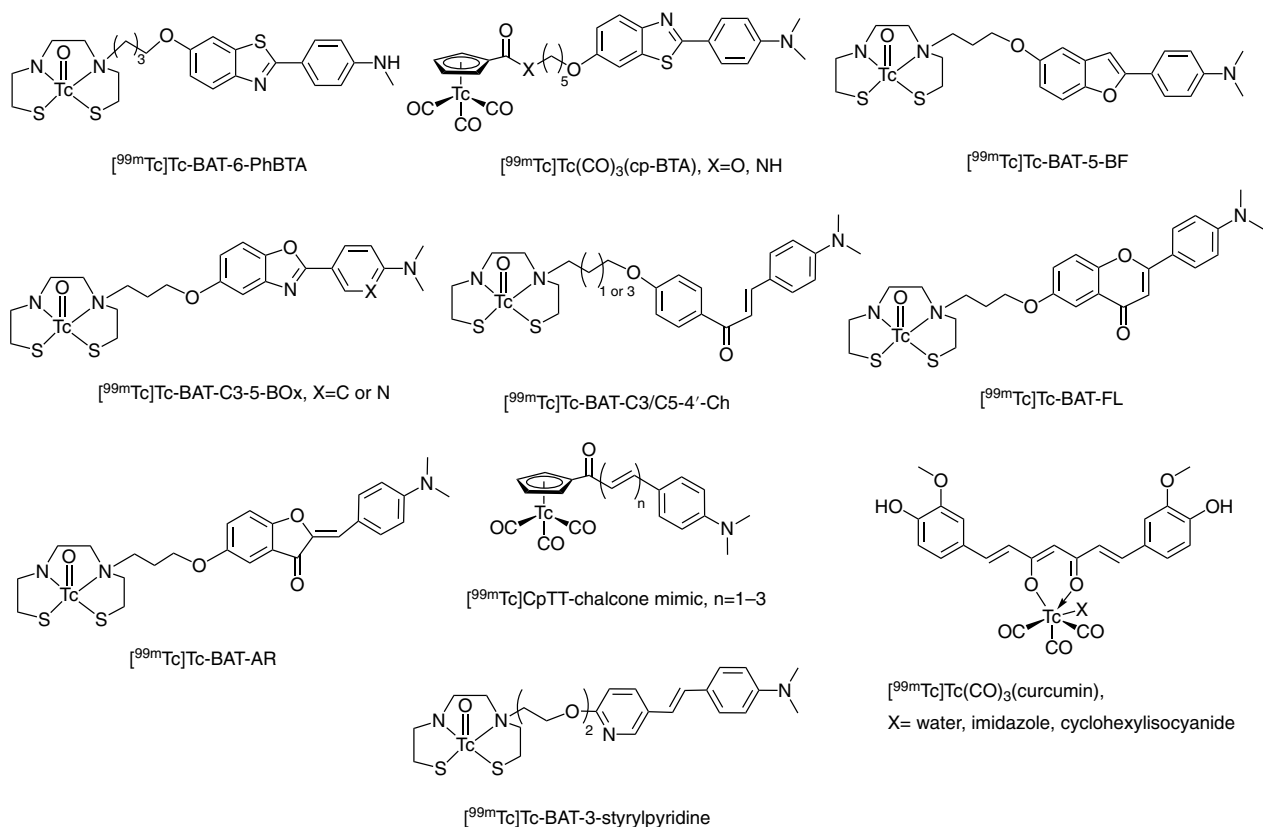


Figure 12.6 Structures of ^{99m}Tc-labelled β-amyloid imaging agents.

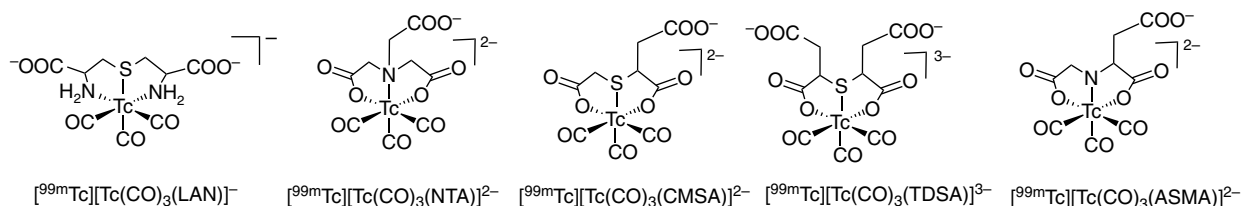


Figure 12.7 Structures of ^{99m}Tc-labelled renal imaging agents.

LAN coordinates via the (N,S,N) donor atoms, while the two dangling carboxylates lead to an overall anionic charge. The diastereomers were separated, and the two preparations of [^{99m}Tc][Tc(CO)₃(*meso*-LAN)]⁻ and [^{99m}Tc][Tc(CO)₃(*DD,LL*-LAN)]⁻ were tested in rats, where their excretion in urine was on average 88% that of [¹³¹I]OIH (each animal was injected with both the ^{99m}Tc-tracer and [¹³¹I]OIH) at 60 minutes *p.i.* In humans, both agents provided excellent renal images, with the plasma clearance averaging 228 ml min⁻¹ for [^{99m}Tc][Tc(CO)₃(*meso*-LAN)]⁻ and 176 ml min⁻¹ for [^{99m}Tc][Tc(CO)₃(*DD,LL*-LAN)]⁻. At three hours, both tracers showed good renal excretion, averaging 85% and 77% that of

$[^{131}\text{I}]\text{OIH}$, respectively [104, 105]. Two other $[^{99\text{m}}\text{Tc}]$ technetium-tricarbonyl complexes were prepared from the ligands carboxymethylmercaptosuccinic acid (CMSAH_3) and thiodisuccinic acid (TDSA_4), of which both $[^{99\text{m}}\text{Tc}][\text{Tc}(\text{CO})_3(\text{CMSA})]^{-2}$ and $[^{99\text{m}}\text{Tc}][\text{Tc}(\text{CO})_3(\text{TDSA})]^{-3}$ are monoanionic with respect to the inner coordination sphere and have additional negative charges due to the dangling carboxylates: one in CMSA and two in TDSA, respectively. Renal excretion in rats was found to be $68 \pm 1\%$ for $[^{99\text{m}}\text{Tc}][\text{Tc}(\text{CO})_3(\text{TDSA})]^{-3}$ and $98 \pm 1\%$ for $[^{99\text{m}}\text{Tc}][\text{Tc}(\text{CO})_3(\text{CMSA})]^{-2}$ as a percentage of $[^{131}\text{I}]\text{OIH}$ at 60 minutes *p.i.* [106]. $[^{99\text{m}}\text{Tc}]\text{Tc}$ -tricarbonyl-nitrilotriacetic acid, $[^{99\text{m}}\text{Tc}][\text{Tc}(\text{CO})_3(\text{NTA})]^{-2}$, was also prepared, which has the advantage of being one single species (without isomers). This tracer was evaluated in normal rats, and the urinary excretion was $108 \pm 9\%$ and $101 \pm 5\%$, respectively, that of $[^{131}\text{I}]\text{OIH}$ at 10 and 60 minutes *p.i.* [107]. In healthy humans, $[^{99\text{m}}\text{Tc}][\text{Tc}(\text{CO})_3(\text{NTA})]^{-2}$ exhibited comparable plasma clearance ($475 \pm 105 \text{ ml min}^{-1}$) and percentage of injected dose in the urine ($91 \pm 4\%$) with $[^{131}\text{I}]\text{OIH}$ (respective values were $472 \pm 108 \text{ ml min}^{-1}$ and $91 \pm 6\%$) at three hours *p.i.* [108]. In patients with chronic kidney disease, the clearance of $[^{99\text{m}}\text{Tc}][\text{Tc}(\text{CO})_3(\text{NTA})]^{-2}$ and $[^{131}\text{I}]\text{OIH}$ were 177 ± 63 and $171 \pm 66 \text{ ml min}^{-1}/1.73 \text{ m}^2$ and the percentage of injected dose in the urine was $77 \pm 9\%$ and $78 \pm 11\%$ at three hours *p.i.*, respectively, indicating the similarity of the two agents [109]. Another tracer developed was $[^{99\text{m}}\text{Tc}]$ technetium-tricarbonyl-aspartic-N-monoacetic acid, $[^{99\text{m}}\text{Tc}][\text{Tc}(\text{CO})_3(\text{ASMA})]^{-2}$, prepared both as a racemate as well as separate D- and L- enantiomers [110]. In healthy humans, the plasma clearance ratio ($[^{99\text{m}}\text{Tc}][\text{Tc}(\text{CO})_3(\text{ASMA})]^{-2}/[^{131}\text{I}]\text{OIH}$) was $81 \pm 3\%$ for D-ASMA, $20 \pm 4\%$ for L-ASMA, and $37 \pm 7\%$ for *rac*-ASMA. In addition, all tracers exhibited rapid urinary excretion where the percentage of activity in the urine ratio $[^{99\text{m}}\text{Tc}][\text{Tc}(\text{CO})_3(\text{ASMA})]^{-2}/[^{131}\text{I}]\text{OIH}$ was $100 \pm 3\%$ for D-ASMA, $80 \pm 2\%$ for L-ASMA, and $88 \pm 1\%$ for *rac*-ASMA at three hours *p.i.* [111].

12.7 BONE IMAGING AGENTS

The $^{99\text{m}}\text{Tc}$ -bisphosphonates (**BP**) $[^{99\text{m}}\text{Tc}]\text{Tc}$ -methylenediphosphonate ($[^{99\text{m}}\text{Tc}]\text{Tc}$ -MDP) and $[^{99\text{m}}\text{Tc}]\text{Tc}$ -hydroxymethylenediphosphonate ($[^{99\text{m}}\text{Tc}]\text{Tc}$ -HMDP) are gold standards for bone scanning. While these agents have widespread use and established clinical value, there are some limitations regarding their relatively slow blood clearance, which requires two hours or longer waiting time before the scan is performed, as well as their *in vivo* dissociation due to the low stability of the technetium-phosphonate bond. To overcome these limitations, new tracers with improved properties were developed by rational drug design, where suitable robust $^{99\text{m}}\text{Tc}$ -chelates were conjugated to a bisphosphonate moiety.

In one effort, aminomethylenediphosphonate (**AMDP**) was conjugated to L,L-ethylene dicysteine (**EC**) chelator, which has been used to form the renal agent $[^{99\text{m}}\text{Tc}]\text{Tc}$ -EC. The respective tracer $[^{99\text{m}}\text{Tc}]\text{Tc}$ -EC-AMDP (Figure 12.8) exhibited improved bone uptake in rats of $29.4\% \text{ ID/g}$ vs. $15.4\% \text{ ID/g}$ for $[^{99\text{m}}\text{Tc}]\text{Tc}$ -MDP at two hours *p.i.* and comparable blood clearance and urinary excretion rates [112].

Alendronate (**ALN**) was conjugated to the chelators MAG_3 and HYNIC, and the respective $^{99\text{m}}\text{Tc}$ -tracers were developed, where the HYNIC complex was prepared with tricine

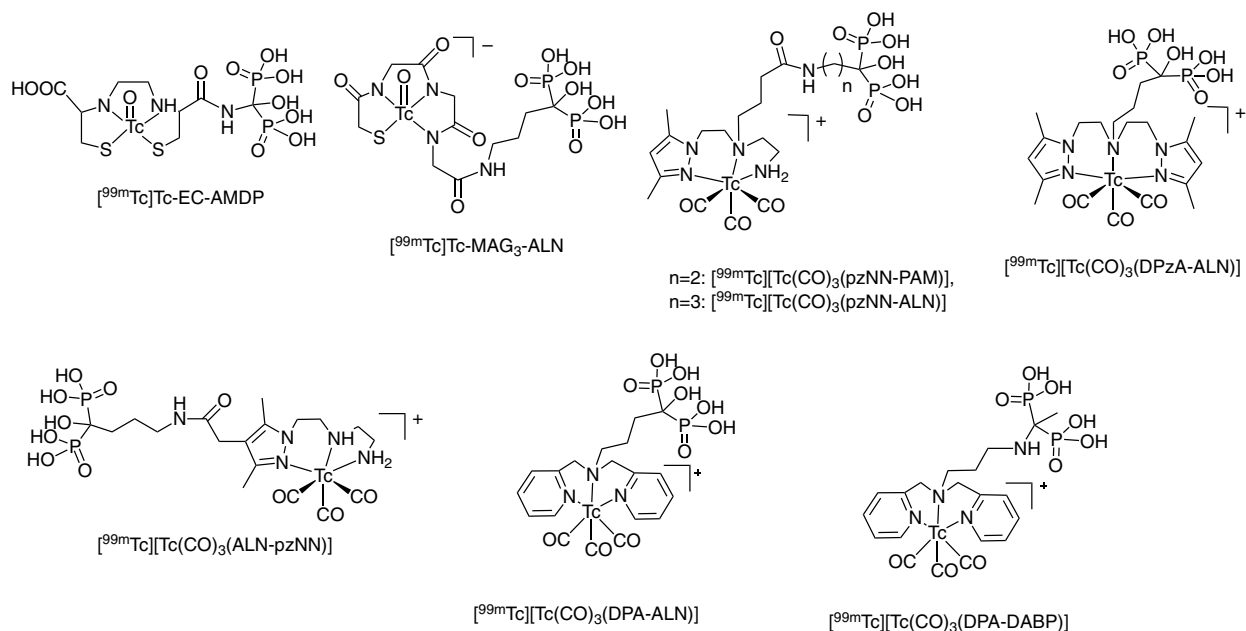


Figure 12.8 Structures of ^{99m}Tc -labelled bone imaging agents.

as co-ligand and 3-acetylpyridine (Acpy) as a ternary ligand. The tracers $[^{99m}\text{Tc}]\text{Tc-MAG}_3\text{-ALN}$ (Figure 12.8) and $[^{99m}\text{Tc}]\text{Tc-(HYNIC-HBP)-tricine-(3-Acpy)}$ exhibited femur uptake in rats of 4.23 ± 0.25 and $3.96 \pm 0.36\%$ ID/g at one hour *p.i.*, which was comparable to that of $[^{99m}\text{Tc}]\text{Tc-HMDP}$ $3.16 \pm 0.51\%$ ID/g [113]. Furthermore, $[^{99m}\text{Tc}]\text{technetium-tricarbonyl-BP}$ complexes were developed. The pyrazolyldiamine (**pzNN**) chelator was conjugated to AMDP, pamidronate (**PAM**), and ALN, and the tracers $[^{99m}\text{Tc}][\text{Tc}(\text{CO})_3(\text{pzNN-PAM})]$ and $[^{99m}\text{Tc}][\text{Tc}(\text{CO})_3(\text{pzNN-ALN})]$ (Figure 12.8) exhibited high bone uptake of $18.3 \pm 0.6\%$ ID/g and $17.3 \pm 6.1\%$ ID/g, respectively, comparable to the uptake of $[^{99m}\text{Tc}]\text{Tc-MDP}$ with value $17.1 \pm 2.4\%$ ID/g at one hour *p.i.* [114, 115]. A modified derivative, where ALN was conjugated to the pyrazolyl moiety of the pyrazolyldiamine chelator via a linker, was developed, $[^{99m}\text{Tc}][\text{Tc}(\text{CO})_3(\text{ALN-pzNN})]$ (Figure 12.8), with high bone uptake of $17.1 \pm 3.6\%$ ID/g at one hour *p.i.* [116]. The tracer $[^{99m}\text{Tc}][\text{Tc}(\text{CO})_3(\text{DPA-ALN})]$ (Figure 12.8) was developed from the DPA chelator that was conjugated to ALN, which exhibited bone uptake of approximately 27%–30% ID/g at 6.5 hours *p.i.*, with values comparable to that of $[^{99m}\text{Tc}]\text{Tc-MDP}$ [117]. Similarly, the dipyrazolylamine (**DPZA**) chelator was conjugated to ALN, and the tracer $[^{99m}\text{Tc}][\text{Tc}(\text{CO})_3(\text{DPZA-ALN})]$ (Figure 12.8) exhibited high bone uptake of $17.7 \pm 3.0\%$ ID/g at one hour *p.i.* [116]. A series of $[^{99m}\text{Tc}]\text{technetium-tricarbonyl}$ complexes was developed, where 1-(3-aminopropylamino)ethane-1,1-diyldiphosphonic acid (**DABP**) were conjugated to various tridentate chelators. The tracer with the DPA chelator, $[^{99m}\text{Tc}][\text{Tc}(\text{CO})_3(\text{DPA-DABP})]$ (Figure 12.8), exhibited the highest bone uptake of $19.44 \pm 1.44\%$ ID/g in comparison to that of $[^{99m}\text{Tc}]\text{Tc-MDP}$ $13.18 \pm 1.96\%$ ID/g at one hour *p.i.* [118]. $[^{99m}\text{Tc}]\text{technetium-tricarbonyl}$ “2+1” complexes of the type $[^{99m}\text{Tc}][\text{Tc}(\text{CO})_3(\text{bipy})]$ (im-BP)] were prepared in high yield with the ligands bipyridine (bipy) and imidazole

conjugated to bisphosphonates (im-BP) such as alendronate. These tracers exhibited high stability as well as skeletal accumulation in mice in scintigraphic studies [27].

12.8 TUMOR-TARGETED IMAGING AGENTS

12.8.1 ^{99m}Tc -Bombesin-like Radioligands

It is known that the transmembrane mammalian Gastrin Releasing Peptide Receptor (**GRPR** or BB_2R) is overexpressed in various tumor types, with a high prevalence in prostate and breast carcinomas, but also in small cell lung cancer, renal cell carcinoma, and gastrointestinal stromal tumors [119]. Bombesin is an amphibian tetradecapeptide that binds selectively to GRPR. A number of ^{99m}Tc radioligands targeted for GRPR have been developed based either on bombesin (**BN**) and its truncated octapeptide BN(7-14) or on the decapeptide neuromedin C, which is the fragment Gastrin Releasing Peptide (GRP) (18-27).

One of the earlier efforts in this area described the development of a BN(7-14) analogue conjugated via the $\text{Me}_2\text{Gly-Ser-Cys}$ (N_3S) chelator and the 5-aminovaleric acid (5Ava) spacer. The tracer $^{99m}\text{Tc}[\text{Tc-N}_3\text{S-G-5Ava-BN(7-14)}]$ ($^{99m}\text{Tc-RP527}$) (Figure 12.9) developed was evaluated in prostate and breast cancer patients. The radioligand detected four out of six breast cancer patients and one out of four prostate cancer patients [120]. Another bombesin analogue, $^{99m}\text{Tc}[\text{Tc-Cys-Aca-Gln-Arg-Leu-Gly-Asn-Gln-Trp-Ala-Val-Gly-His-Leu-Met-NH}_2]$, also exhibited *in vivo* tumor localization in human breast cancer patients [121, 122].

Furthermore, a series of $^{99m}\text{Tc}[\text{Tc-tricarbonyl-BN}]$ complexes were developed, where the $\text{N}\alpha$ -histidinyl acetate ($\text{N}\alpha$ -His-Ac) bifunctional chelator was conjugated to BN(7-14). The peptide ligand $\text{N}\alpha$ -His-Ac-BN(7-14) as well as the Re complex $[\text{Re}(\text{CO})_3(\text{N}\alpha\text{-His-Ac-BN(7-14)})]$ exhibited IC_{50} of 4.3 nM and 0.6 nM, respectively, against $^{125}\text{I}[\text{iodoTyr}^4]\text{BN}$ in PC-3 cells [123]. The tracer $^{99m}\text{Tc}[\text{Tc}(\text{CO})_3(\text{N}\alpha\text{-His-Ac-BN(7-14)})]$ (Figure 12.9) was 75% and 7% intact at 15 and 120 minutes, respectively, in human plasma stability studies, and its tumor uptake in PC-3 tumor-bearing mice was low ($0.89 \pm 0.27\%$ ID/g 30 minutes *p.i.*). To improve the properties, various modifications were implemented, and the replacement of the amino acids Leu^{13} and Met^{14} with the non-natural amino acids cyclohexylalanine (Cha) and norleucine (Nle), respectively, as well as the insertion of spacers with β -amino acids sequences between the chelator, and the peptide improved the biodistribution profile of the tracers [124–126]. Furthermore, pegylation of BN(7-14) [127] was performed, and the tracers $^{99m}\text{Tc}[\text{Tc}(\text{CO})_3(\text{N}\alpha\text{-His}(\text{Ac-}\beta^3\text{hLys}(\text{PEG}_n)\text{-}\beta\text{Ala-}\beta\text{Ala-BN(7-14)} [\text{Cha}^{13}, \text{Nle}^{14}])))]$ exhibited a significant increase in their human plasma stability with $t_{1/2} > 24$ hours, while the receptor affinity was unaffected. The tumor uptake of $^{99m}\text{Tc}[\text{Tc}(\text{CO})_3(\text{N}\alpha\text{-His}(\text{Ac-}\beta^3\text{hLys}(\text{PEG}_5)\text{-}\beta\text{Ala-}\beta\text{Ala-BN(7-14)} [\text{Cha}^{13}, \text{Nle}^{14}])))]$ was $3.91 \pm 0.44\%$ ID/g 60 minutes *p.i.* in PC-3 tumor-bearing mice [127]. In another modification, a series of glycosylated BN analogues were developed by introducing the glycomimetic, shikimic acid, or glucose on the peptide spacer by various methods [128, 129]. In the tracer bearing a clickable glucose moiety,

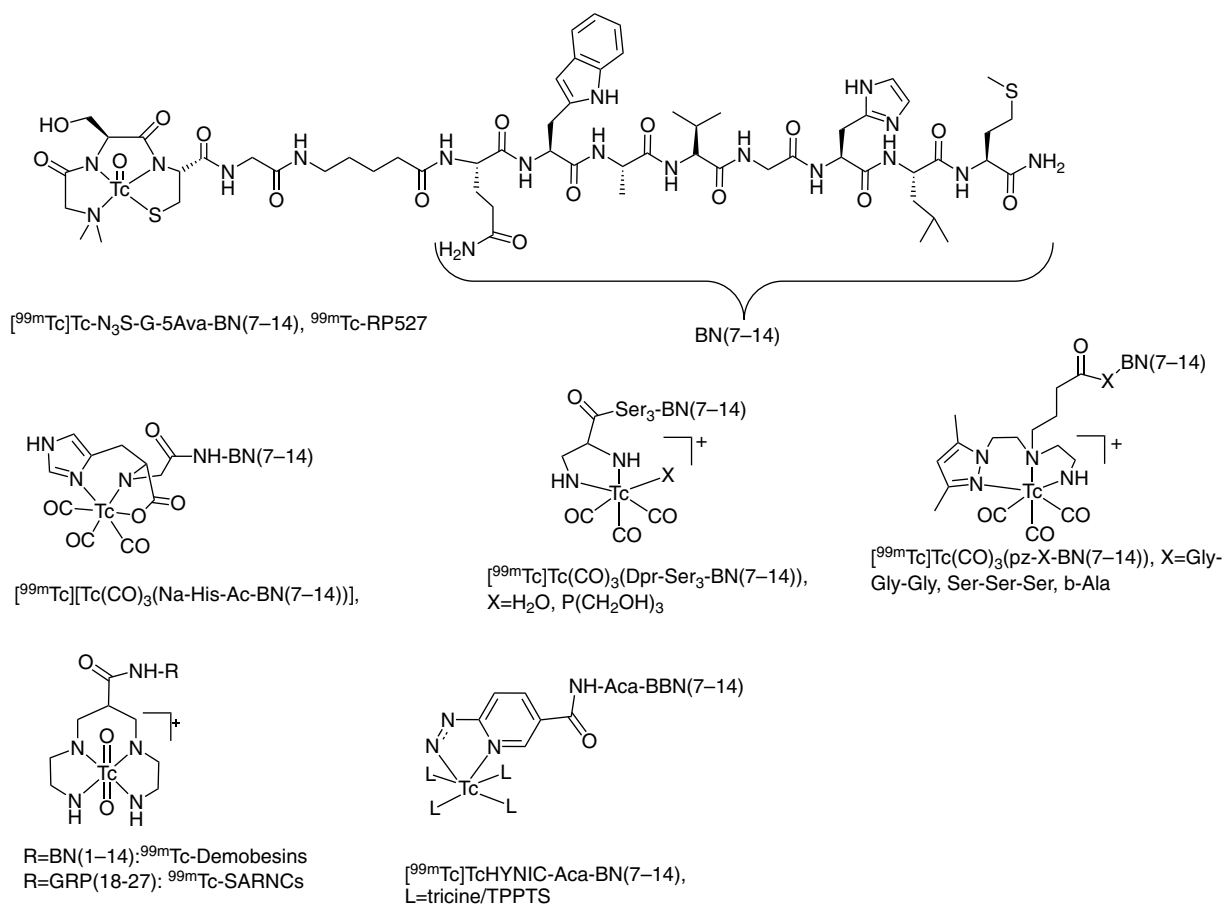


Figure 12.9 Structures of ^{99m}Tc -bombesin-like imaging agents.

increased uptake and retention in tumor tissue (3.6 and 2.5% ID/g at 1.5 and 5 hours *p.i.*, respectively) was observed [128]. Modifications on the chelator were also performed, and the one with the “click” analogue of histidine, triazole-histidine (**TzHis**), resulted in improved tumor-to-background ratios [130–132].

The $[^{99m}\text{Tc}][\text{Tc}(\text{CO})_3(\text{Dpr-SSS-BN(7-14)})(\text{X})]$ tracers (Figure 12.9) were also developed, with the bidentate chelator 2,3 diaminopropionic acid (Dpr) conjugated to BN(7-14) via a triserine spacer (SSS), and water or trishydroxymethylphosphine, P(CH₂OH)₃, as the monodentate co-ligand X. These tracers exhibited tumor uptake of $3.68 \pm 0.92\%$ ID/g at one hour *p.i.*, when X = water, and $2.68 \pm 1.3\%$ ID/g at one hour *p.i.*, when X = P(CH₂OH)₃, in PC-3 tumor-bearing mice [133]. Furthermore, a series of $[^{99m}\text{Tc}(\text{CO})_3\text{-pz-X-BN(7-14)}]$ conjugates were developed, where BN(7-14) was conjugated via the amine terminal to the tridentate pyrazolyl-diamine (pz) chelator with spacers X (X = β -Ala, GGG, and SSS) (Figure 12.9). In PC-3 tumor-bearing mice, tumor uptake of $1.76 \pm 0.79\%$ ID/g and $1.76 \pm 1.20\%$ ID/g at one hour *p.i.* was obtained for SSS- and GGG-containing radioligands,

respectively [134]. Similarly, a series of [^{99m}Tc][$\text{Tc}(\text{CO})_3\text{-DTMA-(X)-BN(7-14)}$] $^+$ complexes were developed where BN(7-14) was conjugated to diethylenetriamine monoacetic acid (DTMA) chelator with the spacers X = β -Ala, GGG, and SSS. All radioligands exhibited high receptor binding affinity as well as high tumor cell uptake *in vitro*. [^{99m}Tc][$\text{Tc}(\text{CO})_3\text{-DTMA-(}\beta\text{-Ala)-BN(7-14)}$] $^+$ was further studied in PC-3 tumor-bearing mice, but low tumor uptake was observed ($0.95 \pm 0.15\%$ ID/g at one hour *p.i.*), probably due to fast elimination [135].

Also, [^{99m}Tc][TcO-DADT-BN]-type derivatives were developed, where BN was conjugated to hexamethyl (Hx) or pentamethyl (Pm) diaminedithiol chelator (DADT) with the pharmacokinetic modifier DTPA. The respective tracers [DTPA 1 , Lys 3 - ^{99m}Tc]Tc-Hx/Pm-DADT, Tyr 4]BN were developed, where the Pm-DADT analogue exhibited higher affinity for the GRPR ($K_i = 4.1 \pm 1.4$ nM) and lower hepatobiliary clearance (in normal mice) [136, 137].

In another approach, a series of BN derivatives were developed with the tetramine chelator 1,4,8,11-tetraazaundecane (Figure 12.9): Demobesin 1, N $_4$ -Bzdig 0 , [(D)Phe 6 , Leu-NHEt 13 , des-Met 14]BN(6-14); Demobesin 3, N $_4$ -[Pro 1 , Tyr 4]BN(1-14); Demobesin 4, N $_4$ -[Pro 1 , Tyr 4 , Nle 14]BN(1-14); Demobesin 5, N $_4$ -Bzdig-BN(7-14); and Demobesin 6, N $_4$ -Bzdig-[Nle 14]BN(7-14) [138, 139]. Their binding affinities were evaluated in PC-3 cells against [^{125}I][iodoTyr 4]BN, and the IC $_{50}$ values were found to be: Demobesin 1, 0.07 ± 0.08 nM; Demobesin 3, 0.06 ± 0.04 nM; Demobesin 4, 0.15 ± 0.04 nM; Demobesin 5, 0.08 ± 0.05 nM; and Demobesin 6, 0.60 ± 0.05 nM. The peptide conjugates were radiolabelled with ^{99m}Tc ; their stability study indicated that the radiotracers remained almost intact in murine plasma after one or two hours of incubation but were metabolized fast in the kidneys, and the radiometabolites were detected in urine. In PC-3 tumor-bearing mice, ^{99m}Tc -Demobesins 3 and 4 exhibited high tumor uptake (9–11% ID/g) at one hour *p.i.*, with high tumor retention (7–9% ID/g) at four hours *p.i.* In the first-in-human pilot study, ^{99m}Tc -Demobesin 4 did not detect metastatic prostate cancer; however, in newly diagnosed patients, local disease was visualized [140]. By a similar approach, neuromedin C was conjugated to the tetramine chelator (demomedin C), and then a series of demomedin C derivatives were developed: [Gly 24 /Met 27]demomedin C (SARNC1), [dAla 24 /Met 27]demomedin C (SARNC2), [dAla 24 /Nle 27]demomedin C (SARNC3), [dAla 24 /Leu 27]demomedin C (SARNC4), [β Ala 24 /Met 27]demomedin C (SARNC5), and [Sar 24 /Met 27]demomedin C (SARNC6). The binding affinity of Demomedin C was performed by *in vitro* receptor autoradiography competition binding assays against the universal radioligand [^{125}I][D-iodoTyr 6 , β Ala 11 , Phe 13 , Nle 14]BN(6-14) in human prostate cancer sections for GRPR, and the IC $_{50}$ value was found to be 1.4 ± 0.02 nM. The binding affinities of the demomedin C derivatives were determined by *in vitro* displacement of [^{125}I][iodo-Tyr 4]BN in PC-3 cell membranes [141], and the IC $_{50}$ values were 2.03 ± 1.06 nM for SARNC2, 2.96 ± 1.33 nM for SARNC3, 9.29 ± 3.55 nM for SARNC4, 0.28 ± 0.02 nM for SARNC5, and 1.78 ± 0.32 nM for SARNC6 [142]. The highest *in vivo* murine plasma stability was displayed by the tracer ^{99m}Tc -SARNC4, which was found to be >50% intact 5 minutes *p.i.* The tracer ^{99m}Tc -demomedin C localized in human PC-3 implants in mice and exhibited tumor uptake of $9.84 \pm 0.81\%$ ID/g at one hour *p.i.* [141]. From the demomedin C series, the highest tumor uptake was exhibited by ^{99m}Tc -SARNC2 with a value of $12.05 \pm 1.22\%$ ID/g at four hours *p.i.* [142].

[^{99m}Tc]Tc-HYNIC-BN derivatives were also developed (Figure 12.9). The tracer [^{99m}Tc]Tc-EDDA-HYNIC-[Lys³BN(1-14)] exhibited tumor uptake of 0.30% ID/g at two hours *p.i.* in tumor-bearing mice [143]. Also, [^{99m}Tc]Tc-[HYNIC-Aca-BN(7-14)]-tricine-TPPTS, where Aca is ϵ -amino-caproic acid, was developed and exhibited tumor uptake of $2.24 \pm 0.64\%$ ID/g after 30 minutes in PC-3 tumor-bearing mice. The latter was evaluated in human patients with established prostate cancer, but the agent failed to detect the tumors by SPECT imaging [144, 145]. Furthermore, the tracer [^{99m}Tc]Tc-[HYNIC-(Aca-BN(7-14))₂]-tricine-TPPTS, where HYNIC was conjugated to 2 Aca-BN(7-14) moieties, was developed, and exhibited comparable tumor targeting with the monomer in tumor-bearing animals [146].

12.8.2 Somatostatin Receptor Imaging Agents

The development of somatostatin receptor (**SSTR**) imaging agents has been shown to be useful in the diagnosis of SSTR-overexpressing tumors, such as neuroendocrine gastroentero-pancreatic tumors. Successful efforts were made to develop a ^{99m}Tc-based SSTR imaging agent by using the octapeptides octreotide, D-Phe-c(Cys-Phe-D-Trp-Lys-Thr-Cys)-Thr(ol), and octreotate, D-Phe-c(Cys-Phe-D-Trp-Lys-Thr-Cys)-Thr, known to have a high binding affinity for the SSTR type-2 receptor. The HYNIC ligand was conjugated to [Tyr]³-octreotide (**TOC**), and the respective [^{99m}Tc]Tc-HYNIC-TOC-tricine and [^{99m}Tc]Tc-EDDA-HYNIC-TOC tracers were developed. The tracer [^{99m}Tc]Tc-EDDA-HYNIC-TOC (Figure 12.10) exhibited the highest stability, its binding affinity in AR42J cell membranes was found to be $K_D = 2.6$ nM, and its tumor uptake in AR42J tumor-bearing mice was $9.65 \pm 2.16\%$ ID/g at four hours *p.i.* [147, 148]. [^{99m}Tc]Tc-EDDA-HYNIC-TOC underwent clinical evaluation and was licensed in Europe [149]. More recently, a dimeric octreotide analogue was developed, where the HYNIC chelator was conjugated to two TOC moieties, (HYNIC-TOC)₂, with a high affinity for SSTR2 ($IC_{50} = 0.74 \pm 0.19$ nM). This tracer, [^{99m}Tc]Tc-EDDA-HYNIC-TOC₂, exhibited high tumor uptake $13.31 \pm 3.14\%$ ID/g at one hour *p.i.*, although high kidney uptake was obtained ($94.40 \pm 6.51\%$ ID/g at one hour *p.i.*) [150].

A series of TOC and [Tyr]³-octreotate (**TATE**) derivatives were conjugated to the acyclic tetramine chelator for labeling with technetium-99m (Demotide/Demotate series). From this series, the tetraamine-functionalized TATE derivative [^{99m}Tc]Tc-[N₄⁰,Tyr³]octreotate, ^{99m}Tc-Demotate-1 (Figure 12.10) exhibited a high binding affinity in AR42J cell membranes ($K_D = 0.07$ nM) as well as high *in vivo* AR42J tumor uptake in mice at one hour *p.i.* (25% ID/g) with high tumor retention (20% ID/g) at four hours *p.i.* [151]. In a pilot study, ^{99m}Tc-Demotate-1 was investigated in humans where tumor imaging was obtained at one hour *p.i.*, making it a promising radiopharmaceutical [152].

Furthermore, [^{99m}Tc][Tc-N₄⁰⁻¹, Asp⁰, Tyr³]octreotate, ^{99m}Tc-Demotate-2, was developed by inserting one aspartate in the sequence, which exhibited a high binding affinity to somatostatin receptors ($IC_{50} = 3.2$ nM) in CA20948 sst2r-expressing tumors. The *in vivo* behavior of this radioligand in tumor-bearing rats was similar to the gold standard, [¹¹¹In][In-DTPA-octreotide] [153]. In the same series, [^{99m}Tc][Tc-N₄-X-TOC], ^{99m}Tc-Demotide, and [^{99m}Tc][Tc-N₄-X-TATE], ^{99m}Tc-Demotate-4 were developed, where X was the (*p*-[(carboxymethoxy)acetyl]aminobenzyl) moiety inserted between the tetramine

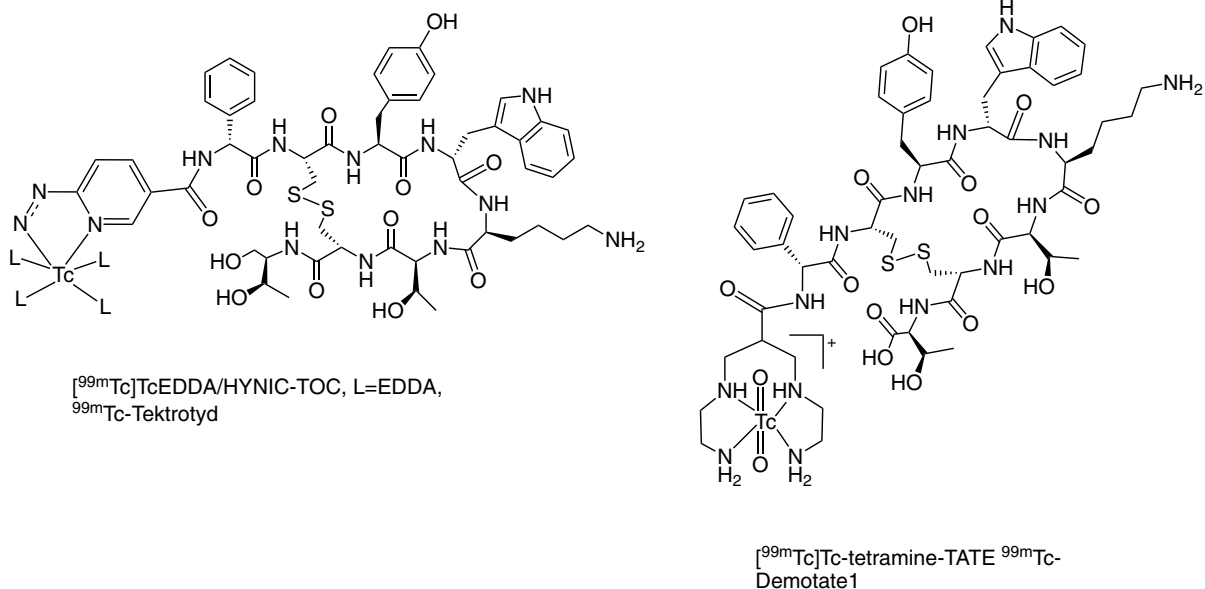


Figure 12.10 Structures of ^{99m}Tc -labelled SSTR2 imaging agents.

chelator and the *N*-terminus of the peptide. Their IC_{50} values in AR42J cells indicated a high binding affinity for SSTR2 receptors, 0.16 ± 0.05 nM and 0.10 ± 0.04 nM for ^{99m}Tc -Demotide and ^{99m}Tc -Demotate-4, respectively. These tracers also exhibited high tumor uptake in AR42J tumor-bearing mice of $27.87 \pm 2.07\%$ ID/g and $29.46 \pm 2.63\%$ ID/g at one hour *p.i.*, for ^{99m}Tc -Demotide and ^{99m}Tc -Demotate-4, respectively, although unfavorably high background activity was observed, especially in the abdomen [154].

In another approach, a series of ^{99m}Tc -cyclized-octreotide and octreotate derivatives were developed, where the oxometal (technetium-99m or rhenium) was coordinated via the two reduced sulfhydryl cysteine moieties and two additional donor atoms of the peptide sequence. The position of the additional coordinating sites greatly influenced the binding affinity as well as the *in vitro* stability. The best analogue in terms of binding affinity was the Re-cyclized-TATE with $\text{IC}_{50} = 29.2 \pm 6.2$ nM; however, the ^{99m}Tc -cyclized-TATE analogue had poor stability [155–157].

Additionally, some effort was made to develop somatostatin receptor antagonist peptides that exhibit different pharmacological properties compared to the agonists octreotide and octreotate, which may translate to different tumor uptake and retention. One such effort described the antagonist peptide 4- NO_2 -Phe-c(DCys-Tyr-DTrp-Lys-Thr-Cys)-DTyr-NH₂ (sst_2 -ANT) that was conjugated to a tridentate (N,S,N) chelator and labelled with $[^{99m}\text{Tc}][\text{Tc}(\text{CO})_3]^+$. The Re complex $\text{Re}(\text{CO})_3(\text{N,S,N-sst}_2\text{-ANT})$ exhibited good binding affinity in AR42J cells ($\text{IC}_{50} = 15 \pm 4$ nM), and the tracer $[^{99m}\text{Tc}]\text{Tc}(\text{CO})_3(\text{N,S,N-sst}_2\text{-ANT})$ successfully targeted SSTR-positive tumors via a receptor-mediated process in AR42J-tumor-bearing mice; however, low tumor uptake was obtained, probably due to unfavorable pharmacokinetics [158].

12.8.3 Prostate-Specific Membrane Antigen Imaging Agents

Prostate-specific membrane antigen (**PSMA**) is a homodimeric type II transmembrane metalloenzyme that functions as a glutamate carboxypeptidase and a folate hydrolase that is overexpressed in prostate cancer. The ^{99m}Tc -PSMA-targeted imaging agents that have been developed for the diagnosis of prostate cancer belong either to the class of ^{99m}Tc -labelled small-molecule inhibitors of the PSMA glutamate carboxypeptidase moiety with glutamate-urea-X sequences of varying X amino acids or to ^{99m}Tc -labelled immunoreactive antibody constructs with improved imaging characteristics for targeting PSMA, compared to the older radiopharmaceutical ^{99m}Tc -Prostascint.

Series of [^{99m}Tc][$\text{Tc}(\text{CO})_3(\text{L-linker-(X-urea-Glu)})$] chelates of the glutamate-urea-type inhibitors with glutamate, lysine, or cysteine as X were developed with various tridentate ligands [159–162]. In these conjugates, the linker length varied from none to 11-carbon. From the structure-activity relationship (SAR) studies that were performed, the nature of the chelate, as well as the length and composition of the linker, significantly influenced the *in vitro* binding affinity. The chelators that exhibited higher binding affinities were those that contained additional carboxylates, such as bis((1-(carboxymethyl)-1H-imidazol-2-yl)methyl)amino (**CIM**) and bis((1-(2-(bis(carboxymethyl)amino)-2-oxoethyl)-1H-imidazol-2-yl)methyl)amino (**TIM**), indicating that perhaps these carboxylates form additional interactions in the PSMA binding area. On the other hand, radioligands that contained the chelators DPA, di-(1-1H-methylimidazol-2-yl) methylamine or PAMA exhibited low binding affinity [160, 161]. Four of the [^{99m}Tc][$\text{Tc}(\text{CO})_3(\text{SAAC-linker-(X-urea-Glu)})$] conjugates developed, with SAAC-type ligands exhibiting higher binding affinities, were evaluated *in vitro* in PSMA and non-PSMA expressing cancer cell lines as well as *in vivo* in tumor-bearing animals, of which ^{99m}Tc -MIP-1404 and ^{99m}Tc -MIP-1405 (Figure 12.11) exhibited the most promising tumor uptake in LNCaP xenografts of 11.1 ± 4.1 and $8.65 \pm 1.88\%$ ID/g at four hours *p.i.*, respectively. Their binding affinities (K_D) on LNCaP cells were calculated to be 1.07 ± 0.89 nM and 4.35 ± 0.35 nM for ^{99m}Tc -MIP-1404 and ^{99m}Tc -MIP-1405, respectively [163]. A first-in-human study in prostate cancer patients was performed for ^{99m}Tc -MIP-1404 and ^{99m}Tc -MIP-1405, and both agents facilitated the detection of radiologically proven prostate cancer in bone, lymph nodes, and the prostate gland by PSMA targeting; however, ^{99m}Tc -MIP-1404 exhibited lower uptake in the kidney, which makes it more promising for the detection of early stages of the disease in the prostate gland and the pelvis [164]. In a phase II study, ^{99m}Tc -MIP-1404 (^{99m}Tc -trofolostat) demonstrated its ability to detect primary prostate cancer (in patients prior to prostatectomy) with high accuracy (94% detection rates) by SPECT/CT [165]. In another clinical study in patients with biochemical recurrence of prostate cancer, overall, a 70% detection rate was obtained [166]. Currently, a phase III study is underway for this agent.

Additionally, [^{99m}Tc][$\text{TcO}(\text{N}_2\text{S}_2$ or $\text{N}_3\text{S})$] and [^{99m}Tc][$\text{Tc}(\text{HYNIC})(\text{tricine})$] probes conjugated to a Glu-urea-Lys moiety were developed with a high affinity for PSMA and the ability to visualize the tumor in PC3-PIP(PSMA+)-bearing mice with SPECT/CT imaging [167]. In the HYNIC approach, also, the inhibitor glutamate-urea-lysine- β -naphthylalanine-HYNIC

(iPSMA) was developed. The tracer $[^{99m}\text{Tc}]\text{Tc-EDDA-HYNIC-iPSMA}$ (Figure 12.11) exhibited high tumor uptake in LNCaP-tumor-bearing mice of $9.84 \pm 2.63\%$ ID/g at three hours *p.i.*. Preliminary images in patients demonstrated the ability of this probe to detect tumors and metastases of prostate cancer [168]. The ligand glutamate-urea-lysine-6-aminohexanoic acid -HYNIC (HYNIC-ALUG) was developed, and the tracer $[^{99m}\text{Tc}]\text{Tc-EDDA-HYNIC-ALUG}$ (Figure 12.11) demonstrated high tumor uptake in PSMA-positive LNCaP xenografts as early as one hour, peaking at two hours *p.i.* ($19.45 \pm 2.14\%$ ID/g) [169].

The monoclonal antibody J591, which binds to an extracellular antigen of PSMA, is being evaluated for the development of radiopharmaceuticals in combination with suitable radionuclides. A diabody derived from J591 bearing a His-tag (J591Cdia) was developed, and it was efficiently labelled with $[^{99m}\text{Tc}][\text{Tc}(\text{CO})_3]$. It was shown that the diabody J591C exhibited a high affinity for PSMA of $\text{IC}_{50} = 3.4 \text{ nM}$ in PSMA-expressing cells; and furthermore, it exhibited $12.1 \pm 1.7\%$ ID/g tumor uptake in mice bearing DU145-(+PSMA) tumors at eight hours *p.i.* [170]. This concept shows promise and has been more recently extended to the development of a J591(scFv) bearing a His-tag for the same purpose [171].

12.8.4 ^{99m}Tc -cyclic-RGD $\alpha_v\beta_3$ Integrin Receptor Imaging Agents

The Arginine-Glycine-Aspartate sequence selectively binds to integrins. In particular, radiolabelled cyclic RGD peptides have been developed as angiogenesis and tumor imaging agents via targeting of the $\alpha_v\beta_3$ integrin receptors. A cyclic RGD peptide was designed with two disulfide bridges, was conjugated to the HYNIC ligand (Cys¹-Cys⁹, Cys³-Cys⁷)HYNIC-HN-Cys-Asp-Cys-Arg-Gly-Asp-Cys-Phe-Cys-COOH (HYNIC-RGD-4C), and was labelled with technetium-99m. The tracers $[^{99m}\text{Tc}]\text{Tc-Tricine}$ -(HYNIC-RGD-4C) [172] and $[^{99m}\text{Tc}]\text{Tc-EDDA}$ -(HYNIC-RGD-4C) [173] were evaluated *in vitro* in human umbilical vein endothelial cells where $[^{99m}\text{Tc}]\text{Tc-EDDA}$ -(HYNIC-RGD-4C) exhibited higher cell accumulation and lower protein binding. The *in vivo* tumor uptake of

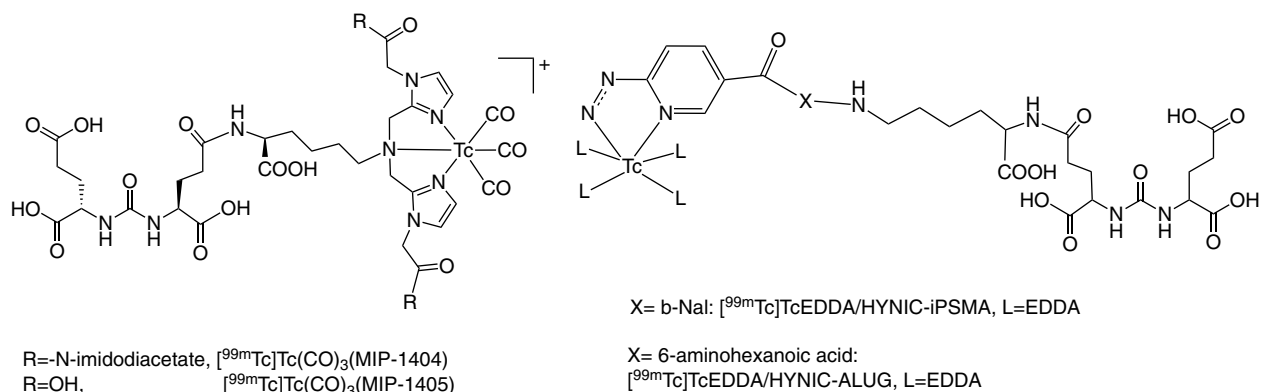


Figure 12.11 Structures of ^{99m}Tc -labelled PSMA imaging agents.

[^{99m}Tc]Tc-Tricine-(HYNIC-RGD-4C) in LS174T and ACHN tumor-bearing mice was 0.75 ± 0.05 and $0.59 \pm 0.10\%$ ID/g at six hours *p.i.*, respectively [172].

Another cyclic RGD tracer, [^{99m}Tc]Tc- (Cys¹-Cys⁹, Cys³-Cys⁷)H₂N-Cys-Asp-Cys-Arg-Gly-Asp-Cys-Lys-Cys-COOH, was developed and used for the imaging of bronchioloalveolar carcinoma in mice [174].

A series of [^{99m}Tc]Tc-HYNIC tracers conjugated to cyclo[Arg-Gly-Asp-D-Phe-Lys] (c[RGDFK]) were developed. The monomeric and the dimeric derivatives (cyclo[Arg-Gly-Asp-D-Phe-(Lys-HYNIC)] (HYNIC-c(RGDFK)) and HYNIC-Glu(cyclo[Lys-Arg-Gly-Asp-D-Phe])-cyclo[Lys-Arg-Gly-Asp-D-Phe] (HYNIC-E[c(RGDFK)]₂) and the respective ^{99m}Tc tracers [^{99m}Tc]Tc-Tricine-TPPTS-(HYNIC-c(RGDFK)) and [^{99m}Tc]Tc-Tricine-TPPTS-(HYNIC-E[c(RGDFK)]₂) were synthesized [175]. The binding affinity of the monomer and the dimer HYNIC ligands to human placental $\alpha_v\beta_3$ integrin was found to be (IC₅₀) 1.0 nM and 0.1 nM, respectively, against biotinylated vitronectin. The tumor uptake of the ^{99m}Tc-dimer tracer in OVAR-3-tumor-bearing mice peaked at $5.8 \pm 0.7\%$ ID/g at one hour *p.i.*, while the tumor uptake of the ^{99m}Tc-monomer tracer peaked at $5.2 \pm 0.6\%$ ID/g at 30 minutes *p.i.* [176]. Also, the cRGD tetramer [^{99m}Tc]Tc-Tricine-TPPTS-(HYNIC-E{E[c(RGDFK)]₂})₂ was developed. The binding affinity of HYNIC-E{E[c(RGDFK)]₂}₂ in MDA-MB-435 human breast cancer cell line, in a competition study against ¹²⁵I-echistatin, was found to be IC₅₀ = 55 ± 11 nM. The tumor uptake of the tetramer tracer [^{99m}Tc]Tc-Tricine-TPPTS-(HYNIC-E{E[c(RGDFK)]₂})₂ was 5.60 ± 0.87 and $7.30 \pm 1.32\%$ ID/g at 5 and 120 minutes *p.i.*, respectively, in MDA-MB-435-tumor-bearing mice [177]. Furthermore, new cyclic RGD peptide dimers conjugated to triglycine (G₃) and polyethyleneglycol (PEG₄) linkers were developed in an effort to increase the distance between two RGD motifs and improve the radiotracers excretion kinetics. The G₃ conjugates HYNIC-E[G₃-c(RGDFK)]₂ and HYNIC-G₃-E[G₃-c(RGDFK)]₂ exhibited binding affinities (IC₅₀) of 60.3 ± 4.4 and 61.1 ± 2.1 nM in U87 MG glioma cells against ¹²⁵I-echistatin. The analogous ^{99m}Tc tracers exhibited high tumor uptake in MDA-MB-435-tumor-bearing mice of 8.48 ± 0.59 and $9.11 \pm 1.83\%$ ID/g for [^{99m}Tc]Tc-Tricine-TPPTS-(HYNIC-E[G₃-c(RGDFK)]₂) and of 8.34 ± 0.39 and $7.60 \pm 0.68\%$ ID/g for [^{99m}Tc]Tc-Tricine-TPPTS-(HYNIC-G₃-E[G₃-c(RGDFK)]₂) (Figure 12.12) at 30 minutes and 120 minutes *p.i.*, respectively. From this study, it was concluded that the G₃ linkers are useful for increasing integrin $\alpha_v\beta_3$ binding affinity of cRGD dimers and improving the tumor uptake and clearance kinetic of their ^{99m}Tc radiotracers [178]. Analogously, the pegylated conjugates HYNIC-E[PEG₄-c(RGDFK)]₂ and HYNIC-PEG₄-E[PEG₄-c(RGDFK)]₂, where PEG₄ was 15-amino-4,7,10,13-tetraoxa-pentadecanoic acid, were developed. The ligands exhibited binding affinities (IC₅₀) of 2.9 ± 0.7 and 2.4 ± 0.7 nM in U87 MG glioma cells against ¹²⁵I-c(RGDYK), respectively. The analogous ^{99m}Tc tracers exhibited high tumor uptake in U87-MG-glioma-bearing mice of 11.17 ± 1.96 and $8.31 \pm 2.31\%$ ID/g for [^{99m}Tc]Tc-Tricine-TPPTS-(HYNIC-E[PEG₄-c(RGDFK)]₂) and 8.17 ± 0.68 and $9.74 \pm 3.22\%$ ID/g for [^{99m}Tc]Tc-Tricine-TPPTS-(HYNIC-PEG₄-E[PEG₄-c(RGDFK)]₂) (Figure 12.12) at 30 minutes and 120 minutes *p.i.*, respectively [179]. The agent [^{99m}Tc]Tc-Tricine-TPPTS(HYNIC-PEG₄-E[PEG₄-c(RGDFK)]₂) has since undergone a series of clinical trials and was evaluated as a potentially useful agent to diagnose rheumatoid arthritis [180], lung cancer [181], non-small-cell lung cancer and lymph node metastases [182], osteolytic bone metastases [183], and refractory

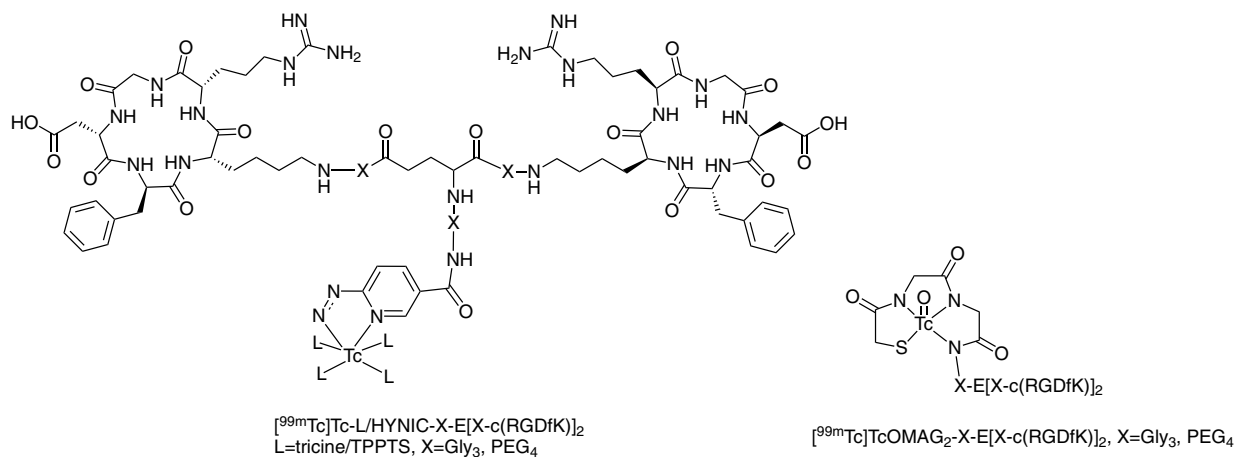


Figure 12.12 Structures of ^{99m}Tc -labelled cRGD imaging agents.

thyroid cancer [184]. Furthermore, the galactosylated dimer (HYNIC-Galacto-RGD₂) developed via “click” conjugation exhibited a high binding affinity (IC_{50}) of 20 ± 2 nM in U87 MG glioma cells against ^{125}I -echistatin. The radiotracer [^{99m}Tc]Tc- tricine-TPPTS-(HYNIC-Galacto-RGD₂) exhibited a high uptake of $8.37 \pm 2.13\%$ ID/g at 30 minutes *p.i.* in athymic nude mice bearing U87 MG gliomas, with advantages from the previous tracers in the imaging of the chest and abdominal regions [185].

The influence of the linker (glutamic acid vs. iminodiacetic acid) was evaluated in the tracer [^{99m}Tc]Tc-Tricine-TPPTS-(HYNIC-I-E[PEG₄-c(RGDfK)]₂) (I = iminodiacetate), whose tumor uptake was found to be similar to that of the tracer with a glutamic linker [^{99m}Tc]Tc-Tricine-TPPTS-(HYNIC-PEG₄-E[PEG₄-c(RGDfK)]₂) and demonstrated advantages in the abdominal area [186].

The influence of the chelator was also evaluated by developing a MAG₂ (mercaptoacetyl diglycine) chelator of the formula MAG₂-G₃-E[G₃-c(RGDfK)]₂. The ligand exhibited a binding affinity (IC_{50}) of 3.6 ± 0.6 nM in U87 MG glioma cells against ^{125}I -c(RGDyK). [^{99m}Tc]TcO(MAG₂-G₃-E[G₃-c(RGDfK)]₂) (Figure 12.12) had a high initial tumor uptake of $12.63 \pm 2.88\%$ ID/g at 30 minutes *p.i.*, with fast tumor washout of $4.70 \pm 1.15\%$ ID/g at 120 minutes *p.i.* in U87 MG-glioma-bearing mice. Due to the fast renal clearance, the tumor-to-kidney ratio increased over time to 2.49 ± 0.25 at two hours *p.i.* [187]. Similarly, the ligands MAG₂-PEG₄-E[c(RGDfK)]₂ and MAG₂-PEG₄-E[PEG₄-c(RGDfK)]₂ were developed, with a binding affinity (IC_{50}) of 8.6 ± 2.8 , 3.9 ± 0.4 nM in U87 MG glioma cells against ^{125}I -c(RGDyK). The tumor uptake of the respective tracers [^{99m}Tc]TcO(MAG₂-PEG₄-E[c(RGDfK)]₂) and [^{99m}Tc]TcO(MAG₂-PEG₄-E[PEG₄-c(RGDfK)]₂) (Figure 12.12) was found to be 11.95 ± 1.90 and $15.36 \pm 2.17\%$ ID/g at one hour *p.i.* in U87 MG-glioma-bearing mice. However, despite the high tumor uptake of the complexes, the target to nontarget ratios were lower compared to the respective highly charged HYNIC tracers, perhaps owing to the higher lipophilicity of the MAG₂ tracers [188]. The dimer HYNIC-G₃-E[PEG₄-c(RGDfK)]₂ and its tracer [^{99m}Tc]Tc-Tricine-TPPTS-(HYNIC-G₃-E[PEG₄-c(RGDfK)]₂) were developed.

The ligand HYNIC-G₃-E[PEG₄-c(RGDfK)]₂ exhibited a binding affinity (IC₅₀) of 3.37 ± 0.84 nM in U87 MG glioma cells against ¹²⁵I-c(RGDyK). The uptake of [^{99m}Tc]Tc-Tricine-TPPTS-(HYNIC-G₃-E[PEG₄-c(RGDfK)]₂) was 7.94 ± 1.74% ID/g at 0.5 hour *p.i.* in U87MG-glioma-bearing mice [189]. Also, the HYNIC ligand was combined with nicotinic acid to form the chelator HYNIC-K(NIC), which was conjugated to E[c(RGDyK)]₂, PEG₄-E[PEG₄-c(RGDfK)]₂ and G₃-E[G₃-c(RGDfK)]₂ via lysine. The conjugates were labelled with ^{99m}Tc to the respective tracers [^{99m}Tc]Tc-Tricine-(HYNIC-K(NIC)-E[c(RGDyK)]), [^{99m}Tc]Tc-Tricine-(HYNIC-K(NIC)-PEG₄-E[PEG₄-c(RGDfK)]₂), and [^{99m}Tc]Tc-Tricine-(HYNIC-K(NIC)-G₃-E[G₃-c(RGDfK)]₂), which exhibited similar tumor uptake of 5.73 ± 0.40, 5.24 ± 1.09, and 4.94 ± 1.71% ID/g at 60 minutes *p.i.* in MDA-MB-435-tumor-bearing mice. Reduced kidney and lung uptake were observed in these tracers compared to the [^{99m}Tc]Tc-Tricine-TPPTS-HYNIC analogue, although conformational isomers were formed with the chelator HYNIC-K(NIC) [190]. Similarly, the K(HYNIC)₂ chelator was used in combination with the dimeric RGD analogues as mentioned previously; and while the tumor uptake of [^{99m}Tc]Tc-Tricine-(K(HYNIC)₂-X-E[X-c(RGDfK)]₂) (where X = none or 3G or PEG₄) was maintained, reduced kidney, lung, and spleen uptake were obtained [191]. Modifications of RGD-HYNIC by the introduction of negative charge from six aspartate moieties [192] as well as the development of a trimer RGD tracer [193] did not improve the imaging properties of the respective tracers in comparison to the previously developed ones.

A similar cyclic RGD conjugated to HYNIC was developed, cyclo[Arg-Gly-Asp-d-Tyr-(Lys-HYNIC)] (HYNIC-c(RGDyK)), as well as the respective tracers [^{99m}Tc]Tc-EDDA-(HYNIC-c(RGDyK)), [^{99m}Tc]Tc-Tricine-(HYNIC-c(RGDyK)), [^{99m}Tc]Tc-Tricine-Nic-(HYNIC-c(RGDyK)) (Nic: nicotinic acid), [^{99m}Tc]Tc-Tricine-TPPTS-(HYNIC-c(RGDyK)), and [^{99m}Tc]Tc(CO)₃(HYNIC-c(RGDyK)) [194]. Of these tracers, [^{99m}Tc]Tc-EDDA-(HYNIC-c(RGDyK)) exhibited the lowest protein binding as well as higher cell uptake. The IC₅₀ of HYNIC-c(RGDyK) for the α_vβ₃ integrin receptors was measured to be 6.0 nM against ¹²⁵I-echistatin. Tumor uptake in nude mice bearing either the human melanoma M21 α_vβ₃-expressing cell line or a human non-small-cell lung carcinoma cell line A549 was found to be 2.73 ± 0.26 and 1.54 ± 0.28% ID/g at one hour *p.i.*, respectively. The effect of the ^{99m}Tc-chelate was evaluated, and c(RGDyK) was conjugated to different chelators: pyrazolyldiamine (pz-c(RGDyK)), isocyanide (CN-c(RGDyK)), and cysteine (Cys-c(RGDyK)). The respective tracers were prepared: [^{99m}Tc][Tc(CO)₃(pz-c(RGDyK))], the "4 + 1" tracer [^{99m}Tc][Tc(N₃S-COOH)(CN-c(RGDyK))], and the nitrido tracer [^{99m}Tc][TcN(PNP)(Cys-c(RGDyK))]. Of these tracers, the previously mentioned [^{99m}Tc]Tc-EDDA-HYNIC-c(RGDyK) exhibited the best biological and pharmacokinetic properties [195]. Also, the ligands [Arg-Gly-Asp-DPhe-Lys(Nε)-His] and [Arg-Gly-Asp-DPhe-Lys(Nε)-CPA] (CPA = cysteine-propionate) were synthesized and radiolabelled with [^{99m}Tc][Tc(H₂O)₃(CO)₃]⁺. The tracers were administered in MDA-MB 435 tumor-bearing mice, where the tumor uptake was found to be 2.8 ± 1.5% ID/g for [^{99m}Tc]Tc-His-cRGDFK and 4.2 ± 1.5% ID/g for [^{99m}Tc]Tc-CPA-cRGDFK at 30 minutes *p.i.* [196, 197]. The tracer [^{99m}Tc][Tc(CO)₃-cyclo-[Arg-Gly-Asp-DTyr-Lys(PZ)]]⁺ was developed with a tridentate dimethyl-pyrazolyl diamine ligand (PZ) carrying the RGD sequence (IC₅₀ = 3 nM), and the complex was administered in M21 melanoma tumor-bearing mice, where the tumor uptake was found to be 2.50 ± 0.29% ID/g at 1 h *p.i.* [198]. Also, c(RGDfK)-(Orn)₃-CGG was

developed, containing three ornithine moieties and the cysteine diglycine (CGG) tripeptide for ^{99m}Tc -labeling [199]. The tracer was evaluated in mice bearing U87MG glioma cells at different days after inoculation of the tumor cells, where maximum uptake was observed at day 21 with tumor uptake of $11.6 \pm 2.1\%$ ID/g at one hour *p.i.* [200].

Another RGD peptide named NC100692 was developed and conjugated to the chelator propylene aminoxime [201]. The ligand NC100692 exhibited $K_D < 1.1 \text{ nmol l}^{-1}$ in isolated $\alpha_v\beta_3$ integrins from human placenta. The tracer ^{99m}Tc -NC100692 was evaluated in breast cancer patients, which detected 86% of the lesions [202]. Also, the ligand IDA-glucosamino-Dc(RGDfK) was used to prepare the tracer $^{99m}\text{Tc}[\text{Tc}(\text{CO})_3(\text{IDA-glucosamino-Dc(RGDfK)})]$, which exhibited a high binding affinity to $\alpha_v\beta_3$ integrins with IC_{50} of 1.5 nM against non-radiolabelled cRGDyV; tumor uptake was $1.03 \pm 0.21\%$ ID/g at one hour *p.i.* in mice bearing RR1022 fibrosarcoma [203]. This tracer was evaluated in monitoring response to paclitaxel therapy in tumor-bearing mice [204]. A cRGD tetramer RAFT-(cyclo[RGDfK])₄ (RAFT-RGD: regioselectivity addressable functionalised template-RGD) was conjugated to histidine and radiolabelled with $^{99m}\text{Tc}[\text{Tc}(\text{H}_2\text{O})_3(\text{CO})_3]^+$. Biodistribution of ^{99m}Tc -RAFT-RGD in tumor-bearing mice showed tumor-specific uptake of $2.4 \pm 0.5\%$ ID/g in B16F0 and in $2.7 \pm 0.8\%$ ID/g TS/A-pc tumors at one hour *p.i.* [205].

12.8.5 Melanocortin 1 Receptor Imaging Agents

It is known that the melanocortin 1 receptor (**MC1R**) is overexpressed in most human and murine melanomas, and it is considered a suitable target for the development of melanoma imaging agents. The ^{99m}Tc -based probes for MC1R targeting are peptide analogues of the tridecapeptide, α -melanocyte stimulating hormone (α -MSH) with the following sequence [Ac-Ser-Tyr-Ser-Met-Glu-His-Phe-Arg-Trp-Gly-Lys-Pro-Val-NH₂]. The required α -MSH sequence for receptor targeting is His-Phe-Arg-Trp.

One of the earlier efforts described a peptide analogue modified with three cysteines at positions 3,4 and 10 of the sequence (Cys^{3,4,10}, D-Phe⁷)- α -MSH₃₋₁₃ (CCMSH), which, after labeling with technetium-99m via glucoheptonate transchelation, formed a metal-cyclized peptide ^{99m}Tc -CCMSH, where ^{99m}Tc oxotechnetium was coordinated via the three cysteine thiols and one amide nitrogen. The tracer ^{99m}Tc -CCMSH was found to be resistant to chemical and proteolytic degradation and had a high binding affinity for MC1R [206]. The tumor uptake of ^{99m}Tc -CCMSH in murine-melanoma (B16/F1)-bearing mice and human-melanoma (TXM-13JQ)-bearing mice was 11.32 ± 3.25 and $2.39 \pm 0.42\%$ ID/g at four hours *p.i.*, respectively, with tumor-to-blood ratios of 39.0 and 11.5 after co-administration of lysine [207]. In the modified tracer ^{99m}Tc -CCMSH (Figure 12.13), where lysine-11 was replaced by arginine, a similar tumor uptake of $11.16 \pm 1.77\%$ ID/g at four hours *p.i.* was obtained in B16/F1-melanoma-bearing mice, but with an improved renal profile, where the kidney uptake was 11 ± 1.44 at one hour *p.i.* (it was $19.71 \pm 1.18\%$ ID/g for ^{99m}Tc -CCMSH) [208, 209]. Additional modifications led to the tracer ^{99m}Tc -RGD-Lys-(Arg¹¹)CCMSH, where the RGD motif {cyclic(Arg-Gly-Asp-DTyr-Asp)} was conjugated to CCMSH via a lysine linker. The modified peptide RGD-Lys-(Arg¹¹)CCMSH displayed binding affinities to both MC1 and $\alpha_v\beta_3$ integrin receptors, with IC_{50} values

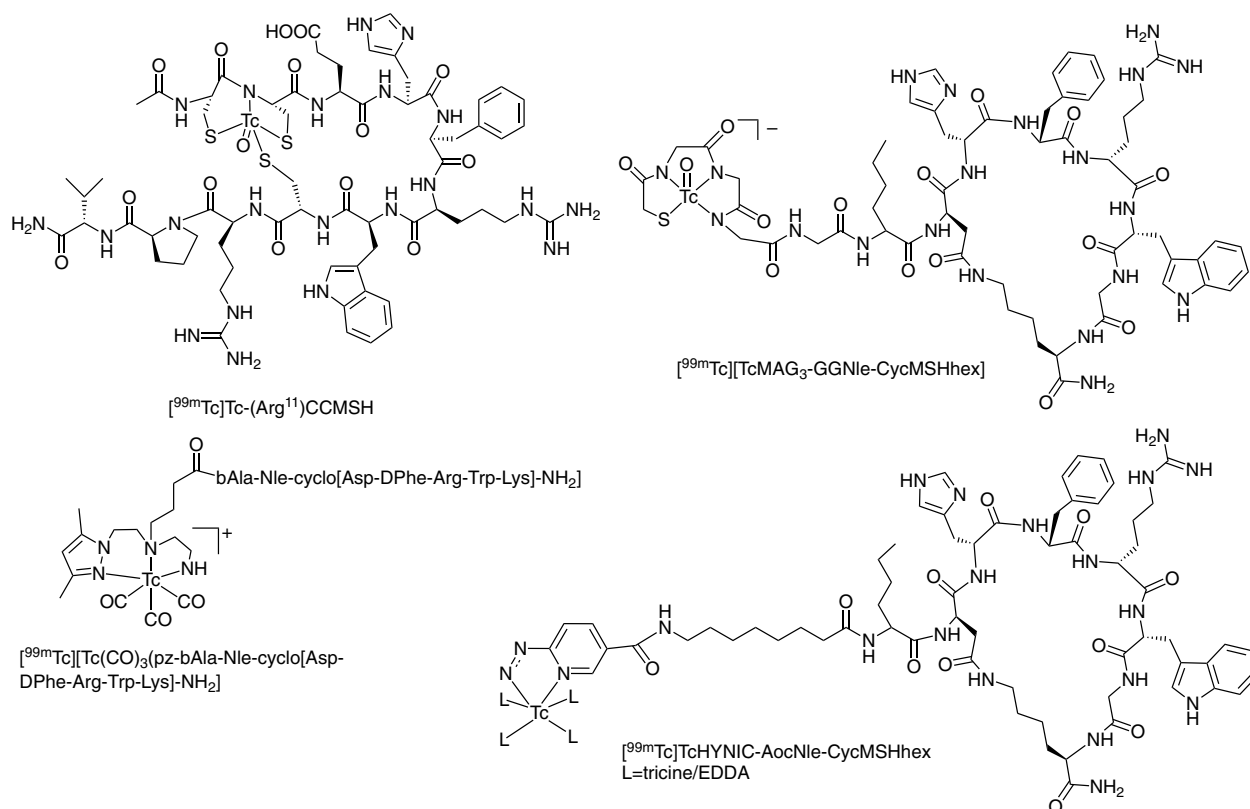


Figure 12.13 Structures of ^{99m}Tc -labelled αMSH imaging agents.

of 2.0 nM and 403 nM, respectively [210]. The tracer $[^{99m}\text{Tc}]\text{Tc-RGD-Lys}-(\text{Arg}^{11})\text{CCMSH}$ exhibited high tumor uptake of $14.83 \pm 2.94\%$ ID/g at two hours *p.i.* and prolonged tumor retention of $7.59 \pm 2.04\%$ ID/g at 24 hours *p.i.* in B16/F1-melanoma-bearing mice [211]. Replacement of the Lys linker with Arg, Gly, or β -Ala reduced kidney uptake [212–214], and replacement of Gly in the RGD sequence with various amino acids was found to improve tumor uptake as well [215–217].

In another approach, a lactam-cyclized α -MSH derivative was developed, cyclized via lysine-aspartate. This lactam-cyclic- α -MSH peptide was conjugated to the pyrazolyl diamine tridentate chelator (pz) and labelled to form the tracer $[^{99m}\text{Tc}]\text{Tc}(\text{CO})_3\text{-pz-}\beta\text{Ala-Nle-cyclo}[\text{Asp-His-DPhe-Arg-Trp-Lys}]\text{-NH}_2$ (Figure 12.13). This tracer exhibited high tumor uptake and retention of 9.26 ± 0.83 and $11.31 \pm 1.83\%$ ID/g at one and four hours *p.i.*, respectively. Unfortunately, high renal and liver uptake were also observed, of 32.12 ± 1.57 and $22.86 \pm 1.17\%$ ID/g at four hours *p.i.*, respectively [218]. The lactam-cyclized short hexapeptide $\text{c}[\text{Asp-His-DPhe-Arg-Trp-Lys}]\text{-CONH}_2$, $\text{CycMSH}_{\text{hex}}$ was conjugated to various chelators suitable for ^{99m}Tc -labelling: MAG_3 , Ac-Cys-Gly-Gly , and HYNIC. The IC_{50} values of the peptides $\text{MAG}_3\text{-GGNle-CycMSH}_{\text{hex}}$, $\text{AcCG}_3\text{-GGNle-CycMSH}_{\text{hex}}$, and $\text{HYNIC-GGNle-CycMSH}_{\text{hex}}$ were 1.0 ± 0.05 , 1.2 ± 0.19 , and 0.6 ± 0.04 nM,

respectively, in B16/F1 melanoma cells. The respective ^{99m}Tc -tracers ^{99m}Tc -MAG₃-GGNle-CycMSH_{hex} (Figure 12.13), ^{99m}Tc -AcCG₃-GGNle-CycMSH_{hex}, ^{99m}Tc -Tc(CO)₃-HYNIC-GGNle-CycMSH_{hex}, and ^{99m}Tc -EDDA-HYNIC-GGNle-CycMSH_{hex} were evaluated in B16/F10 melanoma-bearing mice. The tracer ^{99m}Tc -EDDA-HYNIC-GGNle-CycMSH_{hex} exhibited the highest tumor uptake of $14.14 \pm 4.90\%$ ID/g and the fastest urinary clearance of $91.26 \pm 1.96\%$ ID at two hours *p.i.* [219]. In addition, the insertion of 8-aminooctanoic acid linker (Aoc) between HYNIC and the peptide sequence improved the tumor uptake and pharmacokinetics of ^{99m}Tc -EDDA-HYNIC-AocNle-CycMSH_{hex} (Figure 12.13), which displayed melanoma uptake of $22.3 \pm 1.72\%$ ID/g at two hours *p.i.* and tumor-to-kidney ratios of 3.29, 3.63, and 6.78 at 2, 4, and 24 hours, respectively [220]. It also exhibited improved melanoma uptake in human-melanoma-bearing mice, and it detected melanoma lung metastases in B16/F10 melanoma-bearing mice by SPECT/CT [221, 222].

The linear α -MSH analogue [Ac-Nle-Asp-His-D-Phe-Arg-Trp-Gly-Lys-NH₂] was conjugated to suitable tridentate chelators via the N-terminus or ϵ -Lys of the peptide [218, 223–225]. The respective ^{99m}Tc [Tc(CO)₃]⁺ tracers exhibited lower tumor uptake values compared to the cyclized analogues; however, the tracer ^{99m}Tc [Ac-Nle⁴, Asp⁵, D-Phe⁷, Lys¹¹(pz-Tc(CO)₃)] α -MSH₄₋₁₁, with the chelator conjugated via the ϵ -Lys, exhibited the highest values among them with tumor uptake of 5.88 ± 2.11 and $4.24 \pm 0.94\%$ ID/g at one and four hours *p.i.*, respectively [223].

12.8.6 Neurotensin Receptor Imaging Agents

Neurotensin (NT) (pGlu-Leu-Tyr-Glu-Asn-Lys-Pro-Arg-Arg-Pro-Tyr-Ile-Leu) tridecapeptide and its derivatives have been used in the development of ^{99m}Tc -tracers for imaging of NT receptors that are overexpressed in tumors, such as pancreatic, lung, and colon carcinomas. Many efforts have focused on the development of NT derivatives with improved metabolic stability since the original peptide and its fragments are metabolized quickly *in vivo*. The following derivatives have been selected among those that were developed, based on their improved properties and contain the NT(8-13) sequence Arg⁸-Arg⁹-Pro¹⁰-Tyr¹¹-Ile¹²-Leu¹³:

NT-II: ^{99m}Tc [Tc(CO)₃]⁺-(N α -His-Ac)-Arg-Arg-Pro-Tyr-Ile-Leu [226]

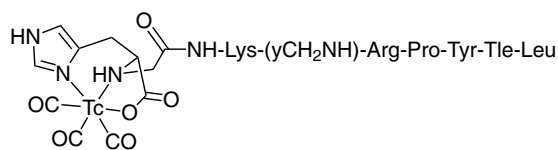
NT-XI: ^{99m}Tc [Tc(CO)₃]⁺-(N α -His-Ac)-Lys- ψ (CH₂NH)-Arg-Pro-Tyr-Tle-Leu [227] (Figure 12.14)

NT-XII: ^{99m}Tc [Tc(CO)₃]⁺-(N α -His-Ac)-Arg-NMeArg-Pro-Tyr-Tle-Leu [228]

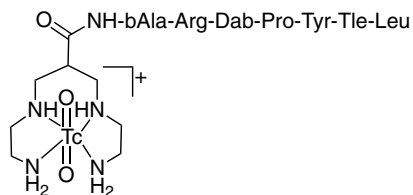
NT-XVIII: ^{99m}Tc [Tc(CO)₃]⁺-(N α -His-Ac)-Lys(shikimic)-Arg-NMeArg-Pro-Tyr-Tle-Leu [229]

NT-XIX: ^{99m}Tc [Tc(CO)₃]⁺-(N α -His-Ac)-Arg-NMeArg-Pro-Dmt-Tle-Leu [229]

In these ^{99m}Tc [Tc(CO)₃]⁺-tracers, the peptide was conjugated to the N α -histidinyl acetate chelator (N α -His-Ac). Modifications in the original sequence include (i) replacement of Arg⁸ with Lys and a reduction of the peptide bond to CH₂NH between the positions 8 and 9 (NT-XI) and (ii) replacement of isoleucine (Ile) by tert-leucine (Tle) at position 12 (NT-XI, NT-XII, NT-XVIII, NT-XIX). NT-XII was stabilized further by methylation of the bond between Arg at positions 8 and 9. In NT-XVIII, the shikimic acid



$[^{99m}\text{Tc}][\text{Tc}(\text{CO})_3(\text{NT-XI})]$,



^{99m}Tc -Demotensin6

Figure 12.14 Structures of ^{99m}Tc -labelled neurotensin imaging agents.

(3,4,5-trihydroxy-1-cyclohexene-1-carboxylic acid) was introduced to obtain a more hydrophilic peptide; and in NT-XIX, Tyr-11 was replaced by 2,6-dimethyltyrosine (Dmt). All the NT derivatives exhibited high binding affinities in human colon adenocarcinoma cell line HT-29, and the dissociation constants (K_D) were calculated to be: NT-II, 0.3 ± 0.2 nM; NT-XI, 0.5 ± 0.3 nM; NT-XII: 2.0 ± 1.6 nM; [NT-XVIII], 4.5 ± 1.7 nM; and NT-XIX: 15.0 ± 6.0 nM. The metabolic stability of the NT derivatives in human plasma at low concentrations (in the nanomolar ranges) showed that NT-II had a biologic $T_{1/2}$ of a few minutes, NT-XI and NT-XII of approximately 21 hours, and NT-XVIII and NT-XIX had very little degradation in 24 hours, respectively. The tumor uptake of NT-II of NT-XII NT-XIX was 0.4 ± 0.1 , 4.6 ± 1.2 , and $5.2 \pm 0.5\%$ ID/g at five hours *p.i.* in HT-29 tumor-bearing mice. The uptake of NT-XI and NT-XVIII was approximately 1.7 and $<1\%$ ID/g at the same time point, respectively. The derivative NT-XIX appears to have a better metabolic profile in conjunction with its reduced kidney uptake. Human studies of NT-XI exhibited the ability of the NT derivative to detect NT-expressing tumors [230].

In another approach, NT derivatives were conjugated to the acyclic tetramine chelator for $[^{99m}\text{Tc}]$ dioxotechnetium labelling. The analogues that were developed were the following:

Demotensin 1: N_4 -Gly-Arg-Arg-Pro-Tyr-Ile-Leu-OH [231]

Demotensin 2: N_4 -Gly-Lys ψ [CH_2NH]Arg-Pro-Tyr-Ile-Leu-OH, [231]

Demotensin 3: N_4 -Gly-Lys ψ [CH_2NH]Arg-Pro-Tyr-Tle-Leu-OH [231]

Demotensin 4: N_4 -Gly-Arg ψ [CH_2NH]Arg-Pro-Tyr-Tle-Leu-OH [231]

Demotensin 5: N_4 -(β)Ala-Arg-Dab-Pro-Tyr-Ile-Leu-OH [232]

Demotensin 6: N_4 -(β)Ala-Arg-Dab-Pro-Tyr-Tle-Leu-OH [232]

In these derivatives, similar modifications were made to improve their metabolic stability, such as the reduction of the Arg-Arg bond in Demotensin 4 and its replacement with lysine in Demotensin 2 and 3. Also, the replacement of isoleucine with tert-leucine in Demotensins 3, 4, 6 was performed. In Demotensins 5 and 6, the 2,4 diaminobutyric acid replaced Arg 9. All the Demotensin derivatives exhibited high binding affinities in the HT-29 cell line, and the IC_{50} values of Demotensin 1–6 against $[^{125}\text{I-Tyr}^3]\text{NT}$ were calculated to be 0.32 ± 0.02 , 0.41 ± 0.02 , 1.50 ± 0.01 , 0.85 ± 0.07 , 0.03 ± 0.01 and 0.08 ± 0.02 nM, respectively. The ^{99m}Tc -Demotensins were evaluated for their *in vivo* biodistribution

properties and their metabolic stability. Metabolic stability in murine plasma showed that ^{99m}Tc -Demotensins 3 and 4 were stable up to one hour, while ^{99m}Tc -Demotensin 2 had a shorter half-life of $t_{1/2} = 20\text{--}25$ minutes and ^{99m}Tc -Demotensin 1 of $t_{1/2} = 3\text{--}5$ minutes [231]. Similarly, ^{99m}Tc -Demotensin 6 was >90% stable for two hours in murine plasma, whereas ^{99m}Tc -Demotensin 5 degraded with a half-life of $t_{1/2} \sim 15$ minutes. The tumor uptake values for ^{99m}Tc -Demotensins 3 and 4 were 3.52 ± 0.66 and $4.94 \pm 0.52\%$ ID/g at one hour *p.i.*, respectively, in HT-29 tumor-bearing mice, while in human NTS1-R-expressing WiDr tumor-bearing mice, their tumor uptake was found to be 3.95 ± 0.64 and $4.72 \pm 0.72\%$ ID/g at one hour *p.i.*, respectively [231]. Tumor uptake in WiDr-bearing mice for ^{99m}Tc -Demotensins 5 and 6 were 1.68 ± 0.15 and $4.30 \pm 0.45\%$ ID/g at one hour *p.i.*, respectively [232]. A pilot study in human patients revealed that ^{99m}Tc -Demotensin 6 (Figure 12.14) could detect tumors in brain metastases [233].

12.8.7 CCK-2 Receptor Imaging Agents

The overexpression of cholecystinin (**CCK**) type-2 receptors (or B receptors or gastrin receptors) has been observed in the majority of medullary thyroid carcinomas as well as in some other carcinomas (e.g. small-cell lung and ovarian). In the efforts to develop ^{99m}Tc -probes for CCK2R imaging, the minigastrin (MG: Leu-Glu-Glu-Glu-Glu-Glu-Ala-Tyr-Gly-Trp-Met-Asp-Phe-NH₂) peptide and its derivatives or the cholecystinin (CCK-8: Asp-Tyr-Met-Gly-Trp-Met-Asp-PheNH₂) peptide were employed. The peptide [D-Glu¹]MG was conjugated to HYNIC (HYNIC-MG) and to the N α -histidinyl acetate chelator (N α -His-Ac-MG), and the respective tracers [^{99m}Tc]Tc-Tricine-HYNIC-MG, [^{99m}Tc]Tc-EDDA-HYNIC-MG (Figure 12.15) and [^{99m}Tc]Tc(CO)₃(N α -His-Ac-MG) exhibited high stability in serum. Competition experiments of the unlabelled peptide conjugates on AR42J membranes versus [^{125}I][iodoTyr¹²]-gastrin I showed a high CCK2R affinity for all conjugates under study. In AR42J tumor-bearing nude mice, the highest tumor uptake was observed in the tracer [^{99m}Tc]Tc-EDDA-HYNIC-MG (8.1% ID/g), followed by [^{99m}Tc]Tc-Tricine-HYNIC-MG (2.2% ID/g) and then [^{99m}Tc]Tc(CO)₃(N α -His-Ac-MG) (1.2% ID/g) at four hours *p.i.*, while the kidney uptake observed was 101.0% ID/g, 53.8% ID/g, and 1.8% ID/g, respectively [234]. To improve kidney uptake, the shortened peptide analogue, which lacks Glu²⁻⁶, [HYNIC⁰,DGlu¹,desGlu²⁻⁶]MG (HYNIC-MG11), was developed. The tracer

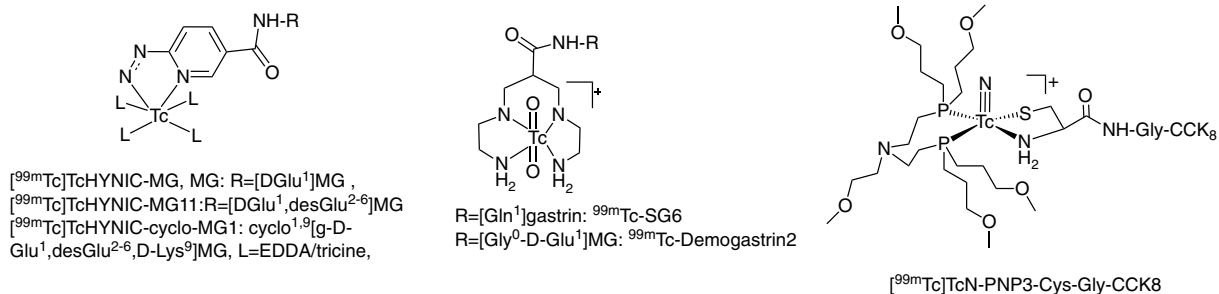


Figure 12.15 Structures of ^{99m}Tc -labelled CCK-2 receptor imaging agents.

[^{99m}Tc]Tc-EDDA-HYNIC-MG11 (Figure 12.15) synthesized exhibited serum stability of 89.4% at 24 hours (the respective stability of [^{99m}Tc]Tc-EDDA-(HYNIC-MG) was 90.5% at 24 hours). A high binding affinity of HYNIC-MG11 for the CCK2R was displayed in displacement studies against [¹²⁵I][iodoTyr¹²]-gastrin I, with IC₅₀ value <2 nM as well as [^{99m}Tc]Tc-EDDA-(HYNIC-MG11) exhibited in a saturation assay K_D of 3.97 nM. [^{99m}Tc]Tc-EDDA-(HYNIC-MG11) exhibited unaltered tumor uptake of 7.11 ± 0.22 %ID/g at four hours *p.i.*, while kidney uptake was reduced by 98% in comparison with the respective biodistribution results of [^{99m}Tc]Tc-EDDA-(HYNIC-MG) [235].

Also, the development of tetramine derivatives of minigastrin was reported. Demogastrin derivatives 1–3 contain the following sequences: Demogastrin 1, [N₄⁰,D-Glu¹]MG; Demogastrin 2, N₄⁰⁻¹,Gly⁰-D-Glu¹]MG; and Demogastrin 3, [N₄⁰,D-Glu¹]MG, with the tetramine ligand N,N',N'',N'''-tetra-(tert-butoxycarbonyl)-6-X-1,4,8,11-tetraazaundecane (where in N₄; X = carboxy and N'; X = p-(carbomethoxy)acetyl]aminobenzyl) [236]. The respective dioxotechnetium complexes ^{99m}Tc-Demogastrin 1–3 prepared were stable for two hours in mouse plasma, but complete degradation was observed in urine. The carrier-added tracers ^{99m}Tc/^{99g}Tc-Demogastrin 1–3 were evaluated for their binding affinities in AR42J cell membranes, and their K_D values were found to be 1.05 ± 0.13, 1.02 ± 0.07, and 1.01 ± 0.09 nM, respectively. Tumor uptake values of ^{99m}Tc-Demogastrins 1–3 were 6.13 ± 3.28, 5.50 ± 0.85, and 4.20 ± 1.22 %ID/g at one hour *p.i.*, respectively, in AR42J tumor-bearing mice. At the same time, high kidney uptake values of 78.97 ± 1.60, 83.92 ± 14.45, and 78.18 ± 11.85% ID/g, respectively, were observed. ^{99m}Tc-Demogastrin 2 (Figure 12.15) was also evaluated in a medullary thyroid carcinoma patient, where all the known lymph node lesions were clearly detected [236]. Similarly, two other gastrin radioligands were developed – the full-length [^{99m}Tc][Tc-N₄-Gln¹]gastrin (^{99m}Tc-SG6) (Figure 12.15) and the truncated [^{99m}Tc][Tc-N₄-D-Glu¹⁰]gastrin(10–17) (^{99m}Tc-DG4) – and were compared to ^{99m}Tc-Demogastrin 2. Competition binding studies of the ligands SG6, Demogastrin 2 and DG4 in A431-CCK2R(+) cell membranes against [¹²⁵I][iodoTyr¹²,Leu¹⁵]gastrin were performed, and the IC₅₀ values of the ligands were found to be 9.3 ± 0.9, 10.7 ± 1.3, and 0.9 ± 0.1 nM, respectively. The tumor uptake of the radiotracers in A431-CCK2R(+) xenografts was found to be 12.89 ± 4.69% ID/g for ^{99m}Tc-Demogastrin 2, 10.25 ± 3.51% ID/g for ^{99m}Tc-SG6, and 0.99 ± 0.13% ID/g for ^{99m}Tc-DG4 at one hour *p.i.*. The *in vivo* mouse plasma stability was measured 5 minutes *p.i.* and found to be: ^{99m}Tc-Demogastrin 2, 60% intact; ^{99m}Tc-SG6, 40% intact; and ^{99m}Tc-DG4, 10% intact. However, prior administration of neutral endopeptidase (**NEP**) and angiotensin-converting enzyme (**ACE**) inhibitors phosphoramidon (**PA**) and Lisinopril (**Lis**), respectively, significantly increased the tracers' stability, as follows: ^{99m}Tc-Demogastrin 2, 85% intact; ^{99m}Tc-SG6, 70% intact; and ^{99m}Tc-DG4, 80% intact. Their tumor uptake was also improved to 18.21 ± 5.97% ID/g (PA + Lis) for ^{99m}Tc-Demogastrin 2, 18.46 ± 3.56% ID/g (PA only) for ^{99m}Tc-SG6, and 8.91 ± 1.61% ID/g (PA + Lis) for ^{99m}Tc-DG4 at four hours *p.i.*. The kidney uptake of ^{99m}Tc-Demogastrin 2 and ^{99m}Tc-SG6 was high [237].

The development of cyclized MG was also reported, where the tracers [^{99m}Tc]Tc-EDDA-HYNIC-cyclo-MG1 (cyclo-MG1: cyclo^{1,9}[γ-D-Glu¹,desGlu²⁻⁶,D-Lys⁹]MG) and [^{99m}Tc]Tc-EDDA-HYNIC-cyclo-MG2 (cyclo-MG2: cyclo^{1,9}[γ-D-Glu¹,desGlu²⁻⁶,D-Lys⁹,Nle¹¹]MG) were developed (Figure 12.15). The *in vitro* stability in human plasma was found to be

88.6–97.6% intact peptide after 24 hours of incubation. The dissociation constant (K_D) of tracers [^{99m}Tc]Tc-EDDA-HYNIC-cyclo-MG1 and [^{99m}Tc]Tc-EDDA-HYNIC-cyclo-MG2 was found to be 19.1 and 21.2 nM, respectively. The tumor uptake values of [^{99m}Tc]Tc-EDDA-HYNIC-cyclo-MG1 and [^{99m}Tc]Tc-EDDA-HYNIC-cyclo-MG2 were 3.61 and 3.17% ID/g one hour *p.i.*, respectively [238].

Using a different approach, the natural octapeptide CCK8 was conjugated to a tetradentate (PN_2S) chelator N-(N-(3-diphenylphosphinopropionyl) glycy)cysteine (Phos-GC), and the respective [^{99m}Tc][TcO(Phos-GC-CCK8)] complex was synthesized in high yield. Its binding affinity was $K_D = 32.0 \pm 5$ nM in A-431 cells, its tumor uptake in A-431 tumor-bearing mice was $2.01 \pm 0.80\%$ ID/g at two hours *p.i.*, and it displayed both renal and hepatobiliary excretion [239]. The development of nitridotechnetium complexes for CCK2R was reported as well, where CCK8 was derivatized with a cysteine residue (Cys-Gly-CCK8) that was used in the tracer [^{99m}Tc][TcN(N,S-Cys-Gly-CCK8)(PNP3)]⁺ (PNP3=N,N-bis(dimethoxypropylphosphinoethyl)methoxyethylamine) (Figure 12.15). Its binding affinity in A-431 cells was found to be $K_D = 19.0 \pm 4.6$ nM ($B_{\text{max}} \sim 10^6$ sites/cell), and its tumor uptake in A-431 tumor-bearing mice was <1 %ID/g at one hour *p.i.*, while high intestinal activity was observed [240].

12.8.8 Folate Receptor Imaging Agents

The vitamin folic acid has been effectively applied for the development of diagnostic radiopharmaceuticals to target folate receptor (**FR**)-positive tumors such as ovarian, non-small-cell lung, endometrial, breast, and renal cell carcinoma. One of the early efforts describes the conjugation of folate to DTPA chelator for standard ^{99m}Tc -labelling as well as for [^{99m}Tc][Tc(CO)₃]⁺-labelling. Intravenous administration of [^{99m}Tc]Tc-DTPA-folate and [^{99m}Tc]Tc(CO)₃(DTPA-folate) to athymic mice bearing KB cell tumor xenografts resulted in tumor uptake of 2.9 ± 0.8 and $3.3 \pm 0.2\%$ ID/g at four hours *p.i.*, respectively. Furthermore, high kidney uptake of 21 ± 3 and $46 \pm 5\%$ ID/g in each kidney was observed at the same time point, due to physiologic FR presence in the renal tubules [241, 242]. Also, a folate-containing peptide with the sequence pteric acid (Pte), D-Glu, β -diaminopropionic acid, Asp, and Cys (EC20) was developed, where the latter three amino acids function as a tetradentate (**NNNS**) chelator for ^{99m}Tc -labelling [243]. ^{99m}Tc -EC20 consists of a mixture of two oxotechnetium(V) complexes characterized as *syn* and *anti* isomers (Figure 12.16). The FR binding affinity of ^{99m}Tc -EC20 in KB cells was measured to be $K_D = 3.2$ nM. The *in vivo* tumor uptake of ^{99m}Tc -EC20 in mice bearing FR-positive M109 cells was $17.2 \pm 1.02\%$ ID/g at four hours *p.i.*, with kidney uptake of $138 \pm 12.4\%$ ID/g at the same time point. Currently, ^{99m}Tc -EC20 (^{99m}Tc -etarfolatide, Endocyte Inc.) is being studied as a companion diagnostic imaging agent to the therapeutic folate-targeted agent vintafolide in multiple clinical trials [244].

A series of [^{99m}Tc][Tc(CO)₃-folate] complexes was developed (Figure 12.16), where folate was conjugated to the PAMA tridentate chelator via a hexylamine linker on either the γ - or α -glutamate, [^{99m}Tc][Tc(CO)₃(PAMA- γ -folate)] and [^{99m}Tc][Tc(CO)₃(PAMA- α -folate)]; and by a similar design, [^{99m}Tc][Tc(CO)₃(PAMA-pterolate)], was synthesized

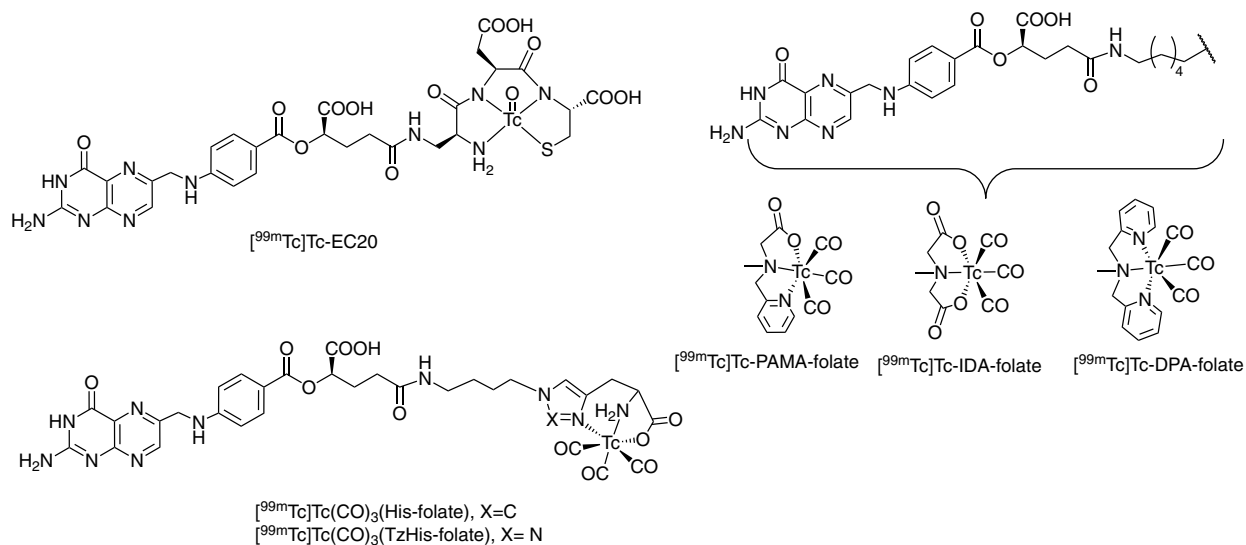


Figure 12.16 Structures of ^{99m}Tc -labelled folate imaging agents.

lacking glutamate [245]. The ^{99m}Tc -folates were also prepared in a kit-like method, where the PAMA conjugates were placed in a kit with the Isolink components, with very high radiochemical yields (>92%). The binding affinities of $[^{99m}\text{Tc}][\text{Tc}(\text{CO})_3(\text{PAMA-}\gamma\text{-folate})]$, $[^{99m}\text{Tc}][\text{Tc}(\text{CO})_3(\text{PAMA-}\alpha\text{-folate})]$, and $[^{99m}\text{Tc}][\text{Tc}(\text{CO})_3(\text{PAMA-pterolate})]$ in KB cells were determined (by the Rosenthal analysis) with K_D values of 2.09, 2.51, and 14.52 nM, respectively. Biodistribution studies in KB-tumor-bearing mice revealed tumor uptake of 2.33 ± 0.36 , 1.24 ± 0.19 , and $0.43 \pm 0.17\%$ ID/g at four hours *p.i.* for the three radiofolates, respectively, with kidney uptake of 18.5 ± 0.7 , 12.4 ± 1.9 , and $3.3 \pm 0.4\%$ ID/g, respectively, and significant hepatobiliary clearance for all the tracers [246]. Importantly, selective FR-blockade in the kidneys was accomplished after administration of antifolates prior to radiofolate administration, while the FR-mediated uptake of radioactivity in KB tumor xenografts was retained [247]. Similar results were obtained with the tracers $[^{99m}\text{Tc}][\text{Tc}(\text{CO})_3(\text{IDA-}\gamma\text{-folate})]$ and $[^{99m}\text{Tc}][\text{Tc}(\text{CO})_3(\text{DPA-}\gamma\text{-folate})]$, with tumor uptake in KB-bearing mice of 2.67 ± 0.27 and $0.94 \pm 0.10\%$ ID/g at four hours *p.i.*, respectively, and with high cell binding of 40–55% in KB cells as well [248]. In a different design, $N(\tau)$ -histidine-folate (His-folate) and its isostructural click 1,2,3-triazole (TzHis-folate) analogue were synthesized, where the γ -glutamate of folate was conjugated via a butylamine linker to the chelator, and the respective $[^{99m}\text{Tc}]\text{Tc}(\text{CO})_3(\text{His-folate})$ and $[^{99m}\text{Tc}]\text{Tc}(\text{CO})_3(\text{TzHis-folate})$ tracers were prepared (Figure 12.16). Their tumor uptake in tumor-bearing mice was 4.29 ± 0.67 and $4.84 \pm 0.10\%$ ID/g at four hours *p.i.*, while their accumulation in the kidney was 24.56 ± 3.17 and $27.33 \pm 3.61\%$ ID/g, respectively [249].

In a recent report, $[^{99m}\text{Tc}]\text{Tc}$ -folate-GGCE (folate-Gly-Gly-Cys-Glu) was developed by ligand-exchange reaction from $[^{99m}\text{Tc}]\text{Tc}$ -tartrate at >95% radiolabelling efficiency. The structure of the technetium complex was not described, but it is assumed that the tetrapeptide, GGCE, is the ^{99m}Tc -chelator. Its binding affinity (K_D) was measured to be

5.19 nM. The KB-tumor uptake of ^{99m}Tc -folate-GGCE was 16.4, 23.2, and 17.6% ID/g, at one, two, and four hours *p.i.*, respectively, and the kidney uptake was 57.04 ± 18.58 %ID/g at four hours *p.i.* [250]. Also, the [^{99m}Tc]Tc-tetraethylenepentamine(**TEPA**)-folate was prepared by direct labelling at >95% radiochemical yield [251]. The binding affinity (K_D) of [^{99m}Tc]Tc-TEPA-folate was found to be 5.00 ± 0.06 , 27.46 ± 0.01 , and 25.85 ± 0.005 nM in KB, U-87MG, and MDA-KB-468 cells, respectively. The tumor uptake of the tracer in KB tumor-bearing mice was 4.26 ± 1.3 % ID/g, kidney uptake was 16.0 ± 1.2 % ID/g, and liver uptake was 16.0 ± 2.0 %ID/g at four hours *p.i.* [251]. Furthermore, [^{99m}Tc]Tc-(DO3A-EA)-folate was synthesized by direct labeling at high efficiency, where DO3A-EA is 1,4,7-tris(carboxymethyl)-10-(4-aminoethyl)-1,4,7,10-tetraazacyclododecane linked to folic acid via its γ -carboxyl group. The *in vitro* receptor binding affinity (K_D) was found to be 4.2 ± 0.8 , 22.54 ± 0.002 , and 16.68 ± 0.01 μM in KB, U-87MG, and OAW, respectively. KB tumor uptake in tumor-bearing mice was 6.26 ± 0.4 at four hours *p.i.*. Both renal and hepatobiliary clearance were observed [252].

12.8.9 ^{99m}Tc -Labelled Glucose Derivatives

The development of a SPECT tracer based on ^{99m}Tc -labelled glucose derivatives is attractive, given the wide usefulness of the PET agent 2-deoxy-2- ^{18}F fluoro-D-glucose. Series of [^{99m}Tc][Tc(CO) $_3$ -glucose] tracers were developed for this purpose by rational drug design. Glucose derivatives were designed for conjugation to a tridentate chelator such as iminodiacetate (**IDA**) at positions, C-1, C-2, C-3, and C-6 (Figure 12.17). The C-1 glucose derivatives were separated by an ethyl spacer from IDA [253], while the C-2 and C-6 [254] derivatives had C3, C8, and triethyleneglycol spacers. Furthermore, glucose derivatives were designed for conjugation to histidine, bisimidazolylamine, and PAMA chelators at position C-3, as well [255]. The tracers [^{99m}Tc][Tc(CO) $_3$ (L-Glucose)] (L = IDA, His, PAMA) were evaluated in a dose-dependent manner for their ability to be transported via GLUT1 glucose transporters in HT29 colon cancer cells, where their uptake was found not to be mediated by GLUT1. The analogous Re-complexes were evaluated for competitive inhibition of hexokinase, where only the C-2 derivatized glucose complexes with extended spacer functionalities were found to be active; in particular, Re(CO) $_3$ (2-IDA-C8-glucose) and [Re(CO) $_3$ (2-deoxyglucose-(PEG) $_3$ IDA)] exhibited K_i values of 5.8 ± 0.9 mM and 0.25 ± 0.01 mM, respectively. The competitive inhibitors, though, were not recognized as substrates of hexokinase [256]. Similar C-1 glucose derivatives [^{99m}Tc][Tc(CO) $_3$ (1 β -IDA-glucose)] and [^{99m}Tc][Tc(CO) $_3$ (1 α -IDA-2-deoxyglucose)] were evaluated in B16F1 melanoma-bearing mice, where low tumor uptake was observed of 0.31 ± 0.23 and 0.40 ± 0.28 % ID/g at one hour *p.i.*, respectively [257].

Another series of [^{99m}Tc]Tc(CO) $_3$ -glucose and -glucosamine tracers were developed, conjugated at the C-1 or C-2 position to various chelators [258, 259] including hydroxypyridone [24], DPA, PAMA, and Schiff-based chelators [260–263], as well as the cyclopentadienyl chelator (Figure 12.17) [264]. From these complexes, the Re analogue Re(CO) $_3$ (2-glucosamine-Cp) was evaluated for competitive inhibition of hexokinase, which exhibited $K_i = 330 \pm 70$ μM , although the complex was not recognized as a substrate

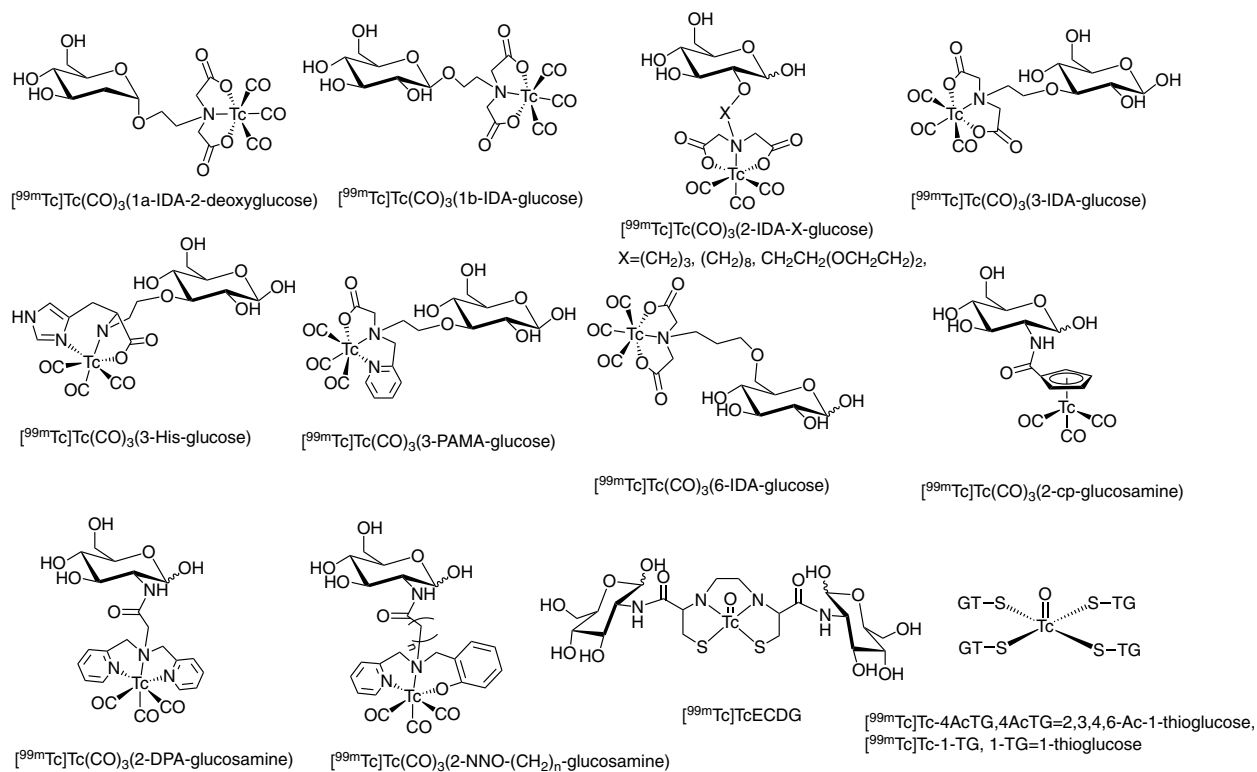


Figure 12.17 Structures of ^{99m}Tc -labelled glucose derivatives.

of hexokinase [264]. The tracers $[^{99m}\text{Tc}][\text{Tc}(\text{CO})_3(2\text{-glucosamine-NNO})]$ with NNO-type chelators exhibited no specific GLUT1 transport in LCC6-HER2 human breast cancer cells. In addition, the Re analogues were not recognized as substrates of HK; however, $\text{Re}(\text{CO})_3(2\text{-glucosamine-CO-C}_7\text{-NNO})$ behaved as a competitive inhibitor of HK with K_i of $70 \pm 20 \mu\text{M}$ [260]. Furthermore, the tracer $[^{99m}\text{Tc}][\text{Tc}(\text{CO})_3(2\text{-glucosamine-DPA})]$ was evaluated in B16F10 murine melanoma tumor-bearing mice and exhibited tumor uptake of $0.47 \pm 0.09\%$ ID/g at two hours *p.i.* [265]. The tracer $[^{99m}\text{Tc}][\text{Tc}(\text{CO})_3(\text{TzHis-C4-2-glucose})]$ was developed by “click” conjugation from a C-2 glucose derivative with a butyl spacer. The tracer was administered in lung carcinoma-bearing mice, and it exhibited tumor uptake values of 0.55 ± 0.05 and $0.35 \pm 0.01\%$ ID/g at one and two hours *p.i.*, respectively [266].

Using a different approach, the tracer $[^{99m}\text{Tc}]\text{oxotechnetium-ethylenebis(L-cysteinyl-D-glucosamine)}$ ($[^{99m}\text{Tc}]\text{Tc-ECDG}$) (Figure 12.17) was developed, and *in vitro* studies showed that its cellular uptake was mediated by a D-glucose transport mechanism and that ECDG was a substrate of hexokinase (HK) [267]. Biodistribution in human A549 lung cancer-bearing mice showed a low tumor uptake of $[^{99m}\text{Tc}]\text{Tc-ECDG}$ of $0.41 \pm 0.16\%$ ID/g at four hours *p.i.*. Furthermore, it was shown that $[^{99m}\text{Tc}]\text{Tc-ECDG}$ was capable of assessing the therapeutic response of tumor-bearing mice post-treatment [268]. An initial

clinical trial in seven human patients showed that the tumor uptake of [^{99m}Tc]Tc-ECDG was three to four times that of normal tissue uptake [269]. Also, the tracer [^{99m}Tc]Tc-DTPA-D D-isomer-glucosamine (DG) was reported. *In vitro*, it was shown that [^{99m}Tc]Tc-DTPA-DG and [^{18}F]FDG exhibited similar uptake values in MCF-7 tumor cells. *In vivo*, in MCF-7 human breast tumor-bearing mice, the tumor uptake of [^{99m}Tc]Tc-DTPA-DG and [^{18}F]FDG was 1.59 ± 0.04 and $1.42 \pm 0.12\%$ ID/g, and the tumor-to-blood ratio was 3.24 ± 0.65 and 7.12 ± 2.12 at four hours *p.i.*, respectively [270].

Furthermore, ^{99m}Tc -labelled thioglucose (TG) analogues were developed; in particular, ^{99m}Tc -1-thio- β -D-glucose ([^{99m}Tc]Tc1-TG) and [^{99m}Tc]Tc-5-thio-D-glucose were prepared by direct labeling in high radiochemical yields (Figure 12.17). The ^{99m}Tc tracers were evaluated for their tumor cell uptake in comparison to [^{18}F]FDG, where they exhibited tumor uptake with a mechanism analogous to that of glucose, although the tracers exhibited higher accumulation in the cell membranes compared to [^{18}F]FDG [271, 272]. [^{99m}Tc]Tc-1-TG was evaluated as an imaging tool for the diagnosis of joint inflammatory disorder [273]. Similarly, 1-thio- β -D-glucose 2,3,4,6-tetra-acetate (4AcTG) was labelled with technetium-99m by ligand exchange from ^{99m}Tc -tartrate. [^{99m}Tc]Tc-4AcTG exhibited high uptake in bacteria and tumor cells expressing GLUT1 transporters, as well as *in vivo* uptake in infection (*Staphylococcus aureus*) and RMA lymphoma in mice, with values of 1.81 ± 0.11 and $3.54 \pm 0.12\%$ ID/g at two hours *p.i.*, while the uptake values of [^{18}F]-FDG were 0.68 ± 0.19 and $0.93 \pm 0.26\%$ ID/g, respectively [274].

In another study, three D-glucosamine (DG) derivatives, N-thioacetyl-D-glucosamine (S-DG), mercaptoacetyltriglycyl-D-glucosamine (MAG₃-DG), and MAMA-butanamide-D-deoxyglucose (MAMA-BA-DG), were labelled by ligand exchange from ^{99m}Tc -glucoheptate in high radiochemical purities. Biodistribution of [^{99m}Tc]Tc-S-DG, [^{99m}Tc]Tc-MAG₃-DG, and [^{99m}Tc]Tc-MAMA-BA-DG was performed in MA891 breast tumor-bearing mice, where their tumor uptake was 1.06 ± 0.18 , 0.82 ± 0.06 , and $0.21 \pm 0.03\%$ ID/g at four hours *p.i.*, respectively, while the respective tumor-to-blood ratio at the same time-point was 0.82 ± 0.15 , 0.94 ± 0.13 , and 0.94 ± 0.16 [275]. In another study, two glucose derivatives were prepared by conjugation of the MAG₃ chelator at the glucopyranose C-1 position of β -D-glucosamine (DG) [276] and β -D-glucopyranose-4-phenylamine (**PhDG**) [277]. The respective tracers [^{99m}Tc]Tc-MAG₃-DG and [^{99m}Tc]Tc-MAG₃-PhDG were evaluated in Ehrlich tumor-bearing mice with tumor uptake of 0.79 ± 0.14 and $0.50 \pm 0.04\%$ ID/g for [^{99m}Tc]Tc-MAG₃-DG and [^{99m}Tc]Tc-MAG₃-PhDG at two hours *p.i.*, respectively [276]. The HYNIC-glucosamine (HYNIC-DG) derivative was labelled by two different methods, and the respective tracers [^{99m}Tc]Tc-(HYNIC-DG)-Tricine-TPPTS and [^{99m}Tc]Tc-(HYNIC-DG)-EDDA were produced. The tumor uptake in S180 murine sarcoma-bearing mice of [^{99m}Tc]Tc-(HYNIC-DG)-Tricine-TPPTS and [^{99m}Tc]Tc-(HYNIC-DG)-EDDA was 0.44 ± 0.13 and $0.46 \pm 0.06\%$ ID/g at two hours *p.i.*, respectively [278]. Dithiocarbamate-Glucose-1 derivatives were prepared by "click" conjugation of a C-1 derivatized glucose, which formed the respective [^{99m}Tc][TcN(dithiocarbamate-glucose-1)₂] tracers. The tracers were evaluated in S180 murine sarcoma-bearing mice, and the maximum tumor uptake was found for the tracer with the longer propyl linker of $4.30 \pm 0.61\%$ ID/g with blood activity of $4.15 \pm 0.53\%$ ID/g at two hours *p.i.* [279].

12.8.10 ^{99m}Tc -Labelled Thymidine Derivatives

Targeting thymidine kinase with radiotracers has been used as an approach to diagnose cancers. In addition, imaging of the non-invasive herpes simplex virus type-1 thymidine kinase (**HSV1-tk**) gene expression has wide interest for research on gene therapy and for confirmation of gene delivery.

In a series of thymidine analogues developed, 5'-carboxamide thymidine was conjugated to the chelators IDA and PAMA with various spacers of length 0–30 Å, which were complexed with the $[\text{M}(\text{CO})_3]^+$ core ($\text{M} = ^{99m}\text{Tc}$, Re) (Figure 12.18). The Re-complexes were tested *in vitro* for their ability to inhibit human cytosolic thymidine kinase (**TK**) with K_i values ranging from 4.4 to 334 μM [280, 281]. By replacing the 5-methyl moiety of thymidine with a 5-ethyl moiety, the respective $\text{Re}(\text{CO})_3(\text{IDA}-5'\text{-carboxamide } 5\text{-ethyl-}2'\text{-deoxyuridine})$ complex was found to be a selective competitive inhibitor of HSV1-TK ($K_i = 4.56 \mu\text{M}$) [282]. In addition, a series of N3- and C3'-functionalized thymidine analogues conjugated by various spacers with tridentate chelators that formed neutral, anionic, and cationic $[\text{M}(\text{CO})_3]^+$ ($\text{M} = ^{99m}\text{Tc}$, Re) chelates were developed (Figure 12.18). A series of N3-functionalized thymidine analogues linked by various spacers to tridentate chelators that form neutral chelates with $[\text{Re}(\text{NO})(\text{CO})_2]^{2+}$ were prepared. The respective Re complexes, as well as some of the ^{99m}Tc tracers, were evaluated as potential substrates for hTK1 by monitoring the formation of the monophosphorylated product, where it was shown that all the complexes were substrates to the enzyme, with the C3'-functionalized thymidine analogues exhibiting higher affinity for the enzyme [283–286]. *In vitro* cell internalization experiments performed in a human neuroblastoma SKNMC cell line revealed low uptake of the ^{99m}Tc tracers, dependent on their lipophilicity; hence it was assumed that they are taken up by diffusion rather than by facilitated transport [283]. A series of thymidine analogues that were functionalized at positions C5', C2', and N3 were linked by various spacers to dipicolylamine and complexed with $[\text{Re}(\text{CO})_3]^+$. Also, a series of N3-functionalised thymidine derivatives linked to bis(quinolin-2-ylmethyl) amino and bis(thiazol-4-ylmethyl)amino tridentate chelators were developed. The Re-complexes were tested against A549 lung carcinoma cell line for their cytotoxicity, and

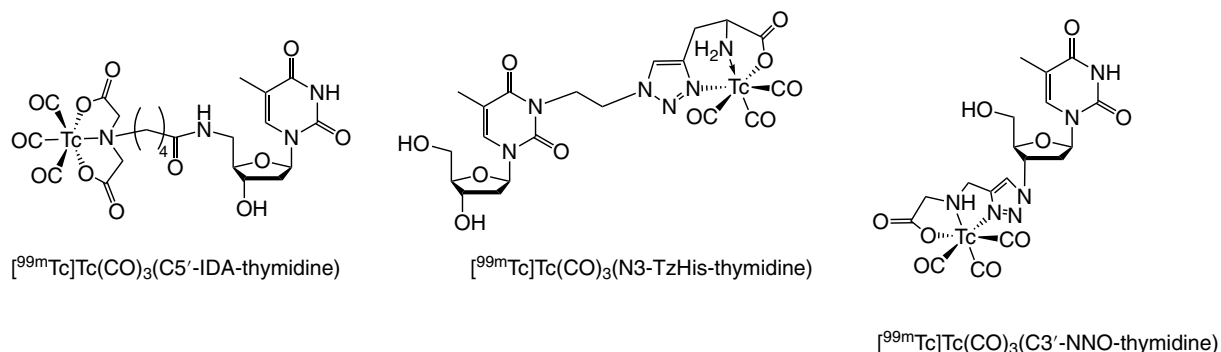


Figure 12.18 Structures of $[\text{M}(\text{CO})_3]$ -thymidine derivatives, $\text{M} = ^{99m}\text{Tc}$ or Re.

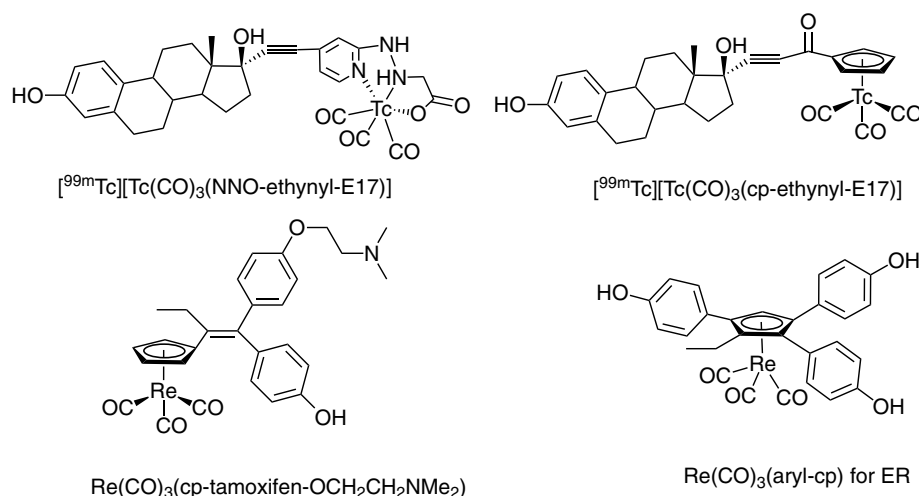
some of these derivatives were found to be quite potent, in particular the N3- and C5'-functionalized derivatives, while low inhibition of TK1 was displayed [287, 288].

Using a different approach, a [^{99m}Tc]oxotechnetium-MAMA-propyl-N3-thymidine derivative was developed; however, it exhibited a low affinity for TK1 and low tumor uptake *in vivo* in a radiation-induced fibrosarcoma (**RIF**) tumor mouse model [289].

12.8.11 Estrogen Receptor Imaging Agents

The development of ^{99m}Tc -labelled imaging agents for the detection of estrogen receptors (**ERs**) overexpressed in ER-positive tumors is of importance in nuclear medicine, especially for the diagnosis of breast cancers. A number of organometallic technetium and rhenium $[\text{M}(\text{CO})_3]^+$ -complexes ($\text{M} = \text{Re}, ^{99m}\text{Tc}$) of 17α -ethynylestradiol have been developed, with various chelators, such as a bidentate dithioether (SS) system, a tridentate dithioether-carboxylate (SSO) system, PAMA, and pyrazolyldiamine (pzNN), as well as cyclopentadienyl (Figure 12.19) [35, 290–292]. The pyridine-2-yl-hydrazine (HYPY) ligand was conjugated to 17α -ethynylestradiol, and the respective $\text{Re}(\text{CO})_3$ (HYPY-E17) complex was evaluated for its relative binding affinity (RBA) to the estrogen receptor, and high ER binding was displayed (RBA = 38%) [293]. The respective pyridin-2-yl-hydrazine acetic acid (NNO) tridentate chelator was conjugated to 17α -ethynylestradiol, and the analogous $\text{Re}(\text{CO})_3$ (NNO-E17) complex exhibited RBA = 20% to $\text{ER}\alpha$ [294]. The linkage effects in ER binding were evaluated after hydrogenation of the triple bond of the complex $\text{Re}(\text{CO})_3$ (NNO-E17) to its double-bonded and single-bonded analogues, where it was shown that the Z-ethenyl (double-bonded) derivative exhibited higher binding to $\text{ER}\beta$ (RBA = 24%) [294]. Preclinical evaluation of the tracer [^{99m}Tc]Tc(CO) $_3$ (NNO-E17) (Figure 12.19) in tumor-bearing mice exhibited low but specific uptake in estrogen receptor-expressing tumors (0.67% for MCF-7 tumors and 0.77% for endometrial tumors at three hours *p.i.*) [295].

Figure 12.19 Structures of $[\text{M}(\text{CO})_3]$ -estradiol derivatives, $\text{M} = ^{99m}\text{Tc}$ or Re.



The 7 α position (E-7) of 3,17 β -estradiol, known to tolerate modifications, was derivatized to synthesize a series of ligands, a thiol (S-E7), an isocyanide (CN-E7), a dithioether (SS-E7), as well as tridentate SSO (SSO-E7) and SNO (SNO-E7) chelators, in order to employ different Re/^{99m}Tc-chelate strategies. The “3+1” oxorhenium complexes ReO-SSS/S-E7, ReO-SOS/S-E7, and ReO-SN(Me)S/S-E7 were synthesized, where a higher affinity of RBA = 45% was observed for ReO-SN(Me)S/S-E7 and a lower binding affinity (RBA = 15%) for the “4+1” complex Re-NS₃/CN-E7. The organometallic Re(CO)₃(SS-E7), Re(CO)₃(SSO-E7), and Re(CO)₃(SNO-E7) complexes exhibited RBA = 15%, 36%, and 27%, respectively [291, 296]. The [^{94m}Tc][Tc(CO)₃(SNO-E7)] analogue was evaluated in rats, but target-specific uptake *in vivo* was not observed.

The DPA tridentate chelator was conjugated to the 16 α -position of estradiol by linkers of varying length, and the respective Re(CO)₃(DPA-Estradiol-16) complexes were prepared, with the hexyl linker derivative exhibiting highest ER α affinity (RBA = 25.7%) among them [297]. In a recent effort, 3-aminoethyl estradiol was conjugated to the DTPA chelator and labelled with ^{99m}Tc. The tracer was studied *in vivo* in estrogen and nonestrogen receptor-expressing tumor cell lines, where significantly higher uptake was observed in MCF-7 (ER+) tumors (6.06 \pm 0.38 %ID/g) than by MDA-MB-231 (ER-) tumors (1.57 \pm 0.28 %ID/g) at four hours *p.i.* [298].

Another class of ER imaging agents was designed based on tamoxifen, where one of the three phenyl groups of tamoxifen (in particular, the β ring) was replaced by the Re-tricarbonyl-cyclopentadienyl moiety, leading to a mixture of isomers Z + E, which maintained a good binding affinity for ER α and ER antagonist activity, with the highest affinity for an isolated Z isomer (RBA = 28% at 0 °C) (Figure 12.19) [299, 300]. Furthermore, new cyclopentadienyl rhenium tricarbonyl complexes that contain two or three aryl moieties as substituents of the cyclopentadiene have been developed, which have exhibited ER binding with RBA values up to 23% (Figure 12.19) [301]. Novel C-ring substituted rhenium cyclopentadienyl analogues of cyclofenil, a nonsteroidal compound known to bind the ER, were also prepared, with low ER binding [302]. Also, a series of mono and diaryl rhenium(I)-carborane derivatives were prepared using microwave heating, which exhibited an affinity for the two isoforms of the ER [38].

12.8.12 Cobalamin Receptor Imaging Agents

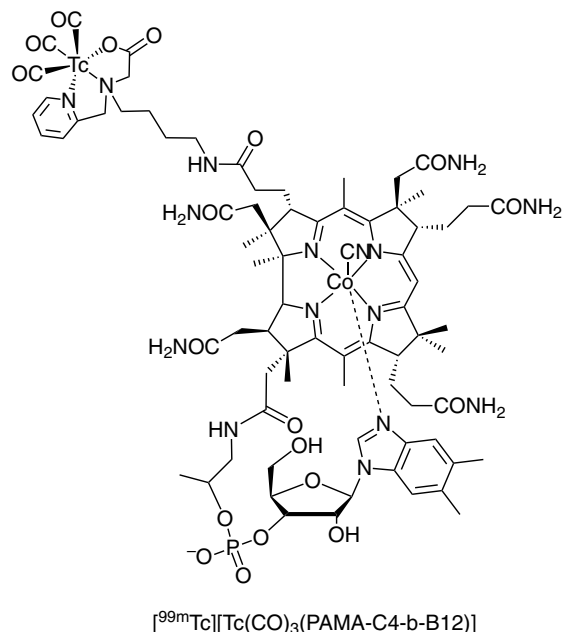
The development of ^{99m}Tc-cobalamin (Vitamin B12) may prove to be useful in oncological imaging. Various proteins recognize and transport cobalamin throughout the body. It is known that certain cancer cells show an increased extracellular density of receptors that bind to cobalamin, and although cobalamin labelled with radioactive cobalt isotopes has been explored for cancer imaging, high uptake in the liver, kidney, and spleen, among other tissues, was observed. A few efforts reported the development of ^{99m}Tc-cobalamin via the [^{99m}Tc]technetium-tricarbonyl approach [303, 304]. First, N(τ)-histidine derivatives were conjugated to the b-acid, c-acid, and d-acid of cyanocobalamin via amide formation. The analogous tracers [^{99m}Tc][Tc(CO)₃(His-B12)] were prepared in high yield and were tested in B16-F10 melanoma-bearing mice. The tumor uptake ranged from 4.4 \pm 0.9% ID/g to 9.2 \pm 2.0% ID/g, while all tracers exhibited significant kidney and liver uptake, similar

to the respective values of [^{57}Co]-cyanocobalamin. The b-acid derivative of B12 among these tracers exhibited an improved excretion profile with a lower percentage of radioactivity in the kidneys and the liver [305]. Another derivative of cyanocobalamin b-acid conjugated to S-derivatized cysteine was also prepared and labelled with $^{99\text{m}}\text{Tc}$ to obtain the tracer [$^{99\text{m}}\text{Tc}$] $\text{Tc}(\text{CO})_3(\text{S-cys-b-B12})$. In B16-F10-bearing mice, it exhibited tumor uptake of $8.1 \pm 0.6\%$ ID/g at four hours *p.i.*, while high liver and kidney uptake were observed as well [19]. The tridentate chelator PAMA was conjugated via C2–C6 spacers to cobalamin b-acid, and these derivatives were labelled to form the respective tracers [$^{99\text{m}}\text{Tc}$] $\text{Tc}(\text{CO})_3(\text{PAMA-C}_{2-6}\text{-b-B12})$ (Figure 12.20). These tracers were evaluated for their interaction with various cobalamin transporters. It was shown that in the short-chain derivatives, their ability to interact with the transport protein transcobalamin II was abolished as well as their mediated uptake in normal tissue; therefore, these tracers might display preferential accumulation in cancer tissue. In particular, the derivative with a butyl spacer exhibited the highest tumor uptake in B16-F10-bearing mice, of approximately 8% ID/g at 24 hours *p.i.*, and low kidney and liver uptake [306]. This agent was also evaluated in a phase I pilot study in human cancer patients, where it was shown that tumor visualization was possible after pretreatment with cobalamin to saturate the circulating haptocorrin [307].

12.9 SENTINEL LYMPH NODE IMAGING AGENTS

Sentinel lymph node (SNL) imaging is helpful in identifying the first lymph node to receive lymphatic flow from the primary tumor site and is also useful intraoperatively. The $^{99\text{m}}\text{Tc}$ -labelled lymph node imaging agents are based on macromolecules whose particulate

Figure 12.20
Structure of
a $^{99\text{m}}\text{Tc}$ -B12
derivative.



properties allow for efficient drainage into the lymphatic system after intradermal or subcutaneous injection. Mannose-bound macromolecules (e.g. dextrans) provide selective recognition via the mannose receptors of the reticuloendothelial system. A modified dextran (Dx) bearing amino-terminal units was conjugated to multiple units of mannose and MAG_3 as the $^{99\text{m}}\text{Tc}$ -chelator, and the final macromolecule contained 3 MAG_3 and 21 mannose units per dextran with a molecular weight of 19389 g/mol and 5.5 nm diameter size [308]. Also, DTPA-mannosyl-dextran was developed, which contained 8 mol DTPA and 55 mol mannose per dextran with a molecular weight of 35800 g/mol and 7.1 nm diameter size [309]. A preliminary SNL-detection study employing footpad injections of $^{99\text{m}}\text{Tc}$ -DTPA-mannosyl-Dx and $^{99\text{m}}\text{Tc}$ -MAG₃-mannosyl-Dx (Figure 12.21) in comparison to $^{99\text{m}}\text{Tc}$ -sulfur colloid (SC) as a standard radiopharmaceutical showed that both mannosyl-Dxs had superior properties compared to $^{99\text{m}}\text{Tc}$ -SC and that $^{99\text{m}}\text{Tc}$ -DTPA-mannosyl-Dx exhibited faster injection-site clearance with a value of $45.7 \pm 8.5\%$ ID at three hours *p.i.* and higher popliteal lymph-node extraction (knee sentinel lymph node for this model) of $97.7 \pm 2.0\%$ ID at three hours *p.i.* in comparison to $^{99\text{m}}\text{Tc}$ -MAG₃-mannosyl-Dx [308, 309]. The $^{99\text{m}}\text{Tc}$ -DTPA-mannosyl-Dx underwent clinical trials and received approval for lymphoscintigraphy and intraoperative application (Lymphoseek, γ -Tilmanocept) [310]. $^{99\text{m}}\text{Tc}$ -Tilmanocept was evaluated in human macrophages with high expression of the C-type lectin mannose receptor (MR; CD206) [311]. Other mannosylated dextrans were developed with tridentate chelators for $^{99\text{m}}\text{Tc}$ -tricarbonyl labeling, which is known for

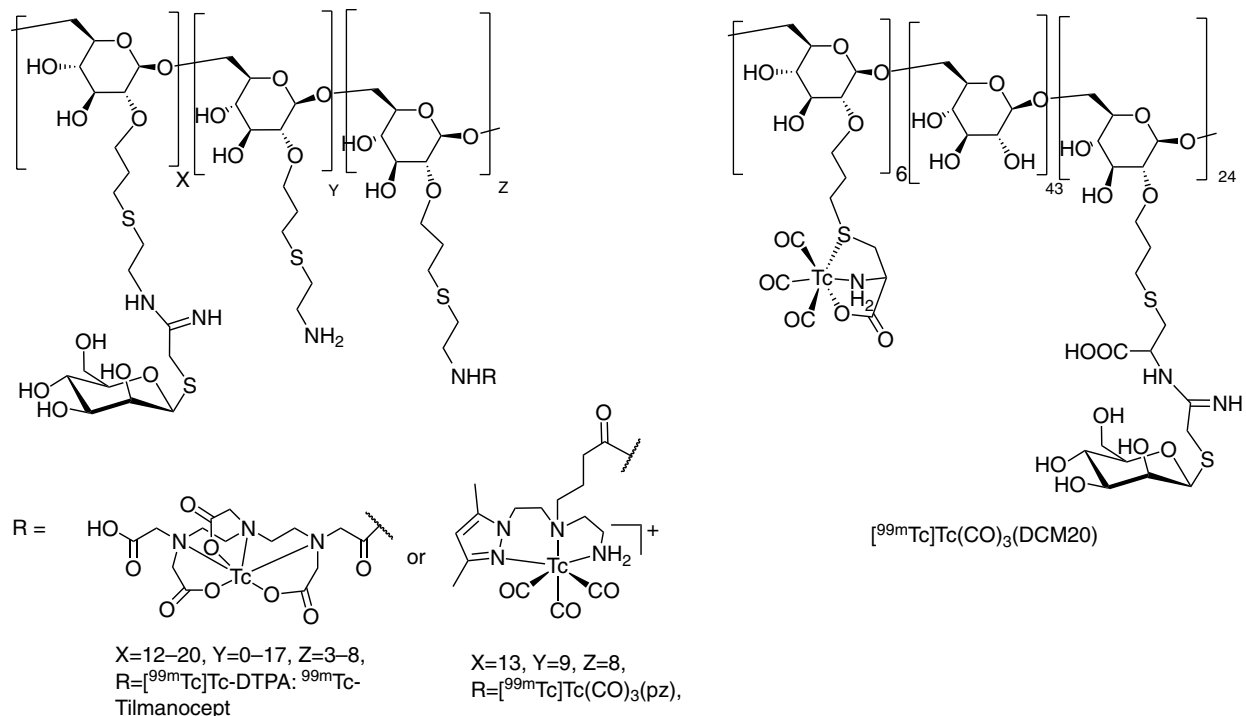


Figure 12.21 Structures of $^{99\text{m}}\text{Tc}$ -labelled SNL imaging agents.

its higher chemical stability compared to the [^{99m}Tc]Tc-DTPA chelate. The pyrazolyl diamine (pz) chelator was conjugated to mannosyl-Dx, and among the derivatives obtained with varying chelator and mannose concentration, the one with 8 mol pz and 13 mol mannose per dextran of 20 kDa weight and 7 nm size (Figure 12.21) exhibited better *in vitro* stability and *in vivo* distribution properties. Its popliteal extraction was $94.47 \pm 2.47\%$ at one hour *p.i.*, higher than that of [^{99m}Tc]Tc-colloid with $78.8 \pm 6.5\%$ and comparable to that of Lymphoseek with $90.1 \pm 10.7\%$ [312]. A modified dextran, S-cysteinyl-mannosylated-Dx, was also developed with 6 mol of S-cysteinyl chelator and 24 mol of mannose per dextran (CDM20, Figure 12.21), 22 kDa weight, and 6.5 nm diameter size. The preliminary biological evaluation of ^{99m}Tc -CDM20 in mice revealed high popliteal lymph-node uptake of 9.2% ID at 30 minutes *p.i.* and fast clearance from the injection site of 67% ID at 30 minutes *p.i.* [313]. Further biological evaluation of ^{99m}Tc -CDM20 showed that there was specific uptake in dendritic cells (that express the mannose receptors) *in vivo* at the injection site, which could explain their slower drainage compared to [^{125}I]radioiodinated mannosyl-neoglycoalbumin [314]. A similar [^{99m}Tc]Tc(CO) $_3$ -S-cysteinyl-mannosylated-Dx with a molecular weight of 30 kDa and 9 and 36 units of cysteine and mannose, respectively, was evaluated in mice, exhibiting $91.05 \pm 9.65\%$ popliteal extraction and $46.35 \pm 3.16\%$ ID remaining at the injection site at 60 minutes *p.i.* [315]. A similar tracer, [^{99m}Tc]Tc(CO) $_3$ -dextran-mannose-dicysteine (**DCCM**) with composition of Dx-(NH $_2$) $_{46}$, mannose $_{13}$, (Cys-Cys) $_{25}$ and molecular weight of 35.5 kDa, was developed. The probe ^{99m}Tc -DCCM was evaluated *in vivo*, and high popliteal extraction of 98% at 60 minutes *p.i.* was obtained [316]. Also, a mannose-dextran derivative bearing isonitrile moieties (DCM30-iso) was developed and was used with the tripodal chelator 2,2',2''-nitriilotris(ethanethiol) (NS $_3$) to form the "4+1" mixed-ligand complex [^{99m}Tc]Tc(NS $_3$)(DCM30-iso). The tracer exhibited $76.4 \pm 12.3\%$ popliteal extraction at 60 minutes *p.i.* and $79.8 \pm 3.0\%$ ID at the injection site in rats [317].

Using a similar approach, HYNIC-mannosyl-neoglycoalbumin (**HYNIC-NMA**) was developed as well and was labelled with technetium-99m in the presence of tricine as co-ligand. In this work, the ^{99m}Tc -labelled non-mannosylated HSA and ^{99m}Tc -colloid were also studied for comparison purposes. After subcutaneous injection of the tracers in mouse footpad, [^{99m}Tc]Tc-(HYNIC-NMA)-tricine demonstrated significantly higher radioactivity levels in the popliteal lymph node than did [^{99m}Tc]Tc-(HYNIC-HSA)-tricine and ^{99m}Tc -colloid, as well as faster clearance from the injection site compared to ^{99m}Tc -colloid [318]. Also, partially reduced mannosyl-HSA was labelled with technetium-99m, and the respective tracer ^{99m}Tc -mannosyl-HSA exhibited higher uptake in the popliteal node in comparison to its analogous non-mannosylated protein, ^{99m}Tc -HSA, and faster clearance from the injection site compared to ^{99m}Tc -colloids [319].

12.10 INFLAMMATION AND INFECTION IMAGING AGENTS

The gold standard for imaging acute inflammation is considered to be the ^{99m}Tc -leukocytes (^{99m}Tc -WBC), an inflammation-specific imaging agent. The preparation of a patient's autologous ^{99m}Tc -WBC is complicated and risky; thus, the agents ^{99m}Tc -Sulesomab

(Leukoscan) and ^{99m}Tc -Besilesomab (Scintimun) were introduced. The first is a murine antibody Fab fragment for the granulocyte surface non-specific cross-reacting antigen NCA-90, and the second is a whole murine monoclonal antibody specific for the granulocyte surface NCA-95. The tracers bind to granulocytes located in the abscess as well as to circulating granulocytes and are used for the diagnosis of osteomyelitis and diabetic foot ulcers. Another radiolabelled antibody, ^{99m}Tc -Fanolesomab [320] (LeuTech or Neutrospect), was introduced, which is a murine monoclonal antibody specific to CD-15 receptors on neutrophils for diagnosis of acute appendicitis; however, it was discontinued due to severe cardiopulmonary side effects. Other macromolecular imaging agents include ^{99m}Tc -human-nonspecific IgG, entrapped in the area of inflammation due to increased vascular permeability, as well as the ^{99m}Tc -nanocolloid, extravasated via the capillary basement membrane followed by phagocytosis from the granulocytes and macrophages; however, these agents are not specific for inflammation. None of these agents is specific for infection.

In an effort to develop infection-specific agents, the ^{99m}Tc -labelled fluoroquinolone antibiotic [^{99m}Tc]Tc-ciprofloxacin (Infecton) (Figure 12.22) was introduced into the clinic for the imaging of bacterial infections [321, 322]. Recent work on the structure of

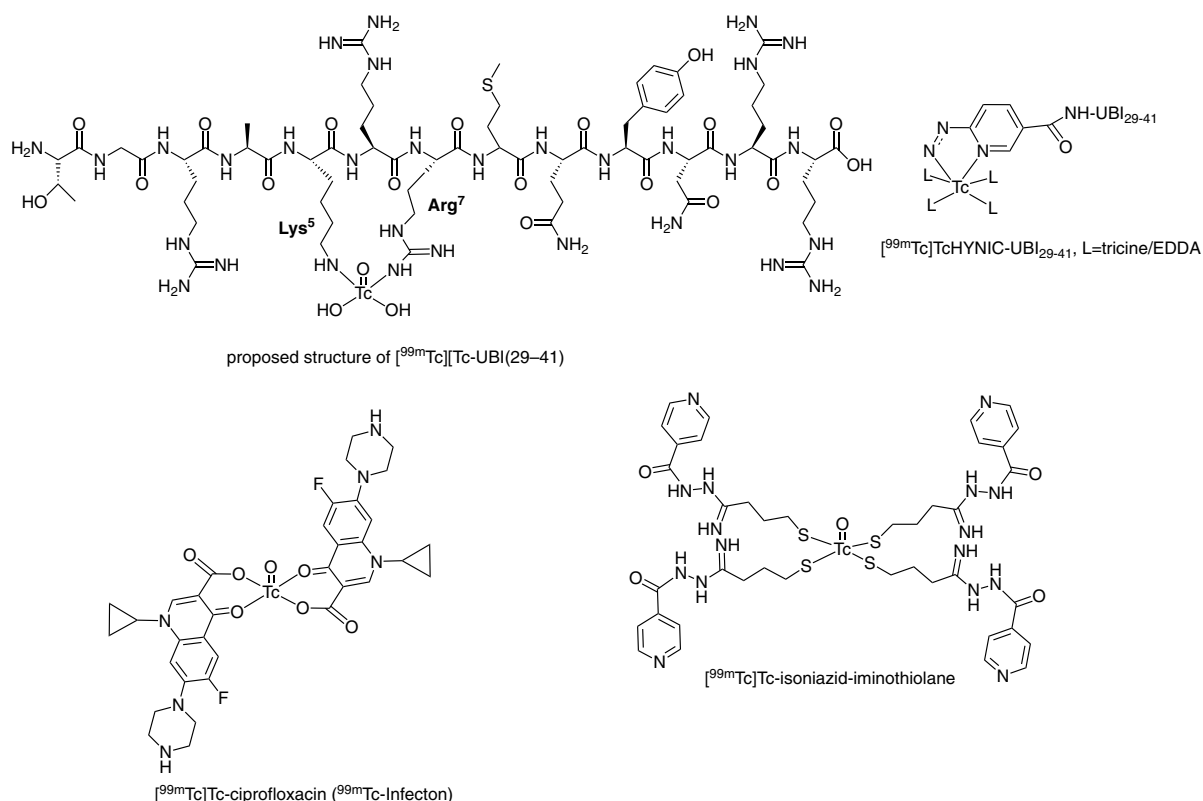


Figure 12.22 Structures of ^{99m}Tc -labelled infection imaging agents.

[^{99m}Tc]Tc-ciprofloxacin indicated that it is an oxotechnetium(V) complex coordinated with two ciprofloxacin molecules that act as O,O bidentate chelator. Similar results were also obtained with the analogous rhenium-ciprofloxacin complex [323]. Although initially, [^{99m}Tc]Tc-ciprofloxacin was considered an infection-specific agent, recent studies revealed accumulation in sterile inflammation as well [324]. In a study that involved the evaluation of both [^{99m}Tc]Tc-ciprofloxacin and [^{99m}Tc]Tc-enrofloxacin for their ability to detect specifically bacterial infections, the ^{99m}Tc-tracers did not demonstrate preferential binding to living bacteria [325]. Using another approach, the fluoroquinolones were derivatized to the respective dithiocarbamate (DTC) and then labelled with nitrodotechnetium, where in the case of norfloxacin-dithiocarbamate (Nfx-DTC), the tracer [^{99m}Tc][TcN(Nfx-DTC)₂] exhibited uptake of 3.43 ± 0.53% ID/g in the infected abscess at four hours *p.i.*, 0.79 ± 0.28% ID/g in the inflammation (turpentine), and high liver and lung uptake [326]. Fluoroquinolones as well as the dithiocarbamate-derivatized fluoroquinolones were also labelled with [^{99m}Tc][Tc(CO)₃]. The tracer [^{99m}Tc][Tc(CO)₃(Ciprofloxacin)] was evaluated in an infection mouse model, where the ratio of infected/noninfected thigh was found to be 3.87:1, while in comparison, it was 3.17:1 for [^{99m}Tc]Tc-ciprofloxacin [327]. The ^{99m}Tc-labelled ciprofloxacin-dithiocarbamate (Cipro-DTC) tracers were evaluated in infected animals *in vivo*, where the abscess uptake was found to be 3.93 ± 0.74% ID/g for [^{99m}Tc][Tc(CO)₃(Cipro-DTC)], 3.21 ± 0.66 for [^{99m}Tc][TcN(Cipro-DTC)₂], and 1.24 ± 0.06 for [^{99m}Tc]Tc-ciprofloxacin at four hours *p.i.* [328].

A number of cephalosporin antibiotics have been labelled with ^{99m}Tc, and of these tracers, [^{99m}Tc]Tc-ceftriaxone was evaluated in infection and inflammation animal models, where the target-to-nontarget ratio was found to be 3.6 for infection and 1.5 for inflammation at four hours *p.i.* This tracer was also evaluated in human skeletal infections, which exhibited a diagnostic accuracy of 83.3%, sensitivity and a specificity of 85.2% and 77.8%, respectively [329].

Antimicrobial peptides, such as the cationic human antimicrobial peptide ubiquicidin, develop electrostatic interactions with negatively charged bacterial membranes, and they have been evaluated in the development of infection-specific radiopharmaceuticals. In particular, the ^{99m}Tc-labelled ubiquicidin fragment UBI 29-41 (Thr-Gly-Arg-Ala-Lys-Arg-Arg-Met-Gln-Tyr-Asn-Arg-Arg) was found to exhibit high binding in gram-positive and -negative bacteria *in vitro*. [^{99m}Tc]Tc-UBI 29-41 (Figure 12.22) shows very high radiochemical yield and stability [330, 331]. The coordination of technetium is postulated to involve the amine nitrogens of lysine and arginine-7, according to theoretical calculations [332, 333]. It exhibited an average infection-to-inflammation ratio of 2.08 ± 0.49, which was superior compared to the respective [⁶⁷Ga]Ga-citrate ratio of 1.14 ± 0.45 [332]. Its bacterial uptake was decreased after pre-treatment of the unlabelled peptide. It exhibits high renal clearance and low hepatobiliary uptake. Clinical trials have proven its ability to detect infection in humans with high sensitivity, selectivity, and accuracy [334]. Furthermore, its binding is proportional to the bacterial number in the infection foci, and therefore it may be suitable to monitor the efficacy and duration of treatment [335]. In patients, ^{99m}Tc-UBI 29-41 has been evaluated in musculoskeletal infections, diabetic foot, and antibiotic treatment monitoring [335, 336]. Furthermore, attempts were made to

develop $[^{99m}\text{Tc}]\text{Tc-HYNIC-UBI}(29-41)$ (Figure 12.22), due to the fact the HYNIC is a well-accepted chelator and could potentially improve the biodistribution and stability of the tracer. The tracer $[^{99m}\text{Tc}]\text{Tc-tricine-HYNIC-UBI}(29-41)$ was suitable for detecting the infection in human patients; however, it exhibited slower blood clearance and similar uptake in the abscess of infected animals in comparison to $[^{99m}\text{Tc}]\text{Tc-UBI}(29-41)$ [333, 337, 338].

The development of a fungal infection-specific imaging agent is also highly desirable, and for this purpose, the tracer $[^{99m}\text{Tc}]\text{Tc-fluconazole}$ was prepared by direct labeling. It was found to be excellent *in vivo* for the detection of *Candida albicans* (T/NT ratio = 3.6 ± 0.47), with low accumulation in bacterial infection (T/NT ratio = 1.3 ± 0.04) and sterile inflammation (lipopolysaccharide: T/NT ratio = 1.4 ± 0.1) in mice [339].

The antitubercular isoniazid (**INH**) was derivatized with 2-iminothiolane and labelled with ^{99m}Tc by the direct method in an effort to develop a tuberculosis-specific imaging agent. The respective tracer $[^{99m}\text{Tc}]\text{Tc-INH-2IT}$ (Figure 12.22) showed promise for tuberculosis imaging in animals, where the lesions were imaged with abscess/muscle ratio of 2:1 at 2 hours *p.i.* and 3.5:1 at 24 hours *p.i.*. Furthermore, this agent was evaluated in human patients and was able to visualize TB lesions [340, 341]. Isoniazid and ethionamide (**ETH**) were conjugated to the cyclopentadienyl (cp) chelator via ligand transfer from the ferrocene analogue and were labelled with $[^{99m}\text{Tc}][\text{Tc}(\text{CO})_3]^+$. The respective tracers $[^{99m}\text{Tc}][\text{Tc}(\text{CO})_3(\text{cp-INH}/\text{cp-ETH})]$ exhibited low uptake in BCG (*Bacillus Calmette-Guérin*) bacterial infection and high liver uptake [342, 343].

12.11 ^{99m}Tc -LABELLED INTERCALATORS FOR THERAPY

Technetium-99m emits, on average, four Auger electrons per decay, and due to this fact, ^{99m}Tc -complexes have been evaluated as radiotherapeutic agents for tumors. Auger electrons have a short range (nm); therefore, in order for the Auger-emitting agent to elicit significant DNA damage, it is required that it possess the ability to accumulate into the nucleus. For this purpose, $[^{99m}\text{Tc}]\text{Tc-tricarbonyl}$ complexes were conjugated to various nuclear intercalators, such as pyrene [344, 345], anthracene [346, 347], acridine orange [348], and doxorubicin [349], and were tested for their ability to enter the cellular nucleus, cause double-strand breaks in circular DNA, and cause cell death. From these efforts, it was shown that the $[^{99m}\text{Tc}]\text{Tc-tricarbonyl-pyrene-NLS}$ tracer conjugated to an NLS (nuclear localization signal) peptide (Figure 12.23) was able to induce cell death in B16 cells by the effect of the Auger electrons emitted by ^{99m}Tc [344]. Similarly, a series of $[^{99m}\text{Tc}]\text{Tc-tricarbonyl}$ complexes conjugated to anthracene (Figure 12.23) were developed, and it was shown that some of these complexes exhibited the ability to target the cell nucleus of B16 cells and induce enhanced cell death by the effect of the technetium's Auger electrons [346, 347]. The $[^{99m}\text{Tc}]\text{Tc-tricarbonyl-dpa-doxorubicin}$ tracer (Figure 12.23) induced cell death in murine cancers [349]. It should be pointed out that the fluorescent Re-tricarbonyl analogues of these ^{99m}Tc -tracers were not always detected in the cell nucleus *in vitro* by fluorescence microscopy, because quenching may occur upon intercalation with DNA [349].

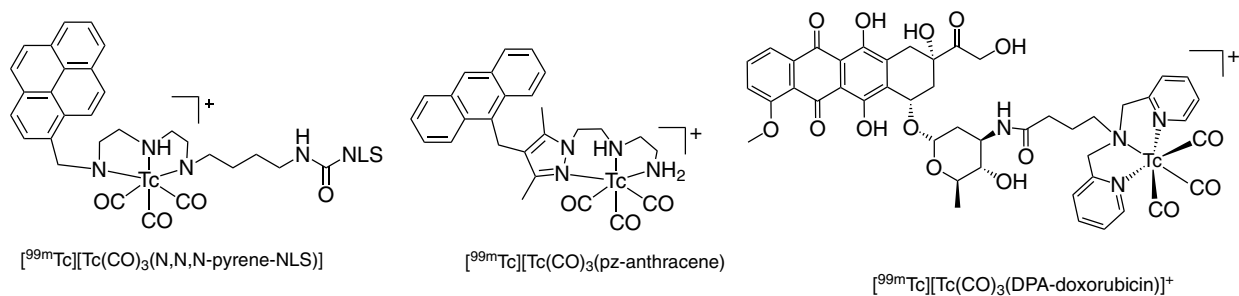


Figure 12.23 Structures of ^{99m}Tc -labelled DNA intercalators.

12.12 CONCLUDING REMARKS

In the previous sections, the literature was reviewed based on the criteria of novelty, established chemistry for the reported tracers, and evidence of biological activity or clinical application. New ^{99m}Tc -labelling methods and chelators were developed, especially in the area of the $[^{99m}\text{Tc}][\text{Tc}(\text{CO})_3]^+$ -complexes. A number of new ^{99m}Tc -based imaging agents developed over the past two decades have shown promise in human patients as, for example, in the detection of gastroenteropancreatic neuroendocrine tumors and the sentinel lymph node. New ^{99m}Tc myocardial and renal agents were developed with advantages over the older radiopharmaceuticals. Many of the ^{99m}Tc -labelled peptides developed are also very attractive, and they may be applied in the clinic in the future. The technetium-99m tricarbonyl complexes were introduced more than 20 years ago as a promising platform for radiopharmaceuticals. It is noteworthy that ^{99m}Tc -Trofolastat is the first technetium-99m tricarbonyl agent currently under clinical trials in phase 3 for prostate cancer imaging in North America. Remarkable efforts were also made in the drug-design of new targeted ^{99m}Tc -probes for estrogen receptors and the beta-amyloid, for example, but also in the development of ^{99m}Tc -labelled glucose derivatives, even though no clinically useful imaging agent has yet emerged.

REFERENCES

1. Francesconi, L.C., Zheng, Y., Bartis, J. et al. (2004). *Inorg. Chem.* 43: 2867–2875.
2. Gali, H., Hoffman, T.J., Sieckman, G.L. et al. (2001). *Bioconjugate Chem.* 12: 354–363.
3. Boschi, A., Bolzati, C., Benini, E. et al. (2001). *Bioconjugate Chem.* 12: 1035–1042.
4. Bolzati, C., Refosco, F., Cagnolini, A. et al. (2004). *Eur. J. Inorg. Chem.* 3: 1902–1913.
5. Meszaros, I.K., Dose, A., Biagini, S.C.G. et al. (2010). *Inorg. Chim. Acta* 363: 1059–1069.
6. Meszaros, I.K., Dose, A., Biagini, S.C.G. et al. (2011). *Dalton Trans.* 40: 6260–6267.
7. Liu, S., Ziegler, M.C., Edwards, D.S. et al. (2000). *Bioconjugate Chem.* 11: 113–117.
8. King, R., Surfraz, M.B.-U., Finucane, C. et al. (2009). *J. Nucl. Med.* 50: 591–598.
9. Pietzsch, H., Gupta, A., Syhre, R. et al. (2001). *Bioconjugate Chem.* 12: 538–544.

10. Seifert, S., Kunstler, J.-U., Schiller, E. et al. (2004). *Bioconjugate Chem.* 15: 856–863.
11. Vitor, R.F., Alves, S., Correia, J.D.G. et al. (2004). *J. Organomet. Chem.* 689: 4764–4774.
12. Banerjee, S.R., Levadala, M.K., Lazarova, N. et al. (2002). *Inorg. Chem.* 41: 6417–6425.
13. Stephenson, K.A., Zubieta, J., Banerjee, S.R. et al. (2004). *Bioconjugate Chem.* 15: 128–136.
14. Maresca, K.P., Marquis, J.C., Hillier, S.M. et al. (2010). *Bioconjugate Chem.* 21: 1032–1042.
15. Schibli, R., La Bella, R., Alberto, R. et al. (2000). *Bioconjugate Chem.* 11: 345–351.
16. van Staveren, D.R., Mundwiler, S., Hoffmanns, U. et al. (2004). *Org. Biomol. Chem.* 2: 2593–2603.
17. Mindt, T.L., Struthers, H., Brans, L. et al. (2006). *J. Am. Chem. Soc.* 128: 15096–15097.
18. Mindt, T.L., Muller, C., Stuker, F. et al. (2009). *Bioconjugate Chem.* 20: 1940–1949.
19. Van Staveren, D.R., Benny, P.D., Waibel, R. et al. (2005). *Helv. Chim. Acta* 88 (3): 447–460.
20. He, H., Morley, J.E., Twamley, B. et al. (2009). *Inorg. Chem.* 48 (22): 10625–10634.
21. Makris, G., Karagiorgou, O., Papagiannopoulou, D.P. et al. (2012). *Eur. J. Inorg. Chem.* 2012: 3132–3139.
22. He, Z., Hsieh, W.-Y., Kim, Y.-S. et al. (2006). *Nucl. Med. Biol.* 33: 1045–1053.
23. Triantis, C., Tsoதாகos, T., Tsoukalas, C. et al. (2013). *Inorg. Chem.* 52: 12995–13003.
24. Ferreira, C.L., Bayly, S.R., Green, D.E. et al. (2006). *Bioconjugate Chem.* 17: 1321–1329.
25. Riondato, M., Camporese, D., Martín, D. et al. (2005). *Eur. J. Inorg. Chem.* 2005: 4048–4055.
26. Gorshkov, N.I., Schibli, R., Schubiger, A.P. et al. (2004). *J. Organomet. Chem.* 689: 4757–4763.
27. Yazdani, A., Janzen, N., Banevicius, L. et al. (2015). *Inorg. Chem.* 54: 1728–1736.
28. Zelenka, K., Borsig, L., and Alberto, R. (2011). *Org. Biomol. Chem.* 9: 1071–1078.
29. Ellis, B.L., Gorshkov, N.I., Lumpov, A. et al. (2013). *J. Labelled Compd. Radiopharm.* 56: 700–707.
30. Waibel, R., Alberto, R., Willuda, J. et al. (1999). *Nat. Biotechnol.* 17: 897–901.
31. Badar, A., Williams, J., de Rosales, R.T. et al. (2014). *EJNMMI Res.* 4: 14.
32. Hofström, C., Orlova, A., Altai, M. et al. (2011). *J. Med. Chem.* 54: 3817–3826.
33. Wenzel, M. (1992). *J. Labelled Compd. Radiopharm.* 31: 641–650.
34. Saidi, M., Seifert, S., Kretzschmar, M. et al. (2004). *J. Organomet. Chem.* 689: 4739–4744.
35. Masi, S., Top, S., Boubekeur, L. et al. (2004). *Eur. J. Inorg. Chem.* 2004: 2013–2017.
36. Peindy N'Dongo, H.W., Liu, Y., Can, D. et al. (2009). *J. Organomet. Chem.* 694: 981–987.
37. Liu, Y., Spingler, B., Schmutz, P. et al. (2008). *J. Am. Chem. Soc.* 130: 1554–1555.
38. Causey, P.W., Besanger, T.R., and Valliant, J.F. (2008). *J. Med. Chem.* 51: 2833–2844.
39. Boschi, A., Bolzati, C., Uccelli, L. et al. (2002). *Nucl. Med. Commun.* 23: 689–693.
40. Boschi, A., Uccelli, L., Bolzati, C. et al. (2003). *J. Nucl. Med.* 44: 806–814.
41. Hatada, K., Riou, L.M., Ruiz, M. et al. (2004). *J. Nucl. Med.* 45: 2095–2101.
42. Bolzati, C., Cavazza-Ceccato, M., Agostini, S. et al. (2008). *J. Nucl. Med.* 49: 1336–1344.
43. Fang, W., Liu, Y., Zhu, L. et al. (2008). *Nucl. Med. Commun.* 29: 775–781.

44. Liu, S., He, Z., Hsieh, W.-Y. et al. (2006). *Nucl. Med. Biol.* 33: 419–432.
45. Kim, Y.-S., Wang, J., Broisat, A. et al. (2008). *J. Nucl. Cardiol.* 15: 535–546.
46. Kim, Y.-S., Shi, J., Zhai, S. et al. (2009). *J. Nucl. Cardiol.* 16: 571–579.
47. Hao, G.Y., Zang, J.Y., Zhu, L. et al. (2004). *J. Labelled Compd. Radiopharm.* 47: 513–521.
48. Liu, S. (2007). *Dalton Trans.* 0: 1183–1193.
49. Liu, Z., Chen, L., Liu, S. et al. (2010). *J. Nucl. Cardiol.* 17: 858–867.
50. Maria, L., Cunha, S., Videira, M. et al. (2007). *Dalton Trans.* 0: 3010–3019.
51. Maria, L., Fernandes, C., Garcia, R. et al. (2009). *Dalton Trans.* 0: 603–606.
52. Goethals, L.R., Santos, I., Caveliers, V. et al. (2011). *Contrast Media Mol. Imaging* 6: 178–188.
53. Mendes, F., Gano, L., Fernandes, C. et al. (2012). *Nucl. Med. Biol.* 39: 207–213.
54. Santos, I., Fernandes, C., Maria, L. et al. (2014). *J. Organomet. Chem.* 760: 138–148.
55. Jung, C.M., Kraus, W., Leibnitz, P. et al. (2002). *Eur. J. Inorg. Chem.* 2002: 1219–1225.
56. Maresca, K.P., Shoup, T.M., Femia, F.J. et al. (2002). *Inorg. Chim. Acta* 338: 149–156.
57. Magata, Y., Kawaguchi, T., Ukon, M. et al. (2004). *Bioconjugate Chem.* 15: 389–393.
58. Cazzola, E., Benini, E., Pasquali, M. et al. (2008). *Bioconjugate Chem.* 19: 450–460.
59. Mathur, A., Subramanian, S., Mallia, M.B. et al. (2008). *Bioorg. Med. Chem.* 16: 7927–7931.
60. Mathur, A., Malslia, M.B., Sarma, H.D. et al. (2011). *J. Labelled Compd. Radiopharm.* 54: 150–156.
61. Walther, M., Jung, C.M., Bergmann, R. et al. (2007). *Bioconjugate Chem.* 18: 216–230.
62. Heintz, A.C., Jung, C.M., Stehr, S.N. et al. (2007). *Nucl. Med. Commun.* 28: 637–645.
63. Mirtschink, P., Stehr, S.N., Pietzsch, H.J. et al. (2008). *Bioconjugate Chem.* 19: 97–108.
64. Mirtschink, P., Stehr, S.N., Walther, M. et al. (2009). *Nucl. Med. Biol.* 36: 833–843.
65. Mirtschink, P., Stehr, S.N., Walther, M. et al. (2009). *Nucl. Med. Biol.* 36: 845–852.
66. Lee, B.C., Kim, D.H., Lee, J.H. et al. (2007). *Bioconjugate Chem.* 18: 1332–1337.
67. Uehara, T., Uemura, T., Hirabayashi, S. et al. (2007). *J. Med. Chem.* 50: 543–549.
68. Lee, B.C., Kim, D.H., Lee, I. et al. (2008). *J. Med. Chem.* 51: 3630–3634.
69. Zeng, H. and Zhang, H. (2014). *S. Eur. J. Med. Chem.* 72: 10–17.
70. Liu, J., Wang, S., Wang, H. et al. (2017). *J. Radioanal. Nucl. Chem.* 312: 543–555.
71. Liu, J., Wang, H., Wang, S. et al. (2017). *J. Labelled Compd. Radiopharm.* 60: 250–262.
72. Heibold, I., Drews, A., Syhre, R. et al. (2002). *Eur. J. Nucl. Med.* 29: 82–87.
73. Drews, A., Pietzsch, H., Syhre, R. et al. (2002). *Nucl. Med. Biol.* 29: 389–398.
74. Heibold, I., Drews, A., Kretzschmar, M. et al. (2002). *Nucl. Med. Biol.* 29: 375–387.
75. Papagiannopoulou, D., Pirmettis, I., Maina, T.P. et al. (2001). *J. Biol. Inorg. Chem.* 6: 256–265.
76. Papagiannopoulou, D., Pirmettis, I., Tsoukalas, C. et al. (2002). *Nucl. Med. Biol.* 29: 825–832.
77. Leon, A., Rey, A., Mallo, L. et al. (2002). *Nucl. Med. Biol.* 29: 217–226.
78. Fernandes, C., Correia, J.D.G., Gano, L. et al. (2005). *Bioconjugate Chem.* 16: 660–668.
79. Bolzati, C., Salvatore, N., Carta, D. et al. (2011). *J. Biol. Inorg. Chem.* 16: 137–155.
80. Chiotellis, A., Tsoukalas, C., Pelecanou, M. et al. (2012). *Appl. Radiat. Isot.* 70: 957–964.
81. Zhang, X., Zhou, P., Liu, J. et al. (2007). *Appl. Radiat. Isot.* 65: 287–292.

82. Garcia, R., Gano, L., Maria, L.P. et al. (2006). *J. Biol. Inorg. Chem.* 11: 769–782.
83. Saied, N.M., Mejri, N., El Aissi, R. et al. (2015). *Eur. J. Med. Chem.* 97: 280–288.
84. Serdons, K., Verduyck, T., Cleynhens, J. et al. (2007). *Bioorg. Med. Chem. Lett.* 17: 6086–6090.
85. Lin, K.S., Debnath, M.L., Mathis, C.A. et al. (2009). *Bioorg. Med. Chem. Lett.* 19: 2258–2262.
86. Pan, J., Mason, N.S., Debnath, M.L. et al. (2013). *Bioorg. Med. Chem. Lett.* 23: 1720–1726.
87. Chen, X., Yu, P., Zhang, L. et al. (2008). *Bioorg. Med. Chem. Lett.* 18: 1442–1445.
88. Zhang, X., Hou, Y., Peng, C. et al. (2018). *J. Med. Chem.* 61: 1330–1339.
89. Zhang, X., Yu, P., Yang, Y. et al. (2016). *Bioconjugate Chem.* 27: 2493–2504.
90. Sagnou, M., Tzanopoulou, S., Raptopoulou, C.P. et al. (2012). *Eur. J. Inorg. Chem.* 2012: 4279–4286.
91. Jia, J., Cui, M., Dai, J. et al. (2014). *Med. Chem. Commun.* 5: 153–158.
92. Jia, J., Cui, M., Dai, J. et al. (2015). *Dalton Trans.* 44: 6406–6415.
93. Jia, J., Zhou, K., Dai, J. et al. (2016). *Eur. J. Med. Chem.* 124: 763–772.
94. Ono, M., Fuchi, Y., Fuchigami, T. et al. (2010). *ACS Med. Chem. Lett.* 1: 443–447.
95. Wang, X., Cui, M., Yu, P. et al. (2012). *Bioorg. Med. Chem. Lett.* 22: 4327–4331.
96. Wang, X., Cui, M., Jia, J. et al. (2015). *Eur. J. Med. Chem.* 89: 331–339.
97. Iikuni, S., Ono, M., Tanimura, K. et al. (2017). *RSC Adv.* 7: 20582–20590.
98. Ono, M., Ikeoka, R., Watanabe, H. et al. (2010). *ACS Chem. Neurosci.* 1: 598–607.
99. Ono, M., Ikeoka, R., Watanabe, H. et al. (2010). *Bioorg. Med. Chem. Lett.* 20: 5743–5748.
100. Yang, Y., Zhu, L., Cui, M. et al. (2010). *Bioorg. Med. Chem. Lett.* 20: 5337–5344.
101. Li, Z., Cui, M., Dai, J. et al. (2013). *J. Med. Chem.* 56: 471–482.
102. Sagnou, M., Benaki, D., Triantis, C. et al. (2011). *Inorg. Chem.* 50: 1295–1303.
103. Yang, Y., Cui, M., Jin, B. et al. (2013). *Eur. J. Med. Chem.* 64: 90–98.
104. He, H., Lipowska, M., Xu, X. et al. (2007). *Inorg. Chem.* 46: 3385–3394.
105. Lipowska, M., He, H., Malveaux, E. et al. (2006). *J. Nucl. Med.* 47: 1032–1040.
106. He, H., Lipowska, M., Christoforou, A.M. et al. (2007). *Nucl. Med. Biol.* 34: 709–716.
107. Lipowska, M., Marzilli, L.G., and Taylor, A.T. (2009). *J. Nucl. Med.* 50: 454–460.
108. Taylor, A.T., Lipowska, M., and Marzilli, L.G. (2010). *J. Nucl. Med.* 51: 391–396.
109. Taylor, A.T., Lipowska, M., and Cai, H. (2013). *J. Nucl. Med.* 54: 578–584.
110. Klenc, J., Lipowska, M., Taylor, A.T. et al. (2012). *Eur. J. Inorg. Chem.* 2012: 4334–4341.
111. Lipowska, M., Klenc, J., Folks, R.D. et al. (2014). *Nucl. Med. Mol. Imaging* 48: 216–224.
112. Verbeke, K., Rozenski, J., Cleynhens, B. et al. (2002). *Bioconjugate Chem.* 13: 16–22.
113. Ogawa, K., Mukai, T., Inoue, Y. et al. (2006). *J. Nucl. Med.* 47: 2042–2047.
114. Palma, E., Oliveira, B.L., Correia, J.D.G. et al. (2007). *J. Biol. Inorg. Chem.* 12: 667–679.
115. Palma, E., Correia, J.D.G., Oliveira, B.L. et al. (2011). *Dalton Trans.* 40: 2787–2796.
116. Fernandes, C., Monteiro, S., Mendes, P. et al. (2014). *J. Organomet. Chem.* 760: 197–204.
117. Torres Martin de Rosales, R., Finucane, C., Mather, S.J. et al. (2009). *Chem Commun.* 3: 4847–4849.

118. Makris, G., Tseligka, E.D., Pirmettis, I. et al. (2016). *Mol. Pharmaceutics* 13: 2301.
119. Reubi, J.C., Wenger, S., Schmuckli-Maurer, J. et al. (2002). *Clin. Cancer Res.* 8: 1139–1146.
120. de Wiele, C., Dumont, F., Vanden Broecke, R. et al. (2000). *Eur. J. Nucl. Med.* 27: 1694–1699.
121. Varvarigou, A., Scopinaro, F., Leondiadis, L. et al. (2002). *Cancer Biother. Radiopharm.* 17: 317–326.
122. Scopinaro, F., Varvarigou, A., Ussof, W. et al. (2002). *Cancer Biother. Radiopharm.* 17: 327–325.
123. La Bella, R., Garcia-Garayoa, E., Bähler, M. et al. (2002). *Bioconjugate Chem.* 13: 599–604.
124. García Garayoa, E., Rüegg, D., Bläuenstein, P. et al. (2007). *Nucl. Med. Biol.* 34: 17–28.
125. García-Garayoa, E., Schweinsberg, C., Maes, V. et al. (2007). *Q J. Nucl. Med. Mol. Imaging* 51: 42–50.
126. García Garayoa, E., Schweinsberg, C., Maes, V. et al. (2000). *Bioconjugate Chem.* 19: 2409–2416.
127. Däpp, S., García, E., Maes, V. et al. (2011). *Nucl. Med. Biol.* 38: 997–1009.
128. Brans, L., Maes, V., García-Garayoa, E. et al. (2008). *Chem. Biol. Drug. Des.* 72: 496–506.
129. Schweinsberg, C., Maes, V., Brans, L. et al. (2008). *Bioconjugate Chem.* 19: 2432–2439.
130. La Bella, R., Garcia-Garayoa, E., Langer, M. et al. (2002). *Nucl. Med. Biol.* 29: 553–560.
131. Mindt, T.L., Struthers, H., Spingler, B. et al. (2010). *ChemMedChem* 5: 2026–2038.
132. Brans, L., García-Garayoa, E., Schweinsberg, C. et al. (2010). *ChemMedChem* 5: 1717–1725.
133. Smith, C.J., Sieckman, G.L., Owen, N.K. et al. (2003). *Cancer Res.* 63: 4082–4088.
134. Alves, S., Correia, J.D.G., Santos, I.V. et al. (2006). *Nucl. Med. Biol.* 33: 625–634.
135. Lane, S.R., Veerendra, B., Rold, T.L. et al. (2008). *Nucl. Med. Biol.* 35: 263–272.
136. Lin, K.-S., Luu, A., Baidoo, K.E. et al. (2004). *Bioconjugate Chem.* 15: 1416–1423.
137. Lin, K.-S., Luu, A., Baidoo, K.E. et al. (2005). *Bioconjugate Chem.* 16: 43–50.
138. Nock, B., Nikolopoulou, A., Chiotellis, E. et al. (2003). *Eur. J. Nucl. Med. Mol. Imaging* 30: 247–258.
139. Nock, B.A., Nikolopoulou, A., Galanis, A. et al. (2005). *J. Med. Chem.* 48: 100–110.
140. Mather, S.J., Nock, B.A., Maina, T. et al. (2014). *Mol. Imaging Biol.* 16: 888–895.
141. Nock, B.A., Cescato, R., Ketani, E. et al. (2012). *J. Med. Chem.* 55: 8364–8374.
142. Marsouvanidis, P.J., Maina, T., Sallegger, W. et al. (2013). *J. Nucl. Med.* 54: 1797–1803.
143. Ferro-flores, G., Arteaga de Murphy, C., Rodriguez-Cortes, J.P. et al. (2006). *Nucl. Med. Commun.* 27: 371–376.
144. Ananias, H.J.K., Yu, Z., Dierckx, R.A. et al. (2011). *Mol. Pharmaceutics* 8: 1165–1173.
145. Ananias, H.J.K., Yu, Z., Hoving, H.D. et al. (2013). *Nucl. Med. Biol.* 40: 933–938.
146. Yu, Z., Carlucci, G., Ananias, H.J.K. et al. (2013). *Amino Acids* 44: 543–553.
147. Decristoforo, C., Jane, K., and Stephen, J. (2000). *J. Nucl. Med.* 41: 1114–1119.
148. Bangard, M., Béhé, M., Gohlke, S. et al. (2000). *Eur. J. Nucl. Med. Mol. Imaging*

- 27: 628–637.
149. Decristoforo, C., Mather, S.J., Cholewinski, W.D. et al. (2000). *Eur. J. Nucl. Med.* 27: 1318–1325.
 150. Dong, C., Zhao, H., Yang, S. et al. (2013). *Mol. Pharmaceutics* 10: 2925–2933.
 151. Maina, T., Nock, B., Nikolopoulou, A. et al. (2002). *Eur. J. Nucl. Med.* 29: 742–753.
 152. Decristoforo, C., Maina, T., Nock, B. et al. (2003). *Eur. J. Nucl. Med. Mol. Imaging* 30: 1211–1219.
 153. Maina, T., Nock, B.A., Cordopatis, P. et al. (2006). *Eur. J. Nucl. Med. Mol. Imaging* 33: 831–840.
 154. Nikolopoulou, A., Maina, T., Sotiriou, P. et al. (2006). *J. Pept. Sci.* 12: 124–131.
 155. Bigott-Hennkens, H.M., Junnotula, S., Ma, L. et al. (2008). *J. Med. Chem.* 51: 1223–1230.
 156. Dannoon, S.F., Bigott-Hennkens, H.M., Ma, L. et al. (2010). *Nucl. Med. Biol.* 37: 527–537.
 157. Bigott-Hennkens, H.M., Dannoon, S.F., Noll, S.M. et al. (2011). *Nucl. Med. Biol.* 38: 549–555.
 158. Radford, L., Gallazzi, F., Watkinson, L. et al. (2017). *Nucl. Med. Biol.* 47: 4–9.
 159. Banerjee, S.R., Foss, C.a., Castanares, M. et al. (2008). *J. Med. Chem.* 51: 4504–4517.
 160. Maresca, K.P., Hillier, S.M., Lu, G. et al. (2012). *Inorg. Chim. Acta* 389: 168–175.
 161. Lu, G., Maresca, K.P., Hillier, S.M. et al. (2013). *Bioorg. Med. Chem. Lett.* 23: 1557–1563.
 162. Kimura, H., Sampei, S., Matsuoka, D. et al. (2016). *Bioorg. Med. Chem.* 24: 2251–2256.
 163. Hillier, S.M., Maresca, K.P., Lu, G.L. et al. (2013). *J. Nucl. Med.* 54: 1369–1376.
 164. Vallabhajosula, S., Nikolopoulou, A., Babich, J.W. et al. (2014). *J. Nucl. Med.* 55: 1791–1798.
 165. Goffin, K.E., Joniau, S., Tenke, P. et al. (2017). *J. Nucl. Med.* 58: 1408–1413.
 166. Reinfelder, J., Kuwert, T., Beck, M. et al. (2017). *Clin. Nucl. Med.* 42: 26–33.
 167. Banerjee, S.R., Pullambhatla, M., Foss, C.a. et al. (2013). *J. Med. Chem.* 56: 6108–6121.
 168. Ferro-Flores, G., Luna-Gutiérrez, M., Ocampo-García, B. et al. (2017). *Nucl. Med. Biol.* 48: 36–44.
 169. Xu, X., Zhang, J., Hu, S. et al. (2017). *Nucl. Med. Biol.* 48: 69–75.
 170. Kampmeier, F., Williams, J.D., Maher, J. et al. (2014). *EJNMMI Res.* 4: 1–10.
 171. Nawaz, S., Mullen, G.E.D., Blower, P.J. et al. (2017). *Nucl. Med. Commun.* 38: 666–671.
 172. Su, Z.-F., Liu, G., Gupta, S. et al. (2002). *Bioconjugate Chem.* 13: 561–570.
 173. Su, Z.-F., He, J., Rusckowski, M. et al. (2003). *Nucl. Med. Biol.* 30: 141–149.
 174. Liu, B., Feng, Y., Zhang, J.-Y. et al. (2013). *Transl. Res.* 162: 174–180.
 175. Liu, S., Edwards, D.S., Ziegler, M.C. et al. (2001). *Bioconjugate Chem.* 12: 624–629.
 176. Janssen, M., Oyen, W.J.G., Massuger, L.F.A.G. et al. (2002). *Cancer Biother. Radiopharm.* 17: 641–646.
 177. Liu, S., Hsieh, W.Y., Jiang, Y. et al. (2007). *Bioconjugate Chem.* 18: 438–446.
 178. Shi, J., Wang, L., Kim, Y.-S. et al. (2008). *J. Med. Chem.* 51: 7980–7990.

179. Wang, L., Shi, J., Kim, Y.-S. et al. (2009). *Mol. Pharmaceutics* 6: 231–245.
180. Huang, C., Zheng, Q., and Miao, W. (2015). *Nucl. Med. Commun.* 36: 1208–1214.
181. Zhang, H., Gao, S., Chen, B. et al. (2016). *Oncol. Lett.* 12: 2517–2523.
182. Jin, X., Liang, N., Wang, M. et al. (2016). *Radiology* 281: 958–966.
183. Shao, G., Gu, W., Guo, M. et al. (2017). *Oncotarget* 8: 75587–75596.
184. Zhao, D., Jin, X., Li, F. et al. (2012). *J. Nucl. Med.* 53: 1872–1877.
185. Ji, S., Czerwinski, A., Zhou, Y. et al. (2013). *Mol. Pharmaceutics* 10: 3304–3314.
186. Xu, D., Zhao, Z.-Q., Chen, S.T. et al. (2017). *Nucl. Med. Biol.* 48: 1–8.
187. Shi, J., Wang, L., Kim, Y.-S. et al. (2009). *Eur. J. Nucl. Med. Mol. Imaging* 36: 1874–1884.
188. Shi, J., Kim, Y.-S., Chakraborty, S. et al. (2009). *Bioconjugate Chem.* 20: 1559–1568.
189. Liu, Z., Jia, B., Shi, J.J. et al. (2010). *Bioconjugate Chem.* 21: 548–555.
190. Zhou, Y., Kim, Y.-S., Lu, X. et al. (2012). *Bioconjugate Chem.* 23: 586–595.
191. Ji, S., Zhou, Y., Shao, G. et al. (2013). *Bioconjugate Chem.* 24: 701–711.
192. Yang, Y., Ji, S., and Liu, S. (2014). *Bioconjugate Chem.* 25: 1720–1729.
193. Zhao, Z.-Q., Yang, Y., Fang, W. et al. (2016). *Nucl. Med. Biol.* 43: 661–669.
194. Decristoforo, C., Faintuch-Linkowski, B., Rey, A. et al. (2006). *Nucl. Med. Biol.* 33: 945–952.
195. Decristoforo, C., Santos, I., Pietzsch, H.J. et al. (2007). *Q J. Nucl. Med. Mol. Imaging* 51: 33–41.
196. Fani, M., Psimadas, D., Zikos, C. et al. (2006). *Anticancer Res.* 26: 431–434.
197. Psimadas, D., Fani, M., Gourni, E. et al. (2012). *Bioorg. Med. Chem.* 20: 2549–2557.
198. Alves, S., Correia, J.D.G., Gano, L. et al. (2007). *Bioconjugate Chem.* 18: 530–537.
199. Tsiapa, I., Loudos, G., Varvarigou, A. et al. (2013). *Nucl. Med. Biol.* 40: 262–272.
200. Tsiapa, I., Loudos, G., Fragogeorgi, E.A. et al. (2014). *Cancer Biother. Radiopharm.* 29: 444–450.
201. Indrevoll, B., Kindberg, G.M., Solbakken, M. et al. (2006). *Bioorg. Med. Chem. Lett.* 16: 6190–6193.
202. Bach-Gansmo, T., Danielsson, R., Saracco, A. et al. (2006). *J. Nucl. Med.* 47: 1434–1439.
203. Lee, B.C., Sung, H.J., Kim, J.S. et al. (2007). *Bioorg. Med. Chem.* 15: 7755–7764.
204. Jung, K.-H., Lee, K.-H., Paik, J.-Y. et al. (2006). *J. Nucl. Med.* 47: 2000–2007.
205. Sancey, L., Ardisson, V., Riou, L.M. et al. (2007). *Eur. J. Nucl. Med. Mol. Imaging* 34: 2037–2047.
206. Giblin, M.F., Wang, N., Hoffman, T.J. et al. (1998). *Proc. Natl. Acad. Sci. U.S.A* 95: 12814–12818.
207. Chen, J., Cheng, Z., Hoffman, T.J. et al. (2000). *Cancer Res.* 60: 5649–5658.
208. Miao, Y., Whitener, D., Feng, W. et al. (2003). *Bioconjugate Chem.* 14: 1177–1184.
209. Miao, Y., Benwell, K., and Quinn, T.P. (2007). *J. Nucl. Med.* 48: 73–80.
210. Yang, J., Guo, H., and Miao, Y. (2010). *Nucl. Med. Biol.* 37: 873–883.
211. Yang, J., Guo, H., Gallazzi, F. et al. (2009). *Bioconjugate Chem.* 20: 1634–1642.
212. Yang, J., Guo, H., Padilla, R.S. et al. (2010). *Bioorganic. Med. Chem.* 18: 6695–6700.

213. Yang, J., Lu, J., and Miao, Y. (2012). *Mol. Pharmaceutics* 9: 1418–1424.
214. Flook, A.M., Yang, J., and Miao, Y. (2014). *J. Med. Chem.* 57: 9010–9018.
215. Flook, A.M., Yang, J., and Miao, Y. (2013). *J. Med. Chem.* 56: 8793–8802.
216. Flook, A.M., Yang, J., and Miao, Y. (2013). *Mol. Pharmaceutics* 10: 3417–3424.
217. Yang, J. and Miao, Y. (2012). *Bioorg. Med. Chem. Lett.* 22: 1541–1545.
218. Raposinho, P.D., Xavier, C., Correia, J.D.G. et al. (2008). *J. Biol. Inorg. Chem.* 13: 449–459.
219. Guo, H., Gallazzi, F., and Miao, Y. (2013). *Mol. Pharmaceutics* 10: 1400–1408.
220. Guo, H. and Miao, Y. (2014). *J. Nucl. Med.* 55: 2057–2063.
221. Liu, L., Xu, J., Yang, J. et al. (2016). *Bioorg. Med. Chem. Lett.* 26: 4724–4728.
222. Liu, L., Xu, J., and Yang, J. (2017). *Bioorg. Med. Chem. Lett.* 27: 4952–4955.
223. Raposinho, P.D., Correia, J.D.G., Alves, S. et al. (2008). *Nucl. Med. Biol.* 35: 91–99.
224. Jiang, H., Kasten, B.B., Liu, H. et al. (2012). *Bioconjugate Chem.* 23: 2300–2312.
225. Kasten, B.B., Ma, X., Liu, H. et al. (2014). *Bioconjugate Chem.* 25: 579–592.
226. García-Garayoa, E., Allemann-Tannahill, L., Bläuenstein, P. et al. (2001). *Nucl. Med. Biol.* 28: 75–84.
227. Bruehlmeier, M., Garayoa, E.G., Blanc, A. et al. (2002). *Nucl. Med. Biol.* 29: 321–327.
228. Bläuenstein, P., Garayoa, E.G., Rüegg, D. et al. (2004). *Cancer Biother. Radiopharm.* 19: 181–188.
229. Maes, V., Garcia-Garayoa, E., Bläuenstein, P. et al. (2006). *J. Med. Chem.* 49: 1833–1836.
230. Buchegger, F., Bonvin, F., Kosinski, M. et al. (2003). *J. Nucl. Med.* 44: 1649–1654.
231. Nock, B.A., Nikolopoulou, A., Reubi, J.-C. et al. (2006). *J. Med. Chem.* 49: 4767–4776.
232. Maina, T., Nikolopoulou, A., Stathopoulou, E. et al. (2007). *Eur. J. Nucl. Med. Mol. Imaging* 34: 1804–1814.
233. Gabriel, M., Decristoforo, C., Wöll, E.E. et al. (2011). *Cancer Biother. Radiopharm.* 26: 557–563.
234. von Guggenberg, E., Behe, M., Behr, T.M. et al. (2004). *Bioconjugate Chem.* 15: 864–871.
235. von Guggenberg, E., Dietrich, H., Skvortsova, I. et al. (2007). *Eur. J. Nucl. Med. Mol. Imaging* 34: 1209–1218.
236. Nock, B.A., Maina, T., Béhé, M. et al. (2005). *J. Nucl. Med.* 46: 1727–1736.
237. Kaloudi, A., Nock, B.A., Lymperis, E. et al. (2016). *Nucl. Med. Biol.* 43: 347–354.
238. von Guggenberg, E., Sallegger, W., Helbok, A. et al. (2009). *J. Med. Chem.* 52: 4786–4793.
239. Aloj, L., Panico, M., Caraco, C. et al. (2004). *Cancer Biother. Radiopharm.* 19: 93–98.
240. Agostini, S., Bolzati, C., Didonè, E. et al. (2007). *J. Pept. Sci.* 13: 211–219.
241. Mathias, C.J., Hubers, D., Low, P.S. et al. (2000). *Bioconjugate Chem.* 11: 253–257.
242. Trump, D.P., Mathias, C.J., Yang, Z. et al. (2002). *Nucl. Med. Biol.* 29: 569–573.
243. Leamon, C.P., Parker, M.A., Vlahov, I.R. et al. (2002). *Bioconjugate Chem.* 13: 1200–1210.
244. Maurer, A.H., Elsinga, P., Fanti, S. et al. (2014). *J. Nucl. Med.* 55: 701–704.

245. Müller, C., Dumas, C., Hoffmann, U. et al. (2004). *J. Organomet. Chem.* 689 (25 SPEC. ISS.): 4712–4721.
246. Müller, C., Hohn, A., Schubiger, P.A. et al. (2006). *Eur. J. Nucl. Med. Mol. Imaging* 33: 1007–1016.
247. Müller, C., Brühlmeier, M., Schubiger, P.A. et al. (2006). *J. Nucl. Med.* 47: 2057–2064.
248. Müller, C., Schubiger, P.A., and Schibli, R. (2006). *Bioconjugate Chem.* 17: 797–806.
249. Mindt, T.L., Müller, C., Melis, M. et al. (2008). *Bioconjugate Chem.*: 1689–1695.
250. Kim, W.H., Kim, C.G., Kim, M.H. et al. (2016). *Ann. Nucl. Med.* 30: 369–379.
251. Panwar, P., Shrivastava, V., Tandon, V. et al. (2004). *Cancer Biol. Ther.* 3: 995–1001.
252. Mishra, G., Hazari, P.P., Kumar, N. et al. (2011). *J. Drug Targeting* 19: 761–769.
253. Jeannine, P., Roger, S., Cécile, D. et al. (2001). *Chem.–A Eur. J.* 7: 1868–1873.
254. Dumas, C., Schibli, R., and Schubiger, P.A. (2003). *J. Org. Chem.* 68: 512–518.
255. Dumas, C., Petrig, J., Frei, L. et al. (2005). *Bioconjugate Chem.* 16: 421–428.
256. Schibli, R., Dumas, C., Petrig, J. et al. (2005). *Bioconjugate Chem.* 16: 105–112.
257. Dapuelto, R., Castelli, R., Fernández, M. et al. (2011). *Bioorg. Med. Chem. Lett.* 21: 7102–7106.
258. Bayly, S.R., Fisher, C.L., Storr, T. et al. (2004). *Bioconjugate Chem.* 15: 923–926.
259. Storr, T., Obata, M., Fisher, C.L. et al. (2004). *Chem.–A Eur. J.* 11: 195–203.
260. Bowen, M.L., Chen, Z.-F., Roos, A.M. et al. (2009). *Dalton Trans.* 0: 9228–9236.
261. Bowen, M.L., Lim, N.C., Ewart, C.B. et al. (2009). *Dalton Trans.* 0: 9216–9227.
262. Storr, T., Sugai, Y., Barta, C.A. et al. (2005). *Inorg. Chem.* 44: 2698–2705.
263. Storr, T., Fisher, C.L., Mikata, Y. et al. (2005). *Dalton Trans.* 0: 654–655.
264. Ferreira, C.L., Ewart, C.B., Bayly, S.R. et al. (2006). *Inorg. Chem.* 45: 6979–6987.
265. Ferreira, C.L., Marques, F.L.N., Okamoto, M.R.Y. et al. (2010). *Appl. Radiat. Isot.* 68: 1087–1093.
266. Fernández, S., Crócamo, N., Incerti, M. et al. (2012). *J. Labelled Compd. Radiopharm.* 55: 274–280.
267. Yang, D.J., Kim, C.-G., Schechter, N.R. et al. (2003). *Radiology* 226: 465–473.
268. Yang, D., Yukihiro, M., Yu, D. et al. (2004). *Cancer Biother. Radiopharm.* 19: 443–456.
269. Schechter, N.R., Erwin, W.D., Yang, D.J. et al. (2009). *Eur. J. Nucl. Med. Mol. Imaging* 36: 1583–1591.
270. Chen, Y., Wen Huang, Z., He, L. et al. (2006). *Appl. Radiat. Isot.* 64: 342–347.
271. Seidensticker, M., Ulrich, G., Muehlberg, F.L. et al. (2014). *Mol. Imaging Biol.* 16: 189–198.
272. Jun Oh, S., Ryu, J.-S., Yoon, E.-J. et al. (2006). *Appl. Radiat. Isot.* 64 (2): 207–215.
273. Brasileiro, C.B., da Fonseca Pacheco, C.M., Queiroz-Junior, C.M. et al. (2010). *Appl. Radiat. Isot.* 68 (12): 2261–2267.
274. Welling, M.M. and Alberto, R. (2010). *Nucl. Med. Commun.* 31: 239.
275. Chen, X., Li, L., Liu, F. et al. (2006). *Bioorg. Med. Chem. Lett.* 16: 5503–5506.
276. de Barros, A.L.B., Cardoso, V.N., Mota, L. et al. (2009). *Bioorg. Med. Chem. Lett.* 19: 2497–2499.
277. de Barros, A.L.B., Cardoso, V.N., Mota, L. et al. (2010). *Bioorg. Med. Chem. Lett.* 20: 2478–2480.

278. Liu, L., Zhao, M., Wang, Z. et al. (2014). *J. Radioanal. Nucl. Chem.* 301: 731–737.
279. Liu, T., Gan, Q., Zhang, J. et al. (2016). *Med. Chem. Commun.* 7: 1381–1386.
280. Schibli, R., Netter, M., Scapozza, L. et al. (2003). *J. Organomet. Chem.* 668: 67–74.
281. Stichelberger, M., Desbouis, D., Spiwok, V. et al. (2007). *J. Organomet. Chem.* 692: 1255–1264.
282. Desbouis, D., Schubiger, P.a., Schibli, R. et al. (2007). *J. Organomet. Chem.* 692: 1340–1347.
283. Desbouis, D., Struthers, H., Spiwok, V. et al. (2008). *J. Med. Chem.* 51: 6689–6698.
284. Struthers, H., Spingler, B., Mindt, T.L. et al. (2008). *Chem.–A Eur. J.* 14: 6173–6183.
285. Struthers, H., Hagenbach, A., Abram, U. et al. (2009). *Inorg. Chem.* 48: 5154–5163.
286. Struthers, H., Viertl, D., Kosinski, M. et al. (2010). *Bioconjugate Chem.* 21: 622–634.
287. Bartholomä, M., Vortherms, A.R., Hillier, S. et al. (2010). *ChemMedChem* 5: 1513–1529.
288. Bartholomä, M.D., Vortherms, A.R., Hillier, S. et al. (2011). *Dalton Trans.* 40: 6216–6225.
289. Celen, S., de Groot, T., Balzarini, J. et al. (2007). *Nucl. Med. Biol.* 34: 283–291.
290. Wüst, F., Carlson, K.E., Katzenellenbogen, J.A. et al. (1998). *Steroids* 63: 665–671.
291. Luyt, L.G., Bigott, H.M., Welch, M.J. et al. (2003). *Bioorg. Med. Chem.* 11: 4977–4989.
292. Neto, C., Oliveira, M.C., Gano, L.M. et al. (2012). *J. Inorg. Biochem.* 111: 1–9.
293. Arterburn, J.B., Corona, C., Rao, K.V. et al. (2003). *J. Org. Chem.* 68: 7063–7070.
294. Ramesh, C., Bryant, B., Nayak, T. et al. (2006). *J. Am. Chem. Soc.* 128: 14476–14477.
295. Nayak, T.K., Hathaway, H.J., Ramesh, C. et al. (2008). *J. Nucl. Med.* 49: 978–986.
296. Skaddan, M.B., Wuest, F.R., and Katzenellenbogen, J.A. (1999). *J. Org. Chem.* 64: 8108–8121.
297. Huang, L., Zhu, H., Zhang, Y. et al. (2010). *Steroids* 75: 905–911.
298. Xia, X., Feng, H., Li, C. et al. (2016). *Nucl. Med. Biol.* 43: 89–96.
299. Jaouen, G., Top, S., Vessières, A. et al. (2001). *Chem. Commun.* 0: 383–384.
300. Top, S., Vessières, A., Pigeon, P. et al. (2004). *ChemBioChem* 5: 1104–1113.
301. Mull, E.S., Sattigeri, V.J., Rodriguez, A.L. et al. (2002). *Bioorg. Med. Chem.* 10: 1381–1398.
302. Bigott, H.M., Parent, E., Luyt, L.G. et al. (2005). *Bioconjugate Chem.* 16: 255–264.
303. Kunze, S., Zobi, F., Kurz, P. et al. (2004). *Angew. Chem. Int. Ed. Engl.* 43: 5025–5029.
304. Mundwiler, S., Waibel, R., Spingler, B. et al. (2005). *Nucl. Med. Biol.* 32: 473–484.
305. van Staveren, D.R., Waibel, R., Mundwiler, S. et al. (2004). *J. Organomet. Chem.* 689: 4803–4810.
306. Waibel, R., Treichler, H., Schaefer, N.G. et al. (2008). *Cancer Res.* 68: 2904–2911.
307. Sah, B.-R., Schibli, R., Waibel, R. et al. (2014). *J. Nucl. Med.* 55: 43–49.
308. Vera, D.R., Wallace, A.M., and Hoh, C.K. (2001). *Nucl. Med. Biol.* 28: 493–498.
309. Vera, D.R., Wallace, a.M., Hoh, C.K. et al. (2001). *J. Nucl. Med.* 42: 951–959.
310. Wallace, A.M., Han, L.K., Povoski, S.P. et al. (2013). *Ann. Surg. Oncol.* 20: 2590–2599.
311. Azad, A.K., Rajaram, M.V.S., Metz, W.L. et al. (2015). *J. Immunol.* 195: 2019.
312. Morais, M., Subramanian, S., Pandey, U. et al. (2011). *Mol Pharm.* 8: 609–620.
313. Pirmettis, I., Arano, Y., Tsoதாக, T. et al. (2012). *Mol. Pharmaceutics* 9: 1681–1692.

314. Yamaguchi, A., Hanaoka, H., Pirmettis, I. et al. (2015). *Mol. Pharmaceutics* 12: 514–519.
315. Núñez, E.G.F., de Oliveira, E.A., da Silva, N.G. et al. (2012). *Nucl Med Biol.* 39: 145–153.
316. Khan, I.U., Shahid, A., Ahmad, F. et al. (2014). *Ann. Nucl. Med.* 28: 248–256.
317. Giglio, J., Fernández, S., Jentschel, C. et al. (2013). *Cancer Biother. Radiopharm.* 28: 541–551.
318. Takagi, K., Uehara, T., Kaneko, E. et al. (2004). *Nucl. Med. Biol.* 31: 893–900.
319. Jeong, J.M., Hong, M.K., Kim, Y.J. et al. (2004). *Nucl. Med. Commun.* 25: 1211–1217.
320. Love, C., Tronco, G.G., and Palestro, C.J. (2006). *Q J. Nucl. Med. Mol. Imaging* 50: 113–120.
321. Britton, K.E., Vinjamuri, S., Hall, A.V. et al. (1997). *Eur. J. Nucl. Med.* 24: 553–556.
322. Vinjamuri, S., Hall, a.V., Solanki, K.K. et al. (1996). *Lancet* 347: 233–235.
323. Lecina, J., Cortés, P., Llagostera, M. et al. (2014). *Bioorg. Med. Chem.* 22: 3262–3269.
324. Sarda, L., Cre, A., Lebellec, Y. et al. (2015). *J. Nucl. Med.* 44: 920–927.
325. Siaens, R.H., Rennen, H.J., Boerman, O.C. et al. (2004). *J. Nucl. Med.* 45 (12): 2088–2095.
326. Zhang, S., Zhang, W., Wang, Y. et al. (2011). *Bioconjugate Chem.* 22: 369–375.
327. Halder, K.K., Nayak, D.K., Baishya, R. et al. (2011). *Metallomics* 3: 1041.
328. Zhang, J., Zhang, S., Guo, H. et al. (2010). *Bioorg. Med. Chem. Lett.* 20: 3781–3784.
329. Kaul, A., Hazari, P.P., Rawat, H. et al. (2018). *Int. J. Infect Dis.* 17: e263–e270.
330. Welling, M.M., Paulusma-Annema, A., Balter, H.S. et al. (2000). *Eur. J Nucl. Med.* 27: 292–301.
331. Welling, M.M., Mongera, S., Lupetti, A. et al. (2002). *Nucl. Med. Biol.* 29: 413–422.
332. Ferro-Flores, G., Arteaga De Murphy, C., Pedraza-López, M. et al. (2003). *Nucl. Med. Biol.* 30: 597–603.
333. Meléndez-Alafort, L., Ramírez, F.D.M., Ferro-Flores, G. et al. (2003). *Nucl. Med. Biol.* 30: 605–615.
334. Akhtar, M.S., Qaisar, A., Irfanullah, J. et al. (2005). *J. Nucl. Med.* 46: 567–573.
335. Akhtar, M.S., Imran, M.B., Nadeem, M.A. et al. (2012). *Int. J. Pept.* 2012: 19.
336. Bunschoten, A., Welling, M.M., Termaat, M.F. et al. (2013). *Bioconjugate Chem.* 24: 1971–1989.
337. Gandomkar, M., Najafi, R., Shafiei, M. et al. (2009). *Nucl. Med. Biol.* 36: 199–205.
338. Welling, M.M., Visentin, R., Feitsma, H.I.J. et al. (2004). *Nucl. Med. Biol.* 31: 503–509.
339. Lupetti, A., Welling, M.M., Mazzi, U. et al. (2002). *Eur. J. Nucl. Med. Mol. Imaging* 29: 674–679.
340. Singh, A.K., Verma, J., Bhatnager, A.S. et al. (2003). *World J. Nucl. Med.* 2 (4): 292–305.
341. Singh, N. and Bhatnagar, A. (2009). *Afr. J. Pharm. Pharmacol.* 3: 110–119.
342. Essouissi, I., Saied, N.M., Bernard, S. et al. (2012). *Radiochim. Acta* 100: 207–214.
343. Essouissi, I., Saied, N.M., Mejri, N. et al. (2014). *J. Radioanal. Nucl. Chem.* 300: 987–996.
344. Haefliger, P., Agorastos, N., Renard, A. et al. (2005). *Bioconjugate Chem.* 16: 582–587.

345. Häfliger, P., Agorastos, N., Spingler, B. et al. (2005). *ChemBioChem* 6: 414–421.
346. Vitor, R.F., Correia, I., Videira, M. et al. (2008). *ChemBioChem* 9: 131–142.
347. Vitor, R.F., Esteves, T., Marques, F. et al. (2009). *Cancer Biother. Radiopharm.* 24: 551–563.
348. Agorastos, N., Borsig, L., Renard, A. et al. (2007). *Chem.–A Eur. J.* 13: 3842–3852.
349. Imstepf, S., Pierroz, V., Raposinho, P. et al. (2015). *Bioconjugate Chem.* 26: 2397–2407.

PART IV

Practical Aspects of Radiopharmaceutical Production and Use

Chapter 13

Automated Synthesis Modules for PET Radiochemistry

Laura Bruton and Peter J.H. Scott

*Department of Radiology, University of Michigan, Ann Arbor, MI,
48109, USA*

13.1 INTRODUCTION

The recent approval of several radiopharmaceuticals for positron emission tomography (**PET**) imaging by the United States Food and Drug Administration (**FDA**) and other regulatory agencies around the world has led to increases in annual PET scan numbers [1]. For example, millions of PET scans are now conducted in the US every year [2] and the increased demand for access to short-lived PET radiopharmaceuticals has created a corresponding need for more efficient means for their production. For some radiochemistry facilities, this requires the production of very large batches of one radiopharmaceutical for distribution (see, for example, [3]), while other facilities need to produce multiple different research radiopharmaceuticals using a single synthesis module (for recent examples, see [4–7]). The field of radiochemistry is thus constantly evolving to meet the needs for increased starting amounts of radioactivity, and in the last couple of decades it has seen a move from manual radiochemistry to the use of automated synthesis modules (for reviews of new developments, see [8, 9]) supported by sophisticated software programs [10]. These modules are enclosed in hot cells and controlled by a computer

Handbook of Radiopharmaceuticals: Methodology and Applications, Second Edition.

Edited by Michael R. Kilbourn and Peter J.H. Scott.

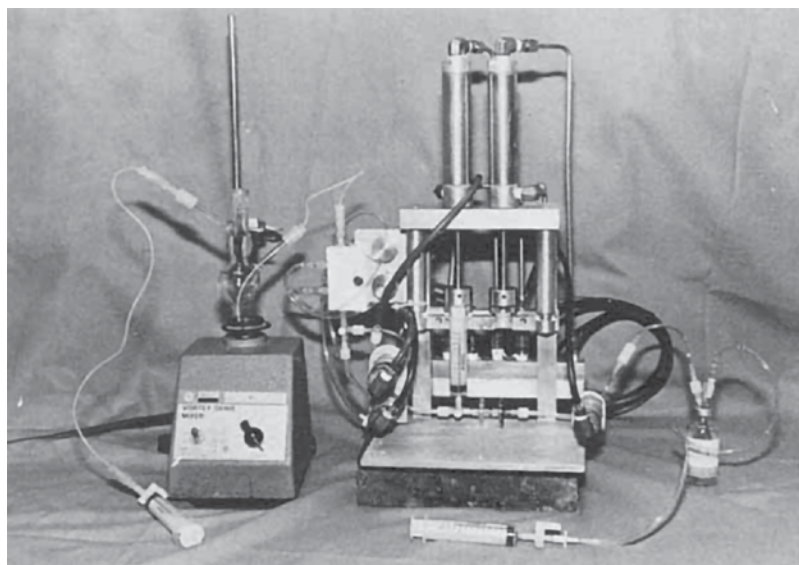
© 2021 John Wiley & Sons Ltd. Published 2021 by John Wiley & Sons Ltd.

from the outside, either using a preprogrammed synthesis sequence (*timelist*) that is executed manually or totally under computer control. The modules are configured for the synthesis and the hot cell is sealed in advance of delivery of radioactivity, thus significantly decreasing worker exposure. Radiochemistry synthesis modules need to be able to deliver doses at a fast pace while maintaining compliance with radiation safety requirements, especially when handling the very large amounts of radioactivity that some facilities use today [3]. The daily synthesis and delivery of PET radiopharmaceuticals create challenges for such systems, including short preparation times, compliance with pharmaceutical quality procedures, reproducibility, and reliability. Through the years, radiochemistry synthesis modules have changed with the increasing pressure of these standards. Compared to the early days of manually operated and hard-wired systems, modern computer-controlled radiopharmaceutical synthesis modules are more advanced in terms of automation, efficiency, and radiochemical yields, as well as the ability to meet the increased demands of FDA-mandated current Good Manufacturing Practice (**cGMP**). This chapter provides an overview of radiopharmaceutical synthesis modules from the homemade systems used in early PET centers when the first edition of this book was published (2002) through to the new modules used today and concludes with thoughts on future directions for the field.

13.2 EARLY RADIOCHEMISTRY SYNTHESIS MODULES

The early radiopharmaceutical synthesis modules (for example, Figure 13.1) were hard-wired systems where valves, fluid movements through lines, gas flows, and temperature

Figure 13.1 A traditional homemade radiochemistry module. Source: Reprinted with permission from Welch et al. 1983 [11], copyright John Wiley and Sons.



changes (heating and cooling) were controlled by manually activated electrical switches that were located externally to lead shielding placed around the module [11]. If physical movement of items was required, this could be done using the manipulator arms of a hot cell. As automation was introduced in the 1980s, the components of the synthesis apparatus began to be controlled using programmable logic controllers and, eventually, small computers; a unique intermediary application was the use of a computer-controlled robot to interact with, and control, an array of work stations that accomplished the individual steps of a complex radiochemical synthesis (Figure 13.2) [12].

By 1990, automated modules were increasingly common in many PET facilities. This was mainly due to the manufacturing and reimbursement approval for [^{18}F]fluorodeoxyglucose ([^{18}F]FDG), which was granted in the USA by the FDA and the Centers for Medicare and Medicaid (**CMS**), respectively. As FDG was the most important PET radiopharmaceutical that needed to be synthesized, there was a move to automate this process (see [13]). Many PET facilities acquired a Coincidence FDG synthesizer (Figure 13.3), which had been commercially released in late 1998; that module was later acquired by General Electric (**GE**) and rebranded as the TRACERlab MX_{FDG} [14]. The module introduced an important new concept: the use of sterile, disposable, pre-assembled synthesis pathways and reagents (termed *kits*) dedicated to single radiopharmaceutical syntheses, such as [^{18}F]FDG. In the following years, GE and a number of third-party companies including Advanced Biochemicals (**ABX**) and Rotem Industries offered (and continue to offer) kits for making different radiopharmaceuticals on the TRACERlab MX_{FDG}, including [^{18}F]FDG, [^{18}F]NaF, [^{18}F]F-L-DOPA, [^{18}F]fluoroethyltyrosine, and [^{18}F]fluorothymidine. While the synthesis module is somewhat dated at this point, because of its very large install base, it continues to be utilized extensively worldwide, and new reports of use of the TRACERlab MX_{FDG} for the syntheses of radiopharmaceuticals such as [^{18}F]fluoromisonidazole [15],

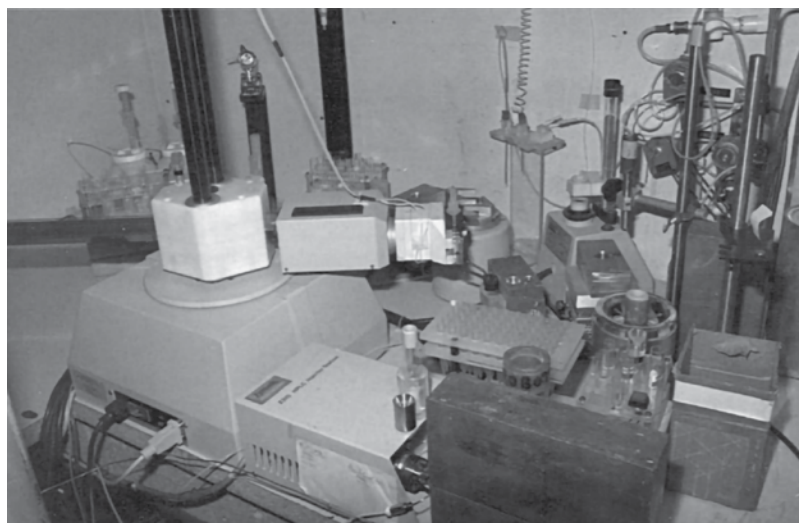


Figure 13.2 An early radiochemistry module run using a computer-controlled robot. Source: Reprinted with permission from Brodack et al. 1988 [12], copyright Elsevier.

Figure 13.3 Early TRACERlab MX_{FDG} cassette-based synthesis module. Source: Image courtesy of GE.



[¹⁸F]fluoromethylcholine [16], [¹⁸F]PSMA-1007 [17, 18], and [¹⁸F]fluoroestradiol [19] continue to be published. Most recently, with the increasing popularity of PET studies using gallium-68 [20, 21], use of the TRACERlab MX module for synthesizing ⁶⁸Ga-labelled tracers has also been disclosed [22].

13.3 MODERN CASSETTE-BASED MODULES

The design and development of synthesis modules have continued to evolve, leading to the improved and more versatile modules that are in use today. For example, in the late 2000s, it became mandatory to prepare PET radiopharmaceuticals for clinical use according to cGMP. Building on lessons learned with early cassette-based systems such as the TRACERlab MX_{FDG} and incorporating cGMP principles, new features such as real-time control, use of information from sensors in pre-run diagnostics, post-run troubleshooting, trend analysis, and process documentation were introduced. For example, GE refined the TRACERlab MX into the FASTlab and, more recently, FASTlab 2 (Figure 13.4a); other modules that have evolved from the TRACERlab MX include the NEPTIS (Figure 13.4b) and the Trasis AllinOne (Figure 13.4c) platforms. Cassette-based module systems were also introduced by Siemens (Explora), IBA (Synthera), and Scintomics (GRP Series). Similar to the TRACERlab MX, this new generation of synthesis modules was primarily developed for the preparation of [¹⁸F]FDG, as it remains the most widely used PET radiopharmaceutical. To improve the control and use of the cassettes used with these modules, they are frequently labeled with a barcode that, when read by the computer, relays information as to which synthesis program should be executed. The use of single-use cassettes is attractive from a cGMP perspective because it eliminates the need for cleaning validation studies [23] and reduces errors during setup and operation. The use of these preconfigured sterile cassettes also enables quick transitions between

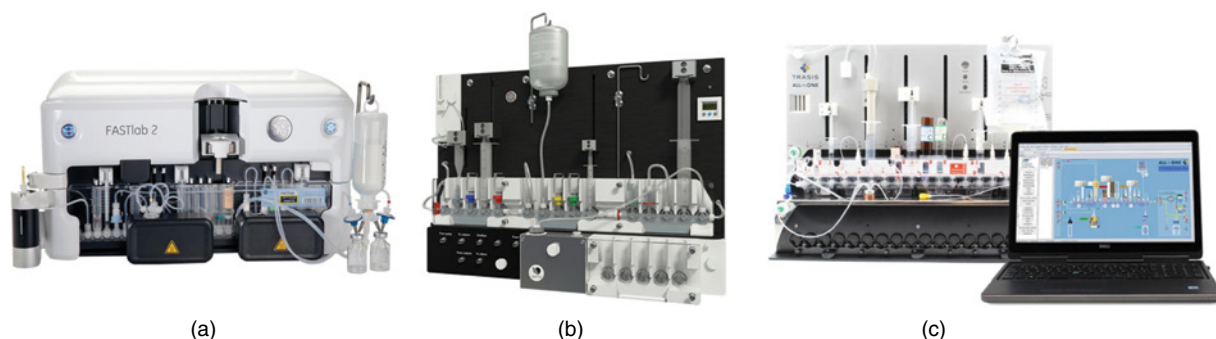


Figure 13.4 Cassette-based synthesis modules. (a) GE FASTlab 2. Source: Image courtesy of GE Healthcare. (b) NEPTIS Perform. Source: Image courtesy of Optimized Radiochemical Applications (ORA). (c) Trasis AllinOne. Source: Image courtesy of Trasis.

syntheses. A common theme with all of these new synthesis modules is that they have been designed to address the challenges of a modern radiochemistry laboratory. Conscious of the space limitations many facilities have, manufacturers have designed many of these new modules in a compact size that allows two (or more) units to fit inside a single mini-cell. Moreover, cassettes have been developed for these new modules that include reagents and cartridges for multiple syntheses of a radiopharmaceutical (e.g. FDG), enabling repeated batches to be prepared without the need to open a hot cell between syntheses [24]. In addition to [^{18}F]FDG, cassettes for these modules are also commercially available for the production of other commonly used radiopharmaceuticals. Alternatively, many of the systems can be adapted to prepare other radiotracers through the use of customizable cassettes, most often for the preparation of ^{18}F -labeled radiopharmaceuticals [4, 5]; custom cassettes have also been developed for products labeled with other radionuclides, such as gallium-68 [25].

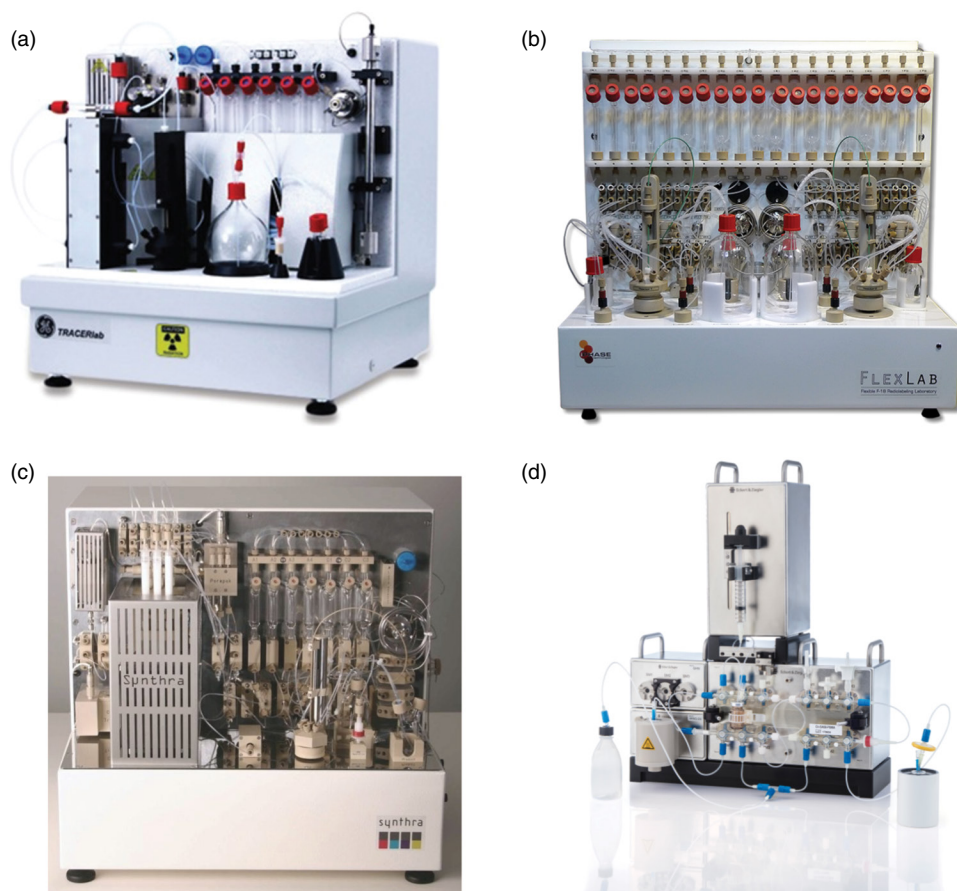
13.4 FULLY AUTOMATED FIXED-TUBING MODULES

The development of new PET radiopharmaceuticals is a very active area of research. Whereas cassette-based modules have become the industry standard for routine daily production of established PET radiopharmaceuticals such as [^{18}F]FDG, they are not always suitable for the synthesis of new PET radiopharmaceuticals. For example, the majority of the modules have limited temperature and pressure tolerances due to the fittings, valves, and materials used to manufacture the cassettes. The systems are usually designed for liquid-phase chemistry (^{68}Ga and ^{18}F ion reactions) and often not compatible with gas-phase chemistry (e.g. ^{11}C). In addition, many modules have only one reaction vessel, which prohibits the synthesis of probes that need multi-reactor protocols (e.g. tracers prepared using radio-click chemistry; see [26]); however, newer systems such as the GE FASTlab 2 and Trasis AllinOne have two reaction vessels, which potentially allow the automation of

more complex chemistry. For the most part, though, cassette-based systems are somewhat limited in how much they can be reconfigured for novel radiochemistry, and new chemistry tends to be developed on fully automated fixed-tubing modules such as the GE TRACERlab FX series (Figure 13.5a), iPhase MultiSyn systems (Figure 13.5b), Synthra radiopharmaceutical synthesizers (Figure 13.5c), and Eckert & Ziegler Modular-Labs (Figure 13.5d). There are systems available for conducting liquid-phase chemistry with [^{18}F]fluoride (e.g. [6, 27, 28]) as well as gas-phase chemistry with [^{11}C]CO₂ or [^{11}C]CH₄ [7]. Recent reports have also demonstrated compatibility with ^{68}Ga [29].

The new fully automated synthesis modules (Figure 13.5) have gradually replaced the early homemade remote systems (Figures 13.1 and 13.2). These synthesis modules contain multiple interconnected parts, including modules for receiving radioactivity from a cyclotron (or generator); the synthesis component, which typically contains one or more reaction vessels and a heater; a vacuum pump for evaporating solvents; a semi-preparative high-performance liquid chromatography (HPLC) purification system; and a module for the reformulation of the purified radiopharmaceutical into a solution suitable for

Figure 13.5 Fully automated fixed-tubing modules. (a) GE TRACERlab. Source: Image courtesy of GE. (b) iPhase F-18 Flex-Lab. Source: Image courtesy of iPhase Technologies. (c) PET radiosynthesizer. Source: Image courtesy of Synthra GMBH. (d) Modular-Lab. Source: Image courtesy of Eckert & Ziegler.



intravenous injection. These fixed-tubing machines are housed in hot cells and controlled by a computer from outside, with a preprogrammed computerized timelist executed manually or under full computer control. A radiotracer-specific program (Figure 13.6) controls every step of the synthesis, from setting the parameters of the reaction (e.g. time, temperature) to the addition of reagents and solvents, purification, reformulation, and delivery of the final product to a sterile vial. During the synthesis, information from numerous components and detectors is sent to the interactive computer, allowing radiochemists to see data such as temperature and pressure measurements in real time, as well as track, trend, and troubleshoot syntheses after completion.

These synthesis modules are often provided by vendors with programs for preparing standard radiolabeling precursors (e.g. [^{11}C]MeI, [^{11}C]MeOTf) as well as established radiotracers, and such radiosyntheses are often accomplished using the basic configuration of the module. However, we and others have also shown that such modules can be easily reconfigured for different applications, including gas-phase reactions [30] and loop chemistry [31, 32]. The basic module configuration is typically designed for the production of radiopharmaceuticals requiring HPLC purification but can be modified to incorporate purification by Sep-Pak cartridge (e.g. [^{18}F]NaF, [^{11}C]carfetanil, etc.) or a reformulation step when using non-injectable HPLC mobile phases. By way of example, in 2011, our group reported the synthesis of 7 ^{18}F -labeled radiotracers and 12 ^{11}C -labeled radiotracers using the TRACERlab FX platform [6, 7].

After a synthesis is completed, the module has to be cleaned and disinfected before the next radiosynthesis. This is done by resetting the module to its basic configuration, cleaning with sterile water, disinfecting with ethanol, and drying with acetone; the process takes approximately 20 minutes. The time needed for cleaning and reset of the modules, and possibly a cleaning validation [23], should be planned for, especially in a smaller lab setting. The need to open hot cells between syntheses to clean and reconfigure modules also potentially increases radioactivity exposure to staff. Moreover, although these systems can be reconfigured for different tracers, to maintain reproducible production conditions (and compliance with cGMP), constant reconfiguration is not always ideal. The need for more flexible automation that matches the increasing demand for the development of radiopharmaceuticals has led to the development of the new hybrid modules and microfluidic systems discussed next.

13.5 HYBRID MODULES

To overcome the limited nature of the cassette-based systems and the impact of reconfiguring fixed-tubing modules on a routine basis, hybrid modules have been developed. These modules aim to combine the simplicity of cassette-based systems with the ability to handle high pressures and temperatures. For example, the Sofie Biosciences ELIXYS FLEX/CHEM (Figure 13.7) offers a three-reactor design suitable for both synthesis development and routine production and is capable of accommodating complex multipot radiochemistry [33–35]. The cassettes for this module include the fluidic paths and various reagent vial sizes, which enables a large number of probes to be produced within

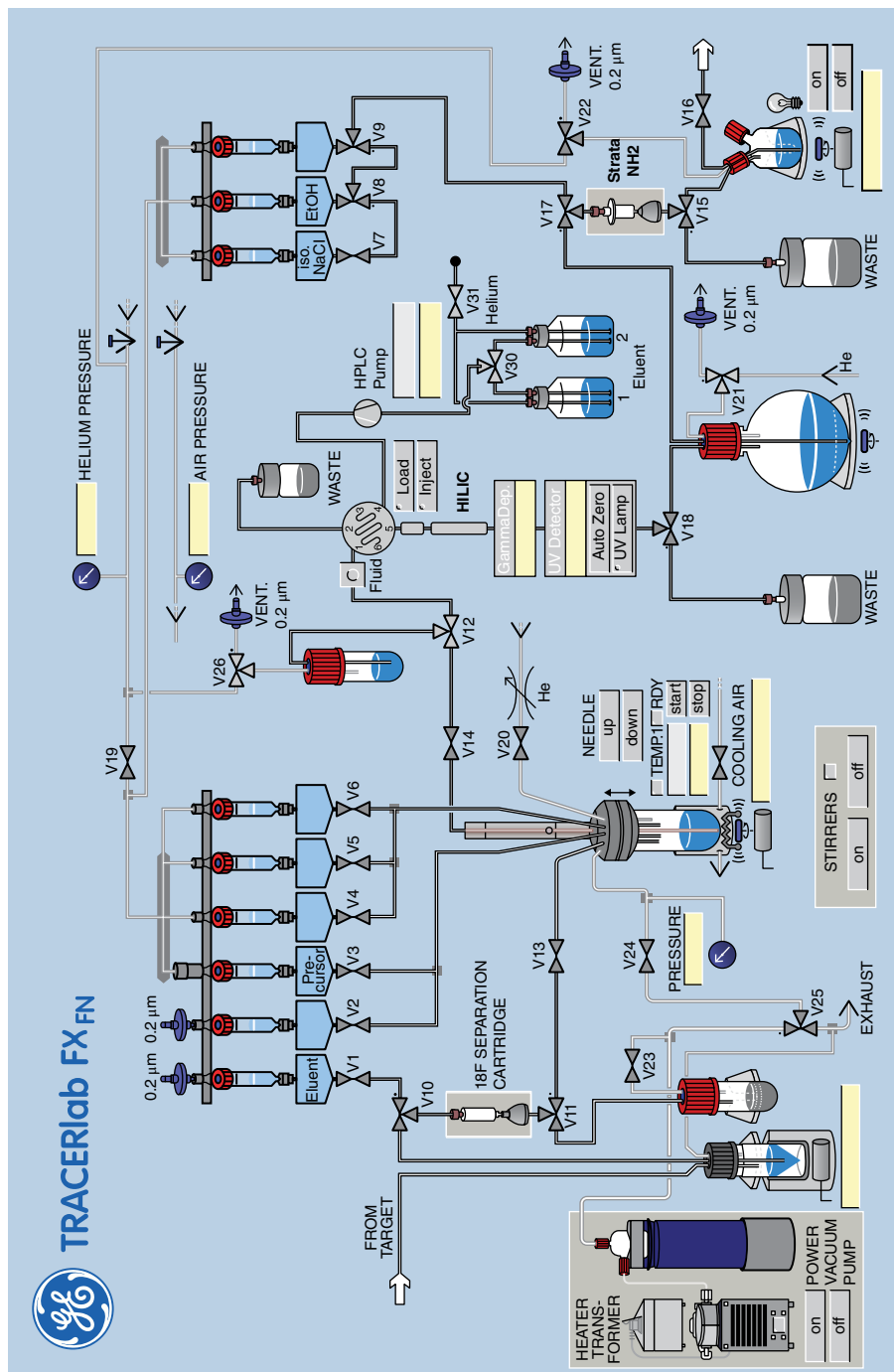


Figure 13.6 Computer program for running a TRACERlab synthesis module. Source: Image courtesy of GE Healthcare.

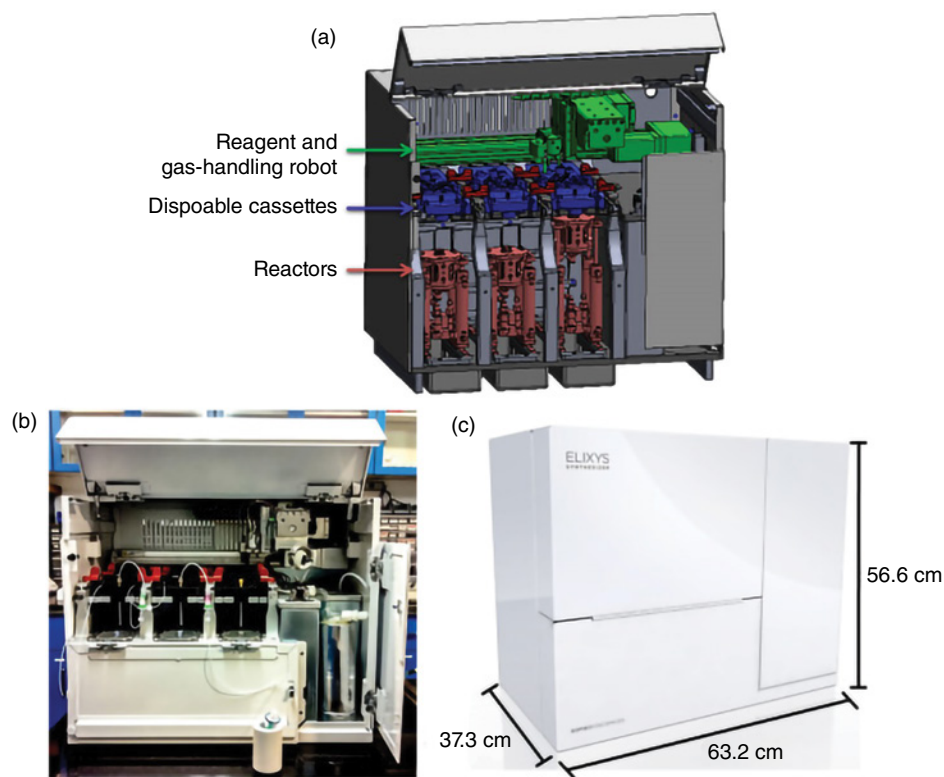


Figure 13.7 ELIXYS hybrid synthesizer. Source: (a) Lazari, M., Quinn, K.M., Claggett, S.B. et al., [33]. Under a creative Commons License (<https://creativecommons.org/licenses/by/2.0/>).

the same module. The only changes between syntheses are the reagents, program, and purification cartridges, as well as a small number of connections between the cassettes. The ELIXYS module also provides access to the reaction vessel, giving the radiochemist the ability to take intermediate measurements while eliminating the need for large numbers of valves: the decreased number of fittings and valves increases module reliability. These features enable the production and development of multiple syntheses in a single system and hot cell, thus requiring less space in smaller lab settings.

The ELIXYS FLEX/CHEM allows for automation without operator intervention up to the final purification step, as this module does not support integrated HPLC purification and formulation; this can, however, be automated by incorporating a separate ELIXYS PURE/FORM module. Cleaning of this latter system is necessary unless disposable cassettes are used as intended. In a recent report, Collins' et al. used ELIXYS FLEX/CHEM to produce 24 different ^{18}F -labeled radiopharmaceuticals and prosthetic groups, showcasing the utility of the hybrid synthesis module in the field [4]. A hybrid system such as ELIXYS therefore has great utility for laboratories that perhaps just have space and/or funding for a single synthesis module but want to be able to conduct both routine production of established radiopharmaceuticals and development of new radiotracers.

13.6 MICROFLUIDIC SYSTEMS

Many of the traditional radiochemistry synthesis modules described in this chapter use a single fluid bus architecture in conjunction with stopcock valve manifold(s), in which every fluid runs through parts of the central pathway, and many have been designed for the express purpose of manufacturing [^{18}F]FDG. However, as stated earlier, there is a need for a more flexible radiopharmaceutical synthesis platform that is compatible with different levels of radioactivity (single dose-on-demand production or multidose batches) as well as a variety of radionuclides and/or radiopharmaceuticals, and that can fit into the space confines of a typical radiochemistry laboratory with only one or two hot cells. In addition to the fixed-tubing modules described in this chapter, significant work has also been undertaken to develop microfluidic approaches for radiopharmaceutical manufacturing (for recent examples, see [36–84]), as well as purification/reformulation [85]. Microfluidic devices have been used to manufacture radiopharmaceuticals for clinical use [86–89], but continuing challenges have limited their commercialization and transition into widespread use [90]. The reasons for the slow uptake are numerous and depend on the particular application, but include (i) cost, (ii) the lack of affordable components due to dependence on specialized chips, and (iii) challenges with the *macro-to-micro interface* (incompatibility between microfluidic volumes [$\leq 0.05\text{ ml}$] and the typical “large-scale” volumes used in cyclotrons and radiopharmaceutical dosing [$\geq 10\text{ ml}$]). Modules that have been commercialized include the Advion NanoTek (Figure 13.8a), used for both PET radiochemistry [91, 92] and standard organic synthesis [93], as well as ABTs BG75 (Figure 13.8b) [38]. Most recently, we have collaborated with GE to introduce ISAR [94]. The ISAR system (Figure 13.8c) offers *parallel fluidics* that overcomes the single fluid bus and associated challenges at the macro-to-micro interface by marrying standard volumes and techniques and off-the-shelf components for radiopharmaceutical synthesis with the established benefits of a microreactor setup; this system offers a promising approach for the automated production of radiopharmaceuticals in the future.

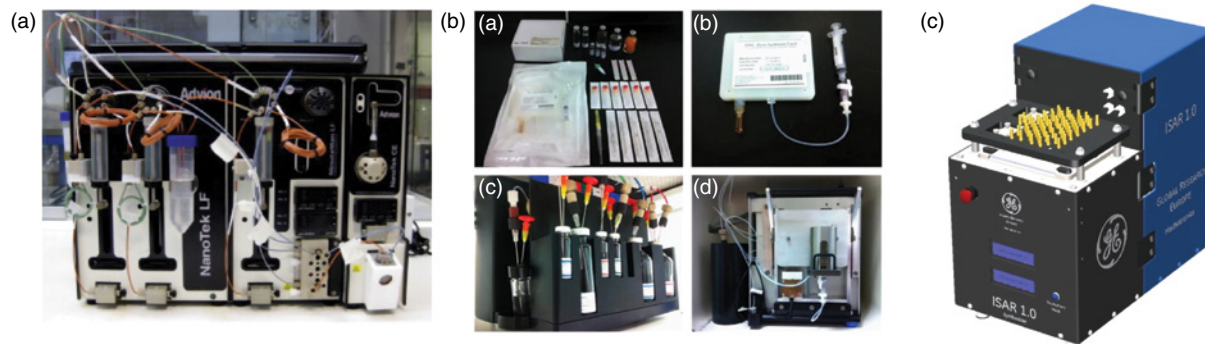


Figure 13.8 (a) Advion NanoTek. Source: Reproduced from Palmieri et al. 2009 with permission from Elsevier. (b) ABT BG75. Source: Reproduced from Awasthi et al. 2014 with permission from Elsevier. (c) ISAR. Source: Reproduced from Frank et al. 2019 under a Creative Commons Attribution 4.0 International License (<http://creativecommons.org/licenses/by/4.0>).

13.7 SYNTHESIS MODULES FOR USE WITH SOLID TARGETS

The increased use of longer-lived PET radionuclides has led to efforts to commercialize methods for their production. Smaller amounts of such radionuclides can be prepared on cyclotrons using liquid targets [95], but large-scale production requires the use of solid targets [96]. Initial solid-target work involved the use of homemade systems, and such systems continue to be reported [97–99], but moving solid targetry from the research arena to a point where it can be used for daily routine production has necessitated the development of dedicated commercially available solutions. These systems usually include the solid targetry, a shuttle method to move the solid target to and from the cyclotron, and a module for the chemistry steps needed to dissolve the solid target and convert the radionuclide to a useable form for subsequent radiochemical syntheses, in the same module or one of the other synthesis modules already described in this chapter. For example, the ALCEO solid target system has been developed by Comcer (Figure 13.9), while IBA introduced Nirta, and ARTMS also offers a solid target system. Both the ALCEO and Nirta systems require electrodeposition steps to manufacture the

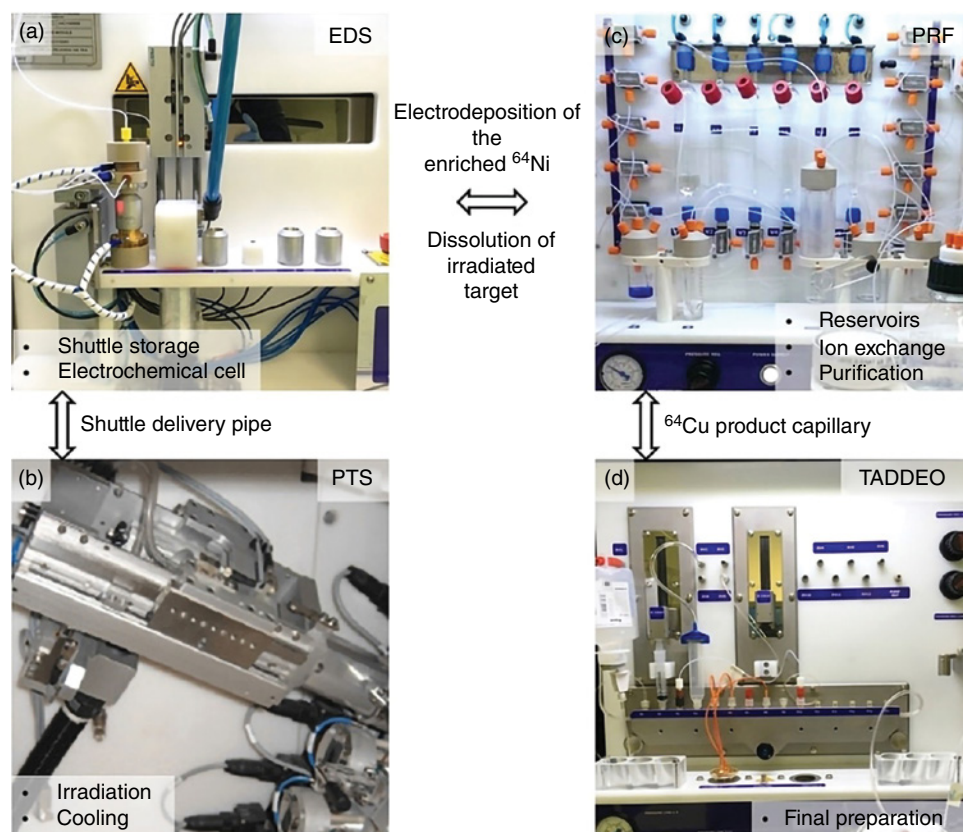


Figure 13.9

Modular setup of the ALCEO system. The shuttle is transported between the EDS (a) and PTS (b) via a delivery pipe; the EDS (a) and PRF (c) are connected by capillaries to enable the circulating fluid transport; and the final product is transferred from the PRF (c) through capillaries to the Taddeo module (d) for final processing. Source: Reproduced from Fiedler et al. 2018 with permission from John Wiley and Sons.

actual target, while ARTMS targets are commercially available. These solid target systems have been developed for cyclotron production of ^{64}Cu , ^{68}Ga , ^{86}Y , ^{89}Zr , ^{123}I , and ^{124}I , etc., and reports on such systems discuss their installation and use in the field [100, 101]. For example, the production of ^{64}Cu using ALCEO was described by Fiedler [100]. ALCEO is composed of a number of different modules for electrodeposition, dissolution, transfer, and storage of targets (**EDS**), an irradiation unit (PTS) connected to the cyclotron, a purification module (PRF) and a synthesis module (Taddeo). The enriched material is deposited on the target by the EDS and shuttled to the PTS on the cyclotron for irradiation. Once irradiation has occurred, the EDS shuttles the target back to the laboratory and dissolves the target. The radionuclide is then sent through capillary lines to the PRF for purification and, finally, Comcer's Taddeo synthesis module for radiochemistry. With the rapid uptick in use of ^{68}Ga radiopharmaceuticals for clinical studies recently, and steady growth in use of both ^{68}Ga and ^{89}Zr use for immuno-PET (for recent reviews, see [102, 103]), the growth in use of these solid-target systems for production and handling of such radioactive metal ions is expected to continue in the future.

13.8 AUTOMATED QUALITY CONTROL TESTING

In addition to advances and automation in synthesis modules, a similar push has been made to automate quality control testing of PET radiopharmaceuticals [104–106]. In order for a dose to be released for clinical use, it must pass a battery of quality control tests such as radiochemical and chemical purity (HPLC and TLC), residual solvent levels gas chromatography (**GC**), visual inspection, pH, osmolarity, radionuclidic identity (half-life), purity, sterile filter integrity, bacterial endotoxin levels, and sterility. These tests generally use separate pieces of analytical equipment, which are expensive to purchase and maintain. To reduce waste and reduce lab space requirements, a push for automation has led to the design of miniaturized systems such as the Tracer-QC (Figure 13.10) and QC1 that can incorporate all of these tests into a single unit. The concept is beyond the scope of this chapter, as it is discussed at length in Chapter 14.

13.9 CONCLUSIONS AND FUTURE DIRECTIONS

Radiochemistry modules have come a long way from the early systems of the 1980s, with a number of advanced systems now commercially available for different radionuclides and a wide range of applications. The increased demand for PET radiopharmaceuticals has led to the development of cassette-based modules that are compliant with cGMP and capable of handling multiple curies of radioactivity, while a continuing need to develop novel radiopharmaceuticals and/or new radiosynthesis methods has also led to the evolution of more flexible fixed-tube synthesis modules and systems for working with solid targetry. For labs that have limited hot-cell space available, hybrid systems that use cassettes capable of both routine cassette-based production and flexibility have been recently introduced. This is the current state of the art at the time of writing. However,



Figure 13.10
Tracer-QC
automated QC
module. Source:
Image courtesy
of LabLogic and
Trace-Ability,
Inc. Other man-
ufacturers of
automated QC
equipment
include QCI.

there remains a desire to reduce the cost and scale of PET radiosyntheses through the use of microfluidics. To this end, the first microfluidic systems for radiosynthesis, reformulation, and automation of quality control have been commercialized since the first edition of the *Handbook of Radiopharmaceuticals*.

The next generation of PET radiochemistry equipment is beginning to be conceived, with two new approaches emerging. The first of these considers the need for rapid and flexible production of new components for automation of new radiochemistry and/or synthesis of novel PET radiotracers, and capitalizes on recent developments in 3-dimensional (3D) printing technologies to translate optimized reaction conditions into synthesis modules and components composed of 3D-printed, electronic, and robotic parts [107]. The second development imagines a future of cGMP PET radiopharmaceutical production that is one of full automation, with little to no interaction by radiochemists. With the increasing connection of PET equipment to the Internet of Things (for more thoughts on PET radiochemistry and the Internet of Things, see [108]), it is possible that in the future, the various systems described in this chapter could communicate with each other to check inventory, order supplies, and ensure the suitability of the cyclotron, synthesis modules, and quality control equipment for use. The synthesis could potentially be set up the day before, and the entire process could be remote-activated so the dose was ready when the radiochemists arrived. Notifications of the synthesis could also be sent to the radiochemists, keeping them up to date on its progress as well as warning them of any

problems, and artificial intelligence (AI) could be used to track, trend, and troubleshoot the big data logged from every radiosynthesis to improve efficiency and reduce the cost of radiopharmaceutical manufacture in the future. The features to enable these advances are becoming available on today's equipment, and it will be exciting to see how the technology develops next.

REFERENCES

1. Vavere, A.L. and Scott, P.J.H. (2017). Clinical applications of small-molecule PET radiotracers: current progress and future outlook. *Semin. Nucl. Med.* 47 (5): 429–453.
2. PET Imaging Market Summary Report 2018. <https://imvinfo.com/product/2020-pet-imaging-market-summary-report>.
3. Eberl, S., Eriksson, T., Svedberg, O. et al. (2012). High beam current operation of a PETtrace™ cyclotron for $^{18}\text{F}^-$ production. *Appl. Radiat. Isot.* 70: 922–930.
4. Collins, J., Waldmann, C.M., Drake, C. et al. (2017). Production of diverse PET probes with limited resources: $^{24}\text{F}^-$ -labeled compounds prepared with a single radiosynthesizer. *Proc. Natl. Acad. Sci. U.S.A.* 114: 11309–11314.
5. Li, S., Schmitz, A., Lee, H., and Mach, R.H. (2016). Automation of the radiosynthesis of six different ^{18}F -labeled radiotracers on the AllinOne. *EJNMMI Radiopharm. Chem.* 1: 15.
6. Shao, X., Hoareau, R., Hockley, B.G. et al. (2011). Highlighting the versatility of the tracerlab synthesis modules. Part 1: Fully automated production of [^{18}F]labelled radiopharmaceuticals using a Tracerlab FX_{FN}. *J. Labelled Compd. Radiopharm.* 54: 292–307.
7. Shao, X., Hoareau, R., Runkle, A.C. et al. (2011b). Highlighting the versatility of the Tracerlab synthesis modules. Part 2: fully automated production of [^{11}C]labeled radiopharmaceuticals using a Tracerlab FXC-Pro. *J. Labelled Compd. Radiopharm.* 54: 819–838.
8. Krasikova, R. (2007). Synthesis modules and automation in F-18 labeling. In: *PET Chemistry*, Ernst Schering Research Foundation Workshop, vol. 62 (eds. P.A. Schubiger, L. Lehmann and M. Friebe), 289–316.
9. Boschi, S., Lodi, F., Malizia, C. et al. (2013). Automation synthesis modules review. *Appl. Radiat. Isot.* 76: 38–45.
10. Claggett, S.B., Quinn, K.M., Lazari, M. et al. (2013). Simplified programming and control of automated radiosynthesizers through unit operations. *EJNMMI Res.* 3: 53.
11. Welch, M.J., Dence, C.S., Marshall, D.R., and Kilbourn, M.R. (1983). Remote system for production of Carbon-11 labeled Palmitic acid. *J. Labelled Compd. Radiopharm.* 20: 1087–1095.
12. Brodack, J.W., Kilbourn, M.R., Welch, M.J., and Katzenellenbogen, J. (1988). Automated production of several positron-emitting radiopharmaceuticals using a single laboratory robot. *Appl. Radiat. Isot.* 39: 689–698.
13. Yu, S. (2006). Review of ^{18}F -FDG synthesis and quality control. *Biomed. Imaging Intervention J.* 2: e57.

14. MJH Life Sciences. 2001. GE plans acquisition of PET device maker Coincidence Technologies. www.diagnosticimaging.com/ge/ge-plans-acquisition-pet-device-maker-coincidence-technologies, accessed 13 Sept 2018.
15. Oh, S.J., Chi, D.Y., Mosdzianowski, C. et al. (2005). Fully automated synthesis of [^{18}F] fluoromisonidazole using a conventional [^{18}F]FDG module. *Nucl. Med. Biol.* 32: 899–905.
16. Kryza, D., Tadino, V., Filannino, M.A. et al. (2008). Fully automated [^{18}F]fluorocho-line synthesis in the TracerLab MX FDG coincidence synthesizer. *Nucl. Med. Biol.* 35: 255–260.
17. Cardinale, J., Martin, R., Remde, Y. et al. Procedures for the GMP-compliant production and quality control of [^{18}F]PSMA-1007: a next generation radiofluorinated tracer for the detection of prostate cancer. *Pharmaceuticals (Basel)* 10: E77.
18. Neels, O., Martin, R., Cardinale, J. et al. (2018). GMP-compliant fully automated single-step radiosynthesis of [^{18}F]PSMA-1007 using SPE cartridge purification. *J. Nucl. Med.* 59 (Suppl. 1): 402.
19. Huang, Y.-Y., Tsai, C.-L., Chang, Y.-N., and Yan, R.-F. (2017). Automated production of GMP-compliant ^{18}F -FES as an estrogen receptor ligand for breast cancer imaging. *Ann. Nucl. Med. Mol. Imaging* 30: 143–250.
20. Prata, M.I. (2012). Gallium-68: a new trend in radiopharmacy. *Curr. Radiopharm.* 5: 142–149.
21. Jayavarapu, R., Waits, T., Chauhan, A. et al. (2018). Our initial experience with ^{68}Ga -DOTATATE in the USA clinical dimension: added value in management decision making. *J. Nucl. Med.* 59 (Suppl. 1): 1225.
22. Nurmi, J. (2016). Leimausolosuhteiden optimointi ^{68}Ga -DOTA- NOC-leimauksessa GE TRACERlab MX-synteesilaitteella. E-thesis, Metropolia Ammattikorkeakoulu. https://www.theseus.fi/bitstream/handle/10024/147310/Nurmi_Jenni.pdf?sequence=1&isAllowed=y, accessed 5 August 2019.
23. Haka, M., Walsh, J., and Webster, E. (2017). P450: cleaning validation concepts for commercial radiopharmaceutical manufacturing. *J. Labelled Compd. Radiopharm.* 60 (Suppl. 1): S632.
24. Sowa, A.R., Jackson, I.M., Desmond, T.J. et al. (2018). Futureproofing [^{18}F]Fludeoxyglucose manufacture at an Academic Medical Center. *EJNMMI Radiopharm. Chem.* 3 (1): 12.
25. Rodnick, M., Hockley, B., Piert, M. et al. (2019). P149 -- clinical implementation of cyclotron-based [^{68}Ga]Ga-PSMA-11 at the University of Michigan. *J. Labelled Compd. Radiopharm.* 62 (Suppl. 1): S304.
26. Meyer, J.-P., Adumeau, P., Lewis, J.S., and Zeglis, B.M. (2016). Click chemistry and radiochemistry: the first 10 years. *Bioconjug Chem* 27 (12): 2791–2807. <https://doi.org/10.1021/acs.bioconjchem.6b00561>.
27. Allott, L., Da Pieve, C., Turton, D.R., and Dmuth, G. (2017). A general [^{18}F]AlF radiochemistry procedure on two automated synthesis modules. *React. Chem. Eng.* 2: 68–74.
28. Antuganov, D.O., Ryzhkova, D.V., Zykova, T.A. et al. (2018). Modification of automatic synthesis of [^{18}F]Fluoromisonidazole on a GE TracerLAB Fx F-N synthesis module. *Radiochemistry* 60: 45–50.

29. Garcia-Arguello, S.F., Lopez-Lorenzo, B., and Ruiz-Cruces, R. (2019). Automated production of [⁶⁸Ga]Ga-DOTANOC and [⁶⁸Ga]Ga-PSMA-11 using a TRACERlab FX_{FN} synthesis module. *J. Labelled Compd. Radiopharm.* 62: 146–153.
30. Shao, X., Hockley, B.G., Hoareau, R. et al. (2011c). Fully automated preparation of [¹¹C]choline and [¹⁸F]fluoromethylcholine using TracerLab synthesis modules and facilitated quality control using analytical HPLC. *Appl. Radiat. Isot.* 69: 403–409.
31. Shao, X. and Kilbourn, M.R. (2009). A simple modification of GE tracerlab FX C Pro for rapid sequential preparation of [¹¹C]carfentanil and [¹¹C]raclopride. *Appl. Radiat. Isot.* 67: 602–605.
32. Dahl, K., Garcia, A., Stephenson, N.A., and Vasdev, N. "In-loop" ¹⁸F-fluorination: a proof-of-concept study. *J. Labelled Compd. Radiopharm.* 62: 292–297.
33. Lazari, M., Quinn, K.M., Claggett, S.B. et al. (2013). ELIXYS - a fully automated, three-reactor high-pressure radiosynthesizer for development and routine production of diverse PET tracers. *EJNMMI Res.* 3 (1): 52.
34. Lazari, M., Collins, J., Shen, B. et al. (2014). Fully automated production of diverse ¹⁸F-labeled PET tracers on the ELIXYS multireactor radiosynthesizer without hardware modification. *J. Nucl. Med. Technol.* 42: 203–210.
35. Waldmann, C.M., Gomez, A., Marchis, P. et al. (2017). An automated multidose synthesis of the potentiometric PET probe 4-[¹⁸F]Fluorobenzyl-triphenylphosphonium ([¹⁸F]FBnTP). *Mol. Imaging Biol.* 20 (2): 205–212.
36. Amaraesekera, B., Marchis, P.D., Bobinski, K.P. et al. (2013). High-pressure, compact, modular radiosynthesizer for production of positron emitting biomarkers. *Appl. Radiat. Isot.* 78: 88–101.
37. Audrain, H. (2007). Positron emission tomography (PET) and microfluidic devices: a breakthrough on the microscale? *Angew. Chem. Int. Ed.* 46: 1772–1775.
38. Awasthi, V., Watson, J., Gali, H. et al. (2014). A "dose on demand" biomarker generator for automated production of [¹⁸F]F⁻ and [¹⁸F]FDG. *Appl. Radiat. Isot.* 89: 167–175.
39. Bejot, R., Kersemans, V., Kelly, C. et al. (2010). Pre-clinical evaluation of a 3-nitro-1,2,4-triazole analogue of [¹⁸F]FMISO as hypoxia-selective tracer for PET. *Nucl. Med. Biol.* 37: 565–575.
40. Bouvet, V.R., Wuest, M., Wiebe, L.I., and Wuest, F. (2011). Synthesis of hypoxia imaging agent 1-(5-deoxy-5-fluoro- α -D-arabinofuranosyl)-2-nitroimidazole using microfluidic technology. *Nucl. Med. Biol.* 38: 235–245.
41. Bouvet, V., Wuest, M., Tam, P.H. et al. (2012). Microfluidic technology: an economical and versatile approach for the synthesis of O-(2-[¹⁸F]fluoroethyl)-L-tyrosine ([¹⁸F]FET). *Bioorg. Med. Chem. Lett.* 22: 2291–2295.
42. Bouvet, V.R. and Wuest, F. (2013). Application of [¹⁸F]FDG in radiolabeling reactions using microfluidic technology. *Lab Chip* 13: 4290–4294.
43. Collier, T., Akula, M., and Kabalka, G. (2010). Microfluidic synthesis of [¹⁸F]FMISO. *J. Nucl. Med.* 51 (Suppl. 2): 1462.
44. Collier, T.L., Liang, S.H., Mann, J.J. et al. (2017). Microfluidic radiosynthesis of [¹⁸F]FEMPT, a high affinity PET radiotracer for imaging serotonin receptors. *Beilstein J. Org. Chem.* 13: 2922–2927.

45. De Leonardis, F., Pascali, G., Salvadori, P.A. et al. (2010). Microfluidic modules for [¹⁸F] activation - Towards an integrated modular lab on a chip for PET radiotracer synthesis. *Proc. MicroTAS* 14: 1604–1606.
46. De Leonardis, F., Pascali, G., Salvadori, P.A. et al. (2011). On-chip pre-concentration and complexation of [¹⁸F]fluoride ions via regenerable anion exchange particles for radiochemical synthesis of positron emission tomography tracers. *J. Chromatogr. A* 1218: 4714–4719.
47. Elizarov, A.M. (2009). Microreactors for radiopharmaceutical synthesis. *Lab Chip* 9: 1326–1333.
48. Elizarov, A.M., van Dam, R.M., Shin, Y.S. et al. (2010). Design and optimization of coin-shaped microreactor chips for PET radiopharmaceutical synthesis. *J. Nucl. Med.* 51: 282–287.
49. Fortt, R. and Gee, A. (2013). Microfluidics: a golden opportunity for positron emission tomography? *Future Med. Chem.* 5: 241–244.
50. Kealey, S., Plisson, C., Collier, T.L. et al. (2011). Microfluidic reactions using [¹¹C]carbon monoxide solutions for the synthesis of a positron emission tomography radiotracer. *Org. Biomol. Chem.* 9: 3313–3319.
51. Keng, P.Y., Chen, S., Ding, H. et al. (2012). Micro-chemical synthesis of molecular probes on an electronic microfluidic device. *Proc. Natl. Acad. Sci. U.S.A.* 109: 690–695.
52. Keng, P.Y. and van Dam, R.M. (2015). Digital microfluidics: a new paradigm for radiochemistry. *Mol. Imaging* 14: 13–14.
53. Lu, S.Y. and Pike, V.W. (2007). Micro-reactors for PET tracer labeling. In: *PET Chemistry*, Ernst Schering Research Foundation Workshop, vol. 62 (PET Chemistry) (eds. P.A. Schubiger, L. Lehmann and M. Friebe), 271–287.
54. Lee, C.C., Sui, G., Elizarov, A. et al. (2005). Multistep synthesis of a radiolabeled imaging probe using integrated microfluidics. *Science* 310: 1793–1796.
55. Liu, K., Lepin, E.J., Wang, M.W. et al. (2011). Microfluidic-based ¹⁸F-labeling of biomolecules for immuno-positron emission tomography. *Mol. Imaging* 10: 168–176.
56. Liu, Y., Tian, M., and Zhang, H. (2013). Microfluidics for synthesis of peptide-based PET tracers. *Biomed. Res. Int.* 2013: 839683.
57. Liow, E., O'Brien, A., Luthra, S. et al. (2005). Preliminary studies of conducting high level production radiosyntheses using microfluidic devices. *J. Labelled Compd. Radiopharm.* 48: 28.
58. Lu, S. and Pike, V.W. (2010). Synthesis of [¹⁸F]xenon difluoride as a radiolabeling reagent from [¹⁸F]fluoride ion in a micro-reactor and at production scale. *J. Fluorine Chem.* 131: 1032–1038.
59. Lu, S.Y., Watts, P., Chin, F.T. et al. (2004). Syntheses of ¹¹C- and ¹⁸F-labeled carboxylic esters within a hydrodynamically driven micro-reactor. *Lab Chip* 4: 523–525.
60. Lu, S., Giamis, A.M., and Pike, V.W. (2009). Synthesis of [¹⁸F]fallypride in a micro-reactor: rapid optimization and multiple-production in small doses for micro-PET studies. *Curr. Radiopharm.* 2: 49–55.
61. Lu, S., Chun, J.H., and Pike, V.W. (2010). Fluorine-18 chemistry in micro-reactors. *J. Labelled Compd. Radiopharm.* 53: 234–238.

62. Matesic, L., Kallinen, A., Greguric, I., and Pascali, G. (2017). Dose-on-demand production of diverse ^{18}F -radiotracers for preclinical applications using a continuous flow microfluidic system. *Nucl. Med. Biol.* 52: 24–31.
63. Miller, P.W. (2009). Radiolabelling with short-lived PET (positron emission tomography) isotopes using microfluidic reactors. *J. Chem. Technol. Biotechnol.* 84: 309–315.
64. Miller, P.W., de Mello, A.J., and Gee, A.D. (2010). Application of microfluidics to the ultra-rapid preparation of fluorine-18 labelled compounds. *Curr. Radiopharm.* 3: 254–262.
65. Miller, P.W., Audrain, H., Bender, D. et al. (2011). Rapid carbon-11 radiolabelling for PET using microfluidics. *Chem. Eur. J.* 17: 460–463.
66. Pascali, G., Mazzone, G., Saccomanni, G. et al. (2010). Microfluidic approach for fast labeling optimization and dose-on-demand implementation. *Nucl. Med. Biol.* 37: 547–555.
67. Pascali, G., Nannavecchia, G., Pitzianti, S., and Salvadori, P.A. (2011). Dose-on-demand of diverse ^{18}F -fluorocholine derivatives through a two-step microfluidic approach. *Nucl. Med. Biol.* 38: 637–644.
68. Pascali, G., Watts, P., and Salvadori, P.A. (2013). Microfluidics in radiopharmaceutical chemistry. *Nucl. Med. Biol.* 40: 776–787.
69. Pascali, G. and Salvadori, P.A. (2016). Opportunities and challenges in the utilization of microfluidic technologies to the production of radiopharmaceuticals. *Chim. Oggi-Chem. Today* 34: 28–32.
70. Rensch, C., Waengler, B., Yaroshenko, A. et al. (2012). Microfluidic reactor geometries for radiolysis reduction in radiopharmaceuticals. *Appl. Radiat. Isot.* 70: 1691–1697.
71. Rensch, C., Jackson, A., Lindner, S. et al. (2013). Microfluidics: a groundbreaking technology for PET tracer production? *Molecules* 18: 7930–7956.
72. Selivanova, S.V., Mu, L., Ungersboeck, J. et al. (2012). Single-step radiofluorination of peptides using continuous flow microreactor. *Org. Biomol. Chem.* 10: 3871–3874.
73. Simms, R.W., Causey, P.W., Weaver, D.M. et al. (2012). Preparation of technetium-99m bifunctional chelate complexes using a microfluidic reactor: a comparative study with conventional and microwave labeling methods. *J. Labelled Compd. Radiopharm.* 55: 18–22.
74. Steel, C.J., O'Brien, A.T., Luthra, S.K., and Brady, F. (2007). Automated PET radiosyntheses using microfluidic devices. *J. Labelled Compd. Radiopharm.* 50: 308–311.
75. Ungersboeck, J., Philippe, C., Mien, L.K. et al. (2011). Microfluidic preparation of ^{18}F FE@SUPPY and ^{18}F FE@SUPPY:2--comparison with conventional radiosyntheses. *Nucl. Med. Biol.* 38: 427–434.
76. Ungersboeck, J., Philippe, C., Haeusler, D. et al. (2012a). Optimization of ^{13}C DASB-synthesis: vessel-based and flow-through microreactor methods. *Appl. Radiat. Isot.* 70: 2615–2620.
77. Ungersboeck, J., Richter, S., Collier, L. et al. (2012b). Radiolabeling of ^{18}F altanse-rin - a microfluidic approach. *Nucl. Med. Biol.* 39: 1087–1092.
78. Voccia, S., Morelle, J.L., Aerts, J. et al. (2009). Mini-fluidic chip for the total synthesis of PET tracers. *J. Labelled Compd. Radiopharm.* 52 (Suppl 1): S11.

79. Wang, M.-W., Lin, W.-Y., Liu, K. et al. (2010). Microfluidics for positron emission tomography (PET) imaging probe development. *Mol. Imaging* 9: 175–191.
80. Wang, J., Chao, P.H., and van Dam, R.M. (2019). Ultra-compact, automated microdroplet radiosynthesizer. *Lab Chip* <https://doi.org/10.1039/c9lc00438f>.
81. Wester, H.J., Schoultz, B.W., Hultsch, C., and Henriksen, G. (2009). Fast and repetitive in-capillary production of [¹⁸F]FDG. *Eur. J. Nucl. Med. Mol. Imaging* 36: 653–658.
82. Wheeler, T.D., Zeng, D., Desai, A.V. et al. (2010). Microfluidic labeling of biomolecules with radiometals for use in nuclear medicine. *Lab Chip* 10: 3387–3396.
83. Yokell, D.L., Leece, A.K., Lebedev, A. et al. (2012). Microfluidic single vessel production of hypoxia tracer 1H-1-(3-[¹⁸F]-fluoro-2-hydroxy-propyl)-2-nitro-imidazole ([¹⁸F]-FMISO). *Appl. Radiat. Isot.* 70: 2313–2316.
84. Zeng, D., Desai, A.V., Ranganathan, D. et al. (2013). Microfluidic radiolabeling of biomolecules with PET radiometals. *Nucl. Med. Biol.* 40: 42–51.
85. Chao, P.H., Collins, J., Argus, J.P. et al. (2017). Automatic concentration and reformulation of PET tracers via microfluidic membrane distillation. *Lab Chip* 17: 1802–1816.
86. Lebedev, A., Miraghaie, R., Kotta, K. et al. (2013). Batch-reactor microfluidic device: first human use of a microfluidically produced PET radiotracer. *Lab Chip* 13: 136–145.
87. Liang, S.H., Yokell, D.L., Jackson, R.N. et al. (2014). Microfluidic continuous-flow radiosynthesis of [¹⁸F]FPEB suitable for human PET imaging. *Med. Chem. Commun.* 5: 432–435.
88. Liang, S.H., Yokell, D.L., Normandin, M.D. et al. (2014). First human use of a radiopharmaceutical prepared by continuous-flow microfluidic radiofluorination: proof of concept with the tau imaging agent [¹⁸F]T807. *Mol. Imaging* 13 <https://doi.org/10.2310/7290.2014.00025>.
89. Rensch, C., Lindner, S., Salvamoser, R. et al. (2014). A solvent resistant lab-on-chip platform for radiochemistry applications. *Lab Chip* 14: 2556–2564.
90. Chiu, D.T., DeMello, A.J., Carlo, D.D. et al. (2017). Small but perfectly formed? Successes, challenges, and opportunities for microfluidics in the chemical and biological sciences. *Chem* 2: 201–223.
91. Matesic, L. (2013). [¹⁸F]radiochemistry using the NanoTek microfluidic synthesis system. *Aust. J. Chem.* 66: 1459–1460.
92. Pascali, G., Berton, A., DeSimone, M. et al. (2014). Hardware and software modifications on the Advion NanoTek microfluidic platform to extend flexibility for radiochemical synthesis. *Appl. Radiat. Isot.* 84: 40–47.
93. Palmieri, A., Ley, S.V., Hammond, K. et al. (2009). A microfluidic flow chemistry platform for organic synthesis: the Hofmann rearrangement. *Tetrahedron Lett.* 50: 3287–3289.
94. Frank, C., Winter, G., Rensei, F. et al. (2019). Parallel fluidics on ISAR: a new paradigm in radiopharmaceutical production. *EJNMMI Radiopharm. Chem.* 4: Article 24.
95. Do Carmo, S.J.C., Scott, P.J.H., and Alvs, F. (2020). Production of radiometals in liquid targets. *EJNMMI Radiopharm. Chem.* 5, article 2.
96. Gelbart, W.Z. and Stevenson, N.R. (1998). Solid targetry systems: a brief history. In: *Proceedings of the 15th International Conference on Cyclotrons and their Applications, Caen, France, 14–19 June* (eds. E. Baron and M. Lieuvin), 90–93. Inst. Phys.

97. Solbach, C., Dieters, J., Machulla, H. et al. (2010). New solid state target construction on a PETtrace cyclotron. *J. Nucl. Med.* 54 (Suppl. 2): 1010.
98. Siikanen, J., Tran, T.A., Olsson, T.G. et al. (2014). A solid target system with remote handling of irradiated targets for PET cyclotrons. *Appl. Radiat. Isot.* 94: 294–301.
99. Gelbart, W.Z. and Johnson, R.R. (2019). Solid target system with in-situ target dissolution. *Instruments* 3: 14.
100. Fiedler, L., Kellner, M., Oos, R. et al. (2018). Fully automated production and characterization of ^{64}Cu and proof-of-principle small-animal PET imaging using ^{64}Cu -Labelled CA XII targeting 6A10 Fab. *ChemMedChem* 13: 1230–1237.
101. Tochon-Danguy, H.J., Poniger, S.S., Sachinidis, J.I., and Panopoulos, H.P. (2012). Implementation of a solid target production facility. In: *AIP Conference Proceedings*, vol. 1509 (eds. M.A. Avila-Rodriguez, J.P. O'Neil, T.E. Barnhart, et al.), 176. AIP.
102. Van Dongen, G.A.M.S. and Vosjan, M.J.W.D. (2010). Immuno-positron emission tomography: shedding light on clinical antibody therapy. *Cancer Biother. Radiopharm.* 25: 375–385.
103. Bailly, C., Bodet-Milin, C., Rousseau, C. et al. (2017). Pretargeting for imaging and therapy in oncological nuclear medicine. *EJNMMI Radiopharm. Chem.* 2: 6.
104. Ha, N.S., Sadeghi, S., and Van Dam, R.N. (2017). Recent progress toward microfluidic quality control testing of radiopharmaceuticals. *Micromachines* 8: 337.
105. Taggart, M.P., Tarn, M.D., Esfahani, M.M. et al. (2016). Development of radiodetection systems towards miniaturised quality control of PET and SPECT radiopharmaceuticals. *Lab Chip* 16: 1605–1616.
106. Ly, J., Ha, N.S., Cheung, S., and van Dam, R.M. (2018). Toward miniaturized analysis of chemical identity and purity of radiopharmaceuticals via microchip electrophoresis. *Anal. Bioanal. Chem.* 410: 2423–2436.
107. Amor-Coarasa, A., Kelly, J.M., and Babich, J.W. (2019). 3D-printed automation for optimized PET radiochemistry. *Sci. Adv.* 5 (9): eaax4762.
108. Thompson, S., Kilbourn, M.R., and Scott, P.J.H. (2016). Radiochemistry, PET imaging, and the internet of chemical things. *ACS Central Sci.* 2 (8): 497–505.

Chapter 14

Automation of PET Radiopharmaceutical Quality Control

Arkadij Mikhailovich Elizarov

Trace-Ability, Inc., Los Angeles, CA 91406, USA

14.1 OVERVIEW

The US Pharmacopeia (USP) is a compendium of drug quality standards. According to the definition offered in USP General Chapter <823>, “Positron Emission Tomography Drugs for Compounding, Investigational, and Research Uses” [1], quality assurance (QA) and quality control (QC) are important elements in the process of making positron emission tomography (PET) drugs. QA is a broad concept that covers all matters that influence the identity, strength, quality, and purity of a PET drug. QC is a subset of QA that deals with testing materials and PET drugs to determine if they meet acceptance criteria. QC functions include the following: (i) evaluate each lot of incoming material to ensure that it meets its established specifications before use in the preparation or testing of PET drugs; (ii) evaluate each batch of a PET drug to ensure the batch meets its established specifications before authorizing the final release or rejection of the batch. It is important to clarify in this context that the scope of QC automation discussed in this chapter relates mostly to pre-release testing required for each batch of a PET drug. It will not cover testing of incoming materials, periodic testing of a PET drug that is not required for release of each batch, or post-release sterility testing.

QC procedures differ between PET tracers and between countries. Therefore, in order to offer a context for meaningful comparison, most of the solutions presented in this chapter will be discussed as they relate to the US environment and clearly distinguishing 2-deoxy-2-^[18F]fluoro-D-glucose (FDG). Other tracers will be discussed as a group only in

Handbook of Radiopharmaceuticals: Methodology and Applications, Second Edition.

Edited by Michael R. Kilbourn and Peter J.H. Scott.

© 2021 John Wiley & Sons Ltd. Published 2021 by John Wiley & Sons Ltd.

aspects of QC that cannot be demonstrated with FDG. It is expected that a discussion in such a narrow context provides the most concise story, which the reader should be able to easily extrapolate to their tracer of interest and local regulatory environment.

While the development of automated systems for radiosynthesis dates back to the 1970s [2, 3] and was immediately fueled by the early success of PET [4, 5], automation of QC has not received much attention until recent years despite its complexity being comparable to or exceeding that of manual radiosynthesis.

In the early days of PET, QC procedures differed among tracer manufacturers and relied mostly on scientific judgment. Mechanisms used to confirm that such judgment was sound included (i) state-regulated practice of medicine and compounding pharmacies [6], putting the liability on the pharmacist; as well as review of procedures via (ii) Radioactive Drug Research Committee (**RDRC**) [7] or (iii) investigational new drug (**IND**) [8] applications. Such mechanisms yielded a variety of QC procedures [9–11], acceptance criteria, and no uniform standards. In such an environment, with diverse QC approaches, there was little structure for the development of QC automation. Furthermore, when most PET was supported only by FDG [12–14], once QC procedures matured, there was no pressure to modify them. However, the evolution of PET in the past decade has catalyzed a wave of QC automation developments across the world, indicating both the need for and feasibility of such innovation.

This chapter will first identify the most important milestones in the PET industry that have led to QC standardization and set the stage for automated solutions. It will then introduce the progression of approaches to automation undertaken by different organizations. Discussion of these approaches, drivers, barriers, and opportunities should put the reader in a position to compare the automated QC solutions available today or arising in the future. It will offer a structure for assessing the value of QC automation for the reader's goals. This discussion will be followed by a regulatory framework and mechanisms available for practical transition from traditional to automated QC. The outlook section at the end will offer the author's perspective on continued innovation and welcome readers to formulate their own.

14.2 PET MILESTONES RELEVANT TO QC AUTOMATION

14.2.1 Milestone 1 – Standardization of PET Tracer QC Requirements

The development of automated solutions can only be justified if they can be applied across a broad set of users. A uniform solution would not be possible in a situation where each manufacturer defined its own QC processes. Thus, standardization of QC procedures was an important prerequisite for QC automation.

The first PET tracer to set a precedent for QC standards was sodium fluoride, [^{18}F]NaF [15]. Its new drug application (**NDA**) was approved by the US Food and Drug Administration (**FDA**) in 1972. The corresponding USP monograph was published in

1979 [16]. This first published PET tracer monograph required the following QC tests: pyrogens (endotoxins), radionuclidic identification, pH, radiochemical purity, assay, and sterility (post-release). This monograph was omitted in 1980 as [F-18]NaF production stopped. Then, until the publication of the 1990 Fludeoxyglucose F 18 Injection (FDG) USP monograph [17], there was no centralized guidance on QC for any PET tracer. Thus, the systematic evolution of standardized QC requirements that we know today practically starts with the latter document.

In 1998, the USP published the first version of General Chapter <823> – “Radiopharmaceuticals for Positron Emission Tomography (PET) – Compounding, Investigational, and Research Uses” – which provided general QA standards for PET drugs [18]. Specifically, it required pH, appearance, radiochemical purity and identity, radionuclidic identity, filter integrity, endotoxin, and sterility (post-release) tests to be performed on each batch for all PET products. Specific activity was required for products with mass-dependent toxicity concerns. Concentrations of residual solvents [19] and other toxic chemical constituents of the final product had to be compliant with the acceptance criteria for each of these compounds. Contaminants needed to be defined based on synthesis and purification processes used to prepare the drug. Products with half-lives under 20 minutes had a special definition of a *batch* where all batches of product made on a given day were to be considered sub-batches of one batch, for which full QC would be performed only once per day.

The requirements defined in the USP are not static. They change based on new developments and risks. For example, when the nucleophilic FDG production method [20] introduced Kryptofix 222 (4,7,13,16,21,24-hexaoxa-1,10-diazabicyclo[8.8.8]hexacosane) as a phase transfer reagent, a test for Kryptofix 222 became necessary, considering the molecule’s toxicity profile [21]. Similar logic applies to new tracers. If their syntheses or formulations involve toxic substances not relevant to FDG, the QC requirements need to be amended accordingly. Current FDG QC requirements based on the 2018 updates to General Chapter <823> [1] and USP Monograph on Fludeoxyglucose F 18 Injection [22] are summarized in Table 14.1. The tests are presented in three groups corresponding to the reasons behind them. The purpose of the tests in the “Identity and Strength” group is to demonstrate the presence of the desired product in the amount needed. Tests in the “Purity” group are performed to confirm that all contaminants that may be reasonably expected in the given tracer formulation are less than the predetermined thresholds. Finally, the “Safety” group of tests confirms that the product is acceptable for parenteral administration to patients.

Sterility is the riskiest factor, since injecting bacterially contaminated drugs may cause serious disease, especially in ill patients. However, the tracers must be injected into patients before the culture test result is known, since the half-life of PET tracers is much shorter than the 14 days needed for microbial colony growth in the sterility test [23]. Therefore, there is always a risk of non-sterile injection. As a result, substantial effort is placed on sterility assurance during drug product preparation. The only pre-release indication of sterility is the final product being filtered through a membrane filter followed by confirming the integrity of that filter.

Table 14.1 The most common QC procedures for PET tracers produced in the US.

	<823> pre-release tests	Method	Example tracer	Specification (for example tracer)	Detection technology
Identity and strength	Radionuclidic identity	Half-life	FDG	105–115 min	Dose calibrator
	Radiochemical identity	TLC	FDG	$R_f = 90\text{--}110\%$ of USP standard R_f	TLC scanner
		HPLC	FMISO	Retention time = standard ± 10 s	HPLC radiation detector
Radioactivity concentration	Radioactivity/volume correlation	FDG	4–300 mCi ml ⁻¹	Dose calibrator	
Purity	Visual inspection	Appearance	FDG	Clear, colorless, free from visible particulates	Human eye
	Radiochemical purity	TLC	FDG	>90%	TLC scanner
		HPLC	FMISO	>95%	HPLC UV and radiation detectors
	Chemical purity and residual compounds used in synthesis	HPLC	FMISO	<35 μ g per dose of UV-absorbing impurities	HPLC UV detector
		Spot test	FDG	<50 μ g ml ⁻¹ (Kryptofix 222)	Human eye
	Specific activity	HPLC	FMISO	>125 Ci mmol ⁻¹	HPLC UV and radiation detectors
Residual solvents used in synthesis or purification	GC	FDG	<0.5% (ethanol)	Flame ionization detector	
		FDG	<0.041% (acetonitrile)	Flame ionization detector	
Safety	pH	pH strip	FDG	4.5–7.5	Human eye
	Bacterial endotoxin	Endosafe PTS	FDG	<175 EU per dose	PTS reader
	Filter integrity test	Bubble point	FDG	>344.8 kPa	Human eye
	<i><823> post-release test</i>				
Sterility (post-release)	14-day culture test	FDG	0 colony forming units	Human eye	
<i><823> periodic tests</i>					
Purity	Radionuclidic purity	Gamma ray spectrometry	FDG	F-18 >99.5% of radionuclides	Multi-channel analyzer (MCA)
	Low-level non-toxic impurities	HPLC	FDG	<1 mg per dose (CIDG)	HPLC pulsed amperometric detector
	Class 3 residual solvents	GC	FMISO	<0.5% (acetone)	Flame ionization detector

Pharmacopeial requirements differ among the USP, European Pharmacopeia (**EP**) [24], British Pharmacopeia (**BP**) [25], and International Pharmacopeia overseen by the World Health Organization (**WHO**) [26]. There are detailed reviews summarizing relevant QC procedures [27] and offering a comparison of various pharmacopeial monographs [28]. There is also draft guidance published by the FDA [29] that includes QC procedures for [N-13]Ammonia, [F-18]NaF and FDG.

These developments have led to large numbers of PET drug manufacturers relying on similar criteria and processes in release testing. This allows an automated solution developed for one user to be applicable across most of the industry.

14.2.2 Milestone 2 – The cGMP Compliance Challenge

Traditional QC testing involves multiple instruments, multiple manual test stations, multiple aliquots of the sample, and many data entries at every step of the way [30, 31]. Moreover, the operator needs to manage and track multiple expiry dates (e.g. for standards or equipment calibration). Until current Good Manufacturing Practice (**cGMP**) regulations took effect, such manual procedures were manageable, as they mostly focused on yielding the information needed for the product release [32].

That paradigm changed with the 21 Code of Federal Regulations (CFR) Part 212 regulations, cGMP for PET Drugs [33], which took effect in 2012. They specify the requirements for a high level of control while executing QC procedures (especially in Subpart G, “Laboratory Controls”). However, these regulations do not specify the details of the test procedures, which still follow the pharmacopeia. Thus, the definition of current QC procedures needs to address both USP and FDA requirements in an inter-related approach [34].

Manual methods have historically been subjective, variable, and dependent on the operator’s experience, judgment, and consistency, with each operator having their own precision and accuracy. Thus, satisfying the increased level of control while running manual methods presented a challenge [35] and called for an increase in resources and operating costs. Analysis of statistics on 21 CFR Part 212 violations published by the FDA [36] leads to the conclusion that the vast majority of them result from poor control of manual processes. This is why cGMP regulation is such an important milestone leading to QC automation development.

Manual procedures are poorly traceable, making them either a high risk from a compliance perspective or costly if mechanisms are put in place to assure traceability of a manual process. Automation, by virtue of taking the person out of the process, eliminates the gaps in cGMP compliance. Every place where pen touches paper provides a data-integrity risk because it compromises compliance. Automation coupled with the data-integrity features of the corresponding software should eliminate all such opportunities. Furthermore, by eliminating the subjectivity and variability of operators, as well as the requirement for operator experience and judgment, automation will further reduce violations.

14.2.3 Milestone 3 – Emergence of New PET Tracers

Compounding the challenge to cGMP compliance has been the growth in PET procedures in the twenty-first century. Now millions of PET scans are performed annually with tracers that are released relying on error-prone, poorly traceable, manual QC processes. With multiple tracer production runs made daily, and two to five different tracers made in some facilities, the chance of error is high. Since QC is the least automated part of production, compliance assurance in this area has quickly become a bottleneck.

FDA approval of [F-18]Florbetapir (Amyvid) [37] as the first proprietary PET tracer in 2012 shows that new tracer development by commercial entities is relatively recent in the PET field. It also marks a critical milestone for the development of QC automation. A spur of new tracers has entered clinical development and received approval since 2012 [38]. PET tracer QC has grown in complexity and diversity as it no longer revolves around one product. It requires more equipment, larger facilities, and, most critically, more skilled staff – who are not readily available.

While manual QC procedures developed in the twentieth century were sustainable when FDG was the only major product, the paradigm shift to multi-tracer portfolios has multiplied the complexity of QC and now limits the number of new tracers a facility can support.

14.3 LABORATORY SETUP FOR QC IN PET TRACER PRODUCTION

The three milestones of standardization of PET QC procedures, cGMP regulations, and new tracer introductions have defined a typical laboratory that can be used to execute the modern QC process. Details of the most common laboratory setup required to execute the most current QC procedures are summarized in Table 14.1. The list of tests is based on the 2020 revision of USP General Chapter <823>. Tracers chosen as examples are FDG and 1-(2-hydroxy-3-[¹⁸F]fluoropropyl)-2-nitroimidazole (FMISO). QC tests for FDG [27] are based on the latest USP monograph, while FMISO QC [39] examples were used to illustrate common tests that are required for non-FDG tracers. The Method and Detection Technology columns illustrate a diverse range of instruments and skills that are required to execute QC for PET tracers.

14.4 DRIVERS OF AUTOMATED QC

Now that the traditional QC procedures are defined, it is important to understand the drivers behind the need for automation as well as the barriers that challenge it. There is a critical difference between QC of short-lived radiopharmaceuticals and all other injectable drugs. The latter are made in large batches with low frequency and ample time for QC. The ratio of product doses per QC analysis is orders of magnitude higher than with PET drugs. In traditional drugs, QC is a minor contributor to the production cost of each

patient dose. In PET, it is a major contributor. Thus, improvements in QC efficiency and cost have an immediate and direct impact on product cost. It is especially important with the increasing number of PET procedures and PET drug diversity.

As will be seen in Section 14.6, independent QC automation efforts started at multiple organizations at about the same time, suggesting that the milestones defined earlier have created a stimulating environment for such innovation. While cGMP compliance and new tracer emergence stress the need for QC automation, process standardization via USP makes it possible to satisfy most users with a single solution. Furthermore, the need for QC automation has been driven incrementally by the following factors:

- (1) *Safety/radiation exposure:* As with radiosynthesis automation, taking the person out of the process is an important factor for personnel safety in consideration of the “As Low as Reasonably Achievable” (ALARA) principle [40]. Radiosynthesis was performed behind shielding even before automation. Meanwhile, the effect of shielding is limited in QC, given the number of manual operations that cannot be performed remotely [41]. Thus, only complete automation of QC can eliminate the radiation exposure associated with these procedures. Although the total amount of starting radioactivity in QC is much lower than that in synthesis, absence of complete shielding in QC leads to higher exposure. Furthermore, the total personnel exposure continues to increase as the number of tracers produced per facility grows further.
- (2) *Human error:* Any manual process is prone to human error. Given the number of FDG batches made every day, there is a high chance that at least one batch is affected by human error in QC. Some of these errors may stay undetected, while others require investigation (which in turn slows production and drives cost). A machine with validated performance and robustness is in a position to eliminate errors.
- (3) *Operational efficiency and throughput:* As the number of PET scans grows every year, so do the volume of FDG production and number of new tracers. This means more production runs per facility per day. Many facilities have already run into their respective efficiency limits, which reduces their ability to take up new tracer production.
- (4) *Skillset dependence:* Radiosynthesis has evolved to a point that any technician with minimal training can perform it. This leaves QC as the part of the PET tracer production process that requires the most operator experience, as well as judgment.
- (5) *Footprint:* Current QC relies on multiple instruments and manual test stations, typically requiring substantial bench space. As labs take on more PET tracers, this space becomes increasingly scarce.
- (6) *Operator variability:* It is inevitable that no two operators can execute QC the same way. In one company, the gold standard for precision and accuracy of gas chromatograph (GC) injections was a person. So, the goal of personnel training was to beat that person’s performance, which was very difficult. As a result, each

operator had their own precision and accuracy, with the best ones getting results close to those of the reference person.

- (7) *Complexity*: Currently, QC requires multiple devices, multiple manual test stations, multiple aliquots of the sample, and a large number of data entries, which are difficult to manage even before considering compliance requirements.

14.5 BARRIERS TO QC AUTOMATION

What has delayed QC automation? *Complexity of development* is one barrier. Automated solution developers need expertise in a broad range of analytical technologies involved in radiopharmaceutical QC. Also, unlike radiosynthesis [42, 43], QC automation cannot be based on predecessor automated devices, because there are none. Therefore, instead of incremental improvements, *ground-up development* has been needed. *Cost* is another factor. Adding automation on top of all the currently used QC instruments would increase the total solution cost. Therefore, either the number of components or the cost per component must be lowered for cost-effective automated solutions. Finally, *regulatory* aspects are a hurdle. Any departure from current QC procedures would require thorough validation. Most of the industry has the opinion that if a procedure does not follow pharmacopeial monographs, it cannot be used. Such a perception limits the motivation for innovation. And it is not far from reality, as the validation burden for new procedures is so great that in practice, it limits users' choices to those that follow monographs.

Despite the fact that both radiosynthesis and QC were required from the onset of PET imaging, automation in the former has preceded that in the latter by decades. The difference in the level of radiation exposure was the most likely reason for this priority. However, the complexity of the required automation efforts remained a major barrier for a long time. Traditional QC requires an assortment of complex instruments that are designed as general-purpose laboratory tools and have little in common among them. In addition, it relies on a set of manual tests (such as the Kryptofix 222 spot test) that have no instrumental analogs.

14.6 QC INNOVATION

14.6.1 Traditional Solutions

A laboratory for executing the procedures outlined in Table 14.1 can be outfitted by the user piece by piece or by purchasing a turn-key laboratory package. The former option involves procuring all the individual pieces of equipment from their respective manufacturers (e.g. GC, thin layer chromatography [TLC] scanner, endotoxin measurement device, dose calibrator), assembling test stations for the manual tests (e.g. pH, Kryptofix 222), developing analytical procedures, writing standard operating procedure (SOP) documents, and training staff. It also requires setting up a system of

batch records with an auditable approval path (either paper or electronic). Meanwhile, a turn-key laboratory option provides all these components as a package. The vendor delivers all equipment, installs and qualifies it, trains personnel, delivers SOPs, establishes a quality management system (QMS), and ties all instruments into a laboratory information management system (**LIMS**) that produces a batch record. Such solutions (Figure 14.1) that enable the tests presented in Table 14.1 are currently available from LabLogic LTD (Sheffield, UK) and Elysia-Raytest GmbH (Straubenhardt, Germany). It is important to note that besides the analytical equipment that is used to make measurements on a QC sample, additional equipment, such as an analytical balance, fume hood, and refrigerator, are required for an operational QC laboratory that executes traditional methods.

The innovation discussed in this section is presented as a stepwise progression along with a reduced correlation with current procedures. Automated methods may (i) match the structure of current procedures, (ii) match the function of current procedures, (iii) match the output of current procedures, or (iv) match only the product release decision. Each subsequent option relies on a greater departure from conventional methods than the previous one. The examples illustrate the progression from (i) to (iii), while approach (iv) is likely to emerge in the future and is discussed at the end of the chapter.

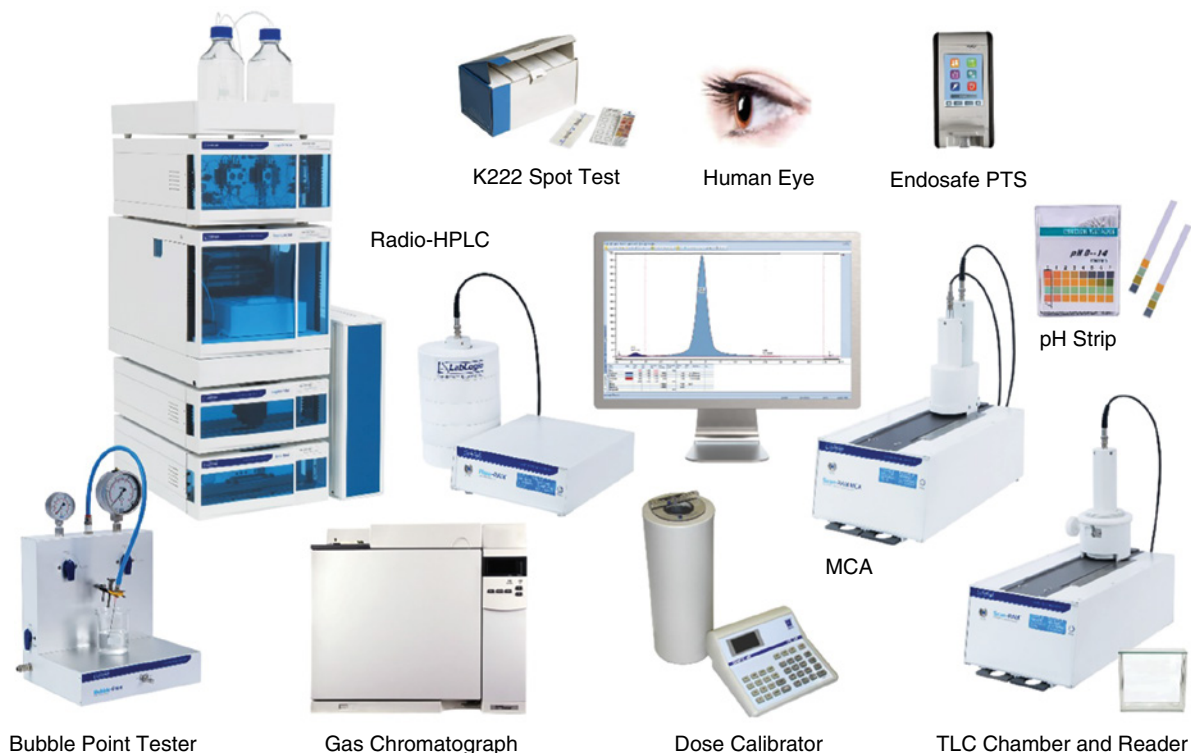


Figure 14.1 Traditional QC laboratory package. Source: Courtesy of LabLogic LTD.

14.6.2 Reducing the Footprint via a Cabinet

One of the issues with QC laboratories is their size. Large laboratory benches with an assortment of equipment and manual test stations on them are poorly scalable. Thus, the first and most logical innovative initiative that presents a measurable improvement over conventional QC is a spatial rearrangement of traditional equipment that reduces the overall floor space requirement while keeping all points of contact with the equipment easily accessible. Typically, laboratory cabinets below and above the equipment are used either to store supplies or not at all. This space is available to be repurposed to host more analytical equipment. Such an approach has been pursued by Elysia-Raytest, yielding a commercially available solution called the QC-Cubicle (Figure 14.2), where a customized cabinet requiring only 1 m² of floor space is configured to host all QC equipment and manual test stations required for the performance of FDG QC tests according to EP. Each instrument can be used in a standalone manner or support a full QC process. The cabinet also contains local shielding to reduce the user's radiation exposure. On-board QC equipment includes a GC with hydrogen generator, dose calibrator, high-performance liquid chromatography (HPLC), camera (for Kryptofix 222 and other visual tests), multi-channel analyzer (MCA), osmometer, TLC scanner, endotoxin test device, and pH strip reader. The user still has to operate all the equipment and perform the individual tests manually, but with a much smaller laboratory.

Figure 14.2 QC-Cubicle by Elysia-Raytest. Source: Courtesy of Elysia-Raytest GmbH.



14.6.3 Adding Automation

The next level of innovation takes the previous concept and adds automation to it. In addition to conventional equipment arranged in a compact space, such solutions also include an automated system for distributing the QC sample between the various test stations. The added benefit of such solutions is that they reduce the dependence on operator variability and risk of human error. Such an approach has been pursued by multiple organizations, including Cardinal Health, Siemens, and Sumitomo.

The best-characterized example is a prototype system (Figure 14.3a) built by *Cardinal Health* (Dublin, OH, USA) [44]. This approach was geared to improve compliance with then-recent cGMP regulations by tying all of the QC processes together with software (Figure 14.3b). Most of the development was focused on the *communication flow*, which allowed an unprecedented degree of control and task coordination. Overall, this system focused on data integrity and eliminating the human in most error-prone aspects of QC. (Some manual operations were still required.)

QC tests enabled on this system included: color, clarity, pH, residual solvents, residual Kryptofix 222, bacterial endotoxin, radionuclidic identity, radionuclidic purity, radiochemical identity, and radiochemical purity. Components of the system included: HPLC (with UV, radiation, and conductivity detectors), GC, Endosafe PTS device (Charles River Laboratories, Inc., Wilmington, MA, USA), pH meter, and dose calibrator with real-time and time-stamped readings.

The expanded range of quality reports generated by this system included: (i) analytical tests performed on the PET tracer product, (ii) product yield, (iii) failure reports for the product, (iv) failure reports for systems or subsystems used to manufacture the product, and (v) operator error reports. The goal was to consider all aspects impacting the quality of the PET tracer in one central system – a powerful concept, built with a focus on cGMP compliance.

The graphical interface allowed the user to choose which tests to run and to set acceptance criteria based on the PET tracers being tested. Moreover, since some manual operations were still required, the system instructed the user what to do and when to do it, to minimize errors and omissions.

The scheduling component of the software allowed automated preparation of multiple QC instruments to be ready for the analysis scheduled on a given date and time. In that environment, it was conceivable that multiple products might be tested at the same time on multiple components of the system followed by the data being channeled to the correct batch records for each given product.

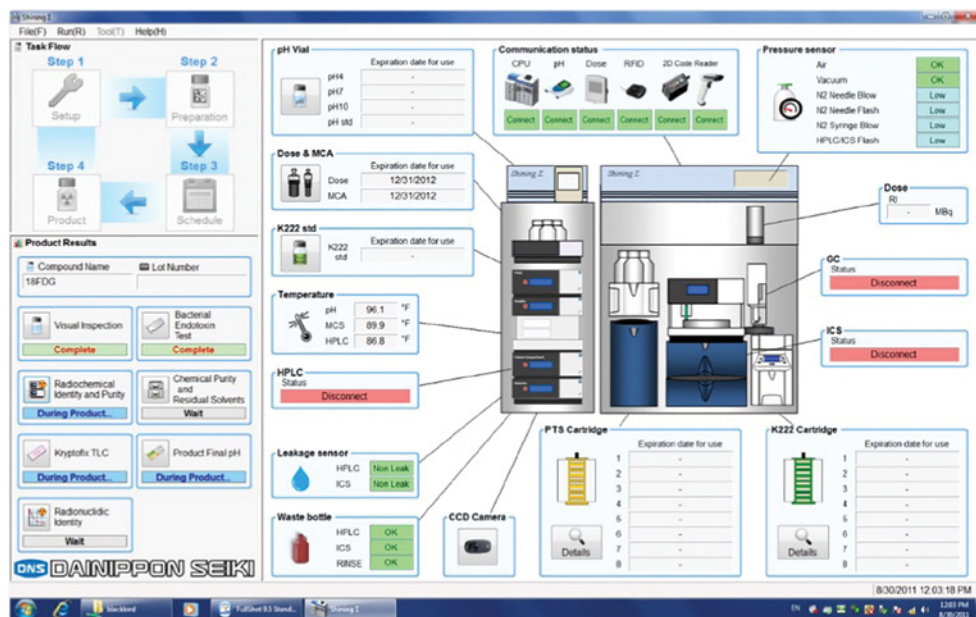
Another development in the “automated cabinet” group was that by *Siemens Molecular Imaging* (Knoxville, TN, USA) [45]. The principle of this system was based on a network of channels and valves that direct syringe-driven liquid. The system included an assembly of commercial instruments and novel test devices that were mounted to a frame. The system was configured to receive a single product sample via a sample delivery cartridge. Downstream of the cartridge was a rotary valve that could meter the sample into multiple aliquots and send them to different test stations via a network of channels and valves.

Figure 14.3

Automated QC prototype (a) and software (b) developed by Cardinal Health. Source: Courtesy of Cardinal Health Nuclear Pharmacy Services.



(a)



(b)

This network was designed such that a single sample injection via an onboard syringe would fill most of the test modules. The modules were: (i) HPLC module used for radiochemical and chemical purity and identity, specific activity, and radioactivity

concentration; (ii) radionuclidic module for radionuclidic purity determination; (iii) color and particulates module based on a flow cell coupled to a light source, detector, and laser for scattering; (iv) filter integrity test module that enabled conclusions by measuring the pressure drop across the used filter; (v) pH module with a pH meter in the flow path of the sample; (vi) Kryptofix 222 module with automated spotting of the sample within the iodine chamber; (vii) Endotoxin module that included an Endosafe PTS device with a disposable cartridge integrated into the sample delivery cartridge; and (viii) residual solvent module based on a compact commercially available GC instrument with sample delivery enabled via one of the channels within the system.

The unique value of the system was that all tests could be performed from one sample injection with no human actions between sample and report. However, after the completion of all tests, the system required cleaning and equilibration before the next run. A functional prototype of the system has been built and demonstrated to produce test results on all of the described parameters.

One more example in this group has been offered by *Sumitomo Heavy Industries* (Tokyo, Japan) [46]. Onboard components included at least an HPLC and a pH meter, and potentially other instruments. Over 40 functional systems rooted in the invention described in the cited patent application have been built and commissioned to date in Japan. The most interesting part of this development is that it yielded a commercial product in the 1990s – much earlier than any other examples and well before the last two of the milestones described at the beginning of this chapter (US cGMP regulations and proprietary tracers). An explanation is that the product was specifically developed for the Japanese market, where stricter regulations exerted pressure for such a solution much earlier than in the rest of the world. The unique value of the Sumitomo system is its integration into a complete solution that also included cyclotron, radiosynthesis, and dose dispensing.

Solutions presented in this group had two types of automation tasks: mechanical and analytical. The former is the delivery of samples and standards to the different instruments that perform the analysis (GC, HPLC, pH meter). Such solutions were based on existing liquid automation technologies and mostly consisted of pumps, channels, and valves. The analytical automation was more challenging as new test devices had to be designed to replace manual operation and assessments where the current detection technology is the human eye (Table 14.1). Innovative approaches amenable to automation had to be developed for Kryptofix 222 [47] and TLC [48] tests that require manual spotting and development.

14.6.4 Adding Miniaturization

Miniaturization of components enables the logical progression from an automated equipment cabinet to a bench-top instrument with similar functionality. Such an approach has been pursued by GE Healthcare (Chicago, IL, USA) and QC1 GmbH (Münster, Germany). A wide range of miniaturized components is required to make such instruments truly bench-top.

Figure 14.4 QC1 concept. Source: Courtesy of QC1 GmbH.



The QC1 concept (Figure 14.4) was designed to receive PET tracer samples via either a sample vial or transfer tubing from either dispensing or production. Downstream of the injection port is a mechanism to distribute the sample between components of the system that perform different tests. The miniaturized components could include a GC, gamma counter and spectrometer, radio-HPLC with different chemical detectors (UV, RI, EC, CC), a column selector, and an isocratic or a gradient pump system. The “sample hub” is configured to perform pH, Kryptofix 222, and radio-TLC tests.

The unique feature of the system is that it was designed to be modular and offered multiple HPLC subsystems with different configurations required for different tracer types. This presented an opportunity for each laboratory to choose the components most relevant to their QC needs and later upgrade the system with added functionality as these needs changed. The main idea of the QC1 approach was to miniaturize and integrate the required components in order to fit all necessary equipment in a small footprint while complying with the appropriate pharmacopoeias (EP, USP). The methods were envisioned to be compendial to avoid validation.

The QC1 solution relied mostly on stationary subsystems that received sample via tubing and therefore needed cleaning with a reliable line-clearance procedure. Only the sample hub used disposable components, which kept consumables to a minimum. Daily system suitability tests and periodic calibration procedures were envisioned to be performed in an automated manner.

The emergence of QC1 as a company was an important milestone in the PET field. For the first time, PET tracer QC was not an exploration of added functionality by a cyclotron

or radiochemistry business. The fact that a standalone entity was formed solely for the purpose of QC automation was a signal that a solution is needed, and the demand for such solutions is confirmed and expected to grow. QC1 also envisioned that the “dose-on-demand” paradigm would become an important part of the industry. In view of that, the easier it became to perform synthesis, the more QC runs per day would be needed, aggravating the bottleneck formed by QC relying on an assortment of instruments and manual procedures.

Only the desired specifications presented earlier for the QC1 system are known. The performance yielded by various prototypes has not been published. The QC1 technology was transferred to Trasis SA (Ans, Belgium) in 2018 for further development.

GE Healthcare presented a concept that went further in its miniaturization innovation [49]. Although it never materialized, it demonstrated a vision where a compact system relying on miniaturized components had a disposable cartridge containing most of the test stations that came in contact with the sample. Meanwhile, the bulk of each miniaturized instrument that was not in any way touched by the sample remained within the stationary system. Such systems were envisioned to operate with minimal cleaning or delays.

In the spirit of the GE approach to radio-synthesis automation with its FASTlab and TRACERlab products, QC automation design revolved around the disposable cassette. Another key innovation was a departure from gas chromatography for the determination of organic solvent concentrations, which were proposed to be measured via head-space analysis mass spectrometer. Furthermore, the fluid path used for fractionating the QC sample and delivering it to the different analysis stations was completely disposable and contained within the cassette.

Separate subsystems were integrated for the following analyses: pH, chemical purity, radiochemical purity, radionuclidic purity, and appearance. The instruments within the system included an HPLC and capillary electrophoresis. Furthermore, innovative testing devices were to be designed within the cassette for endotoxin, pH, and Kryptofix 222 analyses.

Another unique feature of the GE concept was shielding. It was envisioned that the shield would be placed within the instrument to surround only the cassette where all analyses took place. Such arrangements would allow for a dramatic reduction in shielding weight compared to all other approaches, where the entire QC system is shielded on the outside.

Implementation of such a solution relies on the miniaturization of columns and detectors and making them part of a disposable cassette. Furthermore, it requires the development of multiple new miniaturized and highly innovative subsystems. It is feasible that one day a disposable HPLC column with detectors may become technically and commercially viable independently. Then, systems like the proposed concept may need to be revisited.

Representative embodiments show a cleanable path up to the cassette, including a coupling to a Mass Spectrometer (MS) or Gas Chromatograph (GC). The sample would enter the cassette after this coupling. The sample would go through a cleanable pump that would move it into the cassette.

Although the envisioned system has not been built or tested, it provided a conceptual vision radically different from all preceding work that defined subsequent developments in the field. Fluid channels (either permanent or disposable) allow a continuous path between the sample reservoir and every test station as well as eventually to the waste container. All locations are fluidically coupled. Liquids don't get from one location to another without following a fixed and completely enclosed fluid path.

While the two systems just discussed focused on the integration of miniaturized technologies into full-scope QC systems, substantial academic development has focused on the miniaturization of individual QC tests via *microfluidics* [50, 51] or replacement of HPLC by less complex and more compact chromatographic alternatives such as capillary electrophoresis [52]. Once these technologies mature, they are expected to reduce (i) the volume of the QC sample, (ii) the footprint of the instrument, and (iii) the time of analysis.

14.6.5 Exploiting Synergies to Remove Components

While all of the previously described innovation stages were enabled by either addition of components (e.g. cabinet, sample delivery system) or replacement of components (miniaturization), this group of developments aimed at *removing* components to make systems simpler. The premise here is using each component of the system for as many QC tests as possible in order to eliminate other components. Solutions in this group have been presented by ABT Molecular Imaging, Inc. (Louisville, TN, USA) and Trace-Ability, Inc. (Los Angeles, CA, USA).

ABT's ultimate goal was the Biomarker Generator [53], including a compact cyclotron, radiosynthesis module, and QC module integrated together. Such integration allowed opportunities to exploit synergies between the three typically distinct systems and processes.

The ABT team has focused on HPLC being the core of the QC system [54, 55], following a similar approach taken earlier in an academic setting [56]. Innovation in columns, detectors, temperature control, and the mobile phase allowed ABT to enable the following tests on the HPLC: residual solvents (ethanol and acetonitrile), radiochemical identity and purity, and Kryptofix 222. The only additional hardware was the microelectrode measurement device used for pH determination, coupled with a syringe driver for the sample delivery. Meanwhile, the filter integrity test was performed on the synthesis module that was part of the same integrated Biomarker Generator system. Another opportunity was to measure color and clarity inline as the sample was transferred to the final product vial.

The ABT Biomarker Generator system is unique in the way it integrates synthesis and QC. There have not been examples of systems where the QC (even partially) relied on the hardware used in synthesis. Meanwhile, automated sampling and HPLC injection have been enabled in the past on a one-off system at KFA Jülich [57].

The ABT approach was a hybrid between disposable and multi-use components. The synthesis cassette was single-use. Thus, QC functions performed in it (appearance and

filter integrity testing) also relied on the features of the disposable cassette. Meanwhile, chromatographic tests and pH relied on permanent hardware and a system of channels and valves for liquid transfers.

Although some tests, such as radionuclidic purity/identity, sterility, and endotoxin, were not enabled, it is important to recognize that this was not just a concept or a prototype. The solution was released as a product and installed in the field, providing significant simplification of QC compared to traditional methods. According to ABT records, the first complete Biomarker Generator system, including onboard automated QC, was installed and qualified at Sveta Marina Hospital in Varna, Bulgaria in 2013. In 2019, ABT joined the TeamBest group of companies, changing its name to Best ABT, Inc.

Trace-Ability, Inc. took the search for synergies that can reduce the number of components further, to the point where all tests (except filter integrity) required for FDG release in the US were performed on a single analytical instrument – a microplate reader [58, 59]. The Tracer-QC product (Figure 14.5) launched in 2017 is conceptually different from its predecessors as it resulted from a search for the optimal way to obtain the information needed for release testing without being limited by existing test methods. The philosophy followed by Trace-Ability was that what matters is *product quality*, which is manifested in the information yielded by the QC tests. The means of obtaining that information (as long as they are validated and reliable) did not matter. This focus on the goal, rather than means of achieving it, allowed Trace-Ability to expand the arsenal

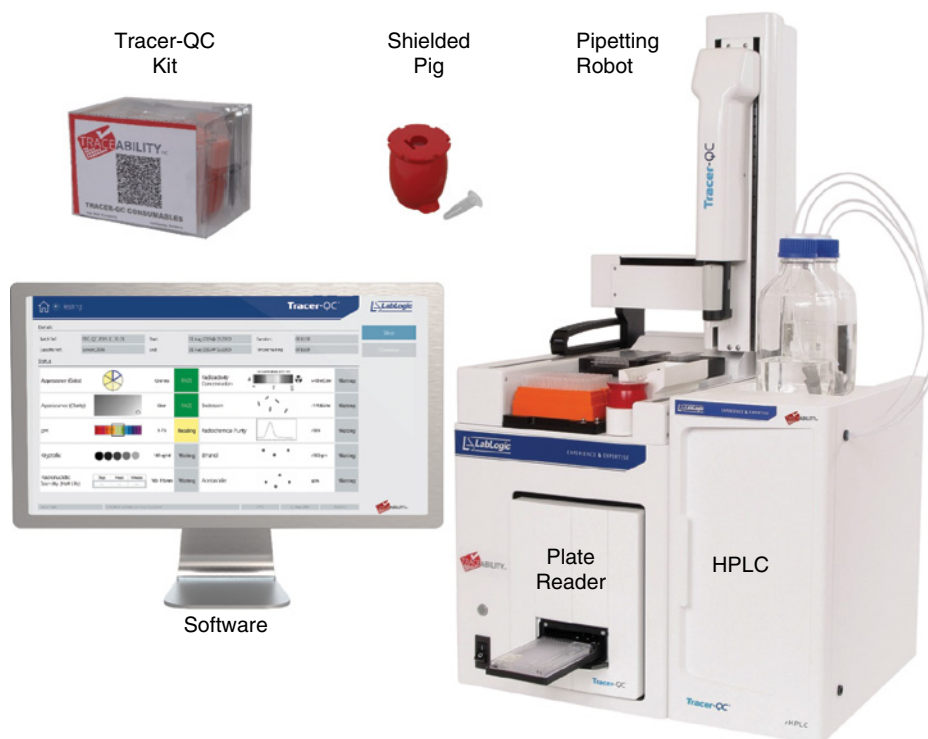


Figure 14.5 Tracer-QC rHPLC product by Trace-Ability. Source: Courtesy of Trace-Ability, Inc.

of applicable technologies and realize synergies that were absent between traditional QC methods.

Trace-Ability chose a plate reader as the core analytical instrument. Plate readers have been developed and perfected over decades for use in diagnostics (60) and other industries. Their performance in measuring absorbed and emitted light from microplates has been continuously improving as a result of competition between multiple manufacturers. A similar evolution has taken place in the microplates used for analysis in plate readers. Trace-Ability built on top of that development and focused the innovation on enabling new methods based on the capabilities offered by state-of-the-art plate readers. Answers for all QC tests are obtained via light measurements (absorbance and luminescence) inside a plate reader. This makes the analytical instrument very simple but requires the development of new tests. These tests and custom plates that enable them became the core innovation yielded by Trace-Ability. FDG QC tests are grouped in the following way:

- *Absorbance tests*, including color and clarity, which can be performed in a microplate on a pure sample by measuring light absorbed by the sample.
- *Indicator-based absorbance tests*, including pH, Kryptofix 222, endotoxin, and organic solvents. These tests require mixing the sample with an indicator that changes color in correlation with the concentration of one of the listed components. That color change is compared to the color change obtained in parallel from multiple standards, yielding a measurement of the concentration of the analyte.
- *Radiation tests*, including radionuclidic identity, radioactivity concentration, radiochemical purity, and radiochemical identity. These tests are enabled via interaction of the sample with scintillating materials within the custom microplate that emit light in response to radiation exposure. The light is measured by the plate reader in luminescence mode and translated into the value of each of the listed properties.

While all of these analyses are performed in a single custom microplate within a plate reader, sample manipulations (distribution and mixing with indicators) are performed by a compact automated pipettor located on top of the plate reader, yielding a completely automated, hands-free process from FDG sample to QC report in a compact footprint measuring under 14 inches in width. Such an approach, not limited by traditional methods, allowed a dramatic simplification of the hardware platform. Since there is no fixed architecture of channels and valves, processes can be easily changed, added, or removed. Microplates have an excessive number of wells, allowing a wide range of analyses to be performed. Thus, samples and standards are analyzed under the same conditions and at the same time, providing *in situ* system suitability confirmation with every run. Furthermore, this allows duplicate testing, which increases accuracy and precision while reducing the chances of invalid test results.

The sample never comes in contact with the instrument, while all contact components and reagents needed for one analysis run are packaged in a single-use kit. The kit is recognized by the system and installed prior to analysis. Then the sample is delivered in a shielded pig keyed to the instrument. Next, the analysis takes place automatically, with

the sample distributed by disposable pipette to the test locations directly from the pig. At the end of the analysis, most of the radioactive waste is aggregated in the same pig for easy removal without user exposure. The rest of the kit can be removed afterward, leaving the system completely free of any radioactive material and ready for the next analysis run.

Unique advantages for the user are presented by a completely disposable path requiring no cleaning and avoiding the risk of cross-contamination. System maintenance is also minimized since no liquids contact any of the permanent components and since the system has so few components. Inventory of consumables required for the analysis is reduced to one kit with a single expiry date. This solution successfully enables users to meet USP quality requirements for FDG while following non-USP methods that have been properly validated. By eliminating all manual operations and human judgments, Tracer-QC yields results that are completely objective and a completely traceable tamper-free data flow from measurement to batch record. These features enable unprecedented ease of compliance with cGMP regulations, further enhanced by software written to 21 CFR Part 11 standards by *LabLogic*. Finally, complete elimination of the person from the process leads to radiation exposure reduction, which is further assured by the compact shielding offered with Tracer-QC systems. Implementation of Tracer-QC in the field has confirmed these advantages along with equivalence to traditional QC methods [61].

To support the diversity of PET tracers beyond FDG, the first Tracer-QC system was closely followed by the second-generation product with integrated HPLC. Although it introduced some cleanable surfaces, the level of automation is such that HPLC cleaning and equilibration take place without user interaction. Moreover, coupling HPLC with a precise automated liquid handler allows the quantitative use of internal standards (supplied within the kit) in every sample injection. This reduces the number of injections required and produces more reliable quantification that has not been possible with standalone HPLCs – even those fitted with automated injectors (that cannot mix sample and standards in precise proportions).

This latest *Tracer-QC rHPLC* product supports a variety of PET tracers by performing all non-specific tests on the plate reader in parallel with running tracer-specific chromatographic tests on the HPLC component. This platform currently enables over 20 QC tests required for the most common PET tracers.

14.7 DISCUSSION OF AUTOMATED QC SOLUTIONS

The previous section presented the progression in PET tracer QC innovation in a sequence correlating with increasing departure from the traditional manual approach. The following discussion focuses on the advantages offered at each step in the context of cGMP production of a variety of PET tracers. At each step, there is a trade-off. Each user must determine the net value that these trade-offs leave them with.

When transitioning from a standard laboratory to a *cabinet*, there is a gain in floor space that is offset by the extra cost of the cabinet. If the user needs to expand their

tracer portfolio within the existing facility, then the extra space is well worth the investment.

When transitioning to an *automated cabinet* solution, there is an investment not only in the cabinet but also in the automation that is added on top of the cost of individual instruments. However, that investment should be balanced by the savings in labor that is eliminated via automation.

Transitioning to *miniaturization* may reduce the overall cost of the solution and offer further space savings compared to both previous solutions. The exact trade-off value will need to be calculated when such solutions are developed and available with known capital and running costs.

Transition to a *synergistic* system offers overall simplification of operation, ease of use, and compliance, all while offering a cost reduction. The trade-off is in the need to validate non-pharmacopeial methods. The latter is clearly a burden for users. However, if the equipment supplier performs such validation, it can dramatically reduce that burden for end users.

Overall, solution complexity goes up and then down as one progresses along this sequence. Adding automation on top of existing instruments increases complexity. Miniaturization may or may not reduce it. And then, only a synergistic approach allows a measurable reduction in solution complexity. A further comparison of the presented solutions is summarized in Table 14.2.

It is also important to recognize the drivers behind each of the presented developments. The GE, Sumitomo, and ABT solutions appear to have been driven by integration within the total tracer-production solution. Specifications were driven by the integration with cyclotron and specific chemistry modules and revolved around the capabilities and needs of the latter. The ABT design was further defined by the dose-on-demand concept. The Siemens and Cardinal systems' specifications were driven by the needs of the corresponding high-volume FDG production networks (PETNET Solutions and Cardinal Health NPS). QC1, and Trace-Ability developments driven by broad use cases.

14.8 CHOOSING AN AUTOMATED QC SYSTEM

As illustrated by the previous summary, there are currently three commercially available automated QC solutions offered by Sumitomo, Best ABT, and Trace-Ability. It is expected that this group will expand, with new solutions offering new features and benefits. Given how different the three systems are from one another, they are very difficult to compare. PET tracer manufacturers' use cases differ as well. Therefore, it is best to review the characteristics of the automated QC solutions that users should compare when choosing a solution for their specific needs. A good start is provided by the list of drivers of QC automation discussed earlier in section 14.4. It provides these reasons to switch to automated solutions: *safety/radiation exposure, human error, operational efficiency and throughput, skillset dependence, footprint, operator variability, and complexity*. Thus, the user can compare the extent of the impacts provided by different automated solutions in

Table 14.2 Automated QC systems for radiopharmaceuticals: concepts, prototypes, and products.

Group	System	Key capabilities and benefits	Key innovative features	Challenges	Fluid path	Maturity
Cabinet	Elysia-Raytest	Compact footprint	Multi-level shielded cabinet	Procedures are still manual	Permanent	Product
Automated cabinet	Cardinal Health	Process controls; coordination of QC and production; data integrity	Software allowing an unprecedented degree of control and integration with synthesis; self-checks.	Some manual operations required; footprint; complexity; cost	Permanent	Prototype
	Siemens	Largest number of tests enabled on a working automated instrument	In-line test stations reached via tubing	Thorough cleaning between runs without feedback on cleanliness; complex maintenance; cost	Permanent	Prototype
	Sumitomo	Integrated with cyclotron, synthesis, and dispensing	Automated sample delivery from synthesis to QC modules	Lack of flexibility	Permanent	Product only in Japan
Miniaturization	GE	Compact instrument with capabilities of a laboratory	Miniaturization; MS for organic solvent analysis; capillary electrophoresis above 2D γ detector; disposable cassette	Requires technologies not currently available	Mostly disposable	Concept
	QC1 (Trasis)	Flexibility	Modular; configurable; single injected sample distributed to different components	Requires additional components to enable complete QC process	Mostly permanent	Prototype
Synergistic	ABT (Best ABT)	Biomarker Generator enablement; simplicity	Synergies enabled via integration of QC with cyclotron and radiosynthesis	Missing tests: appearance, radionuclidic purity/identity, sterility, endotoxin	Mostly permanent	Product
	Trace-Ability	Compact footprint; ease of use, maintenance and compliance	Integrated plate reader pipettor; tests performed within a disposable kit; flexible platform not limited by channels	New tests needed for new tracers	Disposable except for HPLC	Product

these categories. While they all offer an advantage in each category, the impact of that advantage differs in different facilities.

Furthermore, the following criteria that apply to automated solutions should be considered when making a selection: (i) reliability (and how it has been proven); (ii) net cost impact, including a balance of capital, operating, and compliance-driven cost changes yielded by the transition from the current solution to an automated one; (iii) ease of maintenance, driven by the complexity of instruments and skills required for maintenance; (iv) data integrity, which is mostly assured by the level of software compliance with 21 CFR Part 11 regulation; (v) cleaning requirements between runs, especially in systems with a permanent fluid path; (vi) suitability testing, including the complexity of such testing, level of feedback, and degree of automation offered for it; (vii) shielding (whether it is included and sufficient); and (viii) ease of implementation of regulatory transition (discussed next).

14.9 REGULATORY ASPECTS

14.9.1 Regulators' Benefits from Automated QC

While automated QC provides a tool for regulatory compliance that simplifies radiopharmaceutical production, regulators also benefit from its widespread adoption. Automated QC systems give regulators a tangible, verifiable record of manufacturing performance, without having to draw conclusions from secondary data or compare poorly traceable hand-written records.

For example, in the US, the FDA maintains statistics of violations recorded via Form 483 against specific regulatory requirements [36]. A search for 21 CFR Part 212 yields a list of relevant violations referencing the part of the regulation violated and the frequency of such violations. About one-third of all 21 CFR Part 212 violations are in *Laboratory Controls*. Analyzing the requirements and violations in detail, it becomes apparent that most of these violations are rooted in or impacted by manual procedures. The FDA recognizes this but cannot mandate much improvement in the absence of any alternatives to manual procedures. Consequently, the FDA becomes a major stakeholder in and beneficiary of QC automation. QC automation becomes not only a compliance tool for its users but also a QA and inspection tool for regulators. It allows them to have an unquestionable record of cGMP compliance that simplifies inspections and eliminates product quality concerns.

Thus, it is critically important for the developers of QC automation to start interacting with the FDA and regulators in other countries as early in the development process of their products as possible. They should understand the needs of the regulators, manage their expectations, know their concerns, and educate them about upcoming solutions well before the latter are released. Ideally, by the time a solution is on the market, regulatory agencies are aware of it, and the companies know exactly what proof of performance and regulatory submissions are expected by each agency for their products.

In the US, Trace-Ability set a precedent by starting to work with the FDA two years prior to product release, identifying the agency's needs, product performance characteristics, user specifications, and validation approach together with the Technical Committee at the Agency well in advance of these procedures being implemented. *Disclaimer: Funding for this development was made possible, in part, by the Food and Drug Administration through grant U01FD005517. Views expressed in this chapter do not necessarily reflect the official policies of the Department of Health and Human Services; nor does any mention of trade names, commercial practices, or organization imply endorsement by the United States Government.*

14.9.2 Regulatory Approval Mechanism for Automated QC

The following definitions copied from USP General Chapter <823> should be helpful for the discussion of these procedures: "**Validation:** Establishment of documented evidence that a method, process, or system *meets its intended requirements*. **Verification:** Confirmation that an established method, process, or system meets predetermined acceptance criteria. **Performance Qualification (PQ):** PQ demonstrates that the equipment is capable of performing tasks required to make and test PET drugs in the operating environment and that the equipment provides the intended results. PQ should describe the required performance tasks for the equipment. If a USP compendial test procedure is employed, the procedure should be *verified* to demonstrate that the test works under the conditions of actual use. Non-compendial test procedures employed in the testing of a PET drug should be reliable and specific (which can be proven via *validation*).

A change in the process for producing an approved drug, such as the incorporation of automated QC, requires the filing of an NDA supplement with the FDA [62, 63] or similar regulatory submissions in other countries [64]. It is a burden, especially considering that such filings need to contain substantial support for the new method.

If the change uses a USP method, the burden of proof is a *verification*, and a CBE-30 supplement (changes being effected in 30 days in the absence of FDA objections) might suffice [65]. Therefore, USP methods have been the focus of several QC automation efforts. However, the internal complexity of automated systems with diverse instruments integrated via a network of channels and valves requires *validation* of robustness and the absence of cross-contamination. Therefore, most likely the more complex regulatory route of a prior approval supplement (**PAS**) would be required for these systems, despite using USP methods. The PAS mechanism is also appropriate for automated systems using non-USP methods, which require *validation* prior to use.

Radiopharmaceutical manufacturers wishing to adopt an automated QC system could *validate* such changes themselves by following the FDA guidance [66] on bioanalytical method validation. However, few have the resources to do so, which is an adoption barrier. To overcome this barrier, the makers of automated QC systems can validate their systems through collaborative studies with early adopters and present the validation data to the FDA via a drug master file (**DMF**). After the DMF examination is triggered by the

first cross-reference and found acceptable, subsequent adopters may then reference the DMF in their NDA supplements. This mechanism allows them to implement a new solution requiring only PQ without performing the validation study themselves, and may rely on a CBE30 mechanism.

Validation most commonly seeks to establish *equivalence* [67] with the method it is replacing. For automated QC systems that use pharmacopeial methods, this approach is best. However, additional validation is required to demonstrate that methods that are individually equivalent are not affected by other parts of the system. Method performance must be established in the context of the automated process. For example, validation of the robustness of the sample/aliquot management system is needed to ensure that it does not affect tests that may otherwise be equivalent.

The situation is more complicated when new methods are very different from old methods and cannot be considered compendial. Specifically, it can run into the following two types of issues:

- (1) *Comparison is impossible*: The old method was incorporated historically without being properly validated. For example, the spot test for Kryptofix 222 that is in use today has no record on accuracy, precision, linearity, or limit of detection (**LOD**). Thus, it is difficult to come up with criteria for truly comparing the new method to the old one without having to validate the old method first.
- (2) *The new method is inferior to the old one*: This statement may sound absurd. Why would anyone switch to an inferior method? Actually, as discussed earlier, some of the equipment used in QC of PET tracers is general-purpose laboratory equipment that is excessive in its capacity for the purpose of PET tracer QC. A good example is residual solvent analysis. A LOD on a GC is typically in **ppb** (parts per billion). Meanwhile, the release test only needs to answer the question of whether the concentration of acetonitrile in the sample is above or below 400 **ppm** (parts per million). For the purposes of answering this question, sub-ppm LOD is irrelevant. An instrument that has a 200 ppm LOD may answer this question adequately. The purpose for which GC is used in the QC of PET tracers does not require ppb sensitivity. Thus, methods should be compared based on how well they answer the QC question, rather than on their overall characteristics. In view of this, a method with 200 ppm LOD should suffice for acetonitrile test, as long as its accuracy and precision allow 95% confidence in answering the pass/fail question. Such methods should be validated via a mechanism different from overall equivalence or superiority.

Such validation approach is known as *fit for purpose* [68], which relates to the USP definition of *validation*, where the “intended requirements” for the method should be set based on the answer it needs to provide rather than overall analytical performance. Then, the validation study should be designed to determine whether the method meets these requirements. The absence of comparison to old methods eliminates the two issues presented earlier.

To date, the only automated QC solution that has undergone official validation in the US (with corresponding FDA submissions) is Tracer-QC. Both validation approaches

have been used. The *equivalence* approach was used for the TLC test for [N-13]Ammonia because the predicate USP test [69] was similar in principle. The latter method relies on a TLC spotted on the bench, developed vertically in a chamber, dried manually, and read on a TLC scanner, which generates a chromatogram for determining radiochemical identity (based on R_f) and radiochemical purity (peak integration). The Tracer-QC method relies on a horizontal TLC in a disposable kit with automatic spotting, development, and analysis. The study comparing the two methods was designed and executed at the Gordon Center for Medical Imaging at Massachusetts General Hospital (**MGH**). The results obtained on the same samples by both methods demonstrated equivalence. The data were submitted to the FDA via a CBE-30 supplement and resulted in a written approval letter.

The second validation approach used was *fit for purpose* because most of the Tracer-QC tests are different from the compendial ones. This approach was used to validate the entire system with a 10-test protocol for FDG at the Department of Radiology and Biomedical Imaging at the University of California, San Francisco (**UCSF**). Performance criteria were preset based on desired accuracy, precision, specificity, range, linearity in the pass/fail threshold range, and limits of detection and quantification. Additionally, a separate part of the study focused on robustness, with challenges to the system including various environmental conditions or operation near the limits of acceptable conditions (for example, after the kit has stayed open to the atmosphere for the longest allowed time). Multi-parametric validations can quickly become impractical – e.g. a full factorial validation study for a 10-test system can easily require thousands of experiments. Therefore, a more practical study had to be designed. Each experiment in this study assessed multiple tests in parallel, producing data that are parsed for easy review. This approach relied on the Tracer-QC's ability to measure multiple parameters at once. Additionally, this approach allowed for comprehensive testing of potential interferences, essentially placing very stringent requirements on the specificity of the individual tests.

Experimentally, this validation study consisted of repeated analyses of multiple FDG samples spiked with a mixture of specific impurities or water. Spiking solutions were carefully prepared to produce known concentrations of the impurities. For each run, an FDG sample was mixed with the spiking solution. FDG samples were produced according to the standard clinical production protocol. Due to radiation safety concerns, some experiments were performed with decayed FDG samples. This approach allowed measuring the analytical performance of the individual tests on the Tracer-QC platform. Complete validation was achieved over 28 individual runs that generated close to 400 individual data points.

These validation studies have drawn the most benefit from collaboration with the FDA. The development team had a chance to make the agency familiar with the system before designing validation studies. Then, when the studies were designed, they were reviewed with the FDA prior to execution. This approach allowed the Agency to challenge the methods and the validation approach before any of the laborious validation laboratory work. Thus, by the time the laboratory work was started, the developers and regulators had reached concurrence on the validation approach. During the study, interim validation reports were also reviewed with the Agency, resulting in the identification

of areas where additional data had to be gathered. Finally, the body of data was found sufficient by the FDA Technical Committee to conclude that the integrated multi-parametric QC method on Tracer-QC has been successfully validated. Trace-Ability now maintains a Type V DMF (#029891) with the FDA that includes system description and validation reports. Cross-referencing this DMF, enables new users to implement Tracer-QC without extensive validation.

This experience shows that validation of something radically different from compendial methods cannot have a clear prescription. It requires a proactive dialogue with regulators and the joint development of an approval path, which is much more productive than developing a validation strategy in a vacuum in hopes that it matches regulators' expectations after it has been executed. Such a risky approach has a strong chance of having the validation generate a data set that is insufficient or irrelevant for the regulators' decision regarding the new technology.

14.9.3 Pharmacopeia Incorporation

Ultimately, automated methods are expected to become the standard that is incorporated into pharmacopeial monographs. The USP standards-setting process enables anyone to bring a standards-setting issue to the attention of the USP, ranging from establishing a new standard to revising an existing one.

The USP-NF is a combination of two compendia: the USP and the National Formulary (**NF**). Monograph proposals for the USP-NF are submitted in writing to the USP along with explanations for the proposals and data to support them. Monograph submission guidelines [70] published by the USP provide detailed information, including recommendations for what data to submit with specific proposals. The monographs are routinely sponsored by the pharmaceutical companies that hold an approved NDA or abbreviated new drug application (ANDA) for the product of interest. The sponsor's proposal should provide supporting data from its approved application, including method-validation data for the analytical methods used for the drug product. Once an organization sponsors a monograph, a USP panel composed of USP scientific staff and expert volunteers reviews a draft to ensure that it has enough data to provide compelling evidence that the method is either equivalent to existing ones or fit for its intended purpose. Laboratory tests may also be conducted when needed. Once a new standard is developed for the USP-NF, it is proposed for a 90-day public review and comment period in the Pharmacopeial Forum (**PF**). After the public review and comment period, the Expert Committee considers the comments received and determines whether further changes to the standard should be made. To finalize the standard, the Expert Committee members vote independently on the proposal through an electronic balloting system. The standards that the USP deems official are set forth in its various compendia.

The USP allows multiple alternative analytical methods to be included in monographs at the same time for the same drug. As long as a monograph is being maintained by the sponsor, it can stay active, and users can choose the method that they find most appropriate. This process will be appropriate for the incorporation of automated QC solutions

into USP standards. Either the manufacturer of the automated solution or the manufacturer of the PET drug that relies on automated QC will sponsor a monograph (or a revision of one). The review process, including a thorough data analysis, will yield a decision regarding the new monograph.

14.10 FUTURE DEVELOPMENTS

This chapter has presented multiple automation approaches for PET tracer QC. Their relative strengths have been discussed in the context of satisfying today's needs. But what will the PET field look like in a number of years, and how will QC automation support it? To suggest answers to this question, there needs to be a vision for tracer production dynamics. Based on the observed trends, it can be assumed that no single tracer will surpass FDG in the number of doses and batches produced. But it is reasonable to believe that the total batch volume of other tracers will surpass FDG soon, and the total dose volume will do so as well in due time. This means QC laboratories will have to support more and more products each year; and relying on conventional methods if each tracer requires dedicated equipment (as is the case frequently today) will be impractical, as the laboratories will run out of space after the second or third tracer. Automated QC offers a footprint reduction. But if the IP owners of the different tracers demand dedicated equipment, the manufacturers will need an ever-growing number of automated QC machines.

One solution is the disposable path. If the opportunity for cross-contamination is eliminated, then different samples can be run on the same equipment. The disposable path is one measure against cross-contamination, as no surfaces come in contact with more than one sample. However, chromatography such as HPLC cannot yet be made in a disposable fashion (while being economical and practical). Thus, there has to be an automated cleaning procedure coupled with cleaning validation that confirms that any traces of any samples from the previous run are entirely removed before the next run. Also, it is possible that one day, a technology like that envisioned in the GE patent will become available, enabling a cost-effective disposable HPLC.

These trends may cover the immediate need. But if no further evolution takes place in QC automation, it will run into the next bottleneck in a few years when the number of tracers (with unique QC requirements) grows faster than the automated QC procedures available for their support. Even today, with over 100 new PET tracers in development, it is not possible to quickly design automated QC procedures for all tracers prior to Phase I clinical development. However, by the time a much smaller number of tracers enters Phase III, it will be difficult to switch methods, as doing so requires amendments when the sponsor cannot afford to lose any time and delay the NDA approval date. Thus, it is too early in Phase I and too late in Phase III.

To solve this issue, QC automation needs to be very flexible to accommodate methods that are not even conceived today. At the same time, new method development should be so easy that it does not delay tracer development. Thus, it is expected that the

next-generation technology that will replace QC automation summarized here will have these attributes: (i) a more universal platform that can accommodate new tests without hardware modifications, and (ii) a platform that enables method development so easily that it does not require additional resources or time in the tracer development process.

A trend toward merging QC into the total PET tracer production solution is likely to become stronger. Some of the approaches discussed in this chapter have explored this path already. However, within these solutions, synthesis and QC processes are still separate. In the future, it is logical to expect that merging synthesis and QC into one process may offer opportunities for in-process controls that provide early insight into product quality and possibly even enable corrective measures. By merging future innovation in synthesis and QC, the overall value will be greater than the sum of the benefits of the two components.

Yet another possible trend could be toward simplification or refocusing of QC based on the record of production. Automation (in any form) should enable more data that can be analyzed for trending. Such outputs can be used to predict failures before they happen or to prove the robustness of a process that may lead to reduced QC effort (making some per-batch tests periodic). Recent developments in big data analytics [71] should support the emergence of such solutions.

Finally, innovation in the tests themselves should lead to more reliable results. For example, the Kryptofix 222 spot test developed with iodine vapor is non-specific and can respond to a range of compounds besides Kryptofix 222. No such compounds have been observed in formulations of FDG over the years. But it is very possible to see them as intended or unintended constituents of new tracer formulations. Therefore, more specific tests will be needed as the range of PET tracers expands.

Automation approaches may correlate to manual QC in a number of gradually less dependent ways, as illustrated in this chapter. Each subsequent option relies on a greater departure from conventional methods than the previous one:

- (1) Matching the structure of current procedures, such as in the automated cabinet approach
- (2) Matching the function of current procedures, such as in the miniaturization approach
- (3) Matching the output of current procedures, such as in the synergistic approach
- (4) Matching only the product release decision

Currently, the last option remains unexplored. However, a well-supported product release decision is the ultimate purpose of release testing. Future developments are likely to focus on achieving this goal in more effective ways than the ones offered or conceived today. A more systematic approach is likely to take advantage of a combination of in-process controls, merging of synthesis and QC functions, trending analyses, more complex processing of large data sets from the same and different sites, and preventive alarms that trigger action before batches start drifting out of compliance.

The author hopes that there is healthy competition and collaboration between the major players in achieving this vision. It would be best if, yet again, multiple options

are offered by several companies, and possibly a hybrid between different approaches becomes the solution that can support the growth of PET radiotracer production for decades, enabling new diagnostics to reach patients rapidly and save lives.

REFERENCES

1. US Pharmacopeial Convention (USP) (2020). Positron emission tomography drugs for compounding, investigational, and research uses <823>. In: *USP 43-NF 38*, 7100–7109.
2. Winicov, H., Schainbaum, J., Buckley, J. et al. (1978). Chemical process optimization by computer – a self-directed chemical synthesis system. *Anal. Chim. Acta* 103 (4): 469–476.
3. Berger, G., Maziere, M., Knipper, R. et al. (1979). Automated synthesis of ¹¹C-labelled radiopharmaceuticals: imipramine, chlorpromazine, nicotine and methionine. *Int. J. Appl. Radiat. Isot.* 30 (7): 393–399.
4. Comar, D., Zarifian, E., Verhas, M. et al. (1979). Brain distribution and kinetics of ¹¹C-chlorpromazine in schizophrenics: positron emission tomography studies. *Psychiatry Res.* 1 (1): 23–29.
5. Reivich, M., Kuhl, D., Wolf, A. et al. (1979). The [¹⁸F]fluorodeoxyglucose method for the measurement of local cerebral glucose utilization in man. *Circ. Res.* 44 (1): 127–137.
6. Noble, A. (2015). Regulating compounding pharmacies. *NCSL Legisbrief* 23 (23): 1–2.
7. FDA. (2018). Radioactive drugs for certain research use. Code of Federal Regulations Title 21, Volume 5, Part 361, Section 361.1.
8. FDA. (2018). Investigational new drug application. Code of Federal Regulations Title 21, Volume 5, Part 312.
9. Vera-Ruiz, H., Marcus, C.S., Pike, V.W. et al. (1990). Report of an International Atomic Energy Agency's Advisory Group meeting on "Quality control of cyclotron-produced radiopharmaceuticals". *Int. J. Radiat. Appl. Instrum. Part B* 17 (5): 445–456.
10. Pike, V.W., Waters, S.L., Kensett, M.J. et al. (1991). Radiopharmaceutical production for PET: quality assurance practice, experiences and issues. In: *The New Trends in Radiopharmaceutical Synthesis, Quality Assurance, and Regulatory Control* (ed. A.M. Emran), 433–449. Plenum Press.
11. Sharma, S.K. (2016). Quality control of PET radiopharmaceuticals with special reference to ¹⁸F-FDG. In: *Progress in PET Radiopharmaceuticals (Quality Control and Theranostics)* (ed. S.K. Sharma), 105–124. Nova Biomedical.
12. Lovinfosse, P., Visvikis, D., Hustinx, R., and Hatt, M. (2018). FDG PET radiomics: a review of the methodological aspects. *Clin. Transl. Imaging* 6 (5): 379–391.
13. Kelloff, G.J., Hoffman, J.M., Johnson, B. et al. (2005). Progress and promise of FDG-PET imaging for cancer patient management and oncologic drug development. *Clin. Cancer Res.* 11 (8): 2785–2808.
14. Singnurkar, A., Poon, R., and Metser, U. (2017). Comparison of ¹⁸F-FDG-PET/CT and ¹⁸F-FDG-PET/MR imaging in oncology: a systematic review. *Ann. Nucl. Med.* 31 (5): 366–378.

15. Sarikaya, I., Elgazzar, A.H., Sarikaya, A., and Alfeeli, M. (2017). Normal bone and soft tissue distribution of fluorine-18-sodium fluoride and artifacts on 18F-NaF PET/CT bone scan. *Nucl. Med. Commun.* 38 (10): 810–819.
16. US Pharmacopeial Convention (USP) and National Formulary (USP 19-NF 14) (1979). *Rockville, MD: "Sodium Fluoride F 18 Injection" Monograph*, 176–177. United States Pharmacopeial Convention.
17. US Pharmacopeial Convention (USP) (1990). *Fludeoxyglucose F 18 Injection*. USP 22-NF 17, 579–580. Rockville, MD: USP.
18. US Pharmacopeial Convention (USP) (1998). *Radiopharmaceuticals for Positron Emission Tomography (PET) – Compounding, Investigational, and Research Uses <823>*. USP 23-NF 18. Rockville, MD: USP.
19. Tankiewicz, M., Namieśnik, J., and Sawicki, W. (2016). Analytical procedures for quality control of pharmaceuticals in terms of residual solvents content: challenges and recent developments. *TrAC, Trends Anal. Chem.* 80: 328–344.
20. Hamacher, K., Coenen, H.H., and Stöcklin, G. (1986). Efficient stereospecific synthesis of no-carrier-added 2-[¹⁸F]-fluoro-2-deoxy-d-glucose using aminopolyether supported nucleophilic substitution. *J. Nucl. Med.* 27 (2): 235–238.
21. Chaly, T. and Dahl, J.R. (1989). Thin layer chromatographic detection of Kryptofix 2.2.2 in the routine synthesis of [¹⁸F]2-fluoro-2-deoxy-d-glucose. *Int. J. Radiat. Appl. Instrum. Part B* 16 (4): 385–387.
22. US Pharmacopeial Convention (USP) (2018). *Fludeoxyglucose F 18 Injection*. USP 41-NF 36, 1794–1795. Rockville, MD: USP.
23. Bowman, F.W. (1969). The sterility testing of pharmaceuticals. *J. Pharm. Sci.* 58 (11): 1301–1308.
24. European Pharmacopoeia (2002). *Fludeoxyglucose [¹⁸F] Injection*, 4e, 1361–1368. Strasbourg, France: European Directorate for the Quality of the Medicines.
25. British Pharmacopoeia (2000). *Monographs: Radiopharmaceutical Preparation, Fludeoxyglucose [¹⁸F] Injection*, 2000. London: British Pharmacopoeia Commission.
26. World Health Organization. (2009). The international pharmacopoeia: fludeoxyglucose (18F) injection. Document QAS/08.265/FINAL.
27. Yu, S. (2006). Review of ¹⁸F-FDG synthesis and quality control. *Biomed. Imaging Intervention J.* 2 (4):1-11.
28. Hung, J.C. (2002). Comparison of various requirements of the quality assurance procedures for (18)F-FDG injection. *J. Nucl. Med.* 43 (11): 1495–1506.
29. Fludeoxyglucose F 18 Injection (2011). *Sample Formats: Application to Manufacture Ammonia N 13 Injection, Fluorodeoxyglucose F 18 Injection (FDG F 18) and Sodium Fluoride F 18 Injection Chemistry, Manufacturing, and Control Sections*, 24–27. Rockville, MD: US Food and Drug Administration.
30. Ehrenkauf, R.E., Chilton, H., Morton, T., and Jones, B. (1995). Analytical instrumentation in the QC of PET radiopharmaceuticals. In: *Chemists' View of Imaging Centers* (ed. A.M. Emran), 217–224. Plenum Press.
31. Shukla, J., Vatsa, R., Garg, N. et al. (2013). Quality control of positron emission tomography radiopharmaceuticals: an institutional experience. *Indian J. Nucl. Med.* 28 (4): 200–206.

32. Lodi, F. and Boschi, S. (2016). quality control of pet radiopharmaceuticals. In: *Basic Science of PET Imaging* (ed. M.M. Khalil), 105–126. Springer.
33. FDA. (2013). Current good manufacturing practice for positron emission tomography drugs. Code of Federal Regulations, Title 21, Volume 4, Part 212: 171–80.
34. Schwarz, S., Norenberg, J., Berridge, M. et al. (2013). The future of USP monographs for PET drugs. *J. Nucl. Med.* 54 (3): 472–475.
35. Chi, Y.-T., Chu, P.-C., Chao, H.-Y. et al. (2014). Design of CGMP production of ^{18}F - and ^{68}Ga -radiopharmaceuticals. *Biomed Res. Int.* 2014: 680195.
36. FDA. (2018). Inspection observations: data and information summarizing the areas of regulation cited on FDA form 483. <https://www.fda.gov/iceci/inspections/ucm250720.htm>.
37. Patel, N., Fakhry-Darian, D., Nijran, K. et al. (2018). Assessment and optimisation of hermes amyloid BRASS as a quantitative diagnostic tool in reporting ^{18}F -florbetapir (Amyvid) investigations. *J. Nucl. Med.* 59 (Supplement 1): 1011–1011.
38. Clarke, B.N. (2018). PET radiopharmaceuticals: what's new, what's reimbursed, and what's next? *J. Nucl. Med. Technol.* 46 (1): 12–16.
39. Riss, P.J., Ferrari, V., Bielik, R. et al. (2012). Synthesis of [^{18}F]Fluoromisonidazole (1-(2-hydroxy-3- ^{18}F fluoropropyl)-2-nitroimidazole, [^{18}F]FMISO). In: *Radiochemical Syntheses* (eds. P.J.H. Scott and B.G. Hockley), 41–49. Hoboken, NJ, USA: Wiley.
40. Prasad, K.N., Cole, W.C., and Haase, G.M. (2004). Radiation protection in humans: extending the concept of as low as reasonably achievable (ALARA) from dose to biological damage. *Br. J. Radiol.* 77 (914): 97–99.
41. Ferguson, D., McGrath, S., and O'Hara G, Marshall C. (2011). Investigation of staff finger doses during quality control of FDG production. *Health Phys.* 100 (5): 523–529.
42. Alexoff, D.L. (2003). Automation for the synthesis and application of PET radiopharmaceuticals. In: *Handbook of Radiopharmaceuticals* (eds. M.J. Welch and C.S. Redvanly), 283–305. Chichester, UK: Wiley.
43. Krasikova, R. (2013). PET radiochemistry automation: state of the art and future trends in ^{18}F -nucleophilic fluorination. *Curr. Org. Chem.* 17 (19): 2097–2107.
44. Eshima, D., Husnu, M., and Stone, J. (2012). Method and system for automated quality control platform for radiopharmaceuticals. US patent application 13/550,030 filed 16 July 2012.
45. Ball, C.E., Elizarov, A.M., Kolb, H.C., et al. (2009). Apparatus and method for automated quality control. US patent 8,214,159 B2, filed 3 December 2009 and issued 3 July 2012.
46. Sasaki, M. and Tanaka, A. (2000). Quality control system and quality control method for radioactive drug. Japanese patent JP2000356642A, filed 26 December 2000.
47. He, M.Y., Sun, L.Q., and Luo, A.Q. (2012). Spectrophotometric determination of Kryptofix 2.2.2 using TCNQ. *Adv. Mater. Res.* 581–582: 1156–1159.
48. Corkan, L.A., Haynes, E., Kline, S., and Lindsey, J. (1991). Robotic thin layer chromatography instrument for synthetic chemistry. In: *New Trends in Radiopharmaceutical Synthesis, Quality Assurance, and Regulatory Control* (ed. A.M. Emran), 355–370. Boston, MA: Springer US.
49. Hansteen, O.H., Jakobsen, J.B., Lindgaard, S.-E. et al. (2011). Quality control devices and methods for radiopharmaceuticals. US patent 9,291,606 B2 filed 22 August 2011 and issued 22 March 2016.

50. Ha, N., Sadeghi, S., and van Dam, R. (2017). Recent progress toward microfluidic quality control testing of radiopharmaceuticals. *Micromachines* 8 (11): 337.
51. Tarn, M.D., Esfahani, M.M.N., Patinglag, L. et al. (2017). Microanalytical devices towards integrated quality control testing of [¹⁸F]FDG radiotracer. In: *21st International Conference on Miniaturized Systems for Chemistry and Life Sciences (MicroTAS 2017)*, 559–560. Savannah, GA: Chemical and Biological Microsystems Society (CBMS).
52. Cheung, S., Ly, J., and Dam, R.M. (2013). Capillary electrophoresis separation of ¹⁸F-labeled PET tracers from impurities: towards miniaturized quality control. *J. Labelled Compd. Radiopharm.* 56: S458–S458.
53. Awasthi, V., Watson, J., Gali, H. et al. (2014). A “dose on demand” biomarker generator for automated production of [(18)F]F(-) and [(18)F]FDG. *Appl. Radiat. Isot.* 89: 167–175.
54. Anzellotti, A., Bailey, J., Ferguson, D. et al. (2015). Automated production and quality testing of [¹⁸F]labeled radiotracers using the BG75 system. *J. Radioanal. Nucl. Chem.* 305: 387–401.
55. Anzellotti, A.I., McFarland, A.R., Ferguson, D., and Olson, K.F. (2013). Towards the full automation of QC release tests for [¹⁸F]fluoride-labeled radiotracers. *Curr. Org. Chem.* 17 (19): 2153–2158.
56. Kozirowski, J. (2010). A simple method for the quality control of [¹⁸F]FDG. *Appl. Radiat. Isot.* 68 (9): 1740–1742.
57. Crouzel, C., Clark, J.C., Brihaye, C. et al. (1993). Radiochemistry automation for PET. In: *Radiopharmaceuticals for Positron Emission Tomography*, 45–89. Dordrecht: Springer Netherlands.
58. Hennessy, R.C., Stougaard, P., and Olsson, S. (2017). A microplate reader-based system for visualizing transcriptional activity during in vivo microbial interactions in space and time. *Sci. Rep.* 7 (1): 281.
59. Kedar, P., Desai, A., Warang, P., and Colah, R. (2017). A microplate reader-based method to quantify NADH-cytochrome b5 reductase activity for diagnosis of recessive congenital methaemoglobinemia. *Hematology* 22 (4): 252–257.
60. Sun, Y.-P., Zhang, W., Zhao, Q.-J. et al. (2018). An optimized high-throughput fluorescence plate reader-based RSV neutralization assay. *J. Virol Methods* 260: 34–40.
61. Yokell, D., Noel, J., Katorcha, E., and El Fakhri, G. (2020). A comparison of automated quality control using the Trace-Ability Tracer-QC vs traditional quality control for F-18 Fludeoxyglucose (F-18 FDG). *J. Nucl. Med.* 61: 514–514.
62. Marcus, C.S. (2018). How should the FDA review diagnostic radiopharmaceuticals? *J. Nucl. Med.* 59 (6): 868–870.
63. US Department of Health and Human Services Food and Drug Administration Center for Drug Evaluation and Research (CDER). (2014). Guidance for industry CMC postapproval manufacturing changes to be documented in annual reports.
64. Lokesh, M.S., Gupta, N.V., and Belagoankar, B.D. (2015). Comparative study of process of post approval change application submission and approval for marketing authorization variations in EU, US, India, Saudi Arabia and Singapore. *Int. J. Drug Dev. Res.* 7 (1): 10–22.

65. US Department of Health and Human Services; Food and Drug Administration. 2004. Guidance for Industry. Changes to an Approved NDA or ANDA. Center for Drug Evaluation and Research (CDER), CMC.
66. US Department of Health and Human Services; Food and Drug Administration. 2018. Bioanalytical method validation. Guidance for Industry. Center for Drug Evaluation and Research (CDER).
67. Lebrun, P., Govaerts, B., Debrus, B. et al. (2008). Development of a new predictive modelling technique to find with confidence equivalence zone and design space of chromatographic analytical methods. *Chemom. Intell. Lab. Syst.* 91 (1): 4–16.
68. Lee, J.W., Devanarayan, V., Barrett, Y.C. et al. (2006). Fit-for-purpose method development and validation for successful biomarker measurement. *Pharm. Res.* 23 (2): 312–328.
69. US Pharmacopeial Convention (USP) (2018). *Ammonia N 13 Injection*. USP 41-NF 36. Rockville, MD: USP.
70. US Pharmacopeial Convention (USP). 2016. Guideline for submitting requests for revision to USP–NF general information for all submissions. US Pharmacopeial Convention.
71. Wang, Y., Kung, L., and Byrd, T.A. (2018). Big data analytics: understanding its capabilities and potential benefits for healthcare organizations. *Technol. Forecasting Social Change* 126: 3–13.

Chapter 15

Moving PET Drugs from the Lab to the Patient in the USA

David W. Dick

*Department of Radiology, University of Iowa, Iowa City, IA,
52242-1077, USA*

15.1 INTRODUCTION

Positron emission tomography (**PET**) drugs are unique in that they are produced in small batches by decentralized manufacturers/pharmacies due to their physical characteristics, which do not lend them to large-scale production: namely, the shorter half-lives of positron-emitting radionuclides. Until recently, the regulatory pathway for PET drugs was vague and murky due to a lack of rules that considered these unique characteristics. It is worthwhile to look at the history of PET drugs before delving into the current regulatory environment.

15.2 PET DRUGS BEFORE THE FOOD AND DRUG ADMINISTRATION MODERNIZATION ACT

F-18 fluorodeoxyglucose (**F-18 FDG**) was originally developed in the 1970s as a research tool for use in an academic setting [1]. Many other PET drugs were developed in the intervening years, but F-18 FDG showed the most utility for incorporation into clinical practice in the fields of oncology, neurology, and cardiology. The use of F-18 FDG started seeping

into clinical practice, with the manufacturing of the drug usually performed under the practice of pharmacy.

The Food and Drug Administration (**FDA**) was aware of PET drugs and had largely left the field unregulated due to PET drugs being research tools and not part of clinical practice. However, with the shift of F-18 FDG to becoming a clinical drug, FDA decided to regulate the manufacturing of PET drugs to ensure their safety and effectiveness. The FDA published a notice in the *Federal Register* in 1995 stating its intention to regulate PET facilities as drug manufacturers and that the manufacturing of PET radiopharmaceuticals must meet current Good Manufacturing Practice (**cGMP**) standards [2]. The FDA held several stakeholder workshops to educate the PET community on cGMP and how it would regulate PET drug manufacturing. The PET stakeholders soon realized that the regulatory scheme proposed by the FDA would be impossible to meet due to the unique aspects of PET drug production compared with conventional pharmaceutical manufacturing. These unique aspects include distributed, small-scale productions; limited staffing compared to conventional pharmaceutical manufacturers; and quality control concessions due to the short expiration times of PET drugs (e.g. releasing drugs before sterility testing has finished). PET stakeholders realized that legislative action was needed and enlisted the help of Senator Ted Stevens from Alaska.

15.3 FOOD AND DRUG ADMINISTRATION MODERNIZATION ACT

Through congressional action, specific legislative language was added to the Food and Drug Administration Modernization Act (**FDAMA**), which was signed by President Clinton in 1997 [3]. The language in Section 121 directed the FDA to consider the special characteristics of PET radiopharmaceuticals and the unique processes necessary for the manufacturing and quality control of these drugs. The FDA was required to implement new cGMP standards and approval pathways for PET radiopharmaceuticals.

Given that PET radiopharmaceuticals had been used clinically and in research for 20+ years, the FDA first conducted a review of the published literature to evaluate the safety and effectiveness of PET drugs. On 10 March 2000, in the *Federal Register*, the FDA published a notice regarding the safety and effectiveness of F-18 FDG, F-18 sodium fluoride, and N-13 ammonia [4]. This notice allowed potential new drug application (**NDA**) applicants to reference the safety and effectiveness notice when filing an NDA, allowing for a 505(b)(2) application rather than a 505(b)(1) application, and reducing the need for the applicant to provide literature and clinical data proving the safety and effectiveness of PET drugs. The notice also outlined the potential opportunities for reduction or waiver of fees associated with filing an NDA.

The FDA drafted multiple standards for PET drug cGMP, publishing draft rules in 1999, 2002, and 2005. 21 Code of Federal Regulations (**CFR**) Section 212 was officially published on 10 December 2009 [5]. However, it would not go into effect until

12 December 2011, to give PET drug manufacturers time to make sure they were fully compliant. The FDA gave a further extension to PET drug manufacturers that allowed them to continue producing F-18 FDG, F-18 sodium fluoride, and N-13 ammonia as long as they filed abbreviated new drug applications (**ANDAs**) by 12 June 2012. The publication of this rule also meant that all research PET radiopharmaceuticals needed to be produced in good manufacturing practice (**GMP**) conditions and imaged under either approved Radioactive Drug Research Committee (RDRC) or investigational new drug (**IND**) protocols.

15.4 21 CFR 212

The cGMP requirements for PET drugs are located in Title 21, Part 212 of the Code of Federal Regulations (21 CFR Section 212). 21 CFR Section 212 presents the minimum standards necessary for the production of PET drugs for human use, regardless of whether the manufacturer is a commercial producer or a not-for-profit institution. The rule covers the following topics:

- Investigational and research PET drugs
- Batch production and control records
- Equipment and facilities records
- Records of components, containers, and closures
- Process verification
- Laboratory testing records
- Sterility test failure notices
- Conditional final release
- Out-of-specification investigations
- Reprocessing procedures
- Distribution records
- Complaints

These regulations differ from those for traditional pharmaceuticals (21 CFR Section 211) due to the unique characteristics of PET drugs and their manufacturers. The current rule may be accessed on the FDA's website.

15.5 USP GENERAL CHAPTER <823>

21 CFR Section 212 incorporates principles from general Chapter <823> of the 32nd edition of the United States Pharmacopeia (**USP <823>**). USP <823> served as the cGMP requirement for PET drugs from the implementation of FDAMA until the enforcement of 21 CFR Section 212. 21 CFR Section 212 states that research PET drugs may meet cGMP

requirements by either complying with the cGMP standards of USP <823> (32nd Edition) or 21 CFR Section 212.

The FDA announced in 2019 that it intends to amend 21 CFR Section 212 to state that research PET drugs may meet cGMP requirements by complying with either the cGMP standards of the current version of USP <823> or 21 CFR Section 212.

15.6 IMAGING PATIENTS WITH PET DRUGS

Pre-clinical imaging with PET drugs requires not FDA approval, but rather institutional approval from the appropriate animal use committee. Imaging human subjects with PET drugs, be it clinically or in a research setting, requires the PET drug to have some sort of approval from the FDA. The use of research PET drugs in patients occurs under IND or RDRC approval, while clinical PET drugs must be approved under an NDA or ANDA.

15.7 IND

INDs are the mechanism by which most research with PET drugs is performed. The rules and regulations for INDs are found in 21 CFR Section 312. Of particular use is the exploratory IND (**eIND**) mechanism, which is a special type of IND. The eIND is especially suited for PET drugs, as to qualify for an eIND, the administered dose of the test substance should be less than 1/100th of the dose calculated (based on animal data) to yield a pharmacologic effect. Additionally, the maximum administered dose for an eIND must be lower than 30 nmol for a protein or 100 µg for any other drug. PET drugs almost always meet these requirements. The advantage of the eIND approach is that less pharmacology/toxicology data is needed for approval, and it is possible to perform research on a class of closely related compounds rather than just a single compound. eINDs are generally used for a small number of subjects, with the intent that a promising compound would then move on to an IND for the remaining phases of the clinical trial. An example of the use and advantages of an eIND in the PET drug discovery process was published by Avid Radiopharmaceuticals [6].

The content of an IND includes:

- Clinical imaging protocol
- Chemistry, manufacturing, and controls (**CMC**)
- Pharmacology and toxicology
- Previous human experience with the investigational agent or related compounds (if applicable)

Given that this is a book on radiochemistry, the focus of describing the sections will be on the CMC section but will also briefly cover the other sections.

15.7.1 Clinical Imaging Protocol

Inclusion/Exclusion criteria: These criteria need to be set for both normal subjects and those with the disease of interest targeted by the PET drug.

Number of subjects: The number of subjects will be fewer than for traditional therapeutic drug INDs. For example, 20–50 subjects may be sufficient for phase 2 (efficacy) studies of a PET drug, whereas a conventional phase 2 therapeutic study will enroll hundreds of patients.

Imaging procedure: This section needs to fully describe the injected dose range and the rationale for selecting the dose range. Uptake time and the acquisition parameters need to be described in detail. Dynamic acquisition with the injection occurring on the PET camera will be extremely helpful for determining pharmacokinetics in first-in-human studies, while static imaging at a later timepoint is perfectly acceptable for PET drugs that have already been investigated to some extent and are “known quantities.”

Pharmacokinetics: This consists of blood time-activity curves (**TACs**) obtained from blood samples, along with tissue TACs derived quantitatively from the PET scan. Blood samples should be tested for metabolites of the injected radiopharmaceutical, usually using appropriate high-performance liquid chromatography (**HPLC**) separation techniques. Excessive amounts of labeled metabolites may indicate that the PET drug is not stable enough for use.

Monitoring for toxicity/adverse events: The selection of blood tests should be based on the potential effects of the PET drug, based on animal testing. At a minimum, complete blood counts for RBCs, WBCs, and platelets should be done immediately prior to administration of the test drug and one to three hours later if this is a first-in-human study. You may not have to monitor for toxicity if it is not a first-in-human study. All adverse events need to be promptly reported to the FDA.

15.7.2 Chemistry, Manufacturing, and Controls (CMC)

Five sections make up the CMC for an IND: introduction (statement of risk), drug substance, drug product, labeling, and a claim for categorical exclusion for environmental assessment.

Introduction: State whether the investigational drug proposes any risk to the patient. There will be no risk for most PET drugs, as the injected mass is usually well below the limit for any pharmacological response.

Drug substance: This section should include the physical structure of the PET drug, the name/address of the PET drug substance manufacturer, a manufacturing process flow diagram, a radiochemistry scheme, a description of the PET drug manufacturing process, and information on the precursor (identity, strength, quality, purity, stability). The radiochemistry scheme should show all chemical structures

and reaction conditions for the entire synthesis process. The description of the PET drug manufacturing process should include all times, reagent volumes, masses, and temperatures. As a general rule, precursors need to be GMP-grade for phase 3 clinical trials, with R&D-grade precursors acceptable for phase 0/1/2 clinical trials. Regardless of the grade requirement, information needs to be provided on the identity, strength, quality, purity, and stability of the precursor. This information may be obtained from the manufacturer or generated for in-house manufacturing of the precursor. It is critical to ensure that all test methods are appropriately validated.

Drug product: This section should include all the components used to manufacture the finished PET drug, the quantitative composition of the PET drug product, the name/address of the PET drug product manufacturer, and information on the finished PET drug (identity, strength, quality, purity, stability). The components section should include all reagents and fluid pathways, listing the quality of the reagent as well as the amount used. The quantitative composition should list all components of the finished PET drug product (including inactive ingredients) and the composition of the final product vial. All of the quality control tests used to determine identity, strength, quality, and purity should be listed in a table that provides the acceptance criteria and testing schedule (completed prior to release, upon validation, on an annual basis, etc.). Recently, the FDA has been asking manufacturers to validate thin layer chromatography (TLC) tests by using HPLC to corroborate results as part of the validation process. Stability of the PET drug needs to be established through the passing of all quality control tests at expiry.

Labeling: This section should include examples of the labels to be placed on the final product vial and the outside of the lead container that will hold the final product vial. The labels must contain the statement "Caution: New Drug – Limited by Federal (or United States) law to investigational use" (Section 312.6(a)).

Claim for categorical exclusion for environmental assessment: In accordance with 21 CFR Section 25.31(e), PET drug manufacturers are allowed to claim a categorical exclusion from the environmental assessment requirements of 21 CFR Section 25.20 on the basis that the estimated concentration of the PET drug product at the point of entry into the aquatic environment will be below 1 ppb.

15.7.3 Pharmacology and Toxicology

Single-species pharmacology and toxicology studies are required for eIND, and two-species pharmacology and toxicology studies are required for IND applications.

15.7.4 Previous Human Experience with the Investigational Agent or Related Compounds

In this section, you should detail the previous human experience with the PET drug in the application. It is completely appropriate to summarize the literature and provide

references, as this will help the FDA in its assessment of risk with regards to the investigational agent.

15.8 RDRC

There is an alternative approach to the IND that is available only for radioactive drugs. This approach is known as the RDRC. The RDRC is an institutional body that serves as an authorized delegate of the FDA to approve and oversee small studies of radioactive drugs. Typically, RDRCs are found at academic medical centers. The scope of RDRC studies is limited, generally only for a small number of research subjects and for determining basic scientific knowledge of the radioactive drug (i.e. biochemistry, biodistribution, dosimetry, kinetics, localization, pathophysiology, physiology). RDRC studies are never permitted for first-in-human radioactive drugs or studies that are to be used for clinical information. While this may seem limiting, RDRC studies are an efficient mechanism for gaining experience with a radioactive drug and conducting reproducibility studies. Each individual RDRC will have its own submission procedures and requirements. RDRC responsibilities and rules can be found in 21 CFR Section 361.1.

15.9 NDA

Once a radioactive drug has worked its way through the IND pathway, concluding with a successful phase 3 trial(s), the next step is to gain drug approval. An NDA is the method used to gain approval to market and sell a new drug in the United States. The application will contain chemistry, manufacturing, and controls information on the production of the drug; data from pre-clinical animal studies performed to assess safety and efficacy of the drug; and clinical trial data to show that the drug is safe and effective in humans and that the benefits of the drug outweigh the risks. It is beyond the scope of this text to fully expand on the submission requirements of an NDA. However, it is important for the reader to understand that it is not a trivial undertaking. NDAs are submitted in the electronic common technical document (**eCTD**) format, which requires specialized software and resources. The CMC section is much more stringent than for INDs, requiring detailed information on the manufacturing of the radioisotope, precursors, and other key materials. All analytical methods must be validated and the validation information presented in the application. Generally, it will take 9–12 months at a minimum to prepare an NDA for submission. The rules and regulations for DMFs are found in 21 CFR Section 314.

15.10 ANDA

An ANDA is the method used to gain approval to market and sell a drug in the United States that is already on the market. This is the approval pathway used for “generic”

drugs. The applicant must state which reference listed drug (**RLD**) they are using in the application and show that the drug in the application is bioequivalent to the RLD. The RLD will be the radioactive drug with an NDA. The two drugs must be comparable in their characteristics, dosage form, formulation, intended use, quality, route of administration, and strength. The *abbreviated* in ANDA refers to the fact that pre-clinical and clinical data are not needed in the application due to it already being reviewed in the RLD's NDA. However, the chemistry, manufacturing, and controls information is greatly scrutinized in ANDAs to make sure the drug is bioequivalent to the RLD. Some minor differences are allowed between the ANDA drug and the RLD. There can be differences in preservatives, buffers, and antioxidants in the final product formulation. Strength changes can also be considered but require a suitability petition to be filed and approved before submission of the ANDA. The rules and regulations for ANDAs are found in 21 CFR Section 314.

15.11 DRUG MASTER FILE (DMF)

A drug master file (**DMF**) is a compilation of proprietary information about equipment or materials used in the preparation of a drug product or is a drug product itself. Typically, this document is filed by either synthesis module manufacturers or manufacturers of components used in the manufacturing of radioactive drugs (synthesis cassettes, precursors, sterile empty vials, etc.). The DMF allows the manufacturer to provide the information to the FDA without having to worry about any proprietary information becoming public. The FDA also welcomes DMFs, as it simplifies the review process by allowing the FDA to review the DMF rather than having to review the same information presented differently in various INDs, NDAs, and/or ANDAs. The filer of an IND, NDA, or ANDA should obtain letters of authorization from the DMF holder and include those letters of authorization in their IND, NDA, or ANDA submission. The rules and regulations for DMFs are found in 21 CFR Section 314.420.

15.12 SUMMARY

This chapter provided a brief summary of the history and current regulations regarding PET drugs. While the 21 CFR Section 212 regulations may seem cumbersome compared to the regulatory environment before its enactment, the new regulations have provided legitimacy to the field of PET. This is reflected in the number of PET drugs that have been approved since the adoption of 21 CFR Section 212 (Table 15.1). Knowledge of the regulatory pathway is important for radiochemists to consider when developing new PET drugs, as the field only truly advances when PET drugs make it through the approval pathway and are available for clinical use.

Table 15.1 NDAs for PET drugs as of June 2020.

PET drug	NDA #	Institution	Approval year	No. of active ANDAs
Fludeoxyglucose F-18	020306	Downstate Clinical PET Center	1994	38
Fludeoxyglucose F-18	021768	Cornell University	2004	38
Ammonia N-13	022119	Feinstein Institutes for Medical Research	2007	26
Fludeoxyglucose F-18	021870	Feinstein Institutes for Medical Research	2008	38
Sodium fluoride F-18	022494	NIH National Cancer Institute	2011	21
Choline C-11	203155	Mayo Clinic	2012	4
Florbetapir F-18	202008	Avid Radiopharmaceuticals	2012	0 ^a
Flutemetamol F-18	203137	GE Healthcare	2013	0 ^b
Florbetaben F-18	204677	Life Molecular Imaging	2014	0 ^c
Dotatate Ga-68	208547	Advanced Accelerator Applications	2016	0 ^d
Fluciclovine F-18	208054	Blue Earth Diagnostics	2016	0 ^e
Dotatoc Ga-68	210828	University of Iowa	2019	0 ^f
Fluorodopa F-18	200655	Feinstein Institutes for Medical Research	2019	0 ^f
Flortaucipir F-18	212123	Avid Radiopharmaceuticals	2020	0 ^g
Fluoroestradiol F-18	212155	Zionexa US Corp	2020	0 ^h

a Patent expires in 2027.

b Patent expires in 2028.

c Patent expires in 2029.

d Exclusivity expires in 2023; patent expires in 2032.

e Exclusivity expires in 2021; patent expires in 2035.

f No patent; exclusivity was waived.

g Patent expires in 2029.

h Exclusivity expires in 2025.

REFERENCES

1. Ido, T., Wan, C.N., Casella, V. et al. (1978). Labeled 2-deoxy-d-glucose analogs. ¹⁸F-labeled 2-deoxy-2-fluoro-d-glucose, 2-deoxy-2-fluoro-d-mannose and ¹⁴C-2-deoxy-2-fluoro-d-glucose. *J. Labelled Compd. Radiopharm.* 14 (2): 175–183.
2. FDA (1995). Current good manufacturing practice for finished pharmaceuticals; positron emission tomography. *Fed. Regist.* 60: 10517–10520.
3. Food and Drug Administration Modernization Act. 1997. 105–115.
4. FDA (2000). Positron emission tomography drug products; safety and effectiveness of certain PET drugs for specific indications. *Fed. Regist.* 65: 12999–13010.
5. FDA (2009). Current good manufacturing practice for positron emission tomography drugs. *Fed. Regist.* 74: 65409–65436.
6. Carpenter, A. Jr., Pontecorvo, M., Hefti, F., and Skovronsky, D. (2009). The use of the exploratory IND in the evaluation and development of ¹⁸F-PET radiopharmaceuticals for amyloid imaging in the brain: a review of one company's experience. *Q. J. Nucl. Med. Mol. Imaging* 53 (4): 387.

Chapter 16

Moving from the Lab to the Patient in Asia

Dae Yoon Chi

*Department of Chemistry, Sogang University, Seoul,
04107, Korea*

16.1 INTRODUCTION

Radiopharmaceuticals are chiefly divided into two categories: diagnostic drugs using a γ -camera, single photon emission computed tomography (**SPECT**), and positron emission tomography (**PET**); and therapeutic drugs using radioisotopes. While both fields have a long history in nuclear medicine, research into diagnosis through PET and the treatment of radionuclide therapy have entered the spotlight with the emergence of molecular imaging and targeted therapies.

Tc-99m radiopharmaceuticals have been in use for a long time in the detection of cancer. However, this market has been reduced by half over the past 20 years since [^{18}F]fluorodeoxyglucose ([^{18}F]FDG, or simply **FDG**) has been widely recognized as the best radiopharmaceutical to diagnose cancer. FDG has been a wildly successful and popular drug with nuclear medicine doctors, primarily due to its lower cost and readily accessible use of SPECT. The author argues that the last 30 years were the era of FDG, and that it is yielding to a new era of PET drugs. It is well known that PET images are much superior to and more accurate than SPECT, and hence there is an absolute urgency for the development and implementation of new PET radiopharmaceuticals for better diagnosis and care of patients. When people in the field began to look for “the next FDG,” two PET radiopharmaceuticals were approved by the Korea Ministry of Food and Drug Safety (**MFDS**) in 2008, heralding a new era of PET radiopharmaceuticals.

Handbook of Radiopharmaceuticals: Methodology and Applications, Second Edition.

Edited by Michael R. Kilbourn and Peter J.H. Scott.

© 2021 John Wiley & Sons Ltd. Published 2021 by John Wiley & Sons Ltd.

Three PET radiopharmaceuticals capable of imaging β -amyloid in the United States were subsequently approved by the US Food and Drug Administration (**US FDA**): Amyvid (AV-45, Flobetapir F 18 injection) [1, 2] from Lilly in 2012, Vizamyl (Flutemetamol F 18 injection) [3] from GE in 2013, and Neuraceq (AV-1, Florbetaben F18 injection, https://www.accessdata.fda.gov/drugsatfda_docs/label/2014/204677s000lbl.pdf) from Piramal in 2014. In 2016, Axumin (Fluciclovine, (<https://www.fda.gov/news-events/press-announcements/fda-approves-new-diagnostic-imaging-agent-detect-recurrent-prostate-cancer>)) from Blue Earth Diagnostics was registered for prostate cancer imaging. In this review, the scope is limited to PET radiopharmaceuticals and recently developed therapeutics.

16.2 RADIOPHARMACEUTICALS

As mentioned earlier, radiopharmaceuticals are divided into diagnostic radiopharmaceuticals, which use PET or SPECT to diagnose disease, and therapeutic radiopharmaceuticals to treat disease. Since most radiopharmaceuticals so far are diagnostic drugs, radiopharmaceuticals are submitted to the US FDA for approval using a new drug application (**NDA**) through the preclinical phase and clinical phases 1, 2, and 3, and receive new drug approval from the FDA. Drugs developed by the US FDA have an estimated 60% chance of success in phase 1, 30% in phase 2, 60% in phase 3, and 85% at the NDA. In other words, when 100 new drug candidates enter phase 1, only 9.2 of them make it on the market as commercial drugs that are available to the public.

16.2.1 PET Diagnostic Radiopharmaceuticals

Diagnostic radiopharmaceuticals for PET are subject to the same rigorous clinical trials and approval process as therapeutic medicines. There are some key differences that set radiopharmaceuticals apart from other common drugs, but they go through the same approval process as general medicines. For example, the dosage of radiopharmaceuticals used for PET or SPECT is such a minuscule amount that toxicity cannot be an issue in most cases, yet all safety pharmacology data must be obtained. The big advantage of diagnostics over therapeutic drugs in the approval process is that test results can be seen almost immediately after images are taken, rather than having to wait months or years to see if they will be an efficient drug development pathway.

Researchers and scientists have developed new PET diagnostic radiopharmaceuticals with an emphasis on identifying diseases that are difficult to detect using other methods of diagnosis. Chief among these are various oncological and neurological diseases such as Alzheimer's disease and Parkinson's disease. In the case of cancer, it is critical to pinpoint the exact location of the cancer and learn how far it has metastasized in the body. PET diagnostic drugs are also useful for checking the extent and progress of cancer treatment. With regard to dementia, we are trying to find answers to questions such as how much beta-amyloid and tau protein needs to accumulate to diagnose dementia correctly and as early as possible. In the case of beta-amyloid, five compounds have been

developed and approved as commercial products. Radiopharmaceuticals that can measure the accumulation of tau protein are under development.

So far, there is no curative medicine for dementia. Many people ask what the benefit of developing a diagnostic is; after all, what is the use of knowing what disease you have and how severely it has progressed if it cannot be treated? It is important to know the effects of treatment in order to develop a therapeutic drug. What is happening in the brain – are the accumulated proteins removed by the therapeutic drug, and is cognitive function restored by the drug? At the very least, to answer these questions, it is a prerequisite to be able to measure the degree of protein accumulation. In general, the development of a therapeutic agent is preempted by a great diagnostic agent that is capable of accurately measuring any therapeutic effect in addition to providing a simple and elegant method of diagnosis.

16.2.2 Therapeutic Radiopharmaceuticals

In obtaining approval for a drug from the FDA, the guidelines for therapeutic radiopharmaceuticals may be more stringent than those for diagnostic radiopharmaceuticals. If someone gets cancer, the patient will be treated with surgery, chemotherapy, or/and radiation therapy, depending on the progression of the cancer.

A study that began about 20 years ago with peptide receptor radionuclide therapy (**PRRT**) has been able to treat neuroendocrine cancer. Based on these trials, recently, prostate-specific membrane antigen (**PSMA**) has been used to diagnose and treat prostate cancer. Targeted therapeutic potential has been identified using metal radioisotopes emitting β -rays or α -rays, and clinical trials of diagnostic and therapeutic agents are being actively conducted. The most important aspect of radionuclide therapy is the use of compounds that emit radiation. The compound consists of three parts: a moiety that can bind well to the target, a space, and a ligand. The incorporation of Ga-68, which releases positrons, into the ligand of this compound enables determining the biodistribution of the compound *in vivo* by PET scanning. The introduction of Lu-177 into the same compound results in a β -ray-releasing agent, while the incorporation of Ac-225 results in a α -ray-releasing agent.

¹⁷⁷Lu-DOTATATE (Lutathera) is the first PRRT to receive regulatory registration, with approval by the European Commission on 29 September 2017 (<https://www.globenewswire.com/news-release/2017/09/29/1134919/0/en/Advanced-Accelerator-Applications-Announces-European-Approval-of-Lutetium-177Lu-Oxodotreotide-Lutathera-for-Gastroenteropancreatic-Neuroendocrine-GEP-NET-Tumors.html>; https://ec.europa.eu/health/documents/community-register/2017/20170926138665/anx_138665_en.pdf) for the treatment of unresectable or metastatic, progressive, well differentiated, somatostatin receptor positive gastroenteropancreatic neuroendocrine tumors (**GEP-NETs**) in adults. It was approved by the US FDA on 26 January 2018, thereby setting a new bar for safety data for radionuclide therapy (<https://www.fda.gov/news-events/press-announcements/fda-approves-new-treatment-certain-digestive-tract-cancers>). Based on this, there has been a buzz of activity, with new clinical trials being

conducted for new therapeutic agents. A primary distinguishing point of such therapeutic agents from diagnostic agents is that in addition to conventional studies of the safety pharmacology of cold compounds, test results from safety pharmacology, repeated dose toxicity, and genotoxicity of hot compounds are reflected (https://ec.europa.eu/health/documents/community-register/2017/20170926138665/anx_138665_en.pdf).

16.3 TECHNICAL TRANSFER

In a technical transfer, there are licensors who sell licenses of products or technologies, and licensees who purchase the rights to use the products or technologies. Technical transfer may have a variety of purposes, but this review will cover the radiopharmaceutical field only. A company that wants to use the seller's technology buys it either to reduce the production cost of an existing product or to purchase the right to sell a new product. In neither case is a patent required, although having one is desirable.

The transfer of technology related to radiopharmaceuticals is similar to that of general therapeutic drugs. Drug development proceeds in the order of preclinical studies, investigational new drug (**IND** – clinical phase 1, phase 2, phase 3) application, NDA, and finally, approval as a new drug. In the early stages of development, the technology can be bought relatively cheaply, because there is uncertainty about whether it can be developed as a medicine. As a drug continues to perform competitively through the approval process, its chance of obtaining approval from the FDA increases with each next step, as we saw earlier, and the price of technology transfer grows exponentially.

16.3.1 Item Licensing Strategy for Radiopharmaceuticals for PET

When a licensee wishes to buy a technology, the licensee must consider the following issues: (i) how much to pay for the technology – initial payment, milestone, and running royalty; (ii) whether it is possible for the licensee to use the technology to produce a product; and (iii) when it will be possible to pay back the investment. Radiopharmaceuticals are medicines rather than technologies, so most of them are copyrighted; and, like general new drugs, they should undergo clinical trials. Most product licenses in foreign countries are patented, so there is no other means than technology transfer for use in those countries.

A licensee can apply for product registration at the FDA of their own country without a clinical trial by receiving a common technology document (**CTD**, also called a common technology dossier) from a licensor. In Korea, if a radiopharmaceutical is well known and listed in the US or European Pharmacopeia without a patent, it can be used as a pharmacy formulation in a hospital. These pharmacy formulations can only be used in the hospital: outside sales are prohibited. Additionally, a pharmaceutical company can apply to the Korean FDA to commercially produce radiopharmaceuticals that are used as pharmacy

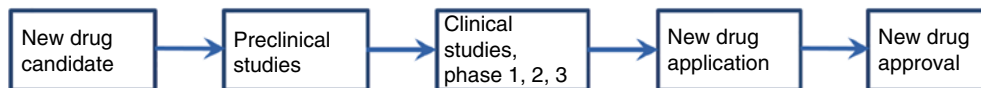
formulations. In this case, the company can submit a document without a CTD to obtain a product registration for commercial purposes.

If a hospital or pharmaceutical company can get a pharmacy formulation for commercial production, hospitals that have already been approved a pharmacy formulation can continue to use it. However, hospitals that do not have a permit for a pharmacy formulation can no longer apply an existing pharmacy formulation and must buy it from a licensed company. Of course, a hospital can apply to the FDA for commercial production and sell to an outside hospital if the hospital gets a product permit. In the case of F-18 radiopharmaceuticals, if they are sold elsewhere, it is more convenient and economical to buy and use them than it is to produce them in the formulation. C-11 radiopharmaceuticals cannot be purchased externally, so there is no alternative but to the formulary.

Even if there are no substance patents for new radiopharmaceuticals that are not listed in the US or European Pharmacopoeia, it is not possible to apply for product registration without a CTD. Therefore, it is economically advantageous to commercialize a product quickly by receiving a technology transfer from a licensor and providing all the product data, including the CTD, rather than conducting a clinical trial to prepare a CTD. Proper compromise will be important, as tedious negotiations between licensors and licensees wastes time for both. The number of these cases are illustrated in Figure 16.1 for clarity.

Selling technology means the sellers are doing a lot of R&D. If new radiopharmaceuticals are available, they must be clinically tested and approved for commercial use. Most hospitals and medical researchers do not have the capital to do this, so companies

1. Most common and typical NDA procedure



2. NDA with technical transfer procedure



3. Hospital production or NDA for known radiopharmaceuticals in american or european pharmacopoeia

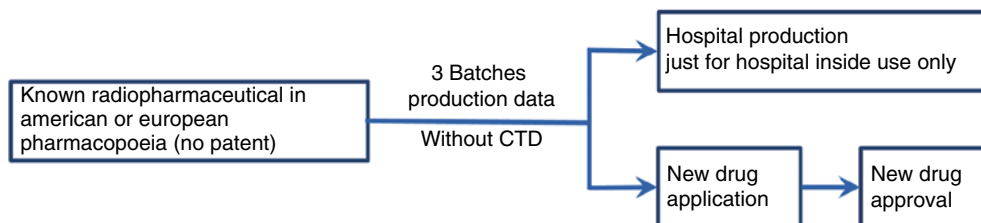


Figure 16.1 Three approaches to radiopharmaceutical NDA in Korea.

that engage in commercial production need to transfer technology. Bayer Healthcare transferred the compound Florbetapir (18F) from Avid, the developer of AV-1, and Lilly purchased Avid along with the compound for \$US 800 million near the end of the AV-45 clinical trial ([https://en.wikipedia.org/wiki/Florbetapir_\(18F\)](https://en.wikipedia.org/wiki/Florbetapir_(18F))).

Lilly Inc. recently introduced ^{68}Ga -DOTATATE (NETSPOT, developed by French cancer specialist Advanced Accelerator Application [AAA]) as a diagnostic agent for neuroendocrine tumors after approval from the US FDA on 21 June 2016. In addition, as a therapeutic agent, ^{177}Lu -DOTATATE (Lutathera) has been used since the European FDA gave permission on 3 October 2017, and it received a US FDA product license on 26 January 2018. AAA is also doing phase I clinical trials for ^{68}Ga - and ^{177}Lu -PSMA-R2, a technology transfer from Professor Martin Pomper of Johns Hopkins University in the US for prostate cancer diagnosis and treatment. Since AAA has a platform for diagnostics and therapeutics in addition to the F-18 PSMA agent (F18 CTT1057), Novartis merged with AAA by paying \$US 3.9 billion on 30 October 2017 (<https://www.reuters.com/article/us-novartis-advanced-accelerator/novartis-to-buy-french-cancer-specialist-aaa-for-3-9-billion-idUSKBN1CZ0HC>). Novartis also merged with Endocyte by paying \$US 2.1 billion on 18 October 2018 (<https://www.novartis.com/news/media-releases/novartis-announces-planned-acquisition-endocyte-expand-expertise-radiopharmaceuticals-and-build-commitment-transformational-therapeutic-platforms>). Thus, Novartis started investing heavily in the area of radiopharmaceuticals.

Most recently, Ga-68-DOTATOC was approved by the FDA on 21 August 2019.

16.3.2 Use of PET Radiopharmaceuticals in Clinical Trials of General Pharmaceuticals

When a pharmaceutical company is developing therapeutic pharmaceutical drugs, PET, a device that can easily measure the biodistribution of new drugs, can significantly reduce the clinical period. Thus, pharmaceutical companies have invested heavily in setting up PET facilities to determine the efficacy of developing therapeutic drugs. At the end of the preclinical and early clinical trials, patients are referred to doctors in hospitals that conduct clinical trials. A general medicine that is entering clinical trials may be produced in one place and provided to clinical trial hospitals, which may be far from the manufacturer or even in a different country. However, PET radiopharmaceuticals should be produced in or near to the clinical trial hospital.

Modern therapeutic pharmaceuticals undergoing clinical trials should be produced in a Good Manufacturing Practice (GMP) facility. PET radiopharmaceuticals that can diagnose therapeutic effects should also be produced in a GMP facility in Korea. When a pharmaceutical company chooses a hospital to conduct clinical trials of therapeutic pharmaceuticals using PET radiopharmaceuticals to evaluate drug efficacy, whether the hospital has a radiopharmaceutical GMP facility or an institution near the hospital can supply it is an important factor. If the PET radiopharmaceuticals needed in clinical trials of a therapeutic drug are available commercially, they can be purchased and used. However, if they are not available, radiopharmaceuticals for PET must first be developed.

16.4 TECHNICAL TRANSFER IN ASIA

16.4.1 Recent Statistics from the International Symposium on Radiopharmaceutical Sciences for Asian Countries

Receiving a technology transfer requires a large number of commercial companies to commercialize the technology, while transferring the technology requires much R&D for the product or manufacturing method. There are good indicators of the R&D capabilities of radiopharmaceuticals. The International Symposium on Radiopharmaceutical Sciences (**ISRS**) is a biennial conference and the most prestigious international meeting of scientists working with radiopharmaceuticals. The percentage of abstracts released by Asian countries divided by the total number of abstracts at each meeting may be used to understand R&D capabilities in Asia (Tables 16.1 and 16.2). This data provides very important indicators of each country's R&D capabilities.

Table 16.2 shows that during 4 conferences, Korea presented 153 abstracts, Japan 115 abstracts, and China 114 abstracts. Taiwan and Iran were next, with 14 and 11, respectively – a large gap from the top three countries.

16.4.2 The Pharmaceutical Inspection Co-operation Scheme in Asia

The Pharmaceutical Inspection Co-operation Scheme (**PIC/S**) was established in 1995 to work in tandem with the Pharmaceutical Inspection Convention (**PIC**) of 1970. PIC began

Table 16.1 Data from recent three meetings of the International Symposium on Radiopharmaceutical Sciences (**ISRS**).

	Number of participants	Number of participating countries	Number of oral presentations	Number of poster presentations	Number of abstracts presented
ISRS 2019 Beijing, China	535 ^a	52	88	380	468
ISRS 2017 Dresden, Germany	847	38	89	352	441
ISRS 2015 Columbia, MO, USA	591	36	78	333	411
ISRS 2013 Jeju, Korea	703	34	87	405	492

^a Excludes exhibit personnel.

Table 16.2 Number of presentations from Asian Countries at recent meetings of the International Symposium on Radiopharmaceutical Sciences (ISRS).

Country	ISRS 2019	ISRS 2017	ISRS 2015	ISRS 2013	Total
	China	Germany	USA	Korea	
Bangladesh	0	0	0	6	6
China	31	41	9	33	114
India	0	1	1	5	7
Iran	0	6	0	5	11
Japan	29	34	24	28	115
Korea	48	35	28	42	153
Kuwait	0	0	1	0	1
Malaysia	0	1	0	1	2
Pakistan	0	0	0	2	2
Philippines	0	0	0	1	1
Saudi Arabia	0	4	2	1	7
Singapore	0	3	1	2	6
Taiwan	0	6	3	5	14
Thailand	1	2	0	2	5
Turkey	0	2	2	0	4
Vietnam	0	0	0	1	1
Total	108	133	71	134	446
% of presentations by Asian countries	27.8	30.2	17.3	27.2	Average 25.6

as a convention of European countries to harmonize GMP requirements for medicinal products for human or veterinary use under a uniform inspection system. When the need for international regulation and collaboration arose, PIC/S was formed to operate in parallel with PIC to provide international coverage. In addition to the 10 original member countries, currently health authorities from 42 countries the world over have earned access to the PIC Scheme, including 10 Asian countries (Table 16.3) (<https://www.pic-scheme.org/en/members>).

16.5 TECHNICAL TRANSFERS IN AND OUT OF ASIA

The development of Western medicine has traditionally meant an influx of technology transfers into many Asian countries, and PET radiopharmaceuticals have been no exception. There are only a handful of cases in which technology has been developed in Asia and transferred to the rest of the world. Most technology transfers occur from an academic university or research institution to a commercial company or from company to company.

Traditional drugs are usually manufactured in one or two GMP plants and then exported worldwide. Due to their short half-life, PET radiopharmaceuticals have a uniquely different production and distribution process. Unlike other medications, PET

Country	Accession year to PIC/S	Name of government institution
Hong Kong SAR	2016	Pharmacy and Poisons Board of Hong Kong (PPBHK)
Indonesia	2012	National Agency for Drug and Food Control (NADFC)
Iran	2018	Iran Food and Drug Administration (IFDA)
Israel	2009	Institute for Standardization and Control of Pharmaceuticals (ISCP)
Japan	2014	Ministry of Health, Labour, and Welfare (MHLW)
Korea (Republic of)	2014	Ministry of Food and Drug Safety (MFDS)
Malaysia	2002	National Pharmaceutical Regulatory Agency (NPRA)
Singapore	2000	Health Sciences Authority (HSA)
Taiwan	2013	Taiwan Food and Drug Administration (TFDA)
Thailand	2016	Food and Drug Administration (Thai FDA)

Table 16.3

Accession of 10 Asian countries' participating authorities to the PIC scheme.

Source: Based on LIST OF PIC/S PARTICIPATING AUTHORITIES. <https://www.picscheme.org/en/members>.

radiopharmaceuticals must be manufactured on the day of administration, because their terms of validity are usually only about six to eight hours. An institution that buys a PET radiopharmaceutical must have its own GMP sites or access to a contract manufacturing organization (**CMO**) site that is capable of producing the radiopharmaceuticals locally on demand. Therefore, each production site must possess automatic modules that can, in turn, produce the necessary radiopharmaceuticals. When a technical transfer is carried out, the licensor hands over to the licensee the technology for both the manufacturing process of the automatic module and the PET radiopharmaceutical.

In Korea, four companies currently produce PET radiopharmaceuticals on a commercial scale: FutureChem, Carecamp, HDX, and Duchembio. Of these four, only FutureChem has a pipeline of proprietary drugs from internal research and development; the other three bring in foreign drugs, such as FDG, obtained by technical transfer. As the first company in Korea to be registered for the manufacture of radiopharmaceuticals on a commercial basis, FutureChem not only produces radiopharmaceuticals but places high importance on pioneering the development and promotion of new radiopharmaceuticals. This dedication to quality and innovation can also be seen in the development of sCUBE, an all-in-one automated synthesis module for simplified manufacturing of FutureChem drugs at any production site.

16.5.1 Aliphatic F-18 Fluorination Method

F-18 fluoride is mainly produced by $^{18}\text{O}(p,n)^{18}\text{F}$ reaction from a medical cyclotron. The F-18 fluoride can be introduced on the position of an aliphatic or aromatic carbon of a drug. The pharmacological effect is changed by the position of the fluorine. Although a method of aromatic fluorination using a metal catalyst has been developed, there is still a need for a practical method for aromatic fluorides having high molar activity.

Radiopharmaceuticals labeled with F-18 fluoride attached to aliphatic carbon have primarily been used because nucleophilic fluorination can provide radiopharmaceuticals with high molar activity. Although there is a weak point of defluorination *in vivo* in a few cases, aliphatic fluoride compounds are used because they can be synthesized in large quantities.

Historically, for the nucleophilic F-18 fluorination reaction, researchers have tried to make naked fluoride, which increases the yield of nucleophilic fluorination. Nucleophilic substitutions are described in organic chemistry textbooks, and the reaction must be carried out in an aprotic solvent. In 2005, the author presented breakthrough fluorination that indicated that nucleophilic substitution could be improved with non-polar protic solvents. The result was illustrated by the synthesis of four [¹⁸F]fluoride-radiolabeled molecular imaging probes – [¹⁸F]FDG, [¹⁸F]FLT, [¹⁸F]FP-CIT (Figure 16.2) [4], and [¹⁸F]FMISO – in high yield and purity, and in shorter times compared to conventional syntheses [5]. After this publication, this new concept was well studied, applied, and reviewed [6]. This technology was patented in 17 countries [7] and transferred to Bayer Schering Pharma on 20 December 2007.

16.5.2 β-Amyloid Imaging Radiopharmaceuticals

16.5.2.1 Florbetaben F18 Injection

Beyond the FDG era, three β-amyloid imaging PET radiopharmaceuticals were launched in the US: Amyvid (florbetapir) from Lilly in 2012, Vizamyl (flutemetamol) from GE in 2013, and Neuraceq (florbetaben) from Piramal in 2014 (Figure 16.3). Neuraceq was

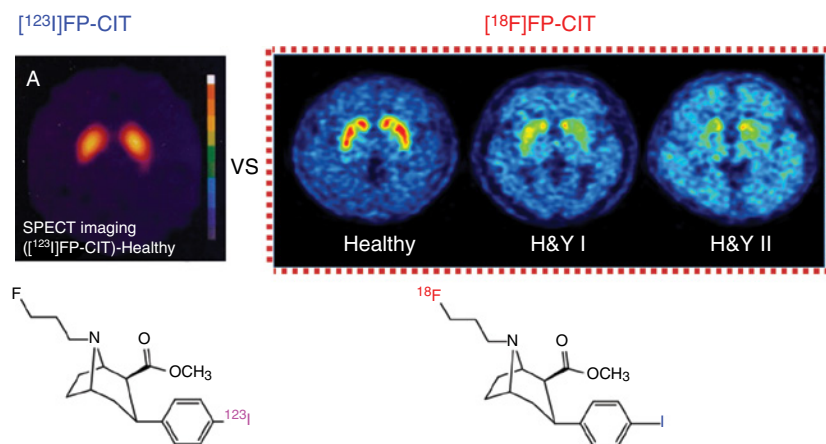


Figure 16.2 Imaging comparison between [¹²³I]FP-CIT and [¹⁸F]FP-CIT to diagnose Parkinson's disease. Source: Michael R. Kilbourn.

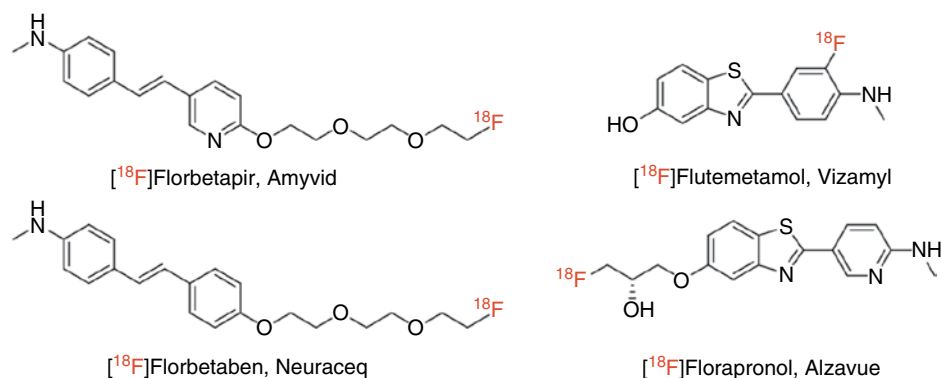


Figure 16.3 Structures of β -amyloid imaging radiopharmaceuticals.

transferred to the Korean company DuchemBio in 2015. Although Neuraceq was the last of the three products to be approved by the US FDA, it was the first to be commercially released in Korea.

16.5.2.2 Flutemetamol F18 Injection

After Neuraceq was launched in Korea, Vizamyl came to the Korean market six months later through technical transfer from GE Healthcare to Carecamp. GE Healthcare's own automatic module (FASTlab) was used in the technical transfer for the production of Vizamyl.

16.5.2.3 Florapronol F18 Injection

In February 2018, FutureChem registered Alzavue (Florapronol F18 injection) as a β -amyloid imaging PET radiopharmaceutical with the Korea MFDS and launched it in the Korean market (<http://www.futurechem.co.kr/eng/business/pet1>). Alzavue is the first new diagnostic agent for Alzheimer's dementia and the 30th new drug to be developed and approved in Korea. The technology of Alzavue was transferred to Moltek in Turkey on 18 December 2018 (http://futurechem.webmaker21.kr/eng/board/news?viewMode=view&ca=&sel_search=&txt_search=&page=1&idx=2). In this case, the technical transfer for the production of Alzavue was facilitated by FutureChem's proprietary all-in-one synthesis module, sCUBE.

16.5.3 Tau Imaging Radiopharmaceuticals

A number of tau radiopharmaceuticals have been developed recently (Figure 16.3), and three have attracted particular attention, as described next. Tau protein aggregates are implicated in neurologic disorder including Alzheimer's disease and traumatic brain injury (TBI).

16.5.3.1 THK5351

THK5351 [8, 9] was discovered at Tohoku University in Sendai, Japan, and licensed by GE Healthcare for commercial distribution (Figure 16.3). Unfortunately, at the Human

Amyloid Imaging (**HAI**) meeting held in January 2017, three groups reported THK5351 binding to the enzyme monoamine oxidase B (MAO B), possibly on astrocytes (<https://www.alzforum.org/news/conference-coverage/next-generation-tau-pet-tracers-strut-their-stuff>). This tau tracer developed in Japan was transferred to global company GE Healthcare, but its commercialization has been hindered by its nonspecific binding.

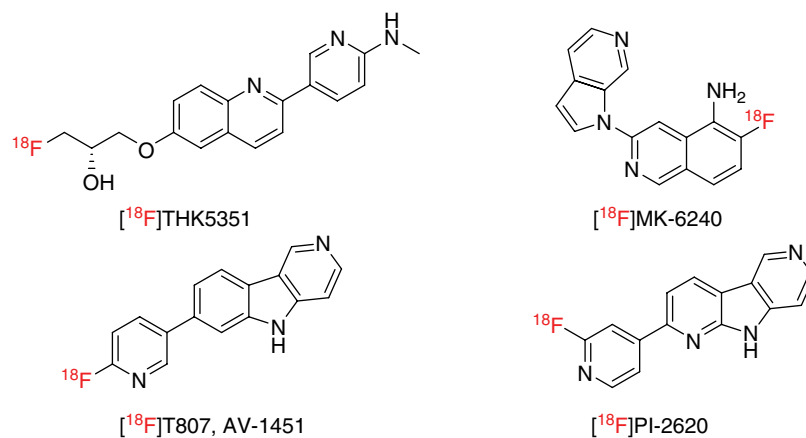
16.5.3.2 TAUVID™

^{18}F -T807 (synonym: ^{18}F -AV-1451) is a PET radiotracer developed for imaging tau protein aggregates (Figure 16.3). ^{18}F -T807 [10, 11] was discovered at Molecular Imaging Biomarker Research, Siemens Medical Solution USA, Inc., Culver City, CA, USA and licensed by Lilly (<https://www.alzforum.org/news/research-news/lilly-buys-tau-tracers-siemens>; <https://www.alzforum.org/news/conference-coverage/tau-tracer-t807av1451-tracks-neurodegenerative-progression>). The FDA approved Tauvid as the first drug to image tau pathology in patients being evaluated for Alzheimer's disease on 28 May 2020 (<https://www.fda.gov/news-events/press-announcements/fda-approves-first-drug-image-tau-pathology-patients-being-evaluated-alzheimers-disease>; <https://investor.lilly.com/news-releases/news-release-details/lilly-receives-us-fda-approval-tauvidtm-flortaucupir-f-18>).

16.5.3.3 MK-6240

^{18}F -MK-6240, developed by Merck, is a promising PET radioligand for *in vivo* imaging of neurofibrillary tau aggregates in AD with minimal off-target binding in the human brain (Figure 16.3) [12–14]. As Merck is a pharmaceutical company, it did not undertake ^{18}F -MK-6240's scale-up, setup of distribution centers, and commercialization. Therefore, in January 2017, Merck licensed out the clinical development and sale of MK-6240 to Cerveau Technologies, a partnership between the Toronto-based company Enigma Biomedical Group and the Beijing-based Sinotau Pharmaceutical Group (<https://www.alzforum.org/news/conference-coverage/next-generation-tau-pet-tracers-strut-their-stuff>). Cerveau Technologies Inc. signed a research agreement with Eisai Inc., for the novel tau

Figure 16.4 Structures of tau imaging radiopharmaceuticals.



imaging agent ^{18}F -MK-6240, on 22 March 2019 (<https://www.businesswire.com/news/home/20190322005317/en/Cerveau-Technologies-Signs-Research-Agreement-Eisai-Tau>).

16.6 CONCLUSION

The earliest studies in the field of radiopharmaceuticals for PET began in the US and Europe. The ISRS, the most authoritative symposium in this field, has been held biannually in America, Europe, and Asia since the inaugural meeting at the Brookhaven National Laboratory on 21–24 September 1976. The ratio of meetings held in America, Europe, and Asia is 2 : 2 : 1. We can see from this tradition and the frequency of participation of Asian countries in the last four meetings that there has been a tremendous increase in participation by Korea, Japan, and China and that these countries have been involved in much R&D as of late. As is the case in many other fields, China has emerged as a force to be reckoned with in the past decade. Not only is much research being done with a new generation of scholars, but the sheer market potential of China makes it an important future target to monitor; keep in mind that the populations of Korea, Japan, and China are 50 million, 130 million, and 1400 million, respectively. Although there has not been much technology transfer in Asia so far, it is expected that more will take place in the future, propelled by up-and-coming R&D.

The transfer of synthesis devices plays a large role in the smooth transfer of technology for the production of radiopharmaceuticals for PET. As many facilities are already producing common drugs such as FDG daily at their existing GMP sites, they often do not have the extra hot-cell capacity required to transfer the technology for the purpose of product approval. It is difficult to immediately increase the number of production hot cells while putting current production on hold, so it would be wise to remember that hot-cell availability is a crucial component in the import of new technology.

REFERENCES

1. Clark, C.M., Schneider, J.A., Bedell, B.J. et al.; for the AV45-A07 Study Group (2011). Use of florbetapir-PET for imaging beta-amyloid pathology. *JAMA* 305: 275–283.
2. Lilly USA, LLC. (2013). Amyvid package insert.
3. GE Healthcare. 2020. Vizmyl package insert. <https://www.gehealthcare.com/-/media/fc6b876ce47d4a7a9f64162aa5f32795.pdf?la=en-us>.
4. Kazumata, K., Dhawan, V., Chaly, T. et al. (1998). Dopamine transporter imaging with fluorine-18-FPCIT and PET. *J. Nucl. Med.* 39: 1521–1530.
5. Kim, D.W., Ahn, D.-S., Oh, Y.-H. et al. (2006). A new class of $S_{\text{N}}2$ reactions catalyzed by protic solvents: facile fluorination for isotopic labeling of diagnostic molecules. *J. Am. Chem. Soc.* 128: 16393–16397.
6. Lee, J.-W., Oliveira, M.T., Jang, H.B. et al. (2016). Hydrogen-bond promoted bimolecular nucleophilic fluorination: concept, mechanism and applications in positron emission tomography. *Chem. Soc. Rev.* 45: 4638–4650.

7. Chi, D.Y., Kim, D.W., Oh, S.J. et al. (2005). A preparation method of organo fluoro compounds in t-alcohol solvents. Korean patent, filed 10 September 2005 and registered 21 December 2007.
8. Betthausen, T.J., Lao, P.J., Murali, D. et al. (2017). In vivo comparison of tau radioligands ^{18}F -THK-5351 and ^{18}F -THK-5317. *J. Nucl. Med.* 58: 996–1002.
9. Harada, R., Okamura, N., Furumoto, S., and Yanai, K. (2018). Imaging protein misfolding in the brain using β -sheet ligands. *Front. Neurosci.* 12: Article 585.
10. Xia, C.-F., Arteaga, J., Chen, G. et al. (2013). [^{18}F]T807, a novel tau positron emission tomography imaging agent for Alzheimer's disease. *Alzheimer's & Dementia* 9 (6): 666–676.
11. Wooten, D.W., Guehl, N.J., Verwer, E.E. et al. (2017). Pharmacokinetic evaluation of the tau PET radiotracer ^{18}F -T807 (^{18}F -AV-1451) in human subjects. *J. Nucl. Med.* 58 (3): 484–491.
12. Walji, A.M., Hostetler, E.D., Selnick, H. et al. (2016). Discovery of 6-(fluoro- ^{18}F)-3-(1H-pyrrolo[2,3-c]pyridin-1-yl)isoquinolin-5-amine ([^{18}F]-MK-6240): a positron emission tomography (PET) imaging agent for quantification of neurofibrillary tangles (NFTs). *J. Med. Chem.* 59: 4778–4789.
13. Hostetler, E.D., Walji, A.M., Zeng, Z. et al. (2016). Preclinical characterization of ^{18}F -MK-6240, a promising PET tracer for in vivo quantification of human neurofibrillary tangles. *J. Nucl. Med.* 57: 1599–1606.
14. Betthausen, T.J., Cody, K.A., Zammit, M.D. et al. (2019). In vivo characterization and quantification of neurofibrillary tau PET radioligand ^{18}F -MK-6240 in humans from Alzheimer disease dementia to young controls. *J. Nucl. Med.* 60: 93–99.

Chapter 17

Moving a Radiotracer from Bench to Bedside in Europe

Koen Vermeulen, Alfons Verbruggen, Guy Bormans
and Frederik Cleeren

*Laboratory for Radiopharmaceutical Research, Department of
Pharmaceutical and Pharmacological Sciences, University of
Leuven, 3000, Leuven, Belgium*

17.1 INTRODUCTION

As the name suggests, a radiopharmaceutical is both a pharmaceutical and radioactive. Therefore, radiopharmaceuticals must comply with the legal requirements for a pharmaceutical, which may need to be adapted with regard to the specific characteristics of radiopharmaceuticals due to their unique properties (e.g. emitting ionizing radiation, produced in low mass amounts, short shelf-life due to the short physical half-life of the radionuclide). During the last two decades, the production of radiopharmaceuticals, and especially positron emission tomography (**PET**) radiopharmaceuticals, has made a quality leap forward toward full Good Manufacturing Practices (**GMPs**). This required technological hot cell innovation, which evolved from crude lead-shielded closets allowing semi-manual synthesis procedures to small high-tech mini clean rooms containing fully automated synthesis modules with disposable cassette kits. Further, the common organic chemistry lab environment has been replaced by restricted access pharmaceutical-grade clean rooms.

Handbook of Radiopharmaceuticals: Methodology and Applications, Second Edition.

Edited by Michael R. Kilbourn and Peter J.H. Scott.

© 2021 John Wiley & Sons Ltd. Published 2021 by John Wiley & Sons Ltd.

National legislation has been partially overruled by stricter European Union (EU) legislation, resulting in a more harmonized landscape. However, the new EU clinical trial regulation is flexible toward requirements for the production of diagnostic radiopharmaceuticals for clinical studies. Different legal requirements still apply for radiopharmaceuticals produced in hospitals vs. commercially available radiopharmaceuticals with marketing authorization. Also, a distinction is made between radiopharmaceuticals prepared from registered generators and labeling kits (e.g. ^{99m}Tc -labeled radiopharmaceuticals) and other radiopharmaceuticals (e.g. ^{11}C - and ^{18}F -labeled radiopharmaceuticals).

The clinical translation of a radiotracer will generally be faster compared to standard pharmaceuticals. However, due to the limited number of clinical doses of the radiotracer that will be produced and injected, clinical translation will generate a relatively high administrative burden. The regulatory environment has changed drastically since 2000, with changes in legislation and the introduction of novel guidelines. This chapter provides an overview of the specific legal requirements that must be followed to move a radiopharmaceutical for PET or single-photon emission computed tomography (SPECT) imaging studies from bench to bedside in Europe.

17.2 GENERAL OVERVIEW

Radionuclide generators, labeling kits, precursors for radiolabeling, and industrially prepared radiopharmaceuticals fall within the scope of EU directive 2001/83/EC (medicinal products for human use) and require a marketing authorization and current Good Manufacturing Practice (cGMP) compliant production. Our interpretation of “precursors for radiolabeling” is chemical precursors containing the radionuclide used to prepare a radiopharmaceutical by the simple addition of the precursor for radiolabeling to a labeling kit. Radiopharmaceuticals prepared from authorized generators, kits, precursors for radiolabeling, and magistral formulas prepared in a pharmacy in accordance with a medical prescription for an individual patient are exempt from requirements of EU directive 2001/83/EC. The directive does also not apply to medicinal products (including radiopharmaceuticals) for clinical trials, which currently fall into the scope of EU Clinical Trials Directive 2001/20/EC, which soon will be replaced by EU Clinical Trial Regulation 536/2014, the requirements of which are discussed in detail in this chapter.

In order to proceed to a clinical trial, a clinical trial application (CTA) needs to be drafted and submitted together with the EudraCT number for review by the local ethical committee and the competent national authorities. Figure 17.1 gives an overview of the requirements to translate a radiotracer to the clinic. In the EU, the CTA consists of an investigator’s brochure (IB), an investigational medicinal product dossier (IMPD), and the study protocol (see <https://ema.europa.eu/en/requirements-chemical-pharmaceutical-quality-documentation-concerning-investigational-medicinal>, www.ema.europa.eu/en/ich-e6-r2-good-clinical-practice).

Before clinical studies with a new radiotracer can be conducted, its safety must be evaluated in non-clinical studies. All this information is collected in the IMPD (www.imp-dossier.eu), which is part of the CTA. The IMPD must also include all the

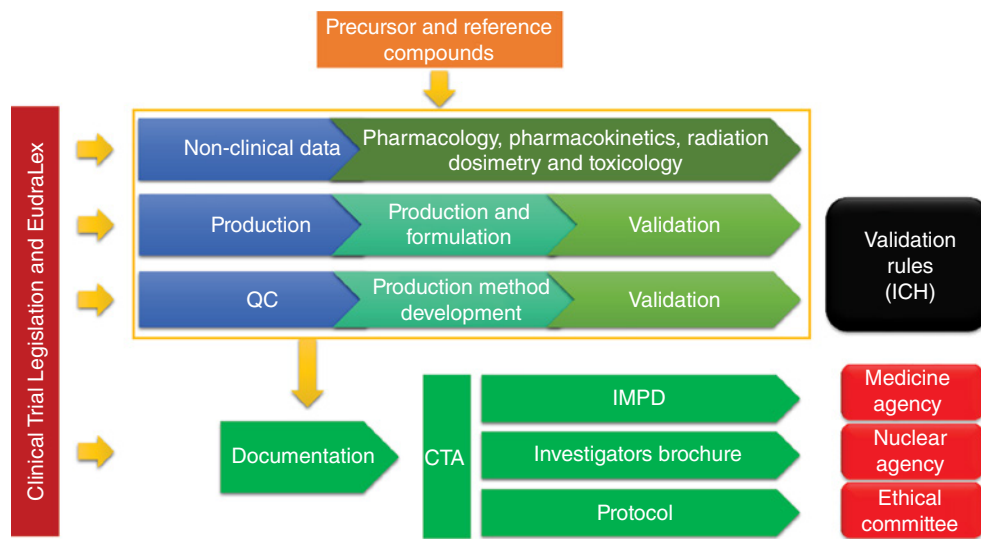


Figure 17.1 Requirements to translate a radio-tracer to the clinic. IMPD, investigational medicinal product dossier; CTA, clinical trial application; ICH, International Council for Harmonization; QC, quality control.

information related to the chemical and pharmaceutical quality of the drug and drug substances, as well as non-clinical data related to pharmacology, pharmacokinetics, radiation dosimetry, and toxicology (Figure 17.1). The information in the IMPD has to be provided in a standardized way based on the common technical dossier (CTD) format, which is also used in applications for marketing authorization. A specific guideline was published by the European Association of Nuclear Medicine (EANM) on the design of an IMPD for a radiopharmaceutical [1].

Several non-legally binding guidelines published by groups such as The International Council for Harmonization (ICH) of Technical Requirements for Pharmaceuticals for Human Use, European Medicines Agency (EMA), and EANM are available. However, these documents provide guidance for the effective implementation of legislation regarding radiopharmaceuticals. Of note, these documents are often incorporated or adapted in the EudraLex legislation and hence are legally binding. Further, the Declaration of Helsinki offers a set of ethical guidelines for physicians and other participants in medical research [2].

In the EU, radiopharmaceuticals for clinical studies need to be produced in agreement with GMP requirements. Detailed GMP guidelines from the EMA are available (EudraLex Volume 4, https://ec.europa.eu/health/documents/eudralex/vol-4_en), and specific guidelines for GMP production of radiopharmaceuticals are provided in Annex 3 (Manufacturing of Radiopharmaceuticals; https://ec.europa.eu/health/sites/health/files/files/eudralex/vol-4/2008_09_annex3_en.pdf) as well as in the Pharmaceutical Inspection Cooperation Scheme (PIC/s) in Annex 3 (<https://picscheme.org/docview/1946>).

Finally, an important reference for the selection of analytical methods and the definition of specifications is the European Pharmacopoeia (Ph. Eur.). Specific monographs for a limited number of radiopharmaceuticals are available, as well as monographs that provide more general guidance. For the US, the Food and Drug Administration (FDA)

publishes specific rules for the production of PET radiopharmaceuticals (<https://www.fda.gov/drugs/pharmaceutical-quality-resources/positron-emission-tomography-pet-questions-and-answers-about-cgmp-regulations-pet-drugs>); and the International Atomic Energy Agency recently published a document providing practical support for the introduction of new radiopharmaceuticals for clinical use (<https://iaea.org/publications/10829/good-practice-for-introducing-radiopharmaceuticals-for-clinical-use>).

Article 11 of Clinical Trials Directive 2001/20/EC established the European Clinical Trials Database (EudraCT) in which all clinical trials in the EU have been registered since 1 May 2004 (<https://eudract.ema.europa.eu>). From 2007 on, the number of clinical trials conducted yearly in the EU has slowly decreased, and the same trend is observed for clinical trials involving radiopharmaceuticals. Figure 17.2 gives an overview of registered clinical trials (phase I–IV) with radiopharmaceuticals labeled with fluorine-18, iodine-124, or iodine-123. Radiotracer clinical studies amount to about 1% of all studies registered in the EU Clinical Trials Register.

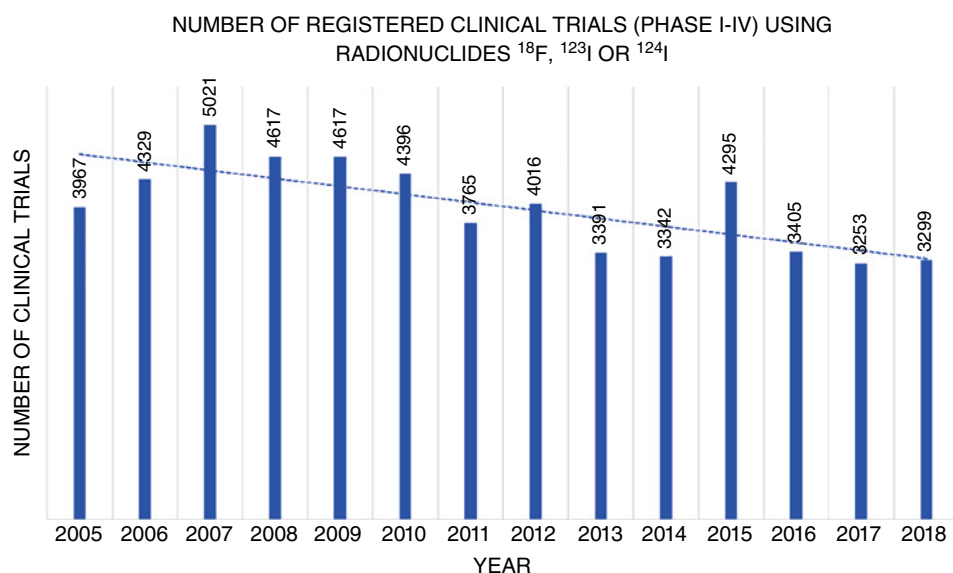
17.3 REGULATORY ENVIRONMENT FOR RADIOPHARMACEUTICALS IN CLINICAL TRIALS

17.3.1 Non-clinical Safety Studies for the Conduct of Human Clinical Trials for Radiopharmaceuticals

The ICH M3(R2) provides harmonized (EU, Japan, US), detailed guidance for non-clinical safety studies in line with the 3R principle (reduction/refinement/replacement) for animal experiments. For small-molecule radiotracer studies, generally, low mass amounts

Figure 17.2

Number of radio-tracer clinical trials (phases I–IV) registered using the radionuclides ^{18}F , ^{123}I , and ^{124}I from 2005 until 2018. Source: Data were provided by the EMA in July 2019.



(<5 µg) are injected so that a “microdose trial approach” can be used (https://www.ema.europa.eu/en/documents/scientific-guideline/ich-guideline-m3r2-non-clinical-safety-studies-conduct-human-clinical-trials-marketing-authorisation_en.pdf). Here, approach 1 (total dose ≤100 µg) or approach 2 (total cumulative dose ≤500 µg, maximum of five administrations) can be applied. For the former, toxicity is evaluated 24 hours or 14 days after single-dose administration to 30 animals of both sexes (15 each). The latter evaluates seven-day repeated-dose toxicity in one species, usually rodents.

Toxicity tests are performed with a 1000-fold higher dose than the intended clinical dose on a mg/kg base and should be conducted in agreement with good laboratory practice (GLP) regulations (<https://publications.europa.eu/en/publication-detail/-/publication/b78b6aee-a9b4-468e-b21e-0d5e54acbe91/language-en>). Genotoxicity studies are not recommended, but appropriate pharmacokinetic and dosimetry estimates should be included.

As radiopharmaceuticals are intrinsically mutagenic, mutagenicity studies are not recommended, and the principles of ICH M7 (mutagenic impurities) can be applied. For pharmaceuticals, a threshold of toxicological concern (TTC) can be established for adjuvants or artifacts present in the pharmaceutical preparation ([https://chemsafetypro.com/Topics/CRA/Introduction_to_Threshold_of_Toxicological_Concern_\(TTC\)_Approach_in_Chemical_Risk_Assessment.html](https://chemsafetypro.com/Topics/CRA/Introduction_to_Threshold_of_Toxicological_Concern_(TTC)_Approach_in_Chemical_Risk_Assessment.html)). This principle determines a threshold for chemicals below which no adverse effects should occur.

However, verification is necessary so that the radiopharmaceutical does not contain any of the structural features of the *cohort of concern* compounds. These compounds were identified to be highly mutagenic. Hence, intake even below the TTC would theoretically be associated with a potential for a significant carcinogenic risk. This group of high potency mutagenic carcinogens comprises aflatoxin-like-, *N*-nitroso-, and alkyl-azoxy compounds (https://www.ema.europa.eu/en/documents/scientific-guideline/ich-guideline-m7r1-assessment-control-dna-reactive-mutagenic-impurities-pharmaceuticals-limit_en.pdf).

A draft of a new EMA guideline stipulates non-clinical requirements specifically for radiopharmaceuticals (<https://www.ema.europa.eu/en/non-clinical-requirements-radiopharmaceuticals>). This draft provides guidance for non-clinical testing of radiopharmaceuticals for diagnostic use as well as radionuclide therapy.

Remarkably, non-clinical safety testing may no longer be needed in certain cases: (i) if a known radiopharmaceutical is labeled with another radionuclide, (ii) when a radionuclide is added to a known non-radioactive pharmaceutical, and (iii) if the non-radioactive part of the radiopharmaceutical is only slightly changed. However, it should be demonstrated that these minimal structural changes do not significantly alter the pharmacology compared to the reference molecule for which the (non-)clinical safety data are available.

For new radiopharmaceuticals for imaging that don't qualify for the previous categories, non-clinical pharmacologic, pharmacokinetic, and toxicity (microdosing approach, mentioned earlier) evaluation should be performed. For high-molecular-mass radiopharmaceuticals (radiolabeled biologicals), microdosing approach 1 may surpass the 100 µg limit based on the molar amount and the potency of the molecule (approach 1 for biologicals).

Finally, the EMA guideline draft recognizes that it might not be possible to conduct all studies in conformity with GLP. However, if a pivotal non-clinical safety study wasn't conducted in conformity with the GLP principles, a scientific justification has to be provided addressing the potential impact of non-compliance on the reliability of the data. Non-clinical safety studies should be performed "as close as possible" to GLP principles, and a prospectively designed study protocol should be used.

17.3.2 Clinical Trial Legislation

17.3.2.1 EudraLex

The EU legal framework for medicinal products for human use guarantees high standards of quality and safety of medicinal products while promoting the good functioning of the internal market with measures that encourage innovation and competitiveness. 2015 marked the 50th anniversary of pharmaceutical legislation in the EU, which began with the adoption of Directive 65/65 in 1965.

EudraLex compiles the EU pharmaceutical legislation in Volume 1 for medicinal products for human use and in Volume 5 for medicinal products for veterinary use (https://ec.europa.eu/health/documents/eudralex_en). The eight other volumes provide detailed guidance on legislation. An outline of EudraLex is depicted in Figure 17.3, and sections relevant to radiopharmaceuticals are discussed in detail underneath.

17.3.2.2 The EU Clinical Trial Directive and the Clinical Trial Regulation

EU Clinical Trials Directive 2001/20/EC was published in 2001 (https://ec.europa.eu/health/human-use/clinical-trials/directive_en). An EU directive requires member countries to incorporate (*transpose*) the objectives of the directive into national law. However, the directive allows flexibility, and this resulted in significant differences in legal requirements toward clinical trials in the different states in the EU, including clinical trials with radiotracers. Soon after its implementation, the negative effects of this directive on clinical research in Europe became apparent, as the lack of harmonization complicates the efficient performance of multinational clinical trials.

EU 2001/20/EC is being replaced by EU Clinical Trial Regulation EU No. 536/2014 (<https://ema.europa.eu/en/human-regulatory/research-development/clinical-trials/clinical-trial-regulation>). Although the regulation was published in 2014, it will only be applied six months after the Clinical Trials Information System (**CTIS**) is fully functional. Starting in June 2019, an iterative delivery model has been developed, with functionalities delivered in short development cycles. Member states are also directly involved in the development of CTIS. As such, their perspectives and concerns are included. Further, this allows for direct testing and verification of the different functionalities. The CTIS audit is currently planned for December 2020.

Unlike a directive, a regulation does not need to be transposed into national law but applies uniformly to all EU countries as soon as it enters into force. The main objectives

Eudralex – EU Legislation

Legislation for medicinal products in the European Union

Volume 1- EU pharmaceutical legislation for medicinal products for human use

Directives (transposed into national law)

e.g. Medicinal Products Directive (2001/83/EC) and Clinical Trial Directive (2001/20/EC)

Regulations (applies uniformly to all EU countries)

e.g. Clinical Trial Regulation (EU No 536/2014)

Volume 5 - EU pharmaceutical legislation for medicinal products for veterinary use

Supporting guidelines

Volume 2 - Notice to applicants and regulatory guidelines for medicinal products for human use

Volume 3 - Scientific guidelines for medicinal products for human use

Volume 4 - Guidelines for good manufacturing practices for medicinal products for human and veterinary use

Annex 1: Manufacture of Sterile Medicinal Products

Annex 3: Manufacture of Radiopharmaceuticals

Annex 11: Computerized Systems

Annex 13: Manufacture of Investigational Medicinal Products

Annex 16: Certification by a Qualified Person and Batch Release

Volume 6 - Notice to applicants and regulatory guidelines for medicinal products for veterinary use

Volume 7 - Scientific guidelines for medicinal products for veterinary use

Volume 8 - Maximum residue limits

Volume 9 - Guidelines for pharmacovigilance for medicinal products for human and veterinary use

Volume 10 - Guidelines for clinical trial

Set of documents applicable to clinical trials authorized under the Clinical Trial Directive “2001/20/EC”

Set of documents applicable to clinical trials that will be authorized under the Clinical Trial Regulation “EU No 536/2014”

Figure 17.3 Outline of EudraLex legislation. Volumes and annexes indicated in bold are important for the manufacturing of radiopharmaceuticals used as medicinal products. Source: EudraLex - EU Legislation, EudraBook V1 - May 2015 / EudraLex V30 - January 2015. https://ec.europa.eu/health/documents/eudralex_en. Reproduced with the permission of European Commission.

of the regulation are simplifying and speeding up approval of clinical trials by implementing an electronic portal (CTIS), increasing the harmonization between the member states to facilitate multicenter transnational clinical trials, augmenting transparency, and increasing participant safety.

The EU Clinical Trial Regulation is flanked by Good Clinical Practice (**GCP**) Directive 2005/28/EC (<https://eur-lex.europa.eu/LexUriServ/LexUriServ.do?uri=OJ:L:2005:091:0013:0019:en:PDF>) describing the ethical and scientific quality standards for designing, recording, and reporting clinical trials. Further, harmonized guidance with regard to GCP is provided by ICH E6(R2) (https://www.ema.europa.eu/en/documents/scientific-guideline/ich-e-6-r2-guideline-good-clinical-practice-step-5_en.pdf) and EudraLex Volume 10 (https://ec.europa.eu/health/documents/eudralex/vol-10_en), which compiles new and revised documents related to changes that will be implemented by Clinical Trial Regulation EU No. 536/2014.

17.3.2.3 Observational Studies, Interventional Studies, and *Individuelle Heilversuche*

Clinical trials are composed of observational and interventional studies. Observational studies imply merely the supervision of disease progression to formulate new ideas for treatment but lack a treatment phase. In contrast, interventional clinical trials,

sometimes referred to as interventional clinical studies, aim to test treatment methods, including the administration of drugs or exercise studies in human beings.

Low-intervention clinical trials assess standard treatments with authorized medicinal products, with the goal of optimizing the use of these medicinal products. Low-intervention clinical trials typically need to comply with less stringent rules (https://www.ema.europa.eu/documents/other/questions-answers-public-consultation-implementation-transparency-requirements-european-clinical_en.pdf).

Non-interventional studies imply studies where the medicinal product is prescribed in accordance with the terms of the marketing authorization. Here, the assignment of the patient to a therapeutic strategy falls within the current practice. Further, no additional monitoring or diagnostic procedures are applied, following article 2(c) of 2001/20/EC. Biological sampling and taking surveys can be performed as part of normal clinical practices [3]. Non-interventional studies are excluded from the scope of EU regulation 536/2014. The Q&A document includes a decision tree to establish whether a trial is a clinical trial, a non-interventional trial, or a low-intervention trial.

In special cases, drugs that are not yet registered can be administered to patients. Off-label-use drugs are drugs intended for an unapproved indication or in an unapproved age group, dosage, or route of administration. Compassionate use allows the use of a drug, currently under investigation, under a strict policy for patients who are not responsive to authorized therapies [4]. In Germany, patients can be treated with medication that is not yet approved by application of an *individuelle Heilver suche* in which full responsibility of the treatment is put on the treating physician [5].

17.3.3 Quality Requirements for Radiopharmaceuticals Used in Clinical Trials

EU Clinical Trials Directive 2001/83/EC requires that investigational medicinal products (**IMPs**), including radiopharmaceuticals, are produced in agreement with GMP regulations.

However, a deviation from those rules is foreseen in the new Clinical Trial Regulation (536/2014, Article 63.2) for diagnostic radiopharmaceuticals used in clinical trials as IMP, if the production process is carried out in hospitals, and when the radiopharmaceuticals are intended to be used exclusively in hospitals taking part in the same clinical trial in the same Member State. In this case, there is no need for GMP production, which facilitates the conduct of a clinical trial and follows the concept of “proportionate risk” in the new regulation.

The Clinical Trial Regulation also makes the distinction between IMPs and auxiliary medicinal products (**AMPs**), known as non-investigational medicinal products (**NIMPs**) in the guidance documents of Clinical Trials Directive 2001/20/EC (https://ec.europa.eu/health/sites/health/files/files/eudralex/vol-10/imp_03-2011.pdf). PET tracers are often used as AMPs in clinical studies: e.g. [¹¹C]raclopride is used to quantify dopamine D₂ receptors [6]. AMPs must be manufactured according to GMP or to at least “an equivalent

standard,” but a GMP manufacturing authorization is not required, as referred to in Article 63(1) of the Clinical Trial Regulation.

Nevertheless, a survey by the EANM [7] showed that currently, most IMPs and AMPs are required to be produced according to GMP standards by the different national authorities throughout the EU, and it can be expected that national authorities will continue to adhere to this requirement after implementation of the EU Clinical Trial Regulation. Furthermore, pharmaceutical companies generally also require GMP-compliant production of PET tracers to be used in their clinical trials. Therefore, it may be difficult to relax production requirements in practice, even if this would be allowed by the new EU Clinical Trial Regulation.

GMP guidelines are described in EudraLex Volume 4; in addition, these guidelines also include several annexes that deal with specific topics related to GMP production (Figure 17.4). In particular, the following EudraLex sections are of importance for the GMP production of radiopharmaceuticals: Manufacture of Sterile Medicinal Products (Annex 1), Computerized Systems (Annex 11), Manufacture of Investigational Medicinal Products (Annex 13), Certification by a Qualified Person and Batch Release (Annex 16), and especially, Manufacture of Radiopharmaceuticals (Annex 3), which came into operation in March 2009.

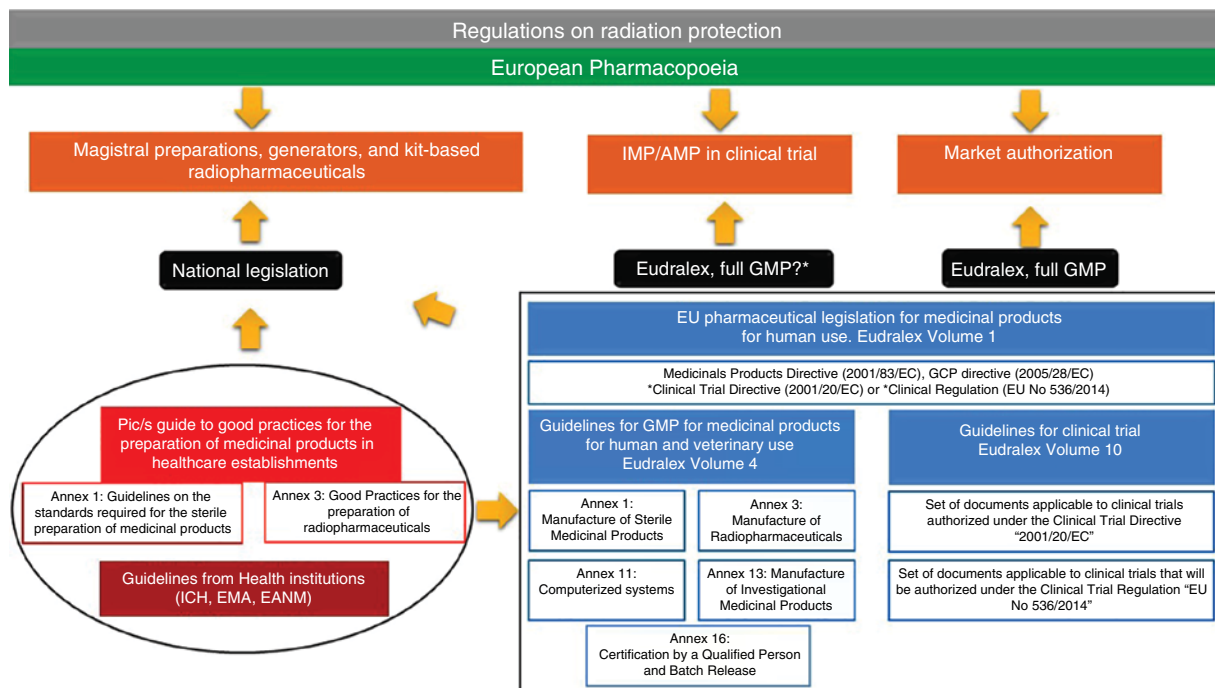


Figure 17.4 Legislation and guidelines that need to be considered for the manufacture of radiopharmaceuticals in the EU.

17.3.3.1 Annex 3 of EudraLex Volume 4: Manufacture of Radiopharmaceuticals

The general principles of GMP for medicinal products are described in EudraLex Volume 4. EudraLex Volume 4, Annex 3, addresses specific requirements for the production of radiopharmaceuticals, radioactive precursors for radiopharmaceutical production, and radionuclide generators. The preparation of radiopharmaceuticals involves adherence to (national) regulations on radiation protection (Figure 17.4). As GMP requirements focus on the protection of the product from its environment and radioprotection requirements and emphasize protection of the environment from the radioactive product, a radiopharmaceutical-specific layout of the production labs is required.

In order to prevent the spread of radioactive gases and particles, the air pressure in the production area of radiopharmaceuticals should be lower compared to surrounding areas. Further, recirculation of air extracted from areas where radioactive products are handled should be avoided. These requirements may be achieved by using barrier technology or airlocks, acting as pressure sinks.

The first step of the radiopharmaceutical production process is the reactor or cyclotron production of the radionuclide, and this can be performed, on site, under non-GMP conditions. The target and transfer system from the cyclotron to the synthesis rig may be considered the first step of active substance manufacture. The subsequent steps in the production process, such as (radio)chemical synthesis, purification, processing, sterile filtration, and formulation, must be performed under GMP conditions and in controlled (air quality and radioactivity) areas to obtain the final medicinal product.

Production of different radiopharmaceuticals in the same hot cell or laminar air flow (LAF) unit at the same time must be avoided to minimize the risk of cross-contamination or mix-up. Further, the critical parameters of the production process should be identified before and during validation, and the ranges necessary for reproducible operation should be validated prospectively. Moreover, a system to verify the quality of starting materials should be in place. Furthermore, the responsible person for production should be different from the person who performs the quality control of the radiopharmaceutical.

As radiopharmaceuticals are mostly used for intravenous injection, they need to be manufactured aseptically or sterilized terminally. Integrity testing of the membrane filter (e.g. bubble-point test) should be performed for aseptically filled products. Cleanliness requirements should comply with the requirements described in EudraLex Volume 4, Annex 1. Clean rooms are classified as grades A, B, C, and D. The corresponding maximum permitted number of particles per cubic meter at rest and in operation are tabulated in Volume 4, Annex 1, as well as the recommended limits for microbial contamination.

Cyclotron-generated radionuclides are typically incorporated into vector molecules in automated synthesis modules present in lead-shielded hot cells. The use of commercially available, preassembled, disposable cassettes allows facile GMP production of multiple tracers with one set of equipment, without the need for individual tracer-specific alterations [8]. In this case, the cassette, consisting of valves, syringes, containers, and connecting tubes, replaces the chemistry part of the module [9]. As computerized systems are often used for the production of radiopharmaceuticals (e.g. in automated

synthesis modules and QC equipment), these need to be in compliance with EudraLex Volume 4, Annex 11, Computerized Systems.

In the case of closed and automated systems (hot cell with a synthesis module), a grade C environment is most suitable for production activities. In contrast, aseptic activities must be carried out in a (shielded) grade A area, including assembly of sterilized equipment and consumables (e.g. sterile filter and vials). Typically, one or two non-shielded pre-chambers are used to unpack and introduce materials in the shielded grade A cell.

Because of the short shelf-life of radionuclides, some radiopharmaceuticals may be released for use before completion of quality control tests. Radiopharmaceutical product release may be carried out in two or more stages, before and after completion of testing.

In the first stage, a designated person should assess batch-processing records, which should cover production conditions and analytical testing performed before the radiopharmaceutical can be transported under quarantine status to the clinical department. In the next stage, the final analytical data should be assessed by a qualified person (QP; the QP responsibilities are elaborated in Eudralex Volume 4, Annex 16), ensuring that all deviations from normal procedures are documented and justified, and the radiopharmaceutical can be conditionally released for human use.

For some tests, samples can be stored to allow sufficient radioactivity decay prior to performing the test. However, all tests, including the sterility test, should be performed "as soon as possible," as stated in Annex 3 of EudraLex Volume 4. Recently, in the United States Pharmacopoeia (USP), former Chapter <797>, providing standards for compounding sterile preparations, has been eliminated and replaced with reference to General Chapter <825> (<https://www.usp.org/sites/default/files/usp/document/our-work/chemical-medicines/proposed-gc-825.pdf>). Additionally, a separate USP monograph was prepared concerning PET radiopharmaceuticals (https://www.uspnf.com/sites/default/files/usp_pdf/EN/USPNF/key-issues/usp35-nf30_general_chapter_823.pdf). The USP states that incubation with the radiopharmaceutical to be examined should begin within 30 hours; this can be exceeded because of weekends or holidays. Further, the endotoxins test should be performed before release, except for short-lived isotopes (^{13}N or ^{15}O), where a sub-batch test is needed.

Upon completion of all the tests, the QP will do the final release of the radiopharmaceutical, which may be more than 14 days after its administration. If unsatisfactory test results (out-of-specification) are obtained after dispatch, proper corrective and preventative measures need to be taken by the QP to prevent future events, and this process must be cautiously documented.

It is important to mention that EudraLex Volume 4, Annex 3 does not apply to radiopharmaceuticals prepared from registered generators and labeling kits. The latter class of radiopharmaceuticals includes the established $^{99\text{m}}\text{Tc}$ -radiopharmaceuticals as well as, recently, ^{68}Ga labeled edotreotide. Both the ^{68}Ga labeling kit (SomaKit TOC, <https://www.adacap.com/our-products>) and the $^{68}\text{Ge}/^{68}\text{Ga}$ generator are registered in the EU (<https://radiopharma.com/product/galliapharm>). For this class of radiopharmaceuticals, diverging, national regulatory requirements apply (Figure 17.4), which are usually in line with those for the preparation of injectables in health care institutions.

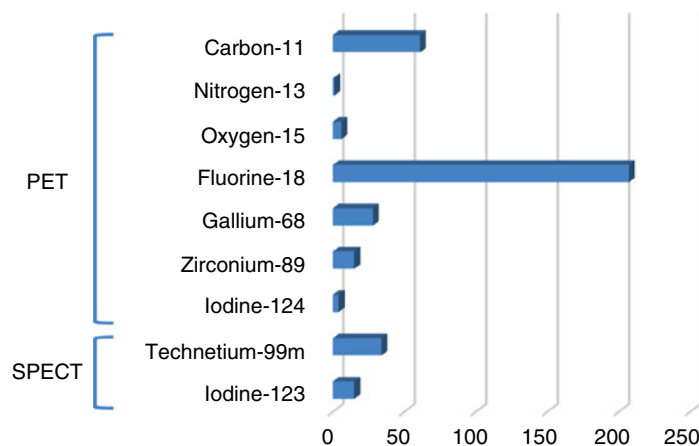
For radiopharmaceuticals used as an IMP in a clinical trial, the requirements described in Eudralex Volume 4, Annex 13 (Manufacture of IMPs) need to be considered. Figure 17.4 gives an overview of regulations and guidelines that must be considered for the manufacture of radiopharmaceuticals as magistral preparations, a radiopharmaceutical used as IMP/AMP in a clinical trial or as a radiopharmaceutical with marketing authorization.

17.4 EU CLINICAL TRIALS REGISTER AND EudraCT DATABASE

The EU Clinical Trials Register contains information on interventional clinical trials for medicines conducted in the EU or the European Economic Area (EEA), which started after 1 May 2004. The EU Clinical Trials Register website (www.clinicaltrialsregister.eu) has been available since 2011 and provides the public with information held in the EudraCT database. This is the database used by national medicines regulators for data related to clinical trial protocols. Data on the results of these trials are entered into the database by the sponsors and are published in this register once the sponsors have validated the data. The EU Clinical Trials Register has been a primary registry in the World Health Organization (WHO's) Registry Network since September 2011 (<https://who.int/ictqp/en>).

The EU Clinical Trials Register provides a searchable overview of phase II to phase IV clinical trials (no phase I clinical trials) that include at least one clinical site in the EEA. Figure 17.5 provides an overview of clinical radiotracer studies retrieved from the EU Clinical Trials Register, showing the dominance of studies using PET over studies using SPECT, with fluorine-18 being the most used radionuclide for phases II–IV radiotracer clinical studies.

Figure 17.5 Distribution of the number of radiotracer clinical trials retrieved from the EU Clinical Trials Register according to the radionuclide used. Source: Data were retrieved in June 2019, and phase I studies are excluded from the EU Clinical Trials Register.



17.5 EANM AND PIC/S GUIDELINES

17.5.1 EANM

The EANM has published several guidelines for proper use of diagnostic and therapeutic nuclear medicine procedures for diseases affecting different organs/tissues, including cardiovascular, central nervous system, bone, respiratory, gastrointestinal, nephro-urinary, endocrine, hematopoietic/lymphatic, oncology, and inflammation/infection (<https://www.eanm.org/publications/guidelines>).

Guidelines related to radiopharmaceuticals are listed in Table 17.1 and provide practical information regarding production, validation, QC, testing, and regulatory issues in the EU.

17.5.2 PIC/s

The Pharmaceutical Inspection Convention (**PIC**) and the PIC/s comprise 52 participating authorities worldwide and aim at harmonizing GMP inspection procedures and developing common GMP standards (<https://picscheme.org/en/picscheme>). PIC/s provides GMP guidelines that are in good agreement with the EU EudraLex GMP guidelines (discussed earlier).

Guideline	Year
Guidance on validation and qualification of processes and operations involving radiopharmaceuticals [10]	2017
Position statement on radiopharmaceutical production for clinical trials [7]	2017
Position paper on requirements for toxicological studies in the specific case of radiopharmaceuticals [11]	2016
Guideline for the preparation of an investigational medicinal product dossier (IMPD) [1]	2014
Guidance on current Good Radiopharmacy Practice for the small-scale preparation of radiopharmaceuticals using automated modules: a European perspective [9]	2014
Guidance on current Good Radiopharmacy Practice for the small-scale preparation of radiopharmaceuticals using automated modules: a European perspective [9]	2014
Guidelines on current Good Radiopharmacy Practice (cGRPP) for the small-scale preparations of radiopharmaceuticals [12]	2010
Guideline to regulations for radiopharmaceuticals in early phase clinical trials in the EU [13]	2008
Guidelines on current Good Radiopharmacy Practice (cGRPP) in the preparation of radiopharmaceuticals (http://eanm.org/publications/guidelines/gl_radioph_cgrpp.pdf)	2007

Table 17.1 EANM guidelines and position papers relevant for clinical translation of radiotracers.

Interestingly, PIC/s also has a guide for good practices for the preparation of medicinal products in healthcare establishments. Annex 1, guidelines on the standards required for the sterile preparation of medicinal products, and especially Annex 3, good practices for the preparation of radiopharmaceuticals, are of great interest to the radiopharmaceutical community (Figure 17.4) (<https://picscheme.org/docview/1946>). The guidance in Annex 3 supplements and amends current guidance for the preparation of radiopharmaceuticals and is divided into personnel, premises and equipment, documentation, production, quality control, and monitoring. A risk assessment-based approach is generally used throughout Annex 3, and a “closed method of preparation,” i.e. typical manipulations associated with kit-based radiopharmaceuticals (transfer of solutions between sealed vials), is allowed in an open class A workstation in a class C environment. Aseptic preparation in a closed workstation (isolator) can be performed in a class D environment.

17.6 EUROPEAN PHARMACPOEIA RADIOPHARMACEUTICALS MONOGRAPHS

The European Pharmacopoeia (Ph. Eur.) functions under the responsibility of the European Directorate for the Quality of Medicines (**EDQM**). The establishment of the Ph. Eur. is the responsibility of the European Pharmacopoeia Commission. It is composed of delegations appointed by the contracting parties (39 member states) and observers from non-member states and international organizations (30 observers are admitted at present).

The purpose of the Ph. Eur. is to promote public health by providing recognised common standards for the quality of medicines and their components. Ph. Eur. monographs and other texts are designed to be appropriate to the needs of regulatory authorities and stakeholders engaged in the manufacture and quality control of medicinal products and their constituents.

In comparison, the USP is a non-profit organization that sets standards for identity, quality, and purity of medicines that are enforced by the FDA.

Monographs on radiopharmaceutical preparations are prepared by Ph. Eur. Expert Group 14 on radiopharmaceutical preparations, composed of about 20 experts from different EU member countries. The preparation of a monograph for the Ph. Eur. is a lengthy and intensive process and proceeds in eight steps. Generally, the introduction of a new monograph on a radiopharmaceutical in the Ph. Eur. takes three to five years from the request for elaboration until implementation.

The requirements, recommendations, and information concerning radiopharmaceutical preparations in the Ph. Eur. are described not only in monographs on individual radioactive preparations but also in five general texts and general chapters, of which two existed in 2000 (and have been updated) and three are new (Table 17.2). For radiopharmaceuticals not described in an individual monograph, the requirements described in the general monographs and general texts apply. This is also the case for non-radioactive and radioactive precursors of radiopharmaceuticals.

The number of monographs related to radiopharmaceuticals in the Ph. Eur. has significantly increased since 2000. In 1999, the first PET radiopharmaceutical monograph

Number	Monograph title
2.2.66	Detection and measurement of radioactivity (new; only short description in Chapter 6.15 up to 2012)
5.7	Table of physical characteristics of radionuclides mentioned in the European Pharmacopoeia (updated)
5.19	Extemporaneous preparation of radiopharmaceuticals (new)
6.2	Chemical precursors for radiopharmaceutical preparations (new)
6.15	Radiopharmaceutical preparations (updated)

Table 17.2
European Pharmacopoeia general monographs on radiopharmaceuticals.

on [^{18}F]Fludeoxyglucose (^{18}F FDG) was introduced. In the meantime, 21 other monographs on PET radiopharmaceutical preparations have become available, three of which are on radioactive precursors [^{18}F] F^- and [^{68}Ga] GaCl_3 , accelerator produced, and [^{68}Ga] GaCl_3 , generator produced. Huang et al. recently reviewed USP and Ph. Eur. monographs [14].

In the most recent volume of the Ph. Eur. (Volume 10.3, published July 2020, implementation January 2021), 82 monographs on individual radiopharmaceutical preparations can be found. The majority (54 monographs) of these preparations are solutions for injection, but apart from these, there are also seven monographs on radioactive precursors (e.g. sodium [^{18}F]fluoride solution for radiolabeling), eight monographs on non-radioactive precursors (e.g. mannose triflate for radiopharmaceutical preparations), four monographs on capsules containing a radioactive compound (e.g. sodium [^{131}I]iodide capsules for therapeutic use), six monographs on radioactive solutions (e.g. sodium [^{131}I]iodide solution, for oral administration), and three monographs on radioactive gases (e.g. [$^{81\text{m}}\text{Kr}$]krypton inhalation gas).

Within the Ph. Eur., a concept unique to radiopharmaceutical preparations is that of *V*: i.e. the maximum recommended patient dose in millilitres. The volume of the radiopharmaceutical preparation to be administered depends on the radioactivity concentration of the preparation and the prescribed radioactivity. Because of the inherent physical decay of radioactivity, the radioactivity concentration of a radiopharmaceutical preparation decreases with time, and the required volume of injection will increase in order to give the desired radioactivity dose. For this reason, the volume of administration is not defined, as it will be specific for a particular product at a particular time and can amount to the total batch volume.

Many tests on radiopharmaceutical preparations measure the analytes (related substances, precursors and catalysts of (radio)synthesis, bacterial endotoxins, etc.) in terms of milligrams or units per millilitre, but the limits are specified in terms of milligrams or units per patient dose *V* (or volume of administration) in millilitres to restrict their total administered amounts independent of the administered volume.

A given Ph. Eur. monograph specifies requirements toward identification and purity (including residual solvents, metal catalysts, and microbiological purity) for precursors for radiolabeling. However, the monograph states that the need for compliance is decided based on a risk assessment considering purification after radiolabeling, quality, and the amount of precursor administered to the patient.

Radiopharmaceuticals in clinical studies are usually new and do not (yet) have a Ph. Eur. monograph, except when they are used as AMPs. Also, for new IMPs, the general Ph. Eur. monographs are valuable, as specifications of Ph. Eur. for established radiopharmaceuticals (e.g. limit for precursor in carbon-11 radiopharmaceuticals) can be used to justify e.g. the amount of impurities specified in the IMPD of a new IMP. Moreover, for validation of the analytical procedures of an IMP, the publicly available guide for the elaboration of monographs on radiopharmaceutical preparations can be used (<https://go.edqm.eu/GuideRadiopharma>).

REFERENCES

1. Todde, S., Windhorst, A.D., Behe, M. et al. (2014). EANM guideline for the preparation of an investigational medicinal product dossier (IMPD). *Eur. J. Nucl. Med. Mol. Imaging* 41 (11): 2175–2185.
2. Carlson, R.V., Boyd, K.M., and Webb, D.J. (2004). The revision of the Declaration of Helsinki: past, present and future. *Br. J. Clin. Pharmacol.* 57 (6): 695–713.
3. These, M.S. (2014). Special issue: responsible writing in science lessons in biostatistics observational and interventional study design types; an overview. *Biochem. Med.* 24 (2): 199–210.
4. Whitfield, K., Huemer, K.H., Winter, D. et al. (2010). Compassionate use of interventions: results of a European clinical research infrastructures network (ECRIN) survey of ten European countries. *Trials* 11 (1): 104.
5. Wedekin, M., Ehrich, J.H.H., and Pape, L. (2011). Effective treatment of anemia in pediatric kidney transplant recipients with methoxy polyethylene glycol-epoetin beta. *Pediatr. Transplant.* 15 (11): 329–333.
6. Van Laere, K., Clerinx, K., D'Hondt, E. et al. (2010). Combined striatal binding and cerebral influx analysis of dynamic ^{11}C -raclopride PET improves early differentiation between multiple-system atrophy and Parkinson disease. *J. Nucl. Med.* 51 (4): 588–595.
7. Bormans, G., Buck, A., Chiti, A. et al. (2017). Position statement on radiopharmaceutical production for clinical trials. *EJNMMI Radiopharm. Chem.* 2 (1): 1–3.
8. Schopf, E., Waldmann, C.M., Collins, J. et al. (2018). Automation of a positron-emission tomography (PET) radiotracer synthesis protocol for clinical production. *J. Vis. Exp.* 140: 1–12.
9. Aerts, J., Ballinger, J.R., Behe, M. et al. (2014). Guidance on current good radiopharmacy practice for the small-scale preparation of radiopharmaceuticals using automated modules: a European perspective. *J. Labelled Compd. Radiopharm.* 57 (10): 615–620.
10. Todde, S., Peitl, P.K., Elsinga, P. et al. (2016). Guidance on validation and qualification of processes and operations involving radiopharmaceuticals. *EJNMMI Radiopharm. Chem.* 2 (8): 1–29.

11. Koziorowski, J., Behe, M., Decristoforo, C. et al. (2016). Position paper on requirements for toxicological studies in the specific case of radiopharmaceuticals. *EJNMMI Radiopharm. Chem.* 1 (1): 1–6.
12. Elsinga, P., Todde, S., Penuelas, I. et al. (2010). Guidance on current good radiopharmacy practice (cGRPP) for the small-scale preparation of radiopharmaceuticals. *Eur. J. Nucl. Med. Mol. Imaging* 37 (5): 1049–1062.
13. Verbruggen, A., Coenen, H.H., Deverre, J.R. et al. (2008). Guideline to regulations for radiopharmaceuticals in early phase clinical trials in the EU. *Eur. J. Nucl. Med. Mol. Imaging* 35 (11): 2144–2151.
14. Huang, Y.Y. (2019). An overview of PET radiopharmaceuticals in clinical use: regulatory, quality and pharmacopoeia monographs of the United States and Europe. In: *Nuclear Medicine Physics*, 1e (eds. A. Shahzad and S. Bashir), 35–58. London: IntechOpen Limited.

PART V

Major Applications of Radiopharmaceuticals

Chapter 18

Radiopharmaceuticals in Oncology

Jeroen A.C.M. Goos^{1,*}, Outi Keinänen^{2,*}, Brian M. Zeglis^{1,2,3,5}, and Jason S. Lewis^{1,4,5}

¹*Department of Radiology, Memorial Sloan Kettering Cancer Center, New York, NY, 10021, USA*

²*Department of Chemistry, Hunter College, The City University of New York, New York, NY, 10021, USA*

³*Ph.D. Program in Chemistry, Graduate Center of the City University of New York, New York, NY, 10021, USA*

⁴*Molecular Pharmacology Program and the Radiochemistry and Molecular Imaging Probes Core, Memorial Sloan Kettering Cancer Center, New York, NY, 10021, USA*

⁵*Departments of Radiology and Pharmacology, Weill Cornell Medical College, New York, NY, 10021, USA*

*Jeroen A.C.M. Goos and Outi Keinänen contributed equally to this work.

18.1 INTRODUCTION

In this chapter, we will discuss recent trends in the use of radiopharmaceuticals in oncology. Although the chapter is divided into two overarching sections – imaging and therapy – the nascent field of theranostics will be a theme throughout. In each section,

we will concentrate on a handful of compelling examples and share the stories of radiopharmaceuticals that have found clinical use in oncology. Although radiopharmaceuticals have been utilized in the diagnosis and treatment of cancer for decades, only a few radiopharmaceuticals have been approved by the European Medicines Agency (**EMA**) and the United States Food and Drug Administration (**US FDA**). However, we fully expect this to change in upcoming years due to the advent of cancer-specific radiopharmaceuticals.

Cancer is a broad term that covers a variety of malignancies, which explains why some cancers lack validated markers for early detection, treatment planning, or targeted therapy. Broadly speaking, *cancer research* aims to identify the molecular mechanisms by which cancers develop, design diagnostic techniques to detect these markers as early as possible, and develop targeted therapeutic strategies for the disease. Non-invasive imaging technologies such as computed tomography (**CT**) and magnetic resonance imaging (**MRI**) can be used to detect the anatomical and morphological changes associated with the disease. However, these methods have limited sensitivity and specificity for early diagnosis in several different forms of cancer. Nuclear imaging techniques – namely positron emission tomography (**PET**) and single-photon emission computed tomography (**SPECT**) – have the potential to detect functional or phenotypic changes in early-developing cancer cells. This type of *functional imaging* is especially useful when combined with anatomical methods (CT, MRI), facilitating the precise, disease-specific collection of molecular information. To manage the highly complex patient-specific tumor biology, the field of molecular imaging has tried to move beyond the workhorse imaging agent [¹⁸F]fluorodeoxyglucose (**[18F]FDG**) and in doing so has shifted its emphasis from the mere detection of cancer to the direction of patient selection for different treatment strategies.

Radiopharmaceuticals can be roughly categorized into two groups – diagnostic and therapeutic – based on their clinical purpose. The relatively new (and occasionally abused) term *theranostic* has been used to describe systems in which diagnostic and therapeutic features are combined in the same platform [1]. However, the concept of theranostics can be traced back to the very beginning of nuclear medicine, specifically to the use of radioiodine for the diagnosis and therapy of benign and malignant thyroid disease. While very effective against tumor cells, treatment modalities like radiotherapy and chemotherapy also strain the human body, and careful, informed patient selection is thus key when implementing these approaches. Theranostic radiopharmaceuticals have the potential to optimize the selection of patients for therapeutic regimens, sparing patients who do not express the drug's target from harmful side effects. In addition, inadequate patient selection can lead to failure in clinical trials with new therapeutic agents when the drug does not reach the target in sufficient quantities to produce an effective response. Theranostics can also help optimize drug dosage. Currently, the general practice is to administer therapeutic agents at their maximum allowed dose, i.e. the maximum tolerated dose in terms of normal tissue toxicity for chemotherapeutic agents and the amount of radioactivity with the highest acceptable whole-body dose or critical tissue radiation dose for radiotherapeutic agents. Optimizing the quantity of the therapeutic agent for each patient will improve "treatment versus side effect" results and thus quality of life.

A theranostic system comprises two components – a diagnostic agent and a therapeutic agent – that are chemically and biologically as similar as possible. For

instance, the diagnostic radiometals indium-111 ($t_{1/2} = 2.8$ days) and gallium-68 ($t_{1/2} = 68$ minutes) both have useful therapeutic counterparts in yttrium-90 ($t_{1/2} = 2.7$ days) and lutetium-177 ($t_{1/2} = 6.7$ days). Conveniently, the same radiometal chelator, 1,4,7,10-Tetraazacyclododecane-1,4,7,10-tetraacetic acid (**DOTA**), can be used to attach all of these radiometals to a targeting moiety. While changing the identity of the radiometal can affect the biological properties of the targeting moiety, subtle differences in the chemical structures do not typically impact the *in vivo* performance of a radiotheranostic pair. As a result, the diagnostic member of the pair can be used to predict the biodistribution of the therapeutic member, even if the two aren't strictly chemically identical. An example of this kind of theranostic pair is ^{68}Ga - and ^{177}Lu -labeled DOTA-(Tyr³-Thr⁶)-octreotide (**TATE**), which are used in the imaging and therapy of neuroendocrine tumors, respectively [2].

18.2 RADIOPHARMACEUTICALS FOR IMAGING CANCER

Radiopharmaceuticals have been used to image cancer since the 1960s. The heterogeneous nature of cancer demands a personalized treatment approach to achieve optimal outcomes. And while the importance of individualized treatment plans has long been known, radiopharmaceuticals are only rarely applied to stage patients and monitor their treatment. Nuclear imaging could add valuable information to these processes. Table 18.1 lists the radiopharmaceuticals approved by the FDA and the EMA for the imaging of cancer. While [^{18}F]FDG-PET has long been – and continues to be – a valuable tool for physicians, it is not a cancer-specific imaging agent [3]. Imaging agents with greater specificity for cancer biomarkers have been developed to fully address the clinical needs of staging patients and monitoring their response to treatment. We will provide examples of how radiopharmaceuticals are utilized in these applications later in this section. First, we will briefly summarize a few key features of PET and SPECT imaging and the radionuclides used for these modalities.

PET and SPECT are sensitive and quantitative molecular imaging methods. The high molar activity of radiotracers and the high sensitivity of nuclear imaging instruments underpin what is known as the *tracer principle* [4]. In short, doses of radiotracers typically lie on the order of 10^{-6} – 10^{-10} mol. As a result, radiopharmaceuticals can be administered without perturbing the biochemical systems with which they interact. As a result, no pharmacological effects are typically observed at such low concentrations, and even toxic and entirely new compounds can be administered fairly safely. Today, radionuclides with a wide range of physical half-lives are used in radiopharmaceuticals. Typically, the physical half-life of the radionuclide is matched to the biological half-life of the targeting moiety. Longer-lived radionuclides (e.g. ^{89}Zr [$t_{1/2} = 3.3$ days] and ^{111}In [$t_{1/2} = 2.8$ days]) are best suited for applications that require a long follow-up time, e.g., as part of an antibody-based radioimmunoconjugate. In contrast, shorter-lived radionuclides (e.g. ^{18}F [$t_{1/2} = 110$ minutes] and ^{68}Ga [$t_{1/2} = 68$ minutes]) are usually chosen for small-molecule radiotracers with fast target accumulation and clearance.

The availability of relatively inexpensive photon-emitting radionuclides – i.e. $^{99\text{m}}\text{Tc}$ and ^{111}In – makes SPECT imaging less expensive than PET imaging and allows for nuclear

Table 18.1 Radiopharmaceuticals approved for imaging of cancer in clinical settings.

Radiopharmaceutical ^a	Tradename	Approved by ^b	Approved for imaging of
Carbon-11 choline	Various	FDA	Prostate cancer, brain tumors
Fluorine-18 fluciclovine	Axumin	FDA and EMA	Prostate cancer
Fluorine-18 sodium fluoride	Various	FDA and EMA	Bone malignancies
Fluorine-18 fludeoxyglucose	Various	FDA and EMA	Abnormal glucose metabolism
Gallium-67 citrate	—	FDA	Hodgkin's disease, lymphoma, bronchogenic carcinoma
Gallium-68 DOTA-TATE	NETSPOT™	FDA	Neuroendocrine tumors
Gallium-68 DOTA-TOC	SomaKit TOC	EMA	Neuroendocrine tumors
Indium-111 pentetate	Octreoscan	FDA and EMA	Neuroendocrine tumors
Iodine I-123 iobenguane	AdreView	FDA	Pheochromocytoma or neuroblastoma
Technetium-99m tilmanocept	Lymphoseek	FDA and EMA	Sentinel lymph nodes draining a primary tumor (intraoperative detection as well)

^aNames are written as approved by FDA and EMA.

^bFDA: Food and Drug Administration; EMA: European Medicines Agency.

imaging in centers without PET facilities. PET has higher sensitivity than SPECT but, unlike SPECT, cannot image multiple targets in one session, since PET scanners record only the 511 keV annihilation photons [5, 6]. On the other hand, imaging only the two annihilation photons means that PET offers much better spatial image resolution. Because high resolution and sensitivity are crucial to detect small metastases, PET is usually the imaging modality of choice for the diagnosis of cancer.

Amongst the array of positron-emitting radionuclides available, gallium-68 and fluorine-18 have received the most attention in recent years. Both allow for same-day follow-up studies, since imaging is usually performed 30 minutes to a few hours after the administration of the radiopharmaceutical. Fluorine-18 – like most positron-emitting radionuclides – can be produced in large quantities using a cyclotron, and its 110 minute half-life enables multistep syntheses and the transfer of ¹⁸F-labeled radiopharmaceuticals from centralized production facilities to remote sites. In contrast, ⁶⁸Ga is produced with a reliable good manufacturing practice (GMP)-compliant ⁶⁸Ge/⁶⁸Ga generator. The drawbacks of ⁶⁸Ga are the relatively low amount of radioactivity available per generator elution and its rather short half-life, both of which limit the centralized production and distribution of the nuclide. The centralized production of ⁶⁸Ga-labeled radiopharmaceuticals would require higher starting amounts of radioactivity, which is why several facilities have initiated studies to produce ⁶⁸Ga with a cyclotron. That said, the demand for centralized production might be lowered upon the emergence of next-generation generators and the arrival of kit-based labeling approaches. The use of metallic radionuclides such as gallium-68 offers a simple one-step radiosynthetic route for the labeling of various compounds [7, 8], complicated only by the need for a metal-binding ligand (i.e. chelator) that can alter the pharmacological profile of the compound of interest. Radiolabeling with fluorine-18, on the other hand, typically requires more complex synthetic methods and specialized equipment but does not require a special ligand moiety for the labeling.

At this juncture, it is important to remember that the decay characteristics of a positron-emitting nuclide can affect the quality of PET images [9]. Simply put, the lower the energy of the emitted positron, the shorter its path before annihilation, and the higher the resolution of the resulting image. Along these lines, one key disadvantage of gallium-68 is that it emits positrons with relatively high energies and thus relatively long ranges, which can compromise the spatial resolution of PET images. When advanced computational methods and improved detector designs are used, however, it is possible to acquire high-quality PET images with all common positron-emitting radionuclides, including ^{68}Ga .

18.3 RADIOPHARMACEUTICALS FOR CANCER THERAPY

The first report of the internal use of radionuclides for cancer therapy emerged in 1913, when Frederick Proescher used intravenous injections of soluble radium-223 salts for the treatment of patients with a variety of diseases, including uterine cancer and leukemia [10]. Radium-223 had been discovered 15 years earlier by Marie Curie, for which she later received the Nobel Prize in Chemistry [11]. The therapeutic potential of ^{223}Ra became evident when Henri Alexandre Danlos and Eugene Bloch applied it to tuberculous skin lesions shortly after Henri Becquerel had reported severe skin inflammation caused by a radium tube that was kept in his pocket for several hours [12]. These discoveries inspired Alexander Graham Bell to publish a letter in *Nature* in 1903 in which he openly questioned “why a tiny fragment of radium sealed up in a fine glass tube should not be inserted into the very heart of the cancer,” suggesting for the first time the use of radium for intratumoral cancer therapy [13]. The initial proof-of-concept for this idea was provided 10 years later by Proescher’s work, which intensified the search for additional radionuclides that could be used for imaging and therapy. In the years since these early discoveries, a remarkable array of radionuclides have been discovered and artificially produced, significantly enriching the arsenal available for the treatment of cancer [14, 15].

The internal application of ionizing radiation to treat patients is referred to as *endoradiotherapy* [16]. Endoradiotherapy is predicated on the ability of radionuclides to cause irreversible damage to the nuclear DNA of cancer cells by inducing double-strand breaks and thus prevent cellular proliferation. Ideally, the particles emitted from therapeutic radionuclides should have relatively short pathlengths over which they deposit the majority of their energy, thereby harming cancer cells without affecting healthy tissues [14]. Of course, the therapeutic efficacy of a radiopharmaceutical is dictated by its physical and biochemical characteristics [62]. These physical parameters include the type of decay and linear energy transfer (**LET**) of the particles emitted by the radionuclide, its physical half-life, the presence of radioactive daughter nuclides, and the methods available for the production of the radionuclide itself. The biochemical characteristics are mainly defined by the choice of vector to which the radionuclide is attached, specifically its ability to localize and remain in target tissues, its *in vivo* stability, and its potential toxicity [12, 63].

Clinical Example 18.1 Targeting Altered Metabolism in Cancer Cells with [¹⁸F]FGln

Cancer cells modify key metabolic pathways and exhibit increased uptake of nutrients (e.g. glucose and glutamine) to support their growth and proliferation. This increased uptake and metabolism is the result of the over-reliance of cancer cells on aerobic glycolysis, a phenomenon known as the *Warburg Effect* [17, 18]. The molecular alterations due to the Warburg Effect are the basis for PET imaging with [¹⁸F]fluorodeoxyglucose ([¹⁸F]FDG), the predominant radiopharmaceutical in nuclear imaging. [¹⁸F]FDG-PET imaging is a valuable clinical tool for diagnosing, grading, and staging cancers and can also be used for monitoring the efficacy of therapy [19]. In many cases, however, [¹⁸F]FDG-PET is not especially sensitive: certain healthy tissues – e.g. the brain – as well as non-malignant inflammatory processes have significant [¹⁸F]FDG uptake. Another nutrient whose processing is affected by the changed metabolism of cancer cells is glutamine. ¹⁸F-labeled glutamine – [¹⁸F]FGln; [¹⁸F]F-(2*S*,4*R*)-4-FGln – has recently shown promising results in human trials [20–23]. Indeed, non-invasive imaging of glutamine metabolism may represent a useful tool for detecting certain cancers as well as evaluating response to therapy.

Clinical trials in glioma patients have shown the advantages of imaging with [¹⁸F]FGln over [¹⁸F]FDG (Figure 18.1) [21, 23]. While [¹⁸F]FDG has high uptake in normal brain tissue that interferes with the detection of tumor lesions, very little uptake of [¹⁸F]FGln is observed in normal brain tissue. [¹⁸F]FGln was also able to differentiate the clinically progressing disease from the stable glioma [21]. Thus, [¹⁸F]FGln could be used to evaluate high-grade gliomas, identify tumors that are undergoing transformation, and monitor tumors after therapy in glioma patients. When studying extracranial primary lesions in patients with gliomas, however, the radioactivity uptake in primary tumors was lower with [¹⁸F]FGln than with [¹⁸F]FDG [23]. In some cases, tumor lesions in the liver were overlooked due to the high uptake of [¹⁸F]FGln in the organ. Furthermore, [¹⁸F]FGln exhibits uptake in the bone due to the defluorination, which may cause confusion in the context of bone metastasis. Despite the flaws in detecting extracranial primary tumors, [¹⁸F]FGln may

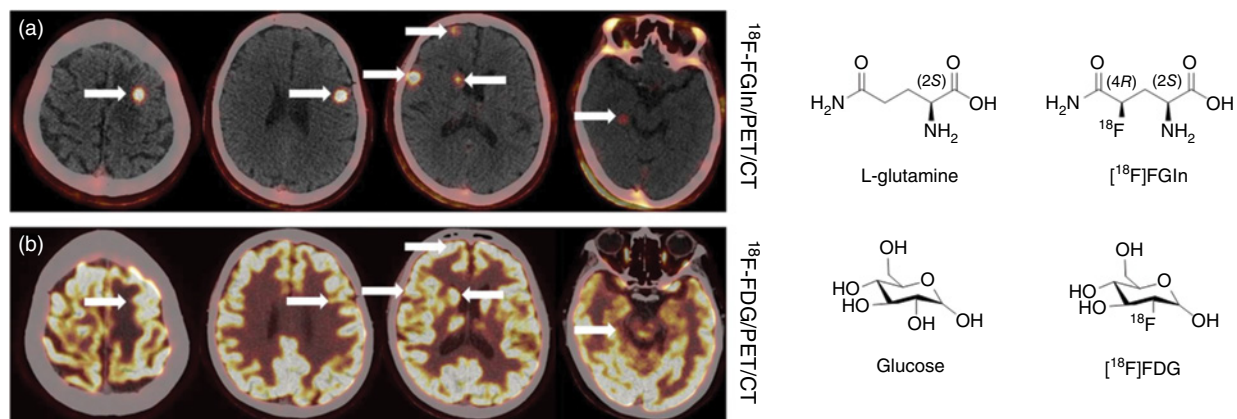


Figure 18.1 Left: Comparison of [¹⁸F]FDG and [¹⁸F]FGln PET-CT imaging in the same brain metastasis patient. (a) [¹⁸F]FGln PET-CT fusion images. (b) [¹⁸F]FDG PET-CT fusion images. White arrows indicate locations of lesions. Right: The structures of L-glutamine, [¹⁸F]FGln, glucose, and [¹⁸F]FDG. Source (a, b) Xu et al. figure 2 (p. e394) [23]. Reproduced with permission from Wolters Kluwer Health, Inc. © 2018 Wolters Kluwer Health, Inc.

provide important metabolic information about glutamine uptake in gliomas that cannot be observed with contrast-enhanced MRI, a method used in the clinic to diagnose brain metastasis. In other human cancers, [^{18}F]FGln PET has also shown a high diagnostic rate and correlation with [^{18}F]FDG-PET [20]. This is especially true for triple-negative breast cancer (**TNBC**), in which [^{18}F]FGln has outperformed [^{18}F]FDG in clinical trials [22]. Finally, unlike with [^{18}F]FDG, fasting prior to PET study is not required with [^{18}F]FGln, thereby accommodating patients who have difficulties fasting for several hours [20, 21].

The central drawback of [^{18}F]FGln is its susceptibility to *in vivo* defluorination. Free [^{18}F]fluoride is a metabolic product of [^{18}F]FGln through glutaminolysis [20]. Following the administration of the radiotracer, the amount of free [^{18}F]fluoride increases with time, leading to the partial clearance of radioactivity from tumor lesions and the accumulation of radioactivity in the bone. Yet because the defluorination is time-dependent, PET imaging carried out in the first 30 minutes after the injection of [^{18}F]FGln most likely provides accurate radioactivity levels in the bone (i.e. the radioactivity seen in bone metastases is likely due to [^{18}F]FGln rather than its radiometabolite [^{18}F]F $^-$ [20]). Moreover, *in vivo* defluorination does not interfere with [^{18}F]FGln PET imaging in glioma patients [21, 23], since gliomas are located in the brain and [^{18}F]FGln uptake in the skull does not hamper the evaluation. In the end, [^{18}F]FDG still has a valuable place in the clinic, but [^{18}F]FGln might provide a more efficient way to detect certain types of cancer and provide metabolic information that could be used to guide the planning of treatment.

Clinical Example 18.2 Imaging the Response to Immunotherapy with the PD-1/PD-L1 Pathway

The immune system uses checkpoint inhibitor pathways to maintain a balance between eliminating disease and maintaining self-tolerance. These systems have sophisticated two signal-activation mechanisms in which antigen recognition must be accompanied by the activation or inhibition of costimulatory molecules. One major checkpoint-inhibitor pathway relies upon programmed cell death protein-1 (PD-1) and its ligand (PD-L1). PD-1 is expressed on the surface of activated T-cells and B-cells, while PD-L1 acts as co-inhibitory factor and limits the T-cell response. PD-L1 is over-expressed on tumor cells of various cancers and can promote the inhibition of anti-tumor immune responses; not surprisingly, elevated PD-L1 expression often correlates with poor prognosis. In response to this correlation, several antibodies against the PD-1/PD-L1 pathway have been developed [24–26]. While immunohistochemistry assays have been developed to predict responses to anti-PD-1 and anti-PD-L1 treatment, collecting representative samples from highly heterogeneous tumor tissue is challenging, and biopsy-based assays are typically limited to one rather small sample per patient. As a result, predicting patient benefit from PD-1/PD-L1 blockade with immunohistochemistry assays has proven to be imprecise: some patients with no PD-L1 staining have benefited from treatment with checkpoint inhibitors, and not all patients with high expression of tumor PD-L1 benefit from treatment [20–23].

Recently, three PET radiopharmaceuticals that target the PD-1/PD-L1 pathway – [^{89}Zr]Zr-deferoxamine (DFO)-atezolizumab, [^{89}Zr]Zr-DFO-nivolumab, and [^{18}F]F-BMS-986192 – were employed in clinical trials [31–33]. [^{89}Zr]Zr-DFO-atezolizumab and [^{89}Zr]Zr-DFO-nivolumab are antibody-based tracers, while the targeting moiety in [^{18}F]F-BMS-986192 is an adnectin. Adnectins are derived from the 10th type III domain of human fibronectin (10Fn3) and resemble antibody variable domains, as both have two sets of antiparallel beta sheets with solvent-accessible loops at each pole. One major difference, however, is that adnectins have no disulfide bonds or free cysteines, facilitating the site-specific modification of adnectins via the introduction of a single cysteine residue. The molecular weight of adnectins is about 10 kDa, which allows

for the fast glomerular clearance of unbound compounds and thus their use with radionuclides with short physical half-lives.

In a study with [^{89}Zr]Zr-DFO-atezolizumab, 22 patients were first imaged with [^{89}Zr]Zr-DFO-atezolizumab and subsequently treated with non-radioactive atezolizumab [31]. The uptake of the tracer in tumors was high, and heterogeneity was observed across lesions, patients, and tumor types. [^{89}Zr]Zr-DFO-atezolizumab also accumulated in lymphoid tissues and sites of inflammation, both locations with abundant PD-L1 expression. Importantly, the clinical responses of the patients to atezolizumab correlated strongly with the uptake of the radiotracer, and the PET imaging results predicted treatment response better than immunohistochemistry results. In another trial, [^{89}Zr]Zr-DFO-nivolumab and [^{18}F]F-BMS-986192 were administered to the same 13 patients with non-small-cell lung cancer that were later treated with nivolumab [32]. Both tracers could be used to detect heterogeneity within tumors and between lesions (Figure 18.2). Brain metastases had lower standardized uptake values (SUVs) compared to extracranial tumors with both radiotracers, which may be the result of the low penetration of the radiopharmaceuticals to the central nervous system. The differences in pharmacokinetics between the two tracers can be clearly observed from the PET images. [^{89}Zr]Zr-DFO-nivolumab has a longer circulation time than [^{18}F]F-BMS-986192, which is excreted through the kidneys. Finally, the PD-L1-mediated uptake of both [^{89}Zr]Zr-DFO-nivolumab and [^{18}F]F-BMS-986192 correlated well with treatment response.

The results of these clinical trials are promising, but larger datasets are nonetheless required for validation. Since the PD-1/PD-L1 pathway controls the immune response, uptake at sites of inflammation and in various normal lymphoid tissues was seen as well. This creates an elevated background signal in

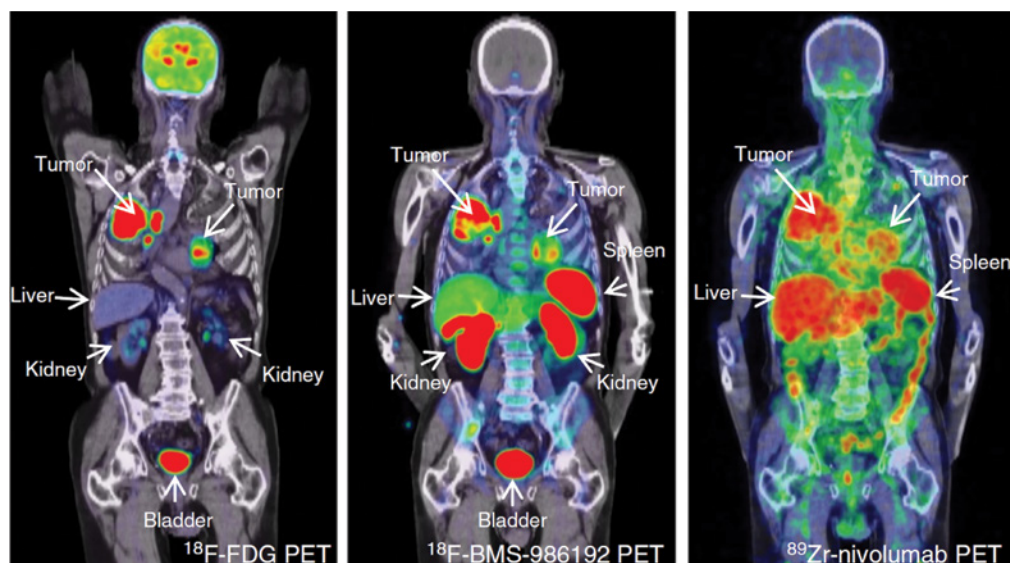


Figure 18.2 Comparison of [^{18}F]FDG, [^{18}F]F-BMS-986192, and [^{89}Zr]Zr-DFO-nivolumab PET-CT imaging in the same patient. [^{18}F]FDG PET demonstrates high glucose metabolism of tumors. [^{18}F]F-BMS-986192 and [^{89}Zr]Zr-DFO-nivolumab demonstrate heterogeneous uptake both within and between lesions. Source: Adapted from Niemeijer AN, et al. 2018, figure 1 (p. 2) [32]. <https://www.nature.com/articles/s41467-018-07131-y/figures/1>. Licensed under Creative Commons 4.0.

some tissues, even compared to [^{18}F]FDG. Like other radioimmunoconjugates, [^{89}Zr]Zr-DFO-nivolumab and [^{89}Zr]Zr-DFO-atezolizumab need time to distribute in the body, with the optimal PET imaging time point determined to be four to seven days after administration. [^{18}F]F-BMS-986192, on the other hand, is smaller and thus has a faster pharmacokinetic profile, enabling same-day PET imaging.

Clinical Example 18.3 Imaging Somatostatin Receptors

Neuroendocrine tumors (**NETs**) are collections of heterogeneous tumors that originate in various areas of the body but are most commonly found in the gastrointestinal or bronchopulmonary system. NETs are considered a rare disease, although their incidence has increased substantially in recent years [34]. Somatostatin receptors (**SSTRs**) are widely distributed in the human body and highly overexpressed in NETs [35], and radiolabeled SSTR-binding peptides have been harnessed for both molecular imaging and peptide receptor radionuclide therapy (**PRRT**) of NETs. Compared to metabolism-targeting tracers (e.g. [^{18}F]FDG), SSTR-targeting radiotracers exhibit superior accuracy for detecting NET lesions (Figure 18.3) [36], although elevated levels of SSTR

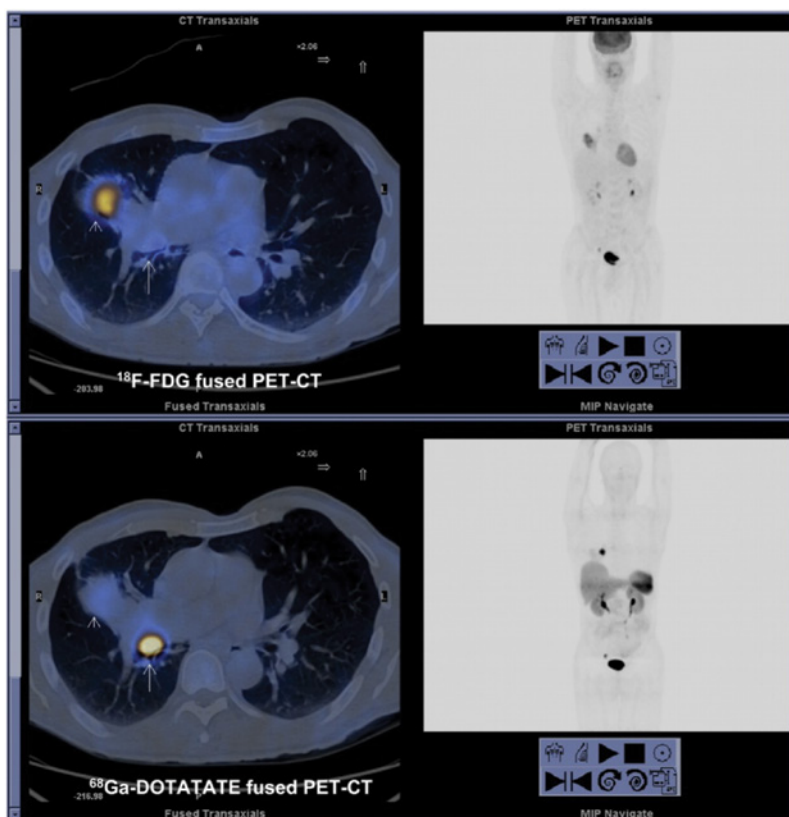


Figure 18.3 Fused PET-CT (left) and maximum intensity projection (right) images of a patient with typical endobronchial carcinoid in middle-lobe bronchus. The lung is collapsed distal to the tumor and shows intense obstructive pneumonia in histology. [^{68}Ga]Ga-DOTA-TATE shows highly selective uptake in the tumor, whereas [^{18}F]FDG shows mild uptake in the tumor and much higher uptake in the collapsed lung. Source: Kayani, et al. 2009, figure 3 (p. 1931) [36]. Reproduced with permission from the Society of Nuclear Medicine and Molecular Imaging, Inc. © 2009 SNMMI.

expression can also be observed at sites of inflammation. For years, the primary SSTR-targeting radiotracer was [¹¹¹In]In-DTPA-octreotide (pentetreotide), but more recently, the emergence of ⁶⁸Ga-labeled SSTR-targeting radiotracers has dramatically improved the sensitivity of imaging and lowered the radiation exposure of patients [37]. Today, ⁶⁸Ga-labeled somatostatin analogues – most notably [⁶⁸Ga]Ga-DOTA-TATE, [⁶⁸Ga]Ga-DOTA-(Tyr³)-octreotide (**TOC**), and [⁶⁸Ga]Ga-DOTA-NOC – are routinely used in the clinic to inform treatment decisions. ⁶⁸Ga-labeled DOTA-TATE has been approved by the US FDA and makes up half of a theranostic pair with ¹⁷⁷Lu-labeled DOTA-TATE, the most frequently used radiopharmaceutical for PRRT. In Europe, however, a different analogue – [⁶⁸Ga]Ga-DOTA-TOC – has been approved by the EMA. Despite minor structural differences, both ⁶⁸Ga-labeled agents are suited to identify patients eligible for PRRT. However, because the centralized production of ⁶⁸Ga-labeled radiopharmaceuticals is impossible, the use of other positron-emitting radionuclides (e.g. ¹⁸F) for SSTR imaging is currently being explored.

Clinical Example 18.4 Prostate Cancer Imaging

Prostate cancer (**PCa**) is the most common type of cancer among men worldwide. And in recent years, the imaging of PCa has become increasingly important in clinical practice for both staging and treatment selection. A large fraction of prostate cancers have limited [¹⁸F]FDG uptake, a fact that has fueled the development of more sensitive radiotracers for the disease. For example, both ¹¹C- and ¹⁸F-labeled choline offer greater sensitivity, but only in patients with high prostate-specific antigen (**PSA**) levels and high Gleason scores [38–41]. The drive to develop tools for the more sensitive and specific detection of PCa ultimately yielded the discovery of prostate-specific membrane antigen (**PSMA**), a transmembrane protein that is overexpressed in 90–100% of PCa lesions [42–44]. PSMA is a reliable tissue marker, and its expression is strongly correlated with tumor grade, pathological stage, and tumor progression.

The antibody-based radiotracer [¹¹¹In]In-cabromab pentetide was one of the first PSMA-targeting radiopharmaceuticals. However, because it only binds the *intracellular* epitope of PSMA, it produces high levels of non-specific uptake and rather poor tumor-to-background activity concentration ratios [45, 46]. Several other anti-PSMA antibodies targeting the extracellular structure of PSMA have been developed, including J415, J533, and J591 [47, 48]. However, radiotracers based on these immunoglobulins have been hampered by long blood-circulation times and poor tumor penetration, leading to low tumor-to-background contrast. As a result, greater emphasis was focused on the development of PSMA-targeting small molecules as vectors for nuclear imaging. The tumoral uptake of these smaller probes peaks within a few hours after injection, a timeframe most appropriate for use in conjunction with ¹⁸F and ⁶⁸Ga. In the past few years, several clinical studies have been conducted to investigate the diagnostic value of radiotracers based on small-molecule PSMA inhibitors. Compounds radiolabeled with ⁶⁸Ga and ¹⁸F for PET imaging have gained the most attention, but the development of analogues for SPECT (labeled with ¹²³I and ^{99m}Tc) has enabled PCa imaging in facilities without a PET scanner.

One of the first ⁶⁸Ga-labeled PSMA inhibitors to reach the clinic was PSMA-11 (*N,N'*-bis(2-hydroxybenzyl)-ethylenediamine-*N,N'*-diacetic acid [**HBED**]-CC-PSMA) (Figure 18.4) [49, 50]. [⁶⁸Ga]Ga-PSMA-11 proved capable of identifying lesions with high tumor-to-background ratios. More specifically, in patients with low PSA levels (<2.2 ng ml⁻¹), [⁶⁸Ga]Ga-PSMA-11 visualized PCa lesions in about 60% of cases; however, in cases with higher PSA levels (>2.2 ng ml⁻¹), PCa lesions were found in all patients. Subsequent clinical studies suggested that [⁶⁸Ga]Ga-PSMA-11 is superior to the current state-of-the-art tracer for prostate cancer, [¹⁸F]fluoromethylcholine [50, 51]. Indeed, lesions that were visible with [¹⁸F]fluoromethylcholine were

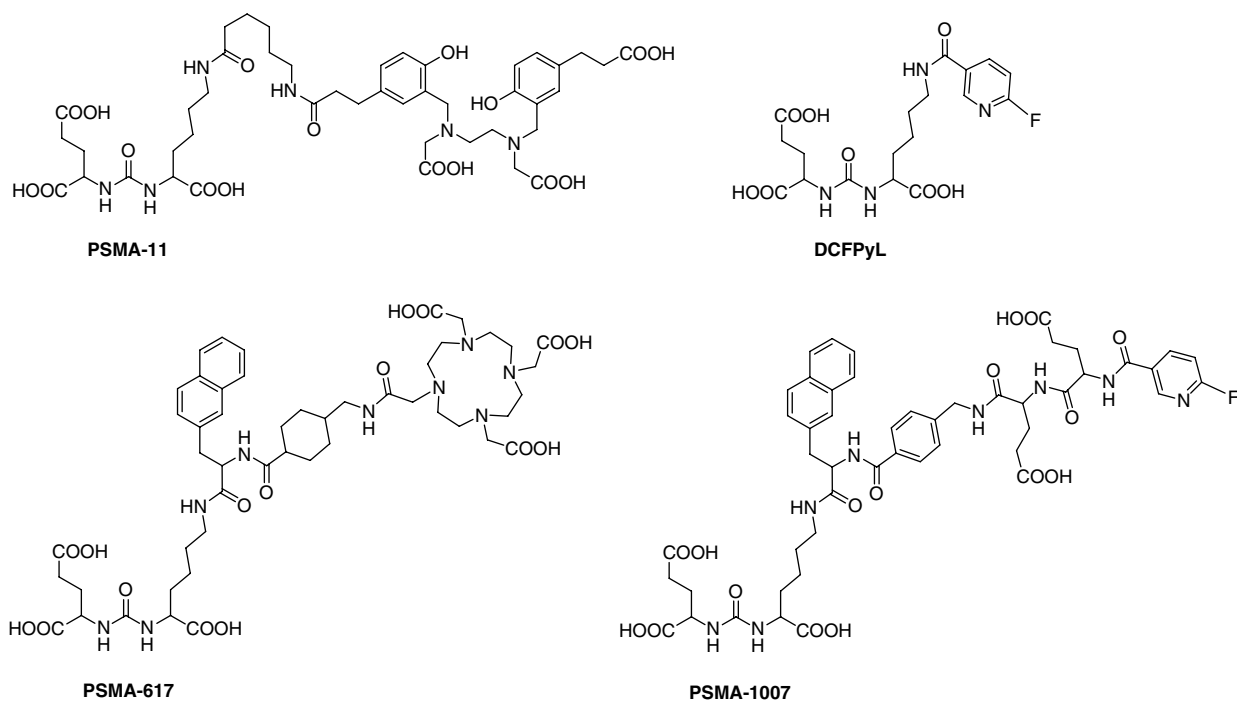


Figure 18.4 Structures of several small-molecule inhibitors of PSMA that have been harnessed for nuclear imaging and therapy.

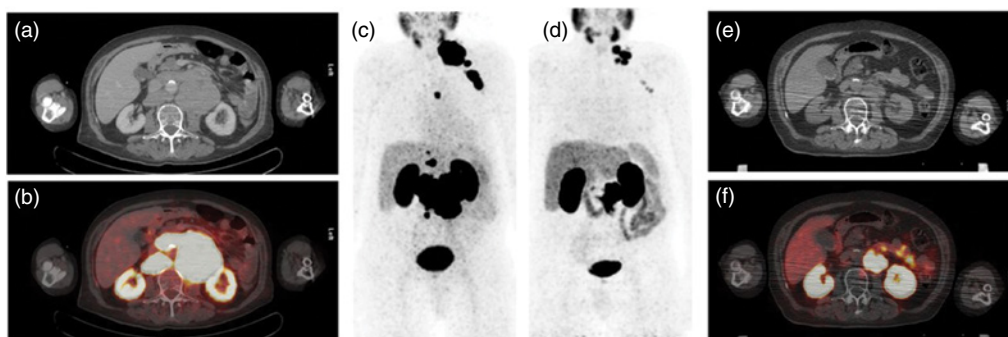


Figure 18.5 Fused [^{68}Ga]Ga-PSMA-11 PET-CT images of the same patient before (a–c) and after (d–f) [^{177}Lu]Lu-PSMA-617 treatment. Extensive PSMA-positive nodal metastases can be seen before treatment, as well as the reduced tumor load after three cycles of [^{177}Lu]Lu-PSMA-617 therapy. Source: Eiber M, et al. 2017, figure 6 (p. 73S) [52]. Reproduced with permission from the Society of Nuclear Medicine and Molecular Imaging, Inc. © 2017 SNMMI.

also visible with [^{68}Ga]Ga-PSMA-11, and [^{68}Ga]Ga-PSMA-11 proved capable of visualizing lesions that were not detectable with [^{18}F]fluoromethylcholine. Furthermore, in most cases, the tumor SUV_{max} values and

tumor-to-background ratios were clearly higher for [^{68}Ga]Ga-PSMA-11 than [^{18}F]fluoromethylcholine. In the years since, [^{68}Ga]Ga-PSMA-11 has been routinely used in the clinic to diagnose PCa (Figure 18.5).

The chelator HBED in [^{68}Ga]Ga-PSMA-11 is an excellent choice for ^{68}Ga , as radiolabeling can be carried out at room temperature, and the resulting metal complex is very stable. However, in the age of theranostics, HBED has the disadvantage of not being suitable for chelating any common therapeutic radiometals. As a result, another small-molecule PSMA ligand – PSMA-617 – was developed [53, 54]. PSMA-617 contains the chelator DOTA and thus can be radiolabeled with ^{68}Ga , ^{111}In , ^{177}Lu , and ^{90}Y , and several centers currently employ [^{177}Lu]Lu-PSMA-617 for the radiotherapy of metastatic PCa. Recently, a clinical trial was carried out to estimate the suitability of [^{68}Ga]Ga-PSMA-617 for diagnosing PCa, as PSMA-617 exhibits slower clearance but has a higher binding affinity than PSMA-11. However, direct intraindividual comparisons between these constructs are lacking, and therefore it is impossible to say which, if either, is superior to the other. One thing that can be said in favor of PSMA-617, however, is that it enables the use of the same substance for both therapeutic and diagnostic procedures.

As we have discussed, the inability to centralize the production of ^{68}Ga -labeled radiopharmaceuticals is a major obstacle to the clinical application of the radionuclide. In light of this, swapping ^{68}Ga for ^{18}F could simultaneously facilitate the production of multiple doses per batch and improve the detection of PCa lesions by improving image resolution. Furthermore, the longer half-life of ^{18}F may also prove beneficial, given that the optimal time point for imaging is three hours after administration. One of the first ^{18}F -labeled PSMA inhibitors that reached clinical trial was [^{18}F]F-DCFBC [55]. [^{18}F]F-DCFBC visualized more lesions than conventional imaging methods (i.e. bone scintigraphy, CT, ultrasound, or MRI), but some of the lesions detected with conventional imaging methods were not observed with PET. A major drawback of [^{18}F]F-DCFBC was its slow clearance, which caused high radioactivity concentrations in the blood pool, led to poor tumor-to-background ratios, and impeded the detection of both small tumors and tumors expressing lower levels of PSMA. These limitations were overcome by a second-generation ^{18}F -labeled PSMA inhibitor – [^{18}F]F-DCFPyL – which produces improved tumor-to-background ratios and a biodistribution profile that better corresponds to the distribution of PSMA [56, 57]. A direct comparison between [^{68}Ga]Ga-PSMA-11 and [^{18}F]F-DCFPyL revealed that the latter could detect more PCa lesions than the former [58]. Furthermore, higher SUV_{max} and tumor-to-background values were also achieved with [^{18}F]F-DCFPyL, though this might be partially explained by the different imaging time points for each radiotracer. Overall, this small study suggests that [^{18}F]F-DCFPyL might be superior to [^{68}Ga]Ga-PSMA-11. [^{18}F]F-DCFPyL – like [^{68}Ga]Ga-PSMA-11 – differs structurally from PSMA-617 and thus is not an identical surrogate for [^{177}Lu]Lu-PSMA-617. As a result, yet another ^{18}F -labeled PSMA inhibitor, [^{18}F]F-PSMA-1007, was developed to better mimic the *in vivo* behavior of [^{177}Lu]Lu-PSMA-617 [59, 60]. In an intra-individual comparison of the diagnostic performance of [^{18}F]F-DCFPyL and [^{18}F]F-PSMA-1007, both radiotracers were shown to be suitable for the imaging of local and metastatic prostate cancer [61]. However, a difference in elimination pathways might affect the choice between these two radiotracers: [^{18}F]F-DCFPyL is predominantly eliminated via the urine, whereas [^{18}F]F-PSMA-1007 is excreted via the hepatobiliary system.

18.3.1 Physical Characteristics

Therapeutic radionuclides commonly decay via the emission of alpha particles (α), beta particles (β), or Auger electrons (Figure 18.6). Alpha particles have a moderate range (50–100 μm) and the highest LET of the three particles (80 $\text{keV } \mu\text{m}^{-1}$). Beta

particles have the longest particle length (≤ 12 mm), but the lowest LET (~ 0.2 keV μm^{-1}). The range of Auger electrons is the smallest (2–500 nm), but their LET is high (4–26 keV μm^{-1}). As a result, alpha particles are particularly suitable for the treatment of small neoplasms or micrometastases, whereas beta particles are generally suited to larger tumors. The biological efficacy of Auger electrons, on the other hand, is mainly restricted to single cells. The short range of Auger electrons requires the radionuclide to cross the nuclear membrane and localize to the DNA in order to induce sufficient damage, although oxidative stress-induced large-range cytotoxic effects have also been suggested [63, 64]. In some cases, the decay of common endoradiotherapeutic nuclides is accompanied by the simultaneous emission of low-abundance gamma (γ) photons. Such gamma radiation allows for the quantification of tumor uptake by SPECT imaging or – in the case of preclinical studies – post-mortem gamma scintigraphy [12, 14].

To maximize the efficacy of treatment, the physical half-life of the radionuclide should be matched to the biological half-life of the vector to which it is attached [65].

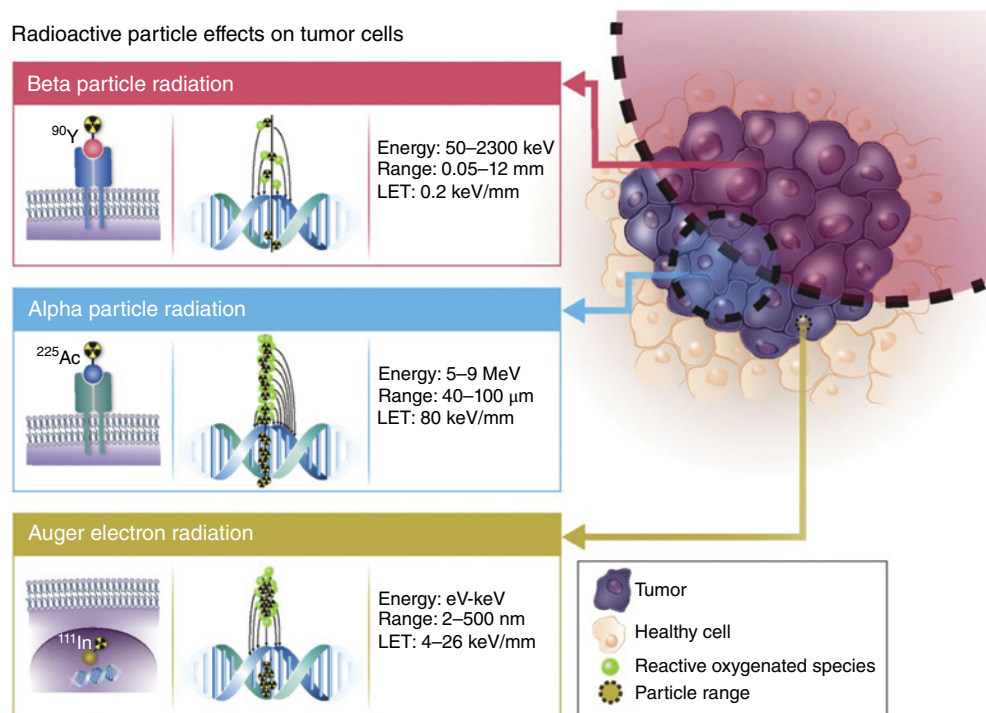


Figure 18.6 Comparison of the energies, ranges, LET values, and DNA damage potencies of therapeutic particles. This research was originally published in JNM. Source: Poty, S., Francesconi, L.C., McDevitt, M.R. et al. [63]. Figure 1 (p. 879). Reproduced with permission from the Society of Nuclear Medicine and Molecular Imaging, Inc.

A common rule of thumb is that the physical half-life of the radionuclide should be 1.5–3 times longer than the time it takes for the radiopharmaceutical to reach optimal contrast between tumor and off-target tissues [65]. Radionuclides with long *physical* half-lives (multiple days or longer) can expose the healthy off-target organs of patients to high radiation doses and often necessitate more elaborate health and safety measures, as patients must be isolated for prolonged periods, and any human waste must be disposed of following radioactive waste guidelines. On the other hand, when the physical half-life of a radionuclide is short (few minutes or less), the efficacy of therapy can be limited, as the majority of radionuclides will have decayed prior to the accumulation of the vector in the tissue. Shifting gears to the issue of *biological* half-lives, if the biological half-life is too long, the retention of the radiopharmaceutical in the blood and clearance organs may result in high off-target doses to healthy tissues. On the other hand, the use of vectors with very short biological half-lives could result in the secretion of high levels of the radiopharmaceutical, resulting in suboptimal therapy [12, 14]. Innovative approaches – such as *in vivo* pretargeting – have been developed to limit the radiation dose to off-target organs typically associated with probes with long biological half-lives and have shown promise in preclinical models [66, 71].

The use of therapeutic radionuclides that form radioactive daughter nuclides upon decay is generally avoided, as radioactive daughters can contribute to the total absorbed dose. This is particularly the case in alpha therapy, as the recoil energy imparted upon the nucleus following the emission of the alpha particle is approximately 1000× greater than the energy contained in a chemical bond. Practically speaking, this phenomenon can result in the release of the daughter radionuclides from the radiopharmaceutical and their subsequent redistribution throughout the body [63]. This *in vivo* redistribution – though hard to quantify – can contribute significantly to total body radiation dose and, consequently, toxicity.

Most therapeutic radionuclides are produced via nuclear fission in a reactor, the bombardment of the target using accelerated ions in a cyclotron, or the decay of a parent radionuclide in a generator [72]. The choice of radionuclide is often informed by the proximity of research labs to production facilities, as well as the decay characteristics and costs of the radionuclides themselves. Generally speaking, the production of radionuclides in a reactor is considered cheaper than the use of cyclotrons, since reactors are often government-subsidized and allow for multiple simultaneous irradiations. Cyclotrons, despite their higher cost, can produce radionuclides with higher purity and superior specific activity. Radionuclide generators are the most cost-effective method of all, and they allow for the in-house production of radionuclides with high specific activity [14]. However, generators are only available for a limited number of therapeutic radionuclides. A more detailed description of the production methods for radionuclides is provided in Chapter 2.

18.3.2 Biochemical Characteristics

Therapeutic radiopharmaceuticals are typically administered in submicromolar concentrations, as their biological effects are predicated on the particles emitted by the

radionuclide rather than the vector responsible for delivery. On the other hand, both the efficacy of tumor targeting and the retention of the probe in the tumor tissue are largely determined by the vector. Probes for endoradiotherapy are typically based on monoclonal antibodies (i.e. **radioimmunotherapy, RIT**) and peptides (i.e. **peptide receptor radionuclide therapy, PRRT**) due to the high specificity and affinity of these biomolecules for their targets. Another reason for the reliance on larger vectors is that the majority of therapeutic radionuclides are *radiometals* and thus require the conjugation of chelators to the vector. This can be hard to do with small molecules without adversely affecting their biochemical properties. That said, some therapeutic radionuclides – i.e. ^{131}I and ^{211}At – can be used in the absence of chelators and are thus more suitable for small molecule probes [73, 74]. Advances in nano- and microparticle chemistry have recently led to several clinical trials using nanometer-to-micrometer-scale particles as vectors for endoradiotherapy. However, major hurdles in this field must still be overcome before these agents become viable clinical options [75, 76].

Many radiopharmaceuticals accumulate within tumors by targeting tumor-associated antigens [77]. While tumor-associated antigens are generally expressed throughout tumors, most radiopharmaceuticals only bind to a subset of tumor cells due to genetic heterogeneity and the limited tissue penetration of the radiopharmaceutical. While this is a major problem for traditional chemotherapeutics – which can only exert a biological effect on the cell they have targeted – therapeutic radiopharmaceuticals can also kill adjacent tumor cells within the range of the emitted particle, even if those cells lack the targeted antigens. This phenomenon is known as the *bystander* or *cross-fire* effect [14, 78]. Although this effect is often considered beneficial, the radiation dose to surrounding cells must be limited in some cases to spare surrounding healthy tissue, prompting the use of radionuclides that emit particles with shorter ranges (such as alpha particles or Auger electrons). Endoradiotherapeutic probes can eliminate disseminated tumor cells with minimal off-target doses to surrounding tissue. Therefore, they can be especially useful in the context of micrometastatic disease [78].

A radiopharmaceutical must be sufficiently stable *in vivo* to guarantee the delivery of radioactivity to the tumor prior to its metabolism, degradation, and excretion. The rapid degradation of a radiopharmaceutical not only decreases its therapeutic efficacy but may result in the formation of radioactive metabolites that can accumulate in off-target tissues. For example, many free radiometals tend to accumulate in bone, which can cause increased toxicity to the radiosensitive bone marrow [72, 79, 80]. However, the use of chelators that form highly stable coordination complexes with radiometals can help prevent the toxicological effects resulting from the release of the radiometal [7].

One limiting factor of endoradiotherapy is the development of radioresistance by cancer cells. *Radioresistance* is the process by which cancer cells adapt to the biological changes induced by radiating particles, thereby limiting the therapeutic effects of the radiopharmaceutical. Although the exact mechanisms of radioresistance remain unknown, combinational approaches that include radiosensitizers may improve patient outcomes [81]. Furthermore, radioresistance may be combatted by selecting suitable

radionuclides; for example, it has been shown that alpha particles can overcome some of the limitations caused by radioresistance to beta particle therapy [82].

18.3.3 Applications

Since Alexander Graham Bell's initial suggestion of using radionuclides for the treatment of cancer, a wide variety of radiopharmaceuticals have been developed, some of which have been approved for clinical use by the US FDA and/or the EMA (Table 18.2). The majority of clinically approved radiopharmaceuticals are for the palliative treatment of bone metastases and rely upon the uptake of the calcimimetic radiometals by hydroxy-apatite. Currently, two radiolabeled monoclonal antibodies have been approved for clinical use: [¹³¹I]-tositumomab and [⁹⁰Y]-ibritumomab tiuxetan, both of which target CD22-positive cells in hematological cancers. Recently, the SSTR-targeting [¹⁷⁷Lu] Lu-DOTA-TATE became the first radiolabeled peptide to be approved by American and European regulatory agencies for the treatment of patients with gastroenteropancreatic

Table 18.2 Radiopharmaceuticals approved for cancer therapy in clinical settings.

Radiopharmaceutical	Tradename	Particle	Target	Approved by ^a	Approved for treatment of
[²²³ Ra]Ra-dichloride	Xofigo	Alpha	Hydroxy-apatite	FDA and EMA	Bone malignancies
[³² P]P-sodium phosphate	—	Beta	Hydroxy-apatite, DNA	FDA and EMA	Bone and hematological malignancies
[⁸⁹ Sr]Sr-dichloride	—	Beta	Hydroxy-apatite	FDA and EMA	Bone malignancies
[¹⁵³ Sm]Sm-lexidronam	—	Beta	Hydroxy-apatite	FDA and EMA	Bone malignancies
[¹⁸⁶ Re]Re-HEDP ^b	—	Beta	Hydroxy-apatite	EMA	Bone malignancies
[¹³¹ I]I-sodium iodide	—	Beta	Iodide trans-porters	FDA and EMA	Endocrinological malignancies
[¹³¹ I]I-iobenguane	Azedra	Beta	Amine trans-porters	FDA and EMA	Neuroendocrine malignancies
[¹³¹ I]I-tositumomab	Bexxar	Beta	CD20	FDA	Hematological malignancies
[⁹⁰ Y]Y-ibritumomab tiuxetan	Zevalin	Beta	CD20	FDA and EMA	Hematological malignancies
[¹⁷⁷ Lu]Lu-DOTA-TATE ^c	Lutathera	Beta	Somatostatin receptor	FDA and EMA	Gastroenteropancreatic neuroendocrine malignancies

^aFDA: Food and Drug Administration; EMA: European Medicines Agency.

^bHEDP: hydroxyethylidenediphosphonate.

^cDOTA-TATE: DOTA-octreotate.

neuroendocrine tumors (**GEP-NETS**). The majority of clinically approved radiopharmaceuticals are labeled with beta-emitting radionuclides, despite the enticing promise of alpha- and Auger electron-emitting radionuclides [80, 83]. At present, the only alpha-emitting radiopharmaceutical that has been clinically approved is [²²³Ra]Ra-dichloride, and no Auger electron-emitting radiopharmaceuticals have been approved. That said, clinical trials with alpha- and Auger electron-emitters are ongoing, and the preliminary results are encouraging [79, 80, 83, 84].

In the ensuing pages, we will highlight several clinical trials from the last decade using endoradiotherapeutic probes labeled with alpha-, beta- or Auger electron-emitting radionuclides (Table 18.3) The production, availability, and purity of the radionuclides used in these radiopharmaceuticals are discussed in Chapter 2.

18.3.4 Alpha Therapy

Endoradiotherapy using alpha-emitting radionuclides has gained renewed interest in the last two decades due to strong (pre)clinical evidence of their clinical benefits [79]. This is particularly true in the context of liquid cancers such as leukemia and lymphomas. In these cases, the advantages of alpha therapy over beta therapy have become especially evident [14, 84]. The high LET and short range of alpha particles allow them to deposit high doses exclusively to cells in the proximity of the radionuclide, thereby delivering a cytotoxic dose of radiation to tumor cells while leaving healthy cells unscathed. A number of clinical trials featuring alpha-emitting radionuclides – either as free radionuclides or as part of small molecule-, peptide-, or antibody-based radiopharmaceuticals for targeted alpha therapy (TAT) – have been undertaken in recent years and have been reviewed extensively by others [79, 80, 84].

18.3.5 Beta Therapy

The majority of clinically approved radiopharmaceuticals rely on beta-emitting radionuclides (Table 5.2). Beta-emitting radiopharmaceuticals are particularly useful in heterogeneous tumors, since the long penetration range of beta particles obviates the need for the radiopharmaceutical to target every single cell within a tumor (a scenario that typically cannot be achieved since the targeted antigens are not expressed on every cell). In addition, the relatively large range of beta particles allows for the penetration of hundreds to thousands of cells, an especially beneficial trait in the treatment of large tumors. An important downside of beta-emitting radiopharmaceuticals is that their long penetration range makes them less useful for the treatment of small tumors – such as micrometastases – due to the deposition of high levels of energy in surrounding healthy tissues. The potential and toxicity of novel beta-emitting radiopharmaceuticals in various cancer types has been the topic of several recent clinical trials, which have focused primarily on peptide- and antibody-based radiopharmaceuticals [80].

Table 18.3 Recent clinical trials of radiopharmaceuticals for cancer therapy.

Radiopharmaceutical	Type of therapy	Target	Phase	Type of cancer	Toxicity	Outcome
[²²³ Ra]Ra-dichloride	Alpha	Hydroxy-apatite	Clinically approved	Bone metastasis	Nausea/vomiting, diarrhea, anemia, pancytopenia in >10% of patients	<ul style="list-style-type: none"> • Improved OS • Improved PFS • Decreased ALP and PSA levels • Pain relief • Tumor remission
[²²⁵ Ac]Ac-PSMA-617	Alpha	PSMA	I	Prostate cancer	Xerostomia	<ul style="list-style-type: none"> • Decreased PSA levels • Circulating blast reduction
[²²⁵ Ac]Ac-DOTA-lintuzumab	Alpha	CD33	I	Acute myeloid leukemia	Myelosuppression	<ul style="list-style-type: none"> • Bone marrow blast reduction • Circulating blast reduction
[²¹³ Bi]Bi-DTPA-lintuzumab	Alpha	CD33	II	Acute myeloid leukemia	Myelosuppression	<ul style="list-style-type: none"> • Bone marrow blast reduction • Long-term remission
[²¹³ Bi]Bi-DOTA-TOC	Alpha	SSTR	First-in-human	Neuroendocrine cancer	Moderate kidney toxicity, low hematological toxicity	<ul style="list-style-type: none"> • Reversible low-grade neurotoxicity
[²¹¹ At]At-ch81C6	Alpha	Tenascin	First-in-human	Brain cancer	Grade 3 or 4 neutropenia, thrombocytopenia, and lymphopenia in <10% of patients	<ul style="list-style-type: none"> • Improved OS
[¹⁷⁷ Lu]Lu-DOTA-TATE	Beta	SSTR	Clinically approved	Neuroendocrine cancer	Grade 3 or 4 neutropenia, thrombocytopenia, and lymphopenia in <10% of patients	<ul style="list-style-type: none"> • Improved OS • Improved PFS • Tumor remission
[¹⁷⁷ Lu]Lu-DOTA-J591	Beta	PSMA	II	Prostate cancer	Myelosuppression	<ul style="list-style-type: none"> • Improved OS • Decreased PSA levels
[¹⁸⁸ Re]Re-6D2	Beta	Melanin	I	Melanoma	—	<ul style="list-style-type: none"> • Improved OS
[¹¹¹ In]In-DTPA-hEGF	Auger electrons	EGFR	First-in-human	Breast cancer	Flushing, chills, nausea/vomiting upon injection	<ul style="list-style-type: none"> • Tumor accumulation • No visible tumor remission

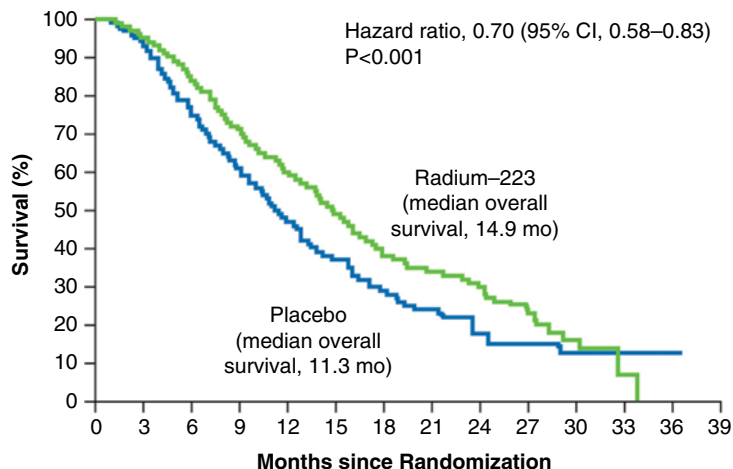
OS: overall survival, PFS: progression-free survival, ALP: alkaline phosphatase, PSA: prostate-specific antigen, PSMA: prostate-specific membrane antigen, SSTR: somatostatin receptor, EGFR: epidermal growth factor receptor.

Clinical Example 18.5 [²²³Ra]Ra-dichloride

Exactly 100 years after Proescher's publication describing the use of ²²³Ra for the treatment of cancer patients, the first alpha-emitting therapy – using the same radionuclide – was clinically approved for the first-line treatment of castration-resistant prostate cancer (CRPC) patients with symptomatic bone metastases [10, 85]. In a phase III clinical trial with 921 patients, six monthly intravenous injections of [²²³Ra]Ra-dichloride plus standard treatment resulted in a median overall survival improvement of 19 weeks, compared to patients receiving a placebo plus standard treatment (Figure 18.7) [86–88]. Furthermore, the offset time to first symptomatic skeletal events was increased, as well as the time to notable increases in alkaline phosphatase (ALP) and PSA levels. These data confirmed the findings of earlier trials with breast and prostate cancer patients, in which reduced ALP levels and significant pain relief were reported [89]. Remarkably, the mechanism here is identical to Proescher's original strategy: ²²³Ra²⁺ ions are incorporated into rapidly growing bone lesions due to their resemblance to Ca²⁺ ions.

²²³Ra has a relatively long half-life ($t_{1/2} = 11.4$ days) and decays to stable ²⁰⁷Pb through a series of α and β^- emissions. Its daughter radionuclides – ²¹¹Pb ($t_{1/2} = 36.1$ minutes) and ²¹¹Bi ($t_{1/2} = 2.1$ minutes) – have the greatest risk of off-target dose distribution, because these nuclides are not necessarily constrained to the bone. The other daughter radionuclides (²¹⁹Rn, ²¹⁵Po, ²¹¹Po, and ²⁰⁷Tl) decay rapidly and therefore only contribute to the total intralésional dose [14]. Treatment with [²²³Ra]Ra-dichloride is generally well-tolerated, with common side-effects such as nausea, diarrhea, vomiting, peripheral edema, and hematological abnormalities such as anemia and pancytopenia occurring in >10% of patients [85].

Overall Survival



No. at Risk

Radium-223	614	578	504	369	274	178	105	60	41	18	7	1	0	0
Placebo	307	288	228	157	103	67	39	24	14	7	4	2	1	0

Figure 18.7 Kaplan-Meier plot depicting a median overall survival difference between CRPC patients treated with [²²³Ra]Ra-dichloride plus standard treatment and patients receiving a placebo plus standard treatment. Source: Parker, C., Nilsson, S., Heinrich, D. et al. [86]. Figure 1 (p. 218).

Clinical Example 18.6 $[^{225}\text{Ac}]\text{Ac-PSMA-617}$

Due to its intrinsic targeting properties, $[^{223}\text{Ra}]\text{Ra-dichloride}$ can only be used for the treatment of bone lesions. Therefore, other alpha-emitting radiopharmaceuticals for metastatic CRPC have been tested, which can also target soft tissue lesions and circulating tumor cells. PSMA-617 is a small-molecule PSMA ligand that has been clinically tested for the PET imaging and beta therapy of prostate cancer patients when labeled with ^{68}Ga or ^{177}Lu , respectively [90, 91]. In a phase I clinical trial with two PSMA-positive patients with metastatic CRPC, treatment with the alpha-emitting analogue $[^{225}\text{Ac}]\text{Ac-PSMA-617}$ led to a complete response without any relevant hematological toxicity [82]. In a subsequent study, the anti-tumor activity of $[^{225}\text{Ac}]\text{Ac-PSMA-617}$ was confirmed in a group of 40 patients, prompting complete remission in numerous patients and an overall reduced radioresistance compared to $[^{177}\text{Lu}]\text{Lu-PSMA-617}$ (Figure 18.8) [92, 93]. The primary adverse response was xerostomia, which is a result of binding of $[^{225}\text{Ac}]\text{Ac-PSMA-617}$ to PSMA epitopes in the salivary glands [80].

The use of ^{225}Ac ($t_{1/2} = 10\text{days}$) as a radionuclide for endoradiotherapy is generally appealing, due to the high cumulative dose delivered to the tumor by the α and β^- particles emitted during its decay to stable ^{209}Bi . Although the literature suggests that daughter radionuclides like ^{213}Bi ($t_{1/2} = 45\text{minutes}$) and ^{209}Pb ($t_{1/2} = 3.2\text{hours}$) are kinetically stable in DOTA, the other daughter radionuclides may escape from the chelator and accumulate elsewhere, leading to toxicity to healthy cells [94, 95]. Critically, however, such adverse effects have appeared minimal in the patients.

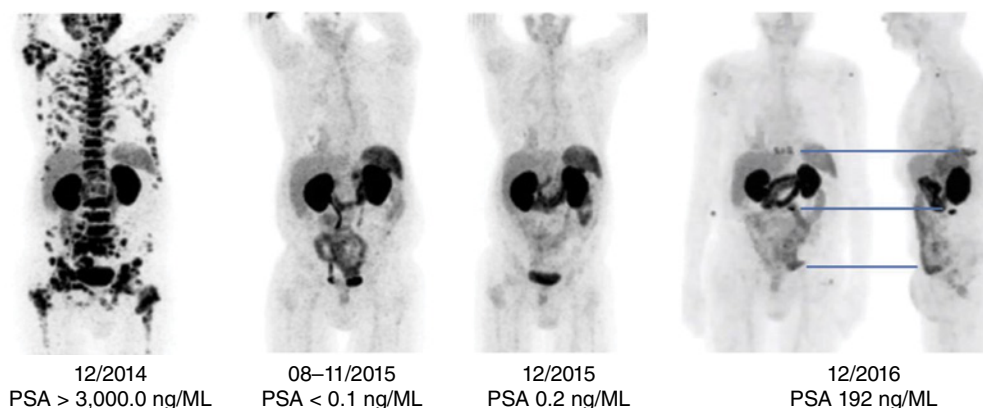


Figure 18.8 PET images and PSA levels of a metastatic CRPC patient pre- and post-treatment with $[^{225}\text{Ac}]\text{Ac-PSMA-617}$. After initial complete remission, slow progression was observed after one year. Due to asymptomatic disease, the treatment-free interval was prolonged to 28 months. Source: Images courtesy of Prof. Felix Mottaghy, Rheinisch-Westfälische Technische Hochschule Aachen.

Clinical Example 18.7 $[^{213}\text{Bi}]\text{Bi-DOTA-TOC}$

Bismuth-213 – one of the daughter radionuclides of ^{225}Ac – has also been tested on its own in clinical settings for alpha therapy. Due to its shorter half-life ($t_{1/2} = 46\text{minutes}$), its cumulative effective doses to off-target organs are significantly lower than those produced by ^{225}Ac , despite its emission of one α and multiple β^- particles during its decay to stable ^{209}Bi . The SSTR-targeting peptide DOTA-TOC was radiolabeled with ^{213}Bi and clinically validated in a first-in-human study [96]. Seven patients with progressive advanced

neuroendocrine liver metastases refractory to DOTA-TOC beta therapy and one patient with bone marrow carcinosis received intraarterial and systemic infusions of [^{213}Bi]Bi-DOTA-TOC, respectively. After bimonthly administration of [^{213}Bi]Bi-DOTA-TOC with increasing activity doses, long-term remission was observed in all treated patients (Figure 18.9). The adverse effects of treatment were limited to moderate kidney toxicity and low hematological toxicity.

Although the minimal toxicity of this modality was largely attributed to the short half-life of ^{213}Bi , the exploitation of such a short-lived radionuclide comes with considerable challenges. More specifically, ^{213}Bi is produced using a generator containing its parent radionuclide ^{225}Ac , which itself has a relatively short half-life for a generator (and thus requires frequent replacements). In addition, the worldwide availability of ^{225}Ac is limited, making the production of ^{213}Bi an expensive endeavor [84]. On top of that, the short half-life can be logistically complicated, since the elution of the generator, the radiolabeling of the probe, and its subsequent purification, quality control, and injection are all time-consuming [95]. These factors – combined with the enhanced potency of ^{225}Ac as compared to ^{213}Bi in preclinical models – has resulted in the preferential use of ^{225}Ac for alpha therapy in recent clinical trials [97].

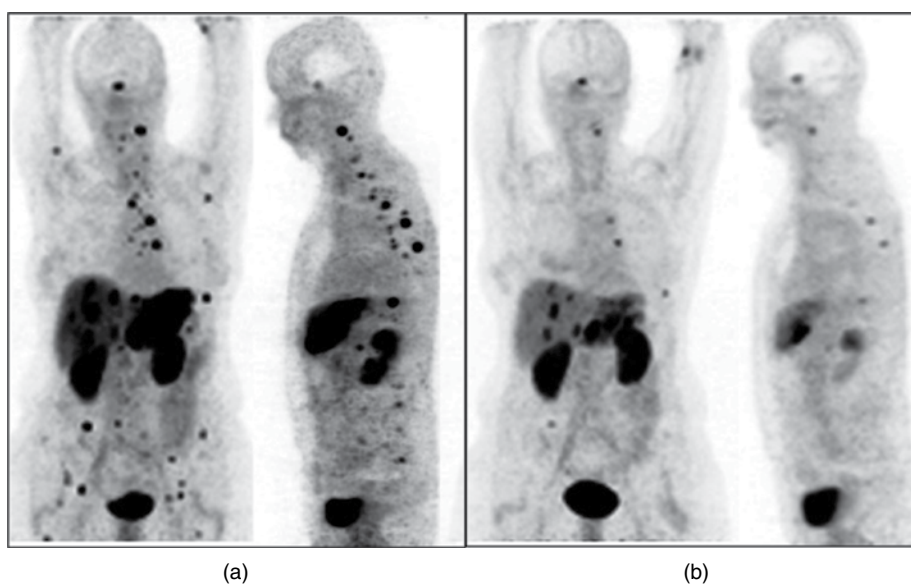


Figure 18.9 PET images of a patient with metastatic neuroendocrine cancer (a) before and (b) six months after treatment with [^{213}Bi]Bi-DOTA-TOC. A significant reduction in the size and number of metastatic lesions was observed. Source: Kratochwil C, et al. 2014, figure 6 (p. 2113) [96]. Licensed under Creative Commons 4.0.

Clinical Example 18.8 $[^{213}\text{Bi}]\text{Bi-DTPA-lintuzumab}$ and $[^{225}\text{Ac}]\text{Ac-DOTA-lintuzumab}$

Moving beyond free radionuclides and radiolabeled small molecules and peptides, radiolabeled monoclonal antibodies are increasingly deployed as radiopharmaceuticals for alpha therapy. Lintuzumab (HuM195, SGN-33) is a humanized monoclonal antibody that targets the CD33 antigen on leukemia cells. Used as an unlabeled drug, lintuzumab promotes complete or partial remissions only infrequently in leukemia patients, even at doses that fully saturate the CD33 binding sites for prolonged periods [98]. However, in 18 patients with relapsed and refractory acute myeloid leukemia (AML) or chronic myelomonocytic leukemia, treatment with $[^{213}\text{Bi}]\text{Bi-DTPA-lintuzumab}$ led to a circulating blast reduction in 93% of patients and a bone marrow blast reduction in 78% of patients [99]. No significant extramedullary toxicity was reported, but myelosuppression was observed in all treated patients. In a follow-up phase I/II study of 31 patients with newly diagnosed or relapsed/refractory AML, $[^{213}\text{Bi}]\text{Bi-DTPA-lintuzumab}$ was administered after partially cytoreductive chemotherapy with cytarabine [100]. Significant bone marrow blast reduction with limited extramedullary toxicity was observed in all patients. In this trial, myelosuppression was the dose-limiting side-effect, and two patients who received the maximum tolerated dose died of infection-related complications. Shifting gears to ^{225}Ac , 18 patients with relapsed or refractory AML were infused with a single dose of $[^{225}\text{Ac}]\text{Ac-DOTA-lintuzumab}$ in another phase I trial [101]. Results were similar to the trials with $[^{213}\text{Bi}]\text{Bi-DTPA-lintuzumab}$, demonstrating circulation blast reductions in 63% of patients and bone marrow blast reductions in 67% of patients, with 20% of patients achieving bone marrow blast levels of 5% or less. The dose-limiting toxicity was myelosuppression, and no notable radiation-induced nephrotoxicity was observed. Two patients died of sepsis during the trial. Phase I and II clinical trials – in which therapy with $[^{225}\text{Ac}]\text{Ac-DOTA-lintuzumab}$ is combined with low-dose cytarabine – are currently in progress, and preliminary results indicate a complete overall response in 28% of patients after one cycle of therapy [102].

Clinical Example 18.9 $[^{211}\text{At}]\text{At-ch81C6}$

Yet another promising alpha-emitting radionuclide is the radiohalogen ^{211}At . ^{211}At is an attractive radionuclide for therapy, since its half-life of 7.2 hours makes it less logistically challenging than ^{213}Bi , and its toxicity to off-target doses is reduced compared to ^{223}Ra and ^{225}Ac . ^{211}At decays to stable ^{207}Pb via the emission of an α particle in combination with the emission of a β^- particle or an electron capture event. Toxicity caused by the redistribution of its daughter radionuclides is negligible, since those have either very short (<1 second) or very long (>33 years) half-lives.

An ^{211}At -labeled variant of the chimeric anti-tenascin monoclonal antibody 81C6 – $[^{211}\text{At}]\text{At-ch81C6}$ – has recently been deployed in a first-in-human study of 18 patients with recurrent brain cancer. $[^{211}\text{At}]\text{At-ch81C6}$ was administered into the resection cavity after the surgical removal of the tumor, followed by adjuvant salvage chemotherapy according to best clinical management practices [103]. The median overall survival of the patients with glioblastoma multiforme ($n = 14$) was 54 weeks, a significant improvement compared to previously reported median survival times of 23–31 weeks [104]. No dose-limiting toxicity or radionecrosis was observed, although some low-grade neurotoxicity was reported (which fully resolved in all but one patient).

It is important to note that radiopharmaceuticals labeled with several other alpha-emitting radionuclides (e.g. ^{212}Pb) are currently being investigated in clinical trials [105, 106]. Although reports describing the use of such radionuclides in the clinic are still scarce, the discovery of new production methods as well as improvements to radiolabeling protocols using novel radionuclides will likely lead to a near-term increase in the number of clinical trials using these alternative radionuclides.

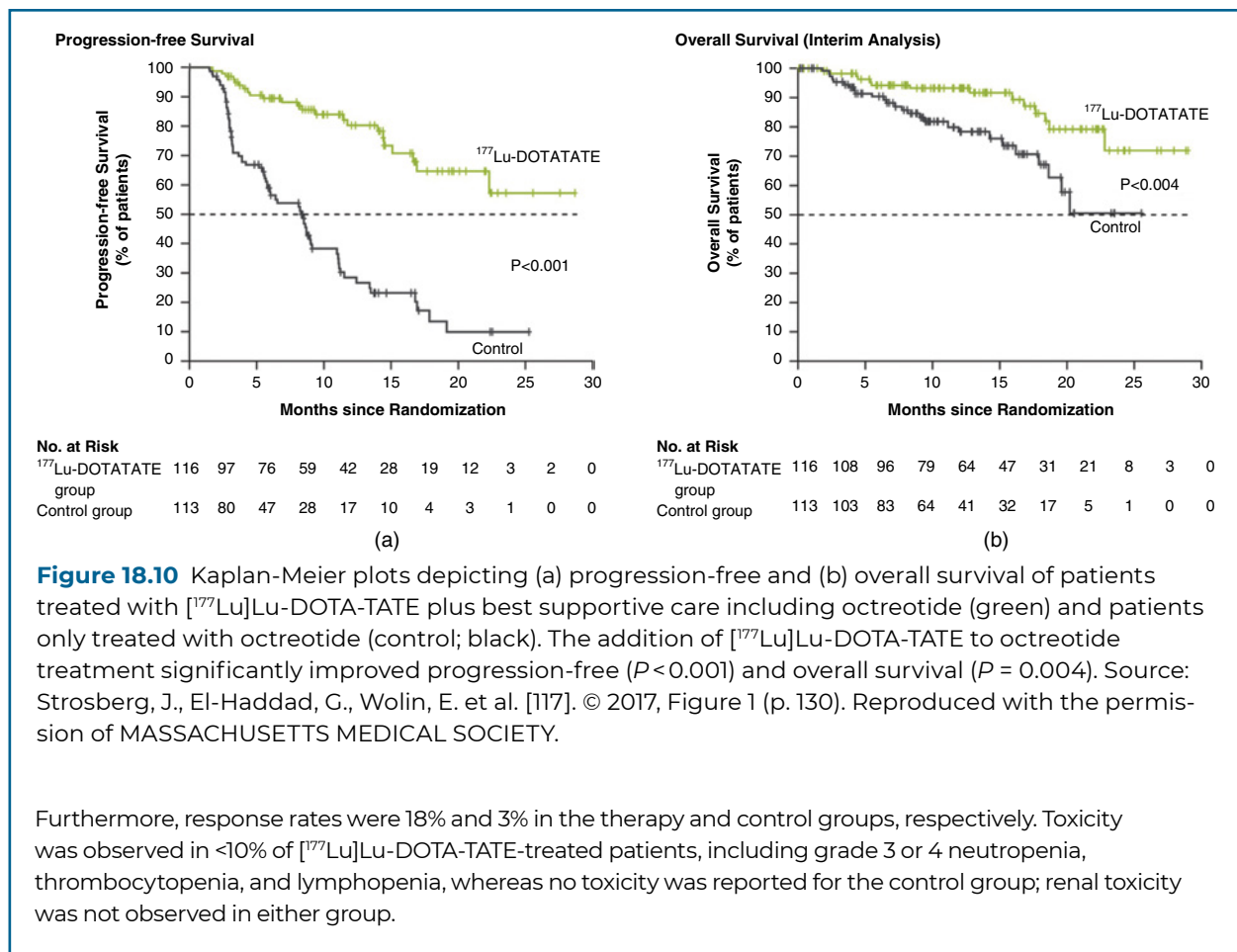
Clinical Example 18.10 [¹⁷⁷Lu]Lu-DOTA-TATE

Due to the ease of its production, very high specific activity, and favorable physical characteristics, ¹⁷⁷Lu has become one of the most widely used radionuclides for endoradiotherapy. ¹⁷⁷Lu ($t_{1/2} = 6.65$ days) decays to stable ¹⁷⁷Hf upon the emission of low-to-medium energy β^- particles as well as the emission of γ photons, which allow for gamma camera imaging. The ability of these β^- particles to traverse cells within a range of several millimeters from the radionuclide in soft tissue facilitates the endoradiotherapy of large and heterogeneous tumors in particular. The major drawback of the high penetration range of ¹⁷⁷Lu is the toxicity associated with the radiation dose to healthy tissues, either surrounding the tumor or from radioactive metabolites that redistribute to other parts of the body. As a result, the use of ¹⁷⁷Lu is less suitable for the treatment of micrometastases or hematological cancers.

Nevertheless, promising results have been achieved with ¹⁷⁷Lu in the clinic. In 2018, [¹⁷⁷Lu]Lu-DOTA-TATE became the first radiolabeled peptide to be approved for the treatment of cancer patients. Based on an abbreviated version of human somatostatin, [¹⁷⁷Lu]Lu-DOTA-TATE accumulates in NETs, which typically require high levels of somatostatin for tumor cell proliferation [107]. Early phase I and II clinical trials demonstrated remission or stable disease in 79% of patients with GEP tumors after regular doses of [¹⁷⁷Lu]Lu-DOTA-TATE ($n = 35$), as well as improved quality of life ($n = 50$) [108, 109]. In a larger follow-up study with 504 GEP-NET patients, [¹⁷⁷Lu]Lu-DOTA-TATE was given in four cycles, with only low-grade hematological toxicity in ~4% of patients and serious adverse effects in <1% of patients [110]. Complete and partial remissions were reported in 30% of evaluable patients ($n = 310$), and minimal response or stable disease was observed in 51% of patients. The median progression-free survival was 40 months, and the median overall survival from the time of diagnosis was 128 months. Considering a historical overall survival of 40–72 months, the survival benefit reported in this study was significant. Long-term toxicity studies indicate that [¹⁷⁷Lu]Lu-DOTA-TATE treatment was well-tolerated with minimal side-effects [111, 112]; persistent hematopoietic neoplasms were reported in 2.2–2.9% of patients.

It was suggested that the efficacy of treatment might be increased by combining [¹⁷⁷Lu]Lu-DOTA-TATE with [⁹⁰Y]Y-DOTA-TATE [113, 114]. In theory, the higher energy of β^- particles emitted from ⁹⁰Y could deposit energy over a longer range, leading to the induction of cell death in a larger number of tumor cells and improving treatment efficacy for larger tumors. In a study with 50 patients with metastatic NETs, treatment with both [¹⁷⁷Lu]Lu-DOTA-TATE and [⁹⁰Y]Y-DOTA-TATE was compared to treatment with [⁹⁰Y]Y-DOTA-TATE alone [115]. It was shown that patients who received [¹⁷⁷Lu]Lu-DOTA-TATE in addition to [⁹⁰Y]Y-DOTA-TATE had a significantly longer overall survival ($P = 0.027$), although no significant differences in event-free survival were noted. Toxicity was assessed in a clinical study with 807 NET patients, demonstrating significantly fewer adverse effects in patients treated with [¹⁷⁷Lu]Lu-DOTA-TATE only, in comparison with patients who received only [⁹⁰Y]Y-DOTA-TATE or a combination of both [¹⁷⁷Lu]Lu-DOTA-TATE and [⁹⁰Y]Y-DOTA-TATE [116]. These data indicated that combined [¹⁷⁷Lu]Lu-DOTA-TATE and [⁹⁰Y]Y-DOTA-TATE therapy may benefit patients with heterogeneous, larger tumors, but due to the added toxicity of [⁹⁰Y]Y-DOTA-TATE treatment without significant improvement of efficacy, treatment with only [¹⁷⁷Lu]Lu-DOTA-TATE was recommended for further commercialization [107].

Based on the promising initial clinical studies, a randomized, controlled phase III clinical trial was initiated with 229 patients with midgut NETs [117]. Patients were assigned to the treatment arm ($n = 116$), in which four intravenous infusions of [¹⁷⁷Lu]Lu-DOTA-TATE plus best supportive care including octreotide were given, or to the control arm ($n = 113$), in which patients only received octreotide. Progression-free ($P < 0.001$) and overall ($P = 0.004$) survival differed significantly between the patients treated with [¹⁷⁷Lu]Lu-DOTA-TATE and the control group. A progression-free survival of 65.2% was observed 20 months after randomization for the cohort of [¹⁷⁷Lu]Lu-DOTA-TATE-treated patients, compared to 10.8% for the control group (Figure 18.10).



Clinical Example 18.11 [¹⁷⁷Lu]Lu-DOTA-J591

J591 is a humanized monoclonal antibody with high affinity for PSMA, and analogues of J591 have been labeled with several radionuclides – including ⁹⁰Y and ¹⁷⁷Lu – and assessed in clinical trials with prostate cancer patients [118, 119]. Phase I studies indicated that tumors could be targeted with radiolabeled J591 with limited toxicity. Due to the higher maximum tolerated dose observed for ¹⁷⁷Lu-labeled J591 compared to ⁹⁰Y-labeled J591, a phase II clinical trial was initiated in which 47 patients with metastatic castration-resistant prostate cancer were treated with one dose of [¹⁷⁷Lu]Lu-DOTA-J591 [120]. A decline in PSA levels was reported for ~60% of patients, as well as an improvement in overall survival time from 11.9 to 21.8 months for patients treated with the maximum tolerated dose. Treatment with [¹⁷⁷Lu]Lu-DOTA-J591 was well-tolerated, and although hematologic toxicity was observed in all patients, adverse effects were all reversible. In contrast to the dose-limiting xerostomia observed in CRPC patients treated with [²²⁵Ac]Ac-PSMA-617, no side-effects

related to the salivary glands were observed for [¹⁷⁷Lu]Lu-DOTA-J591, since J591 is known to bind to different epitopes of PSMA than PSMA-617, which are not expressed in the salivary glands [80]. The myelosuppression, however, limited the maximum dose. Due to the aforementioned promise of alpha therapy, a follow-up phase I dose-escalation study using ²²⁵Ac-labeled J591 in patients with progressive metastatic CRPC is currently ongoing [121].

Clinical Example 18.12 [¹⁸⁸Re]Re-6D2

In light of the successes of radiolabeled antibodies in the clinic, a radioimmunotherapeutic for the broad-spectrum treatment of metastatic melanoma was developed. To this end, the melanin-targeting IgM antibody 6D2 was radiolabeled with beta-emitting radionuclide rhenium-188 (¹⁸⁸Re) [122]. Due to its relatively short half-life of 16.9 hours and emission of high-energy β⁻ particles, ¹⁸⁸Re is an enticing radionuclide for therapy [14]. It decays to stable ¹⁸⁸Os after the emission of both β⁻ and γ particles. Despite the relatively long range of its β⁻ particles, the dose-related toxicity of ¹⁸⁸Re is generally limited due to its relatively short half-life.

In a twofold phase I clinical trial designed to investigate its safety and efficacy, [¹⁸⁸Re]Re-6D2 was administered to patients with stage IIIC/IV metastatic melanoma who failed standard therapies [122]. In the first part of this study (phase Ia, *n* = 13), unlabeled 6D2 was co-administered to assess its effect on the biodistribution and pharmacokinetics of [¹⁸⁸Re]Re-6D2; in the second part of the study (phase Ib, *n* = 7), potential toxicity was measured with increasing [¹⁸⁸Re]Re-6D2 doses. Stable disease was observed in 6 patients after 6 weeks, and the median overall survival was 13 months. This was considerably longer than the historical overall survival of 8.5 months for patients receiving standard care. No severe toxic events were reported – not even for patients receiving the highest doses of [¹⁸⁸Re]Re-6D2, which was explained by the intrinsically fast blood-clearance of IgM antibodies in general, the lack of cross-reactivity with healthy tissue, and the non-residualizing nature, relatively short half-life, and rapid renal excretion of free ¹⁸⁸Re. Dosimetry calculations suggest that follow-up studies with higher doses of [¹⁸⁸Re]Re-6D2 are warranted.

18.3.6 Auger Electron Therapy

Auger electrons are generated when a radionuclide decays by electron capture (**EC**) or internal conversion (**IC**). During these processes, a vacancy is created in one of the inner shells of the atom, which leads to a series of intra-atomic transitions until the atom reaches its ground state. These transitions can cause a cascade of multiplying vacancies toward the valence shell, resulting in the emission of numerous low-energy electrons: the Auger electrons. Due to their short path length and high energy, Auger electrons have a relatively high LET. If the decaying radionuclide is close to the DNA of a cancer cell, this high energy dose can cause multiple double-strand breaks, ultimately leading to the demise of the cell. Due to their nanometer range and high LET, Auger electron-generating radionuclides are very attractive for endoradiotherapy, especially for the eradication of single cells and small tumors (<1 cm) [83]. The main limitation of Auger electron-emitting radiopharmaceuticals is that they must be internalized into the cell and subsequently translocated to the nucleus to facilitate sufficient DNA damage. This may be particularly challenging in the context of radioimmunotherapy, since antibodies only

bind to extracellular antigens, which must then be internalized. Although some clinical trials with Auger electron-emitting radionuclides (e.g. ^{125}I) were published in the 1990s and early 2000s, the number of studies that investigate Auger electron therapy in clinical settings remains limited [83]. However, the potential benefits associated with Auger electron therapy and the development of second-generation endoradiotherapeutic agents is expected to lead to an increase in these trials in the near future.

Clinical Example 18.13 ^{111}In -DTPA-hEGF

The overexpression of epidermal growth factor receptor (**EGFR**) has been associated with many types of cancer, including lung, head-and-neck, pancreatic, colorectal, and breast cancers [123, 124]. In an attempt to exploit this overexpression for Auger electron endoradiotherapy, human epidermal growth factor (**hEGF**) was labeled with ^{111}In . Although ^{111}In is typically considered a radionuclide to achieve therapeutic effects for SPECT, it emits a considerable amount of energy in the form of Auger electrons. ^{111}In ($t_{1/2} = 2.8$ days) decays 100% by electron capture (EC) to ^{111}Cd via emission of γ photons, which in turn leads to internal conversion (IC). The Auger electrons that are generated as a result of this process can be exploited for endoradiotherapy. However, due to the relatively low efficacy of Auger electrons, higher doses are generally needed to achieve therapeutic effects [107].

The safety, pharmacokinetics, biodistribution, and radiation dosimetry of ^{111}In -labeled human EGF (^{111}In -DTPA-hEGF) were recently assessed in a small first-in-human clinical study in patients with EGFR-positive metastatic breast cancer ($n = 16$) [125]. After the injection of a single dose of ^{111}In -DTPA-hEGF, SPECT imaging confirmed the accumulation of the radiopharmaceutical in tumor tissue in 47% of patients (Figure 18.11). No immunogenicity was observed, and adverse effects were limited to flushing, chills, nausea,

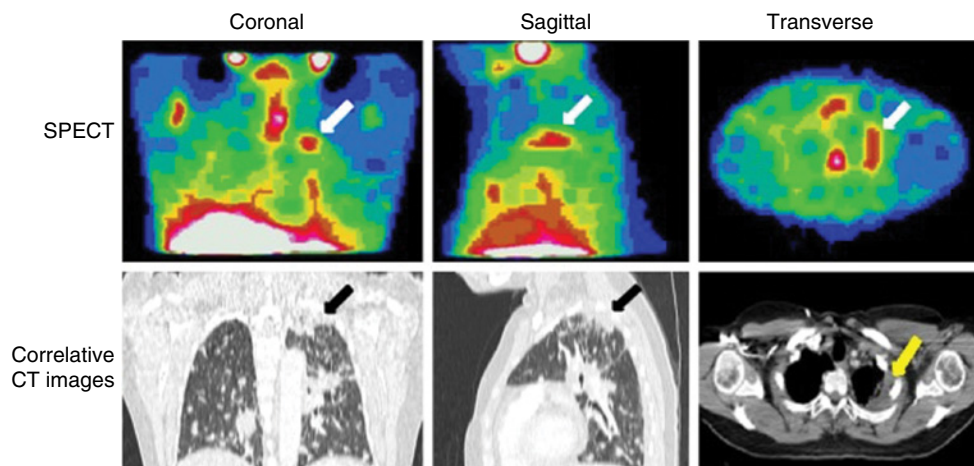


Figure 18.11 Representative SPECT and CT images of a patient with EGFR-positive metastatic breast cancer. The accumulation of ^{111}In -DTPA-hEGF in the tumor after 24 hours indicates the presence of a tumor deposit in the left lung (arrows). Source: Vallis Ka, et al. 2014, figure 1 (p. 186) [125]. Reproduced with permission from *American Journal of Nuclear Medicine and Molecular Imaging*. © 2014 American Journal of Nuclear Medicine and Molecular Imaging.

and vomiting during or immediately after the injection of the radiopharmaceutical; in addition, one patient who had bone marrow infiltration of the cancer experienced grade 3 thrombocytopenia. Although the maximum tolerated radioactive dose was not reached, no significant anti-tumor effects were visible. Despite the safety profile, favorable radiation dosimetric data, and lack of immunogenicity, doses could not be increased any further since most side-effects – i.e. flushing, nausea/vomiting, and hypotension – were attributed to the high mass of EGF administered per patient (0.25mg). A follow-up clinical dose-escalation study involving fractionated doses of [¹¹¹In]In-DTPA-hEGF may overcome these challenges.

18.4 CONCLUSIONS

In this chapter, we have sought to provide a broad overview of the use of radiopharmaceuticals in the diagnosis and treatment of cancer. Currently, a wide range of PET probes beyond [¹⁸F]FDG are being explored and developed, several of which have been applied in clinical practice or clinical trials. While it is unlikely that any of these probes will supplant [¹⁸F]FDG, we anticipate that an increasing number of target-specific imaging agents will be routinely used in clinical practice, helping clinicians realize the ideal of personalized medicine. At present, the short-lived radionuclides ¹⁸F and ⁶⁸Ga are the preferred choices for new diagnostic radiopharmaceuticals. The characteristics of both are well known in the clinic, and adding a new radiopharmaceutical to the arsenal of options is easier when all of the guidelines and instrument settings for the radionuclide are already in place. Yet despite the advantages conferred by ¹⁸F and ⁶⁸Ga, they cannot be used with all targeting moieties. Targeting vectors with longer circulation times (e.g. antibodies) require a longer-lived radiolabel, and the range of available radionuclides with different half-lives should not be forgotten when developing new imaging agents.

Shifting to therapy, a wide variety of endoradiotherapeutic strategies have a place in the treatment of cancer. Above all, it is critical to tailor the choice of radionuclide to the specific type of cancer as well as the individual patient. Until recently, the vast majority of therapeutic radiopharmaceuticals have been labeled with beta-emitting radionuclides. Yet both toxicity and radioresistance can hamper the clinical utility of these radiopharmaceuticals. The latter can be overcome – at least in part – via the use of alpha particle-emitting radionuclides. In light of this, there are several ongoing clinical trials focused on alpha-emitting radiopharmaceuticals, and preliminary results have been very promising. The production and availability of alpha-emitting radionuclides remain a higher-level concern, although these areas are the subject of intense investigation and could very well be resolved soon, facilitating the expanded implementation of alpha radiotherapy in preclinical and clinical settings. Finally, many promising preclinical studies have focused on the use of Auger electron-emitting radionuclides for therapies, and while the translation of these agents to the clinic has been slow, an increasing number of clinical trials are expected in the near future.

As we conclude, it is important to step back and appreciate the bigger picture for a moment. Advances in the understanding of cancer biology, developments in diagnostic

technologies, and the expansion of therapeutic options have combined to fuel the advent of *personalized medicine*. For decades, the medical establishment regarded diagnosis and treatment as two separate enterprises, yet recent years have witnessed a dramatic shift in which diagnosis and therapy are now considered two sides of the same coin. In the context of radiopharmaceuticals, this movement is manifested in the increasing importance of radiotheranostic pairs. Nuclear imaging and therapy can be integrated to form a paradigm in which diagnostic radiotracers are used to visualize tumor lesions and therapeutic analogues are then deployed for treatment. The promise of radiotheranostics has been powerfully demonstrated in both prostate cancer and NETs, and we are both hopeful and confident that new and powerful theranostic innovations will emerge in the near future.

ACKNOWLEDGMENTS

The authors gratefully acknowledge the National Institutes of Health (U01CA221046, R01CA204167) for their support.

REFERENCES

1. Ballinger, J.R. (2018). Theranostic radiopharmaceuticals: established agents in current use. *Br. J. Radiol.* 91 (1091): 20170969.
2. Schottelius, M., Simecek, J., Hoffmann, F. et al. (2015). Twins in spirit - episode I: comparative preclinical evaluation of [⁶⁸Ga]DOTATATE and [⁶⁸Ga]HA-DOTATATE. *EJNMMI Res.* 5: 22.
3. Jiang, L., Tu, Y., Shi, H. et al. (2014). PET probes beyond ¹⁸F-FDG. *J. Biomed. Res.* 28 (6): 435–446.
4. Bergström, M., Grahnen, A., and Långström, B. (2003). Positron emission tomography microdosing: a new concept with application in tracer and early clinical drug development. *Eur. J. Clin. Pharmacol.* 59 (5–6): 357–366.
5. O'Connor, M.K. and Kemp, B.J. (2006). Single-photon emission computed tomography/computed tomography: basic instrumentation and innovations. *Semin. Nucl. Med.* 36 (4): 258–266.
6. Rudin, M. and Weissleder, R. (2003). Molecular imaging in drug discovery and development. *Nat. Rev. Drug Discov.* 2 (2): 123–131.
7. Price, E.W. and Orvig, C. (2014). Matching chelators to radiometals for radiopharmaceuticals. *Chem. Soc. Rev.* 43 (1): 260–290.
8. Boros, E. and Holland, J.P. (2018). Chemical aspects of metal ion chelation in the synthesis and application antibody-based radiotracers. *J. Label. Compd. Radiopharm.* 61 (9): 652–671.
9. Conti, M. and Eriksson, L. (2016). Physics of pure and non-pure positron emitters for PET: a review and a discussion. *EJNMMI Phys.* 3 (1): 8.
10. Proescher, F. (1913). The intravenous injection of soluble radium salts in man. *Radium* i (4): 9–10.

11. MacKee, G.M. (1921). *X-rays and Radium in the Treatment of Diseases of the Skin*. New York: Lea and Febiger.
12. Yeong, C.-H., Cheng, M.-h., and Ng, K.-H. (2014). Therapeutic radionuclides in nuclear medicine: current and future prospects. *J. Zhejiang Univ. Sci. B* 15 (10): 845–863.
13. Bell, A.G. and Sowers, Z.T. (1903). Radium and cancer. *Nature* 68: 320.
14. Knapp, F.F. (2016). *Radiopharmaceuticals for Therapy*, 1e (ed. A. Dash). New Delhi, India: Springer.
15. Blower, P.J. (2015). A nuclear chocolate box: the periodic table of nuclear medicine. *Dalton Trans.* 44 (11): 4819–4844.
16. Zoller, F., Eisenhut, M., Haberkorn, U. et al. (2009). Endoradiotherapy in cancer treatment—basic concepts and future trends. *Eur. J. Pharmacol.* 625 (1–3): 55–62.
17. Ward, P.S. and Thompson, C.B. (2012). Metabolic reprogramming: a cancer hallmark even warburg did not anticipate. *Cancer Cell* 21 (3): 297–308.
18. Vander Heiden, M.G., Cantley, L.C., and Thompson, C.B. (2009). Understanding the Warburg effect: the metabolic requirements of cell proliferation. *Science (New York, N.Y.)* 324 (5930): 1029–1033.
19. Weber, W.A., Schwaiger, M., and Avril, N. (2000). Quantitative assessment of tumor metabolism using FDG-PET imaging. *Nucl. Med. Biol.* 27 (7): 683–687.
20. Dunphy, M.P.S., Harding, J.J., Venneti, S. et al. (2018). In vivo PET assay of tumor glutamine flux and metabolism: in-human trial of ¹⁸F-(2S,4R)-4-fluoroglutamine. *Radiology* 287 (2): 667–675.
21. Venneti, S., Dunphy, M.P., Zhang, H. et al. (2015). Glutamine-based PET imaging facilitates enhanced metabolic evaluation of gliomas in vivo. *Sci. Transl. Med.* 7 (274): 274ra217.
22. Liu, F., Xu, X., Zhu, H. et al. (2018). PET imaging of ¹⁸F-(2 S,4 R)4-fluoroglutamine accumulation in breast cancer: from xenografts to patients. *Mol. Pharm.* 15 (8): 3448–3455.
23. Xu, X., Zhu, H., Liu, F. et al. (2018). Imaging brain metastasis patients with ¹⁸F-(2S,4R)-4-fluoroglutamine. *Clin. Nucl. Med.* 43 (11): e392–e399.
24. Kazandjian, D., Suzman, D.L., Blumenthal, G. et al. (2016). FDA approval summary: nivolumab for the treatment of metastatic non-small cell lung cancer with progression on or after platinum-based chemotherapy. *Oncologist* 21 (5): 634–642.
25. Herbst, R.S., Baas, P., Kim, D.-W. et al. (2016). Pembrolizumab versus docetaxel for previously treated, PD-L1-positive, advanced non-small-cell lung cancer (KEYNOTE-010): a randomised controlled trial. *Lancet* 387 (10027): 1540–1550.
26. Weinstock, M. and McDermott, D. (2015). Targeting PD-1/PD-L1 in the treatment of metastatic renal cell carcinoma. *Ther. Adv. Urol.* 7 (6): 365–377.
27. Daud, A.I., Wolchok, J.D., Robert, C. et al. (2016). Programmed death-ligand 1 expression and response to the anti-programmed death 1 antibody pembrolizumab in melanoma. *J. Clin. Oncol.* 34 (34): 4102–4109.
28. Balar, A.V., Galsky, M.D., Rosenberg, J.E. et al. (2017). Atezolizumab as first-line treatment in cisplatin-ineligible patients with locally advanced and metastatic urothelial carcinoma: a single-arm, multicentre, phase 2 trial. *Lancet (London, England)* 389 (10064): 67–76.

29. Rittmeyer, A., Barlesi, F., Waterkamp, D. et al. (2017). Atezolizumab versus docetaxel in patients with previously treated non-small-cell lung cancer (OAK): a phase 3, open-label, multicentre randomised controlled trial. *Lancet* 389 (10066): 255–265.
30. Shukuya, T. and Carbone, D.P. (2016). Predictive markers for the efficacy of anti-PD-1/PD-L1 antibodies in lung cancer. *J. Thorac. Oncol.* 11 (7): 976–988.
31. Bensch, F., van der Veen, E.L., Lub-de Hooge, M.N. et al. (2018). ⁸⁹Zr-atezolizumab imaging as a non-invasive approach to assess clinical response to PD-L1 blockade in cancer. *Nat. Med.* 24 (12): 1852–1858.
32. Niemeijer, A.N., Leung, D., Huisman, M.C. et al. (2018). Whole body PD-1 and PD-L1 positron emission tomography in patients with non-small-cell lung cancer. *Nat. Commun.* 9 (1): 4664.
33. Donnelly, D.J., Smith, R.A., Morin, P. et al. (2018). Synthesis and biologic evaluation of a novel ¹⁸F-labeled adnectin as a PET radioligand for imaging PD-L1 expression. *J. Nucl. Med.* 59 (3): 529–535.
34. Hallet, J., Law, C.H., Cukier, M. et al. (2015). Exploring the rising incidence of neuroendocrine tumors: a population-based analysis of epidemiology, metastatic presentation, and outcomes. *Cancer* 121 (4): 589–597.
35. Pauwels, E., Cleeren, F., Bormans, G. et al. (2018). Somatostatin receptor PET ligands - the next generation for clinical practice. *Am. J. Nucl. Med. Mol. Imaging* 8 (5): 311–331.
36. Kayani, I., Conry, B.G., Groves, A.M. et al. (2009). A comparison of ⁶⁸Ga-DOTATATE and ¹⁸F-FDG PET/CT in pulmonary neuroendocrine tumors. *J. Nucl. Med.* 50 (12): 1927–1932.
37. Walker, R.C., Smith, G.T., Liu, E. et al. (2013). Measured human dosimetry of ⁶⁸Ga-DOTATATE. *J. Nucl. Med.* 54 (6): 855–860.
38. Umbehrr, M.H., Müntener, M., Hany, T. et al. (2013). The role of ¹¹C-choline and ¹⁸F-fluorocholine positron emission tomography (PET) and PET/CT in prostate cancer: a systematic review and meta-analysis. *Eur. Urol.* 64 (1): 106–117.
39. Krause, B.J., Souvatzoglou, M., and Treiber, U. (2013). Imaging of prostate cancer with PET/CT and radioactively labeled choline derivatives. *Urol. Oncol. Semin. Orig. Investig.* 31 (4): 427–435.
40. Bauman, G., Belhocine, T., Kovacs, M. et al. (2012). ¹⁸F-fluorocholine for prostate cancer imaging: a systematic review of the literature. *Prostate Cancer Prostatic Dis.* 15 (1): 45–55.
41. Castellucci, P., Ceci, F., Graziani, T. et al. (2014). Early biochemical relapse after radical prostatectomy: which prostate cancer patients may benefit from a restaging ¹¹C-choline PET/CT scan before salvage radiation therapy? *J. Nucl. Med.* 55 (9): 1424–1429.
42. Minner, S., Wittmer, C., Graefen, M. et al. (2011). High level PSMA expression is associated with early PSA recurrence in surgically treated prostate cancer. *Prostate* 71 (3): 281–288.
43. Rybalov, M., Ananias, H.J., Hoving, H.D. et al. (2014). PSMA, EpCAM, VEGF and GRPR as imaging targets in locally recurrent prostate cancer after radiotherapy. *Int. J. Mol. Sci.* 15 (4): 6046–6061.

44. Ananias, H.J., van den Heuvel, M.C., Helfrich, W. et al. (2009). Expression of the gastrin-releasing peptide receptor, the prostate stem cell antigen and the prostate-specific membrane antigen in lymph node and bone metastases of prostate cancer. *Prostate* 69 (10): 1101–1108.
45. Franc, B.L., Cho, S.Y., Rosenthal, S.A. et al. (2013). Detection and localization of carcinoma within the prostate using high resolution transrectal gamma imaging (TRGI) of monoclonal antibody directed at prostate specific membrane antigen (PSMA)—proof of concept and initial imaging results. *Eur. J. Radiol.* 82 (11): 1877–1884.
46. Ponsky, L.E., Cherullo, E.E., Starkey, R. et al. (2002). Evaluation of preoperative ProstaScint scans in the prediction of nodal disease. *Prostate Cancer Prostatic Dis.* 5 (2): 132–135.
47. Liu, H., Rajasekaran, A.K., Moy, P. et al. (1998). Constitutive and antibody-induced internalization of prostate-specific membrane antigen. *Cancer Res.* 58 (18): 4055–4060.
48. Bander, N.H., Trabulsi, E.J., Kostakoglu, L. et al. (2003). Targeting metastatic prostate cancer with radiolabeled monoclonal antibody J591 to the extracellular domain of prostate specific membrane antigen. *J. Urol.* 170 (5): 1717–1721.
49. Afshar-Oromieh, A., Malcher, A., Eder, M. et al. (2013). PET imaging with a [⁶⁸Ga] gallium-labelled PSMA ligand for the diagnosis of prostate cancer: biodistribution in humans and first evaluation of tumour lesions. *Eur. J. Nucl. Med. Mol. Imaging* 40 (4): 486–495.
50. Afshar-Oromieh, A., Zechmann, C.M., Malcher, A. et al. (2014). Comparison of PET imaging with a ⁶⁸Ga-labelled PSMA ligand and ¹⁸F-choline-based PET/CT for the diagnosis of recurrent prostate cancer. *Eur. J. Nucl. Med. Mol. Imaging* 41 (1): 11–20.
51. Morigi, J.J., Stricker, P.D., van Leeuwen, P.J. et al. (2015). Prospective comparison of ¹⁸F-fluoromethylcholine versus ⁶⁸Ga-PSMA PET/CT in prostate cancer patients who have rising PSA after curative treatment and are being considered for targeted therapy. *J. Nucl. Med.* 56 (8): 1185–1190.
52. Eiber, M., Fendler, W.P., Rowe, S.P. et al. (2017). Prostate-specific membrane antigen ligands for imaging and therapy. *J. Nucl. Med.* 58 (Suppl 2): 67S–76S.
53. Benesova, M., Schafer, M., Bauder-Wust, U. et al. (2015). Preclinical evaluation of a tailor-made DOTA-conjugated PSMA inhibitor with optimized linker moiety for imaging and endoradiotherapy of prostate cancer. *J. Nucl. Med.* 56 (6): 914–920.
54. Afshar-Oromieh, A., Hetzheim, H., Kratochwil, C. et al. (2015). The theranostic PSMA ligand PSMA-617 in the diagnosis of prostate cancer by PET/CT: biodistribution in humans, radiation dosimetry, and first evaluation of tumor lesions. *J. Nucl. Med.* 56 (11): 1697–1705.
55. Cho, S.Y., Gage, K.L., Mease, R.C. et al. (2012). Biodistribution, tumor detection, and radiation dosimetry of ¹⁸F-DCFBC, a low-molecular-weight inhibitor of prostate-specific membrane antigen, in patients with metastatic prostate cancer. *J. Nucl. Med.* 53 (12): 1883–1891.
56. Szabo, Z., Mena, E., Rowe, S.P. et al. (2015). Initial evaluation of [¹⁸F]DCFPyL for prostate-specific membrane antigen (PSMA)-targeted PET imaging of prostate cancer. *Mol. Imaging Biol.* 17 (4): 565–574.

57. Chen, Y., Pullambhatla, M., Foss, C.A. et al. (2011). 2-(3-{1-Carboxy-5-[[6-¹⁸F]fluoropyridine-3-carbonyl)-amino]-pentyl}-ureido)-pentanedioic acid, [¹⁸F]DCFPyL, a PSMA-based PET imaging agent for prostate cancer. *Clin. Cancer Res.* 17 (24): 7645–7653.
58. Dietlein, M., Kobe, C., Kuhnert, G. et al. (2015). Comparison of [¹⁸F]DCFPyL and [⁶⁸Ga]Ga-PSMA-HBED-CC for PSMA-PET imaging in patients with relapsed prostate cancer. *Mol. Imaging Biol.* 17 (4): 575–584.
59. Cardinale, J., Schafer, M., Benesova, M. et al. (2017). Preclinical evaluation of ¹⁸F-PSMA-1007, a new prostate-specific membrane antigen ligand for prostate cancer imaging. *J. Nucl. Med.* 58 (3): 425–431.
60. Giesel, F.L., Cardinale, J., Schäfer, M. et al. (2016). ¹⁸F-labelled PSMA-1007 shows similarity in structure, biodistribution and tumour uptake to the theragnostic compound PSMA-617. *Eur. J. Nucl. Med. Mol. Imaging* 43 (10): 1929–1930.
61. Giesel, F.L., Will, L., Lawal, I. et al. (2018). Intraindividual comparison of ¹⁸F-PSMA-1007 and ¹⁸F-DCFPyL PET/CT in the prospective evaluation of patients with newly diagnosed prostate carcinoma: a pilot study. *J. Nucl. Med.* 59 (7): 1076–1080.
62. Hoefnagel, C.A. (1991). Radionuclide therapy revisited. *Eur. J. Nucl. Med.* 18 (6): 408–431.
63. Poty, S., Francesconi, L.C., McDevitt, M.R. et al. (2018). α -Emitters for radiotherapy: from basic radiochemistry to clinical studies-part 1. *J. Nucl. Med.* 59 (6): 878–884.
64. Paillass, S., Ladjohounlou, R., Lozza, C. et al. (2016). Localized irradiation of cell membrane by auger electrons is cytotoxic through oxidative stress-mediated nontargeted effects. *Antioxid. Redox Signal.* 25 (8): 467–484.
65. Wessels, B.W. and Meares, C.F. (2000). Physical and chemical properties of radionuclide therapy. *Semin. Radiat. Oncol.* 10 (2): 115–122.
66. Zeglis, B.M., Sevak, K.K., Reiner, T. et al. (2013). A pretargeted PET imaging strategy based on bioorthogonal Diels-Alder click chemistry. *J. Nucl. Med.* 54 (8): 1389–1396.
67. Zeglis, B.M., Brand, C., Abdel-Atti, D. et al. (2015). Optimization of a pretargeted strategy for the PET imaging of colorectal carcinoma via the modulation of radioligand pharmacokinetics. *Mol. Pharm.* 12 (10): 3575–3587.
68. Houghton, J.L., Zeglis, B.M., Abdel-Atti, D. et al. (2016). Pretargeted immuno-PET of pancreatic cancer: overcoming circulating antigen and internalized antibody to reduce radiation doses. *J. Nucl. Med.* 57 (3): 453–459.
69. Houghton, J.L., Membreno, R., Abdel-Atti, D. et al. (2017). Establishment of the in vivo efficacy of pretargeted radioimmunotherapy utilizing inverse electron demand Diels-Alder click chemistry. *Mol. Cancer Ther.* 16 (1): 124–133.
70. Meyer, J.P., Adumeau, P., Lewis, J.S. et al. (2016). Click chemistry and radiochemistry: the first 10 years. *Bioconjug. Chem.* 27 (12): 2791–2807.
71. Keinänen, O., Fung, K., Pourat, J. et al. (2017). Pretargeting of internalizing trastuzumab and cetuximab with a ¹⁸F-tetrazine tracer in xenograft models. *EJNMMI Res.* 7 (1): 95–95.
72. Boros, E. and Packard, A.B. (2019). Radioactive transition metals for imaging and therapy. *Chem. Rev.* 119 (2): 870–901.

73. Zechmann, C.M., Afshar-Oromieh, A., Armor, T. et al. (2014). Radiation dosimetry and first therapy results with a $^{124}\text{I}/^{131}\text{I}$ -labeled small molecule (MIP-1095) targeting PSMA for prostate cancer therapy. *Eur. J. Nucl. Med. Mol. Imaging* 41 (7): 1280–1292.
74. Kiess, A.P., Minn, I., Vaidyanathan, G. et al. (2016). (2S)-2-(3-(1-Carboxy-5-(4- ^{211}At -Astatobenzamido)Pentyl)Ureido)-pentanedioic acid for PSMA-targeted α -particle radiopharmaceutical therapy. *J. Nucl. Med.* 57 (10): 1569–1575.
75. Zhao, J., Zhou, M., and Li, C. (2016). Synthetic nanoparticles for delivery of radioisotopes and radiosensitizers in cancer therapy. *Cancer Nanotechnol.* 7 (1): 9.
76. Wilhelm, S., Tavares, A.J., Dai, Q. et al. (2016). Analysis of nanoparticle delivery to tumours. *Nat. Rev. Mater.* 1: 16014.
77. Sharkey, R.M. and Goldenberg, D.M. (2011). Cancer radioimmunotherapy. *Immunotherapy* 3 (3): 349–370.
78. Institute of M., National Research C (2007). *Advancing Nuclear Medicine Through Innovation*. Washington, DC: The National Academies Press.
79. Makvandi, M., Dupis, E., Engle, J.W. et al. (2018). Alpha-emitters and targeted alpha therapy in oncology: from basic science to clinical investigations. *Target. Oncol.* 13 (2): 189–203.
80. Marcu, L., Bezak, E., and Allen, B.J. (2018). Global comparison of targeted alpha vs targeted beta therapy for cancer: in vitro, in vivo and clinical trials. *Crit. Rev. Oncol. Hematol.* 123: 7–20.
81. Tang, L., Wei, F., Wu, Y. et al. (2018). Role of metabolism in cancer cell radioresistance and radiosensitization methods. *J. Exp. Clin. Cancer Res.* 37 (1): 87–87.
82. Kratochwil, C., Bruchertseifer, F., Giesel, F.L. et al. (2016). ^{225}Ac -PSMA-617 for PSMA-targeted α -radiation therapy of metastatic castration-resistant prostate cancer. *J. Nucl. Med.* 57 (12): 1941–1944.
83. Aghevlian, S., Boyle, A.J., and Reilly, R.M. (2017). Radioimmunotherapy of cancer with high linear energy transfer (LET) radiation delivered by radionuclides emitting α -particles or auger electrons. *Adv. Drug Deliv. Rev.* 109: 102–118.
84. Poty, S., Francesconi, L.C., McDevitt, M.R. et al. (2018). α -Emitters for radiotherapy: from basic radiochemistry to clinical studies—part 2. *J. Nucl. Med.* 59 (7): 1020–1027.
85. Kluetz, P.G., Pierce, W., Maher, V.E. et al. (2014). Radium Ra 223 dichloride injection: US Food and Drug Administration drug approval summary. *Clin. Cancer Res.* 20 (1): 9.
86. Parker, C., Nilsson, S., Heinrich, D. et al. (2013). Alpha emitter radium-223 and survival in metastatic prostate cancer. *N. Engl. J. Med.* 369 (3): 213–223.
87. Sartor, O., Coleman, R., Nilsson, S. et al. (2014). Effect of radium-223 dichloride on symptomatic skeletal events in patients with castration-resistant prostate cancer and bone metastases: results from a phase 3, double-blind, randomised trial. *Lancet Oncol.* 15 (7): 738–746.
88. Nilsson, S., Zhan, L., Shan, M. et al. (2016). Patient-reported quality-of-life analysis of radium-223 dichloride from the phase III ALSYMPCA study. *Ann. Oncol.* 27 (5): 868–874.

- 89 Nilsson, S., Larsen, R.H., Fosså, S.D. et al. (2005). First clinical experience with α -emitting Radium-223 in the treatment of skeletal metastases. *Clin. Cancer Res.* 11 (12): 4451.
90. Afshar-Oromieh, A., Holland-Letz, T., Giesel, F.L. et al. (2017). Diagnostic performance of ^{68}Ga -PSMA-11 (HBED-CC) PET/CT in patients with recurrent prostate cancer: evaluation in 1007 patients. *Eur. J. Nucl. Med. Mol. Imaging* 44 (8): 1258–1268.
91. Brauer, A., Grubert, L.S., Roll, W. et al. (2017). ^{177}Lu -PSMA-617 radioligand therapy and outcome in patients with metastasized castration-resistant prostate cancer. *Eur. J. Nucl. Med. Mol. Imaging* 44 (10): 1663–1670.
92. Kratochwil, C., Bruchertseifer, F., Rathke, H. et al. (2018). Targeted alpha therapy of mCRPC with ^{225}Ac -PSMA-617: swimmer-plot analysis suggests efficacy regarding duration of tumor-control. *J. Nucl. Med.* 59 (5): 795–802.
93. Kratochwil, C., Bruchertseifer, F., Rathke, H. et al. (2017). Targeted α -therapy of metastatic castration-resistant prostate cancer with ^{225}Ac -PSMA-617: dosimetry estimate and empiric dose finding. *J. Nucl. Med.* 58 (10): 1624–1631.
94. Kumar, K., Magerstädt, M., and Gansow, O.A. (1989). Lead(II) and bismuth(III) complexes of the polyazacycloalkane-N-acetic acids nota, dota, and teta. *J. Chem. Soc. Chem. Commun.* 3: 145–146.
95. Scheinberg, D.A. and McDevitt, M.R. (2011). Actinium-225 in targeted alpha-particle therapeutic applications. *Curr. Radiopharm.* 4 (4): 306–320.
96. Kratochwil, C., Giesel, F.L., Bruchertseifer, F. et al. (2014). ^{213}Bi -DOTATOC receptor-targeted alpha-radionuclide therapy induces remission in neuroendocrine tumours refractory to beta radiation: a first-in-human experience. *Eur. J. Nucl. Med. Mol. Imaging* 41 (11): 2106–2119.
97. McDevitt, M.R., Ma, D., Lai, L.T. et al. (2001). Tumor therapy with targeted atomic nanogenerators. *Science* 294 (5546): 1537–1540.
- 98 Feldman, E., Kalaycio, M., Weiner, G. et al. (2003). Treatment of relapsed or refractory acute myeloid leukemia with humanized anti-CD33 monoclonal antibody HuM195. *Leukemia* 17 (2): 314–318.
99. Jurcic, J.G., Larson, S.M., Sgouros, G. et al. (2002). Targeted alpha particle immunotherapy for myeloid leukemia. *Blood* 100 (4): 1233–1239.
100. Rosenblat, T.L., McDevitt, M.R., Mulford, D.A. et al. (2010). Sequential cytarabine and alpha-particle immunotherapy with bismuth-213-lintuzumab (HuM195) for acute myeloid leukemia. *Clin. Cancer Res.* 16 (21): 5303–5311.
101. Jurcic, J.G. and Rosenblat, T.L. (2014). Targeted alpha-particle immunotherapy for acute myeloid leukemia. *Am. Soc. Clin. Oncol. Educ. Book*: e126–e131.
- 102 Jurcic, J., Levy, M., Park, J. et al. (2017). Phase I trial of alpha-particle immunotherapy with ^{225}Ac -lintuzumab and low-dose cytarabine in patients age 60 or older with untreated acute myeloid leukemia. *J. Nucl. Med.* 58 (Suppl. 1): 456.
103. Zalutsky, M.R., Reardon, D.A., Akabani, G. et al. (2008). Clinical experience with alpha-particle emitting ^{211}At : treatment of recurrent brain tumor patients with ^{211}At -labeled chimeric antitenascin monoclonal antibody 81C6. *J. Nucl. Med.* 49 (1): 30–38.

104. Brem, H., Piantadosi, S., Burger, P.C. et al. (1995). Placebo-controlled trial of safety and efficacy of intraoperative controlled delivery by biodegradable polymers of chemotherapy for recurrent gliomas. The polymer-brain tumor treatment group. *Lancet* 345 (8956): 1008–1012.
105. Meredith, R., Torgue, J., Shen, S. et al. (2014). Dose escalation and dosimetry of first-in-human α radioimmunotherapy with ^{212}Pb -TCMC-trastuzumab. *J. Nucl. Med.* 55 (10): 1636–1642.
106. Meredith, R.F., Torgue, J.J., Rozgaja, T.A. et al. (2018). Safety and outcome measures of first-in-human intraperitoneal α radioimmunotherapy with ^{212}Pb -TCMC-trastuzumab. *Am. J. Clin. Oncol.* 41 (7): 716–721.
107. Mitra, E.S. (2018). Neuroendocrine tumor therapy: ^{177}Lu -DOTATATE. *Am. J. Roentgenol.* 211 (2): 278–285.
108. Kwekkeboom, D.J., Bakker, W.H., Kam, B.L. et al. (2003). Treatment of patients with gastro-entero-pancreatic (GEP) tumours with the novel radiolabelled somatostatin analogue [^{177}Lu -DOTA(0),Tyr3]octreotate. *Eur. J. Nucl. Med. Mol. Imaging* 30 (3): 417–422.
109. Teunissen, J.J.M., Kwekkeboom, D.J., and Krenning, E.P. (2004). Quality of life in patients with gastroenteropancreatic tumors treated with [^{177}Lu -DOTA0,Tyr3]octreotate. *J. Clin. Oncol.* 22 (13): 2724–2729.
110. Kwekkeboom, D.J., de Herder, W.W., Kam, B.L. et al. (2008). Treatment with the radiolabeled somatostatin analog [^{177}Lu -DOTA0,Tyr3]octreotate: toxicity, efficacy, and survival. *J. Clin. Oncol.* 26 (13): 2124–2130.
111. Brabander, T., van der Zwan, W.A., Teunissen, J.J.M. et al. (2017). Long-term efficacy, survival, and safety of [^{177}Lu -DOTA0,Tyr3]octreotate in patients with gastroenteropancreatic and bronchial neuroendocrine tumors. *Clin. Cancer Res.* 23 (16): 4617.
112. Bergsma, H., Lom, K.v., Konijnenberg, M. et al. (2017). Therapy-related hematological malignancies after peptide receptor radionuclide therapy with ^{177}Lu -DOTA-octreotate: incidence, course & predicting factors in patients with GEP-NETs. *J. Nucl. Med.*
113. De Jong, M., Valkema, R., Jamar, F. et al. (2002). Somatostatin receptor-targeted radionuclide therapy of tumors: preclinical and clinical findings. *Semin. Nucl. Med.* 32 (2): 133–140.
114. de Jong, M., Breeman, W.A., Valkema, R. et al. (2005). Combination radionuclide therapy using ^{177}Lu - and ^{90}Y -labeled somatostatin analogs. *J. Nucl. Med.* 46 (Suppl. 1): 13s–17s.
115. Kunikowska, J., Królicki, L., Hubalewska-Dydejczyk, A. et al. (2011). Clinical results of radionuclide therapy of neuroendocrine tumours with ^{90}Y -DOTATATE and tandem $^{90}\text{Y}/^{177}\text{Lu}$ -DOTATATE: which is a better therapy option? *Eur. J. Nucl. Med. Mol. Imaging* 38 (10): 1788–1797.
116. Bodei, L., Kidd, M., Paganelli, G. et al. (2015). Long-term tolerability of PRRT in 807 patients with neuroendocrine tumours: the value and limitations of clinical factors. *Eur. J. Nucl. Med. Mol. Imaging* 42 (1): 5–19.
117. Strosberg, J., El-Haddad, G., Wolin, E. et al. (2017). Phase 3 trial of ^{177}Lu -dotatate for midgut neuroendocrine tumors. *N. Engl. J. Med.* 376 (2): 125–135.

118. Milowsky, M.I., Nanus, D.M., Kostakoglu, L. et al. (2004). Phase I trial of yttrium-90-labeled anti-prostate-specific membrane antigen monoclonal antibody J591 for androgen-independent prostate cancer. *J. Clin. Oncol.* 22 (13): 2522–2531.
119. Bander, N.H., Milowsky, M.I., Nanus, D.M. et al. (2005). Phase I trial of ¹⁷⁷Lutetium-labeled J591, a monoclonal antibody to prostate-specific membrane antigen, in patients with androgen-independent prostate cancer. *J. Clin. Oncol.* 23 (21): 4591–4601.
120. Tagawa, S.T., Milowsky, M.I., Morris, M. et al. (2013). Phase II study of lutetium-177-labeled anti-prostate-specific membrane antigen monoclonal antibody J591 for metastatic castration-resistant prostate cancer. *Clin. Cancer Res.* 19 (18): 5182–5191.
121. Tagawa, S.T., Vallabhajosula, S., Jhanwar, Y. et al. (2018). Phase I dose-escalation study of ²²⁵Ac-J591 for progressive metastatic castration resistant prostate cancer (mCRPC). *J. Clin. Oncol.* 36 (Suppl. 6): TPS399–TPS399.
122. Klein, M., Lotem, M., Peretz, T. et al. (2013). Safety and efficacy of ¹⁸⁸rhenium-labeled antibody to melanin in patients with metastatic melanoma. *J. Skin Cancer* 2013: 828329–828329.
123. Yewale, C., Baradia, D., Vhora, I. et al. (2013). Epidermal growth factor receptor targeting in cancer: a review of trends and strategies. *Biomaterials* 34 (34): 8690–8707.
124. Goos, J.A.C.M., Hiemstra, A.C., Coupé, V.M.H. et al. (2014). Epidermal growth factor receptor (EGFR) and prostaglandin-endoperoxide synthase 2 (PTGS2) are prognostic biomarkers for patients with resected colorectal cancer liver metastases. *Br. J. Cancer* 111 (4): 749–755.
125. Vallis, K.A., Reilly, R.M., Scollard, D. et al. (2014). Phase I trial to evaluate the tumor and normal tissue uptake, radiation dosimetry and safety of ¹¹¹In-DTPA-human epidermal growth factor in patients with metastatic EGFR-positive breast cancer. *Am. J. Nucl. Med. Mol. Imaging* 4 (2): 181–192.

Chapter 19

Neurological Applications of Radiopharmaceuticals

Mehdi Djekidel¹ and Nicolaas I. Bohnen^{2,3,4}

¹*Nuclear Medicine and Molecular Imaging, Sidra Medicine,
Doha, Qatar*

²*Radiology, University of Michigan, Ann Arbor, MI 48109 United
States*

³*Neurology, University of Michigan, Ann Arbor, MI 48109 United
States*

⁴*Neurology Service and GRECC, VAAAHS, Ann Arbor, MI 48105
United States*

19.1 INTRODUCTION

Clinical applications of radiopharmaceuticals in the practice of neuro-nuclear medicine are shifting from traditional planar studies of cerebrospinal fluid (**CSF**) and cerebral blood flow (**CBF**) to tomographic single-photon emission computed tomography (**SPECT**) and positron emission tomography (**PET**) studies of brain molecular targets, such as dopamine transporters (**DATs**) and β -amyloid proteinopathy. Despite these shifts, there remains a low but steady volume of traditional CSF and CBF planar imaging that is mainly used for the diagnosis of CSF leaks, obstruction of intrathecal CSF reservoir or baclofen pump, and bedside or portable brain death imaging. The use of ventricular shunt patency studies has also waned significantly due to a newer generation of shunts that allow simple pressure checks to check for patency. The use of radionuclide cisternograms for

CSF leaks has decreased because of low sensitivity. The use of CBF SPECT imaging for diagnosis and management of cerebrovascular disease has waned substantially with the advent of magnetic resonance (MR) perfusion and diffusion stroke imaging. The initial popular application of CBF SPECT imaging for the differential diagnosis of dementing disorders has now shifted to glucose metabolic PET imaging due to its superior spatial resolution. More recently, the field of neuro-nuclear medicine is experiencing a renaissance with the approval for molecular ligands targeting the DAT and β -amyloidopathy.

Molecular imaging has evolved into a major player for the assessment of patients with neurodegenerative disorders, in particular cognitive disorders and dementia. Molecular imaging can serve as a bridge between *in vivo* clinical and *ex vivo* neuropathological criteria. Three major strategies have evolved:

- (i) Imaging the “final” common pathway of neuronal or synaptic degeneration on the basis of the cerebral topography of decreased vs. preserved metabolic or perfusion patterns.
- (ii) Imaging a specific neurochemical substrate, such as the DAT to assist in the differential diagnosis of Parkinson’s disease vs. essential tremor.
- (iii) Imaging specific pathological substrates, such as β -amyloid plaque or neurofibrillary tau proteinopathies. The chapter will give an overview of currently used techniques and will also list some new developments in the field.

19.2 CSF FLOW IMAGING: PLANAR AND SPECT APPLICATIONS

19.2.1 Cerebral Ventricular Shunt Study

Shunting of the ventricular system is performed for decompression in the presence of obstructive hydrocephalus. A catheter is usually located in the lateral ventricle and is connected to a reservoir. The reservoir is connected to a distal catheter with an intervening one-way valve, allowing the flow of CSF away from the ventricle. The second catheter is usually placed subcutaneously with its distal end in the peritoneal cavity or right atrium of the heart. This provides a route for flow and absorption of the CSF. In assessing ventriculo-atrial (**VA**) or ventriculo-peritoneal (**VP**) shunt patency, the passage of the radioactive bolus from the reservoir to the peritoneum is expected, as CSF exits the ventricles by means of the shunt conduit. The study is performed by injection of the radiopharmaceutical (typically diethylenetriamine pentaacetic acid [**DTPA**]) into the shunt reservoir followed by serial images of the head and distal end of the catheter to assess patency and function of the shunt pathway [1] (Table 19.1).

19.2.1.1 Radiopharmaceuticals

[^{99m}Tc]DTPA: Generally preferred to [^{111}In] because of more favorable dosimetry, better counting statistics, and availability. Using [^{99m}Tc]DTPA allows short-interval repeated studies. [^{99m}Tc]DTPA should not be administered intraventricularly (not Food and Drug

Radiopharmaceuticals; (adult) dose ^a , route	Technique	Indication(s)	Main interpretation parameters (presence/absence)
[^{99m} Tc]DTPA, 1 mCi in shunt reservoir	Shunt reservoir injection	Suspected mechanical shunt obstruction	Flow dispersion into peritoneal space (VP shunt) or circulation (VA shunt)
[¹¹¹ In]DTPA, 0.5 mCi in shunt reservoir	Shunt reservoir injection	Suspected mechanical obstruction	Flow dispersion into peritoneal space (VP shunt) or circulation (VA shunt)

^a Need to be adjusted for pediatric patients.

Table 19.1 Summary of cerebral ventricular shunt patency scintigraphy.

Administration [**FDA**] approved for the intracranial CSF compartment). This is achieved by a special injection technique (discussed later). Therefore, it cannot be used for assessment of proximal obstruction of the shunt.

[¹¹¹In]DTPA: Preferred when there is a need for delayed 24-hour views. [¹¹¹In]DTPA is also used to study the afferent part of the shunt, i.e. direct assessment of reflux into the ventricles.

19.2.1.2 Indication

The usual indication for a radionuclide ventricular shunt study is for evaluating a suspected mechanical obstruction. This is the most common complication of shunts. Choroid plexus, brain tissue, tumor, or ventricular debris, including clots, can obstruct the proximal ventricular catheter. The distal catheter can be obstructed by thrombus formation, debris from the ventricles, or loculation of CSF in the abdomen.

19.2.1.3 Interpretation of CSF Ventricular Shunt Studies

These studies can be interpreted only with complete knowledge of the location and types of all shunts present at the time of examination, regardless of their suspected patency. In addition, the anatomy of the ventricular system and the relative position of the proximal catheter relative to this anatomy must be known. Recent plain radiographs of the head, chest, and abdomen need to be reviewed. The injection of the tracer should not disturb the pressures and flow within the shunt system. However, CSF should not be withdrawn for analysis prior to the study, as this may lead to a false-positive scan. If more than one shunt system is in place, the study should be performed on each system independently.

Normal scan findings: After injection, the activity is seen within the reservoir and adjacent catheters. The activity should move spontaneously through the distal catheter. In VP shunts, activity should be visualized within the peritoneum without evidence of loculation. Later, renal excretion of absorbed peritoneal activity should be evident. In the case of VA shunts, the activity should be seen to accumulate rapidly in the bladder due to renal excretion following passage through the distal catheter.

Indeterminate scan findings: Failure to observe movement of the tracer through the system within the first hour of observation, or movement that occurs only following provocative maneuvers such as sitting or standing the patient or “pumping the shunt,” may indicate partial or intermittent shunt occlusion.

Obstruction of the shunt: The tracer remains in the shunt system without significant net movement distally, including over a delayed two- to four-hour examination period. Note that the location of the obstruction cannot be reliably inferred from the study. If activity accumulates slowly within a discrete intraperitoneal region, without evidence for spread within the peritoneal cavity, then loculation of the distal peritoneal catheter is suggested, and a [¹¹¹In]DTPA study may be indicated with delayed 24-hour views.

19.2.1.4 Findings of Ventricular Shunt Study to Assess Patency of Proximal Limb of a Shunt Using [¹¹¹In]DTPA

Normal findings: After injection of the tracer into the reservoir, activity will be seen within the cerebral ventricle if the distal catheter has been manually occluded. Otherwise, reflux into the ventricle may be variable. The tracer then rapidly passes through the shunt tubing into either the peritoneal cavity or the right atrium. Subsequent views within the first hour should demonstrate a rapidly decreasing amount of tracer within the shunt reservoir and ventricles due to the unimpeded flow of CSF. Dispersal of the tracer within the peritoneal cavity should be observed in those patients with VP shunts.

Obstructed proximal shunt limb: If ventricular activity is not achieved after injection of the tracer into the reservoir while occluding the distal catheter, proximal obstruction is suspected. Supporting evidence for proximal catheter obstruction is the lack of decrease in activity within the reservoir throughout the study with some possible passage of tracer down the distal catheter. Occasionally, only antegrade obstruction of the proximal catheter is present. In this scenario, there is ventricular reflux of tracer during injection with delayed, persistent activity in the ventricle. Importantly, there should be activity in the distal catheter if it is patent.

Obstruction of distal shunt: This is shown by a lack of tracer flow into the peritoneum or right atrium and persistently increased activity in the distal catheter.

Localized accumulation of tracer into the abdomen associated with delayed clearance of activity from the tubing strongly suggests intraperitoneal loculation of CSF. If a high-pressure valve is present, there may be a delay in tracer clearance mimicking partial or total obstruction. Placing the patient in an upright position may improve the flow in these cases.

19.2.2 Intrathecal Pump-Catheter Patency Scintigraphy

An intrathecal drug infusion system may be implanted for the administration of intrathecal baclofen or opiates, such as morphine [2]. The pump is implanted subcutaneously

in the anterior abdominal wall with the tip of the catheter in the subarachnoid space in the thoracic or lumbar region. The drug infusion pump may malfunction when the drug flow becomes obstructed due to a catheter malfunction. The introduction of [¹¹¹In]DTPA into the drug infusion pump can be used to follow flow patterns of CSF by taking sequential pictures over a period of time [2]. The use of [¹¹¹In]DTPA is required (Figure 19.1). The study will identify whether the drug leaves the pump if CSF flow is obstructed as well as the location of obstruction or breakage. Only the use of [¹¹¹In]DTPA is approved for this indication. The longer half-life of [¹¹¹In]DTPA is also needed to allow delayed imaging as the flow rate of intrathecal pump-catheter systems is very slow in order to avoid central nervous system (CNS) toxicity (Table 19.2).

19.2.2.1 Radiopharmaceutical

[¹¹¹In]DTPA is approved for intrathecal administration and allows delayed imaging acquisition.

19.2.2.2 Indication

To ascertain the patency and integrity of the pump system and its pathway.

19.2.2.3 Interpretation Intrathecal Pump-Catheter Studies

Normal findings: The activity should be visualized diffusely throughout the subarachnoid space of the lumbar spine followed by ascension into the cerebral subarachnoid space. It is important to increase the intensity of the images due to the low count rate caused by the very slow infusion rate typically used in the pump-catheter systems.

Abnormal findings: Persistent activity is seen at the pump without evidence of intrathecal activity and/or ascending activity.

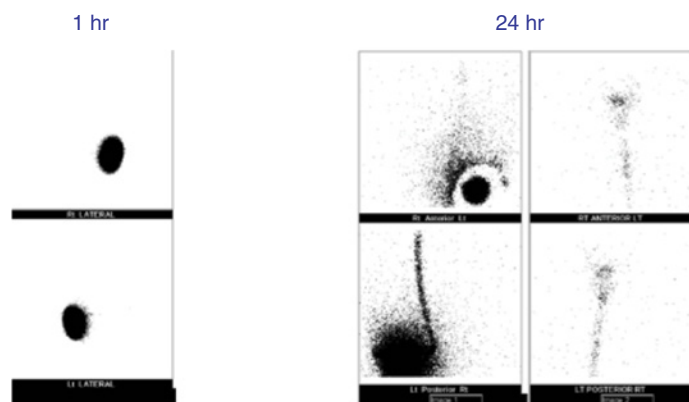


Figure 19.1 Patient example of intrathecal pump-catheter patency scintigraphy. Early (one-hour) images show expected uptake in the reservoir. No appreciable activity in the spinal subarachnoid space is seen at one hour due to the slow flow rate of the system. However, normal ascending spinal and basilar cisternal activity is seen at 24 hours post injection of [¹¹¹In]DTPA in the pump system reservoir.

Table 19.2 Summary of intrathecal pump-catheter patency scintigraphy.

Radiopharmaceutical; (adult) dose^a, route	Technique	Indication(s)	Main interpretation parameters (presence/absence)
[¹¹¹ In]DTPA, 1 mCi in implanted pump reservoir	Injection into implanted pump reservoir	Suspected mechanical obstruction	Flow dispersion/ascension into spinal and cerebral subarachnoid space

^aNeed to be adjusted for pediatric patients.

19.2.3 Radionuclide Cisternography (CSF Leak or Hydrocephalus) and Ventriculography Studies (Ommaya or Rickham Reservoirs for Chemotherapy)

The introduction of a non-irritating radiopharmaceutical into the subarachnoid space can be used to follow flow patterns of CSF by taking sequential pictures over a period of time [3]. This diagnostic procedure is based on the assumption that the radiopharmaceutical travels as a relatively compact bolus rather than diffusing generally throughout the CSF volume. This is a controversial topic, but it is generally believed that CSF imaging can give valuable information concerning CSF dynamics.

The normal adult has approximately 150 ml of CSF contained within the ventricular system and in the extracerebral cisterns and subarachnoid space. The normal rate of CSF production is 0.35 ml min⁻¹ and does not change appreciably with aging. Approximately 80% of the CSF is produced by the choroid plexus in the lateral, third, and fourth ventricles. Bulk movement of brain extracellular fluid into the ventricular system forms the remaining 20%. Several drugs and conditions may affect the rate of CSF secretion (see Table 19.3). Knowledge of these drugs and conditions is important for proper scan interpretation.

Table 19.3 Etiology of decreased vs. increased CSF production.

Decreased CSF production	Increased CSF production
<ul style="list-style-type: none"> • Drugs <ul style="list-style-type: none"> ◦ Cardiac glycosides ◦ Furosemide ◦ Acetazolamide ◦ Glucocorticoids • Conditions <ul style="list-style-type: none"> ◦ Increased intracranial pressure ◦ Hypothermia • Serum hypertonicity 	<ul style="list-style-type: none"> • Drugs <ul style="list-style-type: none"> ◦ Muscarinic stimulation ◦ Hyperthermia • Serum hypotonicity

Patients with leptomeningeal metastases have improved survival when treated with intra-ventricular chemotherapy via a reservoir [4, 5]. However, it has been reported that up to 47% of patients with a reservoir may have an unsuspected CSF block limiting the delivery of chemotherapy to affected sites [6]. This not only may result in a lack of therapeutic efficacy of blocked CNS sites but also increases the risk for neurotoxicity at the site of obstruction. Radiolabeled ventriculograms have been found useful to evaluate the presence of compartmentalization of the CSF system [7]. For example, [¹¹¹In]DTPA scintigraphy can help to differentiate between functioning and malfunctioning infusion systems, guiding appropriate medical or surgical management.

Radionuclide cisternograms can be used to detect CSF leaks or normal pressure hydrocephalus (NPH) [3, 8]. However, the use of radionuclide CSF leak studies has been declining due to its low sensitivity compared to computed tomography (CT) or MR contrast cisternography [3]. Similar declining use has been observed for radionuclide cisternography in the evaluation of hydrocephalus, in particular NPH. There are several reasons for this decline. First, the current concept of NPH as a single disease entity is surrounded by controversy in the neurological community, where it is being viewed as a syndromal manifestation of neurodegenerative disorders like Alzheimer's disease (AD) [9]. Second, there is no established standard of care for the diagnostic work-up of suspected NPH. Therefore, the use of radionuclide cisternography may depend on local practice preferences, where it may compete with procedures like temporary lumbar drain placement to increase the clinical prediction of possible therapeutic response of a definitive CSF shunt. Lastly, the therapeutic efficacy of shunt placement also depends on the duration of presenting symptoms, as there may be a short duration window of opportunity. Therefore, if there is a suspicion of an underlying neurodegenerative condition, alternative diagnostic approaches like fluorodeoxyglucose (FDG) PET may be considered [10]. Interestingly, at least in the relatively isolated syndromal phase of NPH isolated dorsal striatal (i.e. caudate nucleus and putamen), glucose hypometabolism in the setting of preserved cortical metabolism has been observed in "pure" NPH [11]

19.2.3.1 Radiopharmaceutical

[¹¹¹In]DTPA is approved for intrathecal use and also allows delayed imaging acquisition, which is a prerequisite for this type of scintigraphy studies. (Table 19.4).

19.2.3.2 Indications

Radionuclide CSF studies can be useful in:

- (1) The differential diagnosis and localization of CSF leaks
- (2) Evaluating patients suspected of having NPH
- (3) Verifying normal CSF distribution and clearance prior to intraventricular chemotherapy

Cisternography is relatively *contraindicated* in NPH when symptoms may be present for a longer duration or suspected neurodegenerative disorder. In such a scenario, a diagnostic work-up for neurodegeneration like FDG PET would be preferred.

Table 19.4 Radionuclide CSF ventriculography and cisternography studies.

Radiopharmaceutical(s); (adult) dose^a, route	Technique	Main indication(s)	Main interpretation parameters
[¹¹¹ In]DTPA, 1 mCi in implanted reservoir	Injection into implanted reservoir	Suspected ventricular or spinal thecal obstruction prior to giving intra-thecal chemotherapy	<ul style="list-style-type: none"> • Absence of ventricular or supratentorial subarachnoid dispersion • Absence or limited spinal thecal descent
[¹¹¹ In]DTPA, 1 mCi in lumbar subarachnoid space	Lumbar puncture injection	<ul style="list-style-type: none"> • Suspected NPH • Suspected CSF leak 	<ul style="list-style-type: none"> • Delayed CSF migration milestones • Ventricular reflux • Leak

^aNeed to be adjusted for pediatric patients.

19.2.3.3 Limitations

The main limitation of cisternography is in the failure to introduce the radiopharmaceutical into the lumbar subarachnoid space. This results in the non-visualization of activity in the intracranial CSF spaces. Although the correlation of “missed” injections with previous lumbar punctures has not been established, it seems prudent to avoid such procedures prior to radionuclide CSF studies if possible.

19.2.3.4 Interpretation

Radionuclide ventriculography: CSF is produced by the choroid plexuses in the lateral, third, and fourth ventricles and normally flows out of the ventricular system via the spinal canal into the thecal sac. This is followed by ascension into the spinal and subsequent intracranial subarachnoid space. From the level of the basilar cisterns, most of the flow of CSF proceeds in a cephalad fashion around the cerebral hemispheres, terminating at the level of the superior sagittal sinus where the major portion of CSF resorption occurs.

Other abnormal flow patterns that are especially important to note for intraventricular chemotherapy include delay in activity reaching the superior sagittal sinus, asymmetrical flow patterns, and blockage of flow at any level [12]. Occasionally, filling and trapping of the tracer within cysts or surgical defects are seen. It is important to also observe the normal pattern of flow down the spinal subarachnoid space to the level of the cauda equina to look for occult sites of subarachnoid blockage due to tumor. Data obtained from CSF ventriculograms from patients without obstruction yielded the following median CSF compartment appearance times (minutes): ventricular system 1 (0–5); basal cisterns/foramen magnum, 5–10 (5–15); cervical cord, 15 (5–20); thoracic cord, 20 (10–30); lumbar cord, 30 (25–50); and lateral cerebral convexity, 50 (35–90 minutes). It has been suggested that within one hour after reservoir administration, the basal cisterns should be clearly visible.

Radionuclide cisternography: The normal pattern of flow following a lumbar sub-arachnoid injection is for the tracer to migrate upward and reach the lumbar-thoracic subarachnoid space into one to two hours and the basilar cisterns within two to four hours. The activity then ascends symmetrically in front of and along the lateral aspects of both cerebral hemispheres to reach the superior sagittal sinus at approximately 24 hours. Resorption occurs slowly over the next several days. These times may be considerably shorter in children and somewhat longer in elderly patients. Abnormal flow patterns include prolonged entry of the tracer into the ventricles (*ventricular reflux*, Figure 19.2). This is a reversal of normal flow and is consistent with suspected NPH.

In the presence of a CSF leak involving the cribriform plate or paranasal sinuses, activity may be seen in the nasopharyngeal region. Activity may also be seen in the gut from swallowed CSF.

19.3 CBF IMAGING: PLANAR AND SPECT APPLICATIONS

Cerebral function is dependent on blood flow from the internal carotid and vertebral arteries for the supply of nutrients and the removal of metabolic by-products. The tracers [^{99m}Tc]hexamethylpropyleneamine oxime (**HMPAO**), also known as exametazime,

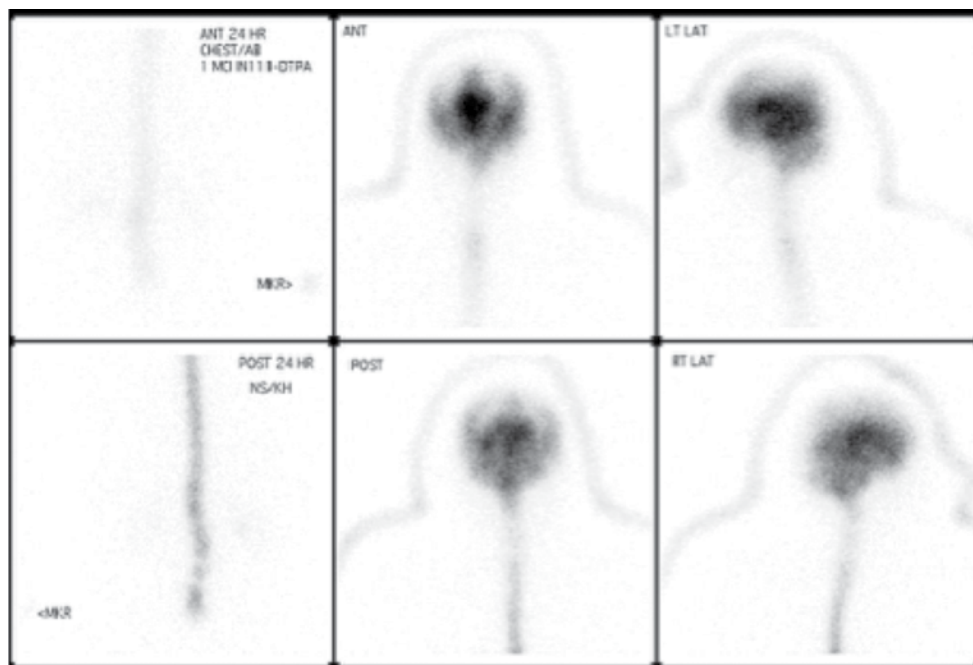


Figure 19.2
Example of ventricular reflux on 24-hour delayed planar [¹¹¹In]DTPA cisternography in a patient presenting with clinical symptoms consistent with syndromal NPH. Although there is mild radio-tracer activity at the subarachnoid lateral convexity, more prominent activity in the ventricles is seen. If additional confirmation is needed, a SPECT or SPECT-CT acquisition can be obtained.

and [^{99m}Tc]ethylcysteine dimer (**ECD**) are useful for determining regional CBF. In particular, these agents have high first-pass extraction fractions (approximately 4–6% of injected dose) and are sufficiently retained in the brain to allow the acquisition of SPECT images [13, 14]. HMPAO and ECD depict perfusion, and once extracted by the brain are converted to polar analogs that do not significantly demonstrate properties of redistribution. Anesthesia or sedatives can be given after HMPAO or ECD are injected to aid in reducing patient motion when needed. The major differences between the available agents HMPAO and ECD are listed in Table 19.5.

CBF imaging can be performed using planar vs. SPECT imaging techniques. The main current remaining clinical indication for planar CBF imaging is evaluating suspected brain death. CBF SPECT imaging was previously used for multiple indications, including assessment of cerebrovascular disease (stroke, vasospasm following subarachnoid hemorrhage, transient ischemic attack), traumatic brain injury, neurotoxicity syndromes, dementia, and epilepsy. However, the advent of MR perfusion and diffusion imaging is now the preferred imaging technique for cerebrovascular disease. Current remaining clinical indications for CBF SPECT are epilepsy, in particular subtraction techniques of interictal from ictal studies for localization of seizure foci and cognitive disorders. FDG PET has become the preferred imaging modality for the differential diagnosis of dementia due to its higher spatial resolution and diagnostic sensitivity compared to CBF SPECT [15]. However, CBF SPECT may still be used when FDG PET is not available or is not covered by the patient's medical insurance.

19.3.1 Brain Death Perfusion Study: Planar CBF Imaging

The main current clinical use of parenchymal CBF planar-flow imaging is for the assessment of suspected brain death. The advantage of planar imaging is that it can be performed at the patient's bedside using a wheeled camera. SPECT imaging may occasionally be performed when needed but generally is not necessary.

Table 19.5 Comparison of [^{99m}Tc]HMPAO and [^{99m}Tc]ECD parenchymal CBF tracers.

Ligand	[^{99m} Tc]HMPAO	[^{99m} Tc]ECD
Mechanism	A steric transformation of the HMPAO chelate linked to intracellular glutathione activity has been proposed. HMPAO is retained intracellularly by interaction of the lipophilic complex with glutathione.	ECD is transformed by intracellular esterases from a diester into a diacid complex. This polar metabolite does not cross the cell membrane and therefore is trapped in the neural cell.
Physiological correlate	Capillary flow and tissue perfusion	Tissue perfusion and a component of cellular metabolism.
Scalp uptake	Relatively more soft tissue scalp uptake that should be distinguished from grey matter uptake.	ECD is cleared more rapidly from the blood than HMPAO and has better brain-to-soft tissue activity ratios that continue to increase over time.

The brain is unique in its relationship to blood flow as the local energy reserves are small by comparison to the rate of cerebral metabolism. Thus, brain function is dramatically compromised by transient lack of perfusion, and loss of adequate flow for more than several minutes results in severe and irreversible injury. In the case of brain death, there is usually a secondary swelling of the necrotic cells due in part to the loss of cell wall integrity. This swelling is sufficient to increase intracranial pressure to the point where perfusion ceases. Thus, the absence of CBF in cases of suspected brain death is pathophysiologically expected and is incompatible with the recovery of cerebral function. The diagnosis of brain death can be made on clinical criteria alone, assuming preset physiological or clinical prerequisites are met [16]. If such clinical prerequisites are not met, then a brain death CBF study may be indicated. The absence of perfusion to both cerebrum and cerebellum supports the clinical diagnosis of brain death.

19.3.1.1 Radiopharmaceuticals

It is recommended that the study be performed with the use of [^{99m}Tc]HMPAO whenever possible. Angiographic phases of studies performed with this CNS parenchymal imaging agent are equivalent to the previously employed [^{99m}Tc]glucoheptonate. A key advantage of [^{99m}Tc]HMPAO is that it can be used for delayed imaging of the brain parenchyma rather than the limited and short transient visualization of the brain vasculature of [^{99m}Tc]glucoheptonate. Furthermore, delayed images with HMPAO are more sensitive for verifying the absence of posterior fossa perfusion, as lateral, oblique, or posterior images can be obtained. In circumstances where [^{99m}Tc]HMPAO cannot be employed (e.g. radiopharmaceutical kits are unavailable), [^{99m}Tc]glucoheptonate (or [^{99m}Tc]DTPA) angiographic phase imaging may be substituted. In addition, if there is doubt as to the interpretation or validity of the study, glucoheptonate imaging may be used in conjunction with (either preceding or following) HMPAO imaging. [^{99m}Tc]ECD is not appropriate for this determination because reduced tracer uptake may not fully represent CBF but also a component of neuronal metabolism.

19.3.1.2 Quality Control Requirements

The FDA-approved labeling for this radiopharmaceutical states that the radiochemical purity of the product must be determined prior to patient administration. The approved product labeling also indicates that radiochemical purity (i.e. % lipophilicity) greater than 80% is necessary for product use. Three potential radiochemical impurities may be present in the prepared injection of the lipophilic complex [^{99m}Tc]HMPAO. These impurities include a secondary, more hydrophilic complex of [^{99m}Tc]HMPAO, free pertechnetate, and reduced-hydrolyzed technetium.

The quality control results should be recorded by the technologist and should be reported in the results or dictated report by the scan interpreter. This is to avoid the risk that no brain activity could be argued as being secondary to poor quality of the tracer or late injection of a good-quality tracer. Therefore, the time after preparation of the kit to time of injection should also be recorded.

19.3.1.3 Limitations

The adequacy of the study depends on rapid and easy injection through a patent intravenous line. In addition, cardiogenic shock precludes interpretation; the study should not be performed when the systolic blood pressure is less than 60 mmHg. Due to the presence of life support equipment, the availability of multiple static views to evaluate delayed tracer retention in the cerebrum and cerebellum may be limited. However, anterior and lateral views should be obtained at a minimum. Pediatric evidence suggests that the lower limits of cerebral perfusion compatible with brain survival in the neonatal period may be substantially less than in the child or adult [17]. Blood-flow determinations for brain death evaluation in children should be performed only after direct contact with the consulting neurologist, and caution must be exercised in the interpretation of the study until further correlative data are available.

The reduced entry of HMPAO into the brain can be the result of injecting beyond 30 minutes after preparation of the tracer; therefore, documentation of the quality control and time between kit preparation and tracer injection is very important.

19.3.1.4 Indication

To provide supportive evidence for the clinical diagnosis of brain death. The diagnosis of brain death is usually established by neurologic or neurosurgical consultation, in accordance with the current local hospital or professional society guidelines for the assessment of brain death. The nuclear medicine CBF study is one of several ancillary tests that may be utilized for confirmation of the clinical diagnosis of brain death. Therefore, the procedure represents a test to *confirm the clinical suspicion of brain death*. This procedure alone does not establish the diagnosis of brain death. Scan interpreters should familiarize themselves with local or national guidelines and policies in the legal definition of brain death that may differ between different jurisdictions.

19.3.1.5 Interpretation

Normal findings angiographic phase ($[^{99m}\text{Tc}]$ glucoheptonate, $[^{99m}\text{Tc}]$ DTPA, or $[^{99m}\text{Tc}]$ HMPAO): Normal CBF is recognized by prompt filling of the internal carotid arteries and major vessels of the cerebrum (anterior and middle cerebral arteries). The sagittal sinus is additionally visualized in the venous phase due to normal incomplete cerebral extraction of HMPAO.

Normal findings parenchymal tissue uptake ($[^{99m}\text{Tc}]$ HMPAO): Within minutes after injection, the parenchymal cerebrum and cerebellum are clearly identified.

Abnormal findings angiographic phase ($[^{99m}\text{Tc}]$ glucoheptonate or $[^{99m}\text{Tc}]$ HMPAO): Arrest of blood flow to the brain and resultant brain death is characterized by visualization of the internal carotid circulation to the level of the base of the skull but lack of visualization of the cerebral circulation and brain parenchyma.

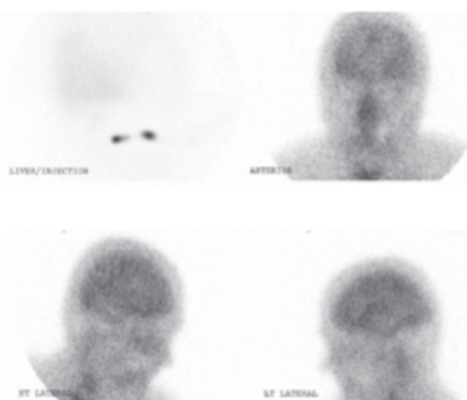
Abnormal findings parenchymal tissue uptake ($[^{99m}\text{Tc}]$ HMPAO): Complete or partial lack of visualization of the brain parenchyma. It should be noted that cerebro-cerebellar

dissociation (i.e. absence of posterior circulation while the anterior circulation remains intact) biologically may represent brainstem death but is not legally accepted as brain death (i.e. absence of total supratentorial anterior and posterior cerebral circulation). Parotid gland HMPAO tracer uptake should not be confused for brainstem uptake on lateral images. Posterior or oblique images may be needed for clarification (Figure 19.3; Table 19.6).

19.3.2 Regional CBF SPECT in ictal and Interictal Epilepsy Imaging

Epileptic syndromes are classified into generalized and partial types of seizures. Primary generalized epilepsy is associated with diffuse and bilateral epileptiform discharges on

(a) Day 1.



(b) Day 2.

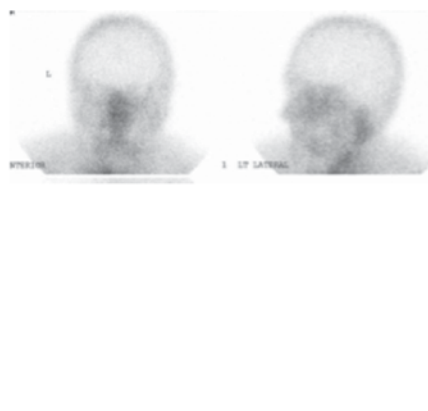


Figure 19.3 Patient example of a bedside ^{99m}Tc HMPAO cerebral CBF study in a patient with an absence of brainstem reflexes on life support and clinically suspected brain death. (a) It shows an absence of posterior fossa perfusion, providing an explanation for the absence of brainstem reflexes. Supratentorial flow was present. Findings indicate a prognosis that is incompatible with non-supported survival. A one-day follow-up study (b) shows an absence of both supratentorial and infratentorial perfusion that supported the clinical diagnosis of brain death.

Radiopharmaceutical(s); (adult) dose, route	Technique	Indication	Main interpretation parameter (presence/absence)
^{99m}Tc glucoheptonate or ^{99m}Tc DTPA, 15–25 mCi, i.v.	Peripheral i.v. injection	Suspected brain death	Intracranial flow
^{99m}Tc HMPAO, 20–30 mCi, i.v.	Peripheral i.v. injection	Suspected brain death	Intracranial flow and parenchymal uptake

Table 19.6 Summary of planar CBF scintigraphy for the assessment of brain death.

an electroencephalogram EEG without evidence for focal brain lesions. Partial epilepsy (i.e. localization-related epilepsy) is thought to arise from a focal gray matter lesion. Partial-onset seizures may remain partial or may secondarily generalize. Medically refractory epilepsy is defined by seizure syndromes that are not effectively controlled by anti-epileptic drugs. The management of medically refractory partial epilepsy has been revolutionized by neurosurgical techniques aimed at the resection of the epileptogenic brain focus. Therefore, precise seizure localization is the prime goal of presurgical work-up in partial epilepsy. Functional neuroimaging is based on an old association of increased regional CBF with seizures (ictal) and an interictal decrease in perfusion [18]. Partial seizures with or without secondary generalization are associated with focal areas of reduced CBF and glucose metabolism at or near the seizure focus during the interictal period and with dramatic increases in glucose metabolism and perfusion in the focus and its anatomic and functional projections during the ictal phase [19]. Interictal imaging of glucose metabolism with FDG PET is more widely established and of greater sensitivity and specificity than interictal SPECT perfusion imaging for evaluating refractory focal epilepsy. However, PET is not regularly available due to restrictions on its reimbursement by major insurers. In cases of temporal lobe epilepsy, the zone of reduced perfusion interictally may involve the mesial or lateral temporal structures or both. In some cases, interictal hypoperfusion or decreased glucose metabolism may extend outside of the temporal regions, involving large areas of adjacent frontal or parietal cortex or the ipsilateral thalamus. These remote areas of hypoperfusion are felt to be part of a network effect. Some cases of complex-partial epilepsy associated with epileptogenic foci in the orbitofrontal cortex may have associated frontal hypoperfusion. In interpreting SPECT perfusion patterns in refractory epilepsy, it is crucial to compare ictal and interictal scans [20–23]. Areas of increased CBF on the ictal scan that are either normal or hypoperfused on interictal images are related either to the focus or to its propagation pathway. Advanced 3D subtraction techniques are superior to visual comparison of the ictal and inter-ictal scans.

19.3.2.1 Radiopharmaceuticals

The tracers [^{99m}Tc]HMPAO and [^{99m}Tc]ECD are also useful for determining regional CBF changes during interictal and ictal states in patients with medically refractory epilepsy (Figure 19.4). The advantage of these tracers for ictal seizure localization is due to their intraneuronal “trapping,” allowing delayed imaging acquisition. [^{99m}Tc]ECD, however, is the preferred ligand due to less scalp soft tissue uptake compared to [^{99m}Tc]HMPAO. It should be noted that [^{99m}Tc]ECD brain studies may show regional variations in ECD clearance with time (higher for the occipital lobe –6.34% per hour, while lower for white matter –2.39% per hour, and thalamus –2.45% per hour [24]). To avoid the “washout effect” with ECD, the acquisition of ictal and interictal data should occur at the same time post-injection in both studies (Table 19.7).

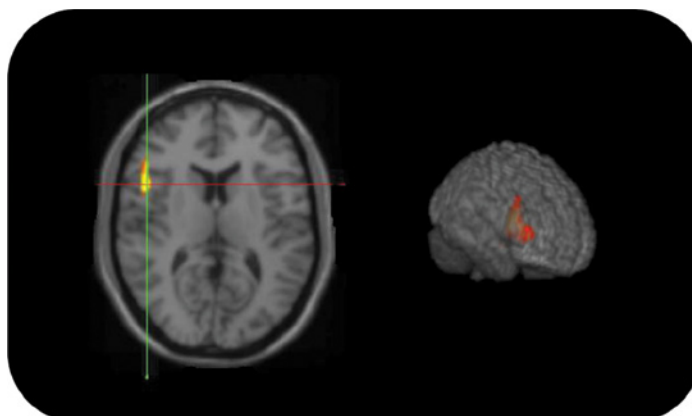


Figure 19.4
Example of ictal-interictal SPECT subtraction coregistered with MRI. A right opercular-insular ictal focus is seen on transaxial slices (a) and anatomic 3D rendering (b).

Table 19.7 Summary of SPECT CBF scintigraphy for seizure localization.

Radiopharmaceutical(s); (adult) dose, route	Technique	Indication	Main interpretation parameter
[^{99m} Tc]ECD, 20–30 mCi, i.v.	Peripheral i.v. injection ictally and interictally	Seizure localization	Ictal minus interictal subtraction with anatomic (MR) registration
[^{99m} Tc]HMPAO, 20–30 mCi, i.v.	Peripheral i.v. injection ictally and interictally	Seizure localization	Ictal minus interictal subtraction with anatomic (MR) registration

19.3.2.2 Patient Preparation

The timing of the injection is essential and should occur as soon as possible after seizure onset for ictal image acquisitions. Anesthesia or sedation can be given to reduce patient motion artifacts in imaging cerebral perfusion. It should be administered at least five minutes following the injection of [^{99m}Tc]HMPAO or [^{99m}Tc]ECD.

19.3.2.3 Interpretation

An automated subtraction program (ictal minus inter-ictal study) and co-registration with magnetic resonance imaging (**MRI**) or CT scan is indispensable for the accurate localization of the seizure onset zone [25]. Visual comparison of interictal and ictal studies is suboptimal and may lead to false-positive or false-negative results. Interpreting and performing ictal regional CBF SPECT studies is challenging as there may be multiple areas of hyperperfusion due to seizure propagation or delayed injections, which may also in some cases be post-ictal (*hyper- to hypoperfusion switch*) [26]. Scan findings should be correlated with the clinical history, recent structural imaging results (MRI or X-ray CT), and EEG results in cases of refractory epilepsy. Digital co-registration of functional imaging data with structural imaging data (MRI, CT) is preferred for interpretation if available.

19.3.3 CBF SPECT in Dementia

Regional CBF SPECT imaging can be used for the differential diagnosis of dementias [15, 27–29]. Several characteristic patterns of abnormal regional perfusion are recognized in the degenerative dementias and are summarized here:

- *Alzheimer's disease*: Relative reduction in perfusion in the posterior cingulate cortex, posterior parietal, or parieto-temporal regions bilaterally, while there is relative preservation of primary visual and sensorimotor cortices and subcortical gray matter (basal ganglia, thalamus, cerebellum activity). Frontal lobe reductions are more variable.
- *Parkinsonian dementia (dementia with Lewy bodies [DLB] or Parkinson's disease with dementia [PDD])*: Similar features can be seen as in Alzheimer's disease with evidence of additional but variable occipital hypoperfusion.
- *Frontotemporal lobar degenerations*: Reduced perfusion in the frontal cortex, anterior cingulum, anterior temporal, and mesiotemporal areas more severely than parietal and lateral temporal cortices or the posterior cingulum.

19.3.3.1 Radiopharmaceuticals

The tracers [^{99m}Tc]HMPAO and [^{99m}Tc]ECD are useful for determining regional CBF changes in neurodegenerative disorders. Generally, perfusion changes parallel glucose metabolic changes in neurodegeneration (Tables 19.8 and 19.10).

19.3.3.2 Patient Preparation

Injections should occur under resting conditions with the patient abstaining from talking, moving, or other behavioral activities. Anesthesia or sedation can be given to reduce patient motion artifacts in imaging cerebral perfusion. It should be administered at least five minutes following the injection of HMPAO or ECD to the awake patient so that tracer distribution is not significantly affected.

19.3.3.3 Interpretation

Recognition of disease-specific patterns of regionally reduced vs. relatively preserved perfusion changes. Scan findings should be correlated with the clinical history and recent

Table 19.8 Summary of SPECT CBF scintigraphy for differential diagnosis of neurodegenerative disorders.

Radiopharmaceutical(s); (adult) dose, route	Technique	Indication	Main interpretation parameters
[^{99m} Tc]ECD, 20–30 mCi, i.v.	Peripheral i.v. injection under resting conditions	Assessment of neurodegenerative disorder(s)	Disease-specific patterns of reduced vs. relatively preserved perfusion
[^{99m} Tc]HMPAO, 20–30 mCi, i.v.	Peripheral i.v. injection under resting conditions	Assessment of neurodegenerative disorders	Disease-specific patterns of reduced vs. relatively preserved perfusion

structural imaging results (MRI or X-ray CT). Digital co-registration of functional imaging data with structural imaging data (MRI, CT) is preferred for interpretation if available.

Qualitative interpretation involves comparison with the contralateral hemisphere and/or observations of obvious diminution of tracer uptake in the brain. Regions of tracer uptake diminution should be localized in comparison with structural imaging studies whenever possible. The normal pattern of regional cerebral perfusion resembles the distribution of gray matter due to the three- to four-fold higher metabolism and perfusion of neurophil and neurons (gray matter constituents) as compared to myelinated axons (white matter).

Statistical comparison of an individual study with a pre-existing database will improve diagnostic assessment and should be performed. This will require additional data processing for anatomic standardization and normalization [30, 31].

19.3.3.4 Limitations

CBF SPECT imaging can provide supportive evidence for a clinical diagnosis of a neurodegenerative condition but cannot be used as a stand-alone diagnostic entity. Occasionally, conditions like alcoholism and auto-immune encephalitis may have regional CBF patterns that mimic those of typical neurodegenerative entities [32].

19.4 DOPAMINE TRANSPORTER SPECT IMAGING

Several specialized neurochemical features are expressed by presynaptic dopaminergic nerve terminals in the mammalian CNS. These include metabolic enzymes for the production of dopamine (DA) as well as transporters for the vesicular storage of DA and for reuptake of DA from the synapse. The dopamine plasmalemmal reuptake transporter (DAT) is targeted by several cocaine-analog radiotracers, and among these, [¹²³I]ioflupane is approved by the FDA for clinical nigrostriatal presynaptic nerve terminal imaging.

19.4.1.1 Radiopharmaceutical

[¹²³I]ioflupane interacts reversibly with the DAT, binding to and inhibiting its function at pharmacologic doses. At tracer mass dosages, [¹²³I]ioflupane binding to the DAT can be imaged with SPECT and used to detect nigrostriatal lesions with no pharmacological effect [33]. Different names for [¹²³I]ioflupane but the same molecule are:

- *N*-ω-fluoropropyl-2β-carbomethoxy-3β-(4-[¹²³I]siodophenyl)nortropane
- [¹²³I]FP-CIT
- DaTscan (US)
- DaTSCAN (Europe)

19.4.1.2 Indications

DAT SPECT imaging is indicated to distinguish tremor due to conditions with nigrostriatal degeneration from those with similar clinical presentations, but with intact projections.

Available data indicate that DAT imaging is not reliable to distinguish among specific degenerations with nigrostriatal damage. For example, striatal DAT reductions are present in several primary extrapyramidal movement disorders, including:

- a. Idiopathic Parkinson's disease
- b. Progressive supranuclear palsy
- c. Multiple system atrophy
- d. Corticobasal syndrome
- e. Dementia with Lewy bodies

In contrast, nigrostriatal projections are relatively preserved in:

- a. Postural and kinetic tremor syndromes (essential, orthostatic, and dystonic tremors)
- b. Psychogenic parkinsonism
- c. Drug-induced parkinsonism
- d. DOPA-responsive dystonia
- e. Alzheimer's disease
- f. Pure vascular parkinsonism (unless stroke affects the nigrostriatal pathway or basal ganglia, resulting in more focal deficits).

DAT SPECT imaging is also approved for the differential diagnosis of DLB from prototypical Alzheimer's disease in Europe.

19.4.1.3 Patient Preparation

The patient's medication or drug intake regimen should be carefully checked for drugs that may interfere with DAT expression [33], such as

- Cocaine
- Amphetamines (D-amphetamine, methamphetamine, methylphenidate)
- Modafinil
- Mazindol (tetracyclic), bupropion
- Adrenergic agonists (phenylephrine, phenylpropranolamine, norephedrine, phentermine)
- Anticholinergic drugs (benztropine)
- Opioids: Fentanyl
- Anesthetics: Ketamine, PCP, isoflurane
- Note carbidopa-levodopa (Sinemet), which may have mild effects but is not a significant issue for qualitative image interpretations

Note that carbidopa-levodopa can be concurrently used and does not significantly affect qualitative image interpretation. DA agonists or neuroleptics are allowed.

Low-dose serotonin-selective reuptake blockers are allowed when image interpretation is qualitative. However, these drugs may affect radioligand binding in reference regions when using quantitative assessment.

19.4.1.4 Interpretation

The normal pattern of DAT distribution in SPECT images shows intense uptake in the head of the caudate nucleus and in the putamen. There should be interhemispheric symmetry of the scan and clear delineation of the putamen compared to the cerebral cortex. Most parkinsonian neurodegenerations affect the putamen earlier and more severely than the caudate, and interhemispheric asymmetry is often present, especially in early Parkinson's disease. Semi-quantitative assessment using occipital or cerebellar reference region may be helpful but will need to be validated for local practice on the department's own camera.

19.4.1.5 Limitations

The main limitation of DAT SPECT imaging is that multiple diseases can have the same DAT imaging pattern – the study can classify individual patients but does not alone result in a specific diagnosis. Current interpretation approaches focus on abnormal patterns of DAT binding in the striatum; however, there may be an advantage in quantitative analyses of the binding. The normal expression of DAT binding is age- and gender-dependent; therefore, the application of quantitative image analyses should be based on appropriate age- and gender-stratified normative data. Finally, several medications can influence the appearance of DAT images, either through direct interaction with the DAT binding site or through interactions with other binding sites in reference regions (see the earlier patient preparation) (Table 19.9).

19.5 GLUCOSE METABOLIC PET IMAGING

[¹⁸F]fluorodeoxyglucose (FDG) PET has largely replaced the use of CBF SPECT in neuro-nuclear medicine due to its superior spatial resolution, more robust imaging acquisition, and physiological principle of coupling between perfusion and metabolism.

Table 19.9 Summary of presynaptic nigrostriatal nerve terminal SPECT imaging.

Radiopharmaceutical(s) (adult) dose, route	Technique	Indication	Main interpretation parameters
[¹²³ I]Ioflupane, 5 mCi, i.v.	Peripheral i.v. injection	Evaluating patients with tremors vs. parkinsonian syndromes (US); additional indication of differential diagnosis of prototypical AD vs. DLB (Europe).	Decreased uptake in the basal ganglia; usually asymmetric: worse on the side contralateral to clinical symptoms; uptake inversely proportional to disease severity.

19.5.1 Indications

The primary intent of the first human research PET scan using [¹⁸F]FDG in 1976 was for brain imaging [34]. Despite its initially intended use for brain imaging, subsequent clinical use of FDG has been dominated by oncological applications. FDG PET has been approved for evaluation of seizure foci in epilepsy and differential diagnosis of brain tumor recurrence vs. radionecrosis. Despite the large body of research literature on FDG PET and dementia, there is no current FDG approval for its use in the differential diagnosis of dementia. In the US, however, there is limited insurance coverage for the use of FDG PET to distinguish Alzheimer's disease from frontotemporal dementia (FTD).

19.5.2 Patient Preparation

Patients should fast for four to six hours prior to the study to reduce blood glucose levels and enhance uptake of FDG by the brain. Diabetic patients may be studied but should have documentation of reasonable blood sugar control prior to the injection of FDG. In addition, the patient must cooperate with scan acquisition for periods of about 15 minutes. In some instances, this may require sedation following the phase of FDG uptake and incorporation.

19.5.3 Interpretation (General Approach)

The normal pattern of regional cerebral glucose utilization resembles the distribution of gray matter due to the four- to five-fold higher metabolic rate of neurophil and neurons (gray matter constituents) as compared to myelinated axons (white matter). Several specific patterns of abnormal regional glucose metabolism are recognized and are summarized in Table 19.9 according to the scan indications. In all instances, an attempt should be made to correlate the scan findings with the clinical history, recent structural imaging results (MRI or CT), and EEG results in cases of refractory epilepsy. Digital co-registration of functional imaging data with structural imaging data (MRI, CT) is preferred for interpretation if available. Statistical comparison of an individual study with a normative database has now become routine in the neuro-nuclear medicine clinic. This will require additional data processing for anatomic standardization and normalization [31] (Tables 19.10 and 19.11).

19.5.4 FDG PET in the Work-up of Cognitive Decline and Dementia

The topography of regional decreased vs. relative preserved glucose metabolic changes in dementia and other neurodegenerative disorders is essentially the same (Figure 19.5), as discussed earlier under CBF SPECT. Table 19.11 provides a simplified interpretation schema FDG PET (or CBF SPECT) for the differential diagnosis of cognitive and dementing disorders.

Table 19.10 Summary overview of [¹⁸F]FDG PET for routine clinical use in neuro-nuclear medicine.

Radiopharmaceutical; (adult) dose, route	Technique	Indication(s)	Main interpretation parameters
[¹⁸ F]FDG, 5–10 mCi, i.v. adult dose	i.v. injection followed by delayed 60 min imaging. Patient is injected while sitting quietly in a dimly lit room with eyes open; obtain a blood sample for determination of plasma glucose before injection. Placement of EEG leads may be useful in patients with epilepsy.	<ul style="list-style-type: none"> • Localization of seizure focus • Differential diagnosis of tumor recurrence vs. radionecrosis • Differential diagnosis of dementia (Alzheimer’s disease vs. FTD) 	<ul style="list-style-type: none"> • Seizure focus: focal photopenia (inter-ictal) vs. focal increase (ictal) • Abnormal FDG uptake within tumor region (tumor recurrence) vs. absence of uptake (radionecrosis) • Neurodegeneration: specific topography of decreased vs. relatively preserved metabolism (see Table 19.11).

A comprehensive review of the FDG PET literature showed that the evidence for [¹⁸F]FDG PET in the assessment of dementia supports the role of [¹⁸F]FDG PET as an effective and useful adjunct to other diagnostic information in the assessment of patients with symptoms of dementia [38]. Findings are in line with revised diagnostic criteria of Alzheimer’s disease that, for the first time, recognize the unique role of biomarker evidence in disease definition [39].

19.5.4.1 Limitations

FDG PET has several limitations that may relate to a lack of sensitivity in (very) early disease. Typically, glucose metabolic changes emerge at the time of symptomatic cognitive impairment along the spectrum of Alzheimer’s disease [40]. Although FDG PET is clinically reimbursed to aid with the differential diagnosis of Alzheimer’s disease vs. FTD, a subset of patients have an FDG pattern consistent with a frontal variant of FTD but also have evidence of amyloid plaques on β -amyloid PET suggestive of a frontal variant of Alzheimer’s disease [41, 42].

19.5.5 FDG PET in Movement Disorders

FDG PET has shown clinical utility in evaluating patients with movement disorders, in particular atypical parkinsonisms [43]. FDG PET was clinically more useful than DA type 2 receptor SPECT imaging in a head-to-head comparison [43].

The following disease-specific topographic profiles of reduced vs. relatively preserved glucose metabolism have been observed:

Table 19.11 Simplified interpretation schema of FDG PET or CBF SPECT for the differential diagnosis of cognitive and dementing disorders.

	MCI. Mild Cognitive impairment (amnesic type)	Alzheimer's disease	Posterior cortical atrophy	Dementia with Lewy bodies	Frontotempo- ral dementia
Bilateral posterior parietal-temporal	Preserved	↓	↓	↓	Preserved
Posterior cingulate	↓	↓	↓	↓	Preserved
Mid-cingulate island sign	[-]	[-]	[-]	[+]	[-]
Anterior cingulate	Preserved	Preserved	Preserved	Variable	↓
Frontal lobe	Preserved	Mild ↓ (more with advanced disease)	Preserved	↓ (more with advanced disease)	↓
Anterior temporal lobe	Preserved	Relatively preserved	Preserved	Variable	↓
Basal ganglia	Preserved	Preserved	Preserved	↓ (caudate)	Variable ↓ to preserved
Thalamus	Preserved	Preserved	Preserved	Variable	Preserved
Primary sensorimotor cortex	Preserved	Preserved	Preserved	Preserved	Variable to preserved
Primary and associative visual cortex	Preserved	Preserved	↓Associative, primary visual cortex relatively preserved.	↓Primary ± associative cortex	Preserved
Hippocampus ^a	↓	↓ esp. if more severe	↓ esp. if more severe	Mild ↓	↓

Posterior cortical atrophy is a variant of Alzheimer's disease with more prominent visuospatial and higher-order visual processing changes.

^aAccurate assessment of hippocampal glucose metabolism is best achieved with statistical parametric mapping and/or quantitative assessment. Visual assessment may be limited to identify hippocampal metabolic impairment because it exhibits a lower resting metabolism than the neocortex. However, MRI-based volume of interest (VOI) sampling indicates significant reductions in AD [35–37]. Sources: Clerici, F., Del Sole, A., Chiti, A. et al. [35].; Mosconi, L., De Santi, S., Li, J. et al. [36]. and Mosconi, L., Tsui, W.H., De Santi, S. et al. [37].

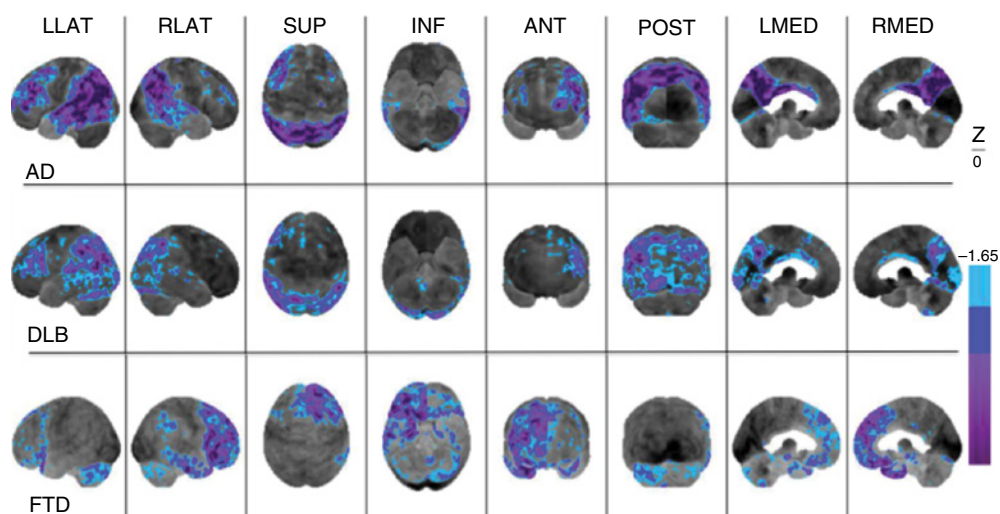


Figure 19.5 Typical regional cerebral [^{18}F]FDG hypometabolism patterns in AD, DLB, and frontotemporal dementia (FTD). Patterns are presented as z score maps based on significantly hypometabolic voxels relative to a normal control database (minimum shown cut-off is z of -1.65). LLAT, left lateral; RLAT, right lateral; SUP, superior; INF, inferior; ANT, anterior; POST, posterior; LMED, left medial; RMED, right medial surface views.

- *Progressive supranuclear palsy*: Reductions in the prefrontal cortex, mid-cingulum, mid-brain, and, to a variable extent, basal ganglia [43].
- *Multiple system atrophy of the cerebellar type (MSA-C)*: Reduced activity in the cerebellar hemispheres, vermis, and pons [39].
- *Multiple system atrophy of the parkinsonian type (MSA-P)*: Reduced activity in the putamen [39].
- *Corticobasal syndrome*: Asymmetric reduced activity in the peri-central (parieto-frontal) cortices and thalamo-striatal subcortical regions [44].
- *Huntington's disease*: Bilateral reductions within the head of the caudate nucleus (more than the putamen) [44].
- *Idiopathic Parkinson's disease without dementia*: Relatively isolated occipital glucose hypometabolism [45]. Relative preservation of striatal metabolism.
- *PDD or DLB*: Similar topographic as Alzheimer's disease but with additional evidence of occipital glucose hypometabolism [46].

Metabolic covariance analysis of FDG PET has provided disease-specific quantitative "network" markers for a number of movement disorders that also allow differential diagnostics between the different parkinsonian disorders [47].

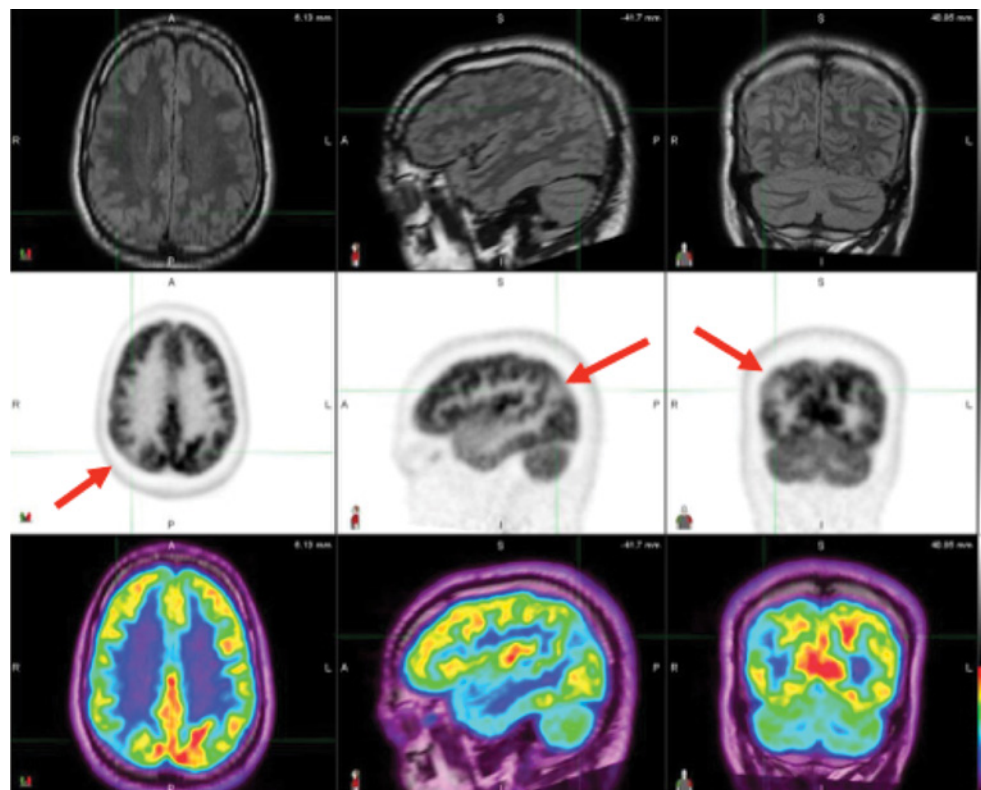
19.5.6 FDG PET in Refractory Epilepsy

The CBF SPECT section provides a more detailed overview of epilepsy and topographic assessment of seizure foci. Similar to CBF SPECT, partial seizures with or without secondary generalization are associated with focal areas of reduced glucose metabolism at or near the seizure focus during the interictal period [48, 49]. An example of focal cortical glucose hypometabolism in a patient with localization-related epilepsy is shown in Figure 19.6. Ictal FDG PET is technically possible but not practical, and its use has been generally limited to patients with very frequent and/or predictable seizures [50]. Therefore, the current clinical practice of ictal minus interictal subtraction is mainly based on CBF SPECT, as discussed earlier.

19.5.7 FDG PET in Brain Tumors

Gliomas can be categorized into different pathologic subtypes. In addition to the pathologic type, World Health Organization classifications also provide histologic grades based on cellular alterations related to cancer aggressiveness. Grades I and II are considered low-grade tumors that have a prolonged clinical course. Grades III and IV tumors are considered high-grade lesions that rapidly lead to death when left untreated [51].

Figure 19.6 Patient example of focal glucose hypometabolism as an interictal expression of a seizure disorder. MRI (upper row), FDG PET (middle row), and fused images (lower row) show focal right parietal cortical hypometabolism (red) arrow corresponding to gyral abnormality on MRI in a patient with lesional focal epilepsy.



The apparent metabolic rate in gliomas is related to the histologic degree of malignancy. Low-grade astrocytoma is associated with metabolic rates less than or equal to those in normal gray matter. In some instances, the metabolic rate may be similar to that of normal white matter. In contrast, the apparent glucose metabolic rate associated with higher-grade malignant astrocytoma is frequently greater than that in normal gray matter. The metabolic rate in regions of necrosis following radiation or chemotherapy is less than normal gray matter and frequently less than normal white matter.

19.5.7.1 Interpretation

The presence of regions of high metabolic rate in cases of glioma is predictive of high-grade primary or recurrent/residual tumor [52, 53]. A low metabolic rate in the region of abnormality does not reliably exclude residual tumor but may favor a lower histologic grade (Figures 19.7 and 19.8).

19.5.7.2 Limitations

A major limitation of FDG PET for the assessment of brain tumors is poor target-to-background ratio because of prominent physiological glucose metabolism of the normal gray matter. Therefore, if FDG PET is used for this purpose, careful registration with MRI would be useful for more precise anatomic delineation.

19.6 β -AMYLOID PET IMAGING

Advances in PET radiochemistry now allow visualization of specific proteinopathies in neurodegenerative disorders (Figure 19.9). The two major proteinopathies in Alzheimer disease are (i) β -amyloid and (ii) tau neurofibrillary tangles (**NFTs**). Neuropathological demonstration of these proteinopathies forms the basis for a definite diagnosis of Alzheimer disorder, which is typically made *postmortem*. Consequently, clinicians can

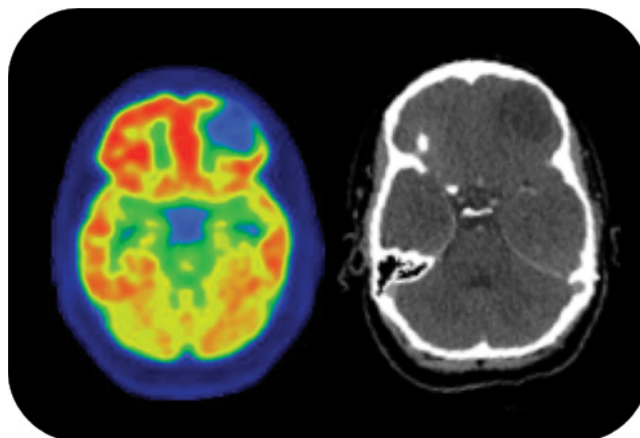


Figure 19.7
Example of FDG PET (a) in a patient with a low-grade neoplasm showing as a large photopenic lesion in the left orbitofrontal region, difficult to delineate on CT (b). MRI not done because of cochlear implants.

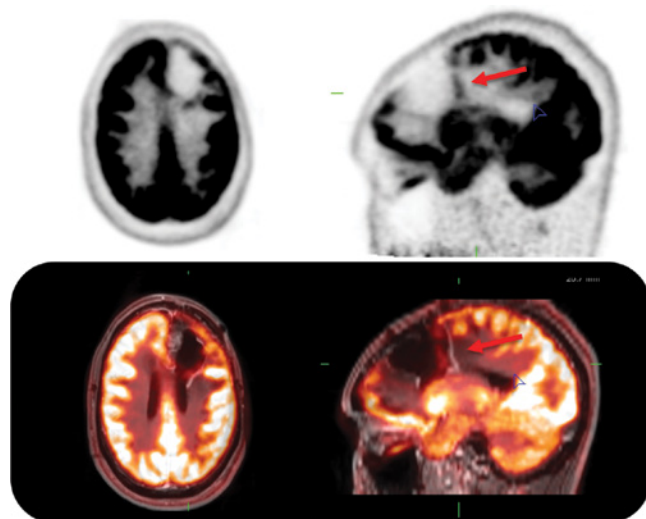


Figure 19.8 Example of FDG PET in a patient. Status: post left frontal lobe brain tumor resection and radiation therapy, showing a large photopenic defect with a rim of uptake corresponding to an area of contrast enhancement on corresponding fused PET and MRI images consistent with recurrent tumor (red arrow) and not radiation necrosis.

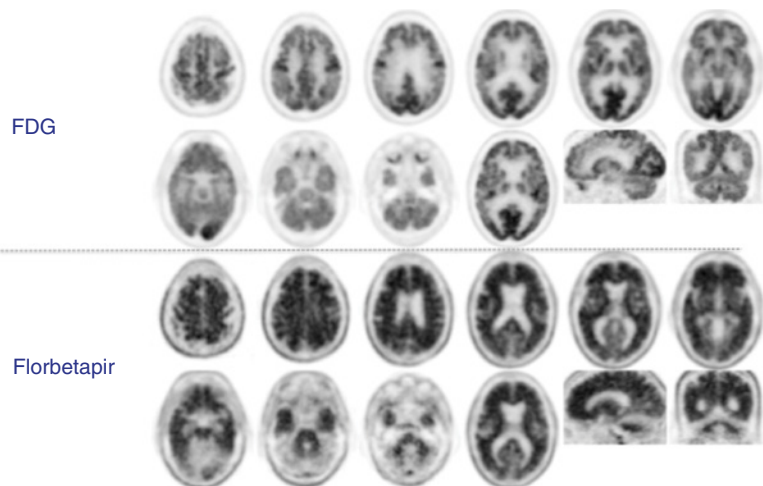


Figure 19.9 Example of abnormal FDG and florbetapir β -amyloid PET scans in a patient with severe dementia of the Alzheimer type. The two upper rows depict the typical glucose metabolic signature of severe Alzheimer's disease, i.e. glucose hypometabolism in the posterior more than anterior association cortices in conjunction with relative metabolic preservation of the primary sensorimotor and visual cortices and subcortical gray matter. The florbetapir β -amyloid PET scan (lower two rows) shows abnormal uptake in the gray matter consistent with evidence of moderate to severe plaques. Source: Images courtesy of Dr. Robert Koeppe.

make an *in vivo* diagnosis of possible or probable Alzheimer's disease at best using clinical criteria alone with information from disease-specific biomarkers. For example, according to the previously used National Institute of Neurological and Communicative Disorders and Stroke and the Alzheimer's Disease and Related Disorders Association (NINCDS–ADRDA) criteria of 1984, a clinical probable AD diagnosis would involve impairment of cognitive function in at least two domains with a decline severe enough to interfere with daily function and independence, age of onset 40–90 years, and absence of other diseases capable of producing a dementia syndrome [54].

Unlike most of medicine practiced in the pathobiological era, the clinical diagnosis has been one of exclusion rather than the typical inclusion diagnostic paradigm. Consequently, a diagnosis of possible or probable Alzheimer's disease would be made after excluding structural causes of brain damage on anatomic CT or MR brain scans and clinical exclusions of metabolic, inflammatory, infectious, vascular, neoplastic, or other laboratory abnormalities.

More recently, the diagnostic field of AD, at least at the research level, is shifting toward incorporation of biomarkers of the AD pathophysiological process: (i) β -amyloid PET, (ii) FDG PET, and (iii) CSF protein signatures [55, 56]. This novel diagnostic inclusion approach opens up the possibility to identify evidence of the AD process in the prodromal and even asymptomatic stages [56].

High β -amyloid PET tracer retention or low CSF $A\beta_{1-42}$ may allow the research definition of *asymptomatic* amyloidosis (stage 1 AD) [56]. Stage 2 would be defined as evidence of amyloidosis and neurodegeneration. Neuronal dysfunction could be assessed based on FDG PET regional glucose hypometabolism or high CSF tau/phospho-tau level as well as evidence of cortical thinning and/or hippocampal atrophy on MR imaging. Finally, stage 3 would encompass both the presence of amyloidosis, neurodegeneration, and evidence of subtle cognitive decline that would be evidenced by the presence of a subtle change from the baseline level of cognition, poor performance on more challenging cognitive tests, but not yet meeting the criteria for mild cognitive impairment. Stage 3 would precede the typical cognitively symptomatic stages of mild cognitive impairment and dementia in AD [56]. Radioligands to assess for β -amyloidopathy are described in (Tables 19.12 and 19.13).

19.6.1 Indication

To estimate β -amyloid neuritic plaque density in adult patients who are being evaluated for AD or other causes of cognitive decline. At present, there is no approved indication to predict the development of dementia or other neurological condition or monitor response to treatment.

19.6.2 Interpretation

Normal – A negative scan indicates sparse to no amyloid neuritic plaques and would be inconsistent with a neuropathological diagnosis of AD at the time of the scan.

Table 19.12 Comparison of currently FDA-approved radioligands to assess for β -amyloidopathy.

	[¹⁸F]florbetapir	[¹⁸F]flutemetamol	[¹⁸F]florbetapen
Dose	i.v. 10 mCi (370 MBq) single bolus (injected through a catheter of ≤ 1.5 in. to minimize drug adsorption to catheter)	i.v. 5 mCi (185 MBq) single bolus (followed by a flush 5–15 ml of sterile 0.9% NaCl)	i.v. 8.1 mCi (300 MBq) slow single bolus
Image acquisition	Obtain 10 min PET image with patient supine starting 30–50 min after injection	Obtain 20 min PET image starting approximately 90 min after injection	Obtain 15–20 min PET image starting approximately 45–130 min after injection
Adverse events	Rare and include headache (2%), musculoskeletal pain, fatigue, and nausea (1% each)	Rare: Flushing (2%), headache (1%), increased blood pressure (1%), nausea (1%), and dizziness (1%)	Rare: Injection site reactions consisting of erythema (1.7%), irritation (1.2%), and pain (3.9%).
Dosimetry	7 mSv	5.9 mSv	5.8 mSv
Contra-indications	None	Known hypersensitivity to Vizamyl or any excipient, including polysorbate 80	None

Table 19.13 Summary of radioligands to assess for β -amyloidopathy.

Radiopharmaceutical(s) (adult) dose, route	Technique	Indication	Main interpretation parameters
[¹⁸ F]florbetapir, 10 mCi, i.v.; [¹⁸ F]flutemetamol, 5 mCi, i.v.; [¹⁸ F]florbetapen, 8.1 mCi, i.v.	Peripheral i.v. injection	To estimate β -amyloid neuritic plaque density in adult patients who are being evaluated for AD or other causes of cognitive decline	Abnormal uptake in the supratentorial cortical gray matter, typically above cerebellar gray matter reference tissue.

A negative scan reduces the likelihood that a patient's cognitive impairment is due to AD.

Abnormal – A positive scan indicates moderate to frequent amyloid neuritic plaques. It should be noted that neuropathological examination has shown this amount of neuritic plaque to be present in patients with AD, but it may also be present in patients with other types of neurological conditions (DLB), as well as older people with normal cognition.

β -amyloid PET radiotracer accumulation limited to the white matter is necessary for a negative scan. On the other hand, radiotracer distribution within the gray matter is necessary for a positive scan. Reporting of these scans requires expertise, as the interpretation can occasionally be challenging, especially in the setting of cortical atrophy.

Registration of the PET scan with either anatomic imaging studies or early post-injection “flow” studies may help to better delineate the gray matter anatomy to ascertain abnormal binding in the cortex.

19.6.3 Limitations

β -amyloid PET imaging is an adjunct to other diagnostic evaluations. Importantly, a positive scan does not establish the diagnosis of AD. However, the future clinical application of phosphorylated tau PET imaging in conjunction with β -amyloid may provide more specific or additional evidence for the in vivo diagnosis of AD. Another reason β -amyloid PET cannot justify a diagnosis of Alzheimer’s disease per se is the fact that other neurodegenerative disorders, such as DLB, may also have β -amyloid plaques [57]

19.7 FUTURE DIRECTIONS

19.7.1 Movement Disorders: DA and Other Tracers

The nigrostriatal nerve terminal has been a popular target for new radioligand development for the last three decades. Figure 19.10 provides a pictorial overview of the main ligands for each class of the major molecular targets (dopamine synthesis, vesicular monoamine transporter type 2 [VMAT2], and plasmalemmal DATs).

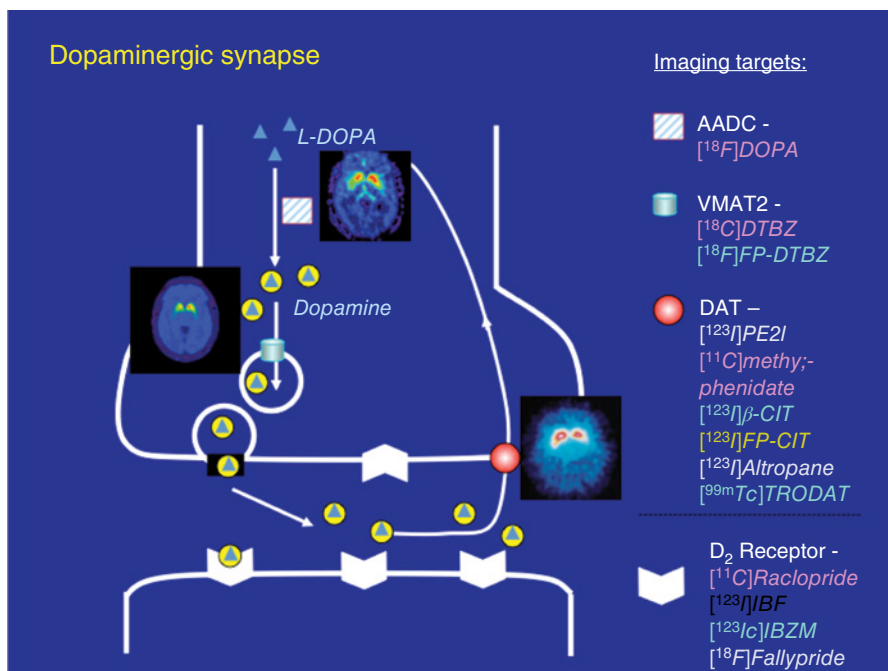


Figure 19.10 Radioligands used for nigrostriatal nerve terminal imaging.

The only ligand that is currently approved for limited clinical use in the US is [¹²³I]-FP-CIT ([¹²³I]ioflupane) for SPECT imaging. The short half-life of [¹¹C]-labeled ligands precludes routine clinical use, but [¹⁸F] labels are in clinical trials [58], such as the VMAT2 ligand ((+)- α -9-*O*-(3-[¹⁸F]fluoropropyl)dihydrotetrabenazine, also known as (+)-[¹⁸F]FP-DTBZ [59]. This ligand not only is more favorable due to the longer half-life but also has a higher affinity for the VMAT2 receptor compared to (+)-[¹¹C]DTBZ. DA PET ligands will provide superior visualization of DA nerve terminals compared to SPECT ligands due to better spatial resolution and more robust and less operator-dependent imaging techniques.

A new direction of research is the development of ligands that target second messenger systems and other elements of the downstream dopamine signaling cascade. For example, ligands targeting the phosphodiesterase (PDE) 10A have shown promise in patients with Parkinson's disease [60]. A PDE 10A PET study using [¹¹C]IMA107 PET found loss of PDE 10A levels very early in the course of PD, associated with the gradual and progressive increase of motor symptoms. Therefore, this class of ligands may have the potential not only for early diagnosis but also to assess the progression of Parkinson's disease as an alternative to presynaptic dopaminergic ligands.

19.7.2 Brain Tumors: Amino Acid PET Imaging

Radiolabeled amino acid analogs may aid in the diagnosis of tumors and differentiate between recurrent tumors and radiation necrosis [61]. The radiolabeled amino acids [¹¹C]methionine, [¹⁸F]3,4-dihydroxyphenylalanine (FDOPA), and *O*-(2-[¹⁸F]fluoroethyl)-L-tyrosine (FET) reflect protein synthesis and ¹⁸F-fluorothymidine (FLT) DNA replication. Low accumulation of amino acid tracers in normal brains allows the detection of low-grade gliomas and facilitates more precise tumor delineation. An important advantage compared to FDG PET is that amino acid ligands generally have a greater target-to-background ratio. Their application has ranged from primary brain tumor evaluation and grading to the evaluation of early and late treatment response, evaluation of pseudo-progression, treatment modulation, prognosis, and the assessment of possible radiation necrosis [62–69]. [¹⁸F]-Fluoromisonidazole (FMISO) as a hypoxia imaging agent is also being explored for radiation treatment planning and prognosis evaluation [70–72]. The increasing availability of integrated PET-MRI scanners is expected to increase the clinical utility of these ligands for more precise anatomic delineation of viable tumor tissue, allowing more precise therapeutic targeting. This class of ligands is expected to gain further importance in neuro-oncological decision-making. Furthermore, combinations of different tracers might provide more in-depth information about tumor characteristics, and current limitations may thus be overcome in the near future.

19.7.3 Tau Proteinopathy Ligands

The number of phosphorylated tau PET imaging ligands is rapidly expanding, with the latest generation having less “off” target binding compared to early-generation ligands.

The availability of reliable and specific tau PET imaging in conjunction with β -amyloid PET ligands has great promise to allow for a reliable *in vivo* diagnosis of Alzheimer's disease.

PET tau imaging probes have been developed with the aim of differentiating tauopathies from non-tau-related pathologies clinically as well as discerning treatment effects and progression of disease. Variability in the types of tau deposition in the brain and their conformation, maturation stage, isoform, and direct relationship to specific pathology have been described [73]. Morphological but also isoform differences can affect the specific binding characteristics of tau tracers [73]. The specificity of these ligands will allow differential diagnostic assessments of various tauopathies ranging from Alzheimer's disease to frontolobar degenerations. For example, a few compounds have aimed at detecting *in vivo* PET tau NFTs composed of paired helical filaments vs. other tau-related deposits in the brain, such as twisted ribbons or straight filaments seen more in FTD-related pathologies. [^{18}F]MK-6240 and [^{18}F]-AV-1451 have been shown with postmortem studies to bind to tau NFT and distinguish to some extent Alzheimer's disease vs. non-Alzheimer tauopathies. These two compounds seem to be able to distinguish AD from other tauopathies, Lewy body disorders, and control brains free of neurodegenerative pathology [74]. They also have a low affinity for monoamine oxidase (**MAO**) enzymes [74]. A number of quantitative measures and threshold parameters are being studied that will facilitate abbreviated and non-invasive imaging-acquisition protocols suitable for clinical practice [75].

19.8 CONCLUSIONS

Single-photon and positron-emitter radiopharmaceuticals play an important role in neuro-nuclear medicine. These applications range from planar scintigraphy to tomographic (SPECT and PET) imaging. Early planar applications, such as brain death CBF and CSF flow imaging, continue to be used in current clinical practice. Recent controversy about the validity of NPH syndrome has been a reason for decreasing indications for cisternography. With the advent of FDG PET, cognitive applications of regional CBF SPECT imaging have declined, but it continues to play an important role in the presurgical evaluation of patients with medically refractory epilepsy. More recently, dopaminergic transporter SPECT and β -amyloid PET imaging have received clinical approval by the FDA in the United States. The very first image acquisition of FDG PET imaging was of the brain, but its clinical application remains limited to indications for seizure focus localization, tumor recurrence vs. radionecrosis detection, and differential diagnosis of dementing disorders. Clinical applications of approved β -amyloid PET imaging are dependent on the presence of national or insurance company approval. However, neuro-nuclear imaging is expected to further expand its current already important role in broad and multifaceted challenging clinical dementia diagnosis and neuro-oncology. Anticipated changes will become even more prominent with the advent of disease-modifying treatments for these conditions.

ACKNOWLEDGMENTS

Nicolaas Bohnen gratefully acknowledges the National Institutes of Health (grant numbers P01 NS015655, P50 NS091856, and RO1 NS070856), Department of Veterans Affairs (grant number I01 RX000317), and the Michael J. Fox Foundation for their support.

REFERENCES

1. Chiewvit, S., Nuntaaree, S., Kanchaanapiboon, P., and Chiewvit, P. (2014). Assessment lumboperitoneal or ventriculoperitoneal shunt patency by radionuclide technique: a review experience cases. *World J. Nucl. Med.* 13 (2): 75–84.
2. Miracle, A.C., Fox, M.A., Ayyangar, R.N. et al. (2011). Imaging evaluation of intrathecal baclofen pump-catheter systems. *AJNR Am. J. Neuroradiol.* 32 (7): 1158–1164.
3. Eljazzar, R., Loewenstern, J., Dai, J.B. et al. (2019). Detection of CSF leaks: is there a radiologic standard of care? A systematic review detection of CSF leaks: a systematic review. *World Neurosurg.* 127: 307–315.
4. Hekster, R.E., Goedhart, Z.D., and Matricali, B. (1976). Neuroradiological applications of the Ommaya reservoir system. *Radiol. Clin. (Basel)* 45 (2–4): 277–281.
5. Grant, R., Naylor, B., Greenberg, H.S., and Junck, L. (1994). Clinical outcome in aggressively treated meningeal carcinomatosis. *Arch. Neurol.* 51 (5): 457–461.
6. Chamberlain, M.C. and Corey-Bloom, J. (1991). Leptomeningeal metastases: 111indium-DTPA CSF flow studies. *Neurology* 41 (11): 1765–1769.
7. Haaxma-Reiche, H., Piers, A., and Beekhuis, H. (1989). Normal cerebrospinal fluid dynamics. A study with intraventricular injection of ¹¹¹In-DTPA in leukemia and lymphoma without meningeal involvement. *Arch. Neurol.* 46 (9): 997–999.
8. Ghosh, D., Ghosh, P.P., Gambhir, S., and Kohli, A. (1997). Normal pressure hydrocephalus role of radionuclide cisternography. *Neurol. India* 45 (4): 231–239.
9. Espay, A.J., Da Prat, G.A., Dwivedi, A.K. et al. (2017). Deconstructing normal pressure hydrocephalus: ventriculomegaly as early sign of neurodegeneration. *Ann. Neurol.* 82 (4): 503–513.
10. Graff-Radford, N.R. and Jones, D.T. (2019). Normal pressure hydrocephalus. *Continuum (Minneap. Minn.)* 25 (1): 165–186.
11. Townley, R.A., Botha, H., Graff-Radford, J. et al. (2018). (18)F-FDG PET-CT pattern in idiopathic normal pressure hydrocephalus. *Neuroimage Clin.* 18: 897–902.
12. Rosenson, A.S., Ali, A., Fordham, E.W., and Penn, R.D. (1990). Indium-111 DTPA flow study to evaluate surgically implanted drug pump delivery system. *Clin. Nucl. Med.* 15 (3): 154–156.
13. Di Rocco, R.J., Silva, D.A., Kuczynski, B.L. et al. (1993). The single-pass cerebral extraction and capillary permeability-surface area product of several putative cerebral blood flow imaging agents. *J. Nucl. Med.* 34 (4): 641–648.
14. Neirinckx, R.D., Canning, L.R., Piper, I.M. et al. (1987). Technetium-99m d,l-HM-PAO: a new radiopharmaceutical for SPECT imaging of regional cerebral blood perfusion. *J. Nucl. Med.* 28 (2): 191–202.

15. O'Brien, J.T., Firbank, M.J., Davison, C. et al. (2014). ^{18}F -FDG PET and perfusion SPECT in the diagnosis of Alzheimer and Lewy body dementias. *J. Nucl. Med.* 55 (12): 1959–1965.
16. Wijdicks, E.F., Varelas, P.N., Gronseth, G.S., and Greer, D.M. (2010). Evidence-based guideline update: determining brain death in adults. Report of the Quality Standards Subcommittee of the American Academy of Neurology. *Neurology* 74 (23): 1911–1918.
17. Schwartz, J.A., Baxter, J., and Brill, D.R. (1984). Diagnosis of brain death in children by radionuclide cerebral imaging. *Pediatrics* 73 (1): 14–18.
18. Horsley, V. (1892). An address on the origin and seat of epileptic disturbance: delivered before the Cardiff Medical Society. *Br. Med. J.* 1 (1631): 693–696.
19. von Oertzen, T.J. (2018). PET and ictal SPECT can be helpful for localizing epileptic foci. *Curr. Opin. Neurol.* 31 (2): 184–191.
20. Laich, E., Kuzniecky, R., Mountz, J. et al. (1997). Supplementary sensorimotor area epilepsy. Seizure localization, cortical propagation and subcortical activation pathways using ictal SPECT. *Brain* 120 (Pt 5): 855–864.
21. Marks, D.A., Katz, A., Hoffer, P., and Spencer, S.S. (1992). Localization of extratemporal epileptic foci during ictal single photon emission computed tomography. *Ann. Neurol.* 31 (3): 250–255.
22. Harvey, A.S., Bowe, J.M., Hopkins, I.J. et al. (1993). Ictal $^{99\text{mTc}}$ -HMPAO single photon emission computed tomography in children with temporal lobe epilepsy. *Epilepsia* 34 (5): 869–877.
23. Harvey, A.S., Hopkins, I.J., Bowe, J.M. et al. (1993). Frontal lobe epilepsy: clinical seizure characteristics and localization with ictal $^{99\text{mTc}}$ -HMPAO SPECT. *Neurology* 43 (10): 1966–1980.
24. Ichise, M., Golan, H., Ballinger, J.R. et al. (1997). Regional differences in technetium- $^{99\text{m}}$ -ECD clearance on brain SPECT in healthy subjects. *J. Nucl. Med.* 38 (8): 1253–1260.
25. O'Brien, T.J., So, E.L., Mullan, B.P. et al. (1998). Subtraction ictal SPECT co-registered to MRI improves clinical usefulness of SPECT in localizing the surgical seizure focus. *Neurology* 50 (2): 445–454.
26. Van Paesschen, W. (2004). Ictal SPECT. *Epilepsia* 45 (Suppl 4): 35–40.
27. Newberg, A.B., Alavi, A., and Payer, F. (1995). Single photon emission computed tomography in Alzheimer's disease and related disorders. *Neuroimaging Clin. N. Am.* 5 (1): 103–123.
28. Bartenstein, P., Grunwald, F., Kuwert, T. et al. (2000). Clinical applications of single photon emission tomography in neuromedicine. 1. Neuro-oncology, epilepsy, movement disorders, cerebrovascular disease. *Nuklearmedizin* 39 (7): 180–195.
29. Farid, K., Caillat-Vigneron, N., and Sibon, I. (2011). Is brain SPECT useful in degenerative dementia diagnosis? *J. Comput. Assisted Tomogr.* 35 (1): 1–3.
30. Minoshima, S., Koeppe, R.A., Mintun, M.A. et al. (1993). Automated detection of the intercommissural line for stereotactic localization of functional brain images. *J. Nucl. Med.* 34 (2): 322–329.
31. Minoshima, S., Koeppe, R.A., Frey, K.A., and Kuhl, D.E. (1994). Anatomic standardization: linear scaling and nonlinear warping of functional brain images. *J. Nucl. Med.* 35: 1528–1537.

32. Kotagal, V., Lorincz, M.T., and Bohnen, N.I. (2012). A frontotemporal dementia-like syndrome mimicking postpartum depression detected by ^{18}F fluorodeoxyglucose positron emission tomography. *Clin. Nucl. Med.* 37 (9): e223–e224.
33. Djang, D.S., Janssen, M.J., Bohnen, N. et al. (2012). SNM practice guideline for dopamine transporter imaging with ^{123}I -ioflupane SPECT 1.0. *J. Nucl. Med.* 53 (1): 154–163.
34. Reivich, M., Kuhl, D.E., Wolf, A. et al. (1979). Local cerebral metabolic rate for glucose. *Circ Res.* 44: 127–137.
35. Clerici, F., Del Sole, A., Chiti, A. et al. (2009). Differences in hippocampal metabolism between amnesic and non-amnesic MCI subjects: automated FDG-PET image analysis. *Q. J. Nucl. Med. Mol. Imaging* 53 (6): 646–657.
36. Mosconi, L., De Santi, S., Li, J. et al. (2008). Hippocampal hypometabolism predicts cognitive decline from normal aging. *Neurobiol. Aging* 29 (5): 676–692.
37. Mosconi, L., Tsui, W.H., De Santi, S. et al. (2005). Reduced hippocampal metabolism in MCI and AD: automated FDG-PET image analysis. *Neurology* 64 (11): 1860–1867.
38. Bohnen, N.I., Djang, D.S., Herholz, K. et al. (2012). Effectiveness and safety of ^{18}F -FDG PET in the evaluation of dementia: a review of the recent literature. *J. Nucl. Med.* 53 (1): 59–71.
39. Kwon, K.Y., Choi, C.G., Kim, J.S. et al. (2007). Comparison of brain MRI and ^{18}F -FDG PET in the differential diagnosis of multiple system atrophy from Parkinson's disease. *Mov. Disord.* 22 (16): 2352–2358.
40. Knopman, D.S., Jack, C.R. Jr., Lundt, E.S. et al. (2015). Role of β -amyloidosis and neurodegeneration in subsequent imaging changes in mild cognitive impairment. *JAMA Neurol.* 72 (12): 1475–1483.
41. Kobylecki, C., Langheinrich, T., Hinz, R. et al. (2015). ^{18}F -florbetapir PET in patients with frontotemporal dementia and Alzheimer disease. *J. Nucl. Med.* 56 (3): 386–391.
42. Brendel, M., Schnabel, J., Schonecker, S. et al. (2017). Additive value of amyloid-PET in routine cases of clinical dementia work-up after FDG-PET. *Eur. J. Nucl. Med. Mol. Imaging* 44 (13): 2239–2248.
43. Hellwig, S., Amtage, F., Kreft, A. et al. (2012). [^{18}F]FDG-PET is superior to [^{123}I]IBZM-SPECT for the differential diagnosis of parkinsonism. *Neurology* 79 (13): 1314–1322.
44. Antonini, A., Leenders, K.L., Spiegel, R. et al. (1996). Striatal glucose metabolism and dopamine D_2 receptor binding in asymptomatic gene carriers and patients with Huntington's disease. *Brain* 119 (Pt 6): 2085–2095.
45. Bohnen, N.I., Minoshima, S., Giordani, B. et al. (1999). Motor correlates of occipital glucose hypometabolism in Parkinson's disease without dementia. *Neurology* 52 (3): 541–546.
46. Albin, R.L., Minoshima, S., D'Amato, C.J. et al. (1996). Fluoro-deoxyglucose positron emission tomography in diffuse Lewy body disease. *Neurology* 47 (2): 462–466.
47. Niethammer, M. and Eidelberg, D. (2012). Metabolic brain networks in translational neurology: concepts and applications. *Ann. Neurol.* 72 (5): 635–647.
48. Kuhl, D.E., Engel, J., Phelps, M.E., and Selin, C. (1980). Epileptic patterns of local cerebral metabolism and perfusion in humans determined by emission computed tomography of ^{18}F FDG and $^{13}\text{NH}_3$. *Ann. Neurol.* 8: 348–360.

49. Engel, J. Jr., Kuhl, D.E., Phelps, M.E., and Mazziotta, J.C. (1982). Interictal cerebral glucose metabolism in partial epilepsy and its relation to EEG changes. *Ann. Neurol.* 12 (6): 510–517.
50. Meltzer, C.C., Adelson, P.D., Brenner, R.P. et al. (2000). Planned ictal FDG PET imaging for localization of extratemporal epileptic foci. *Epilepsia* 41 (2): 193–200.
51. Louis, D.N., Perry, A., Reifenberger, G. et al. (2016). The 2016 World Health Organization classification of tumors of the central nervous system: a summary. *Acta Neuropathol.* 131 (6): 803–820.
52. Glantz, M.J., Hoffman, J.M., Coleman, R.E. et al. (1991). Identification of early recurrence of primary central nervous system tumors by [¹⁸F]fluorodeoxyglucose positron emission tomography. *Ann. Neurol.* 29 (4): 347–355.
53. Janus, T.J., Kim, E.E., Tilbury, R. et al. (1993). Use of [¹⁸F]fluorodeoxyglucose positron emission tomography in patients with primary malignant brain tumors. *Ann. Neurol.* 33 (5): 540–548.
54. McKhann, G., Drachman, D., Folstein, M. et al. (1984). Clinical diagnosis of Alzheimer's disease: report of the NINCDS-ADRDA Work Group under the auspices of Department of Health and Human Services Task Force on Alzheimer's Disease. *Neurology* 34 (7): 939–944.
55. Dubois, B., Feldman, H.H., Jacova, C. et al. (2010). Revising the definition of Alzheimer's disease: a new lexicon. *Lancet Neurol.* 9 (11): 1118–1127.
56. Sperling, R.A., Aisen, P.S., Beckett, L.A. et al. (2011). Toward defining the preclinical stages of Alzheimer's disease: recommendations from the National Institute on Aging-Alzheimer's Association workgroups on diagnostic guidelines for Alzheimer's disease. *Alzheimers Dement.* 7 (3): 280–292.
57. Foster, E.R., Campbell, M.C., Burack, M.A. et al. (2010). Amyloid imaging of Lewy body-associated disorders. *Mov. Disord.* 25 (15): 2516–2523.
58. Peng, S., Doudet, D.J., Dhawan, V., and Ma, Y. (2013). Dopamine: PET imaging and Parkinson disease. *PET Clin.* 8 (4): 469–485.
59. Lin, K.J., Weng, Y.H., Wey, S.P. et al. (2010). Whole-body biodistribution and radiation dosimetry of ¹⁸F-FP-(+)-DTBZ (¹⁸F-AV-133): a novel vesicular monoamine transporter 2 imaging agent. *J. Nucl. Med.* 51 (9): 1480–1485.
60. Pagano, G., Niccolini, F., Wilson, H. et al. (2019). Comparison of phosphodiesterase 10A and dopamine transporter levels as markers of disease burden in early Parkinson's disease. *Mov. Disord.* 34 (10): 1505–1515.
61. Jung, J.H. and Ahn, B.C. (2018). Current radiopharmaceuticals for positron emission tomography of brain tumors. *Brain Tumor Res. Treat.* 6 (2): 47–53.
62. Filss, C.P., Cicone, F., Shah, N.J. et al. (2017). Amino acid PET and MR perfusion imaging in brain tumours. *Clin. Trans. Imaging* 5 (3): 209–223.
63. Galldiks, N. and Langen, K.J. (2017). Amino acid PET in neuro-oncology: applications in the clinic. *Expert Rev. Anticancer Ther.* 17 (5): 395–397.
64. Galldiks, N., Law, I., Pope, W.B. et al. (2017). The use of amino acid PET and conventional MRI for monitoring of brain tumor therapy. *Neuroimage Clin.* 13: 386–394.

65. Langen, K.J., Stoffels, G., Filss, C. et al. (2017). Imaging of amino acid transport in brain tumours: positron emission tomography with *O*-(2-[(18)F]fluoroethyl)-l-tyrosine (FET). *Methods* 130: 124–134.
66. Marner, L., Nysom, K., Sehested, A. et al. (2019). Early postoperative (18)F-FET PET/ MRI for pediatric brain and spinal cord tumors. *J. Nucl. Med.* 60 (8): 1053–1058.
67. Albatly, A.A., Alsamarah, A.T., Alhawas, A. et al. (2018). Value of (18)F-FET PET in adult brainstem glioma. *Clin. Imaging* 51: 68–75.
68. Galldiks, N. and Langen, K.J. (2016). Amino acid PET – an imaging option to identify treatment response, posttherapeutic effects, and tumor recurrence? *Front. Neurol.* 7: 120.
69. Langen, K.J. and Watts, C. (2016). Neuro-oncology: amino acid PET for brain tumours – ready for the clinic? *Nat. Rev. Neurol.* 12 (7): 375–376.
70. Mendichovszky, I. and Jackson, A. (2011). Imaging hypoxia in gliomas. *Br. J. Radiol.* 84 (Spec 2): S145–S158.
71. Tachibana, I., Nishimura, Y., Shibata, T. et al. (2013). A prospective clinical trial of tumor hypoxia imaging with ¹⁸F-fluoromisonidazole positron emission tomography and computed tomography (F-MISO PET/CT) before and during radiation therapy. *J. Radiat. Res.* 54 (6): 1078–1084.
72. Cher, L.M., Murone, C., Lawrentschuk, N. et al. (2006). Correlation of hypoxic cell fraction and angiogenesis with glucose metabolic rate in gliomas using ¹⁸F-fluoromisonidazole, ¹⁸F-FDG PET, and immunohistochemical studies. *J. Nucl. Med.* 47 (3): 410–418.
73. Saint-Aubert, L., Lemoine, L., Chiotis, K. et al. (2017). Tau PET imaging: present and future directions. *Mol. Neurodegener.* 12 (1): 19.
74. Agüero, C., Dhaynaut, M., Normandin, M.D. et al. (2019). Autoradiography validation of novel tau PET tracer [F-18]-MK-6240 on human postmortem brain tissue. *Acta Neuropathol. Commun.* 7 (1): 37.
75. Maass, A., Landau, S., Baker, S.L. et al. (2017). Comparison of multiple tau-PET measures as biomarkers in aging and Alzheimer’s disease. *Neuroimage* 157: 448–463.

Chapter 20

Cardiac

Applications of

Radiopharmaceuticals

John P. Bois¹ and Robert J. Gropler²

¹*Department of Cardiovascular Diseases, Mayo Clinic, Rochester, MN, USA, 55905*

²*Mallinckrodt Institute of Radiology, Washington University School of Medicine, St. Louis, MO, USA, 63110*

20.1 INTRODUCTION

The first assessment of cardiac circulation time in humans utilizing radiopharmaceuticals was performed by Dr. Hermann L. Blumgart at Thorndike Memorial Laboratory in Boston City Hospital in 1927 (Figure 20.1) [1]. In the following decade, the Nobel Prize was awarded to Dr. Ernest Lawrence of the University of California, Berkeley, for his creation of the cyclotron, thus enabling the production of radioactive materials rather than simply searching for naturally occurring radioactive elements. The development of the cyclotron would ultimately result in the production of the first synthetic isotope, technetium-99m (^{99m}Tc). The subsequent rapid development of radiopharmaceuticals capable of imaging the heart coupled with the creation of the scintillation camera in 1958, the introduction of the single-photon emission tomography (**SPECT**) technology in the 1980s, and, ultimately, the application of positron emission tomography (**PET**) for myocardial assessment all contributed to the rapid growth of nuclear cardiologic techniques as invaluable tools in the management of patients with cardiovascular (**CV**) disease and in advancing CV research.

Fundamental to the success of this discipline is has been the availability of radiopharmaceuticals that permit the detection of more macro cardiac processes such

Handbook of Radiopharmaceuticals: Methodology and Applications, Second Edition.

Edited by Michael R. Kilbourn and Peter J.H. Scott.

© 2021 John Wiley & Sons Ltd. Published 2021 by John Wiley & Sons Ltd.

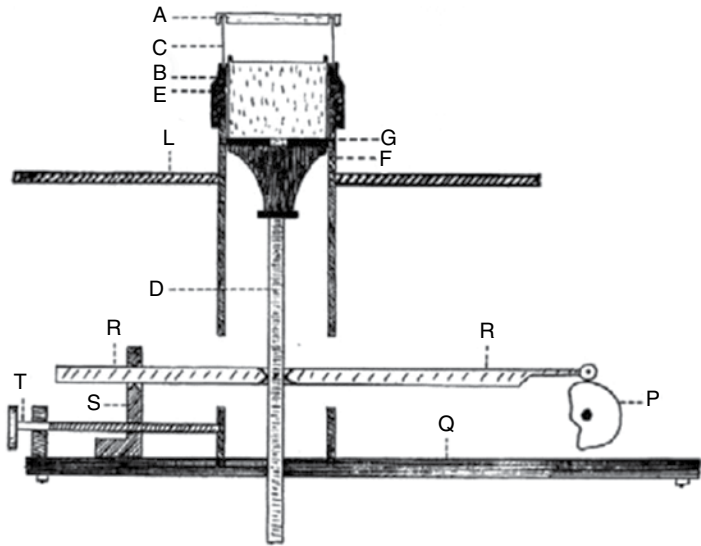


Figure 20.1 Description of the detecting device used to measure the velocity of blood by Blumgart and Yens in 1927. Source: Blumgart, H.L. and Yens, O.C. [1]. © 1927 American Society for Clinical Investigation.

as myocardial perfusion, metabolism, and left ventricular (LV) function. Indeed, the performance of these measurements has been the dominant clinical application of nuclear cardiology since the 1980s. More recently, we have seen the development of radiopharmaceuticals that permit delineation of cellular processes such as neuronal dysfunction, inflammation, and misfolded protein accumulation, that underlies these macro cardiac processes and also provide a better understanding of the biologic underpinnings and systemic nature of CV disease. Further contributing to this success has been the significant advances in SPECT and PET instrumentation as well as the development of hybrid technology that incorporates either computed tomography (**CT**) as is seen with SPECT/CT and PET/CT or magnetic resonance imaging (**MR**) as seen with PET/MR. As a consequence, we are seeing these newer approaches reach clinical application.

The current chapter will discuss the use of radiopharmaceuticals in the study of the heart for both the clinical care for the CV patient and advancing CV research. While the primary aim will be to review developments in radiopharmaceuticals and their consequences for the assessment of CV disease, pertinent developments in nuclear cardiology imaging technology will be noted as these often serve a critical role in enhancing the utilization of the various radiopharmaceuticals currently at our disposal.

20.2 MYOCARDIAL PERFUSION IMAGING (MPI)

Fundamental to myocardial health is the balance between oxygen supply (myocardial perfusion) and demand (myocardial oxygen consumption). Given the ever-changing levels of

myocardial oxygen consumption (e.g. resting vs. exercise conditions), the fundamental importance of adequate myocardial perfusion is unequivocal. The heart meets these changing perfusion demands through vasodilation of the medium and small arterioles, so-called *vasodilator capacity*. In the setting of significant obstructive coronary artery disease (**CAD**), increased vasodilation maintains myocardial perfusion downstream from the coronary artery stenosis under resting conditions. However, this resultant “baseline” vasodilation limits further vasodilation so that under conditions of increased myocardial oxygen consumption, such as exercise, vasodilator capacity is impaired, leading to inadequate oxygen supply to meet oxygen demand and resulting in myocardial ischemia. As a consequence, measurement of myocardial perfusion is an attractive approach to determine the presence and physiological significance of coronary artery stenosis, the central pathological lesion of CAD. For over a half a century, the detection of myocardial ischemia to diagnose the presence of obstructive CAD by myocardial perfusion imaging (**MPI**) during stress and rest has been the most common clinical application of nuclear cardiology. This wide applicability reflects both the accuracy and relatively simplicity of the tracer kinetic approach to measure blood flow.

20.2.1 Radiopharmaceuticals Used for MPI

There are several desirable characteristics for SPECT and PET perfusion radiopharmaceuticals, which include:

- Physiological characteristics:
 - High first-pass extraction fraction with, ideally, minimal myocardial radiopharmaceutical clearance or redistribution
 - Linear relationship between myocardial radiopharmaceutical uptake and myocardial perfusion up to perfusion rates of at least $5 \text{ ml (g min)}^{-1}$ (Figure 20.2) [2]
 - High myocardial-to-lung, -liver, -stomach, and -bowel ratios
- Physical characteristics:
 - Low radiation exposure
 - Physical half-life that permits rapid serial studies but permits both exercise and pharmacological forms of cardiac stress
 - PET: shorter positron range for better image quality and, ideally, unit dosing, obviating the need for expensive generators or on-site cyclotrons

20.2.1.1 SPECT Radiopharmaceuticals

Tc-99m sestamibi and Tc-99m tetrofosmin are lipid-soluble, cationic radiopharmaceuticals that produce 140-keV photons and have a physical half-life of six hours [3]. Their uptake and mitochondrial retention is dependent on blood flow and mitochondrial transmembrane energy potential. Their first-pass extraction fraction is ~50–60% under resting conditions and, thus, exhibits significant roll-off at higher perfusion rates. They

Figure 20.2 Relationship between myocardial uptake of common radiotracers and myocardial blood flow rates. Source: Manabe, O. et al. [2]. 2018 Springer Nature. Licensed Under CCBY 4.0.

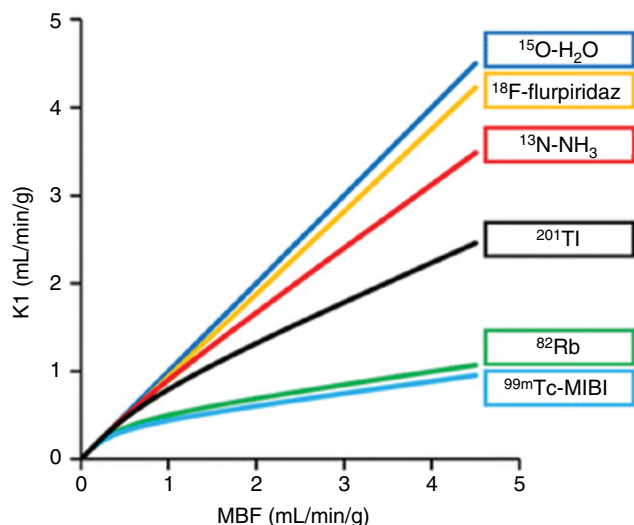


exhibit negligible myocardial washout (redistribution), which offers the advantage of de-coupling radiopharmaceutical injection from imaging but has the disadvantage of requiring separate radiotracer administrations/acquisitions during stress and rest to detect myocardial ischemia. These agents are excreted via the hepatobiliary system and then into the gastrointestinal tract, so increased subdiaphragmatic activity can compromise image quality.

Tl-201 is an analog of potassium (monovalent cation) with a physical half-life of 73.1 hours and decay by electron capture with principal emission of 68- to 80-keV X-rays. It exhibits a high first-pass myocardial extraction of ~85% [3]. Uptake is a combination of primarily active membrane transport and, to a lesser extent, passive diffusion. There is rapid clearance from the intravascular space and monoexponential washout (redistribution), which starts 10–15 minutes after injection. Washout depends on the initial tracer concentration in the myocyte and on myocardial blood flow. This redistribution offers the advantage of obtaining myocardial ischemia information using a single radiopharmaceutical administration and two image acquisitions (initial and three to four hours later) but the disadvantage of coupling of the initial acquisition with radiopharmaceutical administration. Another advantage of Tl-201 is the ability to detect viable myocardium-based initial and delayed imaging (with perhaps re-injection of Tl-201) performed under resting conditions.

20.2.1.2 PET Radiopharmaceuticals

Rubidium-82 is a monovalent cation with several attractive qualities. First, it is produced by a generator from Strontium-82, obviating the need for an on-site cyclotron and thus making its use more widely available [4]. Second, it has a short physical half-life of 76 seconds, allowing for multiple injections of tracer in rapid sequence during stress testing.

However, the short physical half-life essentially precludes the use of exercise as a means of stress. In addition, Rb-82 has the longest positron range of any of the PET radiotracers, which decreases its image resolution. As is the case with all extractible radiopharmaceuticals, the extraction fraction of ^{82}Rb is inversely proportional to flow in a nonlinear fashion, and extraction plateaus at $2\text{--}3\text{ mL (g min)}^{-1}$ (Figure 20.2). Rb-82 is Food and Drug Administration (FDA) approved for clinical use.

Nitrogen-13 ammonia has been used extensively for the assessment of myocardial perfusion with PET. It has a relatively short half-life of ~ 10 minutes. As a consequence, it must be produced by an on-site cyclotron for immediate use [4]. Ammonia appears to enter the myocardium through a carrier-mediated mechanism and has a high extraction fraction in the myocardium as well as long tissue retention (tissue biologic half-life of $80\text{--}400$ minutes) [5]. These attributes, along with the relatively short positron range of N-13, result in excellent tissue-to-blood pool contrast and high image quality. Liver uptake is part of the normal biodistribution of ^{13}N -ammonia. Diffuse lung uptake is also frequently seen in smokers and patients with congestive heart failure. As is the case with ^{82}Rb , the extraction of ^{13}N -ammonia is nonlinear and inversely related to myocardial blood flow (Figure 20.2). Extraction plateaus at flow rates greater than 3 mL (g min)^{-1} . ^{13}N -ammonia is approved for clinical use.

Oxygen-15 water is the only diffusible radiopharmaceutical currently in common use. It has a short physical half-life of ~ 2 minutes that permits rapid sequential evaluations of myocardial perfusion with only modest radiation exposure to the patient [4]. It has a first-pass extraction fraction of nearly 100%, and thus the relationship between radiopharmaceutical uptake and perfusion is linear at physiological flow rates, making it an ideal tracer for absolute measurement of myocardial perfusion (Figure 20.2). The lack of retention in the myocardium means relative perfusion imaging cannot be performed without the use of additional parametric imaging software to delineate myocardium from blood pool. Although some centers in Europe use it clinically, ^{15}O -water use is limited to the research setting in the United States.

^{18}F -Flurpiridaz is a structural analog of the insecticide pyridaben, which is an MC-1 inhibitor [6]. It has a long half-life (108 minutes), and therefore a regional rather than an on-site cyclotron can be utilized in its production, with subsequent widespread distribution [4]. Furthermore, the prolonged half-life of ^{18}F -Flurpiridaz facilitates exercise stress testing, which has been shown to be feasible in clinical trials [7–9]. Its markedly short positron range also improves ^{18}F -Flurpiridaz image resolution. It is currently undergoing a second phase III clinical trial.

20.2.2 Performance of Rest/Stress MPI

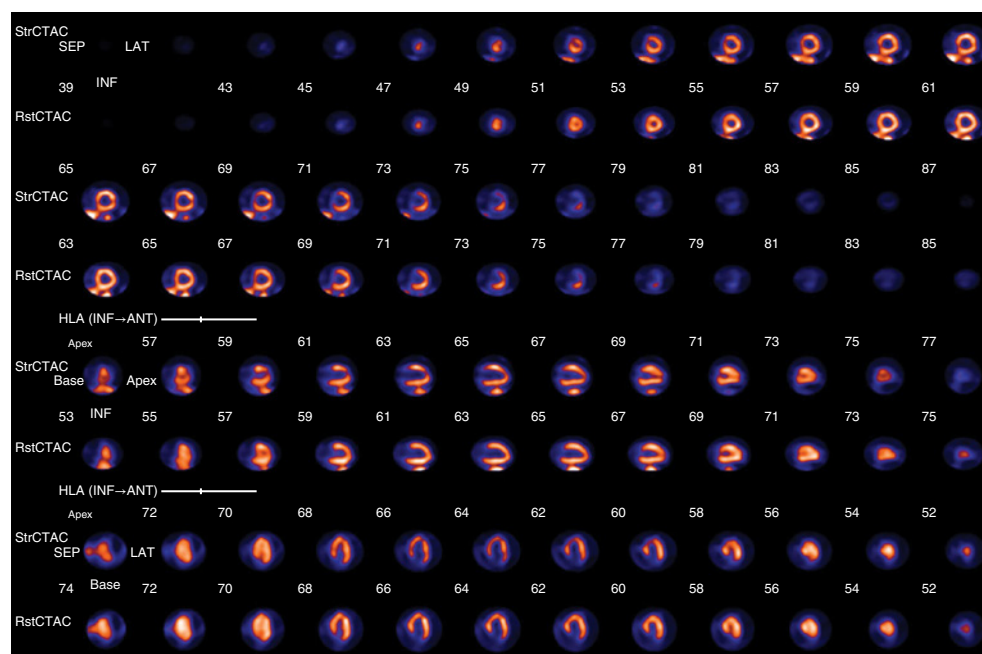
MPI studies are typically performed at rest and during some form of physiological stress. For clinical purposes, physiological stress can be induced by exercise, the use of vasodilators (regadenoson, adenosine, and dipyridamole), or beta-adrenergic stimulation with dobutamine. The type of imaging protocol is dependent upon the type of imaging (SPECT vs. PET), the radiopharmaceutical used, and the form of physiological stress. In addition,

with each of the radiopharmaceuticals, electrocardiographic gating is performed with image acquisition, permitting the assessment of LV morphology and function in addition to myocardial perfusion. It should be noted that electrocardiographically gated imaging with SPECT is typically performed at least 15–30 minutes after the injection of the radiopharmaceutical to allow for blood clearance. Thus, with exercise or pharmacological stress, the LV function assessment is post-stress, which may miss stress-induced functional abnormalities that may have resolved. In contrast, electrocardiographically gated PET measures LV function during stress, so it may provide additional diagnostic information regarding stress-induced functional abnormalities. With the advent of SPECT/CT and PET/CT, accurate attenuation correction is now possible, reducing the likelihood of false-positive studies. Descriptions of these various protocols have been extensively reviewed elsewhere and will not be detailed here [3, 10].

Measurements of myocardial perfusion are most commonly derived from static imaging, which results in a single frame that represents averaged radioactivity throughout the scan. The LV myocardium is divided into 17 segments (American Heart Association Model) with the segment with the highest activity defined as 100% and comparing the other regions to it. Then regional differences are compared between stress and rest conditions to identify reversible (ischemia) and persistent (infarction) perfusion abnormalities (Figure 20.3). The extent and severity of perfusion abnormalities can be further quantified by referencing the individual patient findings to a gender-matched database. Guidelines detailing how to interpret and report imaging findings have been previously reported [3, 10].

Figure 20.3

Example of a stress/rest Tc-99m Tetrofosmin SPECT MPI demonstrating multiple reversible perfusion abnormalities in the inter-ventricular septum, apex, and mid-lateral wall indicative of ischemia in multiple coronary vascular beds.



The strength of the relative MPI approach is the ease of performance and interpretation and extensive database supporting its use. The most notable weakness is the inability to measure global abnormalities in myocardial perfusion since there are no visual regional perfusion abnormalities. Thus, this approach is not useful in conditions of microvascular dysfunction associated with obesity, diabetes mellitus, and hypertrophic cardiomyopathy. Moreover, this relative MPI approach may underestimate the extent of multi-vessel CAD since one segment of the LV myocardium has to serve as the normal reference region even though it may be subtended by a coronary artery with significant stenosis.

Quantitative MPI studies measure myocardial perfusion in absolute terms (e.g. mL/g/min). In this case, dynamic acquisition assesses radiopharmaceutical radioactivity immediately following injection and continues to monitor activity throughout the scan, ultimately allowing the calculation of time-activity curves. These time-activity curves allow the derivation of both myocardial and blood-pool counts over time, from which rate constants are estimated that can be applied to mathematical models that ultimately calculate absolute myocardial perfusion. Measurements are performed during stress and at rest, with the ratio of stress perfusion/rest perfusion equaling the myocardial perfusion reserve (**MPR**), a measure of vasodilator capacity (Figure 20.4) [11]. Because of its better temporal resolution and availability of better perfusion radiopharmaceuticals, PET has been the most widely used method to quantify MPI. With the advent of digital solid-state cadmium zinc telluride SPECT cameras, the potential to quantify MPI is being earnestly explored [12].

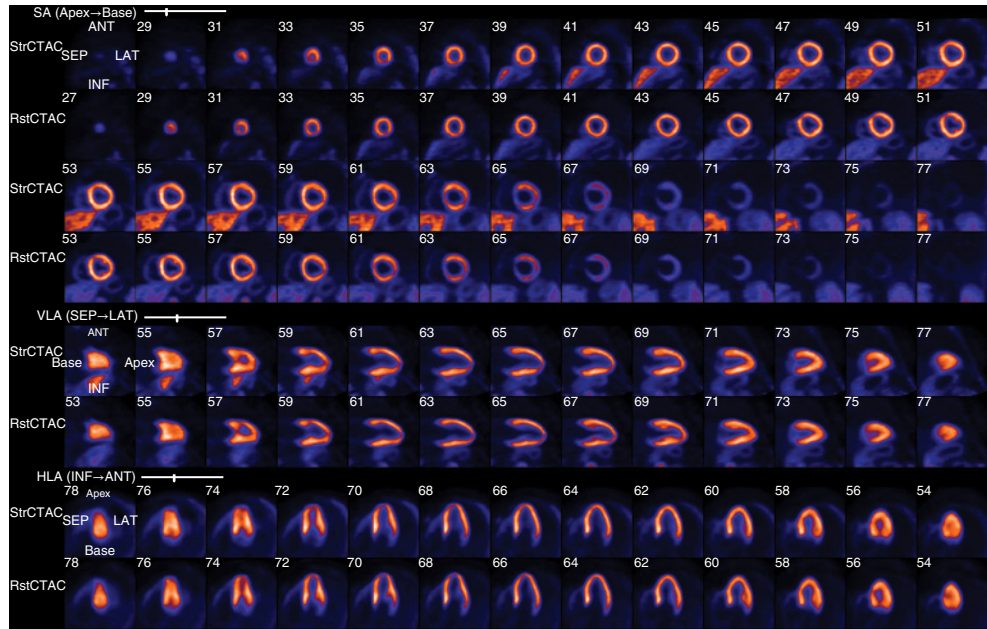
20.2.3 Applications

20.2.3.1 Management of Patients with Suspected CAD

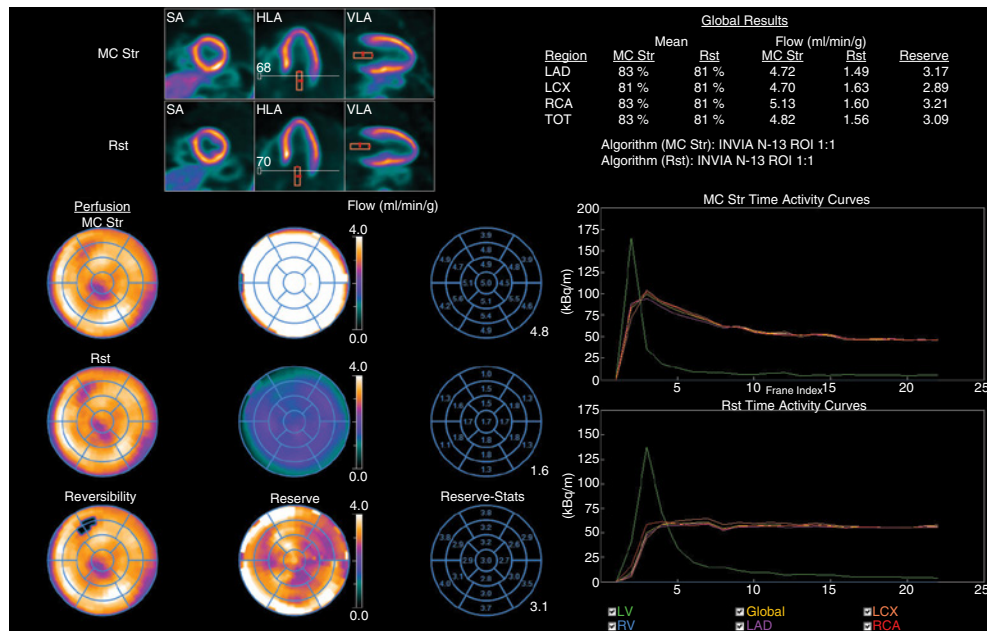
20.2.3.1.1 *Diagnosis*

SPECT and, more recently, PET have been the most commonly used MPI approaches to detect obstructive CAD. Both are highly accurate methods, with PET appearing to offer better sensitivity and specificity. Two recent meta-analyses compared relative MPI using contemporary SPECT methods (Tc-99m perfusion imaging with electrocardiographical gating and attenuation correction) with PET approaches. In one study, PET and SPECT had sensitivities and specificities of 90% and 85% and 88% and 85%, respectively [13, 14]. In the other study, sensitivities of 93% and 88% and specificities 81% and 76% were reported for PET and SPECT, respectively. PET may be more accurate than SPECT for detecting multi-vessel CAD. Because electrocardiographically gated PET measures LV during stress, it has been reported that blunting the LVEF response to stress is a marker of multi-vessel disease and has prognostic significance [15]. Given the rise in hybrid systems, particularly PET/CT, MPI assessments can provide complementary information to the coronary morphologic information provided by CT. For example, moderate-to-severe ischemia has been reported in ~9% of patients with coronary calcium scores >1000, suggesting that most of these patients with atherosclerosis did not have physiologically

Figure 20.4 An example of normal quantitative MBF. Regadenoson stress and rest PET/CT using ^{13}N -ammonia. (a) Tomographic images with CT attenuation demonstrating homogenous MBF. (b) Dynamic PET/CT data showing arterial input and myocardial time-activity curves and calculation of myocardial perfusion with normal stress and rest values and MPR.



(a)



(b)

significant occlusive disease [16]. Furthermore, MPI can be used to determine the hemodynamic significance of coronary artery stenoses identified by coronary CT angiography and perhaps improve the detection of significant CAD (Figure 20.5) [17, 18].

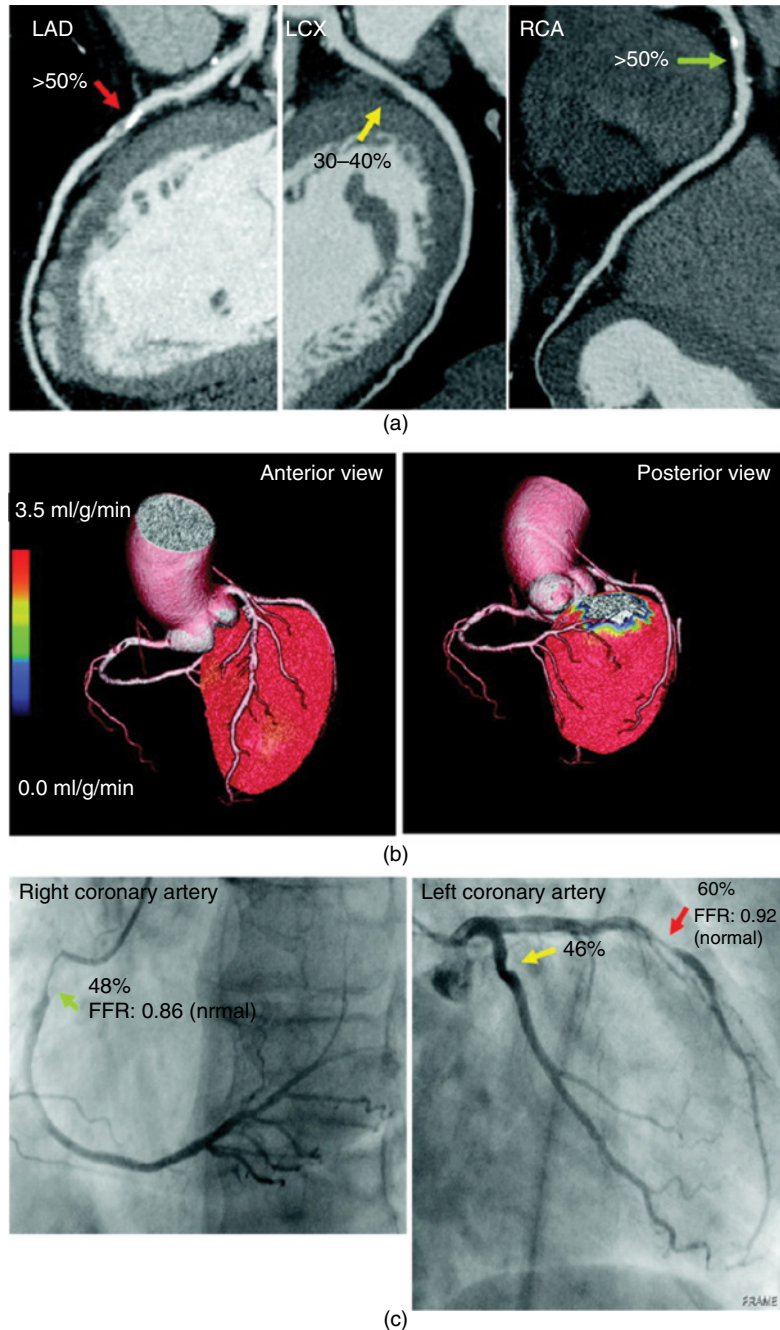


Figure 20.5 A 69-year-old man with attacks of atypical anginal pain. (a) CT showed significant LAD and RCA stenoses with only mild stenosis in the LCx. (b) Hybrid images with normal stress PET perfusion (absolute scale, 0–3.5 mL/g/min⁻¹). Normal perfusion is >2.5 mL/min (yellow or red). (c) ICA with quantitative analysis and FFR. Despite anatomically significant narrowing of the LAD and borderline changes in the RCA, FFR was normal in both vessels, indicating functionally non-significant disease. Source: Kajander, S. et al. [18].

20.2.3.1.2 Risk Stratification

Perhaps the greatest strength of SPECT and PET MPI is their ability to accurately stratify patients into various risk groups based on the integration of the imaging with other

clinical and cardiac anatomical information. Pooled analyses from large observational databases that total nearly 40 000 patients demonstrate that a normal MPI yields an annualized event rate of 0.6%, which is similar to the general population [19]. Although the length of this low-risk period is dependent upon the patient's risk profile, a low event rate has been reported to last as long as seven years [20]. In contrast, an abnormal scan confers a three- to sevenfold increase in annual cardiac events. This risk is directly related to the extent and severity of fixed or reversible perfusion defect and the associated prognostic risk and may be modulated by the baseline risk profile of the individual patient [21]. In addition to perfusion abnormalities, the extent of LV enlargement and dysfunction both at rest and post-stress further impact prognosis [22]. Not surprisingly, numerous studies have documented that PET provides similar strong prognostic information [23, 24]. Compared with SPECT, PET can provide additional insights into prognosis. For example, a blunting or decline in LVEF during stress compared to rest is associated with a worse prognosis independent of the extent and severity of the LV perfusion abnormalities [15].

As mentioned previously, PET can routinely quantify stress and rest myocardial perfusion as well as MPR. Indeed, MPR has been shown to be one of the strongest prognostic factors, and it provides additive information to clinical risk scores as well as relative perfusion abnormalities. Indeed, patients with homogenous radiotracer uptake (e.g. no relative perfusion abnormalities) but with blunted peak myocardial perfusion or MPR can be reclassified to a higher risk category [16, 25, 26].

Both SPECT and PET MPI may also provide important prognostic information to help guide therapy. With SPECT, it has been shown that myocardial ischemia involving 10% of the LV appears to be a threshold for where myocardial revascularization will provide outcome benefits compared with optimal medical therapy [27]. With PET, this threshold appears to be 5% of the LV, which likely reflects its better spatial resolution compared with SPECT (Figure 20.6) [28].

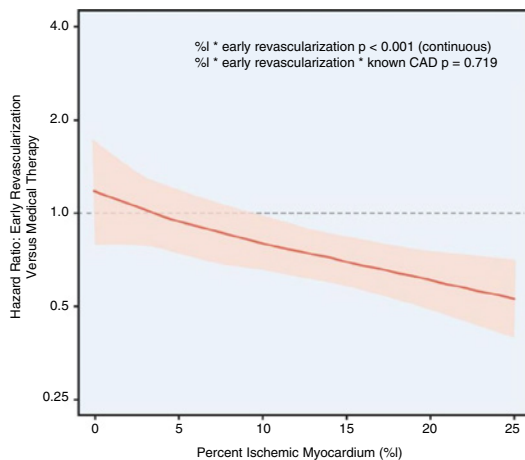


Figure 20.6 Risk vs. benefit for early myocardial revascularization vs. optimal medical therapy as a function of % ischemic myocardium determined by PET MPI. Source: Patel, K.K. et al. [28]. © 2019 Elsevier.

20.2.3.2 Other Disease Processes

Quantitative MPI with PET has made major contributions to our understanding of myocardial microvascular function in a host of diseases separate from CAD. For example, MPR is reduced in patients with hypertension, diabetes mellitus, and cardiomyopathies that are either hypertrophic or non-ischemic dilated in origin [29–32]. In diabetic patients, the impairment in MPR is strongly associated with the degree of albuminuria, suggesting that myocardial vasodilator dysfunction and albuminuria might share common mechanisms separate from CAD [30]. In patients with hypertrophic cardiomyopathy, abnormal MPR more frequently occurs in patients with anginal symptoms and provides prognostic information. Extensive reviews have been developed on the contribution of quantitative MBF to the clinical management and investigation of CV disease [16, 25, 33].

20.3 IMAGING CARDIAC MORPHOLOGY AND FUNCTION

Given the prognostic significance of abnormalities in the size and function of the various cardiac chambers, nuclear cardiologic techniques have been developed to measure cardiac morphology and performance. Equilibrium radionuclide angiography (**ERNA**) is performed by electrocardiographically gated imaging (planar or SPECT) of red blood cells radiolabeled with Tc-99m using *in vivo*, modified *in vivo*, or *in vitro* labeling methods. Planar ERNA was the study of choice to assess cardiac morphology and performance, particularly in patients receiving cardiotoxic chemotherapy. However, it has been largely superseded by echocardiography for this purpose. Currently, cardiac morphology and performance are more commonly assessed based on electrocardiographical gating of an MPI study.

20.4 IMAGING OF MYOCARDIAL METABOLISM

The heart is an omnivore with energy in the form of adenosine triphosphate being primarily generated by mitochondrial oxidative phosphorylation with the remainder derived from glycolytic pathways [34]. Various intermediary biochemical reactions and intracellular transport pathways provide dynamic and reciprocal control of substrate flux through myocardial glycolytic pathways and fatty acid (**FA**) β -oxidation in response to changes in the plasma substrate environment, neurohumoral milieu, and level of cardiac work. The ability to perform these rapid adaptations is central to cardiac myocyte health.

Chronic metabolic adaptations in metabolism can occur when the heart is subject to prolonged stimuli such as sustained increases in plasma FA levels or left ventricular wall stress. Such adaptations are the result of changes at the gene transcriptional level involving various master control points, resulting in the coordinated and sustained upregulation of enzymes and proteins of key metabolic pathways. Thus, in obesity and diabetes mellitus, a prolonged increase in FA delivery activates the nuclear receptor peroxisome

proliferator-activated receptor alpha (**PPAR α**), a key regulator of myocardial FA uptake, oxidation, and storage, resulting in a sustained increase in these processes [35, 36]. In heart failure, a reduction in PPAR α activity downregulates the genes controlling FA metabolism, which in turn leads to an upregulation of glucose use [37, 38]. These chronic changes in myocardial metabolism may be adaptive or maladaptive. An example of the former is observed in hibernating myocardium, where the shift toward glucose use is designed to achieve a more favorable energetic state [39]. Examples of the metabolic response becoming maladaptive include the induction of host processes detrimental to myocardial mechanical function such as an impairment in energy production and transduction, an increase in oxidative stress and inflammation, and overstimulation of cell death and growth pathways [40]. Discussed in the sections that follow are how various radiopharmaceuticals can help characterize these chronic adaptations in various disease processes.

20.4.1 Currently Available PET and SPECT Radiopharmaceuticals

A variety of PET radiopharmaceuticals are currently available to assess different aspects of myocardial metabolism. Currently, ^{123}I - β -Methyl iodophenyl-pentadecanoic acid is the only widely used SPECT radiopharmaceutical to image myocardial metabolism. The choice of radiopharmaceutical is predicated on various important factors, including the biochemical parameter of interest as well as the metabolic fate of the radiotracer. Listed in Table 20.1 are the currently available PET and SPECT radiopharmaceuticals. Many have been available for decades and have been detailed elsewhere [41]. Discussed in more detail next are their clinical and research applications.

20.4.2 Applications

20.4.2.1 Myocardial Viability

The most common clinical use of myocardial metabolic imaging is in the detection of viable myocardium with PET and FDG. The clinical objective of myocardial viability assessment is to prospectively identify patients with CAD and reversible LV dysfunction in whom regional and global LV function, as well as prognosis, may be favorably altered with revascularization. The metabolic patterns that are observed are preserved glucose metabolism in viable tissue and reduced glucose metabolism in scarred or fibrotic tissue. FDG may be preserved or increased in hypoperfused but viable myocardium (termed *metabolism/perfusion mismatch*) and decreased or absent in hypoperfused and scarred myocardium (termed *metabolism/perfusion match*) (Figure 20.7). PET with FDG is the most sensitive approach for predicting recovery of regional systolic function (sensitivity ~90%), which exceeds the performance of SPECT, echocardiographic, and MR approaches to detect viable myocardium [42]. Of note, the presence of viable myocardium is a marker of increased CV risk (Figure 20.8) [43, 44]. Moreover, improvement in LV

Metabolic process	Radiotracer
Oxygen consumption	$^{15}\text{O}_2$, ^{11}C -acetate
<i>Long-chain fatty acid metabolism</i>	
Uptake, oxidation, and storage	^{11}C -palmitate
Uptake and oxidation	^{18}F -FTHA, ^{18}F -FTP, ^{18}F -FTO, ^{18}F -FCPHA
Uptake and storage	^{123}I -BMIPP
<i>Carbohydrate metabolism</i>	
Uptake	FDG
Uptake, glycolysis, and oxidation	^{11}C -glucose
Lactate metabolism	^{11}C -lactate

Table 20.1 PET and SPECT radio-tracers of myocardial metabolism.

^{18}F -FCPHA, *trans*-9(*RS*)- ^{18}F -fluoro-3,4(*RS,RS*) methyleneheptadecanoic acid; FDG, fluorodeoxy-glucose; FTHA, 14-(*R,S*)- ^{18}F -fluoro-6-thia-heptadecanoic acid; FTO, 18- ^{18}F -fluoro-4-thia-oleate; FTP, 16- ^{18}F -fluoro-4-thia-palmitate, ^{123}I - β -Methyl iodophenyl-pentadecanoic acid [41]. Source: Gropler, R.J. [41].

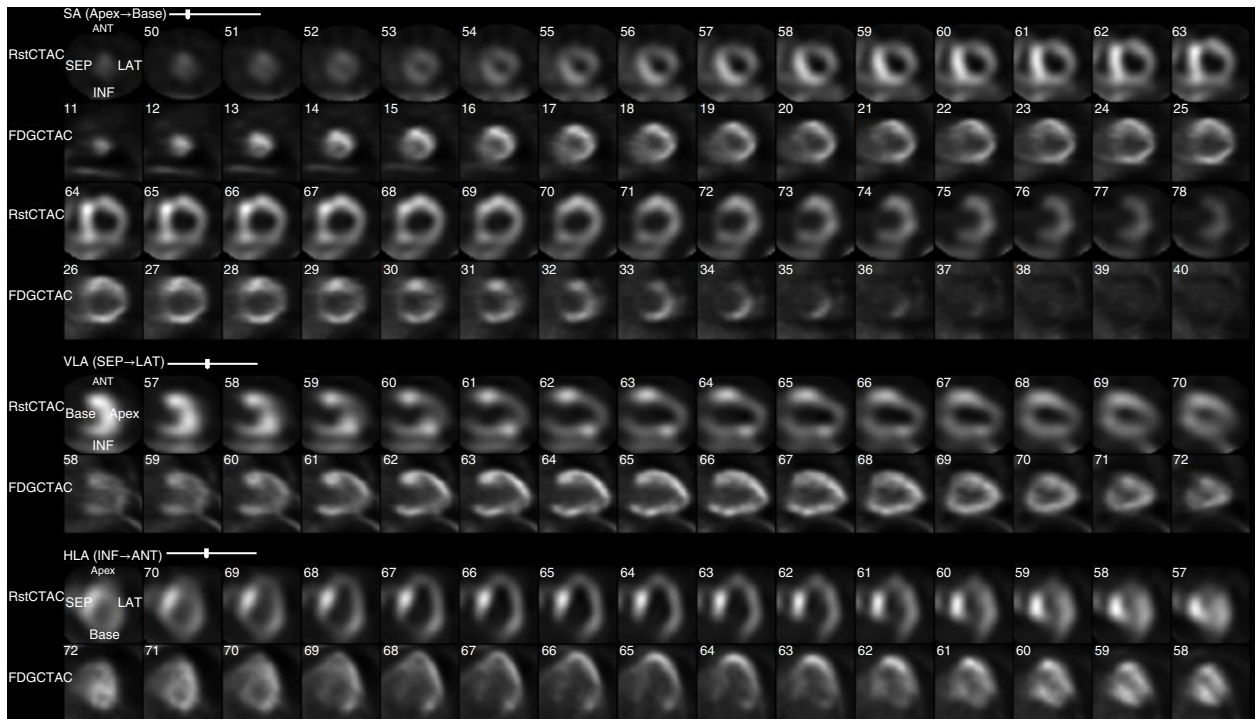


Figure 20.7 T99mTc-Tetrofosmin SPECT MPI and FDG PET/CT of a patient with an ischemic cardiomyopathy. Extensive metabolism-flow mismatches in the antero-apical, mid-basal inferior lateral walls consistent with hibernating myocardium. In addition, FDG uptake in the lateral increased out of proportion relative to the interventricular septum, which has preserved perfusion. This pattern suggests myocardial ischemia.

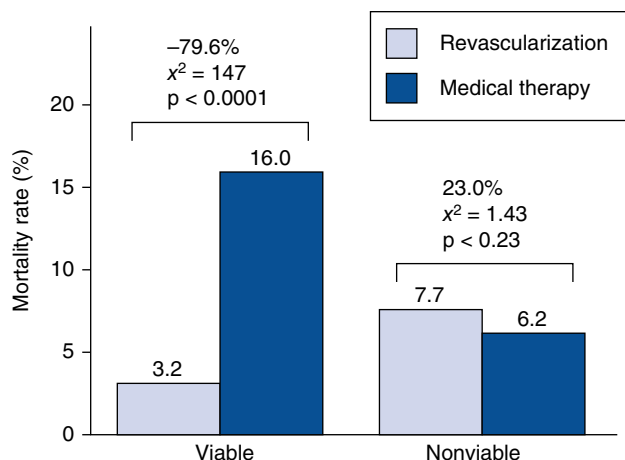


Figure 20.8 Mortality rates for patients with viable or non-viable tissue and response to revascularization. Note the higher mortality rates in patients treated medically with viable tissue compared with patients with non-viable tissue, indicating a higher risk. Source: Tajouri, T.H. and Chareonthaitawee, P. [43]. © 2010 Taylor & Francis.

function after revascularization, the magnitude of improvement in heart failure symptoms, and survival after revascularization correlate with the extent of the “mismatch” pattern present initially [45]. In contrast, in patients with heart failure, the presence of an extensive PET “match” pattern representing predominant infarction, the likelihood of benefiting clinically from revascularization is low. There are few prospective trials to confirm that PET with FDG can be used to help guide myocardial revascularization decisions. The largest such study to date is the Positron Emission Tomography and Recovery Following Revascularization-2 (PARR-2) trial, which evaluated a PET-guided strategy for the management of patients with LV dysfunction due to ischemic cardiomyopathy [46]. Patients were randomized to management assisted by PET with FDG or standard care. The results suggested that in patients who did receive PET-guided therapy, a significant reduction in the primary endpoint was noted and was still present at five years of follow-up [47]. Moreover, at least in the short term, there was improved quality of life [48].

20.4.2.2 Sex Differences in Myocardial Substrate Metabolism

There is sexual dimorphism in myocardial metabolism. Multi-tracer PET studies in healthy young volunteers demonstrated that women exhibited lower levels of glucose metabolism but higher MVO_2 compared with men [49]. In contrast, PET with FDG has demonstrated that as women reach middle age, the dependence of the myocardium on glucose use exceeds that of men, with differences resolving in the elderly [50]. These general trends in myocardial metabolism of female hearts using less glucose and more oxygen and FA than male hearts also generally hold true in multiple

pathological states such as obesity, diabetes mellitus, and non-ischemic dilated cardiomyopathy (Figure 20.9) (discussed in more detail in the following sections). There are likely multiple drivers for the major sex-related differences in myocardial metabolism, such as the influence of sex hormones and greater % FA mass in women whose relative roles in physiological and pathological conditions remains to be determined [51–55].

20.4.2.3 Aging and Myocardial Metabolism

As the heart ages, the contribution of FA oxidation to overall myocardial substrate metabolism declines [56, 57]. The cause of the decrease in FA oxidation seems multifactorial with pre-clinical studies documenting changes in mitochondrial lipid content, oxygen free radical injury, and age-related decline in myocardial PPAR α activity [58–60]. Using a variety of PET metabolic radiotracers, it has been shown that a similar metabolic shift occurs in healthy older humans [61]. However, despite this relative preference for glucose as an energy substrate, older individuals are not able to increase glucose metabolism in

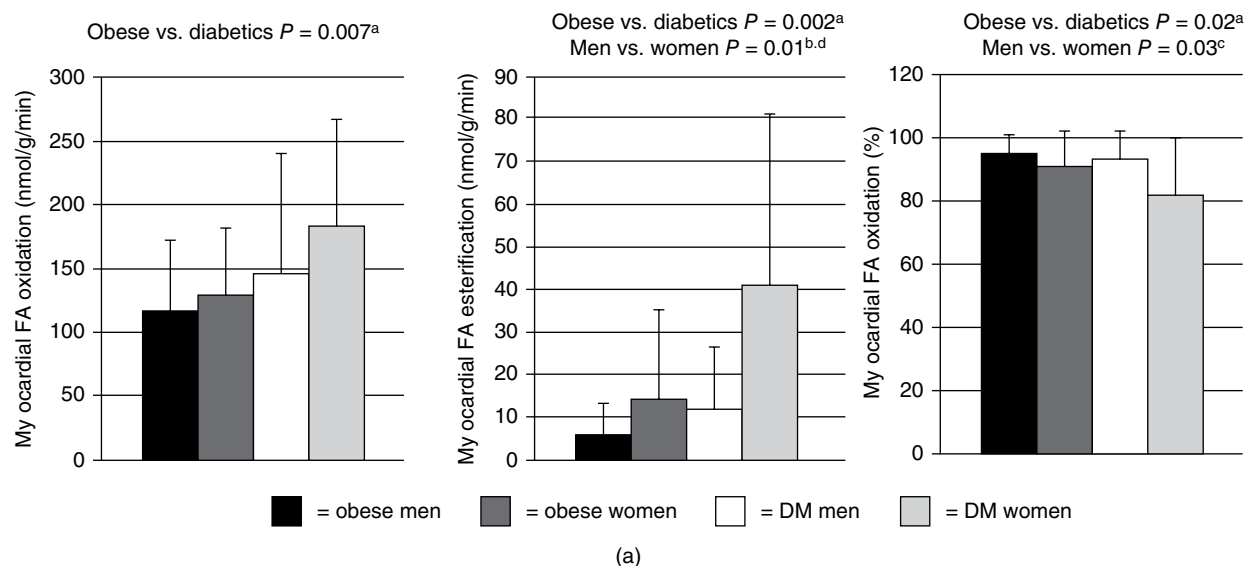
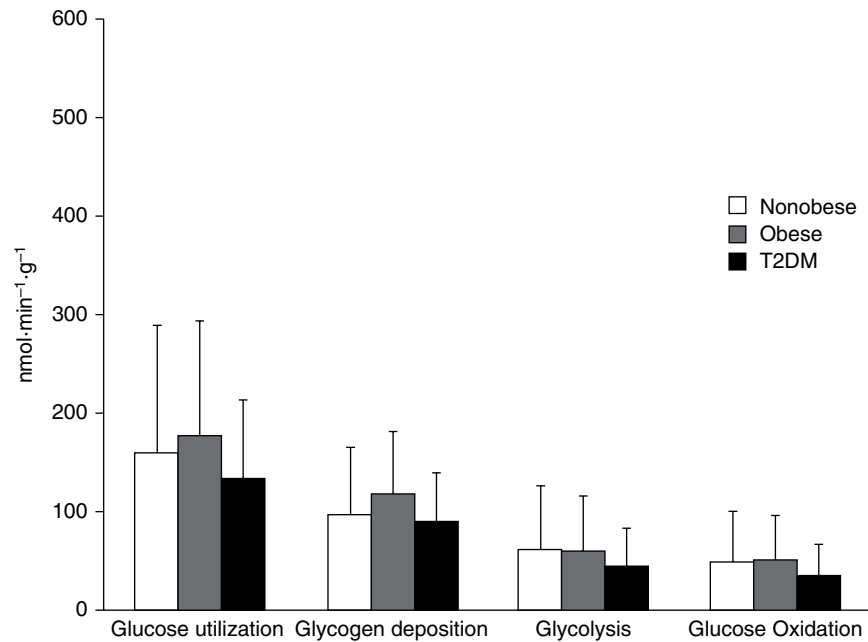
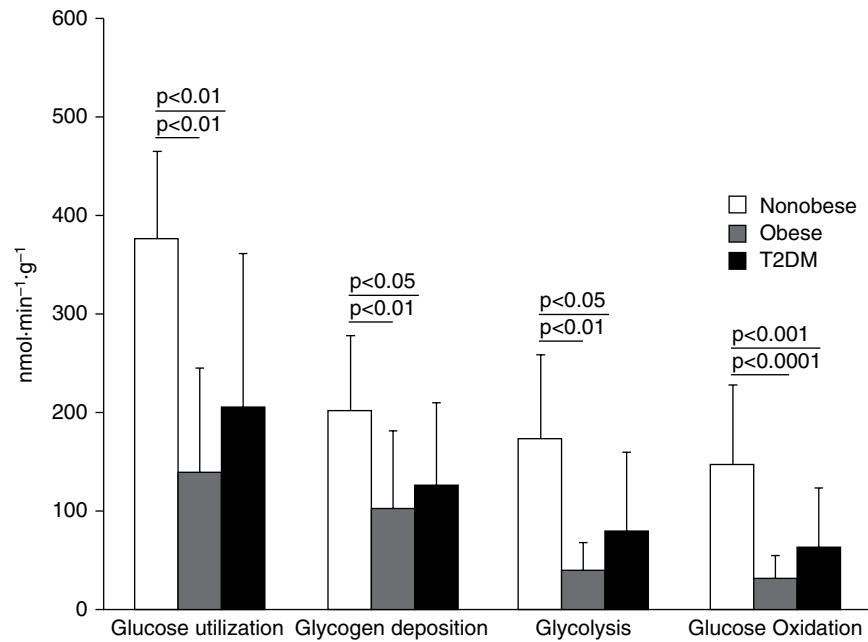


Figure 20.9 Sexual dimorphism of myocardial metabolism. (a) Effects of sex and diabetes (DM) on myocardial FA oxidation, esterification, and % oxidation, suggesting more pronounced effects in women. Source: Peterson, L.R. et al. [74]. (b) Measurements of myocardial glucose utilization, glycogen deposition, glycolysis, and oxidation measured by PET with ^{11}C -glucose in lean, obese, and diabetic men (top) and women (bottom). Data suggest that men exhibit a greater decline in glucose metabolism compared with women as one transitions from lean to obese to diabetes. Source: Peterson, L.R. et al. [72]. © 2015 American Physiological Society.



(b)

Figure 20.9 (Continued).

response to β -adrenergic stimulation with dobutamine to the same extent as younger individuals [62]. However, endurance exercise training can ameliorate this impairment in metabolic reserve in older subjects [63]. Although requiring further study, these sex and

age differences in metabolism may provide a partial explanation for the sex- and age-related outcome differences for various CV diseases where altered myocardial metabolism plays a role.

20.4.2.4 Cardiometabolic Disease

It is now apparent from pre-clinical models of obesity that a significant increase in body mass index induces marked increases in myocardial FA metabolism resulting in excessive intracellular FA accumulation, increased inflammation, oxidative stress, and apoptosis [64]. Multi-radiotracer PET studies in obese humans have demonstrated that an increase in body mass index is associated with a shift in myocardial substrate metabolism toward greater FA use that is more pronounced in women. Moreover, this dependence on myocardial FA metabolism increases with worsening insulin resistance [65]. In contrast, obese men have greater impairment in myocardial glucose metabolism at the same level of plasma insulin, suggesting greater myocardial insulin resistance [66]. Thus it appears there is a complex interplay between sex and obesity in influencing myocardial substrate metabolism. Finally, metabolic imaging with PET has documented the salutary effects of weight loss on myocardial metabolism, structure, and function [67–69].

With the onset of type-2 diabetes mellitus, the metabolic perturbations observed with obesity become more pronounced. In preclinical models with both type-2 diabetes mellitus and humans with the disease, there is a progressive increase in myocardial FA metabolism with a decline in glucose use [40, 70–76]. These metabolic changes are paralleled by a decline in LV diastolic function [74]. It also appears there is sexual dimorphism in these responses, with women exhibiting a greater increase in FA metabolism and a decline in diastolic function compared with male diabetics. In contrast, male diabetics exhibit a greater decline in glucose metabolism [72, 74]. These results are intriguing given the greater susceptibility of females with type-2 diabetes mellitus to developing heart failure and the fact that they exhibit a poorer prognosis when it is present compared with male diabetics.

Human studies employing PET have been useful in demonstrating that the myocardial metabolic response to various classes of antidiabetic agents is independent of the degree of glycemic control. Of note, different therapeutic regimens impact myocardial metabolism in a sex-specific manner [77]. These results suggest that more personalized approaches that incorporate patient sex may be useful in designing diabetic therapies.

20.4.2.5 Myocardial Hypertrophy

With progressive LV and right ventricular (**RV**) hypertrophy, there is a reduction in the expression of β -oxidation enzymes, leading to a fall in myocardial FA oxidation and an increase in glucose use [79, 80]. This adaptive response is considered beneficial to cardiac function under acute conditions; but under exposure to sustained pressure overload, the metabolic switch becomes more permanent, impairing flexibility in myocardial substrate use and inducing mitochondrial dysfunction. In preclinical models of LV hypertrophy, PET

with FDG has demonstrated that these metabolic adaptations may drive the hypertrophic response with respect to its functional and structural consequences [81, 82].

Similar results have been found in humans. PET with $1\text{-}^{11}\text{C}$ -palmitate in humans has shown the reduction in myocardial FA oxidation to be an independent predictor of LV mass in hypertension [83]. Of note, PET with FDG studies demonstrated higher rates of myocardial glucose uptake with PET in hypertensive patients without LV hypertrophy compared with controls, suggesting that the metabolic remodeling preceded structural remodeling in these patients [84]. Similar observations of increased myocardial FDG uptake have been obtained in patients with RV hypertrophy due to pulmonary hypertension (Figure 20.10) [85–87]. It also appears that measuring RV FDG uptake can be used to follow therapeutic responses to the treatment of pulmonary hypertension, as a decrease in RV myocardial glucose uptake parallels a decline in pulmonary hypertension [88, 89]. In summary, these studies raise the possibility of using metabolic imaging for both prognosis assignment and treatment monitoring for patients with pressure-overload conditions of either the left or right ventricle.

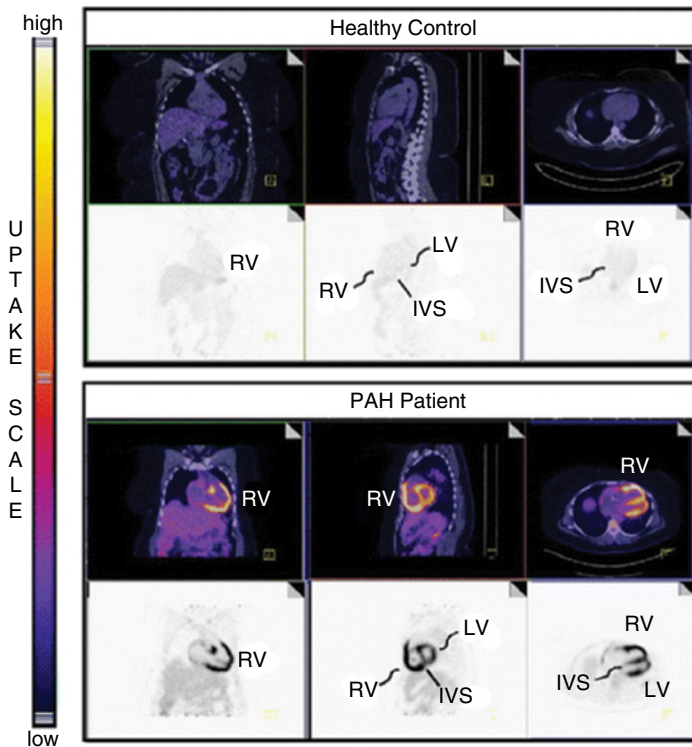


Figure 20.10 Fasting FDG-PET imaging of a control participant and a patient with pulmonary arterial hypertension (PAH). Fasting FDG-PET imaging reveals generalized enhanced FDG standardized uptake value in the PAH heart. IVS, interventricular septum; LV, left ventricle; RV, right ventricle. Source: Lundgrin, E.L. et al. [87].

20.4.2.6 Dilated Nonischemic Cardiomyopathy

Animal models of heart failure have shown that during the progression from cardiac hypertrophy to ventricular dysfunction, changes in the expression of key metabolism-regulating genes result in a shift in myocardial substrate metabolism to primarily glucose use, similar to that seen in the fetal heart [90, 91]. These metabolic changes are paralleled by the re-expression of fetal isoforms of a variety of contractile and calcium regulatory proteins. The reactivation of the metabolic fetal gene program may have numerous detrimental consequences on myocardial contractile function, ranging from energy deprivation to the inability to process FAs, leading to the accumulation of nonoxidized toxic FA derivatives and resulting in lipotoxicity.

In humans with nonischemic dilated cardiomyopathy, the downregulation in myocardial FA metabolism and overdependence on glucose use in heart failure has been well documented with PET techniques [92–94]. Of note, the presence of concomitant insulin resistance appears to be a major contributor to the variability in levels of myocardial glucose and FA metabolism. There are also classic sex-related differences in myocardial metabolism between men and women with cardiomyopathy. Women with heart failure have higher FA uptake and metabolism as well as higher myocardial blood flow than their male counterparts. Interestingly, myocardial blood flow per gram of myocardium predicts event-free survival even in patients with nonischemic heart failure [95]. In addition, numerous PET studies have demonstrated both direct and indirect effects on myocardial metabolism of various therapeutic interventions [96–99].

20.5 MOLECULAR IMAGING

Due to the inherent high sensitivity of the radiopharmaceutical approach and the improved resolution capabilities of hybrid technologies, major advances have been made in the development of radiopharmaceutical-based molecular imaging probes for CV applications. Notable processes of interest include neuronal function, inflammation, calcification, and amyloid deposition. Radiopharmaceuticals that detect processes and their applications are summarized next.

20.5.1 Cardiac Neuronal Function

Cardiac neuronal function encompasses the autonomic nervous system, which is composed of both the sympathetic and parasympathetic nervous systems. Cardiac neuronal function plays a key role in maintaining cardiovascular homeostasis at rest and, in response to a variety of stimuli and its aberrations, contributes to the pathobiology of many CV diseases, including CAD, hypertension, and heart failure [100–103]. Numerous radiopharmaceuticals have been developed to study the autonomic nervous system and are summarized in Figure 20.11. The two most commonly used radiotracers have been ^{123}I -metaiodobenzylguanidine (^{123}I -mIBG) and ^{11}C -meta-hydroxyephedrine (HED).

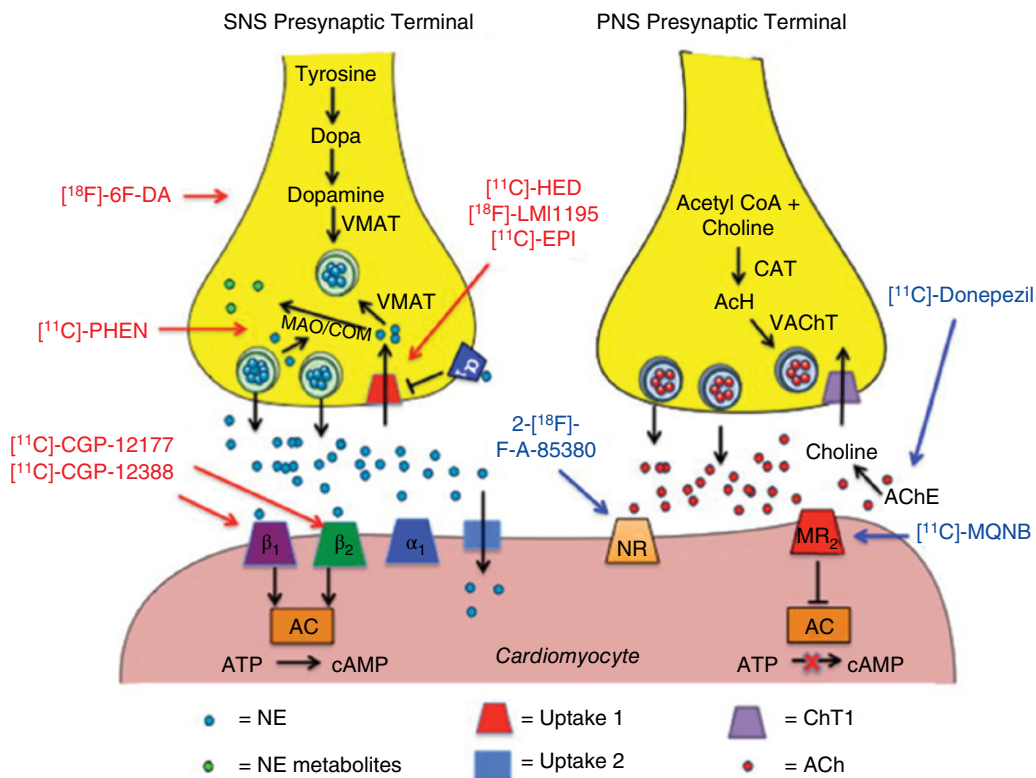


Figure 20.11 Depiction of postganglionic sympathetic nervous system (SNS) and parasympathetic nervous system (PNS) nerve endings. (Left) Synthesis and release of norepinephrine in postganglionic SNS nerve endings and subsequent binding to postsynaptic receptors on cardiomyocytes. The tracers in red depict SNS pre- and postsynaptic radioanalogs. (Right) Synthesis and release of acetylcholine in the terminal nerve ending and varicosities of postganglionic PNS nerve endings and subsequent binding to postsynaptic receptors on cardiomyocytes. Tracers in blue depict PNS pre- and postsynaptic radioanalogs. AC, adenylyl cyclase; ACh, acetylcholine; AChE, acetylcholinesterase; ATP, adenosine triphosphate; CAT, choline-acetyl-transferase; COM, catechol-O-methyltransferase; cAMP, cyclic adenosine monophosphate; MAO, monoamine oxidase; MR₂, muscarinic receptor 2; NE, norepinephrine; NR, α₄β₂ nicotinic receptor; VMAT, vesicular monoamine transporter; ¹⁸F-6F-DA, 6-¹⁸F-fluorodopamine; PHEN, phenylephrine; EPI, epinephrine; HED, hydroxyephedrine; MQNB, (R,S)-N-[¹¹C]-methylquinuclidin-3-yl benzilate. Source: Boutagy, N.E. and Sinusas, A.J. [106]. © 2017 Current Science Inc.

¹²³I-mIBG is a modification of guanethidine, an analog of norepinephrine that is taken up via the uptake-1 pathway. ¹²³I emits predominantly gamma photons with energies of 159 keV, has a half-life of 13.2 hours, and easily is imaged with either planar imaging or SPECT. Interpretation of cardiac ¹²³I-mIBG images are based on the assessment of global tracer uptake on planar images, tracer washout between early and delayed planar images, and regional uptake on tomographic images. The standard measure of global uptake is the heart mediastinal ratio (HMR), derived through assessment of activity in a

region of interest over the heart and referenced to a background area in the upper mediastinum. Assessing regional ^{123}I -mIBG uptake on tomographic images, although less well studied and established, provides information on regional sympathetic nervous system innervation of the heart. This may allow early identification and stratification of patients at risk of sudden cardiac death [104].

^{11}C -meta-hydroxyephedrine (HED) is the most commonly investigated neuronal PET radiotracer. It has higher uptake-1 selectivity than ^{123}I -mIBG, resulting in better differentiation between innervated and denervated myocardium, which may be an advantage in evaluating neuronal heterogeneity in hibernating myocardium [105]. In addition to better image quality, ^{11}C -HED also appears to have more homogeneous uptake than ^{123}I -mIBG. Myocardial HED uptake is typically quantified as the retention index, which represents the activity in the myocardium at the end of a dynamic scan divided by the integral of the image-derived arterial input function [106].

To enhance dissemination and improve the imaging characteristics of ^{123}I -mIBG, [^{18}F]-labeled benzylguanidine, ^{18}F -*N*-[3-bromo-4-(3-fluoro-propoxy)-benzyl]-guanidine ([^{18}F]-LMI1195), was developed [107–109]. Initial studies showed relatively high myocardial selectivity for the uptake-1 mechanism in rabbits and non-human primates, with image quality superior to ^{123}I -mIBG. A first-in-human study demonstrated an acceptable safety and radiation dosimetry profile with promising image quality [108].

20.5.2 Applications

20.5.2.1 Heart Failure

Excessive activation of the cardiac sympathetic nervous system is a hallmark of progressive heart failure and a marker of poor prognosis [110]. It is on this basis that PET with ^{123}I -mIBG and HED have been evaluated as tools to help guide management in these patients [111–114]. The multi-center ADMIRE-HF (AdreView Myocardial Imaging for Risk Evaluation in Heart Failure, AdreV = ^{123}I -mIBG) trial demonstrated that a heart-to-mediastinal ratio of <1.6 separated heart failure patients (New York Heart Association Heart Failure Class II–III and LVEF 35%) with and without events (cardiac death, worsening heart failure class, and life-threatening arrhythmia) [115]. Similar data were observed with HED [112]. Even though ^{123}I -mIBG has been approved by the FDA for prognostication in patients with heart failure with reduced ejection fraction, due to cost and lack of perceived demonstrable added value by clinicians, the technique has not achieved widespread acceptance. Until either it, HED, or another PET imaging approach can more confidently identify patients at very low risk for sudden cardiac death that obviates the need for implantation of a defibrillator, it is unlikely that any of these approaches will achieve routine clinical use in these patients.

20.5.2.2 Cardiac Transplant Rejection

Cardiac transplantation is a common treatment for patient end-stage heart failure that results in denervation of the donor heart. In patients who are post-heart transplantation,

PET with HED has been used to invasively characterize both the cardiac denervation and reinnervation process as well as the cardiac physiological responses to them [116, 117]. Initial cross-sectional studies using PET HED showed regional heterogeneity in myocardial uptake [118]. Longitudinal HED studies demonstrated that the reinnervation process initially occurs in the anteroseptal wall in a basal-to-distal fashion, with reinnervation then proceeding in the lateral wall, inferior wall, and apex [117]. Importantly, reinnervation had beneficial effects on myocardial perfusion, chronotropy, and inotropy in response to aerobic exercise [116].

20.5.3 Inflammation

Inflammatory processes are central to a host of CV disorders ranging from atherosclerosis and its consequences, such as post-MI remodeling, to various cardiomyopathies such as sarcoidosis, to cardiac device infections. As a consequence, there has been growing interest in developing and optimizing nuclear cardiology approaches to detect inflammation of the heart and the arterial system. Numerous radiopharmaceuticals of diverse biological targets have been developed and are listed in Table 20.2. Presented next is a more detailed description of these radiopharmaceuticals and their application in a variety of CV inflammatory conditions.

20.5.4 Radiopharmaceuticals that Detect Inflammation

20.5.4.1 Cell Metabolism

20.5.4.1.1 *Glucose Metabolism*

Due to the overexpression of glucose transporters and the overproduction of glycolytic enzymes, glucose metabolism is increased in inflammatory cells [119]. As a consequence, PET/CT with FDG is currently the most commonly used approach to detect CV inflammation. A key aspect of PET/CT with FDG for imaging myocardial or cardiac inflammation is to standardize the substrate environment to suppress myocardial glucose uptake. In this way, the observed FDG signal will reflect myocardial inflammation and not glucose metabolism by normal cardiac myocytes. Several approaches for myocardial suppression have been proposed, including prolonged fasting, dietary modifications, and a heparin load before imaging. However, inadequate suppression may be seen in between 10% and 20% of patients, which decreases the desirability of FDG for myocardial or cardiac inflammation imaging [120].

20.5.4.1.2 *Amino Acid Metabolism*

Amino acids, particularly methionine, are significant metabolic substrates for activated leukocytes but not a significant metabolic substrate for cardiac myocytes. Thus, they may be more attractive than glucose for targeting cardiac inflammatory processes based on a metabolic readout. Given that ^{11}C -methionine has been used to study tumor amino acid metabolism, it has also been proposed to assess myocardial inflammation. To support this

Table 20.2 Examples of radiotracers for inflammation.

Radiotracer (s)	Biologic target	Demonstrated application	Human imaging
F-18 FDG	Glucose metabolism	Atherosclerosis, post-MI response, inflammatory cardiomyopathies, CIED infections, and AAA	Yes
C-11 methionine	Amino acid metabolism	AAA and post-MI response	Yes
C-11 thymidine			Yes
Ga-68 DOTATAE and DOT-ATAC	SSTR-2	Atherosclerosis, post-MI response, and inflammatory cardiomyopathies	Yes
C-11 PK11195	TSPO	Atherosclerosis and post-MI response	Yes
C-11 PBR28			Yes
F18 flutriclamide			No
Ga-68 Pentixafor	Chemokines	Atherosclerosis, post-MI response, and AAA	Yes
Cu-64 or Ga-68 DOTA-ELCI			Yes
Cu-64 DOTA-vMIP			No
F-18 Galacto-RGD	Integrins	Atherosclerosis and post-MI response	Yes
Tc-99m RP805	MMPs	Atherosclerosis, post-MI response, and AAA	No
Tc-99m RYM1			No
F-18 F12	ROS	Doxorubicin cardiotoxicity	No
F-18 FHMT			No
F-18 NOS	RNS	Post-heart transplant rejection	Yes
Tc-99m Annexin-V	Apoptosis	Atherosclerosis, ischemia/reperfusion, and post-heart transplant rejection	Yes
Tc-99m Duramycin			No
F-18 TPP			No
F-18 WC-116			No

FDG, Fluorodeoxyglucose; MI, Myocardial Infarction; CIED, cardiovascular implantable electronic device; AAA, abdominal aortic aneurysm; SSTR-2, somatostatin receptor 2; TSPO, mitochondrial translocator protein; RGD, arginine-glycine-aspartic acid; FHMT, F6-(4-((1-(2-fluoroethyl)-1*H*-1,2,3-triazol-4-yl)methoxy)phenyl)-5-methyl-5,6-dihydrophenanthridine-3,8-diamine; NOS, nitric oxide synthase; TPP, triphenylphosphonium.

contention, increasing [¹⁴C]methionine myocardial accumulation corresponded to CD68-positive macrophages in the infarct territory in a pre-clinical prior to model of ischemia and reperfusion [121]. Another key process contributing to an inflammatory response is immune cell proliferation. The thymidine analog ¹⁸F-fluoro-3'-deoxy-3'-L-fluorothymidine has been used to assess cellular proliferation of tumor cells. Given the comparable proliferative rates between cancer cells and macrophages found in atherosclerotic plaques and the known hematopoietic tissue uptake of ¹⁸F-FLT uptake, the radiotracer has been proposed to study CV inflammation [122].

20.5.4.2 Somatostatin Receptor 2 (SSTR-2)

Up-regulation of the G-protein-coupled receptor SST2 that occurs on the surface of activated macrophages has been shown by RNA sequencing data, demonstrating a two- to fivefold increase of SSTR2 M1-like macrophages compared to other leukocytes [123].

⁶⁸Ga-DOTATATE and ⁶⁸Ga-DOTATOC target SSTR2 and are routinely used for neuroendocrine tumor imaging. As a consequence, their applicability to assess CV inflammation has also been explored [124, 125]. Compared with FDG, they offer the advantage of not requiring dietary manipulation but tend to have poorer image quality due to the level of expression of SSTR2 being significantly less than the enhancement in glucose metabolism in macrophages.

20.5.4.3 Mitochondrial Translocator Protein (TSPO)

TSPO supports oxidative metabolism at the level of the electron transport chain. It is up-regulated in activated inflammatory cells such as the microglia in the central nervous system and peripheral leukocytes [126, 127]. Numerous carbon-11 and F-18 radiolabeled radiopharmaceuticals have been developed and evaluated in various models of CV inflammation such as atherosclerosis and post-MI remodeling [126, 128–130]. A current challenge using these radiopharmaceuticals is reduced binding in patients with genetic polymorphisms of the receptor.

20.5.4.4 Chemokine System

Chemokines are a superfamily of structurally related, small (most being 8–10 kDa) chemotactic cytokines involved in leukocyte trafficking and activation [131]. The specific effects of the chemokines on their target cells are mediated by members of a family of 7-transmembrane-spanning, G-protein-coupled chemokine receptors through chemokine gradients. The chemokine/chemokine receptor axes play a crucial role in directing the movement of mononuclear cells throughout the body, engendering an immune response, and contributing to the pathogenesis of most common diseases, including those involving the CV system [132, 133]. Thus, they are an attractive target for radiotracer development.

The most heavily studied radiopharmaceutical targeting chemokines is the pentapeptide ⁶⁸Ga-pentixafor, which targets CXCR4. Originally developed for oncologic imaging, this receptor and its specific ligand CXCL12 (or SDF1- α) mediate the trafficking of leukocytes, notably neutrophils. The radiopharmaceutical has demonstrated promise for image inflammatory processes associated with atherosclerosis and post-MI remodeling in both pre-clinical disease models and patients [134–136]. A challenge in interpreting tissue signals is that the CXCL2/CXCR4 axis represents a broad range of cell types besides inflammatory cells [137].

Another approach is to target the monocyte chemoattractant protein-1/C-C chemokine receptor type 2 (MCP-1/CCR2) axis due to its central role in the recruitment of pro-inflammatory monocytes to tissue as well their conversion of pro-inflammatory macrophages [138]. Based on the peptide ECL1i, [139] a non-competitive inhibitor of CCR2, PET radiopharmaceuticals have been developed through radiolabeling with either Cu-64 or Ga-68 [140, 141]. These radiotracers have shown promise in various pre-clinical models of CV inflammation and are now undergoing human evaluation. Due to the redundancy in the chemokine system (e.g. multiple receptor binding by a single chemokine), a third radiopharmaceutical strategy has focused on simultaneously targeting

numerous key chemokine receptors using viral macrophage inflammatory protein II (**vMIP-II**). Cu-64 radiolabeled vMIP-II conjugated to a comb-like nanoparticle (⁶⁴Cu-vMIP-II-comb) has shown the potential to detect elevated expression of F4/80 macrophages and rising expression of several chemokine receptors in a pre-clinical model of vascular injury [142].

20.5.4.5 Integrins

Integrins are cell-adhesion molecules that mediate rolling and extravasation of leukocytes and are expressed by both endothelial cells and activated leukocytes. Numerous radiopharmaceuticals targeting the arginine-glycine-aspartic acid (RGD) peptide sequence expressed by $\alpha_v\beta_3$ integrins have been developed, with several, such as ¹⁸F-fluciclatide and ¹⁸F-Galacto-RGD, showing promise in detecting CV inflammation in humans [143, 144]. Because $\alpha_v\beta_3$ integrins are also up-regulated in angiogenesis, the timing of imaging with RGD-targeted radiopharmaceuticals is essential, as inflammation and angiogenesis typically occur in the same disease processes but with different temporal patterns.

20.5.4.6 Matrix Metalloproteinases (MMPs)

MMPs are a multi-gene family of endopeptidases that selectively digest individual components of the extracellular matrix. However, no in situ enzymatic activity is detectable in normal arteries. Inflammatory cells are an important source of MMPs, so there appears to be a causal relationship between inflammation and destruction of the extracellular matrix in disease processes such as atherosclerosis, post-MI remodeling, and abdominal aortic aneurysm (**AAA**) development and progression [145–147]. So, radiopharmaceuticals of MMP activity provide a readout of the effects of inflammation. Two SPECT radiopharmaceuticals, ^{99m}Tc-RP805 and ^{99m}Tc-RYM1, bind to the active catalytic site of MMPs and have shown promise for detecting the effects of inflammation in pre-clinical models of post-MI remodeling and AAA [148, 149].

20.5.4.7 Superoxide Levels

Not only are oxidative stress machinery and inflammatory signaling interrelated, but their exuberance can lead to a host of maladaptive events that lead to higher CV risk. Oxidative stress reflects the overabundance of both reactive oxygen species (**ROS**) and reactive nitrogen species (**RNS**). Given the importance of superoxide as a ROS, a ¹⁸F-labeled analog (¹⁸F-12) of the well-known fluorescence probe dihydroethidium was developed. When dihydroethidium encounters superoxide, it is converted to the charged molecule ethidium or 2-OH ethidium, which is retained in tissue in contrast to the nonoxidized form of dihydroethidium (which rapidly clears from tissues). This retention allows for determining the amount of superoxide produced in a given tissue. In mice treated with doxorubicin, a well-established model of marked production of superoxide, myocardial uptake of ¹⁸F-12 was approximately twofold higher than in controls [150]. Of note, retention of a similar form of this radiotracer

(¹⁸F-4-((1-(2-fluoroethyl)-1*H*-1,2,3-triazol-4-yl)methoxy)phenyl)-5-methyl-5,6-dihydro-phenanthridine-3,8-diamine) is seen in normal canine myocardium, suggesting potential oxidation by heme proteins [151].

20.5.4.8 Inducible Nitric Oxide Synthase

Increases in RNS and inflammation are both hallmarks of chronic metabolic adaptations in various forms of cardiac disease. The inducible form of nitric oxide synthase (**iNOS**) is a key modulator of both of these processes, with low levels of expression that increase dramatically to a stimulus to produce significantly higher levels of nitric oxide compared with the other nitric oxide synthases. To image iNOS levels, an analog of the reversible NOS inhibitor 2-amino-4-methylpyridine, specific for iNOS, was radiolabeled with fluorine-18 [152]. It showed promise in a murine model of lipopolysaccharide-induced pulmonary inflammation as well as in patients who had undergone orthotopic heart transplantation, using iNOS expression measured on endomyocardial biopsy to detect allograft rejection as the gold standard [153]. However, image quality was compromised by very rapid myocardial washout kinetics, suggesting that further optimization of the radiotracer is needed.

20.5.4.9 Apoptosis

Programmed cell death or apoptosis both plays an important role in the regulation of inflammation and may be the result of inflammation. Thus, noninvasive imaging of apoptosis is an attractive option to understand pathophysiology, track disease activity, and evaluate response to intervention in a variety of CV inflammatory conditions. Numerous radiopharmaceuticals have been developed to image the various components of the apoptotic pathways, including cell surface markers, activation of the intracellular apoptotic machinery, and mitochondrial imaging [154]. Examples of imaging cell surface markers include targeting the cell surface receptors that are externalized during the apoptotic process, such as Tc-99m-Annexin-5 radiotracers (which target phosphatidylserine) and ^{99m}Tc-labeled duramycin (which targets phosphatidylethanolamine), ¹⁸F-fluorophenyltriphenylphosphonium (which targets the mitochondrial membrane potential), and ¹⁸FWC-4-116 (which targets the executioner caspase 3/7) [155–158]. All of the radiotracers have shown some promise but have not achieved significant success in the heart. This may reflect the low levels of apoptosis in most disease processes and the non-specificity for myocardial apoptotic cells.

20.5.5 Applications

20.5.5.1 Cardiac Sarcoidosis

Sarcoidosis is a systemic granulomatous disease of unknown etiology that is characterized histologically by variable contributions of non-necrotizing granulomatous inflammation and concomitant fibrosis, with the lymph nodes and lungs the most frequently involved organs. Cardiac involvement is much less frequent but carries a significantly

worse prognosis, accounting for ~25% of deaths due to sarcoidosis. The clinical manifestations of cardiac sarcoidosis range from asymptomatic evidence of restrictive cardiomyopathy, to conduction abnormalities, to sudden cardiac death [120]. Unfortunately, clinical confirmation of cardiac sarcoidosis has proven elusive due to the non-specificity of disease manifestations, the lack of a clinical gold standard, and the limitations of endomyocardial biopsy. With proper suppression of myocardial glucose uptake, PET/CT and FDG provide early disease detection, image-guided biopsy, and therapy monitoring (Figure 20.12) [47, 159]. There are numerous patterns of myocardial uptake of FDG, with a patchy, focal uptake pattern being the most suggestive for the disease and RV uptake being associated with poorer prognosis [160]. In a recent meta-analysis where PET/CT and FDG were compared with the standard diagnostic criteria devised by the Japanese Ministry of Health, 89% sensitivity and 78% specificity for cardiac sarcoid detection were found [161]. The recent advent of PET/MR may provide unique and valuable information in the management of these patients. For example, the combined approach could provide confirmatory information regarding inflammation (presence of glucose metabolism by PET and increased edema by T_2 -weighted MR), which might increase confidence in proceeding with inflammatory therapy. In contrast, the presence and location of scar tissue (by late gadolinium enhancement MR) could provide evidence for the prediction for ventricular arrhythmias and guidance for potential ablative therapy or lead siting in the setting of implantable cardioverter defibrillator placement [162, 163]. Because of known limitations of myocardial inflammation with FDG PET/CT, the detection of cardiac sarcoidosis using PET/CT with ^{68}Ga -DOTOTAC has been explored. Overall, there was good concordance with CMR criteria for cardiac sarcoidosis, suggesting that further evaluation of this approach is warranted [164]. Of note, not all instances of focal increased FDG uptake

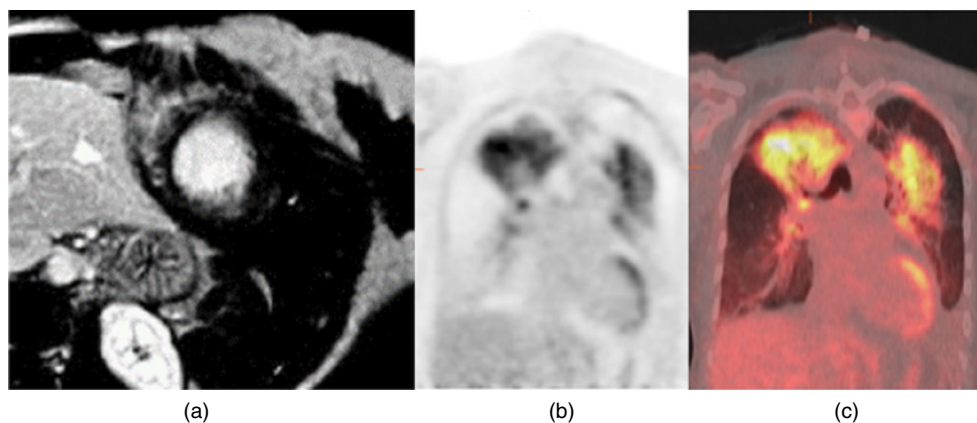


Figure 20.12 Patient with suspected cardiac sarcoidosis. (a) CMR with late gadolinium in the epicardial anteroseptal wall consistent with cardiac sarcoidosis. (b) PET/CT with FDG (no-attenuation correction) demonstrating increased FDG uptake in the anterior wall and apex as well as extensive bilateral lung activity. (c) PET/CT with FDG (co-registered with CT) confirming the myocardial and lung uptake. Tissue diagnosis confirmed cardiac and pulmonary sarcoidosis.

is indicative of cardiac sarcoidosis. In a recent study, the pathology and histology of explanted hearts from cardiac transplant recipients suspected to have cardiac sarcoidosis were compared with the results of FDG PET/CT and CMR performed pre-transplant. It was observed that in cases where cardiac sarcoidosis was deemed as probable by preset criteria, one-third of the patients were found to have an arrhythmogenic cardiomyopathy [165]. A joint consensus document has recently been published on the role of PET/CT with FDG in the management of cardiac sarcoidosis [120].

20.5.5.2 Cardiac Device Infection

The implantation of cardiac devices such as pacemakers, cardioverter defibrillators, and LV assist devices has increased dramatically over the past decade. This is in addition to the common use of prosthetic valve placement for valvular heart disease. The presence of infection of the devices and their localization (e.g. defibrillator pocket, pacemaker lead, annular or periannular valve ring abscesses) remains an important diagnostic challenge. A potential advantage of PET/CT with FDG is its detection of inflammatory cells early in the process, before morphological damage ensues. Indeed, initial studies suggest that among patients with a suspected cardiac mechanical device or prosthetic valve infection, PET/CT with FDG may identify the presence of infection, particularly when anatomic-based imaging studies, such as echocardiography or CT, are uncertain or negative [166–168]. A recent meta-analysis demonstrated that PET/CT with FDG detected cardiac device infection with pooled sensitivity of 87% and specificity of 94% [169]. Moreover, PET with FDG has been incorporated into the 2015 European Society of Cardiology Guidelines for the Management of Infective Endocarditis [170]. Despite this promise, harmonization is still required for the numerous components of study performance, such as dietary preparation, duration and timing of image acquisition, image processing with and without CT attenuation correction, and image interpretation and reporting.

20.5.5.3 Atherosclerosis Imaging

Atherosclerosis is a dynamic immune inflammatory process. It is characterized by cycles of intense activity and progression, followed by intervals of stabilization. To this end, FDG has been evaluated for the detection of “biologically active” atherosclerosis based on the premise that the tracer accumulates in activated macrophages, which are a key component of atherosclerotic plaque. Several groups have established that inflamed arterial vessels have increased uptake of FDG, as measured by PET. It appears that the degree of arterial FDG uptake is associated with certain morphological and blood biomarker risk factors for atherosclerosis. Moreover, it may be an independent predictor of future cardiac events [171]. PET/CT with FDG has been used to track atherosclerotic plaque inflammation following the administration of various statin and anti-diabetic therapies [172–175]. These studies highlight the potential of PET/CT with FDG to be used as a surrogate endpoint in clinical trials designed to assess anti-inflammatory therapies in atherosclerosis. To circumvent the problems with FDG as previously mentioned, other

radiopharmaceuticals that have been explored for this purpose include ^{11}C -PK1195, ^{68}Ga -DOTATATE, and ^{68}Ga -pentixifor [125, 126, 134].

Attempts have been made to perform PET/CT with FDG of the coronary arteries by combining the measurement with CT coronary angiography. The challenges here are substantial and are mostly due to the small size of the coronary arteries, the complex motion of the heart, and the contamination of the FDG signal from the myocardium. To date, imaging the coronary arteries has been limited to the left main coronary arteries and the proximal components of the rest of the coronary tree [176]. Using this approach has permitted noninvasive visualization of the culprit coronary atheroma in patients with acute coronary syndromes. Of interest, an increase in coronary atheroma FDG uptake observed in patients with acute coronary syndrome when compared with patients with stable CAD was associated with increased plasma markers for inflammation. Because ^{68}Ga -DOTATATE and ^{68}Ga -pentixifor do not exhibit cardiac myocyte uptake, they have been explored for this purpose with promising initial results [123, 134].

Recently, preclinical observations have suggested that an acute ischemic event, such as a myocardial infarction, liberates hematopoietic stem and progenitor cells from the bone marrow and spleen [177]. The subsequent pro-inflammatory monocytes is designed to stimulate wound healing but, if prolonged, can actually contribute to post-MI remodeling. The monocytes can also result in atherosclerotic plaque expansion and provide a mechanistic basis for the observed pro-inflammatory conditions following an acute ischemic event. Numerous studies using either PET/CT or PET/MR with FDG, ^{68}Ga -pentixifor, and ^{68}Ga -DOTA-ELCI have confirmed this temporally dependent pro-inflammatory state, paving the way for new diagnostic approaches and strategies to evaluate novel therapies post-MI (Figure 20.13) [136, 140, 178, 179]. Recently, whole-body PET with ^{11}C -PK1195 demonstrated myocardial and neuroinflammation in post-MI patients, providing a mechanistic basis for the cognitive decline frequently observed with myocardial infarction [130].

20.5.5.4 Microcalcification

Microcalcification plays a central role in the pathobiology of a host CV disease, including atherosclerosis, valvular heart disease, and AAA formation and progression [180–182]. Thus, *in vivo* detection of calcification on this microscopic scale with PET/CT and ^{18}F -NaF has been explored for these various conditions. In the case of atherosclerosis, its role is less clear due to the complex relationship between calcification and plaque rupture risk. However, the utility of PET/CT with ^{18}F -NaF as a marker of disease activity in calcific valvular heart disease is currently under evaluation in several clinical trials. While potentially useful as a tool to track the effect of therapeutic interventions on valvular calcification, ^{18}F -NaF PET imaging does not account for the fibrotic component of the disease, potentially limiting its role. In patients with AAA, ^{18}F -NaF uptake was increased compared with control patients, localized to areas of aneurysm disease and active calcification, and was associated with disease progression [181].

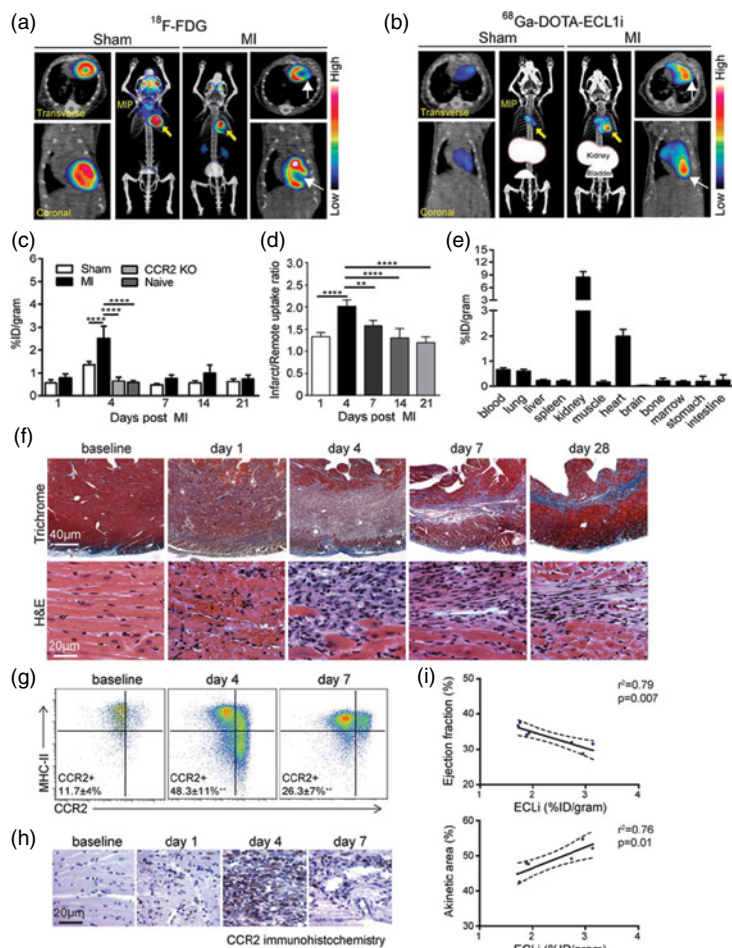


Figure 20.13 PET of ^{68}Ga -DOTA (1,4,7,10-tetraazacyclododecane-1,4,7,10-tetraacetic acid)-ECLi (extracellular loop 1 inverso) in a mouse model of closed-chest ischemia-reperfusion injury. (a) Representative ^{18}F -fluorodeoxyglucose (^{18}F -FDG) PET/CT images obtained five days after 90 minutes of ischemia-reperfusion injury, identifying the infarct region in mice that underwent ischemia-reperfusion injury (myocardial infarction [MI]) compared with sham controls. Transverse, coronal, and maximal-intensity projected (MIP) views are shown, and white arrows denote the infarct area. (b) Representative ^{68}Ga -DOTA-ECLi PET/CT images showing regional accumulation of ^{68}Ga -DOTA-ECLi signal in the infarct and border zone four days after ischemia-reperfusion injury. Transverse, coronal, and MIP views are shown. Yellow arrows identify tracer uptake in hearts that underwent ischemia-reperfusion injury compared with sham controls. White arrows denote the infarct area as determined by ^{18}F -FDG imaging. (c) Quantitative analysis of ^{68}Ga -DOTA-ECLi accumulation in the hearts of naive, sham, MI, and CCR2 (C-C chemokine receptor type 2) **KO** (knockout) mice that underwent ischemia-reperfusion injury at the indicated time points. $n = 4\text{--}5$ per experimental group. (d) Regional accumulation of ^{68}Ga -DOTA-ECLi uptake in the infarct and remote areas of sham and MI mice over the indicated time points. (e) Biodistribution of ^{68}Ga activity four days after ischemia-reperfusion injury measured one hour post-intravenous injection (tail vein) of ^{68}Ga -DOTA-ECLi. $n = 5$ per experimental group. (f) Trichrome and hematoxylin and eosin (H&E) staining showing the evolution of

fibrosis (trichrome-blue, $\times 40$ magnification) and cell infiltration (H&E, $\times 200$ magnification) over time in the closed-chest ischemia-reperfusion injury model. Note the dense accumulation of cells within the infarct four days after ischemia-reperfusion injury. Representative images from six independent experiments. (g) Flow cytometry analysis showing the accumulation of CCR2⁺ monocytes (CCR2 + MHC-II^{low}) and CCR2⁺ macrophages (CCR2 + MHC-II^{high}) four days after ischemia-reperfusion injury and persistence of CCR2⁺ macrophages seven days after ischemia-reperfusion injury compared with sham controls. (h) Immunostaining showing the accumulation of CCR2⁺ cells (brown) in the infarct region peaking at day 4 after ischemia-reperfusion injury. (i) Linear regression analyses showing the relationship between ⁶⁸Ga-DOTA-ECLi heart uptake measured on day 4 after ischemia-reperfusion injury and echocardiographic assessment of LV ejection fraction and akinetic area measured on day 28 after ischemia-reperfusion injury. * $P < 0.05$, ** $P < 0.01$, *** $P < 0.005$, **** $P < 0.001$. MHC indicates major histocompatibility complex. Wolters Kluwer. Source: Reproduced with permission from [140].

20.6 CARDIAC AMYLOIDOSIS

Amyloidosis is a systemic disease with frequent cardiac involvement. Indeed, cardiac amyloidosis (**CA**) is becoming recognized as a significant cause for heart failure with preserved ejection fraction [183]. The restrictive type of physiology in CA is the result of myocardial accumulation of misfolded protein deposits. There are two predominant forms of CA: amyloid immunoglobulin light chain (AL) and amyloid transthyretin (**ATTR**) amyloidosis. In AL CA, the misfolded protein is a monoclonal immunoglobulin light chain commonly produced by bone marrow plasma cells. In ATTR CA, the misfolded protein is transthyretin (**TTR**), a serum transport protein for thyroid hormone and retinol that is synthesized primarily by the liver. Of note, ATTR amyloidosis is further subtyped by the sequence of the TTR protein into wild-type (ATTRwt) or hereditary (ATTRv), the latter resulting from genetic variants in the TTR gene. Cardiac involvement in systemic AL amyloidosis is quite common, with values of up to 75%, depending on the diagnostic criteria used. Cardiac involvement is the dominant feature of ATTRwt amyloidosis [184]. Because of the increased recognition of the importance of CA as a cause of heart failure with preserved ejection fraction, the frequent difficulty in its diagnosis, and the availability of new therapies for both AL CA and ATTR CA, there is growing interest in imaging tools to aid in diagnosis, risk stratification, and therapy monitoring. In this regard, nuclear cardiology approaches are playing a significant role. A multi-societal position paper on the pathophysiology, diagnosis, and management of CA was recently published that comprehensively summarizes CA, diagnostic approaches, and new therapeutic strategies [185, 186].

20.6.1 ATTR CA

Scintigraphy with various bone imaging agents such as ^{99m}Tc-technetium (Tc)-bisphosphonate derivatives (^{99m}Tc-pyrophosphate [PYP], ^{99m}Tc-3,3-diphosphono-1,2-propanodicarboxylic acid [^{99m}Tc-DPD], and ^{99m}Tc hydroxymethylenediphosphonate [^{99m}Tc-HMDP]) have been shown to be highly accurate in the detection of ATTR CA [187–189]. In addition, imaging

with ^{99m}Tc -DPD/HMDP permits evaluation for extra-cardiac amyloid involvement. Imaging protocols are fairly straightforward but are still evolving. In brief, imaging is typically performed from one to three hours post injection and may include both planar and SPECT imaging; the latter may be needed when differentiation of myocardial from blood-pool activity is unclear (Figure 20.14). From an interpretation perspective, when the myocardial uptake is equal to or higher than bone and/or the ratio of heart-to-contralateral lung uptake is elevated, a diagnosis of ATTR-CA is made, provided there is no evidence of monoclonal proteins in blood and urine to suggest AL CA [183]. Moreover, the degree of cardiac uptake appears to correlate with cardiac structural abnormalities (e.g. increased LV mass and decreased LVEF) and provides insights on prognosis [188, 190]. Indeed, the success of cardiac scintigraphy with these bone-avid agents to detect ATTR-CA has led to its central role in a recently developed consensus algorithm for non-invasive diagnosis of CA (Figure 20.15) [183, 191].

20.6.2 AL CA

Numerous PET amyloid-binding radiotracers originally developed to detect image beta-amyloid in various dementia, causing diseases such as Alzheimer's disease, have been successfully used to image CA. Examples include ^{11}C -Pittsburgh compound B, ^{18}F -florbetapir, ^{18}F -florbetaben, and ^{18}F -flutemetamol, with all of the F-18 agents being currently FDA approved for beta-amyloid imaging [192–194]. All of these radiotracers have been evaluated in patients with AL and ATTR CA. A consistent finding is that cardiac radiotracer uptake is higher in CA patients compared to controls, with some reports noting uptake being higher in AL CA compared with ATTR CA. Typical measurements include either a LV myocardial-to-blood ratio or a retention index with increased values signifying CA. As is the case with ^{99m}Tc -DPD/HMDP, these various amyloid-binding PET radiotracers can assess extra-cardiac involvement [195].

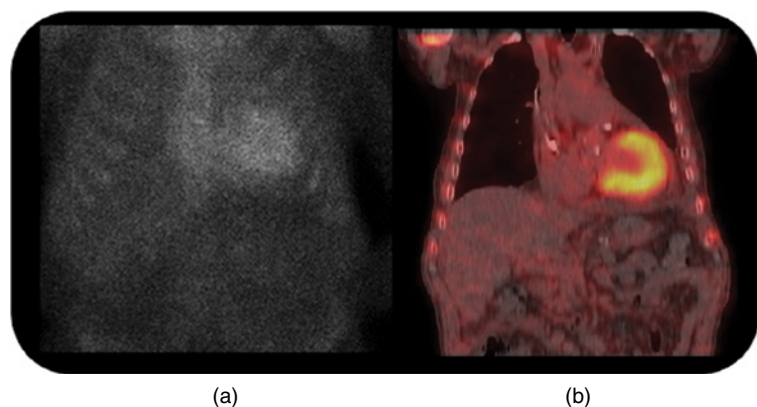


Figure 20.14 Patient with ATTR cardiac amyloidosis. (a) Planar images obtained 60 minutes after the administration of ^{99m}Tc -pyrophosphate. Myocardial uptake greater than ribs (score 3) and heart-to-contralateral-lung ratio of 2.0. (b) SPECT images obtained at 120 minutes confirm myocardial uptake.

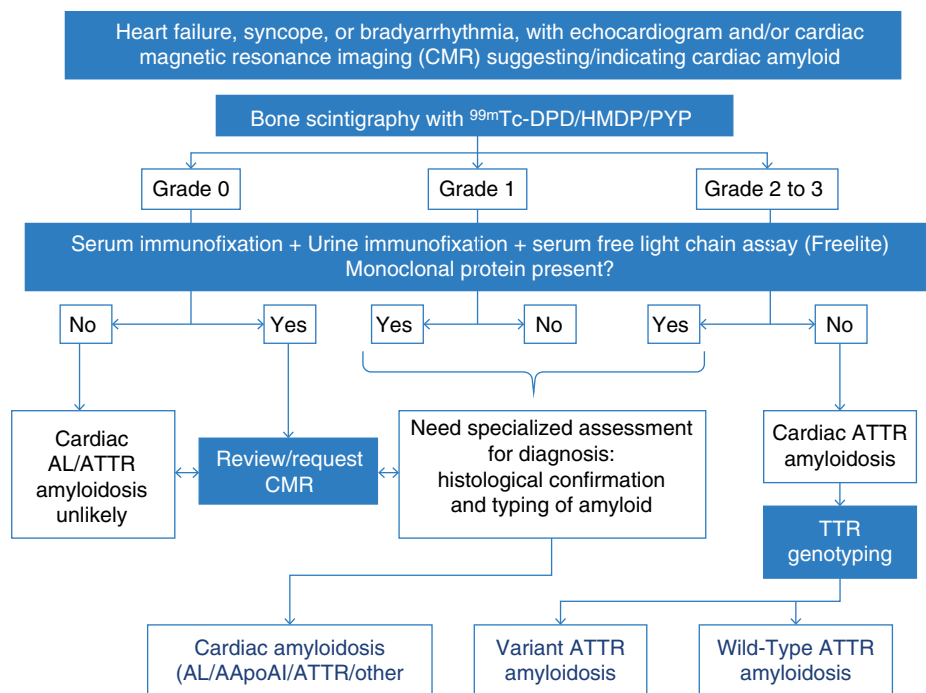


Figure 20.15 Diagnostic algorithm for patients with suspected amyloid cardiomyopathy. Echocardiographic features suggesting/indicating cardiac amyloid include (but are not limited to) increased left ventricular wall thickness, restrictive filling pattern, abnormal left and right ventricular longitudinal strain, and atrial septal thickening. Features suggesting/indicating cardiac amyloid on cardiac magnetic resonance imaging (CMR) include (but are not limited to) restrictive morphology, abnormal gadolinium kinetics, and extracellular volume expansion based on T1 mapping. AApoA1 indicates apolipoprotein A-I; DPD, 3,3-diphosphono-1,2-propanodicarboxylic acid; HMDP, hydroxymethylene diphosphonate; PYP, pyrophosphate. Source: Gillmore, J.D. et al. [191]. © 2016 Wolters Kluwer.

20.7 CONCLUSION

Nuclear cardiology is beginning to expand its clinical application well beyond the detection and risk stratification of the CAD patient via relative MPI and viability detection using FDG PET. Moreover, it is playing an increasingly important role in cardiovascular research. The key drivers of this growth are the integration of our understanding of CV disease pathobiology with innovations in radiopharmaceutical design to characterize key pathological steps and advancements in imaging instrumentation that permit quantification of signals in small animals and humans. Given the anticipated progress in each of these fields, the continued expansion of the role of nuclear cardiology is likely. Needless to say, if Dr. Blumgart were alive today, he would be quite impressed with the field he helped spawn.

REFERENCES

1. Blumgart, H.L. and Yens, O.C. (1927). Studies on the velocity of blood flow: I. The method utilized. *J. Clin. Invest.* 4 (1): 1–13.
2. Manabe, O. et al. (2018). Radiopharmaceutical tracers for cardiac imaging. *J. Nucl. Cardiol.* 25 (4): 1204–1236.
3. Henzlova, M.J. et al. (2016). ASNC imaging guidelines for SPECT nuclear cardiology procedures: stress, protocols, and tracers. *J. Nucl. Cardiol.* 23 (3): 606–639.
4. Dilsizian, V. et al. (2016). ASNC imaging guidelines/SNMMI procedure standard for positron emission tomography (PET) nuclear cardiology procedures. *J. Nucl. Cardiol.* 23 (5): 1187–1226.
5. Schelbert, H.R. et al. (1981). N-13 ammonia as an indicator of myocardial blood flow. *Circulation* 63: 1259–1272.
6. Yalamanchili, P. et al. (2007). Mechanism of uptake and retention of F-18 BMS-747158-02 in cardiomyocytes: a novel PET myocardial imaging agent. *J. Nucl. Cardiol.* 14 (6): 782–788.
7. Berman, D.S., Germano, G., and Slomka, P.J. (2012). Improvement in PET myocardial perfusion image quality and quantification with flurpiridaz F 18. *J. Nucl. Cardiol.* 19 (Suppl. 1): S38–S45.
8. Berman, D.S. et al. (2013). Phase II safety and clinical comparison with single-photon emission computed tomography myocardial perfusion imaging for detection of coronary artery disease: flurpiridaz F 18 positron emission tomography. *J. Am. Coll. Cardiol.* 61 (4): 469–477.
9. Maddahi, J. et al. (2011). Phase I, first-in-human study of BMS747158, a novel 18F-labeled tracer for myocardial perfusion PET: dosimetry, biodistribution, safety, and imaging characteristics after a single injection at rest. *J. Nucl. Med.* 52 (9): 1490–1498.
10. Dorbala, S. et al. (2018). Single photon emission computed tomography (SPECT) myocardial perfusion imaging guidelines: instrumentation, acquisition, processing, and interpretation. *J. Nucl. Cardiol.* 25 (5): 1784–1846.
11. Murthy, V.L. et al. (2018). Clinical quantification of myocardial blood flow using PET: joint position paper of the SNMMI cardiovascular council and the ASNC. *J. Nucl. Med.* 59 (2): 273–293.
12. Agostini, D. et al. (2018). First validation of myocardial flow reserve assessed by dynamic (99m)Tc-sestamibi CZT-SPECT camera: head to head comparison with (15)O-water PET and fractional flow reserve in patients with suspected coronary artery disease. The WATERDAY study. *Eur. J. Nucl. Med. Mol. Imaging* 45 (7): 1079–1090.
13. Mc Ardle, B.A. et al. (2012). Does rubidium-82 PET have superior accuracy to SPECT perfusion imaging for the diagnosis of obstructive coronary disease?: a systematic review and meta-analysis. *J. Am. Coll. Cardiol.* 60 (18): 1828–1837.
14. Parker, M.W. et al. (2012). Diagnostic accuracy of cardiac positron emission tomography versus single photon emission computed tomography for coronary artery disease: a bivariate meta-analysis. *Circ. Cardiovasc. Imaging* 5 (6): 700–707.

15. Dorbala, S. et al. (2009). Incremental prognostic value of gated Rb-82 positron emission tomography myocardial perfusion imaging over clinical variables and rest LVEF. *JACC Cardiovasc. Imaging* 2 (7): 846–854.
16. Acampa, W. et al. (2015). Role of risk stratification by SPECT, PET, and hybrid imaging in guiding management of stable patients with ischaemic heart disease: expert panel of the EANM cardiovascular committee and EACVI. *Eur. Heart J. Cardiovasc. Imaging* 16 (12): 1289–1298.
17. Danad, I. et al. (2013). Hybrid imaging using quantitative H₂¹⁵O PET and CT-based coronary angiography for the detection of coronary artery disease. *J. Nucl. Med.* 54 (1): 55–63.
18. Kajander, S. et al. (2010). Cardiac positron emission tomography/computed tomography imaging accurately detects anatomically and functionally significant coronary artery disease. *Circulation* 122 (6): 603–613.
19. Shaw, L.J. and Iskandrian, A.E. (2004). Prognostic value of gated myocardial perfusion SPECT. *J. Nucl. Cardiol.* 11 (2): 171–185.
20. Elhendy, A. et al. (2003). Long-term prognosis after a normal exercise stress Tc-99m sestamibi SPECT study. *J. Nucl. Cardiol.* 10 (3): 261–266.
21. Klocke, F.J. et al. (2003). ACC/AHA/ASNC guidelines for the clinical use of cardiac radionuclide imaging – executive summary: a report of the American College of Cardiology/American Heart Association task force on practice guidelines (ACC/AHA/ASNC committee to revise the 1995 guidelines for the clinical use of cardiac radionuclide imaging). *Circulation* 108 (11): 1404–1418.
22. Abidov, A. et al. (2003). Transient ischemic dilation ratio of the left ventricle is a significant predictor of future cardiac events in patients with otherwise normal myocardial perfusion SPECT. *J. Am. Coll. Cardiol.* 42 (10): 1818–1825.
23. Dorbala, S. et al. (2013). Prognostic value of stress myocardial perfusion positron emission tomography: results from a multicenter observational registry. *J. Am. Coll. Cardiol.* 61 (2): 176–184.
24. Yoshinaga, K. et al. (2006). What is the prognostic value of myocardial perfusion imaging using rubidium-82 positron emission tomography? *J. Am. Coll. Cardiol.* 48 (5): 1029–1039.
25. Juneau, D. et al. (2016). Clinical PET myocardial perfusion imaging and flow quantification. *Cardiol. Clin.* 34 (1): 69–85.
26. Murthy, V.L. et al. (2018). Clinical quantification of myocardial blood flow using PET: joint position paper of the SNMMI cardiovascular council and the ASNC. *J. Nucl. Cardiol.* 25 (1): 269–297.
27. Hachamovitch, R. et al. (2011). Impact of ischaemia and scar on the therapeutic benefit derived from myocardial revascularization vs. medical therapy among patients undergoing stress-rest myocardial perfusion scintigraphy. *Eur. Heart J.* 32 (8): 1012–1024.
28. Patel, K.K. et al. (2019). Extent of myocardial ischemia on positron emission tomography and survival benefit with early revascularization. *J. Am. Coll. Cardiol.* 74 (13): 1645–1654.

29. Bravo, P.E. et al. (2012). PET/CT assessment of symptomatic individuals with obstructive and nonobstructive hypertrophic cardiomyopathy. *J. Nucl. Med.* 53 (3): 407–414.
30. Potier, L. et al. (2018). Relationship between cardiac microvascular dysfunction measured with ⁸²Rubidium-PET and albuminuria in patients with diabetes mellitus. *Cardiovasc. Diabetol.* 17 (1): 11.
31. Rimoldi, O., Rosen, S.D., and Camici, P.G. (2014). The blunting of coronary flow reserve in hypertension with left ventricular hypertrophy is transmural and correlates with systolic blood pressure. *J. Hypertens.* 32 (12): 2465–2471; discussion 2471.
32. Stolen, K.Q. et al. (2004). Myocardial perfusion reserve and peripheral endothelial function in patients with idiopathic dilated cardiomyopathy. *Am. J. Cardiol.* 93 (1): 64–68.
33. Chen, K., Miller, E.J., and Sadeghi, M.M. (2019). PET-based imaging of ischemic heart disease. *PET Clin.* 14 (2): 211–221.
34. Taegtmeyer, H. et al. (2016). Assessing cardiac metabolism: a scientific statement from the American Heart Association. *Circ. Res.* 118 (10): 1659–1701.
35. Finck, B.N. (2007). The PPAR regulatory system in cardiac physiology and disease. *Cardiovasc. Res.* 73 (2): 269–277.
36. Finck, B.N. et al. (2003). A critical role for PPARalpha-mediated lipotoxicity in the pathogenesis of diabetic cardiomyopathy: modulation by dietary fat content. *Proc. Natl. Acad. Sci. U.S.A.* 100 (3): 1226–1231.
37. Karwi, Q.G. et al. (2018). Loss of metabolic flexibility in the failing heart. *Front. Cardiovasc. Med.* 5: 68.
38. Depre, C. et al. (1998). Unloaded heart in vivo replicates fetal gene expression of cardiac hypertrophy. *Nat. Med.* 4 (11): 1269–1275.
39. Depre, C. and Taegtmeyer, H. (2000). Metabolic aspects of programmed cell survival and cell death in the heart. *Cardiovasc. Res.* 45 (3): 538–548.
40. Boudina, S. and Abel, E.D. (2007). Diabetic cardiomyopathy revisited. *Circulation* 115 (25): 3213–3223.
41. Gropler, R.J. (2013). Recent advances in metabolic imaging. *J. Nucl. Cardiol.* 20 (6): 1147–1172.
42. Schinkel, A.F. et al. (2010). Clinical relevance of hibernating myocardium in ischemic left ventricular dysfunction. *Am. J. Med.* 123 (11): 978–986.
43. Tajouri, T.H. and Chareonthaitawee, P. (2010). Myocardial viability imaging and revascularization in chronic ischemic left ventricular systolic dysfunction. *Expert Rev. Cardiovasc. Ther.* 8 (1): 55–63.
44. Uebleis, C. et al. (2013). The amount of dysfunctional but viable myocardium predicts long-term survival in patients with ischemic cardiomyopathy and left ventricular dysfunction. *Int. J. Cardiovasc. Imaging* 29 (7): 1645–1653.
45. D'Egidio, G. et al. (2009). Increasing benefit from revascularization is associated with increasing amounts of myocardial hibernation: a substudy of the PARR-2 trial. *JACC Cardiovasc. Imaging* 2 (9): 1060–1068.

46. Beanlands, R.S. et al. (2007). F-18-fluorodeoxyglucose positron emission tomography imaging-assisted management of patients with severe left ventricular dysfunction and suspected coronary disease: a randomized, controlled trial (PARR-2). *J. Am. Coll. Cardiol.* 50 (20): 2002–2012.
47. Mc Ardle, B. et al. (2016). Long-term follow-up of outcomes with F-18-fluorodeoxyglucose positron emission tomography imaging-assisted management of patients with severe left ventricular dysfunction secondary to coronary disease. *Circ. Cardiovasc. Imaging* 9 (9).
48. Shukla, T. et al. (2012). Does FDG PET-assisted management of patients with left ventricular dysfunction improve quality of life? A substudy of the PARR-2 trial. *Can. J. Cardiol.* 28 (1): 54–61.
49. Peterson, L.R. et al. (2007). Sex differences in myocardial oxygen and glucose metabolism. *J. Nucl. Cardiol.* 14 (4): 573–581.
50. Kakinuma, Y. et al. (2013). The human female heart incorporates glucose more efficiently than the male heart. *Int. J. Cardiol.* 168 (3): 2518–2521.
51. Campbell, S.E. and Febbraio, M.A. (2001). Effect of ovarian hormones on mitochondrial enzyme activity in the fat oxidation pathway of skeletal muscle. *Am. J. Physiol. Endocrinol. Metab.* 281 (4): E803–E808.
52. Hatta, H. et al. (1988). The effects of ovarian hormones on glucose and fatty acid oxidation during exercise in female ovariectomized rats. *Horm. Metab. Res.* 20 (10): 609–611.
53. Herrero, P. et al. (2005). Impact of hormone replacement on myocardial fatty acid metabolism: potential role of estrogen. *J. Nucl. Cardiol.* 12 (5): 574–581.
54. Mensink, R.P. et al. (2003). Effects of dietary fatty acids and carbohydrates on the ratio of serum total to HDL cholesterol and on serum lipids and apolipoproteins: a meta-analysis of 60 controlled trials. *Am. J. Clin. Nutr.* 77 (5): 1146–1155.
55. Weiner, C.P. et al. (1994). Induction of calcium-dependent nitric oxide synthases by sex hormones. *Proc. Natl. Acad. Sci. U.S.A.* 91 (11): 5212–5216.
56. Abu-Erreish, G.M. et al. (1977). Fatty acid oxidation by isolated perfused working hearts of aged rats. *Am. J. Physiol.* 232 (3): E258–E262.
57. McMillin, J.B. et al. (1993). Mitochondrial metabolism and substrate competition in the aging Fischer rat heart. *Cardiovasc. Res.* 27 (12): 2222–2228.
58. Iemitsu, M. et al. (2002). Aging-induced decrease in the PPAR-alpha level in hearts is improved by exercise training. *Am. J. Physiol. Heart Circ. Physiol.* 283 (5): H1750–H1760.
59. Odiet, J.A., Boerrigter, M.E., and Wei, J.Y. (1995). Carnitine palmitoyl transferase-I activity in the aging mouse heart. *Mech. Ageing Dev.* 79 (2–3): 127–136.
60. Paradies, G. et al. (1992). The effect of aging and acetyl-L-carnitine on the activity of the phosphate carrier and on the phospholipid composition in rat heart mitochondria. *Biochim. Biophys. Acta* 1103 (2): 324–326.
61. Kates, A.M. et al. (2003). Impact of aging on substrate metabolism by the human heart. *J. Am. Coll. Cardiol.* 41 (2): 293–299.
62. Soto, P.F. et al. (2003). Impact of aging on myocardial metabolic response to dobutamine. *Am. J. Physiol. Heart Circ. Physiol.* 285 (5): H2158–H2164.

63. Soto, P.F. et al. (2008). Exercise training impacts the myocardial metabolism of older individuals in a gender-specific manner. *Am. J. Physiol. Heart Circ. Physiol.* 295 (2): H842–H850.
64. Schulze, P.C., Drosatos, K., and Goldberg, I.J. (2016). Lipid use and misuse by the heart. *Circ. Res.* 118 (11): 1736–1751.
65. Peterson, L.R. et al. (2004). Effect of obesity and insulin resistance on myocardial substrate metabolism and efficiency in young women. *Circulation* 109 (18): 2191–2196.
66. Peterson, L.R. et al. (2008). Impact of gender on the myocardial metabolic response to obesity. *JACC Cardiovasc. Imaging* 1 (4): 424–433.
67. Lin, C.H. et al. (2011). Myocardial oxygen consumption change predicts left ventricular relaxation improvement in obese humans after weight loss. *Obesity (Silver Spring)* 19 (9): 1804–1812.
68. Sankaralingam, S. et al. (2015). Lowering body weight in obese mice with diastolic heart failure improves cardiac insulin sensitivity and function: implications for the obesity paradox. *Diabetes* 64 (5): 1643–1657.
69. Viljanen, A.P. et al. (2009). Effect of caloric restriction on myocardial fatty acid uptake, left ventricular mass, and cardiac work in obese adults. *Am. J. Cardiol.* 103 (12): 1721–1726.
70. Devanathan, S. et al. (2013). Genomic and metabolic disposition of non-obese type 2 diabetic rats to increased myocardial fatty acid metabolism. *PLoS One* 8 (10): e78477.
71. Herrero, P. et al. (2006). Increased myocardial fatty acid metabolism in patients with type 1 diabetes mellitus. *J. Am. Coll. Cardiol.* 47 (3): 598–604.
72. Peterson, L.R. et al. (2015). Type 2 diabetes, obesity, and sex difference affect the fate of glucose in the human heart. *Am. J. Physiol. Heart Circ. Physiol.* 308 (12): H1510–H1516.
73. Peterson, L.R. et al. (2008). Fatty acids and insulin modulate myocardial substrate metabolism in humans with type 1 diabetes. *Diabetes* 57 (1): 32–40.
74. Peterson, L.R. et al. (2012). Sex and type 2 diabetes: obesity-independent effects on left ventricular substrate metabolism and relaxation in humans. *Obesity (Silver Spring)* 20 (4): 802–810.
75. Rijzewijk, L.J. et al. (2009). Altered myocardial substrate metabolism and decreased diastolic function in nonischemic human diabetic cardiomyopathy: studies with cardiac positron emission tomography and magnetic resonance imaging. *J. Am. Coll. Cardiol.* 54 (16): 1524–1532.
76. Shoghi, K.I. et al. (2008). Time course of alterations in myocardial glucose utilization in the Zucker diabetic fatty rat with correlation to gene expression of glucose transporters: a small-animal PET investigation. *J. Nucl. Med.* 49 (8): 1320–1327.
77. Lyons, M.R. et al. (2013). Impact of sex on the heart's metabolic and functional responses to diabetic therapies. *Am. J. Physiol. Heart Circ. Physiol.* 305 (11): H1584–H1591.
78. van der Meer, R.W. et al. (2009). Pioglitazone improves cardiac function and alters myocardial substrate metabolism without affecting cardiac triglyceride accumulation and high-energy phosphate metabolism in patients with well-controlled type 2 diabetes mellitus. *Circulation* 119 (15): 2069–2077.

79. Barger, P.M. and Kelly, D.P. (1999). Fatty acid utilization in the hypertrophied and failing heart: molecular regulatory mechanisms. *Am. J. Med. Sci.* 318 (1): 36–42.
80. Tuder, R.M., Davis, L.A., and Graham, B.B. (2012). Targeting energetic metabolism: a new frontier in the pathogenesis and treatment of pulmonary hypertension. *Am. J. Respir. Crit. Care Med.* 185 (3): 260–266.
81. Zhong, M. et al. (2013). Quantitative PET imaging detects early metabolic remodeling in a mouse model of pressure-overload left ventricular hypertrophy in vivo. *J. Nucl. Med.* 54 (4): 609–615.
82. Handa, N. et al. (2007). Quantitative FDG-uptake by positron emission tomography in progressive hypertrophy of rat hearts in vivo. *Ann. Nucl. Med.* 21 (10): 569–576.
83. de las Fuentes, L. et al. (2003). Myocardial fatty acid metabolism: independent predictor of left ventricular mass in hypertensive heart disease. *Hypertension* 41 (1): 83–87.
84. Hamirani, Y.S. et al. (2016). Noninvasive detection of early metabolic left ventricular remodeling in systemic hypertension. *Cardiology* 133 (3): 157–162.
85. Bokhari, S. et al. (2011). PET imaging may provide a novel biomarker and understanding of right ventricular dysfunction in patients with idiopathic pulmonary arterial hypertension. *Circ. Cardiovasc. Imaging* 4 (6): 641–647.
86. Fang, W. et al. (2012). Comparison of 18F-FDG uptake by right ventricular myocardium in idiopathic pulmonary arterial hypertension and pulmonary arterial hypertension associated with congenital heart disease. *Pulm. Circ.* 2 (3): 365–372.
87. Lundgrin, E.L. et al. (2013). Fasting 2-deoxy-2-[18F]fluoro-D-glucose positron emission tomography to detect metabolic changes in pulmonary arterial hypertension hearts over 1 year. *Ann. Am. Thorac. Soc.* 10 (1): 1–9.
88. Oikawa, M. et al. (2005). Increased [18F]fluorodeoxyglucose accumulation in right ventricular free wall in patients with pulmonary hypertension and the effect of epoprostenol. *J. Am. Coll. Cardiol.* 45 (11): 1849–1855.
89. Tatebe, S. et al. (2014). Enhanced [18F]fluorodeoxyglucose accumulation in the right ventricular free wall predicts long-term prognosis of patients with pulmonary hypertension: a preliminary observational study. *Eur. Heart J. Cardiovasc. Imaging* 15 (6): 666–672.
90. Buttrick, P.M. et al. (1994). Alterations in gene expression in the rat heart after chronic pathological and physiological loads. *J. Mol. Cell. Cardiol.* 26 (1): 61–67.
91. Sack, M.N. et al. (1996). Fatty acid oxidation enzyme gene expression is downregulated in the failing heart. *Circulation* 94 (11): 2837–2842.
92. Davila-Roman, V.G. et al. (2002). Altered myocardial fatty acid and glucose metabolism in idiopathic dilated cardiomyopathy. *J. Am. Coll. Cardiol.* 40 (2): 271–277.
93. Sharma, S. et al. (2004). Intramyocardial lipid accumulation in the failing human heart resembles the lipotoxic rat heart. *FASEB J.* 18 (14): 1692–1700.
94. Tuunanen, H. et al. (2006). Decreased myocardial free fatty acid uptake in patients with idiopathic dilated cardiomyopathy: evidence of relationship with insulin resistance and left ventricular dysfunction. *J. Card. Fail.* 12 (8): 644–652.
95. Kadkhodayan, A. et al. (2017). Sex affects myocardial blood flow and fatty acid substrate metabolism in humans with nonischemic heart failure. *J. Nucl. Cardiol.* 24 (4): 1226–1235.

96. Beanlands, R.S. et al. (2000). The effects of beta(1)-blockade on oxidative metabolism and the metabolic cost of ventricular work in patients with left ventricular dysfunction: a double-blind, placebo-controlled, positron-emission tomography study. *Circulation* 102 (17): 2070–2075.
97. Sundell, J. et al. (2004). The effects of cardiac resynchronization therapy on left ventricular function, myocardial energetics, and metabolic reserve in patients with dilated cardiomyopathy and heart failure. *J. Am. Coll. Cardiol.* 43 (6): 1027–1033.
98. Tuunanen, H. et al. (2008). Trimetazidine, a metabolic modulator, has cardiac and extra-cardiac benefits in idiopathic dilated cardiomyopathy. *Circulation* 118 (12): 1250–1258.
99. Yamauchi, S. et al. (2003). Angiotensin-converting enzyme inhibition improves cardiac fatty acid metabolism in patients with congestive heart failure. *Nucl. Med. Commun.* 24 (8): 901–906.
100. Barron, H.V. and Lesh, M.D. (1996). Autonomic nervous system and sudden cardiac death. *J. Am. Coll. Cardiol.* 27 (5): 1053–1060.
101. Esler, M. and Kaye, D. (2000). Sympathetic nervous system activation in essential hypertension, cardiac failure and psychosomatic heart disease. *J. Cardiovasc. Pharmacol.* 35 (7 Suppl 4): S1–S7.
102. Malpas, S.C. (2010). Sympathetic nervous system overactivity and its role in the development of cardiovascular disease. *Physiol. Rev.* 90 (2): 513–557.
103. Olshansky, B. et al. (2008). Parasympathetic nervous system and heart failure: pathophysiology and potential implications for therapy. *Circulation* 118 (8): 863–871.
104. Ji, S.Y. and Travin, M.I. (2010). Radionuclide imaging of cardiac autonomic innervation. *J. Nucl. Cardiol.* 17 (4): 655–666.
105. Raffel, D.M. et al. (2013). Radiotracers for cardiac sympathetic innervation: transport kinetics and binding affinities for the human norepinephrine transporter. *Nucl. Med. Biol.* 40 (3): 331–337.
106. Boutagy, N.E. and Sinusas, A.J. (2017). Recent advances and clinical applications of PET cardiac autonomic nervous system imaging. *Curr. Cardiol. Rep.* 19 (4): 33.
107. Higuchi, T. et al. (2015). Myocardial kinetics of a novel [(18)F]-labeled sympathetic nerve PET tracer LMI1195 in the isolated perfused rabbit heart. *JACC Cardiovasc. Imaging* 8 (10): 1229–1231.
108. Sinusas, A.J. et al. (2014). Biodistribution and radiation dosimetry of LMI1195: first-in-human study of a novel 18F-labeled tracer for imaging myocardial innervation. *J. Nucl. Med.* 55 (9): 1445–1451.
109. Werner, R.A. et al. (2015). Retention kinetics of the 18F-labeled sympathetic nerve PET tracer LMI1195: comparison with 11C-hydroxyephedrine and 123I-MIBG. *J. Nucl. Med.* 56 (9): 1429–1433.
110. Kaye, D.M. et al. (1994). Neurochemical evidence of cardiac sympathetic activation and increased central nervous system norepinephrine turnover in severe congestive heart failure. *J. Am. Coll. Cardiol.* 23 (3): 570–578.
111. Agostini, D. et al. (2000). Improvement of cardiac neuronal function after carvedilol treatment in dilated cardiomyopathy: a 123I-MIBG scintigraphic study. *J. Nucl. Med.* 41 (5): 845–851.

112. Bengel, F.M. et al. (2001). Relationship between altered sympathetic innervation, oxidative metabolism and contractile function in the cardiomyopathic human heart; a non-invasive study using positron emission tomography. *Eur. Heart J.* 22 (17): 1594–1600.
113. Matsunari, I. et al. (2010). Iodine-123 metaiodobenzylguanidine imaging and carbon-11 hydroxyephedrine positron emission tomography compared in patients with left ventricular dysfunction. *Circ. Cardiovasc. Imaging* 3 (5): 595–603.
114. Yamada, T. et al. (2003). Comparison of the prognostic value of cardiac iodine-123 metaiodobenzylguanidine imaging and heart rate variability in patients with chronic heart failure: a prospective study. *J. Am. Coll. Cardiol.* 41 (2): 231–238.
115. Jacobson, A.F. et al. (2009). 123I-mIBG scintigraphy to predict risk for adverse cardiac outcomes in heart failure patients: design of two prospective multicenter international trials. *J. Nucl. Cardiol.* 16 (1): 113–121.
116. Bengel, F.M. et al. (2001). Effect of sympathetic reinnervation on cardiac performance after heart transplantation. *N. Engl. J. Med.* 345 (10): 731–738.
117. Bengel, F.M. et al. (1999). Serial assessment of sympathetic reinnervation after orthotopic heart transplantation. A longitudinal study using PET and C-11 hydroxyephedrine. *Circulation* 99 (14): 1866–1871.
118. Schwaiger, M. et al. (1991). Evidence for regional catecholamine uptake and storage sites in the transplanted human heart by positron emission tomography. *J. Clin. Invest.* 87 (5): 1681–1690.
119. Satomi, T. et al. (2013). Comparison of contrast agents for atherosclerosis imaging using cultured macrophages: FDG versus ultrasmall superparamagnetic iron oxide. *J. Nucl. Med.* 54 (6): 999–1004.
120. Chareonthitawee, P. et al. (2017). Joint SNMMI-ASNC expert consensus document on the role of (18)F-FDG PET/CT in cardiac sarcoid detection and therapy monitoring. *J. Nucl. Med.* 58 (8): 1341–1353.
121. Thackeray, J.T. et al. (2016). Targeting amino acid metabolism for molecular imaging of inflammation early after myocardial infarction. *Theranostics* 6 (11): 1768–1779.
122. Ye, Y.X. et al. (2015). Imaging macrophage and hematopoietic progenitor proliferation in atherosclerosis. *Circ. Res.* 117 (10): 835–845.
123. Tarkin, J.M. et al. (2017). Detection of atherosclerotic inflammation by (68)Ga-DOTATATE PET compared to [(18)F]FDG PET imaging. *J. Am. Coll. Cardiol.* 69 (14): 1774–1791.
124. Lapa, C. et al. (2015). Imaging of myocardial inflammation with somatostatin receptor based PET/CT – a comparison to cardiac MRI. *Int. J. Cardiol.* 194: 44–49.
125. Schatka, I. et al. (2013). Peptide receptor-targeted radionuclide therapy alters inflammation in atherosclerotic plaques. *J. Am. Coll. Cardiol.* 62 (24): 2344–2345.
126. Gaemperli, O. et al. (2012). Imaging intraplaque inflammation in carotid atherosclerosis with 11C-PK11195 positron emission tomography/computed tomography. *Eur. Heart J.* 33 (15): 1902–1910.
127. Vivash, L. and O'Brien, T.J. (2016). Imaging microglial activation with TSPO PET: lighting up neurologic diseases? *J. Nucl. Med.* 57 (2): 165–168.

128. Borchert, T., Hess, A., Lukačević, M, Ross, T.L., Bengel, F.M., and Thackeray, J.T., (2020 Jul). Angiotensin-converting enzyme inhibitor treatment early after myocardial infarction attenuates acute cardiac and neuroinflammation without effect on chronic neuroinflammation. *Eur J Nucl Med Mol Imaging*. 47 (7): 1757–1768 doi: 10.1007/s00259-020-04736-8. Epub 2020 Mar 3.
129. Hellberg, S. et al. (2017). 18-kDa translocator protein ligand (18)F-FEMPA: biodistribution and uptake into atherosclerotic plaques in mice. *J. Nucl. Cardiol*. 24 (3): 862–871.
130. Thackeray, J.T. et al. (2018). Myocardial inflammation predicts remodeling and neuroinflammation after myocardial infarction. *J. Am. Coll. Cardiol*. 71 (3): 263–275.
131. Murdoch, C. and Finn, A. (2000). Chemokine receptors and their role in inflammation and infectious diseases. *Blood* 95 (10): 3032–3043.
132. Majmudar, M.D. et al. (2013). Monocyte-directed RNAi targeting CCR2 improves infarct healing in atherosclerosis-prone mice. *Circulation* 127 (20): 2038–2046.
133. Swirski, F.K. et al. (2010). Myeloperoxidase-rich Ly-6C⁺ myeloid cells infiltrate allografts and contribute to an imaging signature of organ rejection in mice. *J. Clin. Invest*. 120 (7): 2627–2634.
134. Derlin, T. et al. (2018). Imaging of chemokine receptor CXCR4 expression in culprit and nonculprit coronary atherosclerotic plaque using motion-corrected [(68)Ga]pentixafor PET/CT. *Eur. J. Nucl. Med. Mol. Imaging* 45 (11): 1934–1944.
135. Lapa, C. et al. (2015). [(68)Ga]Pentixafor-PET/CT for imaging of chemokine receptor 4 expression after myocardial infarction. *JACC Cardiovasc. Imaging* 8 (12): 1466–1468.
136. Thackeray, J.T. et al. (2015). Molecular imaging of the chemokine receptor CXCR4 after acute myocardial infarction. *JACC Cardiovasc. Imaging* 8 (12): 1417–1426.
137. Doring, Y. et al. (2014). The CXCL12/CXCR4 chemokine ligand/receptor axis in cardiovascular disease. *Front. Physiol*. 5: 212.
138. Gautier, E.L., Jakubzick, C., and Randolph, G.J. (2009). Regulation of the migration and survival of monocyte subsets by chemokine receptors and its relevance to atherosclerosis. *Arterioscler. Thromb. Vasc. Biol*. 29 (10): 1412–1418.
139. Auvynet, C. et al. (2016). ECL1i, d(LGTFLKC), a novel, small peptide that specifically inhibits CCL2-dependent migration. *FASEB J*. 30.
140. Heo, G.S. et al. (2019). Molecular imaging visualizes recruitment of inflammatory monocytes and macrophages to the injured heart. *Circ. Res*. 124 (6): 881–890.
141. Li, W. et al. (2018). Visualization of monocytic cells in regressing atherosclerotic plaques by intravital 2-photon and positron emission tomography-based imaging-brief report. *Arterioscler. Thromb. Vasc. Biol*. 38 (5): 1030–1036.
142. Luehmann, H.P. et al. (2016). PET/CT imaging of chemokine receptors in inflammatory atherosclerosis using targeted nanoparticles. *J. Nucl. Med*. 57 (7): 1124–1129.
143. Beer, A.J. et al. (2014). PET/CT imaging of integrin alphavbeta3 expression in human carotid atherosclerosis. *JACC Cardiovasc. Imaging* 7 (2): 178–187.
144. Jenkins, W.S. et al. (2017). Cardiac alphaVbeta3 integrin expression following acute myocardial infarction in humans. *Heart* 103 (8): 607–615.
145. Johnson, J.L. (2017). Metalloproteinases in atherosclerosis. *Eur. J. Pharmacol*. 816: 93–106.
146. Rabkin, S.W. (2017). The role matrix metalloproteinases in the production of aortic aneurysm. *Prog. Mol. Biol. Transl. Sci*. 147: 239–265.

147. Vanhoutte, D. et al. (2006). Relevance of matrix metalloproteinases and their inhibitors after myocardial infarction: a temporal and spatial window. *Cardiovasc. Res.* 69 (3): 604–613.
148. Razavian, M. et al. (2010). Molecular imaging of matrix metalloproteinase activation to predict murine aneurysm expansion in vivo. *J. Nucl. Med.* 51 (7): 1107–1115.
149. Toczek, J. et al. (2017). Preclinical evaluation of RYM1, a matrix metalloproteinase-targeted tracer for imaging aneurysm. *J. Nucl. Med.* 58 (8): 1318–1323.
150. Chu, W. et al. (2014). Development of a PET radiotracer for non-invasive imaging of the reactive oxygen species, superoxide, in vivo. *Org. Biomol. Chem.* 12 (25): 4421–4431.
151. Boutagy, N.E. et al. (2018). In vivo reactive oxygen species detection with a novel positron emission tomography tracer, (18)F-DHMT, allows for early detection of anthracycline-induced cardiotoxicity in rodents. *JACC Basic Transl. Sci.* 3 (3): 378–390.
152. Zhou, D. et al. (2009). Design and synthesis of 2-amino-4-methylpyridine analogues as inhibitors for inducible nitric oxide synthase and in vivo evaluation of [18F]6-(2-fluoropropyl)-4-methyl-pyridin-2-amine as a potential PET tracer for inducible nitric oxide synthase. *J. Med. Chem.* 52 (8): 2443–2453.
153. Herrero, P. et al. (2012). Feasibility and dosimetry studies for 18F-NOS as a potential PET radiopharmaceutical for inducible nitric oxide synthase in humans. *J. Nucl. Med.* 53 (6): 994–1001.
154. Shekhar, A. et al. (2018). Targeted imaging for cell death in cardiovascular disorders. *JACC Cardiovasc. Imaging* 11 (3): 476–493.
155. Higuchi, T. et al. (2011). Stable delineation of the ischemic area by the PET perfusion tracer 18F-fluorobenzyl triphenyl phosphonium after transient coronary occlusion. *J. Nucl. Med.* 52 (6): 965–969.
156. Kolodgie, F.D. et al. (2003). Targeting of apoptotic macrophages and experimental atheroma with radiolabeled annexin V: a technique with potential for noninvasive imaging of vulnerable plaque. *Circulation* 108 (25): 3134–3139.
157. Thukkani, A.K. et al. (2016). PET imaging of in vivo caspase-3/7 activity following myocardial ischemia-reperfusion injury with the radiolabeled isatin sulfonamide analogue [(18)F]WC-4-116. *Am. J. Nucl. Med. Mol. Imaging* 6 (2): 110–119.
158. Wang, L. et al. (2015). The feasibility of imaging myocardial ischemic/reperfusion injury using (99m)Tc-labeled duramycin in a porcine model. *Nucl. Med. Biol.* 42 (2): 198–204.
159. Osborne, M.T. et al. (2014). Reduction in (1)(8)F-fluorodeoxyglucose uptake on serial cardiac positron emission tomography is associated with improved left ventricular ejection fraction in patients with cardiac sarcoidosis. *J. Nucl. Cardiol.* 21 (1): 166–174.
160. Blankstein, R. et al. (2014). Cardiac positron emission tomography enhances prognostic assessments of patients with suspected cardiac sarcoidosis. *J. Am. Coll. Cardiol.* 63 (4): 329–336.
161. Youssef, G. et al. (2012). The use of 18F-FDG PET in the diagnosis of cardiac sarcoidosis: a systematic review and metaanalysis including the Ontario experience. *J. Nucl. Med.* 53 (2): 241–248.

162. LaForest, R., Woodard, P.K., and Gropler, R.J. (2016). Cardiovascular PET/MRI: challenges and opportunities. *Cardiol. Clin.* 34 (1): 25–35.
163. Schatka, I. and Bengel, F.M. (2014). Advanced imaging of cardiac sarcoidosis. *J. Nucl. Med.* 55 (1): 99–106.
164. Lapa, C. et al. (2016). Somatostatin receptor based PET/CT in patients with the suspicion of cardiac sarcoidosis: an initial comparison to cardiac MRI. *Oncotarget* 7 (47): 77807–77814.
165. Divakaran, S. et al. (2019). Diagnostic accuracy of advanced imaging in cardiac sarcoidosis. *Circ. Cardiovasc. Imaging* 12 (6): e008975.
166. Bensimhon, L. et al. (2011). Whole body [(18)F]fluorodeoxyglucose positron emission tomography imaging for the diagnosis of pacemaker or implantable cardioverter defibrillator infection: a preliminary prospective study. *Clin. Microbiol. Infect.* 17 (6): 836–844.
167. Saby, L. et al. (2013). Positron emission tomography/computed tomography for diagnosis of prosthetic valve endocarditis: increased valvular 18F-fluorodeoxyglucose uptake as a novel major criterion. *J. Am. Coll. Cardiol.* 61 (23): 2374–2382.
168. Sarrazin, J.F. et al. (2012). Usefulness of fluorine-18 positron emission tomography/computed tomography for identification of cardiovascular implantable electronic device infections. *J. Am. Coll. Cardiol.* 59 (18): 1616–1625.
169. Juneau, D. et al. (2017). Positron emission tomography and single-photon emission computed tomography imaging in the diagnosis of cardiac implantable electronic device infection: a systematic review and meta-analysis. *Circ. Cardiovasc. Imaging* 10 (4).
170. Habib, G. et al. (2015). 2015 ESC guidelines for the management of infective endocarditis: the task force for the management of infective endocarditis of the European Society of Cardiology (ESC) endorsed by: European Association for Cardio-Thoracic Surgery (EACTS), the European Association of Nuclear Medicine (EANM). *Eur. Heart J.* 36 (44): 3075–3128.
171. Rominger, A. et al. (2009). 18F-FDG PET/CT identifies patients at risk for future vascular events in an otherwise asymptomatic cohort with neoplastic disease. *J. Nucl. Med.* 50 (10): 1611–1620.
172. Mizoguchi, M. et al. (2011). Pioglitazone attenuates atherosclerotic plaque inflammation in patients with impaired glucose tolerance or diabetes a prospective, randomized, comparator-controlled study using serial FDG PET/CT imaging study of carotid artery and ascending aorta. *JACC Cardiovasc. Imaging* 4 (10): 1110–1118.
173. Tahara, N. et al. (2006). Simvastatin attenuates plaque inflammation: evaluation by fluorodeoxyglucose positron emission tomography. *J. Am. Coll. Cardiol.* 48 (9): 1825–1831.
174. Tawakol, A. et al. (2013). Intensification of statin therapy results in a rapid reduction in atherosclerotic inflammation: results of a multicenter fluorodeoxyglucose-positron emission tomography/computed tomography feasibility study. *J. Am. Coll. Cardiol.* 62 (10): 909–917.
175. Tawakol, A. et al. (2014). Effect of treatment for 12 weeks with rilapladi, a lipoprotein-associated phospholipase A2 inhibitor, on arterial inflammation as assessed with 18F-fluorodeoxyglucose-positron emission tomography imaging. *J. Am. Coll. Cardiol.* 63 (1): 86–88.

176. Rogers, I.S. et al. (2010). Feasibility of FDG imaging of the coronary arteries: comparison between acute coronary syndrome and stable angina. *JACC Cardiovasc. Imaging* 3 (4): 388–397.
177. Dutta, P. et al. (2012). Myocardial infarction accelerates atherosclerosis. *Nature* 487 (7407): 325–329.
178. Rischpler, C. et al. (2016). Prospective evaluation of 18F-fluorodeoxyglucose uptake in postischemic myocardium by simultaneous positron emission tomography/magnetic resonance imaging as a prognostic marker of functional outcome. *Circ. Cardiovasc. Imaging* 9 (4): e004316.
179. Wollenweber, T. et al. (2014). Characterizing the inflammatory tissue response to acute myocardial infarction by clinical multimodality noninvasive imaging. *Circ. Cardiovasc. Imaging* 7 (5): 811–818.
180. Dweck, M.R. et al. (2014). 18F-sodium fluoride uptake is a marker of active calcification and disease progression in patients with aortic stenosis. *Circ. Cardiovasc. Imaging* 7 (2): 371–378.
181. Forsythe, R.O. et al. (2018). (18)F-sodium fluoride uptake in abdominal aortic aneurysms: the SoFIA(3) study. *J. Am. Coll. Cardiol.* 71 (5): 513–523.
182. Raggi, P. et al. (2019). (18)F-sodium fluoride imaging of coronary atherosclerosis in ambulatory patients with diabetes mellitus. *Arterioscler. Thromb. Vasc. Biol.* 39 (2): 276–284.
183. Dorbala, S. et al. (2019). ASNC/AHA/ASE/EANM/HFSA/ISA/SCMR/SNMMI expert consensus recommendations for multimodality imaging in cardiac amyloidosis: part 1 of 2 – evidence base and standardized methods of imaging. *J. Card. Fail.* 25.
184. Siddiqi, O.K. and Ruberg, F.L. (2018). Cardiac amyloidosis: an update on pathophysiology, diagnosis, and treatment. *Trends Cardiovasc. Med.* 28 (1): 10–21.
185. Dorbala, S. et al. (2019). ASNC/AHA/ASE/EANM/HFSA/ISA/SCMR/SNMMI expert consensus recommendations for multimodality imaging in cardiac amyloidosis: part 2 of 2 – diagnostic criteria and appropriate utilization. *J. Card. Fail.* 25.
186. Dorbala, S. et al. (2019). ASNC/AHA/ASE/EANM/HFSA/ISA/SCMR/SNMMI expert consensus recommendations for multimodality imaging in cardiac amyloidosis: part 1 of 2 – evidence base and standardized methods of imaging. *J. Nucl. Cardiol.* 26.
187. Bokhari, S. et al. (2013). (99m)Tc-pyrophosphate scintigraphy for differentiating light-chain cardiac amyloidosis from the transthyretin-related familial and senile cardiac amyloidoses. *Circ. Cardiovasc. Imaging* 6 (2): 195–201.
188. Galat, A. et al. (2015). Usefulness of (99m)Tc-HMDP scintigraphy for the etiologic diagnosis and prognosis of cardiac amyloidosis. *Amyloid* 22 (4): 210–220.
189. Rapezzi, C. et al. (2008). Usefulness of ^{99m}Tc-DPD scintigraphy in cardiac amyloidosis. *J. Am. Coll. Cardiol.* 51 (15): 1509–1510; author reply 1510.
190. Castano, A. et al. (2016). Multicenter study of planar technetium 99m pyrophosphate cardiac imaging: predicting survival for patients with ATTR cardiac amyloidosis. *JAMA Cardiol.* 1 (8): 880–889.
191. Gillmore, J.D. et al. (2016). Nonbiopsy diagnosis of cardiac transthyretin amyloidosis. *Circulation* 133 (24): 2404–2412.

192. Antoni, G. et al. (2013). In vivo visualization of amyloid deposits in the heart with 11C-PIB and PET. *J. Nucl. Med.* 54 (2): 213–220.
193. Dorbala, S. et al. (2014). Imaging cardiac amyloidosis: a pilot study using (1)(8)F-florbetapir positron emission tomography. *Eur. J. Nucl. Med. Mol. Imaging* 41 (9): 1652–1662.
194. Law, W.P. et al. (2016). Cardiac amyloid imaging with 18F-florbetaben PET: a pilot study. *J. Nucl. Med.* 57 (11): 1733–1739.
195. Wagner, T. et al. (2018). Extracardiac (18)F-florbetapir imaging in patients with systemic amyloidosis: more than hearts and minds. *Eur. J. Nucl. Med. Mol. Imaging* 45 (7): 1129–1138.

Chapter 21

Radiopharmaceuticals in Pediatric Nuclear Medicine

Scott E. Snyder, Elizabeth R. Butch and Barry L. Shulkin
*Department of Diagnostic Imaging, St Jude Children's Research
Hospital, Memphis, TN, USA*

21.1 INTRODUCTION

Many diseases such as epilepsy, autism, and neuroblastoma are associated with developmental anomalies that manifest in utero or during early childhood or are associated with genetic mutations that specifically affect children and adolescents. In other diseases, such as glioblastoma, the pediatric forms have genetic signatures distinct from those found in the adult disease. However, as with most pharmaceutical developments, the vast majority of nuclear medicine procedures that are applied to pediatric disorders and investigations utilize radiopharmaceuticals and imaging methods developed for adults. As such, many of the radiopharmaceuticals used in these procedures have been extensively reviewed elsewhere. This chapter summarizes these well-established or clinically approved nuclear medicine procedures but focuses on studies more commonly performed in pediatric populations. We summarize the initial development of key radiopharmaceuticals used in pediatric imaging and therapy, citing relevant previous reviews, and present representative studies and applications in young populations. This is not a comprehensive review of each radiopharmaceutical, particularly with regard to studies in adult populations, as we focus on pediatric applications. A few disorders, such as neuroblastoma, are almost exclusively found in children and are therefore described in more detail.

21.2 CLINICALLY APPROVED SINGLE-PHOTON PROCEDURES AND RADIOPHARMACEUTICALS

21.2.1 Technetium Tc-99m (^{99m}Tc)

After more than four decades of use, ^{99m}Tc remains the radiotracer of choice for most conventional nuclear imaging procedures. Numerous functional processes are studied using ^{99m}Tc -labeled radiotracers. In pediatric nuclear medicine, ^{99m}Tc is most commonly used in skeletal scintigraphy, renal and genitourinary reflux studies, hepatobiliary scintigraphy, gastric emptying and esophageal reflux studies, and thyroid scanning. ^{99m}Tc -methylene diphosphonate (^{99m}Tc -MDP) is a bone-seeking tracer [1]. Three-phase bone scanning with ^{99m}Tc -MDP is both highly sensitive and specific for the early detection of osteomyelitis in children. It is also valuable, particularly with SPECT/CT, for evaluating low back pain in teenagers. Before FDG PET/CT became widely available, skeletal scintigraphy was the principal functional imaging technique for evaluating children with malignant diseases for the presence of osseous metastases, but it is now used much less often for that purpose. Renal imaging to evaluate obstruction, ectopia, or function is usually performed with ^{99m}Tc -MAG3 (mecaptoacetyltriglycine) [2]. At our institution, overall renal function is assessed without imaging by using ^{99m}Tc -DTPA (diethylenetriaminepentaacetic acid) [3]. This agent is largely cleared by glomerular filtration, and blood samples are obtained at one, two, and four hours post-administration to determine the glomerular filtration rate. Direct cystoscintigraphy is performed with $^{99m}\text{TcO}_4$ (pertechnetate) [4, 5]. Tracer is administered into the bladder via an external catheter, along with fluid, to detect vesico ureteral reflux. ^{99m}Tc -IDA labeled compounds (i.e. disofenin, mebrofenin) are used to distinguish neonatal hepatitis and biliary atresia [6]. In older children, it is useful for the diagnosis of suspected cholecystitis, particularly in patients with abnormal ultrasonographic findings and abdominal pain. ^{99m}Tc -pertechnetate is used for thyroid scanning. In neonates, ^{99m}Tc -pertechnetate scans can distinguish various causes for hypothyroidism, such as thyroid agenesis, thyroid ectopia, organification disorders, and maternal antibody suppression [7]. It remains the agent of choice for evaluating patients with gastrointestinal bleeding due to Meckel's diverticulum. It may also be used to determine cerebrospinal fluid shunt patency. ^{99m}Tc -MAA (macroaggregated albumin) scans are used to evaluate regional and global pulmonary perfusion and to quantify the magnitude of right-to-left shunts [8]. ^{99m}Tc -SC (sulfur colloid) is trapped by cells of the reticuloendothelial system, particularly the spleen and liver. It is primarily used to detect splenic function in patients with hematologic disorders, principally sickle cell disease, who are at risk for splenic dysfunction [9]. ^{99m}Tc -ECD (ethyl cysteinyl dimer) can be used to evaluate cerebral blood flow, in particular as part of a multidisciplinary effort to detect a seizure focus [10].

21.2.2 Infection/Inflammation Radiopharmaceuticals

Multiple radiotracers can be used to evaluate infectious/inflammatory conditions in pediatric patients [11]. In addition to bone scanning for suspected osteomyelitis, [^{67}Ga]gallium citrate and *in vitro* radiolabeled white blood cell imaging (using [^{111}In]indium oxine or [$^{99\text{m}}\text{Tc}$]technetium hexamethyl-propylene-amine-oxime [**HMPAO**]-labeled white blood cells) may be useful. [^{67}Ga]Gallium citrate is not commonly used in pediatric patients because the resulting image quality is poor and the patient receives a relatively high radiation dose, in part because of the long half-life of ^{67}Ga and the physiologic uptake of the tracer in the lungs, liver, and particularly bowel. Indium-111 (**111In**)-labeled leukocytes also impart a relatively high radiation burden, but the resulting image quality is better. Physiologic uptake in the spleen and liver can be intense, however. Leukocytes can also be labeled with $^{99\text{m}}\text{Tc}$ -HMPAO. The image quality obtained with this tracer is often very good due to the near-optimization of modern gamma cameras for detecting the $^{99\text{m}}\text{Tc}$ 140 keV gamma emission. Delayed images may show considerable activity in the bowel.

21.2.3 Radioiodine for Thyroid Disease

For thyroid diseases, iodine-123 (**123I**) is used for imaging, and iodine-131 (**131I**) is used to treat hyperthyroidism and thyroid cancer in both children and adults [12–14]. The iodine radionuclides ^{123}I and ^{131}I are a theranostic pair. Compared to ^{131}I , the decay characteristics of ^{123}I are more favorable for imaging. Iodine-123 decays by electron capture with a photon emission of 159 keV, suitable for gamma camera imaging. Its physical half-life is approximately 13 hours, and it lacks the beta particle emission of ^{131}I . Compared to ^{123}I , ^{131}I has a longer physical half-life (approximately eight days), a high-energy photon emission of 364 keV, and a beta emission that cannot be imaged but adds to the overall patient radiation burden. The latter feature is favorable for treatment but not for imaging. However, imaging of thyroid cancer post-therapy with ^{131}I is often of very high quality as a result of the large photon flux and favorable tumor-to-non-tumor ratios following treatment.

21.3 ESTABLISHED CLINICAL PET RADIOPHARMACEUTICALS AND THEIR USES

21.3.1 2- [^{18}F]Fluoro-2-deoxy-D-glucose ([^{18}F]FDG)

In pediatric oncology, [^{18}F]FDG PET/CT is frequently used in the management of disease, particularly in the selection of biopsy sites, tumor staging, risk stratification, radiation treatment planning, monitoring of response to treatment, and surveillance of tumors [15]. It is useful in many pediatric tumors, including lymphoma and sarcomas [16–18]. It can be very helpful in locating the primary site of a malignant neoplasm,

differentiating benign from malignant lesions, and monitoring for malignant transformation of known benign lesions such as those seen in neurofibromatosis [19, 20]. [^{18}F]FDG PET/CT is used to assess the distribution of disease activity and to monitor treatment in Langerhans histiocytosis [21]. With regard to infectious/inflammatory conditions, ^{18}F -FDG-PET/CT has proven useful in evaluating tuberculosis, sarcoidosis, chronic recurrent multifocal osteomyelitis, chronic granulomatous disease, Takayasu arteritis, and Crohn's disease, and in children with fever of unknown origin (**FUO**) [22–28]. [^{18}F]FDG PET/CT of the brain can be performed not only for tumor imaging but also to localize epileptogenic foci [29–31].

21.3.2 [^{13}N]Ammonia ([^{13}N]NH₃)

Studies for myocardial perfusion reserve using [^{13}N]NH₃ are not commonly performed in children and adolescents. Coronary artery disease, the main indication for [^{13}N]NH₃ myocardial perfusion studies, is rare in children. [^{13}N]NH₃ is an excellent tracer for measuring myocardial blood flow because of the relatively linear relationship between [^{13}N]NH₃ uptake and blood flow ([32]; NDA 22-119/S-001). Myocardial perfusion analysis with [^{13}N]NH₃ in adolescents with Kawasaki disease [33] showed that the myocardial perfusion reserve in children with a history of that disease who have normal coronary arteries is lower (mean: 3.2) than that in young adult healthy volunteers (mean: 4.6; $p = 0.003$). The vasodilator used in that study was adenosine. A similar study using [^{13}N]NH₃ and with adenosine as the coronary vasodilator was performed in infants with congenital heart disease [34]. That study showed that infants with repaired heart disease have higher resting flow and less coronary flow reserve than do adults. Also, patients who have undergone Norwood palliation of hypoplastic left heart syndrome have perfusion lower than that of patients with repaired congenital heart disease.

21.3.3 Sodium [^{18}F]fluoride ([^{18}F]NaF)

Although [^{18}F]NaF was the first radiotracer to be widely used for bone scanning [35], its use declined with the introduction of $^{99\text{m}}\text{Tc}$ compounds, and the tracer subsequently became unavailable. Compared to $^{99\text{m}}\text{Tc}$ -based compounds, [^{18}F]NaF has the advantage of being a positron emitter, which enables PET detection with its intrinsic high-quality three-dimensional display. Additional desirable features of [^{18}F]NaF bone scans include fast clearance of the radiotracer from non-bony structures, quick acquisition, and the potential for quantification. One study used [^{18}F]NaF in the evaluation of 94 patients aged 4–26 years with back pain, resulting in the discovery of a potential cause of back pain in more than 50% of these patients [36]. The use of [^{18}F]NaF to evaluate non-accidental trauma has also been reported [37]. In that study, 22 patients younger than two years with suspected non-accidental skeletal injuries who had both [^{18}F]NaF bone scans and skeletal surveys were examined. More skeletal lesions were found with [^{18}F]NaF bone scanning than with skeletal surveys. Despite the favorable imaging features and positive clinical experience, however, the use of [^{18}F]NaF for PET bone scanning remains limited.

21.4 RESEARCH RADIOPHARMACEUTICALS AND METHODS

21.4.1 Neuroscience

The human brain undergoes dramatic anatomic and functional transformation in the first two decades of life (for a review, see Kumar and Chugani [38]). Neurogenesis and dendritic growth continue after birth, resulting in the whole-brain and cortical gray-matter volumes peaking in the early teens. Different brain regions develop at different rates: critical motor and sensory areas mature first, followed by areas involved in basic language and spatial skills, with cortical areas associated with higher functions developing last. Most areas mature slightly earlier, typically by one to two years, in girls than in boys. Because of this high level of growth and reorganization, both cerebral blood flow (CBF) and regional glucose metabolic rates are higher in the developing brain than in the mature brain. Accordingly, there have been many imaging studies of normal brain and neuronal development, as well as of the typical neurodevelopmental, neurocognitive, and neuromotor disorders that afflict pediatric populations (most notably epilepsy, autism spectrum disorder, and attention-deficit/hyperactivity disorder [ADHD]). There have been detailed examinations of abnormal brain metabolism (with [¹⁸F]FDG) and CBF (with [¹⁵O]water, ^{99m}Tc-HMPAO, and ^{99m}Tc-ECD) in children and adolescents, and these studies have been extensively reviewed [38–43]. It is typically not permissible to image completely healthy children for research purposes due to the small but significant radiation doses involved. However, sufficient data can still be obtained from patients undergoing whole-body scans for non-neuronal clinical indications (e.g. peripheral tumors) and from patients with suspected neurologic disorders who later prove to be neurologically normal. In addition to general metabolic measures, several of the neurotransmitter systems implicated in pediatric development and neurologic disorders have been examined using radiotracers selective for serotonin (α -[¹¹C]methyl-*L*-tryptophan) and dopamine (6-[¹⁸F]fluoro-*L*-dihydroxyphenylalanine) synthesis and gamma aminobutyric acid (GABA) receptor complexes ([¹¹C]flumazenil and [¹²³I]lomazenil), among others. As described hereafter, molecular imaging has provided critical insights into normal neuronal development as well as into disease progression and has assisted with guiding therapy.

21.4.1.1 α -Methyl Tryptophan

Tryptophan is an essential amino acid and the precursor of the neurotransmitter serotonin (5-hydroxytryptamine, **5-HT**). Most tryptophan in the blood (approximately 90%) is bound to plasma proteins, and only the 10–15% of tryptophan that is free enters cerebral metabolism via the large neutral amino acid carrier (LAT1) [44, 45]. Serotonin is synthesized from tryptophan in a two-step enzymatic process, with the first enzyme, tryptophan hydroxylase (**TPH**), which is found only in serotonergic neurons, being the rate-limiting step [46–48].

There was a high demand for an *in vivo* method for detecting serotonin due to the number of pathologic disease states that are thought to involve serotonergic signaling, such as depression and impulse-control, mood, sleep, and eating disorders [49]. α -Methyl-*L*-tryptophan (**AMT**) labeled with ^{11}C [50–52], ^{14}C , or ^3H [53] was chosen as this *in vivo* probe because it is not incorporated into protein as are other amino acid radiotracers [54] but is rather converted to α -methyl-serotonin (**AMS**) [55, 56]. AMS, in turn, is not a substrate for deamination by monoamine oxidase [57], thus allowing accumulation in serotonergic neurons and theoretically making a radiotracer based on AMT more amenable to quantification. Numerous elegant kinetic studies have been performed with radiolabeled AMT in rats [47, 53], dogs [46], non-human primates [58, 59], and human subjects [45, 49, 60, 61] to characterize the metabolic trapping of AMT in serotonergic neurons. Collectively, these studies demonstrated that AMT displays a net uptake from the plasma into brain tissue followed by conversion into AMS and storage in the releasable neurotransmitter pool. This suggests that AMT can serve as an *in vivo* biomarker for serotonin synthesis and for assessing serotonergic neurons [45, 53, 62]. This process has been described as following first-order kinetics in a three-compartment model similar to that for 6- ^{18}F fluoro-*L*-dihydroxyphenylalanine (^{18}F FDOPA); however, the limited amount of free (i.e. not plasma protein-bound) AMT available for transport, the significant competition for LAT1 transport by endogenous amino acids, and the modest rate of AMT conversion to α -methyl-serotonin (with a 20-minute biological half-life), purportedly leading to a large unmetabolized pool of AMT, limit the absolute quantification of serotonin synthesis using ^{11}C AMT [63, 64]. Despite these limitations, a unidirectional rate constant for AMT metabolic trapping (K^* or K -complex) can be calculated that corresponds to the *serotonin synthesis capacity*; this correlates with regional serotonin levels in the human brain [49, 60] and is highly reproducible within individuals [58].

The primary users of ^{11}C AMT in pediatric patients have been Chugani, Muzik, and colleagues at Children's Hospital of Michigan/Wayne State University [38, 43]. ^{11}C AMT was first used in pediatric patients with autism, based on the well-established increase in platelet serotonin observed in many autistic individuals [65, 66]. An early ^{11}C AMT imaging study conducted by Chugani et al. in autistic boys revealed decreased serotonin synthesis in the frontal cortex and thalamus and increased serotonin synthesis in the contralateral dentate nucleus of the cerebellum in all seven boys studied [67]. There was no asymmetry in the PET scan of the one girl in the study. The authors concluded that this might be due to gender differences, but further studies would need to be performed to confirm this. A somewhat larger study in autistic children ($n = 30$), their non-autistic siblings ($n = 8$) and epileptic children without autism ($n = 16$) revealed both age and gender differences in serotonin synthesis capacity, with levels in children younger than five years being more than twice those in normal adults [68]. In children with autism, significant differences were detected in both the level of serotonin synthesis capacity and the rate of change with age when these children were compared with healthy siblings and with children with epilepsy. A more recent study also demonstrated that the location of serotonergic differences affects language development and possibly handedness [69]. In a therapeutic trial of buspirone (a serotonin $5\text{HT}_{1\text{A}}$ receptor partial agonist) in children with

autism, the number of foci with increased tryptophan synthesis identified by [¹¹C]AMT PET before treatment was predictive of therapeutic response [70].

PET imaging with [¹¹C]AMT has also been used in numerous pediatric studies to detect epileptogenic foci in patients with intractable epilepsy [71]. The use of [¹¹C]AMT in epilepsy was initially based on reports of elevated levels of serotonin and dopamine and their metabolites in these brain regions [72–74]. In 39% of patients with intractable epilepsy, [¹¹C]AMT uptake in the epileptic focus correlated with the frequency of interictal spikes [75]. [¹¹C]AMT PET has proved particularly useful for presurgical identification of epileptogenic foci that result from defined brain lesions, such as tuberous sclerosis complex (**TSC**), [75–78] cortical dysplasia [71, 79], or other developmental malformations [71, 80, 81], not all of which result in epileptic activity. Post-surgical studies of [¹¹C]AMT uptake in patients with intractable epilepsy have identified areas of incomplete resection of epileptogenic tissue [82] and have also shown increased radiotracer accumulation in striatal regions that is indicative of functional reorganization of cortico-striatal pathways [83]. Although apparently less sensitive than other imaging methods, including [¹⁸F]FDG PET [71, 84], for identifying such lesions (the sensitivity of [¹¹C]AMT PET is <50%), the specificity of [¹¹C]AMT PET for identifying epileptogenic foci is essentially 100% [80, 81]. Presurgical [¹¹C]AMT uptake abnormality was predictive of poor surgical outcomes, even in patients whose resected tissue had normal histopathology [71]. Additional studies have investigated the relation between autism and epilepsy in patients with TSC [85], and one group has recently begun to investigate specific genetic profiles associated with epileptogenic, high-[¹¹C]AMT cortical TSC lesions in the hope of better defining the underlying mechanisms of that disease [86].

Another metabolic route for tryptophan in the brain is via the kynurenine pathway in which tryptophan is converted to quinolinic acid by tryptophan 2,3-dioxygenase and indoleamine 2,3-dioxygenase (for a review, see Chugani and Muzik [63], Jones [44], and Lovelace et al. [87]). Normally, the levels of these metabolites are smaller by a factor of 100 to 1000 than the tryptophan concentration in the brain [88]. There is recent evidence that in pathologic conditions such as ischemic brain injury, immune activation (e.g. in multiple sclerosis or ALS), and epilepsy, the metabolism of tryptophan (and AMT) via the kynurenine pathway leads to the accumulation of quinolinic acid, a convulsant and known agonist of the *N*-methyl-D-aspartate (**NMDA**) receptors [63, 87]. The increased levels of quinolinic acid in epileptogenic tubers [89] and the observed mismatches between tryptophan hydroxylase activity (serotonin synthesis) and [¹¹C]AMT accumulation in some epileptogenic tubers suggest that at least some fraction of the [¹¹C]AMT signal represents kynurenine pathway activation.

A clear role for kynurenine pathway activation and, in particular, for indoleamine 2,3-dioxygenase (**IDO**) activity in tumor immunoresistance has been reported [86, 90], prompting interest in examining the utility of [¹¹C]AMT for imaging this pathway as a potential therapeutic target. Accumulation of [¹¹C]AMT has been demonstrated in pediatric astrocytoma, dysembryoplastic neuroepithelial tumors, ependymoma, ganglioma, and oligodendroglioma, including several low-grade tumors that were not contrast-enhancing on MRI [91–95]. As described previously, [¹¹C]AMT shares the same

tumor-uptake mechanism via the LAT1 transporter with the other amino acid radiotracers discussed hereafter ($[^{11}\text{C}]\text{MET}$, $[^{18}\text{F}]\text{FET}$, and $[^{18}\text{F}]\text{FDOPA}$). Also like other amino acid radiotracers, $[^{11}\text{C}]\text{AMT}$ has been used in pediatric patients primarily to evaluate brain tumors. The tumor-to-normal brain tissue difference is smaller for $[^{11}\text{C}]\text{AMT}$ than for other amino acid tracers because of the specific accumulation of the tracer in serotonergic neurons. However, unlike the other radiotracers, $[^{11}\text{C}]\text{AMT}$ metabolism lends itself to kinetic analysis and quantification. Differential kinetics of $[^{11}\text{C}]\text{AMT}$ have been observed in various tumor types [91, 92, 94, 96], and these differences correlate with IDO expression [91]. The additional biochemical information provided by $[^{11}\text{C}]\text{AMT}$ creates opportunities to study the role of IDO in tumor therapy resistance and, potentially, to develop novel therapeutic agents.

21.4.1.2 Benzodiazepine Receptors

Central benzodiazepine (**BZD**) receptors are found at high levels throughout the human cerebral cortex and hippocampus, and they are also found in the basal ganglia, thalamus, and hypothalamus [97, 98]. They are associated with the subtypes of the GABA_A receptor complex, serving as allosteric modulators of GABA_A -gated chloride ion flux [99]. This broad expression of BZD receptors throughout the cerebral cortex has proved valuable in the study of cortical development and injury [38]. The involvement in epileptogenesis of an imbalance between the inhibitory GABA_A and excitatory glutamate neurotransmitter systems is well established, leading to radiolabeled BZD ligands being used to detect epileptic foci. The use of functional imaging in the management of epilepsy has been reviewed previously [40–42, 100]. Although not as sensitive as $[^{18}\text{F}]\text{FDG}$ for detecting many epileptic foci, the high level of binding of BZD radiotracers to the cortex and hippocampus makes these agents particularly useful for identifying the cortical asymmetries associated with temporal lobe epilepsy and the mild deficits typical of hippocampal sclerosis and epilepsy with dual pathology [41, 101].

21.4.1.2.1 $[^{11}\text{C}]\text{Flumazenil}$

Shortly after its disclosure by F. Hoffman-La Roche & Co. in 1981 [102], the reversible BZD receptor antagonist ethyl 8-fluoro-5,6-dihydro-5-methyl-6-oxo-4*H*-imidazo[1,5-*a*] [1,4]benzodiazepine-3-carboxylate (RO 15-1788, Flumazenil, FMZ) was radiolabeled with ^{11}C by Mazière et al. [103]. $[^{11}\text{C}]\text{FMZ}$ was shown to bind selectively and reversibly to BZD receptors in the brain [104]. Several subsequent studies evaluated the kinetic analysis of this reversible radiotracer [104–109]. Although most groups agree that full kinetic modeling of $[^{11}\text{C}]\text{FMZ}$ at steady state, using arterial blood sampling to define a radiotracer input function, yields the best results for detailed studies of neural development [39, 110, 111], a reference region approach or simple asymmetry ratios provide adequate semi-quantitative data for clinical applications in epilepsy or brain injury and are far more practical in a pediatric population [112–117].

Chugani and colleagues have conducted several investigations of GABA_A/BZD distribution in the developing brains of humans ranging in age from newborns through

young adults [39, 110, 113], and they have examined how this distribution is altered by injury [118] and developmental abnormalities [111]. Collectively, these studies demonstrate the tremendous plasticity of the developing brain. The researchers observed a completely different overall binding pattern in newborns compared with older children and adults. The amygdala, hippocampus, sensory-motor cortex, thalamus, brainstem, and basal ganglia showed the highest level of [¹¹C]FMZ binding, whereas binding in the cerebellum and the rest of the cerebral cortex was much lower. This contrasts with the relatively low level of [¹¹C]FMZ binding to the basal ganglia and brainstem and the higher level of binding to most of the cerebral and cerebellar cortices in adults [113]. There was a progressive decrease in receptor density by 25–50%, depending on the region, with advancement in age from childhood (to approximately two years of age) to adolescence and young adulthood [110]. This group also observed differences in [¹¹C]FMZ binding that were attributable to injury or cortical malformations [111, 118]. Whether [¹¹C]FMZ binding was increased or decreased relative to that in controls was dependent on the particular malformation, but the binding was often increased in adjacent regions beyond those areas detected by MRI.

The early evaluation of [¹¹C]FMZ PET in epileptic patients focused on correlation with [¹⁸F]FDG and electroencephalogram (EEG) measurements [119–121]. All three methods correlated well in terms of localization of epileptic foci; however, the [¹¹C]FMZ abnormality was typically larger than the structural abnormalities seen on MRI but smaller than those observed using [¹⁸F]FDG [120]. Resection of these [¹¹C]FMZ-defined regions was strongly correlated with good surgical control of seizures, whereas neither the size of the [¹⁸F]FDG abnormality nor that of the structural abnormality was correlated with outcome [119]. This supports the existence of a functional link between GABA_A/BZD receptor activity and seizure onset even beyond those associations with genetic abnormalities (such as succinic semialdehyde dehydrogenase deficiency [117, 122] and trisomy 18 [123]) that are known to directly affect GABA signaling. The demonstration of this strong relationship gave rise to further studies using [¹¹C]FMZ PET to define surgical interventions and electrode placement for intracranial EEG [124–127]. Several patients in these latter studies had areas of [¹¹C]FMZ abnormality outside the primary seizure focus, and intracranial EEG electrodes placed with respect to these abnormalities verified neuronal spiking in these areas. Expanding the surgical site to include these remote spiking regions proved more effective than surgery without such expansion of the site.

21.4.1.2.2 [¹²³I]Iomazenil

Prompted by the successful use of [¹¹C]FMZ for *in vivo* BZD receptor imaging by French researchers in Orsay, the group of Schubiger at the Paul Scherrer Institute, in collaboration with Hoffman-La Roche, soon after developed the iodinated analog 5,6-dihydro-7-iodo-5-methyl-6-oxo-4*H*-imidazo[1,5-*a*][1,4]benzodiazepine-3-carboxylate (RO 16-0154, lomazenil, IMZ) and radiolabeled it with ¹²³I for SPECT imaging. Their rationale was that the importance of BZD receptors as drug targets and the utility of BZD imaging in a wide range of central nervous system (CNS) disorders warranted disseminating this technology to hospitals and institutes that did not have an on-site cyclotron as is required for

^{11}C labeling. The preparation and initial evaluation of [^{123}I]IMZ was reported in 1989 [128, 129]. The retention pattern of [^{123}I]IMZ in human brain was comparable to that of [^{11}C]FMZ and was displaced in a dose-dependent fashion by unlabeled FMZ [129].

The development and use of [^{123}I]IMZ over the next 10 years closely paralleled that of [^{11}C]FMZ with *in vitro* and preclinical validation, kinetic studies, and human trials being conducted in adult patients with epilepsy, stroke, and other neurologic disorders [130, 131]. Despite the fact that [^{123}I]IMZ was developed in Switzerland and most early studies were performed there, only in Japan was there any commercial interest in this successful radiotracer. Thus, nearly all reports of the pediatric use of [^{123}I]IMZ have come from groups in Japan. Pediatric [^{123}I]IMZ imaging has been used in studies of brain maturation [132, 133], autism [134], neuropsychiatric disorders such as ADHD [135] and anorexia nervosa [136], and, in particular, epilepsy [137–145].

21.4.1.3 *R*-[^{11}C]PK11195

First described by Le Fur et al. (Pharmuka Laboratories) [146, 147], 1-(2-chlorophenyl)-*N*-methyl-*N*-(1-methylpropyl)-3-isoquinolinecarboxamide (PK11195) is a potent (low nM) inhibitor of the peripheral benzodiazepine receptor (**PBR**), a small (18 kDa) mitochondrial membrane protein that is ubiquitous throughout the body and is thought to help regulate cell proliferation, immunomodulation, steroid synthesis, and apoptosis, among other functions [148, 149]. The mitochondrial localization of the PBR, more recently known as the 18 kDa translocator protein (**TSPO**), and the high level of expression of this “peripheral” receptor on activated microglia in various brain regions, have led to the use of PBR/TSPO ligands, including PK11195, for investigating and quantifying microglial-activated neuroinflammation in several neurologic disorders [149, 150]. Radiolabeling of racemic PK11195 with ^{11}C for PET was reported in 1984 by Camsonne et al. [151] in Orsay, France. This group subsequently demonstrated the specific binding of [^{11}C]PK11195 to cardiac muscle in both dogs and human volunteers [152]. Shortly thereafter, a group at the University of Michigan used [^{11}C]PK11195 to image 10 patients with astrocytoma [153]. The preparation of the radiolabeled active enantiomer *R*-[^{11}C]PK11195 was reported by Shah et al. in 1994, and the process was automated for routine production by Chakraborty et al. in 2006 [154]; this latter approach has been used in most subsequent studies. Unfortunately, the ubiquitous expression of TSPO and the lipophilicity of PK11195 result in high radiotracer background, typically resulting in a <10% difference in signal between normal and compromised tissues. This poor signal quality and the variable plasma kinetics make quantification and kinetic analysis challenging [155]. Despite these limitations, imaging with *R*-[^{11}C]PK11195 continues and has undergone a resurgence as a consequence of the recent search for a reliable *in vivo* marker of neuroinflammation.

Radiolabeled PK11195 has been used to investigate the involvement of inflammatory processes in several neuropathologies of children and young adults, including ADHD [156], encephalitis [38, 157], cerebral palsy [158, 159], autism spectrum disorder [160], and some less common disorders [157, 161–163]. The group at Children’s Hospital of Michigan has been particularly active in this area, reporting the normal distribution of *R*-[^{11}C]PK11195 in children [164] and age-related changes in radiotracer

binding [165] in addition to imaging neuroinflammation in children [161, 162, 166]. This group recently published the results of a study of 17 children with pediatric autoimmune neuropsychiatric disorders associated with streptococcal infection (**PANDAS**) and 12 children with Tourette syndrome, and their findings illustrate both the strength of neuroinflammation imaging and its limitations (at least with respect to R -[^{11}C]PK11195 PET) [162]. The study used 60-minute dynamic imaging, and the resulting time-activity data were analyzed using a modified reference region method to calculate the R -[^{11}C]PK11195 binding potential. As no brain region is completely devoid of TSPO, the researchers had to use cluster analysis of all gray-matter areas to identify the set of image voxels with the lowest maximal standardized uptake values (**SUVs**) and fastest radiotracer clearance. This cluster of voxels was then defined as the reference region. The binding potential values thus calculated were small (0.1–0.38), as were differences between the values for the disease and control groups (e.g. values for the caudate nucleus were 0.15 for patients with PANDAS vs. 0.09 for controls). However, despite these challenges, statistically significant increases in R -[^{11}C]PK11195 PET binding were observed in both patient groups as compared to adult controls. Other neuroinflammatory conditions have been less difficult to discern but still require the use of dynamic imaging and cluster analysis-based reference regions [161]. Although R -[^{11}C]PK11195 has remained the most used radiotracer for neuroinflammation for over three decades despite these limitations, several groups are actively developing alternatives [167–170]. These second-generation tracers have been used in some adult studies, but none has yet been used in pediatric patients.

21.4.2 Oncology

21.4.2.1 Amino acid Imaging

Radiolabeled amino acids have been used for many decades for imaging tumors in both adults and children [171–181]. This application was based on a chance observation by the group of Herrera, et al. at Danbury Hospital (Connecticut) and the Yale University School of Medicine [174]. The researchers noted a large, well-defined intraabdominal region of high [^{75}Se]selenomethionine uptake during a scan to measure pancreatic function in a patient with jaundice. This signal was subsequently proven to be associated with a lymphosarcoma, and the team proceeded to demonstrate the uptake of [^{75}Se]selenomethionine in several other lymphoid neoplasms. The accumulation of [^{75}Se]selenomethionine and several ^{11}C -labeled amino acids was subsequently reported in various peripheral solid tumors, including lung carcinoma [176, 182], pancreatic adenocarcinoma [183], hepatoma [184], thymoma [185], and glioma [175].

The preferential accumulation of amino acids, particularly neutral amino acids, by tumor tissue is well established [186]. It is thought to occur primarily via either LAT1 (SCL7A5) or the ASC system transporter type 2 (ASCT2, SLC1A5), both of which are upregulated in many types of cancer [187–189]. Most amino acids then go on to be incorporated into proteins or to participate in other metabolic processes. However, tumor imaging using radiolabeled amino acids primarily reflects this upregulated transport, and

synthetic molecules that do not participate in metabolic processes, such as [¹⁸F]fluoroethyltyrosine (FET) [190] and the cyclic leucine analog 1-amino-3-[¹⁸F]fluorocyclobutane-1-carboxylic acid ([¹⁸F]FACBC) [191], work equally well for imaging [179]. In fact, image analysis can be simplified for these non-natural amino acid radiotracers because of the lack of metabolites.

Amino acid radiotracers have shown particular utility in the area of brain tumor imaging, in which the avidity of brain tissue for glucose severely limits the contrast between normal brain glucose consumption and tumor metabolism when [¹⁸F]FDG is used as the radiotracer. The standard of care for imaging patients with brain tumors is anatomical imaging, including CT and MR with T2-weighted and fluid-attenuated inversion recovery (**FLAIR**) sequences [192]. Although CT is faster (and thus does not always necessitate sedation in children), the specialized MR sequences (FLAIR, susceptibility-weighted imaging, and diffusion-weighted imaging) give higher sensitivity for distinguishing tumor margins and identifying anatomical details such as cellularity [193, 194]. MR also has the advantage of limiting the exposure of pediatric patients to radiation, although this is a minor advantage given the typical therapy regimens for pediatric cancers. However, even specialized MRI sequences do not adequately differentiate between tumor grades, and they sometimes cannot reliably distinguish radiation necrosis from recurrent tumor; nor do they identify the extent of metabolically active tumor or address tumor heterogeneity, which are critical factors for guiding therapy [195].

The initial molecular imaging of brain tumors with [¹⁸F]FDG showed areas of easily distinguishable high radiotracer accumulation in high-grade gliomas. There was also a clear distinction between high- and low-grade disease and between active tumor and areas of scarring or necrosis [196, 197]. [¹⁸F]FDG PET has become a valuable tool for improving biopsy yield, guiding surgery, and detecting residual or recurrent tumor in pediatric patients, particularly in combination with advanced MRI [15, 194, 198]. However, [¹⁸F]FDG imaging of brain tumors suffers from high background, such that many low-grade tumors are indistinguishable from normal brain tissue [15, 196, 197]. Also, many benign pediatric tumors show accumulation of [¹⁸F]FDG [15].

It was observed early on that radiolabeled amino acids could penetrate the blood-brain barrier, but that radioactivity retention in normal brain tissue was quite low [172]. Further studies demonstrated preferential accumulation of ¹¹C-labeled methionine, valine, and tryptophan in brain neoplasms, which are difficult to image with [¹⁸F]FDG [171, 175, 199]. Whether this effect was specific tumor radiotracer uptake due to the high utilization of amino acids in rapidly proliferating tissue of most tumors or simply non-specific accumulation resulting from disruptions of the blood-brain barrier integrity was not initially addressed.

For adult brain tumor detection, amino acid radiotracers, predominantly [¹¹C]methionine ([¹¹C]MET), *O*-(2-[¹⁸F]fluoroethyl)-*L*-tyrosine ([¹⁸F]FET), or 3,4-dihydroxy-6-[¹⁸F]fluoro-*L*-phenylalanine ([¹⁸F]FDOPA), provide dramatically improved contrast between tumor and normal brain tissue when compared with traditional [¹⁸F]FDG imaging [178, 200–203]. However, pediatric brain tumors represent a distinct group of diseases in terms of their genetic profiles and lesion locations [193, 204], which gives rise to specifically pediatric

neoplasms such as ependymoma, medulloblastoma, and diffuse intrinsic pontine glioma (**DIPG**) [204]. Therefore, early amino acid PET studies focused on validating in the pediatric brain tumor population trends and protocols already established in adults. Although brain tumors in the aggregate are the second most common pediatric cancer, behind leukemia, the populations with individual pediatric brain tumor types are still small, limiting our ability to perform human subjects research on a specific tumor population (such as ependymoma) [204]. Most reports of pediatric brain tumor imaging include patient groups comprising multiple histologic tumor types, and studies often included both pediatric and adult patients in order to acquire sufficient participants within a reasonable time frame (see Kaschten et al. [202] and Utriainen et al. [203]). Thus, while the utility of amino acid PET for identifying pediatric brain tumors is obvious, the ability of researchers to evaluate the prognostic value of these radiopharmaceuticals is limited by the low number of available study participants and the population differences between tumor types [180, 202, 203, 205, 206].

21.4.2.1.1 [¹¹C]methionine ([¹¹C]MET)

O'Tuama, et al. reported the first use of [¹¹C]MET in children with brain tumors [180]. They studied a small group of children (aged 2–16 years) with various brain tumors typical of the pediatric population (ependymoma, medulloblastoma, and different grades of astrocytoma/glioma). Significant [¹¹C]MET accumulation was observed in 11 of 13 tumors, with the tumor vs. normal brain uptake ratio ranging from 1.18 to 2.91. These data likewise verified that the mechanism of [¹¹C]MET accumulation, via LAT1, was the same in these genetically distinct pediatric brain tumors as the mechanism demonstrated in adult tumors. Further examinations verified the expected higher contrast of [¹¹C]MET in pediatric brain tumors as compared with FDG [203]. Likewise, [¹¹C]MET could distinguish tumor from non-tumorous brain lesions [205]. However, in contrast to observations in adults [207–209], no clear difference was detected in [¹¹C]MET accumulation between high- and low-grade tumors [203, 205]. This is probably an artifact of the study group, including patients with tumors of multiple histologic types [180, 203, 205]. Even in adults, some overlap in [¹¹C]MET uptake between tumors of different histological types has been observed [207]. Nevertheless, there was a statistically significant difference in [¹¹C]MET accumulation between WHO grade II and grade III astrocytomas, indicating that it might be possible to use [¹¹C]MET to grade tumors within a given histologic type or to perform intra-individual sequential non-invasive monitoring of tumor progression [205].

Our recent studies have examined the utility of [¹¹C]MET in more homogeneous pediatric populations of patients with craniopharyngioma [210], high-grade glioma [211], and DIPG [212]. In 10 patients with newly diagnosed craniopharyngioma, [¹¹C]MET demonstrated a median tumor-to-background ratio of 2.2:1 ($P=0.0001$) based on measures of SUV_{max} within the MR-defined tumor volume [210]. In contrast, [¹⁸F]FDG, although having slightly higher absolute radiotracer accumulation ($SUV_{max}=2.65$, vs. 2.2 for [¹¹C]MET), showed no significant difference between tumor and normal brain (tumor-to-background ratio = 0.83, $P=0.3272$).

Interpreting [¹¹C]MET imaging results with respect to prognostic value and tumor heterogeneity was more complicated. We have shown that in patients with high-grade glioma, [¹¹C]MET PET rarely added to the MRI tumor volume and that the regions of most intense [¹¹C]MET accumulation (SUV > 3) were different for a given tumor when imaged at diagnosis, post-treatment, and at recurrence [211]. However, the overlap between [¹¹C]MET accumulation and site of recurrence was 90%. Also, when >10% of the [¹¹C]MET-positive tumor volume was also non-contrast enhancing by MR FLAIR imaging, the time to progression was shorter (5.8 vs. 10.5 months). In patients with DIPG, we observed significant [¹¹C]MET accumulation in 18 of 22 baseline scans, yet 11 of these showed [¹¹C]MET avidity in <25% of the MR-defined tumor volumes [212]. Also, while neither the intensity nor the extent of [¹¹C]MET accumulation correlated with outcome, in this study there was a 100% overlap between the baseline [¹¹C]MET accumulation and the site of eventual tumor recurrence. Thus, [¹¹C]MET delineated regions at increased risk for recurrence, but not the likelihood of recurrence.

Another area in which [¹¹C]MET has had an important impact for adult patients is image-guided stereotactic biopsy and therapy planning [213–218]. In children, using [¹¹C]MET for functional brain mapping, in combination with anatomical MR imaging, has been reported to improve accuracy in stereotactic brain biopsy and has enabled a reduction in the number of trajectories probed [216, 219, 220]. In many cases, the improved planning information provided by PET has enabled physicians to limit sampling to only one biopsy trajectory. In fact, these studies were sufficiently successful to lead the researchers to suggest that biopsy might be unnecessary for patients with intrinsic infiltrative brain stem lesions [220].

PET imaging with [¹¹C]MET was demonstrated to improve neurosurgical outcomes by better defining areas of active tumor in cases where the initial diagnosis was an incidental finding or where tumors were infiltrative or poorly defined on MR [216]. A combination of [¹¹C]MET imaging with MR and other radiotracers ([¹⁸F]FDG and [¹⁵O]water) for surgical planning was shown to provide not only an accurate assessment of the active tumor location(s) but also localization of adjacent active cortical areas to minimize the risk to adjacent healthy, functional brain tissue [201].

Recent pediatric applications of [¹¹C]MET have returned to the original focus of using this radiolabeled amino acid for imaging peripheral tumors [173, 174, 176, 208]. Our group is currently conducting both preclinical research [221, 222] and an imaging trial in children and young adults (NCT00840047, PI: Shulkin) to investigate the normal distribution of [¹¹C]MET in this population and to evaluate the utility of [¹¹C]MET imaging in several peripheral pediatric neoplasms, including lymphoma, osteosarcoma, rhabdomyosarcoma, and Ewing sarcoma, among others [223, 224]. We found only minor differences in normal organ [¹¹C]MET levels in our pediatric patients. In particular, age-related increases in testicular, left ventricular, and bone marrow uptake were observed, and there was some decrease in bone marrow activity in patients previously treated with antineoplastic agents, probably due to a decline in their bone marrow reserve [223]. Although the utility of [¹¹C]MET for abdominal lesions may be limited by the high normal background in liver and pancreas [223, 224], it appears to offer added value, as compared to [¹⁸F]FDG, in terms of predicting therapy response and recurrent disease [221, 224].

21.4.2.1.2 *O*-(2-[¹⁸F]fluoroethyl)-*L*-tyrosine ([¹⁸F]FET)

[¹⁸F]FET was introduced in 1999 by Wester et al. as a substitute for [¹¹C]MET and other ¹¹C-labeled amino acids used for tumor imaging [190]. The longer half-life of ¹⁸F enabled centralized production (in contrast to the production of ¹¹C-labeled amino acids), and the more efficient radiochemistry of [¹⁸F]FET, as compared with that of other ¹⁸F-labeled amino acids such as 4-[¹⁸F]fluoro-*L*-phenylalanine and 2-[¹⁸F]fluoro-*L*-tyrosine, enabled more widespread adoption of this radiotracer at sites without easy access to the on-site radiochemistry needed for ¹¹C-labeling. The initial radiosynthesis method, [¹⁸F]fluoroalkylation of the tyrosine disodium salt by using [¹⁸F]fluoroethyltosylate [190], was later automated [225], as was a comparable synthesis using direct [¹⁸F]fluorination of a protected *O*-(2-tosyloxyethyl)-*L*-tyrosine, as reported by Hamacher and Coenen [226].

It had earlier been reported that the accumulation of amino acid radiotracers in tumors depended primarily on transport rather than on the subsequent incorporation of the labeled amino acids into proteins or involvement in other metabolic processes [179, 181, 190]. This finding supported the use of synthetic amino acids such as [¹⁸F]FET, which undergo minimal metabolism, resulting in images of improved quality that reflect the distribution of the radioactive compound as administered without being confounded by radioactive metabolites, thus simplifying image analysis. Initial evaluation *in vitro* demonstrated that, as expected, [¹⁸F]FET accumulated in cells primarily via LAT1, accounting for >80% of the accumulation [227]. Murine tumor models revealed prolonged [¹⁸F]FET retention at significant levels only in pancreas and tumor [190, 227]. However, in the absence of incorporation into proteins, [¹⁸F]FET slowly cleared from tumors, with a peak concentration at approximately 60 minutes post-injection. Unlike other synthetic amino acids, [¹⁸F]FET showed protracted retention in mouse brain, peaking at approximately 60 minutes post-injection, but only at low levels (approximately 2% of the injected dose per gram) that were comparable to those in other non-target organs. No accumulation in the brain or pancreas was observed in the initial human imaging study [190]. This species difference was confirmed in subsequent biodistribution and dosimetry evaluations that showed only low levels of radioactivity in all nontarget organs except the kidney and bladder (in which levels were increased as a result of urinary excretion) [228, 229]. A direct comparison with [¹¹C]MET in adult patients with suspected brain tumors revealed slightly lower uptake of [¹⁸F]FET in normal brain tissue (SUVs of 1.1 and 0.8 for normal gray and white matter, respectively) as compared with [¹¹C]MET accumulation (SUVs of 1.4 and 0.9, respectively), but as the [¹⁸F]FET tumor uptake was also slightly lower (2.7 for [¹⁸F]FET vs. 3.3 SUV for [¹¹C]MET), the tumor-to-normal brain contrast did not differ significantly between these two radiotracers [230].

Researchers in Europe, mostly in Germany, have reported several studies in which [¹⁸F]FET was used in pediatric patients with brain tumors [231–246]. Most of these included groups containing both adults and children, likely to ensure sufficient patient numbers, as discussed previously. An early pediatric study utilized [¹⁸F]FET and MR spectroscopy for image-guided biopsy in two children with suspected diffuse bithalamic astrocytoma, which is a difficult tumor to assess with anatomic imaging alone [239].

PET-guided biopsy in a group of 26 children and adolescents further demonstrated the utility of [¹⁸F]FET, which showed 83% sensitivity and 91% specificity [240]. Two patients in that study had [¹⁸F]FET signal in suspicious lesions, but biopsy proved these to be localized inflammation, although no specific uptake data were provided for these patients. In a separate case study of a 6-year old patient treated with proton beam irradiation, a positive [¹⁸F]FET scan later proved to show pseudoprogression. Thus, although [¹⁸F]FET demonstrated much-improved sensitivity and specificity for tumor versus inflammation in preclinical models as compared with FDG [247, 248], there were limitations on imaging efficiency in cases of reactive gliosis as a result of injury (as in the proton therapy cases) or neurodegeneration in human subjects [235]. There is evidence that mismatch between [¹⁸F]FET accumulation and contrast enhancement on MR images might help distinguish active tumor from gliosis [233, 241].

In addition to the difficulty of distinguishing tumor from reactive gliosis, it is not always possible to separate low- and high-grade tumors based solely on the absolute uptake values (SUV) or tumor-to-brain ratios. However, at least part of the overlap observed in children with brain tumors could be due to the heterogeneity of the patient populations examined, as discussed previously [180, 203, 205]. The slow clearance of [¹⁸F]FET from brain lesions at later time points provides an opportunity to evaluate the use of radiotracer kinetics to distinguish neoplastic from benign lesions and possibly to predict tumor grade. Even simple evaluations of the time-activity curve shape and relative intensity in pediatric patients with suspected tumor recurrence identified distinctions between low- and high-grade tumors [231, 238, 244, 246]. In general, high-grade tumors show rapid [¹⁸F]FET uptake and subsequent clearance, whereas low-grade tumors exhibit a slow, continuous accumulation of radiotracer. This curve-shape analysis has given rise to simplified kinetic parameters such as time to peak activity (TTP), which has been evaluated in both pediatric and adult patients and shows great promise as a compromise between full kinetic analysis and simple SUV measurement [243–245, 249–252]. In fact, in a mixed group of adult and pediatric patients with diffuse astrocytoma, a longer TTP was predictive of improved outcome [243]. Similar analyses do not appear to improve the diagnostic value of [¹¹C]MET as they do for [¹⁸F]FET [253].

21.4.2.1.3 3,4-dihydroxy-6-[¹⁸F]fluoro-L-phenylalanine (6-[¹⁸F]FDOPA)

6-[¹⁸F]FDOPA was developed in the early 1980s by Firnau and colleagues at the McMaster University Medical Center as a radiotracer for measuring dopamine synthesis in patients with Parkinson's disease [254, 255]. Like other radiolabeled amino acids, 6-[¹⁸F]FDOPA is taken into cells via amino acid transporters. In neurons, 6-[¹⁸F]FDOPA is further converted by aromatic acid decarboxylase into 6-[¹⁸F]fluorodopamine, and it has provided an imaging biomarker for presynaptic dopaminergic innervation in numerous neuroimaging studies for movement disorders (for a review, see [256]). More recently, 6-[¹⁸F]FDOPA, similar to other amino acid radiotracers, has proved valuable for tumor images. In addition to brain tumor imaging, 6-[¹⁸F]FDOPA has been reported to have particular utility for the identification of neuroendocrine tumors, in which both the system L amino acid transport mechanism and neurotransmitter synthesis pathways likely contribute to

radiotracer accumulation [257–260]. Recent advances in the radiochemistry of high-specific-activity 6-^[18F]FDOPA promise to expand the availability of this versatile and highly useful radiotracer [261, 262].

Unsurprisingly, the initial pediatric application of 6-^[18F]FDOPA was to image brain dopamine synthesis in children with various rare developmental neurobiology disorders [263–270]. One study even looked at the utility of 6-^[18F]FDOPA as a reporter for gene therapy to correct aromatic amino acid decarboxylase deficiency [271]. However, the focus of 6-^[18F]FDOPA imaging in children quickly moved from brain imaging to neuroendocrine function, and particularly the pancreatic lesions responsible for congenital hyperinsulinism [177, 272–274]. Chronic hyperinsulinism (CHI) is a genetic abnormality most often linked to mutations in genes encoding the ATP-sensitive potassium channel (K_{ATP}) in pancreatic β -cells [274, 275]. The resulting overactive β -cells present in infants and children as chronic hypoglycemia that is resistant to medication. The CHI defect can be focal or diffuse, and although focal disease can be treated with surgery, the focal defect is difficult to detect through functional tests or even during surgery. Diffuse disease requires complete or near-complete pancreatectomy, which leaves the infant dependent on medication for life. Based on the propensity of neuroendocrine cells, like pancreatic β -cells, to accumulate the amino acid precursors of neurotransmitters, Otonkoski et al. first reported the use of FDOPA to identify focal hyperinsulinism in 2003 [276]. Since then, numerous studies have demonstrated the clinical utility of 6-^[18F]FDOPA for distinguishing focal and diffuse CHI with nearly 100% accuracy, enabling image-guided, limited resection in cases of focal disease [272, 274, 277, 278].

As with other amino acid radiotracers, 6-^[18F]FDOPA has been used in both children and adults for imaging brain tumors [178, 279–284]. Morana and colleagues at the Istituto Giannina Gaslini pediatric hospital in Genoa, Italy, have published multiple papers on the utility of 6-^[18F]FDOPA PET for detecting pediatric diffuse infiltrative astrocytomas [285–290]. This group has demonstrated that 6-^[18F]FDOPA can distinguish between low- and high-grade disease and that uptake was strongly correlated with progression-free and overall survival [286, 287]. Combining 6-^[18F]FDOPA PET with MR perfusion imaging (arterial spin labeling) and diffusion-weighted imaging further improved the prognostic value [288]. However, because brain activity associated with 6-^[18F]FDOPA accumulation could result from a combination of amino acid transport and participation in monoamine neurotransmitter synthesis, care must be taken when interpreting images. Individual cases of increased 6-^[18F]FDOPA accumulation in brain parenchyma resulting from epileptogenic tumors [285] or developmental abnormalities of cerebral blood flow [291] have been reported. In a recent report, this group demonstrated the ability of 6-^[18F]FDOPA PET to detect the presence of a specific histone mutation (H3K27M) that is thought to contribute to abnormal cell-cycle regulation and possibly to radiotherapy resistance [290].

6-^[18F]FDOPA has also been used to investigate neuroendocrine tumors, including paraganglioma, pheochromocytoma, and neuroblastoma [257, 292, 293]. The vast majority of pediatric studies are in patients with neuroblastoma and will be described in detail in a separate section. Although paraganglioma and pheochromocytoma occur

mainly in adult patients, a few imaging studies, including pediatric patients, have been published. An early case report described a 16-year-old patient with three lesions suspicious for paraganglioma on MR, only one of which was positive by SPECT imaging using [¹²³I]MIBG, the standard radiotracer imaging method for neuroendocrine tumors. All three lesions showed intense 6-[¹⁸F]FDOPA accumulation and subsequently proved to be paragangliomas by histology [258]. Pacak and colleagues have reported on the utility of 6-[¹⁸F]FDOPA for imaging paraganglioma associated with polycythemia [294, 295]. Imaging in these patients is complicated by the multiple tumor types that develop over time, and the patients usually present with widespread disease. In both studies, 6-[¹⁸F]FDOPA outperformed [¹⁸F]FDG and ⁶⁸Ga-DOTATATE in identifying paraganglioma in terms of both the number of lesions visualized and the intensity of the signal.

21.4.2.2 Neuroblastoma

Neuroblastoma is the most common extra-cranial solid malignant neoplasm of childhood. Approximately 650 new cases are expected yearly in the United States. The median age at diagnosis is 18 months. Although uncommon, neuroblastoma may occur in newborns or in middle-aged adults. The disease originates from neuroectodermal cells that normally develop into the sympathetic nervous system. Evaluation with noninvasive functional and anatomic imaging procedures is used to assign patients to risk groups and determine their subsequent treatment [296, 297].

Indications for radionuclide imaging in neuroblastoma are as follows [298]: (i) confirmation of suspected neuroectodermally derived tumors, including neuroblastoma, pheochromocytoma, and ganglioneuroma; (ii) staging of disease; (iii) monitoring of disease response; and (iv) surveillance for disease recurrence following treatment.

21.4.2.2.1 Radioiodinated meta-iodobenzylguanidine (*mIBG*)

This is a norepinephrine analog initially developed by Wieland and colleagues at the University of Michigan for imaging the sympathetic innervation of the heart [299–301]. *mIBG* has been used for evaluating pheochromocytoma and neuroblastoma for more than 35 years [302]. *mIBG* is an aralkylguanidine derived from the combination of the benzyl group of bretylium (an obsolete anti-arrhythmic, antihypertensive agent) with the guanidine group of guanethidine (an adrenergic neuronal blocker). It was initially labeled with ¹³¹I for human use and represented a major breakthrough in the management of pheochromocytoma [303]. It was subsequently tested in patients with neuroblastoma [304]. *mIBG* is most commonly labeled with ¹²³I for diagnostic purposes and with ¹³¹I for therapy. [¹²³I]*mIBG* was widely used in Europe before it became commercially available in the United States. *mIBG* is taken up by tissues with rich adrenergic innervation. Expected physiologic sites of uptake include the salivary glands, heart, liver, bowel, and bladder [305, 306]. [¹²³I]*mIBG* has high sensitivity for detecting neuroblastoma, ranging from 88–92%, with a specificity of 83–92% [307]. Imaging of [¹²³I]*mIBG* is commonly performed with SPECT/CT and is a critical component of disease monitoring in national and international trials. It is currently the best commercially available functional imaging

agent for neuroblastoma. Many reviews of and guidelines for the use of *m*IBG in neuroblastoma have been published, most recently by Bar-Sever [308].

Many drugs interfere with the uptake and/or retention of *m*IBG, particularly tricyclic antidepressants (such as amitriptyline), sympathomimetics (vasoconstrictors present in nasal sprays, such as phenylephrine, ephedrine, and pseudoephedrine), cocaine, and certain anti-hypertensives (labetalol). Calcium-channel blockers most likely do not interfere with *m*IBG uptake, so it is not necessary to withdraw them [309]. Most of the drugs known to interfere with *m*IBG uptake are rarely used in children. Patients should not receive interfering medications until *m*IBG imaging is complete, as these drugs will also cause the discharge of *m*IBG already stored within tumors. Typically, an *m*IBG scan of a patient receiving an interfering medication shows poor uptake in the salivary glands and heart and widespread soft tissue/muscle activity.

*m*IBG has also been radiolabeled with the positron emitter ^{124}I ; however, this is a sub-optimal radionuclide for imaging [310]: it has a long physical half-life of 4.2 days, a low rate of disintegration by positron emission (approximately 23%), and a complex decay scheme that results in multiple high-energy gamma photons. Nevertheless, high-quality images can be achieved with radiotracers labeled with this radionuclide. ^{124}I *m*IBG has been synthesized as a no-carrier-added preparation [311]. The radiochemical purity was >95% and the stability high: $\geq 90\%$ at 120 hours and $\geq 95\%$ at 48 hours. The method was derived to provide ^{124}I *m*IBG to support a multicenter clinical trial to compare ^{124}I *m*IBG PET/CT with ^{123}I *m*IBG scintigraphy in patients with metastatic neuroblastoma.

^{124}I *m*IBG has had very little usage in patients with neuroblastoma. PET/CT using ^{124}I *m*IBG provided high-resolution, high-quality studies in two patients with advanced disease [312]. The radiation dose from ^{124}I *m*IBG is much higher than that from ^{123}I *m*IBG (0.25 mSv/MBq vs. 0.019 mSv/MBq), but the radiation exposure in the context of preparation for ^{131}I *m*IBG therapy is minimal and of no biologic importance.

21.4.2.2.2 Meta- ^{18}F fluorobenzylguanidine (^{18}F *m*FBG)

A ^{18}F -labeled analog of benzylguanidine has great promise for imaging neuroblastoma [313]. In an initial study, Pandit-Taskar and colleagues showed that PET/CT imaging with ^{18}F *m*FBG in neuroblastoma is safe and yields very high image quality. Imaging is performed within a few hours after injection because of the rapid uptake of the tracer and its fast clearance from background tissues. Quantification of the uptake in lesions is possible due to the inherent quantitative characteristics of PET. The overall distribution of ^{18}F *m*FBG within tissues was similar to that of ^{123}I *m*IBG. However, compared with *m*IBG imaging, more lesions were localized with ^{18}F *m*FBG PET/CT in patients with neuroblastoma and those with paraganglioma/pheochromocytoma.

The dosimetry of ^{18}F *m*FBG is comparable to that of ^{18}F FDG PET imaging. Advantages of using ^{18}F *m*FBG PET imaging, as compared with conventional ^{123}I *m*IBG scintigraphy, include the ability to perform single-day imaging, the lack of a need to protect the thyroid from radioiodine (as the compound does not contain radioiodine), and the shorter time required to complete imaging. Another advantage is the ability to image patients using a PET MR scanner, further reducing the radiation doses. Further data on this

radiotracer is being generated in an ongoing study (NCT02348749; PI: N. Pandit-Taskar). Clearly, [¹⁸F]mFBG has the potential for commercial distribution, and if it becomes widely available, it might assume a prominent role in investigations of neuroblastoma and pheochromocytoma.

21.4.2.2.3 3,4-Dihydroxy-6-[¹⁸F]fluoro-L-phenylalanine (6-[¹⁸F]FDOPA)

As mentioned previously, 6-[¹⁸F]FDOPA is the fluorinated, radiolabeled analog of DOPA, the precursor of the catecholamines dopamine, norepinephrine, and epinephrine. It is transported into cells by LAT1 and then converted into [¹⁸F]fluorodopamine by the enzyme aromatic amino acid decarboxylase (AADC) [314]. 6-[¹⁸F]FDOPA may currently be the best alternative to [¹²³I]mIBG for PET imaging of neuroblastoma, because of its ability to track the metabolism of catecholamines [315–319].

The patient should fast for four or more hours before the study and should be well-hydrated. The normal biodistribution of ¹⁸F-DOPA includes uptake in the pancreas, adrenal glands, and basal ganglia. There may be variable, sometimes intense, uptake in the excretory organs, such as the gallbladder and biliary tract, kidneys, ureters, and bladder. In pediatric patients, some uptake may be evident in the epiphyseal growth plates [293, 314].

Piccardo reported 6-[¹⁸F]FDOPA PET/CT to be superior, overall, to [¹²³I]mIBG planar scintigraphy [259, 320–323]. Lopci et al. reported their findings in 21 patients with advanced neuroblastoma, mostly studied at restaging, who underwent 6-[¹⁸F]FDOPA PET/CT [324]. The PET studies were compared with CT or MRI and were largely concordant (in 30 of 37 cases). Four false-positive findings with 6-[¹⁸F]FDOPA were due to biliary duct stasis. CT/MRI did not identify bone lesions in two patients who had positive results on 6-[¹⁸F]FDOPA PET/CT. For lesion detection, the sensitivity of 6-[¹⁸F]FDOPA PET/CT was 91%, and that of CT/MRI was 48%. 6-[¹⁸F]FDOPA PET/CT detected 95% of bone/bone marrow lesions (55/58), whereas CT/MRI detected only 7% (4/58). 6-[¹⁸F]FDOPA PET/CT may detect bone and lymph node metastases that are negative on diagnostic [¹²³I]mIBG scintigraphy but confirmed on post-treatment [¹³¹I]mIBG imaging.

Lu reported on 55 patients with neuroblastoma who underwent 6-[¹⁸F]FDOPA PET (202 studies), [¹⁸F]FDG PET (205 studies), and [¹²³I]mIBG imaging (80 scans) [325]. Three of four tumors with negative [¹²³I]mIBG imaging were positive on both 6-[¹⁸F]FDOPA PET and [¹⁸F]FDG PET, whereas one false negative was visualized only on 6-[¹⁸F]FDOPA PET. The sensitivity of 6-[¹⁸F]FDOPA PET (16/16: 100%) was higher than that of [¹²³I]mIBG imaging (12/16: 75%). The authors of this study concluded that there is a complementary role for 6-[¹⁸F]FDOPA PET in evaluating neuroblastoma but that [¹²³I]mIBG imaging is still required, particularly if [¹³¹I]mIBG therapy is being considered.

21.4.2.2.4 Radiolabeled somatostatin analogs (⁶⁸Ga-DOTATXX)

Many neuroblastomas express somatostatin receptors (SSTRs). The presence of SSTRs allows imaging and therapy with somatostatin binding agents. In tissue studies, SSTRs

are found in 77–89% of neuroblastoma cells by autoradiography and immunohistochemistry [326–330]. SSTR scintigraphy was performed with ^{111}In -pentetretotide [331, 332]. Data suggested that the prognosis was better for patients with higher uptake, but imaging of neuroblastoma with ^{111}In -pentetretotide was not widely adopted.

PET agents are now available to probe SSTRs *in vivo*. They are ^{68}Ga -DOTA-based peptides (DOTA is dodecanetetraacetic acid, a macrocyclic metal chelator), such as ^{68}Ga -DOTA-NOC (^{68}Ga -DOTA-Nal3-octreotide), ^{68}Ga -DOTA-TATE (^{68}Ga -DOTA-Tyr3-octreotate), and ^{68}Ga -DOTA-TOC (^{68}Ga -DOTA-Tyr3-octreotide). Kong et al. performed imaging with ^{68}Ga -DOTA-TATE of eight children, aged two–nine years, with refractory, heavily pretreated neuroblastoma [333] and compared the results with those of *mIBG* imaging (either [^{123}I]*mIBG* diagnostic scans ($n = 5$), or [^{131}I]*mIBG* post-therapy scans ($n = 3$)). ^{68}Ga -DOTA-TATE binds principally to SSTR type 2. The authors of that study found additional sites of disease using ^{68}Ga -DOTA-TATE in three of the eight patients. In six of the patients, the ^{68}Ga -DOTA-TATE uptake in the tumor was considered sufficiently intense (i.e. greater than that in the liver) to qualify the patients for radiolabeled peptide therapy, leading to four patients receiving radiolabeled peptide therapy. With therapy, each of the patients had temporary symptomatic and partial imaging responses.

Abonga et al. described the safety and accuracy of ^{68}Ga -DOTA-TOC in children and young adults with solid tumors [334]. Of the 26 patients in the study, 18 were aged 16 months to 18 years. One patient, a 17-month old, had neuroblastoma. ^{68}Ga -DOTA-TOC PET/CT demonstrated radiotracer uptake in the primary right adrenal mass and regional lymph node, whereas the [^{123}I]*mIBG* scan was negative. The authors concluded that ^{68}Ga -DOTA-TOC is safe for use detecting SSTR type 2-positive neoplasms in children.

Gains et al. used ^{68}Ga -DOTA-TATE PET/CT to identify patients with refractory or relapsed neuroblastoma for treatment with ^{177}Lu -DOTA-TATE [335]. The criterion for treatment was tumor uptake of ^{68}Ga -DOTA-TATE greater than the liver uptake. Six patients qualified and were subsequently treated. The authors concluded that ^{68}Ga -DOTA-TATE PET/CT could be used to identify patients with neuroblastoma with SSTR-positive disease that was appropriate for therapy and that ^{68}Ga -DOTA-TATE PET/CT imaging could be used to assess therapy response.

Different forms of ^{68}Ga -DOTA-peptides differ in their affinity profiles for SSTR subtypes, with ^{68}Ga -DOTA-TATE having the highest affinity to SSTR2, ^{68}Ga -DOTA-TOC the highest for SSTR 5, and ^{68}Ga -DOTA-NOC predominantly for SSTRs 3 and 5 [336]. ^{68}Ga has a short half-life of 68 minutes, resulting in a low radiation dose to the patient (an effective dose of 2.1 mSv for a 100 MBq administration) [337–339]. The primary target organ is the spleen, followed by the kidneys and urinary bladder [340]. Other normal sites of uptake include the adrenals and pituitary glands, with less intense uptake in the liver, salivary gland, thyroid gland, and bowel. Acquisition is usually performed 45–90 minutes (typically 60 minutes) after injection [340]. The field of view of a pediatric acquisition for neuroblastoma covers the patient from the vertex to the toes.

^{68}Ga -DOTA-Octreotate uptake in pathologic lesions usually has very high focal tumor-to-background contrast, which is reflected in high SUVs, even for subcentimeter lesions [333]. The absence of radiotracer accumulation in normal brain enables the

evaluation of skull osseous and brain metastases. Other sites of non-tumor uptake include the pancreatic uncinata process, splenunculi or splenosis, meningioma, inflammatory processes (reactive nodes, post-radiotherapy changes), and osteoblastic activity such as that arising from fracture, vertebral hemangioma, or epiphyseal growth plates. Uptake in inflammatory and benign osteoblastic processes is usually low grade [336, 340]. Similarly, uptake at physiologic sites, particularly in the liver and bowel, may mask small-volume disease in these regions.

21.4.2.2.5 Radiolabeled Anti-GD2 Antibodies

GD2 is a disialoganglioside that is widely expressed by pediatric solid tumors (e.g. by >98% of neuroblastomas) but minimally expressed in most other tissues [341–344], making it an excellent target for immunotherapy [345, 346]. This low expression in normal tissue and the reported link between ganglioside expression and increased cell migration and invasion make GD2 a particularly attractive target for both imaging and radioimmunotherapy [347].

Two families of anti-GD2 antibodies have been examined for therapeutic efficacy in GD2-positive tumors [348]. The first anti-GD2 monoclonal antibody studied in humans was 3F8, a murine antibody developed in 1985 by Nai-Kong Cheung and colleagues at Case Western Reserve [341]. In the three decades since then, 3F8 has been studied in numerous neuroblastoma immunotherapy trials, either alone or in combination with cytokines and immune effectors [349]. Many of these studies showed significant improvements in event-free survival and even some long-term remissions (>20 years). More recently, a humanized 3F8 has been developed to minimize the induction of the human anti-mouse antibody (**HAMA**) response in patients [349, 350]

The second antibody family derives from the murine anti-GD2 antibody 14.18 (IgG 3 isotype) [351] and from the subsequent IgG2a switch variant 14.G2a [352]. The murine 14G.2a antibody [353–355], as well as the chimeric (ch14.18) [344, 356–358] and humanized (hu14.18 and hu14.18K322A) [359–361] versions of 14.18, have shown promise in several clinical trials [344, 358, 362, 363]. A recent Children's Oncology Group (**COG**) study demonstrated that consolidation therapy using ch14.18 in conjunction with a cytokine regimen resulted in a 20% increase in 2-year event-free survival and a 10% increase in overall survival of patients with neuroblastoma. This is an exceptional improvement in a population that heretofore had a survival rate of only 40% [344]. Based on these results, immunotherapy with anti-GD2 antibodies has become the standard of care for metastatic neuroblastoma.

The humanized version of 14.18 containing a single lysine-to-alanine point mutation at position 322, hu14.18K322A, was developed to exhibit decreased complement activation, with a concomitant decrease in both the severity and duration of drug-associated pain while preserving therapeutic efficacy [364]. This modification renders the therapy much more tolerable for pediatric patients and enables an increase in the maximum tolerated dose (**MTD**), with a corresponding increase in the therapeutic benefit [360].

The 3F8, 14.G2a, and ch14.18 antibodies have been radiolabeled previously with ^{99m}Tc and iodine radioisotopes (^{131}I , ^{124}I) for imaging [345]. Initial human imaging trials using ^{131}I -3F8 in children with neuroblastoma demonstrated tumor-to-nontarget tissue ratios

greater than 10:1 and a more protracted retention of radioactivity in tumors (with a clearance half-life of 60 vs. 40 hours for normal tissue) with optimal imaging 2–3 days post-injection of radiotracer [365]. Further imaging studies proved ^{131}I -3F8 to be better than [^{123}I]mIBG for identifying distant metastases [366, 367]. Likewise, $^{99\text{m}}\text{Tc}$ -ch14.18 was superior to [^{123}I]mIBG for early identification of tumor recurrence for both skeletal and soft-tissue metastases [368]. In patients treated with the 14.G2a antibody, pre-therapy imaging with ^{131}I -14.G2a was used to verify antibody uptake in the tumor [355]. Post-therapy imaging with either ^{131}I - or $^{99\text{m}}\text{Tc}$ -14.G2a revealed that the GD2 binding was not saturated by therapeutic dosing [369], indicating that imaging can be performed at multiple stages throughout therapy. Several phase I trials validated the safety (relative to other forms of neuroblastoma therapy) and feasibility of radioimmunotherapy with ^{131}I -3F8 [345, 349] including intrathecal injection of the radiolabeled antibody for patients with CNS metastases [370, 371]. A phase II trial is ongoing at the Memorial Sloan Kettering Cancer Center [345, 372].

Diagnostic imaging with ^{131}I has multiple limitations: The emitted photon of ^{131}I is quite energetic (364 keV), which degrades image quality, and the images are inherently non-quantitative due to the single-photon emission. Furthermore, ^{131}I has a prominent β^- -emission (192 keV, 90%), which adds to the patient radiation exposure and significantly limits the injected dose. In an early study, Larson et al. successfully used ^{124}I -3F8 PET to estimate the dosimetry in a patient scheduled for ^{131}I -3F8 radioimmunotherapy. [373] The images obtained had a direct impact on patient care in that the low accumulation of radiotracer in tumor resulted in a decision not to treat with radioimmunotherapy. More recently, 14G.2a, ch14.18 [206], and hu14.18K322A [374, 375] were labeled with copper-64 (^{64}Cu) and evaluated in mouse models of neuroblastoma, osteosarcoma, and melanoma. A parallel study with ch14.18- ΔCH2 , examining the effect of chelators on biodistribution, found that the 5-2-benzyl-1,4,7-triazacyclononane-1,4,7-triacetic acid (NOTA) chelator connected via a thiourea linkage provides the optimum signal-to-noise profile [376]. The accumulation of [^{64}Cu]Cu-Bn-NOTA-hu14.18K322A in osteosarcoma tumor xenografts was proportional to the GD2 expression as measured by flow cytometry [374]. The authors also reported that lesions as small as 29 mm³ were identified in a 34% GD2-positive model of metastatic osteosarcoma of the lung. Thus, imaging GD2 expression with PET shows great promise for improving on the successes already reported with SPECT and provides a highly impactful biomarker for therapy design.

21.4.2.3 [^{18}F]Fluorothymidine ([^{18}F]FLT)

Fluorothymidine (**FLT**) is being investigated for its safety and utility in pediatric brain tumors (Clinicaltrials.gov ID NCT01244737). The purpose of this phase II study is “to evaluate the utility of 3′-deoxy-3′-[^{18}F]fluorothymidine ([^{18}F]FLT) as a PET imaging agent to assess cellular proliferation for the characterization and evaluation of central nervous system tumors in children” and “to better define the biodistribution of ^{18}F -FLT administered to children and adolescents.” Preliminary findings have been published [377].

Brain tumors are the most common solid tumor in children and are sources of considerable morbidity and mortality. [^{18}F]FDG PET/CT imaging is hampered by the high

background uptake of FDG in normal cerebral cortex, which often renders distinction between normal brain uptake and tumor difficult. We have found [^{11}C]methionine to be of extraordinary value in numerous cerebral neoplasms of childhood [210–212]. [^{18}F]FLT, a surrogate marker of cellular proliferation, has been studied in adults with brain tumors, but it had not previously been evaluated in children.

[^{18}F]FLT PET scans were conducted on 22 pediatric patients (aged 6–21 years) with newly diagnosed ($n = 8$) or recurrent ($n = 9$) brain tumor. Five patients were later demonstrated to have a cerebral lesion other than a neoplasm, such as inflammation, vasculitis, or lymphomas. PET/CT was performed 30–45 minutes after intravenous administration of 5.2 MBq/kg of [^{18}F]FLT. No or minimal background uptake was observed in normal brain tissue.

Tumor uptake of [^{18}F]FLT was quite variable, ranging from similar to background brain (an oligoastrocytoma had minimal uptake with SUV_{max} of 0.11) to intense (SUV_{max} 4.00) in a pilocytic astrocytoma. Pilocytic astrocytoma was the most common tumor. Tumor uptake of [^{18}F]FLT (SUV_{max}) correlated significantly with the Ki-67 labeling index (a measure of cellular proliferation) in the 17 patients with new or recurrent brain tumor (Pearson $r = 0.74$, $p < 0.001$). In the nine patients with tumor recurrence, the SUV_{max} ranged from 1.54 to 4.00, and the Ki-67 labeling index ranged from 3–66%, reflecting the variety of tumor types with variable proliferation. Thus, in pediatric brain tumors, uptake of [^{18}F]FLT is related to the degree of cellular proliferation. These findings may help direct biopsy and may help identify tumors in patients with suspected recurrence and non-diagnostic MRI findings.

The use of [^{18}F]FLT PET/CT in pediatric lymphoma has also been explored [378]. The purpose of that study was to evaluate the normal biodistribution of [^{18}F]FLT and to compare the uptake of [^{18}F]FLT at disease sites in patients with lymphoma who had equivocal [^{18}F]FDG uptake. Eight patients with equivocal findings underwent [^{18}F]FLT PET/CT within three to five days of [^{18}F]FDG PET/CT. The authors of the study found much higher uptake of [^{18}F]FLT than of [^{18}F]FDG within the bone marrow and liver. There was much lower uptake of [^{18}F]FLT than of [^{18}F]FDG within the brain and heart. Reactive lymph nodes also concentrated [^{18}F]FLT. The clinical utility of [^{18}F]FLT was unclear because of the small number of patients and the patient selection criteria. Future studies may address this issue.

21.5 SUMMARY

Many radiotracers, labeled with either single-photon- or positron-emitting radionuclides, have been used to probe a wide variety of pediatric disorders. Most of these radiotracers were initially developed for applications in adults and were then applied to pediatric disorders. For example, mIBG was first developed for imaging the sympathetic nervous system of the heart and pheochromocytoma before being evaluated in the pediatric tumor neuroblastoma. Likewise, [^{18}F]FDG was evaluated in adult patients with neurodegenerative disorders and cerebral neoplasms prior to being used in pediatric patients.

As pediatric disorders and diseases are generally much less common than those in adults, fewer tracers have been developed specifically for application in pediatrics. A rare example of a radiotracer synthesized for use principally in pediatric patients is the series of radiolabeled antibodies directed at the GD2 disialoganglioside expressed on neuroblastoma cells (and also on osteosarcoma and melanoma). Additional radiolabeled probes for use in specific pediatric conditions await development.

REFERENCES

1. Schauwecker, D.S. (1992). The scintigraphic diagnosis of osteomyelitis. *Am. J. Roentgenol.* 158 (1): 9–18.
2. Jafri, R.A., Britton, K.E., Nimmon, C.C. et al. (1988). Technetium-99m MAG3, a comparison with iodine-123 and iodine-131 orthoiodohippurate, in patients with renal disorders. *J. Nucl. Med.* 29 (2): 147–158.
3. Rodman, J.H., Maneval, D.C., Magill, H.L., and Sunderland, M. (1993). Measurement of Tc-99m DTPA serum clearance for estimating glomerular filtration rate in children with cancer. *Pharmacotherapy* 13 (1): 10–16.
4. Willi, U. and Treves, S. (1983). Radionuclide voiding cystography. *Urol. Radiol.* 5 (3): 161–173.
5. Conway, J.J., Belman, A.B., and King, L.R. (1974). Direct and indirect radionuclide cystography. *Semin. Nucl. Med.* 4 (2): 197–211.
6. Nadel, H.R. (1996). Hepatobiliary scintigraphy in children. *Semin. Nucl. Med.* 26 (1): 25–42.
7. Treves, S.T., Baker, A., Fahey, F.H. et al. (2011). Nuclear medicine in the first year of life. *J. Nucl. Med.* 52 (6): 905–925.
8. Lu, G., Shih, W.J., Chou, C., and Xu, J.Y. (1996). Tc-99m MAA total-body imaging to detect intrapulmonary right-to-left shunts and to evaluate the therapeutic effect in pulmonary arteriovenous shunts. *Clin. Nucl. Med.* 21 (3): 197–202.
9. Rogers, Z.R., Wang, W.C., Luo, Z. et al. (2011). Biomarkers of splenic function in infants with sickle cell anemia: baseline data from the BABY HUG trial. *Blood* 117 (9): 2614–2617.
10. Sasaki, M. (2015). SPECT findings in autism spectrum disorders and medically refractory seizures. *Epilepsy. Behav.* 47: 167–171.
11. Parisi, M.T., Otjen, J.P., Stanescu, A.L., and Shulkin, B.L. (2018). Radionuclide imaging of infection and inflammation in children: a review. *Semin. Nucl. Med.* 48 (2): 148–165.
12. Remiker, A.S., Chuang, J., Corathers, S. et al. (2019). Differentiated thyroid cancer in the pediatric/adolescent population: evolution of treatment. *J. Pediatr. Hematol. Oncol.* 41 (7): 532–536.
13. Hamburger, J.I. (1985). Management of hyperthyroidism in children and adolescents. *J. Clin. Endocrinol. Metab.* 60 (5): 1019–1024.
14. Clark, J.D., Gelfand, M.J., and Elgazzar, A.H. (1995). Iodine-131 therapy of hyperthyroidism in pediatric patients. *J. Nucl. Med.* 36 (3): 442–445.

15. Uslu, L., Donig, J., Link, M. et al. (2015). Value of 18F-FDG PET and PET/CT for evaluation of pediatric malignancies. *J. Nucl. Med.* 56 (2): 274–286.
16. Dong, Y., Zhang, X., Wang, S. et al. (2017). 18F-FDG PET/CT is useful in initial staging, restaging for pediatric rhabdomyosarcoma. *Q. J. Nucl. Med. Mol. Imaging* 61 (4): 438–446.
17. Hurley, C., McCarville, M.B., Shulkin, B.L. et al. (2016). Comparison of (18) F-FDG-PET-CT and bone scintigraphy for evaluation of osseous metastases in newly diagnosed and recurrent osteosarcoma. *Pediatr. Blood Cancer* 63 (8): 1381–1386.
18. Treglia, G., Salsano, M., Stefanelli, A. et al. (2012). Diagnostic accuracy of (1)(8)F-FDG-PET and PET/CT in patients with Ewing sarcoma family tumours: a systematic review and a meta-analysis. *Skeletal. Radiol.* 41 (3): 249–256.
19. Tsai, L.L., Drubach, L., Fahey, F. et al. (2012). [18F]-Fluorodeoxyglucose positron emission tomography in children with neurofibromatosis type 1 and plexiform neurofibromas: correlation with malignant transformation. *J. Neurooncol.* 108 (3): 469–475.
20. Van Der Gucht, A., Zehou, O., Djelbani-Ahmed, S. et al. (2016). Metabolic tumour burden measured by 18F-FDG PET/CT predicts malignant transformation in patients with neurofibromatosis type-1. *PLoS One* 11 (3): e0151809.
21. Phillips, M., Allen, C., Gerson, P., and McClain, K. (2009). Comparison of FDG-PET scans to conventional radiography and bone scans in management of Langerhans cell histiocytosis. *Pediatr. Blood Cancer* 52 (1): 97–101.
22. Basu, S., Chryssikos, T., Moghadam-Kia, S. et al. (2009). Positron emission tomography as a diagnostic tool in infection: present role and future possibilities. *Semin. Nucl. Med.* 39 (1): 36–51.
23. Basu, S., Zhuang, H., Torigian, D.A. et al. (2009). Functional imaging of inflammatory diseases using nuclear medicine techniques. *Semin. Nucl. Med.* 39 (2): 124–145.
24. Bomanji, J., Almuhaideb, A., and Zumla, A. (2011). Combined PET and X-ray computed tomography imaging in pulmonary infections and inflammation. *Curr. Opin. Pulm. Med.* 17 (3): 197–205.
25. Guleria, R., Jyothidasan, A., Madan, K. et al. (2014). Utility of FDG-PET-CT scanning in assessing the extent of disease activity and response to treatment in sarcoidosis. *Lung India* 31 (4): 323–330.
26. Jasper, N., Dabritz, J., Frosch, M. et al. (2010). Diagnostic value of [(18)F]-FDG PET/CT in children with fever of unknown origin or unexplained signs of inflammation. *Eur. J. Nucl. Med. Mol. Imaging* 37 (1): 136–145.
27. Saboury, B., Salavati, A., Brothers, A. et al. (2014). FDG PET/CT in Crohn's disease: correlation of quantitative FDG PET/CT parameters with clinical and endoscopic surrogate markers of disease activity. *Eur. J. Nucl. Med. Mol. Imaging* 41 (4): 605–614.
28. Theobald, I., Fischbach, R., Hulskamp, G. et al. (2002). Pulmonary aspergillosis as initial manifestation of septic granulomatosis (chronic granulomatous disease, CGD) in a premature monozygotic female twin and FDG-PET diagnosis of spread of the disease. *Radiologe* 42 (1): 42–45.
29. Kim, S., Salamon, N., Jackson, H.A. et al. (2010). PET imaging in pediatric neuroradiology: current and future applications. *Pediatr. Radiol.* 40 (1): 82–96.

30. Patil, S., Biassoni, L., and Borgwardt, L. (2007). Nuclear medicine in pediatric neurology and neurosurgery: epilepsy and brain tumors. *Semin. Nucl. Med.* 37 (5): 357–381.
31. Stanescu, L., Ishak, G.E., Khanna, P.C. et al. (2013). FDG PET of the brain in pediatric patients: imaging spectrum with MR imaging correlation. *Radiographics* 33 (5): 1279–1303.
32. Demer, L.L., Gould, K.L., Goldstein, R.A. et al. (1989). Assessment of coronary artery disease severity by positron emission tomography. Comparison with quantitative arteriography in 193 patients. *Circulation* 79 (4): 825–835.
33. Muzik, O., Paridon, S.M., Singh, T.P. et al. (1996). Quantification of myocardial blood flow and flow reserve in children with a history of Kawasaki disease and normal coronary arteries using positron emission tomography. *J. Am. Coll. Cardiol.* 28 (3): 757–762.
34. Donnelly, J.P., Raffel, D.M., Shulkin, B.L. et al. (1998). Resting coronary flow and coronary flow reserve in human infants after repair or palliation of congenital heart defects as measured by positron emission tomography. *J. Thorac. Cardiovasc. Surg.* 115 (1): 103–110.
35. Grant, F.D., Fahey, F.H., Packard, A.B. et al. (2008). Skeletal PET with 18F-fluoride: applying new technology to an old tracer. *J. Nucl. Med.* 49 (1): 68–78.
36. Lim, R., Fahey, F.H., Drubach, L.A. et al. (2007). Early experience with fluorine-18 sodium fluoride bone PET in young patients with back pain. *J. Pediatr. Orthop.* 27 (3): 277–282.
37. Drubach, L.A., Johnston, P.R., Newton, A.W. et al. (2010). Skeletal trauma in child abuse: detection with 18F-NaF PET. *Radiology* 255 (1): 173–181.
38. Kumar, A. and Chugani, H.T. (2008). PET in the assessment of Pediatric brain development and developmental disorders. *PET Clin.* 3 (4): 487–515.
39. Chugani, H.T. (2018). Imaging brain metabolism in the Newborn. *J. Child Neurol.* 33 (13): 851–860.
40. Ergun, E.L., Saygi, S., Yalnizoglu, D. et al. (2016). SPECT-PET in epilepsy and clinical approach in evaluation. *Semin. Nucl. Med.* 46 (4): 294–307.
41. Juhasz, C. and Chugani, H.T. (2003). Imaging the epileptic brain with positron emission tomography. *Neuroimaging Clin. N. Am.* 13 (4): 705–716. viii.
42. Kumar, A. and Chugani, H.T. (2013). Functional imaging: PET. *Handb. Clin. Neurol.* 111: 767–776.
43. Zurcher, N.R., Bhanot, A., McDougle, C.J., and Hooker, J.M. (2015). A systematic review of molecular imaging (PET and SPECT) in autism spectrum disorder: current state and future research opportunities. *Neurosci. Biobehav. Rev.* 52: 56–73.
44. Jones, S.P., Guillemin, G.J., and Brew, B.J. (2013). The kynurenine pathway in stem cell biology. *Int. J. Tryptophan Res.* 6: 57–66.
45. Muzik, O., Chugani, D.C., Chakraborty, P. et al. (1997). Analysis of [C-11]alpha-methyl-tryptophan kinetics for the estimation of serotonin synthesis rate in vivo. *J. Cereb. Blood Flow Metab.* 17 (6): 659–669.
46. Diksic, M., Nagahiro, S., Chaly, T. et al. (1991). Serotonin synthesis rate measured in living dog brain by positron emission tomography. *J. Neurochem.* 56 (1): 153–162.

47. Diksic, M., Nagahiro, S., Sourkes, T.L., and Yamamoto, Y.L. (1990). A new method to measure brain serotonin synthesis in vivo. I. Theory and basic data for a biological model. *J. Cereb. Blood Flow Metab.* 10 (1): 1–12.
48. Kuhar, M.J., Aghajanian, G.K., and Roth, R.H. (1972). Tryptophan hydroxylase activity and synaptosomal uptake of serotonin in discrete brain regions after midbrain raphe lesions: correlations with serotonin levels and histochemical fluorescence. *Brain Res.* 44 (1): 165–176.
49. Nishizawa, S., Leyton, M., Okazawa, H. et al. (1998). Validation of a less-invasive method for measurement of serotonin synthesis rate with alpha-[11C]methyl-tryptophan. *J. Cereb. Blood Flow Metab.* 18 (10): 1121–1129.
50. Chakraborty, P.K., Mangner, T.J., Chugani, D.C. et al. (1996). A high-yield and simplified procedure for the synthesis of alpha-[11C]methyl-L-tryptophan. *Nucl. Med. Biol.* 23 (8): 1005–1008.
51. Chaly, T. and Diksic, M. (1988). Synthesis of "no-carrier-added" alpha-[11C]methyl-L-tryptophan. *J. Nucl. Med.* 29 (3): 370–374.
52. Huang, X., Xiao, X., Gillies, R.J., and Tian, H. (2016). Design and automated production of 11C-alpha-methyl-L-tryptophan (11C-AMT). *Nucl. Med. Biol.* 43 (5): 303–308.
53. Cohen, Z., Tsuiki, K., Takada, A. et al. (1995). In vivo-synthesized radioactively labelled alpha-methyl serotonin as a selective tracer for visualization of brain serotonin neurons. *Synapse* 21 (1): 21–28.
54. Madras, B.K. and Sourkes, T.L. (1965). Metabolism of alpha-methyltryptophan. *Biochem. Pharmacol.* 14 (11): 1499–1506.
55. Roberge, A.G., Missala, K., and Sourkes, T.L. (1972). Alpha-methyltryptophan: effects on synthesis and degradation of serotonin in the brain. *Neuropharmacology* 11 (2): 197–209.
56. Sourkes, T.L. (1971). Alpha-methyltryptophan and its actions on tryptophan metabolism. *Fed. Proc.* 30 (3): 897–903.
57. Missala, K. and Sourkes, T.L. (1988). Functional cerebral activity of an analogue of serotonin formed in situ. *Neurochem. Int.* 12 (2): 209–214.
58. Shoaf, S.E., Carson, R., Hommer, D. et al. (1998). Brain serotonin synthesis rates in rhesus monkeys determined by [11C]alpha-methyl-L-tryptophan and positron emission tomography compared to CSF 5-hydroxyindole-3-acetic acid concentrations. *Neuropsychopharmacology* 19 (5): 345–353.
59. Shoaf, S.E. and Schmall, B. (1996). Pharmacokinetics of alpha-methyl-L-tryptophan in rhesus monkeys and calculation of the lumped constant for estimating the rate of serotonin synthesis. *J. Pharmacol. Exp. Ther.* 277 (1): 219–224.
60. Chugani, D.C., Muzik, O., Chakraborty, P. et al. (1998). Human brain serotonin synthesis capacity measured in vivo with alpha-[C-11]methyl-L-tryptophan. *Synapse* 28 (1): 33–43.
61. Nishizawa, S., Benkelfat, C., Young, S.N. et al. (1997). Differences between males and females in rates of serotonin synthesis in human brain. *Proc. Natl. Acad. Sci. U.S.A.* 94 (10): 5308–5313.

62. Abbott, N.J., Chugani, D.C., Zaharchuk, G. et al. (1999). Delivery of imaging agents into brain. *Adv. Drug Delivery Rev.* 37 (1–3): 253–277.
63. Chugani, D.C. and Muzik, O. (2000). Alpha[C-11]methyl-L-tryptophan PET maps brain serotonin synthesis and kynurenine pathway metabolism. *J. Cereb. Blood Flow Metab.* 20 (1): 2–9.
64. Diksic, M., Nagahiro, S., and Sourkes, T.L. (1990). Biological model for the in vivo measurement of rate of serotonin synthesis in the brain. *J. Neural. Transm. Suppl.* 29: 131–140.
65. Anderson, G.M., Horne, W.C., Chatterjee, D., and Cohen, D.J. (1990). The hyperserotonemia of autism. *Ann. N.Y. Acad. Sci.* 600: 331–340. discussion 41-2.
66. Schain, R.J. and Freedman, D.X. (1961). Studies on 5-hydroxyindole metabolism in autistic and other mentally retarded children. *J. Pediatr.* 58: 315–320.
67. Chugani, D.C., Muzik, O., Rothermel, R. et al. (1997). Altered serotonin synthesis in the dentatohalamocortical pathway in autistic boys. *Ann. Neurol.* 42 (4): 666–669.
68. Chugani, D.C., Muzik, O., Behen, M. et al. (1999). Developmental changes in brain serotonin synthesis capacity in autistic and nonautistic children. *Ann. Neurol.* 45 (3): 287–295.
69. Chandana, S.R., Behen, M.E., Juhasz, C. et al. (2005). Significance of abnormalities in developmental trajectory and asymmetry of cortical serotonin synthesis in autism. *Int. J. Dev. Neurosci.* 23 (2–3): 171–182.
70. Chugani, D.C., Chugani, H.T., Wiznitzer, M. et al. (2016). Efficacy of low-dose buspirone for restricted and repetitive behavior in young children with autism spectrum disorder: a randomized trial. *J. Pediatr.* 170: 45–53. e1–4.
71. Chugani, H.T., Kumar, A., Kupsky, W. et al. (2011). Clinical and histopathologic correlates of 11C-alpha-methyl-L-tryptophan (AMT) PET abnormalities in children with intractable epilepsy. *Epilepsia* 52 (9): 1692–1698.
72. Louw, D., Sutherland, G.R., Glavin, G.B., and Girvin, J. (1989). A study of monoamine metabolism in human epilepsy. *Can. J. Neurol. Sci.* 16 (4): 394–397.
73. Trottier, S., Evrard, B., Vignal, J.P. et al. (1996). The serotonergic innervation of the cerebral cortex in man and its changes in focal cortical dysplasia. *Epilepsy Res.* 25 (2): 79–106.
74. Pintor, M., Mefford, I.N., Hutter, I. et al. (1990). Levels of biogenic amines, their metabolites, and tyrosine hydroxylase activity in the human epileptic temporal cortex. *Synapse* 5 (2): 152–156.
75. Fedi, M., Reutens, D.C., Andermann, F. et al. (2003). Alpha-[11C]-methyl-L-tryptophan PET identifies the epileptogenic tuber and correlates with interictal spike frequency. *Epilepsy Res.* 52 (3): 203–213.
76. Chugani, D.C., Chugani, H.T., Muzik, O. et al. (1998). Imaging epileptogenic tubers in children with tuberous sclerosis complex using alpha-[11C]methyl-L-tryptophan positron emission tomography. *Ann. Neurol.* 44 (6): 858–866.
77. Kagawa, K., Chugani, D.C., Asano, E. et al. (2005). Epilepsy surgery outcome in children with tuberous sclerosis complex evaluated with alpha-[11C]methyl-L-tryptophan positron emission tomography (PET). *J. Child Neurol.* 20 (5): 429–438.

78. Bagla, S., Cukovic, D., Asano, E. et al. (2018). A distinct microRNA expression profile is associated with alpha-[¹¹C]-methyl-L-tryptophan (AMT) PET uptake in epileptogenic cortical tubers resected from patients with tuberous sclerosis complex. *Neurobiol. Dis.* 109 (Pt A): 76–87.
79. Fedi, M., Reutens, D., Okazawa, H. et al. (2001). Localizing value of alpha-methyl-L-tryptophan PET in intractable epilepsy of neocortical origin. *Neurology* 57 (9): 1629–1636.
80. Juhasz, C., Chugani, D.C., Muzik, O. et al. (2003). Alpha-methyl-L-tryptophan PET detects epileptogenic cortex in children with intractable epilepsy. *Neurology* 60 (6): 960–968.
81. Wakamoto, H., Chugani, D.C., Juhasz, C. et al. (2008). Alpha-methyl-L-tryptophan positron emission tomography in epilepsy with cortical developmental malformations. *Pediatr. Neurol.* 39 (3): 181–188.
82. Juhasz, C., Chugani, D.C., Padhye, U.N. et al. (2004). Evaluation with alpha-[¹¹C]methyl-L-tryptophan positron emission tomography for reoperation after failed epilepsy surgery. *Epilepsia* 45 (2): 124–130.
83. Chugani, H.T., Juhasz, C., Chugani, D.C. et al. (2008). Increased striatal serotonin synthesis following cortical resection in children with intractable epilepsy. *Epilepsy Res.* 78 (2–3): 124–130.
84. Rintahaka, P.J. and Chugani, H.T. (1997). Clinical role of positron emission tomography in children with tuberous sclerosis complex. *J. Child Neurol.* 12 (1): 42–52.
85. Asano, E., Chugani, D.C., Muzik, O. et al. (2001). Autism in tuberous sclerosis complex is related to both cortical and subcortical dysfunction. *Neurology* 57 (7): 1269–1277.
86. Uyttenhove, C., Pilotte, L., Theate, I. et al. (2003). Evidence for a tumoral immune resistance mechanism based on tryptophan degradation by indoleamine 2,3-dioxygenase. *Nat. Med.* 9 (10): 1269–1274.
87. Lovelace, M.D., Varney, B., Sundaram, G. et al. (2017). Recent evidence for an expanded role of the kynurenine pathway of tryptophan metabolism in neurological diseases. *Neuropharmacology* 112 (Pt B): 373–388.
88. Saito, K., Nowak, T.S. Jr., Suyama, K. et al. (1993). Kynurenine pathway enzymes in brain: responses to ischemic brain injury versus systemic immune activation. *J. Neurochem.* 61 (6): 2061–2070.
89. Huttenlocher, P.R. and Heydemann, P.T. (1984). Fine structure of cortical tubers in tuberous sclerosis: a Golgi study. *Ann. Neurol.* 16 (5): 595–602.
90. Munn, D.H. and Mellor, A.L. (2016). IDO in the tumor microenvironment: inflammation, counter-regulation, and tolerance. *Trends Immunol.* 37 (3): 193–207.
91. Batista, C.E., Juhasz, C., Muzik, O. et al. (2009). Imaging correlates of differential expression of indoleamine 2,3-dioxygenase in human brain tumors. *Mol. Imaging Biol.* 11 (6): 460–466.
92. Juhasz, C., Chugani, D.C., Muzik, O. et al. (2006). In vivo uptake and metabolism of alpha-[¹¹C]methyl-L-tryptophan in human brain tumors. *J. Cereb. Blood Flow Metab.* 26 (3): 345–357.

93. Peng, F., Juhasz, C., Bhambhani, K. et al. (2007). Assessment of progression and treatment response of optic pathway glioma with positron emission tomography using alpha-[(11)C]methyl-L-tryptophan. *Mol. Imaging Biol.* 9 (3): 106–109.
94. Juhasz, C., Muzik, O., Chugani, D.C. et al. (2011). Differential kinetics of alpha-[(11)C]methyl-L-tryptophan on PET in low-grade brain tumors. *J. Neurooncol.* 102 (3): 409–415.
95. Alkonyi, B., Mittal, S., Zitron, I. et al. (2012). Increased tryptophan transport in epileptogenic dysembryoplastic neuroepithelial tumors. *J. Neurooncol.* 107 (2): 365–372.
96. Bosnyak, E., Kamson, D.O., Guastella, A.R. et al. (2015). Molecular imaging correlates of tryptophan metabolism via the kynurenine pathway in human meningiomas. *Neuro. Oncol.* 17 (9): 1284–1292.
97. Shinotoh, H., Yamasaki, T., Inoue, O. et al. (1986). Visualization of specific binding sites of benzodiazepine in human brain. *J. Nucl. Med.* 27 (10): 1593–1599.
98. Zezula, J., Cortes, R., Probst, A., and Palacios, J.M. (1988). Benzodiazepine receptor sites in the human brain: autoradiographic mapping. *Neuroscience* 25 (3): 771–795.
99. Gammill, R.B. and Carter, D.B. (1993). Neuronal BZD receptors: new ligands, clones and pharmacology. *Ann. Rep. Ned. Chem.* 28: 19–27.
100. Hodolic, M., Topakian, R., and Pichler, R. (2016). (18)F-fluorodeoxyglucose and (18)F-flumazenil positron emission tomography in patients with refractory epilepsy. *Radiol. Oncol.* 50 (3): 247–253.
101. Juhasz, C., Nagy, F., Muzik, O. et al. (1999). [11C]flumazenil PET in patients with epilepsy with dual pathology. *Epilepsia* 40 (5): 566–574.
102. Hunkeler, W., Mohler, H., Pieri, L. et al. (1981). Selective antagonists of benzodiazepines. *Nature* 290 (5806): 514–516.
103. Mazière, M., Hantraye, P., Prenant, C. et al. (1984). Synthesis of ethyl 8-fluoro-5,6-dihydro-5-[11C]methyl-6-oxo-4H-imidazo [1,5-a] [1,4]benzodiazepine-3-carboxylate (RO 15.1788-11C): a specific radioligand for the in vivo study of central benzodiazepine receptors by positron emission tomography. *Int. J. Appl. Radiat. Isot.* 35 (10): 973–976.
104. Samson, Y., Hantraye, P., Baron, J.C. et al. (1985). Kinetics and displacement of [11C] RO 15-1788, a benzodiazepine antagonist, studied in human brain in vivo by positron tomography. *Eur. J. Pharmacol.* 110 (2): 247–251.
105. Iyo, M., Itoh, T., Yamasaki, T. et al. (1991). Quantitative in vivo analysis of benzodiazepine binding sites in the human brain using positron emission tomography. *Neuropharmacology* 30 (3): 207–215.
106. Koeppe, R.A., Holthoff, V.A., Frey, K.A. et al. (1991). Compartmental analysis of [11C]flumazenil kinetics for the estimation of ligand transport rate and receptor distribution using positron emission tomography. *J. Cereb. Blood Flow Metab.* 11 (5): 735–744.
107. Lassen, N.A., Bartenstein, P.A., Lammertsma, A.A. et al. (1995). Benzodiazepine receptor quantification in vivo in humans using [11C]flumazenil and PET: application of the steady-state principle. *J. Cereb. Blood Flow Metab.* 15 (1): 152–165.

108. Meyer, M., Koeppe, R.A., Frey, K.A. et al. (1995). Positron emission tomography measures of benzodiazepine binding in Alzheimer's disease. *Arch. Neurol.* 52 (3): 314–317.
109. Ishiwata, K., Itou, T., Ohyama, M. et al. (1998). Metabolite analysis of [¹¹C]flumazenil in human plasma: assessment as the standardized value for quantitative PET studies. *Ann. Nucl. Med.* 12 (1): 55–59.
110. Chugani, D.C., Muzik, O., Juhasz, C. et al. (2001). Postnatal maturation of human GABAA receptors measured with positron emission tomography. *Ann. Neurol.* 49 (5): 618–626.
111. Hammers, A., Koeppe, M.J., Richardson, M.P. et al. (2001). Central benzodiazepine receptors in malformations of cortical development: a quantitative study. *Brain* 124 (Pt 8): 1555–1565.
112. Asahina, N., Shiga, T., Egawa, K. et al. (2008). [¹¹C]flumazenil positron emission tomography analyses of brain gamma-aminobutyric acid type a receptors in Angelman syndrome. *J. Pediatr.* 152 (4): 546–549, 9 e1–3.
113. Chugani, H.T., Kumar, A., and Muzik, O. (2013). GABA(A) receptor imaging with positron emission tomography in the human newborn: a unique binding pattern. *Pediatr. Neurol.* 48 (6): 459–462.
114. Holopainen, I.E., Metsahonkala, E.L., Kokkonen, H. et al. (2001). Decreased binding of [¹¹C]flumazenil in Angelman syndrome patients with GABA(A) receptor beta3 subunit deletions. *Ann. Neurol.* 49 (1): 110–113.
115. Nagy, F., Chugani, D.C., Juhasz, C. et al. (1999). Altered in vitro and in vivo flumazenil binding in human epileptogenic neocortex. *J. Cereb. Blood Flow Metab.* 19 (9): 939–947.
116. Niimura, K., Muzik, O., Chugani, D.C. et al. (1999). [¹¹C]flumazenil PET: activity images versus parametric images for the detection of neocortical epileptic foci. *J. Nucl. Med.* 40 (12): 1985–1991.
117. Pearl, P.L., Gibson, K.M., Quezado, Z. et al. (2009). Decreased GABA-A binding on FMZ-PET in succinic semialdehyde dehydrogenase deficiency. *Neurology* 73 (6): 423–429.
118. Niimura, K., Chugani, D.C., Muzik, O., and Chugani, H.T. (1999). Cerebellar reorganization following cortical injury in humans: effects of lesion size and age. *Neurology* 52 (4): 792–797.
119. Juhasz, C., Chugani, D.C., Muzik, O. et al. (2001). Relationship of flumazenil and glucose PET abnormalities to neocortical epilepsy surgery outcome. *Neurology* 56 (12): 1650–1658.
120. Juhasz, C., Chugani, D.C., Muzik, O. et al. (2000). Electroclinical correlates of flumazenil and fluorodeoxyglucose PET abnormalities in lesional epilepsy. *Neurology* 55 (6): 825–835.
121. Muzik, O., da Silva, E.A., Juhasz, C. et al. (2000). Intracranial EEG versus flumazenil and glucose PET in children with extratemporal lobe epilepsy. *Neurology* 54 (1): 171–179.
122. Pearl, P.L., Shukla, L., Theodore, W.H. et al. (2011). Epilepsy in succinic semialdehyde dehydrogenase deficiency, a disorder of GABA metabolism. *Brain Dev.* 33 (9): 796–805.

123. Kumada, T., Nishii, R., Higashi, T. et al. (2010). Epileptic apnea in a trisomy 18 infant. *Pediatr. Neurol.* 42 (1): 61–64.
124. Juhasz, C., Asano, E., Shah, A. et al. (2009). Focal decreases of cortical GABAA receptor binding remote from the primary seizure focus: what do they indicate? *Epilepsia* 50 (2): 240–250.
125. Shiraishi, H., Takano, K., Shiga, T. et al. (2007). Possible involvement of the tip of temporal lobe in Landau-Kleffner syndrome. *Brain Dev.* 29 (8): 529–533.
126. Sood, S. and Chugani, H.T. (2006). Functional neuroimaging in the preoperative evaluation of children with drug-resistant epilepsy. *Childs Nerv. Syst.* 22 (8): 810–820.
127. Stanasic, M., Coello, C., Ivanovic, J. et al. (2015). Seizure outcomes in relation to the extent of resection of the perifocal fluorodeoxyglucose and flumazenil PET abnormalities in anteromedial temporal lobectomy. *Acta. Neurochir. (Wien).* 157 (11): 1905–1916.
128. Beer, H.F., Blauenstein, P.A., Hasler, P.H. et al. (1990). In vitro and in vivo evaluation of iodine-123-Ro 16-0154: a new imaging agent for SPECT investigations of benzodiazepine receptors. *J. Nucl. Med.* 31 (6): 1007–1014.
129. Holl, K., Deisenhammer, E., Dauth, J. et al. (1989). Imaging benzodiazepine receptors in the human brain by single photon emission computed tomography (SPECT). *Int. J. Rad. Appl. Instrum. B.* 16 (8): 759–763.
130. Jibiki, I. and Yamaguchi, N. (1994). Epilepsy and SPECT. *Neurosci. Biobehav. Rev.* 18 (2): 281–290.
131. Kung, H.F., Kung, M.P., and Choi, S.R. (2003). Radiopharmaceuticals for single-photon emission computed tomography brain imaging. *Semin. Nucl. Med.* 33 (1): 2–13.
132. Ikemoto, S., Hamano, S.I., Hirata, Y. et al. (2018). Maturational changes of gamma-Aminobutyric acid receptors measured with benzodiazepine binding of iodine 123 Iomazenil single-photon emission computed tomography. *Pediatr. Neurol.* 82: 19–24.
133. Nomura, S., Koizumi, H., Suehiro, E. et al. (2016). Unique distribution of benzodiazepine receptors in the brain during the first two years of life. *Pediatr. Neurosurg.* 51 (5): 244–248.
134. Mori, T., Mori, K., Fujii, E. et al. (2012). Evaluation of the GABAergic nervous system in autistic brain: (123)I-iomazenil SPECT study. *Brain Dev.* 34 (8): 648–654.
135. Nagamitsu, S., Yamashita, Y., Tanigawa, H. et al. (2015). Upregulated GABA inhibitory function in ADHD children with child behavior checklist-Dysregulation profile: 123I-Iomazenil SPECT study. *Front Psychiatry.* 6: 84.
136. Nagamitsu, S., Sakurai, R., Matsuoka, M. et al. (2016). Altered SPECT (123)I-iomazenil binding in the cingulate cortex of children with anorexia nervosa. *Front Psychiatry.* 7: 16.
137. Matsuda, K., Mihara, T., Tottori, T. et al. (2001). Neuroradiologic findings in focal cortical dysplasia: histologic correlation with surgically resected specimens. *Epilepsia* 42 (Suppl 6): 29–36.
138. Fujimoto, A., Okanishi, T., Kanai, S. et al. (2018). Double match of (18)F-fluorodeoxyglucose-PET and Iomazenil-SPECT improves outcomes of focus resection surgery. *Acta Neurochir. (Wien).* 160 (9): 1875–1882.

139. Higurashi, N., Hamano, S., Oritsu, T. et al. (2011). Iomazenil hyperfixation in single photon emission computed tomography study of malformations of cortical development during infancy. *Eur. J. Paediatr. Neurol.* 15 (4): 372–375.
140. Horino, A., Kawawaki, H., Fukuoka, M. et al. (2016). A case of succinic semialdehyde dehydrogenase deficiency with status epilepticus and rapid regression. *Brain Dev.* 38 (9): 866–870.
141. Ishikawa, N., Kobayashi, Y., and Kobayashi, M. (2010). A case of frontal lobe epilepsy in which amplitude-integrated EEG combined with conventional EEG was useful for evaluating clusters of seizures. *Epilepsy Behav.* 18 (4): 485–487.
142. Kaido, T., Otsuki, T., Kakita, A. et al. (2012). Novel pathological abnormalities of deep brain structures including dysplastic neurons in anterior striatum associated with focal cortical dysplasia in epilepsy. *J. Neurosurg. Pediatr.* 10 (3): 217–225.
143. Sata, Y., Matsuda, K., Mihara, T. et al. (2002). Quantitative analysis of benzodiazepine receptor in temporal lobe epilepsy: [(125)I]iomazenil autoradiographic study of surgically resected specimens. *Epilepsia* 43 (9): 1039–1048.
144. Mori, T., Mori, K., Fujii, E. et al. (2011). Neuroradiological and neurofunctional examinations for patients with 22q11.2 deletion. *Neuropediatrics* 42 (6): 215–221.
145. Mori, K., Mori, T., Toda, Y. et al. (2012). Decreased benzodiazepine receptor and increased GABA level in cortical tubers in tuberous sclerosis complex. *Brain Dev.* 34 (6): 478–486.
146. Le Fur, G., Guilloux, F., Rufat, P. et al. (1983). Peripheral benzodiazepine binding sites: effect of PK 11195, 1-(2-chlorophenyl)-N-methyl-(1-methylpropyl)-3 isoquinolinecarboxamide. II. In vivo studies. *Life Sci.* 32 (16): 1849–1856.
147. Le Fur, G., Vaucher, N., Perrier, M.L. et al. (1983). Differentiation between two ligands for peripheral benzodiazepine binding sites, [3H]RO5-4864 and [3H]PK 11195, by thermodynamic studies. *Life Sci.* 33 (5): 449–457.
148. Casellas, P., Galiegue, S., and Basile, A.S. (2002). Peripheral benzodiazepine receptors and mitochondrial function. *Neurochem. Int.* 40 (6): 475–486.
149. Scott, G., Mahmud, M., Owen, D.R., and Johnson, M.R. (2017). Microglial positron emission tomography (PET) imaging in epilepsy: applications, opportunities and pitfalls. *Seizure* 44: 42–47.
150. Venneti, S., Lopresti, B.J., Wang, G. et al. (2009). PK11195 labels activated microglia in Alzheimer's disease and in vivo in a mouse model using PET. *Neurobiol. Aging* 30 (8): 1217–1226.
151. Camsonne, R., Crouzel, C., Comar, D. et al. (1984). Synthesis of N-(¹¹C) methyl, N-(methyl-1 propyl), (chloro-2 phenyl)-1-isoquinoline carboxamide-3 (PK 11195): a new ligand for peripheral benzodiazepine receptors. *J. Labelled Compds Radiopharm.* 21 (10): 985–991.
152. Charbonneau, P., Syrota, A., Crouzel, C. et al. (1986). Peripheral-type benzodiazepine receptors in the living heart characterized by positron emission tomography. *Circulation* 73 (3): 476–483.
153. Junck, L., Olson, J.M., Ciliax, B.J. et al. (1989). PET imaging of human gliomas with ligands for the peripheral benzodiazepine binding site. *Ann. Neurol.* 26 (6): 752–758.

154. Chakraborty, P., Maiti, D., Mangner, T. et al. (2006). High yield and semi-automated synthesis procedure for (R)-[¹¹C]PK11195. *J. Nucl. Med.* 47 (Suppl 1): 522P.
155. Anderson, A.N., Pavese, N., Edison, P. et al. (2007). A systematic comparison of kinetic modelling methods generating parametric maps for [(11)C]-(R)-PK11195. *Neuroimage* 36 (1): 28–37.
156. Weizman, R., Dar, D.E., Landa, S. et al. (1993). "Peripheral" benzodiazepine receptor density is not altered by methylphenidate treatment in children with attention-deficit hyperactivity disorder. *J. Child Adolesc. Psychopharmacol.* 3 (2): 63–69.
157. Kannan, S., Balakrishnan, B., Muzik, O. et al. (2009). Positron emission tomography imaging of neuroinflammation. *J. Child Neurol.* 24 (9): 1190–1199.
158. Kannan, S., Saadani-Makki, F., Balakrishnan, B. et al. (2011). Magnitude of [(11)C]PK11195 binding is related to severity of motor deficits in a rabbit model of cerebral palsy induced by intrauterine endotoxin exposure. *Dev Neurosci.* 33 (3–4): 231–240.
159. Kannan, S., Saadani-Makki, F., Muzik, O. et al. (2007). Microglial activation in perinatal rabbit brain induced by intrauterine inflammation: detection with 11C-(R)-PK11195 and small-animal PET. *J. Nucl. Med.* 48 (6): 946–954.
160. Suzuki, K., Sugihara, G., Ouchi, Y. et al. (2013). Microglial activation in young adults with autism spectrum disorder. *JAMA Psychiatry.* 70 (1): 49–58.
161. Kumar, A., Chugani, H.T., Chakraborty, P., and Huq, A.H. (2011). Evaluation of neuroinflammation in X-linked adrenoleukodystrophy. *Pediatr. Neurol.* 44 (2): 143–146.
162. Kumar, A., Williams, M.T., and Chugani, H.T. (2015). Evaluation of basal ganglia and thalamic inflammation in children with pediatric autoimmune neuropsychiatric disorders associated with streptococcal infection and tourette syndrome: a positron emission tomographic (PET) study using 11C-[R]-PK11195. *J. Child Neurol.* 30 (6): 749–756.
163. Leong, D.K. and Butterworth, R.F. (1996). Neuronal cell death in Wernicke's encephalopathy: pathophysiologic mechanisms and implications for PET imaging. *Metab. Brain Dis.* 11 (1): 71–79.
164. Kumar, A., Muzik, O., Chugani, D. et al. (2010). PET-derived biodistribution and dosimetry of the benzodiazepine receptor-binding radioligand (11)C-(R)-PK11195 in children and adults. *J. Nucl. Med.* 51 (1): 139–144.
165. Kumar, A., Muzik, O., Shandal, V. et al. (2012). Evaluation of age-related changes in translocator protein (TSPO) in human brain using (11)C-[R]-PK11195 PET. *J. Neuroinflammation* 9: 232.
166. Kumar, A., Chugani, H.T., Luat, A. et al. (2008). Epilepsy surgery in a case of encephalitis: use of 11C-PK11195 positron emission tomography. *Pediatr. Neurol.* 38 (6): 439–442.
167. Albrecht, D.S., Granziera, C., Hooker, J.M., and Loggia, M.L. (2016). In vivo imaging of human neuroinflammation. *ACS Chem. Neurosci.* 7 (4): 470–483.
168. Marques, T.R., Ashok, A.H., Pillinger, T. et al. (2019). Neuroinflammation in schizophrenia: meta-analysis of in vivo microglial imaging studies. *Psychol. Med.* 49 (13): 2186–2196.

169. Nag, S., Krasikova, R., Airaksinen, A.J. et al. (2019). Synthesis and biological evaluation of [(18)F]fluorovinpocetine, a potential PET radioligand for TSPO imaging. *Bioorg. Med. Chem. Lett.* 29 (16): 2270–2274.
170. Van Weehaeghe, D., Van Schoor, E., De Vocht, J. et al. (2019). TSPO versus P2X7 as target for neuroinflammation—an in vitro and in vivo study. *J. Nucl. Med.*
171. Bergstrom, M., Collins, V.P., Ehrin, E. et al. (1983). Discrepancies in brain tumor extent as shown by computed tomography and positron emission tomography using [68Ga]EDTA, [11C]glucose, and [11C]methionine. *J. Comput. Assisted Tomogr.* 7 (6): 1062–1066.
172. Comar, D., Cartron, J., Maziere, M., and Marazano, C. (1976). Labelling and metabolism of methionine-methyl-11 C. *Eur. J. Nucl. Med.* 1 (1): 11–14.
173. Fujiwara, T., Matsuzawa, T., Kubota, K. et al. (1989). Relationship between histologic type of primary lung cancer and carbon-11-L-methionine uptake with positron emission tomography. *J. Nucl. Med.* 30 (1): 33–37.
174. Herrera, N.E., Gonzalez, R., Schwartz, R.D. et al. (1965). Se methionine as a diagnostic agent in malignant lymphoma. *J. Nucl. Med.* 6 (11): 792–804.
175. Hubner, K.F., Purvis, J.T., Mahaley, S.M. Jr. et al. (1982). Brain tumor imaging by positron emission computed tomography using 11C-labeled amino acids. *J. Comput. Assisted Tomogr.* 6 (3): 544–550.
176. Kubota, K., Ito, M., Fukuda, H. et al. (1983). Cancer diagnosis with positron computed tomography and carbon-11-labelled L-methionine. *Lancet* 2 (8360): 1192.
177. Chamroonrat, W., Houseni, M., Li, G. et al. (2008). PET and PET/CT in pediatric gastrointestinal tract oncology. *PET Clin.* 3 (2): 227–238.
178. Juhasz, C., Dwivedi, S., Kamson, D.O. et al. (2014). Comparison of amino acid positron emission tomographic radiotracers for molecular imaging of primary and metastatic brain tumors. *Mol. Imaging* 13.
179. Laverman, P., Boerman, O.C., Corstens, F.H., and Oyen, W.J. (2002). Fluorinated amino acids for tumour imaging with positron emission tomography. *Eur. J. Nucl. Med. Mol. Imaging* 29 (5): 681–690.
180. O’Tuama, L.A., Phillips, P.C., Strauss, L.C. et al. (1990). Two-phase [11C]L-methionine PET in childhood brain tumors. *Pediatr. Neurol.* 6 (3): 163–170.
181. Ogawa, T., Miura, S., Murakami, M. et al. (1996). Quantitative evaluation of neutral amino acid transport in cerebral gliomas using positron emission tomography and fluorine-18 fluorophenylalanine. *Eur. J. Nucl. Med.* 23 (8): 889–895.
182. Critchley, M., Testa, H.J., and Stretton, T.B. (1974). Combined use of 99mtechnetium-labelled macroaggregates of albumin and 75selenium-selenomethionine in the diagnosis of lung cancer. *Thorax* 29 (4): 421–424.
183. Washburn, L.C., Sun, T.T., Byrd, B.L. et al. (1979). DL-[Carboxyl-11C]tryptophan, a potential agent for pancreatic imaging; production and preclinical investigations. *J. Nucl. Med.* 20 (8): 857–864.
184. Kubota, K., Yamada, K., Fukada, H. et al. (1984). Tumor detection with carbon-11-labelled amino acids. *Eur. J. Nucl. Med.* 9 (3): 136–140.

185. Bose, A., Tanaka, T., and Mishkin, F.S. (1982). Selenomethionine uptake in the thorax. *Semin. Nucl. Med.* 12 (2): 220–221.
186. Busch, H., Davis, J.R., Honig, G.R. et al. (1959). The uptake of a variety of amino acids into nuclear proteins of tumors and other tissues. *Cancer Res.* 19: 1030–1039.
187. Ganapathy, V., Thangaraju, M., and Prasad, P.D. (2009). Nutrient transporters in cancer: relevance to Warburg hypothesis and beyond. *Pharmacol. Ther.* 121 (1): 29–40.
188. Huang, C. and McConathy, J. (2013). Radiolabeled amino acids for oncologic imaging. *J. Nucl. Med.* 54 (7): 1007–1010.
189. Nakanishi, T. and Tamai, I. (2011). Solute carrier transporters as targets for drug delivery and pharmacological intervention for chemotherapy. *J. Pharm. Sci.* 100 (9): 3731–3750.
190. Wester, H.J., Herz, M., Weber, W. et al. (1999). Synthesis and radiopharmacology of O-(2-[18F]fluoroethyl)-L-tyrosine for tumor imaging. *J. Nucl. Med.* 40 (1): 205–212.
191. Shoup, T.M., Olson, J., Hoffman, J.M. et al. (1999). Synthesis and evaluation of [18F]1-amino-3-fluorocyclobutane-1-carboxylic acid to image brain tumors. *J. Nucl. Med.* 40 (2): 331–338.
192. Wen, P.Y., Macdonald, D.R., Reardon, D.A. et al. (2010). Updated response assessment criteria for high-grade gliomas: response assessment in neuro-oncology working group. *J. Clin. Oncol.* 28 (11): 1963–1972.
193. Braunstein, S., Raleigh, D., Bindra, R. et al. (2017). Pediatric high-grade glioma: current molecular landscape and therapeutic approaches. *J. Neurooncol.* 134 (3): 541–549.
194. Zukotynski, K., Fahey, F., Kocak, M. et al. (2014). 18F-FDG PET and MR imaging associations across a spectrum of pediatric brain tumors: a report from the pediatric brain tumor consortium. *J. Nucl. Med.* 55 (9): 1473–1480.
195. Suchorska, B., Albert, N.L., and Tonn, J.C. (2016). Usefulness of PET imaging to guide treatment options in Gliomas. *Curr. Treat Options Neurol.* 18 (1): 4.
196. Delbeke, D., Meyerowitz, C., Lapidus, R.L. et al. (1995). Optimal cutoff levels of F-18 fluorodeoxyglucose uptake in the differentiation of low-grade from high-grade brain tumors with PET. *Radiology* 195 (1): 47–52.
197. Di Chiro, G., DeLaPaz, R.L., Brooks, R.A. et al. (1982). Glucose utilization of cerebral gliomas measured by [18F] fluorodeoxyglucose and positron emission tomography. *Neurology* 32 (12): 1323–1329.
198. Gatidis, S., Bender, B., Reimold, M., and Schafer, J.F. (2017). PET/MRI in children. *Eur. J. Radiol.* 94: A64–A70.
199. Ericson, K., Lilja, A., Bergstrom, M. et al. (1985). Positron emission tomography with ([11C]methyl)-L-methionine, [11C]D-glucose, and [68Ga]EDTA in supratentorial tumors. *J. Comput. Assisted Tomogr.* 9 (4): 683–689.
200. Dunet, V., Pomoni, A., Hottinger, A. et al. (2016). Performance of 18F-FET versus 18F-FDG-PET for the diagnosis and grading of brain tumors: systematic review and meta-analysis. *Neuro. Oncol.* 18 (3): 426–434.

201. Kaplan, A.M., Bandy, D.J., Manwaring, K.H. et al. (1999). Functional brain mapping using positron emission tomography scanning in preoperative neurosurgical planning for pediatric brain tumors. *J. Neurosurg.* 91 (5): 797–803.
202. Kaschten, B., Stevenaert, A., Sadzot, B. et al. (1998). Preoperative evaluation of 54 gliomas by PET with fluorine-18-fluorodeoxyglucose and/or carbon-11-methionine. *J. Nucl. Med.* 39 (5): 778–785.
203. Utraiainen, M., Metsahonkala, L., Salmi, T.T. et al. (2002). Metabolic characterization of childhood brain tumors: comparison of 18F-fluorodeoxyglucose and 11C-methionine positron emission tomography. *Cancer* 95 (6): 1376–1386.
204. Gajjar, A., Bowers, D.C., Karajannis, M.A. et al. (2015). Pediatric Brain Tumors: Innovative Genomic Information Is Transforming the Diagnostic and Clinical Landscape. *J. Clin. Oncol.* 33 (27): 2986–2998.
205. Galldiks, N., Kracht, L.W., Berthold, F. et al. (2010). [11C]-L-methionine positron emission tomography in the management of children and young adults with brain tumors. *J. Neurooncol.* 96 (2): 231–239.
206. Voss, S.D.. (2018). Staging and following common pediatric malignancies: MRI versus CT versus functional imaging. *Pediatr. Radiol.* 48 (9): 1324–1336.
207. Herholz, K., Holzer, T., Bauer, B. et al. (1998). 11C-methionine PET for differential diagnosis of low-grade gliomas. *Neurology* 50 (5): 1316–1322.
208. Jager, P.L., Vaalburg, W., Pruijm, J. et al. (2001). Radiolabeled amino acids: basic aspects and clinical applications in oncology. *J. Nucl. Med.* 42 (3): 432–445.
209. Poetsch, N., Woehrer, A., Gesperger, J. et al. (2018). Visual and semiquantitative 11C-methionine PET: an independent prognostic factor for survival of newly diagnosed and treatment-naive gliomas. *Neuro. Oncol.* 20 (3): 411–419.
210. Laser, B.S., Merchant, T.E., Indelicato, D.J. et al. (2013). Evaluation of children with craniopharyngioma using carbon-11 methionine PET prior to proton therapy. *Neuro. Oncol.* 15 (4): 506–510.
211. Lucas, J.T. Jr., Serrano, N., Kim, H. et al. (2017). (11)C-Methionine positron emission tomography delineates non-contrast enhancing tumor regions at high risk for recurrence in pediatric high-grade glioma. *J. Neurooncol.* 132 (1): 163–170.
212. Tinkle, C.L., Duncan, E.C., Doubrovin, M. et al. (2019). Evaluation of (11)C-Methionine PET and Anatomic MRI Associations in Diffuse Intrinsic Pontine Glioma. *J. Nucl. Med.* 60 (3): 312–319.
213. Goldman, S., Levivier, M., Pirotte, B. et al. (1997). Regional methionine and glucose uptake in high-grade gliomas: a comparative study on PET-guided stereotactic biopsy. *J. Nucl. Med.* 38 (9): 1459–1462.
214. Levivier, M., Wikler, D. Jr., Massager, N. et al. (2002). The integration of metabolic imaging in stereotactic procedures including radiosurgery: a review. *J. Neurosurg.* 97 (5 Suppl): 542–550.
215. Massager, N., David, P., Goldman, S. et al. (2000). Combined magnetic resonance imaging- and positron emission tomography-guided stereotactic biopsy in brain-stem mass lesions: diagnostic yield in a series of 30 patients. *J. Neurosurg.* 93 (6): 951–957.

216. Pirotte, B., Acerbi, F., Lubansu, A. et al. (2007). PET imaging in the surgical management of pediatric brain tumors. *Childs Nerv. Syst.* 23 (7): 739–751.
217. Pirotte, B., Goldman, S., Dewitte, O. et al. (2006). Integrated positron emission tomography and magnetic resonance imaging-guided resection of brain tumors: a report of 103 consecutive procedures. *J. Neurosurg.* 104 (2): 238–253.
218. Pirotte, B., Goldman, S., Massager, N. et al. (2004). Combined use of 18F-fluorodeoxyglucose and 11C-methionine in 45 positron emission tomography-guided stereotactic brain biopsies. *J. Neurosurg.* 101 (3): 476–483.
219. Pirotte, B., Goldman, S., Salzberg, S. et al. (2003). Combined positron emission tomography and magnetic resonance imaging for the planning of stereotactic brain biopsies in children: experience in 9 cases. *Pediatr. Neurosurg.* 38 (3): 146–155.
220. Pirotte, B.J., Lubansu, A., Massager, N. et al. (2007). Results of positron emission tomography guidance and reassessment of the utility of and indications for stereotactic biopsy in children with infiltrative brainstem tumors. *J. Neurosurg.* 107 (5 Suppl): 392–399.
221. Snyder, S.E., Sherman, P.S., Davis, M.A. et al. (2004). Evaluation of [¹¹C]methionine and [¹⁸F]FDG in a rodent model of radiotherapy response. *J. Nucl. Med.* 45 (Suppl 1): 332P.
222. Stewart, E., Goshorn, R., Bradley, C. et al. (2014). Targeting the DNA repair pathway in Ewing sarcoma. *Cell Rep.* 9 (3): 829–841.
223. Harris, S.M., Davis, J.C., Snyder, S.E. et al. (2013). Evaluation of the biodistribution of 11C-methionine in children and young adults. *J. Nucl. Med.* 54 (11): 1902–1908.
224. Kaste, S.C., Snyder, S.E., Metzger, M.L. et al. (2017). Comparison of (11)C-Methionine and (18)F-FDG PET/CT for Staging and Follow-up of Pediatric Lymphoma. *J. Nucl. Med.* 58 (3): 419–424.
225. Stadlbauer, A., Prante, O., Nimsky, C. et al. (2008). Metabolic imaging of cerebral gliomas: spatial correlation of changes in O-(2-18F-fluoroethyl)-L-tyrosine PET and proton magnetic resonance spectroscopic imaging. *J. Nucl. Med.* 49 (5): 721–729.
226. Hamacher, K. and Coenen, H.H. (2002). Efficient routine production of the 18F-labelled amino acid O-2-18F fluoroethyl-L-tyrosine. *Appl. Radiat. Isot.* 57 (6): 853–856.
227. Heiss, P., Mayer, S., Herz, M. et al. (1999). Investigation of transport mechanism and uptake kinetics of O-(2-[18F]fluoroethyl)-L-tyrosine in vitro and in vivo. *J. Nucl. Med.* 40 (8): 1367–1373.
228. Pauleit, D., Floeth, F., Herzog, H. et al. (2003). Whole-body distribution and dosimetry of O-(2-[18F]fluoroethyl)-L-tyrosine. *Eur. J. Nucl. Med. Mol. Imaging* 30 (4): 519–524.
229. Tang, G., Wang, M., Tang, X. et al. (2003). Pharmacokinetics and radiation dosimetry estimation of O-(2-[18F]fluoroethyl)-L-tyrosine as oncologic PET tracer. *Appl. Radiat. Isot.* 58 (2): 219–225.
230. Weber, W.A., Wester, H.J., Grosu, A.L. et al. (2000). O-(2-[18F]fluoroethyl)-L-tyrosine and L-[methyl-11C]methionine uptake in brain tumours: initial results of a comparative study. *Eur. J. Nucl. Med.* 27 (5): 542–549.

231. Dunkl, V., Cleff, C., Stoffels, G. et al. (2015). The usefulness of dynamic O-(2-18F-fluoroethyl)-L-tyrosine PET in the clinical evaluation of brain tumors in children and adolescents. *J. Nucl. Med.* 56 (1): 88–92.
232. Floeth, F.W., Pauleit, D., Wittsack, H.J. et al. (2005). Multimodal metabolic imaging of cerebral gliomas: positron emission tomography with [18F]fluoroethyl-L-tyrosine and magnetic resonance spectroscopy. *J. Neurosurg.* 102 (2): 318–327.
233. Floeth, F.W., Sabel, M., Stoffels, G. et al. (2008). Prognostic value of 18F-fluoroethyl-L-tyrosine PET and MRI in small nonspecific incidental brain lesions. *J. Nucl. Med.* 49 (5): 730–737.
234. Garibotto, V., Heinzer, S., Vulliemoz, S. et al. (2013). Clinical applications of hybrid PET/MRI in neuroimaging. *Clin. Nucl. Med.* 38 (1): e13–e18.
235. Hutterer, M., Nowosielski, M., Putzer, D. et al. (2013). [18F]-fluoro-ethyl-L-tyrosine PET: a valuable diagnostic tool in neuro-oncology, but not all that glitters is glioma. *Neuro. Oncol.* 15 (3): 341–351.
236. Kasper, B.S., Struffert, T., Kasper, E.M. et al. (2011). 18Fluoroethyl-L-tyrosine-PET in long-term epilepsy associated glioneuronal tumors. *Epilepsia* 52 (1): 35–44.
237. Korchi, A.M., Garibotto, V., Ansari, M., and Merlini, L. (2013). Pseudoprogression after proton beam irradiation for a choroid plexus carcinoma in pediatric patient: MRI and PET imaging patterns. *Childs Nerv. Syst.* 29 (3): 509–512.
238. Marner, L., Henriksen, O.M., Lundemann, M. et al. (2017). Clinical PET/MRI in neurooncology: opportunities and challenges from a single-institution perspective. *Clin. Transl. Imaging* 5 (2): 135–149.
239. Messing-Junger, A.M., Floeth, F.W., Pauleit, D. et al. (2002). Multimodal target point assessment for stereotactic biopsy in children with diffuse bithalamic astrocytomas. *Childs Nerv. Syst.* 18 (8): 445–449.
240. Misch, M., Guggemos, A., Driever, P.H. et al. (2015). (18)F-FET-PET guided surgical biopsy and resection in children and adolescence with brain tumors. *Childs Nerv. Syst.* 31 (2): 261–267.
241. Pauleit, D., Floeth, F., Hamacher, K. et al. (2005). O-(2-[18F]fluoroethyl)-L-tyrosine PET combined with MRI improves the diagnostic assessment of cerebral gliomas. *Brain* 128 (Pt 3): 678–687.
242. Rapp, M., Heinzl, A., Galldiks, N. et al. (2013). Diagnostic performance of 18F-FET PET in newly diagnosed cerebral lesions suggestive of glioma. *J. Nucl. Med.* 54 (2): 229–235.
243. Suchorska, B., Giese, A., Biczok, A. et al. (2018). Identification of time-to-peak on dynamic 18F-FET-PET as a prognostic marker specifically in IDH1/2 mutant diffuse astrocytoma. *Neuro. Oncol.* 20 (2): 279–288.
244. Tscherpel, C., Dunkl, V., Ceccon, G. et al. (2017). The use of O-(2-18F-fluoroethyl)-L-tyrosine PET in the diagnosis of gliomas located in the brainstem and spinal cord. *Neuro. Oncol.* 19 (5): 710–718.
245. Vettermann, F.J., Felsberg, J., Reifenberger, G. et al. (2018). Characterization of Diffuse Gliomas With Histone H3-G34 Mutation by MRI and Dynamic 18F-FET PET. *Clin. Nucl. Med.* 43 (12): 895–898.

246. Weckesser, M., Langen, K.J., Rickert, C.H. et al. (2005). O-(2-[¹⁸F]fluoroethyl)-L-tyrosine PET in the clinical evaluation of primary brain tumours. *Eur. J. Nucl. Med. Mol. Imaging* 32 (4): 422–429.
247. Kaim, A.H., Weber, B., Kurrer, M.O. et al. (2002). (¹⁸F)-FDG and (¹⁸F)-FET uptake in experimental soft tissue infection. *Eur. J. Nucl. Med. Mol. Imaging* 29 (5): 648–654.
248. Rau, F.C., Weber, W.A., Wester, H.J. et al. (2002). O-(2-[¹⁸F]Fluoroethyl)- L-tyrosine (FET): a tracer for differentiation of tumour from inflammation in murine lymph nodes. *Eur. J. Nucl. Med. Mol. Imaging* 29 (8): 1039–1046.
249. Popperl, G., Kreth, F.W., Herms, J. et al. (2006). Analysis of ¹⁸F-FET PET for grading of recurrent gliomas: is evaluation of uptake kinetics superior to standard methods? *J. Nucl. Med.* 47 (3): 393–403.
250. Galldiks, N., Rapp, M., Stoffels, G. et al. (2013). Response assessment of bevacizumab in patients with recurrent malignant glioma using [¹⁸F]Fluoroethyl-L-tyrosine PET in comparison to MRI. *Eur. J. Nucl. Med. Mol. Imaging* 40 (1): 22–33.
251. Koopman, T., Verburg, N., Schuit, R.C. et al. (2018). Quantification of O-(2-[¹⁸F] fluoroethyl)-L-tyrosine kinetics in glioma. *EJNMMI Res.* 8 (1): 72.
252. Kunz, M., Albert, N.L., Unterrainer, M. et al. (2019). Dynamic ¹⁸F-FET PET is a powerful imaging biomarker in gadolinium-negative gliomas. *Neuro. Oncol.* 21 (2): 274–284.
253. Moulin-Romsee, G., D'Hondt, E., de Groot, T. et al. (2007). Non-invasive grading of brain tumours using dynamic amino acid PET imaging: does it work for ¹¹C-methionine? *Eur. J. Nucl. Med. Mol. Imaging* 34 (12): 2082–2087.
254. Firnau, G., Chirakal, R., Sood, S., and Garnett, S. (1980). Aromatic fluorination with xenon difluoride: L-3,4-dihydroxy-6-fluoro-phenylalanine. *Can. J. Chem.* 58: 1449–1450.
255. Garnett, E.S., Firnau, G., and Nahmias, C. (1983). Dopamine visualized in the basal ganglia of living man. *Nature* 305 (5930): 137–138.
256. Seibyl, J.P., Chen, W., and Silverman, D.H. (2007). 3,4-dihydroxy-6-[¹⁸F]-fluoro-L-phenylalanine positron emission tomography in patients with central motor disorders and in evaluation of brain and other tumors. *Semin. Nucl. Med.* 37 (6): 440–450.
257. Fliedner, S.M., Lehnert, H., and Pacak, K. (2010). Metastatic paraganglioma. *Semin. Oncol.* 37 (6): 627–637.
258. Levine, D.S., Metzger, D.L., Nadel, H.R. et al. (2011). Novel use of F-DOPA PET/CT imaging in a child with paraganglioma/pheochromocytoma syndrome. *Pediatr. Radiol.* 41 (10): 1321–1325.
259. Piccardo, A., Lopci, E., Conte, M. et al. (2012). Comparison of ¹⁸F-dopa PET/CT and ¹²³I-MIBG scintigraphy in stage 3 and 4 neuroblastoma: a pilot study. *Eur. J. Nucl. Med. Mol. Imaging* 39 (1): 57–71.
260. Piccardo, A., Lopci, E., Foppiani, L. et al. (2014). (¹⁸F)-DOPA PET/CT for assessment of response to induction chemotherapy in a child with high-risk neuroblastoma. *Pediatr. Radiol.* 44 (3): 355–361.
261. Qin, L., Hu, B., Neumann, K.D. et al. (2015). A mild and general one-pot synthesis of densely functionalized diaryliodonium salts. *Eur. J. Org. Chem.* 2015 (27): 5919–5924.

262. Mossine, A.V., Tanzey, S.S., Brooks, A.F. et al. (2019). One-pot synthesis of high molar activity 6-[(18F)fluoro-L-DOPA by Cu-mediated fluorination of a BPIn precursor. *Org. Biomol. Chem.* 17 (38): 8701–8705.
263. Ernst, M., Zametkin, A.J., Matochik, J.A. et al. (1997). Low medial prefrontal dopaminergic activity in autistic children. *Lancet* 350 (9078): 638.
264. Ernst, M., Zametkin, A.J., Matochik, J.A. et al. (1999). High midbrain [18F]DOPA accumulation in children with attention deficit hyperactivity disorder. *Am. J. Psychiatry* 156 (8): 1209–1215.
265. Fernell, E., Watanabe, Y., Adolfsson, I. et al. (1997). Possible effects of tetrahydrobiopterin treatment in six children with autism—clinical and positron emission tomography data: a pilot study. *Dev. Med. Child Neurol.* 39 (5): 313–318.
266. Minami, T., Otsuka, M., Ichiya, Y. et al. (1994). Different patterns of [18F]dopa uptake in siblings with hereditary dentato-rubro-pallido-luysian atrophy. *Brain Dev.* 16 (4): 335–338.
267. Ernst, M., Zametkin, A.J., Jons, P.H. et al. (1999). High presynaptic dopaminergic activity in children with Tourette's disorder. *J. Am. Acad. Child Adolesc. Psychiatry* 38 (1): 86–94.
268. Chutorian, A.M., Bojko, A., Heier, L. et al. (2003). Toxic pediatric parkinsonism: report of a child with metabolic studies and response to treatment. *J. Child Neurol.* 18 (11): 812–815.
269. Dunn, H.G. (2001). Neurons and neuronal systems involved in the pathophysiologies of Rett syndrome. *Brain Dev.* 23 (Suppl 1): S99–S100.
270. Kawano, H., Takeuchi, Y., Misawa, A. et al. (2000). Putaminal necrosis presenting with hemidystonia. *Pediatr. Neurol.* 22 (3): 222–224.
271. Hwu, W.L., Muramatsu, S., Tseng, S.H. et al. (2012). Gene therapy for aromatic L-amino acid decarboxylase deficiency. *Sci. Transl. Med.* 4 (134): 134ra61.
272. Hardy, O.T., Hernandez-Pampaloni, M., Saffer, J.R. et al. (2007). Diagnosis and localization of focal congenital hyperinsulinism by 18F-fluorodopa PET scan. *J. Pediatr.* 150 (2): 140–145.
273. Hernandez-Pampaloni, M., Zhuang, H., Fanti, S., and Alavi, A. (2007). Positron emission tomography imaging and hyperinsulinism. *PET Clin.* 2 (3): 377–383.
274. Shah, P., Rahman, S.A., Demirbilek, H. et al. (2017). Hyperinsulinaemic hypoglycaemia in children and adults. *Lancet Diabetes Endocrinol.* 5 (9): 729–742.
275. Stanley, C.A. (1997). Hyperinsulinism in infants and children. *Pediatr. Clin. North Am.* 44 (2): 363–374.
276. Otonkoski, T., Veijola, R., Huopio, H. et al. (2003). Diagnosis of focal persistent hyperinsulinism of infancy with ¹⁸F-fluoro-L-DOPA PET. *Horm. Res.* 60: 2.
277. Barthlen, W., Blankenstein, O., Mau, H. et al. (2008). Evaluation of [18F]fluoro-L-DOPA positron emission tomography-computed tomography for surgery in focal congenital hyperinsulinism. *J. Clin. Endocrinol. Metab.* 93 (3): 869–875.
278. Otonkoski, T., Nanto-Salonen, K., Seppanen, M. et al. (2006). Noninvasive diagnosis of focal hyperinsulinism of infancy with [18F]-DOPA positron emission tomography. *Diabetes* 55 (1): 13–18.

279. Albert, N.L., Weller, M., Suchorska, B. et al. (2016). Response assessment in neuro-oncology working group and European association for neuro-oncology recommendations for the clinical use of PET imaging in gliomas. *Neuro. Oncol.* 18 (9): 1199–1208.
280. Becherer, A., Karanikas, G., Szabo, M. et al. (2003). Brain tumour imaging with PET: a comparison between [18F]fluorodopa and [11C]methionine. *Eur. J. Nucl. Med. Mol. Imaging* 30 (11): 1561–1567.
281. Chondrogiannis, S., Marzola, M.C., Al-Nahhas, A. et al. (2013). Normal biodistribution pattern and physiologic variants of 18F-DOPA PET imaging. *Nucl. Med. Commun.* 34 (12): 1141–1149.
282. Gauvain, K., Ponisio, M.R., Barone, A. et al. (2018). (18)F-FDOPA PET/MRI for monitoring early response to bevacizumab in children with recurrent brain tumors. *Neurooncol. Pract.* 5 (1): 28–36.
283. Karunanithi, S., Sharma, P., Kumar, A. et al. (2014). Can (18)F-FDOPA PET/CT predict survival in patients with suspected recurrent glioma? A prospective study. *Eur. J. Radiol.* 83 (1): 219–225.
284. Tripathi, M., Sharma, R., D'Souza, M. et al. (2009). Comparative evaluation of F-18 FDOPA, F-18 FDG, and F-18 FLT-PET/CT for metabolic imaging of low grade gliomas. *Clin. Nucl. Med.* 34 (12): 878–883.
285. Morana, G., Bottoni, G., Mancardi, M.M. et al. (2018). Seizure-induced increased 18F-DOPA uptake in a child with diffuse astrocytoma and transient brain mri abnormalities related to status epilepticus. *Clin. Nucl. Med.* 43 (5): e149–e150.
286. Morana, G., Piccardo, A., Milanaccio, C. et al. (2014). Value of 18F-3,4-dihydroxyphenylalanine PET/MR image fusion in pediatric supratentorial infiltrative astrocytomas: a prospective pilot study. *J. Nucl. Med.* 55 (5): 718–723.
287. Morana, G., Piccardo, A., Puntoni, M. et al. (2015). Diagnostic and prognostic value of 18F-DOPA PET and 1H-MR spectroscopy in pediatric supratentorial infiltrative gliomas: a comparative study. *Neuro. Oncol.* 17 (12): 1637–1647.
288. Morana, G., Piccardo, A., Tortora, D. et al. (2017). Grading and outcome prediction of pediatric diffuse astrocytic tumors with diffusion and arterial spin labeling perfusion MRI in comparison with 18F-DOPA PET. *Eur. J. Nucl. Med. Mol. Imaging* 44 (12): 2084–2093.
289. Morana, G., Puntoni, M., Garre, M.L. et al. (2016). Ability of (18)F-DOPA PET/CT and fused (18)F-DOPA PET/MRI to assess striatal involvement in paediatric glioma. *Eur. J. Nucl. Med. Mol. Imaging* 43 (9): 1664–1672.
290. Piccardo, A., Tortora, D., Mascelli, S. et al. (2019). Advanced MR imaging and (18) F-DOPA PET characteristics of H3K27M-mutant and wild-type pediatric diffuse midline gliomas. *Eur. J. Nucl. Med. Mol. Imaging* 46 (8): 1685–1694.
291. Morana, G., Piccardo, A., Garre, M.L. et al. (2016). 18F-DOPA uptake of developmental venous anomalies in children with brain tumors. *Clin. Nucl. Med.* 41 (7): e351–e352.
292. Castinetti, F., Kroiss, A., Kumar, R. et al. (2015). 15 YEARS OF PARAGANGLIOMA: Imaging and imaging-based treatment of pheochromocytoma and paraganglioma. *Endocr. Relat. Cancer* 22 (4): T135–T145.

293. Chondrogiannis, S., Grassetto, G., Marzola, M.C. et al. (2012). 18F-DOPA PET/CT biodistribution consideration in 107 consecutive patients with neuroendocrine tumours. *Nucl. Med. Commun.* 33 (2): 179–184.
294. Darr, R., Nambuba, J., Del Rivero, J. et al. (2016). Novel insights into the polycythemia-paraganglioma-somatostatinoma syndrome. *Endocr. Relat. Cancer* 23 (12): 899–908.
295. Janssen, I., Chen, C.C., Zhuang, Z. et al. (2017). Functional imaging signature of patients presenting with polycythemia/paraganglioma syndromes. *J. Nucl. Med.* 58 (8): 1236–1242.
296. Wilson, L.M. and Draper, G.J. (1974). Neuroblastoma, its natural history and prognosis: a study of 487 cases. *Br. Med. J.* 3 (5926): 301–307.
297. Young, J.L. Jr., Ries, L.G., Silverberg, E. et al. (1986). Cancer incidence, survival, and mortality for children younger than age 15 years. *Cancer* 58 (2 Suppl): 598–602.
298. Shulkin, B.L. and Shapiro, B. (1998). Current concepts on the diagnostic use of MIBG in children. *J. Nucl. Med.* 39 (4): 679–688.
299. Wieland, D.M., Wu, J., Brown, L.E. et al. (1980). Radiolabeled adrenergi neuron-blocking agents: adrenomedullary imaging with [131I]iodobenzylguanidine. *J. Nucl. Med.* 21 (4): 349–353.
300. Kline, R.C., Swanson, D.P., Wieland, D.M. et al. (1981). Myocardial imaging in man with I-123 meta-iodobenzylguanidine. *J. Nucl. Med.* 22 (2): 129–132.
301. Wieland, D.M., Brown, L.E., Rogers, W.L. et al. (1981). Myocardial imaging with a radioiodinated norepinephrine storage analog. *J. Nucl. Med.* 22 (1): 22–31.
302. Taieb, D., Jha, A., Treglia, G., and Pacak, K. (2019). Molecular imaging and radionuclide therapy of paraganglioma and pheochromocytoma. *Endocr. Relat. Cancer.*
303. Sisson, J.C., Frager, M.S., Valk, T.W. et al. (1981). Scintigraphic localization of pheochromocytoma. *N. Engl. J. Med.* 305 (1): 12–17.
304. Treuner, J., Feine, U., Niethammer, D. et al. (1984). Scintigraphic imaging of neuroblastoma with [131-I]iodobenzylguanidine. *Lancet* 323 (8372): 333–334.
305. Nakajo, M., Shapiro, B., Copp, J. et al. (1983). The normal and abnormal distribution of the adrenomedullary imaging agent m-[I-131]iodobenzylguanidine (I-131 MIBG) in man: evaluation by scintigraphy. *J. Nucl. Med.* 24 (8): 672–682.
306. Parisi, M.T., Sandler, E.D., and Hattner, R.S. (1992). The biodistribution of metaiodobenzylguanidine. *Semin. Nucl. Med.* 22 (1): 46–48.
307. Vik, T.A., Pfluger, T., Kadota, R. et al. (2009). (123)I-MIBG scintigraphy in patients with known or suspected neuroblastoma: Results from a prospective multicenter trial. *Pediatr. Blood Cancer* 52 (7): 784–790.
308. Bar-Sever, Z., Biassoni, L., Shulkin, B. et al. (2018). Guidelines on nuclear medicine imaging in neuroblastoma. *Eur. J. Nucl. Med. Mol. Imaging* 45 (11): 2009–2024.
309. Jacobson, A.F. and Travin, M.I. (2015). Impact of medications on MIBG uptake, with specific attention to the heart: Comprehensive review of the literature. *J. Nucl. Cardiol.* 22 (5): 980–993.
310. Braghirolli, A.M., Waissmann, W., da Silva, J.B., and dos Santos, G.R. (2014). Production of iodine-124 and its applications in nuclear medicine. *Appl. Radiat. Isot.* 90: 138–148.

311. Green, M., Lowe, J., Kadirvel, M. et al. (2017). Radiosynthesis of no-carrier-added meta-[(124)I]iodobenzylguanidine for PET imaging of metastatic neuroblastoma. *J. Radioanal. Nucl. Chem.* 311 (1): 727–732.
312. Cistaro, A., Quartuccio, N., Caobelli, F. et al. (2015). 124I-MIBG: a new promising positron-emitting radiopharmaceutical for the evaluation of neuroblastoma. *Nucl. Med. Rev. Cent. East Eur.* 18 (2): 102–106.
313. Pandit-Taskar, N., Zanzonico, P., Staton, K.D. et al. (2018). Biodistribution and Dosimetry of (18)F-Meta-Fluorobenzylguanidine: A First-in-Human PET/CT Imaging Study of Patients with Neuroendocrine Malignancies. *J. Nucl. Med.* 59 (1): 147–153.
314. Jager, P.L., Chirakal, R., Marriott, C.J. et al. (2008). 6-L-18F-fluorodihydroxyphenylalanine PET in neuroendocrine tumors: basic aspects and emerging clinical applications. *J. Nucl. Med.* 49 (4): 573–586.
315. Brodeur, G.M. and Saylor, R.L. 3rd. (1991). Neuroblastoma, retinoblastoma, and brain tumors in children. *Curr. Opin. Oncol.* 3 (3): 485–496.
316. Jacobson, A.F., Deng, H., Lombard, J. et al. (2010). 123I-meta-iodobenzylguanidine scintigraphy for the detection of neuroblastoma and pheochromocytoma: results of a meta-analysis. *J. Clin. Endocrinol. Metab.* 95 (6): 2596–2606.
317. Kauhanen, S., Seppanen, M., Ovaska, J. et al. (2009). The clinical value of [18F] fluoro-dihydroxyphenylalanine positron emission tomography in primary diagnosis, staging, and restaging of neuroendocrine tumors. *Endocr. Relat. Cancer* 16 (1): 255–265.
318. LaBrosse, E.H., Comoy, E., Bohuon, C. et al. (1976). Catecholamine metabolism in neuroblastoma. *J. Natl. Cancer Inst.* 57 (3): 633–638.
319. Timmers, H.J., Chen, C.C., Carrasquillo, J.A. et al. (2009). Comparison of 18F-fluoro-L-DOPA, 18F-fluoro-deoxyglucose, and 18F-fluorodopamine PET and 123I-MIBG scintigraphy in the localization of pheochromocytoma and paraganglioma. *J. Clin. Endocrinol. Metab.* 94 (12): 4757–4767.
320. Piccardo, A., Morana, G., Massollo, M. et al. (2015). Brain Metastasis from Neuroblastoma Depicted by (18)F-DOPA PET/CT. *Nucl. Med. Mol. Imaging* 49 (3): 241–242.
321. Piccardo, A., Lopci, E., Conte, M. et al. (2013). PET/CT imaging in neuroblastoma. *Q. J. Nucl. Med. Mol. Imaging* 57 (1): 29–39.
322. Piccardo, A., Lopci, E., Conte, M. et al. (2014). Bone and lymph node metastases from neuroblastoma detected by 18F-DOPA-PET/CT and confirmed by post-therapy 131I-MIBG but negative on diagnostic 123I-MIBG scan. *Clin. Nucl. Med.* 39 (1): e80–e83.
323. Piccardo, A., Puntoni, M., Lopci, E. et al. (2014). Prognostic value of (1)(8)F-DOPA PET/CT at the time of recurrence in patients affected by neuroblastoma. *Eur. J. Nucl. Med. Mol. Imaging* 41 (6): 1046–1056.
324. Lopci, E., Piccardo, A., Nanni, C. et al. (2012). 18F-DOPA PET/CT in neuroblastoma: comparison of conventional imaging with CT/MR. *Clin. Nucl. Med.* 37 (4): e73–e78.
325. Lu, M.Y., Liu, Y.L., Chang, H.H. et al. (2013). Characterization of neuroblastic tumors using 18F-FDOPA PET. *J. Nucl. Med.* 54 (1): 42–49.

326. O'Dorisio, M.S., Hauger, M., and Cecalupo, A.J. (1994). Somatostatin receptors in neuroblastoma: diagnostic and therapeutic implications. *Semin. Oncol.* 21 (5 Suppl 13): 33–37.
327. O'Dorisio, M.S., Chen, F., O'Dorisio, T.M. et al. (1994). Characterization of somatostatin receptors on human neuroblastoma tumors. *Cell Growth Differ.* 5 (1): 1–8.
328. Albers, A.R., O'Dorisio, M.S., Balster, D.A. et al. (2000). Somatostatin receptor gene expression in neuroblastoma. *Regul. Pept.* 88 (1–3): 61–73.
329. Moertel, C.L., Reubi, J.C., Scheithauer, B.S. et al. (1994). Expression of somatostatin receptors in childhood neuroblastoma. *Am. J. Clin. Pathol.* 102 (6): 752–756.
330. Georgantzi, K., Tsolakis, A.V., Stridsberg, M. et al. (2011). Differentiated expression of somatostatin receptor subtypes in experimental models and clinical neuroblastoma. *Pediatr. Blood Cancer* 56 (4): 584–589.
331. Kropp, J., Hofmann, M., and Bihl, H. (1997). Comparison of MIBG and pentetretotide scintigraphy in children with neuroblastoma. Is the expression of somatostatin receptors a prognostic factor? *Anticancer Res.* 17 (3B): 1583–1588.
332. Schilling, F.H., Bihl, H., Jacobsson, H. et al. (2000). Combined (111)In-pentetretotide scintigraphy and (123)I-MIBG scintigraphy in neuroblastoma provides prognostic information. *Med. Pediatr. Oncol.* 35 (6): 688–691.
333. Kong, G., Hofman, M.S., Murray, W.K. et al. (2016). Initial experience with Gallium-68 DOTA-Octreotate PET/CT and peptide receptor radionuclide therapy for pediatric patients with refractory metastatic neuroblastoma. *J. Pediatr. Hematol. Oncol.* 38 (2): 87–96.
334. Abongwa, C., Mott, S., Schafer, B. et al. (2017). Safety and accuracy of (68)Ga-DOT-ATOC PET/CT in children and young adults with solid tumors. *Am. J. Nucl. Med. Mol. Imaging* 7 (5): 228–235.
335. Gains, J.E., Bomanji, J.B., Fersht, N.L. et al. (2011). 177Lu-DOTATATE molecular radiotherapy for childhood neuroblastoma. *J. Nucl. Med.* 52 (7): 1041–1047.
336. Hofman, M.S., Lau, W.F., and Hicks, R.J. (2015). Somatostatin receptor imaging with 68Ga DOTATATE PET/CT: clinical utility, normal patterns, pearls, and pitfalls in interpretation. *Radiographics* 35 (2): 500–516.
337. Walker, R.C., Smith, G.T., Liu, E. et al. (2013). Measured human dosimetry of 68Ga-DOTATATE. *J. Nucl. Med.* 54 (6): 855–860.
338. Sandstrom, M., Velikyan, I., Garske-Roman, U. et al. (2013). Comparative biodistribution and radiation dosimetry of 68Ga-DOTATOC and 68Ga-DOTATATE in patients with neuroendocrine tumors. *J. Nucl. Med.* 54 (10): 1755–1759.
339. Hartmann, H., Freudenberg, R., Oehme, L. et al. (2014). Dosimetric measurements of (68)Ga-high affinity DOTATATE: twins in spirit - part III. *Nuklearmedizin* 53 (5): 211–216.
340. Virgolini, I., Ambrosini, V., Bomanji, J.B. et al. (2010). Procedure guidelines for PET/CT tumour imaging with 68Ga-DOTA-conjugated peptides: 68Ga-DOTA-TOC, 68Ga-DOTA-NOC, 68Ga-DOTA-TATE. *Eur. J. Nucl. Med. Mol. Imaging* 37 (10): 2004–2010.

341. Cheung, N.K., Saarinen, U.M., Neely, J.E. et al. (1985). Monoclonal antibodies to a glycolipid antigen on human neuroblastoma cells. *Cancer Res.* 45 (6): 2642–2649.
342. Schulz, G., Cheresch, D.A., Varki, N.M. et al. (1984). Detection of ganglioside GD2 in tumor tissues and sera of neuroblastoma patients. *Cancer Res.* 44 (12 Pt 1): 5914–5920.
343. Svennerholm, L., Bostrom, K., Fredman, P. et al. (1994). Gangliosides and allied glycosphingolipids in human peripheral nerve and spinal cord. *Biochim. Biophys. Acta* 1214 (2): 115–123.
344. Yu, A.L., Gilman, A.L., Ozkaynak, M.F. et al. (2010). Anti-GD2 antibody with GM-CSF, interleukin-2, and isotretinoin for neuroblastoma. *N. Engl. J. Med.* 363 (14): 1324–1334.
345. Modak, S. and Cheung, N.K. (2007). Disialoganglioside directed immunotherapy of neuroblastoma. *Cancer Invest.* 25 (1): 67–77.
346. Ahmed, M. and Cheung, N.K. (2014). Engineering anti-GD2 monoclonal antibodies for cancer immunotherapy. *FEBS Lett.* 588 (2): 288–297.
347. Shibuya, H., Hamamura, K., Hotta, H. et al. (2012). Enhancement of malignant properties of human osteosarcoma cells with disialyl gangliosides GD2/GD3. *Cancer Sci.* 103 (9): 1656–1664.
348. Roth, M., Linkowski, M., Tarim, J. et al. (2014). Ganglioside GD2 as a therapeutic target for antibody-mediated therapy in patients with osteosarcoma. *Cancer* 120 (4): 548–554.
349. Dobrenkov, K. and Cheung, N.K. (2014). GD2-targeted immunotherapy and radioimmunotherapy. *Semin. Oncol.* 41 (5): 589–612.
350. Cheung, N.K., Guo, H., Hu, J. et al. (2012). Humanizing murine IgG3 anti-GD2 antibody m3F8 substantially improves antibody-dependent cell-mediated cytotoxicity while retaining targeting in vivo. *Oncimmunology* 1 (4): 477–486.
351. Mujoo, K., Cheresch, D.A., Yang, H.M., and Reisfeld, R.A. (1987). Disialoganglioside GD2 on human neuroblastoma cells: target antigen for monoclonal antibody-mediated cytotoxicity and suppression of tumor growth. *Cancer Res.* 47 (4): 1098–1104.
352. Mujoo, K., Kipps, T.J., Yang, H.M. et al. (1989). Functional properties and effect on growth suppression of human neuroblastoma tumors by isotype switch variants of monoclonal antiganglioside GD2 antibody 14.18. *Cancer Res.* 49 (11): 2857–2861.
353. Handgretinger, R., Baader, P., Dopfer, R. et al. (1992). A phase I study of neuroblastoma with the anti-ganglioside GD2 antibody 14.G2a. *Cancer Immunol. Immunother.* 35 (3): 199–204.
354. Saleh, M.N., Khazaeli, M.B., Wheeler, R.H. et al. (1992). Phase I trial of the murine monoclonal anti-GD2 antibody 14G2a in metastatic melanoma. *Cancer Res.* 52 (16): 4342–4347.
355. Murray, J.L., Cunningham, J.E., Brewer, H. et al. (1994). Phase I trial of murine monoclonal antibody 14G2a administered by prolonged intravenous infusion in patients with neuroectodermal tumors. *J. Clin. Oncol.* 12 (1): 184–193.
356. Gillies, S.D., Lo, K.M., and Wesolowski, J. (1989). High-level expression of chimeric antibodies using adapted cDNA variable region cassettes. *J. Immunol. Methods* 125 (1–2): 191–202.

357. Saleh, M.N., Khazaeli, M.B., Wheeler, R.H. et al. (1992). Phase I trial of the chimeric anti-GD2 monoclonal antibody ch14.18 in patients with malignant melanoma. *Hum. Antibodies Hybridomas* 3 (1): 19–24.
358. Yu, A.L., Uttenreuther-Fischer, M.M., Huang, C.S. et al. (1998). Phase I trial of a human-mouse chimeric anti-disialoganglioside monoclonal antibody ch14.18 in patients with refractory neuroblastoma and osteosarcoma. *J. Clin. Oncol.* 16 (6): 2169–2180.
359. Federico, S.M., McCarville, M.B., Shulkin, B.L. et al. (2017). A pilot trial of humanized anti-GD2 monoclonal antibody (Hu14.18K322A) with chemotherapy and natural killer cells in children with recurrent/refractory neuroblastoma. *Clin. Cancer Res.* 23 (21): 6441–6449.
360. Navid, F., Sondel, P.M., Barfield, R. et al. (2014). Phase I trial of a novel anti-GD2 monoclonal antibody, Hu14.18K322A, designed to decrease toxicity in children with refractory or recurrent neuroblastoma. *J. Clin. Oncol.* 32 (14): 1445–1452.
361. Talleur, A.C., Triplett, B.M., Federico, S. et al. (2017). Consolidation therapy for newly diagnosed pediatric patients with high-risk neuroblastoma using busulfan/melphalan, autologous hematopoietic cell transplantation, anti-GD2 antibody, granulocyte-macrophage colony-stimulating factor, interleukin-2, and haploidentical natural killer cells. *Biol. Blood Marrow Transplant* 23 (11): 1910–1917.
362. Navid, F., Armstrong, M., and Barfield, R.C. (2009). Immune therapies for neuroblastoma. *Cancer Biol. Ther.* 8 (10): 874–882.
363. Navid, F., Santana, V.M., and Barfield, R.C. (2010). Anti-GD2 antibody therapy for GD2-expressing tumors. *Curr. Cancer Drug. Targets* 10 (2): 200–209.
364. Sorkin, L.S., Otto, M., Baldwin, W.M. 3rd et al. (2010). Anti-GD(2) with an FC point mutation reduces complement fixation and decreases antibody-induced allodynia. *Pain* 149 (1): 135–142.
365. Miraldi, F.D., Nelson, A.D., Kraly, C. et al. (1986). Diagnostic imaging of human neuroblastoma with radiolabeled antibody. *Radiology* 161 (2): 413–418.
366. Yeh, S.D., Larson, S.M., Burch, L. et al. (1991). Radioimmunodetection of neuroblastoma with iodine-131-3F8: correlation with biopsy, iodine-131-metaiodobenzylguanidine and standard diagnostic modalities. *J. Nucl. Med.* 32 (5): 769–776.
367. Cheung, N.K., Kushner, B.H., Cheung, I.Y. et al. (1998). Anti-G(D2) antibody treatment of minimal residual stage 4 neuroblastoma diagnosed at more than 1 year of age. *J. Clin. Oncol.* 16 (9): 3053–3060.
368. Reuland, P., Geiger, L., Thelen, M.H. et al. (2001). Follow-up in neuroblastoma: comparison of metaiodobenzylguanidine and a chimeric anti-GD2 antibody for detection of tumor relapse and therapy response. *J. Pediatr. Hematol. Oncol.* 23 (7): 437–442.
369. Reuland, P., Handgretinger, R., Smykowsky, H. et al. (1991). Application of the murine anti-Gd-2 antibody 14.Gd-2a for diagnosis and therapy of neuroblastoma. *Int. J. Rad. Appl. Instrum. B.* 18 (1): 121–125.
370. Kramer, K., Humm, J.L., Souweidane, M.M. et al. (2007). Phase I study of targeted radioimmunotherapy for leptomeningeal cancers using intra-ommaya 131-I-3F8. *J. Clin. Oncol.* 25 (34): 5465–5470.

371. Kramer, K., Kushner, B.H., Modak, S. et al. (2010). Compartmental intrathecal radioimmunotherapy: results for treatment for metastatic CNS neuroblastoma. *J. Neurooncol.* 97 (3): 409–418.
372. Kramer, K., Pandit-Taskar, N., Zanzonico, P. et al. (2015). Low incidence of radionecrosis in children treated with conventional radiation therapy and intrathecal radioimmunotherapy. *J. Neurooncol.* 123 (2): 245–249.
373. Larson, S.M., Pentlow, K.S, Volkow, N.D et al. (1992). PET scanning of iodine-124-3F9 as an approach to tumor dosimetry during treatment planning for radioimmunotherapy in a child with neuroblastoma. *J. Nucl. Med.* 33 (11): 2020–2023.
374. Butch, E.R., Mead, P.E., Amador Diaz, V. et al. (2019). Positron emission tomography detects in vivo expression of disialoganglioside GD2 in mouse models of primary and metastatic osteosarcoma. *Cancer Res.* 79 (12): 3112–3124.
375. Vavere, A.L., Butch, E.R., Dearling, J.L. et al. (2012). ⁶⁴Cu-p-NH₂-Bn-DOTA-hu14.18K322A, a PET radiotracer targeting neuroblastoma and melanoma. *J. Nucl. Med.* 53 (11): 1772–1778.
376. Dearling, J.L., Paterson, B.M., Akurathi, V. et al. (2015). The ionic charge of copper-64 complexes conjugated to an engineered antibody affects biodistribution. *Bioconjugate Chem.* 26 (4): 707–717.
377. Grant, F., Sexton-Stallone, B., Falone, A. et al. (2019). [¹⁸F]FLT PET predicts cellular proliferation in pediatric brain tumors. *J. Nucl. Med.* 60 (Suppl. 1): 156.
378. Costantini, D.L., Vali, R., McQuattie, S. et al. (2016). A pilot study of 18F-FLT PET/CT in pediatric lymphoma. *Int. J. Mol. Imaging.* 2016: 6045894.

Chapter 22

PET Imaging in Drug Discovery and Development

David J. Donnelly, Ph.D

*Discovery Chemical Platforms-PET Radiochemical Synthesis,
Bristol Myers Squibb Pharmaceutical Research and Development,
Princeton, NJ, 08543, USA*

22.1 INTRODUCTION

The hunt for substances that can cure human maladies is as old as we are. Serendipitously, our ancestors searched and cataloged the natural world to find plants and extracts that could help ease their ailments. As they encountered these substances within natural products, they reported how these materials affected human health accordingly. Centuries later, the discovery and development of pharmaceuticals has had a major impact on the field of medicine and increased both the health and lifespan of the human race. Drug discovery as we know it today has its roots in the mid to late 1800s [1]. During the latter half of the nineteenth century, a boom in synthetic dyes was occurring in Europe for the emerging textile industry. Synthetic clothing dyes were synthesized and developed as replacements for perishable sources. As these dyes were significantly cheaper to produce and not perishable, hundreds of dye variants were made to produce a vast array of colors for this industry. This evolution of synthetic dye chemistry for textiles had a profound influence on the start of the field of medicinal chemistry: a young medical student named Paul Ehrlich, while searching for a thesis topic, began to use these myriad dyes to stain biological samples to enhance the field of microscopy [2]. This early work using dyes in cultures of parasites with various microorganisms and cancer cells led Ehrlich to postulate that different chemical molecules interact with different chemoreceptors and

Handbook of Radiopharmaceuticals: Methodology and Applications, Second Edition.

Edited by Michael R. Kilbourn and Peter J.H. Scott.

© 2021 John Wiley & Sons Ltd. Published 2021 by John Wiley & Sons Ltd.

that these synthetic compounds could be designed as chemical treatments for human maladies. From this work, the field of chemotherapy arose around the use of specific chemicals to heal the diseased body. The beginning of modern medicinal chemistry and the concept of the magic bullet were spawned.

Advances in analytical chemistry led to the purification of drugs from natural sources, making drugs such as morphine and papaverine available in pharmacies. The field of pharmacology was also founded during this time period to study how these compounds interact within the body; as such, a new “drug” industry was created, within pharmacies and as a branch of chemical dye companies. In 1910, arsphenamine became the first synthetic “chemotherapeutic” drug for the treatment of syphilis [3]. In the 1930s, penicillin and subsequent synthetic and semi-synthetic antibiotics were developed [4]. In the 1960s began the quantitative structure-activity relationships theory of drug discovery, followed by monoclonal antibody (**mAb**) technology in the 1970s. Human insulin was approved for use in the 1980s and combinatorial chemistry in the 1990s. High-throughput screening and molecular modeling gave the industry new tools to discover drugs, and the early 2000s gave rise to the genomics and proteomics eras.

As the field and industry have matured, advances in biology, biochemistry, pharmacology, molecular modeling, genomics, proteomics, combinatorial chemistry, and high-throughput screening methods have propelled the discovery of novel medicines into the current area. We can examine the work of synthetic antibiotics and vaccines that have eradicated deadly diseases such as smallpox and polio as major medical advancements, as well as the search for compounds to treat leukemia (once considered a disease that could not be cured) and the groundbreaking drug research in the field of antivirals, which has changed the course of human immunodeficiency virus/acquired immunodeficiency syndrome (**HIV/AIDS**) from a death sentence to a chronic illness. Fast forward to research within the field of immuno-oncology that has changed the treatment of many forms of cancer over the past few years [5]. The successes in the pharmaceutical industry are vast and incredible. To put this into context, we can examine how life expectancy and major causes of death in 1900 compare to those same numbers in 2018. The leading causes of death in 1900 were pneumonia/flu, tuberculosis, and gastrointestinal infections; as late as 1940, the chances of dying from one of these causes was 1 in 11 [6]. Through the discovery of modern medicines, the leading causes of death are now heart disease, cancer, and stroke—it’s no wonder life expectancy has risen in America from 50 to 77 years of age in the early 2000s. Of course, many factors have led to this drastic increase in life expectancy. However, one cannot deny that a major contributor to this increase in human lifespan and health has been the discovery and development of new drugs to cure human maladies.

As a consequence of this success, drug targets are now more focused on chronic conditions within heart disease, cancer, metabolic diseases, and neuroscience targets, as they have assumed more dominant roles in causes of human death. These conditions are far more challenging to treat, as the discovery of novel targets is challenging. The mechanisms often associated with potential treatments for these targets carry with them a higher risk, as clinical validation is lacking. As such, the process of discovering and developing new drugs remains a risky and costly endeavor. The cost of developing a drug

to market approval is now estimated to be ~US\$3 billion, with development timelines between 5 and 10 years [7]. With these costs steadily increasing, a recent trend within the field of drug discovery and development (**DDD**) has been to focus on translational techniques that can provide decisional information to reduce both the cycle times and costs associated with this process. The goal of this chapter is to describe the tremendous challenges and costs of discovering and developing a new pharmaceutical and how we can de-risk this process through translational and personal medicine approaches. Our focus is on how positron emission tomography (**PET**) and novel PET radioligands are used to gain better understanding of a drug and its target, and how this technology can be used to gain important insight into human biology quantitatively in real time at the receptor level. The use of PET across the DDD process can help guide smarter decisions earlier in the process to ensure that the proper drug candidate is developed, for the right target, with limited side effects, for the right patient population, to thus have maximal impact on human health and lifespan.

22.2 THE DRUG DISCOVERY AND DEVELOPMENT PROCESS

A more efficient and refined drug discovery process is evolving within the industry. The evolving drug discovery process has been captured in two case studies that have recently been published. These reports highlight the impact of the decline in pharmaceutical industry productivity and recommend a new approach to address these issues. First, in a retrospective analysis of 44 programs in phase II clinical trials, the team identified “lack of efficacy” as the most common cause of attrition in their discovery programs [8]. To improve drug discovery effectiveness, the authors suggested a model of “three pillars” for evaluating potential investment in non-validated drug targets: (i) sufficient exposure of ligands at the site of action, (ii) proof of target engagement, and (iii) expression of functional pharmacological activity. The authors’ conclusion was that projects that are able to demonstrate all “three pillars of survival” should have the highest probability of translating to human clinical studies.

In a second interesting case study, AstraZeneca recently published an exhaustive review of its small-molecule pipeline from 2005 to 2010 [9]. The authors define a revised drug discovery strategy with a focus on early decision-making based on a five-dimensional framework. These five determinants or “5Rs,” as they are called, include right target, right safety, right tissue, right patient, and right commercial potential. The sixth determinant was the right culture that rewards truth-seeking behaviors. In particular, the “right tissue” is defined as the appropriate exposure of the drug candidate in the target organ, leading to sufficient pharmacological activity. To assess the “right tissue,” it is necessary to evaluate pharmacokinetic (**PK**) properties and target engagement to develop an understanding of the PKs/pharmacodynamic (**PD**) correlations relative to the target organ. In a follow-up case study, Morgan and coworkers reported an increased success rate from 2012 to 2016 after implementing this framework into their research

and development (**R&D**) model. After implantation of the 5R model, they reported an increase in the success rate for compounds entering phase III clinical trial completions of only 4% from 2005 to 2010 to 19% in 2012–2016 [10]. Within the industry, these case studies have changed the way drugs are being discovered and have focused on the need for translational biomarkers throughout the DDD process.

PET imaging is a tool within molecular imaging that uses a radiolabeled molecule, generally referred to as a *PET tracer*, *PET ligand*, or *PET radioligand*, that has been synthesized to include a PET radionuclide. This ligand is delivered to living animals (from mice to human), and the emitted positron collides with a local electron, which results in the production of a pair of photons that travel 180° to each other. These photons are detected in a PET scanner and generate real-time quantitative data about a molecule (usually in the picomolar range) localized within a tissue of interest; this occurs non-invasively within a living animal. PET data can be used in combination with anatomical imaging techniques like magnetic resonance imaging or computed tomography to give both functional and anatomical readouts.

PET is a translational biomarker that is used in preclinical rodent studies to human clinical studies and has been used throughout the drug discovery process [11]. But obviously, PET imaging is not the only technique to provide critical decisional information within drug discovery. A good biomarker strategy is one that can use numerous biomarkers together to answer the questions presented by the 5R framework. To illustrate this, Figure 22.1 shows how a PET probe can be incorporated into this 5R framework. In this diagram, the modified 5R criteria are represented on the

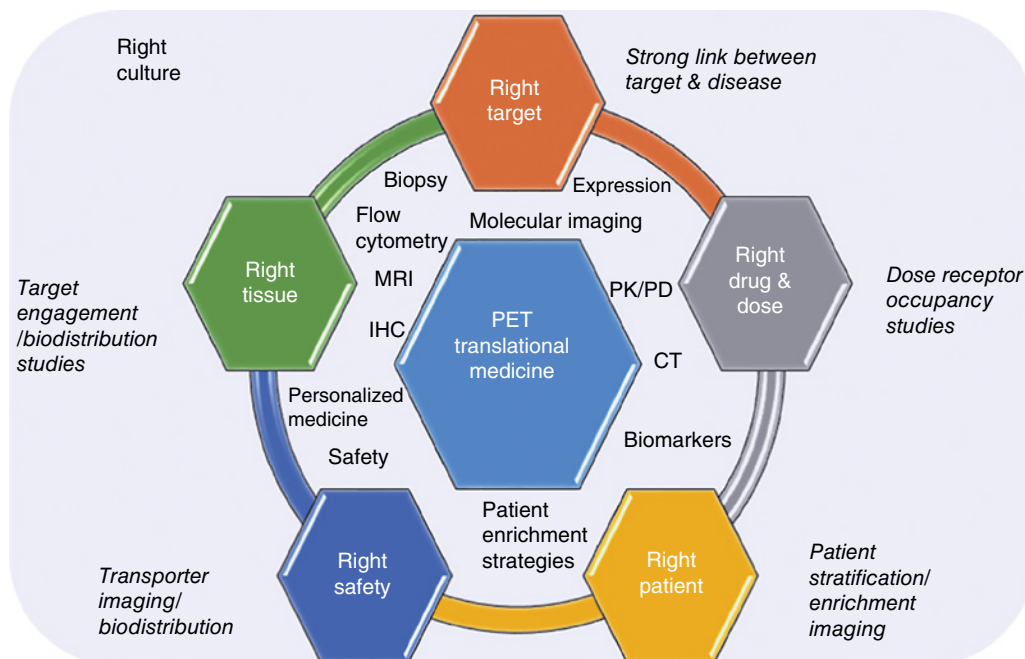
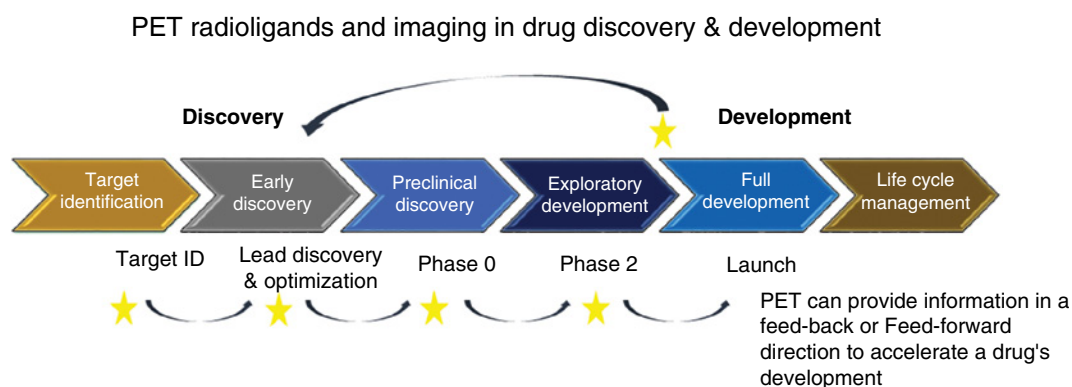


Figure 22.1 The PET 5R framework.

outer portion of the circle. In the inner portion are examples of tools that modern translational medicine departments use to interrogate this framework. At the center of this discussion are PET/PET ligands and the types of studies and information provided to DDD teams using this technology. Finally, the entire framework is encompassed by having the right culture to follow the science and present well-vetted drug candidates into clinical medicine.

The evaluation of modern DDD has been described in several recent publications [12–15]. The drug discovery process continues to evolve from a series of linear decision gates to a model that embraces the flow of information in both a feedforward and feedback manner across all stages of the DDD process. Translational medicine departments have been established within the industry with the daunting task of understanding a drug’s targeting within animal models and forward-translating this to humans to guide decision-making for a novel therapy. Biomarkers are essential for a translational medicine approach to work; these biomarkers focus on understanding the disease state in question, proper patient enrichment strategies, pharmacokinetic and pharmacodynamic responses, target validation, and safety margins. Given the translational nature of PET, the technology fits nicely into this paradigm because the same radioligand and imaging technique are used from mouse to humans.

Molecular imaging using a PET ligand can accelerate cycle times in drug discovery. Early phase I clinical trials can be designed to link protocols that integrate safety and tolerability studies with target engagement studies using PET imaging. This provides an early link between the right safety and right target at peak levels of plasma exposure for a potential drug. These studies provide decisional information for go/no-go decisions in a feedforward manner early within drug development by providing guidance for dose selection in later clinical trials. As shown in Figure 22.2, PET can be integrated in early clinical development, providing information in both a feedback and a feedforward manner. The information obtained from using a PET radioligand within lead optimization



Molecular imaging using PET radioligands provides quantitative, translational information used to accelerate the drug discovery and development process using a personalized medicine approach

Figure 22.2 PET ligands use in drug discovery and development.

provides an import feedback loop to the early discovery portion of the process. PET imaging can feedback information to drug discovery programs focusing on contingency back-up clinical candidates to deliver a higher-quality drug candidate for these programs, as well.

There is growing interest within the field in developing more personalized medicine approaches to the DDD process [16, 17]. PET and novel ligands have been developed to help enrich patient pools to ensure that potential drug candidates are selecting the right patients. One of the biggest challenges of using PET within drug discovery is shifting from qualitative use of PET tracers such as FDG, which are clinically used to detect disease, to a more quantitative approach that provides decisional and quantifiable measurements of the drug/target interaction within a clinical trial setting. New mathematical estimation approaches using quantitative modeling algorithms and analysis techniques have allowed the determination of tissue-level drug/receptor occupancy measurements to be obtained [18]. Using these methods, drug hunters receive real-time information about a potential drug and its target all along the DDD timeline. Over the remaining portion of the chapter, I will provide literature examples of how PET imaging studies are performed in both the preclinical and clinical settings and how the data obtained from these types of studies guide a drug's discovery.

22.3 DESIGN CRITERIA OF A NOVEL PET RADIOLIGAND

PET is a nascent field: the first clinical images with ^{18}F -fluorodeoxyglucose (FDG) were generated in the late 1970s [19]. PET imaging's true potential is now being realized with numerous novel ligands developed for preclinical and clinical imaging applications within the fields of neuroscience, oncology, immuno-oncology, and cardiovascular and fibrotic diseases [20–24]. The goal for developing these translational tools is to impact a drug's discovery by delivering novel radioligands to the clinic with a focus on speed to patient in a cost-effective manner. If we can accomplish this as a field, we will unlock the true potential of this technique.

Real-time microdosing biodistribution and target engagement studies will have the largest impact on a drug's development only if the cost and time to accomplish these studies remain reasonable. If these studies become too expensive or take too long to return data to enable critical decisions for a program, this field will struggle to make a long-term impact on the industry. Advances in molecular imaging, particularly PET imaging, play an increasingly important role in translational medicine to test new molecular entities, their mechanisms of action, and the therapeutic hypotheses of these potential new drugs.

The success of using this technique to answer these critical DDD questions relies on the design and synthesis of novel PET radioligands. Development of a novel PET radioligand requires a disciplined approach, and one of the most important considerations when designing a novel PET radioligand is timelines. Developing a novel PET ligand for

a new target is as challenging as developing a novel drug for a target. Discovery efforts should be planned in a parallel manner to ensure the ligand can be used at the proper time clinically. If the ligand is developed too late, the impact on early go-no/go decisions will be lost, and these efforts will be wasted along with the investment in the discovery effort for the program. This is why it is important to build a multidisciplinary team that includes talented drug hunters, skilled radiochemists with a strong background in medicinal chemistry, biologists, and imaging specialists early in a drug discovery program. Early engagement of this team is key to developing a successful ligand. This biomarker will be useful only if it provides the right answer at the right time within a drug's development.

PET radioligands are versatile and are designed to track a drug's biodistribution, non-invasively visualize a drug target, or monitor a biochemical or physiological process. Novel PET radioligands are rarely used across multiple drug targets, and the cost of developing a ligand must be accounted for in the context of a specific drug discovery program. The intended use of the ligand dictates the design and success criteria for the ligand. Certainly, when discussing the characteristics of a successful novel PET radioligand, the intended target for application plays a major role. For example, a small-molecule ligand intended to determine target engagement within a neuroscience application will have different success criteria than a ligand designed for imaging within the tumor microenvironment. In the neuroscience example, a molecule that has rapid distribution to the brain and reaches equilibrium rapidly at the target level is certainly important, whereas in tumor imaging, brain exposure is not necessarily a positive attribute of a ligand, and a longer target off rate may provide better signal to noise within the tumor microenvironment. Therefore, we will look to define these characteristics for the majority of ligands and suggest that they can be modified in a fit-for-purpose manner for the target and application of use.

Design criteria for potential PET radioligand candidates start with determining the proper molecular platform for the ligand and its intended use. Modern drug pipelines consist of a multitude of drug modalities. These modalities include a myriad of drug platforms such as small molecules, antisense oligonucleotides, peptides, and monoclonal antibodies, to name a few. All of these drug platforms have pros and cons as potential frameworks for a PET radioligand and must be carefully chosen to ensure that the ligand can provide quantitative results for the program. Typically, discovery teams screen the relevant compounds within a discovery program for molecular matter that can incorporate a PET radionuclide. It is also important to note during this screening process that what makes a successful drug may not make an ideal PET radioligand candidate. For example, small-molecule drug candidates are designed with properties that can allow longer circulating biological half-lives, lower clearances and oral bioavailability, and so on. These are properties that a PET ligand would not necessarily need to provide a quantitated answer around target engagement, since most PET ligands are delivered via IV injection and have short circulating blood half-lives. Once the molecular framework is chosen for the ligand, the proper PET radionuclide can be selected for its intended use.

As a PET radiochemist within the field of drug discovery, it is important to remain platform and radionuclide agnostic. This requires the modern radiochemist to have a diverse skill set in radiochemistry to accommodate the synthesis of any PET radionuclide to support a drug's discovery. When designing a novel PET ligand, one must choose the proper radionuclide to match the biological half-life of the drug. This is important for several reasons. The first is to reduce the radiation burden to a patient, while introducing the radionuclide into the molecule without loss of selectivity or affinity. As an example, it wouldn't be beneficial to label a small-molecule drug candidate with Zr-89, as the incorporation would likely change the affinity of the molecule toward its target, and the half-life of over 78 hours would lead to an unnecessary radiation burden to patients. Conversely, it would be equally unproductive to label a mAb with carbon-11. Table 22.1 lists the common radionuclides used in PET ligand design for DDD.

Once the molecular framework and radionuclide are chosen, the design of the ligand focuses on the medicinal chemistry aspects of both the potential ligand and its target. Two specific parameters regarding the biological target are particularly important in ligand design: the maximum concentration of target binding sites (B_{\max}) and the equilibrium dissociation constant (K_d), which is a measure of the affinity of the ligand toward the target. There have been several reports of the ideal target concentration/ligand receptor affinity ratio, commonly referred to as the *binding potential* (**BP**) for the ligand, being between 5 and 10 for a successful PET ligand [18, 19, 25, 26]. High affinity for the target (typically in the pM to nM range) is seen in successful ligands, as typical drug targets may have lower expression levels, and thus a higher affinity is required for a ligand to show specific binding. If an exploratory drug target has a B_{\max} value that is less than 1 nM, it is nearly impossible to identify a PET ligand lead with enough affinity to drive the binding potential to a point where a quantifiable PET signal can be obtained. An early estimation of B_{\max} within a target tissue of interest gives the drug discovery/ligand discovery teams important information around the likelihood of success that a PET ligand can be developed for the target. This data is often not available for early drug discovery programs, and studies to determine this value are amongst the first to be completed when discovering novel PET ligands [27]. This data can be used for target validation in both animal and human tissues coupled with immunohistochemistry (IHC) stains [28].

Table 22.1 List of common radionuclides used in PET radioligands for drug discovery and development.

Radionuclide	Half-life (h)	Max energy (MeV)	% Decay by positron emission	Maximum theoretical specific activity (Ci μmol^{-1})
^{11}C	0.34	0.87	99%	9250
^{68}Ga	1.1	1.90	89%	2700
^{18}F	1.8	0.64	97%	1700
^{64}Cu	12.7	0.65	19%	246
^{89}Zr	78.4	0.40	22.5%	40
^{124}I	100.8	2.14	25%	0.4

The binding potential of the ligand gives a glimpse into the maximum potential signal-to-noise ratio for a ligand and its target. Most importantly, it provides data to suggest whether there will be enough target signal within the tissue to quantitate with a potential ligand. Maximizing signal to noise is a key success factor for any PET radioligand, independent of its intended application. A useful ligand must provide imaging results that are “amenable to quantification” because analog/visual images are likely to be of limited utility. The signal-to-noise ratio should be at least 1.5 in the tissue of interest to be able to accurately quantitate data for a PET radioligand.

Several physicochemical properties of PET ligand candidates should also be taken into consideration. These properties include the calculated partition coefficient (ClogP), calculated distribution coefficient at pH 7.4 (ClogD), molecular weight, polar surface area, hydrogen bond donors, and the acid dissociation constant (pKa) of the molecule all can play an important role in ligand design. These properties can be fine-tuned in a fit-for-purpose manner. The ideal properties for a ligand are compound, platform, and intended use dependent. Computational methods to assess physicochemical properties to help accelerate the discovery of novel small-molecule PET ligands have recently been reported for central nervous system (CNS) ligands [29]. In this study, Zhang and coworkers described a multiparameter optimization design tool. This tool incorporated six physicochemical properties commonly used by medicinal chemistry teams in compound design to guide ligand design. Using this tool led to the discovery of several novel CNS ligands, specifically a phosphodiesterase 2A ligand. The team suggested that by this using this tool, ligand discovery was successfully accomplished with reduced resources and shortened timelines. Additionally, parameters such as permeability, volume of distribution, routes, and rates of clearance also play important roles in designing a PET radioligand. Another key component to ligand design is target selectivity. Typically, our teams look for ligand candidates with at least 30- to 100-fold higher affinities to desired targets, which also helps to increase the signal-to-noise ratio in target tissues.

Ligand candidates must be metabolically stable over the course of the PET imaging study. The positron emission generates the signal within a PET scan, and thus the data generated from a PET scan is a factor of the radionuclide distribution alone. Ensuring that the ligand is intact throughout the PET scan and binds to the target tissue of interest is important for quantification. The presence of radiolabeled metabolites can limit occupancy studies [30]. When a ligand is designed to measure a signal within the CNS, it is common to place the radionuclide within the portion of molecule that generates hydrophilic radiometabolites, since these types of metabolites do not typically cross the blood-brain barrier. A nice example of this is a workaround generating a ligand for the serotonin 1A (5-HT_{1A}) receptor. The original ligand design placed the C-11 label in the *O*-methyl position and gave an excellent signal to noise within the rodent brain for the target [31]. However, when this ligand was translated to human, the primary route of metabolism gave a C-11 labeled metabolite that entered the brain. This reduced the ligand’s signal to noise within the region of interest, and thus this ligand missed its primary objective. With this data, the team was able to redesign the PET synthesis to incorporate the C-11 label in a different position on the molecule, resulting in a radiometabolite

profile that did not show brain uptake and thus increased the signal to noise for this ligand, enabling quantification of this target [32]. For ligands designed for periphery tumor targets, the absence of the blood-brain barrier that keeps radiometabolites from entering the tissue of interest represents a high hurdle to overcome in ligand design. An example of this principle is represented in a recent study with an ^{18}F -labeled version of dasatinib. In this study, Veach et al. showed how an ^{18}F -dasatinib analog could visualize K562 tumors in a mouse model [33]. However, they reported high levels of radiolabeled metabolites throughout the PET study, leading to a significant amount of non-specific uptake in non-tumor tissues and thus poor signal to noise within the tumor microenvironment. Another example of understanding the metabolic profile of a lead ligand candidate is a recent study conducted in our lab using an ^{18}F -labeled adnectin for program death ligand 1 (**PD-L1**) positive tumors [34]. Our team chose the adnectin platform as our targeting vector for this PET ligand because it does not generate any radiometabolites in vivo. This ligand also was cleared as an intact entity through the kidneys and, as such, offers the best visualization of tumors with lung tissues. By focusing on the metabolic profile of the ligand and its in vivo clearance parameters, our team discovered a successful same-day imaging agent to determine human PD-L1 expression in lung tumors [22].

Next, we focus on the synthesis of the ligand. Given the short half-lives of most PET radionuclides, a successful ligand candidate must be amenable for labeling. Generating PET radioligands with high specific activity can be some of the most synthetically challenging chemistry to complete effectively and repeatedly. PET synthesis requires a unique synthesis for each time point within a study. The synthesis starts from raw materials and continues through synthesis, purification, and formulation of the final injectable. This process is typically completed within a one- to three-hour timeframe for most ligands. PET radiochemical synthesis is completed under microscale conditions, where the limiting reagent is the radionuclide. Reaction yields rarely go to completion, and there is a constant balance between the speed of synthesis, chemical purity, radiochemical purity, isolated yields, radiochemical yields, and specific activity of the ligand. Careful ligand design requires a multidisciplinary approach, one in which the medicinal and radiochemists retrosynthetically plan radionuclide incorporation into the labeled portion of the molecule at the latest possible synthetic step. Careful planning of ligand and appropriate precursor synthesis can accelerate novel ligand discovery and shorten timelines for these teams. New advances in the field of PET radiochemistry, particularly within the field of ^{18}F -fluorination chemistry, have increased access to a broader range of chemical matter as potential PET radioligand candidates [35–40]. Advances in late-stage ^{18}F -labeling techniques, such as electron-deficient and neutral aryl rings using metal-mediated fluorination of boronic acids, boronic esters, stannyl, and iodonium precursors, now give our teams access to molecules once thought not viable for radiolabeling.

By considering all of the factors summarized in Figure 22.3, discovery teams can begin the challenge of generating novel PET radioligands. This is an iterative discovery process with many opportunities for innovation along the way. Once ligand candidates have been identified, synthesized, and validated, the hard work of utilizing them in the DDD process begins.

Key design considerations for a novel PET radioligand

- Define target of interest and the ideal characteristics of ligand for this target.
- Choose the molecular platform that best fits these characteristics.
- Match biological half-life to half-life of PET radionuclide.
- Synthetically feasible for radionuclide incorporation.
- High affinity for the target (Typically in the nM-pM range).
- High target: off target ratios.
 - Rapid localization in target tissues.
 - Rapid clearance from non-target tissues.
 - K_d/B_{max} ratio >5–10.
 - 30–100 fold selective to ensure low non-specific/off target binding.
- Chemically and metabolic stable.
- Tunable parameters for a fit for purpose ligand such as:
 - log P, log D, pKa, polar surface.
 - volume of distribution, clearance rates, and routes.

Figure 22.3 Key design considerations for novel PET radioligands.

22.4 PET IMAGING AND PET RADIOLIGANDS IN DRUG DISCOVERY AND DEVELOPMENT

Generally, there are four main approaches to using PET radioligands in the DDD process. The first is using a radiolabeled drug candidate to evaluate the distribution and PK of the drug candidate. The second is to use a known radioligand from the literature for a specific target. The radioligand database initiative that is sponsored by the National Institute of Mental Health and the Society for Non-invasive Imaging in Drug Development and the Molecular Imaging and Contrast Agent Database (<https://www.ncbi.nlm.nih.gov/books/NBK5330>) are excellent resources to search for specific PET radioligands for a given drug target. The third approach is to use a PET radioligand as an imaging biomarker of a known biochemical, metabolic, or physiologic process (such as ^{18}F -fluorodeoxyglucose [FDG]) to evaluate the efficacy of a candidate drug. The final approach is to design, synthesize, and discover a novel ligand for an exploratory molecular target of interest. In this case, the PET radioligand is no longer a drug candidate and is a derivative of either of the main drug or a derivative of a molecule that is known to bind to the target of interest. Ligands discovered through de novo methods are usually the most resource-intensive but can provide the most impactful data sets to the discovery teams.

FDG is a biomimetic radioligand for glucose: it is taken up by the cell and partially metabolized with the cell, and its radiometabolite remains trapped within the cell. This powerful radioligand non-invasively tracks glucose metabolism in a wide variety of tissues and disease states. FDG-PET has become a standard imaging procedure for the staging of many types of cancer. FDG is used within drug development as a tool to assess

metabolic response to therapy and is the most widely used PET tracer within the industry. It is routinely used as an early response marker to novel therapeutics. There are many examples in the literature of using FDG within drug development, and excellent reviews have already covered this topic extensively [41–43]. As such, it is not within the scope of this chapter to cover all of these examples. Instead, a couple of recent examples highlight the general use of ^{18}F -FDG within drug development.

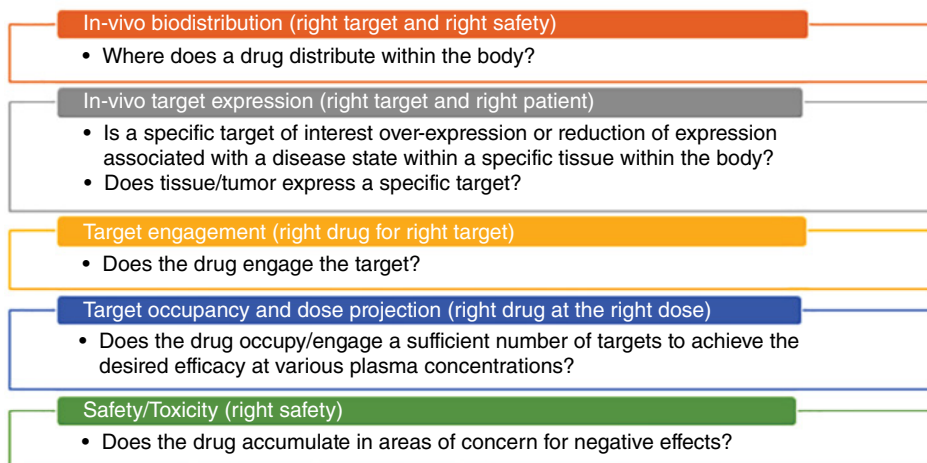
FDG was used to predict the outcome of metastatic melanoma patients treated with imatinib by measuring the metabolic response of FDG and associating the mutational status of the tumor [44]. This team evaluated both baseline and four-week follow-up PET scans in a small patient subset and found a positive correlation using FDG in patients who had a partial response to imatinib [44]. This study highlights the potential of FDG to predict responses to a drug treatment using this imaging technique. FDG was also determined to be an effective tool to evaluate early response of gastrointestinal stromal tumors (**GISTs**) to imatinib treatment [45]. In this study, 70 FDG PET scans were obtained for 63 patients to evaluate for an early response to neoadjuvant imatinib treatment. The authors noted that “utilizing FDG PET for early evaluation of response often results in a change of management in GIST patients harboring the non-*KIT* exon 11 mutation and should be considered the standard of care in GIST patients treated with neoadjuvant intent” [45]. Both of these studies are nice examples of how FDG is used within the context of a drug’s development to gain a better understanding of early responses to therapeutic interventions using novel therapies. FDG is an important tool, as decreases in tracer accumulation within tumors (from either decreased glucose metabolism or cell loss) represent a non-invasive way to assess whether a potential drug may show promise in affecting the tumor and tumor microenvironment.

Figure 22.4 highlights the common uses of PET imaging and novel PET ligands to guide drug discovery. The bio-distribution of drug candidates labeled with a PET radionuclide allows for the investigation of the drug’s PK parameters. These studies are used to ensure

Figure 22.4

Common uses of PET imaging in drug discovery and development.

PET imaging in drug discovery and development



that the right drug target and right drug safety profile from the 5R analysis are being fulfilled in both the preclinical and clinical imaging settings.

In these studies, information obtained often overlaps, allowing researchers to gain important target engagement and biodistribution data simultaneously. Establishing that a drug candidate can localize within a tissue of known target expression with confidence is a critical point for a potential drug at this phase of development. A dynamic PET biodistribution study using a PET labeled drug candidate can provide concentration-time course information in the tissue of interest as well as uptake in non-target expressing tissues. Additionally, tissues of known toxicity can be examined for accumulation of the radiolabeled drug candidate as a measure of safety. This information can be decisional, as only the most promising candidates that localize in tissues of known expression are carried forward, to reduce lengthy and costly clinical phases. Also, in these clinical phases, PET radioligands can be used as imaging biomarkers that can, often quantitatively, assess the clinical efficacy of the drugs being tested and thus provide important tools for the assessment of clinical endpoints.

There are many examples of biodistribution studies, as PET radioligands enable human microdosing studies to generate a non-invasive image of a molecule's biodistribution while delivering only picomoles of the drug molecule to the patient. As PET ligands generally have high effective specific activities ($>1 \text{ mCi nmol}^{-1}$), they are always dosed under microdosing criteria. This makes using PET imaging an ideal choice within phase 0 clinical microdosing studies during drug development. *Microdosing* is defined as the use of less than 1/100th of the dose calculated to yield a pharmacological effect of a test substance, up to a maximum dose of less than 100 μg or 30 nmol for biologic drugs [46]. Valuable information regarding the PK, bioavailability, biodistribution, and targeting properties of new drugs is obtained from microdosing studies. Figure 22.5 shows the chemical structures of recently reported ^{11}C and ^{18}F labeled drug candidates that have been used in both preclinical and clinical PET studies to study biodistribution [47].

These six examples demonstrate how PET radiolabeled drug candidates can be used within drug development as biomarkers for biodistribution, ensuring the right target and right safety of the drug. The first example is ^{11}C -zofenoprilat, which was used in a human microdosing study: this study confirmed that the C-11 labeled drug accumulates in human tissues that express high levels of angiotensin-converting enzymes such as lungs, kidneys, and (to a minor extent) the heart, where it can afford organ protection as a drug [47]. Another example of a microdosing/biodistribution study was with ^{11}C -docetaxel [48]. In this study, ^{11}C -docetaxel at microdosing levels was quantified in lung tumors, and uptake in the tumor was variable across 34 patient tumors. The authors suggest that this variable uptake in lung tumors may predict sensitivity to docetaxel therapy. ^{11}C -erlotinib has been extensively studied in lung cancer tumors as well [49, 50]. In these studies, the carbon-11 epidermal growth factor receptor (**EGFR**) tyrosine kinase inhibitor was dosed in lung cancer patients, and biodistribution studies were conducted to determine the amount of ^{11}C -erlotinib within the tumor. In these studies, the team confirmed that the right target was achieved and was able to show significantly higher uptake in lung cancer tumors with activating mutations

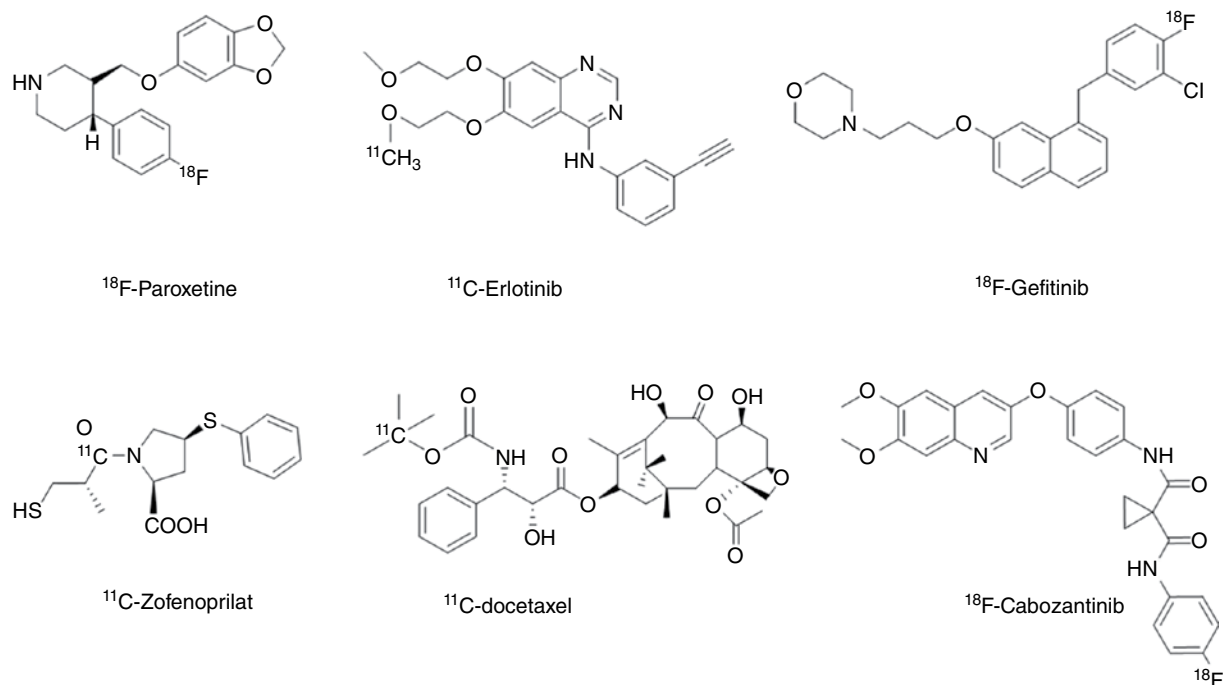


Figure 22.5 ^{18}F and ^{11}C labeled drug candidates for biodistribution studies.

(exon 19 deletions). This study showed that the PET signal within the EGFR-expressing tumors correlated with IHC stains of the tumor and showed little accumulation of the ligand in tissues for safety concerns. ^{18}F -Cabozantinib has recently been described and was used to understand the biodistribution of the drug in various preclinical tumor models to confirm ligand distribution to tumors [51, 52]. These examples provide critical information to the team that the drug candidates have the right target and right safety profiles.

^{18}F -Gefitinib was studied in preclinical biodistribution studies in several EGFR-specific tumor xenografts. These studies showed little to no uptake of ^{18}F -gefitinib within tumors, highlighting the importance of early tumor biodistribution studies for drug programs [53]. Within neuroscience, the selective serotonin reuptake inhibitor (**SSRI**) medication ^{18}F -paroxetine was studied in a series of preclinical non-human primate studies to look at brain penetrance [40]. This group showed that the radiolabeled drug crossed into the brain but had significant amounts of non-specific binding. If we use these two reports as hypothetical scenarios, the information from them highlights the importance of understanding a potential drug candidate's biodistribution. If these studies were conducted before a drug candidate was filed, the information from these biodistribution studies could be used as a feedback biomarker to the drug discovery team to have better selectivity criteria or better tumor penetration. Using PET would have provided information to support no-go decisions for these potential assets.

In vivo target engagement and receptor occupancy studies using PET imaging ensure that we have selected the right drug candidate at the right dose. Determining target engagement is the most common use of molecular imaging within the pharmaceutical industry. Early in the DDD process, PET ligands can be used to confirm a new potential drug target within cells and tissues to confirm a target expression within a human disease condition [54]. This target confirmation information can be used in the DDD process to provide important confidence in a target’s expression within a disease condition. Techniques such as in vitro, ex vivo, and quantitative whole-body autoradiography can be used to detect the presence of a target within cells, tissues, and animal models [55–57]. This information is also used to validate the PET ligand for future translational imaging studies. These techniques are by no means a replacement for high-throughput assays in this phase of the drug discovery process and typically deliver data much more slowly than traditional assays. Target engagement and receptor occupancy studies can be conducted in preclinical animals to select potential doses, and a PET ligand can help medicinal chemistry teams by prioritizing lead chemical series (chemotypes). These studies provide important decisional information regarding which of these series to progress along the process. A generic example of this type of study is shown in Figure 22.6.

In this hypothetical example, a success criterion for the drug candidate indicates that a potential drug for this target would need to obtain >90% receptor occupancy to obtain efficacy. In these studies, the same non-human primate is serially imaged first at baseline and again after administration of increasing concentrations of a lead compound of series A, B, or C. From the quantitative PET data set, the medicinal chemist would receive

Hypothetical example: Using a PET radioligand to compare occupancy of several lead chemotypes in vivo using same tracer and same animal for go/no-go decisions

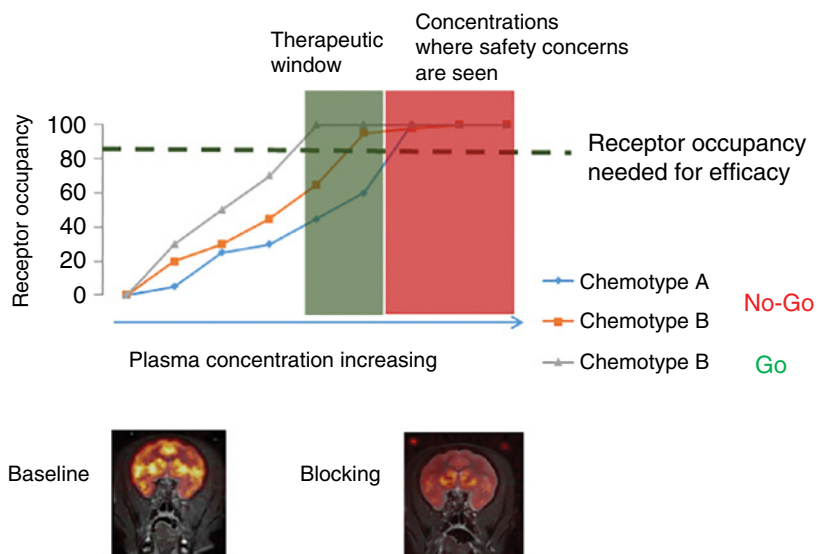


Figure 22.6 A hypothetical example of using a PET radioligand to measure preclinical target engagement to drive go/no-go decisions within the DDD process.

important information regarding which of these series to advance. In this example, chemotype C would differentiate itself against the other series of compounds. The quantitative PET imaging studies would provide the team with critical target engagement data and a clear go decision to progress this asset to clinical development. Compounds from chemotype A would be discontinued, as they reach only 90% occupancy at plasma concentrations that cause safety concerns, and chemotype B also would not be advanced as its therapeutic window would be too narrow for development. This example provides a glimpse into the type of target engagement studies that are routinely performed during preclinical drug discovery programs. An example of a similar approach used for a non-CNS target is ^{11}C -BMT-136088 [58]. ^{11}C -BMT-136088 is a novel PET radioligand for the lysophosphatidic acid type 1 (**LPA1**) receptor [58]. This lung-imaging PET ligand was used to measure the target engagement of a lead drug candidate (BMS-986020) within the lung of a non-human primate. This ligand was advanced to human studies to measure dose-dependent receptor occupancy of this drug within the lung.

Probably the best example of using a PET radioligand to guide drug development from the literature is ^{18}F -SPA-RQ. ^{18}F -SPA-RQ is a small-molecule PET radioligand that binds to the neurokinin-1 (**NK-1**) receptor [20]. In a series of studies, the ligand was used in human imaging studies to determine NK1 receptor levels in the healthy volunteer cohort, and the receptor occupancy of the drug candidate aprepitant was measured at multiple plasma concentrations. The researchers established the dose/receptor occupancy relationship of aprepitant and the NK1 receptor occupancy using this ligand. A clear concentration versus receptor occupancy relationship was observed using this PET radioligand that confirmed aprepitant's in vivo target engagement. The researchers used this data to show that high levels of NK1 receptor occupancy (>90%) were required to achieve optimal anti-emetic effects for the drug candidate [59]. These studies were also used to pick the lowest dose that demonstrated occupancy to optimize the therapeutic window of aprepitant [60]. In a separate study, ^{18}F -SPA-RQ was used to guide dose selection of aprepitant in an antidepressant trial. This study elegantly showed that NK-1R antagonists needed to block central NK-1 receptors continuously, which ultimately led to a no-go decision for that indication for this drug [61]. These studies represent the value of using a PET ligand in drug development. Over the course of several human PET studies, the team was able to discover the right drug for the right target in the right patient population. A critical no-go decision was also reached for this drug program using the PET ligand, preventing further clinical studies for the flawed indication and saving valuable resources for the team.

Why is target engagement so important? In drug trials, particularly during neuroscience drug discovery, drug candidates are typically run in clinical trials using a placebo arm to avoid the so-called *placebo effect*. The placebo effect is a phenomenon in which a group within a trial receives an inactive substance but receives benefit from this inactive substance. In a recent review, a series of studies were summarized in which dopamine, serotonin, opioid, or endocannabinoid pathways were studied in conjunction with the placebo effect [62]. Over several of these studies, researchers found single-nucleotide polymorphisms that can modify outcomes in placebo arms of drug trials. Data from these

studies show consistent levels of individuals who have higher dopamine or dopaminergic activity and are more likely to respond to a placebo [58]. Placebos are valuable control arms within clinical drug trials, and they significantly contribute to how clinical outcomes are determined for these trials. These results highlight why both biodistribution studies using a PET radioligand and target engagement studies are crucial to understanding whether a new drug or new drug target has a valid clinical hypothesis.

Target engagement studies are also important in terms of combination therapies for cancer treatments. In a recent study, the chemotherapy drug temozolomide was labeled with carbon-11, and tumor target engagement studies that co-administered the cancer drug bevacizumab were conducted in patients with glioblastomas [63, 64]. These studies showed that ^{11}C -temozolomide uptake was decreased after initiation of bevacizumab treatment in most patients [64]. The authors concluded that temozolomide had less access to its tumor target and thus less target engagement when administered in combination with bevacizumab. The decrease of temozolomide in tumors was hypothesized to result from decreased tumor permeability when treated in combination with bevacizumab. A similar result was seen using ^{11}C -docetaxel in combination studies with bevacizumab [65]. These studies suggest that PET gives drug development teams the ability to serially interrogate target engagement of a drug in a tumor setting and provides key information about that drug's engagement in combination therapy regimens.

These examples also extend to non-small-molecule drugs such as the human epidermal growth factor receptor 3 (**HER3**) specific mAb, GSK-2849330 [66]. In this study, the lead drug candidate was a mAb and was labeled with ^{89}Zr . This team used PET imaging mAb in cancer patients to determine the biodistribution and target engagement of ^{89}Zr -GSK-2849330 in solid tumors. In a small 16-patient study, patients were given a baseline scan followed by a treatment scan. Using a mathematical model (Patlak model), this group predicted the ID_{90} (which, for a cancer agent, stands for the concentration of a drug that inhibits 90% of tumor growth) of this drug. They determined an optimal dose of 18 mg kg^{-1} that could cover the ID_{90} within HER3-positive tumors. This target engagement information was used for a quicker decision in dose selection and faster development of this potential drug [66]. These types of studies can narrow the dosing arms within a clinical trial, accelerate asset development, and generate huge cost savings during drug development. The estimated cost of pivotal efficacy trials between 2015 and 2016 was estimated between US\$ 252 and 441 million for a noninferiority trial [67]. Narrowing the number of dosing arms in these pivotal trials can have a direct cost savings for clinical trials. There is also an opportunity cost savings, as resources and research efforts can be redirected to targets that have the best potential for clinical success. This example also shows the impact of the serial nature of PET imaging. In this study, PET images of the entire tumor burden were taken before and after treatment. Biopsy is the gold standard in tumor diagnosis. However, biopsies are traditionally taken at a single time point within a tumor's lifespan. A complementary tool is needed, given the imperfect nature of a biopsy. Most cancers are heterogeneous by nature, and the expression of a particular target is both heterogeneous and dynamic within the tumor microenvironment. PET radioligands that are designed to understand the dynamics of a target expression can

provide insight into both primary and combination therapy options. This was the design criteria for our ^{18}F -ligand for the PD-L1 target BMS-986192. This tool showed in both pre-clinical and clinical studies that uptake of ^{18}F -BMS-986192 increased with PD-L1 expression in tumors as determined by IHC [22, 34]. This tool allows the drug development team a same-day imaging agent to determine PD-L1 expression in all tumors non-invasively and avoid any heterogeneity seen with IHC samples. Teams could use tools like these to examine the dynamics of a tumor target as a function of monotherapy or within combination therapies. This tool could provide data to explore novel tumor biology and quickly optimize the proper dose to influence target expression within the tumor micro-environment.

Finally, PET ligands like BMS-986192 can also be used as patient selection/patient enrichment tools for trials. A nice example of this is the Zr-89 labeled trastuzumab studies [68, 69]. Trastuzumab is a mAb that targets human epidermal growth factor receptor 2 (**HER2**), a cell-surface receptor implicated in an aggressive form of breast cancer [70]. However, not all tumors exhibit HER2 positivity within the tumors, and tools that enrich patient populations with the proper disease state in clinical trials can accelerate a drug's development. In the first example, ^{89}Zr -trastuzumab was imaged a 20-patient study where HER2 status could not be determined by standard methods. The authors of this study concluded that ^{89}Zr -trastuzumab PET imaging supported clinical decision-making of trastuzumab treatment when HER2 status could not be determined by standard workup [69]. In the second study, an assessment of ^{89}Zr -trastuzumab uptake resulted in a positive predictive value of 72% and a negative predictive value of 88% for prediction of clinical outcome for 55 patient studies on new antibody-drug conjugate (**ADC**) treatment. When combining ^{89}Zr -trastuzumab-PET with early FDG-PET response after one cycle of treatment with an ADC, a negative predictive value of 100% was obtained for all patients. These two studies highlight the use of PET as a potential tool to populate trials with patients who will benefit from the treatment and offer a more personalized medicine approach to the DDD process. The authors also suggest in this study that ^{89}Zr -trastuzumab was able to separate patients with a median time to treatment failure of 2.8 month from patients with a median time to treatment failure of 15 months [68]. This personalized medicine approach will affect patients the most: it allows them more information around their treatment plans and provides data to the drug developers to make informed decisions about drug potential more rapidly during this phase of the development process. Additional PET ligands such as ^{18}F -MK-6240 and ^{18}F -florbetapir are currently being investigated as potential tools to help the enrichment of early stage Alzheimer's disease clinical trials [71, 72].

22.5 CONCLUSION

PET imaging and novel PET radioligands play an important role in the evaluation and development of new molecular entities. These translational biomarkers provide insight into important biological targets across multiple therapeutic areas. In drug discovery, PET imaging provides value to medicinal chemistry programs by providing a non-invasive

glimpse at the drug/target interaction in animals. These tools provide decisional, translational information around target engagement, receptor occupancy, and a drug's bio-distribution in a timely manner. The use of imaging biomarkers helps to focus research endeavors on patients who need treatments and drug candidates that are most likely to achieve satisfactory clinical outcomes for them. The future of PET imaging in drug discovery is bright, and its use continues (both early and often) within the discovery and development process. This chapter has provided examples of how PET imaging drives down the cost of developing a drug by eliminating expensive late-stage failures. Using PET as a truth-seeking tool, our goal is to ensure that we are selecting the proper drug candidate for development, for the right target, with limited side effects, for the right patient population, thus having a positive impact on human health and lifespan.

REFERENCES

1. Drews, J. (2000). Drug discovery: a historical perspective. *Science* 287 (5460): 1960–1964.
2. Mukherjee, S. (2010). *The Emperor of All Maladies: A Biography of Cancer*. New York, NY: Scribner.
3. Williams, K.J. (2009). The introduction of “chemotherapy” using arsphenamine – the first magic bullet. *J. R. Soc. Med.* 102 (8): 343–348.
4. Aminov, R.I. (2010). A brief history of the antibiotic era: lessons learned and challenges for the future. *Front. Microbiol.* 1: 134.
5. Xin Yu, J., Hubbard-Lucey, V.M., and Tang, J. (2019). Immuno-oncology drug development goes global. *Nat. Rev. Drug Discovery* 18 (12): 899–900.
6. Jones, D.S., Podolsky, S.H., and Greene, J.A. (2012). The burden of disease and the changing task of medicine. *N. Engl. J. Med.* 366 (25): 2333–2338.
7. Mullard, A. (2014). New drugs cost US\$2.6 billion to develop. *Nat. Rev. Drug Discovery* 13 (12): 877.
8. Morgan, P., Van Der Graaf, P.H., Arrowsmith, J. et al. (2012). Can the flow of medicines be improved? Fundamental pharmacokinetic and pharmacological principles toward improving phase II survival. *Drug Discovery Today* 17 (9–10): 419–424.
9. Morgan, P., Brown, D.G., Lennard, S. et al. (2018). Impact of a five-dimensional framework on R&D productivity at AstraZeneca. *Nat. Rev. Drug Discovery* 17 (3): 167–181.
10. Cook, D., Brown, D., Alexander, R. et al. (2014). Lessons learned from the fate of AstraZeneca’s drug pipeline: a five-dimensional framework. *Nat. Rev. Drug Discovery* 13: 419.
11. Donnelly, D.J. (2017). Small molecule PET tracers in drug discovery. *Semin. Nucl. Med.* 47 (5): 454–460.
12. Eder, J. and Herrling, P.L. (2016). Trends in modern drug discovery. In: *New Approaches to Drug Discovery* (eds. U. Nielsch, U. Fuhrmann and S. Jaroch), 3–22. Cham: Springer International Publishing.
13. Zheng, W., Thorne, N., and McKew, J.C. (2013). Phenotypic screens as a renewed approach for drug discovery. *Drug Discovery Today* 18 (21–22): 1067–1073.

14. Jones, L.H. (2016). An industry perspective on drug target validation. *Expert Opin. Drug Discovery* 11 (7): 623–625.
15. Vaidya, A., Roy, A., and Chaguturu, R. (2018). How to rekindle drug discovery process through integrative therapeutic targeting? *Expert Opin. Drug Discovery* 13 (10): 893–898.
16. Dugger, S.A., Platt, A., and Goldstein, D.B. (2018). Drug development in the era of precision medicine. *Nat. Rev. Drug Discovery* 17 (3): 183–196.
17. Ginsburg, G.S. and McCarthy, J.J. (2001). Personalized medicine: revolutionizing drug discovery and patient care. *Trends Biotechnol.* 19 (12): 491–496.
18. Naganawa, M., Gallezot, J.D., Rossano, S., and Carson, R.E. (2019). Quantitative PET imaging in drug development: estimation of target occupancy. *Bull. Math. Biol.* 81 (9): 3508–3541.
19. Reivich, M., Kuhl, D., Wolf, A. et al. (1979). The [¹⁸F]fluorodeoxyglucose method for the measurement of local cerebral glucose utilization in man. *Circ. Res.* 44 (1): 127–137.
20. Solin, O., Eskola, O., Hamill, T.G. et al. (2004). Synthesis and characterization of a potent, selective, radiolabeled substance-P antagonist for NK1 receptor quantitation: ([¹⁸F]SPA-RQ). *Mol. Imag. Biol.* 6 (6): 373–384.
21. Nanni, C., Zanoni, L., Pultrone, C. et al. (2016). (18)F-FACBC (anti-1-amino-3-(18)F-fluorocyclobutane-1-carboxylic acid) versus (11)C-choline PET/CT in prostate cancer relapse: results of a prospective trial. *Eur. J. Nucl. Med. Mol. Imaging* 43 (9): 1601–1610.
22. Niemeijer, A.N., Leung, D., Huisman, M.C. et al. (2018). Whole body PD-1 and PD-L1 positron emission tomography in patients with non-small-cell lung cancer. *Nat. Commun.* 9 (1): 4664.
23. Melero-Ferrer, J.L., López-Vilella, R., Morillas-Climent, H. et al. (2016). Novel imaging techniques for heart failure. *Card. Fail. Rev.* 2 (1): 27–34.
24. Gallezot, J.-D., Nabulsi, N.B., Holden, D. et al. (2018). Evaluation of the lysophosphatidic acid receptor type 1 radioligand ¹¹C-BMT-136088 for lung imaging in rhesus monkeys. *J. Nucl. Med.* 59 (2): 327–334.
25. Patel, S. and Gibson, R. (2008). In vivo site-directed radiotracers: a mini-review. *Nucl. Med. Biol.* 35 (8): 805–815.
26. Van de Bittner, G.C., Ricq, E.L., and Hooker, J.M. (2014). A philosophy for CNS radiotracer design. *Acc. Chem. Res.* 47 (10): 3127–3134.
27. Patel, S., Hamill, T., Hostetler, E. et al. (2003). An in vitro assay for predicting successful imaging radiotracers. *Mol. Imag. Biol.* 5 (2): 65–71.
28. Haeusler, D., Grassinger, L., Fuchshuber, F. et al. (2015). Hide and seek: a comparative autoradiographic in vitro investigation of the adenosine A₃ receptor. *Eur. J. Nucl. Med. Mol. Imaging* 42 (6): 928–939.
29. Zhang, L., Villalobos, A., Beck, E.M. et al. (2013). Design and selection parameters to accelerate the discovery of novel central nervous system positron emission tomography (PET) ligands and their application in the development of a novel phosphodiesterase 2A PET ligand. *J. Med. Chem.* 56 (11): 4568–4579.
30. Tonietto, M., Rizzo, G., Veronese, M. et al. (2016). Plasma radiometabolite correction in dynamic PET studies: insights on the available modeling approaches. *J. Cereb. Blood Flow Metab.* 36 (2): 326–339.

31. Pike, V.W., McCarron, J.A., Lammerstma, A.A. et al. (1995). First delineation of 5-HT_{1A} receptors in human brain with PET and [¹¹C]WAY-100635. *Eur. J. Pharmacol.* 283 (1–3): R1–R3.
32. Pike, V.W., McCarron, J.A., Lammertsma, A.A. et al. (1996). Exquisite delineation of 5-HT_{1A} receptors in human brain with PET and [carbonyl-¹¹C]WAY-100635. *Eur. J. Pharmacol.* 301 (1–3): R5–R7.
33. Veach, D.R., Namavari, M., Pillarsetty, N. et al. (2007). Synthesis and biological evaluation of a fluorine-18 derivative of dasatinib. *J. Med. Chem.* 50 (23): 5853–5857.
34. Donnelly, D.J., Smith, R.A., Morin, P. et al. (2018). Synthesis and biologic evaluation of a novel (18)F-labeled adnectin as a PET radioligand for imaging PD-L1 expression. *J. Nucl. Med.* 59 (3): 529–535.
35. Mossine, A.V., Brooks, A.F., Makaravage, K.J. et al. (2015). Synthesis of [¹⁸F]arenes via the copper-mediated [¹⁸F]fluorination of boronic acids. *Org. Lett.* 17 (23): 5780–5783.
36. McCammant, M.S., Thompson, S., Brooks, A.F. et al. (2017). Cu-mediated C–H ¹⁸F-fluorination of electron-rich (hetero)arenes. *Org. Lett.* 19 (14): 3939–3942.
37. Lee, S.J., Brooks, A.F., Ichiishi, N. et al. (2019). C–H ¹⁸F-fluorination of 8-methylquinolines with Ag[¹⁸F]F. *Chem. Commun.* (Cambridge, UK) 55 (20): 2976–2979.
38. Lee, S.J., Makaravage, K.J., Brooks, A.F. et al. (2019). Copper-mediated aminoquinoline-directed radiofluorination of aromatic C–H bonds with K¹⁸F. *Angew. Chem. Int. Ed.* 58 (10): 3119–3122.
39. Tredwell, M., Preshlock, S.M., Taylor, N.J. et al. (2014). A general copper-mediated nucleophilic ¹⁸F-fluorination of arenes. *Angew. Chem. Int. Ed.* 53 (30): 7751–7755.
40. Kamlet, A.S., Neumann, C.N., Lee, E. et al. (2013). Application of palladium-mediated ¹⁸F-fluorination to PET radiotracer development: overcoming hurdles to translation. *PLoS One* 8 (3): e59187.
41. Tomasi, G. and Rosso, L. (2012). PET imaging: implications for the future of therapy monitoring with PET/CT in oncology. *Curr. Opin. Pharmacol.* 12 (5): 569–575.
42. Kurdziel, K.A., Lindenberg, L., Mena, E. et al. (2013). The role of PET/CT and SPECT/CT in oncology drug development. *Curr. Mol. Imaging.* 2 (1): 42–52.
43. Gjedde, A. (2014). Positron emission tomography of brain glucose metabolism with [¹⁸F]fluorodeoxyglucose in humans. *NeuroMethods* 90 (Brain Energy Metabolism): 341–364.
44. Zukotynski, K., Yap, J.T., Giobbie-Hurder, A. et al. (2014). Metabolic response by FDG–PET to imatinib correlates with exon 11 KIT mutation and predicts outcome in patients with mucosal melanoma. *Cancer Imaging* 14 (1): 30.
45. Farag, S., Geus-Oei, L.F., van der Graaf, W.T. et al. (2018). Early evaluation of response using (18)F-FDG PET influences management in gastrointestinal stromal tumor patients treated with neoadjuvant imatinib. *J. Nucl. Med.* 59 (2): 194–196.
46. Rani, P.U. and Naidu, M.U.R. (2008). Phase 0 – microdosing strategy in clinical trials. *Indian J. Pharmacol.* 40 (6): 240–242.
47. Matarrese, M., Salimbeni, A., Turolla, E.A. et al. (2004). ¹¹C-Radiosynthesis and preliminary human evaluation of the disposition of the ACE inhibitor [¹¹C]zofenoprilat. *Bioorg. Med. Chem.* 12 (3): 603–611.

48. van der Veldt, A.A., Lubberink, M., Greuter, H.N. et al. (2011). Absolute quantification of [(11)C]docetaxel kinetics in lung cancer patients using positron emission tomography. *Clin. Cancer Res.* 17 (14): 4814–4824.
49. Bahce, I., Smit, E.F., Lubberink, M. et al. (2013). Development of [(11)C]erlotinib positron emission tomography for in vivo evaluation of EGF receptor mutational status. *Clin. Cancer Res.* 19 (1): 183–193.
50. Bahce, I., Yaqub, M., Errami, H. et al. (2016). Effects of erlotinib therapy on [(11)C]erlotinib uptake in EGFR mutated, advanced NSCLC. *EJNMMI Res.* 6 (1): 10.
51. Xu, W., Donnelly, D.J., Chow, P.L., and Henley, B.J. (2016). Method of preparing fluorine-18 labeled cabozantinib and its analogs. Patent WO2016019285A1.
52. Lien, V.T., Klaveness, J., and Olberg, D.E. (2018). One-step synthesis of [(18)F]cabozantinib for use in positron emission tomography imaging of c-Met. *J. Labelled Compd. Radiopharm.* 61 (1): 11–17.
53. Su, H., Seimbille, Y., Ferl, G.Z. et al. (2008). Evaluation of [¹⁸F]gefitinib as a molecular imaging probe for the assessment of the epidermal growth factor receptor status in malignant tumors. *Eur. J. Nucl. Med. Mol. Imaging* 35 (6): 1089–1099.
54. Marquié, M. Validating novel tau positron emission tomography tracer [F-18]-AV-1451 (T807) on postmortem brain tissue. *Ann. Neurol.* 78 (5): 787–800.
55. Wang, Y., Zhang, Y.-L., Hennig, K. et al. (2013). Class I HDAC imaging using [(3)H]CI-994 autoradiography. *Epigenetics* 8 (7): 756–764.
56. Koeppe, M.J., Hand, K.S., Labbe, C. et al. (1998). In vivo [¹¹C]flumazenil-PET correlates with ex vivo [³H]flumazenil autoradiography in hippocampal sclerosis. *Ann. Neurol.* 43 (5): 618–626.
57. Riccobene, T.A., Miceli, R.C., Lincoln, C. et al. (2003). Rapid and specific targeting of ¹²⁵I-labeled B lymphocyte stimulator to lymphoid tissues and B cell tumors in mice. *J. Nucl. Med.* 44 (3): 422–433.
58. Gallezot, J.D., Nabulsi, N.B., Holden, D. et al. (2018). Evaluation of the lysophosphatidic acid receptor type 1 radioligand (11)C-BMT-136088 for lung imaging in rhesus monkeys. *J. Nucl. Med.* 59 (2): 327–333.
59. Bergstrom, M., Hargreaves, R.J., Burns, H.D. et al. (2004). Human positron emission tomography studies of brain neurokinin 1 receptor occupancy by aprepitant. *Biol. Psychiatry* 55 (10): 1007–1012.
60. Hargreaves, R., Ferreira, J.C., Hughes, D. et al. (2011). Development of aprepitant, the first neurokinin-1 receptor antagonist for the prevention of chemotherapy-induced nausea and vomiting. *Ann. N.Y. Acad. Sci.* 1222: 40–48.
61. Keller, M., Montgomery, S., Ball, W. et al. (2006). Lack of efficacy of the substance p (neurokinin1 receptor) antagonist aprepitant in the treatment of major depressive disorder. *Biol. Psychiatry* 59 (3): 216–223.
62. Hall, K.T., Loscalzo, J., and Kaptchuk, T.J. (2015). Genetics and the placebo effect: the placebome. *Trends Mol. Med.* 21 (5): 285–294.
63. Moseley, C.K., Carlin, S.M., Neelamegam, R., and Hooker, J.M. (2012). An efficient and practical radiosynthesis of [¹¹C]temozolomide. *Org. Lett.* 14 (23): 5872–5875.

64. Gerstner, E.R., Emblem, K.E., Chang, K. et al. (2019). Bevacizumab reduces permeability and concurrent temozolomide delivery in a subset of patients with recurrent glioblastoma. *Clin. Cancer Res.*
65. Van der Veldt, A.A., Lubberink, M., Bahce, I. et al. (2012). Rapid decrease in delivery of chemotherapy to tumors after anti-VEGF therapy: implications for scheduling of anti-angiogenic drugs. *Cancer Cell* 21 (1): 82–91.
66. Menke-van der Houven van Oordt, C.W., McGeoch, A., Bergstrom, M. et al. (2019). Immuno-PET imaging to assess target engagement: experience from (89)Zr-Anti-HER3 mAb (GSK2849330) in patients with solid tumors. *J. Nucl. Med.* 60 (7): 902–909.
67. Moore, T.J., Zhang, H., Anderson, G., and Alexander, G.C. (2018). Estimated costs of pivotal trials for novel therapeutic agents approved by the US Food and Drug Administration, 2015–2016. *JAMA Intern. Med.* 178 (11): 1451–1457.
68. Jauw, Y.W.S., Menke-van der Houven van Oordt, C.W., Hoekstra, O.S. et al. (2016). Immuno-positron emission tomography with zirconium-89-labeled monoclonal antibodies in oncology: what can we learn from initial clinical trials? *Front. Pharmacol.* 7: 131.
69. Bensch, F., Brouwers, A.H., Lub-de Hooge, M.N. et al. (2018). (89)Zr-trastuzumab PET supports clinical decision making in breast cancer patients, when HER2 status cannot be determined by standard work up. *Eur. J. Nucl. Med. Mol. Imaging* 45 (13): 2300–2306.
70. Moja, L., Tagliabue, L., Balduzzi, S. et al. (2012). Trastuzumab containing regimens for early breast cancer. *Cochrane Database Syst. Rev.* (4) (Art. No.: Cd006243).
71. Sevigny, J., Suhy, J., Chiao, P. et al. (2016). Amyloid PET screening for enrichment of early-stage Alzheimer disease clinical trials: experience in a phase 1b clinical trial. *Alzheimer Dis. Assoc. Disord.* 30 (1): 1–7.
72. Pascoal, T.A., Shin, M., Kang, M.S. et al. (2018). In vivo quantification of neurofibrillary tangles with [(18)F]MK-6240. *Alzheimers Res. Ther.* 10 (1): 74–84.

Index

A

- abbreviated new drug applications (ANDAs), 493, 497–498
- abdominal aortic aneurysm (AAA), 631
- absorbance tests, 474
- ABT Biomarker Generator system, 472
- ABT Molecular Imaging, Inc., 472
- ABTs BG75, 446
- [²²⁵Ac]Ac-DOTA-lintuzumab, 556
- [²²⁵Ac]Ac-PSMA-617, 554
- ²²⁵Ac-PSMA-617, 35
- acute myeloid leukemia (AML), 556
- adenosine triphosphate, 617
- S-adenosyl-L-methionine (ADM), 261
- ADME, 15
- advanced accelerator application (AAA), 506
- advanced biochemicals (ABX), 439
- Advion NanoTek, 446
- ALCEO solid target system, 447–448
- alendronate (ALN), 390
- aliphatic [¹⁸F]trifluoromethyl methodology, 258–259
- alkaline phosphatase (ALP), 553
- O-alkylation, 182–183
- S-alkylation, 183–186
- alkylations with [¹¹C]alkyl halides, 178–179
 - C-alkylation, 186
 - [¹¹C]methyl iodide vs. [¹¹C]methyl triflate as labelling agents, 179
 - metal-free coupling reactions, 193–196
 - N-alkylation, 179–182
 - Negishi coupling reactions, 192, 193
 - O-alkylation, 182–183
 - S-alkylation, 183–186
 - Sonogashira-like coupling reaction, 192
 - stille coupling reactions, 187–189
 - Suzuki coupling reactions, 189–191
 - transition metal-mediated
 - ¹¹C-methylation, 186–187
- allylic fluorinations, 256–257
- alpha emitters production, 95
- alpha-emitting radioisotopes, 26
- alpha (α)-methyl-serotonin (AMS), 658
- alpha (α)-methyl tryptophan (AMT), 657–660
- alzavue (florapronol), 510, 511
- Alzheimer's disease (AD), 386, 511
- amino acid imaging
 - (6-[¹⁸F]FDOPA), 668–669
 - [¹¹C]methionine ([¹¹C]MET), 665–666
 - O-(2-[¹⁸F]fluoroethyl)-L-tyrosine ([¹⁸F]FET), 667–668
 - radiotracers, 664
- amino acid metabolism, 628–629
- amino acid PET imaging, 600
- amino acids biocatalysis, 121–123
- amino acids synthesis, 120–121
- aminodiphosphane (P,N,P) ligand, 378
- 1-amino-3-[¹⁸F]fluorocyclobutane-1-carboxylic acid ([¹⁸F]FACBC), 664
- aminomethylenediphosphonate (AMDP), 390
- 1-(3-aminopropylamino)ethane-1,1-diylidiphosphonic acid (DABP), 391
- amyloid immunoglobulin light chain (AL), 638
- amyloidosis, cardiac. *See* cardiac amyloidosis (CA)
- amyloid transthyretin (ATTR), 637–639
- amyvid (florbetapir), 502, 510, 511
- analogous aurone (AR), 386
- anilines, 267
- antibody-drug conjugate (ADC), 720
- antitubercular isoniazid (INH), 421
- apoptosis, 632
- arginine-Glycine-Aspartate sequence, 398

arkel-de Boer process, 344
aromatic [¹⁸F]trifluoromethyl methodology, 259–260
artificial intelligence (AI), 450
ARTMS targets, 448
aryl-benzothiazole (BTA) derivatives, 386
aryl fluorides, 262
aryliodonium salts, 265–267
AstraZeneca, 705
[²¹¹At]At-ch81C6, 556
atherosclerosis, 634–637
attention-deficit/hyperactivity disorder (ADHD), 656
Auger electrons, 27, 421, 422
 emitters production, 96–97
 therapy, 559–560
auxiliary medicinal products (AMPs), 522, 530
Avid Radiopharmaceuticals, 494
axumin, 502
azobisisobutyronitrile (AIBN), 176

B

beam dump, 100
benzodiazepine (BZD) receptors
 [¹¹C]FMZ, 660–661
 [¹²³I]lomazenil, 661–662
 R-[¹¹C]PK11195, 662–663
benzofuran (BF) derivatives, 386
benzguanidine molecule, 24
benzoisoquinoline tetrabenazine, 11
benzylic and allylic fluorinations, 256–257
Berzelius, Jöns Jacob, 344
beta (β)-amyloid imaging agents, 386–389
beta (β)-amyloid imaging radiopharmaceuticals
 florapronol F18 injection, 511
 florbetaben F18 injection, 510–511
 flutemetamol F18 injection, 511
beta (β)-amyloid PET imaging
 indication, 596
 interpretation, 597–599
 limitations, 599
 neurodegenerative disorders, 595, 596
 radioligands, 597, 598
beta emitters production, 94–95
beta therapy, 555
Bexxar, 36
[²¹³Bi]Bi-DTPA-lintuzumab, 556

bidentate (S,S) chelators, 378
bifunctional chelates
 of ⁸⁹Zr-based radiotracers, 358, 359
bifunctional chelator (BFC), 298
²¹³Bi-lintuzumab, 37
biomarker generator, 472
bisaminethiols (BAT), 377
bis((1-(2-(bis(carboxymethyl)amino)-2-oxoethyl)-1H-imidazol-2-yl)methyl)amino (TIM), 397–398
bis((1-(carboxymethyl)-1H-imidazol-2-yl)methyl)amino (CIM), 397–398
blood-brain barrier (BBB), 5
brain death perfusion
 indication, 582
 interpretation, 582–583
 limitations, 582
 quality control requirements, 581
 radiopharmaceuticals, 581
brain tumors, 594–596, 600
breast cancer resistance protein (BCRP), 5
Bremsstrahlung radiation, 97
British Pharmacopeia (BP), 461

C

CAD. *see* coronary artery disease (CAD)
C-alkylation, 186
cancer
 clinical examples
 ([¹¹¹In] In-DTPA-hEGF), 560–561
 [²²⁵Ac]Ac-DOTA-lintuzumab, 556
 [²²⁵Ac]Ac-PSMA-617, 554
 [²¹¹At]At-ch81C6, 556
 [²¹³Bi]Bi-DOTA-TOC, 554–555
 [²¹³Bi]Bi-DTPA-lintuzumab, 556
 [¹⁷⁷Lu]Lu-DOTA-J591, 558–559
 [¹⁷⁷Lu]Lu-DOTA-TATE, 557–558
 PD-1/PD-L1 pathway, 541–543
 PSMA, 544–546
 [¹⁸⁸Re]Re-6D2, 559
 somatostatin receptors, 543–544
 targeting altered metabolism, [¹⁸F]FGln, 540–541
 definition, 536
 diagnosis and treatment of, 536
 PET, 537–539
 positron-emitting radionuclides, 538

research, 536
 SPECT imaging, 538
 theranostic system, 536–537
 therapy
 alpha therapy, 551
 applications, 550–551
 auger electron therapy, 559–560
 beta therapy, 551, 552
 biochemical characteristics, 549–550
 endotherapy, 539
 physical characteristics, 546–548
 candesartan, 10
 carbon-11, 51–52
 alkylations with [¹¹C]alkyl halides, 178–179
 C-alkylation, 186
 [¹¹C]methyl iodide vs. [¹¹C]methyl triflate as labelling agents, 179
 metal-free coupling reactions, 193–196
 N-alkylation, 179–182
 Negishi coupling reactions, 192, 193
 O-alkylation, 182–183
 S-alkylation, 183–186
 Sonogashira-like coupling reaction, 192
 stille coupling reactions, 187–189
 Suzuki coupling reactions, 189–191
 transition metal-mediated
 ¹¹C-methylation, 186–187
 biological considerations, 144–145
 chemical reactions with
 diazomethane, 211–212
 fluoroform, 210
 lithium [¹¹C]methyl(2-thienyl)cuprate, 214
 lithium trimethylsilylnolate, 213
 methyl azide, 212–213
 nitromethane, 210–211
 enzymatic reactions with, 214–217
 history, 143–144
 “loop” method, 158–159
 microfluidic chemistry, 160
 “On-Cartridge” method, 157–158
 primary precursors, 145–147
 purification and quality control, 160
 reactions with [¹¹C]CO, 168
 flow-based carbonylation methods, 177–178
 high-pressure carbonylation methods, 169–173
 low-pressure carbonylation methods, 173–177
 preconcentration and recirculation systems, 169
 reactions with [¹¹C]CO₂, 160–161
 carboxylation using reactive nucleophiles, 161–163
 C-C bond formation, 167–168
 fixation-agent, 163–167
 reaction with [¹¹C]carbon disulfide, 208–210
 reaction with [¹¹C]cyanide, 196–200
 reaction with [¹¹C]formaldehyde, 200–202
 reaction with [¹¹C]phosgene, 202–208
 secondary precursors, 147
 acetylene, 157
 ¹¹C-alkylating agents, 152–153
 [¹¹C]carbon disulfide, 155
 [¹¹C]carbon monoxide, 147–149
 [¹¹C]diazomethane, 156
 [¹¹C]fluoroform, 155–156
 [¹¹C]formaldehyde, 154–155
 [¹¹C]hydrogen cyanide, 153–154
 [¹¹C]methyl azide, 156–157
 [¹¹C]methyl iodide, 149
 [¹¹C]methyl triflate, 152
 [¹¹C]nitromethane, 156
 [¹¹C]phosgene, 154
 “gas-phase” method, 149–152
 wet method, 149
 Ynolates, 157
 synthetic considerations, 144
 carboranes, 380
 cardiac amyloidosis (CA)
 AL, 638
 ATTR, 637–639
 cardiac applications
 assessment of, 607, 608
 CA (*see* cardiac amyloidosis (CA))
 CAD, 613–617
 imaging cardiac morphology and function, 617
 molecular imaging
 apoptosis, 632
 atherosclerosis imaging, 634–637
 cardiac device infection, 634
 cardiac neuronal function, 625–627
 cardiac transplant rejection, 627–628
 cell metabolism, 628–629

- cardiac applications (*Contd.*)
 - chemokine system, 630–631
 - heart failure, 627
 - inducible nitric oxide synthase, 632
 - inflammation, 628
 - integrins, 631
 - microcalcification, 635
 - MMPs, 631
 - sarcoidosis, 632–634
 - SSTR-2, 629–630
 - superoxide levels, 631–632
 - TSPO, 630
- MPI, 608–611
- myocardial metabolism imaging, 617–625
- cardiac device infection, 634
- cardiac neuronal function, 625–627
- cardiac sarcoidosis, 632–634
- cardiometabolic disease, 623
- carfentanil, 9
- cassette-based synthesis modules, 440–441
- castration-resistant prostate cancer (CRPC)
 - patients, 553
- catecholamine *O*-methyl transferase (COMAT), 7
- cationic *trans*-[^{99m}Tc]dioxotechnetium(V)
 - complexes, 378
- CBF. *see* cerebral blood flow (CBF)
- ¹¹C-BMT-136088, 718
- CD33, 37
- ¹¹C-docetaxel, 715, 716
- cell metabolism
 - amino acid metabolism, 628–629
 - glucose metabolism, 628
- Centers for Medicare and Medicaid (CMS), 439
- central nervous system (CNS), 5, 711
- cerebral blood flow (CBF), 656
 - glucose metabolic PET imaging (*see* glucose metabolic PET imaging)
- planar imaging
 - brain death perfusion, 580–583
 - [^{99m}Tc]ECD, 580
 - [^{99m}Tc]HMPAO, 580
- SPECT
 - in dementia, 586–587
 - dopamine transporter, 587–589
 - in ictal and interictal epilepsy imaging, 583–585
- cerebral ventricular shunt
 - indication, 573
 - [¹¹¹In]DTPA, 574
 - interpretation of, 573–574
 - [^{99m}Tc]DTPA, 572–573
- cerebrospinal fluid (CSF)
 - planar and SPECT applications
 - cerebral ventricular shunt study, 572–574
 - intrathecal pump-catheter patency scintigraphy, 574–576
 - radionuclide cisternography, 576–579
 - ventriculography studies, 578
- ¹¹C-erlotinib, 715, 716
- [¹¹C]flumazenil, 660–661
- cGMP regulations. *see* Current Good Manufacturing Practice (cGMP)
- chalcone (Ch) derivatives, 386
- charged-particle reactions, 94
 - alpha emitters production, 95
 - Auger electron emitters production, 96–97
 - beta emitters production, 94–95
- chemistry, manufacturing, and controls (CMCs), 495–496
- chemokine system, 630–631
- Children's Oncology Group (COG) study, 674
- chiral aldehydes, 194
- chloride process, 344
- cholecystokinin (CCK) type-2 receptors, 406–408
- chronic metabolic adaptations, 617
- clinical trial application (CTA), 516
- Clinical Trial Regulation, 522
- Clinical Trials Information System (CTIS), 520
- ¹¹C-meta-hydroxyephedrine (HED), 625, 626
- [¹¹C]methionine ([¹¹C]MET), 665–666
- [¹¹C]methyl iodide vs. [¹¹C]methyl triflate as labelling agents, 179
- cobalamin receptor imaging agents, 415–416
- cobalt-58m, 96
- cocaine, 16, 17
- 21 Code of Federal Regulations 212 (21 CFR Section 212), 493
- 21 Code of Federal Regulations (CFR), 461, 492
- common technical dossier (CTD) format, 517
- common technology document (CTD), 504, 505
- Compton backscattering, 98

computed tomography (CT), 4, 536
contract manufacturing organization (CMO), 509
copper-mediated radiofluorination (CMRF), 253
coronary artery disease (CAD)
 diagnosis, 613–614
 myocardial microvascular function, 617
 risk stratification, 615–616
corticobasal syndrome, 593
¹¹C-Pittsburgh compound B, 638
CSF. *see* cerebrospinal fluid (CSF)
Cu-catalyzed alkyne-azide cycloaddition (CuAAC), 212
Cu-mediated fluorination, of organoboranes, 328
 aryl boronic esters, 327
 heavy halide, 332–336
 optimization, 330
 positron emission tomography, 327
 radiosynthesis, 331–332
 scope and limitations of, 329
 strategies, 325–326
Current Good Manufacturing Practice (cGMP), 61, 438, 440, 461, 516
CXC-chemokine receptor-4 (CXCR4), 37
cyclotron, 607
cyclotron-induced (p,x)-type transmutation reactions, 346
cyclotron-produced radionuclides, 75
¹¹C-zofenoprilat, 715, 716

D

DDD. *see* drug discovery and development (DDD)
DDNP, 12
dementia, 586–587
density functional theory (DFT), 264, 356
deoxy-2-[¹⁸F]fluoro-d-glucose (FDG), 457
diamidedithiols (DADS), 377
diaminedithiols (DADT), 377
2,3-diaminopropionic acid (Dpr), 393
diaryliodonium salts, 263
1,8-diazabicyclo[5.4.0]undec-7-ene (DBU), 270
diazomethane, 211–212
dicysteine (EC) chelator, 390
diffuse intrinsic pontine glioma (DIPG), 665
3,4-dihydroxy-6-[¹⁸F]fluoro-L-phenylalanine (6-[¹⁸F]FDOPA), 668–669, 672
dihydroxyphenylalanine (DOPA), 7

di-isopropyl ether (DIPE), 77
dilated nonischemic cardiomyopathy, 625
N,N-dimethylformamide (DMF), 155, 254
dimethyl sulfoxide (DMSO), 179, 258
dipicolylamine (DPA), 379
dipyrazolylamine (DPzA) chelator, 391
dithiocarbamate, 378
DLB, 593
D,L-[^{99m}Tc]
 oxotechnetium-
 hexamethylpropyleneamineoxime, 378
dopamine transporter (DAT), 9
dopamine transporter SPECT imaging
 indications, 587–588
 interpretation, 589
 limitations, 589
 patient preparation, 588–589
 radiopharmaceutical, 587
drug discovery and development (DDD)
 evaluation of, 707
 medicine approaches, 708
 non-validated drug targets, 705
 PET imaging in, 713–720
 PET ligands, 707
 PET radioligand
 ¹¹C-BMT-136088, 718
 database initiative, 713
 design criteria of, 708–713
 exploratory molecular target, 713
 ¹⁸F-SPA-RQ, 718
 generic example of, 717
 glucose, 713
 imaging biomarkers, 715
 molecule's biodistribution, 715
 non-invasively tracks glucose metabolism, 713
 radiolabeled drug candidate, 713
 target expression, 719
 PET 5R framework, 705, 706
 drug master file (DMF), 479, 498
 dual-use targets, 54–55

E

Eckert & Ziegler Modular-Labs, 442
electrodeposition, dissolution, transfer, and storage of targets (EDS), 448

electron capture (EC), 26
electronic common technical document (eCTD) format, 497
electron linear accelerators (eLINACs), 89
electrophilic aromatic substitution (SEAr), 262
electrophilic radiofluorination, 263
ELIXYS FLEX/CHEM, 443, 445
elysia-raytest GmbH, 464
end-of-bombardment (EOB), 60, 151
endoradiotherapy, 25, 539, 551
epidermal growth factor receptor (EGFR), 9, 171, 560, 715
epileptic syndromes, 583
equilibrative nucleoside transporter 1 (ENT1), 7
equilibrium radionuclide angiography (ERNA), 617
estrogen receptor imaging agents, 414–415
ethionamide (ETH), 419, 421
EudraLex legislation, 520, 521
European Association of Nuclear Medicine (EANM), 517, 523, 527
European Directorate for the Quality of Medicines (EDQM), 528
European Economic Area (EEA), 526
European Medicines Agency (EMA), 32, 517–520, 536
European Pharmacopeia (EP), 461
European Pharmacopoeia Radiopharmaceuticals monographs, 528–530
European Union (EU) legislation, 516
exametazime, 579
exploratory IND (eIND) mechanism, 494, 496

F

FASTlab, 440, 441
fatty acids, technetium-99m, 382–384
¹⁸F-cabozantinib, 716
¹⁸F-dasatinib, 712
Federal Register in 1995, 492
[¹⁸F]F-BMS-986192, 541
[F-18]florbetapir (Amyvid), 462
[¹⁸F]fludeoxyglucose ([¹⁸F]FDG), 439, 529
[¹⁸F]fluoride, 442
2-[¹⁸F]fluoro-2-deoxy-D-glucose ([¹⁸F]FDG), 655–656
[¹⁸F]fluorodeoxyglucose ([¹⁸F]FDG), 491–492, 501, 536, 540, 589
¹⁸F-fluoro-3'-deoxy-3'-L-fluorothymidine, 629
[¹⁸F]fluorodihydroxyphenylalanine ([¹⁸F]FDOPA), 269
[¹⁸F]fluoroestradiol, 440
[¹⁸F]fluoromethylcholine, 440
[¹⁸F]fluorothymidine ([¹⁸F]FLT), 675–676
¹⁸F-flurpiridaz, 611
[¹⁸F]FP-CIT, 510
¹⁸F-gefitinib, 716
¹⁸F-labeled glutamine-[¹⁸F]Gln, 540
florbetapir F 18 injection, 502
florbetaben F18 Injection, 510–511
florbetapir (18F), 506
fludeoxyglucose F 18 Injection, 459
fluid-attenuated inversion recovery (FLAIR) sequences, 664
flumazenil, 9
fluorine-18, 47–51
 aliphatic C–F bond formation methods, 260–261
 aliphatic fluorination with, 255–257
 aromatic fluorination with
 aryl fluorides, 262
 aryliodonium salts, 265–267
 diaryliodonium salts, 263
 electrophilic radiofluorination, 263
 phenols and anilines, 267
 radiofluorination, 262
 S_NAr, 263–265
 transition-metal-mediated late-stage, 267–270
 CF₃ chemistry, 257–260
 elutions and solvents, 253–254
 feature of, 251–252
 positron emission tomography, 252
 prosthetic group methods, 270–272
 radiochemistry, 252
 radiofluorination, of acceptor chemistry, 273–274
fluoroform, 210
fluorohydrins, 255–256
¹⁸F-MK-6240, 512–513
folate receptor (FR)-positive tumors, 408
Food and Drug Administration (FDA), 27, 56, 258, 437, 458, 509, 517, 611
Food and Drug Administration Modernization Act (FDAMA), 491–493
¹⁸F-paroxetine, 716
[¹⁸F]PI-2620, 512
[¹⁸F]PSMA-1007, 440
frontotemporal dementia (FTD), 590

¹⁸F-SPA-RQ, 718
¹⁸F-T807, 512
[¹⁸F] THK5351, 511–512
[¹⁸F]trifluoromethyl groups, 259
FutureChem, 509

G

⁶⁸Ga-DOTA-ELCI, 635, 636
⁶⁸Ga-DOTATATE, 506
⁶⁸Ga-DOTATXX, 672–674
[⁶⁸Ga]Ga-PSMA-11, 544, 545, 546
⁶⁸Ga-labeled radiopharmaceuticals, 538
gallium-67, 77–78
gallium-68, 55–56, 56–57
 automation, integration and novel chemical processes, 316–317
 chelator library impact, 316
 clinical tracers, 309
 PSMA-targeting radiotracers, 312–315
 somatostatin receptor, 309–312
 design an ideal chelator, 297–303
 general development areas, 315–316
 isotope production, 292–296
 kits and tracer production, 316
 neuroendocrine tumors, 291
 positron emission tomography, 291
 practical aspects of, 303–305
 future of pre-purification, 305
 synthesis units vs. kits, 306–309
 prostate-specific membrane antigen, 291
 radiochemistry, 296–297
 somato-statin receptors, 291
 therapeutic isotope congeners and dosimetry, 317–318
gas chromatography (GC), 448
gas-phase reduction, 148
gastroenteropancreatic neuroendocrine tumors (GEP-NETs), 503, 551
gastrointestinal stromal tumors (GISTs), 714
⁶⁸Ge/⁶⁸Ga generators, 57–63
 aqueous target development, 61–62
 cyclotron production, 58, 62–63
 future of, 63
 liquid target production, 59–60, 60–61
 solid target production, 58–59

General Electric (GE), 439, 440
GE TRACERlab FX series, 442
glucose metabolic PET imaging
 FDG PET in
 in brain tumors, 594–596
 cognitive and dementing disorders, 590–593
 in movement disorders, 591, 593
 in refractory epilepsy, 594
 indications, 590
 interpretation, 589, 590
 limitations, 591
 patient preparation, 590
glucose metabolism, 628
Good Clinical Practice (GCP) Directive, 521
Good Laboratory Practice (GLP) regulations, 519
Good Manufacturing Practice (GMP), 188, 493, 506, 515, 538

H

hafnium, 344
Health Sciences Authority (HSA), 509
heart mediastinal ratio (HMR), 626
hematological cancers, 37
herpes simplex virus type-1 thymidine kinase (HSV1-tk)
 gene expression, 412
hexafluoroisopropanol (HFIP), 260
highly enriched ²³⁵U (HEU), 72
high-performance liquid chromatography (HPLC), 57, 158, 254, 466
high-performance liquid chromatography (HPLC)
 purification, 360, 442
high-throughput screening (HTS), 14
HPLC. *see* high-performance liquid chromatography (HPLC)
human amyloid imaging (HAI), 511–512
human anti-mouse antibody (HAMA), 674
human epidermal growth factor receptor 2 (HER2), 720
human epidermal growth factor receptor 3 (HER3), 719
human immunodeficiency virus/acquired immunodeficiency syndrome (HIV/AIDS), 704
Huntington's disease, 593
6-hydrizinonicotinic acid (HYNIC) ligand, 378
hydrofluoric acid (HF), 95
hydrophilic interaction chromatography (HILIC), 160
hydroxamate resin, 353, 359

4-(2-hydroxyethyl)-1-piperazineethanesulfonic acid (HEPES), 360
1-(2-hydroxy-3-[¹⁸F]fluoropropyl)-2-nitroimidazole (FMISO), 462
6-hydroxy-4'-*N,N*-dimethylamino-flavone (FL), 386
hydroxypyridinonate (HOPO) donors, 360
5-hydroxytryptamine (5-HT), 657
hypertrophy, 623–624

I

ictal and inter-ictal scans., 584–585
idiopathic Parkinson's disease without dementia, 593
[¹²³I]FP-CIT, 510
[¹²³I]ioflupane, 587
[¹²³I]iomazenil, 661–662
¹²³I-metaiodobenzylguanidine (¹²³I-MIBG), 625, 626
¹³¹I-MIBG, 29
iminodiacetate (IDA), 410
immunotherapy, 36
indicator-based absorbance tests, 474
indium-111, 78–80
indoleamine 2,3-dioxygenase (IDO), 659
IND protocols. *see* investigational new drug (IND)
[¹¹¹In]DTPA, 574, 575
inducible nitric oxide synthase (iNOS), 632
inhibitor glutamate-urea-lysine-εA-naphthylalanine-HYNIC (iPSMA), 398
[¹¹¹In] In-DTPA-hEGF, 560–561
instant thin-layer chromatography (ITLC), 296
Institute for Standardization and Control of Pharmaceuticals (ISCP), 509
integrins, 631
International Atomic Energy Agency (IAEA), 76
International Council for Harmonization (ICH), 517
International Symposium on Radiopharmaceutical Sciences (ISRS), 507, 508
intrathecal pump-catheter patency scintigraphy, 574–576
investigational medicinal product dossier (IMPD), 516, 517
investigational medicinal products (IMPs), 522
investigational new drug (IND), 458, 493
 chemistry, manufacturing, and controls (CMCs), 495–496
 clinical imaging protocol, 495

 pharmacology and toxicology, 496
 previous human experience, 496–497
iodine-123, 80–82
iodine-131, 74, 75
iodobenzamide, 11
iodonium salts, 266
iPhase MultiSyn systems, 442
Iran Food and Drug Administration (IFDA), 509
ISAR system, 446
Isotope Technologies Garching (ITG), 295

K

Klaproth, Martin Heinrich, 344
Kroll process, 344
Kroll, William J., 344
Kryptofix 222 (4,7,13,16,21,24-hexaoxa-1,10-diazabicyclo[8.8.8]hexacosane), 459

L

LabLogic LTD, 464
laboratory information management system (LIMS), 464
laminar air flow (LAF) unit, 524
lanthionine (LAN)
large amino acid transporter 1 (LAT1), 7
leukemia, 36–38, 539
linear energy transfer (LET), 25, 26, 89, 546
lithium [¹¹C]methyl(2-thienyl)cuprate, 214
lithium trimethylsilylolate, 213
“loop” method, 158–159
losartan, 10
low enriched ²³⁵U (LEU), 72
¹⁷⁷Lu-DOTATATE (Lutathera), 503
¹⁷⁷Lu-labeled DOTA-(Tyr³-Thr⁶)-octreotide (TATE), 537
[¹⁷⁷Lu]Lu-DOTA-J591, 558–559
[¹⁷⁷Lu]Lu-DOTA-TATE, 557–558
[¹⁷⁷Lu]Lu-PSMA-617, 546
lymphoma, 36–38

M

magnetic resonance imaging (MRI), 4, 536
Massachusetts General Hospital (MGH), 481
matrix metalloproteinases (MMPs), 631
maximum tolerated dose (MTD), 674

Mealey, John, 348
 melanocortin 1 receptor (MC1R), 402–404
 mercaptoacetyltriglycine (MAG3), 377
 meta-¹⁸F fluorobenzylguanidine (¹⁸FmFBG), 671–672
 meta-iodobenzylguanidine (MIBG), 27
 meta-iodobenzylguanidine (mIBG), 670–671
 metal-free coupling reactions, 193–196
 metallic radionuclides, 538
 metastatic castration-resistant prostate cancer (mCRPC), 33, 35
 methyl azide, 212–213
 1-methyl-4-phenyl-1,2,3,6-tetrahydropyridine (MPTP), 13
 microcalcification, 635
 microdose trial approach, 519
 microdosing, 715
 microfluidic systems, 446
 Ministry of Food and Drug Safety (MFDS), 501, 509
 Ministry of Health, Labour, and Welfare (MHLW), 509
 mitochondrial oxidative phosphorylation, 617
 mitochondrial translocator protein (TSPO), 630
 “3+1” mixed-ligand [^{99m}Tc]oxotechnetium(V) complexes, 377
 “2+1” mixed-ligand [^{99m}Tc][Tc(CO)₃]⁺ complexes, 379
 “4+1” mixed-ligand system, 379
 molar activity, 91
 monoamine oxidase (MAO), 7
 monoamine oxidase B (MAO B), 512
 monoamino monoamido dithiols (MAMA), 377
 monoclonal antibody (mAb), 24, 704
 morphine, 16, 17, 574
 movement disorders, 591, 593, 599–600
 MPI. *see* myocardial perfusion imaging (MPI)
^{99m}Tc-benzoxazole (BOx) derivatives, 386
^{99m}Tc-besilesomab (Scintimun), 418
^{99m}Tc-bisphosphonates (BP), 390
 [^{99m}Tc]CpTT-chalcone, 389
 [^{99m}Tc]CpTT complexes, 379
 [^{99m}Tc]CpTT-*o*MPP, 385
 [^{99m}Tc]CpTT-15-oxo-PTA, 382, 384
 [^{99m}Tc]CpTT-PA, 382, 383
^{99m}Tc-demobesins, 393
^{99m}Tc-demogastrin 2, 406, 407
^{99m}Tc-demotate-1, 395, 396
^{99m}Tc-demotensin 6, 405, 406
^{99m}Tc-DTPA (diethylenetriaminepentaacetic acid), 654
 [^{99m}Tc]ECD, 584, 585
 [^{99m}Tc]ethylcysteine dimer, 600
 [^{99m}Tc]hexamethylpropyleneamine oxime (HMPAO), 579
 [^{99m}Tc]HMPAO, 584, 585
^{99m}Tc-labelled dibenzylideneacetone (DBAC) derivatives, 386
^{99m}Tc-labelled fluoroquinolone antibiotic [^{99m}Tc]Tc-ciprofloxacin (Infecton), 418
^{99m}Tc-labelled myocardial imaging agents, 380
^{99m}Tc-labelled peptides, 377
^{99m}Tc-leukocytes (^{99m}Tc-WBC), 418
^{99m}Tc-methylene diphosphonate (^{99m}Tc-MDP), 654
^{99m}Tc-MIP-1404, 397, 398
^{99m}Tc-MIP-1405, 397, 398
 [^{99m}Tc]nitridotechnetium(V) complexes, 378
 [^{99m}Tc]oxotechnetium(V) complexes, 377, 378
 [^{99m}Tc]oxotechnetium-ethylenebis(L-cysteinyl-D-glucosamine) ([^{99m}Tc]Tc-ECDG), 411
 [^{99m}Tc]oxotechnetium-MAMA-propyl-N3-thymidine derivative, 414
^{99m}Tc-SARNCS, 393
^{99m}Tc-sestamibi, 381
^{99m}Tc-sulesomab, 418
 [^{99m}Tc]Tc(CO)₃(1 α -IDA-2-deoxyglucose), 410, 411
 [^{99m}Tc][Tc(CO)₃(1 β -IDAgucose)], 410, 411
 [^{99m}Tc][Tc(CO)₃(15C5-PNP)]⁺, 380, 381
 [^{99m}Tc][Tc(CO)₃(ALN-pzNN)], 391
 [^{99m}Tc][Tc(CO)₃(ASMA)]²⁻, 389, 390
 [^{99m}Tc]Tc(CO)₃(C3'-NNO-thymidine), 413
 [^{99m}Tc]Tc(CO)₃(C5'-IDA-thymidine), 413
 [^{99m}Tc][Tc(CO)₃(CMSA)]²⁻, 389, 390
 [^{99m}Tc]Tc(CO)₃(cp-BTA), 386, 389
 [^{99m}Tc]Tc(CO)₃(curcumin), 388, 389
 [^{99m}Tc]Tc(CO)₃(DMIB-bis-*o*MPP), 385
 [^{99m}Tc][Tc(CO)₃(DPA-ALN)], 391
 [^{99m}Tc][Tc(CO)₃(DPA-DABP)], 391
 [^{99m}Tc][Tc(CO)₃(DPA-doxorubicin)]⁺, 421, 422
 [^{99m}Tc][Tc(CO)₃(Dpr-SSS-BN(7-14)(X)) tracers, 393
 [^{99m}Tc][Tc(CO)₃(H₂O)₃]⁺, 380
 [^{99m}Tc][Tc(CO)₃(His-B12)], 415
 [^{99m}Tc][Tc(CO)₃(LAN)], 388, 389
 [^{99m}Tc][Tc(CO)₃(N,N,N-pyrene-NLS)], 421, 422
 [^{99m}Tc]Tc(CO)₃(N₃-TzHis-thymidine), 413

- [^{99m}Tc][Tc(CO)₃(Na-His-Ac-BN(7-14))], 392, 393
- [^{99m}Tc]Tc(CO)₃(NNO-E17), 414–415
- [^{99m}Tc][Tc(CO)₃(NT-XI)], 404, 405
- [^{99m}Tc][Tc(CO)₃(NTA)]²⁻, 388, 389
- [^{99m}Tc][Tc(CO)₃(PAMA-C2-6-b-B12)], 416
- [^{99m}Tc][Tc(CO)₃(pz-anthracene), 421, 422
- [^{99m}Tc][Tc(CO)₃(pzNN-ALN)], 391
- [^{99m}Tc][Tc(CO)₃(pzNN-PAM)], 391
- [^{99m}Tc][Tc(CO)₃(TDSA)]³⁻, 389, 390
- [^{99m}Tc]Tc(NS3)(CN-C11S), 382
- [^{99m}Tc]Tc(NS₃)(CN-Cn-*o*MPP), 385
- [^{99m}Tc]Tc-(Arg¹¹)CCMSH, 402, 403
- [^{99m}Tc]Tc-BAT-AR, 388, 389
- [^{99m}Tc]Tc-BAT-5-BF, 387, 389
- [^{99m}Tc]Tc-BAT-C3-5-BOX, 387, 389
- [^{99m}Tc]Tc-BAT-C3/C5-4'-Ch, 387, 389
- [^{99m}Tc]Tc-BAT-FL, 388, 389
- [^{99m}Tc]Tc-BAT-6-PhBTA, 386, 389
- [^{99m}Tc]Tc-BAT-3-styrylpyridine, 388, 389
- [^{99m}Tc][Tc(CO)₃C₂B₉H₁₀] complex, 380
- [^{99m}Tc]Tc-ciprofloxacin, 419
- [^{99m}Tc][Tc(CO)₃(*h*5-Cp)] complexes
([^{99m}Tc]CpTT), 379
- [^{99m}Tc]Tc-DPA-folate, 408
- [^{99m}Tc]Tc-DTPA-mannosyl-Dx, 416
- [^{99m}Tc]Tc-EC20, 408, 409
- [^{99m}Tc]Tc-EC-AMDP, 390, 391
- [^{99m}Tc]Tc-EDDA-HYNIC-ALUG, 398
- [^{99m}Tc]Tc-EDDA-HYNIC-AocNle-CycMSH_{hex}, 403, 404
- [^{99m}Tc]Tc-EDDA-HYNIC-cyclo-MG2 (cyclo-MG2: cyclo^{1,9}[g-D-Glu¹,desGlu²⁻⁶,D-Lys⁹,Nle¹¹]MG), 406, 407
- [^{99m}Tc]Tc-EDDA-HYNIC-iPSMA, 398
- [^{99m}Tc]Tc-EDDAHYNIC- MG, 406
- [^{99m}Tc]Tc-EDDA-HYNIC-MG11, 406–407
- [^{99m}Tc]Tc-EDDA-HYNIC-TOC, 395, 396
- [^{99m}Tc]Tc-enrofloxacin, 418
- [^{99m}Tc][Tc(CO)₃-folate] complexes, 408, 409
- [^{99m}Tc]Tc-hydrazino complexes, 378
- [^{99m}Tc]Tc-hydroxymethylenediphosphonate
([^{99m}Tc]Tc-HMDP), 390
- [^{99m}Tc]Tc-HYNIC-BN derivatives, 393, 395
- [^{99m}Tc]Tc-HYNIC-EDDA complexes, 378
- [^{99m}Tc]Tc-HYNIC-tricine complexes, 378
- [^{99m}Tc]Tc-HYNIC-UBI(29-41), 419, 421
- [^{99m}Tc]Tc-IDA-folate, 408
- [^{99m}Tc]Tc-INH-2IT, 419, 421
- [^{99m}Tc]Tc-isoniazid-iminothiolane, 419
- [^{99m}Tc]Tc-MAG₃, 377
- [^{99m}Tc]Tc-MAG₃-ALN, 391
- [^{99m}Tc]Tc-MAG3-mannosyl-Dx, 416
- [^{99m}Tc]Tc-methylenediphosphonate
([^{99m}Tc]Tc-MDP), 390
- [^{99m}Tc][TcN(N,S-Cys-Gly-CCK8)(PNP3)]+ (PNP3=N,N-bis(dimethoxypropylphosphinoethyl) methoxyethylamine), 406, 408
- [^{99m}Tc][TcN(PNP3)(DBODC)]⁺, 380, 381
- [^{99m}Tc][TcN(PNP3)(DTC11)]⁺, 382
- [^{99m}Tc][TcN(PNP⁵)(MPO)]⁺, 380
- [^{99m}Tc][TcN(S,S)₂], 378
- [^{99m}Tc][Tc-N₄-Gln1]gastrin (^{99m}Tc-SG6), 406, 407
- [^{99m}Tc]TcN-NOET, 378
- [^{99m}Tc]Tc-N₃S-G-5Ava-BN(7-14)
(^{99m}Tc-RP527), 392, 393
- [^{99m}Tc]TcN-(SPiso)-DTC-Cn-*o*MPP), 385
- [^{99m}Tc]TcO(MAG₂-G₃-E[G₃-c(RGDfK)]₂), 399, 400
- [^{99m}Tc]TcO(MAG₂-PEG₄-E[PEG₄-c(RGDfK)]₂), 399, 400
- [^{99m}Tc]TcO(S,X,S)(S)], 378
- [^{99m}Tc]TcO(S₂NMe)(S-C₆-*o*MPP), 385
- [^{99m}Tc]TcO-BAT, 377
- [^{99m}Tc]TcO-DADT, 377
- [^{99m}Tc]TcO-DADT-*o*MPP, 385
- [^{99m}Tc]TcO-MAG₃, 377
- [^{99m}Tc]TcO-MAMA, 377
- [^{99m}Tc]TcO-MAMA-HDA, 382
- [^{99m}Tc]Tc-PAMA-folate, 408
- [^{99m}Tc]Tc(CO)₃-pz-βAla-Nle-cyclo[Asp-His-DPhe-Arg-Trp-Lys]-NH₂, 403
- [^{99m}Tc]Tc-TMEOP, 380, 381
- [^{99m}Tc]Tc(CO)₃(TzHis-folate) tracers, 409
- [^{99m}Tc]Tc-Tricine-TPPTS-(HYNIC-G₃-E[G₃-c(RGDfK)]₂), 399, 400
- [^{99m}Tc]Tc-Tricine-TPPTS-(HYNIC-PEG₄-E[PEG₄-c(RGDfK)]₂), 399, 400
- [^{99m}Tc]technetium hexamethyl-propylene-amine-oxime (HMPAO), 655
- [^{99m}Tc]technetium-tricarbonyl complexes, 381
- ^{99m}Tc-Tetrofosmin, 381
- ^{99m}Tc-tracers [^{99m}Tc]Tc-MAG₃-GGNle-CycMSH_{hex}, 403, 404
- multichannel analyzer (MCA), 466

multiple system atrophy of the cerebellar type (MSA-C), 593
multiple system atrophy of the parkinsonian type (MSA-P), 593
myocardial hypertrophy, 623–624
myocardial metabolism
 aging and myocardial metabolism, 621–623
 cardiometabolic disease, 623
 dilated nonischemic cardiomyopathy, 625
 myocardial hypertrophy, 623–624
 myocardial viability, 618–620
 PET and SPECT radiopharmaceuticals, 618
 sex differences in, 620–621
myocardial perfusion, 612
myocardial perfusion imaging (MPI)
 PET radiopharmaceuticals, 610–611
 physical characteristics, 609
 physiological characteristics, 609
 rest/stress, 611–614
 SPECT radiopharmaceuticals, 609–610
myocardial perfusion reserve (MPR), 613
myocardial viability, 618–620

N

N-alkylation, 179–182
[¹³N]Ammonia ([¹³N]NH₃), 656
nanoparticles (NPs), 91, 124
National Agency for Drug and Food Control (NADFC), 509
National Nuclear Decay Center (NNDC), 345
National Pharmaceutical Regulatory Agency (NPRA), 509
Negishi coupling reactions, 192, 193
NEPTIS, 440, 441
Neuraceq (florbetaben), 502, 510, 511
neuroblastoma
 6-[¹⁸F]FDOPA, 672
 [¹⁸F]mFBG, 671–672
 mIBG, 670–671
 radiolabeled anti-GD2 antibodies, 674–675
 radiolabeled somatostatin analogs, 672–674
neurodegenerative disorders, 572
neuroendocrine tumors (NETs), 23, 291, 543–544
neurokinin-1 (NK-1) receptor, 718
neurotensin (NT), 404
neurotensin receptor imaging agents, 404–406
new drug application (NDA), 458, 492, 497, 499, 502
N-fluorobenzenesulfonimide (NFSI), 263
niobium, 346
nirta systems, 447
nitrogen-13, 52–53, 109–110
 amino acids biocatalysis, 121–123
 amino acids synthesis, 120–121
 biocatalysis, 123–124
 clinical applications, 127–128
 compounds, 124–127
 nanoparticles, 124
 ¹³N-labeled amines and amides, 116–117
 ¹³N-labeled azo compounds, 120
 ¹³N-labeled nitrosamines, 118–119
 ¹³N-labeled nitrosothiols, 118
 [¹³N]NH₃ production, 113–115
 [¹³N]N₂O production, 116
 [¹³N]NO₂- production, 115–116
 [¹³N]NO₃- production, 115
 [¹³N]N₂ production, 111–113
 nuclear reactions for, 110
nitrogen-13 ammonia, 611
nitromethane, 210–211
¹³N-labeled amines and amides, 116–117
¹³N-labeled azo compounds, 120
¹³N-labeled nitrosamines, 118–119
¹³N-labeled nitrosothiols, 118
N-methyl-D-aspartate (NMDA) receptors, 659
N,N'-ethylenediamine-diacetic acid (EDDA), 378
[¹³N]NH₃ production, 113–115
[¹³N]N₂O production, 116
[¹³N]NO₂- production, 115–116
[¹³N]NO₃- production, 115
[¹³N]N₂ production, 111–113
No-carrier-added (n.c.a) iodine, 27
non-investigational medicinal products (NIMPs), 522
non-radioactive contaminant, 92
norepinephrine transporter (NET), 7
NorthStar Medical Technologies, 74
N₂S₂ chelators, 377
N₃S chelators, 377
nuclear medicine, 3
nucleophilic aromatic substitution (SNAr), 262
nucleophilic substitutions, 510

- O**
- [¹⁵O] butanol synthesis, 132
 - [¹⁵O]CO, 130–131
 - [¹⁵O]CO₂, 130–131
 - [¹⁵O]DG synthesis, 133
 - O-(2-[¹⁸F]fluoroethyl)-L-tyrosine ([¹⁸F]FET), 667–668
 - [¹⁵O]H₂O, 131
 - [¹⁵O]H₂O₂, 132–133
 - Ommaya reservoir, 576–579
 - “On-Cartridge” method, 157–158
 - oncology, pediatric nuclear medicine. *See also* cancer
 - amino acid imaging, 663–670
 - [¹⁸F]FLT, 675–676
 - neuroblastoma, 670–675
 - one-pot photoradiochemical conjugation and labelling
 - of antibodies, 365
 - [¹⁵O]N₂O, 130
 - [¹⁵O]O₂, 130
 - [¹⁵O]O₃, 132
 - organoboranes
 - Cu complexes, 326
 - Cu-mediated fluorination, 328
 - aryl boronic esters, 327
 - heavy halide, 332–336
 - optimization, 330
 - positron emission tomography, 327
 - radiosynthesis, 331–332
 - scope and limitations of, 329
 - strategies, 325–326
 - radioiodination method, 325
 - transition-metal species, 326
 - utilization of, 325
 - organolithium reagents, 161
 - organometallic ^{99m}Tc(III)-complexes, 379
 - orthomethoxyphenyl- piperazine (oMPP), 384
 - oxalate anions, 354
 - oxotechnetium(V) complexes, 377
 - oxygen-15, 53–54
 - administration of, 134
 - biological processes, 129
 - clinical applications of, 134
 - [¹⁵O]CO, 130–131
 - [¹⁵O]CO₂, 130–131
 - [¹⁵O]H₂O, 131
 - [¹⁵O]N₂O, 130
 - [¹⁵O]O₂, 130
 - [¹⁵O]O₃, 132
 - production of, 129–130
 - properties, 128–129
 - radiochemistry of, 132
 - [¹⁵O] butanol synthesis, 132
 - [¹⁵O]DG synthesis, 133
 - [¹⁵O]H₂O₂ synthesis, 132–133
 - oxygen-15 water, 611
- P**
- parasympathetic nervous system (PNS), 625, 626
 - Parkinson’s disease with dementia (PDD), 593
 - pediatric autoimmune neuropsychiatric disorders
 - associated with streptococcal infection (PANDAS), 663
 - pediatric nuclear medicine
 - infection/inflammation radiopharmaceuticals, 655
 - neuroscience
 - benzodiazepine receptors, 660–663
 - α-methyl tryptophan, 657–660
 - oncology
 - amino acid imaging, 663–670
 - [¹⁸F]FLT, 675–676
 - neuroblastoma, 670–675
 - PET radiopharmaceuticals and their uses
 - [¹⁸F]FDG, 655–656
 - [¹⁸F]NaF, 656
 - [¹³N]NH₃, 656
 - radioiodine for thyroid disease, 655
 - technetium Tc-99m (^{99m}Tc), 654
 - peptide receptor radionuclide therapy (PRRT), 25, 503, 549
 - performance qualification (PQ), 479
 - peripheral benzodiazepine receptor (PBR), 662
 - PET. *see* positron emission tomography (PET)
 - p-glycoprotein (PGP), 5, 381
 - Pharmaceutical Inspection Convention (PIC), 507–509, 527–528
 - Pharmaceutical Inspection Co-operation Scheme (PIC/S), 507–508, 517, 527–528
 - Pharmacopeial Forum (PF), 482
 - Pharmacy and Poisons Board of Hong Kong (PPBHK), 509

phenols, 267

phenyliodonium diacetate (PIDA), 267

phosphodiesterase 10A (PFD10A) enzyme, 14

photonuclear reactions, 97–100

- bremsstrahlung radiation, 97
- Compton backscattering, 98
- isomers, 99–100

picolylamine acetic acid (PAMA), 379

Pittsburgh compound B (PIB), 12

polar surface area (PSA), 14

polyether ether ketone (PEEK), 50

polytetrafluoroethane (PTFE), 50, 158

- applications of, 45
- automated quality control (QC)
 - barriers to, 464
 - cGMP compliance challenge, 461
 - concepts, prototypes, and products, 476, 477
 - criteria, 478
 - drivers of, 462–464
 - functions, 457
 - future developments, 483–485
 - innovation (*see* quality control (QC) innovation, PET)
 - laboratory setup for, 460, 462
 - mechanisms, 458
 - new tracers, 462
 - pharmacopeia incorporation, 482–483
 - regulators' benefits from, 478–479
 - regulatory approval mechanism for, 479–482
 - requirements, 458–461
- automated synthesis modules for
 - automated quality control testing, 448
 - daily synthesis and delivery of, 438
 - early radiopharmaceutical synthesis modules, 438–440
 - fully automated fixed tubing modules, 441–443
 - hybrid modules, 443, 445
 - microfluidic systems, 446
 - modern cassette-based modules, 440–441
 - solid target system, 447–448

cancer

- [²²⁵Ac]Ac-PSMA-617, 552
- [¹⁸F]FDG, 540
- [¹⁸F]FGLn, 540–541
- fused [⁶⁸Ga]Ga-PSMA-11, 552
- neuroendocrine cancer, 555
- PD-1/PD-L1 pathway, 541–543
- PSMA, 544–546
 - somatostatin receptors, 543–544
- cyclotron targets, 45

DDD (*see* drug discovery and development (DDD))

drugs from the lab to the patient in the USA

- ANDA, 497–498
- 21 CFR 212, 493
- DMF, 498
- Food and Drug Administration Modernization Act, 491–493
- imaging patients, 494
- INDs (*see* investigational new drug (IND))
- NDA, 497, 499
- RDRC, 497
- USP 823, 493–494

⁶⁸Ge/⁶⁸Ga generators, 57–63

- aqueous target development, 61–62
- cyclotron production, 58, 62–63
- future of, 63
- liquid target production, 59–60, 60–61
- solid target production, 58–59

moving from the lab to the patient in Asia

- diagnostic radiopharmaceuticals, 502–503
- technical transfer (*see* technical transfer, PET radiopharmaceuticals)
- therapeutic radiopharmaceuticals, 503–504

production, 46–47

- carbon-11, 51–52
- dual-use targets, 54–55
- fluorine-18, 47–51
- gallium-68, 55–56, 56–57
- nitrogen-13, 52–53
- oxygen-15, 53–54
- rubidium-82, 55–56, 56
- tandem targets, 54–55

radioligand

- biochemical, metabolic, or physiologic process, 713
- ¹¹C-BMT-136088, 718
- database initiative, 713
- design criteria of, 708–713
- exploratory molecular target, 713
- ¹⁸F-SPA-RQ, 718

positron emission tomography (PET) (*Contd.*)
generic example of, 717
glucose, 713
imaging biomarkers, 715
molecule's biodistribution, 715
non-invasively tracks glucose metabolism, 713
radiolabeled drug candidate, 713
target expression, 719
tau proteinopathy ligands, 600–601
Positron Emission Tomography and Recovery Following
Revascularization-2 (PARR-2) trial, 620
prior approval supplement (PAS), 479
production, 46–47
program death ligand 1 (PD-L1), 712
programmed cell death protein-1 (PD-1), 541
progressive supranuclear palsy, 593
proliferator-activated receptor alpha (PPAR α), 618
propyleneaminoxime chelator, 378
prostate cancer (PC), 23, 544
prostate-specific antigen (PSA), 33–36, 544
prostate-specific membrane antigen (PSMA), 28, 291,
397–398, 503, 544
prosthetic group methods, 270–272
purification module (PRF), 448

Q

QC1 concept, 470–471
QC-Cubicle, 466
qualified person (QP), 524
quality assurance (QA), 457
quality control (QC) innovation, PET
automated prototype, 467–469
exploit synergies, 472–475
footprint via a cabinet, 466
miniaturization, 469–471
traditional solutions, 464–465
quality management system (QMS), 464
quaternary methyl-ammonium (QMA), 253
quaternary methyl ammonium ion (QMA), 354, 355
quiniclidinyl benzilate (QNB), 13

R

radiation-induced fibrosarcoma (RIF) tumor mouse
model, 414
radiation tests, 474

Radioactive Drug Research Committee (RDRC), 458,
493, 497
radiochemical yield (RCY), 147, 253
radiofluorination, 262
radioimmunotherapy (RIT), 23, 24, 25, 549
radiolabeled anti-GD2 antibodies, 674–675
radiolabeled endogenous compounds, 6–9
radiolabeled somatostatin analogs, 672–674
radioligand therapy (RLT), 23
radionuclide cisternography, 576–579, 577–579
radionuclides
of zirconium, 345–347
radionuclide therapy, 29
radioresistance, 549–550
radiotracer
clinical translation of, 516
clinical trial legislation
EU Clinical Trial Regulation, 521
EU Clinical Trials Directive 2001/20/EC, 520–521
EudraLex, 520, 521
individuelle Heilversuche, 522
interventional studies, 521–522
observational studies, 521
clinical trials (phase I-IV), 517, 518
EANM, 527
EU clinical trials register, 526
EudraCT database, 526
Eudralex Volume 4, Annex 13, 523–526
European Pharmacopoeia Radiopharmaceuticals
monographs, 528–530
GMP requirements, 522
non-clinical safety studies, 518–520
PIC/s, 527–528
requirements to translate, 516, 517
radiotracers
development of, 4
efflux transporters, 5
emphasis in, 3–4
endogenous compound label, 6–9
high-throughput screening, 14–15
from in vitro reagents to in vivo imaging, 12–13
natural products, 15–17
pharmaceutical or derivative, 9–12
site-specific delivery, 4
radiotracer-specific program, 443, 444

radium-223, 539
[²²³Ra]Ra-dichloride, 553
R-[¹¹C]PK11195, 662–663
reactive nitrogen species (RNS), 631
reactive oxygen species (ROS), 631
reference listed drug (RLD), 498
[¹⁸⁸Re]Re-6D2, 559
rickham reservoirs, 576–579
rubidium-82, 55–56, 56, 610–611

S

sarcoidosis, 632–634
saturation point, 90
secondary precursors, in Carbon-11, 147
 acetylene, 157
 ¹¹C-alkylating agents, 152–153
 [¹¹C]carbon disulfide, 155
 [¹¹C]carbon monoxide, 147–149
 [¹¹C]diazomethane, 156
 [¹¹C]fluoroform, 155–156
 [¹¹C]formaldehyde, 154–155
 [¹¹C]hydrogen cyanide, 153–154
 [¹¹C]methyl azide, 156–157
 [¹¹C]methyl iodide, 149
 [¹¹C]methyl triflate, 152
 [¹¹C]nitromethane, 156
 [¹¹C]phosgene, 154
 “gas-phase” method, 149–152
 wet method, 149
 Ynolates, 157
selective serotonin reuptake inhibitors (SSRIs), 12
sentinel lymph node (SNL) imaging, 416–418
D-Serine, 201
serotonin synthesis capacity, 658
serotonin transporter (SERT), 11
[⁷⁵Se]selenomethionine, 663
single amino acid chelate (SAAC), 379
single photon emission computed tomography (SPECT), 5, 25, 501, 516
 cerebral blood flow
 in dementia, 586–587
 dopamine transporter, 587–589
 in ictal and interictal epilepsy imaging, 583–585
 cerebrospinal fluid
 cerebral ventricular shunt study, 572–574

 intrathecal pump-catheter patency
 scintigraphy, 574–576
 radionuclide cisternography, 576–579
 ventriculography studies, 578
cyclotron-produced radionuclides, 75
dopamine transporter
 indications, 587–588
 interpretation, 589
 limitations, 589
 patient preparation, 588–589
 radiopharmaceutical, 587
gallium-67, 77–78
indium-111, 78–80
iodine-123, 80–82
iodine-131, 74, 75
radionuclides, 71, 72
technetium-99m, 72–74
thallium-201, 75–77
xenon-133, 74
Slow neutrons, 91
S_NAr, 263–265
Society for Nuclear Medicine and Molecular Imaging (SNMMI), 291
sodium [¹⁸F]fluoride ([¹⁸F]NaF), 656
Sofie Biosciences ELIXYS FLEX/CHEM, 443, 445
solid-phase extraction (SPE), 160, 353
solution-phase techniques, 148
somatostatin receptor 2 (SSTR-2), 629–630
somatostatin receptor (SSTR), 28, 291, 395–396, 543, 672–673
Sonogashira-like coupling reaction, 192
SPECT. *see* single photon emission computed tomography (SPECT)
⁸⁹Sr, 30
standardized uptake values (SUVs), 542, 663
standard operating procedure (SOP)
 documents, 464
sterility, 459
Stille coupling reactions, 187–189
Stockley, Matthew, 348, 349
sulpiride, 11
superoxide levels, 631–632
Suzuki coupling reactions, 189–191
sympathetic nervous system (SNS), 625, 626
Synthra radiopharmaceutical synthesizers, 442

T

- Taiwan Food and Drug Administration (TFDA), 509
- tandem targets, 54–55
- targeted alpha therapy (TAT), 32, 551
- “targeted” radiopharmaceuticals, 4
- tau imaging radiopharmaceuticals
 - MK-6240, 512–513
 - TAUVIDTM, 512
 - THK5351, 511–512
- tau proteinopathy ligands, 600–601
- TAUVID™, 512
- Tc-99m sestamibi, 609
- Tc-99m tetrofosmin, 609, 619
- technetium 99m (^{99m}Tc), 72–74
 - bone imaging agents, 390–391
 - brain imaging agents
 - beta-amyloid imaging agents, 386–389
 - 5-HT_{1A} imaging agents, 384–385
 - chelators and complexes, 377–379
 - diagnostic procedures, 375, 376
 - fatty acids, 382–384
 - myocardial imaging agents, 380–381
 - pediatric nuclear medicine, 654
 - renal imaging agents, 388–389
 - structures of, 375, 376
 - tumor-targeted imaging agents
 - Auger electrons, 421, 422
 - bombesin-like radioligands, 392–394
 - CCK-2 receptor imaging agents, 406–408
 - cobalamin receptor imaging agents, 415–416
 - cyclic RGD peptides, 398–402
 - estrogen receptor imaging agents, 414–415
 - folate receptor imaging agents, 408–410
 - inflammation and infection, 418–420
 - labelled glucose derivatives, 410–412
 - melanocortin 1 receptor (MC1R), 402–404
 - neurotensin receptor imaging agents, 404–406
 - prostate-specific membrane antigen imaging agents, 397–398
 - sentinel lymph node, 416–418
 - somatostatin receptor imaging agents, 395–396
 - targeting thymidine kinase, 412–413
- technical transfer, PET radiopharmaceuticals
 - in Asia
 - ISRS, 507, 508
 - PIC/S, 507–508
 - in clinical trials of general pharmaceuticals, 506
 - item licensing strategy, 504–506
 - in and out of ASIA
 - aliphatic F-18 fluorination method, 509–510
 - β-amyloid imaging radiopharmaceuticals, 510–511
 - tau imaging radiopharmaceuticals, 511–513
- ternary phosphines, 378
- 1,4,7,10-tetraazacyclododecane-1,4,7,10-tetraacetic acid, 537
- tetrahydrocannabinol (THC), 17
- tetrahydrofuran (THF), 149
- tetramethylethylenediamine (TMEDA), 167
- tetramine chelators, 378
- tetra-*n*-butylammonium fluoride (TBAF), 148
- tetra-*n*-butylammonium (TBA) salt, 183
- tetrapeptide chelator, 377
- thallium-201, 75–77
- THC. *See* tetrahydrocannabinol (THC)
- theranostic radiopharmaceuticals, 536
- theranostics, 27–28
- therapeutic radionuclides
 - decay particles, 89
 - in-flight projectile fragmentation, 100
 - isotope production, 90
 - nuclear reactions, 90
 - reactor production of
 - direct neutron-induced reactions, 91–92
 - fission, 92–93
 - using charged-particle reactions, 94
 - alpha emitters production, 95
 - Auger electron emitters production, 96–97
 - beta emitters production, 94–95
 - using photonuclear reactions, 97–100
 - bremsstrahlung radiation, 97
 - Compton backscattering, 98
 - isomers, 99–100
- therapeutic radiopharmaceuticals
 - ¹³¹I-MIBG, 29
 - lymphoma and leukemia, 36–38

prostate-specific membrane antigen, 33–36
 radiotherapy, of bone metastases, 29–31
 somatostatin receptor-targeted ligands, 31–33
 theranostics, 27–28
 viral, fungal, and infectious diseases, 37, 39
 thermal iodide process, 344
 thin layer chromatography (TLC), 464
 threshold of toxicological concern (TTC), 519
 thyroid disease, 655
 Tl-201, 610
 Trace-Ability, Inc., 472, 473–474
 TRACERlab MX_{F_{FDG}}, 439, 440
 tracer principle, 537
 tracer-QC automated QC module, 448, 449
 tracer-QC system, 473, 475
 traditional homemade radiochemistry
 module, 438
 transition metal-mediated ¹¹C-methylation, 186–187
 translocator protein (TSPO), 662
 translocator protein 18 kDa (TSPO), 170
 transthyretin (TTR), 637
 Trasis AllinOne, 440, 441
 traumatic brain injury (TBI), 511
 triazole-histidine (TzHis), 393
 tributyl phosphate (TBP)-functionalized extraction
 resin, 355
 tridentate dithiolate, 377
 tripeptide chelator, 377
 triphenylphosphine oxide (TOPO), 63
 triphenylphosphine-3,3',3'-trisulfonate
 (TPPTS), 378
 triple-negative breast cancer (TNBC), 541
 tris(hydroxypyridinone) (THP), 301
 true theranostic pairs, 28
 tryptophan hydroxylase (TPH), 657
 [Tyr]³-octreotate (TATE) derivatives, 395
 (Tyr³)-octreotide (TOC), 31
 (Tyr³-Thr⁶)-octreotide (TATE), 31

U

United States Food and Drug Administration (US
 FDA), 536
 United States Pharmacopeia (USP 823), 493–494
 University of California, San Francisco (UCSF), 481

uranium-thorium-lead radiometric dating
 methods, 344
 US Food and Drug Administration (US FDA), 502
 US Pharmacopeia (USP), 457
 USP Monograph on Fludeoxyglucose F 18
 Injection, 459
 uterine cancer, 539
²³⁵U, thermal neutron fission of, 72, 73

V

vasodilator capacity, 609
 ventriculography, 576–579
 vesicular monoamine transporter type 2
 (VMAT2), 7
 vesicular transporter for acetylcholine (VACHT), 13
 viral macrophage inflammatory protein II
 (vMIP-II), 631
 vizamyl (flutemetamol), 502, 510, 511

W

Warburg effect, 540
 World Health Organization (WHO), 461, 526

X

xenon-133, 74

Y

⁹⁰Y-DOTATOC, 32

Z

zevalin, 36–37
 zircalloys, 345
 zircon, 343–344
 zirconium
 coordination compounds of, 356–359
 fundamentals, 355
 historical background of, 343–345
 of radionuclides, 345–347
 zirconium-89 radiolabelling, 359–360
 zirconium desferrioxamine B complex ([Zr(HDFO)
 (H₂O)_n]⁺, 356, 357
 zirconium dioxide (ZrO₂), 343

zirconium-89 radiochemistry
 aqueous solution, 353–355
 citrate formulation of, 348
 clinical use, 348
 concentrations of, 348
 custom-made solid target, 348, 349
 decay properties of, 350–352
 excitation functions, 348, 349
 irradiation yields of, 349, 350
 pharmacokinetic studies of, 348
 radiolabelling, 359–360
 separation chemistry, 352–353
 ⁸⁹Zr-radiolabelled antibodies, 361–365
zirconium silicate (ZrSiO₄), 343

zirconocene hydrochloride, 356
⁸⁹Zr-chloride, 354, 355
Zr(MeAHA)₄ complex, 358, 359
⁸⁹Zr-immuno-PET radiotracers, 361
⁸⁹Zr-radiolabelled antibodies
 in animals and in human trials, 361–363
 automated production, 361, 364
 simultaneous bioconjugation and
 radiolabelling, 364–365
⁸⁹Zr-radiolabelled trastuzumab, 360
[⁸⁹Zr][Zr(C₂O₄)₄]₄, 359
[⁸⁹Zr]Zr-Deferoxamine (DFO)-atezolizumab, 541, 542
[⁸⁹Zr]Zr-DFO-nivolumab, 541–543
[⁸⁹Zr][Zr(HDFO) (H₂O)_n]²⁺, 360

WILEY END USER LICENSE AGREEMENT

Go to www.wiley.com/go/eula to access Wiley's ebook EULA.